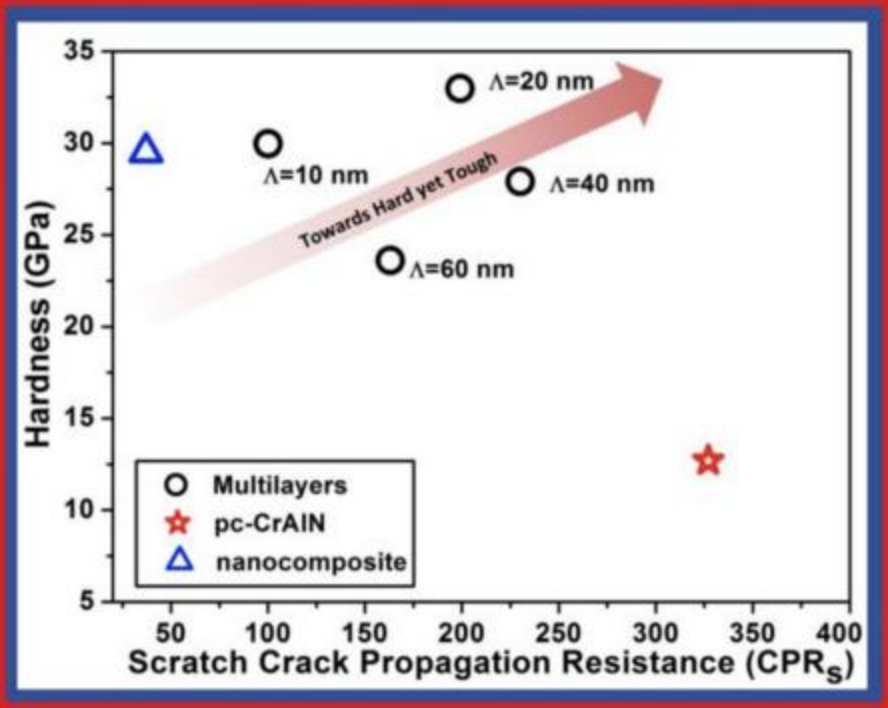
Advances in Materials Science and Engineering

Thin Films and Coatings

Toughening and Toughness Characterization



Edited by Sam Zhang

CRC Press
Taylor & Francis Group

Thin Films and Coatings

Toughening and Toughness Characterization

Advances in Materials Science and Engineering

Series Editor

Sam Zhang

Aerospace Materials Handbook, *edited by Sam Zhang and Dongliang Zhao*

Biological and Biomedical Coatings Handbook: Applications, *edited by Sam Zhang*

Biological and Biomedical Coatings Handbook: Processing and Characterization, *edited by Sam Zhang*

Hierarchical Micro/Nanostructured Materials: Fabrication, Properties, and Applications, *Weiping Cai, Guotao Duan, Yue Li*

Hydroxyapatite Coatings for Biomedical Applications, *edited by Sam Zhang*

Nanobiomaterials: Development and Applications, *edited by Dong Kee Yi and Georgia C. Papaefthymiou*

Nanostructured and Advanced Materials for Fuel Cells, *edited by San Ping Jiang and Pei Kang Shen*

Micro- and Macromechanical Properties of Materials, *Yichun Zhou, Li Yang, and Yongli Huang*

Thin Films and Coatings: Toughening and Toughness Characterization, *edited by Sam Zhang*

Thin Films and Coatings

Toughening and Toughness Characterization

Edited by Sam Zhang

Nanyang Technological University
Singapore



CRC Press
Taylor & Francis Group
Boca Raton London New York

CRC Press is an imprint of the
Taylor & Francis Group, an **informa** business

CRC Press
Taylor & Francis Group
6000 Broken Sound Parkway NW, Suite 300
Boca Raton, FL 33487-2742

© 2016 by Taylor & Francis Group, LLC
CRC Press is an imprint of Taylor & Francis Group, an Informa business

No claim to original U.S. Government works
Version Date: 20150610

International Standard Book Number-13: 978-1-4822-2291-3 (eBook - PDF)

This book contains information obtained from authentic and highly regarded sources. Reasonable efforts have been made to publish reliable data and information, but the author and publisher cannot assume responsibility for the validity of all materials or the consequences of their use. The authors and publishers have attempted to trace the copyright holders of all material reproduced in this publication and apologize to copyright holders if permission to publish in this form has not been obtained. If any copyright material has not been acknowledged please write and let us know so we may rectify in any future reprint.

Except as permitted under U.S. Copyright Law, no part of this book may be reprinted, reproduced, transmitted, or utilized in any form by any electronic, mechanical, or other means, now known or hereafter invented, including photocopying, microfilming, and recording, or in any information storage or retrieval system, without written permission from the publishers.

For permission to photocopy or use material electronically from this work, please access www.copyright.com (http://www.copyright.com/) or contact the Copyright Clearance Center, Inc. (CCC), 222 Rosewood Drive, Danvers, MA 01923, 978-750-8400. CCC is a not-for-profit organization that provides licenses and registration for a variety of users. For organizations that have been granted a photocopy license by the CCC, a separate system of payment has been arranged.

Trademark Notice: Product or corporate names may be trademarks or registered trademarks, and are used only for identification and explanation without intent to infringe.

Visit the Taylor & Francis Web site at
http://www.taylorandfrancis.com

and the CRC Press Web site at
http://www.crcpress.com



"Tough," a Chinese calligraphy by Sam Zhang

Contents

Series Statement ix
Preface xi
Editor xiii
Contributors xv

Chapter 1 Present Status of Hard-Yet-Tough Ceramic Coatings 1
Yu Xi Wang and Sam Zhang

Chapter 2 Toughness Evaluation of Thin Hard Coatings and Films 47
Xiaomin Zhang, Ben D. Beake, and Sam Zhang

Chapter 3 Nanoindentation for Fracture Toughness of Coatings 123
Jinju Chen

Chapter 4 Toughness and Toughening Mechanisms of Porous Thin Films 179
Yanan Xu, Mingchao Wang, John M. Bell, and Cheng Yan

Chapter 5 Toughness of Laser-Treated Surface Layers Obtained by Alloying and Feeding of Ceramic Powders 225
Tomasz Tański, Ewa Jonda, Krzysztof Labisz, and Leszek A. Dobrzański

Chapter 6 Interfacial Adhesion of Film/Substrate System Characterized By Nanoindentation 315
Mingyuan Lu and Han Huang

Chapter 7 Advanced Hard Coatings with Enhanced Toughness and Resistance to Cracking 377
Jindrich Musil

Chapter 8 Characterization of Coating Adhesion Strength 465
Kun Zhou, Zhaoxiang Chen, and Hsin Jen Hoh

Chapter 9 Sliding-Contact Fracture of Brittle Layers 529
Oscar Borrero-Lopez and Mark Hoffman

Index 591

Series Statement

ADVANCES IN MATERIALS SCIENCE AND ENGINEERING

Materials form the foundation of technologies that govern our everyday life, from housing and household appliances to handheld phones, drug delivery systems, airplanes, and satellites. Development of new and increasingly tailored materials is a key to further advancing important applications with the potential to dramatically enhance and enrich our experiences.

The *Advances in Materials Science and Engineering* series by CRC Press/Taylor & Francis Group is designed to help meet new and exciting challenges in the field of materials science and engineering. The books and monographs in the series are based on cutting-edge research and development, and thus are up to date with new discoveries, new understanding, and new insights in all aspects of materials development, including processing and characterization and applications in metallurgy, bulk or surface engineering, interfaces, thin films, coatings, and composites, to name just a few.

The series aims at delivering an authoritative information source to readers in academia, research institutes, and industry. The publisher and its series editor are committed to making this series the most comprehensive and accurate literary source to serve the materials' world and associated fields.

As the series editor, I would like to thank all authors and editors of the books in this series for their noble contributions to the advancement of materials science and engineering and to the advancement of humankind.

Sam Zhang

Preface

Cutting tools, drills, molds, and dies used in today's industries are likely made of high-speed steels, tungsten carbides, and so on. Applying a thin layer of ceramic coating could extend their service life up to many folds. However, if the coatings applied are only hard and not "tough" enough, chipping of the coatings occurs, which renders the coatings ineffective. Hardness of thin films and coatings has been sought after for years. Researchers have now realized that toughness is as important as hardness, if not more so, in all mechanical application areas. Toughening of films and coatings thus has attracted research attention worldwide, especially during recent years. Meanwhile, toughness measurement/characterization for thin films and coatings is still a pertinent research area although that for bulk materials has been classic. Thus, these two areas prompted me to gather forces and examine the most recent endeavors and results scattered across disciplines to formulate a logical chain of references, hence, the birth of this book *Thin Films and Coatings: Toughening and Toughness Characterization*.

As such, this book captures recent hardening, toughening and development in relation to the toughness measurement of thin films and coatings to provide a timely reference book for researchers to refer to and for newcomers to learn from. Being the first of its kind, this book provides the most recent developments in toughening of hard coatings and methodologies in the measurement of toughness of thin films and coatings.

This book is written in such a way that both novices and veterans will find it useful. Researchers in the materials fields, materials scientists, engineers, postgraduate students, especially those dealing with films and coatings, will find this book timely and useful.

The book contains nine chapters contributed by experts from Australia, China, Czech Republic, Poland, Singapore, Spain, and the United Kingdom. Chapter 1 presents the current status of hard-yet-tough ceramic coatings. Chapter 2 reviews various toughness evaluation methodologies for films and hard coatings, old and new. Chapter 3 focuses on nanoindentation determination of fracture toughness of coatings, and Chapter 4 further focuses on toughness and toughening mechanisms of porous thin films. Laser-treated surface toughness is dealt with in Chapter 5. Chapter 6 looks into the adhesions of the film/substrate interface while Chapter 7 focuses on resistance to cracking. Chapter 8 especially deals with characterization of coating adhesion strength. Finally, Chapter 9 looks specifically at sliding contact fracture phenomena.

Toughening and toughness measurement (of films and coatings) are two related, yet separate, fields of great importance in today's nanotechnology world. I dream that one day a technology will be developed such that a device/apparatus is available for toughness of thin films and coatings just like nanoindentation is to hardness of films and coatings. I hope that this book contributes to that aim along the way.

As with my other books, I paid special attention to be sure that enough details to the chapters were included by their respective contributing authors, noting that this book is one of the reliable resources for readers searching for knowledge. A book chapter is not a journal paper, thus it should be written in such a way that novices will find it a stepping stone to the field and veterans will find it a rich source of information for their research. I hope that I have achieved this.

I thank all the contributing authors for their painstaking work that finally resulted in this informative and timely book in the area of toughening and toughness measurement of films and coatings. Special thanks to the reviewers of the chapters who patiently went through the long chapters (one or two reviewers per chapter) to provide their professional critique, which enabled the authors to improve the chapters to their current form. Their professional contributions guaranteed the quality of the book. Last, but not least, I thank the staff at CRC Press, especially Allison Shatkin and Jennifer Ahringer, for their invaluable assistance throughout the endeavor that made the smooth publication of the book a reality.

Sam Zhang
Professor
Nanyang Technological University
Singapore

Editor



Professor Sam Zhang Shanyong, better known as Sam Zhang, earned his PhD in ceramics in 1991 from the University of Wisconsin-Madison, USA, and is a tenured full professor (since 2006) at the School of Mechanical and Aerospace Engineering, Nanyang Technological University, Singapore. Professor Zhang serves as the founding editor-in-chief for *Nanoscience and Nanotechnology Letters* (USA) since 2008 and principal editor for *Journal of Materials Research* (USA) since 2003. He has been in processing and characterization of nanocomposite thin films and coatings for more than 20 years and has authored/coauthored more than 290 peer-reviewed international journal articles, 11 books, more than 20 book chapters, and guest-edited more than 10 journal volumes. His books are

1. Sam Zhang (ed.), *Thin Films and Coatings: Toughening and Toughness Characterization,* CRC Press, Taylor & Francis Group, 2015.
2. Guojun Qi and Sam Zhang (eds.), *Handbook of Manufacturing Engineering and Technology*, Springer, 2014.
3. Sam Zhang (ed.), *Hydroxyapatite Coatings for Biomedical Applications*, CRC Press, Taylor & Francis Group, 784 pp., 2013, ISBN: 9781439886939.
4. Sam Zhang and Dongliang Zhao (eds.), *Aerospace Materials Handbook*, CRC Press, Taylor & Francis Group, 784 pp., 2012, ISBN: 9781439873298.
5. Sam Zhang (ed.), *Biological and Biomedical Coatings Handbook: Processing and Characterization*, CRC Press, Taylor & Francis Group, 2011, ISBN: 978-1-4398-4995-8.
6. Sam Zhang (ed.), *Biological and Biomedical Coatings Handbook: Applications*, CRC Press, Taylor & Francis Group, 2011, ISBN: 978-1-4398-4996-5.
7. Sam Zhang (ed.), *Nanostructured Films and Coatings: Mechanical Properties*, CRC Press, Taylor & Francis Group, 550 pp., 2010, ISBN: 9781420094022.
8. Sam Zhang (ed.), *Nanostructured Films and Coatings: Functional Properties*, CRC Press, Taylor & Francis Group, 422 pp., 2010, ISBN: 9781420093957.
9. Sam Zhang (ed.), *Organic Nanostructured Thin Film Devices and Coatings for Clean Energy*, CRC Press, Taylor & Francis Group, 254 pp., 2010, ISBN: 9781420093933.

10. Sam Zhang, Lin Li, and Ashok Kumar, *Materials Characterization Techniques*, CRC Press, Taylor & Francis Group, 344 pp., 2008, ISBN 9781420042948.
11. Sam Zhang and Nasar Ali (eds.), *Nanocomposite Films and Coatings—Processing, Properties and Performance*, Imperial College Press, UK, 628 pp., 2007, ISBN 978-1-86094-784-1.

His textbook *Materials Characterization Techniques* has been adopted by eight American universities and one European university: Purdue University, Department of Materials Engineering; New York University, Department of Biomaterials and Biomimetics; Louisiana State University, Department of Mechanical Engineering; California Polytechnic State University, Department of Materials Engineering; University of Missouri, Department of Chemical and Biological Engineering; Rutgers University-Camden, Department of Physics; Johns Hopkins University, Department of Materials Science and Engineering; and North Seattle Community College, Math, Science, and Social Sciences; and in Europe: University of Southern Denmark, Centre for Nanotechnology. This book was also translated into Chinese and published by the China Science Press in October 2010, and is adopted by many Chinese universities as a textbook.

Professor Zhang was conferred the title of honorary professor of the Institute of Solid State Physics, Chinese Academy of Sciences. He also holds guest professorship at Zhejiang University and Harbin Institute of Technology. He was featured in the first ever *Who's Who in Engineering Singapore* (2007), and featured in the 26th and 27th editions of *Who's Who in the World*. He became a fellow of the Institute of Materials, Minerals and Mining, United Kingdom, in October 2007. He has been invited to present plenary keynote lectures nearly 60 times at international conferences in Japan, the United States, France, Spain, China, Portugal, New Zealand, Germany, among others. He has also been invited by universities or industries to conduct short courses and workshops more than 20 times. He founded the biennial *International Conference on Technological Advances of Thin Films & Surface Coatings* conference series in 2002 and has been the chair of this very successful conference series ever since. Professor Zhang is also the founding president of the Thin Films Society.

Professor Zhang's research centers on the following four aspects: hard-yet-tough nanocomposite coatings for tribological applications, biological coatings and drug delivery application, electronic thin films, and energy films and coatings. On hard-yet-tough nanocomposite coatings alone, he has published approximately 50 journal articles. Professor Zhang's articles have been cited more than 4,860 times as of March 2015, citation per paper more than 17 times. His H-index is 38. An online live update of these data is available at Professor Zhang's researcher ID website: http://www.researcherid.com/rid/A-3867-2011. (Details are also easily accessible at his personal website http://www.ntu.edu.sg/home/msyzhang)

Contributors

Ben D. Beake
Micro Materials Ltd
Wrexham, United Kingdom

John M. Bell
School of Chemistry, Physics and Mechanical Engineering
Queensland University of Technology
Brisbane, Queensland, Australia

Oscar Borrero-Lopez
Departamento de Ingeniería Mecánica, Energética y de los Materiales
Universidad de Extremadura
Badajoz, Spain

Jinju Chen
School of Mechanical and System Engineering
Newcastle University
Newcastle upon Tyne, United Kingdom

Zhaoxiang Chen
School of Mechanical and Aerospace Engineering
Nanyang Technological University
Singapore

Leszek A. Dobrzański
Institute of Engineering Materials and Biomaterials
Silesian University of Technology
Gliwice, Poland

Mark Hoffman
School of Materials Science and Engineering
University of New South Wales
Sydney, New South Wales, Australia

Hsin Jen Hoh
School of Mechanical and Aerospace Engineering
Nanyang Technological University
Singapore

Han Huang
School of Mechanical and Mining Engineering
University of Queensland
Brisbane, Queensland, Australia

Ewa Jonda
Institute of Engineering Materials and Biomaterials
Silesian University of Technology
Gliwice, Poland

Krzysztof Labisz
Institute of Engineering Materials and Biomaterials
Silesian University of Technology
Gliwice, Poland

Mingyuan Lu
School of Mechanical and Mining Engineering
University of Queensland
Brisbane, Queensland, Australia

Jindrich Musil
Department of Physics
University of West Bohemia
Plzeň, Czech Republic

and

Institute of High Technology Physics
Tomsk Polytechnic University
Tomsk, Russia

Tomasz Tański
Institute of Engineering Materials and Biomaterials
Silesian University of Technology
Gliwice, Poland

Mingchao Wang
School of Chemistry, Physics and Mechanical Engineering
Queensland University of Technology
Brisbane, Queensland, Australia

Yu Xi Wang
Ningde Amperex Technology Limited
Fujian, People's Republic of China

Yanan Xu
School of Chemistry, Physics and Mechanical Engineering
Queensland University of Technology
Brisbane, Queensland, Australia

Cheng Yan
School of Chemistry, Physics and Mechanical Engineering
Queensland University of Technology
Brisbane, Queensland, Australia

Sam Zhang
School of Mechanical and Aerospace Engineering
Nanyang Technological University
Singapore

Xiaomin Zhang
College of Materials and Mineral Resources
Xi'an University of Architecture and Technology
Shaanxi, People's Republic of China

Kun Zhou
School of Mechanical and Aerospace Engineering
Nanyang Technological University
Singapore

1 Present Status of Hard-Yet-Tough Ceramic Coatings

Yu Xi Wang and Sam Zhang

CONTENTS

1.1 Hardness and Toughness in Ceramic Coatings 1
1.2 Toward Hard-Yet-Tough Ceramic Coatings 3
1.2.1 Ways toward Hardening of Ceramic Coatings 3
1.2.1.1 Hardening via Grain-Size Refinement 3
1.2.1.2 Hardening via Grain-Boundary Reinforcement 5
1.2.1.3 Hardening via Solid-State Solution and Precipitation 7
1.2.1.4 Hardening via Ion Bombardment 11
1.2.1.5 Hardening via Multilayering 13
1.2.2 Ways toward Toughening of Ceramic Coatings 15
1.2.2.1 Toughening through Toughening Agent 17
1.2.2.2 Phase Transformation Toughening 28
1.2.2.3 Compressive Stress Toughening 28
1.2.2.4 Toughening through Optimization of Coatings Architecture 28
1.3 Summary 36
References 37

1.1 HARDNESS AND TOUGHNESS IN CERAMIC COATINGS

Ceramic coatings have been widely used in various engineering systems, for instance, for protecting structural materials in harsh environment, prolonging life of manufacturing tools by improving wear/corrosion resistance, and enhancing efficiency in energy storage and/or conversion. However, a low toughness limits the use of ceramic coatings. Most typical example is the sudden failure of machining tools with hard ($H > 20$ GPa) or superhard coatings ($H > 40$ GPa) when they are in contact with large foreign impact [1]. To solve this problem, a number of studies have been conducted to understand the origin of cracks in hard or superhard coatings [2–5]. Accordingly, several toughening methods have been developed to obtain coatings of both improved hardness and toughness [6,7]. In this chapter, we reviewed the academic journey targeting hard-yet-tough ceramic coatings in the past decades.

Hardness, for either bulky materials or thin films, is referred to the resistance of a material against plastic deformation. Experimentally, it is measured using a very stiff and hard indenter. Normally, this indenter is a diamond pyramid of a given shape, which is pressed into the surface of a material with a given load *P*. The remnant contact area of the plastically deformed area *A* can be observed with a microscope. And, the indentation hardness *H* is obtained as

$$H = \frac{P}{A} \tag{1.1}$$

In modern times, an automatic load-depth-sensing indentation instrument can automate this process and the hardness is determined from an analysis of the loading–unloading curve (i.e., Oliver–Pharr method [8]). It should be emphasized that the hardness values measured using indentation are sensitive to a number of factors: indenter geometry, tip rounding, indentation size effect, and substrate condition in terms of, surface roughness, surface oxidation, and surface piling-up/sinking-in [9]. According to the recommendations of UK National Physical laboratory, the indentation depth should not exceed one-tenth of the thickness of the region of the specimen that is being tested [10].

The properties of materials that find particular use for tough coating have been described by a variety of terms such as fracture tough, tough, ductile, resilient, crack tolerant, and likewise. This often renders considerable ambiguity. Herein, it is necessary to understand what "tough" refers to. When a desirable material is subjected to an externally applied driven force, that is, stress, the material could be terminated by fracture. If the fracture is abrupt with less plastic deformation and a sharp drop in stress, the behavior is referred to as brittle fracture. If the fracture behavior requires considerable plastic work to accomplish and is accompanied without abrupt but steady drop in stress for complete separation, this response is termed as ductile fracture. Obviously, higher energy absorption takes place for ductile fracture and the material that undergoes such fracture possesses larger fracture toughness, or is tougher. To evaluate the toughness, a stress intensity factor K_{1c} (with unit of MPa $m^{1/2}$) is introduced and can be readily determined according to American Society for Testing and Materials (ASTM) standards [11,12]. The subscript "1c" stands for the mode 1 crack opening, where the crack opens under a normal tensile stress perpendicular to the plane of the crack. In 1921 [13], Griffith employed an energy-balance approach to quantify fracture toughness (under plain strain condition) as

$$K_{1c} = \sqrt{\frac{EG_c}{1-\nu^2}} \tag{1.2}$$

$$G_c = \sqrt{\frac{\sigma^2 \pi a}{E}} \tag{1.3}$$

where

E is the elastic modulus

G_c is the energy release rate

ν is Poisson's ratio
a is the width of the crack flank
σ is the stress at the crack tip

For thin films, toughness measurements are difficult due to the dimensional limitation. In other words, the measured toughness is influenced by the substrate on which the films are coated. The existed evolution methods are divided into two groups, that is, qualitative and quantitative methods [6]. Qualitatively, toughness is estimated by the plasticity, the microhardness dissipation parameter, and scratch crack propagation resistance. Quantitatively, the toughness is measured via bending, buckling, indentation, and tensile methods [5]. However, a universally accepted method is not yet available [2,3]. A detailed discussion of thin film toughness measurement is presented in Chapter 2 in this handbook.

1.2 TOWARD HARD-YET-TOUGH CERAMIC COATINGS

The foremost feature of a machining tool is high hardness that measures the resistance of a material against plastic deformation or penetration. Toughness, however, measures the resistance to crack propagation or energy consumed to fracture a precracked sample. Over the past decades, hard and superhard ceramic coatings have been developed and widely used in various industrial applications. Meanwhile, an increasing number of studies have signaled that the toughness is just as crucial as, if not more than, hardness especially for ceramic coatings. However, hardness and toughness do not go hand in hand. In other words, hard coatings are usually brittle and less durable while toughened coatings are of lower strength. For practical engineering applications, it is more desirable to have coatings with high hardness without too much sacrificing of toughness. That is why hard-yet-tough ceramic coatings have been the focal point of research for the last few decades. Needless to say, fabricating such a coating is difficult because of the natural conflict between hardness and toughness. Figure 1.1 shows the typical dilemma in hard ceramic coatings [6] and the engineer's dream (hard yet tough). To realize a hard-yet-tough ceramic coating, one needs to consider the ways toward both hardening and toughening. In the following section, different routines toward hardening and toughening will be discussed.

1.2.1 Ways toward Hardening of Ceramic Coatings

Hardness is defined as the resistance of a material to plastic deformation. Under applied load, plastic deformation occurs predominantly through dislocation. In this regard, increasing the resistance to the dislocation movement is the essence of hardening. Several strengthening mechanisms are active in hard coatings: (i) grain-size refinement, (ii) grain-boundary reinforcement, (iii) solid-solution hardening, (iv) multilayer hardening, and (v) ion bombardment/stressing hardening.

1.2.1.1 Hardening via Grain-Size Refinement

The dominant mechanism of plastic deformation of a crystalline material is the generation and motion of dislocations. Under an applied stress, existing dislocations

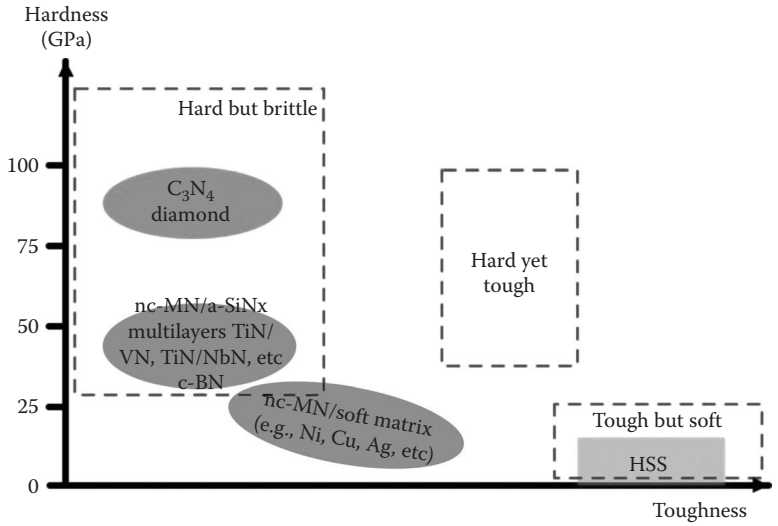


FIGURE 1.1 Schematic of current status of hard ceramic coatings. (Redrawn from Zhang S. et al., *Plasma Processes and Polymers* 2007;4:219.)

and dislocations nucleated mostly from Frank–Read Sources will move through the crystal structure until encountering a grain boundary, where the large atomic mismatch between different grains creates a repulsive stress field to oppose continued dislocation movement. As more and more dislocations propagate to this boundary, a "pileup" occurs. These dislocations will generate repulsive stress fields, countering the energy barrier to cross the boundary. As the energy barrier is overcome, dislocations move across the boundary, leading to a further deformation in the material. Decrease of grain size, however, decreases the amount of possible pileups at the boundary but increases the threshold of applied stress to move a dislocation across a grain boundary, thus increasing strength. A schematic representative of the crystal atoms and boundary atoms is shown in Figure 1.2. The crystal atoms are those with neighbor configuration corresponding to the lattice. The boundary atoms are those with a wide variety of interatomic spacing. In the boundary regions, the coordination between nearest-neighbor atoms deviates or reduces from the one in the crystallites. Theoretically, the stress needed for such generation and motion of dislocations increases in inverse proportion to the distance of the pinning points in the dislocation network, and the increase of strength with decreasing crystallite size is well governed by the Hall–Petch relation [14–16]:

$$H = H_0 + kd^{-1/2} \tag{1.4}$$

where

H_0 is the intrinsic hardness
d is the grain size
k is a constant parameter for a given material

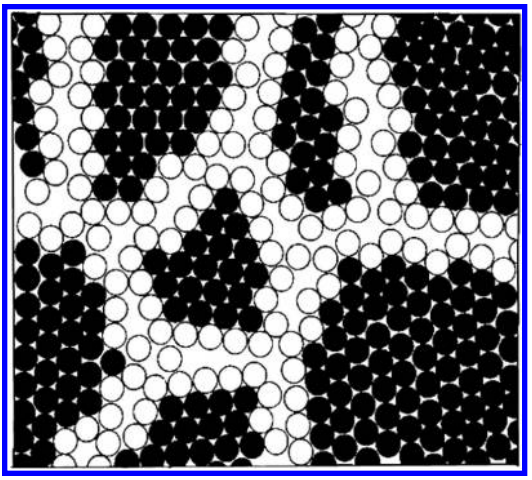


FIGURE 1.2 A schematic representative of the crystal atoms (solid black) and boundary atoms (open circle). (From Tjong SC, Chen H. *Materials Science and Engineering R: Reports* 2004;45.)

1.2.1.2 Hardening via Grain-Boundary Reinforcement

The Hall–Petch effect governs the coarse-grained materials ($d >$ ca. 30 nm). However, as the grain size is decreased down to the order of a few tens or even a few nanometers, this rule ceases to function perfectly. Many researchers have reported an abnormal behavior and correlated it to an inverse or reverse Hall–Petch effect. As seen in Figure 1.3, a maximum hardness is achieved when d is close to ca. 10 nm [4]. It is suggested that the traditional view of dislocation-driven plasticity in polycrystalline materials needs to be revisited and the way of achieving further hardening

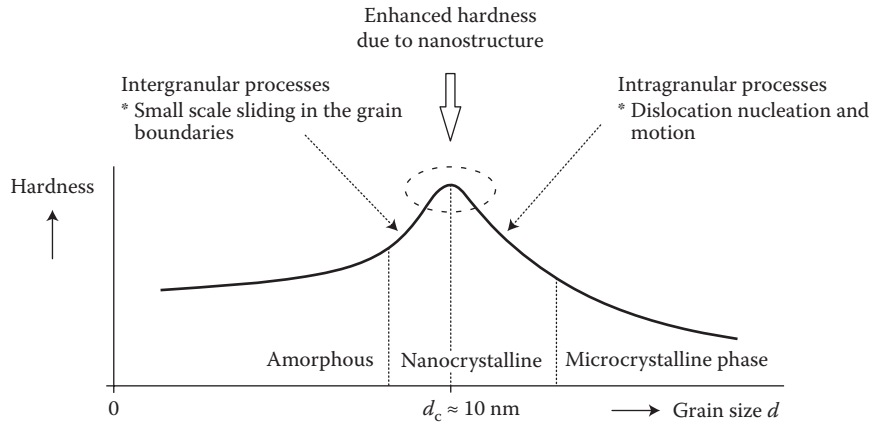


FIGURE 1.3 Schematic illustration of coating hardness as a function of the size d of grains. (From Musil J. *Surface and Coatings Technology* 2012;207:50.)

needs to be reconsidered. Several factors such as grain-boundary sliding, creep diffusion, triple junctions, and impurities could contribute to inverse Hall–Petch effect. Among them, the grain-boundary sliding via a certain accommodation mechanism is considered as the most primary cause. When grain sizes are below a critical value, nanocrystallites contain a large fraction of atoms at interfaces. In this case, pileup of the dislocations against grain boundaries are hardly expected to occur since the size of a Frank–Read source is smaller than the grain size. With a phenomenological mesoscopic model, Hahn et al. [17,18] have predicted a critical grain size at which the grain-boundary sliding becomes dominant. An empirical equation is obtained and thus exhibiting an inverse Hall–Petch effect:

$$H = H_0 - m/d^{1/2} \tag{1.5}$$

where

H_0 is the intrinsic hardness
d is the grain size
m is a constant parameter for a given material.

Coupled with the numerical study, molecular dynamics (MD) modeling was employed to predict the nanocrystalline plasticity in the nanograins with size below 10 nm [19]. The primary cause for the nanograins Ni (<10 nm) deformation was verified as localized sliding of atoms in the grain boundary, which was triggered by atomic shuffling and stress-assisted free volume migration.

To overhaul the size limitation in hardening mechanism, Veprek and Reiprich proposed a ternary nanocomposite, formed by thermodynamically driven spinodal segregation. A nanocomposite coating comprises at least two phases: a nanocrystalline phase and an amorphous phase, or two different nanocrystalline phases. Veprek and Reiprich focused on such system, which has a type nc-Me_nN/a-Si_3N_4, where Me_n represents transition metal such as Ti, W, V, Zr; nc represents nanocrystalline; and a represents amorphous. It should be pointed out that "a-" refers to x-ray amorphous only with no signal of Bragg reflections [20,21]. The use of transition metals lies on the large cohesive energy and high-bulk modulus (K_b), allowing formation of carbides, nitrides, borides, or oxides with very low compressibility and high strength. In a typical TiSiN nanocomposite (Figure 1.4), the crystallites of transition metal nitride (d < 10 nm) were separated by about one or two monolayer of a-Si_3N_4. The thin layer of Si_3N_4 serves as strong "glue" among MeN nanocrystals, effectively suppressing the occurrence of grain-boundary sliding and thus the super-high hardness (>50 GPa) [22]. For instance, the nc-TiN/a-Si_3N_4 and the nc-W_2N/a-Si_3N_4 nanocomposite appeared to increase the hardness with decreasing crystallite size down to 4 nm. Although the claimed ultra-high hardness value ranged from 80 to 105 GPa has evoked an intensive debate [23,24], the concept brings about a remarkable progress in pursuing coatings with super-high hardness.

Similar results have been found in other ternary systems, for example, nc-TiN/a-BN, nc-TiN/a-BN/a-TiB_2 [25], nc-TiC/a-C [26,27], nc-WC/a-C [28], and in quandary system [1] such as nc-CrAlN/a-SiN_x and nc-TiAlN/a-SiN_x. According to the design

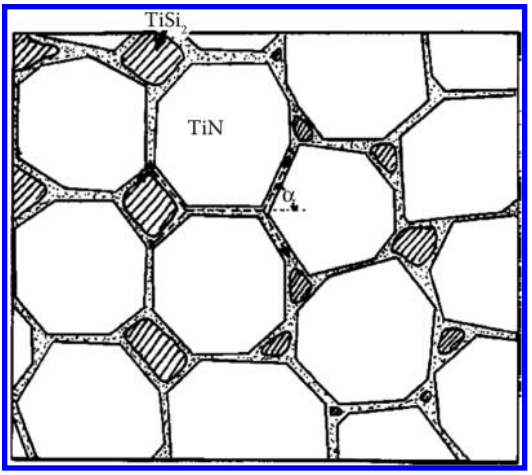


FIGURE 1.4 Schematics of the nanostructure of nc-TiN/a-Si_3N_4 and nc-$TiSi_2$. (From Veprek S. et al., *Surface and Coatings Technology* 2000;133–134:152.)

concept, the most promising option in creating a strong and hard material is the realization of an isotropic nanocomposite consisting of two strongly immiscible materials, which are generated from a strong thermodynamically driven spinodal phase segregation. In addition, an extreme thin interfacial layer (i.e., close to one monolayer as reported in nc-TiN/a-Si_3N_4 system) is beneficial to further minimize internal weakening in interfacial material and diminish misfit dislocations associated with the interface. The crucial effect of the interfacial layer thickness has been recently explained in terms of the critical thickness of a pseudomorphic or heteroepitaxial growth [29]. The experimental results of Söderberg et al. [30] and theoretical calculations of Zhang et al. [31] and Hao et al. [32] confirmed that one interfacial monolayer is the most stable configuration in coherent TiN–Si_3N_4 system. In this system, the decohesion strength was found greater than that of single-crystal Si_3N_4. It was also found that a thicker interfacial layer would lead to the formation of real amorphous SiN_x, resulting in the loss of structural coherence between TiN and SiN and thus the loss of strength or hardness. Figure 1.5 illustrates the hardness tendency of TiSiN as a function of Si_3N_4 content [33]. Estimation of the mean grain separation at the composition of 15–20 at.% Si_3N_4 (inset B) shows only a few monolayers of silicon nitride in the interfacial layer. At high silicon nitride fractions, the mean grain separation becomes greater, leading to the large degradation of coherence between TiN and SiN, and eventually the hardness drop.

1.2.1.3 Hardening via Solid-State Solution and Precipitation

The development of solid-state solution (or solid solution) can be traced back to the Bronze Age when the use of alloy emerged. The insertion of atoms of an alloying element into the interstitial or substitutional position of the matrix atoms leads to physical homogeneity disruption with crystal lattice distortion. This distortion introduces a local stress field, impeding the motion of dislocations and thus increases the

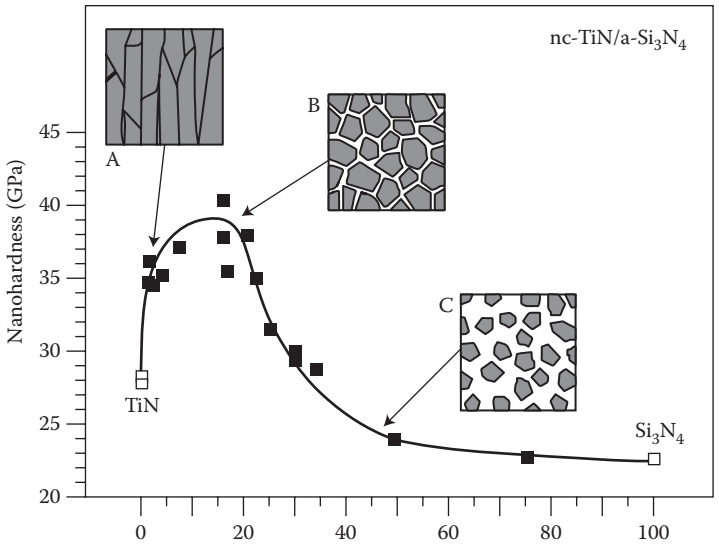


FIGURE 1.5 Hardness of nc-TiN/a-Si3N4 as a function of silicon nitride fraction. Insets illustrate the schematic nanostructure for different compositions. (From Diserens M., Patscheider J., Levy F., *Surface and Coatings Technology* 1999;120–121:158.)

strength. In thin films and coatings, this principle works in the same way. Insertion of B into TiN proved strength improvement, since the gliding of the dislocations formed inside the crystallites is hindered by the lattice distortion resultant strain [34]. In bulk material, solid solutioning can be achieved through heat treatment, while in thin films and coatings, the solid solutioning can be realized through nonequilibrium growth in physical/chemical vapor deposition. In reactive arc evaporation, a highly ionized flux of ions was used to synthesize a promising metastable super-saturated Ti–B–N solid solution. The maximum hardness is obtained at 34.5 GPa. An effective way of optimizing hardness of solid solution is changing the soluble content of the foreign element. It was once reported that a maximum 17.4 at.% of B rendered an increased hardness up to 43 GPa [34]. Other examples are TiCN [35], CrZrN [36], TiAlN [37], CrAlN [38], and so on. TiAlN and CrAlN are intensively studied in recent years since the insertion of Al in TiN or CrN can provide improved thermal stability in addition to the enhanced strength [39].

In particular, CrAlN coatings are studied from different physical vapor deposition (PVD) techniques, such as cathodic arc evaporation [40], cathodic arc ion plating [41,42,43], reactive magnetron sputtering [38,44,45], and beam plasma-assisted PVD [46]. The strength of CrAlN was found largely dependent on the Al content, which can be directly tailored by altering power applied to the metal source (i.e., targets) [43,44,47–50]. Using reactive magnetron sputtering, Ding et al. [48] investigated the influence of Al/Cr atomic ratio (between 0 and 0.6) on the mechanical properties of CrAlN coatings. With the addition of Al, coating hardness gradually increased. An optimized Al/Cr atomic ratio was ~0.4–0.5, at which the hardness reached up to ~30 GPa (Figure 1.6). The substitution of Cr (radius of 0.139 nm)

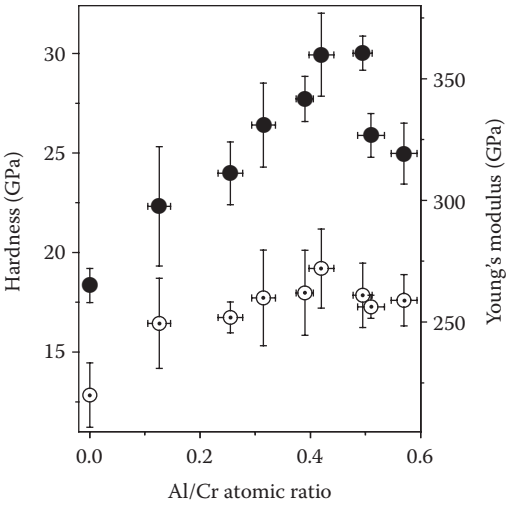


FIGURE 1.6 Hardness (●) and Young's modulus (⊙) of the as-deposited CrAlN coatings as a function of Al/Cr atomic ratio. (From Ding X-Z., Zeng XT. *Surface and Coatings Technology* 2005;200:1372.)

by a smaller Al (radius of 0.121 nm) atom led to the formation of solid-solution fcc-CrAlN. The lattice distortion caused by the substitution rendered the solid-solution hardening. However, this hardening effect was weakened when Al content was further increased. The decrease of hardness was attributed to the emergence of hcp-AlN phase, which was less strengthened than the fcc-AlN. Reiter et al. [43] verified the microstructure change by varying the content of Al in CrAlN with a full range from 0 to 100 at.%. From their results (Figure 1.7a), a threshold at 46 at.% was identified, below which the Al substituted the Cr in the fcc-CrN lattice and thus kept a fcc-CrAlN solid solution. Between 46 and 71 at.%, segregation of fcc-AlN occurred as seen from the evident peak shift. When Al content exceeded 71 at.%, the fcc-AlN completely transformed into hcp-AlN phase. The lattice parameter reduction is shown in Figure 1.7b. As compared to the maximum value (i.e., 40 GPa) of fcc-CrAlN solid solution, a considerable decrease by 47% was observed in the hardness due to the formation of the soft hcp-AlN phase. In addition, a decrease of crystalline size (i.e., from 11 to 6 nm) was reported by Rafaja et al. [51]. In their study, an increase of mutual disorientation of the grains from 0.5 to several degrees was also found when Al content increased. So far, it has been commonly recognized that the threshold (Al/(Al + Cr) ratio) of solubility of Al in CrN is ~0.7, below which CrAlN coatings retains the fcc structure without segregation of hcp-AlN [43,49,52,53].

Unlike solid-solution hardening, which relies on the process of merging two or more different elements into one crystalline structure, precipitation hardening comes from the decomposition of multiple elemental composite, and can be achieved by altering solid-state solubility through heat treatment (i.e., annealing) [54]. Supersaturated phases can be easily obtained by PVD or chemical vapor deposition

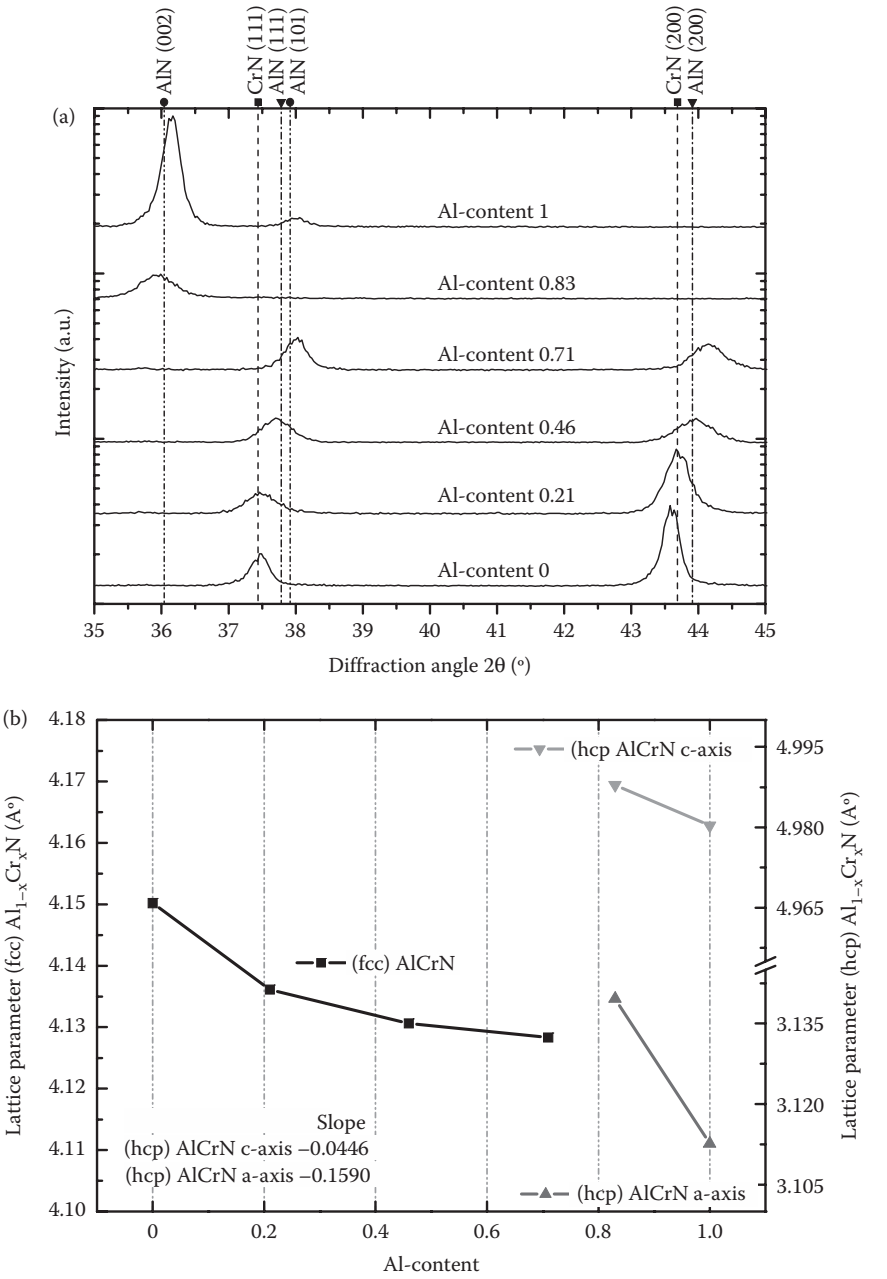


FIGURE 1.7 (a) XRD spectra of various CrAlN coatings ($0 < x < 1$); (b) Lattice parameter of various CrAlN coatings ($0 < x < 1$). (From Reiter AE. et al., *Surface and Coatings Technology* 2005;200:2114.)

(CVD) due to limited atomic kinetic energy. As-deposited (TiAl)N [55] and Ti(BN) [56] exhibited a dense columnar microstructure of supersaturated NaCl structure, in which Ti position in fcc-TiN was occupied by Al and N position was substituted by B, respectively. During annealing, these two coatings underwent spontaneous spinodal decomposition and transformed into coherent cubic phase domains with nanograins, leading to hardness increase.

1.2.1.4 Hardening via Ion Bombardment

The energetic bombardment in magnetron sputtering can come from the energy of the sputtered atoms, the flux of energetic neutrals, and flux of gas ions from the plasma impinging on the biased substrate [53,57]. Studies have demonstrated that ion bombardment during deposition at low temperature can be used to increase coating density [58], modify coating morphology [59,60] in addition to improving the adhesion between coating and substrate [39]. Normally, increasing ion bombardment produces resputtering on the film surface and nudges the sputtered atoms to fill the "valley" and "hump" that naturally occur from the shadowing effects, thus the increased film density. Also, bombarding ions can retard the grain growth, increase the nucleation sites, and allow the formation of nanocrystalline microstructure. This process has been interpreted in terms of Thorton–Messier structure–zone diagram [61,62]. In parallel with microstructural change, biaxial compressive stress is built up and is mainly attributed to the lattice defect arrangements induced by energetic ions [63,64]. During deposition, incoming ions with enough kinetic energy will knock atoms in the films out of their original positions if the recoil energy transfer exceeds about 25 eV, creating a sequence of intensive collisions (i.e., collision cascades). Usually, the initial collision leads to the most energy transfer and exchange among the atoms. And the resultant atomic motion along the trajectory contributes to the eventual rearrangement of the lattice atoms [65].

The development of hard coatings utilizing a synergetic effect of the decrease of grain size, densification of grain boundaries, and compressive stress upon ion bombardment is a subject of intensive research. Common methods to study the effect of ion energy and ion flux bombardment are manipulating plasma [53,59] or applying a negative substrate bias [66,67]. Lin et al. demonstrated the influence of ion energies on the microstructure and the mechanical properties of CrAlN coatings prepared via pulsed closed field unbalanced magnetron sputtering. At lower ion energy of 72 eV, the coating favored in (200) for minimization of the surface energy. With increased ion energy and ion flux, the preferential orientation turned into (111) in order to lower the strain energy. A super-high hardness of 48 GPa was achieved when the total ion energies were about 177–200 eV. The increased hardness was attributed to the high residual stress and lattice distortion (Figure 1.8), which restricted the plastic deformation and dislocation movement [53]. Wang et al. [68] prepared the CrAlN coating using magnetron sputtering at various negative bias voltage. It was found that with increased negative bias voltage (from –50 to –260 V), columnar grains were transformed to glassy dense structure, thereby hardness was increased monotonically up to 26 GPa (Figure 1.9). Similar results can also be found in preparing other nitride coatings, such as TiN [69].

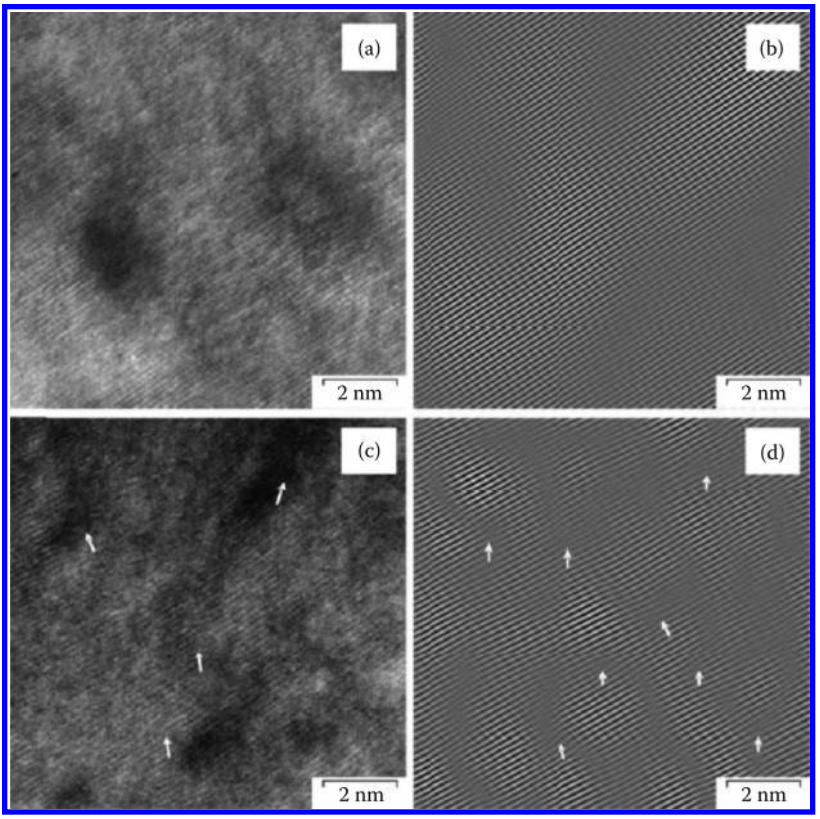


FIGURE 1.8 High-resolution TEM lattice images of CrAlN fabricated at ion energy of (a) 122 eV and (c) 188 eV, (b) and (d) are the FFT filtered image of (a) and (c), respectively. (From Lin J. et al., *Surface and Coatings Technology* 2008;202:1418.)

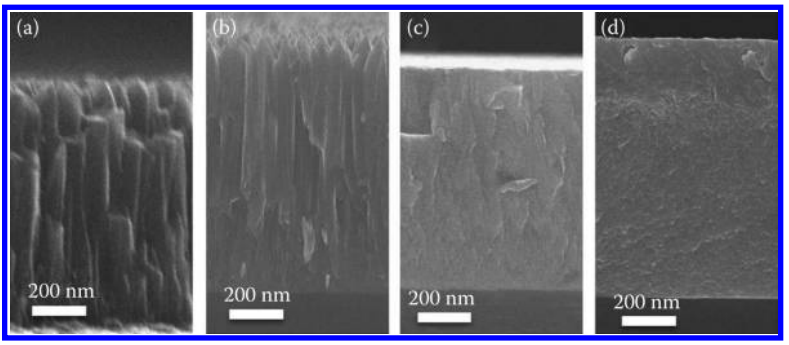


FIGURE 1.9 Cross-sectional morphology of CrAlN at different Vb (a) 50 V, (b) 160 V, (c) 210 V, and (d) 260 V.

However, the resultant hardness improvement may be annealed out upon heat treatment at a certain temperature due to the stress relaxation [70]. However, too much stress will cause coating delamination as a result of increased residual stress when coating thickness increases.

1.2.1.5 Hardening via Multilayering

Multilayer and/or superlattice coatings are materials prepared on atomic scales, with structures consisting of layers in thickness of tens or only a few nanometers. In 1970, Koehler demonstrated that by employing alternate ultra-thin layers of materials with higher and lower elastic constants, materials with superior mechanical properties can be achieved [71]. In 1987, Helmersson et al. showed that single-crystal transition metal nitride multilayers presented hardness 2–3 times those of the single-layered nitrides. A maximum hardness value of 56 GPa was obtained for the TiN/VN multilayer with a period thickness of 5.2 nm [72]. The choice of component materials for the constituent layer and the thickness of the individual layers are essential in obtaining the desired properties. Combinations in terms of metal/metal, metal/ceramic, and ceramic/ceramic have been investigated by many researchers (see Table 1.1). The increased interest in the ceramic/ceramic multilayer coatings is driven by their great potential application in diverse fields. Currently, the most technologically important ceramic/ceramic nitride multilayer systems are as follows: TiN/NbN [73,74,75], CrN/NbN [76], TiN/VN [72,77], TiN/CrN [78,79], TiN/AlN [80], TiN/TiAlN [81], CrN/TiAlN [82,83,84], CrN/CrAlN [85] CrAlN/VN [86], CrAlN/CrAlSiN [87], multilayering DLC [88,89], and TiC/DLC [90], to name but a few.

TABLE 1.1
A Summary of Common Multilayers with Different Layers Combination

Combinations	Period Thickness (nm)	Maximum Hardness (GPa)	Reference
TiN/NbN	4.8	40	[73]
TiN/NbN	6	52	[74]
TiN/NbN	4.6	49	[75]
CrN/NbN	3.4–7.4	35–36	[76]
TiN/VN	5–10	50	[77]
TiN/VN	5.2	56	[72]
TiN/CrN	2.3	35	[78]
TiN/CrN	10	40	[79]
CrN/TiAlN	6.4	39	[82]
CrN/TiAlN	4.8	35	[83]
CrN/TiAlN	5–10	29.7	[84]
CrN/CrAlN	7.2	31	[85]
CrAlN/VN	20	32.4	[86]
CrAlN/CrAlSiN	20	33	[87]
Multilayers DLC	45	27	[88]

The improved hardness is attributed to several reinforcement mechanisms, including dislocation blocking by layer interfaces, Hall–Petch effect, dislocation motion in an alternating strain field and supermodulus effect. Among them, dislocation blocking by layer interfaces are the most studied and considered effective in predicting hardness improvement. Koehler explained the dislocations moving across layer by introducing image force [71]. Theoretically, the dislocation motion would be inhibited in a multilayered structure due to the image force on dislocations created by the different dislocation line energies in each layer. The model assumed that the multilayers consist of layers with two different shear moduli, lower one (layer *A*) and higher one (layer *B*). Under this circumstance, a shear stress of the order of $G_A/100$ (*G* stands for the shear modulus) would be required to drive dislocations through the multilayers given that the individual layer is thin enough. Assuming that the dislocation glide plane and the interface were orthogonal, Pacheco et al. [91] derived the shear stress on the dislocation on the basis of Peierls dislocation model. The maximum shear stress acting on a screw dislocation occurs when it is located at the interface and is given by

$$\tau_{\max} = \frac{\sin\theta(G_B - G_A)}{\pi} \tag{1.6}$$

where

τ is the shear stress
θ is the angle of dislocation slip plane with respect to the interface

In this model, the dislocation would be constrained in layer *A* unless a shear stress of $\tau_A + \tau_{\max}$ was applied to the system, where τ_A is the shear stress required to move the dislocation in material *A*. With the predictable value of shear stress, the yield stress can be obtained using Schmid's law, as given by

$$\sigma = \frac{\tau}{m} \tag{1.7}$$

where

σ is the yield stress
τ is the shear stress
m is the Taylor factor

For transition metal nitrides in the NaCl-type structure, $m \approx 0.3$ [71]. The estimated hardness from the yield stress can then be obtained using $H \approx 3\sigma$. Therefore, the maximum expected hardness of a multilayer due to image effects in the system is

$$H_{\max} = \frac{H_A + 3\sin\theta(G_B - G_A)}{m\pi^2} \tag{1.8}$$

where

H_A is the hardness of layer *A*
θ is the angle of dislocation slip plane with respect to the interface

G is the shear modulus
m is the Taylor factor

This simple model gives a good approximation for polycrystalline materials and can be further improved by taking into consideration many other factors, in terms of layer thickness, layer numbers, and interface diffusion. Koehler mentioned that the layer thickness must be thin enough so that the dislocation generation cannot occur within the layers. While if the individual layer thickness is large, dislocations will confine within the layer without encountering an interface, thus no significant image force effect would occur. With these concerns, Chu et al. [92] proposed a model on the basis of Kzanowski's model for image force effect. With this model, they managed to predict the tendency of hardness versus individual layer thickness, so as to find out the optimal layer thickness to inhibit dislocation motion across the boundaries between the layers without having dislocation motion within a layer. To highlight, this model matched well with the experimental data of TiN/NbN multilayers [92].

For multilayers, another significant factor that should be considered is the residual stress, since large accumulated stress may lead to layer exfoliation, detrimental to the coating system. To solve this problem, attempts have been made on optimizing the multilayer structure. For instance, Li et al. [88] prepared a multilayered diamond-like carbon (DLC) with alternate soft and hard carbon layers by varying bias voltage during magnetron sputtering. The hardness of the sublayers' layer was adjusted as a function of sp^3 sites fraction. Increased bias voltage resulted in increased sp^3 sites fraction and thus the increased hardness. By optimizing the sublayer thickness and total thickness, the hardness of multilayer DLC with soft/hard sublayers improved from 18.9 to 21 GPa while the residual stress decreased from 6.0 to 2.8 GPa. Figure 1.10 demonstrates the comparison of hardness and residual stress between monolayer and multilayer DLC coatings fabricated using various bias voltage combination.

1.2.2 Ways toward Toughening of Ceramic Coatings

Toughness is used to measure the resistance to crack propagation, indicative of the amount of energy needed to break the material. Practically, load-induced deformations of a coated surface generate surface stresses, which can lead to the surface fracture, starting from the cracking in a molecular level such as atomic bonds breaking. Normally, the fracture can be categorized as ductile cracking and brittle cracking. Ductile fracture is characterized by a large amount of plastic deformation in the vicinity of an advancing crack. For ceramic materials, brittle fracture often occurs since the cracks spread extremely rapidly, with little plastic deformation accompanied (i.e., typically less than 5%). A fracture process involves three steps: crack nucleation, crack propagation, and failure through material separation. Crack nucleation and initiation may take place according to different mechanisms depending on material structure, geometrical features, and the state of applied and residual stress. For example, the dislocations in a work-hardened region are piled up by shear stresses, which can lead to the crack initiation as shown in the case of rolling bearings [93]. In a ceramic coating with columnar structure, the crack nucleation is expected to occur between the columnar grains. Crack propagation theory for

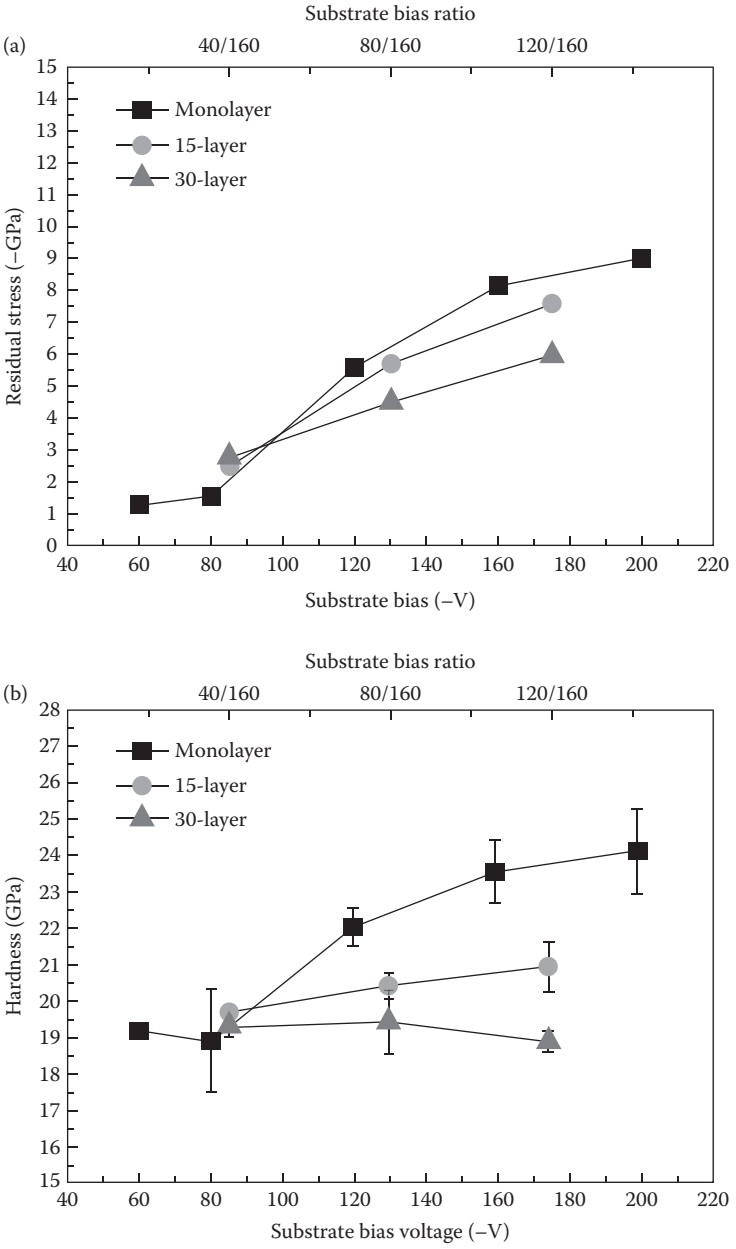


FIGURE 1.10 (a) Residual stress of monolayer and multilayer DLC coatings as a function of substrate bias and substrate bias ratio. (b) Hardness in monolayer and multilayer DLC as a function of substrate bias and substrate bias ratio. (From Li F. et al., *Thin Solid Films* 2011;519:4910.)

systems with cracks longer than about 1 mm is well established based on linear elastic fracture mechanics (LEFM) [94]. Depending on different crack dimensions, the crack growth behavior was analyzed using Kitagawa–Takahashi diagram. However, crack propagation for the case of a loaded very thin-coated surface is much more complicated and no general model can be used to predict.

In principle, materials will be tougher if more energy has to be consumed during crack propagation. Design of tough ceramic coatings can therefore be realized via (i) introducing toughening agent, including metal ductile phase and carbon nanotube (CNT) additive, (ii) utilizing phase transformation, (iii) inducing compressive stress, and (iv) optimizing the coating architecture. Herein, it should be highlighted that in thin films community, there is not yet a universally accepted toughness measurement methodology [2,3]. Current measurement methods are divided into two groups, that is, qualitative and quantitative methods [6]. Qualitatively, toughness can be estimated by the plasticity, the microhardness dissipation parameter and scratch crack propagation resistance. Quantitatively, toughness can be measured via bending, buckling, indentation, and tensile elongation [5]. Owing to the different measurement method used, the following discussion on toughening effect would be different in terminology.

1.2.2.1 Toughening through Toughening Agent

1.2.2.1.1 Ductile Phase Toughening

Incorporating a ductile phase is the most straightforward route in toughening hard ceramic coatings. The toughness increment comes from extra work consumed during plastic deformation, in two primary mechanisms (Figure 1.11): (1) the relaxation of the strain field around the crack tip through the ductile phase and (2) the yielding and bridging of cracks by ligaments of the ductile phase. More often, metals are the promising candidates as ductile phases due to their ductility.

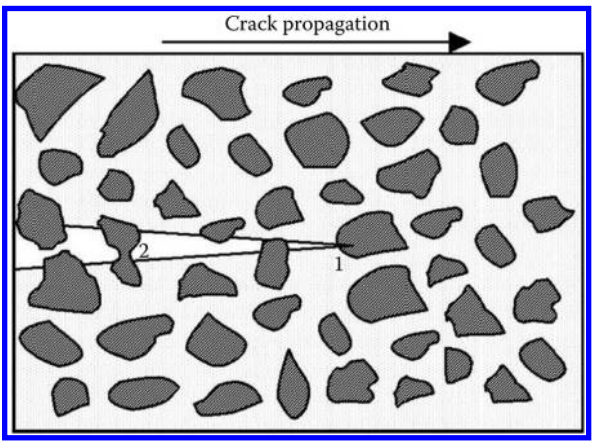


FIGURE 1.11 Schematic diagram of ductile phase toughening through (1) ductile phase deformation or crack blunting, and (2) crack bridging. (From Zhang S. et al., *Surface and Coatings Technology* 2005;198:2.)

In ceramic coatings, the ductile phase may serve as matrix (i.e., metal matrix composite) or dopant (i.e., ceramic matrix composite). In the studies of metal matrix composites, less attention on toughening effect has been given but more are focused on microstructure optimization to obtain the maximum hardness, as reported in ZrTiN/Cu [95], ZrN/Cu [96,97], TiN/Cu [98], CrN/Cu [99], TiN/Ag, CrN/Ag, ZrN/Ag [100,101], Mo_2N/Ag [102], ZrN/Ni [103], and so on. In the ceramic matrix composite, toughening effect via metallic dopant has been widely studied. In the case of TaN/Cu deposited on tool steel substrate [104], the crack resistance was determined by the content of Cu diffused into the TaN matrix via the rapid thermal annealing process. The coating with 1.4 at.% Cu exhibited the least amount of cracks after indentation test, attributed to the Cu network. Similar results can be found in Cu into ZrO_x [105]. The enhanced toughness was ascribed to the amorphous structure and compressive macrostress introduced.

As mentioned, nc-Me_nN/a-SiN_x is a significant hard/superhard nanocomposite coating and has been widely used in industrial applications [1]. Recently, the limitation of intrinsic lower toughness has been increasingly recognized. To toughen the nc-TiN/a-SiN_x nanocomposite, Ni was introduced via cosputtering of Ti, TiNi, and Si_3N_4 targets in an Ar/N_2 atmosphere [106,107]. When Ni ranged from 0 to ~40 at.%, the toughness increased from 1.15 to 2.6 MPa $m^{1/2}$. Wang et al. [108] did a similar work but investigated the toughening effect of Ni in a more complicated nanocomposite, nc-CrAlN/a-SiN_x. Figure 1.12 illustrates the bright field high-resolution transmission electron microscope (HRTEM) image of nc-CrAlN/a-SiN_x with 12 at.% Ni. It was observed that the nanocrystallites (ca. 3 nm) were embedded in the a-SiN_x and Ni network, which limited the grain growth. An analysis of the selected area diffraction (SAD) pattern indicated that these nanocrystallites were polycrystalline CrAlN in face-centered cubic structure. The measured hardness and scratch toughness (Figure 1.13) suggested that doping 4.3 at.% Ni lead to the best balance in strength and crack resistance. The increase of toughness is from (1) relaxation of the strain field around the crack tip through

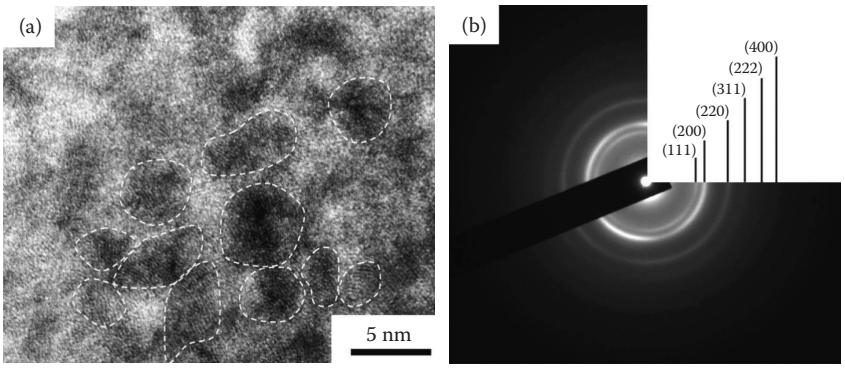


FIGURE 1.12 HRTEM image (a) and corresponding selected area diffraction patterns (b) of nc-CrAlN/a-SiN*x* with 12.0 at.% Ni. (From Wang YX. et al., *Applied Surface Science* 2013;265:418.)

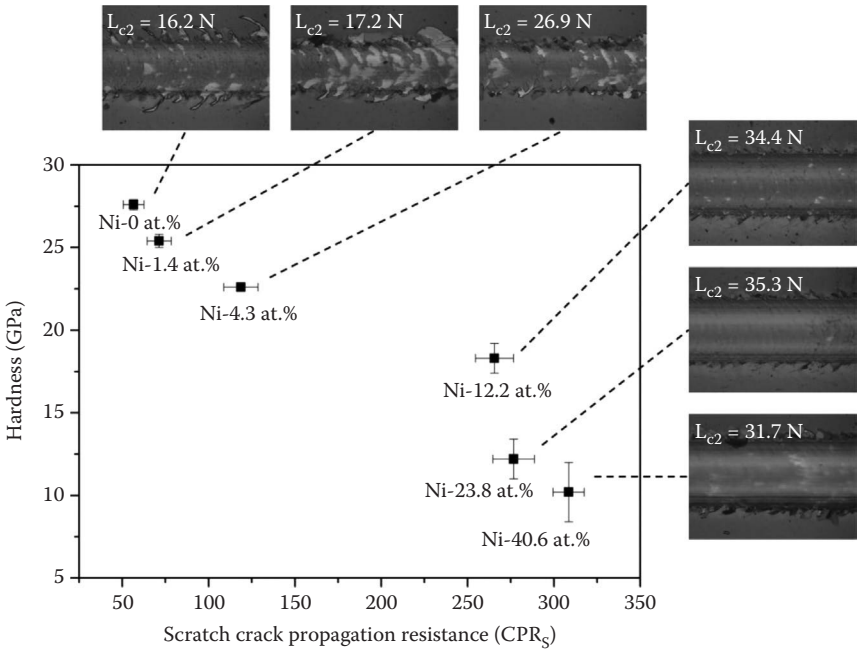


FIGURE 1.13 Plot of hardness versus scratch toughness and fracture behavior after scratch of nc-CrAlN/a-SiN*x* with varied Ni contents. (From Wang YX. et al., *Applied Surface Science* 2013;265:418.)

the ductile phase (metallic Ni) deformation or crack blunting, whereby the work for plastic deformation is increased, and (2) a network of amorphous Ni atoms together with a-SiN_x surrounding the CrAlN nanocrystallites. Pei et al. once proposed a toughening theory based on crack localization in an amorphous matrix. Under this circumstance, crack nucleation may be suppressed by the introduction of nanoparticles [109].

DLC is another extensively used coating owing to their high hardness, low friction coefficient, superior wear resistance, and chemical inertness [110–114]. However, a large compressive stress from the ion bombardment during deposition and intrinsic brittle feature make this type of coating less durable when exposed to sudden impact. To overcome these problems, Tay et al. [115] doped Al in amorphous carbon (a-C) to decrease the accumulated stress as well as improve the toughness. In spite of the amelioration of the residual stress and toughness, an inevitable significant drop of hardness was observed. With increase of Al from 1 to 10 at.%, the hardness decreased from 27 to 18 GPa accordingly. Bui et al. [116] utilized the similar methodology and performed a systematic investigation on the microstructure, residual stress, hardness, and scratch toughness on a-C/Al. Results from XRD and TEM indicated that Al is in x-ray amorphous state. With different contents of Al, mechanical properties of a-C/Al were varied as expected. Without Al, the hardness of pure DLC coating was 32.5 GPa with a high residual stress of 4.1 GPa.

When Al content reached 19 at.%, the residual stress declined largely to 0.2 GPa while the hardness was only 7.8 GPa. In parallel, the addition of Al significantly improved the coating toughness and adhesion. Without Al, a lower critical scratch force at only 118 mN can lead to a brittle delamination with severe chipping and buckling. In contrast, with 19 at.% Al, the lower critical scratch force can reach to 180 mN without rendering brittle cracking. No coating fracture or interfacial failure was observed even when the scratch load is up to 455 mN, suggesting the coating is of enhanced toughness.

Doping ductile phase is an effective way of toughening, but loses too much hardness. To achieve hard-yet-tough coating, hardness must be restored, which is the motivation of doping another reinforcing phase. Following this concept, nc-TiC nanoparticles were incorporated into a-C/Al to form nc-TiC/a-C(Al) nanocomposite coatings [116,117]. The existence of randomly oriented TiC nanograins (~5 nm) surrounded by a-C/Al phase was achieved. With the addition of nc-TiC, the hardness was recovered at a large magnitude. Figure 1.14 illustrates the difference of scratch tests in comparing a-C, bias-graded a-C, nc-TiC/a-C, and nc-TiC/a-C(Al). Among these coatings, nc-TiC/a-C(Al) presents a hard-yet-tough feature. To qualitatively determine the toughness, a related parameter-plasticity was used to show the benchmark and a scratch test was carried out to verify. Plasticity here is defined as the ratio of plastic strain over the total strain. Considering plastic deformation is the major source of stress relaxation, a larger plasticity should be associated with (but not equal to) higher toughness inherent in the material. In such nc-TiC/a-C(Al) nanocomposites, the plasticity was as high as 55%. As a comparison, the super-hard

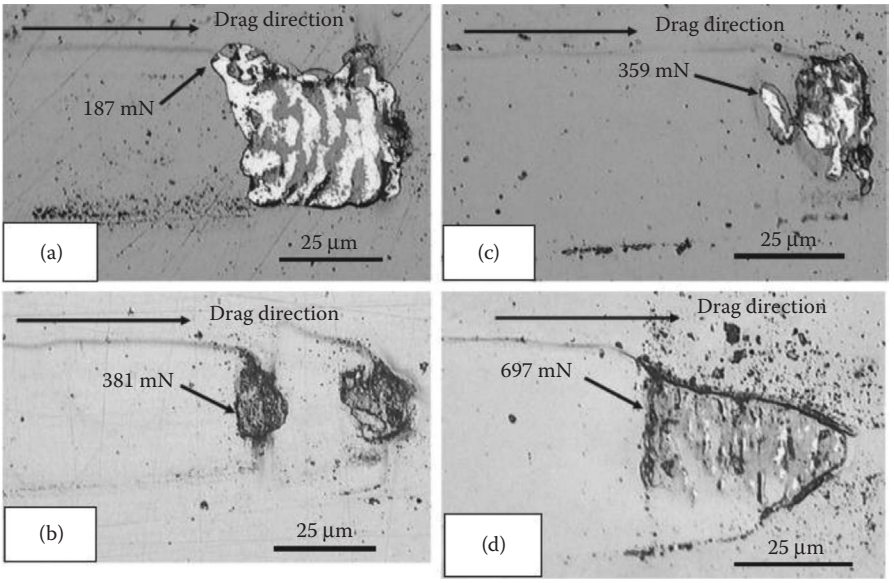


FIGURE 1.14 Scratch tracks on (a) a-C $H = 28.1$ GPa, (b) bias-graded a-C $H = 25.1$ GPa, (c) nc-TiC/a-C $H = 27.4$ GPa, and (d) nc-TiC/a-C(Al) $H = 19.6$ GPa. (From Zhang S. et al., *Thin Solid Films* 2005;482:138.)

nc-TiN/a-Si_3N_4 shows almost no plasticity and the nc-TiC/a-C coating of 30 GPa hardness had a plasticity of ~40%.

1.2.2.1.2 Carbon Nanotube Toughening

Since discovered in 1991 [118,119], CNTs have been considered versatile due to its unique features in mechanical, electronic, and chemical aspects. CNTs compose one (i.e., single-walled nanotube [SWNT]) or several (i.e., multiwalled nanotube [MWNT]) graphite basal planes rolling into a cylinder [120]. Rolled graphite basal planes with coaxial structure make CNTs the stiffest and most robust materials; this is so because the constituent carbon–carbon bond on the basal plane is predicted to be one of the strongest in nature. SWNTs present tensile strength 100 times than that of steel with weight of only 1/6. In particular, SWNTs have shown tensile strength greater than 65 GPa (predicted value up to 200 GPa) and modulus of elasticity in the magnitude of 1000 GPa, allowing them to withstand 10–30% elongation before brittle breakage, plastic deformation, or bond rupture [121]. The Young's modulus of MWNT has been measured up to ~1800 GPa, which is much higher than that of their predecessors, namely carbon fiber (~680 GPa) and carbon whisker (~800 GPa). Reversibility of deformation in MWNT is also good and has been observed with the aid of TEM [122]. Similar results regarding the outstanding mechanical properties of CNTs have been reported by different research groups [123,124], indicating CNTs would be the ideal candidate for the toughening agent.

Highly flexible and resilient CNTs are first composited in bulk ceramics, in order to increase the inherent low toughness. However, uniform dispersion of CNTs and maintaining their integrity when mixing with ceramic matrix are difficult. Unlike using traditional hot-press with high temperature for a long period, Zhan et al. [125] proposed spark plasma sintering (SPS) process (Figure 1.15). SPS process advances in generating high-temperature plasma to complete sintering within a short time, ensuring the intrinsic mechanical properties of CNTs. In particular, a fully dense SWNTs/Al_2O_3 composite could be obtained within only 3 min by using SPS at 1150°C. A significant improvement of fracture toughness (9.7 MPa $m^{1/2}$) was achieved by the addition of 10 vol.% CNTs. In comparison, the fracture toughness of monolithic Al_2O_3 was only 3.3 MPa $m^{1/2}$. The essence of toughness enhancement are the intact and the homogenous distribution of CNTs, encapsulating the nano-sized Al_2O_3 grains along the grain boundaries. Vasiliev et al. [126] further studied this unique tube–grain interface, proposing a novel grain-boundary structure in a ceramic/CNT composite. Jiang et al. [127] adopted the same methodology but focused more on the effect of sintering temperature. It was reported that temperature higher than 1150°C was detrimental to the hardness, toughness, and density of the composites, since elevated temperature was likely to result in CNTs degradation.

Compared to the powder process, precursor polymer routes demonstrate an advantage in preparing well-dispersed CNT-imbedded ceramics. In addition, the polymerization process enables the densification of the composites at a relatively low temperature. The most typical case is the SiCN/CNTs composite fabricated using polymerization process [128–130]. In this system, carbon is in a thermodynamic equilibrium with the SiCN phase and no reactions can take place between CNTs and SiCN matrix. Katsuda et al. [129] prepared the SiCN/CNTs composite by

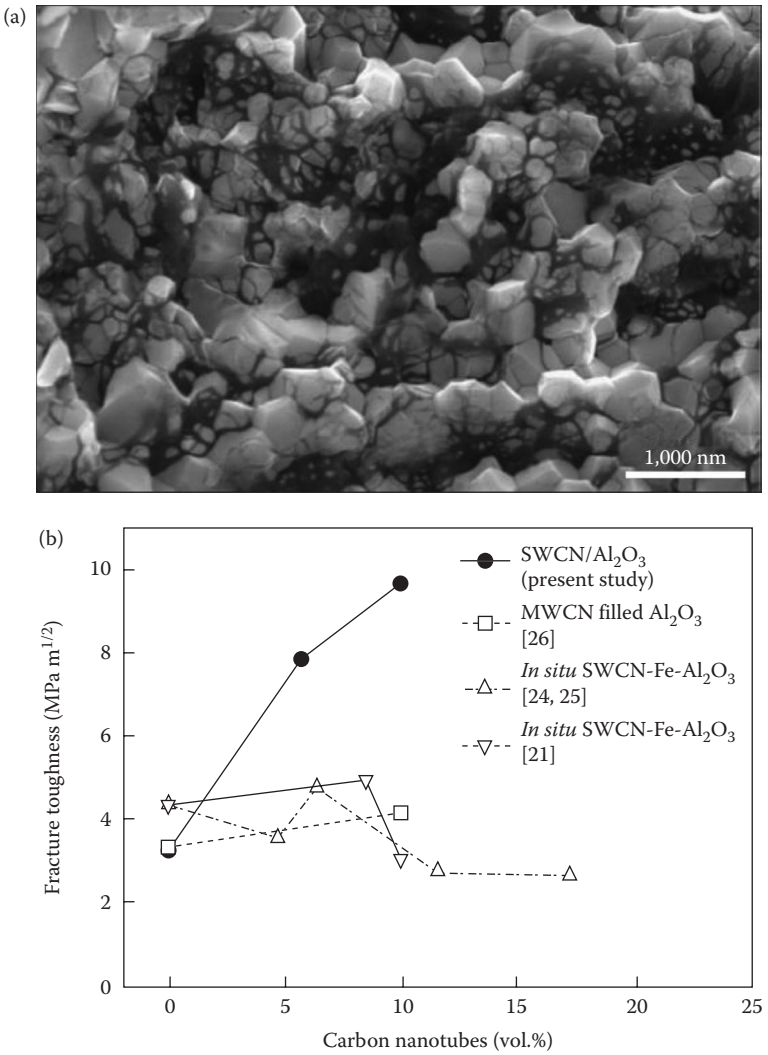


FIGURE 1.15 (a) Fracture surface of composite 5.7 vol.% SWNT-Al_2O_3. (b) Fracture toughness as a function of CNT content. (From Zhan GD. et al., *Nature Materials* 2003;2:38.)

using catalytic cross-linking and pressure-assisted thermolysis from mixtures of a ply (ureamethylvinyl) silazane precursor and MWNTs. More than 60% increase in toughness can be achieved if a high aspect ratio (length over diameter) type of CNTs were used (Figure 1.16). The toughness increase comes from the tube pull-out and crack bridging after examining the fracture surface.

To date, not many studies have been carried out on CNTs-toughened ceramic coatings. The difficulty, primarily, is the uniform dispersion of nanotubes into the ceramic matrix. *In situ* growth of CNTs is one way out as reported in the case of CNTs/Al_2O_3 composite with thickness of 400 μm [131]. With the aid of CVD and

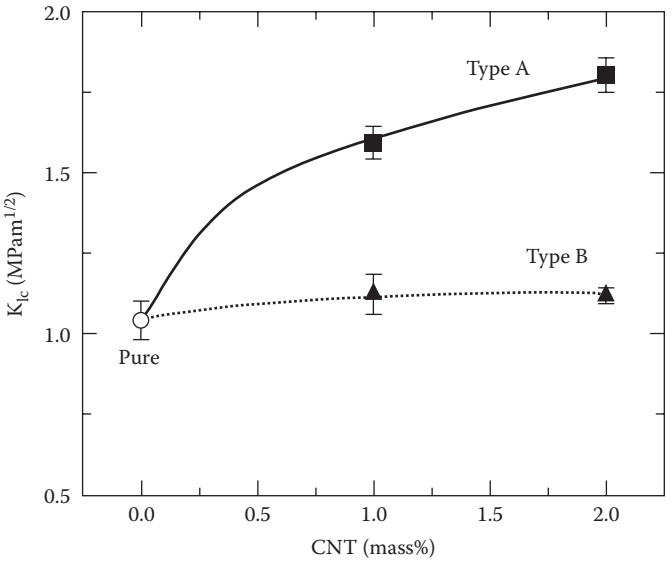


FIGURE 1.16 Fracture toughness behavior of Si-C-N nanocomposites as a function of the CNT content type A (high aspect ratio CNT) and type B (low aspect ratio CNT). (From Katsuda Y. et al., *Journal of the European Ceramic Society* 2006;26:3399.)

plasma spray, well-dispersed CNT was obtained. Figure 1.17a demonstrates the interface between CNT and Al_2O_3, where a 0.5 nm thick amorphous interlayer can be identified. It was believed that such interlayer acts as a buffer layer to accommodate imperfect surface termination. And, because of the tube anchoring (Figure 1.17b) in the Al_2O_3 phase, the composite presented a balance between hardness (~9 GPa) and toughness (~4.62 MPa $m^{1/2}$).

However, in most CNT-embedded composites, nanotube tangling is the major problem and thus declining the toughening effect. To optimize the strengthening effect of CNTs, Xia et al. [132] prepared Al_2O_3 coatings (20–90 μm) with highly oriented CNTs. The CNTs *in situ* grew (CVD assistant) from the anodized aluminum template with pore diameter of 30–40 nm and Co or Ni catalyst particles at the bottom. Microscopic analyses confirmed the formation of MWNTs inside the pore walls, as seen from Figure 1.18. And the nanotube toughening behaviors were observed in terms of crack deflection at the tube–matrix interface, crack bridging from tube, and tube pull-out from the field-emission scanning electron microscope (FESEM) image as shown in Figure 1.19.

Wang et al. proposed a novel way of introducing toughening whiskers (i.e., carbon nanofiber [CNF]) into ceramic coatings via magnetron sputtering and rapid thermal annealing (RTA). It should be pointed out that even though the mechanical properties of carbon nanofiber is not at par with that of CNT, CNF is still a good candidate for materials reinforcement and has been used widely in industrial applications. To prepare *in situ* CNF in ceramic coatings (e.g., nc-TiC/a-C coatings), a two-step fabrication process is followed: First is the cosputtering of graphite, titanium, and nickel

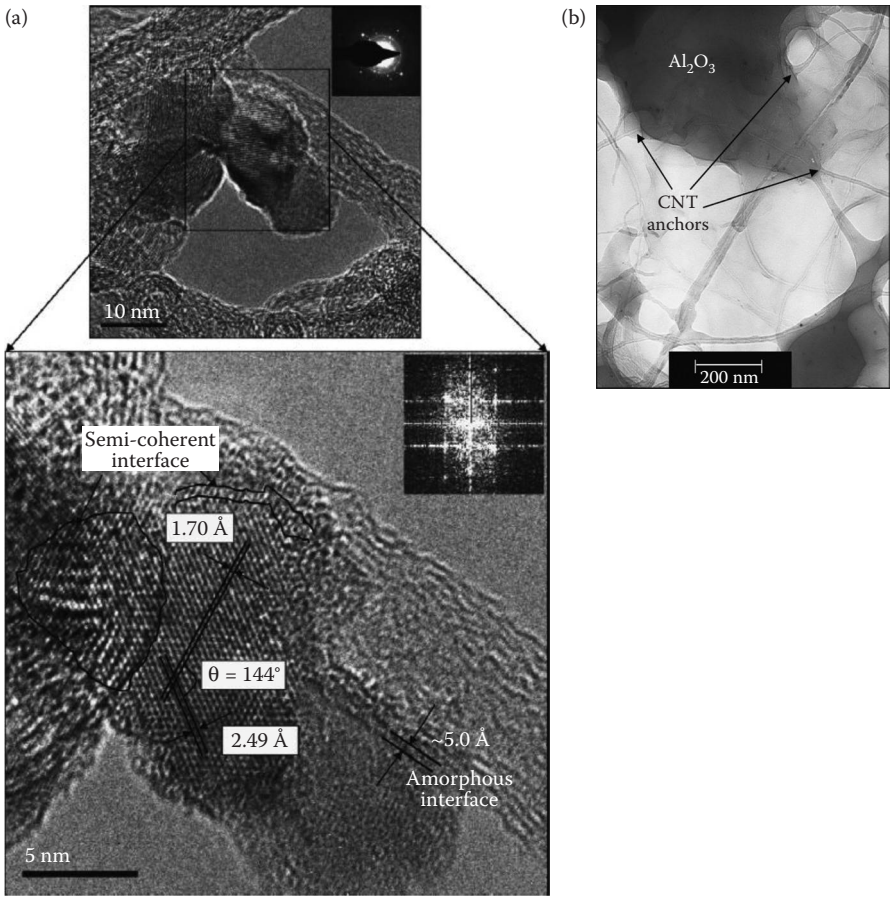


FIGURE 1.17 (a) HR-TEM image showing 0.5 nm amorphous interface and embedded Al_2O_3 crystallite in CNT with lattice spacing of 2.49 and 1.70 Å, (b) CNT anchored with Al_2O_3crystallite. (From Balani K. et al., *Acta Materialia* 2008;56:571.)

targets to deposit a nanocomposite coating rich in amorphous carbon; Second, the coating is rapid thermal annealed during which nickel sputtered serves as the catalyst for CNF formation. The RTA temperature is controlled at the maximum of 1100°C and the RTA duration is no more than 180 s. Figure 1.20 shows a typical morphology of nc-TiC/a-C with *in situ* CNF. The toughness of nc-TiC is about doubled from 3.25 to 6.09 MPa $m^{1/2}$. The formation of *in situ* CNF lies on the diffusion of a-C into the Ni nanoparticles, whereby solid-solution droplets form. Upon saturation, the excess carbon will precipitate out of the Ni nanoparticles. With the catalytic reaction, the precipitated carbon atoms nucleate on the surface of the catalyst and nanofibers start to grow from the nuclei. An Al_2O_3 barrier layer can also be introduced to improve the CNF quality. With similar synthesis procedures, Wang et al. [133] also demonstrated that CNTs could be formed if proper amount of hydrogen was introduced

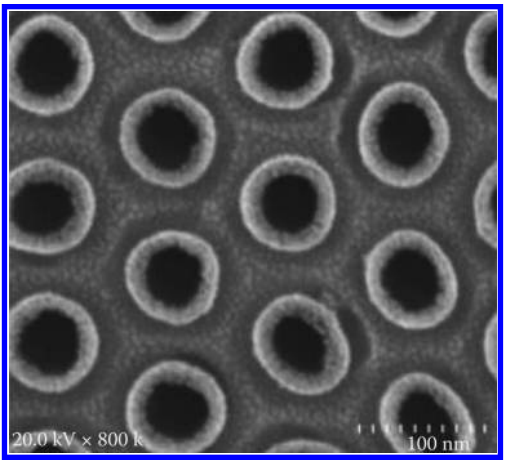


FIGURE 1.18 Top view of as-fabricated highly orientated CNT/Al_2O_3 composites. (From Xia Z. et al., *Acta Materialia* 2004;52:931.)

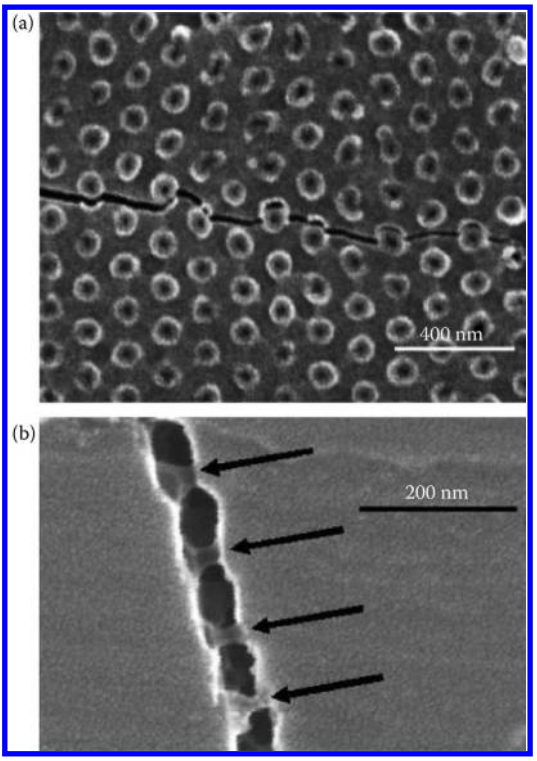


FIGURE 1.19 (a) Crack deflection at CNT/Al_2O_3 interface, (b) CNT bridging longitudinal Al_2O_3 matrix and tube pull-out. (From Xia Z. et al., *Acta Materialia* 2004;52:931.)

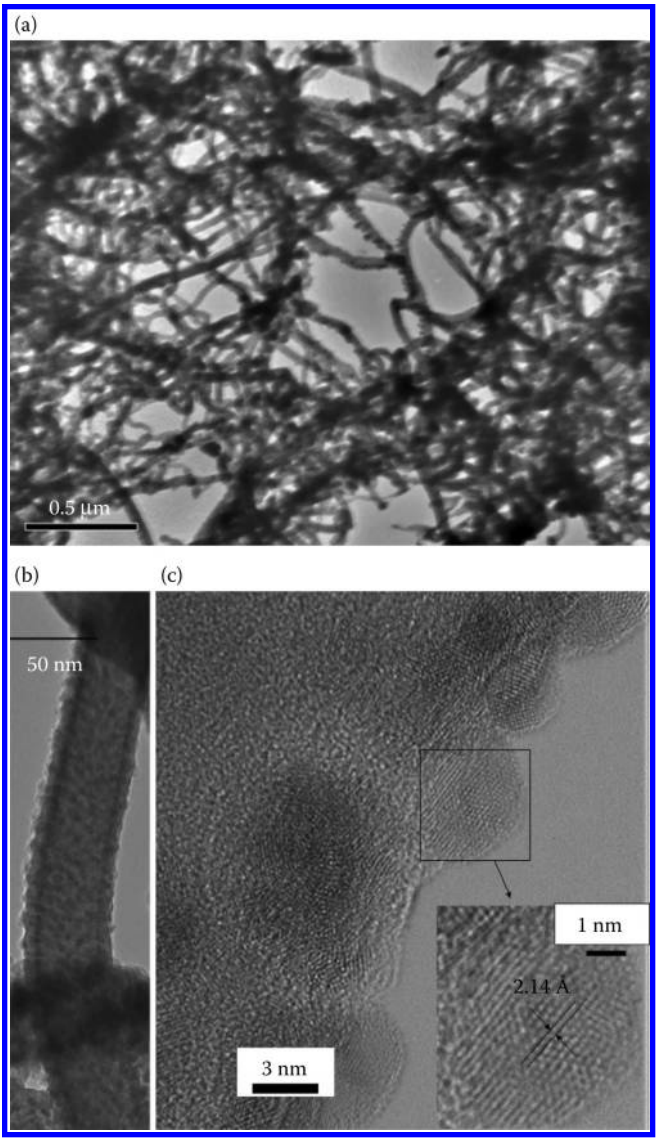


FIGURE 1.20 Image of nc-TiC/(CNFs:a-C)$_{0.05}$ coating showing (a) uniformly distributed CNFs, (b) a single carbon nanofiber, and (c) nc-TiC crystallites well adhered to the fiber; inset: enlarged square part.

during sputtering. Figure 1.21a–d illustrated CNT formed using different content of hydrogen during sputtering. The authors emphasized that hydrogen played a key role in ensuring the formation of nanotubes. Hydrogen is well-known to be a reduction agent, preventing catalyst oxidation and promoting catalytic activity. However, the nucleated carbon can be subsequently converted into methane by interacting with the

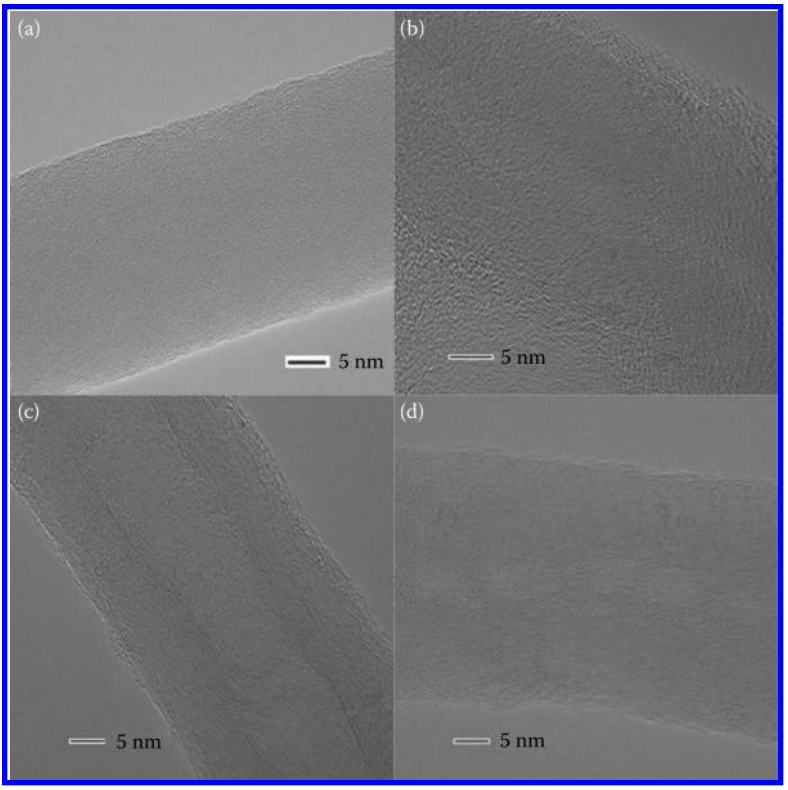


FIGURE 1.21 HRTEM image of (a) carbon nanofiber, 0 at.% H_2 introduced, (b) CNT, 35 nm outer diameter, 5 nm inner diameter, 0.6 at.% H_2 introduced, (c) CNT, 35 nm outer diameter, 12 nm inner diameter, 1.0 at.% H_2 introduced, and (d) CNT, 40 nm outer diameter, 5 nm inner diameter, 1.5 at.% H_2 introduced. (From Wang H. et al., *Nanoscience and Nanotechnology Letters* 2011;3:491.)

adsorbed hydrogen at the surface of the catalysis dots. During the hydrocarbonization reaction, the catalyst dot retraced its original catalytic path removing the core component and leaving behind the outer, more structurally ordered skin, which is highly graphitic. In contrast to carbon nanofiber produced from hydrocarbon vapor source, the nanofibers obtained with amorphous carbon film as the source were grown via a plausible solid–liquid–solid growth regime. The inclusion of hydrogen promotes the catalytic activity of the catalyst dots as well as the gasification of the amorphous inner cores of the nanofibers. A further study on the thickness of catalysis layer was done recently. To obtain a highly purified multiwalled CNTs with lowest catalyst inclusions, an upper limit of the catalysis thickness must be set. In this work, a conservative upper limit of Ni catalysis layer was 50 nm [134]. To date, no results are available to demonstrate the toughening effect of *in situ* CNT prepared using the above procedures, but it would be very interesting to see the outcome in further studies.

1.2.2.2 Phase Transformation Toughening

Phase transformation process readily toughens brittle ceramics, since the process consumes a large amount of energy due to the dimensional variation in crystalline structure. In previous studies [135,136], transformation occurs under stress leading to crystallites changing from tetragonal phase to monoclinic phase. This change is accompanied by a 4% volume expansion, which releases the stress accumulated and consumes the fracture energy from the resultant strain. ZrO_2 is one typical material with such characteristics and ZrO_2 toughened ZrB_2 is one of the examples [135]. In this case, retention of the tetragonal phase of ZrO_2 is essential, since it has a high toughness against the brittle fracture behavior [136].

1.2.2.3 Compressive Stress Toughening

Open surfaces of cracks are generally initiated by the tensile stress. Therefore, the toughness will be likely increased if compressive residual stress is properly induced in the coatings, in which extra energy is required to overcome that stress before a crack is driven in tension. When a coating has a high compressive residual stress to start with, the coating is able to take more tensile strain before a fracture. In practice, there are many ways to introduce stress into the coatings. For instance, Halitim et al. [137] did it by ion implantation while Abe et al. [138,139] by phase change. In the case of $NiAl/Al_2O_3$, the formation of $NiAl_2O_4$ was the source of stress as a result of volume change. The induced 127 MPa compressive stress led to the large increase of toughness from 3.91 to 6.22 MPa $m^{1/2}$.

Compressive stress-induced high toughness can also be found in the coating systems such as TiN, DLC, MoS_2, TiC, and CrAlN [68,69,140,141]. Wang et al. measured the toughness of TiC with different compressive stress originated from the bias voltage during sputtering. The increased bias voltage led to the increase of stress as well as the restrained columnar structure, and thus the increased toughness from 1.19 to 1.89 MPa $m^{1/2}$ [69]. However, too much compressive stress is detrimental, resulting in poor adhesion, delamination, and microcracks in the as-deposited coatings and in turn renders decrease of toughness [142]. Similar results were also reported in CrAlN-coating system [68]. The measured toughness increased from 1.67 to 2.02 MPa $m^{1/2}$ when bias voltage increased from 50 to 210 V (Figure 1.22a). But further increasing bias voltage led to the drop of toughness and adhesion. Figure 1.22b illustrates the fracture behavior of such CrAlN coatings prepared at varied bias voltage when they are subjected to the scratch test. A poor adhesion along with severe chipping and buckling was observed when the bias voltage was at 260 V.

1.2.2.4 Toughening through Optimization of Coatings Architecture

1.2.2.4.1 Gradient Structure Toughening

In practical applications, requirements on a coating can vary throughout the coating thickness (from the coating/substrate interface all the way up to the top of the coating surface). For example, a good adhesion is required at the coating–substrate interface, while at the coating surface a very stable material is needed (against penetration, scratching, corrosion, and so on (Figure 1.23) [143]). However, in a homogeneous single-layer coating, these desired properties are rarely achieved simultaneously.

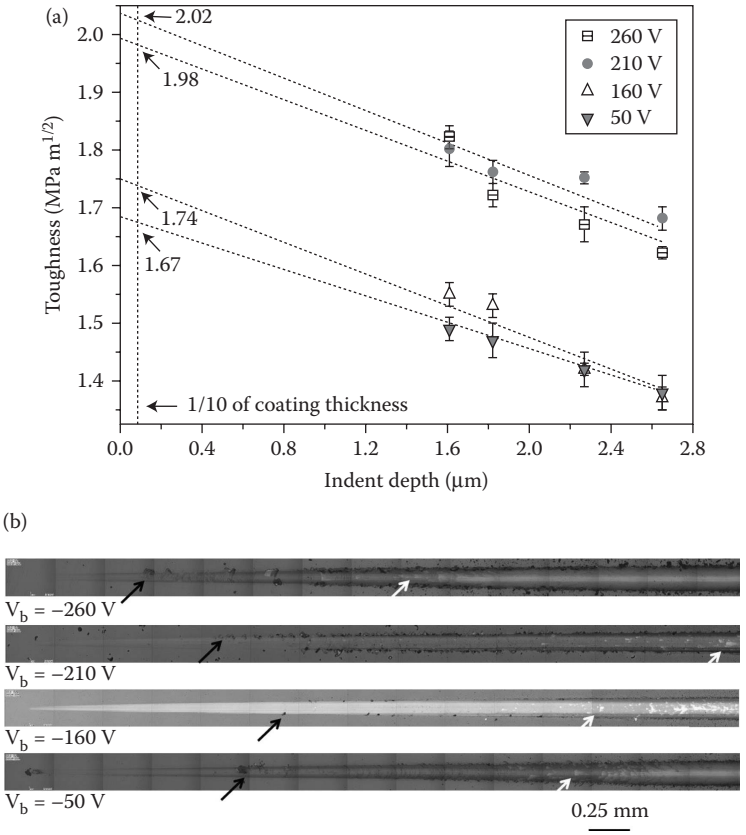


FIGURE 1.22 (a) Fracture toughness of CrAlN prepared at different bias voltage via sputtering. (From Wang YX. et al., *Surface and Coatings Technology* 2012;206:5103); (b) Scratch tracks of CrAlN prepared at different bias voltage (black arrow: lower critical load, white arrow higher critical load). (Data based on Wang YX. et al., *Surface and Coatings Technology* 2012;206:5103.)

Therefore, it is apt to apply graded coatings, consisting of a sequence of coating materials, to satisfy different requirements at different coating thickness.

In the gradient design, the substrate is first coated with a high adhesion layer and then the coating constituents are allowed to vary homogeneously or heterogeneously while the coating thickness builds up. The gradually changed coating constituents can be achieved by varying various deposition conditions. Wang et al. adjust the target power during sputtering and fabricate CrAlSiN nanocomposite with heterogeneously gradient structure (Figure 1.24). An obvious structure change can be identified from the bottom to the top. The toughness was increased 300% as compared to the monolayer CrAlSiN while the hardness can be maintained at ~25 GPa.

By gradually changing the bias voltage, Zhang et al. [144] prepared a 1.5 μm thick a-C gradient coating on the tool steel with moderately high hardness (25 GPa) and high toughness (plasticity ratio ~58%). As the negative bias voltage varied from 20 to

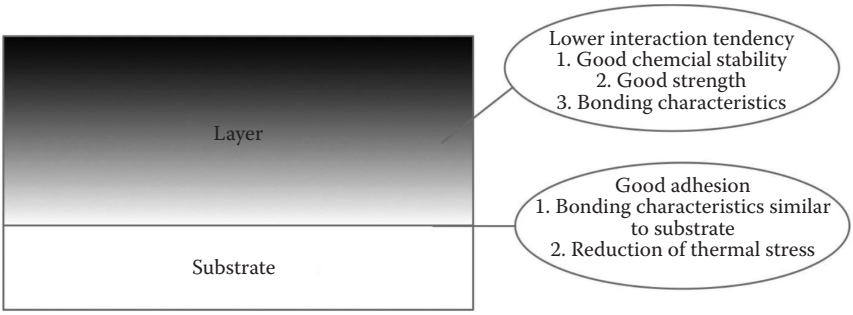


FIGURE 1.23 A schematic of gradient layer coatings. (Redrawn from Fella R, Holleck H, Schulz H., *Surface and Coatings Technology* 1988;36:257.)

150 V, sp^3/sp^2 ratio of the carbon gradually increased from the bottom layer to the top surface. The lower sp^3/sp^2 ratio ensured the good adhesion at the coating–substrate interface, while the higher sp^3/sp^2 ratio gave rise to the high hardness, as well as the coating of the improved tribological performance. The graded coatings became hard yet tough (Figure 1.25). In other gradient coating systems, such as commercial grading TiCN [145,146], TiN–TiCN–TiC–DLC [89], and Ti–TiC–DLC [90], high hardness with enhanced adhesion was also achieved. Gradient structure is beneficial for the suppression of crack initiation due to the absence of sharp interface.

1.2.2.4.2 Multilayering Structure Toughening

Multilayering structure is considered another effective way to improve toughness of ceramic coatings. The main mechanisms include crack deflection at interface among the sublayers, interface delamination, ductile interlayer ligament bridging, and crack

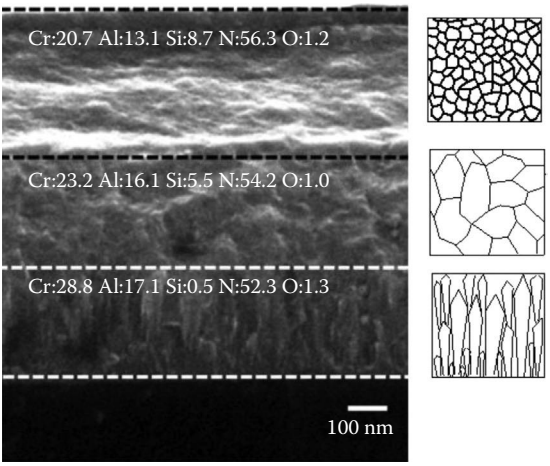


FIGURE 1.24 Cross-sectional image of heterogeneously gradient CrASiN nanocomposites, chemical compositions are listed accordingly in the unit of at.%.

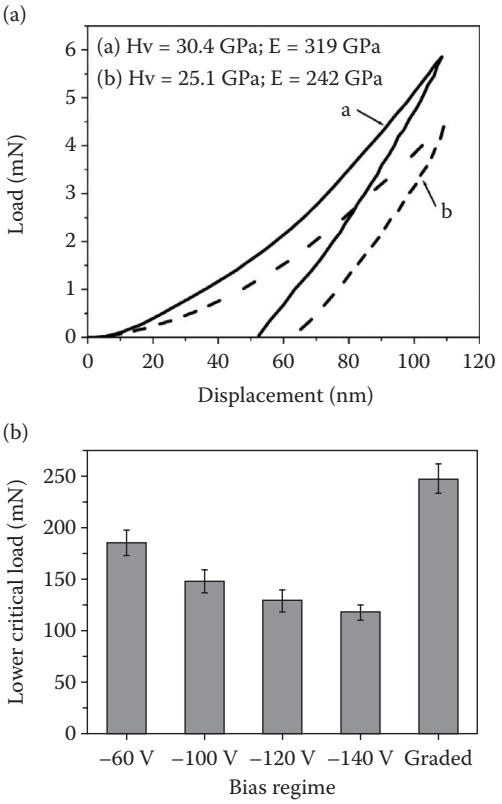


FIGURE 1.25 (a) Hardness of graded DLC coatings, (b) scratch adhesion strength of the nonhydrogenated DLCs deposited under various constant bias voltage or bias-graded conditions. (From Zhang S. et al., *Diamond and Related Materials* 2004;13:867.)

tip blunting because of nanoplasticity, which will cause extra energy consumption and dissipation during crack propagation [147] (Figure 1.26).

These toughening mechanisms have been validated by a number of experimental observations. Suresha et al. [148] demonstrated the cracking patterns in monolayer TiN and multilayered TiN/AlTiN at indentation load of 20 N. Severe edge cracking was observed in the monolayer while much less cracking was found in the multilayers (Figure 1.27). In particular, TiN/AlTiN with bilayer thickness of 650 nm showed two edge cracks, whereas that with bilayer thickness of 130 nm showed only one. Figure 1.28 illustrates the cross-sectional images of the fracture region under indentation with normal load of 5 N. Continuous shear cracks were evident in monolayer TiN. Multilayers of bilayer thickness of 650 nm displayed discontinuous shear cracks, whereas such cracks were absent in the multilayers of bilayer thickness of 130 nm. These results indicated the positive effects of the layered structure in preventing crack propagation.

For the same multilayer system, Lee et al. [149] investigated the toughening effect using scratch test in addition to nanoindentation. Multilayers presented great

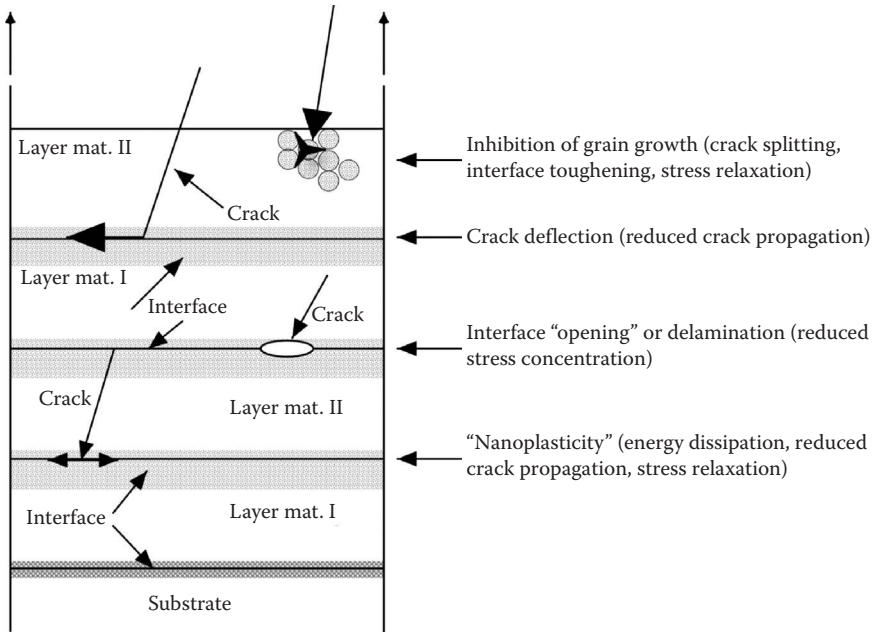


FIGURE 1.26 Multilayering structure toughening mechanisms. (Redrawn from Holleck H, Schier V., *Surface and Coatings Technology* 1995;76–77, Part 1:328.)

resistance to crack initiation and propagation, in great contrast with the monolayer, which exhibited extreme brittleness accompanied by severe coating chipping off at the fringe of the groove track (Figure 1.29). Nanoindentation tests further confirmed the advantage of the multilayers in fracture resistance. Only a few cracks spread out radially within the multilayers, whereas delamination was obvious in the monolayer, together with radial cracks.

Karimi et al. [150] fabricated a variety of nanostructured TiAlN(Si, C). A summary of the results for several samples is given in Figure 1.30, in which "M" stands for

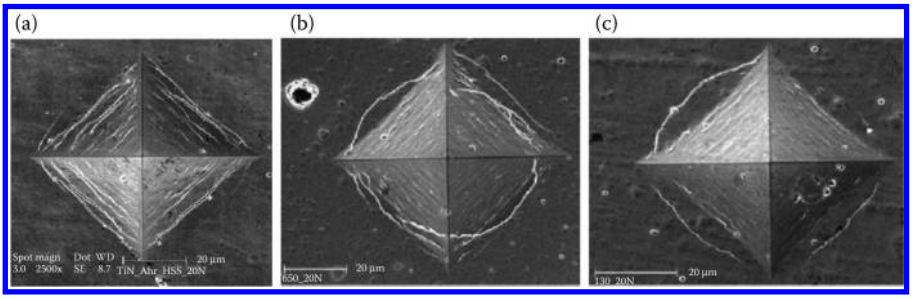


FIGURE 1.27 Surface view of the indentation with a load of 20 N showing dependence of edge cracking on layer spacing: (a) monolayer TiN, (b) multilayer TiN/TiAlN with bilayer thickness of 650 nm, and (c) multilayer TiN/TiAlN with bilayer thickness of 130 nm. (From Suresha SJ. et al., *Philosophical Magazine* 2007;87:2521.)

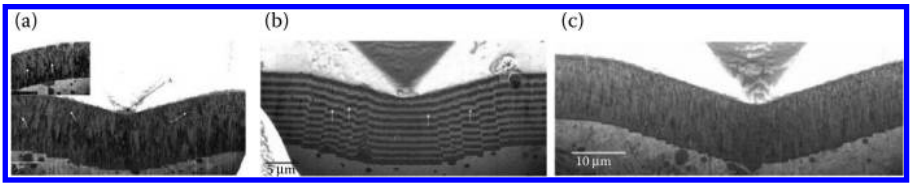


FIGURE 1.28 Cross-sectional images of the indentation under 5 N showing inclined shear cracks: (a) monolayer TiN, (b) multilayer TiN/TiAlN with bilayer thickness of 650 nm, and (c) multilayer TiN/TiAlN with bilayer thickness of 130 nm. (From Suresha SJ. et al., *Philosophical Magazine* 2007;87:2521.)

multilayers. It was shown that multilayers (4) exhibited the best performances, both in hardness and toughness. A similar result was obtained in the case of CrN/AlN multilayer, subjected to the Rockwell C-Brale indentation test [151]. Practically, the number of the interlayers, the thickness of each sublayer, and the thickness ratio of different sublayers all affect the toughness. The dependence of the toughness on these factors is evaluated in coating systems such as TiC/TiB_2 [152], TiC/TiB_2 [153], TiC/CrC [154],

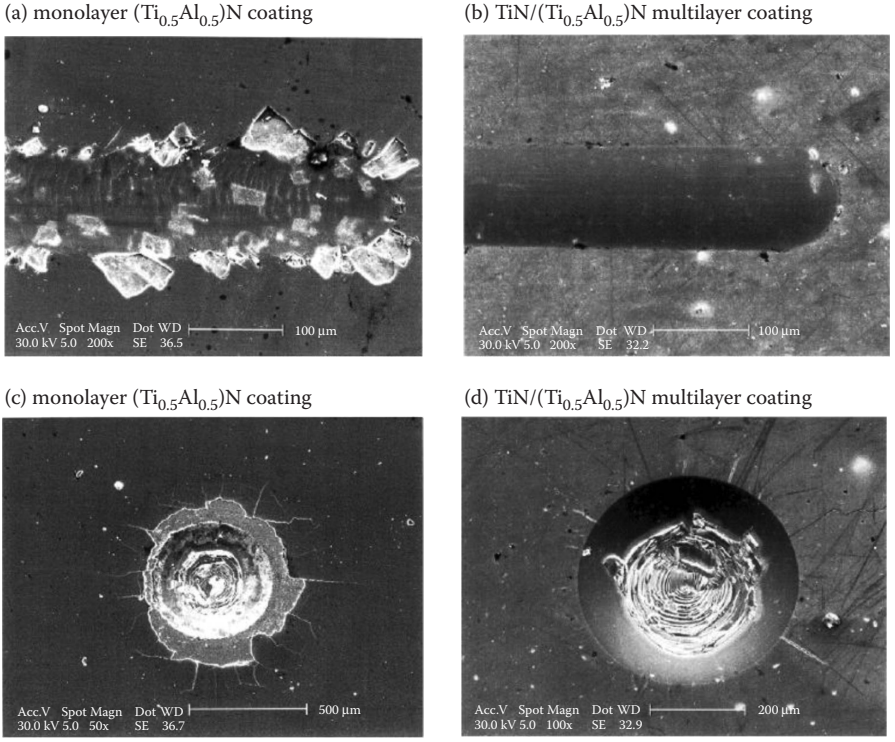


FIGURE 1.29 Scratch channels (a) and (b) and indent marks (c) and (d) of monolayer $(Ti_{0.5}Al_{0.5})N$ and $TiN/(Ti_{0.5}Al_{0.5})N$ multilayer coatings. (From Lee D-K, Lee S-H, Lee J-J., *Surface and Coatings Technology* 2003;169–170:433.)

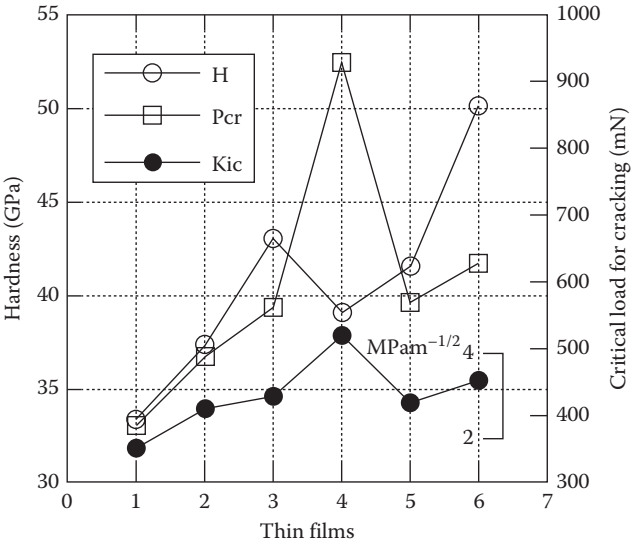


FIGURE 1.30 Variation of hardness, critical load for cracking, and fracture toughness for a number of coatings: 1. TiN; 2. TiCN; 3. TiAlN; 4. TiAlN(M); 5. TiAlSiN(M); 6. TiAlCN. (From Karimi A. et al., *Thin Solid Films* 2002;420–421:275.)

CrN/AlN [155], and TiN/Ti [156]. In general, increased number of the interface leads to improved toughness. Besides the dimensional effect of the sublayers, studies have been carried out on the crystalline structure of the constituent layers. Yau et al. [157] investigated the multilayers with the bilayers of nanocrystalline/amorphors phases, such as nc-TiAlN/a-Si_3N_4. Maximum critical scratching load of the multilayers was increased by 165% as compared to monolayer TiAlN. The improvement was attributed to the crack deflection at the layer interfaces (Figure 1.31). In the more recent researches of TiN/SiN_x [158,159] and CrAlN/SiN_x multilayers [160,161], the crystallite structure of the SiN_x layers was found to be dependent on their thickness. At very small thickness, for example, a few tense of angstrom, the SiN_x was in an epitaxial crystalline structure. However, when the thickness was larger than a certain threshold, the epitaxial crystalline structure could transform into an amorphous phase. The hardness was varied accordingly due to the phase change of the SiN_x. Although the tendency of the toughness is not reported, it is believed that the epitaxial crystalline structure will influence the ability of coating in preventing crack growth and propagation.

By investigating the hardness and toughness of homogeneously gradient CrAlSiN nanocomposite [162] and polycrystalline CrAlN (pc-CrAlN) [68], Wang et al. integrated them into multilayer structure consisting of alternative layer of nanocomposite CrAlSiN and pc-CrAlN (Figure 1.32). The interfaces shown by the white arrows in Figure 1.32a are enlarged in Figure 1.32b. The continuous growth of the columnar pc-CrAlN grains was periodically interrupted due to the insertion of nanocomposite layer, as also observed in Reference 68. No epitaxial relation was found to take place within the adjacent layers. However, the interface was not sharp. At the interface, pc-CrAlN layer with large grains (~10 nm) was observed. pc-CrAlN layer combined

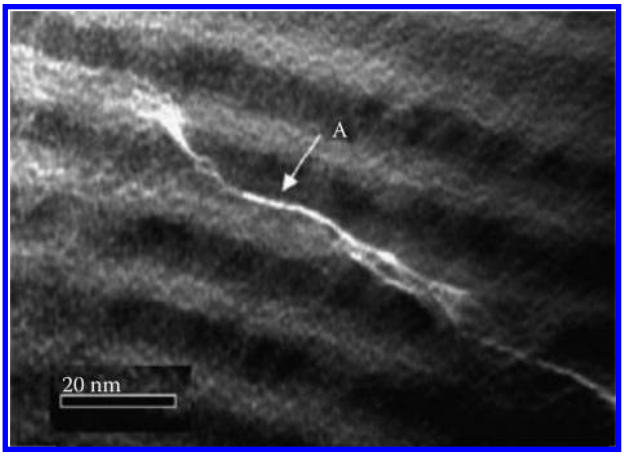


FIGURE 1.31 Cross-section TEM micrograph showed the propagation of nanocracks in nc-TiAlN/a-Si_3N_4 nanolaminate coatings with $\Lambda = 20$ nm. (From Yau B-S. et al., *Surface and Coatings Technology* 2005;194:119.)

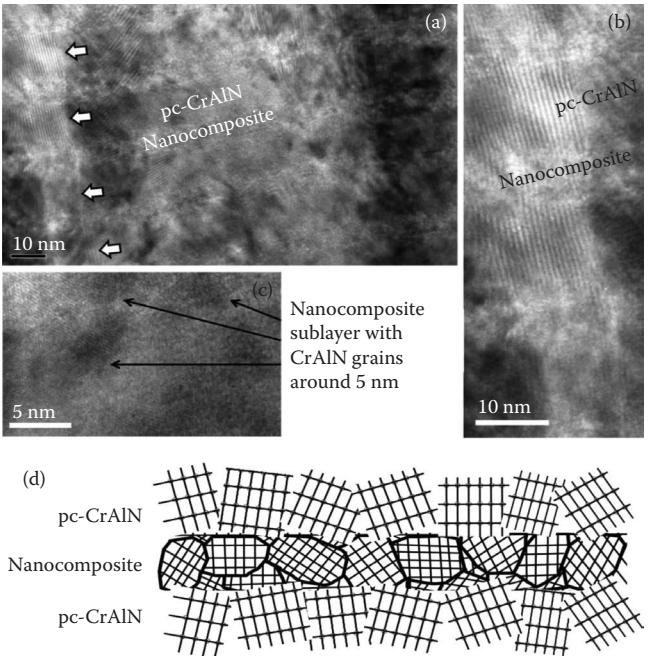


FIGURE 1.32 (a) HRTEM image of the multilayer coating with period thickness of 20 nm, (b) an enlarged interface at the white arrows in (a), (c) HRTEM image of the nanocomposite (i.e., nc-CrAlN in a-SiN_x) sublayer, and (d) the schematic representative of the sandwich structure.

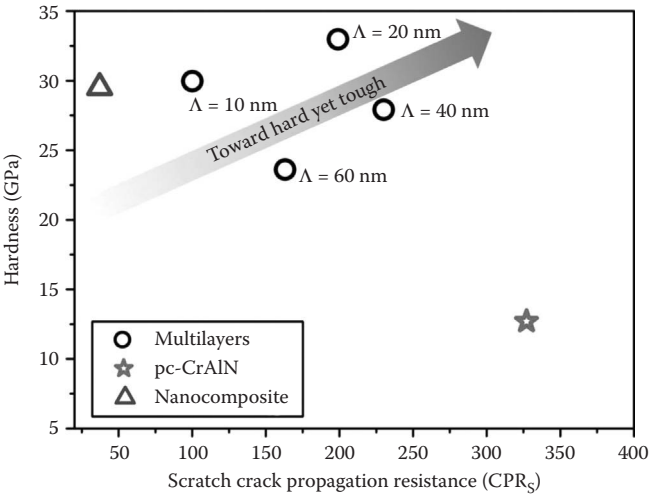


FIGURE 1.33 Hardness versus scratch toughness of multilayer and monolayer CrAlSiN. (From Wang YX. et al., *Nanoscience and Nanotechnology Letters* 2012;4.)

with the nanocomposite layer (with nanocrystallites ~5 nm as seen in Figure 1.32c), leading to complex interface boundaries (Figure 1.32d). In nanocomposite layer, only a few nanocrystallites, whose lattice planes oriented parallel to the electron beam, appeared in the lattice resolution due to random orientation. With such structure, the multilayer coatings (the open circles) do appear toward hard-yet-tough direction with varying period thickness (Λ) [87]: Λ = 10 nm, the hardness of the multilayer coating matches that of the nanocomposite monolayer, meanwhile, its toughness is better (moving toward right in the hardness vs. toughness space). At even larger period thickness, Λ = 60 nm, the multilayer's hardness drops with increased toughness; at Λ = 40 nm, hardness returns with much improved toughness (seven times as much as that of nanocomposite monolayer); at Λ = 20 nm, the hardness further improves, and even surpasses that of the nanocomposite (from less than 30 to 33 GPa) at a slight drop in toughness from that at Λ = 40 nm. With this architecture (Λ = 20 nm), the multilayer coating's toughness increased fivefold from that of the hard nanocomposite (the open triangle, Figure 1.33).

1.3 SUMMARY

Increasing studies have proven that toughness is just as crucial as hardness. In this chapter, a comprehensive discussion on hardening and toughening mechanisms of ceramic coatings has been attempted. Microstructural design at nanoscale effectively engineers the hardening. Decreasing crystallite size (ca. to 10 nm) increases grain boundaries thereby increasing hindering of dislocation movements, resulting in Hall–Petch strengthening. As crystallite size goes below 10 nm (i.e., nanocomposite hardening), further strengthening is achievable through multilayering. Multilayering

renders hardening by blocking dislocation movement between the layers. Hardening effect can be maximized through manipulation of the layer thickness, total number of layers, and interfaces.

Toughening can be achieved via similar nanoscale optimization. Individual toughening techniques such as toughening agent (e.g., metallic additives and carbon nanofibers/nanotubes) and coating structure optimization (e.g., gradient structure and multilayering) have achieved a lot. The key of toughening lies in the creation of complex coherent boundaries at interfaces, whereby more energy is consumed during crack initiation and propagation. This principle can be applied to any coating system. The challenge now is how to properly integrate these hardening and toughening mechanisms in one, so as to make hard-yet-tough ceramic coatings practical. Nanomultilayers containing nanocomposite layers have switched on a beacon light in this direction.

Last but not least, in studies of toughening of thin films and coatings, it is inevitable that one needs to have a precise evaluation of toughness. Toughness measurement of bulk materials has been achieved by the generous use of indentation method [163], but obtaining good toughness estimation of thin films remains a challenge [164]. A universally accepted single method is not yet established for thin films or coatings, but the field has seen much effort in this arena, as detailed in Chapters 2 and 8.

REFERENCES

1. Veprek S, Veprek-Heijman MJG. Industrial applications of superhard nanocomposite coatings. *Surface and Coatings Technology* 2008;202:5063.
2. Chen J. Indentation-based methods to assess fracture toughness for thin coatings. *Journal of Physics D: Applied Physics* 2012;45.
3. Chen J, Bull SJ. Modelling the limits of coating toughness in brittle coated systems. *Thin Solid Films* 2009;517:2945.
4. Musil J. Hard nanocomposite coatings: Thermal stability, oxidation resistance and toughness. *Surface and Coatings Technology* 2012;207:50.
5. Zhang S, Zhang X. Toughness evaluation of hard coatings and thin films. *Thin Solid Films* 2012;520:2375.
6. Zhang S, Wang HL, Ong SE, Sun D, Bui XL. Hard yet tough nanocomposite coatings: Present status and future trends. *Plasma Processes and Polymers* 2007;4:219.
7. Zhang S, Sun D, Fu Y, Du H. Toughening of hard nanostructural thin films: A critical review. *Surface and Coatings Technology* 2005;198:2.
8. Harding DS, Oliver WC, Pharr GM. *Cracking During Nanoindentation and Its Use in the Measurement of Fracture Toughness*. vol. 356. Boston, MA, USA: Materials Research Society, 1995. p.663.
9. Fischer-Cripps AC. *Nanoindentation*. New York: Springer, 2004.
10. Peggs GN, Leigh IC, *National Physical Laboratory Division of Mechanical and Optical Metrology*. *Recommended Procedure for Micro-indentation Vickers Hardness Test*. Great Britain: National Physical Laboratory Division of Mechanical and Optical Metrology, 1983.
11. Standard test for plane strain fracture toughness of metallic materials (E399-90). *Fatigue Standards and Fracture Standards*. Philadelphia, PA: American Society for Testing and Materials, 1997.
12. Cherepanov G. *Mechanics of Brittle Fracture*. New York: McGraw-Hill International Book Co., 1979.

13. Griffith AA. The phenomena of rupture and flow in solids. *Philosophical Transactions of the Royal Society of London. Series A, Containing Papers of a Mathematical or Physical Character* 1921;221:163.
14. Hall EO. The deformation and ageing of mild steel: III Discussion of results. *Proceedings of the Physical Society. Section B* 1951;64:747.
15. Petch NJ. The cleavage strength of polycrystals. *Journal of the Iron and Steel Institute* 1953;174:25.
16. Tjong SC, Chen H. Nanocrystalline materials and coatings. *Materials Science and Engineering R: Reports* 2004;45.
17. Hahn H, Mondal P, Padmanabhan KA. Plastic deformation of nanocrystalline materials. *Nanostructured Materials* 1997;9:603.
18. Hahn H, Padmanabhan KA. A model for the deformation of nanocrystalline materials. *Philosophical Magazine B: Physics of Condensed Matter; Statistical Mechanics, Electronic*, *Optical and Magnetic Properties* 1997;76:559.
19. Van Swygenhoven H, Farkas D, Caro A. Grain-boundary structures in polycrystalline metals at the nanoscale. *Physical Review B* 2000;62:831.
20. Vepřek S, Reiprich S. A concept for the design of novel superhard coatings. *Thin Solid Films* 1995;268:64.
21. Vepřek S, Reiprich S, Shizhi L. Superhard nanocrystalline composite materials: The TiN/Si3N4 system. *Applied Physics Letters* 1995:2640.
22. Veprek S, Niederhofer A, Moto K, Bolom T, Männling HD, Nesladek P, Dollinger G, Bergmaier A. Composition, nanostructure and origin of the ultrahardness in nc-TiN/a-Si_3N_4/a- and nc-$TiSi_2$ nanocomposites with HV=80 to ≥105 GPa. *Surface and Coatings Technology* 2000;133–134:152.
23. Fischer-Cripps AC, Bull SJ, Schwarzer N. Critical review of claims for ultra-hardness in nanocomposite coatings. *Philosophical Magazine* 2012;92:1601.
24. Veprek S. Recent attempts to design new super-and ultrahard solids leads to nano-sized and nano-structured materials and coatings. *Journal of Nanoscience and Nanotechnology* 2011;11:14.
25. Veprek S, Veprek-Heijman MGJ, Karvankova P, Prochazka J. Different approaches to superhard coatings and nanocomposites. *Thin Solid Films* 2005;476:1.
26. Voevodin AA, Prasad SV, Zabinski JS. Nanocrystalline carbide/amorphous carbon composites. *Journal of Applied Physics* 1997;82:855.
27. Voevodin AA, Zabinski JS. Load-adaptive crystalline–amorphous nanocomposites. *Journal of Materials Science* 1998;33:319.
28. Voevodin AA, O'Neill JP, Prasad SV, Zabinski JS. Nanocrystalline WC and WC/a-C composite coatings produced from intersected plasma fluxes at low deposition temperatures. *Journal of Vacuum Science and Technology A: Vacuum, Surfaces and Films* 1999;17:986.
29. Veprek S, Veprek-Heijman MGJ. The formation and role of interfaces in superhard nc-MenN/a-Si3N4 nanocomposites. *Surface and Coatings Technology* 2007;201:6064.
30. Söderberg H, Oďn M, Molina-Aldareguia JM, Hultman L. Nanostructure formation during deposition of TiN SiN*x* nanomultilayer films by reactive dual magnetron sputtering. *Journal of Applied Physics* 2005;97(11):114327.
31. Veprek S, Argon AS, Zhang RF. Origin of the hardness enhancement in superhard nc-TiN/a-Si_3N_4 and ultrahard nc-TiN/a-Si_3N_4/$TiSi_2$ nanocomposites. *Philosophical Magazine Letters* 2007;87:955.
32. Hao S, Delley B, Veprek S, Stampfl C. Superhard nitride-based nanocomposites: Role of interfaces and effect of impurities. *Physical Review Letters* 2006;97:086102.
33. Diserens M, Patscheider J, Levy F. Mechanical properties and oxidation resistance of nanocomposite TiN-SiN*x* physical-vapor-deposited thin films. *Surface and Coatings Technology* 1999;120–121:158.

34. Mayrhofer PH, Stoiber M, Mitterer C. Age hardening of PACVD TiBN thin films. *Scripta Materialia* 2005;53:241.
35. Sundgren JE, Hentzell HTG. A review of the present state of art in hard coatings grown from the vapor phase. *Journal of Vacuum Science and Technology A* 1986;4.
36. Kim G, Kim B, Lee S, Hahn J. Structure and mechanical properties of Cr-Zr-N films synthesized by closed field unbalanced magnetron sputtering with vertical magnetron sources. *Surface and Coatings Technology* 2005;200:1669.
37. Löffler FHW. Systematic approach to improve the performance of PVD coatings for tool applications. *Surface and Coatings Technology* 1994;68–69:729.
38. Sanchez-Lopez JC, Martinez-Martinez D, Lopez-Cartes C, Fernandez A, Brizuela M, Garcia-Luis A, Onate JI. Mechanical behavior and oxidation resistance of Cr(Al)N coatings. *Journal of Vacuum Science and Technology A: Vacuum, Surfaces and Films* 2005;23:681.
39. PalDey S, Deevi SC. Single layer and multilayer wear resistant coatings of (Ti,Al)N: A review. *Materials Science and Engineering: A* 2003;342:58.
40. Romero J, Gómez MA, Esteve J, Montal F, Carreras L, Grifol M, Lousa A. CrAlN coatings deposited by cathodic arc evaporation at different substrate bias. *Thin Solid Films* 2006;515:113.
41. Uchida M, Nihira N, Mitsuo A, Toyoda K, Kubota K, Aizawa T. Friction and wear properties of CrAlN and CrVN films deposited by cathodic arc ion plating method. *Surface and Coatings Technology* 2004;177–178:627.
42. Le Bourhis E, Goudeau P, Staia MH, Carrasquero E, Puchi-Cabrera ES. Mechanical properties of hard AlCrN-based coated substrates. *Surface and Coatings Technology* 2009;203:2961.
43. Reiter AE, Derflinger VH, Hanselmann B, Bachmann T, Sartory B. Investigation of the properties of Al1-xCrxN coatings prepared by cathodic arc evaporation. *Surface and Coatings Technology* 2005;200:2114.
44. Banakh O, Schmid PE, Sanjinés R, Lévy F. High-temperature oxidation resistance of Cr1-xAlxN thin films deposited by reactive magnetron sputtering. *Surface and Coatings Technology* 2003;163–164:57.
45. Ulrich S, Holleck H, Ye J, Leiste H, Loos R, Stüber M, Pesch P, Sattel S. Influence of low energy ion implantation on mechanical properties of magnetron sputtered metastable (Cr,Al)N thin films. *Thin Solid Films* 2003;437:164.
46. Spain E, Avelar-Batista JC, Letch M, Housden J, Lerga B. Characterisation and applications of Cr-Al-N coatings. *Surface and Coatings Technology* 2005;200:1507.
47. Sanchéz JE, Sanchéz OM, Ipaz L, Aperador W, Caicedo JC, Amaya C, Landaverde MAH, Beltran FE, Muńoz-Saldańa J, Zambrano G. Mechanical, tribological, and electrochemical behavior of Cr1-xAlxN coatings deposited by r.f. reactive magnetron co-sputtering method. *Applied Surface Science* 2009;256:2380.
48. Ding X-Z, Zeng XT. Structural, mechanical and tribological properties of CrAlN coatings deposited by reactive unbalanced magnetron sputtering. *Surface and Coatings Technology* 2005;200:1372.
49. Wang L, Zhang G, Wood RJK, Wang SC, Xue Q. Fabrication of CrAlN nanocomposite films with high hardness and excellent anti-wear performance for gear application. *Surface and Coatings Technology* 2010;204:3517.
50. Scheerer H, Hoche H, Broszeit E, Schramm B, Abele E, Berger C. Effects of the chromium to aluminum content on the tribology in dry machining using (Cr,Al)N coated tools. *Surface and Coatings Technology* 2005;200:203.
51. Rafaja D, Wüstefeld C, Dopita M, Ruzicka M, Klemm V, Schreiber G, Heger D, Sima M. Internal structure of clusters of partially coherent nanocrystallites in Cr-Al-N and Cr-Al-Si-N coatings. *Surface and Coatings Technology* 2007;201:9476.

52. Kimura A, Kawate M, Hasegawa H, Suzuki T. Anisotropic lattice expansion and shrinkage of hexagonal TiAlN and CrAlN films. *Surface and Coatings Technology* 2003;169–170:367.
53. Lin J, Moore JJ, Mishra B, Pinkas M, Sproul WD, Rees JA. Effect of asynchronous pulsing parameters on the structure and properties of CrAlN films deposited by pulsed closed field unbalanced magnetron sputtering (P-CFUBMS). *Surface and Coatings Technology* 2008;202:1418.
54. Mayrhofer PH, Mitterer C, Hultman L, Clemens H. Microstructural design of hard coatings. *Progress in Materials Science* 2006;51:1032.
55. Mayrhofer PH, Hörling A, Karlsson L, Sjölén J, Larsson T, Mitterer C, Hultman L. Self-organized nanostructures in the Ti-Al-N system. *Applied Physics Letters* 2003;83:2049.
56. Wen JG, Mayrhofer PH, Mitterer C, Greene JE, Petrov I. Self-hardening of nanocrystalline Ti-B-N thin films. *Microscopy and Microanalysis* 2006;12:720.
57. Window B. Issues in magnetron sputtering of hard coatings. *Surface and Coatings Technology* 1996;81:92.
58. Mattox DM. Particle bombardment effects on thin-film deposition: A review. *Journal of Vacuum Science and Technology A* 1989;7:1105.
59. Karkari SK, Vetushka A, Bradley JW. Measurement of the plasma potential adjacent to the substrate in a midfrequency bipolar pulsed magnetron. *Journal of Vacuum Science and Technology A: Vacuum, Surfaces and Films* 2003;21:L28.
60. Audronis M, Leyland A, Kelly PJ, Matthews A. The effect of pulsed magnetron sputtering on the structure and mechanical properties of CrB2 coatings. *Surface and Coatings Technology* 2006;201:3970.
61. Thornton JA, Hoffman DW. Stress-related effects in thin films. *Thin Solid Films* 1989;171:5.
62. Messier R, Giri AP, Roy RA. Revised structure zone model for thin film physical structure. *Journal of Vacuum Science & Technology A: Vacuum, Surfaces, and Films* 1984;2:500.
63. Sproul WD. Physical vapor deposition tool coatings. *Surface and Coatings Technology* 1996;81:1.
64. Ljungcrantz H, Hultman L, Sundgren JE, Karlsson L. Ion induced stress generation in arc-evaporated TiN films. *Journal of Applied Physics* 1995;78:832.
65. Chapman B. *Glow Discharge Processes: Sputtering and Plasma Etching*. New York: John Wiley & Sons, Inc., 1980.
66. Mayrhofer PH, Kunc F, Musil J, Mitterer C. A comparative study on reactive and non-reactive unbalanced magnetron sputter deposition of TiN coatings. *Thin Solid Films* 2002;415:151.
67. Musil J, Kadlec S, Vyskočil J, Valvoda V. New results in d.c. reactive magnetron deposition of TiN*x* films. *Thin Solid Films* 1988;167:107.
68. Wang YX, Zhang S, Lee J-W, Lew WS, Li B. Influence of bias voltage on the hardness and toughness of CrAlN coatings via magnetron sputtering. *Surface and Coatings Technology* 2012;206:5103.
69. Wang H, Zhang S, Li Y, Sun D. Bias effect on microstructure and mechanical properties of magnetron sputtered nanocrystalline titanium carbide thin films. *Thin Solid Films* 2008;516:5419.
70. Karvánková P, Männling HD, Eggs C, Veprek S. Thermal stability of ZrN-Ni and CrN-Ni superhard nanocomposite coatings. *Surface and Coatings Technology* 2001;146–147:280.
71. Koehler JS. Attempt to design a strong solid. *Physical Review* B 1970;2:547.
72. Helmersson U, Todorova S, Barnett SA, Sundgren JE, Markert LC, Greene JE. Growth of single-crystal TiN/VN strained-layer superlattices with extremely high mechanical hardness. *Journal of Applied Physics* 1987;62:481.
73. Barshilia HC, Rajam KS. Structure and properties of reactive DC magnetron sputtered TiN/NbN hard superlattices. *Surface and Coatings Technology* 2004;183:174.

74. Chu X, Barnett SA, Wong MS, Sproul WD. Reactive unbalanced magnetron sputter deposition of polycrystalline TiN/NbN superlattice coatings. *Surface and Coatings Technology* 1993;57:13.
75. Shinn M, Hultman L, Barnett SA. Growth, structure, and microhardness of epitaxial TiN/NbN superlattices. *Journal of Materials Research* 1992;7:901.
76. Hovsepian PE, Lewis DB, Müunz WD, Rouzaud A, Juliet P. Chromium nitride/niobium nitride superlattice coatings deposited by combined cathodic-arc/unbalanced magnetron technique. *Surface and Coatings Technology* 1999;116–119:727.
77. Chu X, Wong MS, Sproul WD, Barnett SA. Deposition, structure, and hardness of polycrystalline transition-metal nitride superlattice films. *Journal of Materials Research* 1999;14:2500.
78. Yashar P, Barnett SA, Rechner J, Sproul WD. Structure and mechanical properties of polycrystalline CrN/TiN superlattices. *Journal of Vacuum Science and Technology A: Vacuum, Surfaces and Films* 1998;16:2913.
79. Yang Q, He C, Zhao LR, Immarigeon JP. Preferred orientation and hardness enhancement of TiN/CrN superlattice coatings deposited by reactive magnetron sputtering. *Scripta Materialia* 2002;46:293.
80. Madan A, Kim IW, Cheng SC, Yashar P, Dravid VP, Barnett SA. Stabilization of cubic AlN in epitaxial AlN/TiN superlattices. *Physical Review Letters* 1997;78:1743.
81. Knutsson A, Johansson MP, Persson POÅ, Hultman L, Odn M. Thermal decomposition products in arc evaporated TiAlN/TiN multilayers. *Applied Physics Letters* 2008;93.
82. Barshilia HC, Prakash MS, Jain A, Rajam KS. Structure, hardness and thermal stability of TiAlN and nanolayered TiAlN/CrN multilayer films. *Vacuum* 2005;77:169.
83. Lewis DB, Wadsworth I, Münz WD, Kuzel Jr R, Valvoda V. Structure and stress of TiAlN/CrN superlattice coatings as a function of CrN layer thickness. *Surface and Coatings Technology* 1999;116–119:284.
84. Luo Q, Rainforth WM, Münz WD. TEM observations of wear mechanisms of TiAlCrN and TiAlN/CrN coatings grown by combined steered-arc/unbalanced magnetron deposition. *Wear* 1999;225–229:74.
85. Barshilia HC, Deepthi B, Selvakumar N, Jain A, Rajam KS. Nanolayered multilayer coatings of CrN/CrAlN prepared by reactive DC magnetron sputtering. *Applied Surface Science* 2007;253:5076.
86. Qiu Y, Zhang S, Lee JW, Li B, Wang Y, Zhao D. Self-lubricating CrAlN/VN multilayer coatings at room temperature. *Applied Surface Science* 2013;279:189.
87. Wang YX, Zhang S, Lee J-W, Lew WS, Sun D, Li B. Hard yet tough ceramic coating: Not a dream any more-I. via nanostructured multilayering. *Nanoscience and Nanotechnology Letters* 2012;4.
88. Li F, Zhang S, Kong J, Zhang Y, Zhang W. Multilayer DLC coatings via alternating bias during magnetron sputtering. *Thin Solid Films* 2011;519:4910.
89. Voevodin AA, Schneider JM, Rebholz C, Matthews A. Multilayer composite ceramicmetal-DLC coatings for sliding wear applications. *Tribology International* 1996;29:559.
90. Voevodin AA, Capano MA, Laube SJP, Donley MS, Zabinski JS. Design of a Ti/TiC/DLC functionally gradient coating based on studies of structural transitions in Ti-C thin films. *Thin Solid Films* 1997;298:107.
91. Pacheco ES, Mura T. Interaction between a screw dislocation and a bimetallic interface. *Journal of the Mechanics and Physics of Solids* 1969;17:163.
92. Chu X, Barnett SA. Model of superlattice yield stress and hardness enhancements. *Journal of Applied Physics* 1995;77:4403.
93. Nelias D, Dumont ML, Champiot F, Vincent A, Girodin D, Fougeres R, Flamand L. Role of inclusions, surface roughness and operating conditions on rolling contact fatigue. *Journal of Tribology* 1999;121:240.

94. Anderson TL. *Fracture Mechanics Foundamentals and Applications*. USA: CRC Press. 1995.
95. Musil J, Daniel R. Structure and mechanical properties of magnetron sputtered Zr-Ti-Cu-N films. *Surface and Coatings Technology* 2003;166:243.
96. Musil J, Zeman P, Hrubý H, Mayrhofer PH. ZrN/Cu nanocomposite film—A novel superhard material. *Surface and Coatings Technology* 1999;120–121:179.
97. Musil J, Zeman P. Structure and microhardness of magnetron sputtered ZrCu and ZrCu-N films. *Vacuum* 1999;52:269.
98. He JL, Setsuhara Y, Shimizu I, Miyake S. Structure refinement and hardness enhancement of titanium nitride films by addition of copper. *Surface and Coatings Technology* 2001;137:38.
99. Musil J, Leipner I, Kolega M. Nanocrystalline and nanocomposite CrCu and CrCu-N films prepared by magnetron sputtering. *Surface and Coatings Technology* 1999;115:32.
100. Kelly PJ, Li H, Benson PS, Whitehead KA, Verran J, Arnell RD, Iordanova I. Comparison of the tribological and antimicrobial properties of CrN/Ag, ZrN/Ag, TiN/Ag, and TiN/Cu nanocomposite coatings. *Surface and Coatings Technology* 2010;205:1606.
101. Aouadi SM, Debessai M, Filip P. Zirconium nitride/silver nanocomposite structures for biomedical applications. *Journal of Vacuum Science and Technology B: Microelectronics and Nanometer Structures* 2004;22:1134.
102. Gulbiński W, Suszko T. Thin films of Mo2N/Ag nanocomposite—The structure, mechanical and tribological properties. *Surface and Coatings Technology* 2006;201:1469.
103. Aouadi SM, Maeruf T, Debessai M, Filip P. Zirconium nitride/nickel nanocomposite structures. *Vacuum* 2005;79:186.
104. Hsieh JH, Liu PC, Li C, Cheng MK, Chang SY. Mechanical properties of TaN-Cu nanocomposite thin films. *Surface and Coatings Technology* 2008;202:5530.
105. Jirout M, Musil J. Effect of addition of Cu into ZrOx film on its properties. *Surface and Coatings Technology* 2006;200:6792.
106. Zhang S, Sun D, Fu Y, Pei YT, De Hosson JTM. Ni-toughened nc-TiN/a-SiN*x* nanocomposite thin films. *Surface and Coatings Technology* 2005;200:1530.
107. Zhang S, Sun D, Fu Y, Du H. Effect of sputtering target power on microstructure and mechanical properties of nanocomposite nc-TiN/a-SiN*x* thin films. *Thin Solid Films* 2004;447–448:462.
108. Wang YX, Zhang S, Lee J-W, Lew WS, Li B. Toughening effect of Ni on nc-CrAlN/a-SiN*x* hard nanocomposite. *Applied Surface Science* 2013;265:418.
109. Pei YT, Chen CQ, Shaha KP, De Hosson JTM, Bradley JW, Voronin SA, Čada M. Microstructural control of TiC/a-C nanocomposite coatings with pulsed magnetron sputtering. *Acta Materialia* 2008;56:696.
110. Robertson J. Properties of diamond-like carbon. *Surface and Coatings Technology* 1992;50:185.
111. Lifshitz Y. Hydrogen-free amorphous carbon films: Correlation between growth conditions and properties. *Diamond and Related Materials* 1996;5:388.
112. Lifshitz Y. Diamond-like carbon—Present status. *Diamond and Related Materials* 1999;8:1659.
113. Voevodin AA, Zabinski JS. Supertough wear-resistant coatings with 'chameleon' surface adaptation. *Thin Solid Films* 2000;370:223.
114. Robertson J. Diamond-like amorphous carbon. *Materials Science and Engineering: R: Reports* 2002;37.
115. Tay BK, Cheng YH, Ding XZ, Lau SP, Shi X, You GF, Sheeja D. Hard carbon nanocomposite films with low stress. *Diamond and Related Materials* 2001;10:1082.
116. Zhang S, Lam Bui X, Zeng XT, Li X. Towards high adherent and tough a-C coatings. *Thin Solid Films* 2005;482:138.

117. Zhang S, Bui XL, Fu Y. Magnetron-sputtered nc-TiC/a-C(Al) tough nanocomposite coatings. *Thin Solid Films* 2004;467:261.
118. Thostenson ET, Ren Z, Chou T-W. Advances in the science and technology of carbon nanotubes and their composites: A review. *Composites Science and Technology* 2001;61:1899.
119. Iijima S. Helical microtubules of graphitic carbon. *Nature* 1991;354:56.
120. Baughman RH, Zakhidov AA, de Heer WA. Carbon nanotubes—The route toward applications. *Science* 2002;297:787.
121. Guo Y, Guo W. Mechanical and electrostatic properties of carbon nanotubes under tensile loading and electric field. *Journal of Physics D: Applied Physics* 2003;36:805.
122. Ajayan PM. Nanotubes from Carbon. *Chemical Reviews* 1999;99:1787.
123. Colbert DT. Single-wall nanotubes: A new option for conductive plastics and engineering polymers. *Plastics, Additives and Compounding* 2003;5:18.
124. Srivastava D, Wei C, Cho K. Nanomechanics of carbon nanotubes and composites. *Applied Mechanics Reviews* 2003;56:215.
125. Zhan GD, Kuntz JD, Wan J, Mukherjee AK. Single-wall carbon nanotubes as attractive toughening agents in alumina-based nanocomposites. *Nature Materials* 2003;2:38.
126. Vasiliev AL, Poyato R, Padture NP. Single-wall carbon nanotubes at ceramic grain boundaries. *Scripta Materialia* 2007;56:461.
127. Jiang D, Thomson K, Kuntz JD, Ager JW, Mukherjee AK. Effect of sintering temperature on a single-wall carbon nanotube-toughened alumina-based nanocomposite. *Scripta Materialia* 2007;56:959.
128. An L, Xu W, Rajagopalan S, Wang C, Wang H, Fan Y, Zhang L, Jiang D, Kapat J, Chow L, Guo B, Liang J, Vaidyanathan R. Carbon-nanotube-reinforced polymer-derived ceramic composites. *Advanced Materials* 2004;16:2036.
129. Katsuda Y, Gerstel P, Narayanan J, Bill J, Aldinger F. Reinforcement of precursor-derived Si-C-N ceramics with carbon nanotubes. *Journal of the European Ceramic Society* 2006;26:3399.
130. Li Y, Fernandez-Recio L, Gerstel P, Srot V, Van Aken PA, Kaiser G, Burghard M, Bill J. Chemical modification of single-walled carbon nanotubes for the reinforcement of precursor-derived ceramics. *Chemistry of Materials* 2008;20:5593.
131. Balani K, Zhang T, Karakoti A, Li WZ, Seal S, Agarwal A. *In situ* carbon nanotube reinforcements in a plasma-sprayed aluminum oxide nanocomposite coating. *Acta Materialia* 2008;56:571.
132. Xia Z, Riester L, Curtin WA, Li H, Sheldon BW, Liang J, Chang B, Xu JM. Direct observation of toughening mechanisms in carbon nanotube ceramic matrix composites. *Acta Materialia* 2004;52:931.
133. Wang H, Zhang S, Ong SE, Guo J. Carbon nanofiber or carbon nanotube?—The role of hydrogen during rapid thermal processing. *Nanoscience and Nanotechnology Letters* 2011;3:491.
134. Li FJ, Zhang S, Sun GZ, Kong JH, Rawat RS, Ilyas U, Li B. Entrapping of inclusions within carbon nanotubes during catalytic decomposition of C2H4 on a "thick" nickel film. *Nanoscience and Nanotechnology Letters* 2012;4:1194.
135. Basu B, Venkateswaran T, Kim DY. Microstructure and properties of spark plasma-sintered ZrO 2-ZrB2 nanoceramic composites. *Journal of the American Ceramic Society* 2006;89:2405.
136. Ruddell DE, Stoner BR, Thompson JY. The effect of deposition parameters on the properties of yttria-stabilized zirconia thin films. *Thin Solid Films* 2003;445:14.
137. Halitim F, Ikhlef N, Boudoukha L, Fantozzi G. Microhardness, young's modulus and fracture toughness of alumina implanted with Zr+, Cr+, Ti+ and Ni+. The effect of the residual stresses. *Journal of Physics D: Applied Physics* 1997;30:330.

138. Abe O, Ohwa Y. Oxidation of NiAl/Al2O3 composites for controlled development of surface layers and toughening. *Solid State Ionics* 2004;172:553.
139. Abe O, Takata S, Ohwa Y. Toughening of NiAl-alumina composites by self-constructed compressive surface layers under oxidation. *Journal of the European Ceramic Society* 2004;24:489.
140. Holmberg K, Ronkainen H, Laukkanen A, Wallin K, Hogmark S, Jacobson S, Wiklund U, Souza RM, Ståhle P. Residual stresses in TiN, DLC and MoS2 coated surfaces with regard to their tribological fracture behaviour. *Wear* 2009;267:2142.
141. Chunyan Y, Linhai T, Yinghui W, Shebin W, Tianbao L, Bingshe X. The effect of substrate bias voltages on impact resistance of CrAlN coatings deposited by modified ion beam enhanced magnetron sputtering. *Applied Surface Science* 2009;255:4033.
142. Lim SHN, McCulloch DG, Bilek MMM, McKenzie DR. Minimisation of intrinsic stress in titanium nitride using a cathodic arc with plasma immersion ion implantation. *Surface and Coatings Technology* 2003;174–175:76.
143. Fella R, Holleck H, Schulz H. Preparation and properties of WC-TiC-TiN gradient coatings. *Surface and Coatings Technology* 1988;36:257.
144. Zhang S, Bui XL, Fu Y, Butler DL, Du H. Bias-graded deposition of diamond-like carbon for tribological applications. *Diamond and Related Materials* 2004;13:867.
145. Bull SJ, Bhat DG, Staia MH. Properties and performance of commercial TiCN coatings. Part 1: Coating architecture and hardness modelling. *Surface and Coatings Technology* 2003;163–164:499.
146. Bull SJ, Bhat DG, Staia MH. Properties and performance of commercial TiCN coatings. Part 2: Tribological performance. *Surface and Coatings Technology* 2003;163–164:507.
147. Holleck H, Schier V. Multilayer PVD coatings for wear protection. *Surface and Coatings Technology* 1995;76–77, Part 1:328.
148. Suresha SJ, Math S, Jayaram V, Biswas SK. Toughening through multilayering in TiN-AlTiN films. *Philosophical Magazine* 2007;87:2521.
149. Lee D-K, Lee S-H, Lee J-J. The structure and mechanical properties of multilayer TiN/(Ti0.5Al0.5)N coatings deposited by plasma enhanced chemical vapor deposition. *Surface and Coatings Technology* 2003;169–170:433.
150. Karimi A, Wang Y, Cselle T, Morstein M. Fracture mechanisms in nanoscale layered hard thin films. *Thin Solid Films* 2002;420–421:275.
151. Lin J, Moore JJ, Moerbe WC, Pinkas M, Mishra B, Doll GL, Sproul WD. Structure and properties of selected (Cr-Al-N, TiC-C, Cr-B-N) nanostructured tribological coatings. *International Journal of Refractory Metals and Hard Materials* 2010;28:2.
152. Holleck H, Lahres M, Woll P. Multilayer coatings, Äîinfluence of fabrication parameters on constitution and properties. *Surface and Coatings Technology* 1990;41:179.
153. Wolfe DE, Singh J, Narasimhan K. Synthesis and characterization of multilayered TiC/TiB2 coatings deposited by ion beam assisted, electron beam, Äìphysical vapor deposition (EB-PVD). *Surface and Coatings Technology* 2003;165:8.
154. Wolfe DE, Singh J, Narasimhan K. Synthesis of titanium carbide/chromium carbide multilayers by the co-evaporation of multiple ingots by electron beam physical vapor deposition. *Surface and Coatings Technology* 2002;160:206.
155. Lin J, Moore JJ, Mishra B, Pinkas M, Sproul WD. Nano-structured CrN/AlN multilayer coatings synthesized by pulsed closed field unbalanced magnetron sputtering. *Surface and Coatings Technology* 2009;204:936.
156. Ma KJ, Bloyce A, Bell T. Examination of mechanical properties and failure mechanisms of TiN and Ti/TiN multilayer coatings. *Surface and Coatings Technology* 1995;76–77, Part 1:297.
157. Yau B-S, Huang J-L, Lu H-H, Sajgalik P. Investigation of nanocrystal-(Ti1-*x*Al*x*)Ny/amorphous-Si3N4 nanolaminate films. *Surface and Coatings Technology* 2005;194:119.

158. Hultman L, Bareno J, Flink A, Soderberg H, Larsson K, Petrova V, Oden M, Greene JE, Petrov I. Interface structure in superhard TiN-SiN nanolaminates and nanocomposites: Film growth experiments and ab initio calculations. *Physical Review B–Condensed Matter and Materials Physics* 2007;75:155437.
159. Kong M, Zhao W, Wei L, Li G. Investigations on the microstructure and hardening mechanism of TiN/Si3N4 nanocomposite coatings. *Journal of Physics D: Applied Physics* 2007;40:2858.
160. Lin C-H, Tsai Y-Z, Duh J-G. Effect of grain size on mechanical properties in CrAlN/SiN*x* multilayer coatings. *Thin Solid Films* 2010;518:7312.
161. Tsai SH, Duh JG. Microstructure and mechanical properties of CrAlN/SiN*x* nanostructure multilayered coatings. *Thin Solid Films* 2009;518:1480.
162. Wang YX, Zhang S, Lee J-W, Lew WS, Sun D, Li B. Toward hard yet tough CrAlSiN coatings via compositional grading. *Surface and Coatings Technology* 2013;213:346.
163. Blau PJ, Lawn BR, Testing ASf, Metallography MCE-o, Society IM. *Microindentation Techniques in Materials Science and Engineering: A Symposium Sponsored by ASTM Committee E-4 on Metallography and by the International Metallographic Society*, Philadelphia, PA, 15-18 July 1984: American Society for Testing Materials, 1985.
164. Zhang S, Sun D, Fu Y, Du H. Toughness measurement of thin films: A critical review. *Surface and Coatings Technology* 2005;198:74.

2 Toughness Evaluation of Thin Hard Coatings and Films

Xiaomin Zhang, Ben D. Beake, and Sam Zhang

CONTENTS

2.1 Introduction: Toughness Evaluation of Thin Hard Coatings and Films 48
2.2 Overview of the Qualitative Assessment of Toughness for Hard Coatings ... 49
2.2.1 Indentation Plasticity 49
2.2.2 Scratch Toughness 52
2.2.3 Impact Toughness 53
2.2.3.1 Nanoimpact Testing 54
2.2.3.2 Experimental Test Procedure 56
2.2.3.3 Progression of Damage with Continued Impact 56
2.2.3.4 Interfacial Toughness 58
2.2.3.5 Cutting-Tool Coatings 59
2.2.3.6 Postdeposition Coating Modification by Microblasting 60
2.2.3.7 Load Dependence, Substrate, and Microstructural Influences on Impact Toughness 62
2.2.3.8 Impact and Erosion of Thermal Barrier Coatings in Aero-Engines 63
2.3 Overview of the Quantitative Characterization of the Fracture Toughness for Hard Coatings 65
2.3.1 Toughness Evaluation from Radial Cracks 67
2.3.2 Toughness Evaluation from Circumferential Cracking and Spallation 71
2.3.2.1 Methodology of the Toughness Evaluation from Circumferential Cracking and Spallation 71
2.3.2.2 Debates About the Extraction of the Irreversible Work W_{irr} 71
2.3.2.3 Argument on the Methodology of Circumferential Cracking and Spallation for the Fracture Toughness of Thin Hard Coatings 77
2.3.3 Toughness Evaluation from Channel Cracking 83
2.4 Overview of the Microtensile Testing of Fracture Toughness for Standalone Thin Films 88
2.4.1 Inchworm Actuation 89

2.4.2 Membrane Deflection 89
2.4.3 Tension by Residual Stress 91
2.4.4 Bulging of Films 92
2.4.5 Macrotension of Substrate 95
2.4.5.1 Substrate Configuration 95
2.4.5.2 Loading Stage 96
2.4.5.3 Preparation of the Substrate Precrack 97
2.4.5.4 Preparation of Film Microbridges 98
2.4.5.5 *In Situ* Inspection in Testing 98
2.4.5.6 Extraction of the Fracture Toughness 98
2.4.5.7 A CNx Film Case Study 101
2.4.5.8 Loose-Columnar Aluminum Layer: A New Lift-Off Material for the Testing of a Film Deposited at an Elevated Temperature 106
2.4.5.9 Advantage of the Tension on Substrate Method 111
2.5 Summary 111
2.5.1 Hard Coatings 111
2.5.2 Thin Films 111
Acknowledgments 112
Abbreviations 112
Symbols 112
References 113

2.1 INTRODUCTION: TOUGHNESS EVALUATION OF THIN HARD COATINGS AND FILMS

Toughness is one of the crucial mechanical properties of a material. Toughness refers to the ability of a material to absorb energy during deformation up to fracture [1,2], usually measured in terms of fracture toughness. In classic mechanics, fracture toughness refers to the stress resistance of a material to fracture in the presence of a flaw, that is, the highest stress intensity that the material can withstand without fracture [3]. It is measured as the maximum stress intensity factor under plane strain condition [4,5]. To meet the "plane strain" condition, the specimen dimensions should satisfy

$$t, a, (W - a) \geq 2.5\left(\frac{K_{IC}}{\sigma_y}\right)^2 \tag{2.1}$$

where t and W are specimen thickness and width respectively, a is flaw size, σ_y is yield stress, and here K_{IC} is the critical stress intensity that a material can withstand without fracture. In essence, Equation 2.1 requires that the sample thickness should be large enough, the initial crack length and the "no-crack" region (i.e., $W - a$) should not be too small. For brittle bulk materials, the minimum thickness t is several to tens of micrometers [5,6].

For a hard coating deposited on a substrate, indentation and scratch methods provide effective ways to qualitatively evaluate the toughness of a coating material. "Indentation plasticity" is well correlated with durability of a coating in contact situations where contact stresses are high and some ductility is required to avoid brittle fracture. And the parameter, the so-called "scratch toughness" is a type of index indicating the damage tolerance of a coating when a diamond stylus, subjected to a linearly increasing load, is drawn across the coated surface.

Impact toughness was proposed for the evaluation of the fatigue fracture resistance of a coating. It is important that coated components display high impact toughness, particularly in applications involving severe mechanical contact such as high speed machining of hard-to-cut aerospace materials or the erosive conditions of aero-engines.

Measurement of fracture toughness for bulk materials is classical, and is done routinely in research or production, for instance, Charpy test, four-point or three-point bending, and so on [7,8]. However, because of the size limitation, making standalone thin films into specimens for classical fracture toughness measurement is difficult.

Based on radial cracking, circumferential cracking, as well as channel cracking patterns introduced through indentation upon the coating or bending of the substrate, several modes have been proposed yet for a quantitative analysis of the fracture toughness of the coating.

Microtensile testing is the most straightforward test to measure the fracture toughness of thin films. However, it is very challenging to prepare freestanding sample with microscale size and conduct a tensile test on them. Notable progress has been made in the micro- and nanoscale tensile testing in recent years. Quite a few methods have been proposed: the inchworm actuation method, membrane deflection method, residual stress tension method, film bulging method, as well as the most recent macrotension on substrate method.

In this chapter, the term "films" refers to freestanding films (i.e., without substrate), while "coatings" refers to that with a substrate. It is necessary to make this distinction because a substrate renders support and also brings constraints on the deformation and fracture of the coating on it.

2.2 OVERVIEW OF THE QUALITATIVE ASSESSMENT OF TOUGHNESS FOR HARD COATINGS

2.2.1 Indentation Plasticity

In 1960, before advanced testing techniques such as nanoindentation were even thought of, Greenwood and Williamson introduced a plasticity index that related the deformation in rough contacts to the ratio of E_r/H multiplied by a geometric factor [9]. Their equation is as shown in Equation 2.2:

$$\psi = (E_r/H)\sqrt{(\sigma/\beta)} \tag{2.2}$$

where ψ = a plasticity index, σ = standard deviation of the height of the contacting asperities, and β = their average radius. When $\psi \gg 1$, plastic deformation of

asperities occurs, even at minimal contact pressure. If $\psi < 0.6$ deformation is largely elastic and plastic contact can only be caused if surfaces are forced together under very large nominal pressure. This original plasticity index was considered as a general surface texture parameter combining material and topographic properties of solids in contact.

More recently, several researchers have observed that in addition to providing a direct route to the determination of hardness and modulus by contact mechanics based analysis of unloading curves, the entire indentation curve could be considered in terms of the energies involved and, therefore, provide a fingerprint for the relative elastic and plastic properties of the material being tested.

For an elastoplastic contact where fracture does not occur we can define a simple plasticity index as the ratio of plastic (irreversible) work done in indentation to the total work done (Equation 2.3). In a nanoindentation test it is simple to obtain the value of plasticity index since the plastic work done during indentation (W_p), and elastic (W_e) work done during the indentation since these parameters are direct outputs of the instrument software (Figure 2.1).

$$PI = W_p/W_{total} = W_p/(W_p + W_e) \tag{2.3}$$

In Equation 2.3, PI = plasticity index, plastic work = W_p, and elastic work = W_e. This simpler dimensionless plasticity index is also related to H/E_r (Equation 2.4) and often shows good correlation with tribological performance. Using a self-similar indenter, such as Berkovich, the approximate relationship between PI and H/E_r is given by Equation 2.4.

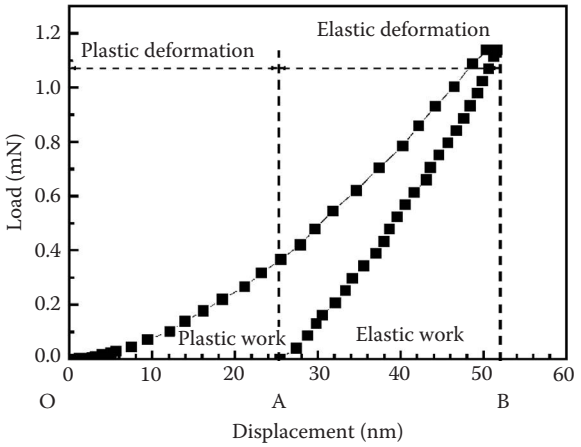


FIGURE 2.1 Schematic plot of a load–displacement curve obtained from nanoindentation. Plasticity is calculated as OA/OB and plastic work/(plastic work + elastic work.) (From Fox-Rabinovich, G.S. et al., *Thin Solid Films*, 2004. 469–470: 505–512; Fox-Rabinovich, G.S. et al., *Surface and Coatings Technology*, 2006. 200(20–21): 5738–5742.)

$$W_p/W_{total} \approx 1 - x(H/E_r) \tag{2.4}$$

Using FEA, Cheng and Cheng proposed that for an ideal pyramidal Berkovich geometry (equivalent conical angle 70.3°) the constant x should be ~5 [12,13]. This has been tested experimentally by several groups and it has been found that on bulk metallic materials and hard coatings x is typically closer to 7 with only ~5 for glasses [14–16]. Choi and coworkers [16] have suggested that the relative importance of pile-up and sink-in is responsible but since the higher values are also observed for hard brittle coatings that do not pile up the situation is more complex. A high H/E_r ratio also increases radial dilation effects on unloading, which cause the size of the residual indentation to be underestimated by calculation of the projected contact area from the contact depth [17]. Another possibility is that on materials with high H/E the displaced material is accommodated elastically under the indent and much of this is not recoverable due to the plastic deformation around the indentation; so the irreversible term, W_p, may contain a contribution from locked-in elastic deformation in addition to normal plastic deformation. When using sharp indenters to measure hardness, the applied load should be high enough to ensure that the coating exhibits full plasticity and indenter rounding at the low indentation depths required to measure coating properties is minimized.

Milman [18] has postulated that the underlying relationship is more complex, involving the material's Poisson ratio, as proposed in Equation 2.5.

$$PI = 1 - x(1 - \nu - 2\nu^2)H/E \tag{2.5}$$

with $x = 10.2$ the best fit, although the reported data did not precisely fit this, particularly below $PI = 0.5$ where the data were far from the fitted line. Beake et al. reported data showing that $x = 11.2$ is a better fit over the range of PI of 0.6–1 [15]. In this relationship, and the simpler Equation 2.4, it is important to note that the behavior only approximates to linearity. Deviation from linearity is more significant above $\sim H/E > 0.1$. An elastic recovery parameter (termed η in ISO14577 [19]) has been defined as $(1 - PI)$ so that

$$\eta = W_e/W_t \tag{2.6}$$

Although the formulations in Equations 2.2 and 2.4 are somewhat different, both these plasticity indices reflect essentially the same behavior with varying mechanical properties; namely that in both cases increasing H/E results in a lower plasticity index and more elastic contact. Matthews and Leyland have shown that the H/E index can be directly linked to wear [20,21]. A higher H/E (lower plasticity index) is beneficial for improved wear resistance in many tribological contact situations. Higher H/E values result in higher critical loads for the onset of yield (nonelastic deformation) in indentation or sliding contact, since the coatings with higher H/E usually have higher values of H^3/E_r^2, which is a measure of their resistance to plastic deformation. For a given applied load contact is more elastic and wear should be minimized.

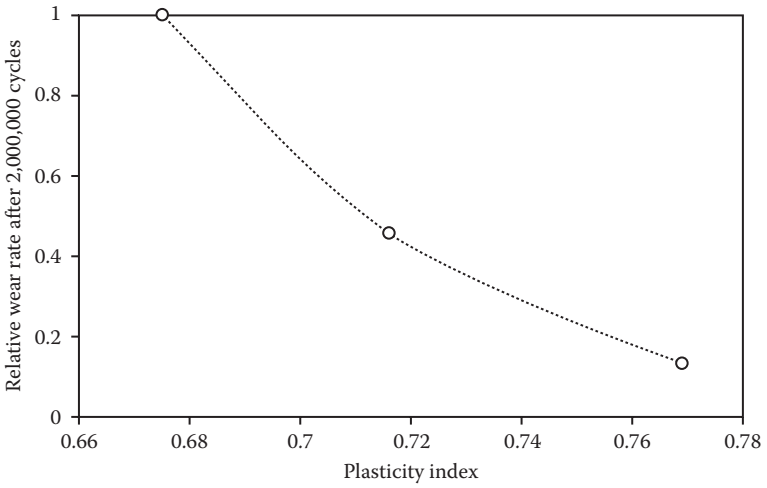


FIGURE 2.2 Variation in relative wear rate in high-performance stamping of magnetic steels with plasticity index for different cemented carbide grades.

However, when coatings are developed for highly loaded contact applications higher plasticity in indentation has been correlated with higher toughness and durability in application conditions since fracture dominated wear can be life-limiting [11,16,22,23]. Toughness is not the same as plasticity, but under highly loaded conditions cracks can propagate to failure where dissipative mechanisms such as plasticity do not exist so the two properties can be very well correlated. For example, in high-performance stamping, it is the harder grades of carbide that show much higher wear rates [15,23]. In contrast, grades that combine (slightly) lower hardness with higher stiffness, resulting in higher plasticity, dramatically outperform the hardest grade. This is illustrated in Figure 2.2. Higher plasticity in the carbides improves their chipping resistance. SEM images of the worn surface of a cemented carbide grade with high hardness but at the expense of plasticity showed numerous cracks forming on a surface as a result of intensive adhesive-fatigue wear.

2.2.2 Scratch Toughness

Scratch testing is most widely used in evaluating adhesion strength of hard coatings. During the test, a diamond stylus subjected to a linearly increasing load is drawn across the coated surface until adhesion failure is induced at a critical load. Generally (but not necessarily), for hard coatings, microcracks appear in the scratch track before failure occurs [24]. The minimum load at which the first crack occurs is termed as the "lower critical load" L_{c1}, and the load corresponding to the complete peeling off of the coating is the "higher critical load" L_{c2} (Figure 2.3). Some researchers directly used the lower critical load to indicate crack resistance, or even termed it "scratch toughness" [25–30].

An interesting concept for providing a qualitative assessment of differences in coating toughness has been recently developed by Zhang and coworkers [32,33].

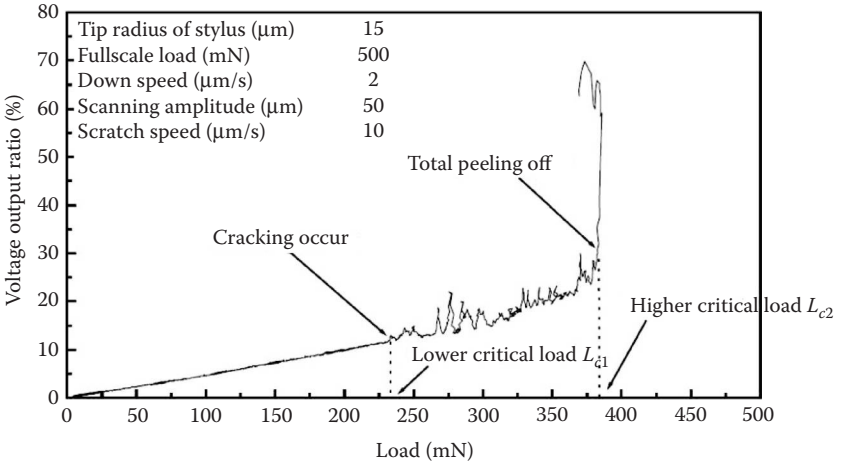


FIGURE 2.3 Scratch adhesion profile. (From Zhang, S. et al., *Thin Solid Films*, 2004. 447–448: 462–467.)

They equated L_{c1} with the resistance to the initiation of cracks and $(L_{c2} - L_{c1})$ as a measure of the toughness (L_{c2} = load for total fail). They defined a parameter representing resistance to crack initiation and also propagation as follows:

$$\text{Scratch crack propagation resistance parameter (CPR)} = L_{c1}(L_{c2} - L_{c1}) \qquad (2.7)$$

The assumption is that the crack systems responsible for the L_{c1} and L_{c2} failures are linked, which may not be true in all cases. Nevertheless, scratch test data on hard coatings show large differences in CPR with a maximum in scratch toughness being reported at intermediate values of hardness.

Colligon and coworkers proposed that the dimensionless scratch durability ratio given by Equation 2.8 could also be a suitable parameter for assessing film durability and toughness [34,35].

$$\text{Scratch durability ratio} = (L_{c2} - L_{c1})/L_{c1} \qquad (2.8)$$

This ratio more strongly emphasizes the durability of the coating after the initial cracking occurs and can be considered as a type of damage tolerance index. It may enable useful comparison between critical loads obtained in scratch tests with different end radius indenters more easily due to the normalizing effect of dividing by the lower critical load.

2.2.3 Impact Toughness

It is important that coated components display high impact toughness, particularly in applications involving severe mechanical contact such as high speed machining of hard-to-cut aerospace materials or the erosive conditions of aero-engines.

2.2.3.1 Nanoimpact Testing

Nanoimpact testing is a nanomechanical test technique involving high strain rate contact. It was primarily designed to assess the toughness and fatigue fracture resistance of thin films although it has a much wider range of applications, as illustrated in Tables 2.1 and 2.2. The strain rates are typically ~10^2–10^3 s^{-1} [36], which is much larger than in a nanoindentation test (commonly ~10^{-2}–10^{-4} s^{-1}). This high strain rate contact allows much closer simulation of the performance of coatings systems under highly loaded intermittent contact (such as interrupted cutting and erosive wear) and the evolution of wear under these conditions. The repetitive contacts are true impact events where the probe leaves the surface between each subsequent impact, which occurs at the same location on the sample surface. The progression of surface damage is followed using the depth-sensing capability of the instrumentation. Practice has shown a high degree of correlation between results of nanoimpact tests and the performance of coated systems operating in extreme intermittent contact environments.

The nanoimpact test does not immediately provide a value of the *quasi-static* fracture toughness K_{1c} but rather an assessment of the sample's resistance to fatigue fracture, or effective *dynamic* toughness, under dynamic and repetitive loading that can be more representative of actual contact conditions in applications.

TABLE 2.1
Applications of Single Nanoimpacts

Property Investigated	Materials Studied	Reference
Strain rate sensitivity	Polymers	[37]
Dynamic hardness	Al, Mg alloys, NiW	[36,38]
Dynamic *H*/*E*	Al-12Si UFG cladding	[39]
Energy absorption	Tissues and tissue surrogates	[40]

TABLE 2.2
Applications of Repetitive Nanoimpacts

Property Investigated	Materials Studied	Reference
Fracture resistance	Ni-5%Al coatings deposited by HVOF, APS, and CS	[41]
	PEO coatings on Ti6Al4V	[42]
	Nanocomposite films on polymers	[43]
	TiAlN coatings	[11,14]
	CrAl(Si)N coatings deposited by cathodic arc	[44,45]
Fracture toughness	Intermetallic $Al_{12}(Fe,Cr)_3Si_2$ coatings on 316L stainless steel	[46]
	NiTi on Silicon	[47]
Evolution of dynamic hardness and debonding	Sol–gel on stainless steel	[48]
Debonding	DLC on Si	[49–51]
	250 nm Pt–Ir coatings on binder-less cemented carbide tools	[52]
Erosive wear	EB-PVD thermal barrier coatings	[53]

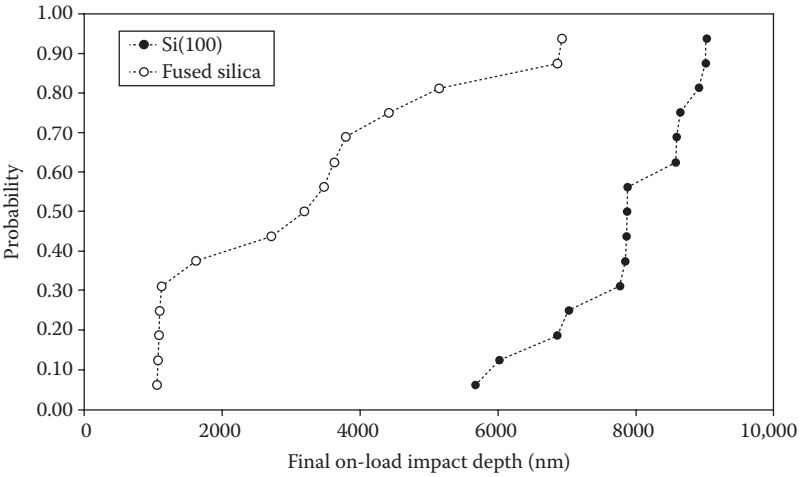


FIGURE 2.4 Nanoimpact behavior of fused silica and Si(100) impacted with a 4.6 μm end radius spheroconical diamond at 40 mN.

As an illustration, the behavior of two bulk materials, fused silica and Silicon (100), under repetitive impact is shown in Figure 2.4. This figure shows the results of an impact with a 4.6 μm end radius spheroconical diamond at 40 mN at 15 different positions on the surface. Both materials show a stochastic response, with a wide variation in the final impact depth. Under the test conditions, the depth at 50% probability was 3200 nm on fused silica but 7900 nm on Silicon (100). Although they are reported to have similar quasi-static fracture toughness values (~0.9 MPa $m^{1/2}$) it is clear that under the repetitive high strain rate conditions the silicon wafer behaves in a more brittle manner. Silicon is known to exhibit rate sensitivity to indentation contact and complex wear behavior in intermittent contact situations such as abrasive water jet machining [54]. Since the phase transformations that occur on loading and unloading have been shown to exhibit some rate sensitivity [55,56] it seems plausible that this may be implicated in the impact behavior (strain relief by phase transformation being much less efficient when contact occurs at high strain rate) [57].

Nevertheless, Frutos and coworkers [46] have recently reported quantitative measurements of the quasistatic fracture toughness K_{1c} of intermetallic coatings using the repetitive nanoimpact test. The intermetallic $Al_{12}(Fe,Cr)_3Si_2$ coatings were deposited on medical grade stainless steel by hot dipping in an Al-12.6 wt.% Si alloy for 60–600 s. With repetitive contact by a cube-corner diamond indenter they were able to generate well-developed cracks at loads/depths well below those in quasistatic indentation. Since the depths were lower the crack system developed without any interference from the interface and substrate, which is not typically the case when measuring the toughness of thin films by indentation-induced crack propagation methods. Hardness, compressive residual stress, and fracture toughness were reported to decrease with continued immersion time although Young's modulus was unaffected and the supplied impact energy to coating failure increased.

2.2.3.2 Experimental Test Procedure

In the nanoimpact test parameters such as probe geometry, acceleration distance, coil force, impact angle, number of cycles, and test frequency can all be controlled to alter the severity of the test and its duration. The position of the impacting diamond probe is recorded throughout the test allowing the progression of damage to be monitored. At the beginning of the test, the surface contact by the impact probe under a minimum contact load determines the depth zero. The static coil force is then applied producing elastoplastic deformation by indentation. By electromagnetic actuation the impact probe is rapidly removed to ~10–15 μm from the surface and then accelerated over this distance to impact the surface. Periodic actuation produces repetitive impacts. A cube-corner diamond indenter whose geometry induces high contact strain is commonly chosen, as this high contact strain is beneficial in inducing fracture within a quite short test time.

Typical impact test parameters for testing hard coatings are as follows:

- Impact probe cube-corner diamond, impact angle 90°.
- Applied load 25–150 mN, accelerating distance 15 μm.
- Impact frequency 0.25 Hz, test duration 300 s (75 impacts in total).
- Number of repeats 10 for each load chosen.

2.2.3.3 Progression of Damage with Continued Impact

A single impact is essentially a high strain rate indentation test. Analysis of the impact-time data can determine the "dynamic hardness" of material, that is, its effective hardness at a given strain rate, following the procedures explained by Schuh, van Vliet, and others [36,37,48].

When multiple impacts are performed on a ductile material there is a gradual increase in probe penetration depth, which decreases with continued impacts, particularly for strongly work-hardening materials. In contrast, for a brittle material there are often several abrupt increases in probe depth during the test. Jennett and Nunn have shown that there is a clear increase in the energy absorbed for impacts causing immediate fracture [58]. For example, Figure 2.5 shows the initial response of fused silica to repetitive impact data at 8 mN with a cube-corner diamond indenter. The impact resulting in a large abrupt change in depth in this test (the eight impact) is correlated with enhanced energy absorption. The nanoimpact behavior of a $Ti_{0.4}Al_{0.6}N$ coating has been simulated by 3D-FEM by Bouzakis and coworkers [59]. Their model used the failure of constrained tied nodes to simulate crack formation and propagation as the plastic strain develops and exceeds the coating failure strain with repetitive impact. The nanoimpact FEM simulation was able to predict the film failure initiation and evolution on repetitive impacting with a cube-corner diamond indenter at 10–50 mN impact force.

The general response of a brittle material to repetitive contact in the nanoimpact test has been summarized as [60]

i. *Initial impact*—some plastic deformation occurs and cracks begin to nucleate subsurface.
ii. *Fatigue*—growth of cracks subsurface and further nucleation with little or no change in probe depth.

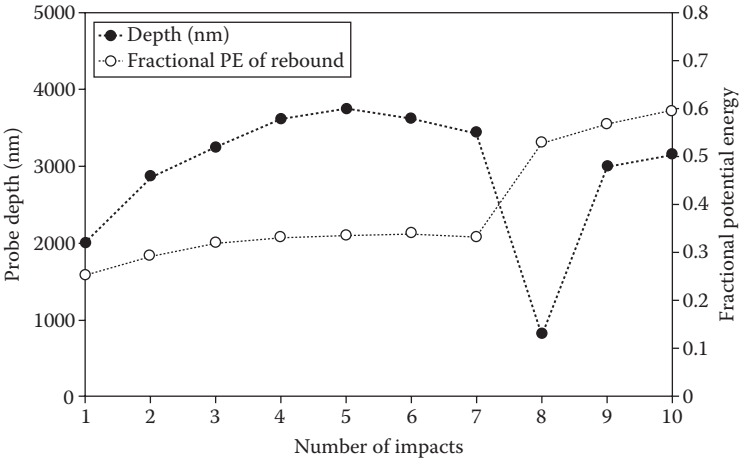


FIGURE 2.5 Correlation between fractional potential energy and probe depth in the repetitive impact test.

iii. *Crack coalescence and fracture*—rapid change in probe depth on material removal.
iv. *Repetition of the fatigue cycle*—long periods where the depth remaining fairly constant separated by abrupt fracturing events.

Impact data on Si (100) are consistent with this and are stochastic in nature (Figure 2.4). Brittle behavior is also observed on hard ceramic coatings. Figure 2.6 illustrates this for two coatings with similar initial impact behavior but clear differences in impact toughness upon repetitive contact [61].

Impact resistance of different coatings can be compared by the time required for failure (fracture) to occur in 50% of the tests, enabling comparison between similar materials. Fracture probability can be estimated by ranking the time-to-failure events in order of increasing fatigue resistance and then assigning a probability of failure (Equation 2.9)

$$P(f) = n/(N + 1) \tag{2.9}$$

to the nth ranked failure event in a total sample size of N, analogously to the treatment of distributions of failure stresses in Weibull statistics. The probability of failure with a given time (usually the end of the test) is a convenient way to compare all the films together. By combining fracture probability data at different loads it is possible to produce a graph of median time or number of impacts to fracture versus impact force (analogously to a stress life diagram) [60]. The energy supplied for coating failure can be calculated from the time-to-failure data using Equations 2.10 and 2.11.

$$\text{Energy per impact} = \text{force} \times \text{accelerating distance} \tag{2.10}$$

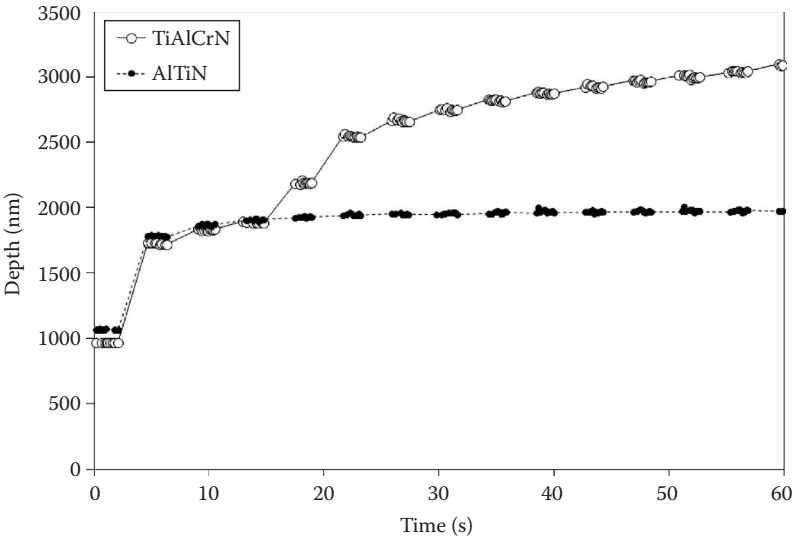


FIGURE 2.6 Impact test on TiAlCrN and AlTiN coatings on WC-Co.

$$\text{Total energy supplied} = \text{number of impacts} \times \text{energy per impact} \quad (2.11)$$

For typical test conditions of 1 impact every 4 s the number of impacts to failure = 0.25 × time-to-failure in seconds.

2.2.3.4 Interfacial Toughness

Film failure by fracture with high contact strain (e.g., cube corner) indenters is typically associated with large abrupt increases in probe depth during the test. The time-to-fracture and final impact depth can be highly stochastic. Nevertheless, Beake has shown that for DLC coatings the depth-at-failure can be remarkably constant [62]. In contrast, when spherical probes are used at low impact forces a backward depth evolution can be observed (i.e., the on-load probe depth decreases with continued impacts) [48,51]. This behavior has been confirmed by posttest AFM imaging of impact scars showing volume uplift and has been interpreted as due to interfacial delamination without (or before) the accompanying fracture that results in the increase in depth. Under these conditions stresses are relatively low and impact-induced plasticity is minimized. This raises the intriguing possibility that the impact test may be used to assess adhesion and interfacial toughness. Faisal and coworkers reported that in the repetitive impact testing of 100 nm DLC film on Si, the geometry of the impact probe influenced the deformation [51]. Using a 10 μm end radius spheroconical indenter resulted in delamination and uplift, and a Berkovich resulted in extensive fracture. When testing ~500 nm CVD DLC films on Si with a 25 μm end radius spherical indenter at 1 mN, Beake and coworkers reported the probability of interfacial and cohesive failures that varied slightly with deposition power [49]. Films deposited at higher RF power failed more rapidly but films did not delaminate as readily as films

deposited at lower RF power suggesting improved adhesion strength. The nanoimpact test has been used to assess the influence of depositing thin adhesion promoting interlayer of 15–50 nm Ni or Cr prior to the deposition of 250 nm Pt-Ir coatings on binder-less cemented carbide tools used for precision glass molding [52]. On coatings without interlayer the probe depth continued to increase dramatically as the repetitive impact test progressed but coatings with interlayer were more impact-resistant with the best impact resistance for a Pt-Ir coating with a 50 nm Cr interlayer.

2.2.3.5 Cutting-Tool Coatings

Cutting-tool coatings operating in demanding machining operations such as face and end milling need to display high resistance to adhesive wear and excellent fatigue properties to extend tool life. A typical failure mechanism of cutting tools during milling is low cycle thermal fatigue due to thermal cycling impact. For example, this failure mechanism is important for end milling of Ti alloys when intensive adhesive interaction between work piece material and cutting tool surfaces take place. The adhered material tears off during further cutting resulting in intensive adhesive-fatigue wear of tool accompanied by intensive chipping of its cutting edges. The severity of the cutting conditions and the material being machined both influence the relative importance of factors such as energy dissipation (plasticity) and high temperature hardness. Nevertheless, room temperature nanoimpact tests have been used successfully by several groups to simulate end and face milling. The test results correlate well with the longer, more laborious, and expensive tests of cutting tool life, ranking coating performance in terms of tool life in end milling and simulating the evolution of the tool wear.

Since their introduction three decades ago, TiAlN coatings with equal Ti and Al fractions have proved to be highly popular coatings for a wide variety of applications requiring high wear resistance. Nevertheless, a growing body of experimental and theoretical evidence shows that they combine high hardness with relatively low toughness and therefore perform less well in demanding applications where toughness and fatigue resistance are important. Newer coatings have been developed based on compositional change, such as alloying (e.g., with Cr), and/or increasing the Al fraction is proving successful in challenging applications such as high-speed machining of hard-to-cut materials. Sangiovanni and coworkers have applied density functional theory calculations to estimate the ductility of $(TiAl)_{1-x}M_xN$ films with the cubic B1 structure where M = V, Nb, Ta, Mo, and W [63,64]. Their calculations suggested increased ductility due to enhanced occupancy of $d - t_{2g}$ metallic states induced by the valence electrons of the substitutional elements. Ductility was assessed by G/B ratio and Cauchy pressure ($C_{12}-C_{44}$) criteria where ductile behavior is predicted for $G/B < 0.5$ and $(C_{12}-C_{44}) > 0$. TiAlN has a rather high G/B ratio of 0.665 consistent with its observed brittleness. Many of the alloyed compositions they investigated showed lower G/B together with retention of hardness. They reported that the "super toughening" effect was more pronounced with increasing valence electron concentration leading to a layered electronic structure on shearing and a selective response to applied stress. If tensile/compressive stresses are applied the structure responds in a hard manner but if shear stresses are applied the layered structure forms and the system could display ductile/tough behavior by dislocation

glide on an activated slip system. Super toughening of B1 transition metal nitride alloys by valence electron tuning is an intriguing approach. However, the extent of correlation between the theoretical ductility parameters and their predicted mechanical properties is not yet clear. For the TiAlMoN and TiAlWN systems the *lower G/B* values were typically associated with *higher H/E* (which experimentally has lower plasticity in indentation), which may cast some doubt on the ability of the approach to reliably predict ductility in these complex coatings.

TiAlN variants with differing Ti:Al ratios have been developed. The results of cutting tool tests show that increasing the Al content from 50% to 67% is beneficial for end and face milling applications despite the small drop in hardness that results. High-Al coatings (AlTiN, AlCrN) can show less fracturing than TiAlN and consequently abrupt/unstable wear in face and end milling is minimized. The highly loaded and high strain rate contact conditions in the interrupted cutting tests have been simulated in nanoimpact tests, which can assess the coating system behavior under low cycle fatigue. In Figure 2.7, illustrative data on TiAlN- and AlCrN-coated inserts are compared with end milling tests on 1040 structural steel. Abrupt changes in slope in the nanoimpact test correspond to fracture. There is obvious correlation between the two tests, with AlCrN-coated inserts showing greater fracture resistance on repetitive nanoimpact and longer tool life in the end milling cutting test. The evolution of tool wear process in the longer cutting test is mirrored in the nanoimpact test.

Elevated temperature nanoimpact tests have been performed for TiAlN- and AlTiN-coated WC-Co cutting tool inserts [65]. The brittleness of TiAlN and AlTiN has been assessed by fracture probability data analysis, which allows for the stochastic nature of the impact fracture process to be examined. Although the room temperature plasticity is similar the nanoimpact test showed significantly more brittle behavior for TiAlN. Fracture probability data from nanoimpact tests at 500°C on TiAlN- and AlTiN-coated WC-Co inserts have been shown to correlate with the plasticity index and cutting tool life data (Table 2.3). At 500°C the fracture probability decreased, consistent with the higher plasticity shown by high temperature nanoindentation. TiAlN fractures more extensively than AlTiN at high temperature, consistent with more unstable and greater wear in interrupted cutting applications that generate significant heat (milling) as has been observed in machining tests. The lower brittleness of the AlTiN coating helps provide more favorable, low wear conditions for effective tribo-film formation. The tribo-films produced from higher Al-fraction coatings are also predominantly alumina-based while those from TiAlN are more futile and less protective. The alumina tribo-films protect the cutting tool surface against the chipping that is typical for cutting operations with intensive adhesive interaction with work piece materials such as machining of Ti-based alloys.

2.2.3.6 Postdeposition Coating Modification by Microblasting

Microblasting induces compressive stresses that can be beneficial in reducing wear although the results are highly dependent on pressure and grain size and the geometry of the abrasive materials since the induced compressive stresses can result in increased brittleness. In studying the optimum parameters in post deposition wet microblasting for improved cutting performance of PVD-coated tools Bouzakis and

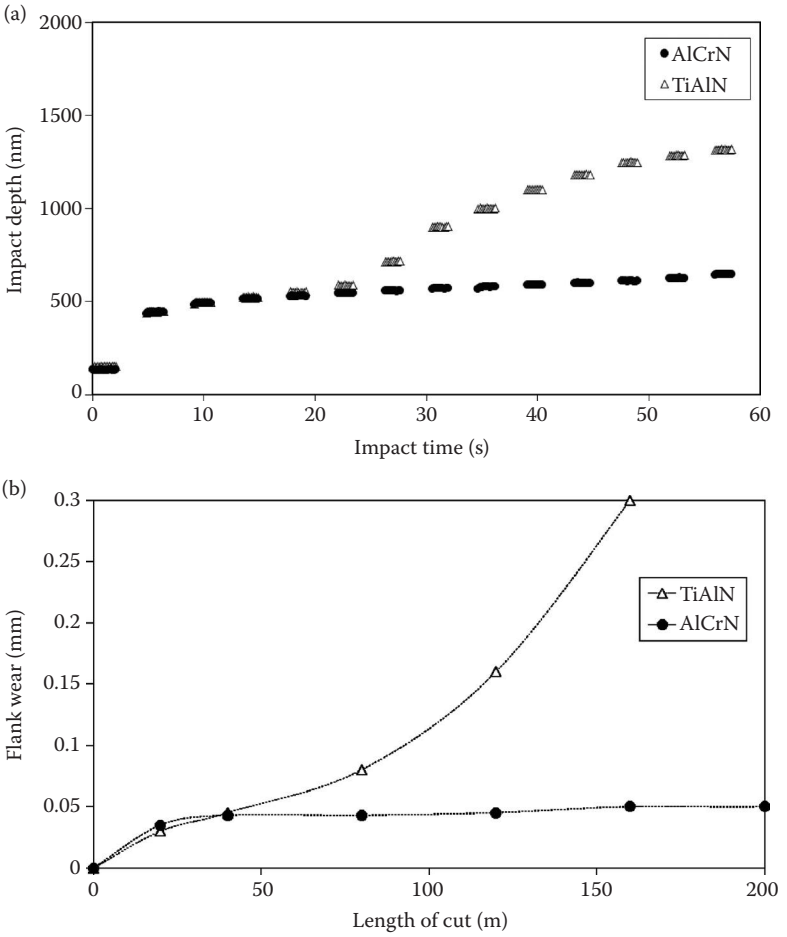


FIGURE 2.7 (a) Nanoimpact tests on TiAlN and AlCrN coated inserts. (b) End milling tests on structural steel using TiAlN and AlCrN.

coworkers supplemented their tool life data with nanomechanical testing and FEM [64–68]. For the same microblasting conditions and abrasive diameter, the abrasion with ZrO_2 was less intense than Al_2O_3 due to the spherical nature of the ZrO_2 [66]. To investigate the influence of the developed compressive stresses on the film brittleness they performed nanoimpact tests. Data from their studies is illustrated in Figure 2.8, which shows correlation between the results of the nanoimpact tests and the cutting performance when milling hardened steel (AISI 4140). Under these conditions, low-impact depth (high impact resistance) is strongly correlated with cutting tool life. The trends in tool life with microblasting pressure are well reproduced by the nanoimpact test. The relative ranking of cutting performance after microblasting with ZrO_2 and Al_2O_3 at a given pressure, and the switch in relative performance between 0.2 and 0.4 MPa are well reproduced.

TABLE 2.3
Correlation between Plasticity Index in Nanoindentation, Fracture Probability in the Nanoimpact Test, and Tool Life in Face and End Milling

Test Temperature/°C	Coating	Plasticity Index[a]	Fracture Probability[b]	Relative Tool Life in End Milling[c]	Relative Tool Life in Face Milling[d]
25	AlTiN	0.52	0.4		
25	TiAlN	0.48	0.8		
500	AlTiN	0.73	<0.2	1.2	1.9
500	TiAlN	0.70	0.5	1	1

[a] From nanoindentation.
[b] Defined as probability of fracture occurring within the duration of the impact test.
[c] End milling of 4340 steel.
[d] Face milling of 1040 steel.

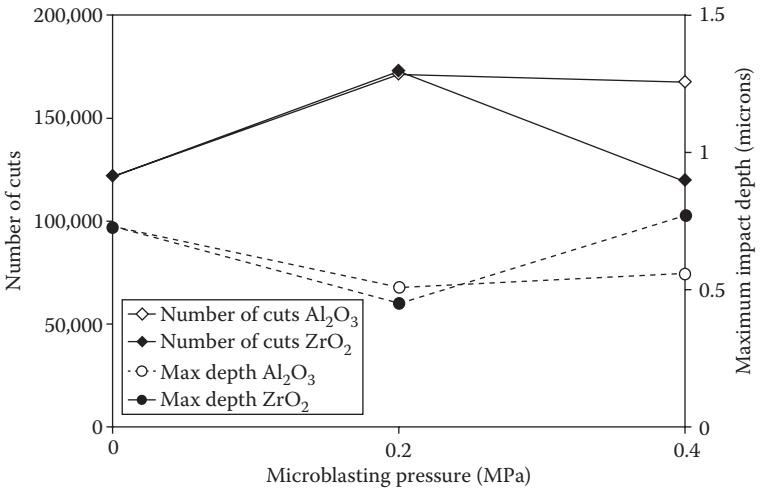


FIGURE 2.8 Greater impact resistance correlates with greater cutting performance in studies of postdeposition microblasting.

2.2.3.7 Load Dependence, Substrate, and Microstructural Influences on Impact Toughness

The mechanical behavior of the substrate influences the strain accumulation under impact. A good illustration is the impact wear of TiAlN and TiN coatings on ductile (AISI D2 steel) and brittle (WC-Co) substrates [69]. On D2 steel, the coating system with higher H^3/E^2, TiAlN, showed a reduced impact wear volume and a greater number of impact cycles required to cause fracture. The more ductile substrate minimizes the accumulation of elastic strain at high load. The behavior was completely

different when the coatings were deposited on the more brittle WC-Co. Although initially more resistant than the TiN, with continued impacts the TiAlN showed pronounced brittle cracking so that the impact wear volume was increased dramatically.

Chen and coworkers have studied the load dependence of the impact behavior of multilayer TiAlSiN ($H = 32$ GPa) and monolayer TiN ($H = 29$ GPa) coatings on M2 steel [70]. The parameters H/E_r and H^3/E_r^2 were significantly higher on the TiAlSiN. Using a well-worn cube-corner indenter they performed nanoimpact tests over 10–150 mN using subsequent SEM imaging of FIB-sectioned impact craters to determine the failure mechanisms across the load range. At the lowest load of 10 mN, cracks were observed on the monolayer TiN but were absent on the multilayer TiAlSiN, which required 30 mN for the onset of cracking. The higher crack initiation threshold for the multilayer is consistent with its higher H^3/E_r^2. When the load was increased spallation was observed in both coatings. The multilayer TiAlSiN coating showed less spallation, presumably as its multilayered structure aided crack deflection and minimized crack propagation.

By investigating individual impact depth versus time curves in detail, it is possible to separate film behavior into three distinct regimes as the test progresses: (i) load support (preimpact), (ii) initial impact, and (iii) subsequent impacts. This procedure enables the role of film properties on load support, initial resistance to crack nucleation, and subsequent crack propagation to be determined [71]. In Figure 2.9, the data for a TiFeN film with very high H^3/E_r^2 is contrasted with the data for a TiFeMoN film with lower H^3/E_r^2. Although resistance to single impact is improved by increasing H^3/E_r^2, durability at high dynamic contact load is not. At lower impact load, the ratio of impact depth to film thickness is low so higher H^3/E_r^2, in the film is beneficial by preventing cracks from forming in the first place. Increasing H^3/E_r^2 has been associated with high resistance to cracking and hence high fracture toughness. However, without a beneficial microstructure such as multilayer [72] or nanolaminate, simply depositing a coating with very high H^3/E_r^2 does not guarantee improved impact resistance at high load, particularly if the coating is unable to protect the underlying substrate from deforming. At higher impact load, effective durability and damage tolerance requires resistance to both formation and propagation of cracks under dynamic loading.

2.2.3.8 Impact and Erosion of Thermal Barrier Coatings in Aero-Engines

In the hostile environment of an aero-engine, thermal barrier coatings (TBCs) must display the optimum combination of mechanical and thermal protection to the underlying super alloy substrate. They can be subjected to a wide range of damage modes and microstructural changes including oxidation, erosion, foreign object damage, compaction, calcium–magnesium–aluminum–silicate attack, and sintering. Along with bond coat oxidation, erosion of TBCs has been acknowledged as one of the key factors influencing their service life. The three main mechanisms of erosive damage on EB-PVD TBCs have been determined as (i) erosion (lateral cracking/subsurface cracking), (ii) compaction, and (iii) foreign object damage. The ratio between the contact diameter of the impacting particle (D) and the column diameter of the coating (d) has been shown by Wellman and Nicholls to correlate with the type of erosion

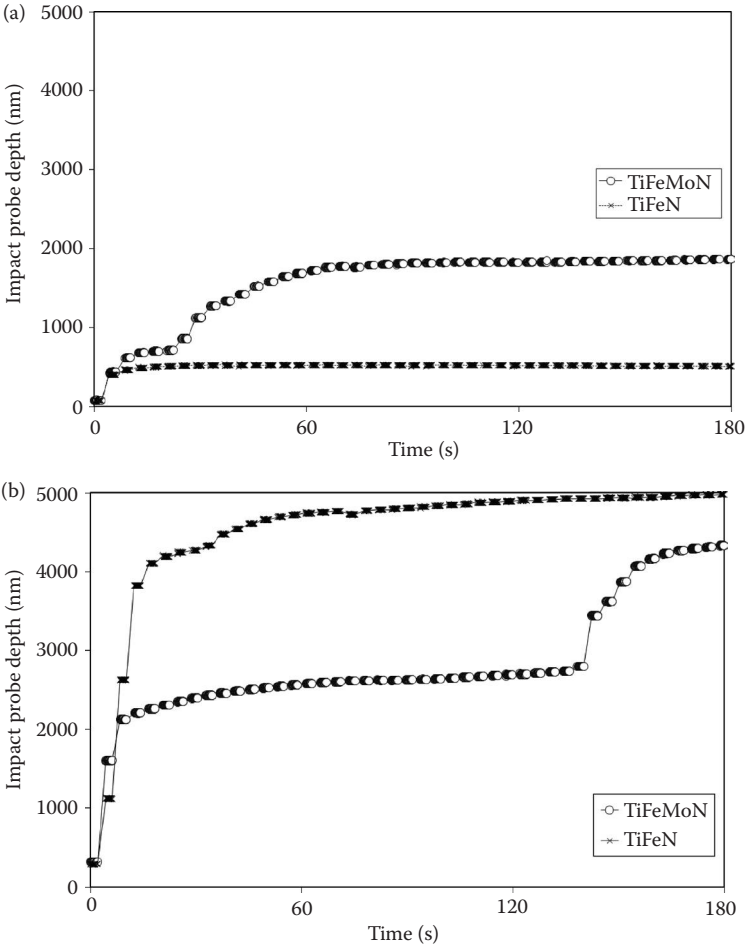


FIGURE 2.9 Impact performance of TiFeN and TiFeMoN films at (a) 5 mN and (b) 25 mN.

behavior observed [73]. A value of *D*/*d* of less than 2 indicates an erosion mechanism, while a value greater than 2 indicates a compaction mechanism, and greater than 12 a foreign object damage mechanism. For EB-PVD TBCs the columns are usually 10–15 μm in diameter and in the erosion mechanism the contact footprints are 5–25 μm in diameter so that *D*/*d* is <2.

To reliably simulate the erosion mode mechanism it is necessary that the test be performed at the correct length scale since many mechanical properties (such as hardness and yield stress) usually depend on the length scale probed by different methods, particularly for materials with complex microstructures such as TBCs. Chen et al. have recently investigated the role of coating microstructure and mechanical properties of 150 μm thick TBCs after thermal aging at 1100–1500°C and investigating the extent of correlation with their behavior

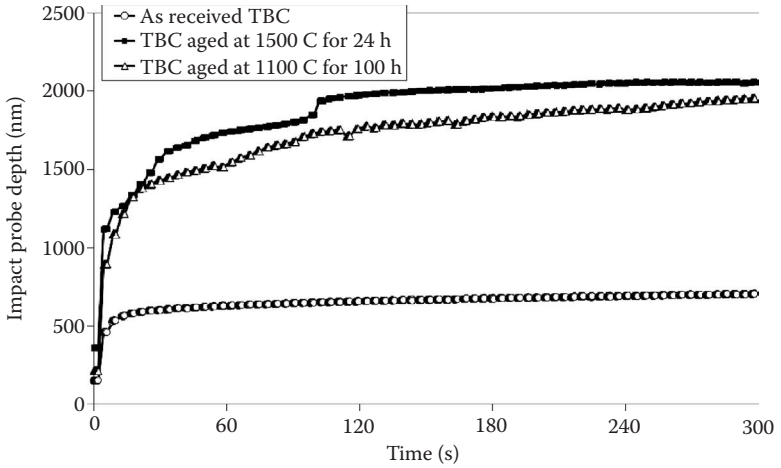


FIGURE 2.10 Influence of thermal aging for 24 h at 1500°C and 100 h at 1100°C on the impact resistance of an EB-PVD TBC at 10 mN.

in repetitive nanoimpact and conventional erosion tests [53]. The thermal aging changes the microstructure and mechanical properties of EB-PVD TBC systems, increasing their hardness, stiffness, H/E, and H^3/E_r^2. The columnar microstructure undergoes intercolumn sintering, particularly at 1500°C. This results in an increased bulk erosion rate after aging since damage can extend across several columns resulting in more material removal. As a repetitive dynamic test producing damage on the correct length scale, the nanoimpact test was highly effective in simulating the erosion mechanism. It showed greater impact wear after aging (Figure 2.10), correlating with differences in the measured bulk erosion rate. Nanoindentation alone would not be able to predict this since there was no clear correlation between any of the TBC mechanical properties and the bulk erosion rate. For this application, the nanoimpact test is preferred to conventional nanoindentation as the dynamic strain rates are much higher. The nanoimpact test could potentially be used as a rapid screening test to evaluate the erosion resistance of novel TBCs compositions.

2.3 OVERVIEW OF THE QUANTITATIVE CHARACTERIZATION OF THE FRACTURE TOUGHNESS FOR HARD COATINGS

Scratch testing is most widely used in evaluating adhesion strength of hard coatings. During the test, a diamond stylus subjected to a linearly increasing load is drawn across the coated surface until adhesion failure is induced at a critical load. Generally, for hard coatings, microcracks appear in the scratch track before failure occurs [24]. Some researchers directly used the critical load to indicate crack resistance, or even termed it "scratch toughness" [25–30]. Hoehn et al. proposed

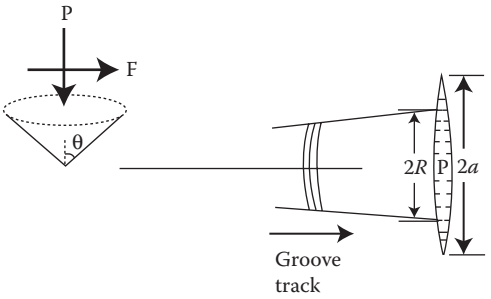


FIGURE 2.11 Schematic diagram of the microscratch fracture toughness measurement with a pressure P opening a crack (2*a*) out of a groove width 2*R*. (From Hoehn, J.W. et al., *Materials Science and Engineering A*, 1995. 192–193(Part 1): 301–308.)

simplified model of scratch trying to obtain the fracture toughness from the cracking of the coating (Figure 2.11) [74]:

$$K_{IC} = \frac{2pf_g}{R^2 \cot\theta}\left(\frac{a}{\pi}\right)^{1/2} \sin^{-1}\frac{R}{a} \tag{2.12}$$

where p is the pressure opening the crack, R is the radius of the indenter cone into the groove, $2a$ is the total crack length, and f_g is the coefficient of grooving friction, which depends on the cone angle 2θ and can be obtained from the scratch track width and the depth of penetration.

Holmberg et al. divided the material response during scratch into three components: ploughing, interface sliding, and pulling a freestanding coating as shown in Figure 2.12, and then proposed a 3D finite element model for the fracture toughness of a coating [75]:

$$K_{IC} = \sigma\sqrt{b} f(a,b) \tag{2.13}$$

where σ is the tensile stress that induces the crack, a is the crack length, and b is the crack spacing, $f(a,b)$ is a nondimensional function.

The above methods try to obtain the fracture toughness of a coating through analyzing the stress state of the coating beneath the scratch stylus. But these models are not practically applicable because of the complexity of the actual state of forces in the groove ahead and right below the stylus tip are much complex. The deformation of the coating and the strain–stress state are nonaxial symmetric, which make it extremely hard for the extraction of the tensile stress responsible for the coating cracking. Besides, the moving of the stylus on the coating surface makes the strain–stress of the coating overcomplicated by the existence of the friction.

For a hard coating well bonded with substrate, three types of cracking patterns may be introduced through indentation upon the coating or bending of the substrate: radial cracking, circumferential cracking, as well as channel cracking. All these

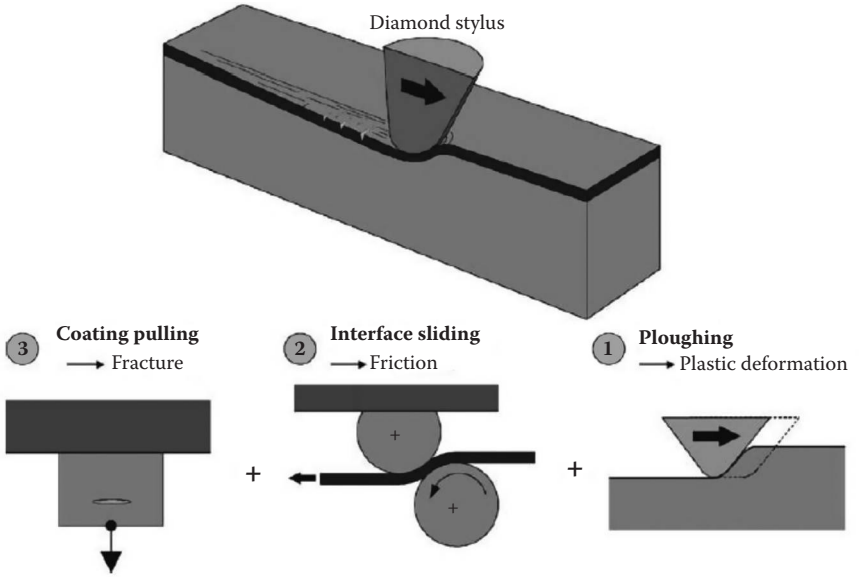


FIGURE 2.12 Schematic illustration of the stylus drawn along the coated sample. The material loading and response can be divided into three components: ploughing, interface sliding, and pulling a freestanding coating. (From Holmberg, K. et al., *Wear*, 2003. 254(3–4): 278–291.)

modes of cracking are quite simple in mechanics and are used for quantitative analysis of the fracture toughness of the coating.

2.3.1 Toughness Evaluation from Radial Cracks

Radial cracks may be introduced at the surface of a ceramic material when indenting with a sharp edge indenter, a Vickers or a Berkovich indenter (Figure 2.13a).

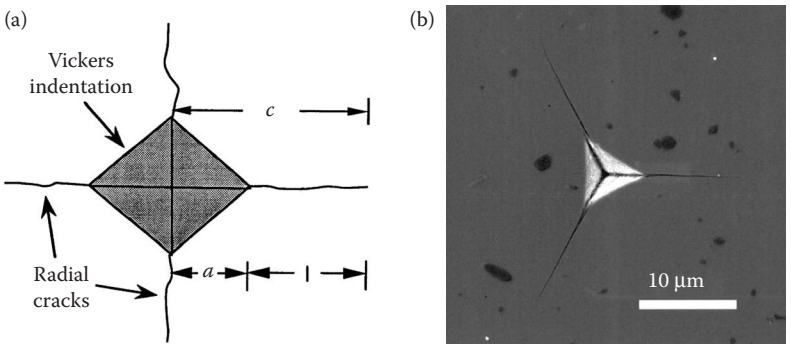


FIGURE 2.13 (a) Schematic illustration of radial cracking at a Vickers indentation, and (b) Ultralow load nanoindentation radial crack. (From Pharr, G.M., *Materials Science and Engineering A*, 1998. 253(1–2): 151–159.)

Radial cracking indentation method was initially proposed for bulk materials [76]. The relationship between the fracture toughness and the length of radial cracks had been established decades ago [77,78]:

$$K_c = \alpha\left(\frac{E}{H}\right)^{1/2}\left(\frac{P}{c^{3/2}}\right) \tag{2.14}$$

where P is the peak load at indentation; c is the crack length; and α is the empirical constant, which depends on the geometry of the indenter, $\alpha = 0.016$ for both a Berkovich and Vickers type indenter. The elastic/plastic indentation fracture mechanics requires a median/radial crack pattern being well developed (Figure 2.14). Geometrically, it is required that $c \geq 2a$ (a is the radius of the impression [Figure 2.14c]) to ensure a complete formation of the half-penny cracking pattern and that the depth d of the half-penny crack beneath the surface be less than one-tenth of the height of geometry to avoid the influence of the lower boundary [79].

The radial cracking indentation method was introduced into hard coatings by applying an ultralow load with nanoindentation in order to avoid the effect from the coating/substrate interface [76] (Figure 2.13b). For a coating with residual stress σ_r, the following relationship is commonly used [80,81]:

$$K_{IC} = \alpha\left(\frac{E}{H}\right)^{1/2}\left(\frac{P}{c^{3/2}}\right) + Z\sigma_r c^{1/2} \tag{2.15}$$

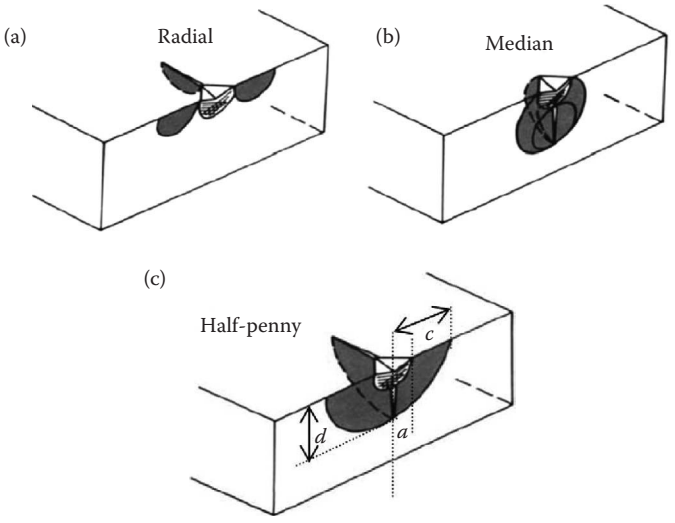


FIGURE 2.14 Crack patterns of a brittle material upon Vickers indentation: (a) the radial crack; (b) the median crack; (c) the half-penny cracking (a combination of the radial crack and the median crack).

where Z is the crack shape factor given by [81]

$$Z = 1.12\sqrt{\pi}\,\frac{d/c}{(3\pi/8) + (\pi/8)(d/c)^2} \tag{2.16}$$

$Z = 1.26$ for an idealized half-penny, that is, the depth d of the crack is equal to the crack length c, making the half-penny an ideal semicircle.

To meet the geometrical requirement of Equations 2.14 or 2.15, the indentation depth (smaller than the depth d of the crack induced) should be much less than 10% of the coating thickness. However, a load threshold exists for the occurrence of the radial crack during indentation. For most ceramic materials, the threshold load of a Vickers or Berkovich indentation is 250 mN or more, and the corresponding impression produced is several micrometers in depth [76,82]. A sharper angle indenter greatly reduces the threshold load for radial cracks. For instance, indenting with a cube-corner indenter reduces the load threshold by at least an order of magnitude compared with that with a Vickers indenter [76]. Yet even such, the indentation depth would still be a few hundred nanometers for many brittle materials to induce a radial crack [83]. Therefore, for coatings, to introduce well-developed radial cracks, the depth limitation of a nanoindentation to exclude the substrate effect is usually very difficult to meet.

Unlike standardized test with a single crack in a well-defined loading configuration (like the uniaxial tensile testing) [84], indentation induces a relatively complex crack network and residual damages around the impression. This makes the mechanical analysis difficult [78,85]. The simplified "expanding cavity" model is adopted to depict the damage zone of an indentation [77,86]. However, its reliability has been questioned [87,88]: Experiments on bulk ceramic materials revealed that the crack patterns are material-dependent and often not the idealized half-penny as assumed in the model [89,90]. In bulk ceramic materials, the actual crack patterns is obtained through observing the cross section of the median/radial crack (Figure 2.14c) [90,91], but it is extremely hard for the operation on coatings to make a judgment of the restriction of the substrate surface on the actual cracking patterns.

A substrate indentation method was proposed to tackle the problem of the substrate influence [92]: indentation is conducted on the uncoated side of the substrate surface and the radial crack on the substrate propagates into the coating. In this way, a single through-thickness crack is induced in the coating (Figure 2.15a). The tougher the coating is, the shorter it cracks into the coating (Figure 2.15b). Based on the energy balance principle the following equation is obtained:

$$A_f G_f + A_s G_s = A_{sf} A_s + A_{ss} G_s \tag{2.17}$$

where G_f and G_s are the strain energy release rates for coating and substrate, A_f and A_s are true cracked films and substrate areas, respectively. A_{sf} and A_{ss} are cracked areas when coating properties are identical to those of the substrate. Through comparing

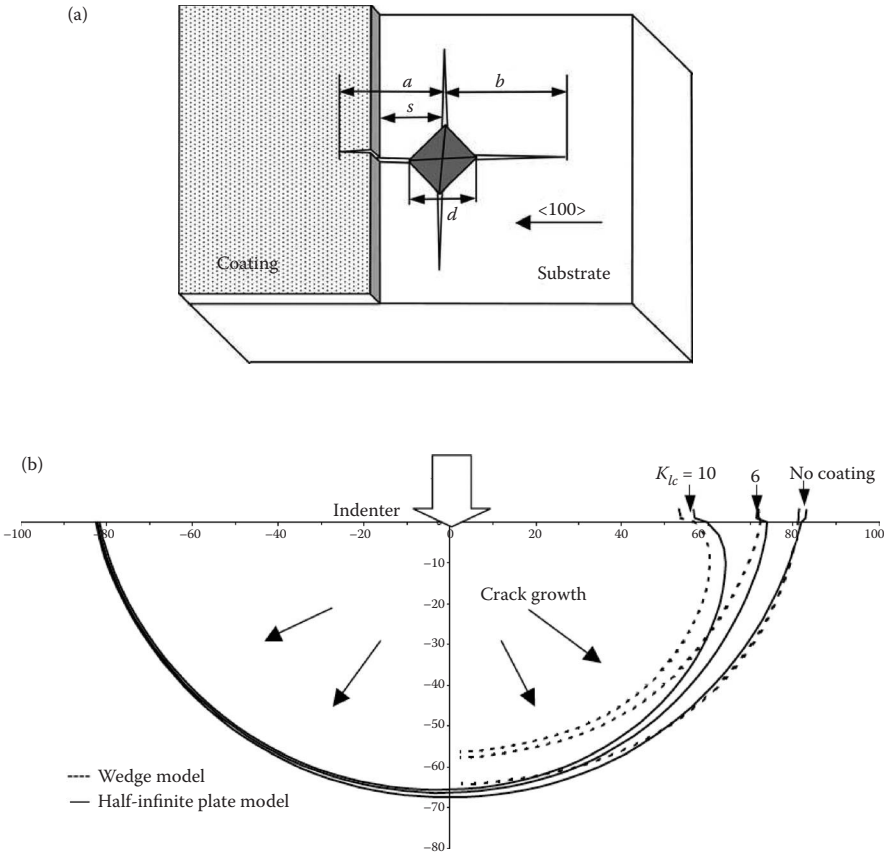


FIGURE 2.15 (a) Schematic of indentation geometry; (b) crack growth front for different film fracture toughness K_c. (From Basak, A.K. et al., *Wear*, 2010. 269(3–4): 269–277.)

the crack lengths of coated and uncoated side, an expression is obtained for toughness of the coating

$$K_f = \left\{ K_s^2 \left[1 + \lambda \frac{(\phi b - a)}{t} \sqrt{\frac{E_f}{E_s} \frac{(1 - \upsilon_s^2)}{(1 - \upsilon_f^2)}} \right]^2 + \left[2\psi_c \sigma_r \sqrt{t} \sqrt{\frac{E_f}{E_s} \frac{(1 - \upsilon_s^2)}{(1 - \upsilon_f^2)}} \right]^2 \right\}^{1/2} \tag{2.18}$$

where subscript "f" refers to the film and "s" to the substrate; K_s is the fracture toughness of substrate; ϕ is the slope of a versus b; a and b are crack lengths as shown in Figure 2.15a; and the dimensionless factors λ and ψ_c are 0.45 and 0.95 respectively, obtained from finite element modeling (FEM) calculations.

2.3.2 Toughness Evaluation from Circumferential Cracking and Spallation

2.3.2.1 Methodology of the Toughness Evaluation from Circumferential Cracking and Spallation

Circumferential cracking and spallation describes peeling off of the coating around indentation (Figure 2.16a). For a very brittle coating, it is generated upon nanoindentation. At spallation, a plateau forms in the load–displacement curve (Figure 2.16b) [83,93–96], which can be made use of to produce quantitative estimation of the fracture toughness of the coating. Li et al. (Figure 2.16a) [83] suggested that the fracture proceeds as follows: (1) the first circumferential through-thickness crack forms around the indenter by high stress in the contact area; (2) delamination and buckling occur around contact area at the coating/substrate interface by high lateral pressure; (3) a second circumferential through-thickness crack forms, and spallation is generated by high bending stresses at the edges of the buckled thin coating. The third stage, circumferential through thickness cracking and spallation of the coating, causes a sudden excursion of the indenter in displacement, which induces a step in load–displacement curve (Figure 2.16b). Given area ABC in Figure 2.16b representing the energy U dissipated on the coating cracking, the fracture toughness is obtained

$$K_C = \left[\frac{EU}{(1-\nu^2)A}\right]^{1/2} \tag{2.19}$$

where $A = 2\pi C_R t$ is the crack area, $2\pi C_R$ is the crack length in the coating plane, C_R is the radius of circumferential through-thickness crack formed around the indenter, t is coating thickness. E and ν are Young's modulus and Poisson's ratio of the coating, respectively. In Equation 2.19, the coating fracture energy U comes from the irreversible work W_{irr} of the indenter during the excursion from A to B.

2.3.2.2 Debates About the Extraction of the Irreversible Work W_{irr}

However, the extraction of the irreversible work W_{irr} became the focal point of much debate: Toonder et al. [93] suggested the lower and upper boundaries of the W_{irr} as shown in Figure 2.17: the areas of OAB and ABFR, which corresponds to the cases of full elastic deformation and full plastic deformation of coated system, respectively. Chen et al. [96] considered the ABQE representing the irreversible work W_{irr}, given AE and BQ being the unloading curves at excursion start point and end point. Further, they provided a way to obtain the unloading curve AE through following linear relationship between the ratio of displacement δ_f/δ_1 and that of hardness over Young's modulus (H_s/E_s)

$$\frac{\delta_f}{\delta_1} = 1 - \lambda\frac{H_s}{E_s} \tag{2.20}$$

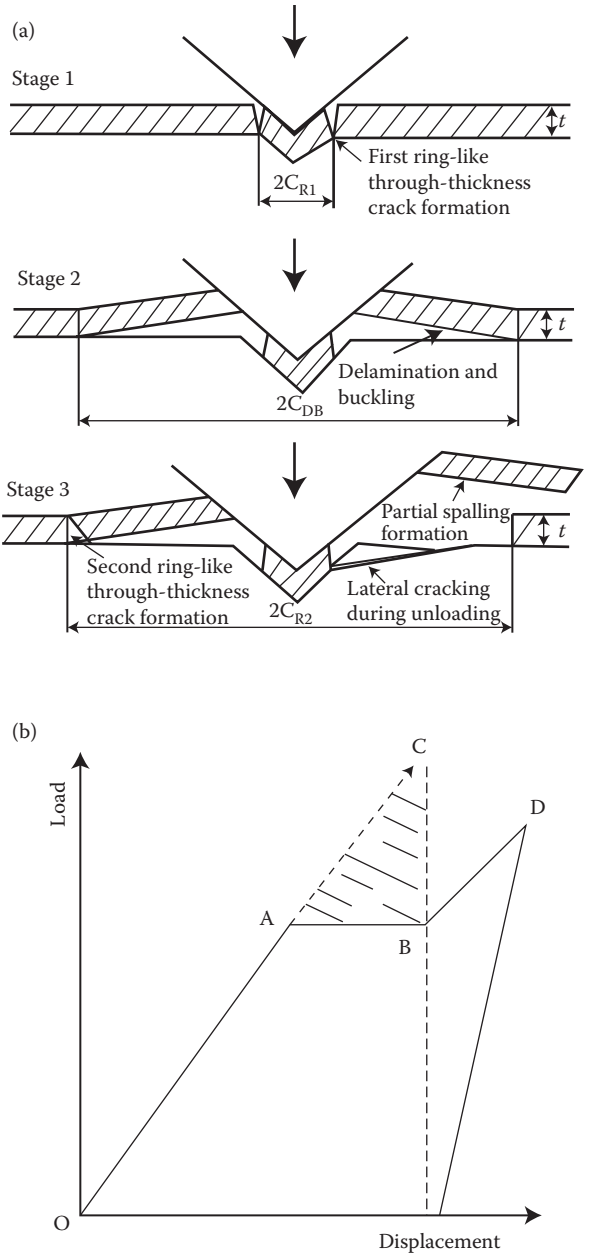


FIGURE 2.16 (a) Schematic of the three stages in nanoindentation fracture for thin coatings coated system; (b) schematic of a load–displacement curve, showing a step during the loading cycle and associated energy release. (From Li, X., D. Diao, and B. Bhushan, *Acta Materialia*, 1997. 45(11): 4453–4461.)

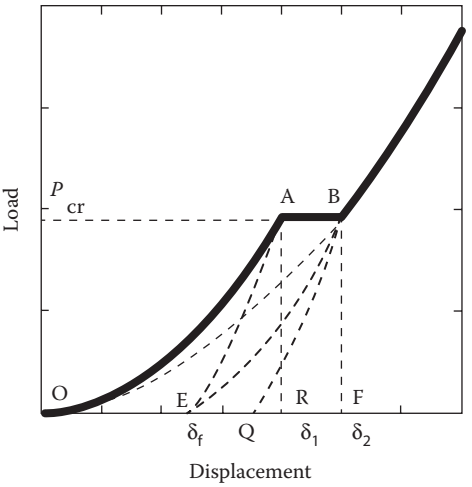


FIGURE 2.17 Schematic of the boundaries of the irreversible work W_{irr} at the plateau in a load–displacement curve of a nanoindentation. (From Chen, J. and S.J. Bull, *Thin Solid Films*, 2009. 517(9): 2945–2952.)

where H_s and E_s are the hardness and Young's modulus of substrate. $\lambda = 4.5$ for Berkovich indenter. δ_f and δ_1 are the residual displacement and full displacement of an indentation, respectively, as shown in Figure 2.17. Expression (2.20) is developed for bulk materials without fracture [97]. It was approximately applied for the coated system as the substrate dominates the deformation in deep indentation. In this way, the lower boundary ABE and the upper boundary ABFE of the irreversible work W_{irr} are obtained.

Michel et al. [95] realized that apart from the fracture energy U of the coating, the energy consumed in substrate deformation is also included in the work done by indenter. Roughly, he proposed ABH in Figure 2.18 as the fracture energy U of the coating. In Figure 2.18, ABEF represents the total work of the indenter during circumferential cracking and spallation of the coating, and segment GB represents a partial loading curve of the silicon substrate.

Malzbender et al. [93,98] studied the change of the irreversible energy W_{irr} versus load P through conducting a set of loading–unloading cycles before and after the spallation of a coating. They found that the curve of $W_{irr} - P$ was divided into several segments of straight lines representing different events during cracking: radial cracking, delamination, circumferential through-thickness cracking, and chipping (Figure 2.19a). Apparently, the irreversible work W_{irr} was obtained from the energy jump U^c_{fr}. Further, they found that W_{irr} is coating-thickness dependent [99]: the thinner the coating is, the larger the irreversible energy W_{irr} dissipates. The authors claimed that it is due to the fact that more substrate deformation is involved for a thinner coating during indentation. Accordingly, the fracture energy U is obtained through extrapolating the W_{irr} of the coating with infinite coating thickness from those coatings with finite thickness (Figure 2.19b).

Chen et al. [94,100] extracted the fracture energy U of a coating from the curve of total work W_t versus displacement D (Figure 2.20). First, the initial W_t–D curve

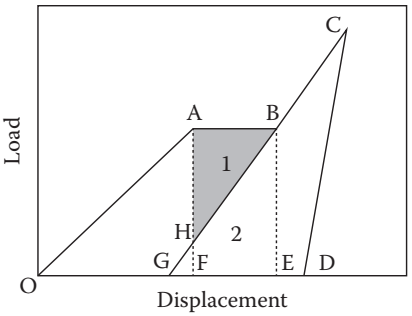


FIGURE 2.18 Schematic representing the fracture energy U of a coating at the plateau in the load–displacement curve of a nanoindentation: the segment (GB) represents a partial loading curve of the Si substrate; the dotted area (ABEF) represents the total work under the step (done by indenter); The gray area 1 (ABH) indicated represents the energy released on circumferential cracking and spallation, while that area 2 (BEF), represents the energy of Si deformation. (From Michel, M.D. et al., *Thin Solid Films*, 2006. 496(2): 481–488.)

is extrapolated from the cracking start point A to the cracking end point C. Then the W_t–D curve after cracking is extrapolated backward to the cracking start point. Vertical difference AB and CD are thus obtained. AB represents the work difference consumed in the elastic–plastic deformation of the coating/substrate system before and after the coating fracture, and CD is the total work done during the cracking. The difference between CD and AB is thus deemed as the fracture energy U.

Displacement-controlled nanoindentation of thin ceramic coatings with sharp indenter (cube-corner tip with radius of 40 nm when new) was investigated by Chen et al. [94,100]. Displacement-controlled indentation was supposed to be more sensitive to the coating cracking. It is because that the load drop at coating fracture is unambiguously related to the loss of the contact of the indenter with the coating/substrate system. On the contrary, in addition to the indenter movement due to the loss of the contact, there is an additional movement of the indenter due to the deformation of the coating/substrate system at the fracture load. Figure 2.21a is the typical load–displacement curve of a displacement-controlled nanoindentation conducted upon a 400 nm TiO_xN_y coating on a glass substrate, in which, the load jump between B and C is associated with the radial through-thickness cracking of the coating [94]. W_t–D method was used to obtain the fracture energy U, and the fracture toughness was thus obtained according to Equation 2.19.

However, during nanoindentation of a thin hard coating coated system, besides the second circumferential cracking and spallation, radial cracking of the coating [101–103], delamination of the interface [104,105], cracking or spallation of the brittle substrate [101,106], or even the dislocation nucleation and phase transformation of the substrate material [107] are possible to induce a step in loading curve of a nanoindentation. Zhang et al. pointed out the possible blending of the event of the second ring-like through-thickness crack formation with other catastrophic cracking events [108]. The following one-dimensional (1D) blister model of a coating was taken to illustrate the overlap of the catastrophic delamination of a compressively stressed

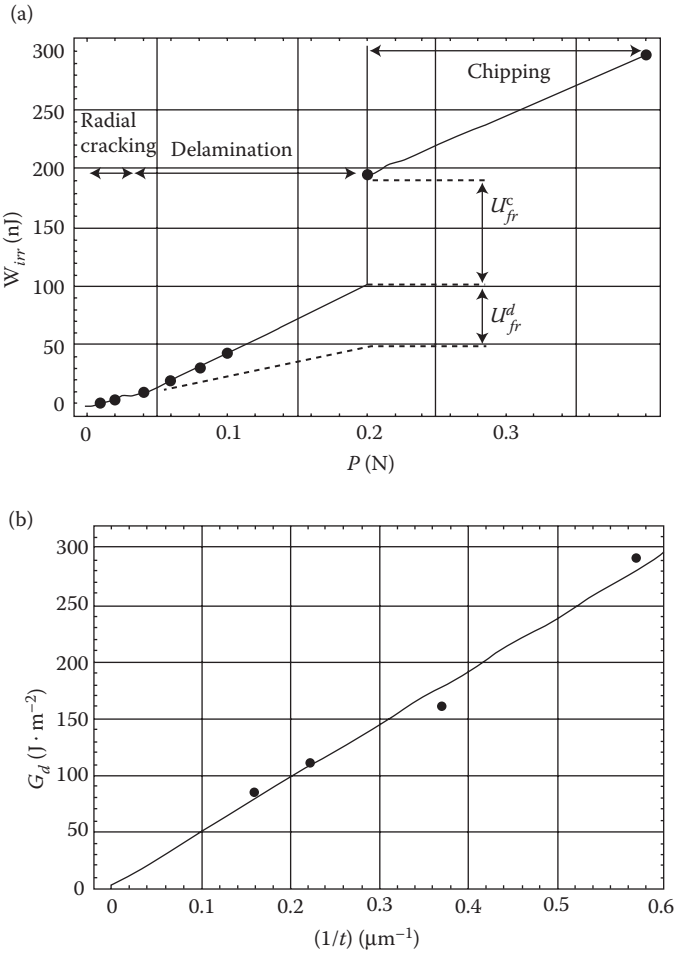


FIGURE 2.19 (a) Energy irreversibly dissipated during indentation, as a function of the peak load applied during indentation (From Malzbender, J. et al., *Materials Science and Engineering: R: Reports*, 2002. 36(2–3): 47–103.); (b) the energy irreversibly dissipated during indentation as a function of the inverse coating thickness *t*. (From Malzbender, J. and G. de With, *Surface and Coatings Technology*, 2000. 135(1): 60–68.)

coating after bulking up with the event of circumferential cracking and spallation that followed:

The driving force (energy release rate of the interface) G_i of the interfacial delamination after bulking is [109–111]

$$\frac{G_i}{G_0} = m\left[1 - \left(\frac{\sigma_c}{\sigma_r}\right)^2\right] \tag{2.21}$$

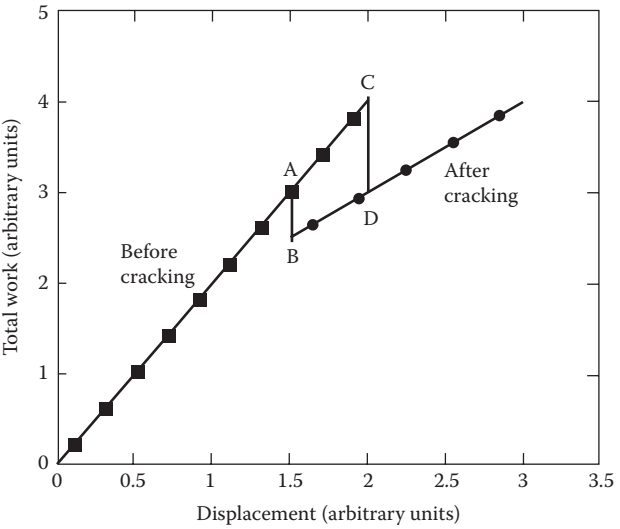


FIGURE 2.20 Schematic of extrapolating the total work versus displacement curve before and after cracking to determine the fracture dissipated energy CD–AB. Here, the point A and D are the start and end points of excursion in the measured work–displacement curve. (From Chen, J. and S.J. Bull, *Thin Solid Films*, 2006. 494(1–2): 1–7.)

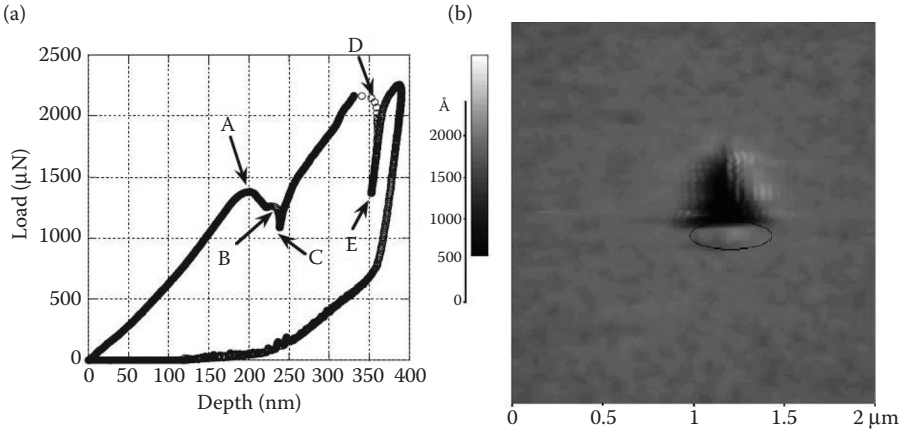


FIGURE 2.21 Displacement-controlled nanoindentation of 400 nm TiO_xN_y coating on a glass substrate. The circle in (b) marks an area of uplift associated with interfacial fracture. In (a), position A is where plastic deformation of the softer substrate starts; points B and C are the start point and end point of through-thickness cracking; D and E are the start point and end point of interfacial fracture. (From Chen, J. and S.J. Bull, *Thin Solid Films*, 2006. 494(1–2): 1–7.)

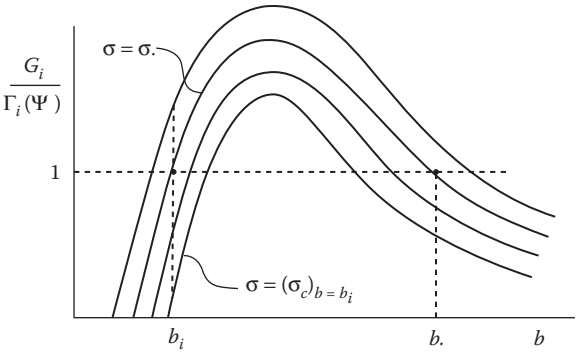


FIGURE 2.22 The schematic of instability analyses of 1D blister. (From Hutchinson, J.W. and Z. Suo, *Advances in Applied Mechanics*, 1992. 29: 63–191.)

where $G_0 = (1 - \upsilon)t\sigma_r^2/E$ and $m = [1 + 0.9021(1 - \upsilon)]^{-1}$; σ_r is the residual stress of the coating, and $\sigma_c = 1.2235(E/(1 - \upsilon^2))(t/b)^2$ is the buckling stress; t is coating thickness; and b is radius of delaminated zone.

Equation 2.21 is schematically represented by Figure 2.22, where $\Gamma_i(\psi)$ is the fracture toughness of the interface. Given an initially delaminated region of width $2b_i$, the coating would buckle up at $\sigma_r = \sigma_c$. The blister (buckled coating) would then spread dynamically when σ_r attains σ_* (where $G_i = \Gamma_i(\psi)$), and would arrest at $b = b_*$ (where $G_i = \Gamma_i(\psi)$. The buckling also favors the cracking and spallation of the coating because a tensile stress in the coating on the inner side near the edge is induced after the bending. When the driving force G_f for the cracking of the coating satisfies the equation $G_f/G_i > \Gamma_f/\Gamma_i(\psi)$, where Γ_f is the fracture toughness of the coating, the coating cracks and spalls away from substrate in a particular angle [112]. Both the dynamic processes, that is, the interfacial delamination and the cracking and spallation of the coating, blend together. In this case, the energy used to calculate the coating toughness is overestimated if the possible existing process of delamination was ignored.

2.3.2.3 Argument on the Methodology of Circumferential Cracking and Spallation for the Fracture Toughness of Thin Hard Coatings

Recent study by Zhang et al. on the circumferential cracking and spallation methodology posed a question about the validity of the Equation 2.19 for the fracture toughness of coatings by rethinking the role of the "step" in fracture toughness calculation [113]. The authors examined those literatures directly using this "step method" to determine fracture toughness of hard coatings and scrutinized the reported curves and the fracture topography and noticed that only a handful of them had detailed indentation and measurements on various hard coatings: DLC coating [83,114,115], a-C:H coating [95,116], CNx coating [96,117], and so on. These are tabulated in Table 2.4. The step sizes in these literatures are measured from the load–displacement curves (Figures 2.23 through 2.28) and are also entered in Table 2.4 together with the respective coating thickness.

TABLE 2.4
Mechanical Properties of Four Kind Coatings as well as the Thickness and the "Step" Size

Example	Coating Type	Coating Hardness H (GPa)	Coating Young's Modulus E (GPa)	Substrate[a]	Indenter Shape[b]	Coating Thickness t (nm)	"Step" Size D (nm)	$(t - D)/t$
1. Figure 2.23	ECRCVD DLC coating (Figure 3 in Reference 115)	/	180	Si wafer	Cube	100	87.7	12.3%
2. Figure 2.24	Ion beam carbon coating (Figure 2 in Reference 114)	/	150	Si wafer	Conical	400	350	12.5%
3. Figure 2.25	a-C:H coating[c] (Figure 8 in Reference 95)	9.5	83	Si wafer	Cube	1000	1052 (745)[d]	–5.2% (25.5%)
4. Figure 2.26	a-C:H coating[e] (Figure 1 in Reference 116)	7.9	62	Si wafer	Berkovich	1000	1040	–4.5%
5. Figure 2.27	CNx coating (Figures 6,7 in Reference 96)	9	100	SiC	Berkovich	1000	750	25%
6. Figure 2.28	CNx coating (Figure 17 in Reference 117)	/	/	SiC	Berkovich	1000	892	11.8%

Note: The mechanical properties and coating thickness were taken from original papers; the "step" size was measured according to the load–displacement curve and the discrepancy between "step" size and coating thickness were calculated by the authors of this chapter.

[a] Silicon wafer (100): (H = 11.5 GPa, E = 130 GPa); SiC ((001) 3C): (H = 42 GPa, E = 450 GPa).

[b] Cube indenter (tip radius 100 nm); Conical indenter (included angle 90°, tip radius 100 nm); Berkovich indenter (tip radius of 250 nm).

[c] a-C:H coating: (the deposited condition is: pres 8 Pa; bias 250 V).

[d] The size of the "jump" given in original paper.

[e] a-C:H coating: (the deposited condition is: pres 8 Pa; bias 220 V).

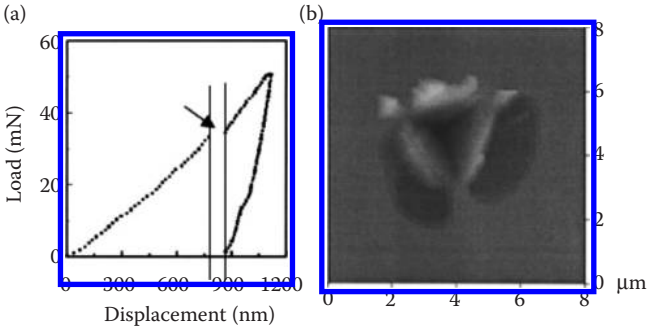


FIGURE 2.23 Load–displacement curve of an indentation made at 50 mN peak indentation loads using cube indenter (a) and the AFM images of the indentation (b) on the ECRCVD DLC coating on silicon (coating Example 1 in Table 2.4). The figure is adapted from Figure 3 in Reference 117. Two vertical dot lines in (a) were added by the authors of this chapter to indicate the span of the step.

The first line in the table is a 100 nm DLC coating indented with a cube indenter [115]. The estimated "step" size in the load–displacement curve (Figure 2.23a) is 87.7 nm. The indent is shown in Figure 2.23b. Example 2 is 400 nm thick DLC coating indented with a conical indenter [114]. The step size is 350 nm. The micrograph of the indent (Figure 2.24b) reveals some residual crushed coating beneath the indenter tip. Example 3 is a 1000 nm a-C:H coating (Figure 2.25a, Cube indenter) [95]. Though the authors took point B to point C as the step size, the fracture of the coating should have started at point A. From point A to point B, partial fracture of the coating occurred. Taking this into account, the step size from A to C is 1052 nm. The fracture topography in Figure 2.25b reveals a clean substrate surface. Reference 116 indented a-C:H coating of 1000 nm (Example 4 in Table 2.4, Berkvich indenter). The step size in Figure 2.26a is 1040 nm. References 96 and 117 indented

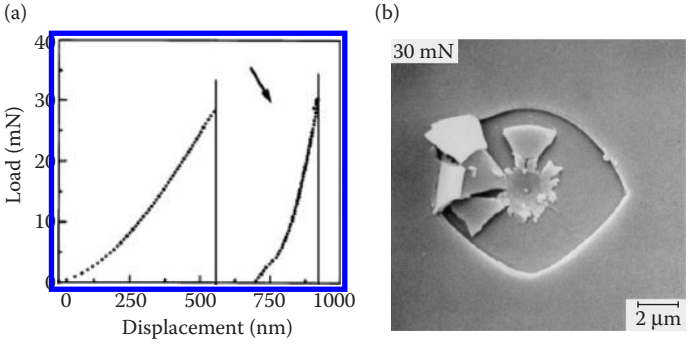


FIGURE 2.24 Load–displacement curve of an indentation made at 30 mN peak indentation loads using conical indenter (a) and the SEM micrograph of the indentation (b) on the ion beam carbon film on silicon (coating Example 2 in Table 2.4). The figure is adapted from Figure 2 in Reference 114. Two vertical dot lines in (a) were added by the authors of this chapter to indicate the span of the step.

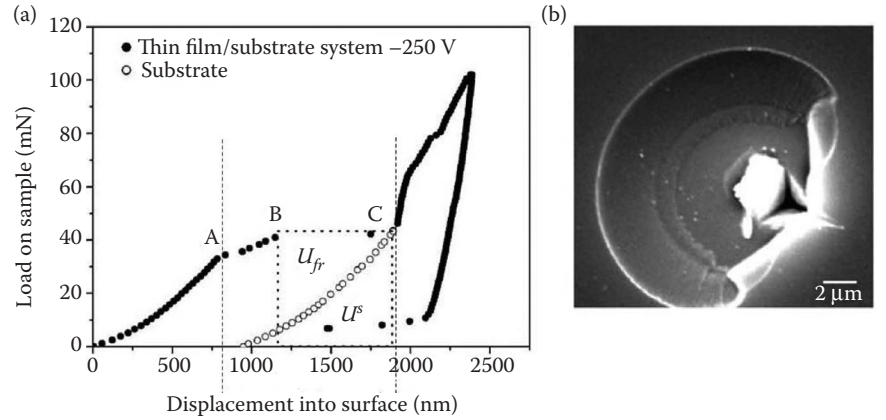


FIGURE 2.25 Load–displacement curve of a nanoindentation made at 100 mN peak indentation loads using cube indenter (a) and the SEM micrograph of the indentation (b) on the a-C:H coating deposited on silicon at 8 Pa at Vb = –250 V (coating Example 3 in Table 2.4). The figure is adapted from Figure 8 in Reference 95. Two vertical dot lines in (a) were added by the authors of this chapter to indicate the span of the step.

on 1000 nm CNx coatings deposited on SiC substrate (42 GPa in hardness [96]). The step size from Reference 96 is 750 nm (Example 5), and from Reference 117 is 892 nm (Example 6). Figures 2.27b and 2.28b are the fractured surface of the coatings, showing no residual coating fragment beneath indenter. Obviously, examination of Table 2.4 reveals an astonishing similarity between the size of the "step" and the thickness of the coating. Is this accidental or logical?

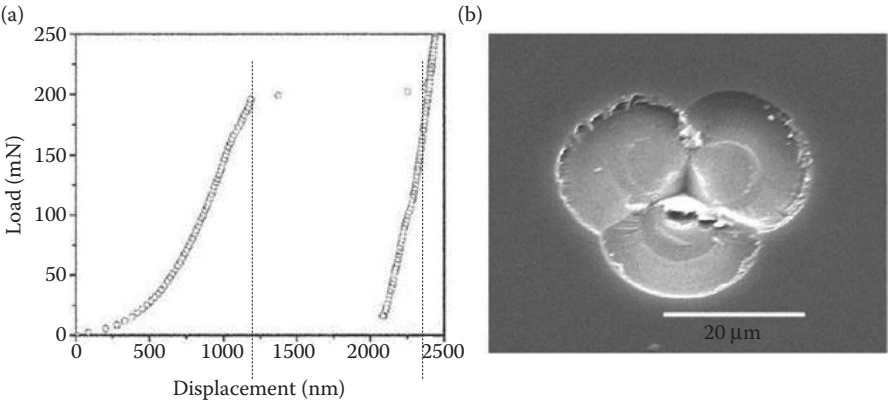


FIGURE 2.26 Load–displacement curve of a nanoindentation made at 250 mN peak indentation loads using Berkovich indenter (a) and the SEM micrograph of the indentation (b) on the a-C:H coating deposited on silicon at 8 Pa at Vb = –200 V (coating Example 4 in Table 2.4). The figure is adapted from Figure 1 in Reference 116. Two vertical dot lines in (a) were added by the authors of this chapter to indicate the span of the step.

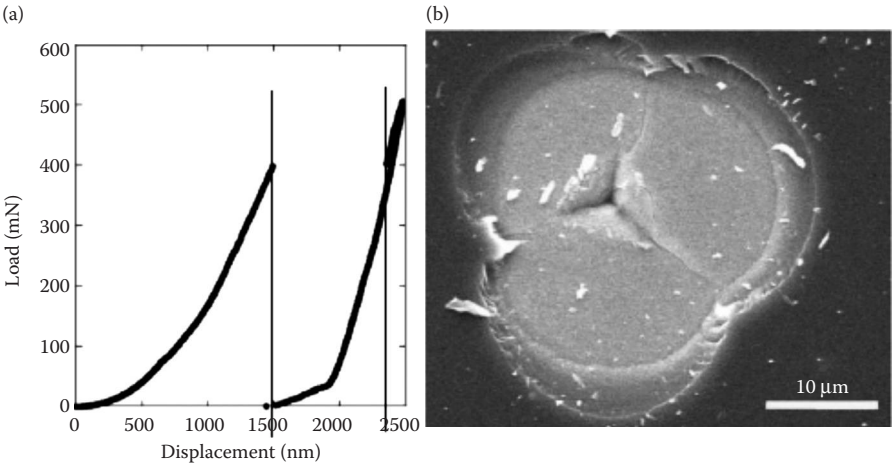


FIGURE 2.27 Load–displacement curve of a nanoindentation made at 500 mN peak indentation loads using Berkovich indenter (a) and the micrograph of the indentation (b) on CNx coatings on (100) 3C SiC (coating Example 5 in Table 2.4). The figure is adapted from Figures 6 and 7 in Reference 96. Two vertical dot lines in (a) were added by the authors of this chapter to indicate the width of the step.

Further examination of the micrograph of the indentation indicates that two factors caused the little discrepancy between the step size and the coating thickness: completeness of the coating spallation and hardness of the sample.

Completeness of the coating spallation: Obviously, if the coating does not totally spalls away, that is, coating residual exists beneath the indenter, the "step" span

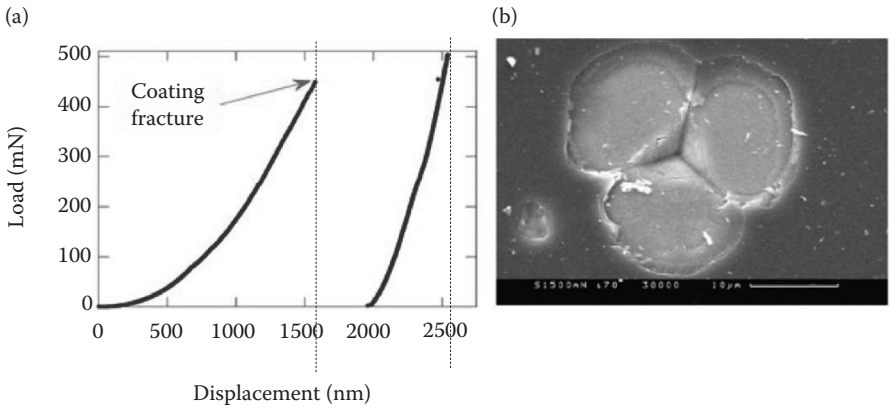


FIGURE 2.28 Load–displacement curve of a nanoindentation made at 500 mN peak indentation loads using Berkovich indenter (a) and the micrograph of the indentation (b) on CNx coatings on (100) 3C SiC (coating Example 6 in Table 2.4). The figure is adapted from Figure 17 in Reference 117. Two vertical dot lines in (a) were added by the authors of this chapter to indicate the width of the step.

would be smaller than coating thickness, depending on how much is the leftover. The other extreme of this is the chipping of brittle substrate. If this happens, the "step" could be more than the coating thickness as there is an additional advancement of the indenter before it comes to be in contact with the substrate again. In Figure 2.24b, the residual coating beneath the indenter reduces the "step size" (in comparison with coating thickness) while the chipping of the substrate in Figures 2.25b and 2.26b cause a slight increase in the "step size."

Hardness of the sample: the hardness of the sample includes two aspects: the hardness of the coating and the hardness of the substrate. When the coating is softer than the substrate, the indenter would penetrate more into the coating before the spallation (at A in Figure 2.16b), and less into the substrate after the spallation (at B in Figure 2.16b). This gives rise to a shorter "step size" than the coating thickness. If the coating hardness and the substrate hardness are about the same, the "step size" would be very close to the coating thickness. Examples 1, 2, 3, and 4 in Table 2.4 fall in this category: the coatings are deposited on silicon wafer (11.5 GPa in hardness [96]), which has similar hardness with substrate, thus indentation does not cause significant difference between the indenting depth before and after the spalling of the coating. As a result, the step is almost the coating thickness. For CNx coatings on SiC substrate (Examples 5 and 6 in Table 2.4), the hardness of coating is much lower than substrate (42 GPa in hardness [96]), the indenter penetrates into a deeper depth in the coating before spallation occurs. This results in a shorter "freefall" of the indenter, thus a smaller "step" than the coating thickness.

Through a careful examination of the steps in nanoindentation load–displacement curves, a fact was revealed that the load–displacement curve is discontinuous at the step (cf., Figure 2.23 through 2.28) (or, in Figure 2.16b, point A and point B are in fact not connected). As the vertical axis in the load–displacement curve is the load exerted on the coating via the tip of the indenter, a straight line in the curve means that the indenter would move from, say, A to C in Figure 2.16b to form AC at a constant load; discontinuity of the curve signifies that the load is not detected while the indenter advances. In other words, the indenter loses its physical contact with the sample (at point A) and resumes it (at point C). As such, gap AC is formed. From the indenter's point of view, it is a "jump" from A to C (as there is no physical contact with the sample). As the "step size" is so close to the coating thickness, it makes sense to suspect that the "jump" comes from the "freefall" of the indenter when coating suddenly fractures away.

The freefall (loss of contact) is more clearly exhibited in the depth-controlled loading curve reported by Warren and Wyrobek [118]: In load control, Figure 2.29a has the classical jump in load–displacement curve. In depth control (Figure 2.29b), the load goes to zero at the start of the gap. It resumes after the indenter touches the exposed substrate. Figure 2.29b also revealed a small portion of the indenter displacement caused by the deformation of substrate before the load rises to the value at the end of the gap.

During the freefall of the indenter from A to B (Figure 2.16b), the indenter does not do any work because, as illustrated by the Figure 2.29b, the load is zero during advancement of the indenter from A to B. The straight line connecting A and B is thus arbitrary and misleading. The energy that fractures the coating is accumulated during the indentation from start (as the indenter touches the coating) to the point where the fracture occurs. In this process, the material beneath the indenter is forced to move outside,

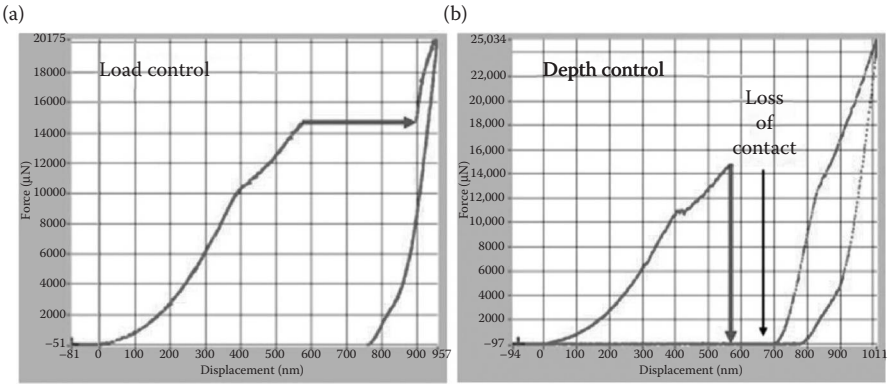


FIGURE 2.29 Load- and depth-controlled force–displacement curves obtained from proprietary brittle coating deposited onto Si. Major transient event at a depth between 500 and 600 nm results in large displacement excursion in the load-controlled case and 100% load relaxation in the depth-controlled case (displacement or load discontinuity indicated by thick arrow). Details of the load-controlled curve suggest loss of contact brought on by transient event but this interpretation is inconclusive because pumped-in energy during displacement excursion might have caused additional permanent deformation. The depth-controlled curve unambiguously shows loss of contact attributed to spalling accompanying fracture. (From Warren, O.L. and T.J. Wyrobek, *Measurement Science & Technology*, 2005. 16(1): 100–110.)

inducing a gradually increasing compressive stress in the coating until delamination or/and fracture of the coating occurs [109–111,119]. The event of the "through-thickness cracking and spalling," as illustrated by Figure 2.16a, takes place catastrophically in a fraction of time [111]. At this moment, all the stored energy is completely released (c.f. Figure 2.16b: at point A, not during A to B). As the stored energy is not dissipated during A to C, the fracture energy is not logically linked to area ABC.

2.3.3 Toughness Evaluation from Channel Cracking

Channel cracking is a "through thickness cracking" where the coating is cracked all the way through to the substrate as the crack propagates; the "through-thickness" characteristic maintains at its propagation, forming a channel-like crack (Figure 2.30). In tensile loading, as the crack length reaches about three times of the coating thickness, the channel crack propagates at a steady state till complete fracture [120].

Taking into consideration the substrate constraint on cracking of the coating, the stress intensity factor of the coating can be expressed as [111,120–124]

$$K_I = \sigma\left(\frac{1-\nu^2}{2}\pi tg\right)^{1/2} \tag{2.22}$$

where $g = g(\alpha,\beta,\sigma/\sigma_{sy},n_s)$, in which, α and β are Dunders parameter describing the elastic mismatch between the coating and the substrate, σ_{sy} and n_s are yielding stress and strain hardening exponent of the substrate.

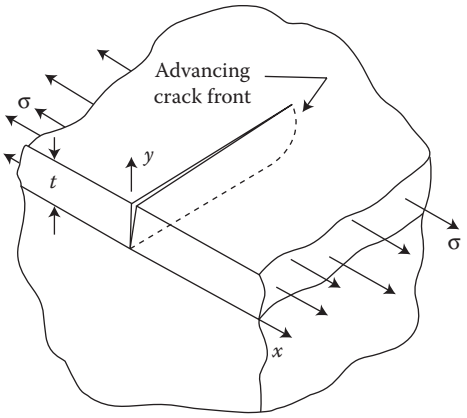


FIGURE 2.30 3D channeling of a crack across a thin bonded coating. (From Beuth, J.L. and N.W. Klingbeil, *Journal of the Mechanics and Physics of Solids*, 1996. 44(9): 1411–1428.)

In Equation 2.22, the substrate effect is contained in g. Studies [120–121] on g indicate that a ductile substrate promotes channel cracking (i.e., bigger g, as can also be seen in ratio σ/σ_{sy} in the g expression, ductile materials have much smaller yielding stress than brittle ones) and thus requires less stress to reach K_I in Equation 2.22.

For a thin ceramic coating on a ductile substrate, bending of the ductile substrate causes channel cracking of the coating. Multistrain flexure test [125,126] or sphere indentation test [123,124] have thus been proposed for the fracture toughness of the coating.

Multistrain flexure test [125,126] is shown in Figure 2.31. Ceramic coating is deposited on a ductile (metallic) substrate and patterned into strips. The sample is then put under flexure such that the ceramic coating strips are on the side surface of the bending beam, and the strips are aligned along the beam axis. During bending, a linear strain gradient is induced into the beam from the bottom to the top: tensile strain on the top, compressive strain at the bottom, and zero strain along the neutral. Thus, coating strips at different position are subjected to different strain. Coating strips with strains over a critical value fracture. As such, critical strain can be identified and the critical stress is thus obtained from the stress–strain relationship (Young's Equation, assuming the ceramic coating fractures in elastic deformation). Plugging in the critical stress in Equation 2.22 yields the fracture toughness of the coating.

In sphere indentation, a sphere indenter of large radius is indented on the coating to cause circular cracking of the coating (Figure 2.32) [123,124]. The strain of the coating under the indenter is axisymmetric and is a function of the location (r), as given by [21]

$$\frac{\varepsilon_r}{\varepsilon_{sy}} = m_1(\varepsilon_{sy})\left(\frac{r}{D}\right) + m_2(\varepsilon_{sy}, n_s)\left(\frac{r}{D}\right)^3 \tag{2.23}$$

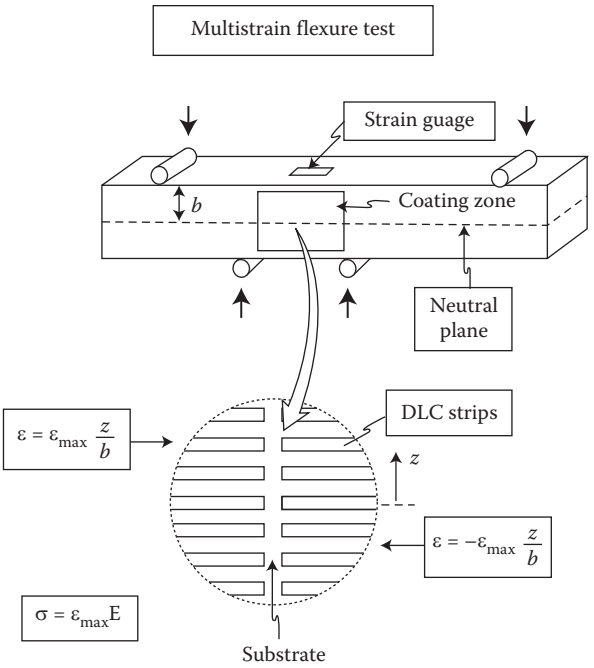


FIGURE 2.31 The multistrain specimen and test configuration. (From Leung, D.K., M.Y. He, and A.G. Evans, *Journal of Materials Research*, 1995. 10(7): 1693–1699.)

where ε_r is the strain in radial direction; r and D are radius of impression and sphere indenter, respectively; ε_{sy} and n_s are the yielding strain and hardening exponent of ductile substrate;

$$m_1(\varepsilon_{sy}) = 1.45 + \frac{0.14}{\varepsilon_{sy}}$$

and

$$m_2(\varepsilon_{sy}, n_s) = [1466 - 118n_s] + [-22.7 + 1.8n_s]\left(\frac{1}{\varepsilon_{sy}}\right) + [0.075 - 0.003n_s]\left(\frac{1}{\varepsilon_{sy}}\right)^2$$

Once the critical strain is identified, the critical stress is thus obtained through the Young's equation; thus Equation 2.22 yields the ceramic coating's fracture toughness.

Expression 2.23is suitable for most of the metallic substrates [123].

The parameter g in Equation 2.22 describes the constraint of the substrate on the channel cracking of the coating. It is much complicated for ductile substrates [121],

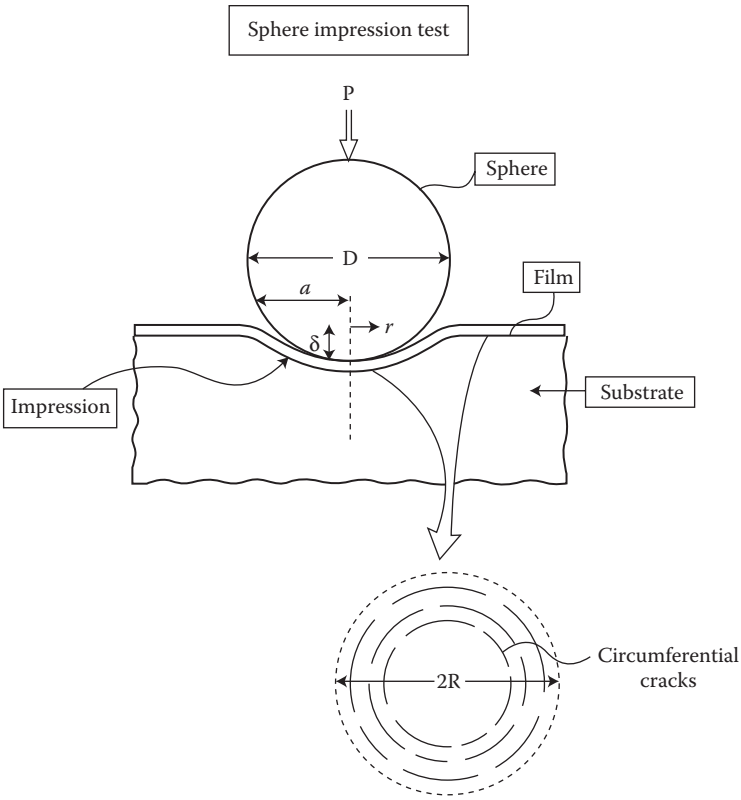


FIGURE 2.32 The sphere indentation test. Circumferential cracks develop within the impression. (From Begley, M.R., A.G. Evans, and J.W. Hutchinson, *International Journal of Solids and Structures*, 1999. 36(18): 2773–2788.)

which hinders its application. In practice, it is difficult to make coating strips on a metallic substrate by lithography as metallic substrate is not the mainstream substrate in micro-electromechanical system (MEMS) practice. Also, with the sphere indentation it is difficult to accurately locate the first crack on the unloaded impression (it tends to close-up upon unloading).

For a thin hard coating deposited on a rigid (ceramic) substrate, nanoindentaiton with a sharp edge indenter can be used to generate radial channel cracks [19,55], as shown in Figure 2.33. A hemispherical plastic zone is generated under the contact at the beginning of indentation; with load increasing, the plastic zone expands further and its hemispherical shape changes upon impinging on the substrate; finally, the radial cracks emanated from the sharp corners. With further loading, the plastic zone transforms into a cylindrical shape and the radial cracks become a channel crack configuration (Figure 2.33b) [127,128].

According to the rigid substrate hypothesis, the indented volume of the coating material is solely accommodated via deformation of the coating. This requires the substrate material to be much harder and tougher than the coating [129]. Otherwise,

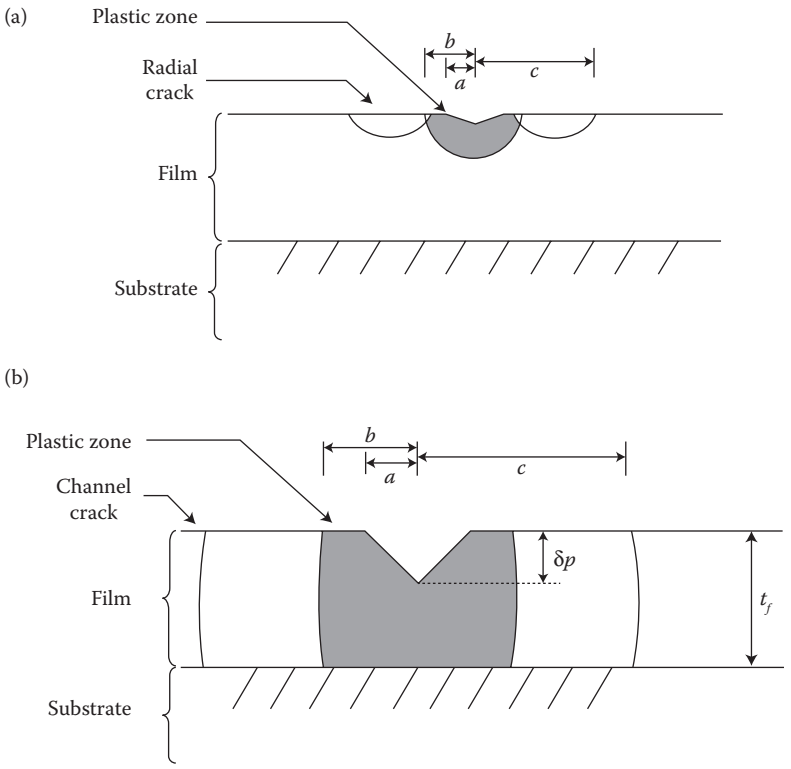


FIGURE 2.33 (a) Schematic cross section of indent-induced partial-penetration radial fracture in a mechanically thick coating. Here, when the coating is thick compared to the plastic zone, the plastic zone is spherical in shape and the radial cracks are seen as surface traces; (b) schematic cross section of indent-induced channel cracking in a mechanically thin coating. Here, the plastic zone is cylindrically shaped due to the constraint of the substrate and the channel cracks extend through the coating. (From Jungk, J.M. et al., *Acta Materialia*, 2006. 54(15): 4043–4052; Thurn, J. and R.F. Cook, *Journal of Materials Science*, 2004. 39(15): 4809–4819.)

the plastic zone may extend into substrate [107] or even worse, cause extensive substrate deformation [130]. Assuming there is no deformation in the substrate, the stress intensity factor of the indentation driven channel cracking is derived as [111,131]

$$K_I = \lambda V^* \frac{(E_f H_f^2)^{1/3}}{t_f} \frac{a^2}{c^{1/2}} \tag{2.24}$$

where the subscript '*f*' refers to "film" or coating properties, and λ is approximately 0.013 for Vickers geometry and 0.016 for cube-corner geometry. *a* is the radius of indented impression, and *c* is the crack length. For a well-developed channel crack, it is required that crack length is larger than three times of film thickness as shown in Figure 2.34. The parameter V^* is used to exclude the portion

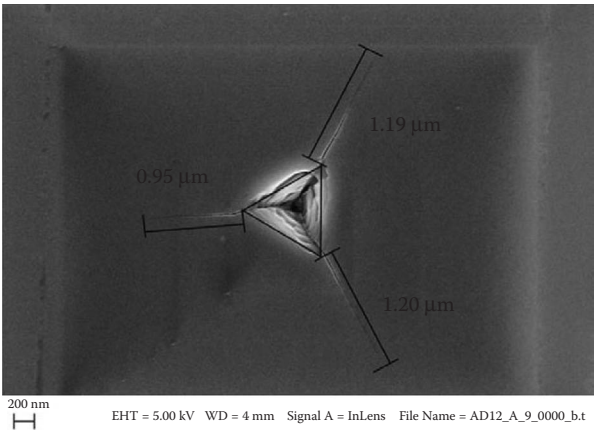


FIGURE 2.34 An SEM images of ta-C coating fracture. The thickness is 248 nm. (From Jungk, J.M. et al., *Acta Materialia*, 2006. 54(15): 4043–4052.)

of indent-displaced volume accommodated by substrate when indenter tip penetrates through coating [127]

$$V^* = \begin{cases} 1 & h_p \le t_f \\ 1 - ((h_p - t_f)^3 / h_p^3) & h_p > t_f \end{cases} \tag{2.25}$$

where h_p refers to indentation depth; t_f is coating thickness. Residual stresses σ_r contained in coating act as an additional crack driving or retarding force. The residual stress resulted stress intensity factor has the form

$$K_r = \psi' \sigma_r t_f^{1/2} \tag{2.26}$$

where ψ' is a constant that depends on the stiffness mismatch of the coating and substrate [111,121]. At equilibrium, the fracture toughness can be obtained by summation of Equations 2.24 and 2.26.

2.4 OVERVIEW OF THE MICROTENSILE TESTING OF FRACTURE TOUGHNESS FOR STANDALONE THIN FILMS

Uniaxial tensile testing has been established for the measurement of the fracture toughness of a bulk material [7,8]. In a uniaxial tensile testing with a central crack, the stress intensity factor is

$$K_I = \sigma \sqrt{\pi l} \tag{2.27}$$

where σ is the stress in sample, and here l is half length of the central crack. For a tensile testing specimen with an edge crack, the stress intensity factor becomes

$$K_I = \sigma\sqrt{\pi a}\, f(a/W) \tag{2.28}$$

where the sample dimensional function $f(a/W) = 1.12 - 0.23(a/W) + 10.55(a/W)^2 - 21.72(a/W)^3 + 30.41(a/W)^4$, a is the length of the edge precrack and W is the width of the gauge region. Equation 2.28 is valid for $a/W \leq 0.6$ [132].

A microtensile testing is most straightforward to measure the fracture toughness of thin films according to the Equations 2.27 and 2.28. However, it is very challenging to prepare freestanding sample with microscale size and conducting a tensile test on them. Notable progress has been made in the micro- and nanoscale tensile testing in recent years [5,133–144]. Photolithographic techniques are made use of in the preparation of the freestanding films. According to classic fracture toughness measurement, atomic sharp precracks of known lengths are needed. Vickers indentation and focused ion beam are most commonly used in making precracks in the film. Loading of the precracked standalone films can be very delicate and difficult. Quite a few methods have been proposed: the inchworm actuation by Chasiotis et al. [141], membrane deflection by Espinosa et al. [144], tension by residual stress by Kahn et al. [138,139,145], bulging of films by Xiang et al. [136,137], and the most recent macrotension on substrate by Zhang and Zhang [146]. The key points of these methods are described below.

2.4.1 Inchworm Actuation

The inchworm actuation method [85] is illustrated in Figure 2.35. The "dog-bone" shape film is made with lithographic technique. An edge precrack is fabricated by indentation of the adjacent substrate. To facilitate griping of sample, one end of the "dog-bone" is not released from substrate, while the other end is made freestanding. UV adhesion and electrostatic control combined to provide bonding of the freestanding end of the "dog-bone" to the loading beam. The tensile load is applied to the film via an inchworm actuator. The resolution of the actuator is 4 nm and the load cell is of an accuracy of 10^{-4} N. The fracture toughness is obtained according to Equation 2.28 given the critical stress at fracture.

The technique was used successfully in the fracture toughness measurement of DLC films and polycrystalline silicon films [140,142,147].

2.4.2 Membrane Deflection

In the membrane deflection method [144], the film to be tested is deposited on silicon wafer and patterned into strips with lithographic techniques. The gauge section of film strips are made freestanding by etching away the silicon wafer material through thickness from backside with MEMS method (Figure 2.36). The loading is accomplished vertically using a nanoindenter with line-load tip at the middle of the freestanding span (Figure 2.37). A microscope interferometer positioned directly below the specimen measures the deflection Δ of film from the fringes generated as a result of phase differences of the monochromatic light reflecting off the film after traveling different length of path. The angle that the film turned upon deflection is given as

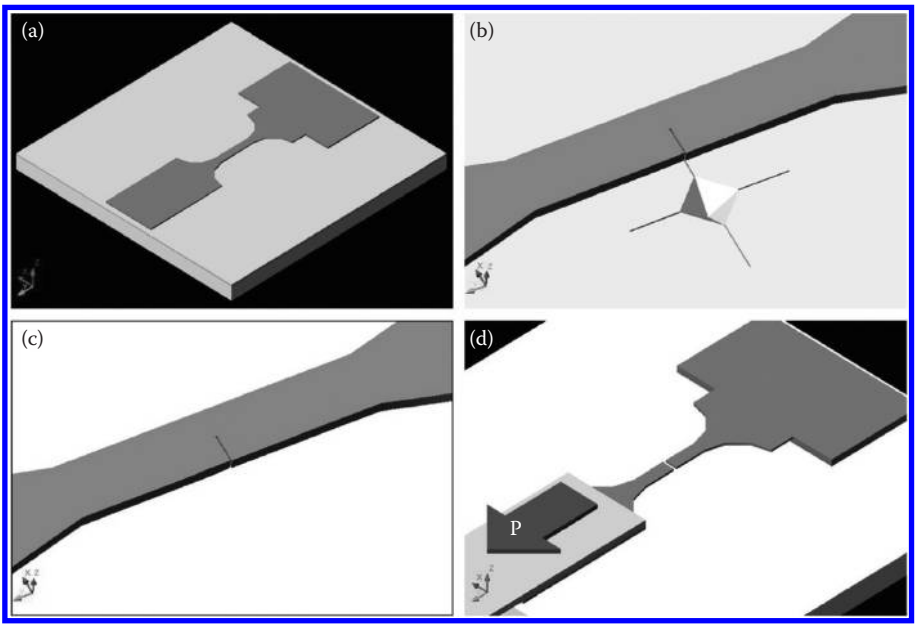


FIGURE 2.35 Microscale fracture specimen preparation and testing: (a) specimen before indentation of SiO_2 substrate, (b) specimen with edge precrack after indentation, (c) free-standing specimen with edge precrack after substrate removal (release), and (d) fracture of specimen at applied force P. (From Jonnalagadda, K. et al., *Journal of the Mechanics and Physics of Solids*, 2008. 56(2): 388–401.)

$$\tan\theta = \frac{\Delta}{L_M} \tag{2.29}$$

where L_M is the initial length of the film. Then the tensile load P_M and the stress σ in the film is obtained through Equations 2.30 and 2.31

$$P_M = \frac{P_V}{2\sin\theta} \tag{2.30}$$

$$\sigma = \frac{P_M}{A} \tag{2.31}$$

where P_V is the load on the film by indentation (vertical); A is the cross-sectional area of the film in gauge section.

At fracture of the film, the fracture toughness is calculated according to Equation 2.28. The method was used in the ultrananocrystalline diamond film, polycrystalline gold film [143,148–152].

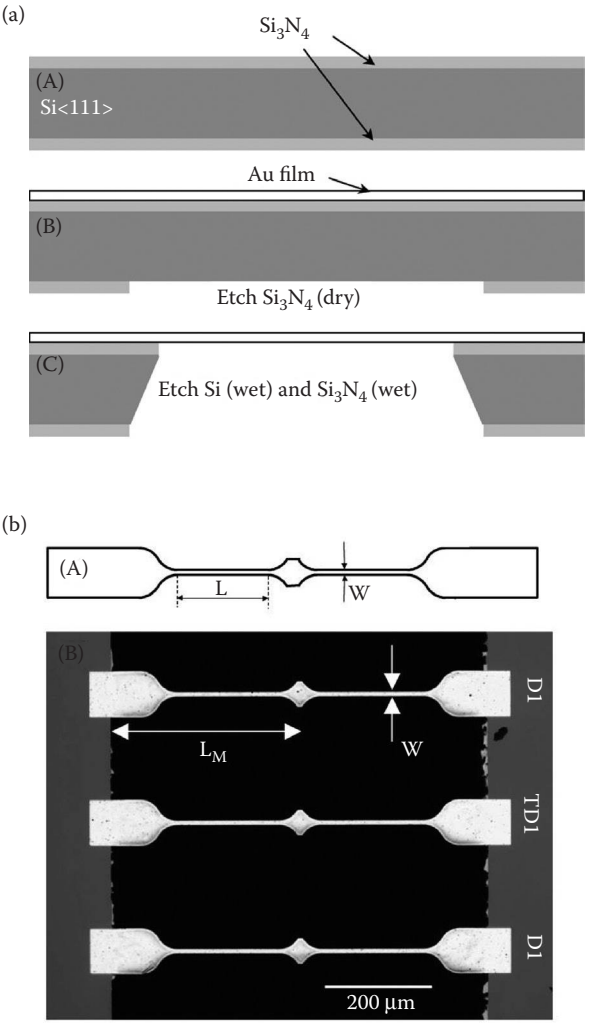


FIGURE 2.36 (a) Schematic representation of the three general microfabrication steps used to process the specimens; (b) optical image of three Au membranes showing characteristic dimensions. L_M is half the membrane span, and W is the membrane width. (From Espinosa, H.D., B.C. Prorok, and M. Fischer, *Journal of the Mechanics and Physics of Solids*, 2003. 51(1): 47–67.)

2.4.3 Tension by Residual Stress

In this ingenious way of loading, the residual tensile stress in a thin film is made use of to serve as the loading to fracture the film for fracture toughness measurement [138,139,145]. The film to be tested is made into bridges with lithographic technologies (a film strip that is freestanding from substrate while both sides still adhere well

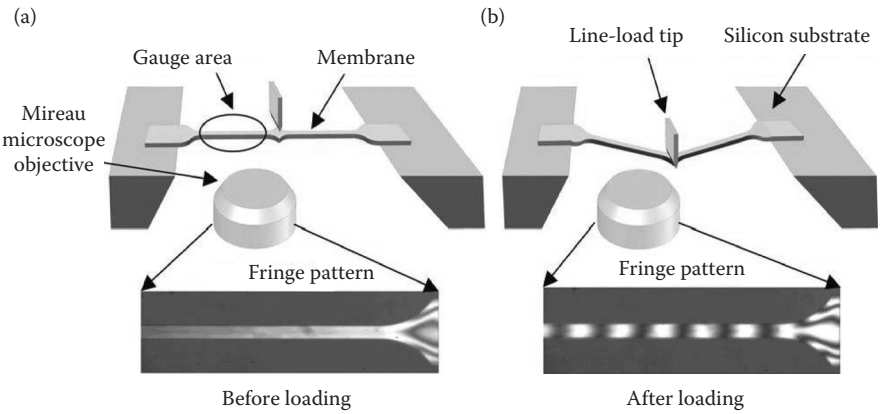


FIGURE 2.37 Schematic drawing of the MDE setup and monochromatic images of the bottom side of a membrane in the unloaded state (a) and under load (b). (From Peng, B., N. Pugno, and H.D. Espinosa, *International Journal of Solids and Structures*, 2006. 43(11–12): 3292–3305.)

on the substrate) (Figure 2.38b). A sharp precrack is made into film bridges before freestanding from substrate with indentation (Figure 2.38a and c). After the freestanding, film bridges are stressed automatically due to unleashing of the residual stress. The stress intensity is related to the initial crack length as shown of K versus a curves in Figure 2.38d. Bridge cracks if stress intensity factor is above the fracture toughness. Thus, the fracture toughness lies between the stress intensity factors of those broken and unbroken (dot line in Figure 2.38d). For the successful application of this method, the residual stress must be tensile (not compressive) and the magnitude should only be in the range of a few tens of megapascals.

2.4.4 Bulging of Films

The bulge test was originally proposed for the accurate measurement of elastic properties of freestanding films [153], and was later used in the measurement of fracture toughness [136,137,154]. In the bulge test, a rectangular "window" of the silicon substrate was etched away to reveal the film to be tested (Figure 2.39a). Focused ion beam was used to prepare a precrack of $2l$ in length in the film along the longer side at the middle of the window (Figure 2.40). A uniform air or water pressure was applied at the window to "bulge up" the film as shown in Figure 2.39b. As the window's length over width is greater than 4, the stress σ and strain ε of the film will be uniformly distributed across the width of the bulged film [136] (Figure 2.39b):

$$\sigma = \frac{p(a^2 + h^2)}{2ht} \tag{2.32}$$

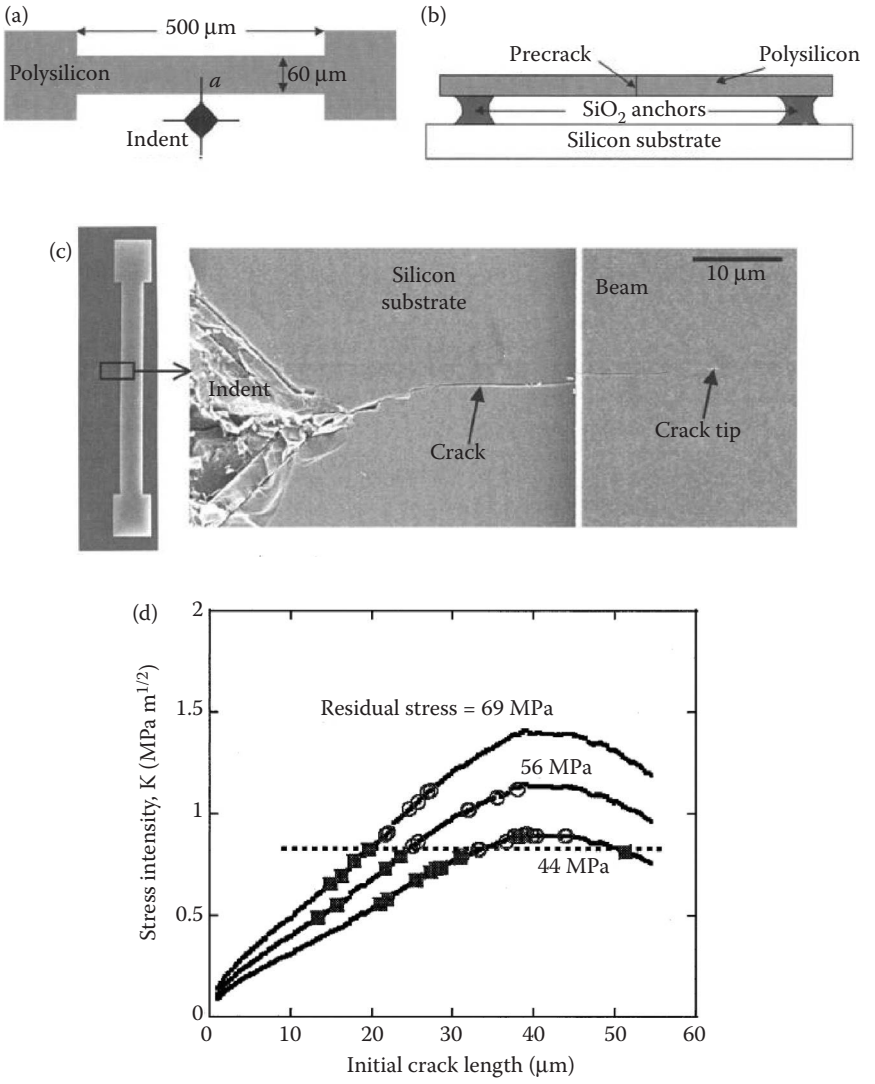


FIGURE 2.38 Images of the film bridges used to measure fracture toughness and stress corrosion. (a) Schematic top view showing the dimensions. (b) Schematic side view. (c) Scanning electron micrograph (SEM) of a 60 µm-wide beam with an indent placed near its center, with a higher magnification SEM of the area near the indent showing the precrack traveling from the substrate into the beam. The indent was made on the SiO_2 release layer, which was subsequently removed by the HF release acid. (d) Plot of stress intensity K versus crack length a for polysilicon film bridges. The solid lines show the relation between K and a for three values of residual stress; the dotted line is fracture toughness K_{Ic} determined from these data. (From Kahn, H. et al., *Science*, 2002. 298(5596): 1215–1218.)

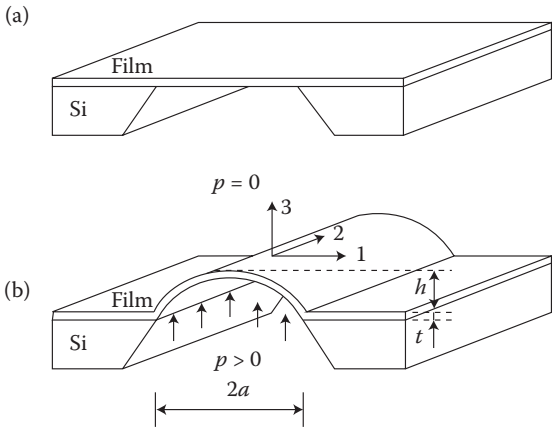


FIGURE 2.39 Schematic illustration of the bulge test for a section of a long rectangular membrane: perspective views of the freestanding film, (a) before and (b) after a pressure (p) is applied. (From Xiang, Y. et al., *International Journal of Fracture*, 2007. 144(3): 173–179.)

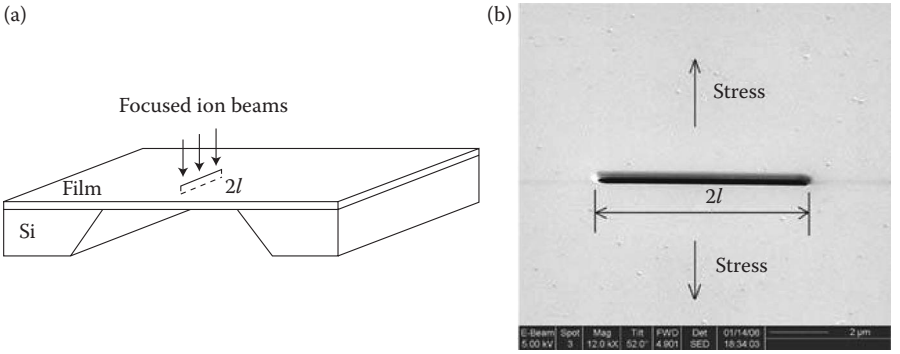


FIGURE 2.40 (a) Schematic illustration of the microfabrication of a precrack of length 2l at the center of a freestanding membrane using a focused ion beam and (b) SEM image of a typical precrack. The arrows indicate the transverse direction of the membrane. (From Xiang, Y. et al., *International Journal of Fracture*, 2007. 144(3): 173–179.)

and

$$\varepsilon = \varepsilon_0 + \frac{a^2 + h^2}{2ah}\arcsin\left(\frac{2ah}{a^2 + h^2}\right) - 1 \tag{2.33}$$

where p is the applied pressure, h is the membrane deflection, t is the film thickness, $2a$ is the width of the membrane, and ε_0 is the residual strain in the films.

At critical pressure, Equation 2.32 gives rise to the crucial stress. Plugging into Equation 2.27 yields the fracture toughness of the film.

2.4.5 Macrotension of Substrate

A recently proposed method is microtensile testing of film microbridges via macrotension to a substrate [146]. In this method, the film is deposited on a rectangular silicon wafer substrate, in which an initial edge crack is introduced using a diamond cutter with a manual application of a small force. After film deposition, a section of the film ahead of the substrate crack is patterned into strips as shown in Figure 2.41. Precracks on each film strip are made with Vickers indentation into the adjacent substrate region. The film strips are then released from the substrate by etching away a ZnO sacrificial layer to form film microbridges; that is, the middle of the strip is released while both ends are still affixed to the substrate. As the surface tension of the etchant would fracture the microbridges easily when the sample is taken out of the liquid, a sample holder is made to allow testing in water. On testing, a displacement-controlled loading is applied to the substrate by manually dialing a micrometer. The tensile loading opens the substrate crack beneath the microbridges, causing the bridges to fracture.

2.4.5.1 Substrate Configuration

Figure 2.41 is the schematic of the sample configuration: a crack is made at one edge of a rectangular silicon wafer with two pin-holes made at each side of the crack. The rectangular shape of the substrate is of the so-called double cantilever beam, which ensures that the cracking of the substrate takes place in a stable manner upon displacement-controlled loading [155,156].

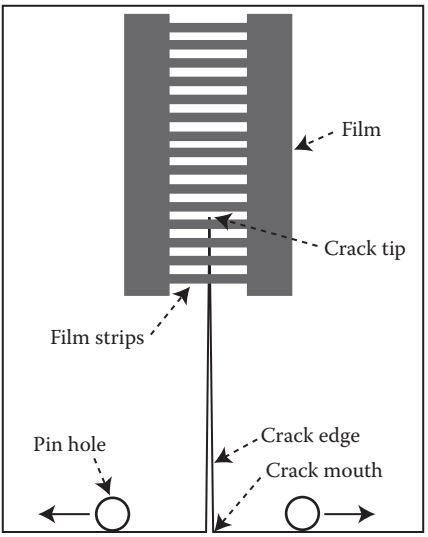


FIGURE 2.41 Schematic of the testing configuration: a rectangular silicon wafer substrate containing an edge crack and two pin-holes; a series of film strips just ahead of the tip of substrate crack. Just before testing, the film strips will be released from substrate through etching away the sacrificial layer between the film and the substrate; upon loading, the substrate crack extends in a stable manner and travels beneath film bridges.

Ensuring a straight propagation of the crack in an isotropic ceramic plate have been shown to be a big challenge [157], but not a problem to a silicon wafer as in the single crystal material the crack tends to propagate perfectly straightly along a crystal plane.

2.4.5.2 Loading Stage

Figure 2.42 is the loading stage comprising

1. Two aluminum blocks as the loading platform, one of which is mobile and the other is stationary; each block has a steel pin of 1 mm in diameter to match the pin-holes in the wafer. Two blocks are placed tightly side by side. In testing, the double cantilever beam wafer substrate is placed on the blocks so that the pins go through the pin-hole in the wafer.
2. A commercially obtained differential micrometer with displacement sensitivity of 0.5 μm is attached to the mobile block. Turn of the micrometer results in the movement of the mobile block, then the loading is applied on the wafer through the movement of the pin affixed on the mobile block.

   Though this simple loading stage is not strictly displacement controlled, it is stiff enough to ensure the substrate crack propagating in a semistable manner. Each turn of the micrometer results in about 0.5 μm opening up of the crack mouth, giving rise to about 50 μm crack propagation before it ceases, as shown in Figure 2.43.
3. A water tank in which the testing sample and part of the blocks are placed.

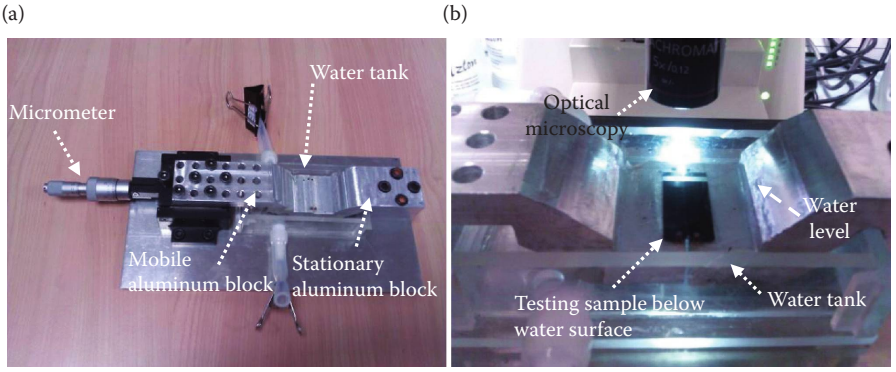


FIGURE 2.42 Testing stage: In (a) the whole stage is shown: two aluminum blocks, a micrometer, and a water tank. The right aluminum block is fixed and therefore stationary; the left aluminum block is able to move toward left driven by the micrometer with 0.5 μm resolution. Two pins, fixed at the platform of the two blocks separately, are for loading; the water tank is used for etching and in-water testing. In (b) the stage is shown during testing: the optical microscopy is to inspect the etching process of sacrificial layer, and to observe fracture events of film strips during testing; sample is submerged in water during etching and testing.

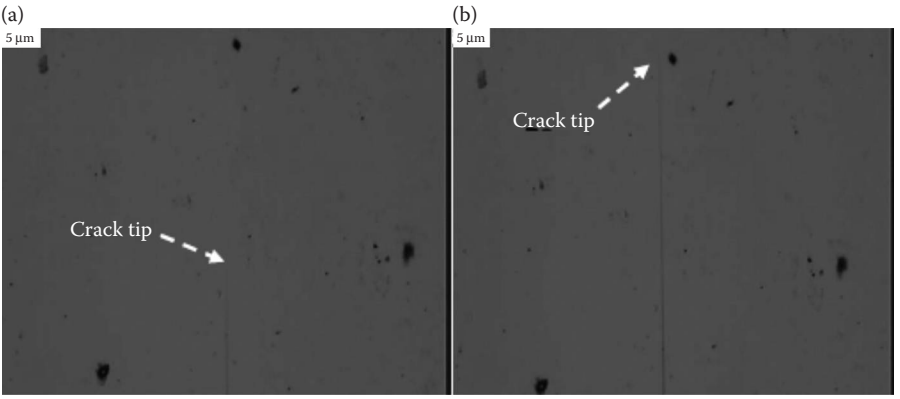


FIGURE 2.43 A substrate crack before (a) and after (b) a single loading step, the crack extension distance is about 50 µm.

2.4.5.3 Preparation of the Substrate Precrack

In order to achieve a gradual propagation of the substrate cracking, it is necessary to start with a sharp crack. A number of methods have been proposed in literatures on making sharp cracks in ceramic plates: Knoop indentation [158], three-point bending of sandwiched specimen [159], contact stresses between the sample and two polymer blocks [160], indentation and scratch [161,162], and so on. Here, a simple cutting is adopted. A diamond cutter is placed at the edge of the wafer, and a small force is applied to make a tiny notch. A sharp crack is easily obtained in the notch that immediately propagates into the wafer as shown in Figure 2.44. Once the crack



FIGURE 2.44 A crack on silicon wafer substrate introduced on cutting at an edge with a diamond tip.

forms, it usually travels through the wafer and breaks it into two. To prevent this simultaneous catastrophic propagation, the cut is performed after a layer of photoresist is spin-coated on the wafer (the photoresist layer is needed in making the microbridges). The photoresist layer effectively restrains the initial propagation to less than 10 mm.

2.4.5.4 Preparation of Film Microbridges

To make the film microbridges, the film is first patterned into strips using the standard photolithographic technique and then etching away the sacrificial layer between the film and the substrate.

Though SiO_2 is traditionally used as the material for sacrificial layer in MEMS technology, it is not used in this work for two reasons:

1. The etching rate of SiO_2 is extremely low: to release a film strip of 60 μm over 4 h are needed, which is in most cases intolerable. To overcome the slow etching, some authors even patterned small holes in the film to allow multiple entry of etchant [138], but that inevitably compromises the integrity of the film.
2. HF etchant used in the processing is highly toxic.

In this method, sputtered ZnO is used as the sacrificial layer due to its remarkable lateral etching rate [163,164]: only about 10 min are needed to etch through a 60 μm wide film strip using 0.25% HCl etchant. The etchant is not only nontoxic, but more importantly, most metals can survive in such a mild HCl solution for such a short time—thus making the test for thin metallic films also becomes possible.

After the film is patterned into strips and before the sacrificial layer is etched away, Vickers indentation is applied on the adjacent substrate region to induce a precrack in each film strip [144,145,147]. Then, upon etching away of the sacrificial layer, the microbridges are realized with each bridge containing a sharp precrack (of various lengths) at the edge.

2.4.5.5 *In Situ* Inspection in Testing

A capillary force exists when the etching solution is drained away [165], which easily fractures the thin "bridges" as they already contain precracks at the edge. This is a classical capillary force problem in MEMS [166]. A water tank (c.f., Figure 2.42) is thus used to house the platform so that the tensile testing can be carried out without subjecting the microbridges to the capillary force. In practice, immediately when the etching is completed, fresh water is allowed to flow in from the bottom to overflow the etchant away. An optical microscopy is used to observe the etching process and the breakage of the bridges during testing.

2.4.5.6 Extraction of the Fracture Toughness

Let ε_f be the strain of the freestanding film, and E_f its Young's modulus, thus within the elastic range, the stress σ_f on the film is

$$\sigma_f = E_f \varepsilon_f \tag{2.34}$$

And, the stress intensity factor K_I at the tip of the precrack is obtained by [132]

$$K_I = \sigma_f \sqrt{\pi a} f(a/W) \tag{2.35}$$

where $f(a/W) = 1.12 - 0.23(a/W) + 10.55(a/W)^2 - 21.72(a/W)^3 + 30.41(a/W)^4$, W is the width of the film bridge and a is the length of the precrack, and $a/W \leq 0.6$ is required. Fracture toughness K_{IC} is obtained if the strain is obtained at fracture (critical strain).

The film strain ε_f can be measured through the extension δ of the film during testing

$$\varepsilon_f = \frac{\delta}{L_o} \tag{2.36}$$

where L_o is the original length of the freestanding film before loading.

For a nonprestressed bridge, δ is obtained from the substrate displacement δ_s between the two points where the two ends of the bridge anchor. The total displacement of the substrate δ_s contains two parts: the elastic displacement δ_{se} and the crack opening distance δ_{so}

$$\delta_s = \delta_{se} + \delta_{so} \tag{2.37}$$

The substrate displacement δ_s of a (100) silicon wafer is determined using finite element method. In the coordinate system referred to as x,y-axis along the ⟨110⟩ direction, and z-axis along the thickness ⟨100⟩ direction, the following symmetric stiffness matrix C ($\times 10^2$ GPa) is calculated [167,168]:

$$C = \begin{bmatrix} 1.944 & 0.352 & 0.639 & & & & \\ 0.352 & 1.944 & 0.639 & & & & \\ 0.639 & 0.639 & 1.657 & & & & \\ & & & 0.509 & & & \\ & & & & 0.796 & & \\ & & & & & 0.796 & \end{bmatrix}$$

Eight-node anisotropic elements were used to model the large deflection of double cantilever beam silicon wafer specimen. Due to the symmetry of the loading configuration, only half of the substrate was simulated. Figure 2.45 shows the FEM results of the half substrate. Figure 2.45a is the substrate total displacement (δ_s in Equation 2.37) at various locations from the edge into the wafer along an imaginary line for three scenarios, where the line is (1) 0 mm (dots); (2) 0.5 mm (+); and (3) 1.5 mm (open circles) from one side of the crack edge. As scenario 1 is for the crack opening only, no substrate is involved, thus δ_{se} is zero. If there is noticeable elastic

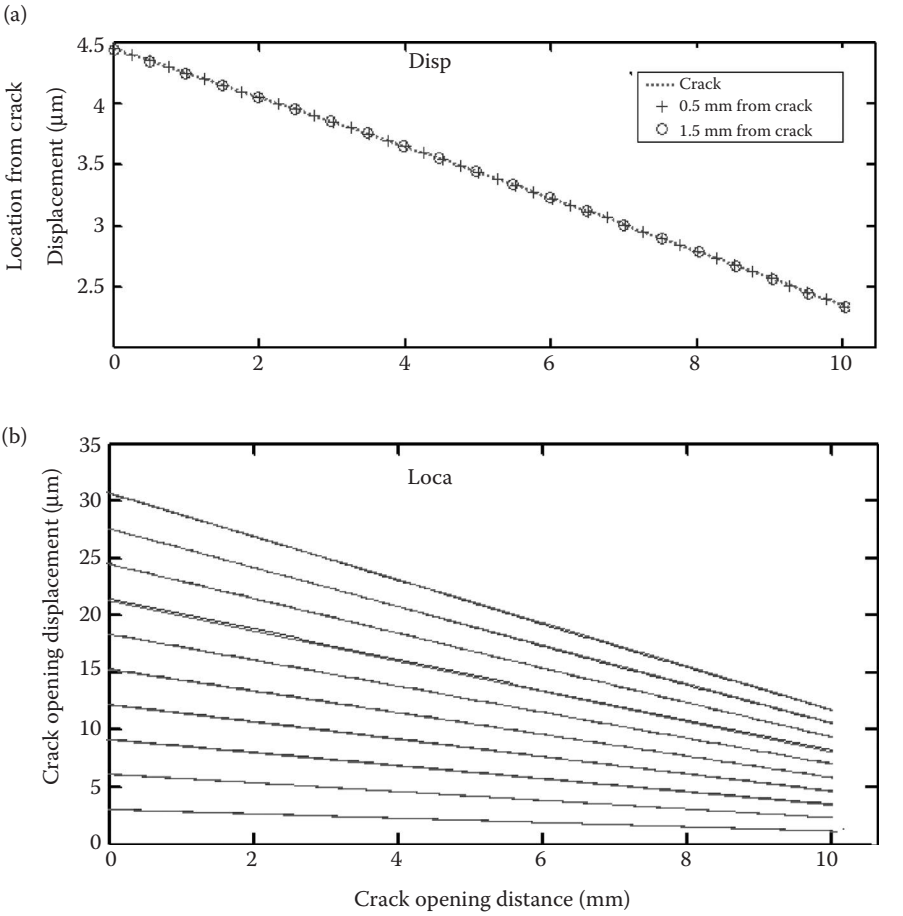


FIGURE 2.45 FEM results of the displacement of silicon substrate. In (a) the displacements are shown along three lines: Red line is the displacement along crack, "+" and "o" are on lines 0.5 mm and 1.5 mm from the side of the crack edge, respectively. In (b) the crack opening distance as the crack mouth opens from 0 to 35 μm are shown: blue lines are FEM results and the red lines are linear fitting.

displacement from the substrate, the distance δ_s for scenario 2 and 3 would be different from scenario 1 (see Equation 2.37). In Figure 2.45a, the results for scenario 2 and 3 completely overlap with that of scenario 1, indicating that the elastic displacement δ_{se} on the substrate is negligible at least 1.5 mm away from the edge of the crack (sufficiently long enough for any possible length of the microbridge). Thus, Equation 2.37 reduces to

$$\delta_s = \delta_{so} \tag{2.38}$$

that is, the substrate displacement is just the crack opening distance.

Figure 2.45b is the crack opening distance δ_{so} as the crack mouth opens from 0 to 35 μm (vertical axis). As seen, the relationship of δ_{so} with the location is linear. Thus, given the crack opening distance δ_{so} at the crack mouth (the largest δ_{so} value) and the crack length into the wafer, calculation of the crack opening distance δ_{so} becomes easy.

A residual stress is generally generated during the deposition process. The residual stress will be released upon the sacrificial layer is etching away. This stress release causes the microbridge to bend or stretch with an extension δ_r:

$$\delta_r = \frac{\sigma_r}{E_f} * L_o \tag{2.39}$$

Thus, the total displacement of the bridge becomes

$$\delta = \delta_s + \delta_r \tag{2.40}$$

Inserting δ from Equation 2.40 into Equation 2.36 obtains strain ε_f of the film, which returns stress σ_f of the film through Equation 2.34. Consequently, Equation 2.35 gives rise to the stress intensity factor K_I. In theory, as δ obtained is at the fracture, K_I becomes K_{IC}.

In practice, as the loading is step-wise (not continuous) and the initial crack length made in the microbridges is discrete, direct attainment of the critical crack length is not possible. Then, K_{IC} value of the film can be identified as "in between" of the K_I values of the broken and the unbroken bridge.

As the tensile force exerted on the film bridge is via opening of the substrate crack, the wedge-shaped substrate crack makes the tensile force not completely uniaxial tensile. The stress (and strain) difference across the width of the film bridge is assessed with a deviation factor ε_d:

$$\varepsilon_d = \frac{(\delta_{top} - \delta_{bottom})}{\delta_{top}} \tag{2.41}$$

where δ_{top} and δ_{bottom} are crack opening distances at top and bottom locations where the film bridge anchors.

2.4.5.7 A CNx Film Case Study

A CNx film (0.31 μm) was tested as a case study. Films were sputter-deposited on silicon wafers. Table 2.5 tabulates the mechanical and the physical properties of the film. Young's modulus and hardness are obtained by nanoindentation. The residual stress is calculated with the Stoney equation through curvature measurement before and after the film deposition [169] on 2″ (100) silicon wafer of 315 μm in thickness. The thickness of film is measured by profilometry and verified by FESEM cross-sectional examination. XPS is used to measure the elemental concentration.

TABLE 2.5
The Properties of Sputter-Deposited CNx and CuZr Films

	CNx Film	CuZr Amorphous Film
Concentration (at.%)	C:N = 60.60:39.40	Cu:Zr = 18.64:44.64
Thickness (μm)	0.31	1.10
Young's modulus E (GPa)	77.4	124.1
Hardness H (GPa)	6.5	6.04
Residual stress σ_r (MPa)	348.0	183.6
Strip width W ()	58.0	80.0
Strip length (μm)	600.0	600.0

The sample preparation for testing of the CNx film is as follows:

1. *Deposition of sacrificial layer*: ZnO (0.5 μm thick) is sputter deposited on a 4″ (100) silicon wafer of 425 μm in thickness.
2. *Deposition of the testing film*: CNx film (0.31 μm thick) is sputter deposited on ZnO layer.
3. *Creating the initial substrate crack*: 10 μm AZ400 photoresist is spin coated on top of the CNx coated Si wafer, which is then cured on a hot plate at 110° for 4 min; the wafer is then cut into a rectangle of 16 mm × 33 mm; at the middle of shorter edge, a notch is made with a diamond tip to produce a crack of about 10 mm perpendicular to the edge.
4. *Patterning the film into strips*: Standard MEMS patterning method is used in patterning. Oxygen plasma is employed to etch away the unwanted film and expose the wafer. When the photoresist on the film is washed away, roughly 200 strips per wafer measuring 58 μm × 600 μm and 102 μm apart are obtained. The strip number patterns are also made during the patterning of the films for easy recognition (the last strip from the crack mouth as number 1, then when the strip is made into microbridge it is referred to as "Bridge No. 1").
5. *Creating the precracks on the strips*: Vickers indentation at a load of 500 mN is used to induce a sharp crack on each strip. The precrack length is measured at scanning electron microscope and recorded along with the strip number.
6. *Making the "pin-holes"*: Two U-shaped grooves 5 mm apart were cut into the edge of the wafer with a diamond wafer blade to serve as the pin-hole.

Figure 2.46a shows the rectangular wafer with "pin-holes" and the initial substrate crack. Film strips and corresponding number labels close to the left-side edge are visible. Figure 2.46b shows the enlarged film strips, in which the substrate crack and Vickers indentations for precrack are clear. Figure 2.46c has the enlarged indentation impression and Figure 2.46d demonstrates precrack made into the film.

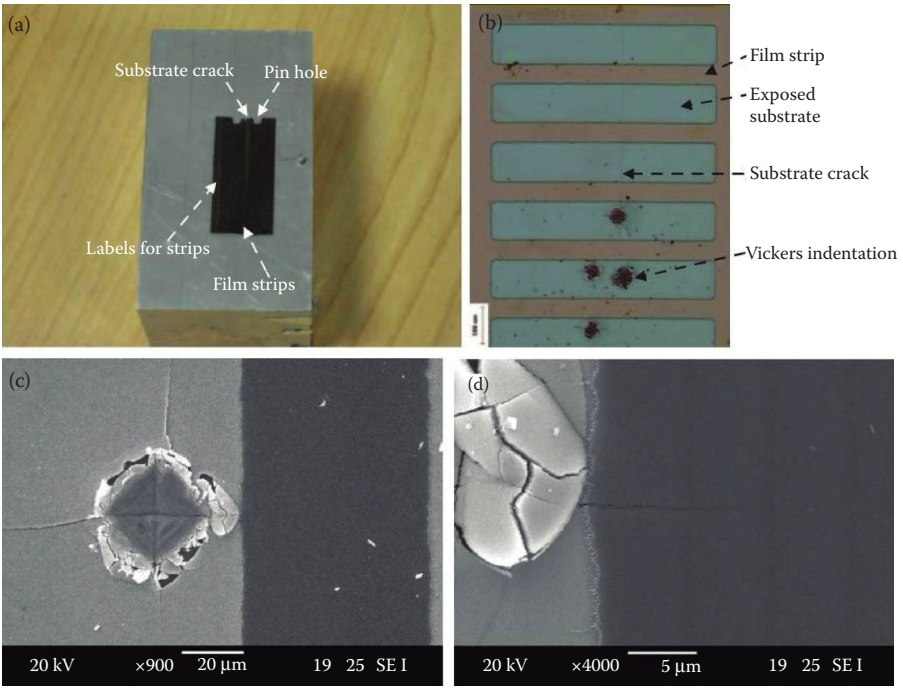


FIGURE 2.46 The prepared testing sample of CN film: (a) the whole sample of rectangular shape (16 × 33 mm), (b) some part of the film strips, (c) a Vickers impression for precrack preparation, and (d) the magnification of (c) showing the perpendicular precrack prepared in the film strip. During etching process, the sacrificial layer between film and substrate will be etched away and thus film strips become freestanding. Upon testing, substrate crack will travel beneath freestanding film strips and the opening up of the substrate crack will exert a tensile force on film strips until they fracture at precracks introduced by Vickers indentation.

The etching of the sacrificial layer and the testing of the precracked CNx film microbridges are as follows:

The etching of the sacrificial layer come right before the tensile testing. The testing sample is assembled in the water tank under an optical microscope; the 0.25% HCl etchant is poured into the tank to submerge the sample. As the microscopic observation indicates the completion of the etching process, pure water is allowed to flow in from the bottom tube to overflow the etchant out of the tank from the upper tube. In this way, the height of the liquid in tank is kept constant to ensure smooth exchange of the liquids without subjecting the microbridges to capillary force. Effectively, no breakage of the microbridges occurs in the process.

Seven loadings (termed "fracture event" in Table 2.6) are conducted. For each loading, the length of the substrate crack into the wafer and the opening distance at crack mouth is measured, and the fracture of the microbridges is optically surveyed and recorded. Figure 2.47 has two optical image showing five mircobridges under stress during testing. In Figure 2.47a, only bridge No. 3 fractures. Upon next loading, shown in Figure 2.47b, bridge No. 2 fractures as well. Calculated stress

TABLE 2.6
Testing Results of the Fracture Toughness of CNx Film (MPa m$^{1/2}$)

Strip Number			10	11	12	13	14	15
Precrack Length a (μm)			5.42	1.94	0	2.71	4.26	6.78
Fracture Events	Substrate Crack Length and Opening Displacement δ_{so} at Crack Mouth (μm)		Stress Intensity Factor K_I (MPam$^{1/2}$)					
C1	32,000	49.4	0.14	0.0069	NA	0.21	0.41	0.72
C2	32,000	61.7	0.24	0.24	\	0.55	0.88	1.38
C3	32,000	66.0	0.37	0.33	\	0.67	1.04	1.62
C4	32,000	77.2	0.72	0.55	\	0.98	1.47	2.22
C5	32,000	86.4	1.01	0.73	\	1.24	1.82	2.72
C6	32,000	93.8	1.24	0.88	\	1.44	2.10	(3.12)
C7	32,000	113.4	1.85	1.26	\	1.98	2.84	4.17
Estimated fracture toughness K_{IC}(MPa m$^{1/2}$)			$1.85 < K_{IC}$	$1.26 < K_{IC}$	\	$1.98 < K_{IC}$	$2.84 < K_{IC}$	$2.72 < K_{IC} < 3.12$
Deviation $\varepsilon_d = (\delta_{top} - \delta_{bottom})/\delta_{top}$			0.0375	0.0340	0.0312	0.0288	0.0267	0.025

16	17	18	19	20	21	22	23	24
5.85	0	5	7.9	5.4	0	6.65	6.5	0
Stress Intensity Factor K_I (MPa m$^{1/2}$)								
0.82	NA	1.04	1.59	1.39	NA	1.94	2.08	NA
1.46	\	1.70	2.52	2.16	\	2.90	3.07	\
1.69	\	1.93	2.84	2.43	(\)	(3.24)	(3.42)	(\)
2.27	\	2.53	(3.69)	(3.13)	\	4.11	4.32	\
2.76	\	(3.02)	4.39	3.70	\	4.83	5.06	\
(3.14)	\	3.42	4.95	4.17	\	5.41	5.66	\
4.17	(\)	4.47	6.43	5.39	\	6.94	7.24	\
$2.76 < K_{IC} < 3.14$	\	$2.53 < K_{IC} < 3.02$	$2.84 < K_{IC} < 3.69$	$2.43 < K_{IC} < 3.13$	\	$2.90 < K_{IC} < 3.24$	$3.07 < K_{IC} < 3.42$	\
0.0234	0.022059	0.0208	0.0197	0.0187	0.0178	0.0170	0.0163	0.0156

(*Continued*)

TABLE 2.6 (*Continued*)
Testing Results of the Fracture Toughness of CNx Film (MPa m$^{1/2}$)

25	**26**	**27**	**28**	**29**	**30**	**31**	
2.9	**5.23**	**0**	**12.15**	**6.5**	**8.45**	**7.05**	**Estimated Fracture Toughness K_{IC} (MPa m$^{1/2}$)**
			Stress Intensity Factor K_I (MPa m$^{1/2}$)				
1.53	2.28	NA	(4.68)	(3.12)	(3.93)	(3.65)	$2.28 < K_{IC} < 3.12$
2.21	(3.25)	\	6.59	4.37	5.47	5.06	$3.07 < K_{IC} < 3.25$
2.44	3.60	\	7.26	4.81	6.01	5.55	$2.84 < K_{IC} < 3.24$
(3.06)	4.49	(\)	9.00	5.94	7.42	6.80	$2.53 < K_{IC} < 3.06$
3.57	5.22	\	10.43	6.88	8.57	7.89	$2.76 < K_{IC} < 3.02$
3.98	5.81	\	11.59	7.63	9.50	8.73	$2.10 < K_{IC} < 3.12$
5.06	7.37	\	14.63	9.62	11.95	10.98	$2.84 < K_{IC}$
$2.44 < K_{IC} < 3.06$	$2.28 < K_{IC} < 3.25$	\	$K_{IC} < 4.68$	$K_{IC} < 3.12$	$K_{IC} < 3.93$	$K_{IC} < 3.65$	
0.015	0.0144	0.0138	0.0133	0.0129	0.0125	0.0120	

Note: All calculating results of the stress intensity factor are listed; the film strips that break at seven fracture events are highlighted in round parentheses; the fracture toughness obtained from each fracture event and each film bridge is listed in the last column and the second last row, respectively; the last row is the calculated error from uniaxial tensile testing condition for each bridge.

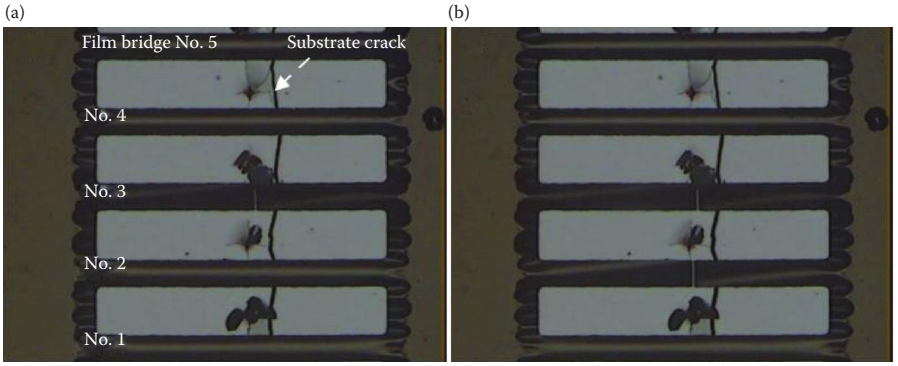


FIGURE 2.47 Five freestanding film strips (film bridges) of CNx film during testing just before and after a fracture event: In (a) film strip No. 3 is already fractured but others are not. In (b) the film strip No. 2 fractured upon a further loading. Film strip fractures at the place where a precrack exists induced by a Vickers indentation.

intensity factor K_I at fracture events C1–C7 is tabulated in Table 2.6 for microbridges numbered with 10 to 31. Some of the bridges do not have good initial cracks (strips of No. 12, 17, 21, 24, and 27), thus is labeled NA. The bridges fractured under each loading are highlighted in parentheses. For example, at fracture event C1, bridges numbered 28 and above fractured and thus are in parentheses. At each fracture event, K_{IC} should lie in between the smallest K_I of the broken and the largest K_I of the unbroken bridges. For instance, at fracture event C1, K_{IC} is between 2.28 MPa $m^{1/2}$ of bridge No. 26 and 3.12 MPa $m^{1/2}$ of bridge No. 29; K_{IC} can also be identified by observing the stress response of a particular microbridge at adjacent two fracture events. For example, bridge No. 15 does not break at C5 with K_I of 2.72 MPa $m^{1/2}$ but breaks at C6 with K_I of 3.12 MPa $m^{1/2}$. Therefore, K_{IC} should be in between 2.72 MPa $m^{1/2}$ and 3.12 MPa $m^{1/2}$. Consequently, a series of K_{IC} ranges are obtained. The results are tabulated in Table 2.6, and also plotted in Figure 2.48. In theory, the upper bounds and the lower bounds should converge to the true K_{IC} of the film. In practice, K_{IC} should lie in between the smallest "gap" of the bounds. Reading from the dotted line in Figure 2.48, the fracture toughness of the film is therefore 3.05 MPa $m^{1/2}$.

The deviation from complete uniaxial tensile condition is also evaluated with the deviation factor ε_d as given in Equation 2.41. As entered in the last row in Table 2.6, ε_d decreases as the bridge number increases: 0.0375 at No. 10 and 0.012 at No. 31. In other words, the bridge closer to the substrate crack mouth has smaller deviation. The largest deviation of all the bridges tested is 0.0375 or less than 4%.

2.4.5.8 Loose-Columnar Aluminum Layer: A New Lift-off Material for the Testing of a Film Deposited at an Elevated Temperature

For the etching of the above CNx film to form strip patterns, oxygen plasma was adopted. However, for those films that have no ready etchant, lift-off process is usually used to prepare the film patterns (Figure 2.49): before film deposition,

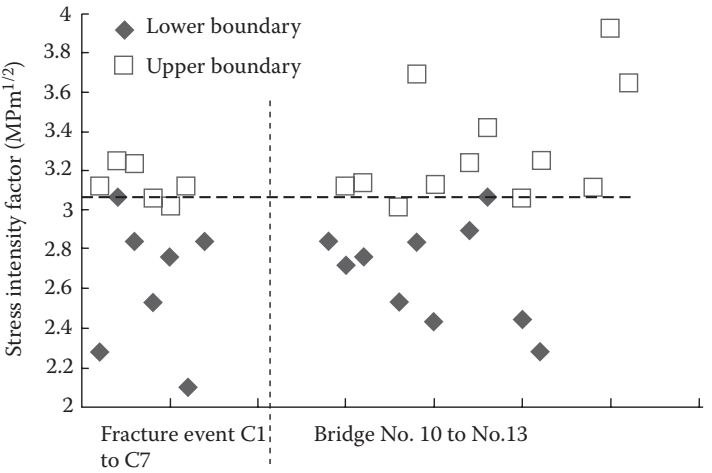


FIGURE 2.48 Upper and lower boundaries of the fracture toughness of CNx film, indicating that the pinpointed fracture toughness is 3.05 MPa m$^{1/2}$: the first seven pairs of data are from C1 to C7 (the last column in Table 2.6), and others are from bridges No. 10 to 31 (the second last row in Table 2.6).

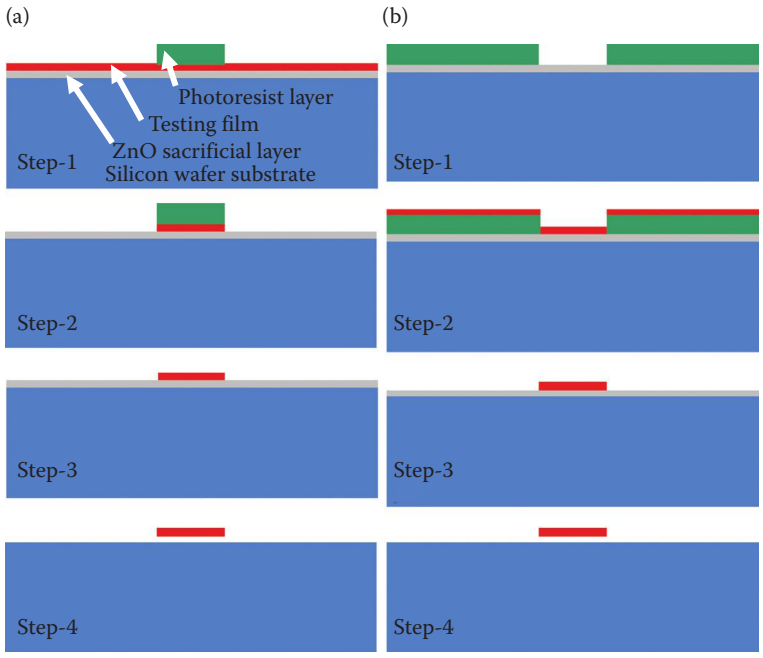


FIGURE 2.49 Illustration of the etching away (a) and the lift-off method (b) to produce film patterns.

a layer of photoresist is spin-coated on the wafer and then patterned onto the desired region with standard photolithographic technique to expose substrate surface. After deposition of desired film, dissolution of the photoresist is done to realize the stripping of the film. However, for those films prepared with sputtering technology at elevated temperatures, the photoresist cannot survive during film deposition. To solve the problem, a loose-columnar aluminum material (melting point of 660°C) is introduced with magnetron sputtering method to serve as the lift-off layer.

Figure 2.50a and b are the surface topographies of the *dense* Al layer prepared with sputtering technique. Figure 2.50c–e are surface topographies of loose Al layer proposed by the authors. It is clear that *dense* Al layer consists of equiaxed grains (100–300 nm) and bright surface. No pores and voids appear at grain boundaries, while loose Al layer exhibited a matt surface and consists of tapered crystallites separated by voids. Gaps between grains are about 50 nm. Figure 2.50f is tensile-fracture cross-section of the loose Al layer showing the columnar structure through the thickness. *Dense* Al layer exhibited ductile and could not be fractured, while loose Al is much brittle due to its loose structure.

Patterning of the loose Al layers is conducted as in Figure 2.51.

Step 1: A layer of photoresist is spin-coated on the surface of the samples.
Step 2: Patterning the photoresist layer into strips pattern with photolithography technique. AZ9260 developer is used in the developing process of the photoresist layer after exposure.
Step 3: Keeping the sample in the AZ9260 developer for about 5 s, intensive reaction was observed that lasted for about 1 min. Microscopy examination confirmed that 5 μm thick Al (series-1) has been etched through completely.
Step 4: Washing away the residual photoresist top layer with acetone solution.

Following the above four steps, patterned loose Al layer is realized. It is notable that the ZnO sacrificial layer is well preserved during the etching process of the loose Al layer by AZ9260 developer. The compatibility of the loose Al layer with the ZnO sacrificial layer is crucial for the combination of "the loose Al/ZnO sacrificial layer" to be used in the preparation of the film microbridges.

For comparison, the etching of dense Al with AZ9260 developer is conducted in the same procedure as above. No visible etching was detected. Prolonged etching of 1 h only produced subtle etching impression on the dense Al surface. The quick etching character of the loose Al layer with AZ9260 developer is owed to its loose structure. The loose Al layer has about 20% void in-between column crystals (Figure 2.50e), which enables the etchant to go through the thickness instantly resulting in rapid etching rate. Tests show that only less than 1 min is required to etch away 5 μm loose Al in thickness.

The application of the loose Al layer to replace the photoresist layer as the lift-off material makes it possible for the testing of the films prepared with sputtering techniques at raised substrate temperatures.

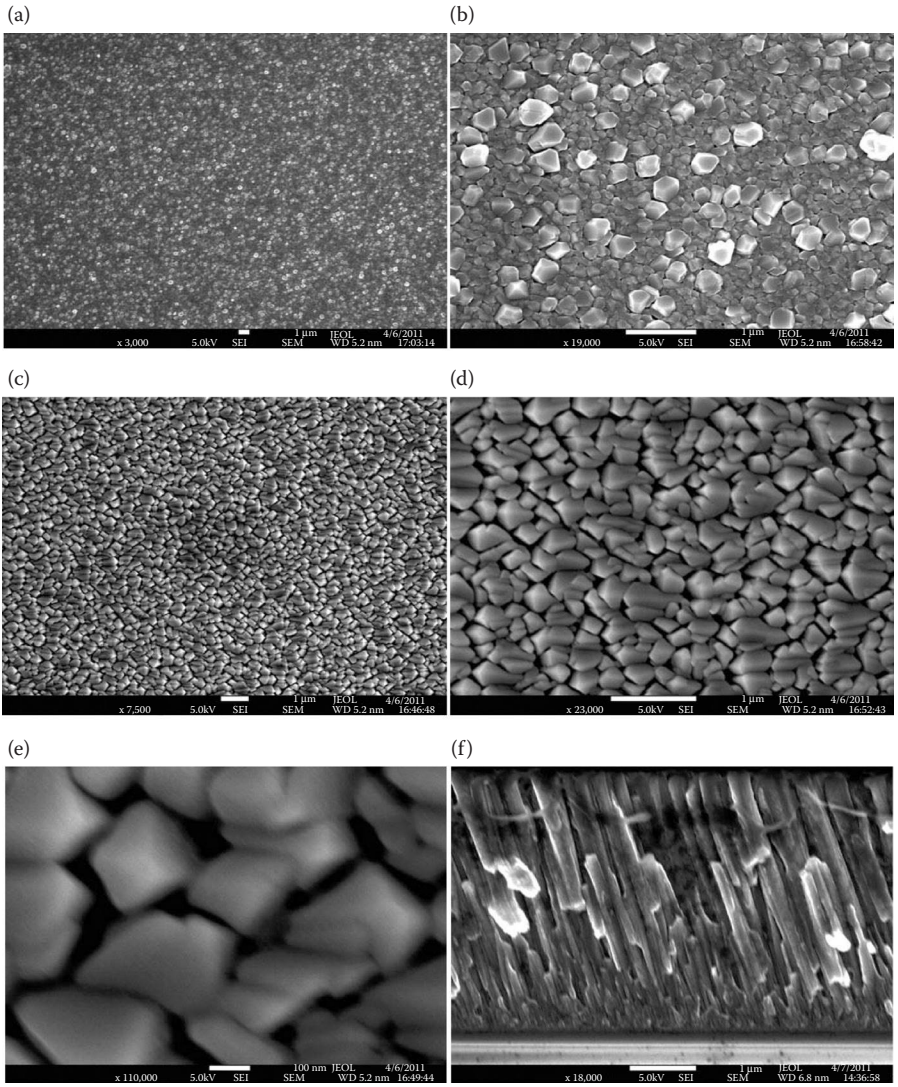


FIGURE 2.50 Structure of the sputter-deposited Al films. (a,b) are the surface topographies of dense Al; (c–e) are surface topographies of loose Al; (f) is the tensile-fracture cross section of loose Al.

The combination of "the loose Al/ZnO sacrificial layer" is used in the preparation of the film microbridges for the testing of the fracture toughness of CuZr amorphous film. After all processing steps and testing, the fracture results at 4 fracture events on 5 bridges (No. 5 to No. 9) are plotted as in Figure 2.52, from which, a K_{IC} value of 1.10–1.20 MPa $m^{1/2}$ is obtained.

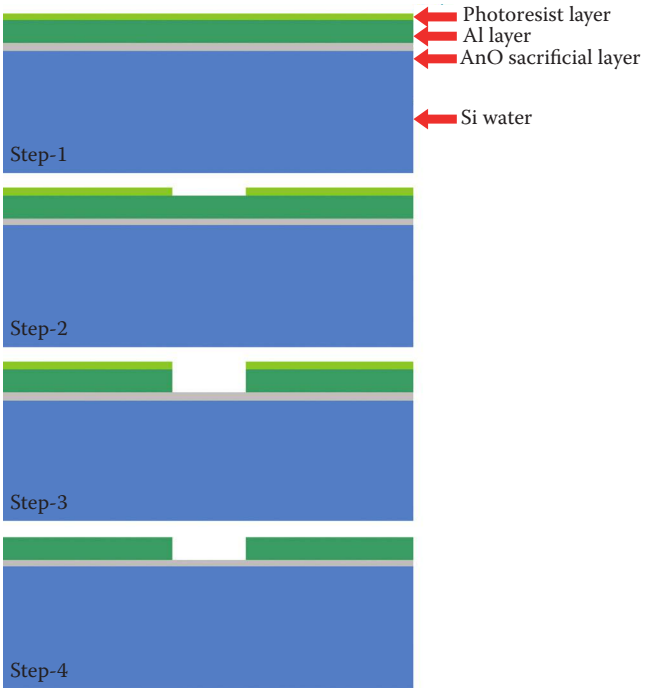


FIGURE 2.51 Illustration to produce Al patterns: Step-1, ZnO (300 nm) and Al (5 μm) is sputtering-deposited. And, then a layer of photoresist is spin-coated; Step-2, patterning the photoresist with standard exposure and develop procedure (AZ9260 developer); Step-3, Al layer is etched with AZ9260; Step-4, residual photoresist removed by acetone and aluminum pattern formed.

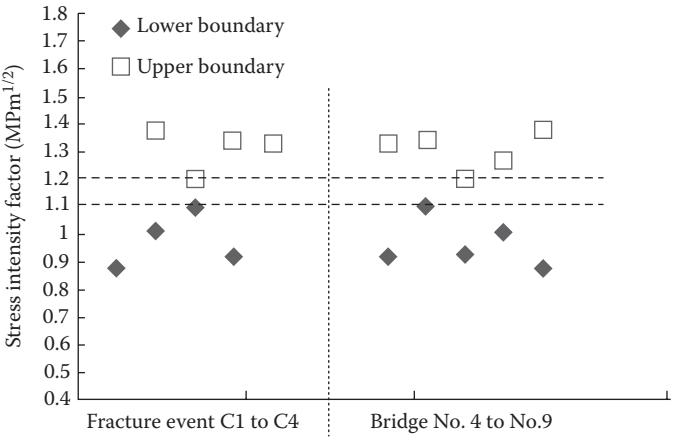


FIGURE 2.52 Upper and lower boundaries of the fracture toughness of CuZr film, indicating that the fracture toughness is between 1.10 and 1.20 MPa m$^{1/2}$: the first four pairs of data are from fracture events and the left are from film bridges.

2.4.5.9 Advantage of the Tension on Substrate Method

1. This method successfully turns the tensile testing of the film into tensile loading of the substrate, avoided the delicate clamping, and a direct loading on the film itself.
2. A series of freestanding film strips are loaded at the same time during testing. This make the critical strain of film fracture easily determinable from the broken–unbroken dividing position of film strips and the opening distance of the substrate crack, which avoids the awful difficulty of a direct measurement of the film stress/strain.
3. The introduction of the loose-columnar Al layer to replace the photoresist as the lift-off material extends the macrotension of substrate method to most PVD films.
4. The shortcoming of the method is its in-water testing.

2.5 SUMMARY

2.5.1 Hard Coatings

Effective coating toughness is dependent on the type of loading conditions experienced in the application. Indentation plasticity is well correlated with durability in contact situations where contact stresses are high and some ductility is required to avoid brittle fracture. Scratch toughness more emphasizes the damage tolerance of hard coatings under highly loaded sliding. The nanoimpact test determines the fatigue fracture resistance of the coating at contact and impact situations. It extends the range of nanomechanical test techniques to much higher strain rates than are possible in standard quasistatic nanoindentation. Repetitive high-strain contact allows the durability of coatings under intermittent highly loaded contact to be determined. The fatigue fracture resistance determined in the nanoimpact shows a very high level of correlation with coating performance in these types of contact situations—such as hard coatings for cutting tools or TBCs subject due to erosive impacts in jet engines—due to the closer simulation than in quasistatic tests.

2.5.2 Thin Films

To probe the intrinsic characteristics of the toughness of a coating/film, notable progresses have been made to conduct a measurement of the fracture toughness of a coating/film, like standard methods for bulk materials.

The methods developed on the coated system based on the radial cracking, the circumferential cracking, as well as the channel cracking patterns give a quantitative analysis of the fracture toughness of a coating. Among them, the nanoindentation ultralow loading method based on the radial cracking is most simple, but there is a difficulty in excluding the substrate effect; the nanoindentation method based on circumferential cracking has been heavily investigated and most debated. The channel cracking pattern was mechanically well studied, however, there is still a tough job to determine the substrate effect factor. Overall, all these methods conducted on coated systems are semiquantitative at most.

A microtensile testing is most straightforward to measure the fracture toughness of thin films. Notable progress has been made in the micro- and nanoscale tensile testing in recent years. Quite a few methods have been proposed to challenge the difficulties coming from the preparation of freestanding film sample with microscale size and conducting a tensile test on them: Inchworm actuation, membrane deflection, tension by residual stress, bulging of film, and the most recent macrotension on substrate. The macrotension on substrate method successfully avoids the delicate clamping and a direct loading on the film itself by turning the tensile testing of the film into tensile loading of the substrate. The advantage of the method lies in its simplicity in conducting the tensile testing of thin films and the lack of expense involved in loading apparatus. Preliminary testing results are encouraging.

ACKNOWLEDGMENTS

This work was supported by Project No. T208A1218 of the Ministry of Education, Singapore, and partly by Project No. 51001084 of the National Natural Science Foundation, China, and Project No. 2012JM6002 of the Natural Science Foundation of Shaanxi Province, China.

ABBREVIATIONS

PI	plasticity index
CPR	crack propagation resistance
DLC	diamond like carbon
CVD	chemical vapor deposition
PVD	physic vapor deposition
AFM	atomic force microscope
SEM	scanning electron microscope
FEM	field emission microscopy
TBC	thermal barrier coating
MEMS	micro-electromechanical system

SYMBOLS

K	Stress intensity factor
K_C	Critical stress intensity factor
K_{IC}	Critical stress intensity in opening mode
U	Fracture energy
W_{irr}	Irreversible energy
W_p	Plastic work
W_e	Elastic work
W_t	Total work
Γ	Fracture toughness
σ_y	Yield stress

t	Thickness
E	Young's modulus
H	Hardness
P	Pressure
σ	Stress
ε	Strain
δ	Displacement
υ	Poisson's ratio
n	Hardening exponent
f	Film
s	Substrate
i	Interface
η	Elastic recovery parameter

REFERENCES

1. Dieter, G.E., *Mechanical Metallurgy*, 2nd ed. 1976: McGraw-Hill, London.
2. Wong, E.W., P.E. Sheehan, and C.M. Lieber, Nanobeam mechanics: Elasticity, strength, and toughness of nanorods and nanotubes. *Science*, 1997. 277(5334): 1971–1975.
3. Broek, D., *Elementary Engineering Fracture Mechanics*, 4nd ed. 1986: M. Nijhoff, Boston.
4. Anderson, T., *Fracture Mechanics: Fundamental and Applications*. 2005: CRC Press, Boca Raton, FL.
5. Hosokawa, H., A.V. Desai, and M.A. Haque, Plane stress fracture toughness of free-standing nanoscale thin films. *Thin Solid Films*, 2008. 516(18): 6444–6447.
6. Jiang, Z. et al., Accurate measurement of fracture toughness of free standing diamond films by three-point bending tests with sharp pre-cracked specimens. *Diamond and Related Materials*, 2000. 9(9–10): 1734–1738.
7. ASTM1421–99, Standard Test Methods for the Determination of Fracture Toughness of Advanced Ceramics at Ambient Temperature. Annual Book Standards, Vol. 15.01. ASTM Int., West Conshohocken, PA. ASTM C 1421-99 Standard Test Methods, 1999. 15.01.
8. ASTM E399-90(1997), Standard Test Method for Plane-Strain Fracture Toughness of Metallic Materials, ASTM International, West Conshohocken, PA, 1997.
9. Greenwood, J.A. and J.B.P. Williamson, Contact of nominally flat surfaces, *Proceedings of the Royal Society of London A*, 1960. 295: 300.
10. Fox-Rabinovich, G.S. et al., Elastic and plastic work of indentation as a characteristic of wear behavior for cutting tools with nitride PVD coatings. *Thin Solid Films*, 2004. 469–470: 505–512.
11. Fox-Rabinovich, G.S. et al., Effect of mechanical properties measured at room and elevated temperatures on the wear resistance of cutting tools with TiAlN and AlCrN coatings. *Surface and Coatings Technology*, 2006. 200(20–21): 5738–5742.
12. Cheng, Y.T. and C.M. Cheng, Relationships between hardness, elastic modulus, and the work of indentation. *Applied Physics Letters*, 1998. 73(5): 614–616.
13. Cheng, Y.T. and C.M. Cheng, Scaling, dimensional analysis, and indentation measurements. *Materials Science & Engineering R-Reports*, 2004. 44(4–5): 91–149.
14. Beake, B.D. et al., Coating optimisation for high speed machining with advanced nanomechanical test methods. *Surface & Coatings Technology*, 2009. 203(13): 1919–1925.
15. Beake, B.D. et al., Using Nanomechanics to Optimise Coatings for Cutting Tools in Handbook of Nanostructured Thin Films and Coatings, Mechanical Properties. 2010: CRC Press, Boca Raton, FL.

16. Choi, Y., H.S. Lee, and D. Kwon, Analysis of sharp-tip-indentation load-depth curve for contact area determination taking into account pile-up and sink-in effects. *Journal of Materials Research*, 2004. 19(11): 3307–3315.
17. Chudoba, T. and N.M. Jennett, Higher accuracy analysis of instrumented indentation data obtained with pointed indenters. *Journal of Physics D-Applied Physics*, 2008. 41(21): 215407.
18. Milman, Y.V., Plasticity characteristic obtained by indentation. *Journal of Physics D-Applied Physics*, 2008. 41(7): 074013.
19. ISO14577, ISO 14577: Metallic Materials—Instrumented Indentation Test for Hardness and Materials Parameters, Part 4—Test Method for metallic and non-metallic coatings, CEN, Brussels, Belgium.
20. Leyland, A. and A. Matthews, Design criteria for wear-resistant nanostructured and glassy-metal. *Surface & Coatings Technology*, 2004. 177: 317–324.
21. Leyland, A. and A. Matthews, On the significance of the H/E ratio in wear control: A nanocomposite coating approach to optimised tribological behaviour. *Wear*, 2000. 246(1–2): 1–11.
22. Beake, B.D. and J.F. Smith, Nano-impact testing-an effective tool for assessing the resistance of advanced wear-resistant coatings to fatigue failure and delamination. *Surface & Coatings Technology*, 2004. 188: 594–598.
23. Fox-Rabinovich, G. et al., Physical and mechanical properties to characterize tribological compatibility of Heavy Loaded Tribo-systems (HLTS), pp 121–150, in Self-Organization during Friction: Advanced Surface Engineered Materials and Systems Design, G.S. Fox-Rabinovich, G. Totten (eds.) . 2007: Taylor and Francis Books, CRC Press LLC, Boca Raton, FL.
24. Bull, S.J., Failure mode maps in the thin film scratch adhesion test. *Tribology International*, 1997. 30(7): 491–498.
25. Pei, Y.T., D. Galvan, and J.T.M. De Hosson, Nanostructure and properties of TiC/a-C:H composite coatings. *Acta Materialia*, 2005. 53(17): 4505–4521.
26. Voevodin, A.A. and J.S. Zabinski, Supertough wear-resistant coatings with 'chameleon' surface adaptation. *Thin Solid Films*, 2000. 370(1–2): 223–231.
27. Voevodin, A.A. and J.S. Zabinski, Load-adaptive crystalline-amorphous nanocomposites. *Journal of Materials Science*, 1998. 33(2): 319–327.
28. Voevodin, A.A. et al., Wear-resistant composite coatings deposited by electron enhanced closed field unbalanced magnetron sputtering. *Surface & Coatings Technology*, 1995. 73(3): 185–197.
29. Harry, E. et al., Failure and adhesion characterization of tungsten-carbon single layers, multilayered and graded coatings. *Surface & Coatings Technology*, 1999. 116: 172–175.
30. Ligot, J., S. Benayoun, and J.J. Hantzpergue, Analysis of cracking induced by scratching of tungsten coatings on polyimide substrate. *Wear*, 2000. 243(1–2): 85–91.
31. Zhang, S. et al., Effect of sputtering target power on microstructure and mechanical properties of nanocomposite nc-TiN/a-SiNx thin films. *Thin Solid Films*, 2004. 447–448: 462–467.
32. Zhang, S. et al., Toughening of hard and superhard thin films: A critical review. *Surface & Coatings Technology*, 2005. 198(1–3): 2–8.
33. Zhang, S. et al., Toughness measurement of thin films: A critical review. *Surface & Coatings Technology*, 2005. 198(1–3): 74–84.
34. Colligon, J.S., V.M. Visnhyakov, R. Valizadeh, and B.D. Beake, 18th International Conference on Ion-Surface Interactions, (ISI-2007) Zvenigorod, Russia. 2007.
35. Beake, B.D., S.R. Goodes, and B. Shi, Nanomechanical and nanotribological testing of ultra-thin carbon-based and MoST films for increased MEMS durability. *Journal of Physics D-Applied Physics*, 2009. 42(6): 065301.

36. Trelewicz, J.R. and C.A. Schuh, The Hall-Petch breakdown at high strain rates: Optimizing nanocrystalline grain size for impact applications. *Applied Physics Letters*, 2008. 93(17): 3.
37. Constantinides, G. et al., Quantitative impact testing of energy dissipation at surfaces. *Experimental Mechanics*, 2009. 49(4): 511–522.
38. Constantinides, G. et al., Quantifying deformation and energy dissipation of polymeric surfaces under localized impact. *Materials Science and Engineering a-Structural Materials Properties Microstructure and Processing*, 2008. 489(1–2): 403–412.
39. Arreguin-Zavala, J. et al., Characterization of nanostructured and ultrafine-grain aluminum-silicon claddings using the nanoimpact indentation technique. *Journal of Materials*, 2013. 65(6): 763–768.
40. Kalcioglu, Z.I. et al., Dynamic impact indentation of hydrated biological tissues and tissue surrogate gels. *Philosophical Magazine*, 2011. 91(7–9): 1339–1355.
41. Choi, W.B. et al., Modified indentation techniques to probe inelasticity in Ni-5%Al coatings from different processes. *Journal of Thermal Spray Technology*, 2009. 18(1): 65–74.
42. Wheeler, J.M. et al., Evaluation of micromechanical behaviour of plasma electrolytic oxidation (PEO) coatings on Ti-6Al-4V. *Surface & Coatings Technology*, 2010. 204(21–22): 3399–3409.
43. Moghal, J. et al., Nanomechanical study of thin film nanocomposite and PVD thin films on polymer substrates for optical applications. *Journal of Physics D-Applied Physics*, 2013. 46(48): 5303.
44. Mosquera, A. et al., Advantages of nanoimpact fracture testing in studying the mechanical behavior of CrAl(Si)N coatings. *Nanoscience and Nanotechnology Letters*, 2010. 2(4): 352–356.
45. Mosquera, A., L. Mera., G.S. Fox-Rabinovich, R. Martínez, I. Azkona, and J.L. Endrino, Statistical analysis of nanoimpact testing of Hard CrAl(Si)N coatings. *Materials Research Society Symposium Proceedings*, 2011. 1339: 44–49.
46. Frutos, E. and J.L. Gonzalez-Carrasco, A method to assess the fracture toughness of intermetallic coatings by ultramicroindentation techniques: Applicability to coated medical stainless steel. *Acta Materialia*, 2013. 61(6): 1886–1894.
47. Faisal, N.H., R. Ahmed, and R. Fu, Nano-impact (Fatigue) characterization of as-deposited amorphous nitinol thin film. *Coatings*, 2012. 2(3): 195–209.
48. Wheeler, J.M. and A.G. Gunner, Analysis of failure modes under nano-impact fatigue of coatings via high-speed sampling. *Surface & Coatings Technology*, 2013. 232: 264–268.
49. Beake, B.D. et al., Investigating the fracture resistance and adhesion of DLC films with micro-impact testing. *Diamond and Related Materials*, 2002. 11(8): 1606–1609.
50. Faisal, N.H., R. Ahmed, and Y. Fu, Nano-impact testing and failure mechanism of solar panel DLC film. Proc. ATMC 2011, KACST, Saudi Arabia, 2011: 36–44.
51. Faisal, N.H. et al., Influence of test methodology and probe geometry on nanoscale fatigue failure of diamond-like carbon film. *Surface & Coatings Technology*, 2014. 242: 42–53.
52. Klocke, F. et al., Adhesive interlayers' effect on the entire structure strength of glass molding tools' Pt-Ir coatings by nano-tests determined. *Surface & Coatings Technology*, 2011. 206(7): 1867–1872.
53. Chen, J. et al., An investigation into the correlation between nano-impact resistance and erosion performance of EB-PVD thermal barrier coatings on thermal ageing. *Surface & Coatings Technology*, 2012. 206(23): 4992–4998.
54. Basak, A.K. et al., Material removal mechanisms of monocrystalline silicon under the impact of high velocity micro-particles. *Wear*, 2010. 269(3–4): 269–277.
55. Beake, B.D. et al., Accelerated nano-fretting testing of Si(100). *Tribology International*, 2012. 46(1): 114–118.

56. Beake, B.D., T.W. Liskiewicz, and J.F. Smith, Deformation of Si(100) in spherical contacts—Comparison of nano-fretting and nano-scratch tests with nano-indentation. *Surface & Coatings Technology*, 2011. 206(7): 1921–1926.
57. Beake, B.D., S. Achanta, and T.W. Liskiewicz, Microtribology: New tools to fill measurement gap. *Tribology*, 2010. 4(3): 152–61.
58. Jennett, N.M. and J. Nunn, High resolution measurement of dynamic (nano) indentation impact energy: A step towards the determination of indentation fracture resistance. *Philosophical Magazine*, 2011. 91(7–9): 1200–1220.
59. Bouzakis, K.D. et al., Nano-impact test on a TiAlN PVD coating and correlation between experimental and FEM results. *Surface & Coatings Technology*, 2011. 206(7): 1936–1940.
60. Beake, B.D., S.R. Lau, and J.F. Smith, Evaluating the fracture properties and fatigue wear of tetrahedral amorphous carbon films on silicon by nano-impact testing. *Surface & Coatings Technology*, 2004. 177: 611–615.
61. Fox-Rabinovich, G.S. et al., Design and performance of AlTiN and TiAlCrN PVD coatings for machining of hard to cut materials. *Surface & Coatings Technology*, 2009. 204(4): 489–496.
62. Beake, B.D., Evaluation of the fracture resistance of DLC coatings on tool steel under dynamic loading. *Surface & Coatings Technology*, 2005. 198(1–3): 90–93.
63. Sangiovanni, D.G., V. Chirita, and L. Hultman, Toughness enhancement in TiAlN-based quarternary alloys. *Thin Solid Films*, 2012. 520(11): 4080–4088.
64. Sangiovanni, D.G., L. Hultman, and V. Chirita, Supertoughening in B1 transition metal nitride alloys by increased valence electron concentration. *Acta Materialia*, 2011. 59(5): 2121–2134.
65. Beake, B.D. et al., Investigating the correlation between nano-impact fracture resistance and hardness/modulus ratio from nanoindentation at 25-500 degrees C and the fracture resistance and lifetime of cutting tools with Ti(1 – x)Al(x)N (x = 0.5 and 0.67) PVD coatings in milling operations. *Surface & Coatings Technology*, 2007. 201(8): 4585–4593.
66. Bouzakis, K.D. et al., Optimization of wet micro-blasting on PVD films with various grain materials for improving the coated tools' cutting performance. *Cirp Annals-Manufacturing Technology*, 2011. 60(1): 587–590.
67. Bouzakis, K.D. et al., Influence of dry micro-blasting grain quality on wear behaviour of TiAlN coated tools. *Wear*, 2011. 271(5–6): 783–791.
68. Bouzakis, K.D. et al., Effect of PVD films wet micro-blasting by various Al2O3 grain sizes on the wear behaviour of coated tools. *Surface & Coatings Technology*, 2011. 205: S128–S132.
69. Yoon, S.Y. et al., Impact-wear behaviors of TiN and Ti-Al-N coatings on AISI D2 steel and WC-Co substrates. *Surface & Coatings Technology*, 2004. 177: 645–650.
70. Chen, J. et al., Effects of mechanical properties and layer structure on the cyclic dynamic loading of TiN-based coatings. *Surface & Coatings Technology*, 2011. 206(2–3): 522–529.
71. Beake, B.D., V.M. Vishnyakov, and J.S. Colligon, Nano-impact testing of TiFeN and TiFeMoN films for dynamic toughness evaluation. *Journal of Physics D-Applied Physics*, 2011. 44(8): 85301.
72. Fox-Rabinovich, G.S. et al., Emergent behavior of nano-multilayered coatings during dry high-speed machining of hardened tool steels. *Surface & Coatings Technology*, 2010. 204(21–22): 3425–3435.
73. Wellman, R.G. and J.R. Nicholls, Erosion, corrosion and erosion-corrosion of EB PVD thermal barrier coatings. *Tribology International*, 2008. 41: 657–662.
74. Hoehn, J.W. et al., Micromechanical toughness test applied to NiAl. *Materials Science and Engineering A*, 1995. 192–193(Part 1): 301–308.

75. Holmberg, K. et al., A model for stresses, crack generation and fracture toughness calculation in scratched TiN-coated steel surfaces. *Wear*, 2003. 254(3–4): 278–291.
76. Pharr, G.M., Measurement of mechanical properties by ultra-low load indentation. *Materials Science and Engineering A*, 1998. 253(1–2): 151–159.
77. Lawn, B.R., A.G. Evans, and D.B. Marshall, Elastic/plastic indentation damage in ceramics: The Mediad Radial crack system. *Journal of the American Ceramic Society*, 1980. 63(9–10): 574–581.
78. Evans, A.G. and E.A. Charles, Fracture toughness determinations by indentation. *Journal of the American Ceramic Society*, 1976. 59(7–8): 371–372.
79. Anstis, G.R. et al., A critical-evaluation of indentation techniques for measuring fracture-toughness. 1. Direct crack measurements. *Journal of the American Ceramic Society*, 1981. 64(9): 533–538.
80. Marshall, D.B. and B.R. Lawn, Indentation technique for measuring stresses in tempered glass surfaces. *Journal of the American Ceramic Society*, 1977. 60(1–2): 86–87.
81. Broek, D., Elementary Engineering Fracture Mechanics. 1997: Kluwer Academic Publishers, Dordrecht.
82. Lankford, J. and D.L. Davidson, Crack-initiation threshold in ceramic materials subject to elastic-plastic indentation. *Journal of Materials Science*, 1979. 14(7): 1662–1668.
83. Li, X., D. Diao, and B. Bhushan, Fracture mechanisms of thin amorphous carbon films in nanoindentation. *Acta Materialia*, 1997. 45(11): 4453–4461.
84. Methods, A.C.-S.T., Standard Test Methods for the Determination of Fracture Toughness of Advanced Ceramics at Ambient Temperature. Annual Book Standards, Vol. 15.01. ASTM Int., West Conshohocken, PA. 1999. 15.01.
85. Leonardi, A. et al., Numerical analysis of brittle materials fractured by sharp indenters. *Engineering Fracture Mechanics*, 2010. 77(2): 264–276.
86. Niihara, K., A Fracture-mechanics analysis of indentation-induced Palmqvist crack in ceramics. *Journal of Materials Science Letters*, 1983. 2(5): 221–223.
87. Kruzic, J.J. and R.O. Ritchie, Comments on "Measurement of the microstructural fracture toughness of cortical bone using indentation fracture". *Journal of Biomechanics*, 2008. 41(6): 1379–1380.
88. Quinn, G.D. and R.C. Bradt, On the Vickers indentation fracture toughness test. *Journal of the American Ceramic Society*, 2007. 90(3): 673–680.
89. Sakai, M. and R.C. Bradt, Fracture-toughness testing of brittle materials. *International Materials Reviews*, 1993. 38(2): 53–78.
90. Cook, R.F. and G.M. Pharr, Direct observation and analysis of indentation cracking in glasses and ceramics. *Journal of the American Ceramic Society*, 1990. 73(4): 787–817.
91. Zhang, T.Y., L.Q. Chen, and R. Fu, Measurements of residual stresses in thin films deposited on silicon wafers by indentation fracture. *Acta Materialia*, 1999. 47(14): 3869–3878.
92. Xia, Z.H., W.A. Curtin, and B.W. Sheldon, A new method to evaluate the fracture toughness of thin films. *Acta Materialia*, 2004. 52(12): 3507–3517.
93. den Toonder, J. et al., Fracture toughness and adhesion energy of sol-gel coatings on glass. *Journal of Materials Research*, 2002. 17(1): 224–233.
94. Chen, J. and S.J. Bull, Assessment of the toughness of thin coatings using nanoindentation under displacement control. *Thin Solid Films*, 2006. 494(1–2): 1–7.
95. Michel, M.D. et al., Fracture toughness, hardness and elastic modulus of hydrogenated amorphous carbon films deposited by chemical vapor deposition. *Thin Solid Films*, 2006. 496(2): 481–488.
96. Chen, J. and S.J. Bull, Modelling the limits of coating toughness in brittle coated systems. *Thin Solid Films*, 2009. 517(9): 2945–2952.

97. Cheng, Y.T., Z.Y. Li, and C.M. Cheng, Scaling, relationships for indentation measurements. *Philosophical Magazine a-Physics of Condensed Matter Structure Defects and Mechanical Properties*, 2002. 82(10): 1821–1829.
98. Malzbender, J. et al., Measuring mechanical properties of coatings: A methodology applied to nano-particle-filled sol-gel coatings on glass. *Materials Science and Engineering: R: Reports*, 2002. 36(2–3): 47–103.
99. Malzbender, J. and G. de With, Energy dissipation, fracture toughness and the indentation load-displacement curve of coated materials. *Surface and Coatings Technology*, 2000. 135(1): 60–68.
100. Chen, J. and S.J. Bull, Indentation fracture and toughness assessment for thin optical coatings on glass. *Journal of Physics D-Applied Physics*, 2007. 40(18): 5401–5417.
101. Hainsworth, S.V., T. Bartlett, and T.F. Page, The nanoindentation response of systems with thin hard carbon coatings. *Thin Solid Films*, 1993. 236(1–2): 214–218.
102. Page, T.F. and S.V. Hainsworth, Using nanoindentation techniques for the characterization of coated systems: A critique. *Surface and Coatings Technology*, 1993. 61(1–3): 201–208.
103. Rabe, R. et al., Observation of fracture and plastic deformation during indentation and scratching inside the scanning electron microscope. *Thin Solid Films*, 2004. 469: 206–213.
104. Bahr, D.F. et al., Adhesion and acoustic emission analysis of failures in nitride films with a metal interlayer. *Acta Materialia*, 1997. 45(12): 5163–5175.
105. Haq, A.J. et al., Berkovich indentation of diamondlike carbon coatings on silicon substrates. *Journal of Materials Research*, 2008. 23(7): 1862–1869.
106. Whitehead, A.J. and T.F. Page, Nanoindentation studies of thin film coated systems. *Thin Solid Films*, 1992. 220(1–2): 277–283.
107. Haq, A.J. et al., Effect of coating thickness on the deformation behaviour of diamond-like carbon-silicon system. *Thin Solid Films*, 2010. 518(8): 2021–2028.
108. Zhang, S. and X. Zhang, Toughness evaluation of hard coatings and thin films. *Thin Solid Films*, 2012. 520(7): 2375–2389.
109. Marshall, D.B. and A.G. Evans, Measurement of adherance of residually stressed thin-films by indentation. 1. Mechanics of interface delamination. *Journal of Applied Physics*, 1984. 56(10): 2632–2638.
110. Evans, A.G. and J.W. Hutchinson, On the mechanics of delamination and spalling in compressed films. *International Journal of Solids and Structures*, 1984. 20(5): 455–466.
111. Hutchinson, J.W. and Z. Suo, Mixed-mode cracking in layered materials, in *Advances in Applied Mechanics*, J.W. Hutchinson and T.Y. Wu (eds.) 1992. Vol. 29, pp. 63–191. Springer, Netherlands.
112. He, M.-Y. and J.W. Hutchinson, Kinking of a crack out of an interface. *Journal of Applied Mechanics-Transactions of the Asme*, 1989. 56(2): 270–27827.
113. Zhang, X. and S. Zhang, Rethinking the role that the "step" in the load–displacement curves can play in measurement of fracture toughness for hard coatings. *Thin Solid Films*, 2012. 520(9): 3423–3428.
114. Li, X. and B. Bhushan, Measurement of fracture toughness of ultra-thin amorphous carbon films. *Thin Solid Films*, 1998. 315(1–2): 214–221.
115. Li, X.D. and B. Bhushan, Evaluation of fracture toughness of ultra-thin amorphous carbon coatings deposited by different deposition techniques. *Thin Solid Films*, 1999. 355: 330–336.
116. Lepienski, C.M. et al., Indentation fracture of a-C : H thin films from chemical vapour deposition. *Philosophical Magazine*, 2006. 86(33–35): 5397–5406.
117. Bull, S.J., Nanoindentation of coatings. *Journal of Physics D: Applied Physics*, 2005. 38: R319.
118. Warren, O.L. and T.J. Wyrobek, Nanomechanical property screening of combinatorial thin-film libraries by nanoindentation. *Measurement Science & Technology*, 2005. 16(1): 100–110.

119. He, M.Y. et al., Kinking of a crack out of an interface—Role of inplane stress. *Journal of the American Ceramic Society*, 1991. 74(4): 767–771.
120. Beuth, J.L., Cracking of thin bonded films in residual tension. *International Journal of Solids and Structures*, 1992. 29(13): 1657–1675.
121. Beuth, J.L. and N.W. Klingbeil, Cracking of thin films bonded to elastic-plastic substrates. *Journal of the Mechanics and Physics of Solids*, 1996. 44(9): 1411–1428.
122. Xia, Z.C. and J.W. Hutchinson, Crack patterns in thin films. *Journal of the Mechanics and Physics of Solids*, 2000. 48(6–7): 1107–1131.
123. Begley, M.R., A.G. Evans, and J.W. Hutchinson, Spherical impression of thin elastic films on elastic-plastic substrates. *International Journal of Solids and Structures*, 1999. 36(18): 2773–2788.
124. Wang, J.S. et al., The mechanical performance of DLC films on steel substrates. *Thin Solid Films*, 1998. 325(1–2): 163–174.
125. Leung, D.K. et al., Crack progression and interface debonding in brittle-ductile nanoscale multilayers. *Journal of Materials Research*, 1995. 10(8): 1958–1968.
126. Leung, D.K., M.Y. He, and A.G. Evans, The cracking resistance of nanoscale layers and films. *Journal of Materials Research*, 1995. 10(7): 1693–1699.
127. Jungk, J.M. et al., Indentation fracture toughness and acoustic energy release in tetrahedral amorphous carbon diamond-like thin films. *Acta Materialia*, 2006. 54(15): 4043–4052.
128. Thurn, J. and R.F. Cook, Mechanical and thermal properties of physical vapour deposited alumina films—Part II—Elastic, plastic, fracture, and adhesive behaviour. *Journal of Materials Science*, 2004. 39(15): 4809–4819.
129. Tsui, T.Y., J. Vlassak, and W.D. Nix, Indentation plastic displacement field: Part I. The case of soft films on hard substrates. *Journal of Materials Research*, 1999. 14(6): 2196–2203.
130. Tsui, T.Y., J. Vlassak, and W.D. Nix, Indentation plastic displacement field: Part II. The case of hard films on soft substrates. *Journal of Materials Research*, 1999. 14(6): 2204–2209.
131. Cook, R.F., Deformation and fracture by sharp rolling contacts. *Journal of the American Ceramic Society*, 1994. 77(5): 1263–1273.
132. Murakami, Stress Intensity Factors Handbook. 1987: Pergamon, Oxford.
133. Ballarini, R. et al., The fracture toughness of polysilicon microdevices: A first report. *Journal of Materials Research*, 1997. 12(4): 915–922.
134. Haque, M.A. and M.T.A. Saif, In-situ tensile testing of nano-scale specimens in SEM and TEM. *Experimental Mechanics*, 2002. 42(1): 123–128.
135. Haque, M.A. and M.T.A. Saif, A review of MEMS-based microscale and nanoscale tensile and bending testing. *Experimental Mechanics*, 2003. 43(3): 248–255.
136. Xiang, Y., X. Chen, and J.J. Vlassak, Plane-strain bulge test for thin films. *Journal of Materials Research*, 2005. 20(9): 2360–2370.
137. Xiang, Y. et al., Measuring the fracture toughness of ultra-thin films with application to AlTa coatings. *International Journal of Fracture*, 2007. 144(3): 173–179.
138. Hatty, V. et al., Fracture toughness of low-pressure chemical-vapor-deposited polycrystalline silicon carbide thin films. *Journal of Applied Physics*, 2006. 99(1): 013517.
139. Bellante, J.J. et al., Fracture toughness of polycrystalline silicon carbide thin films. *Applied Physics Letters*, 2005. 86(7): 071920.
140. Jonnalagadda, K. et al., Effect of intrinsic stress gradient on the effective mode-I fracture toughness of amorphous diamond-like carbon films for MEMS. *Journal of the Mechanics and Physics of Solids*, 2008. 56(2): 388–401.
141. Chasiotis, I. and W.G. Knauss, A new microtensile tester for the study of MEMS materials with the aid of atomic force microscopy. *Experimental Mechanics*, 2002. 42(1): 51–57.

142. Cho, S.W., K. Jonnalagadda, and I. Chasiotis, Mode I and mixed mode fracture of polysilicon for MEMS. *Fatigue & Fracture of Engineering Materials & Structures*, 2007. 30(1): 21–31.
143. Espinosa, H.D. et al., Elasticity, strength, and toughness of single crystal silicon carbide, ultrananocrystalline diamond, and hydrogen-free tetrahedral amorphous carbon. *Applied Physics Letters*, 2006. 89(7): 073111.
144. Espinosa, H.D., B.C. Prorok, and M. Fischer, A methodology for determining mechanical properties of freestanding thin films and MEMS materials. *Journal of the Mechanics and Physics of Solids*, 2003. 51(1): 47–67.
145. Kahn, H. et al., Fatigue failure in polysilicon not due to simple stress corrosion cracking. *Science*, 2002. 298(5596): 1215–1218.
146. Zhang, X. and S. Zhang, A., Microbridge method in tensile testing of substrate for fracture toughness of thin films. *Nanoscience and Nanotechnology Letters*, 2011. 3(6): 735–743.
147. Chasiotis, I., S.W. Cho, and K. Jonnalagadda, Fracture toughness and subcritical crack growth in polycrystalline silicon. *Journal of Applied Mechanics-Transactions of the Asme*, 2006. 73(5): 714–722.
148. Peng, B., N. Pugno, and H.D. Espinosa, An analysis of the membrane deflection experiment used in the investigation of mechanical properties of freestanding submicron thin films. *International Journal of Solids and Structures*, 2006. 43(11–12): 3292–3305.
149. Pugno, N., B. Peng, and H.D. Espinosa, Predictions of strength in MEMS components with defects—A novel experimental-theoretical approach. *International Journal of Solids and Structures*, 2005. 42(2): 647–661.
150. Peng, B. et al., Fracture size effect in ultrananocrystalline diamond: Applicability of Weibull theory. *Journal of Materials Research*, 2007. 22(4): 913–925.
151. Espinosa, H.D. and B.C. Prorok, Size effects on the mechanical behavior of gold thin films. *Journal of Materials Science*, 2003. 38(20): 4125–4128.
152. Espinosa, H.D., B.C. Prorok, and B. Peng, Plasticity size effects in free-standing submicron polycrystalline FCC films subjected to pure tension. *Journal of the Mechanics and Physics of Solids*, 2004. 52(3): 667–689.
153. Vlassak, J.J. and W.D. Nix, A new bulge test technique for the determination of young modulus and poisson ratio of thin-films. *Journal of Materials Research*, 1992. 7(12): 3242–3249.
154. Merle, B. and M. Göken, Fracture toughness of silicon nitride thin films of different thicknesses as measured by bulge tests. *Acta Materialia*, 2011. 59(4): 1772–1779.
155. Bäcklund, J. and J. Mackerle, Stress intensity and crack opening of compact tension specimens. *Engineering Fracture Mechanics*, 1979. 12(1): 99–101.
156. Srawley, J.E. and B. Gross, Stress intensity factors for bend and compact specimens. *Engineering Fracture Mechanics*, 1972. 4(3): 587–589.
157. Davalos, J.F. et al., Compliance rate change of tapered double cantilever beam specimen with hybrid interface bonds. *Theoretical and Applied Fracture Mechanics*, 1998. 29(2): 125–139.
158. Chen, C.P. and M.H. Leipold, Fracture-toughness of silicon. *American Ceramic Society Bulletin*, 1980. 59(4): 469–472.
159. Pancheri, P. et al., Production of sharp cracks in ceramic materials by three-point bending of sandwiched specimens. *Engineering Fracture Mechanics*, 1998. 59(4): 447–456.
160. Hashimoto, A. and D. Kovar, Controlled precracking of fracture mechanics specimens using contact stresses. *Journal of the American Ceramic Society*, 2002. 85(9): 2251–2255.

161. Evans, A.G., Method for evaluating time-dependent failure characteristics of brittle materials—And its application to polycrystalline alumina. *Journal of Materials Science*, 1972. 7(10): 1137–1146.
162. Xin, Y.B. and K.J. Hsia, A technique to generate straight through thickness surface cracks and its application to studying dislocation nucleation in Si. *Acta Materialia*, 1996. 44(3): 845–853.
163. Bhatt, V., Pal, and S. Chandra, Feasibility study of RF sputtered ZnO film for surface micromachining. *Surface & Coatings Technology*, 2005. 198(1–3): 304–308.
164. Xu, T. et al., The compatibility of ZnO piezoelectric film with micromachining process. *Sensors and Actuators a-Physical*, 2003. 104(1): 61–67.
165. Kim, C.J., J.Y. Kim, and B. Sridharan, Comparative evaluation of drying techniques for surface micromachining. *Sensors and Actuators a-Physical*, 1998. 64(1): 17–26.
166. Tas, N. et al., Stiction in surface micromachining. *Journal of Micromechanics and Microengineering*, 1996. 6(4): 385–397.
167. Brantley, W.A., Calculated elastic-constants for stress problems associated with semiconductor devices. *Journal of Applied Physics*, 1973. 44(1): 534–535.
168. Chouaf, A. et al., Stress analysis at singular points of micromachined silicon membranes. *Sensors and Actuators a-Physical*, 2000. 84(1–2): 109–115.
169. Janssen, G. et al., Celebrating the 100th anniversary of the Stoney equation for film stress: Developments from polycrystalline steel strips to single crystal silicon wafers. *Thin Solid Films*, 2009. 517(6): 1858–1867.

3 Nanoindentation for Fracture Toughness of Coatings

Jinju Chen

CONTENTS

3.1 Introduction 123
3.2 Indentation Test Methods 124
3.2.1 What Is Nanoindentation? 124
3.2.2 Different Nanoindentation Test Approaches 130
3.2.3 Young's Modulus and Hardness of Coatings 132
3.2.4 Detect Indentation-Induced Fracture 136
3.3 Residual Stress in the Coating 138
3.4 Failure Mechanisms during Nanoindentation Tests 141
3.5 Stress-Based Models to Assess Indentation Fracture Toughness 144
3.5.1 Radial Cracks 145
3.5.1.1 Half-Penny-Like Radial Cracks 145
3.5.1.2 Palmqvist Radial Cracks 148
3.5.2 Lateral Cracks 148
3.6 Energy-Based Models 149
3.6.1 Extrapolate Load–Displacement Curve 150
3.6.2 Extrapolate Total Work–Displacement Curve 153
3.6.3 Method Based on Analyzing Irreversible Work and Plastic Work 154
3.6.4 Extrapolating Irreversible Work versus Load 155
3.6.5 Modeling the Limits of Fracture-Dissipated Energy 156
3.6.6 Assess the Interfacial Fracture-Dissipated Energy 161
3.7 Numerical Analysis of Indentation-Induced Cracking 165
3.8 Summary 169
Acknowledgments 170
References 170

3.1 INTRODUCTION

Ceramics and ceramic coatings have been widely used in many types of engineering systems and have fulfilled a wide range of functions [1–10], such as protecting structural materials in harsh environment, wear resistance, energy storage, and optical properties. The coating deposition techniques and process conditions affect residual

stress and microstructure in the coating, which consequently affect the mechanical properties of the coating (e.g., Young's modulus, hardness, fracture toughness, and interface adhesion). Therefore, evaluation of key mechanical properties can be followed as quality control for the coating systems.

One of the key challenges in measuring the mechanical properties of the coatings is in isolating or eliminating the influence of the substrate. In this context, nanoindentation techniques have been developed to study the mechanical properties of coatings. Nanoindentation tests are nondestructive and efficient, which makes it convenient for such assessments. These techniques are based on pressing an indenter of known geometry into materials, with the load and displacement continuously recorded. Such a load–displacement curve provides a "mechanical fingerprint" of the indented materials [11]. By analyzing the load–displacement curves and images of indented materials, a wide range of mechanical responses such as phase transformation [3,12,13], dislocation burst [14–17], and creep [18–22] can be identified. Based on appropriate models, various mechanical properties at very small scales can be obtained.

For several ceramic coatings, fracture toughness is one of the key mechanical parameters that may limit their application. For a given contact condition, the fracture mechanism of the coatings will be affected by the elastic–plastic responses of the materials, fracture toughness of the coating, and interface toughness between coating and substrate. An evaluation of the mechanical properties of the coatings could guide the optimization of the materials' selection, design, and fabrication. The characterization of the elastic–plastic responses of the coatings (e.g., Young's modulus and hardness) would be discussed before the assessment of toughness.

3.2 INDENTATION TEST METHODS

The difference in microstructure and residual stress in the coatings makes the hardness of the coatings different from their bulk counterpart. For the coatings, the indentation test may be the only viable technique that can be applied to assess their hardness. The indentation (usually referred to as microindentation) is to press a probe (or indenter) into the material, usually at a given load. A microscope will then be used to measure the residual impression left by the indenter. Nanoindentation not only reduces the spatial scale of the test compared to traditional indentation methods but also makes it possible to estimate properties such as hardness and elastic modulus without reliance on post facto microscopy to measure the small indentations formed for many materials. However, post facto microscopy is still very important if more details (such as pile-up, cracking, delamination, and phase transformation) about the deformation response are required.

3.2.1 What Is Nanoindentation?

The typical nanoindenter apparatus employs magnetic coils (see Figure 3.1) or electrical capacitance gages (Figure 3.2) to drive the indenter into the sample. For some commercial indenters, the probe also serves as a scanning probe, which enables

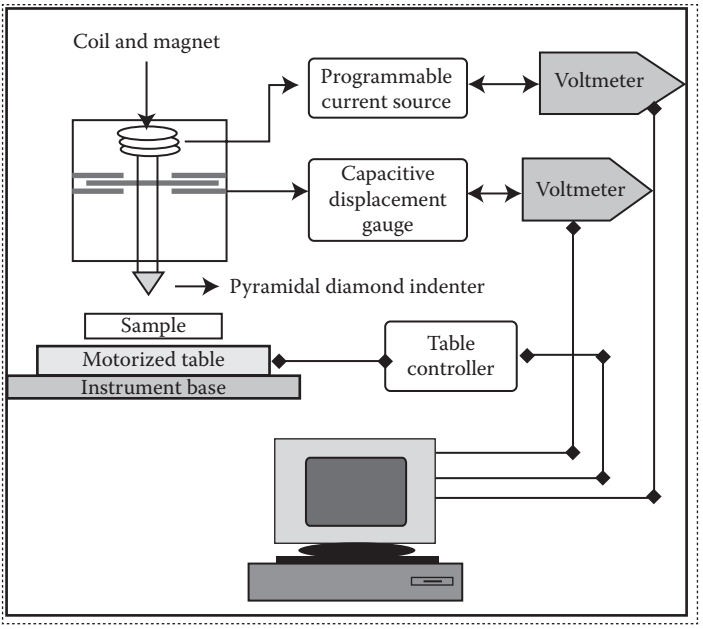


FIGURE 3.1 Schematic drawing of the Nano Indenter® with coil and magnetic gauge.

pre- and postindentation imaging. This is very useful to locate the indentation on some desired small features [23–26]. In addition, it also enables to reveal important indentation-induced deformation mechanisms, such as dislocation slip and crack [15,27]. But one cannot rely on this for quantitative analysis of the contact area because the indenter tip may be relatively blunt unless a specialized sharp indenter is used. The latest nanoindenters (e.g., Micromaterials, Hysitron, and CSM

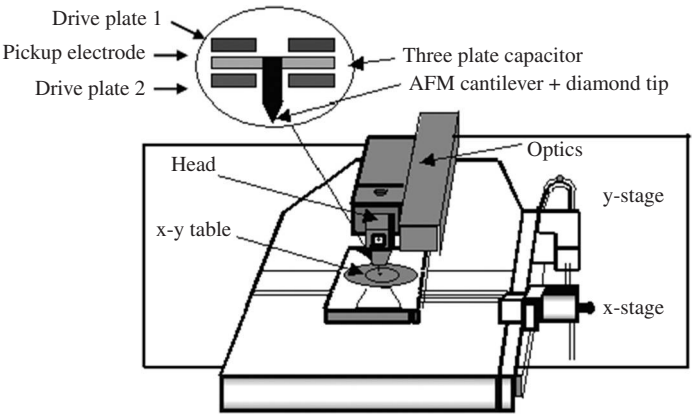


FIGURE 3.2 Schematic of the head and the positioning table where the main parts in a Hysitron triboscope.

nanoindeners) are also equipped with control environmental conditions to assess true "in-service" properties. In addition, it also enables one to do the nanotribological tests [28–30].

Figure 3.3 displays a typical load–displacement curve (P–δ) from a nanoindentation test. The basic parameters in a load–displacement curve are illustrated as follows, which are very useful to derive various mechanical properties of both bulk materials and coatings.

- P_{max}: the maximum applied load.
- S: the contact stiffness at peak load calculated from the slope of the upper part of the unloading curve. It is also known as unloading stiffness.
- δ_{max}: the maximum displacement at the indenter at the maximum applied load. δ_c: the contact depth, which is the actual depth that the indenter in contact with material in the absence of elastic deflection of the surface as shown in Figure 3.4.
- δ_{res}: the residual displacement after the elastic recovery of the material.
- W_t: total work of indentation (the area under the loading curve, i.e., area ADH in Figure 3.3).
- W_e: the elastic work of indentation (the area under the unloading curve, i.e., area GDH in Figure 3.3).
- W_{irr}: irreversible work, which is equal to W_t minus W_e. If the plastic deformation is the only mechanism for energy dissipation, irreversible work equals the energy dissipated by plastic deformation.
- *Segment AB*: the elastic portion of the loading curve where $P\alpha\delta^{1.5}$.
- *Segment BC*: the transition from elastic behavior to elastic–plastic behavior.
- *Segment CD*: the plastic portion of the loading curve where $P\alpha\delta^{2}$.

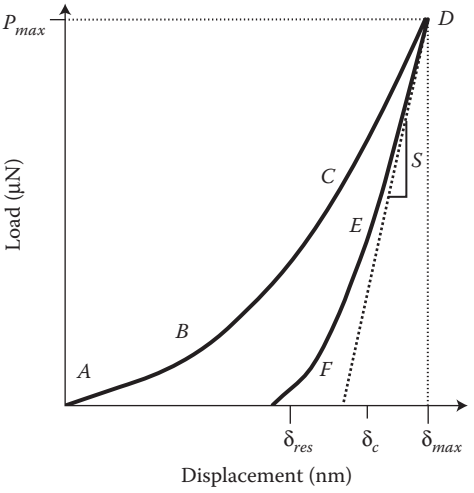


FIGURE 3.3 Schematic of a typical load–displacement curve for an elastic–plastic material indented by a pyramidal tip.

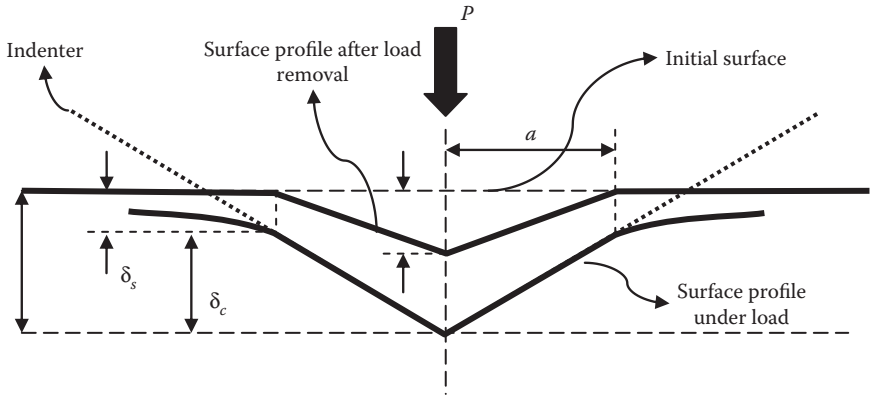


FIGURE 3.4 Schematic of surface profile for an indentation by a pyramidal tip in O&P analysis. Pile-up and sink-in are ignored here. (From Oliver, W.C. and G.M. Pharr, *Journal of Materials Research*, 1992. **7**(6): 1564–1583.)

- *Segment DE*: the initial part of the unloading curve where the recovery of the surface flexure occurs. No change of indent shape occurs in this range.
- *Segment EF*: the region in which full elastic recovery occurs, and the impression changes shape.

Based on the analysis for the elastic unloading of a flat punch, it was suggested that the elastic modulus can be given by [31],

$$E_r = \frac{S}{2}\sqrt{\frac{\pi}{A_C}} \tag{3.1}$$

Considering that a Berkovich tip is actually not axially symmetric, an extra parameter β (β = 1.034) is introduced to correct this equation, which has been widely adopted [33]. If considering a flat-ended triangular tip, the value of β will be a little higher [34]. Since most indenters are not flat punches, a correction for the elastic radial inward displacement in the Sneddon equation when indenting an elastic half space by a rigid indenter is required. This correction factor γ is given by Hay et al. [35].

$$\gamma = \pi\frac{(\pi/4) + 0.15483073\cot\theta((1-2\nu)/4(1-\nu))}{\left((\pi/2) - 0.83119312\cot\theta((1-2\nu)/4(1-\nu))\right)^2} \tag{3.2}$$

where θ is the half included angle of the indenter (which in the case of a Berkovich is 70.32°) and ν is the Poisson's ratio of the material indented. For a very sharp tip (e.g., cube corner indenter (θ = 42.28°)) the expression derived for γ is

$$\gamma = 1 + \frac{(1-2\nu)}{4(1-\nu)\tan\theta} \tag{3.3}$$

Taking these corrections into consideration, Equation 3.9 can be rewritten as,

$$E_r = \frac{S}{2\beta\gamma}\sqrt{\frac{\pi}{A_C}} \tag{3.4}$$

The reduced modulus E_r is given by,

$$\frac{1}{E_r} = \frac{(1-\nu_s^2)}{E_s} + \frac{(1-\nu_i^2)}{E_i} \tag{3.5}$$

The subscripts *i* and *s* refer to the indenter and specimen, respectively. For a diamond tip, $E_i = 1140$ GPa and the Poisson's ratio, ν_i is 0.070. For many ceramics, a value of $\nu = 0.25$ can be used without introducing significant errors into the moduli values calculated.

A_C is the contact area which is given by [32],

$$A_C = C_0\delta_C^2 + C_1\delta_C^1 + C_2\delta_C^{1/2} + C_3\delta_C^{1/4} + \ldots + C_8\delta_C^{1/128} \tag{3.6}$$

where $C_0 = 24.5$ and 2.596 for Berkovich and cube corner indenters, respectively. The constants C_1 to C_8 are fitting parameters that are obtained by calibration tests on fused quartz, a material with well-known mechanical properties that are independent with depth. The contact depth is given by,

$$\delta_c = \delta_{max} - \varepsilon\frac{P_{max}}{S} \tag{3.7}$$

where ε is a geometric constant, which can be experimentally determined or calculated from finite element analysis (FEA). For a typical pyramid indenter (such as a Berkovich tip) $\varepsilon = 0.75$; for a conical tip equivalent to a Berkovich tip, $\varepsilon = 0.72$; for a flat punch, $\varepsilon = 1$.

In order to obtain the unloading stiffness *S*, it is necessary to analyze the unloading curve. Oliver and Pharr (O&P) found that the unloading curve is better described by a power law as given by [32],

$$P = B(\delta - \delta_{res})^m \tag{3.8}$$

where *B* and *m* are fitting constants. Thus, the unloading stiffness *S* is given by,

$$S = \left.\frac{dP}{d\delta}\right|_{\delta=\delta_{max}} = mB(\delta_{max} - \delta_{res})^{m-1} \tag{3.9}$$

The nanoindentation hardness is given by,

$$H = \frac{P}{A_C} \tag{3.10}$$

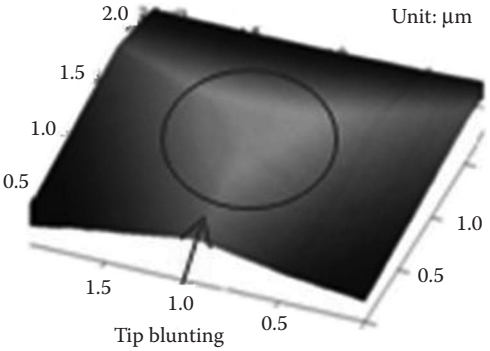


FIGURE 3.5 Atomistic force microscope (AFM) image that shows the tip blunting.

Please note that in the nanoindentation hardness the contact area is used, which is different from the residual projection area or the surface area used in microindentation.

O&P method is very popular and has been implemented in all the commercial nanoindenters. In practice, the indenter tip is not perfectly sharp but has a blunted tip (see Figure 3.5). In such case, the O&P method may encounter some problems for indentation at a shallow depth, which is particularly important when the tip is used for a while. In addition, this method cannot cope with significant pile-up or sink-in (see Figure 3.6), which may cause up to 50% inaccuracy on the determined Young's modulus [36].

Based on analytical modeling and numerical simulation for a wide range of materials including the materials with sink-in and pile-up, an alternative method has been developed by Chen et al. [37], as shown below:

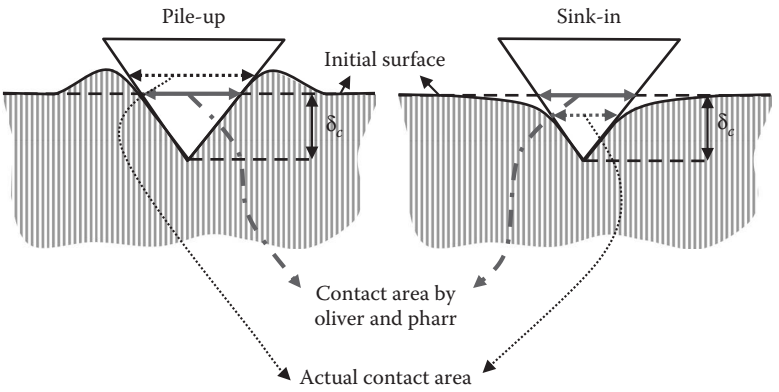


FIGURE 3.6 Schematic of pile-up and sink-in during nanoindentation, which result in underestimation or overestimation of the contact area, respectively. (From Bolshakov, A. and G.M. Pharr, *Journal of Materials Research*, 1998. **13**(4): 1049–1058.)

$$E_r = \frac{(1 - (\delta_r/\delta_m))S_u^2 \cot\theta}{2\beta P_m((1.24 + 0.2n) - (1 - (\delta_r/\delta_m))\varepsilon)} \tag{3.11}$$

$$H = \frac{(1 - (\delta_r/\delta_m))^2 S_u^2 \cot^2\theta}{\pi\beta P_m((1.24 + 0.2n) - (1 - (\delta_r/\delta m))\varepsilon)^2} \tag{3.12}$$

where δ_r and δ_m are the residual and maximum depths as defined earlier, P_m is the maximum force, S_u is the unloading stiffness, and n is the work-hardening exponent.

The alternative expressions are given by [37],

$$E_r = \frac{W_e/W_t}{(1.5\pi(1.24 + 0.2n)/(2.24 + 0.2n)) - \pi\varepsilon W_e/2W_t}\cot\theta/\frac{4\beta P_m}{\pi S_u^2} \tag{3.13}$$

$$H = \left(\frac{W_e/W_t}{1.5\pi(1.24 + 0.2n)/(2.24 + 0.2n) - \pi\varepsilon W_e/2W_t}\right)^2 / \frac{4P_m}{\pi S_u^m} \tag{3.14}$$

To validate Equations 3.13 and 3.14, it is necessary to choose materials with known properties. For example, Figure 3.7 displays a comparison of the determination of hardness and reduced modulus based on the O&P method and the model given by Equations 3.13 and 3.14 for fused silica. The values of reduced modulus determined by both methods at various loads agree very well. For the hardness, reasonably good agreement is achieved at large penetrations where tip blunting has a negligible effect on the contact area. However, the hardness determined by O&P method is unrealistically high at low loads. This could be due to the erroneous fitting of the tip area function experimentally, which implies that O&P method can be significantly affected by the tip blunting.

In addition, further comparisons have been done for various materials with pile-up during nanoindentation [37]. These also suggested that Equations 3.20 and 3.21 are improvements over the O&P method due to the capability to account for the pile-up.

3.2.2 Different Nanoindentation Test Approaches

Conventional nanoindentation is an open-loop method, which utilizes voltage applied for a fixed time period to generate the required load. It is basically a force control system, but it does not do a real-time correction for the internal spring in the transducer. This means that when a particular force is requested, part of the force will be used by the internal spring in the transducer, resulting in the force in the sample not being the same as requested. It is precisely controlled by time only. Due to a small portion of the load absorbed by the springs of the transducer, it presents great challenges in doing creep studies because it does not maintain a constant load when holding at a peak load. A closed loop indentation is run by

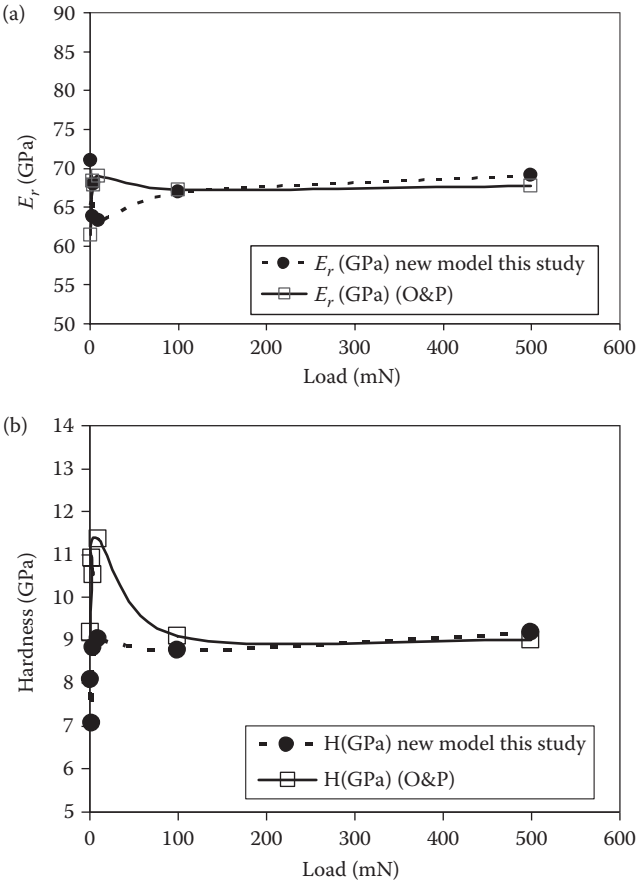


FIGURE 3.7 Comparison of (a) hardness and (b) reduced modulus of fused silica using the O&P method and the new model given by Equations 3.13 and 3.14. (From Chen, J. and S.J. Bull, *Journal of Materials Research*, 2009. **24**(3): 590–598.)

feedback control. When running in closed loop control (force control or displacement control), there is actually a digital feedback loop that is controlled by the computer. The closed loop force control corrects internal spring force in real time, so the force applied to the sample is exactly as the user requests. In displacement control, the indentation is driven based on the displacement that the user requests, and thus measures the force.

Typical load–displacement curves for all types of tests are depicted in Figure 3.8. Note a hold period at peak load or displacement is used to illustrate the differences between them.

In addition, nanoindentation instruments also commonly enable one to perform nanoscratch and nanowear tests, which are very useful to evaluate mechanical reliability of various coatings [38–45].

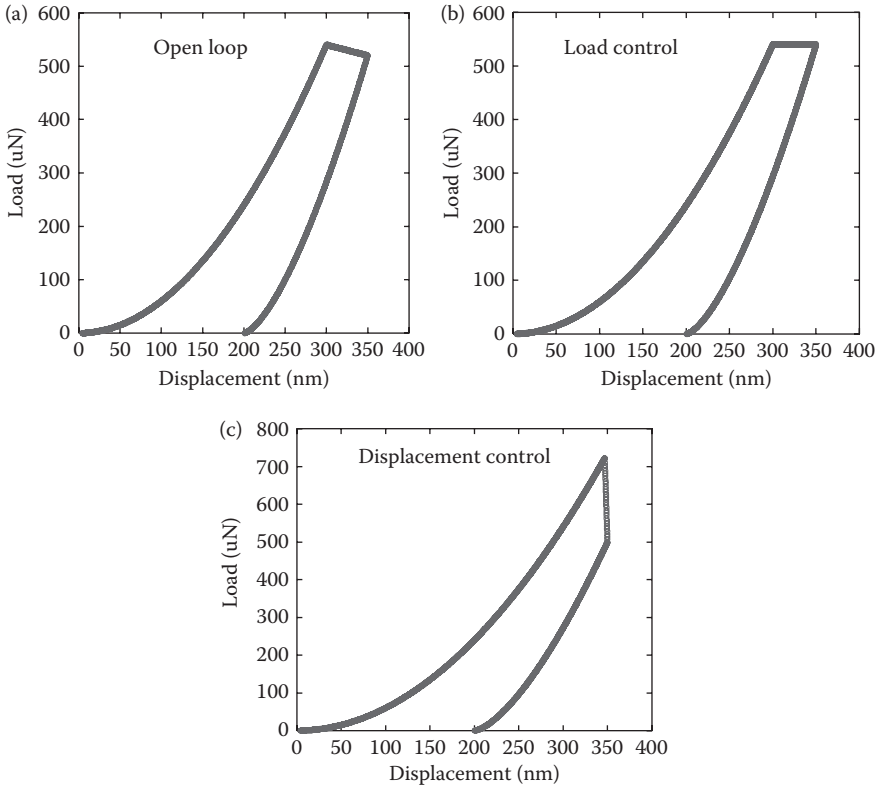


FIGURE 3.8 Schematic of the load displacement curve under (a) open-loop control; (b) close-loop load control, and (c) close-loop displacement control. (From Chen, J., 2006, University of Newcastle upon Tyne: Newcastle upon Tyne.)

3.2.3 Young's Modulus and Hardness of Coatings

When measuring the elastic modulus, the influence from the substrate is unavoidable. Therefore, various methods have been proposed to account for this. For example, combining the empirical model by Doerner and Nix and the finite element method, it gives the following equation to determine the effective modulus of the coating/substrate composite, E_{eff}, [47]

$$\frac{1}{E_{eff}} = \left(\frac{1 - v_s^2}{E_s} - \frac{1 - v_C^2}{E_c} \right) e^{-\alpha t/\sqrt{A}} + \frac{1 - v_C^2}{E_c} + \frac{1 - v_i^2}{E_i} \tag{3.15}$$

where the subscripts *f*, *s*, and *i* refer to the film, substrate, and indenter, respectively. Where t is the film thickness, and the empirical constant α can be determined by experimental results on the films with known property and thicknesses. Gao et al. [48] used a moduli-perturbation method to obtain the following closed form solution,

$$E_{eff} = E_s + (E_f - E_s)I_o \tag{3.16}$$

where I_o is a weighting function, which is related to the ratio of film thickness and the contact radius.

Another empirical power law relationship was proposed by Jung et al. [49],

$$E_{eff} = E_s + (E_f/E_s)^L \tag{3.17}$$

where

$$L = \frac{1}{1 + \psi(h/t)^b} \tag{3.18}$$

where the constants ψ and b can be obtained by calibration tests on specimens with known elastic modulus.

These equations are important because the measurement of modulus for the film is connected with that of the substrate. As a rough approximation, the stiffness of the two elastic elements comprising the thin film and substrate are essentially in series as shown in Figure 3.9a [50]. No matter how low a force is applied, there is always a contribution from the substrate. As commented in Reference 50, the indenter load is supported not only by compression in the vertical direction, as shown in Figure 3.9a, but also by compressive stresses acting inward from the sides. As there is always some elastic displacement of the substrate during an indentation test, the traditional 10% rule does not strictly apply for nanoindentation measurements for modulus determination of thin film systems [50]. Instead, it is usually suggested to extrapolating E_{eff}, to zero value of the contact radius over the coating thickness (i.e., a/t) as shown in Figure 3.9b.

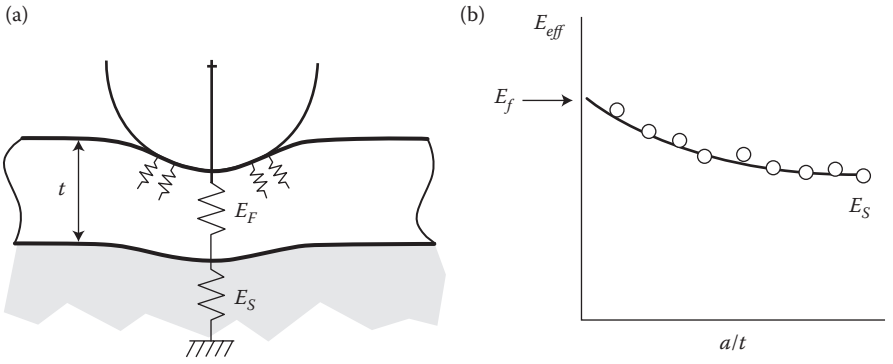


FIGURE 3.9 Schematic of (a) the contribution to the effective modulus from the film including the localized support from the indentation stress field, and (b) the modulus of the film E_f can be obtained by extrapolating measured values of E_{eff} to a/t, for a typical stiffer coating on the substrate. (From Fischer-Cripps, A.C., 2002, Springer-Verlag GmbH.)

The hardness of the coating/substrate is more difficult to quantify due to the complex plastic zone interacting with the substrate. In addition, it is also affected by the elastic deformation of the substrate as well.

For a typical harder and stiffer coating on a softer substrate, Bückle proposed that the composite hardness is given by [51],

$$H_{eff} = H_s + \alpha(H_f - H_s) \tag{3.19}$$

the subscripts *f*, *s*, refer to the film, substrate, and is an empirical parameter.

Based on area of mixtures, Jonsson and Hogmark proposed the following equation [52],

$$H_{eff} = H_f \frac{A_f}{A} + H_s \frac{A_s}{A} \tag{3.20}$$

where A_f, A_s, and A are the relative parts of the contact carried by the film and the substrate and the total area. A similar mixtures rule based on deformation volume was proposed by Burnett and Rickerby [53,54].

For a soft film on a hard substrate, Bhattacharya and Nix revealed that the elastic mismatch between the film and substrate also contributed to the effective hardness of the film/substrate [55].

$$H_{eff} = H_s + (H_f - H_s)\exp\left(-\frac{Y_f}{Y_s}\frac{E_s}{E_f}\left(\frac{\delta}{t}\right)^2\right) \tag{3.21}$$

where Y_f and Y_s are the material yield stresses for the film and substrate, respectively. The δ and t are the indentation penetration and the coating thickness, as defined previously.

For the hard film on a soft substrate, this expression becomes [55],

$$H_{eff} = H_s + (H_f - H_s)\exp\left(-\frac{H_f}{H_s}\frac{Y_s}{Y_f}\frac{\delta}{t}\sqrt{\frac{E_s}{E_f}}\right) \tag{3.22}$$

For the coating–substrate combinations (i.e., a stiffer and harder coating on the more compliant and softer substrate, and vice verse) discussed above, here is a 10% thumb rule (i.e., the critical thickness is around 10% of the coating thickness), for measuring the coating hardness. These have been confirmed as reasonable approximation by FEA (see Figures 3.10 and 3.11) [56].

However, this 10% rule does not apply to the more compliant but harder coating on a stiffer and softer substrate as demonstrated by Chen et al. [56]. Figure 3.12 displays how the hardness changes with the relative indentation depth (i.e., δ/t) for a typical softer but stiffer coating on a harder but less stiffer substrate. From which, it

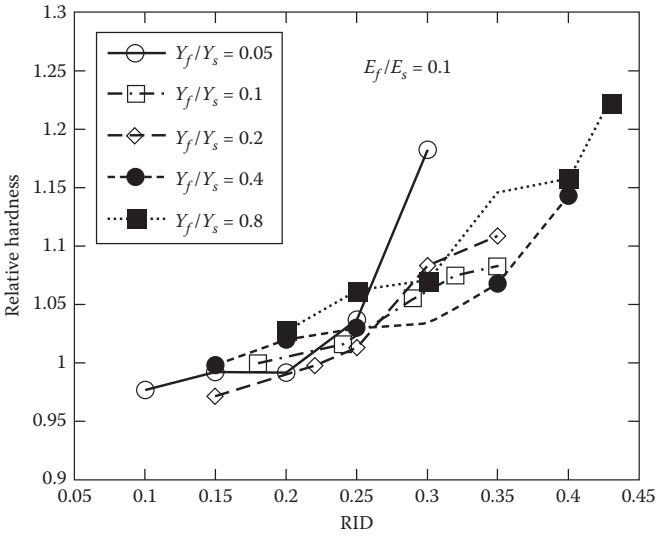


FIGURE 3.10 Simulated relative hardness for various softer coatings on a harder and stiffer substrate. Young's modulus of the coatings are fixed at 60 GPa. Y_f/Y_s is the yield strength ratio of the film to substrate. (From Chen, J. and S.J. Bull, *Vacuum*, 2009. **83**(6): 911–920.)

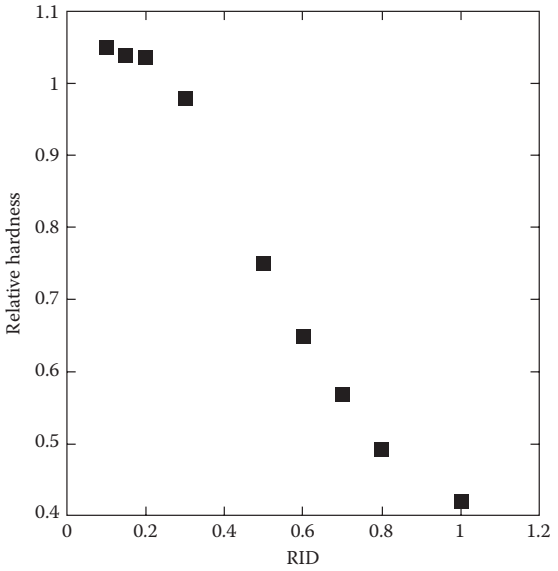


FIGURE 3.11 Simulated relative hardness for a hard coating with $E_f = 120$ GPa and $Y_f = 8$ GPa on a softer substrate with $E_s = 60$ GPa and $Y_s = 1$ GPa. (From Chen, J. and S.J. Bull, *Vacuum*, 2009. **83**(6): 911–920.)

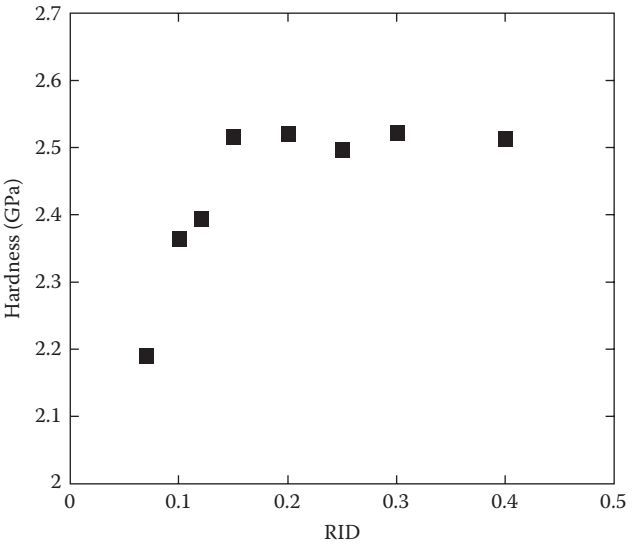


FIGURE 3.12 Simulated hardness for a typical softer but stiffer coating ($E_f = 120$ GPa and $Y_f = 1$ GPa) on a harder but less stiffer substrate ($E_f = 60$ GPa and $Y_f = 4$ GPa). (From Chen, J. and S.J. Bull, *Vacuum*, 2009. **83**(6): 911–920.)

can be seen that the true hardness can only be measured at a very limited region for this type of coating/substrate combination.

3.2.4 Detect Indentation-Induced Fracture

Not all the cracking in the coating could be readily imaged due to the limited length and cracking open displacement. In order to analyze the nanoindentation response of the coated systems, Hainsworth et al. [11] proposed a method by analyzing P/δ^2 versus δ (or δ^2). This analysis was based on the following relationship, which was developed for a monolithic material indented by a geometrically self-similar indenter such as the conical or pyramidal tips,

$$P = E\left(\varphi\sqrt{\frac{H}{E}} + \phi\sqrt{\frac{E}{H}}\right)^{-2}\delta^2 = K_m\delta^2 \tag{3.23}$$

where E and H are the Young's modulus and the hardness, respectively. The constants $\phi = 0.194$ and $\varphi = 0.930$ were experimentally determined for a Berkovich indenter. A similar equation was derived for a perfect Berkovich tip elsewhere.

It has been shown that P/δ^2 versus δ (i.e., K_m) curve can be expected to identify the transition from coating-dominated deformation behavior at low displacement (usually less than the coating thickness) to substrate-dominated deformation. But such model is not sensitive enough to detect fracture behavior, therefore, an alternative

method was proposed by McGurk and Page, that is, a plot of $\partial P/\partial(\delta^2)$ versus δ (known as K_{exp} curve) [57]. Figure 3.13a displays the K_{exp} curve of 2.81 μm NbN coating on stainless steel, from which it can be seen that three drops in the K_{exp} curve are visible when the penetration exceeds 600 nm. Such events are related to through-thickness fracture in the coated steel, which has been verified by scanning electron microscope (SEM) analysis (see Figure 3.13b). Some spikes were also observed in the region between 250 and 400 nm, which are caused by the imperfect geometry of the tip.

This method works well for the hard coatings on a softer substrate but it does not work well for hard coatings on a hard substrate because it leads to quite noisy curves. For example, when it is applied to sol–gel coatings on glass and solar control coatings on glass (see Figure 3.14), the K_{exp} curve is too noisy to provide any useful information in these brittle coated systems.

Acoustic emission (AE) signal can be used to detect rapid phase transformation [58,59], fracture initiation [60–63], and dislocation bursts [64] during nanoindentation. For the TiO_xN_y coatings, no evidence of phase transformation occurs when indented by a relatively blunt Berkovich tip. Therefore, the AE events occurring after the plastic deformation are likely to correlate to the fracture initiation in these amorphous brittle coating systems. As displayed in Figure 3.14, it is obvious that there are many more excursions in a plot of K_{exp} versus δ than AE events and the correlation between them is poor.

In order to remove the noise in the K_{exp} curve, Malzbender et al. [65] suggested smoothing the data. However, it is difficult to choose a reasonable smoothing interval that can effectively remove the noise influence without changing the nature of loading curve and retaining the useful information. In fact, it is found that the smoothing procedure may change the nature of the indentation response, which is discussed later. Furthermore, Malzbender et al. [65] argued that the smoothed K_{exp} curve did not provide more information than the plot of P/δ^2 versus δ in their sol–gel coatings.

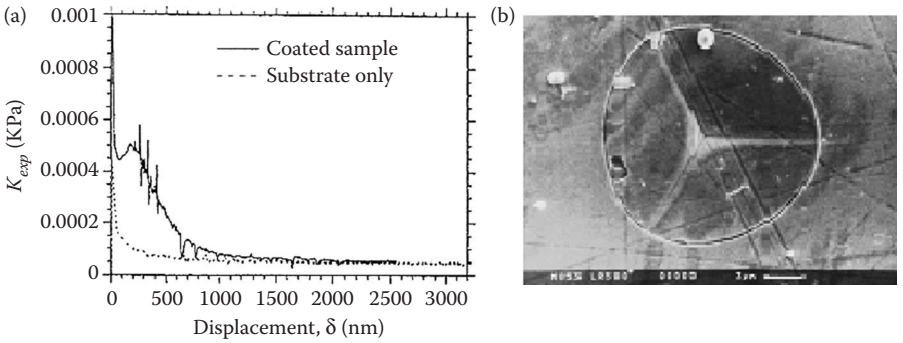


FIGURE 3.13 (a) The K_{exp} curve for both coated sample and the stainless-steel substrate only and (b) SEM image for the indentation-induced crack in the coated sample. (After McGurk, M.R. and T.F. Page, *Journal of Materials Research*, 1999. **14**(6): 2283–2295.)

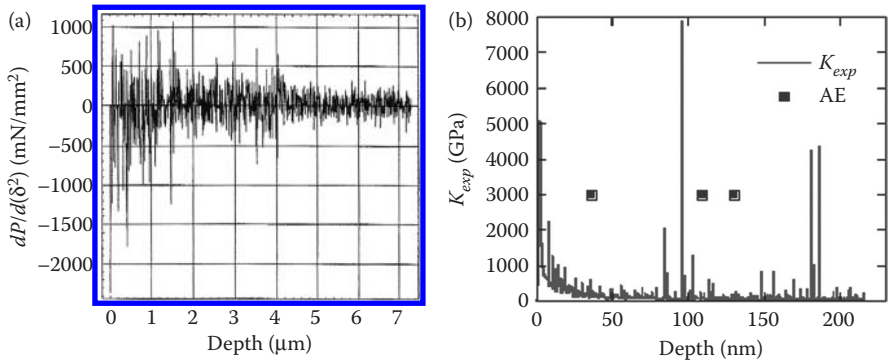


FIGURE 3.14 The K_{exp} curve of (a) sol–gel coatings on glass. (From Malzbender, J. and G. de With, *Surface & Coatings Technology*, 2001. **137**(1): 72–76.) (b) 200 nm TiO_xN_y single layer on glass. (From Berasategui, E.G., S.J. Bull, and T.F. Page, *Thin Solid Films*, 2004. **447**: 26–32.)

To solve this problem, it is suggested analyzing the instantaneous loading rate curve, $\partial P/\partial t$ versus δ. This method avoids the presence of a singularity and it is quite sensitive to the change of mechanical deformation during nanoindentation. For a comparison, Figure 3.16 displays the plots of $\partial P/\partial(\delta^2)$ versus δ at different averaging levels (i.e., number of data points for the moving average) and a scatter plot of $\partial P/\partial(\delta^2)$.

In Figure 3.15, the raw line plot of K_{exp} curve is very noisy, which does not give useful information about fracture. Although the noise can be removed with a smoothing interval of 50 data points (see Figure 3.15b), the K_{exp} curve after smoothing considerably deviates from the initial one. It is obvious that the second event is more significant than the first one in the scatter plot (i.e., Figure 3.15c), however, this phenomena has been reversed in the smoothed curve in Figure 3.15b.

In contrast, the plot of instantaneous loading rate provides good information without smoothing as shown in Figure 3.16. Although there are obvious events in the K_{exp} and scatter $\partial P/\partial(\delta^2)$ curves, it is difficult to reliably distinguish the fracture initiation point from them. However, it is much easier to find the fracture initiation point based on the events in the instantaneous loading rate curve. From Figure 3.16 we can see a significant drop in the loading rate in some regions or even negative loading rates. This may be due to slow crack growth in such brittle coatings, which is not obvious in the in situ AFM image due to its limited scanning resolution. The negative values of K_{exp} in Figure 3.15 do not have any physical meaning, while, the negative loading rate in Figure 3.16 is related to cracking propagation. In summary, the plot of instantaneous loading rate improves the sensitivity to detect fracture events during indentation.

3.3 RESIDUAL STRESS IN THE COATING

In many coatings, the residual stress in the coating is in evitable and this could also affect the fracture mechanism and fracture toughness assessment for the coating. The residual stress in the coating may cause spontaneous interface failure as shown in Figure 3.17.

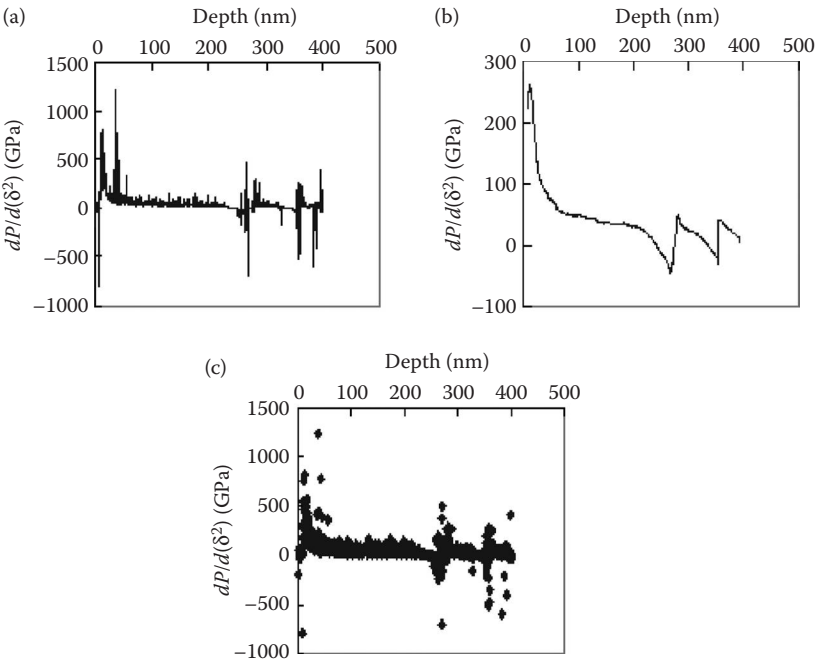


FIGURE 3.15 Line plots (a) without smoothing and (b) with smoothing level of 50 data and (c) a scatter plot of $\partial P/\partial(\delta^2)$ versus δ for a 240 nm indium tin oxide (ITO) cap layer multilayer stack on glass.

One of the main origins of the residual stress is the thermal stress. The thermal stress is generated on cooling after deposition due to thermal expansion mismatch between coating and substrate. It can be tensile or compressive depending on the combination of coating and substrate. The thermal stresses increase proportional to temperature. The other origin is the growth stress, which is generated during the deposition by the competitive growth of the columnar structure. Usually, it is compressive due to the energetic ion bombardment in the deposition chamber. It may be

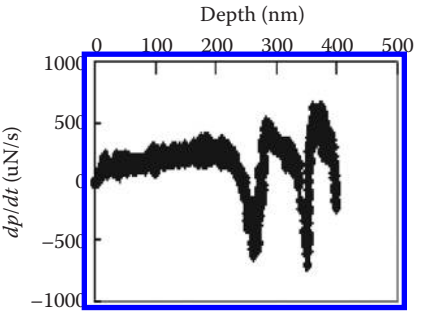


FIGURE 3.16 Plot of $\partial P/\partial t$ versus δ for a 240 nm ITO cap layer multilayer stack on glass.

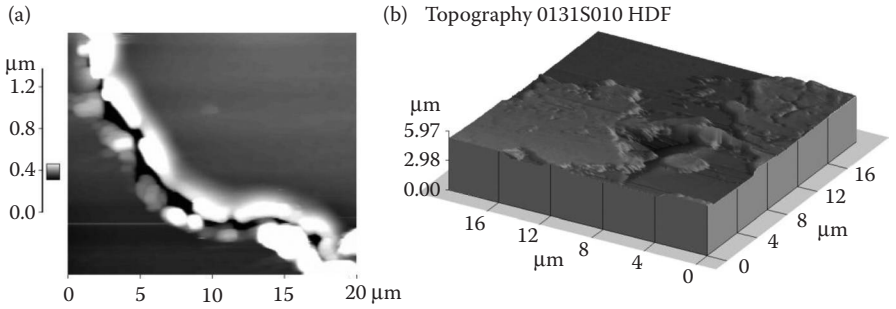


FIGURE 3.17 AFM image of (a) spontaneous blister in 400 nm ITO on glass and (b) an indentation around the blister.

tensile stress if the grain boundaries, small voids, and pores in the films are significant [67]. With the increase of temperature, the film becomes denser and the tensile growth stress decays to zero.

Figure 3.18 displays how the growth, thermal, and total residual stresses change with temperature. The thermal and growth stresses are assumed to be of the same sign.

The total residual stress in the coating can be measured by various techniques [69–72]. If the coating is crystalline, x-ray diffraction (XRD) can be used [73].

$$\sigma_{\phi} = \frac{E}{(1+\nu)\sin^2 \Psi}\left(\frac{d_i - d_n}{d_n}\right) \tag{3.24}$$

where E and ν are Young's modulus and Poisson's ratio for the coating, d_n is the spacing between planes parallel to the coating surface, and d_i are the planes whose normal is inclined to the coating surface at an angle ψ (see Figure 3.19).

If the coating is amorphous, the residual stress can be determined by measuring the residual stress-induced deflection of the coating substrate. The deflection can be measured by profilometer or light interferometry [74], laser beams [8,28], and x-rays [75].

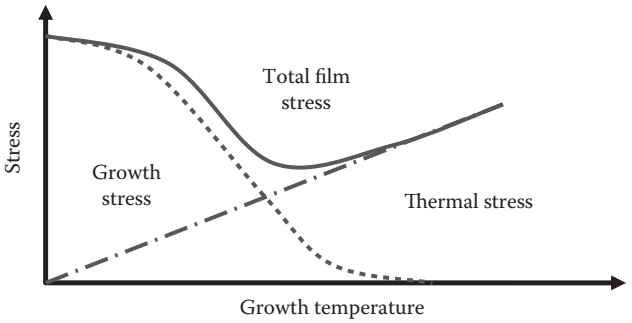


FIGURE 3.18 Schematic of how the growth, thermal, and total residual stresses change with temperature. Where thermal and growth stresses are assumed to be of the same sign. (From Hultman, L. et al., *Physical Review Letters*, 2001. **8722**(22): p. art. no.-225503.)

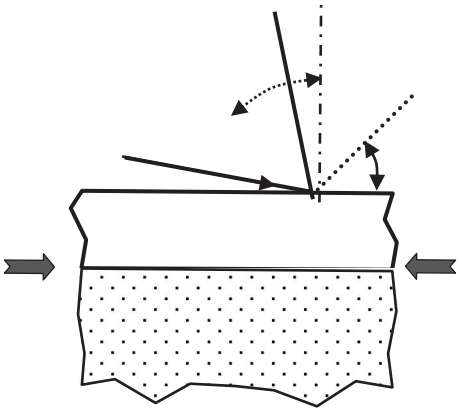


FIGURE 3.19 Illustration of determination of residual stresses by the sin 2ψ method. (From Fernández-Palacio, J., 2006, Newcastle University: Newcastle.)

Then, the residual stress can be determined by the Stoney equation [76],

$$\sigma = \frac{E_s h_s^2}{6(1 - v_s)h_f}\left(\frac{1}{R} - \frac{1}{R_0}\right) \tag{3.25}$$

where R_0 and R are the radii of curvature of the substrate before and after deposition, and h is the thickness with the subscript s and f refers to the substrate and film.

If the coating is sufficiently thick or the difference of the Young's modulus of the coating and the substrate is significant, then the coating thickness and mechanical properties of the coating should be considered. To account for these, the following equation has been proposed [77],

$$\sigma = \frac{E_s\left(h_s + E_f(1 - \nu_s)/E_s(1 - \nu_f)h_f\right)^3}{6(1 - v_s)h_s h_f}\left(\frac{1}{R} - \frac{1}{R_0}\right) \tag{3.26}$$

3.4 FAILURE MECHANISMS DURING NANOINDENTATION TESTS

If the coating thickness is much bigger than the indentation depth, the failure mechanism of the coating is similar to that of bulk materials, provided that the microstructure effect is not important. In such case, the typical indentation-induced fracture modes will be as illustrated in Figure 3.20. The fracture mode is dependent on the materials, the indenter, and test conditions as has been demonstrated in various studies [78–89].

a. *Cone crack*: This crack is typically generated by a flat punch or spherical indenter. It is related to the elastic deformation, and initiates in a ring crack due to the high tensile stresses near the edge of the contact. With increasing

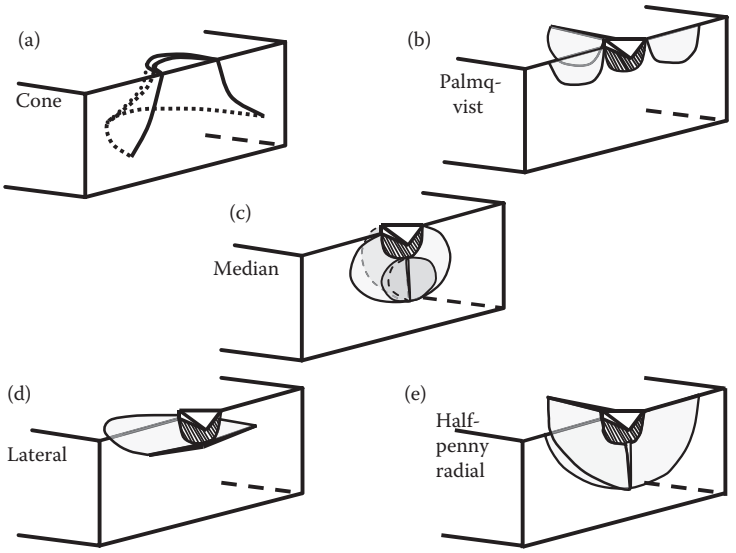


FIGURE 3.20 Schematic of five major types of cracks: (a) cone, (b) palmqvist radial, (c) median, (d) lateral, and (e) half-penny radial cracks. (From Cook, R.F. and G.M. Pharr, *Journal of the American Ceramic Society*, 1990. **73**(4): 787–817.)

load, the maximum tensile stresses distribute around a cone producing a cone crack.

b. *Palmqvist radial crack*: This is related to the plastic deformation of the material when indented with sharp indenters or blunt indenters at high loads, beyond the Hertzian regime. It is created parallel to the axis of the load starting from the edge of the plastic impression left by the indenter, which is driven by a tensile hoop stress. It usually occurs in tough materials such as carbides and zirconia ceramics.
c. *Median crack*: This type of crack propagates parallel to the axis of the load but is created beneath the plastic deformation zone due to the wedging action of a conical or pyramidal indenter.
d. *Lateral crack*: It generates beneath the plastic deformation zone and propagate initially almost parallel to the surface of the material before turning upward to the surface and forming a chip. It usually originates during the unloading cycle (for most ceramics), although for some glasses it also appears during the loading cycle. The lateral crack usually occurs in the very brittle materials such as glass during unloading. However, it may also appear in the tough materials in cyclic loading.
e. *Half Penny radial crack*: This type of crack may be formed on unloading starting from a radial crack running downward or a median crack running upward or a mixture between the two of them.

For the coating/substrate, the radial cracks may be confined within the coating (see Figure 3.21a) but may also propagate to the coating/substrate interface (see

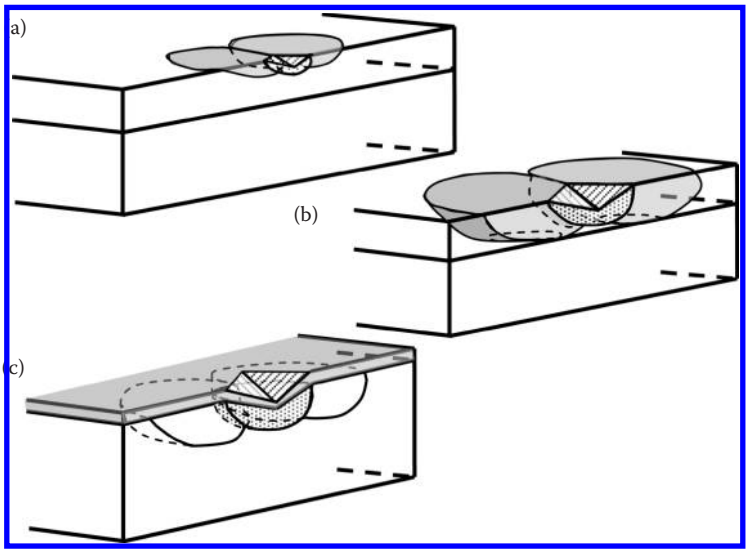


FIGURE 3.21 Schematic diagrams of lateral cracks occurring in (a) coating only, (b) coating/substrate interface, and (c) substrate only. (From Fernández-Palacio, J., 2006, Newcastle University: Newcastle.)

Figure 3.21b). The crack may initiate within the brittle substrate and it may propagate toward the coating (see Figure 3.21c).

For thin coatings, in addition to the crack pattern described above, the picture-frame cracks may occur, which is caused by the bending of the thin stiffer films enhanced by the plastic deformation in the substrate as illustrated in Figure 3.22.

In addition, the lateral crack may also occur at interface (see Figure 3.23), which will cause the delamination and consequent chipping.

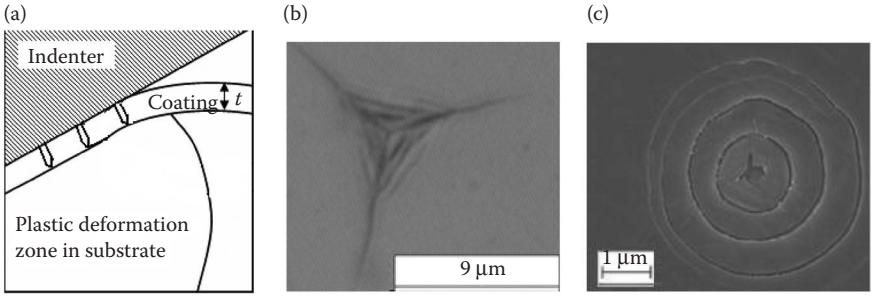


FIGURE 3.22 (a) Schematic of substrate bending induced picture-frame crack (From Chen, J. and S.J. Bull, *Journal of Physics D-Applied Physics*, 2007. **40**(18): 5401–5417.); and picture-frame cracks induced by (b) a Berkovich (From Chen, J., *Journal of Physics D: Applied Physics*, 2012. **45**: 203001.); and (c) conical tip (From Fu, K. et al., *Journal of Physics D-Applied Physics*, 2013. **46**(50): 505314.), respectively.

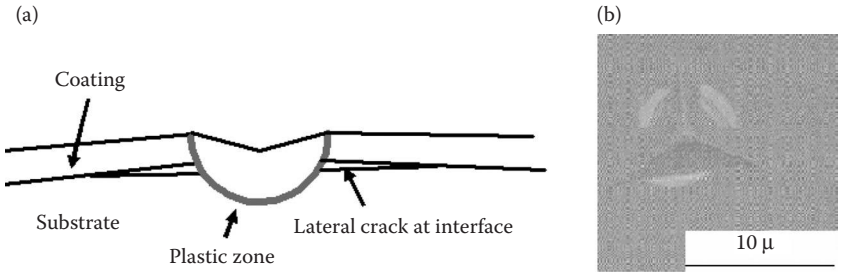


FIGURE 3.23 (a) A schematic illustration of lateral cracks initiated at coating/substrate interface generated and (b) a lateral crack in a coated glass induced by a Berkovich indenter. (From Chen, J. and S.J. Bull, *Journal of Physics D-Applied Physics*, 2007. **40**(18): 5401–5417.)

3.5 STRESS-BASED MODELS TO ASSESS INDENTATION FRACTURE TOUGHNESS

Fracture toughness (represented by K_C) is to measure the resistance to crack propagation. A typical test is to apply a ramping stress σ to a sample with a notch as shown in Figure 3.24. The stress at crack tip (K_I) is determined by

$$K_I = A\sigma(\pi c)^{1/2} \tag{3.27}$$

where A and c are the shape of the sample and the length of the crack.

When the stress is sufficiently big, the crack will propagate spontaneously. In which case, it is mode I failure and the critical stress intensity factor (or the fracture toughness), K_{IC}, can be obtained.

However, such tensile tests do not apply to the coatings, particularly when the coating is thin. Therefore, indentation tests have been introduced. For a given material, the indentation fracture toughness is the same as that determined by tensile tests if the size effect is not significant. If the microstructure effect is significant, more complex stress analysis is required [94–98] as seen in thermal barrier coatings.

As discussed above, there are various types of cracks. Stress-based approaches can be used to determine the fracture toughness for the radial cracks and lateral crack, which are commonly observed cracks in the coatings. To enable the crack to occur, usually a sharp tip (such as pyramid or conical tip) is preferred. In such case, the commonly observed fracture is radial crack and lateral crack. Therefore, we will mainly focus on these two types of cracks.

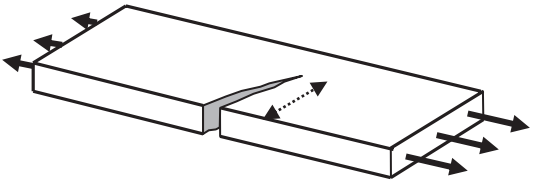


FIGURE 3.24 Schematic of a typical tensile test to measure fracture toughness.

3.5.1 Radial Cracks

3.5.1.1 Half-Penny-Like Radial Cracks

Figure 3.25 shows the well-developed radial cracking caused by indentation with a Vickers indenter and a typical radial crack in glass. Experimental observations found that the toughness K_{Ic} of indented materials was proportional to applied load P multiplied by crack length, c, raised to the power of −1.5, in the case of well-developed radial/median crack system (half-penny-like cracking) caused by indentation. Combining stress analysis based on the model of the analogous expanding spherical cavity problem and simplistic dimensional analysis, Lawn et al. [99] developed the following expression to assess the toughness of ceramics and glass,

$$K_c = \chi P/c^{3/2} = \xi_v^R (E/H)^m P/c^{3/2} \tag{3.28}$$

where ξ_v^R is a calibration coefficient, which depends on indenter geometry; the commonly used value of exponent m is 1/2, and E and H are Young's modulus and hardness, respectively. For well-developed radial cracking produced by a Vickers or Berkovich indenter, $\xi_v^R = 0.016 \pm 0.004$ [100]. There is a considerable uncertainty (±25%) in the constant itself, leading to an inherent uncertainty in the calculated toughness. With the decrease of indenter semiangle (θ), ξ_v^R increases since it is proportional to $(\cot\theta)^{2/3}$, which was derived based on the expanding cavity model and was verified by indentation in different brittle materials. Such geometry-dependent phenomena have been validated for different tip angles in the range of 35.3–75° [101].

The Young's modulus and hardness (E and H) of the coating can be easily determined by nanoindentation, and crack length c can be measured by various microscopy imaging. The simplicity and reliability of this method leads to its convenience of application and thus it becomes a common method for bulk materials indented at high loads. However, it requires the crack to be sufficiently developed (i.e., $c \gg 2a_c$, where a_c is the contact impression radius as depicted in Figure 3.25), which

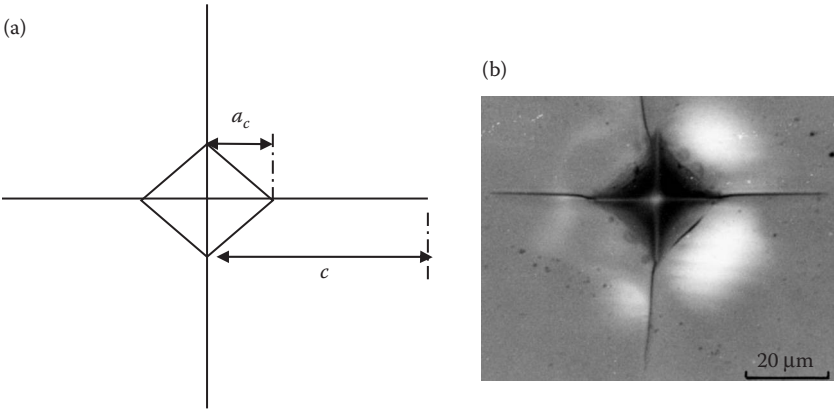


FIGURE 3.25 (a) Schematic of well-developed radial cracking caused by indentation with a Vickers indenter, (b) radial crack in glass.

accordingly requires a high load. For thin films, high loads lead to large penetration, which may result in plastic deformation in the substrate. In such cases, the initial residual stress field to drive the fracture may be disturbed by the interface and substrate so that the fracture shape will also change. This reduces the reliability of the conventional indentation method.

Due to the mismatch between the coatings and their substrates and the different coating processes used, it is inevitable that preexisting residual stress will occur, which has not been considered in Equation 3.28. In order to solve this problem, a modified expression has been suggested as follows [102,103]:

$$K_c = \xi_v^R (E/H)^{1/2} P/c^{3/2} + 2\sigma(c/\pi)^{1/2} \tag{3.29}$$

However, it should be noted that the constant π is crack geometry dependent and corresponds to the well-developed half-penny crack. It can be expected that both the stress field and crack shape will be disturbed by the substrate. When the substrate effect becomes more important, a shape factor initially defined by Broek can be introduced to account for crack shape modification. Therefore, Equation 3.28 can be modified as [104],

$$K_c = \xi_v^R (E/H)^{1/2} P/c^{3/2} + Z\sigma c^{1/2} \tag{3.30}$$

$$Z = 1.12\sqrt{\pi}\,\frac{d/c}{(3\pi/8) + (\pi/8)(d/c)^2} \tag{3.31}$$

where d is the depth of the radial crack. Although it is difficult to accurately measure the crack depth, den Toonder et al. argued that the fracture toughness can be obtained without the knowledge of Z, and Z is only important for determining the residual stress.

When the coating thickness decreases, the radial cracking may not be well developed as observed in References 103, 105, and 106. In such cases, the applicability of the above equations will be uncertain. For example, Laugier [107] and Nihara [108] reported that the linear relation between K_{Ic} and $P/c^{3/2}$ stopped when $c < 2.5a_c$. However, it was found elsewhere that such a scaling relationship remained even when the radial crack length was down to $1.1a_c$ for typical materials [109,110].

Even if Equations 3.28 through 3.31 are still valid for small crack lengths (i.e., c is slightly bigger than a_c), the difficulty to accurately measure the crack length will be a major issue. Therefore, an alternative method that eliminates the imaging system has been suggested by Field et al. [111] based on the concept of crack opening displacement (COD) and utilizing the feature of a pop-in in the load–displacement curve. For a typical pyramid indenter, the COD, δ_{COD}, can be given by

$$\delta_{\mathrm{COD}} = 2h_{ex} \cot\varphi \tan 30^\circ \tag{3.32}$$

where φ is the face-to-center angle of the tip, and h_{ex} is the extra penetration caused by the entry of the indenter into the crack. Field et al. [111] suggested that h_{ex} can be estimated as the difference between the actual displacement with pop-in and the extrapolated displacement without pop-in (i.e., $h_{m2} - h_{m1}$ is regarded to be h_{ex} as

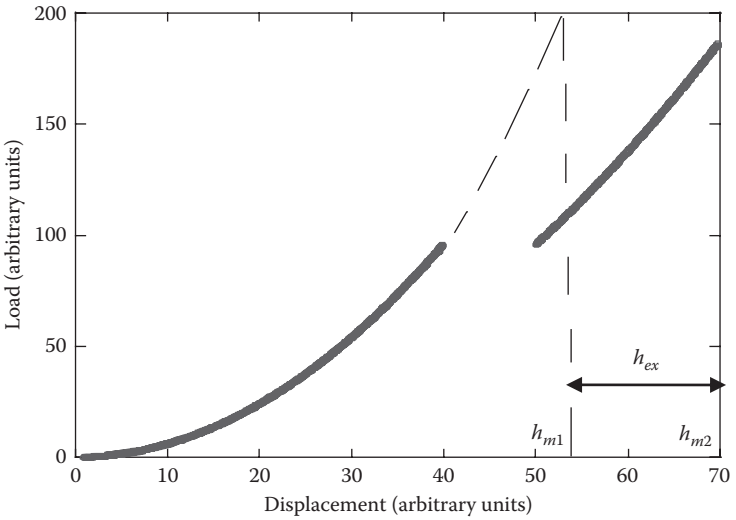


FIGURE 3.26 Schematic of a pop-in in a load–displacement curve.

depicted in Figure 3.26). Figure 3.27 depicts the schematic of a triangular pyramid indenter wedging open radial crack in the brittle material surface. Field et al. [111] proposed the following equation to estimate the crack length.

$$c = (h_{m2} - h_{ex})\cot\varphi + \frac{\pi E_r h_{ex} \cot\varphi \tan 30^\circ}{4pD} \tag{3.33}$$

where p is the pressure at the center of the crack, and D is a constant.

Since p is likely to be proportional to the Meyer's hardness, H_M, Equation 3.33 can be rewritten as follows:

$$c = h_{m2}\cot\varphi + \left(Q\frac{E_r}{H_M} - 1\right)h_{ex}\cot\varphi \tag{3.34}$$

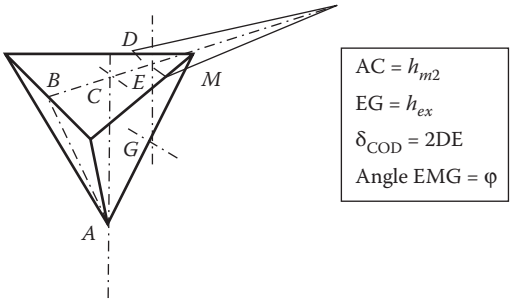


FIGURE 3.27 Schematic of a triangular pyramid indenter wedging open radial crack in the brittle material surface.

where Q is a combined constant that can be obtained by curve fitting the relationship between c and h_{ex}.

3.5.1.2 Palmqvist Radial Cracks

In addition to half-penny (or approximately half-penny) crack patterns, palmqvist radial cracks may also occur [111–113]. These usually occur at high load for much tougher materials compared to glass. Palmqvist cracks tend to appear during loading, initiating at corners due to the high stress concentration and are driven by the hoop tensile stress. In this case, there is a similar scaling relation as shown in Equation 3.28. However, the exponent of E/H was found to be 2/3 and an additional term depending on the crack dimension over contact size (c/a_c) is required to get reasonable toughness values. The c/a_c term will affect the proportional coefficient [111]. Such Palmqvist cracks tend to occur at relatively high loads in relatively tough materials. Thus, it may not be suitable for the assessment of thin coatings because substrate influence can be significant at a high load.

3.5.2 Lateral Cracks

For lateral cracking, based on the expanding cavity model as used in the analysis of radial/median crack pattern [114] and a simple plate theory, Marshall et al. [115] proposed a model to relate the toughness of brittle bulk materials to the critical load where lateral cracks occur during unloading.

$$K_c = 0.147H\left(\frac{P_0}{E}(\cot\theta)^{2/3}\right)^{1/4} \tag{3.35}$$

Here, P_0 is threshold load for lateral cracking, and θ is the half-included angle for an indenter [115]. A wide range of indentation tests can be performed until the lateral cracks are observed. By plotting the force against the lateral crack length, the threshold load can be determined. This approach is also applicable to the assessment of interfacial toughness. For example, Chen et al. applied such a method to solar control coatings and found the energy release rate of ZnO/Ag to be 1.9 J/m^2. When using the double cantilever bead technique, nanoscratch technique and overlayer method, the values of the energy release rate of the ZnO/Ag were found to be 2, 2, and 2.1 J/m^2, respectively. These results agree well with the values (1.1–2.2 J/m^2) predicted by atomistic simulations.

Based on combined expanding cavity model and numerical analysis, a semianalytical model could be obtained to determine the fracture toughness for indentation-induced lateral crack. Figure 3.28 displays the schematic of lateral cracking and plastic deformation zone induced by a spherical indentation.

If the critical contact radius (a_{cr}) for the lateral cracking can be identified, the energy release rate G can be given by the following equation [116]:

$$G = \frac{W_{cr}^2}{9.1Ea_{cr}{}^5} \tag{3.36}$$

where W_{cr} is the critical indentation work when the lateral crack occurs.

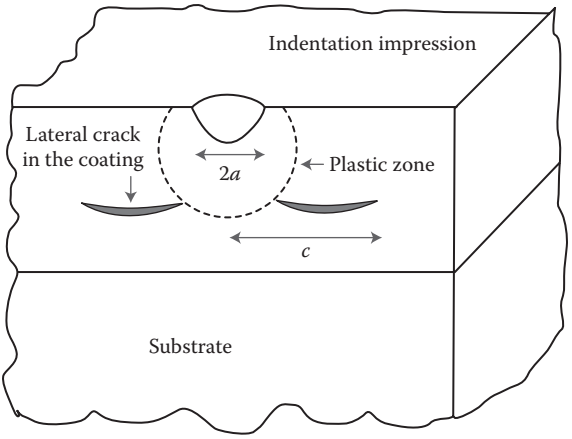


FIGURE 3.28 Schematic of lateral cracking in the coating induced by a spherical tip. (Modified after Chen, X., J.W. Hutchinson, and A.G. Evans, *Journal of the American Ceramic Society*, 2005. **88**(5): 1233–1238.)

Based on empirical fitting to the numerical simulations, it gives [116],

$$G = \frac{0.0484W^2}{Ea^3c^2} \tag{3.37}$$

where W, a, and c are the indentation work, contact radius, and crack length.

Under certain circumstance, these methods can be extended to assess the interfacial failure of a coated system [40].

3.6 ENERGY-BASED MODELS

For stress-based models, the fracture toughness is strongly dependent on the crack length. In practice, the crack length may vary significantly at indenter corners due to the defect, in which case the experimentalists are unsure which crack length should be used. In addition, with the development of complex coating stacks (e.g., multilayered coated systems) and the decrease of coating thickness, stress analysis-based solution becomes very complicated. Therefore, it is necessary to develop energy-based models to deal with various cracking patterns in complex coatings. The energy-based methods are also useful for the assessment of interface toughness [117–121].

A typical mechanism of nanoindentation-induced fracture for a brittle coating on a hard substrate is depicted in Figure 3.29. Considering that the buckling interfacial failure is more likely than the shear-induced delamination when the coating is relatively tough compared to the interface, some modification was made on the originally proposed indentation-induced failure as indicated in Reference 122.

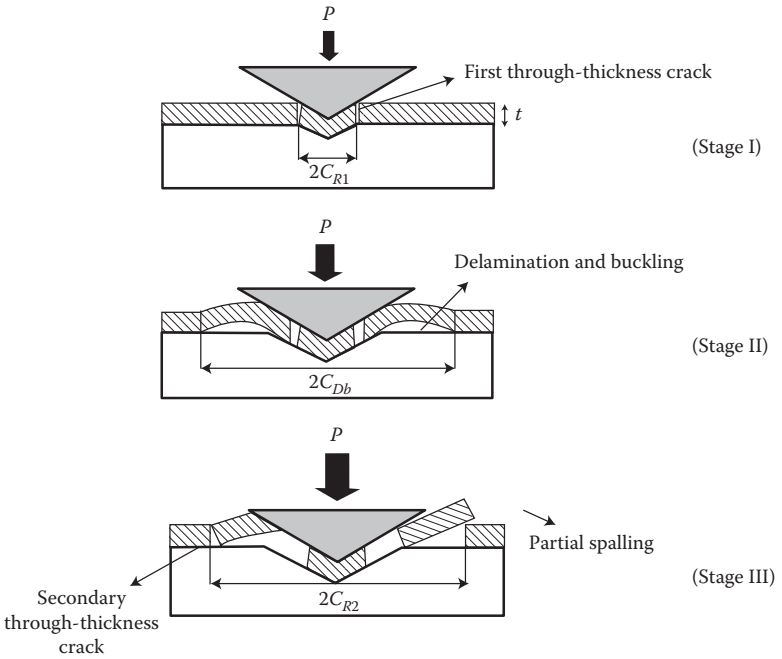


FIGURE 3.29 Schematic of the different stages in nanoindentation fracture for a brittle coating on a hard substrate. (Adapted from Chen, J. *Journal of Physics D: Applied Physics*, 2012. **45**: 203001.)

The fracture evolution in a typical brittle coating (Figure 3.29) on a hard substrate can be described in the following.

Stage I: a ring, picture frame, or radial crack may occur depending on the coating/substrate system and indenter geometry.
Stage II: with the increase of the load, the crack opening increases and the coating delaminates and buckles.
Stage III: secondary through-thickness cracks form and coating spallation (either partial or full) may occur depending on the flaw size distribution at the interface.

3.6.1 Extrapolate Load–Displacement Curve

When indenting a typical brittle coating, the pop-in and load-drop is commonly associated with through-thickness cracks for the tests under load control and displacement control, respectively (see Figures 3.30 and 3.31).

Based on such observations, Li et al. [122,124] proposed an approach based on extrapolating the loading curve. In this model, the load–displacement curve is extrapolated from the step start point (assumed to be the onset of fracture) to its end point, and the difference between the extrapolated curve and the measured curve

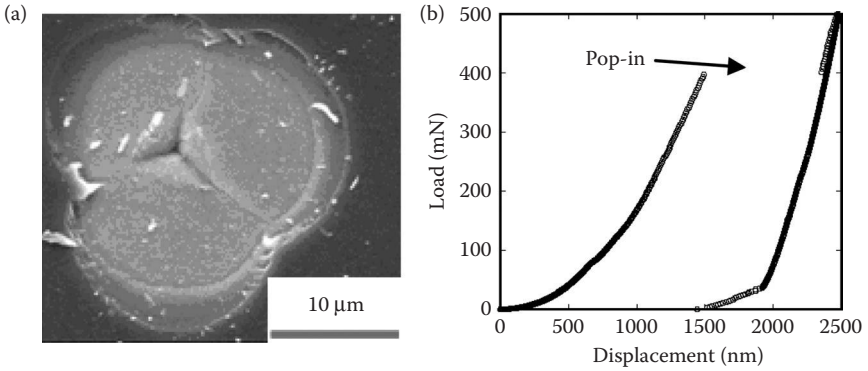


FIGURE 3.30 (a) SEM image of the indentation-induced through-thickness cracks in 1 µm CN_x coating on 3C SiC and (b) the associated load–displacement curve during load control (Ld-ctrl). (From Chen, J., *Surface & Coatings Technology*, 2012. **206**: 3064–3068.)

is regarded as the fracture-dissipated energy, that is, area ACD in Figure 3.32. For convenience, this method is denoted as the ld–dp method.

The fracture toughness is then related to the released elastic strain energy during fracture, U_{fra}, effective film thickness, t, the total length of the crack in the film plane $C_{tot,}$ Young's modulus of the film, E, and Poisson's ratio of the film, ν, and it is given by,

$$K_{IC} = \sqrt{\frac{U_{fra}E}{(1-\nu^2)C_{tot}t'}} \tag{3.38}$$

where $t' = (t/\sin\beta)$, since the crack may propagate at an angle of β rather than be exactly perpendicular to the coating/substrate interface (see Figure 3.33). The angle, β, can be measured by microscopy.

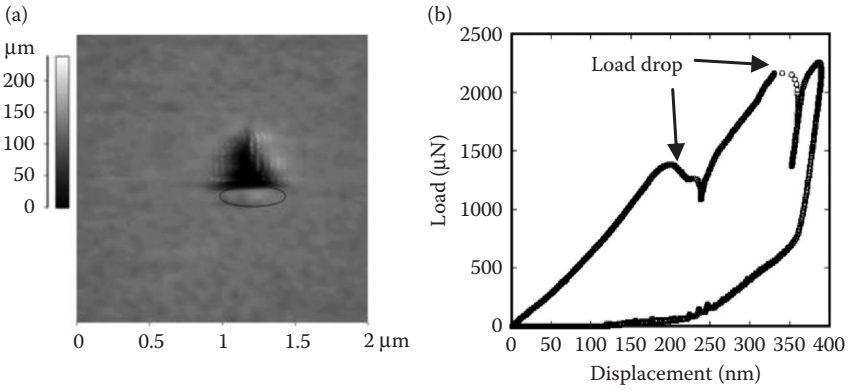


FIGURE 3.31 (a) AFM image of the indentation-induced through-thickness cracks in 400 nm TiO_xN_y glass substrate and (b) the associated load–displacement curve during displacement control (Dp-ctrl).

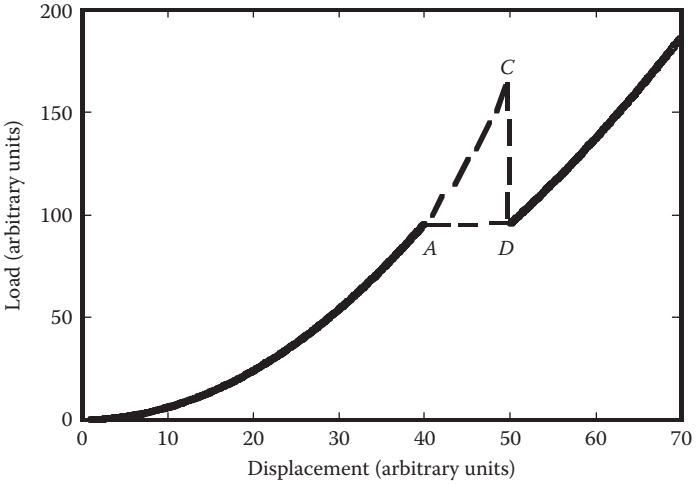


FIGURE 3.32 Schematic of the ld–dp method to determine the fracture-dissipated energy. The area ACD is regarded as fracture-dissipated energy. (From Chen, J. and S.J. Bull, *Thin Solid Films*, 2006. **494**(1–2): 1–7.)

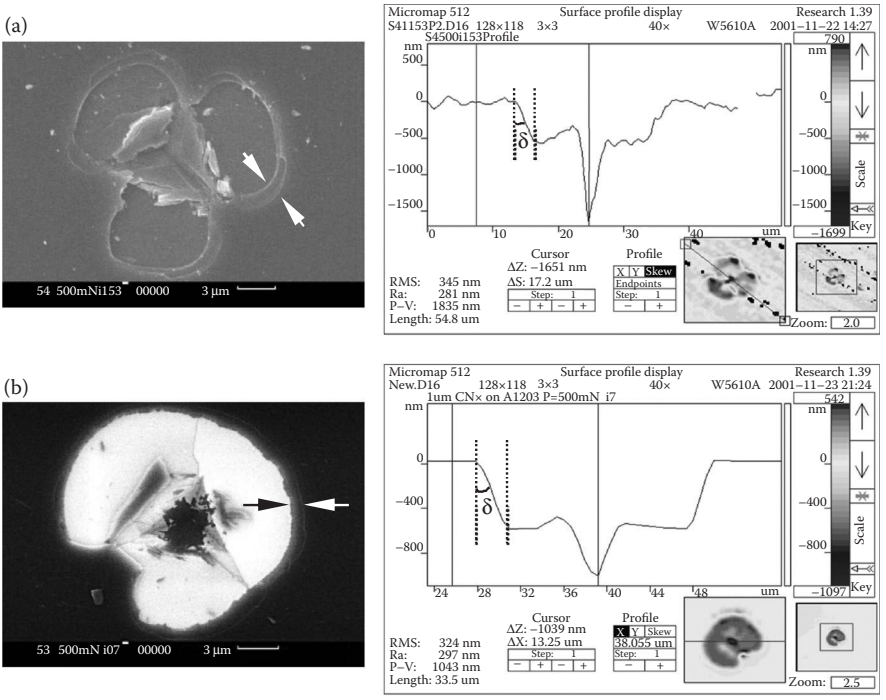


FIGURE 3.33 SEM images and corresponding profiles of indentation-induced fracture on 1 µm CN*x* coating deposited on (a) Si(001) and (b) Al_2O_3. Where the through-thickness propagates at an angle, β. (From Fernández-Palacio, J., 2006, Newcastle University: Newcastle.)

However, this method ignores the change in elastic–plastic response in the coated system before and after fracture, which can be essential as commented by Wu et al. [125] and Gao et al. [48]. It can be anticipated that ld–dp method tends to overestimate the toughness for harder coatings on softer substrate and underestimate the toughness vice versa. These predictions agree with the experimental results in Reference 91.

3.6.2 Extrapolate Total Work–Displacement Curve

Therefore, another approach was developed by Chen et al. [105] based on analyzing the total work versus displacement curve (W_t–dp method). This method is explained in Figure 3.34. First, it is proposed to extrapolate the initial W_t–dp curve from the cracking start point *A* to the cracking end point *C*, to get the work difference CD after fracture; then extrapolate the W_t–dp curve after cracking backward to the cracking start point and thus obtaining the work difference AB at the onset of fracture. AB represents the work caused by different elastic–plastic deformation behavior of the material before and after fracture, whereas CD represents the total work difference caused by the presence of cracking, which consists of the change of elastic–plastic deformation behavior between the uncracked system and cracked system plus the fracture-dissipated energy. The difference between the two (i.e., CD minus AB in Figure 3.34) is the fracture-dissipated energy. The CD in Figure 3.34 can be positive or negative depending on the coated systems.

Table 3.1 summarizes the toughness results determined by ld–dp and W_t–dp methods. For ld–dp method, it showed that the carbon coating prepared by cathodic arc is even tougher than the diamond. In addition, for the same coating indented with different probes, the toughness values varied more than 10%. It can be seen that W_t–dp method yields more consistent results.

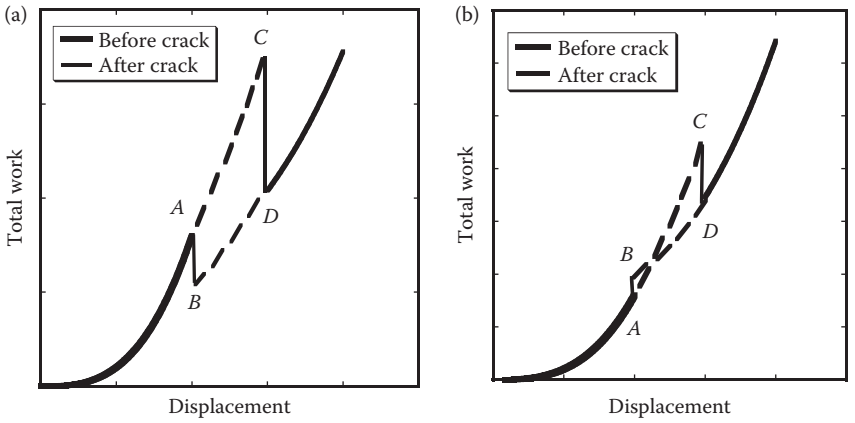


FIGURE 3.34 Schematic of extrapolating the total work versus displacement curve before and after cracking to determine the fracture-dissipated energy CD–AB. Compared to CD, AB can be positive as displayed in (a) or negative as depicted in (b) depending on the actual coated systems. (From Chen, J., *Journal of Physics D: Applied Physics*, 2012. **45**: 203001.)

TABLE 3.1
Toughness Results of Carbon Coating on Silicon Determined by ld–dp Method and W_t–dp Method

	K_{IC}, MPa$\sqrt{m}$	
	ld–dp Method	**W_t–dp Method**
Ion beam conical tip	5.4	5.8
Ion beam cube tip	4.9	6.0
Cathodic arc cube tip	10.9	6.2

Source: Chen, J. and S.J. Bull, *Journal of Physics D-Applied Physics*, 2007. **40**(18): 5401–5417.

3.6.3 Method Based on Analyzing Irreversible Work and Plastic Work

All the energy-based models discussed above are based on features in the load–displacement curve associated with fracture, otherwise, no slope change or excursion in P–δ, W_{irr}–P, and W_t–dp can be observed. However, it is not unusual that fracture does not cause any excursion in the load–displacement curve. For example, a number of picture-frame cracks have been observed in indentations on solar control coatings on glass, which do not cause obvious slope change or excursions (see Figure 3.35). These types of cracks usually occur in hard coatings on the soft substrate. However, for hard coatings on the hard substrate, the appearance of the picture-frame cracks actually depends on the ratio of H/E in the coating and substrate as discussed in References 91 and 126.

To deal with this case, another energy-based model to estimate coating toughness in the case of no excursion in P–δ curve was proposed by Chen et al. [91,127]. The key requirement is to obtain the plastic work during nanoindentation. The method of irreversible work difference (denoted as W_{irr}–W_p) is explained as follows.

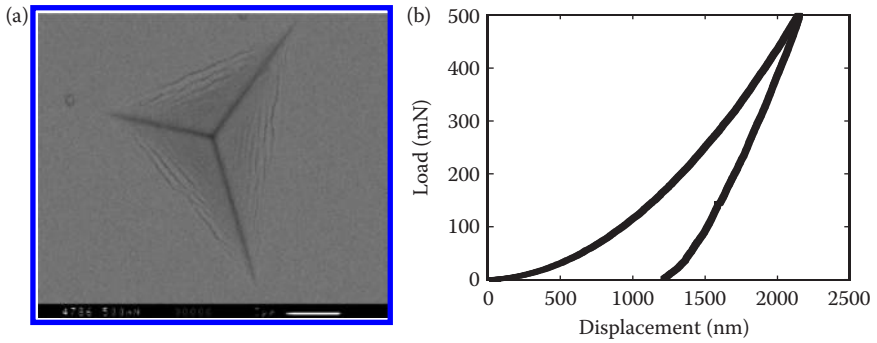


FIGURE 3.35 (a) SEM image of picture frame cracks in a 400 nm ZnO coating on glass indented by a Berkovich tip at 500 mN and (b) its associated load–displacement curve. No excursion in the P–δ curve was observed.

The work of indentation can be written in the following form:

$$W_t = W_P + U_{fra} + W_e + W_{other} \tag{3.39}$$

where W_t is the total work, W_P is work of plastic deformation, W_e is work of elastic deformation, U_{fra} is the fracture-dissipated energy, and W_{other} represents other items such as the heat dissipated during indentation, the energy dissipated in creep and microcracking. The sum of all the other items except W_e in Equations 3.47 and 3.48 is the irreversible energy W_{irr} (here, we ignore any reversible plastic behavior). Given an indentation procedure, we can easily measure W_t and W_e, by integrating the loading and unloading curves. The key point is to determine W_P, which will be discussed as follows.

It is assumed that the crack influence on the plastic and elastic deformation can be averaged over the whole loading curve. This is reasonable if E/H remains almost constant despite the presence of fracture and the picture frame cracking appears and propagates during loading in our coated systems as is usually observed [126]. The value of W_P can be approximately determined by [128],

$$\frac{W_p}{W_t} = 1 - \gamma \frac{H}{E_r} \tag{3.40}$$

where γ is an indenter geometry-dependent constant. This gives good approximation only for materials with $H/E < 0.17$.

A more generalized expression is given by [37],

$$\frac{W_p}{W_t} = 1 - \frac{3m\pi}{2\beta(m+1)} \frac{H}{E_r} \tan\theta \left(\frac{1}{1 + (\pi\varepsilon/2\beta)(H/E_r)\tan\theta} \right) \tag{3.41}$$

However, there is always some deviation between the numerical fitting and the actual experiment data. At the high loads investigated here this is dominated by deformation processes in the substrate. Therefore, we analyze the uncoated substrate to determine the W_{other} term. Now U_{fra} can be obtained using Equation 3.39. Ideally, this approach can separate the influence of elastic–plastic deformation from fracture for coated systems with features similar to what has been described here (i.e., no excursion associated with fracture and no significant change in the slope of the load-displacement curve). It can also be applied to brittle bulk materials given the condition that measurable cracking occurs and the fracture does not lead to a discontinuity in the load–displacement curve. The fracture-dissipated energy for oxide coatings determined by this approach is presented in Table 3.2. This approach is only applicable to the case where there is a relatively small mismatch in Young's modulus and hardness between coating and substrate.

3.6.4 Extrapolating Irreversible Work versus Load

Another energy-based model was proposed by Malzbender and de With based on analysis of the change in W_{irr}–P. It is assumed that a slope change in the W_{irr} versus

TABLE 3.2
Fracture Dissipated Energy for Oxide Coatings on Glass Substrate Indented by Different Indenters Determined by Various Methods

			G (J/m²)	
Coating	**Indenter**	**Excursion**	W_t–dp	W_{irr}–dp
400 nm SnO_2	Cube corner tip	Yes	29.3 +/– 9.8	19.9 +/– 6.3
240 nm ITO	Berkovich tip	No	36.3 +/– 8.2	39.4 +/– 15.9

Source: Chen, J., *Journal of Physics D: Applied Physics*, 2012. **45**: 203001.

applied load (W_{irr}–P) curve and the step change are correlated with delamination and chipping. The step change in the irreversible work due to chipping was regarded to be the energy dissipated by chipping (i.e., $\Delta W_{irr}^{c} = U_{fr}^{c}$), as depicted in Figure 3.36. Based on the Equation 3.38, it enables the determination of the fracture toughness.

3.6.5 Modeling the Limits of Fracture-Dissipated Energy

For the same experimental observation that the crack is associated with the pop-in in the load–displacement curve, a simple model to determine the limits of fracture-dissipated energy was originally proposed in Reference 104. This approach assumes the load (P) scales with displacement squared (δ^2) in the loading part and in the unloading procedure before and after fracture-induced pop-in in the load–displacement curve. The illustration of this model is provided in Figure 3.37. The additional assumptions in this model and the lower and upper limits of fracture-dissipated energy, U_{min}

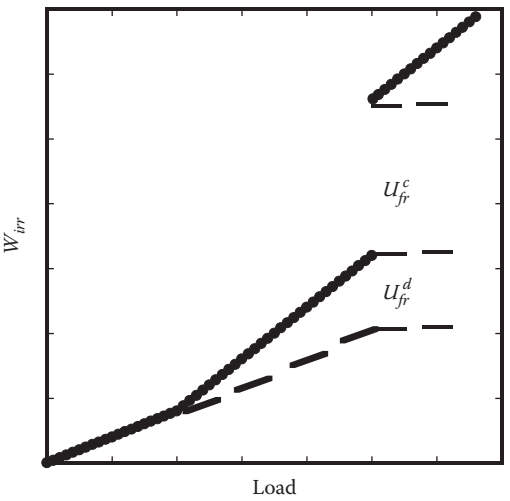


FIGURE 3.36 Schematic of analyzing W_{irr}–P curve to determine the fracture-dissipated energy by the delamination and chipping in the coating.

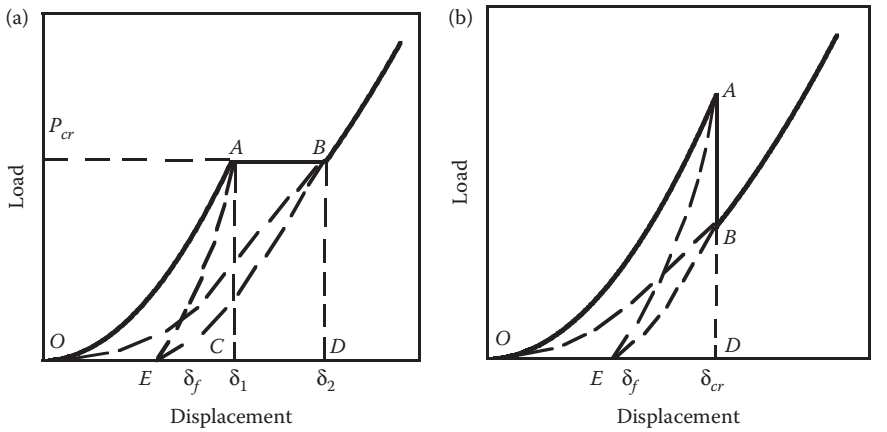


FIGURE 3.37 Schematic of the existing toughness limits models for (a) load control and (b) displacement control.

and U_{max}, are summarized in Table 3.3. From this, it can be seen that this model is unable to provide the lower toughness limit for the displacement control. With the same assumption, however, it gives the lower bound for load control but upper bound for the displacement control. The area ABDC in Figure 3.37 is the work done by indenter, which consists of elastic and plastic working together with the fracture-dissipated energy.

Therefore, this model has been further developed in References 129 and 130, in which case the unloading curve is assumed to be a power law relationship as follows:

$$P = A(\delta - \delta_f)^m \quad \text{before cracking at Point A} \tag{3.42}$$

$$P = B(\delta - \delta_f)^n \quad \text{after cracking at Point B} \tag{3.43}$$

where the A, B, m, n are constants, δ_f is the final depth.

TABLE 3.3
Summary of the Initial Toughness Bound Model Proposed in for the Nanoindentation Tests under Load Control (Ld-ctrl) and Displacement Control (Dp-ctrl)

	Lower Bound			Upper Bound		
Test Mode	**Assumption**	U_{min}	**Expression**	**Assumption**	U_{max}	**Expression**
Ld ctrl	Fully elastic recovery	Area OAB	$2/3P_{cr}(\delta_2-\delta_1)$	No recovery	Area ABDC	$P_{cr}(\delta-\delta_1)$
Dp ctrl	NA	NA	NA	Fully elastic recovery	Area OAB	$1/3\delta_{cr}(P_2-P_1)$

TABLE 3.4
Summary of the Toughness Limits Model

	Lower Bound			Upper Bound		
Test Mode	**Assumption**	U_{min}	**Expression**	**Assumption**	U_{max}	**Expression**
Ld ctrl	No increase in δ_f after crack	ABE	$\int_0^{P_{cr}} \left[\left(\frac{P}{B}\right)^{1/n} - \left(\frac{P}{A}\right)^{1/m} \right] dP$	No recovery	ABDE	$\int_{\delta_f}^{\delta_1} A(\delta - \delta_f)^m d\delta + P_{cr}(\delta_2 - \delta_1)$
Dp ctrl	No increase in δ_f after crack	ABE	$\int_{\delta_f}^{\delta_{cr}} \left[\left[A(\delta - \delta_f)^m - B(\delta - \delta_f)^n \right] \right] d\delta$	No recovery	ABDE	$\int_{\delta_f}^{\delta_{cr}} A(\delta - \delta_f)^m d\delta$

Source: Proposed by Chen, J., *Surface & Coatings Technology*, 2012. **206**: 3064–3068.

Unloading the curve at point B, the associated final depth should be between δ_f and δ_2 as shown in Figure 3.37. Therefore, the areas ABE and ABDE in Figure 3.37 are the lower and upper bounds of fracture-dissipated energy for both load and displacement control. The corresponding assumptions and generalized expressions for the lower and upper limits of fracture-dissipated energy proposed by Chen et al. are summarized in Table 3.4. This approach works equally for both load and displacement control.

However, there is a need to tighten this upper bound model as explained below. Under the load control, the indentation work associated with fracture event, that is, the area ABDC, is composed of the elastic and plastic work. Of which, only the stored elastic energy can be dissipated by the fracture. Although no work is done by indentation during the fracture event under the displacement control, the stored energy is not completely dissipated by fracture unless the load at Point B drops to zero. Therefore, the model above was further refined by Chen in 2012 [123]. Figure 3.38 displays the schematic to illustrate this refined lower and upper bound method developed by Chen.

In principle, the area ABFE should be fracture-dissipated energy. Based on the mathematical analysis, one could derive its expression, which is to relate to the power (i.e., *m* and *n*) of the unloading curves AE and BF, as summarized in Table 3.5. If the commercial nanoindenter softwares can be reprogrammed to do automatical unloading at the fracture end point B, it enables the assessment of the fracture-dissipated energy. At the moment, the existing nanoindenters do not have such function. Therefore, it is important to determine the lower and upper bounds of the fracture-dissipated energy. Table 3.6 summarizes the lower and upper limits of fracture-dissipated energy for both load and displacement control.

The equations above have been applied to various coatings when the nanoindentation tests were performed under both load and displacement control. For example,

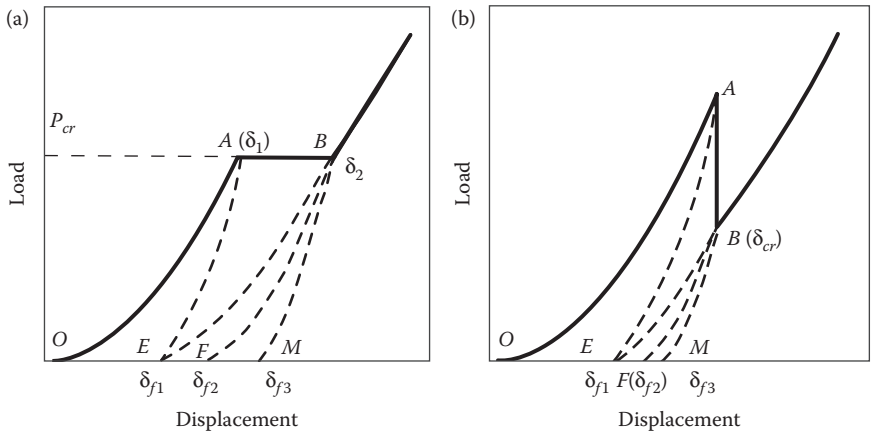


FIGURE 3.38 Schematic of the lower bound method developed in this work under (a) load control and (b) displacement control. The areas ABE and ABME are regarded as the lower and upper bounds of the fracture-dissipated energy, respectively.

TABLE 3.5
Summary of Fracture Dissipated Energy

Test Mode	Fracture Dissipated Energy, U_{fr}	Expression of U_{fr}
Ld control	Area ABFE	$\frac{P_{cr}(\delta_1 - \delta_{f1})}{m+1} + P_{cr}(\delta_2 - \delta_1) - \frac{P_{cr}(\delta_2 - \delta_{f2})}{n+1}$
Dp control	Area ABFE	$\frac{P_1(\delta_1 - \delta_{f1})}{m+1} - \frac{P_2(\delta_2 - \delta_{f2})}{n+1}$ $\quad \delta_1 = \delta_2 = \delta_{cr}$[a] $\quad \delta_1 \neq \delta_2$[b]

Source: Proposed by Chen, J., *Surface & Coatings Technology*, 2012. **206**: 3064–3068.

[a] Where the displacement at Point A and B is the same.

[b] Where the displacement at Point B is larger than Point A.

TABLE 3.6A
Summary of the Lower and Upper Limits of Fracture Dissipated Energy for Load Control

	Lower Bound	
Test Mode	Assumption	Expression of Fracture Dissipated Energy
Ld ctrl	No increase in the residual depth	$\left[\frac{(\delta_2 - \delta_{f1})}{1 + 1/n} - \frac{(\delta_1 - \delta_{f1})}{1 + 1/m}\right] P_{cr}$
Dp ctrl	No increase in the residual depth	$(\delta_{cr} - \delta_{f1})\left[\frac{P_1}{m+1} - \frac{P_2}{n+1}\right]$

Source: Chen, J., *Surface & Coatings Technology*, 2012. **206**: 3064–3068.

TABLE 3.6B
Summary of the Lower and Upper Limits of Fracture Dissipated Energy for Displacement Control

	Upper Bound	
Test Mode	Assumption	Expression of Fracture Dissipated energy
Ld ctrl	No change in the stiffness	$P_{cr}(\delta_1 - \delta_{f1})\left(\frac{1}{m+1} - \frac{1}{n+1}\right) + P_{cr}(\delta_2 - \delta_1)$
Dp ctrl	No change in the stiffness	$P_1(\delta_{cr} - \delta_{f1})\left(\frac{1}{m+1} - \frac{1}{n+1}\right) + \frac{P_2}{n+1}(\delta_{cr} - \delta_{f1})\left(\frac{P_1 - P_2}{P_1}\right)^{1/m}$

Source: Chen, J., *Surface & Coatings Technology*, 2012. **206**: 3064–3068.

TABLE 3.7
Summary of Fracture Toughness Determined by Various Models for the 1 μm Fullerene–Like CN_x Coating on Various Substrates Indented by a Berkovich Tip under Load Control

	K_{IC} (MPa*m $^{0.5}$)						
Substrate	**W_t–dp**	**Lower Limit**			**Upper Limit**		
Al_2O_3	5.4 ± 0.2	4.3 ± 0.2[a]	4.2 ± 0.1[b]	4.2 ± 0.1[c]	5.4 ± 0.3[a]	6.3 ± 0.3b	6.3 ± 0.3[c]
(100) 3C SiC	5.5 ± 0.2	5.5 ± 0.2[a]	5.1 ± 0.2[b]	5.1 ± 0.2[c]	6.7 ± 0.3[a]	7.4 ± 0.3[b]	6.4 ± 0.3[c]

Source: Chen, J., *Surface & Coatings Technology*, 2012. **206**: 3064–3068.
[a] Model proposed in Reference 104.
[b] Model proposed in Reference 130.
[c] Improved model proposed in Reference 123.

TABLE 3.8
Summary of Fracture Toughness Determined by Various Models for the 400 nm Oxides Coatings on Glass Indented by a Cube Corner Tip under Displacement Control

	K_{IC} (MPa*m $^{0.5}$)						
Coating	**W_t–dp**		**Lower Limit**			**Upper Limit**	
TiO_xN_y	1.8 ± 0.2	NA[a]	1.8 ± 0.2[b]	1.8 ± 0.2[c]	2.0 ± 0.3[a]	3.9 ± 0.5[b]	2.3 ± 0.3[c]
ITO	2.1 ± 0.2	NA[a]	2.0 ± 0.2[b]	2.0 ± 0.2[c]	2.2 ± 0.3[a]	5.5 ± 0.6[b]	2.6 ± 0.3[c]

Source: Chen, J., *Surface & Coatings Technology*, 2012. **206**: 3064–3068.
[a] Model proposed in Reference 104.
[b] Model proposed in Reference 130.
[c] Improved model proposed in Reference 123.

the chipping causes the big discontinuity in the P–δ curve for the indentation tests on CN_x coating under load control as shown in Figure 3.30. The radial cracks lead to the load drop in the P–δ curve for the indentation tests on oxide coating under displacement control as shown in Figure 3.31. The corresponding values of fracture toughness K_{IC} have been summarized in Tables 3.7 and 3.8, in which case it is assumed that $m = n = 1.48$ as it is closer to the experimental results.

3.6.6 Assess the Interfacial Fracture-Dissipated Energy

Hainsworth et al. [27] treated the indentation-induced delaminated coating as a centrally loaded disc. It was assumed that the fracture-dissipated energy associated with delamination equals the elastic energy stored in the flexed annular coating segment. In which case, the energy dissipated by delamination is given by [27],

$$U_{fr}^{d} = \frac{2\pi E t^3 (\delta_m - \delta_r)^2}{3C_R^2} \tag{3.44}$$

The energy release rate for the delamination is given by,

$$G_{int} = \frac{U_{fr}^{d}}{\pi C_R^2} = \frac{2E t^3 (\delta_m - \delta_r)^2}{3C_R^4} \tag{3.45}$$

This method gave G_{int} = 173–716 J/m^2 for 4 μm TiN/ZrN multilayers on steel and 20,000 J/m^2 for submicro solar control coatings on glass, which are unrealistically high. Such significant overestimation is due to the fact that the stored elastic energy in the cracked coating is only partially released by the fracture. From Equation 3.45, it can be seen that this method is extremely sensitive to the measured delamination length. Any measurement uncertainty in crack length will lead to significant errors in the energy release rate.

It was often observed that the unloading induced delamination would cause the extra linear recovery in the unloading curve [40,42,117–119,131] (e.g., Figure 3.39a). Therefore, another method was proposed by analyzing the extra linear recovery caused by delamination for indentations of various coated systems. Such observations were also found in the numerical simulations [120], as shown in Figure 3.39b. It was assumed that the additional recovery work (i.e., the extra recovery area as shown in Figure 3.39a) was the fracture-dissipated energy. This method gave the G_{int} = 32–64 J/m^2 for 4 μm TiN/ZrN multilayers on steel and 35–80 J/m^2 for submicro solar control coatings on glass, which are more sensible compared to Equations 3.44 and 3.45.

However, this method still overestimated the interface fracture toughness because only small portion of such energy is associated with fracture-dissipated energy.

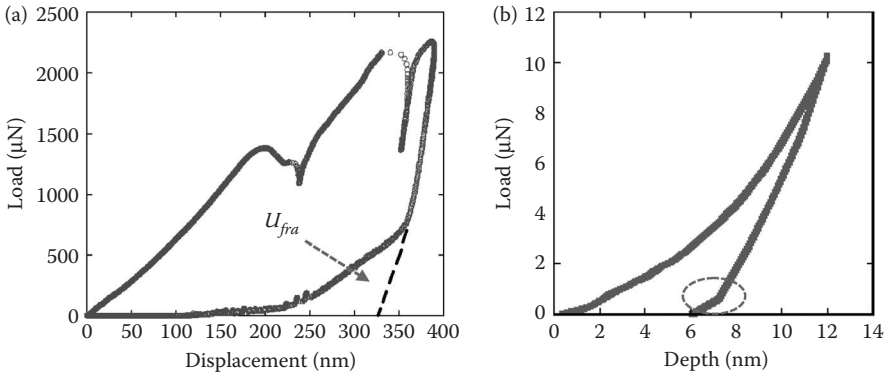


FIGURE 3.39 (a) Extra linear elastic recovery in the load–displacement curve observed during unloading for an ITO/Ag/ZnO/TiO2 multilayer on commercial soda-lime glass. (From Chen, J. and S.J. Bull, *Journal of Physics D-Applied Physics*, 2007. **40**(18): 5401–5417.) (b) Finite element simulation of unloading induced delamination for coated glass, which shows extra linear recovery. (From Chen, J.J. and S.J. Bull, *Thin Solid Films*, 2009. **517**(13): 3704–3711.)

Another energy-based method is based on analyzing W_{irr}–P curve to determine the fracture-dissipated energy by delamination. The difference between the irreversible work at a given delamination dimension r_d and the extrapolated irreversible (see Figure 3.36) was assumed to be the energy dissipated by delamination (i.e., $\Delta W_{irr}^{d} = U_{fr}^{d}$). This method has yielded reasonable estimation of interfacial toughness for various sol–gel coatings on glass. But it requires performing indentation tests at a wide range of loads to generate W_{irr}–P curve.

Recently, alternative approaches have been proposed [117,118]. They propose to perform sequential dual-indentation and analyzing the corresponding two unloading curves. The key point is to perform the sequential indentation of the delaminated thin film.

It suggested that the fracture-dissipated energy due to the interfacial delamination is the difference between W_1 and W_2 (W_1–W_2). For the 0.5 μm compressive SiN and Dl-com SiN coatings, it gave the values of interfacial energy release rate of 1.06 and 2.31 J/m^{2,} respectively [118]. In that study, a 60° conical indenter with a tip radius of 5.6 μm was used. The applied loads were in the range of 100–200 mN.

However, the deformation mechanisms including the failure mechanisms depend on the indenter geometries and applied force [91,92]; for example, when these coatings were indented by a 120° conical indenter with a tip radius of 3 μm with the applied load from 0.5 to 28 mN. In which case, a pop-in induced by the formation of the slip bands always occur prior to the delamination associated with pop-out. Furthermore, it was observed that the unloading curves in the two sequential indentations are parallel during certain period. In this case, the method proposed in their earlier work (i.e., W_1–W_2 in Figure 3.40) would lead to overestimation of the fracture-dissipated energy. Therefore,

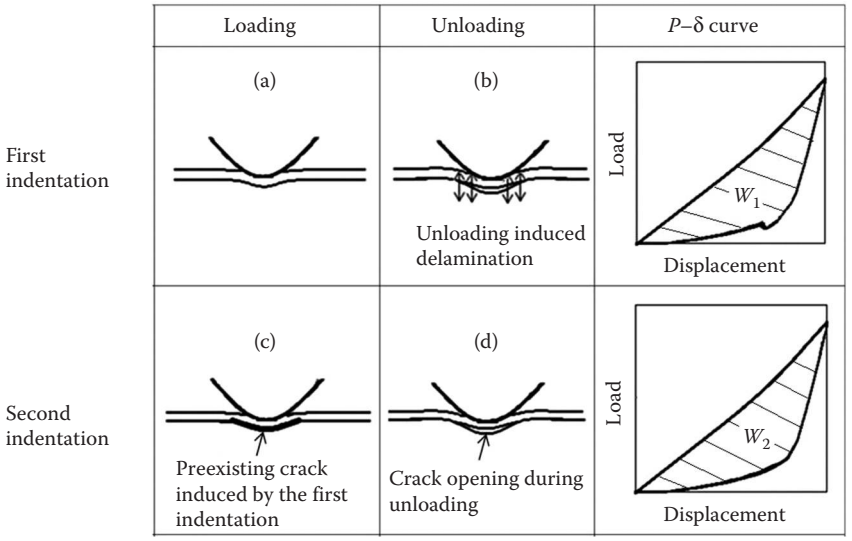


FIGURE 3.40 Schematic of two sequential indentation-induced deformation during loading and unloading. (Modified after Xie, H.T. and H. Huang, *Journal of Materials Research*, 2013. **28**: 3137–3145.)

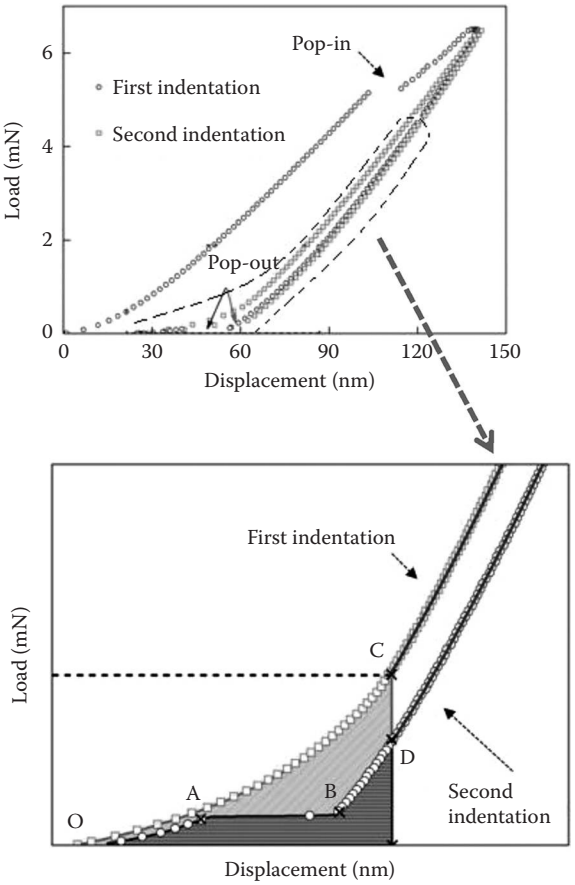


FIGURE 3.41 Schematic of using the unloading curves of two sequential indentations to determine the fracture-dissipated energy by delamination. (Modified after Lu, M. and H. Huang, *Journal of Materials Research*, 2014. **29**: 801–810.)

this method has been refined by finding the critical point where the unloading curves are no longer parallel [117]. This has been illustrated in Figure 3.41. This method enables extracting the stored energy caused by the deflection of suspended film. For the 0.5 μm compressive SiN and Dl-com SiN coatings, it gave the values of interfacial energy release rate of 1.6 and 0.98 J/m^2, respectively [117]. These values are similar to the previous reported results determined by the approach illustrated in Figure 3.40.

Based on equation similar to Equation 3.38, by replacing the E with the interface elastic modulus (E_{int}), which is given by [132],

$$\frac{1}{E_{int}} = \frac{1}{2}\left(\frac{1}{E_c} + \frac{1}{E_s}\right) \tag{3.46}$$

where E_c and E_s are the Young's modulus of the coating and substrate, respectively.

3.7 NUMERICAL ANALYSIS OF INDENTATION-INDUCED CRACKING

There are also some numerical analyzes based on finite element modeling (FEM) to study indentation-induced cracking. For example, the cohesive zone model (CZM) [133–138] has been implemented to FEA to model crack nucleation and propagation. This technique enables to remove the crack tip stress singularity and cope with the nonlinear process.

A cohesive zone is a surface along which a small displacement jump between the two sides is allowed with normal and tangential components δ_n and δ_t, respectively. There are different CZMs such as bilinear CZM and exponential CZM. The commonly used one is exponential CZM proposed by Xu and Needleman [138]. In this case, the traction components at normal and tangential directions, T_n and T_t, are determined by two potentials Φ_n and Φ_t at normal and tangential directions.

$$T_n = \frac{\partial \varphi_n}{\partial \delta_n} \tag{3.47}$$

$$T_t = \frac{\partial \varphi_t}{\partial \delta_t} \tag{3.48}$$

The traction–separation relations are illustrated in Figure 3.42. The maximum traction represents the cohesive strength and the area under the curve is the work of the fracture.

Figure 3.43 shows how to implement the CZM into an indentation model.

Here, coating cracking is represented by inserting cohesive zones into the coating, perpendicular to the surface. A cohesive zone is also used to model the interface between coating and substrate.

Abdul-Baqi and Van der Giessen have demonstrated that three through-thickness cracks occur in the coating and the corresponding load–displacement curve. This confirms that three load drops are indeed correlated to the through-thickness cracks in the coating.

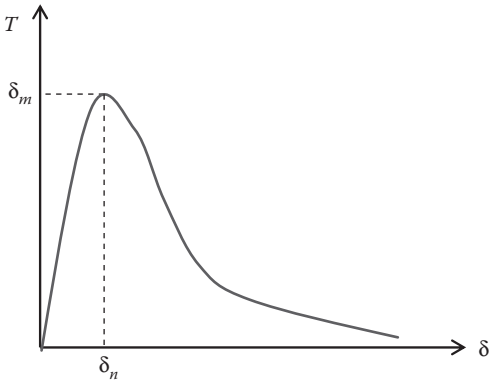


FIGURE 3.42 Schematic of traction–separation (T–δ) relationship in the bilinear CZM.

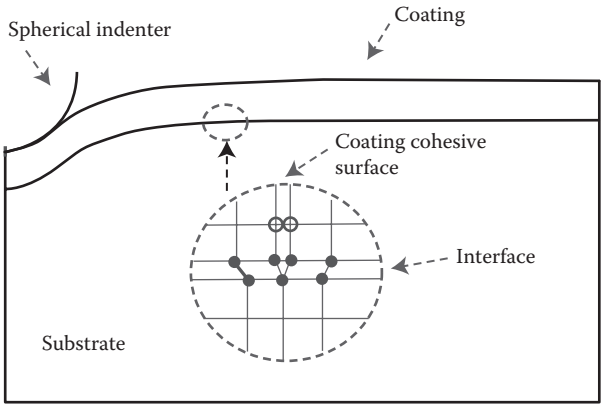


FIGURE 3.43 Schematic of the indentation modeling with details of the layout of the continuum elements and cohesive elements along the interface. (Modified after Abdul-Baqi, A. and E. Van der Giessen, *International Journal of Solids and Structures*, 2002. **39**(6): 1427–1442.)

Based on these load drops, there are some simple empirical models to estimate the fracture-dissipated energy. For example, Li et al. [140] proposed that the area ABCD in Figure 3.44 was the fracture-dissipated energy, while, Kanninen and Popelar [141] suggested that area OAC or area OAB were the fracture-dissipated energy instead. With CZM implemented to finite element simulation, it enables the evaluation of the existing empirical models.

For the indentation-induced through-thickness crack, the crack is dominated by mode I. In this case, only Φ_n is needed. Abdul-Baqi and Van der Giessen have studied the estimated values of the energy release rate (i.e., $(\Delta U/A_{fra}) = \varphi_n^{est}$, where ΔU can be obtained as shown in Figure 3.44) of the coating, with regard to different

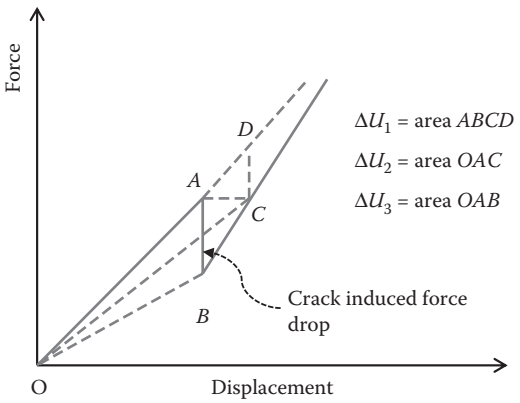


FIGURE 3.44 Schematic of the load drop in a load–displacement curve induced by fracture in the coating. (Modified after Abdul-Baqi, A. and E. Van der Giessen, Numerical analysis of indentation-induced cracking of brittle coatings on ductile substrates. *International Journal of Solids and Structures*, 2002. **39**(6): 1427–1442.)

values of intrinsic φ_n of the coating and coating thickness t. It has been demonstrated that the first method (i.e., ΔU_1 in Figure 3.44) underestimates the fracture energy, whereas the second (i.e., ΔU_2 in Figure 3.44) and third method (i.e., ΔU_3 in Figure 3.44) give reasonable estimation for small values of Φ_n or t. However, at large values of Φ_n or t, the second and third methods overestimate the fracture-dissipated energy, whereas the estimation by the first method seems reasonable [139]. The plastic deformation of the substrate leads to highly nonlinear process during indentation. However, the simples models illustrated in Figure 3.44, are based on the assumption of linear elastic deformation, which is the major reason to cause the significant discrepancy between the estimated fracture energy dissipation and the intrinsic one. Nevertheless, it is interesting to observe the linear correlation between $\varphi_n^{est}/\varphi_n$ and the coating thickness. This suggests that when Φ_n is higher, the substrate plastic deformation would play more contribution. Here, the models (i.e., W_t–dp method discussed previously) that could subtract the effect caused by plastic deformation of the substrate will be particularly useful.

Similarly, the FEA implemented with CZM also enables evaluation of analytical/empirical models to determine the interface toughness [120,142].

To tackle the difficulty in updating the mesh so as to match the geometry of the discontinuity, a few other techniques have been developed to model cracks and crack growth without remeshing. These include the moving mesh technique [143], incorporation of a discontinuous mode on an element level [144], and the technique based on a partition-of-unity [145,146]. Among which, the technique based on partition-of-unity is also known as the extended finite element method (XFEM), which has been widely used [147–149]. This technique allows the presence of discontinuities in an element by enriching degrees of freedom with special displacement functions. Therefore, it allows crack to be modeled independent of the mesh and enables simulation of initiation and propagation of a discrete crack along an arbitrary, solution-dependent path without the requirement of remeshing.

Another technique that enables modeling the crack behavior in the coatings is virtual crack closure technique (VCCT) [150–153], which is illustrated in Figure 3.45.

In this case, the mode I (G_I) and mode II (G_{II}) energy release rates are given as follows [150–153]:

$$G_I = \frac{-Z_i(w_j - w_{j^*})}{2\Delta a} \tag{3.49}$$

$$G_{II} = \frac{-X_i(u_j - u_{j^*})}{2\Delta a} \tag{3.50}$$

where Z_i and X_i are the forces required to close the crack; u and w are the shear and opening displacement for the upper and lower nodes as shown in Figure 3.45; Δa is the crack surface of the crack extension. This technique could be used to model indentation tests to determine the fracture-dissipated energy [154,155]. Figure 3.46 illustrates the schematic of numerical model incorporated with VCCT used for the finite element simulation of indentation-induced crack.

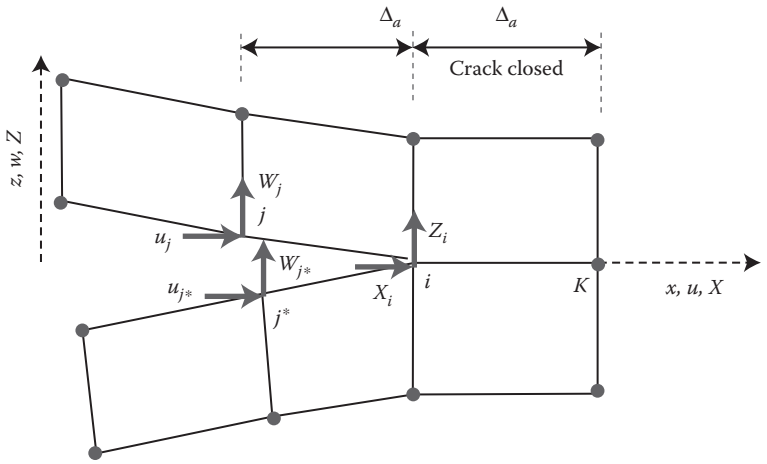


FIGURE 3.45 VCCT for a four-noded element. (Modified after Krueger, R., *Applied Mechanics Reviews*, 2004. **57**(2): 109–143.)

When using this technique to determine the energy release rate for the indentation-induced picture-frame crack (also known as circumference crack), it gives consistent results to those determined by the J-integral [156–159] for various indentation penetrations as demonstrated in Reference 155. These VCCT techniques could also be used to determine interface toughness [160]. As it can be seen from Figure 3.46, this type of crack is due to the plastic deformation of the substrate, which induce the bending of the film [91].

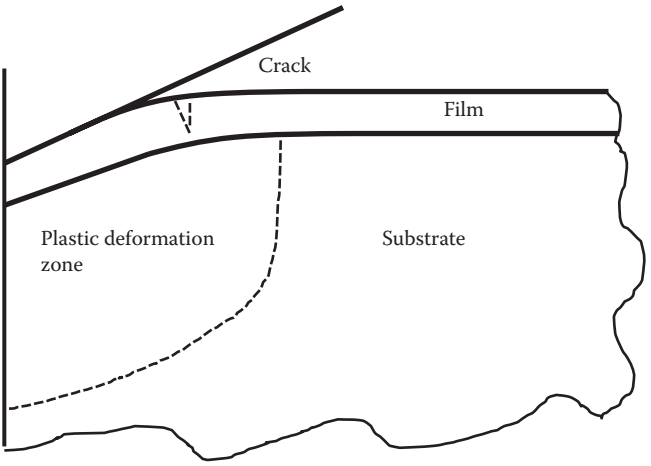


FIGURE 3.46 Numerical model used for the finite element simulation of indentation-induced crack. (Modified after Steffensen, S. and H.M. Jensen, *European Journal of Mechanics a-Solids*, 2014. **43**: 133–141.)

3.8 SUMMARY

As a nondestructive method, nanoindentation tests have been proved effective to determine fracture toughness, which do not require special specimen preparation.

This chapter illustrated the nanoindentation techniques and discussed how to use nanoindentation to obtain reliable Young's modulus and hardness of thin coatings, which are essential for determining the fracture toughness of the coatings. Furthermore, a comprehensive discussion on fracture mechanisms of indentation-induced cracks and a range of indentation-based methods (i.e., stress analysis and energy-based models) to assess fracture toughness. Table 3.9 presents a summary for the stress- and energy-based models. From these it can be seen that the stress analysis-based models usually require empirical fitting parameters and the specific model is required with regard to crack pattern. In contrast, the energy-based models do not involve empirical constants and are independent of crack morphology, provided that the specific assumptions outlined in the models can be satisfied. However, they usually require that the crack propagates during the loading cycle only, while, stress analysis-based models can take account of this if they are carefully constructed. In practice, it is good to use a sharper indenter, such as a cube corner tip, to induce the cracks at lower load, which could reduce the substrate effect.

The models based on the analysis of the fracture-induced excursion (or step) in the load–displacement curve have been applied to coatings with thickness down to 100 nm so far. Zhang and Zhang [89] pointed out that the step size of the load–displacement curve induced by fracture is correlated to the coating thickness. Usually, the step size is similar to the coating thickness but it may be down to 75% of the coating thickness. So, one may expect that the method based on step in the load–displacement curve should work well for coatings with thickness above 50 nm.

The accuracy of such method is also dependent on how sensitive the instrument is to be able to detect the excursions.

In addition, various techniques such as CZM and VCCT could be implemented into finite element simulations to study fracture initiation and propagation. These could be employed to evaluate the models to determine fracture-dissipated energy.

TABLE 3.9
Summary of Stress-Based Models and Energy-based Models

	Stress-Based Models	Energy-Based Models
No need for empirical fitting parameters	N	Y
Independent for crack morphology	N	Y
Independent for indenter	N	Y
Account for residual stress	Y	Y
Valid for cracks that occur during loading	Y	Y
Valid for cracks that occur during unloading	Y	

ACKNOWLEDGMENTS

Professors B. Beake and H. Huang are acknowledged for constructive comments. Professors S.J. Bull and A.M. Korsunsky are acknowledged for useful discussions. Most of the works, were sponsored by The Engineering and Physical Sciences Research Council (EPSRC) and Newcastle University.

REFERENCES

1. Beake, B.D. et al., Coating optimisation for high speed machining with advanced nano-mechanical test methods. *Surface & Coatings Technology*, 2009. **203**(13): 1919–1925.
2. Alfano, M. et al., The influence of high-temperature sintering on microstructure and mechanical properties of free-standing APS CeO2-Y2O3-ZrO2 coatings. *Journal of Materials Science*, 2011. **45**: 2662–2669.
3. Chen, J. and S.J. Bull, Multi-cycling nanoindentation study on thin optical coatings on glass. *Journal of Physics D: Applied Physics*, 2008. **41**(7): 074009.
4. Liu, Z. et al., Magnetron sputtered Ni-rich nickel oxide nano-films for resistive switching memory applications. *International Journal of Applied Ceramic Technology*, 2013. **10**(1): 20–25.
5. Qiu, Y. et al., Self-lubricating CrAlN/VN multilayer coatings at room temperature. *Applied Surface Science*, 2013. **279**: 189–196.
6. Zhao, X. et al., Investigations on B-doped SiO2 thermal protective coatings by hybrid sol–gel method. *Thin Solid Films*, 2011. **519**: 4849–4854.
7. Zhou, Z.B. et al., Schottky solar cells with amorphous carbon nitride thin films prepared by ion beam sputtering technique. *Solar Energy Materials and Solar Cells*, 2002. **70**(4): 487–493.
8. Treglio, J.R., S. Trujillo, and A.J. Perry, Deposition of TiB2 at low-temperature with low residual-stress by a vacuum-arc plasma source. *Surface & Coatings Technology*, 1993. **61**(1–3): 315–319.
9. Huang, J. et al., Microstructure and thermal cycling behavior of CeO2 coatings deposited by the electron beam physical vapor technique. *Thin Solid Films*, 2013. **544**: 270–275.
10. Ilyas, U. et al., Enhanced ferromagnetic response in ZnO:Mn thin films by tailoring composition and defect concentration. *Journal of Magnetism and Magnetic Materials*, 2013. **344**: 171–175.
11. Hainsworth, S.V., H.W. Chandler, and T.F. Page, Analysis of nanoindentation load–displacement loading curves. *Journal of Materials Research*, 1996. **11**(8): 1987–1995.
12. Juliano, T., Y. Gogotsi, and V. Domnich, Effect of indentation unloading conditions on phase transformation induced events in silicon. *Journal of Materials Research*, 2003. **18**(5): 1192–1201.
13. Ruffell, S. and J.S. Williams, Effect of oxygen on nanoscale indentation-induced phase transformations in amorphous silicon, in *Probing Mechanics at Nanoscale Dimensions*, *Materials Research Society Symposium Proceedings,* N. Tamura et al., Editors. 2009. Boston, USA: Materials Research Society, pp. 1–6.
14. Feng, G. and A.H.W. Ngan, Creep and strain burst in indium and aluminium during nanoindentation. *Scripta Materialia*, 2001. **45**(8): 971–976.
15. Chen, J. and S.J. Bull, The investigation of creep of electroplated Sn and Ni-Sn coating on copper at room temperature by nanoindentation. *Surface & Coatings Technology*, 2009. **203**(12): 1609–1617.
16. Shin, C. and S. Shim, Dislocation mechanisms of radius effect on displacement bursts during spherical nanoindentations. *Journal of Materials Research*, 2012. **27**(16): 2161–2166.

17. Caer, C. et al., Stress induced pop-in and pop-out nanoindentation events in CuAlBe shape memory alloys. *Materials Science and Engineering a-Structural Materials Properties Microstructure and Processing*, 2013. **587**: 304–312.
18. Bartosik, M. et al., Lateral gradients of phases, residual stress and hardness in a laser heated Ti0.52Al0.48N coating on hard metal. *Surface & Coatings Technology*, 2012. **206**(22): 4502–4510.
19. Wei, J. et al., Effect of Ni-Coated carbon nanotubes on the creep behavior of Sn-Ag-Cu solder by nanoindentation. *Proceedings of the Asme International Mechanical Engineering Congress and Exposition*, 2011. **112012**: 843–847.
20. Yi, L.-H. et al., Analyzing mechanical properties of a nanocrystalline Fe-Ni coating by nanoindentation. *Journal of Materials Research*, 2011. **26**(19): 2533–2542.
21. Takagi, H. and M. Fujiwara, Set of conversion coefficients for extracting uniaxial creep data from pseudo-steady indentation creep test results. *Materials Science and Engineering a-Structural Materials Properties Microstructure and Processing*, 2014. **602**: 98–104.
22. Geranmayeh, A.R. et al., Indentation creep of lead-free Sn-5Sb solder alloy with 1.5 wt% Ag and Bi additions. *Journal of Electronic Materials*, 2014. **43**(3): 717–723.
23. Fernández-Palacio, J., *Mechanical and Tribological Characterisation of Fullerene-like Materials*, 2006, Newcastle University: Newcastle.
24. Maharaj, D. and B. Bhushan, Scale effects of nanomechanical properties and deformation behavior of Au nanoparticle and thin film using depth sensing nanoindentation. *Beilstein Journal of Nanotechnology*, 2014. **5**: 822–836.
25. Zhang, L. et al., *Mechanical properties of atomic layer deposition-reinforced nanoparticle thin films.* Nanoscale, 2012. **4**(20): 6543–6552.
26. Chakraborty, H. et al., A study on nanoindentation and tribological behaviour of multifunctional ZnO/PMMA nanocomposite. *Materials Letters*, 2013. **93**: 137–140.
27. Hainsworth, S.V., M.R. McGurk, and T.F. Page, The effect of coating cracking on the indentation response of thin hard-coated systems. *Surface & Coatings Technology*, 1998. **102**(1–2): 97–107.
28. Chen, J. et al., Mechanical analysis and in situ structural and morphological evaluation of Ni-Sn alloy anodes for Li ion batteries. *Journal of Physics D-Applied Physics*, 2008. **41**(2): 025302.
29. Chen, J. et al., Nanoindentation and nanowear study of Sn and Ni-Sn coatings. *Tribology International*, 2009. **42**(6): 779–791.
30. Polychronopoulou, K. et al., Deposition and Nanotribological Characterization of Sub-100-nm Thick Protective Ti-Based Coatings for Miniature Applications. *Tribology Letters*, 2011. **44**(2): 213–221.
31. Sneddon, I.N., The relationship between load and penetration in the axisymmetric Boussinesq problem for a punch of arbitrary profile. *International Journal of Engineering Science*, 1965. **3**: 47–57.
32. Oliver, W.C. and G.M. Pharr, An improved technique for determining hardness and elastic-modulus using load and displacement sensing indentation experiments. *Journal of Materials Research*, 1992. **7**(6): 1564–1583.
33. King, R.B., Elastic analysis of some punch problems for a layered medium. *International Journal of Solids and Structures*, 1987. **23**(12): 1657–1664.
34. Vlassak, J.J. and W.D. Nix, Measuring the elastic properties of anisotropic materials by means of indentation experiments. *Journal of the Mechanics and Physics of Solids*, 1994. **42**(8): 1223–1245.
35. Hay, J.C., A. Bolshakov, and G.M. Pharr, A critical examination of the fundamental relations used in the analysis of nanoindentation data. *Journal of Materials Research*, 1999. **14**: 2296–2305.

36. Bolshakov, A. and G.M. Pharr, Influences of pileup on the measurement of mechanical properties by load and depth sensing indentation techniques. *Journal of Materials Research*, 1998. **13**(4): 1049–1058.
37. Chen, J. and S.J. Bull, Relation between the ratio of elastic work to the total work of indentation and the ratio of hardness to Young's modulus for a perfect conical tip. *Journal of Materials Research*, 2009. **24**(3): 590–598.
38. Lahijania, Y.Z.K., M. Mohseni, and S. Bastani, Characterization of mechanical behavior of UV cured urethane acrylate nanocomposite films loaded with silane treated nanosilica by the aid of nanoindentation and nanoscratch experiments. *Tribology International*, 2014. **69**: 10–18.
39. Nikkhah, S.J., H. Hojati, and M.R. Moghbeli, Self-cross-linking acrylate copolymer/organoclay nanocomposite–emulsion coating: Nanoindentation and nanoscratch behavior. *Polymer-Plastics Technology and Engineering*, 2014. **53**(3): 268–277.
40. Chen, J. and S.J. Bull, Approaches to investigate delamination and interfacial toughness in coated systems: An overview. *Journal of Physics D: Applied Physics*, 2011. **44**(3): 034001.
41. Jellad, A. et al., Nanomechanical and nanowear properties of Cr3C2 thin films deposited by rf sputtering. *Wear*, 2008. **264**(9–10): 893–898.
42. Chen, J. et al., Experimental and modelling techniques for assessing the adhesion of very thin coatings on glass. *Journal of Physics D: Applied Physics*, 2009. **42**: 214003.
43. Chen, L. et al., Is 2 nm DLC coating enough to resist the nanowear of silicon. *Wear*, 2013. **302**(1–2): 909–917.
44. Chen, J. et al., Mechanical analysis and in situ structural and morphological evaluation of Ni-Sn alloy anodes for Li ion batteries. *Journal of Physics D: Applied Physics*, 2008. **41**(2): 025302.
45. Chen, J. et al., Nanoindentation and nanowear study of Sn and Ni-Sn coatings. *Tribology International*, 2009. **42**(6): 779–791.
46. Chen, J., *Energy Based Models to Determine Fracture Toughness of Thin Coated Systems by Nanoindentation*, 2006, University of Newcastle upon Tyne: Newcastle upon Tyne.
47. Doerner, M.F. and W.D. Nix, A method for interpreting the data from depth-sensing indentation instruments. *Journal of Materials Research*, 1986. **1**(4): 601–609.
48. Gao, H.J., C.H. Chiu, and J. Lee, Elastic contact versus indentation modeling of multilayered materials. *International Journal of Solids and Structures*, 1992. **29**(20): 2471–2492.
49. Jung, Y.G. et al., Evaluation of elastic modulus and hardness of thin films by nanoindentation. *Journal of Materials Research*, 2004. **19**(10): 3076–3080.
50. Fischer-Cripps, A.C., *Nanoindentation* 2002: Springer-Verlag GmbH: New York.
51. Bückle, H., Chapter 33 in *The Science of Hardness Testing and its Applications*, J.W. Westbrook and H. Conrad, Editors. 1973, American Society for Metals: Metals Park, OH. pp. 453–491.
52. Jonsson, B. and S. Hogmark, Hardness measurements of thin films. *Thin Solid Films*, 1984. **114**: 257–269.
53. Burnett, P.J. and D.S. Rickerby, The mechanical properties of wear-resistance coatings I: Modelling of hardness behaviour. *Thin Solid Films*, 1987. **148**: 41–50.
54. Burnett, P.J. and D.S. Rickerby, The mechanical properties of wear-resistance coatings II: Experimental studies and interpretation of hardness. *Thin Solid Films*, 1987. **148**: 51–65.
55. Bhattacharya, A.K. and W.D. Nix, Finite element simulation of indentation experiments. *International Journal of Solids and Structures*, 1988. **24**(12): 1287–1298.
56. Chen, J. and S.J. Bull, On the factors affecting the critical indenter penetration for measurement of coating hardness. *Vacuum*, 2009. **83**(6): 911–920.
57. McGurk, M.R. and T.F. Page, Using the P-delta(2) analysis to deconvolute the nanoindentation response of hard-coated systems. *Journal of Materials Research*, 1999. **14**(6): 2283–2295.

58. Swain, M.V. and M. Wittling, Comparison of acoustic emission from pointed and spherical indentation of TiN films on silicon and sapphire. *Surface & Coatings Technology*, 1995. **76–77**(1–3): 528–533.
59. Faisal, N.H., R. Ahmed, and R.L. Reuben, Indentation testing and its acoustic emission response: applications and emerging trends. *International Materials Reviews*, 2011. **56**(2): 98–142.
60. G-Berasategui, E., S.J. Bull, and T.F. Page, Mechanical modelling of multilayer optical coatings. *Thin Solid Films*, 2004. **447**: 26–32.
61. Dyjak, P. and R.P. Singh, Acoustic emission analysis of nanoindentation-induced fracture events, in *Fundamentals of Nanoindentation and Nanotribology III*, *Materials Research Society Symposium Proceedings,* K.J. Wahl et al., Editors. 2005. Boston, USA: Materials Research Society. pp. 393–398.
62. Faisal, N.H. et al., The use of acoustic emission to characterize fracture behavior during vickers indentation of HVOF thermally sprayed WC-Co coatings. *Journal of Thermal Spray Technology*, 2009. **18**(4): 525–535.
63. Irwan, R. and H. Huang, Removal and fracture characteristics of cemented tungsten carbide under nanoindenting and nanoscratching, *Key Engineering Materials*, 2010. **447–448**: 16–20.
64. Bahr, D.F. and W.W. Gerberich, Relationships between acoustic emission signals and physical phenomena during indentation. *Journal of Materials Research*, 1998. **13**(4): 1065–1074.
65. Malzbender, J. and G. de With, The use of the indentation loading curve to detect fracture of coatings. *Surface & Coatings Technology*, 2001. **137**(1): 72–76.
66. Berasategui, E.G., S.J. Bull, and T.F. Page, Mechanical modelling of multilayer optical coatings. *Thin Solid Films*, 2004. **447**: 26–32.
67. Bull, S.J. and D.S. Rickerby, Characterization of hard coatings, in *Handbook of Hard Coatings*, R.F. Bunshah, Editor. 2001, Noyes Publications/William Andrew Publishing: Norwich–New York. p. 181–228.
68. Hultman, L. et al., Cross-linked nano-onions of carbon nitride in the solid phase: Existence of a novel C48N12 aza-fullerene. *Physical Review Letters*, 2001. **8722**(22): p. art. no.-225503.
69. Perry, A.J., J.A. Sue, and P.J. Martin, Practical measurement of the residual stress in coatings. *Surface & Coatings Technology*, 1996. **81**(1): 17–28.
70. Perry, A.J. et al., The residual-stress in tin films deposited onto cemented carbide by high-rate reactive sputtering. *Surface & Coatings Technology*, 1989. **39**(1–3): 387–395.
71. Perry, A.J. et al., Aspects of residual-stress measurements in TiN prepared by reactive sputtering. *Surface and Coatings Technology*, 1990b. **43–4**(1–3): 234–244.
72. Bull, S.J. and D.S. Rickerby, Evaluation of coatings. *British Ceramic Transactions and Journal*, 1989. **88**(5): 177–183.
73. Perry, A.J., V. Valvoda, and D. Rafaja, X-Ray residual-stress measurement in tin, Zrn and Hfn films using the seemann-bohlin method. *Thin Solid Films*, 1992. **214**(2): 169–174.
74. Hoffman, R.W., in The mechanical properties of thin condensed films, *Physics of Thin Films*, G. Haas and R.E. Thun, Editors. 1966, Academic Press: New York. vol. 3, pp. 211–273.
75. Kondrashov, P.E. et al., Capabilities of combined studies of DLC films by X-ray methods. *Diamond and Related Materials*, 1997. **6**(12): 1784–1788.
76. Stoney, G.G., The tension of metallic deposited by electrolysis. *Proceedings of the Royal Society*, 1909. **A82**: 172–175.
77. Senderoff, S. and A. Brenner, Calculation of the stress in electron deposits from the curvature of plated strip. *Journal of Research of the National Bureau of Standards*, 1949. **42**: 105–123.

78. An, L. et al., Damage-resistant alumina-based layer composites. *Journal of Materials Research*, 1996. **11**(1): 204–210.
79. Fischer-Cripps, A.C. et al., Stress analysis of elastic plastic contact damage in ceramic coatings on metal substrates. *Journal of the American Ceramic Society*, 1996. **79**(10): 2619–2625.
80. Lardner, T.J., J.E. Ritter, and G.Q. Zhu, Spherical indentation and fracture of glass plates. *Journal of the American Ceramic Society* 1997. **80**(7): 1851–1862.
81. Pajares, A. et al., Mechanical characterization of plasma sprayed ceramic coatings on metal substrates by contact testing. *Materials Science and Engineering*., 1996. **A208**: 158–165.
82. Swain, M.V. and J. Mencik, Mechanical property characterization of thin films using spherical tipped indenters. *Thin Solid Films*, 1994. **253**: 204–211.
83. Miranda, P. et al., Contact fracture of brittle bilayer coatings on soft substrates. *Journal of Materials Research*, 2001. **16**(1): 115–126.
84. Lee, K.S. et al., Contact-induced transverse fracture in brittle layers on soft substrates: A study on silicon nitride bilayers. *Journal of the American Ceramic Society*, 1998. **81**(3): 571–580.
85. Lawn, B.R. et al., Damage-resistant brittle coatings. *Advanced Engineering Materials* 2000. **2**(11): 745–748.
86. Chai, H., B. Lawn, and S. Wuttiphan, Fracture modes in brittle coatings with large interlayer modulus mismatch. *Journal of Materials Research*, 1999. **14**(9): 3805–3817.
87. Chai, H. and B.R. Lawn, Fracture mode transitions in brittle coatings on compliant substrates as a function of thickness. *Journal of Materials Research*, 2004. **19**(6): 1752–1761.
88. Zhang, S. and X. Zhang, Toughness evaluation of hard coatings and thin films. *Thin Solid Films*, 2012. **520**: 2375–2389.
89. Zhang, X. and S. Zhang, Rethinking the role that the "step" in the load–displacement curves can play in measurement of fracture toughness for hard coatings. *Thin Solid Films*, 2012. **520**(9): 3423–3428.
90. Cook, R.F. and G.M. Pharr, Direct observation and analysis of indentation cracking in glasses and ceramics. *Journal of the American Ceramic Society*, 1990. **73**(4): 787–817.
91. Chen, J. and S.J. Bull, Indentation fracture and toughness assessment for thin optical coatings on glass. *Journal of Physics D-Applied Physics*, 2007. **40**(18): 5401–5417.
92. Chen, J., Indentation-based methods to assess fracture toughness for thin coatings. *Journal of Physics D: Applied Physics*, 2012. **45**: 203001.
93. Fu, K. et al., Analysis on multiple ring-like cracks in thin amorphous carbon film on soft substrate under nanoindentation. *Journal of Physics D-Applied Physics*, 2013. **46**(50): 505314.
94. Tang, Y. et al., On radial crack and half-penny crack induced by Vickers indentation. *Proceedings of the Royal Society a-Mathematical Physical and Engineering Sciences*, 2008. **464**(2099): 2967–2984.
95. Yan, J. et al., On stresses induced in a thermal barrier coating due to indentation testing. *Computational Materials Science*, 2009. **44**(4): 1178–1191.
96. Chen, X. et al., Foreign object damage in a thermal barrier system: Mechanisms and simulations. *Materials Science and Engineering a-Structural Materials Properties Microstructure and Processing*, 2003. **352**(1–2): 221–231.
97. Chen, X. et al., Mechanisms governing the high temperature erosion of thermal barrier coatings. *Wear*, 2004. **256**(7–8): 735–746.
98. Chen, X., J.W. Hutchinson, and A.G. Evans, Simulation of the high temperature impression of thermal barrier coatings with columnar microstructure. *Acta Materialia*, 2004. **52**(3): 565–571.

99. Lawn, B.R., A.G. Evans, and D.B. Marshall, Elastic/plastic indentation damage in ceramics: The median/radial crack system. *Journal of the American Ceramic Society*, 1980. **63**: 574.
100. Anstis, G.R. et al., A critical-evaluation of indentation techniques for measuring fracture-toughness.1. Direct crack measurements. *Journal of the American Ceramic Society*, 1981. **64**(9): 533–538.
101. Jang, J. et al., Cracking and phase transformation in silicon during nanoindentation. *Material Research Society Symposium*, 2004. **795**: U8.15.11–U8.15.16.
102. Marshall, D.B. and B.R. Lawn, Indentation technique for measuring stresses in tempered glass surfaces. *Journal of the American Ceramic Society*, 1977. **60**(1–2): 86–87.
103. Malzbender, J. and G. de With, Elastic modulus, hardness and fracture toughness of SiO2-filled methyltrimethoxysilane coatings on glass substrates. *Journal of Non-Crystalline Solids*, 2000. **265**: 51–60.
104. den Toonder, J. et al., Fracture toughness and adhesion energy of sol-gel coatings on glass. *Journal of Materials Research*, 2002. **17**(1): 224–233.
105. Chen, J. and S.J. Bull, Assessment of the toughness of thin coatings using nanoindentation under displacement control. *Thin Solid Films*, 2006. **494**(1–2): 1–7.
106. Malzbender, J. and G. de With, Elastic modulus, hardness and fracture toughness of SiO2-filled methyltrimethoxysilane coatings on glass substrates. *Journal of Non-Crystalline Solids*, 2000. **265**(1–2): 51–60.
107. Laugier, M.T., Palmqvist indentation toughness in Wc-Co composites. *Journal of Materials Science Letters*, 1987(6): 897–900.
108. Niihara, K., R. Morena, and D.P.H. Hasselman, Evaluation of Klc of brittle solids by the indentation method with low crack-to-indent ratios. *Journal of Materials Science Letters*, 1982. **1**: 13–16.
109. Tanaka, K., Evaluation of elastic plastic indentation stress to determine fracture toughness. *Journal of the Japan Institute of Metals*, 1984. **48**: 1157–1162.
110. Scholz, T. et al., Fracture toughness from submicron derived indentation cracks. *Applied Physics Letters*, 2004. **84**(16): 3055–3057.
111. Field, J.S., M.V. Swain, and R.D. Dukino, Determination of fracture toughness from the extra penetration produced by indentation-induced pop-in. *Journal of Materials Research*, 2003. **18**(6): 1412–1419.
112. Chicot, D. et al., Vickers Indentation Fracture (VIF) modeling to analyze multi-cracking toughness of titania, alumina and zirconia plasma sprayed coatings. *Materials Science and Engineering a-Structural Materials Properties Microstructure and Processing*, 2009. **527**(1–2): 65–76.
113. Demidova, N.V., X.J. Wu, and R. Liu, A fracture toughness model for brittle coating on ductile substrate under indentation loading. *Engineering Fracture Mechanics*, 2012. **82**: 17–28.
114. Lawn, B.R., Indentation of ceramics with spheres: A century after Hertz. *Journal of the American Ceramic Society*, 1998. **81**(8): 1977–1994.
115. Marshall, D.B., B.R. Lawn, and A.G. Evans, Elastic plastic indentation damage in ceramics—the lateral crack system. *Journal of the American Ceramic Society*, 1982. **65**(11): 561–566.
116. Chen, X., J.W. Hutchinson, and A.G. Evans, The mechanics of indentation induced lateral cracking. *Journal of the American Ceramic Society*, 2005. **88**(5): 1233–1238.
117. Lu, M. and H. Huang, Determination of the energy release rate in the interfacial delamination of silicon nitride film on gallium arsenide substrate via nanoindentation. *Journal of Materials Research*, 2014. **29**: 801–810.
118. Xie, H.T. and H. Huang, Characterisation of the interfacial strength of SiN/GaAs film/substrate systems using energy balance in nanoindentation. *Journal of Materials Research*, 2013. **28**: 3137–3145.

119. Chen, J. and S.J. Bull, Assessment of the adhesion of ceramic coatings. *Advances in Science and Technology*, 2006. **45**: 1299–1308.
120. Chen, J.J. and S.J. Bull, Finite element analysis of contact induced adhesion failure in multilayer coatings with weak interfaces. *Thin Solid Films*, 2009. **517**(13): 3704–3711.
121. Chen, J.J. and S.J. Bull, Approaches to investigate delamination and interfacial toughness in coated systems: An overview. *Journal of Physics D-Applied Physics*, 2011. **44**(3): 034001.
122. Li, X.D., D.F. Diao, and B. Bhushan, Fracture mechanisms of thin amorphous carbon films in nanoindentation. *Acta Materialia*, 1997. **45**(11): 4453–4461.
123. Chen, J., On the determination of coating toughness during nanoindentation. *Surface & Coatings Technology*, 2012. **206**: 3064–3068.
124. Li, X.D. and B. Bhushan, Measurement of fracture toughness of ultra-thin amorphous carbon films. *Thin Solid Films*, 1998. **315**(1–2): 214–221.
125. Wu, T.W., M. Moshref, and P.S. Alexopoulos, The effect of the interfacial strength on the mechanical-properties of aluminum films. *Thin Solid Films*, 1990. **187**(2): 295–307.
126. Chen, J., Energy based models to determine fracture toughness of thin coated systems by nanoindentation, Ph.D thesis, University of Newcastle, UK., 2006.
127. Chen, J. and S.J. Bull, An energy based model to estimate coating toughness in the case that there is no excursion in the load–displacement curve. *Proc. Int. Conf. Materials Science and Technology (MS&T): Fundamentals and Characterization*, Cincinnati, Ohio, USA: 2006. **2**: 61–70.
128. Cheng, Y.T. and C.M. Cheng, Relationships between hardness, elastic modulus, and the work of indentation. *Applied Physics Letters*, 1999. **73**(5): 614–616.
129. Chen, J. and S.J. Bull, Modified model to determine limiting values of coating toughness. *Tribology: Materials, Surfaces and Interfaces*, 2008. **2**: 219–224.
130. Chen, J. and S.J. Bull, Modelling the limits of coating toughness in brittle coated systems. *Thin Solid Films*, 2009. **517**(9): 2945–2952.
131. McGurk, M.R. and T.F. Page, Exploration of the plate bending model for predicting the hardness response of coated systems. *Surface & Coatings Technology*, 1997. **92**(1–2): 87–95.
132. Hutchinson, J.W. and Z. Suo, Mixed-mode cracking in layered materials. *Advances in Applied Mechanics*, 1992. **29**: 63–191.
133. Barenblatt, G.I., The mathematical theory of equilibrium cracks in brittle fracture. *Advances in Applied Mechanics*, 1962. **7**: 55–129.
134. Tvergaard, V., Theoretical investigation of the effect of plasticity on crack growth along a functionally graded region between dissimilar elastic-plastic solids. *Engineering Fracture Mechanics*, 2002. **69**(14–16): 1635–1645.
135. Zhang, C. and D. Gross, Ductile crack analysis by a cohesive damage zone model. *Engineering Fracture Mechanics*, 1994. **47**(2): 237–248.
136. Needleman, A., Numerical modeling of crack growth under dynamic loading conditions. *Computational Mechanics*, 1997. **19**: 463–469.
137. Tvergaard, V. and J.W. Hutchinson, The relation between crack growth resistance and fracture process parameters in elastic-plastic solids. *Journal of the Mechanics and Physics of Solids*, 1992. **40**: 1377–1397.
138. Xu, X.P. and A. Needleman, Void nucleation by inclusion debonding in a crystal matrix. *Modelling and Simulation in Materials Science and Engineering*, 1993. **1**: 111–132.
139. Abdul-Baqi, A. and E. Van der Giessen, Numerical analysis of indentation-induced cracking of brittle coatings on ductile substrates. *International Journal of Solids and Structures*, 2002. **39**(6): 1427–1442.
140. Li, X.D., D.F. Diao, and B. Bhushan, Fracture mechanisms of thin amorphous carbon films in nanoindentation. *Acta Materialia*, 1997. **45**: 4453–4461.

141. Kanninen, M.F. and C.H. Popelar, *Advanced Fracture Mechanics*, 1985, New York: Oxford University Press.
142. Chen, J. and S.J. Bull, Finite element modelling of delamination in multilayer coatings. *Nanoscience and Nanotechnology Letters*, 2013. **5**(7): 795–800.
143. Rashid, M., The arbitrary local mesh renement method: an alternative to remeshing for crack propagation analysis. *Computer Methods in Applied Mechanics and Engineering*, 1998. **154**: 133–150.
144. Oliver, J., Continuum modelling of strong discontinuities in solid mechanics using damage models. *Computational Mechanics*, 1995. **17**: 49–61.
145. Belytschko, T. and T. Black, Elastic crack growth in finite elements with minimal remeshing. *International Journal for Numerical Methods in Engineering*, 1999. **45**(5): 601–620.
146. Moes, N., J. Dolbow, and T. Belytschko, A finite element method for crack growth without remeshing. *International Journal for Numerical Methods in Engineering*, 1999. **46**(1): 131–150.
147. Wan, H. et al., A plastic damage model for finite element analysis of cracking of silicon under indentation. *Journal of Materials Research*, 2010. **25**(11): 2224–2237.
148. Wu, H. and S.N. Melkote, Study of ductile-to-brittle transition in single grit diamond scribing of silicon: Application to wire sawing of silicon wafers. *Journal of Engineering Materials and Technology-Transactions of the Asme*, 2012. **134**(4): 041011.
149. Yang, X.S. et al., Finite element analysis of crack propagation and fracture mechanical properties of freestanding 8 wt.% Y2O3-ZrO2 coatings. *Surface & Coatings Technology*, 2013. **223**: 87–91.
150. Rybicki, E.F. and M.F. Kanninen, Finite-element calculation of stress intensity factors by a modified crack closure integral. *Engineering Fracture Mechanics*, 1977. **9**(4): 931–938.
151. Singh, R. et al., Universal crack closure integral for SIF estimation. *Engineering Fracture Mechanics*, 1998. **60**(2): 133–146.
152. Krueger, R., Virtual crack closure technique: History, approach, and applications. *Applied Mechanics Reviews*, 2004. **57**(2): 109–143.
153. Pirondi, A. et al., Comparative study of cohesive zone and virtual crack closure techniques for three-dimensional fatigue debonding. *Journal of Adhesion*, 2014. **90**(5–6): 457–481.
154. Chen, S.Y., T.N. Farris, and S. Chandrasekar, Contact mechanics of hertzian cone cracking. *International Journal of Solids and Structures*, 1995. **32**(3–4): 329–340.
155. Steffensen, S. and H.M. Jensen, Energy release rate for circular crack due to indentation in a brittle film on a ductile substrate. *European Journal of Mechanics a-Solids*, 2014. **43**: 133–141.
156. Rice, J.R., A path independent integral and the approximate analysis of strain concentration by notches and cracks. *Journal of Applied Mechanics*, 1968. **35**: 379–386.
157. Li, F.Z., C.F. Shih, and A. Needleman, A comparison of methods for calculating energy release rates. *Engineering Fracture Mechanics*, 1985. **21**(2): 405–421.
158. Shih, C.F., B. Moran, and T. Nakamura, Energy release rate along a three dimensional crack front in a thermally stressed body. *International Journal of Fracture*, 1986. **30**: 79–102.
159. Steffensen, S., N.D. Madsen, and H.M. Jensen, Numerical estimation of fracture toughness from indentation-induced circumferential cracking in thin films on ductile substrates. *International Journal of Solids and Structures*, 2013. **50**(20–21): 3406–3417.
160. Lee, C.-C., Overview of interfacial fracture energy predictions for stacked thin films using a four-point bending framework. *Surface & Coatings Technology*, 2013. **237**: 333–340.

4 Toughness and Toughening Mechanisms of Porous Thin Films

Yanan Xu, Mingchao Wang, John M. Bell, and Cheng Yan

CONTENTS

4.1 Introduction 179
4.2 Fundamental Mechanical Properties of Porous Thin Films 181
4.2.1 Highly Ordered Porous Thin Films 181
4.2.1.1 Porous Anodic Alumina Thin Film 182
4.2.1.2 TiO_2 Nanotube Array Thin Film 183
4.2.1.3 Silica Foam Thin Film 186
4.2.2 Disordered Porous Thin Films 188
4.3 Fracture Behavior of Disordered Porous Thin Films 190
4.3.1 Fracture Toughness and Interfacial Toughness 190
4.3.2 Failure and Toughening Mechanisms 202
4.4 Nanoindentation Testing 209
4.4.1 Basic Theory 209
4.4.1.1 Measurement of Young's Modulus and Hardness 209
4.4.1.2 Measurement of Fracture Toughness 210
4.4.2 Nanoindentation on Thin Films 211
4.4.2.1 Fully Densed Thin Films 211
4.4.2.2 Porous Thin Films 215
4.5 Summary 217
Acknowledgment 218
References 218

4.1 INTRODUCTION

Porous materials are referred to those containing pores, cavities, channels, and interstices. According to the pore size d, porous systems are generally classified using the standard specified by International Union of Pure and Applied Chemistry (IUPAC): microporous ($d < 2$ nm), mesoporous ($d \sim 2$–50 nm), and macroporous ($d > 50$ nm) [1]. In recent years, there has been a rapid growth in the research of porous materials owing to their exceptional physical properties, with potential applications as adsorbents, catalysts, and catalyst supports. Combined with the advantages brought

by thin-film structure, porous thin films are attracting increased attention. Typical porous thin films include porous low dielectric constant films [2,3], nanoporous thin-film glasses [4], highly ordered TiO_2 nanotube array thin films [5–7], meso- and macroporous SiO_2 thin films [8], as shown in Figure 4.1.

Depending on compositions and microstructures, porous thin films may have unique properties such as strong oxidizing ability, chemical inertness, nontoxicity, and high surface to volume ratio. Possible applications include biosensors [10], size selective membranes [11], photovoltaic cells [12], photocatalysis [13–17], and insulators in microelectronics [18,19]. To realize these potentials, a good understanding of their mechanical properties is essential for structure design, processing, and reliability assessment. For example, biomedical applications generally require long-term *in vivo* structural stability. In general, porous materials are fragile, the corresponding devices have a high possibility of mechanical failure including adhesive and cohesive fracture of the porous layers [4,20]. Cracks, delamination, and fractures are expected due to the mechanical stresses arising from thermal expansion coefficient mismatch, pressure gradients, and external mechanical loading [21–23]. Obviously, these failure and damage will lead to material degradation or loss of functionalities in the devices. Therefore, it is important to establish a structure–property relationship and gain a better understanding of the toughness and toughening

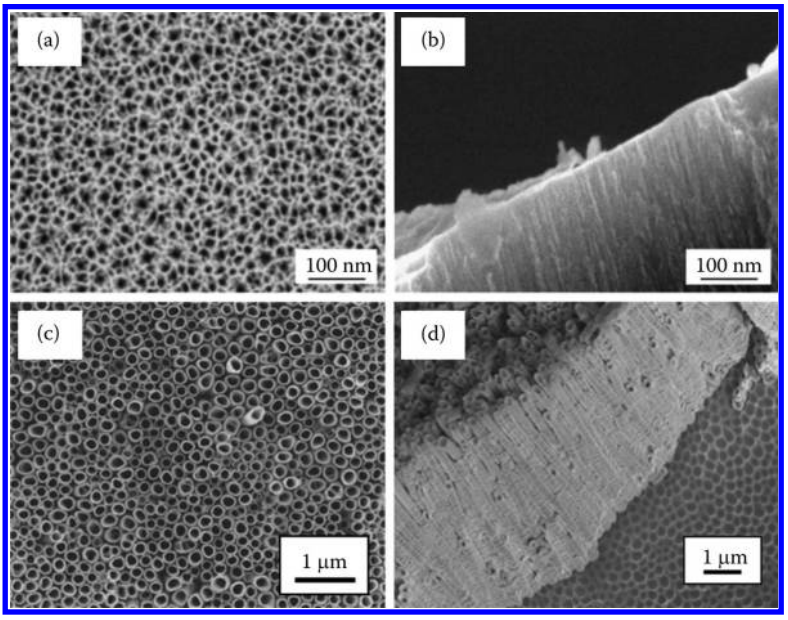


FIGURE 4.1 Typical porous thin films: Scanning electron microscopy (SEM) images of porous silicon low dielectric constant thin film (a) top surface and (b) cross section. (Reprinted from *Thin Solid Films*, 518, K. Rahmoun. et al., A multilayer model for describing hardness variations of aged porous silicon low-dielectric-constant thin films, 213–21, Copyright 2009, with permission from Elsevier.) SEM images of highly ordered TiO_2 nanotube array thin film (c) top surface and (d) cross section.

mechanism in porous thin films. In principle, toughness of thin films can be evaluated using various methods including nanoindentation [22,24], microbeam cantilever deflection [25], bulge testing of free-standing thin films [26], and so on. Among all these methods, nanoindentation measurements can be conducted without lifting a film from its substrate. Therefore, it is regarded as one of the simplest methods for investigating the mechanical behavior of thin films [24]. However, it is not very clear whether this can be effectively applied to porous thin films.

In spite of some publications discussing the synthesis and properties of porous thin film, a comprehensive review of the mechanical behavior, especially toughness and toughening mechanisms of porous thin films is still lacking. In this chapter, we present a comprehensive review of recent development on characterization of toughness and toughening mechanisms of porous thin films. Fundamental mechanical properties of porous thin films are reviewed first, with a focus on theoretical and experimental investigation of toughness and toughing mechanisms.

4.2 FUNDAMENTAL MECHANICAL PROPERTIES OF POROUS THIN FILMS

To fabricate devices and structures from porous thin films and take advantage of their excellent electrical, thermal, and chemical properties, it is critical to maintain adequate mechanical integrity. To this, an understanding of the mechanical properties of porous thin films is essential. In addition, it is necessary to identify the key material and structural parameters (such as thin-film thickness and porosity) that may affect their mechanical behavior. In this section, the fundamental mechanical properties of highly ordered and disordered porous thin films are discussed. The possible underlying deformation and failure mechanisms are also introduced.

4.2.1 Highly Ordered Porous Thin Films

Highly ordered porous thin films possess regular pore patterns and microstructural features, which govern their overall mechanical properties. Figure 4.2 shows some highly ordered thin films including anodic alumina thin film [27], titanium dioxide

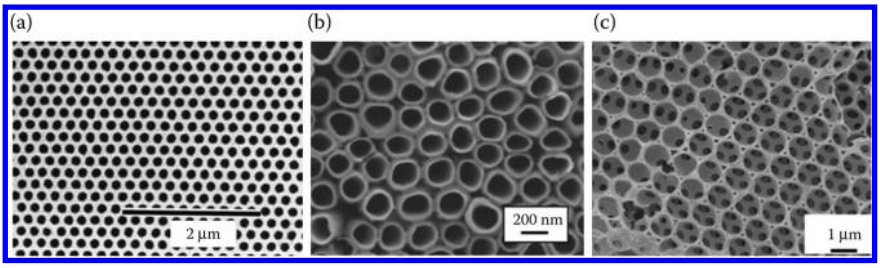


FIGURE 4.2 SEM images of (a) anodic alumina thin film (Adapted from H. Asoh et al., *Journal of the Electrochemical Society* 148, 2001: B152–56. Copyright 2001, with permission from the Electrochemical Society.) (b) TiO_2 nanotube array thin film, and (c) ordered silica foam thin film. (Reproduced from Y. Toivola, A. Stein, and R. F. Cook. *Journal of Materials Research* 19, 2004: 260–71. Copyright 2004, with permission from Cambridge University Press.)

(TiO_2), nanotube array thin film [28], and silica foam thin film [29]. The sizes of pores in these highly ordered porous ceramics are normally larger than 50 nm, in the range of macroporous materials. Although pores have been considered to be detrimental to mechanical property in bulk ceramics, highly ordered ceramic thin films, due to their unique properties, have found their applications in high-temperature thermal insulation, catalytic reactions, and sustainable energy (e.g., hetero-junction solar cells).

4.2.1.1 Porous Anodic Alumina Thin Film

Porous anodic alumina thin film, which is prepared by the anodic oxidation of aluminum with an acidic electrolyte, is a self-organized fine structure with a nanohole array [30–32]. As shown in Figure 4.2a, porous anodic alumina has a packed array of columnar hexagonal cell with uniformly sized holes. Due to the porous microstructures along thickness direction, porous anodic alumina thin film has unidirectional structures, which are transversely isotropic.

To measure its mechanical properties, nanoindentation tests are usually adopted [30–32]. In nanoindentation tests on thin films, substrate materials may have a significant effect on the evaluated properties. For porous anodic alumina thin films, the evaluated elastic modulus and hardness decrease with increasing indentation depth, owing to the effect of aluminum substrate, which has much lower elastic modulus and hardness. In order to eliminate the substrate effect, the indentation depth should be less than 10% of the thickness of thin film [33].

From nanoindentation tests, the measured values of hardness and elastic modulus of porous anodic alumina thin film at 10% porosity are about 13 and 140 GPa, respectively [34]. It is clear that the pore size (i.e., the porosity P) dominates the mechanical behavior of these thin films, as shown in Figure 4.3, both measured hardness and elastic modulus of porous anodic alumina thin film decrease with the porosity, which is consistent with Dukhyun's work [35]. Generally, the mechanical properties and the porosity can be related by empirical equations, like [34]

$$\frac{M}{M_0} = (1 - \phi)^{\alpha}, \quad \frac{H}{H_0} = (1 - \phi)^{\alpha} \tag{4.1}$$

where M_0 is the mechanical property at 0% porosity; H_0 is the hardness at 0% porosity; ϕ and α represent the porosity, and an empirical coefficient, respectively.

Vojkuvka et al. [36] study three types of porous anodic alumina samples with different porosity. In their study, porous anodic alumina is produced using sulfuric, oxalic, or phosphoric acid, referred as type I, type II, and type III, which have interpore sizes of 60, 105, and 455 nm, respectively. From the load–displacement curves in Figure 4.4, it can be observed that the indentation depth increases with the porosity in all samples.

Figure 4.5 shows the cleavage propagating through the hexagonal cells along the length direction. It increases in width as the sample porosity increases. Hence, it is reasonable to assume that cleavage occurs during the loading cycle of the nanoindentation test [36].

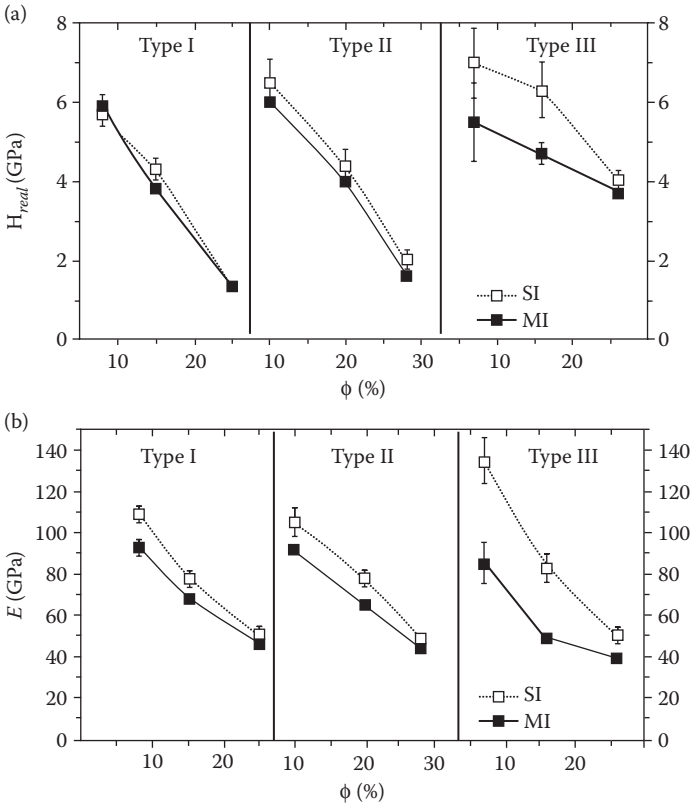


FIGURE 4.3 (a) Hardness and (b) elastic modulus with respect to the porosity ϕ of porous anodic alumina samples. (Reproduced from *Surface and Coatings Technology*, 206, L. Vojkuvka et al., On the mechanical properties of nanoporous anodized alumina by nanoindentation and sliding tests, 2115–24, Copyright 2012, with permission from Elsevier.)

Besides elastic modulus and hardness, bending modulus is another important mechanical property of thin films. The atomic force microscopy (AFM) test by Dukhyun et al. [35] indicates that bending modulus decreases nonlinearly with porosity. When the porosity increases from 10% to 40%, the bending modulus drops from 36 GPa to only about 10 GPa, indicating the significant effect of porosity on the mechanical performance.

4.2.1.2 TiO_2 Nanotube Array Thin Film

Highly ordered TiO_2 nanotubes grown directly on Ti substrate can be regarded as another type of porous thin film. As shown in Figure 4.2b, TiO_2 nanotubes are vertical to the Ti substrate and the length can be controlled from several to 1000 μm using electrochemical anodization method. The outer surface of these TiO_2 nanotubes can have a spring-like shape. TiO_2 nanotube-array thin film has been widely used for various applications, such as solar cells [37], photoelectrocatalysis [13,15,16], and purification of environmental pollutants [38,39]. Due to excellent biocompatibility,

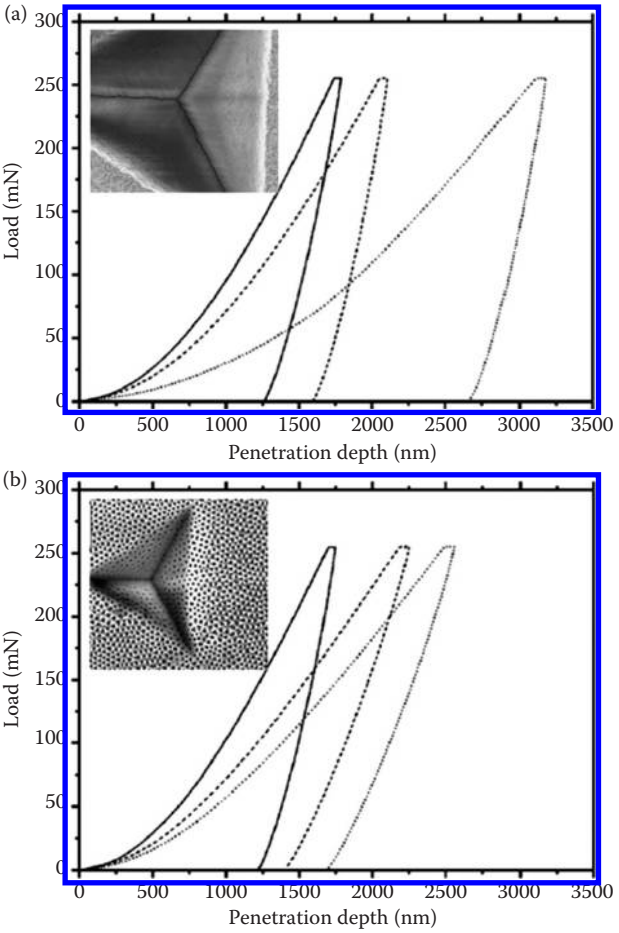


FIGURE 4.4 Load–displacement curves of nanoindentation tests at the applied load of 250 mN for samples with low (solid lines), medium (dashed lines), and high (dotted lines) porosity: (a) Type II. (b) Type III. (Reprinted from *Surface and Coatings Technology*, 206, L. Vojkuvka et al., On the mechanical properties of nanoporous anodized alumina by nanoindentation and sliding tests, 2115–24, Copyright 2012, with permission from Elsevier.)

Ti and Ti alloys have been also used to make various biomedical devices. Recent research has demonstrated that TiO_2 nanotube array thin film can improve cellular activities [40,41] and accelerate the growth of osteoblast cells [42]. The adhesion between body cells and such thin film can be largely strengthened because body cells could grow into the nanotube pores and generate locked-in cell structures [42], indicating potential applications as implants.

In order to fully take advantage of the excellent properties of TiO_2 nanotube arrays, their fundamental mechanical behavior has been recently studied. For instance, Shokuhfar et al. [43] report for the first time that the Young's modulus of single TiO_2 nanotubes with outside diameters of 75 and 110 nm and wall thicknesses of

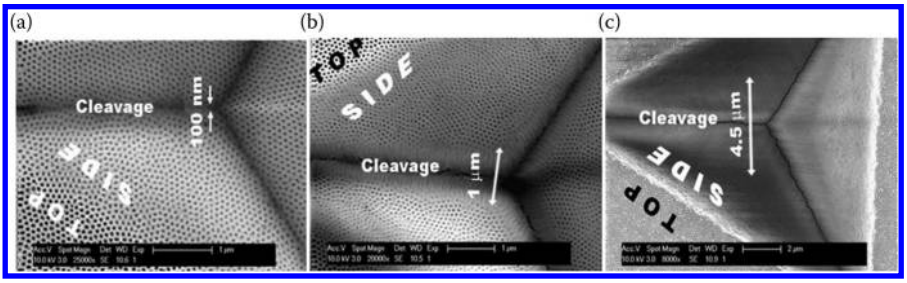


FIGURE 4.5 Top view SEM images of the indents on type II with different porosities under applied load of 250 mN. (a) II_{low}. (b) II_{medium}. (c) II_{high}. (Reprinted from *Surface and Coatings Technology*, 206, L. Vojkuvka et al., On the mechanical properties of nanoporous anodized alumina by nanoindentation and sliding tests, 2115–24, Copyright 2012, with permission from Elsevier.)

5 and 15 nm are in the range of 23–44 GPa. Tang et al. [44] and Crawford et al. [45] investigate the mechanical properties of the whole TiO_2 nanotube arrays by using nanoindentation tests. Tang et al. [44] point out that Young's modulus and hardness decrease with increasing the thickness of TiO_2 nanotube-array thin film. This is owing to the reduced critical load for the buckling of long nanotubes. The measured apparent Young's modulus decreases from 29.8 to 11.7 GPa and the measured hardness decreases from 42.6 to 5.9 HV when the thickness of TiO_2 nanotubular array films increases from 18 to 99 μm [44]. Crawford et al. [45] find that there are three distinct stages in the variation of Young's modulus with indentation displacement, as shown in Figure 4.6. Region I is characterized by a linear increase in the indentation modulus. In this region, the rise of modulus is owing to increased densification of the

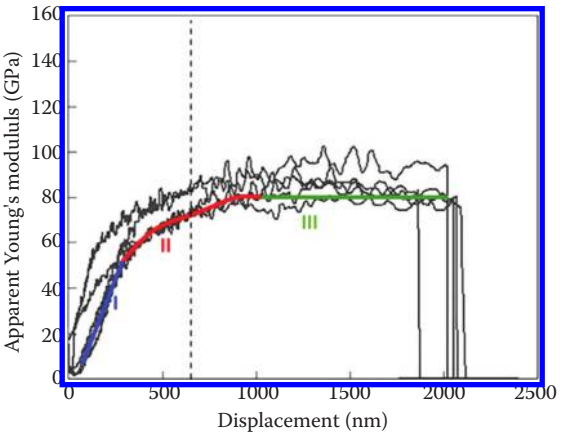


FIGURE 4.6 Typical apparent Young's modulus as a function of displacement. Dotted vertical line represents the average coating thickness. (Reprinted from *Acta Biomaterialia*, 3, G. A. Crawford et al., Microstructure and deformation behavior of biocompatible TiO_2 nanotubes on titanium substrate, 359–67, Copyright 2007, with permission from Elsevier.)

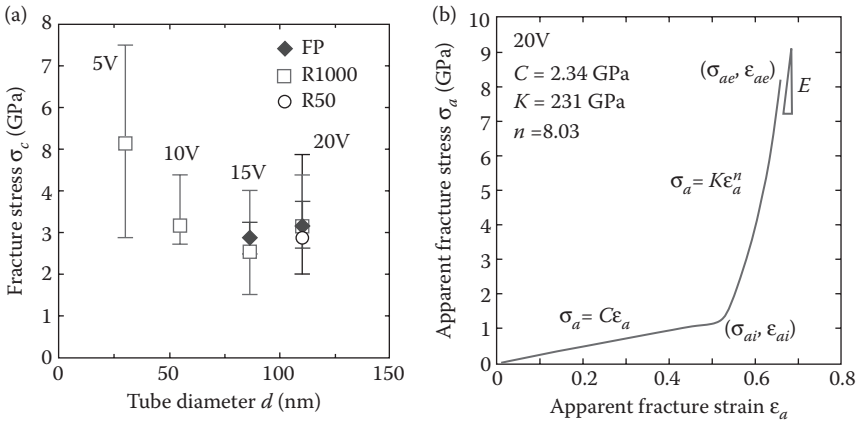


FIGURE 4.7 (a) Fracture stress of the TiO_2 nanotubes as a function of tube diameter, and (b) constitutive relationship between apparent fracture stress and strain. (Reproduced from *Acta Materialia*, 58, H. Hirakata et al., Strength of self-organized TiO_2 nanotube arrays, 4956–67, Copyright 2010, with permission from Elsevier.)

TiO_2 nanotubes. Region II is characterized by a parabolic increase in the indentation modulus, as a result of increased contribution from the substrate. Finally, in Region III, the coating has become almost fully dense, responsible for a stable indentation modulus [45].

Hirakata et al. [46] explore the underlying mechanisms governing the strength of TiO_2 nanotube array thin film and present a stress-based fracture model to evaluate its fracture stress. Figure 4.7a shows the fracture strength σ_c of TiO_2 nanotube array thin film as a function of the tube diameter d. For TiO_2 nanotubes with diameters of about 55, 86, and 110 nm, σ_c keeps almost the same about 3 GPa regardless of the tube size [46]. For TiO_2 nanotubes with diameters of about 30 nm, σ_c is about 5 GPa, which is higher than that for TiO_2 nanotubes with diameters of 55–110 nm. A phenomenological model is also proposed to describe the densification behavior of TiO_2 nanotube array [46]. Figure 4.7b shows the constitutive relation of the model that represents both linear and densification stages. With complete densification, the slope of the apparent stress–strain curve is close to the Young's modulus of bulk TiO_2 material. The load–displacement curve evaluated by such model is in agreement with that measured by nanoindentation tests, indicating the validity of the model.

4.2.1.3 Silica Foam Thin Film

Macroporous silica in the form of three-dimensionally ordered foams can be synthesized by a simple, efficient, and relatively inexpensive method, namely colloidal crystal templating. The ordered silica foam structures synthesized by this method consist of a skeleton surrounding uniform close-packed macropores that are interconnected through voids, as shown in Figure 4.2c.

Depth-sensing indentation method is suggested to be utilized to quantify the mechanical behavior of macroporous silica foam [29]. Based on this technique, the

typical load–displacement (P–h) relation for macroporous silica foam at peak load $P_{max} = 1$ mN is given in Figure 4.8a. It can be seen that there are obvious pop-ins in the loading part for macroporous silica foam and the slope of unloading part is nearly vertical. In contrast, the loading part for dense silica is smooth, and elastic recovery can be observed during unloading [29,47]. These pop-in events in the P–h relation are believed to be related to the densification process of the spherical porous shells. As shown in Figure 4.8b, the impression on the macroporous silica foam reveals homogeneous deformation. Interestingly, the pores close to the impression are undeformed, indicating that there is no significant strain transfer from the indenter to the material adjacent to the impression [29]. The deformation mechanism of macroporous silica foams is complicated, consisting of cell-wall bending, cell-wall fracture, pore collapse, and local densification. Therefore, their load–displacement relations are independent of indentation tip geometry after initial deformation [29].

The indentation deformation mechanisms in these macroporous silica foam are predominantly nonelastic and nonvolume conserving, rendering the modulus and hardness obtained from standard P–h methods inapplicable. Owing to the rigid-perfectly plastic nature of such materials, the load–displacement (P–h) relations can be converted into pressure–volume (p–V) relations using the shape profile of the Berkovich indenter at a large indentation depth [29], that is,

$$p = P/(24.5h^2), V = (24.5h^3)/3 \tag{4.2}$$

Figure 4.9 shows the p–V relations in dense silica and two types of macroporous silica foams. For dense silica, the indentation pressure is almost constant over three to four orders of magnitude of swept indenter volume. For macroporous silica foam,

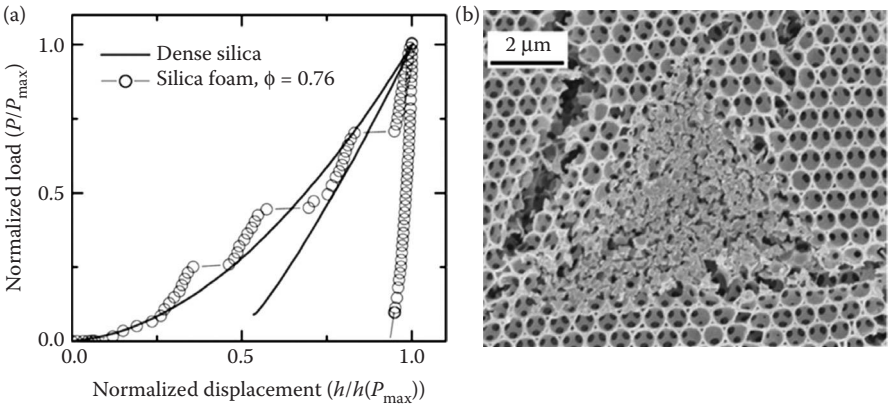


FIGURE 4.8 (a) The normalized load–displacement relation in macroporous silica foam ($P_{max} = 1$ mN) and dense silica ($P_{max} = 100$ mN) using Berkovich indenter. (b) Residual Berkovich indentation impression from a 1 mN indentation in macroporous silica foam. (Reproduced from Y. Toivola, A. Stein, and R. F. Cook. *Journal of Materials Research* 19, 2004: 260–71. Copyright 2004, with permission from Cambridge University Press.)

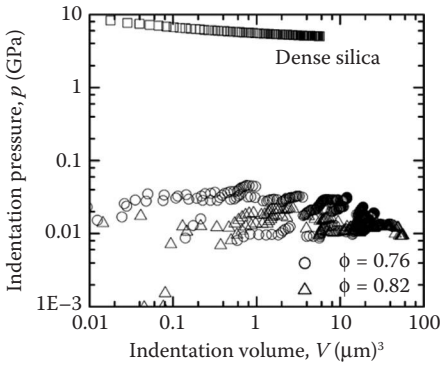


FIGURE 4.9 Pressure–volume (p–V) relations for P_{max} = 1 mN with Berkovich indenter in two silica foams (porosity $\phi = 0.76, 0.82$) and for P_{max} = 100 mN in dense silica. (Reproduced from Y. Toivola, A. Stein, and R. F. Cook. *Journal of Materials Research* 19, 2004: 260–71. Copyright 2004, with permission from Cambridge University Press.)

it appears that the indentation pressure of the more porous foam is slightly smaller, about 0.015 GPa for the $\phi = 0.82$ foam in comparison with 0.026 GPa for the $\phi = 0.76$ foam, which are both about two orders of magnitude less than that for dense silica (6 GPa).

4.2.2 Disordered Porous Thin Films

Besides the thin films with uniform pores, thin films with disordered pores are attracting more attention from a number of research communities owing to their unique physical properties. One of the most popular disordered porous thin films is low dielectric constant (κ) thin film, which contains randomly distributed nanopores. A range of κ values is available based on the introduction of open volume or pores in a Si-O-Si matrix, with Si-CH_3 groups acting to stabilize the pores. Low-κ thin films play a significant role in interconnects used throughout the semiconductor industry, because the reduction of signal delay, power dissipation, and cross talk between metal conductors can be achieved by lowering the dielectric constant. Popular low-κ materials include organosilicate glasses (OSG) and silsesquioxane (SSQ) spin-on glasses, which have similar chemical structures. Among these materials, higher porosity leads to lower κ [48,49]. One disadvantage of lower κ is the reduction in mechanical properties such as elastic modulus and hardness [50]. In order to achieve better functions in applications, it is necessary to understand the mechanical performance of the low-κ thin film in the low-κ/substrate system.

In terms of P–h curves, elastic modulus E and hardness H can be evaluated. Figure 4.10 shows the plane strain modulus of four hydrogen-silsesquioxane (HSSQ) thin films cured at different temperatures. The modulus and hardness increase with displacement (indentation depth). Within 20% of the film thickness, the measured modulus is invariant and therefore can represent the intrinsic properties of these thin films. When the indentation depth is larger than 20% of the film thickness, the

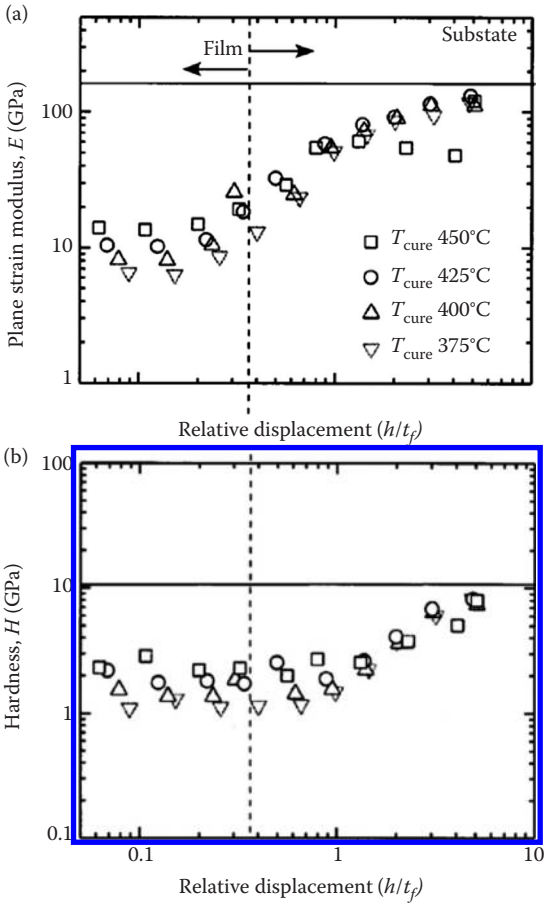
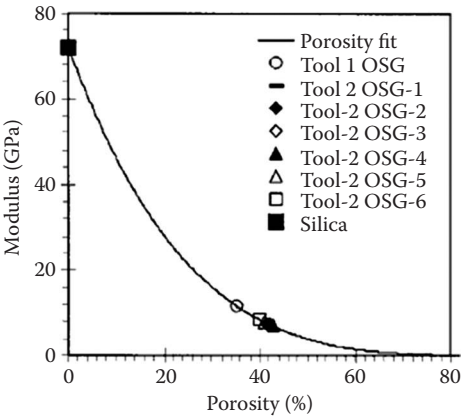


FIGURE 4.10 (a) Plane strain modulus and (b) hardness as a function of relative displacement in HSSQ thin films. (Reproduced from Y. Toivola, J. Thurn, and R. F. Cook. *Journal of the Electrochemical Society* 149, 2002: F9–17. Copyright 2002, with permission from The Electrochemical Society.)

measured modulus increases, attributed to the strong substrate effect. The similar trend is observed for the measured hardness.

Porosity also plays a big role in the mechanical properties of low-κ thin films as other porous thin films discussed above. Vella et al. [52] show that increasing porosity can remarkably lead to the reduction of elastic modulus of OSG low-κ thin films, as shown in Figure 4.11. An empirical model can be used to predict the effect of porosity not only on elastic modulus but also on hardness and fracture toughness of OSG low-κ thin films. The model is in the form of $X^*/X^0 = \alpha(1 - p^*/p_0)^f$, where X represents mechanical properties such as Young's modulus, hardness and fracture strength; f and α are fitting parameters; ϕ is porosity. Superscripts * and 0 represent to a given and reference materials, respectively.



	Modulus (GPa)	Percolation porosity (%)
Tool 1 OSG	11.7	35.1
Tool 2 OSG-1	7.60	41.4
Tool 2 OSG-2	7.49	41.6
Tool 2 OSG-3	7.24	42.1
Tool 2 OSG-4	6.90	42.8
Tool 2 OSG-5	7.92	40.9
Tool 2 OSG-6	8.32	40.1
Silica	72.00	0.0

FIGURE 4.11 Elastic modulus as a function of porosity. (Reproduced from J. B. Vella et al., *International Journal of Fracture* 120, 2003: 487–99. Copyright 2003, with permission from Kluwer Academic Publishers.)

4.3 FRACTURE BEHAVIOR OF DISORDERED POROUS THIN FILMS

4.3.1 Fracture Toughness and Interfacial Toughness

Low-κ dielectric materials, such as OSG and SSQ spin-on glasses have higher porosity (>30%) and sustain compromises in either thermal or mechanical integrity with respect to traditional SiO_2 dielectrics. The ceramic nature of OSG and SSQ thin films gives the materials a higher degree of thermal stability but low fracture toughness of thin films themselves, as well as low interfacial toughness between them and substrates. The practical applications of low-κ thin films require them to withstand chemical or mechanical polishing without fracturing or delaminating. Therefore, it is necessary to develop techniques that can evaluate the fracture toughness of low-κ thin films and interfacial adhesion between them and substrate (e.g., silicon).

In general, fracture toughness of thin films can be evaluated by nanoindentation technique. OSG material has a high hardness to modulus ratio and low fracture toughness [53]. The low modulus, makes delamination hard to be observed during regular indentation due to poor stress transfer from the indenter to the film/substrate

interfaces. Practically, a superlayer of high hardness and modulus, capable of effectively supporting and storing elastic energy, can be deposited on the thin films. This technique is referred as superlayer indentation. Upon indentation, a delamination blister forms around the indent, and its area can be used to calculate the strain energy release rate. Volinsky et al. [52,53] use conical diamond tip to indent OSG thin films with a superlayer of TiW. Figure 4.12a shows the formed blister in the low-κ/TiW film structure. From the cross-sectioned sample prepared using focused ion beam (FIB), it can be found that the crack kinks from the low-κ/substrate to the low-κ/TiW interface, as given in Figure 4.12b and c.

Generally, fracture toughness K_c of a bulk brittle material can be evaluated using the following equation [53]:

$$K_c = \alpha\left(\frac{E}{H}\right)^{1/2}\left(\frac{P_{\max}}{c^{3/2}}\right) \tag{4.3}$$

where α is an empirical constant depending on the geometry of the indenter (0.0139 for cube corner indenter) [54]; E is elastic modulus; H is hardness; $P_{\max}$ is maximum indentation load; c is crack length. For low-κ thin films, it is often assumed that the failure of thin films is mainly caused by residual stress. Wafer curvature technique

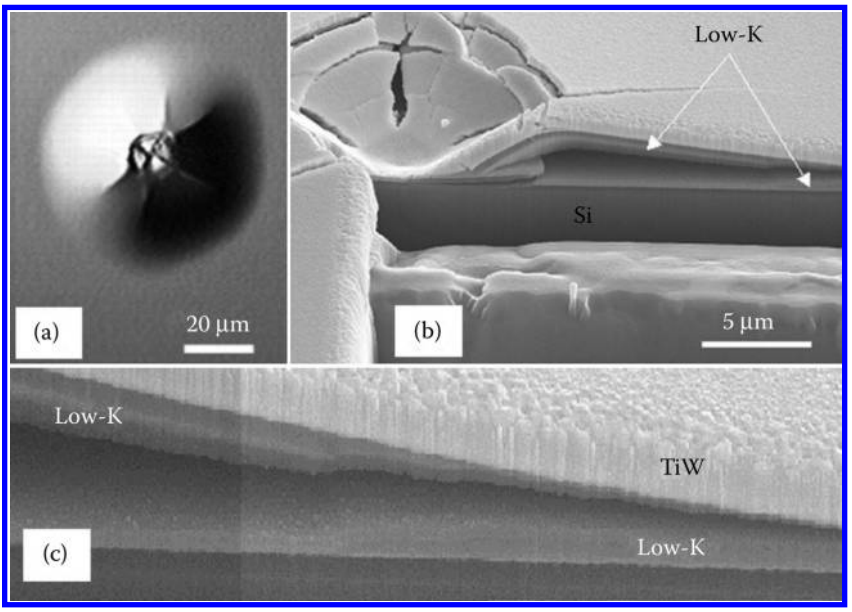


FIGURE 4.12 (a) Optical image of the TiW/400 nm low-κ thin film blister; (b) SEM image of the FIB cross section of the blister; (c) SEM image showing cohesive failure of low-κ thin film. (Reprinted from *Thin Solid Films*, 429, A. A. Volinsky, J. B. Vella, and W. W. Gerberich, Fracture toughness, adhesion and mechanical properties of low-*k* dielectric thin films measured by nanoindentation, 201–10, Copyright 2003, with permission from Elsevier.)

[55] can be used to evaluate the residual stress and a simple relationship is established between the film thickness h and the residual stress σ_R,

$$\sigma_R = A + B\ln(h) \tag{4.4}$$

where A and B are the fitting parameters. In classical fracture mechanics, the stress intensity factor (SIF) K is related to the strain energy release rate G as follows:

$$K^2(1 - \upsilon_f^2) = GE_f \tag{4.5}$$

where υ_f is Poisson's ratio. G can also be estimated using the method described in Hutchinson and Suo's work [56],

$$G = Z\frac{(1 - \upsilon_f^2)\sigma_R^2 h}{E} \tag{4.6}$$

where Z ranges from 0.5 to 4 [56], depending on the sample geometry and the nature of residual stresses (tensile and compressive stresses). From Equations 4.5 and 4.6, K_C can be related to residual stress in the form of

$$K_C = \sigma_R\sqrt{Zh} \tag{4.7}$$

Therefore, the failure criterion based on the residual stress and film thickness can be given as

$$K_C \le \sigma_R\sqrt{Zh} \tag{4.8}$$

It is clear that thicker films with a constant level of residual stress are more susceptible to failure. It is noted that the criterion is similar to the general relation between fracture toughness, applied stress, and crack length [57]. With Equation 4.8, assuming 25 MPa tensile residual stress exhibits in a 3 μm film [53] and taking $Z = 1.976$ for a channel crack [54], the evaluated K_C value is 0.06 MPa·m$^{1/2}$. K_C can be rewritten as in a logarithmic form, that is,

$$K_C \le \left|A + B\log h\right|(Zh)^{1/2} \tag{4.9}$$

As shown in Figure 4.13b, the measured fracture toughness of low-κ ranges from 0.02 to 0.03 MPa·m$^{1/2}$, less than delamination fracture resistance K_C, that is, 0.06–0.13 MPa·m$^{1/2}$ [53]. This demonstrates that the fracture toughness of low-κ thin film itself controls the fracture process rather than interfacial adhesion. Also shown in Figure 4.13b, at about 1.5 μm film thickness, the measured fracture toughness of low-κ thin film is much higher than that predicted by Equation 4.9 due to the really existed residual stress in thin film. Moreover, according to Equation 4.8, larger magnitude of residual stress in thin films is more susceptible to lead failure of low-κ thin films.

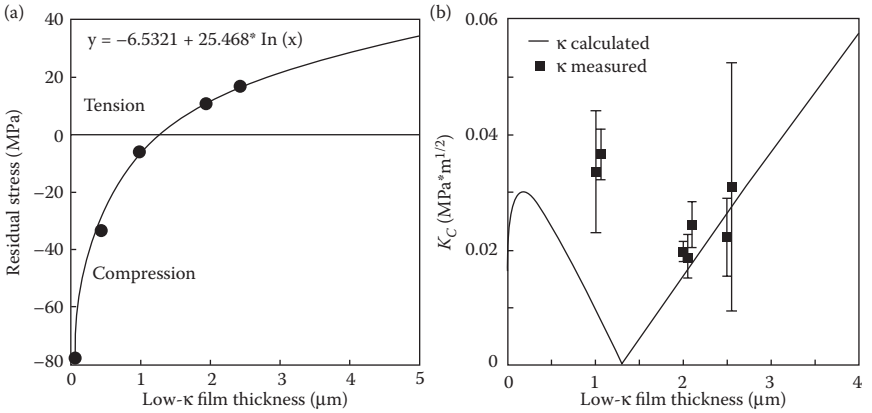


FIGURE 4.13 (a) Residual stress in low-κ thin film as a function of film thickness. (b) Fracture toughness of low-κ thin film as a function of film thickness. (Reprinted from *Thin Solid Films*, 429, A. A. Volinsky, J. B. Vella, and W. W. Gerberich, Fracture toughness, adhesion and mechanical properties of low-*k* dielectric thin films measured by nanoindentation, 201–10, Copyright 2003, with permission from Elsevier.)

Even though the failure criterion discussed above can simply and clearly describe the failure process in low-κ thin film, the effect of underlying substrate should also be taken into account to get more accurate fracture toughness. Morris et al. [58,59] explored the instrumented indentation of a variety of OSG thin films, and developed a fracture mechanics model to measure fracture toughness of low-κ thin films. Figure 4.14 shows the load–displacement curves of half-cycle loading

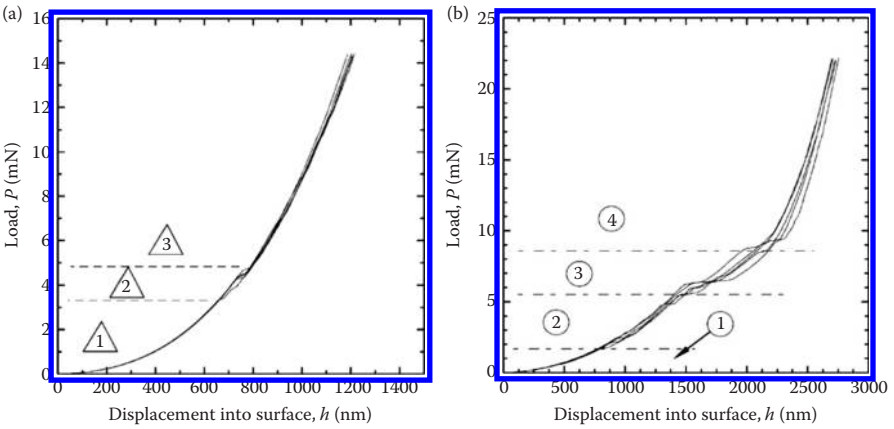


FIGURE 4.14 Load–displacement curves of half-cycle loading for (a) five 15 mN peak load Berkovich indentations on 2.4 μm-thick OSG thin film, and (b) five cube-corner indentation on 2 μm-thick OSG thin film. (Reproduced from D. J. Morris and R. F. Cook. *Journal of Materials Research* 23, 2008: 2429–42. Copyright 2008, with permission from Cambridge University Press.)

for both Berkovich and cube-corner indentations on OSG thin films. In these load–displacement curves, there are obvious pop-in events, which correspond to the fracture process in low-κ thin films [51,60–62]. For the Berkovich result presented in Figure 4.14a, the pop-in events occur in the second stage but the indentation modulus is unaffected by these pop-in events. While for the cube-corner result shown in Figure 4.14b, in the third stage, the so-called "large" pop-in regime, the indentation modulus decreases and the uncertainty in indentation modulus increases greatly. After pop-in, the *P*–*h* curves change discontinuously, in contrast to the behavior of Berkovich indentation [58].

In addition, for the cube-corner geometry, the indenter drives fracture by wedging the cracks apart [63], instead of driving fracture by residual stresses caused by plastic deformation gradients. The wedging deformation is different since the materials under nanoindentation test have a large free volume, which is unlikely to store residual stress during plastic deformation. In Figure 4.15a, well-formed cracks of length *c* after indentation can be seen on the film surface. Figure 4.15b and c shows two typical cases of cracking in low-κ thin film.

Moreover, the existence of a stiff and relatively tough substrate, such as silicon for low-κ thin film, provides severe constraint on the evolution of radial cracks. This constraint can lead to two basically different crack geometries when radial cracks are contained within the low-κ thin film. When the radial cracks are contained well within the thin film (Figure 4.15b), the film is partially cracked, any subsequent

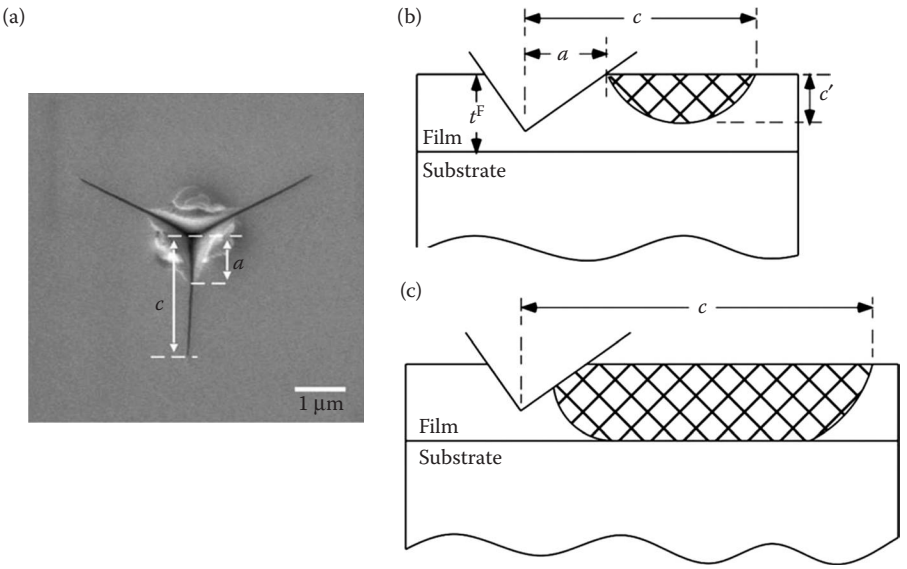


FIGURE 4.15 (a) SEM image of a cube-corner indentation on a low-κ thin film, in which *a* is the contact dimension and *c* is the surface crack length. Schematic cross-sectional diagrams of (b) a partially cracked film and (c) a one-dimensional channel crack with surface crack length *c*. (Reproduced from D. J. Morris and R. F. Cook. *Journal of Materials Research* 23, 2008: 2443–57. Copyright 2008, with permission from Cambridge University Press.)

crack propagation may occur toward the substrate and moves away from the axis of indentation. The SIFs at load P for both wedging stress field K_{PC}^{W} and elastic contact stress field K_{PC}^{E} can be written as [64]

$$K_{PC}^{I} = K_{PC}^{W} + K_{PC}^{E},\ K_{PC}^{W} = \chi_{PC}^{W}\frac{P}{c^{3/2}},\ K_{PC}^{E} = \chi_{PC}^{E}\frac{P}{c^{3/2}}\ln(2c/a) \tag{4.10}$$

where K_{PC}^{I} is the total SIF; χ^{W} and χ^{E} are semiempirical terms related to Poisson's ratio υ of the material, suggested by both experimental [65] and theoretical [64] studies. Here, the subscript PC refers to the partially cracked condition.

Another type of crack is the fully cracked one, namely channeling crack, which is shown in Figure 4.15c. Such channeling crack is constrained by the tougher and stiffer substrate, and only propagates outward the low-κ thin film. Here, the SIFs at load P for both wedging stress field K_{CH}^{W} and contact stress field K_{CH}^{E} can be expressed as

$$K_{CH}^{I} = K_{CH}^{W} + K_{CH}^{E},\ K_{CH}^{W} = \chi_{CH}^{W}\frac{P}{c^{3/2}}\left[\frac{c}{a} + \frac{a}{c}\ln(2c/a)\right],\ K_{CH}^{E} = \chi_{CH}^{E}\frac{P}{c^{3/2}}\left[\frac{c}{a}\right] \tag{4.11}$$

Here, the subscript CH refers to channeling crack. To use Equations 4.10 and 4.11, some corrections are still needed for both wedging and elastic contact stresses for radial cracks. Generally, many low-κ thin films have a preexisting tensile stress σ^{F} at room temperature, providing an additional driving force for crack propagation.

To estimate the fracture toughness, all components contributing to SIFs need to be considered. It is further assumed that the toughness of the film is insensitive to the crack length and therefore there is no R-curve behavior [59]. This is a reasonable assumption for brittle materials. In equilibrium, we have

$$K^{W} + K^{E} = T^{F} - K^{F} \tag{4.12}$$

where K^{W} includes K_{PC}^{W} and K_{CH}^{W}; K^{E} consists of K_{PC}^{E} and K_{CH}^{E}; T^{F} is the fracture toughness of thin film; K^{F} is the SIF caused by residual stress.

The left side of equation ($K^{W} + K^{E}$) is interpreted as the total driving force for fracture caused by indentation, and right part ($T^{F} - K^{F}$) is the material resistance to fracture associated with material properties, film thickness, and residual stress. The toughness of 2.0, 1.5, and 1.0 μm thick low-κ thin film can be calculated with the film stresses measured by wafer-curvature method, and the values of T^{F} are $T^{F} \approx 0.091$ MPa.m$^{1/2}$ for 2.0 μm thick film, $T^{F} \approx 0.089$ MPa·m$^{1/2}$ for 1.5 μm thick film, and $T^{F} \approx 0.083$ MPa·m$^{1/2}$ for 1.0 μm thick film. The mean fracture toughness is about 1/8 that of dense fused silica, as is the elastic modulus of thin film [66].

The stability of crack propagation is another important issue in evaluation of the fracture response in the low-κ thin film. The condition to achieve stability in an ideal brittle material is $dK^{T}/dc < 0$. Figure 4.16 shows that there are three possible crack lengths that satisfy the equilibrium condition, that is, $K/T^{F} = 1$. The channeling

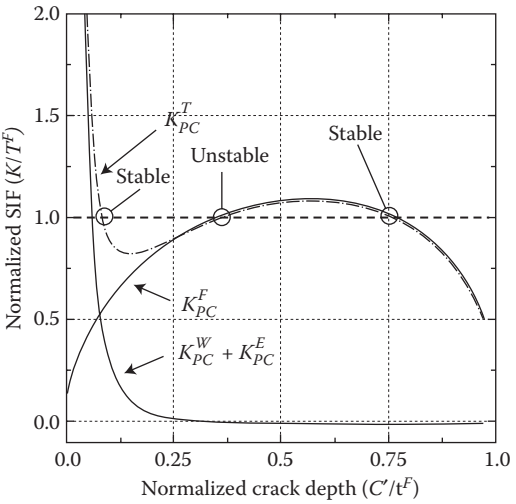


FIGURE 4.16 Normalized SIFs, K/T^F as a function of normalized crack depth, c'/t^F for a hypothetical indentation + film SIF fracture field. (Reproduced from D. J. Morris and R. F. Cook. *Journal of Materials Research* 23, 2008: 2443–57. Copyright 2008, with permission from Cambridge University Press.)

film-stress SIF is always neutral with respect to the surface crack length. While the partial-crack film-stress SIF should satisfy the condition [59]

$$\frac{dK^T_{PC}}{dc} = -\frac{3}{2c}\left[K^W_{PC} - \frac{1}{W}K^E_{PC}\right] - \frac{1}{W}\frac{K^W_{PC}}{c} - K^F_{PC}\left(\frac{1}{2c} - \frac{(1/2 - s)}{(1 - \ell c/t^F)t^F}\frac{\ell}{t^F}\right) < 0 \tag{4.13}$$

Figure 4.17b gives the c–P relation with and without substrate attenuation for the thinnest film, 0.5 μm-thick low-κ thin film [59]. The substrate attenuation plays a key role in developing the low-κ film fracture model. Such substrate attenuation is to increasingly reduce the indentation SIFs as the substrate may accommodate a larger fraction of strain energy with increasing indenter penetration. A lack of substrate attenuation could lead to longer crack lengths at fixed indentation load. In general, fracture behavior of low-κ thin films depends on film stress, thickness, and substrate effect.

However, interfacial toughness is another significant parameter affecting the overall mechanical integration of low-κ film/substrate systems. The interfacial delamination in such system is normally driven by various stresses, such as thermal stresses induced during cooling and heating and intrinsic residual stresses generated during deposition processes [49,67,68]. Nanoindentation has been widely utilized to characterize the interfacial properties in a numbers of ways, including using a range of indenters (spherical, wedge, and conical) and combining with other techniques (cross section and superlayer).

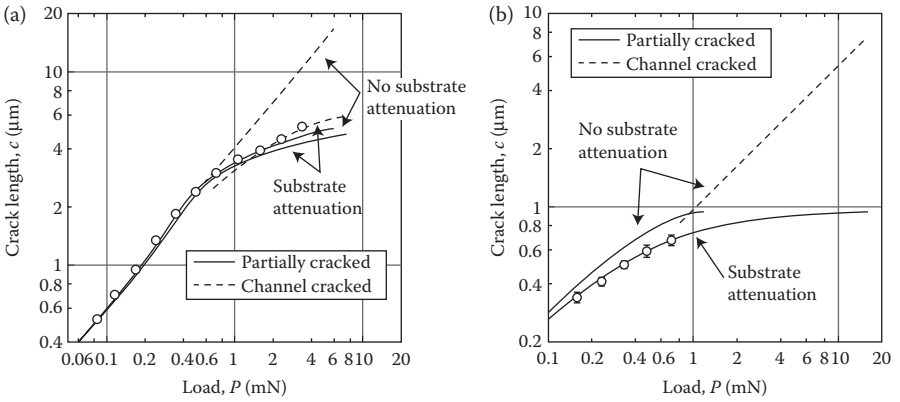


FIGURE 4.17 Crack length c as a function of indentation load P for cube-corner indentation, with and without substrate attenuation on (a) 2.4-μm-thick and (b) 0.5-μm-thick low-κ thin films. (Reproduced from D. J. Morris and R. F. Cook. *Journal of Materials Research* 23, 2008: 2443–57. Copyright 2008, with permission from Cambridge University Press.)

As for the low-κ methyl-silsesquioxane (MSSQ) thin film, Yeap et al. [69,70] demonstrate that wedge indentation can make the interfacial delamination occur at a relatively lower load in comparison with Berkovich or other axisymmetrical indentation. The load–displacement (P–h) curves for the MSSQ thin film with three types of indenters are given in Figure 4.18. It is clear that wedge tips can lead to pop-in events in P–h curves, while the Berkovich tip results in a smooth P–h curve [69]. The indentation under a 90° wedge tip produces much clearer pop-ins in the curves than that under a 120° wedge tip, due to the fact that the 90° wedge tip introduces higher stress at a particular load. By examining field emission scanning electron microscopy (FESEM) images of the wedge indents (Figures 4.19 and 4.20) [69], it was found that the pop-in event is associated with a central crack along the wedge tip, whereas the interface crack is actually initiated at a load higher than that for the pop-ins.

With FIB sectioning technique, it is found that the corner crack and the interfacial crack tend to occur at the same time. For the 90° wedge indentation, the corner cracks are actually part of the interfacial cracks. Therefore, the corner crack can be seen as the indicator of interfacial delamination.

In the low-κ/substrate systems, the interfacial delamination occurs when the indentation depth is less than the film thickness. The methods developed by de Boer and Gerberich [71,72] can be adopted to evaluate the interfacial adhesion. According to de Boer's and Gerberich's methods, indentation-induced stress is the main driving force for interfacial delamination and the residual stress is ignored. Without buckling, the interfacial toughness Γ can be expressed as

$$\Gamma = \frac{(1-\upsilon_f^2)t\sigma_0^2}{2E_f} \tag{4.14}$$

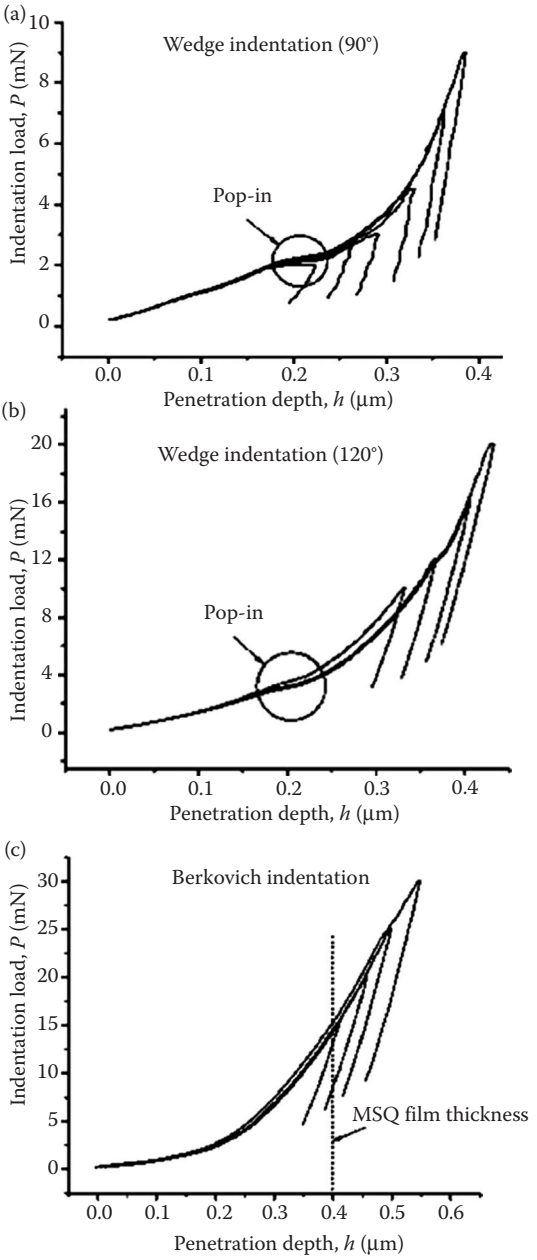


FIGURE 4.18 Nanoindentation load–displacement depth (*P*–*h*) curves of the MSSQ thin film using (a) a 90° wedge tip, (b) a 120° wedge tip, and (c) a Berkovich tip. (Reprinted from K. B. Yeap et al., *Journal of Applied Physics*, 101, 123531 and 2007. Copyright 2007 by the American Physical Society.)

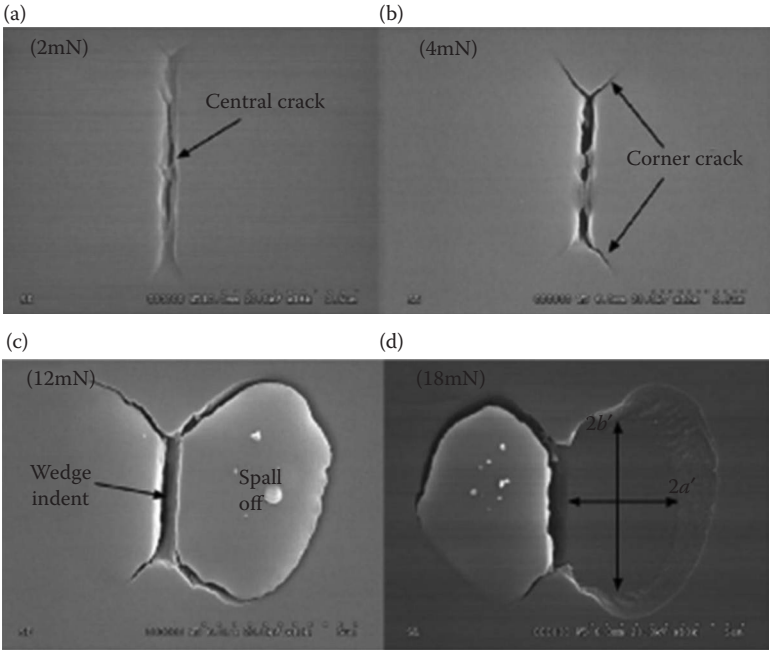


FIGURE 4.19 FESEM images of 90° wedge indentation on the MSSQ thin film. Each figure represents (a) central crack, (b) corner cracks, and (c,d) delamination cracks at the film surface. (Reprinted from K. B. Yeap et al., *Journal of Applied Physics*, 101, 123531 and 2007. Copyright 2007 by the American Physical Society.)

where υ_f and E_f are the Poisson's ratio and elastic modulus of thin film; σ_0 and t are the indentation-induced stress and thickness. The 90° wedge indentation gives the interfacial toughness, $\Gamma = G_c = 1.89 \pm 0.28$ J/m^2, while the 120° wedge indentation gives $\Gamma = G_c = 1.92 \pm 0.08$ J/m^2 [69]. These results are also consistent with Guyer's work [4], which reports that the interfacial toughness of MSSQ with less than 40% porosity ranges from 1.7 to 2.4 J/m^2. For the induced deformation field after nanoindentation, it can be found that the front of the interface crack is slightly curved, indicating the buckling of the nearly delaminated thin film. However, for both 90° and 120° wedge indentations, the indentation-induced stresses are much lower than the buckling stress. In this case, buckling is unlikely to occur. Comparing Berkovich indentations and wedge indentations, Berkovich indentations can also create interface delamination. However, it requires higher indentation load for Berkovich indentations to induce interface delamination than wedge indentations. Hence, the Berkovich tip penetrates into the substrate and leads to plastic deformation on the substrate.

In addition to the MSSQ thin film, the interfacial behavior of low-κ OSG thin film is also investigated by using wedge indentations. Similar to the MSSQ thin film, pop-in events are also exhibited in the *P–h* curve of OSG thin film during the wedge indentation [73]. The difference is the appearance of two obvious pop-in events.

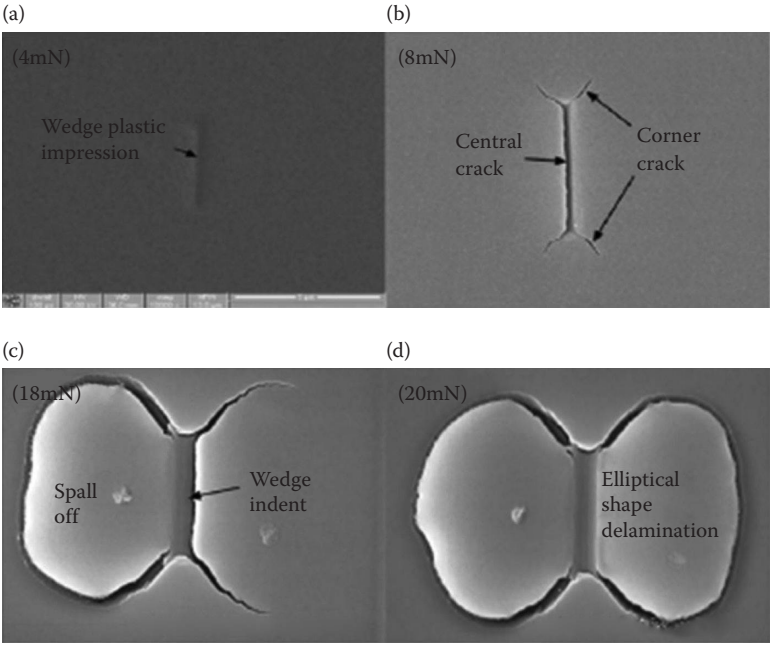


FIGURE 4.20 FESEM images of 120° wedge indentation on the MSSQ thin film. Each figure represents (a) central crack, (b) corner cracks, and (c,d) delamination cracks at the film surface. (Reproduced from K. B. Yeap et al., *Journal of Applied Physics*, 101, 123531 and 2007. Copyright 2007 by the American Physical Society.)

As shown in Figure 4.21a, the first pop-in event is related to the cohesive cracking along the wedge length and at each corner of the wedge indentation. The second can be correlated to the interfacial delamination. Moreover, the range B of the *P–h* curve highlighted in Figure 4.21a is used to determine the critical energy release rate for steady-state crack propagation [73].

The effects of various parameters such as density and porosity on the fracture behavior of low-κ thin films (e.g., fracture toughness, interfacial toughness, and crack velocity) have been investigated. At a given crack velocity, a linear relationship between the density and interfacial toughness has been observed in MSSQ thin films [4,50]. Corresponding to a fixed interfacial toughness, decreasing the film density from 1.3 to 0.8 g/cm^3 results in over four orders of magnitude increase in the crack velocity. Theoretically, the relationship among crack velocity *da*/*dt*, interfacial toughness Γ, and density ρ can be described as [74]

$$\frac{da}{dt} \propto \frac{1}{\rho}\exp\left(\frac{b}{RT}\frac{\Gamma}{\rho}\right) \tag{4.15}$$

where *b* is the activation area for the reaction; *T* is the absolute temperature, and *R* is the ideal gas constant. This model unveils the importance of increasing the interfacial toughness of low-κ thin films in order to decrease the rate of crack

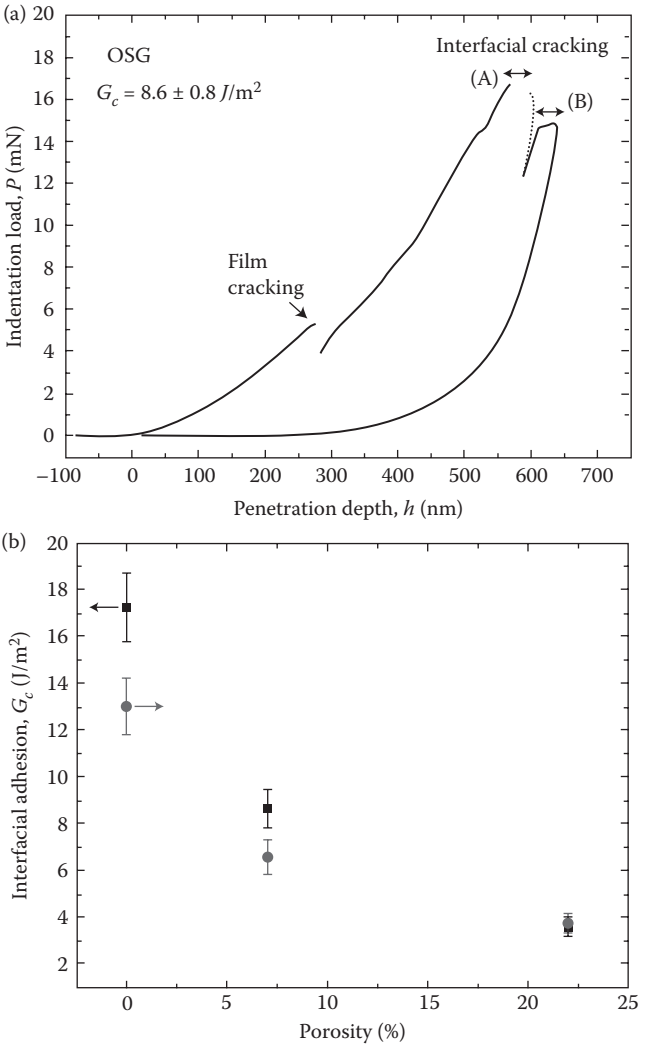


FIGURE 4.21 (a) Load–displacement (*P*–*h*) curve obtained from wedge indentation on a 660 nm-thick OSG thin film. (b) Interfacial toughness of OSG films (black boxes) with respect to porosity. (Reprinted from *Microelectronic Engineering*, 106, K. Boon et al., Nanoindentation for reliability assessment of ULK films and interconnects structures, 182–87, Copyright 2013, with permission from Elsevier.)

growth and increase material yields as well as long-term reliability. As for the effect of porosity, Figure 4.21b shows that the interfacial toughness of OSG thin films decreases drastically with the increase of porosity. The trends observed here are in agreement with previous experimental and simulation results [75]. The calculated interfacial toughness here is also consistent with the results from four-point-bending tests [76,77].

4.3.2 Failure and Toughening Mechanisms

The previous section discusses the basic fracture properties of popular low-κ thin films, including fracture toughness and interfacial toughness. In practice, the integration of these materials into microelectronic devices has been limited not only due to their brittle nature but the susceptibility to stress-corrosion cracking in a moist environment. In this section, the effects of moist or chemically active environment on crack evolution and possible failure and toughening mechanisms are reviewed.

Stress-corrosion cracking is a time-dependent failure that occurs at a load well below those required for general fracture. It can be initiated due to crack-tip bond rupture in moist environments. To macroscopically reflect such atomic-scale bond-rupture behavior, crack velocity is generally used to characterize the phenomenon of stress-corrosion cracking in moist or chemically active environments [4,20,51,78–84]. Generally, crack velocity versus strain energy release rate can be divided into four typical regions, as schematically shown in Figure 4.22. The first region represents a threshold strain energy release rate below which no crack growth is observed. In the second region (also called reaction-controlled regime), crack velocity is determined by the kinetics of the chemical reaction between crack-tip bonds and environmental reactants. In this region, the crack velocity increases rapidly with the driving force. In the third region (also called transport-limited regime), crack velocity is limited by transport of environmental reactants to the crack tip. As a result, the crack velocity is nearly independent of the strain energy release rate, but depends strongly on environment. In the final stage, catastrophic failure takes place and the crack velocity no longer depends on environmental factors.

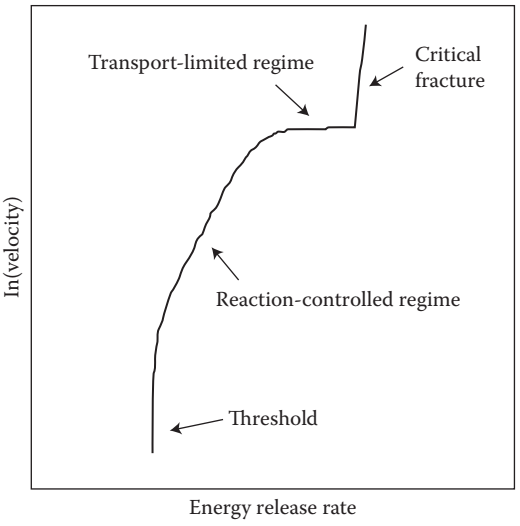


FIGURE 4.22 Schematic graph of crack velocity as a function of strain energy release rate. (Reprinted from *Materials Science and Engineering*, A 391, J. J. Vlassak, Y. Lin, and T. Y. Tsui, Fracture of organosilicate glass thin films: environmental effects, 159–74, Copyright 2005, with permission from Elsevier.)

Some analytical models have been developed to understand the relationship between crack velocity $v = da/dt$ and strain energy release rate G. For example, Vlassak et al. [78] developed a theoretical model to describe the reaction-controlled region. Based on Maxwell–Boltzmann statistics, the crack-growth rate v can be expressed as

$$\nu = \nu_0 \sin h\left(\frac{G - 2\gamma}{2N\kappa T}\right) \tag{4.16}$$

where ν_0 is a reference velocity; N is the number of bonds per unit area; γ is the surface energy of the material in the presence of reactants; and κ is the Boltzmann constant. In this model, the effect of reactants governs the value of γ; the velocity curve as a function of G shifts with the concentration of environmental reactants [78]. This model agrees well with experimental results as shown in Figure 4.23. Similar model is also proposed by Hall et al. [83].

The crack-growth rate in the transport-limited region is also proposed and can be written as [78,84]:

$$\nu = \frac{64(1 - \upsilon^2)Gp_X}{3\pi nNE\sqrt{2\pi m_X \kappa T}\,\ln(l/b)} \tag{4.17}$$

where p_X is the partial pressure of the reactants X in the environment, m_X the molecular mass of the reactant, l the mean free path length, n the number of reactants adsorbed per bond; b the bond length. This equation describes the transport-limited crack velocity quite well as evidenced by experimental results reported in previous studies [85]. When the crack velocity is a constant value in reaction-controlled region, the strain energy release rate to drive a crack in the reaction-controlled region varies linearly with the chemical potential of water in the environment [80–82,84,85]. Such relationship can be given as

$$G = B - nNRT \ln p_{H_2O} \tag{4.18}$$

where B is a constant value that depends on crack velocity. As shown in Figure 4.24, the theoretical results predicted by this model fits well with experimental results. It is thus indicated that it is possible to incorporate the water diffusion profile to the energy release rate, which is required to drive a crack at constant velocity. Lin et al. [80] also report that water diffusion in OSG thin films is remarkably fast with the activation energy being 0.27 eV. Moreover, it is reported that water diffuses predominantly along the interfaces and not through the low-κ thin films [80,81].

To further understand the stress-corrosion cracking of low-κ materials in water-containing environments, some atomistic-scale cracking mechanisms are also proposed to explain the effect of aqueous solutions on the cracking evolution. Guyer et al. [79] report the relationship between crack velocity (also called crack-growth rate) da/dt and strain-energy release rate G under different conditions, and also relate it to corresponding atomistic-scale molecular reaction mechanisms. For instance, similar

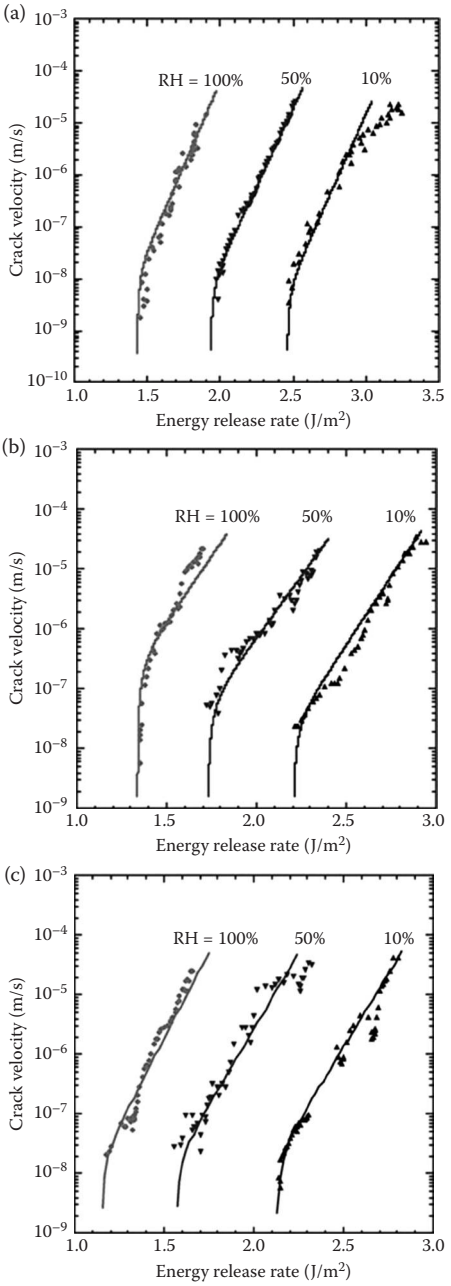


FIGURE 4.23 Representative subcritical crack-growth curves in ambient environment for (a) the OSG/TaN system, (b) OSG/SiN_x system, and (c) the OSG/SiO_2 system. Curves are fitted to the experimental results using Equation 4.16. (Reprinted from *Materials Science and Engineering*, A 391, J. J. Vlassak, Y. Lin, and T. Y. Tsui, Fracture of organosilicate glass thin films: environmental effects, 159–74, Copyright 2005, with permission from Elsevier.)

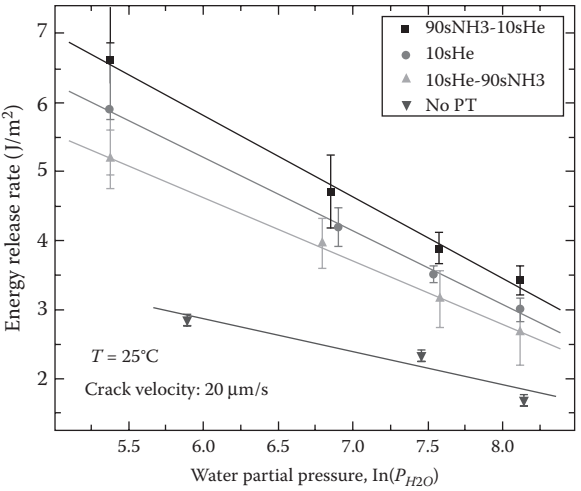


FIGURE 4.24 Linear relationship between the energy release rate to drive an interfacial crack at a given velocity and the natural logarithm of the water partial pressure in the environment for OSG/SiNx and OSG/SiCN systems. (Reprinted from *Acta Materialia*, 55, Y. Lin, T. Y. Tsui, and J. J. Vlassak, Water diffusion and fracture in organosilicate glass film stacks, 2455–64, Copyright 2007, with permission from Elsevier.)

to bulk glasses [86,87], the accelerating effect of basic solutions and the inhibiting effect of acidic solutions is clearly evident. Generally, stress-corrosion is caused by stress-enhanced, heterogeneous chemical reaction between highly strained crack-tip bonds and a reactive environmental species in low-κ materials. Such chemical reaction leads to Si–O bond rupture, as shown in Figure 4.25a. In Figure 4.25b, the nucleophilic attack of strained Si–O crack-tip bonds by hydroxide ions leads to the accelerated cracking rates and the reduction of G (operationally defined at $da/dt \sim 10^{-10}$ m/s) with increasing pH [79]. The attack changes the coordination number of the Si atom from four to five, and reduces the electron density in the Si–O bond.

However, the crack-growth behavior measured in the H_2O_2 (hydrogen peroxide) solution is quite different from the expected one on the basis of solution pH [79]. The red line in Figure 4.26 demonstrates the existence of a transport-limited regime between the two reaction-controlled regions (and higher than 2.2 J/m^2). In the first reaction-controlled region (G lower than ~1.4 J/m^2), the production of $SiO^{\bullet}$ surface group during reaction between H_2O_2 and Si–O bonds would be hydrolyzed by water molecule, and the highly reactive hydroxide radical may also attack other crack-tip bonds, further accelerating crack-growth rates, as shown in Figure 4.25c [79]. In the transport-limited region (G between 1.4 and 2.2 J/m^2), owing to the lower diffusivity of H_2O_2 than that of water, it therefore limits crack propagation rate. The resulting crack-growth rate is nearly independent of G. In the second reaction-controlled region (G larger than 2.2 J/m^2), the crack-growth rate again increases with G.

In order to retard the crack evolution to maintain the mechanical integration, it is necessary to find out possible ways to improve the fracture toughness of low-κ

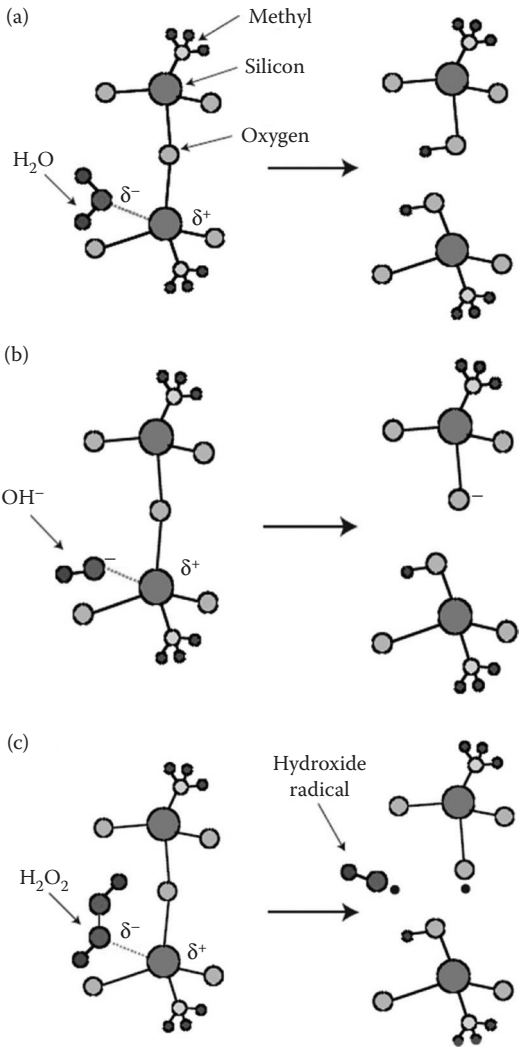


FIGURE 4.25 Simplified molecular reaction mechanisms. (a,b) Reaction between strained crack-tip Si–O bonds and (a) water and (b) hydroxide ions. (c) The proposed mechanism for hydrogen peroxide. (Reprinted from E. P. Guyer and R. H. Dauskardt. *Nature Materials* 3, 2004: 53–57. Copyright 2004, with permission from Nature Publishing Group.)

and other porous thin films. Kim et al. [88] investigated the influence of surfactants on the crack evolution in MSSQ thin films. It was found that even small changes in the lengths of either the hydrophobic or hydrophilic groups of the surfactants have dramatic effects on the crack-growth rates. The suppression of crack-growth rates is caused by the bridging of crack surfaces due to the formation of surfactant nano-bubbles, which is demonstrated in Figure 4.27 [88]. Alternatively, the acceleration of crack-growth rates is caused by reducing the free energy of the fracture surfaces.

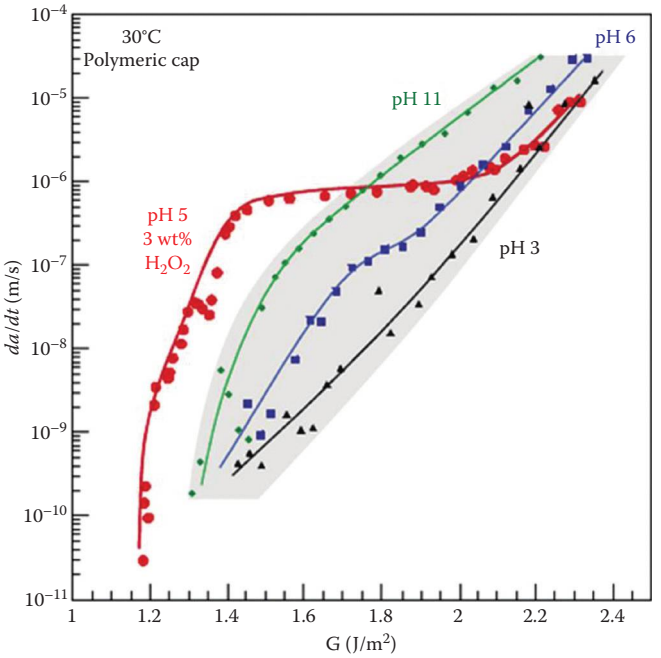


FIGURE 4.26 The crack propagating rate as a function of applied strain energy release rate in 3 wt% hydrogen peroxide solution, buffered solution, and water. (Reprinted by permission from E. P. Guyer and R. H. Dauskardt. *Nature Materials* 3, 2004: 53–57. Copyright 2004, with permission from Nature Publishing Group.)

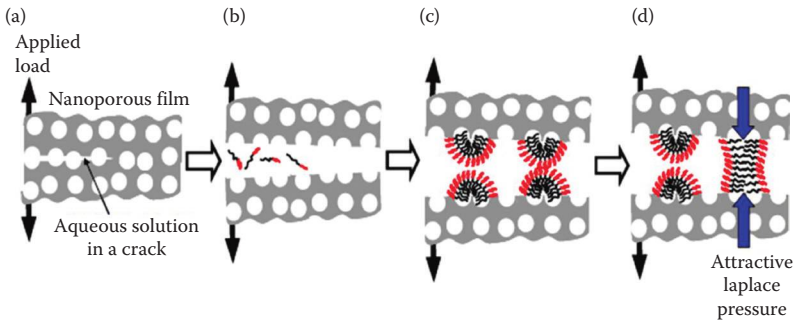


FIGURE 4.27 A crack bridging phenomenon by surfactant-enhanced nanobubble cavitations consisting of four steps. (a) Crack propagates in a hydrophobic nanoporous organosilicate film and nanobubbles nucleate instantly on crack surfaces in contact with an aqueous solution. (b) Surfactants are attracted to air-water nanobubble interfaces. (c) Surfactants adsorb on nanobubbles and facilitate the growth of nanobubbles. (d) Finally, nanobubbles coalesce and the resulting cavity generates an attractive Laplace pressure at large range. (Reprinted from *Acta Materialia*, 57, T.-S. Kim, T. Konno, and R. H. Dauskardt, Surfactant-controlled damage evolution during chemical mechanical planarization of nanoporous films, 4687–96, Copyright 2009, with permission from Elsevier.)

All these conclusions provide useful guidance for tailoring surfactant additions as crack-inhibiting agents.

Besides the formation of surfactant-enhanced nanobubble cavitations, which can result in crack bridging in low-κ thin films, Maidenberg et al. [89] also demonstrated that controlled decomposition of porogen molecules during preparation of low-κ thin films may lead to significant increase in interfacial toughness. By the remnants of porogen molecules used to create nanoscale pores, the interfacial toughness of ~2.6 J/m^2 for dense MSSQ thin films increases by over one order of magnitude to larger than 30 J/m^2 for MSSQ containing 50 vol.% porosity, as indicated in Figure 4.28. The possible mechanism of significant increase in interfacial toughness is related to molecular bridges that exist behind the debonding crack tip [89]. The porogen remnants present at the surface are stretched across the opening crack front, providing molecular-bridging effect. The bridging contribution to the debond energy, $G_{bridging}$, is given by [89]

$$G_{bridging} = 1/2(f_{\max} A\delta_0) \tag{4.19}$$

where $f_{\max}$ is the maximum force each molecular bridge can sustain; A is the areal density of the molecules; δ_o is the fully extended molecular length. According to this equation, the molecular-bridging contribution scales with the areal density and maximum extension of the molecular bridges. The measured interfacial toughness

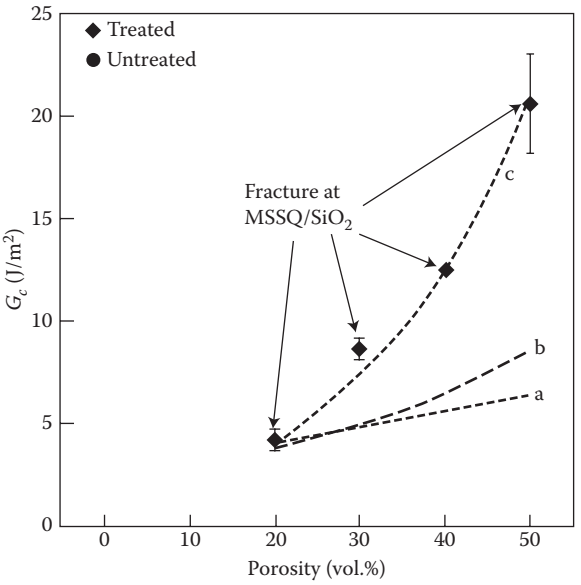


FIGURE 4.28 Interfacial toughness of MSSQ thin films as a function of porosity with and without UV/ozone exposure. (Reprinted by permisssion from D. A. Maidenberg et al., *Nature Materials* 3, 2004: 464–69. Copyright 2004, with permission from Nature Publishing Group.)

is the sum of the bridging contribution $G_{bridging}$, and the intrinsic energy necessary to separate the interface G_o,

$$G_c = G_o + G_{bridging} \tag{4.20}$$

The previous analysis are important for a large range of emerging optical, electronic, and biological technologies that use low-κ materials, but are limited by the degradation of mechanical properties with increasing porosity.

4.4 NANOINDENTATION TESTING

Indentation test is a useful method to measure the mechanical properties under contact-induced stress. Nanoindentation is capable of testing materials in nanoscale. The contact area can be determined indirectly from the recorded indentation depth and the indenter geometry, instead of measuring the impressions afterwards. This is of great importance as direct measurements of impressions lead to inconvenience and inaccuracy at micro- and nanoscale.

4.4.1 Basic Theory

4.4.1.1 Measurement of Young's Modulus and Hardness

When an indenter is placed in contact with a sample, both load and displacement are recorded during loading and unloading, as shown in Figure 4.29. The loading part of the indentation cycle may involve an initial elastic deformation, followed by

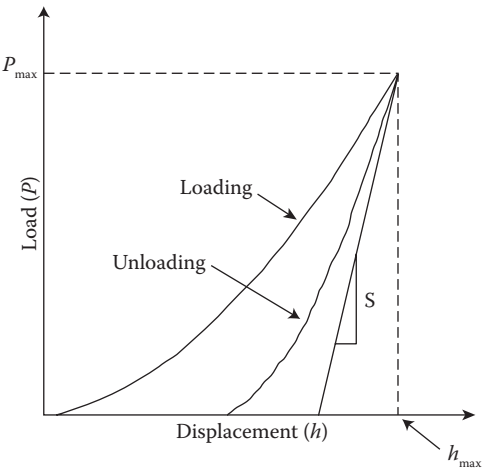


FIGURE 4.29 Typical indentation load–displacement data defining key experimental quantities. h_{max} is the total depth of penetration, P_{max} is the maximum applied load, and S is the contact stiffness. (Reprinted from *Materials Science and Engineering*, A 253, G. M. Pharr, Measurement of mechanical properties by ultra-low load indentation, 151–59, Copyright 1998, with permission from Elsevier.)

plastic deformation, or yield. Upon unloading, if plastic deformation or yield occurs, a residual impression will be left in the specimen when the load is removed.

From the recorded curves, the reduced modulus M_r can be obtained by the slope of unloading curve at the point of maximum depth, as follows [33]:

$$M_r = \frac{1}{2}\frac{dP}{dh}\frac{\sqrt{\pi}}{\sqrt{A}} = \frac{\sqrt{\pi}}{2}\frac{S}{\sqrt{A}} \tag{4.21}$$

where $S = dP/dh$ is often referred to as the contact stiffness, which can be evaluated at the beginning of the unloading response. Reduced modulus M_r combines the modulus of the indenter and the specimen and is given by [91]:

$$\frac{1}{M_r} = \frac{(1-\nu^2)}{E} + \frac{(1-\nu'^2)}{E'} \tag{4.22}$$

where E and ν are the elastic modulus and Poisson's ratio of the specimen, respectively; E' and ν' are the elastic modulus and Poisson's ratio of the indenter, respectively. For a standard diamond indenter, E' is 1140 GPa and ν' is 0.07.

The value of hardness H is usually evaluated by the mean contact pressure at full loading and is given by:

$$H = \frac{P_{\max}}{A} \tag{4.23}$$

where A is the contact area (as distinct from the actual curved area of contact), and $P_{\max}$ is the maximum applied load. One thing needs to be mentioned is that the measurement of hardness needs to be undertaken under a condition of fully developed plastic zone because within this region, the mean contact pressure generally becomes independent of load and is only related to the material's response [33].

4.4.1.2 Measurement of Fracture Toughness

Nanoindentation technique has been widely used to evaluate the fracture toughness of materials by using sharp indenters (e.g., Vickers, and Berkovich). The lengths of radial cracks are always used to calculate the fracture toughness of specimens. Figure 4.30 shows radial cracks induced by Vickers indenter and Berkovich indenter, respectively. For Vickers indenter, fracture toughness K_c can be found from [33,92]:

$$K_c = k\left(\frac{E}{H}\right)^n \frac{P}{c^{3/2}} \tag{4.24}$$

where c is the crack length measured from the center of contact to the end of crack at the specimen surface; k is an empirical calibration constant, which depends on the geometry of the indenter. For standard Vickers, value of k is taken as 0.016 [93]. P is indentation load and $n = 1/2$. E and H are Young's modulus and hardness,

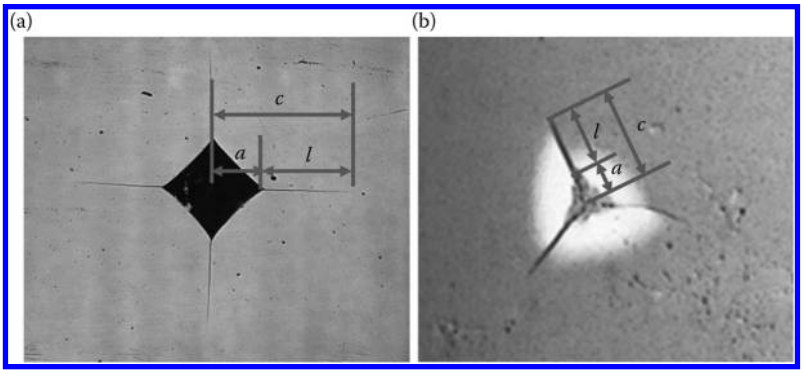


FIGURE 4.30 Crack parameters for (a) Vickers indenter. (Reprinted from *Wear*, 239, R. J. Anton and G. Subhash, Dynamic Vickers indentation of brittle materials, 27–35, Copyright 2000, with permission from Elsevier.) (b) Berkovich indenter. (Reprinted from *Thin Solid Films*, 366, J. Malzbender, G. de With, and J. M. J. den Toonder, Elastic modulus, indentation pressure and fracture toughness of hybrid coatings on glass, 139–49, Copyright 2000, with permission from Elsevier.) Crack length c is measured from the center of contact to the end of crack at the specimen surface.

which can be determined from nanoindentation tests with small load. Other methods have been developed for evaluation of fracture toughness using Vickers indenters [93–95].

In comparison with Vickers indenter, Berkovich indenter has been less used due to the loss of symmetry. However, Dukino et al. [96] found that Berkovich indenter gives more consistent estimations of fracture toughness over the complete load range than Vickers indenter. Thus, it has been suggested that Berkovich indenter is more suitable for evaluation of fracture toughness, especially at very low load levels. Figure 4.30b shows the crack parameters for Berkovich indenter. Fracture toughness K_c can be written in the form of [96]:

$$K_c = 1.073 x_v (a/l)^{1/2} \left(\frac{E}{H}\right)^{2/3} \frac{P}{c^{3/2}} \tag{4.25}$$

where a, l, and c can be measured from the indentation impression. The constant x_v is set to be 0.015 in the calculation.

4.4.2 Nanoindentation on Thin Films

4.4.2.1 Fully Densed Thin Films

4.4.2.1.1 Measurement of Young's Modulus and Hardness

It is very difficult to assess the properties of thin coatings (below 10 μm) using traditional indentation tests as the measurement of deformed areas or depths become more difficult with reduced contact area [99]. Considering the ability of precise and continuous record of load or displacement at nanoscale, nanoindentation is regarded as an ideal and powerful tool to explore the near-surface mechanical properties of

materials, especially for thin films, coatings, and layered or small-sized materials. In addition, the combined effect of thin films and substrate can be estimated with increasing indentation depth, providing a means of investigating a thin film system, from film- to substrate-dominated responses. Thus, nanoindentation method has been massively employed in testing different coated systems including hard coatings on soft substrates for tribological applications, hard coatings on hard substrates (e.g., semiconductor metallization), hard coatings on hard substrates (e.g., antireflection coatings on optical elements), and soft coatings on soft substrates (e.g., protective polymer coatings on steel) [99].

Nanoindentation tests can be performed without removal of the film from its substrate. Obviously, substrate may have a significant effect on the mechanical properties of film materials [101]. For different thin-film systems (soft film/hard substrate or hard film/soft substrate), so-called pile-up or sink-in of materials may occur during indentation, as shown in Figure 4.31. This will lead to an underestimation or overestimation of the contact area, which is generally estimated based on Oliver–Pharr model [102]. Whether a pile-up or sink-in will be produced for thin film systems depends on the hardness ratio between film and substrate [100]. In the case of a soft film on a hard substrate, the soft film is prevented by the hard material from moving downwards, thus increasing the degree of pile-up. In the case of a hard film on a soft substrate, the plastic region in the soft substrate is much larger than that in the hard film, thus enhances the sink-in effect.

Generally, we can neglect the substrate effect when the penetration depth is smaller than 10% of the total thickness of thin film [33], although this rule has no physical basis [103]. Considering the substrate effect, Gao et al. [104] assume indentation modulus M can be estimated as

$$M = \frac{2\mu_{eff}}{1 - \nu_{eff}} \tag{4.26}$$

where

$$\begin{cases} \nu_{eff} = \nu_s + (\nu_f - \nu_s) I_1(h/a) \\ \mu_{eff} = \mu_s + (\mu_f - \mu_s) I_0(h/a) \end{cases} \tag{4.27}$$

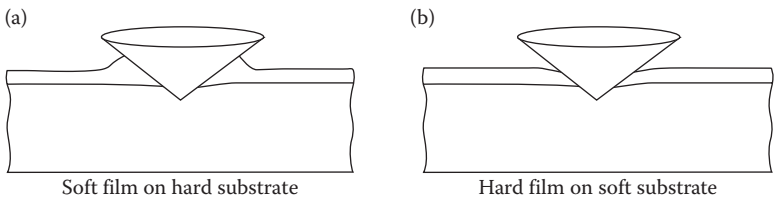


FIGURE 4.31 (a) Pile-up or (b) sink-in of materials in thin film systems. (Reproduced from X. Chen and J. J. Vlassak. *Journal of Materials Research* 16, 2001: 2974–82. Copyright 2004, with permission from Cambridge University Press.)

The materials are assumed to be isotropic with shear modulus μ and Poisson's ratio ν. Subscripts *f* and *s* represent the film and the substrate, respectively. μ_{eff} and ν_{eff} are the effective shear modulus and Poisson's ratio of the thin film system. The indentation modulus *M* is given by the plane strain modulus, $E/(1-\nu^2)$, for isotropic materials [105]. I_0 and I_1 are weight functions that reflect the substrate effect and can be calculated using the following equations:

$$I_1(\xi) = \frac{2}{\pi}\arctan\xi + \frac{\xi}{\pi}\ln\frac{1+\xi^2}{\xi^2}$$
$$I_0(\xi) = \frac{2}{\pi}\arctan\xi + \frac{1}{2\pi(1-\nu)}\left[(1-2\nu)\xi\ln\frac{1+\xi^2}{\xi^2} - \frac{\xi}{1-\xi^2}\right] \tag{4.28}$$

where $\xi = h/a$ is the ratio between the thickness of thin film *h* and the radius of the circle of contact *a*. When *h/a* is very large, both I_0 and I_1 approach unity and the measured indentation modulus is equal to the film. However, when *h/a* is small, both I_0 and I_1 approach zero and the modulus is determined by the substrate.

4.4.2.1.2 Measurement of Fracture Toughness

The technical difficulties in evaluation of fracture toughness in thin films are associated with accurate measurement of crack length under limited indentation depth. There exists a cracking threshold below which indentation cracking does not occur during indentation [106]. With a sharp indenter, that is, Berkovich indenter, such cracking threshold could be significantly reduced. The crack formation is much easier under Cube corner indenter than Berkovich indenter, because it will induce more than three times indentation volume than Berkovich indenter under the same load, leading to much lower cracking threshold. Furthermore, it is often difficult to accurately measure the radial crack length even under SEM [107]. Besides the methods introduced in Section 4.1, a more reliable method for evaluation of fracture toughness is the energy method [108–110]. The energy release rate G_c (strain energy release per unit crack area) can be defined as

$$G_c = \frac{dU}{dA} \tag{4.29}$$

where *U* is the strain energy; *A* is the area of the crack. Then, the fracture toughness can be calculated based on classic fracture mechanics, that is,

$$K_c = \sqrt{EG_c} \text{ (for plane stress mode I fracture)} \tag{4.30}$$

$$K_c = \sqrt{\frac{EG_c}{1-\nu^2}} \text{ (for plane strain mode I fracture)} \tag{4.31}$$

For example, Li et al. [107,108] investigate the fracture mechanisms of thin amorphous carbon films by nanoindentation. They proposed three stages in the fracture

during indentation: (1) first ring-like through thickness cracks form around the indenter by high stresses in the contact area, (2) delamination and buckling around contact area at the film/substrate interface due to high lateral pressure, and (3) a second ring-like through thickness crack and spalling generated by high bending stresses at the edge of the buckled film, as shown in Figure 4.32.

The strain energy released in the first/second ring-like crack and spalling can be calculated from the corresponding steps in the load–displacement curves [108], as shown in Figure 4.33. OACD and DE are the loading and unloading curves, respectively. Since the first ring-like through thickness crack does not always lead to step stage in the loading curve for some films (e.g., ion beam carbon film), the second ring-like through thickness crack should be considered [108]. Suppose that the second ring-like through thickness crack occurs at AC, this crack formation changes the loading curve OAB into OAC. Thus, the energy difference before and after the crack generation is the energy stored in the area of ABC. This energy will be released as strain energy to create the ring-like through thickness crack. In this case, the fracture toughness can be estimated as [108]

$$K_c = \left(\frac{E}{(1 - \nu_f^2) 2\pi C_R} \frac{\Delta U}{t} \right)^{1/2} \tag{4.32}$$

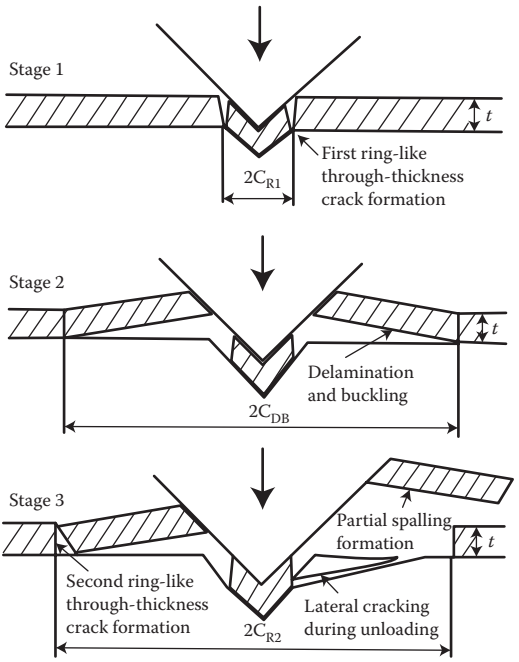


FIGURE 4.32 Schematic of various stages in nanoindentation fracture for the film/substrate system. (Reprinted from *Thin Solid Films*, 315, X. Li and B. Bhushan, Measurement of fracture toughness of ultra-thin amorphous carbon films, 214–21, Copyright 1998, with permission from Elsevier.)

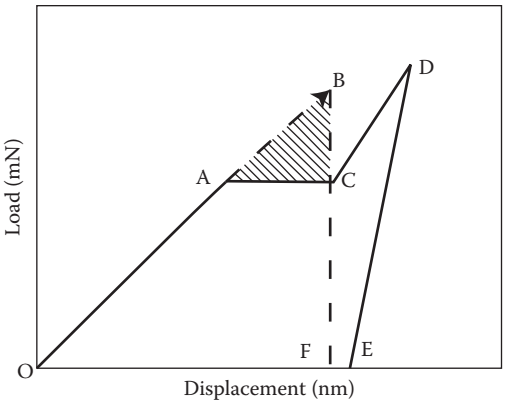


FIGURE 4.33 Schematic of a load–displacement curve, showing a step during the loading cycle and associated energy release. (Reprinted from *Thin Solid Films*, 315, X. Li and B. Bhushan, Measurement of fracture toughness of ultra-thin amorphous carbon films, 214–21, Copyright 1998, with permission from Elsevier.)

where E is the elastic modulus of the thin film; ν_f is the Poisson's ratio of film; $2\pi C_R$ is the crack length in the film plane; ΔU is the strain energy difference before and after cracking; t is the film thickness.

4.4.2.2 Porous Thin Films

When a thin film is composed of porous materials, it is more complicated to evaluate its mechanical properties by nanoindentation. This is attributed to the fact that pores, surface roughness exist and fracture and densification can happen during indentation [22]. Consequently, mechanical responses of porous thin films are largely different from their fully densed counterparts [24].

First, porosity may lead to a transition in fracture mechanisms. For example, when the relative porosity increases, the compression behavior shows a transition from a brittle failure with cracks parallel to the applied load, to cellular-like behavior, featured by progressive densification [111].

Figure 4.34 shows the load–displacement curves recorded during indentation of porous alumina with different amount of pores. The load–displacement curves for less porous samples are characterized by elastic deformation followed by sudden rupture, similar to dense ceramics. Macrocracks parallel to the direction of the applied load can be observed on the exterior surface of the sample [111]. On the contrary, the behavior of highly porous samples is more like ceramic foams. After an initial elastic deformation, the load–displacement curve is featured by a plateau due to a progressive collapse of the solid walls between the pores.

To fully understand the effect of porosity on porous thin films in nanoindentation, the number of unit cells that are sampled by the indenter is important. If a small number of unit cells are sampled, the measured elastic modulus tends to be underestimated. It has been demonstrated that a minimum of five unit cells of thin-film samples in each direction should be sampled to properly measure the modulus of low

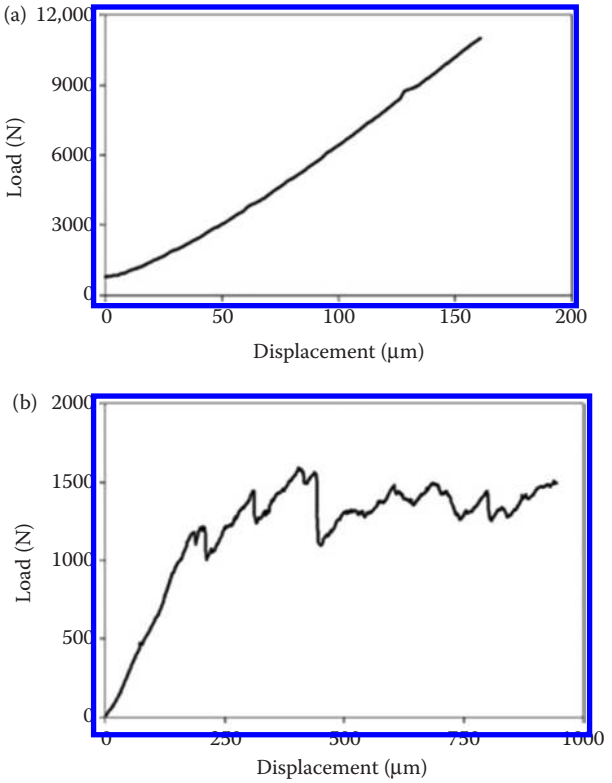


FIGURE 4.34 Typical load–displacement curves for porous alumina prepared with: (a) 40 vol% and (b) 65 vol% of pore former (small spheres). (Reprinted from *Journal of the European Ceramic Society*, 32, S. Meille et al., Mechanical properties of porous ceramics in compression: On the transition between elastic, brittle, and cellular behavior, 3959–67, Copyright 2012, with permission from Elsevier.)

density porous materials [112]. To this, blunt indenters are always adopted in testing porous materials, such as conical indenter with large radius.

An important parameter in nanoindentation tests is the contact area, which is used to calculate the modulus and hardness. Due to the presence of pores, the real contact area is smaller than the estimated one based on the indentation depth and the geometrical parameters of the indenters. Therefore, a corrected contact area is required. The relative contact radius $\hat{a}$ between samples and a conical indenter can be estimated as [113]

$$\hat{a}^3 = \left(\frac{a_A}{a_B}\right)^3 = \frac{M_A}{M_B} \tag{4.33}$$

where M_A and M_B are the indentation modulus of material A and B; a_A and a_B are the contact radius between indenter and material A and B. The relative contact area can be determined by subtracting the pore area, which can be estimated as [113]

$$A_r = \pi\hat{a}^2 - \left[\frac{\pi\hat{a}^2}{\sqrt{3}/4d^2}\right]\left[\frac{1}{2}\pi r^2\right] = \pi\hat{a}^2(1-\phi) \tag{4.34}$$

where ϕ is the porosity of porous anodic alumina samples; d is the interpore distance; r is the pore radius.

Surface roughness could lead to underestimation of E and H at small indentation depths. The reason for this lies in the overestimated contact area, given that the indentation depth is comparable to the roughness [114]. To eliminate such effect in data analysis, a critical indentation depth is required [115]. The densification (crushing) of porous thin films under indentation also plays a critical role in mechanical characterization of porous thin films. In general, densification of porous material under indenter increases the local elastic modulus. To what extent the densification affects the measured mechanical properties by nanoindentation depends on the detailed microstructures of the thin films. Chen et al. [24] conclude that the densification-induced stiffness gradient only plays a role when the elastic properties of dense and porous phases are very distinct (e.g., $E_{dense}/E_{porous} > 3$). In the case of polymer films ($E_{dense}/E_{porous} = 1.4$), however, the difference between the contact stiffness with stiffness gradient and the reference curve is less than 1%. In this case, the densification is relatively small as compared with the elastically deformed region under the indenter. Consequently, the effect of densification on stiffness measurements of polymer films ($E_{dense}/E_{porous} = 1.4$) is marginal.

In nanoindentation tests on porous thin films, substrate also has a significant effect on the evaluated mechanical properties [22]. To remove the substrate effect, the plastic deformation region induced should be minimized within the film. Taking a 10 μm-thick $La_{0.6}Sr_{0.4}Co_{0.2}Fe_{0.8}O_{3-\delta}$ film as an example, Figure 4.35 shows the top surface and cross-sectional SEM images using conical indenter [22]. The microstructural changes can be observed near the indents in the film. The compression force on the porous thin film generates an approximately parabolic-shaped plastic zone. Different from the plastic deformation zone induced by viscous flow or dislocation motion, such plastic zone is governed by densification of porous structure [22]. When the indentation depth increases to a critical value, such plastic zone reaches the substrate and the substrate starts to play a role. As a benchmark, the indentation depth should be controlled within this critical value. Alternatively, substrate effect should be considered using some methods introduced in Section 4.4.2.1.

4.5 SUMMARY

Porous thin films have been widely used in various fields owing to their excellent optical, electrical, chemical, and transport properties. To fully take the advantage of these unique properties, adequate mechanical integrity needs to be maintained. In this chapter, we present a brief review of mechanical and fracture properties of both highly ordered (such as TiO_2 nanotube array thin film and silica foam thin film) and disordered (low-κ) porous thin films, largely based on nanoindentation technique. In general, their mechanical properties strongly depend on material structures and porosity. As for the fracture behavior of these porous films, especially for low-κ

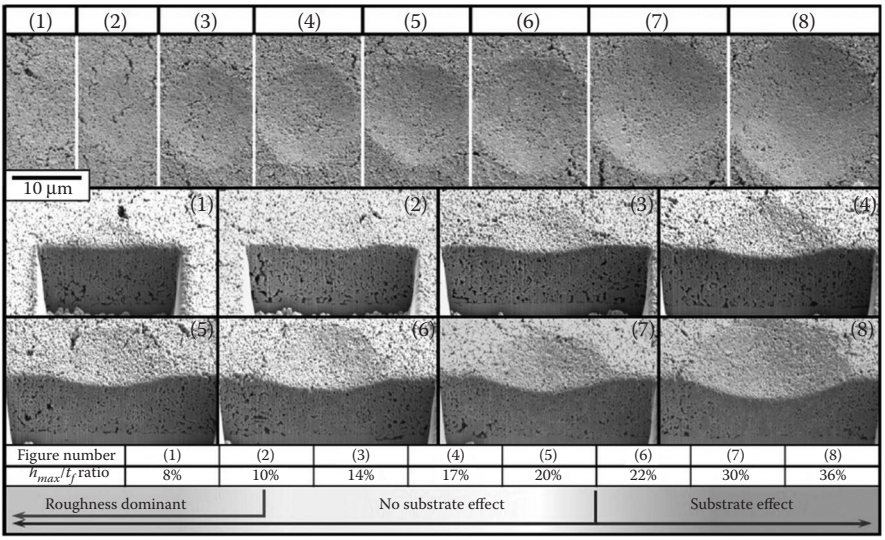


FIGURE 4.35 Top surface and cross-sectional SEM images of indents in a 10 µm thick $La_{0.6}Sr_{0.4}Co_{0.2}Fe_{0.8}O_3$-δ film corresponding to maximum indentation depths from 800 to 3600 nm. (Reprinted from *Acta Materalia*, 61, Z. Chen et al., Nanoindentation of porous bulk and thin films of $La_{0.6}Sr_{0.4}Co_{0.2}Fe_{0.8}O_{3-\delta}$. 5720–34, Copyright 2013, with permission from Elsevier.)

thin films, it exhibits typical brittle nature and the fracture toughness is much lower than that of fully densed thin films. Controlled decomposition of the porogen molecule during processing of low-κ thin films can significantly increase their interfacial toughness by over one order of magnitude. In addition, the fracture evolution of these low-κ thin films can be induced by environmental reactants, such as water and surfactant. This chapter not only provides a detailed review of mechanical and fracture performance of porous thin films, but also gives insight into the novel design of porous materials in future.

ACKNOWLEDGMENT

Support from the ARC Discovery Project (DP150101717) is gratefully acknowledged.

REFERENCES

1. K. S. W. Sing, D. H. Everett, R. A. W. Haul, L. Moscou, R. A. Peirotti, and J. Rouquerol. IUPAC commission on colloid and surface chemistry including catalysis. *Pure and Applied Chemistry* 57, 1985: 603–19.
2. L. Shen and K. Zeng. Comparison of mechanical properties of porous and non-porous low-*k* dielectric films. *Microelectronic Engineering* 71, 2004: 221–28.
3. H-J. Lee, E. K. Lin, H. Wang, W-l. Wu, W. Chen, and E. S. Moyer. Structural comparison of hydrogen silsesquioxane based porous low-k thin films prepared with varying process conditions. *Chemistry of Materials* 14, 2002: 1845–52.

4. E. P. Guyer, M. Patz, and R. H. Dauskardt. Fracture of nanoporous methyl silsesquioxane thin-film glasses. *Journal of Materials Research* 21, 2006: 882–94.
5. P. Roy, S. Berger, and P. Schmuki. TiO_2 nanotubes: Synthesis and applications. *Angewandte Chemie International Edition* 50, 2011: 2904–39.
6. C. A. Grimes and G. K. Mor. *TiO_2 Nanotube Arrays: Synthesis, Properties and Applications*. New York: Springer, 2009.
7. S. P. Albu, A. Ghicov, J. M. Macak, R. Hahn, and P. Schmuki. Self-organized, free-standing TiO_2 nanotube membrane for flow-through photocatalytic applications. *Nano Letters* 7, 2007: 1286–89.
8. O. Sel, S. Sallard, T. Brezesinski, J. Rathouský, D. R. Dunphy, A. Collord, and B. M. Smarsly. Periodically ordered meso- and macroporous SiO_2 thin films and their induced electrochemical activity as a function of pore hierarchy. *Advanced Functional Materials* 17, 2007: 3241–50.
9. K. Rahmoun, A. Iost, V. Keryvin, G. Guillemot, and N. E. Chabane Sari. A multilayer model for describing hardness variations of aged porous silicon low-dielectric-constant thin films. *Thin Solid Films* 518, 2009: 213–21.
10. T. A. Desai, D. J. Hansford, L. Leoni, M. Essenpreis, and M. Ferrari. Nanoporous antifouling silicon membranes for biosensor applications. *Biosensors and Bioelectronics* 15, 2000: 453–62.
11. A. K. Cheetham, G. Férey, and T. Loiseau. Open-framework inorganic materials. *Angewandte Chemie International Edition* 38, 1999: 3268–92.
12. K. M. Coakley and M. D. McGehee. Photovoltaic cells made from conjugated polymers infiltrated into mesoporous titania. *Applied Physics Letters* 83, 2003: 3380–82.
13. H. F. Zhuang, C. J. Lin, Y. K. Lai, L. Sun, and J. Li. Some critical structure factors of titanium oxide nanotube array in its photocatalytic activity. *Environmental Science and Technology* 41, 2007: 4735–40.
14. X. Tang and D. Li. Sulfur-doped highly ordered TiO_2 nanotubular arrays with visible light response. *Journal of Physical Chemistry C* 112, 2008: 5405–09.
15. Z. Liu, X. Zhang, S. Nishimoto, M. Jin, D. A. Tryk, T. Murakami, and A. Fujishima. Highly ordered TiO_2 nanotube arrays with controllable length for photoelectrocatalytic degradation of phenol. *Journal of Physical Chemistry C* 112, 2008: 253–59.
16. Z. Zhang, Y. Yuan, G. Shi, Y. Fang, L. Liang, H. Ding, and L. Jin. Photoelectrocatalytic activity of highly ordered TiO_2 nanotube arrays electrode for azo dye degradation. *Environmental Science and Technology* 41, 2007: 6259–63.
17. Z. Zhang, Y. Yuan, Y. Fang, L. Liang, H. Ding, and L. Jin. Preparation of photocatalytic nano-ZnO/TiO_2 film and application for determination of chemical oxygen demand. *Talanta* 73, 2007: 523–28.
18. C. V. Nguyen, K. R. Carter, C. J. Hawker, J. L. Hedrick, R. L. Jaffe, R. D. Miller, J. F. Remenar, H-W. Rhee, P. M. Rice, and M. F. Toney. Low-dielectric, nanoporous organosilicate films prepared via inorganic/organic polymer hybrid templates. *Chemistry of Materials* 11, 1999: 3080–85.
19. J. L. Hedrick, R. D. Miller, C. J. Hawker, K. R. Carter, W. Volksen, D. Y. Yoon, and M. Trollsås. Templating nanoporosity in thin-film dielectric insulators. *Advanced Materials* 10, 1998: 1049–53.
20. R. F. Cook and E. G. Liniger. Stress-corrosion cracking of low-dielectric-constant spin-on-glass thin films. *Journal of the Electrochemical Society* 146, 1999: 4439–48.
21. O. Bellon, N. M. Sammes, and J. Staniforth. Mechanical properties and electrochemical characterisation of extruded doped cerium oxide for use as an electrolyte for solid oxide fuel cells. *Journal of Power Sources* 75, 1998: 116–21.
22. Z. Chen, X. Wang, V. Bhakhri, F. Giuliani, and A. Atkinson. Nanoindentation of porous bulk and thin films of $La_{0.6}Sr_{0.4}Co_{0.2}Fe_{0.8}O_{3-\delta}$. *Acta Materialia* 61, 2013: 5720–34.

23. A. Atkinson and A. Selcuk. Mechanical behaviour of ceramic oxygen ion-conducting membranes. *Solid State Ionics* 134, 2000: 59–66.
24. X. Chen, Y. Xiang, and J. J. Vlassak. Novel technique for measuring the mechanical properties of porous materials by nanoindentation. *Journal of Materials Research* 21, 2006: 715–24.
25. S. P. Baker, and W. D. Nix. Mechanical properties of compositionally modulated Au-Ni thin films: Nanoindentation and microcantilever deflection experiments. *Journal of Materials Research* 9, 1994: 3131–44.
26. J. J. Vlassak and W. D. Nix. A new bulge test technique for the determination of Young's modulus and Poisson's ratio of thin films. *Journal of Materials Research* 7, 1992: 3242–49.
27. H. Asoh, K. Nishio, M. Nakao, T. Tamamura, and H. Masuda. Conditions for fabrication of ideally ordered anodic porous alumina using pretextured Al. *Journal of the Electrochemical Society* 148, 2001: B152–B56.
28. C. A. Grimes. Synthesis and application of highly ordered arrays of TiO_2 nanotubes. *Journal of Materials Chemistry* 17, 2007: 1451–57.
29. Y. Toivola, A. Stein, and R. F. Cook. Depth-sensing indentation response of ordered silica foam. *Journal of Materials Research* 19, 2004: 260–71.
30. H. Masuda and K. Fukuda. Ordered metal nanohole arrays made by a two-step replication of honeycomb structures of anodic alumina. *Science* 268, 1995: 1466–68.
31. G. E. Thompson and G. C. Wood. Porous anodic film formation on aluminium. *Nature* 290, 1981: 230–32.
32. T-H. Fang, T. Wang, C-H. Liu, L-W. Ji, and S-H. Kang. Physical behavior of nanoporous anodic alumina using nanoindentation and microhardness tests. *Nanoscale Research Letters* 2, 2007: 410–15.
33. A. C. Fischer-Cripps. *Nanoindentation*. New York: Springer, 2011.
34. S. Ko, D. Lee, S. Jee, H. Park, K. Lee, and W. Hwang. Mechanical properties and residual stress in porous anodic alumina structures. *Thin Solid Films* 515, 2006: 1932–37.
35. C. Dukhyun, L. Sangmin, L. Changwoo, L. Pyungsoo, L. Junghyun, L. Kunhong, P. Hyunchul, and H. Woonbong. Dependence of the mechanical properties of nanohoneycomb structures on porosity. *Journal of Micromechanics and Microengineering* 17, 2007: 501.
36. L. Vojkuvka, A. Santos, J. Pallarès, J. Ferré-Borrull, L. F. Marsal, and J. P. Celis. On the mechanical properties of nanoporous anodized alumina by nanoindentation and sliding tests. *Surface and Coatings Technology* 206, 2012: 2115–24.
37. K. Zhu, N. R. Neale, A. Miedaner, and A. J. Frank. Enhanced charge-collection efficiencies and light scattering in dye-sensitized solar cells using oriented TiO_2 nanotubes arrays. *Nano Letters* 7, 2007: 69–74.
38. G. J. Liu, X. R. Zhang, L. Mcwilliams, J. W. Talley, and C. R. Neal. Influence of ionic strength, electrolyte type, and NOM on As (V) adsorption onto TiO_2. *Journal of Environmental Science and Health Part A* 43, 2008: 430–36.
39. X. Quan, S. Yang, X. Ruan, and H. Zhao. Preparation of titania nanotubes and their environmental applications as electrode. *Environmental Science and Technology* 39, 2005: 3770–75.
40. J. Park, S. Bauer, K. A. Schlegel, F. W. Neukam, K. von der Mark, and P. Schmuki. TiO_2 nanotube surfaces: 15 nm—an optimal length scale of surface topography for cell adhesion and differentiation. *Small* 5, 2009: 666–71.
41. J. Park, S. Bauer, K. von der Mark, and P. Schmuki. Nanosize and vitality: TiO_2 nanotube diameter directs cell fate. *Nano Letters* 7, 2007: 1686–91.
42. S. Oh and S. Jin. Titanium oxide nanotubes with controlled morphology for enhanced bone growth. *Materials Science and Engineering: C* 26, 2006: 1301–06.

43. T. Shokuhfar, G. K. Arumugam, P. A. Heiden, R. S. Yassar, and C. Friedrich. Direct compressive measurements of individual titanium dioxide nanotubes. *ACS Nano* 3, 2009: 3098–102.
44. X. Tang and D. Li. Fabrication, geometry, and mechanical properties of highly ordered TiO_2 nanotubular arrays. *Journal of Physical Chemistry C* 113, 2009: 7107–13.
45. G. A. Crawford, N. Chawla, K. Das, S. Bose, and A. Bandyopadhyay. Microstructure and deformation behavior of biocompatible TiO_2 nanotubes on titanium substrate. *Acta Biomaterialia* 3, 2007: 359–67.
46. H. Hirakata, K. Ito, A. Yonezu, H. Tsuchiya, S. Fujimoto, and K. Minoshima. Strength of self-organized TiO_2 nanotube arrays. *Acta Materialia* 58, 2010: 4956–67.
47. Z. Wang, F. Li, N. S. Ergang, and A. Stein. Effects of hierarchical architecture on electronic and mechanical properties of nanocast monolithic porous carbons and carbon–carbon nanocomposites. *Chemistry of Materials* 18, 2006: 5543–53.
48. S. M. Gates, G. Dubois, E. T. Ryan, A. Grill, M. Liu, and D. Gidley. Adjusting the skeleton and pore structure of porous SiCOH dielectrics. *Journal of the Electrochemical Society* 156, 2009: G156–G62.
49. K. Maex, M. R. Baklanov, D. Shamiryan, F. lacopi, S. H. Brongersma, and Z. S. Yanovitskaya. Low dielectric constant materials for microelectronics. *Journal of Applied Physics* 93, 2003: 8793–841.
50. M. W. Lane, L. X. Hu, and T. M. Shaw. Environmental effects on cracking and delamination of dielectric films. *Device and Materials Reliability, IEEE Transactions on* 4, 2004: 142–47.
51. Y. Toivola, J. Thurn, and R. F. Cook. Structural, electrical, and mechanical properties development during curing of low-*k* hydrogen silsesquioxane films. *Journal of the Electrochemical Society* 149, 2002: F9–F17.
52. J. B. Vella, I. S. Adhihetty, K. Junker, and A. A. Volinsky. Mechanical properties and fracture toughness of organo-silicate glass (OSG) low-*k* dielectric thin films for microelectronic applications. *International Journal of Fracture* 120, 2003: 487–99.
53. A. A. Volinsky, J. B. Vella, and W. W. Gerberich. Fracture toughness, adhesion and mechanical properties of low-*k* dielectric thin films measured by nanoindentation. *Thin Solid Films* 429, 2003: 201–10.
54. W. C. Oliver, B. N. Lucas, and G. M. Pharr. Mechanical characterization using indentation experiments. In *Mechanical Properties and Deformation Behavior of Materials Having Ultra-Fine Microstructures*, ed. M. Nastasi, D. M Parkin, and H. Gleiter, 417–28. Springer, Netherlands, 1993.
55. M. G. Allen, M. Mehregany, R. T. Howe, and S. D. Senturia. Microfabricated structures for the insitu measurement of residual stress, Young's modulus, and ultimate strain of thin films. *Applied Physics Letters* 51, 1987: 241–43.
56. J. W. Hutchinson and Z. Suo. Mixed mode cracking in layered materials. *Advances In Applied Mechanics* 29, 1992: 63–191.
57. D. B. Marshall, B. R. Lawn, and A. G. Evans. Elastic/plastic indentation damage in ceramics: The lateral crack system. *Journal of the American Ceramic Society* 65, 1982: 561–66.
58. D. J. Morris and R. F. Cook. Indentation fracture of low-dielectric constant films: Part I. Experiments and observations. *Journal of Materials Research* 23, 2008: 2429–42.
59. D. J. Morris and R. F. Cook. Indentation fracture of low-dielectric constant films: Part II. Indentation fracture mechanics model. *Journal of Materials Research* 23, 2008: 2443–57.
60. S. Kim, Y. Toivola, R. F. Cook, K. Char, S-H. Chu, J-K. Lee, D. Y. Yoon, and H-W. Rhee. Organosilicate spin-on glasses: I. effect of chemical modification on mechanical properties. *Journal of the Electrochemical Society* 151, 2004: F37–F44.

61. Y. Toivola, S. Kim, R. F. Cook, K. Char, J-K. Lee, D. Y. Y, H-W. Rhee, S. Youl Kim, and M. Young Jin. Organosilicate spin-on glasses: II. Effect of physical modification on mechanical properties. *Journal of the Electrochemical Society* 151, 2004: F45–F53.
62. R. J. Nay, O. L. Warren, D. Yang, and T. J. Wyrobek. Mechanical characterization of low-*k* dielectric materials using nanoindentation. *Microelectronic Engineering* 75, 2004: 103–10.
63. D. J. Morris and R. F. Cook. In situ cube-corner indentation of soda–lime glass and fused silica. *Journal of the American Ceramic Society* 87, 2004: 1494–501.
64. D. J. Morris and R. F. Cook. Radial fracture during indentation by acute probes: I. Description by an indentation wedging model. *International Journal of Fracture* 136, 2005: 237–64.
65. D. J. Morris, A. M. Vodnick, and R. F. Cook. Radial fracture during indentation by acute probes: II. Experimental observations of cube-corner and vickers indentation. *International Journal of Fracture* 136, 2005: 265–84.
66. S. M. Wiederhorn. Fracture surface energy of glass. *Journal of the American Ceramic Society* 52, 1969: 99–105.
67. M. Amagai. Mechanical reliability in electronic packaging. *Microelectronics Reliability* 42, 2002: 607–27.
68. Y. Xiang, X. Chen, T. Y. Tsui, J-I. Jang, and J. J. Vlassak. Mechanical properties of porous and fully dense low-κ dielectric thin films measured by means of nanoindentation and the plane-strain bulge test technique. *Journal of Materials Research* 21, 2006: 386–95.
69. K. B. Yeap, K. Zeng, H. Jiang, L. Shen, and D. Chi. Determining interfacial properties of submicron low-*k* films on Si substrate by using wedge indentation technique. *Journal of Applied Physics* 101, 2007: 123531.
70. K. B. Yeap, K. Zeng, and D. Chi. Determining the interfacial toughness of low-*k* films on Si substrate by wedge indentation: Further studies. *Acta Materialia* 56, 2008: 977–84.
71. M. P. De Boer, and W. W. Gerberich. Microwedge indentation of the thin film fine line—I. Mechanics. *Acta Materialia* 44, 1996: 3169–75.
72. M. P. De Boer and W. W. Gerberich. Microwedge indentation of the thin film fine line—II. Experiment. *Acta Materialia* 44, 1996: 3177–87.
73. K. B. Yeap, F. Iacopi, H. Geisler, U. Hangen, and E. Zschech. Nanoindentation for reliability assessment of ULK films and interconnects structures. *Microelectronic Engineering* 106, 2013: 182–87.
74. E. P. Guyer and R. H. Dauskardt. 2005. Effect of porosity on reducing cohesive strength and accelerating crack growth in ultra low-k thin-films. *Paper Read at Proceedings of the 5th IEEE International Interconnect Technology Conference*, Burlingame, CA, USA, June.
75. H. Li, Y. Lin, T. Y. Tsui, and J. J. Vlassak. The effect of porogen loading on the stiffness and fracture energy of brittle organosilicates. *Journal of Materials Research* 24, 2009: 107–16.
76. F. Iacopi, G. Beyer, Y. Travaly, C. Waldfried, D. M. Gage, R. H. Dauskardt, K. Houthoofd et al. Thermomechanical properties of thin organosilicate glass films treated with ultraviolet-assisted cure. *Acta Materialia* 55, 2007: 1407–14.
77. Y. Lin, Y. Xiang, T. Y. Tsui, and J. J. Vlassak. PECVD low-permittivity organosilicate glass coatings: Adhesion, fracture and mechanical properties. *Acta Materialia* 56, 2008: 4932–43.
78. J. J. Vlassak, Y. Lin, and T. Y. Tsui. Fracture of organosilicate glass thin films: Environmental effects. *Materials Science and Engineering A* 391, 2005: 159–74.
79. E. P. Guyer and R. H. Dauskardt. Fracture of nanoporous thin-film glasses. *Nature Materials* 3, 2004: 53–57.
80. Y. Lin, T. Y. Tsui, and J. J. Vlassak. Water diffusion and fracture in organosilicate glass film stacks. *Acta Materialia* 55, 2007: 2455–64.

81. H. Li, T. Y. Tsui, and J. J. Vlassak. Water diffusion and fracture behavior in nanoporous low-*k* dielectric film stacks. *Journal of Applied Physics* 106, 2009: 033503.
82. Y. Lin, T. Y. Tsui, and J. J. Vlassak. Adhesion degradation and water diffusion in nanoporous organosilicate glass thin film stacks. *Journal of the Electrochemical Society* 157, 2010: G53–G56.
83. A. B. Hall, G. J. Irvine, S. M. Gates, and M. W. Lane. Corrosion of Si-O based porous low-*k* dielectrics. *Applied Physics Letters* 101, 2012: 202901.
84. T. Y. Tsui, A. J. McKerrow, and J. J. Vlassak. The effect of water diffusion on the adhesion of organosilicate glass film stacks. *Journal of the Mechanics and Physics of Solids* 54, 2006: 887–903.
85. M. W. Lane, J. M. Snodgrass, and R. H. Dauskardt. Environmental effects on interfacial adhesion. *Microelectronics Reliability* 41, 2001: 1615–24.
86. S. M. Wiederhorn and H. Johnson. Effect of electrolyte pH on crack propagation in glass. *Journal of the American Ceramic Society* 56, 1973: 192–97.
87. G. S. White, S. W. Freiman, S. M. Wiederhorn, and T. D. Coyle. Effects of counterions on crack growth in vitreous silica. *Journal of the American Ceramic Society* 70, 1987: 891–95.
88. T-S. Kim, T. Konno, and R. H. Dauskardt. Surfactant-controlled damage evolution during chemical mechanical planarization of nanoporous films. *Acta Materialia* 57, 2009: 4687–96.
89. D. A. Maidenberg, W. Volksen, R. D. Miller, and R. H. Dauskardt. Toughening of nanoporous glasses using porogen residuals. *Nature Materials* 3, 2004: 464–69.
90. G. M. Pharr. Measurement of mechanical properties by ultra-low load indentation. *Materials Science and Engineering A* 253, 1998: 151–59.
91. S. P. Timoshenko and J. N. Goodier. Theory of elasticity. *International Journal of Bulk Solids Storage in Silos* 1, 2011: 567–67.
92. B. R. Lawn, A. G. Evans, and D. B. Marshall. Elastic/plastic indentation damage in ceramics: The median/radial crack system. *Journal of the American Ceramic Society* 63, 1980: 574–81.
93. G. R. Anstis, P. Chantikul, B. R. Lawn, and D. B. Marshall. A critical evaluation of indentation techniques for measuring fracture toughness: I, direct crack measurements. *Journal of the American Ceramic Society* 64, 1981: 533–38.
94. P. G. R. B. R. Chantikul, G. R. Anstis, B. R. Lawn, and D. B. Marshall. A critical evaluation of indentation techniques for measuring fracture toughness: II, strength method. *Journal of the American Ceramic Society* 64, 1981: 539–43.
95. M. T. Laugier. Palmqvist indentation toughness in WC-Co composites. *Journal of materials science letters* 6, 1987: 897–900.
96. R. D. Dukino and M. V. Swain. Comparative measurement of indentation fracture toughness with Berkovich and Vickers indenters. *Journal of the American Ceramic Society* 75, 1992: 3299–304.
97. R. J. Anton and G. Subhash. Dynamic Vickers indentation of brittle materials. *Wear* 239, 2000: 27–35.
98. J. Malzbender, G. de With, and J. M. J. den Toonder. Elastic modulus, indentation pressure and fracture toughness of hybrid coatings on glass. *Thin Solid Films* 366, 2000: 139–49.
99. S. J. Bull. Nanoindentation of coatings. *Journal of Physics D: Applied Physics* 38, 2005: R393.
100. X. Chen and J. J. Vlassak. Numerical study on the measurement of thin film mechanical properties by means of nanoindentation. *Journal of Materials Research* 16, 2001: 2974–82.
101. R. Saha and W. D. Nix. Effects of the substrate on the determination of thin film mechanical properties by nanoindentation. *Acta Materialia* 50, 2002: 23–38.

102. W. C. Oliver and G. M. Pharr. Improved technique for determining hardness and elastic modulus using load and displacement sensing indentation experiments. *Journal of Materials Research* 7, 1992: 1564–83.
103. J. L. Hay, M. E. O'Hern, and W. C. Oliver. Tie importance of contact radius for substrate-independent property measurement of thin films. *MRS Proceedings* 522, 1998: 1–27.
104. G. Huajian, C. Cheng-Hsin, and L. Jin. Elastic contact versus indentation modeling of multi-layered materials. *International Journal of Solids and Structures* 29, 1992: 2471–92.
105. H. Li and J. J. Vlassak. Determining the elastic modulus and hardness of an ultra-thin film on a substrate using nanoindentation. *Journal of Materials Research* 24, 2009: 1114–26.
106. S. Zhang, D. Sun, Y. Fu, and H. Du. Toughness measurement of thin films: A critical review. *Surface and Coatings Technology* 198, 2005: 74–84.
107. X. Li, D. Diao, and B. Bhushan. Fracture mechanisms of thin amorphous carbon films in nanoindentation. *Acta Materialia* 45, 1997: 4453–61.
108. X. Li and B. Bhushan. Measurement of fracture toughness of ultra-thin amorphous carbon films. *Thin Solid Films* 315, 1998: 214–21.
109. B. Bhushan. Chemical, mechanical and tribological characterization of ultra-thin and hard amorphous carbon coatings as thin as 3.5 nm: Recent developments. *Diamond and Related Materials* 8, 1999: 1985–2015.
110. J. Malzbender and G. de With. Energy dissipation, fracture toughness and the indentation load–displacement curve of coated materials. *Surface and Coatings Technology* 135, 2000: 60–68.
111. S. Meille, M. Lombardi, J. Chevalier, and L. Montanaro. Mechanical properties of porous ceramics in compression: On the transition between elastic, brittle, and cellular behavior. *Journal of the European Ceramic Society* 32, 2012: 3959–67.
112. E. W. Andrews, G. Gioux, P. Onck, and L. J. Gibson. Size effects in ductile cellular solids. Part II: Experimental results. *International Journal of Mechanical Sciences* 43, 2001: 701–13.
113. D. Choi, S. Lee, S. Kim, P. Lee, K. Lee, H. Park, and W. Hwang. Dependence of adhesion and friction on porosity in porous anodic alumina films. *Scripta Materialia* 58, 2008: 870–73.
114. C. Walter and C. Mitterer. 3D versus 2D finite element simulation of the effect of surface roughness on nanoindentation of hard coatings. *Surface and Coatings Technology* 203, 2009: 3286–90.
115. J. Menčík, and M. V. Swain. Errors associated with depth-sensing microindentation tests. *Journal of Materials Research* 10, 1995: 1491–1501.

5 Toughness of Laser-Treated Surface Layers Obtained by Alloying and Feeding of Ceramic Powders

Tomasz Tański, Ewa Jonda, Krzysztof Labisz, and Leszek A. Dobrzański

CONTENTS

5.1 Literature Overview 226
5.1.1 Introduction 226
5.1.2 Hot Work Tool Steels and Their Application 226
5.1.2.1 Heat Treatment 230
5.1.2.2 Production Technology 231
5.1.3 Lasers and Their Application in Material Engineering 233
5.1.3.1 Physical Basics of Lasers 233
5.1.4 Surface Layer Systems Characteristics 237
5.1.5 Wear of Parts and the Machines 241
5.2 Investigation Procedure 247
5.2.1 Aim of the Work 247
5.2.2 Material for Investigation 247
5.2.3 Investigation Methodology 249
5.3 Technical Application 252
5.4 Microstructure and Properties 254
5.4.1 Structural Characteristic of the Surface 254
5.4.1.1 Morphology and Microstructure of the Laser-Treated Surface Layer 261
5.4.1.2 Phase and Chemical Composition of the Surface Layers 282
5.4.2 Toughness Measurements of the Obtained Surface Layers 287
5.4.2.1 Hardness Measurement 287
5.4.2.2 Microhardness Measurement 292
5.4.2.3 Wear Resistance Measurements in the Metal–Metal Arrangement 296

5.4.3 Thermal Fatigue.....300
5.5 Summary and Conclusion.....308
References.....310

5.1 LITERATURE OVERVIEW

5.1.1 Introduction

Properties of cooperating elements are primarily dependent on two factors: the internal microstructure of the analyzed material and the structure of the outer surface, which is in direct contact with both the chemical and mechanical environmental factors, involving interaction with machining tools as well as with collaborating surfaces of other elements. The nature of the surface morphology and its properties have a significant impact on the functional characteristics of the finished product. The surface layer of the material is characterized by different properties of the core material, which has a significant impact on a variety of mechanisms occurring within the surface layer, including, among others, friction, fatigue, corrosion resistance, erosion, diffusion, and conductivity, and decide on possible applications of surface-treated components. Often due to technological and economic requirements the substrate material is chosen in such a way as to satisfy the general objectives concerning the strength of the finished product, and special surface treatment is applied to increase the functional properties or to enhance protection against damage. During the design process of machine parts or equipments, particular attention should be paid to the resistance of the working elements on both tribological (mechanical, fatigue, adhesion, abrasion) and nontribological damage (corrosion, erosion, diffusion, ablation). It is, therefore, important to pay attention during the design process and material choice to the particular environmental processes that can have an influence on the wear destruction of the produced device. Regeneration of the damaged surface of the components or the production of new materials, including the coating gives the opportunity to discover previously unidentified structural mechanisms, as well as extend the range of existing knowledge. Characteristics of these mechanisms and interdependencies are not only of cognitive nature but also allow a broader methodological and application perspective of the described grades of hot work tool steels. This is important especially when there is a need for the production of new engineering materials or regeneration of the existing ones.

This work presents the investigation results of the microstructure and mechanical properties as well as functional properties of the surface layers of the selected hot work tool steel grades after heat and surface treatment.

5.1.2 Hot Work Tool Steels and Their Application

Among all the applicable materials, the tool steels represent the largest and most widely used group of tool materials. Intensively developing industry sets increasingly higher demands on tool materials, ensuring that the geometrical stability of tools made from these materials, as well as resistance to carrying loads without plastic deformation and wear resistance, which is usually dependent on the hardness of steel. The service life of tools depends on the proper selection of the material in terms of

chemical composition and structure as well as the proper design, implementation, and correct operation [1,2]. Tools made from this group of steels are used for hot forming, such as dies for presses, pins, punches, dies, anvils, and cutters. There are difficult working conditions for this type of material, since the working surfaces of the tools are subjected to tempering temperature and rapid changes, as it is in contact with hot, processed materials that are subsequently cooled. Moreover, they are exposed to high pressures; even if the force of hot plastic deformation is smaller compared to that which occurred during the cold plastic deformation, hot work tool charge is charged with forces of considerable value, and the character of the pressure is often dynamic, for example, during forging in matrix. Alloying hot work tool steels used for tools operate in the temperature range of 250–700°C [3–9]. A characteristic feature of hot work tool steels is the average carbon concentration of 0.30–0.6%. These steels generally contain a significant concentration of alloying elements (3–15%), such as Cr, V, Mo, and W, and sometimes also Si, Ni, Co, Mn, and B (Table 5.1) [7,10–13]. The main alloying elements are Cr, Mo, W, and V, which are dissolved during the austenitizing process causing precipitation of MC and M2C carbides, responsible for the effect of hardness increase during tempering [10,14,15]. This is particularly important because hot work steels due to the properties stability are tempered at a temperature of about 550°C higher than the operating temperature of the tool [5,6,16].

Chromium as an alloying additive in tool steels is responsible for increasing hardenability, and in the case of higher concentration it also improves oxidation resistance and heat resistance [15,17,18]. Tungsten as an alloying additive in steels considerably increases the resistance to tempering temperatures. It also increases the mechanical properties at elevated temperature, however, it greatly reduces the thermal conductivity and plastic properties, and thus the thermal fatigue resistance. Silicon in a concentration of up to about 1% results in some grades of steels with an increase in the oxidation resistance at temperatures up to 800°C. The addition of vanadium increases

TABLE 5.1
Approximate Chemical Composition of the Hot Work Tool Steels According to PN-EN ISO 4957:2004

	Average Mass Concentration of the Elements (%)						
Steel Grade	**C**	**Si**	**Mn**	**Cr**	**Mo**	**V**	**Other**
55NiCrMoV7	0.55	0.25	0.75	1.0	0.45	0.10	Ni: 1.7
32CrMoV12-28	0.32	0.25	0.30	3.0	2.75	0.55	–
X37CrMoV5-1	0.37	1.00	0.40	5.2	1.30	0.40	–
X38CrMoV5-3	0.38	0.40	0.40	5.0	2.95	0.50	–
X40CrMoV5-1	0.40	1.00	0.40	5.2	1.35	1.00	–
50CrMoV13-15	0.50	0.50	0.70	3.3	1.50	0.25	–
X30WCrV9-3	0.30	0.25	0.30	2.9	–	0.40	W: 9.0
X35CrWMoV5	0.35	1.00	0.35	5.1	1.45	0.35	W: 1.4
38CrCoWV18-17-17	0.38	0.35	0.35	4.4	0.40	1.90	W: 4.2 Co: 4.3

Source: Polish standard: Chemical composition of hot work tool steels PN-EN ISO 4957:2002.
Content: P ≤ 0.03%, S ≤ 0.02%.

the erosive wear resistance of steel. Nickel is used as an additive for steels for forging tools to achieve an increase in hardenability, which can therefore be replaced by other elements. Steels with nickel addition reveals very good impact strength at room temperature, while at elevated temperature the impact strength can be compared to steel without the addition of nickel, hence the use of nickel is often not reasonable [6,7].

The working surfaces of the tools are subjected to frequent temperature changes, which are the result of cyclic contact with deformable material heated to a high temperature and cooled after forming is completed. This causes thermal fatigue and is the primary reason for the wear of the hot work tools [6,9]. As a result of disadvantageous developments affecting the tool during its operation, there occurs a mesh of surface cracking. These cracks are caused by thermal and mechanical stress and are formed mainly at grain boundaries, which is the reason for spalling of grains and formation of stress concentration. Increase of silicon and chromium concentration counteracts the effect of the formation of surface crack formation, since these elements increase the fatigue strength, resistance to oxidation, and high temperature strength, reducing the wear processes of the tool. They do not ensure a high strength at elevated temperature of the steel without the addition of other alloying elements [5]. While using the tool there can also occur thermo-mechanical fatigue in case of overlapping of thermal fatigue and stress caused by, for example, external pressure or friction [13,18].

Taking into account the working conditions, tools made from the hot work tool steel should be characterized by the following properties [5,7,8,19–22]:

- Fatigue resistance
- Wear resistance in elevated temperature (particularly in case of the metal–metal arrangement)
- High toughness and resistance to the notch influence (low carbon concentration)
- Erosion resistance
- Corrosion and oxidation resistance of the treated material
- High heat transfer rate
- Low thermal expansion coefficient
- Low possible volume changes during heat treatment (tempering, austenitization in mediums with low cooling intensity rates, requires high hardenability)
- Strength in the range between 850 and 1000 MPa
- High resistance to elevated temperature during tempering
- High ductility (resistance to cracking)
- Structure, shape, and volume stability

Hot work tool steels currently produced and applied cover a large number of grades. Taking chemical composition as a criterion several basic groups can be distinguished [6,7]:

- Cr–Mo–V
- Cr–W–V
- Cr–Mo–W–V

- Multicompound
- Low alloyed

Chromium–molybdenum steels containing vanadium are a very important group of hot work tool steels. They are used to produce a variety of tools for hot work. These steels are characterized by a high hardenability and tempering resistance, good toughness and oxidation resistance, as well as very good thermal fatigue resistance [7,23]. Chromium–molybdenum steels have higher thermal conductivity compared to the thermal conductivity of steels containing tungsten addition. They are also more resistant as those steels to extreme temperature changes [5,9]. Chromium steels with the addition of tungsten, molybdenum, and vanadium exhibit even greater resistance to tempering, compared to steels without tungsten addition, but lower ductility and thermal fatigue resistance [7].

Tungsten steels are currently losing their technical importance. They are characterized by lower thermal fatigue resistance and lower ductility, but reveals instead greater abrasion resistance and are more resistant to tempering at elevated temperature compared to the properties of chromium–molybdenum steels. Multicomponent steels contain several percentage of chromium, tungsten, and molybdenum, up to 2% vanadium, cobalt, and often titanium or niobium as microadditives. This is a relatively new group of steel, still being investigated concerning the chemical composition and resulting mechanical properties [7,24,25]. In the low-alloy steels the alloying elements concentration does not exceed 5%. They exhibit low resistance to tempering and thermal fatigue, but their impact strength is increased compared to steels containing more kinds of alloying elements, especially those that are responsible for the occurrence of carbide phase.

Hot work steels are often melted using argon blowing in the ladle, vacuum refining, or electroslag remelting. These methods are beneficial for increasing the purity and homogeneity of the steel, and to increase its functional properties. Crystallization takes place after casting of the steel in the conventional molds, and during remelting crystallization occurs in intensively cooled crystallizers. Phase transformation during solidification and subsequent cooling of ingots depend on the chemical composition of steel as well as the crystallization conditions. During crystallization of these steels, most often ferrite crystallization occurs directly from the liquid solution, and then a peritectic reaction, resulting finally in the formation of austenite. Depending on the concentration of carbon and other alloying elements and part or even the entire austenite can also be separated directly from the liquid. Lowering the temperature of steel in the solid state causes the decomposition of austenite to ferrite and carbides. During crystallization there occurs a change of chemical concentration of the liquid components and precipitation of austenite crystals. This causes the macro- and microsegregation of the chemical composition in the whole ingot volume. After conventional casting as the last part solidifies the upper and middle part of the ingot, this area has the highest difference of the chemical composition compared to the surface layer. These steels in as-cast state, despite microsegregation, reveal also macrosegregation of the chemical composition within the particular grains. After solidification of the steel, the level of segregation can be evaluated, by determining the concentration of alloying elements in the core material and at the dendrite boundaries [15,26–28].

5.1.2.1 Heat Treatment

Hot work tool steels are provided in a softened state, ensuring good workability. Tools made by machining are subjected to a heat treatment consisting of quenching and high-temperature tempering. Table 5.2 shows the heat treatment conditions and hardness of hot work tool steels after heat treatment. In order to reduce thermal stress, a multistage heating is applied to the austenitizing temperature. To protect the tool against decarburization and oxidation, heating and tempering at a temperature above 650°C takes place in furnaces with protective atmospheres. Austenitizing temperature of hot work tool steels is in the range of 840–1140°C and is selected to prevent excessive growth of the primary austenite grains, because of the decrease of ductility of the steel [15,29–33].

During heating to the austenitizing temperature, after exceeding the A_{c1} temperature there begins the transformation of ferrite to austenite. At first the M_3C carbides dissolve in austenite containing mainly iron and manganese. As a result of increase of the austenitizing temperature there occurs subsequent dissolution of $M_{23}C_6$ and M_7C_3 carbides containing mainly chromium, followed by the dissolution of M_6C carbides as well as finally of the interstitial MC and M_2C phases, containing mainly tungsten. Austenite grain embryos occurring at grain boundaries between the ferrite and carbides grow with time and because of temperature increase. Carbides, which are dissolved in the resulting austenite cause its enrichment in carbon and other alloying elements [15,34,35].

Optimal austenitizing conditions ensure proper dissolution of most of the carbides in austenite, whereby a desired hardenability of the steel will be achieved, and after quenching—a structure consisting of lath martensite, saturated with the alloying elements and carbon. Such a structure allows during tempering the precipitation of the type of carbides of the type M_4C_3, M_2C, M_7C_3 with occurrence of the secondary hardness effect [6,15,36].

TABLE 5.2
Heat Treatment Conditions and Hardness of Hot Work Tool Steels According to the Standard

	Temperature (°C)		
Steel Grade	**Quenching**	**Tempering**	**Hardness, HRC**
55NiCrMoV7	850	500	42
32CrMoV12-28	1040	550	46
X37CrMoV5-1	1020	550	48
X38CrMoV5-3	1040	550	50
X40CrMoV5-1	1020	550	50
50CrMoV13-15	1010	510	56
X30WCrV9-3	1150	600	48
X35CrWMoV5	1020	550	48
38CrCoWV18-17-17	1120	600	48

Source: Polish standard: Chemical composition of hot work tool steels PN-EN ISO 4957:2002.

The alloying elements, except cobalt and aluminum, reduce the M_s temperature, influencing thereby the morphology of the formed martensite, which occurs in most of the hot work tool steels in the form of laths, wherein within a single austenite grains there is formed a series of packages separated by wide-angle martensite boundaries. Inside the packages, the individual martensite laths are separated by low angle boundaries or twin-like boundaries. Since the martensite transformation does not practically reach completion, in the structure of martensite there remains austenite dependent on the chemical composition and the quenching conditions of the steel. There is also the possibility of transformation of the supercooled austenite to bainite-type structure [7,15,37–39].

Tempering is performed directly after quenching, without lowering the temperature of the tools below approximately 80–200°C. In order to facilitate the transformation of retained austenite repeatable tempering is applied, sometimes three times. The tempering temperature is chosen on the basis of the analysis of tool operating condition and information about changes of the steel properties as a function of tempering temperature. Most often, the tempering temperature corresponds to the temperature of the secondary hardness effect—that is, 50–100°C higher. As a result of this, the hardness decreases slightly and is associated with an increase of toughness and thermal fatigue resistance of steel [5,15,18,40]. The highest influence on phase transformation during tempering of steel has the density of decomposition products of the supercooled austenite enriched with the alloying elements and carbon. In terms of low-temperature annealing, the transformation kinetics depends mainly on carbon supersaturation of the martensite. Delay of the transformation of retained austenite caused by chromium, silicon, and manganese is responsible for an increase of strength, while after medium-temperature tempering vanadium and molybdenum have less impact. During high-temperature tempering of steels, which do not contain carbide-forming elements there occurs further precipitation and coagulation and alloying cementite, recovery, and recrystallization of the matrix. This results in a continuous decrease of hardness of the steel, together with the increase of tempering temperature. Carbide-forming elements such as chromium, tungsten, molybdenum, and vanadium at a temperature of about 500°C achieve sufficiently high growing rates to form $M_{23}C_6$, M_7C_3, M_6C, M_2C, and MC type particles.

This carbides are formed by “in situ” conversion, meaning that the primary carbide achieving a sufficiently high concentration of other alloying elements, transforms to a mesh-shaped phase with different crystalline structure, such as M_7C_3 combining with M_3C, while during the precipitation of interstitial simple phases, for example, M_2C, there occurs independent nucleation by dissolving one of the solid solution carbides and subsequent precipitation of a new carbide. Figure 5.1 shows the effect of tempering temperature on hardness of the hot work tool steels [11,13,15].

5.1.2.2 Production Technology

Hot work tool steels enable the hot-forming of work-pieces made of iron and nonferrous metals as well as alloy derivatives at high temperatures. They are utilized in processes such as pressure die casting, extrusion, and drop forging as well as in tube and glass manufacturing.

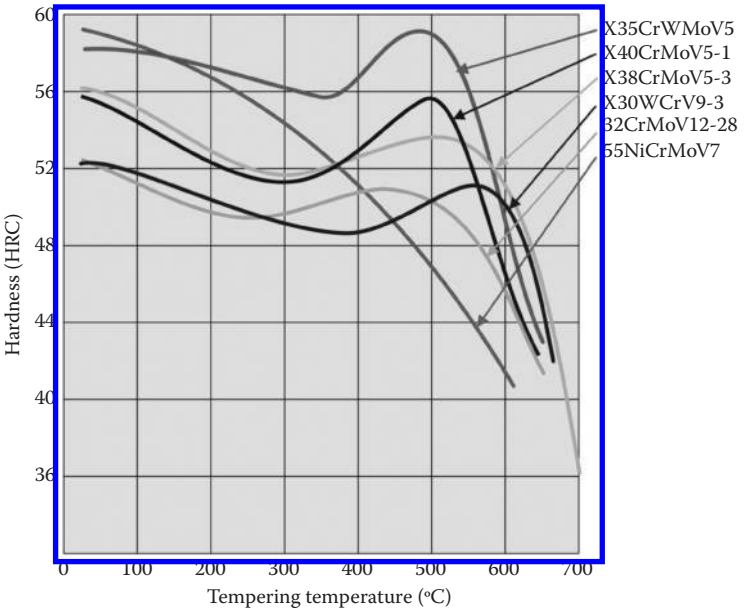


FIGURE 5.1 Influence of the tempering temperature on hardness of the hot work tool steels. (From Dobrzański. L.A.: Basics of material science metal science. *Engineering Materials with Basics of Material Design*. WNT, Gliwice—Warszawa, 2006.)

Tools made from hot work tool steels are not only subjected to constantly high temperatures when employed, but also to fluctuating thermic loads occurring where the tool surfaces come into contact with the materials to be processed.

The significance of tool steels extends far beyond what is generally perceived as commonplace. Nearly, all the objects that surround us and encounter on a daily basis are manufactured with the help of tool steels. The application spectrum for hot work tool steels is extensive and the tools manufactured are used in the most diverse areas. These steels enable the hot-forming of work-pieces made of iron and nonferrous metals as well as alloy derivatives at high temperatures. They are utilized in processes such as pressure die casting, extrusion, and drop forging as well as in tube and glass manufacturing.

To withstand such service conditions, red hardness and high resistance to softening by tempering or drawing action are essential criteria of hot work steels. The amount of thermal shock in service is of extreme importance in this whole family of hot work tooling. In operations such as those encountered in piercing, the temperature is high and contact time long; therefore, to prevent softening by annealing, the tool face must be cooled between each piercing operation. Since the most intense heating is on the working surface, this cyclic heating and cooling has the effect of expanding and contracting the surface layer. To withstand such service, the steel must be very ductile through the entire temperature range encountered in service; otherwise, the surface of the tool develops heat checks.

5.1.3 Lasers and Their Application in Material Engineering

A huge interest in the application of lasers in industry is mainly due to the properties of laser radiation, which enables the exact execution of multiple processing operations on different materials, ranging from materials that are difficult to machine, such as diamonds, hard metal, as well as soft foam, and brittle ceramic, with a precision and performance often considerably higher compared to the earlier used method [64,17].

Lasers are a source of time- and space-coherent light. Compared to the light emitted by thermal sources, laser light is particularly useful in materials science, and first of all in surface engineering because of its coherency, intensity, and the possibility of generating short- and ultrashort pulses [41–43].

The term laser is an acronym of the description "Light Amplification by Stimulated Emission of Radiation."

Laser is a device generating a beam of coherent electromagnetic radiation in the wavelength range from ultraviolet to infrared, where in its active medium, by reversing the energy levels of electrons, there occur a strengthening phenomenon by the stimulated emission of radiation. Optical light waves spread out in an irregular manner, while the laser light is coherent, that is, consists only of rays of the same wave length, running in the same direction and synchronized with each other. Light wave propagates from the source in various directions, while laser beam does not expand and remains consistent even at very long distances [44–50].

Some of the characteristic properties of light, difficult or even impossible to achieve in other electromagnetic radiation sources with other wave length that the visible light for human eyes, are [51,52]

- Very small width of the emission line
- Polarization of the light beam
- Coherence of the beam in time and space
- Monochromatic beam
- A very small divergence of the laser beam
- High power density of the beam

5.1.3.1 Physical Basics of Lasers

Matter in condensed states is formed from a large number of atoms or particles coming into direct close contact. Mutual influence of these basic matter elements, that is, the interatomic or intermolecular forces ensures consistency of the matter. The result of these forces are—in most of the materials used in material engineering—its characteristic for a given atoms or molecules, physical and chemical properties. For this reason, because of the existence of different physical basics there exists three types of interaction of photons with atoms [43,46,53]:

- Stimulated absorption
- Stimulated emission
- Spontaneous emission

One of the simplest quantum systems is a two-level system, that is, such a system where may occur emission and absorption processes of radiation between two discrete energy levels [54,55]:

- Basic state with energy E_0
- Excited state with energy E_1

Each atom is located at the ground energy state E_0, and can absorb a certain portion of energy [46,56]:

$$\Delta E = h\nu_{01} = \frac{h \cdot c}{\lambda_{01}} = E_1 - E_0 \tag{5.1}$$

where

h—Planck's constant, ($h = 6625 \times 10^{-34}$ J · s)
ν_{01}—wave frequency, Hz
c—propagation rate of radiation in vacuum, ($c = 2998 \times 10^8$ m/s)
λ_{01}—wavelength, nm

The transition of an atom from a lower level to a higher one occurs after external energy delivery by a radiation quantum (Figure 5.2). The atom is then raised to a state of higher energy E_1. Excited atom stays in this state for some time. Lifetime of such an energy state is inverse to the so-called spontaneous emission constant, meaning probability of a spontaneous transition from level 1 to level 0 within 1 s. The lifetime depends on the type of atoms as well as the particular energy level [52,53,57]. This phenomenon is known as stimulated absorption.

Typical lifetime of an atom in the excited state is very short, and if during this very short time, no photon will be able to "force" the excited atom to the return to a lower level, then the atom spontaneously, without any external influence, will

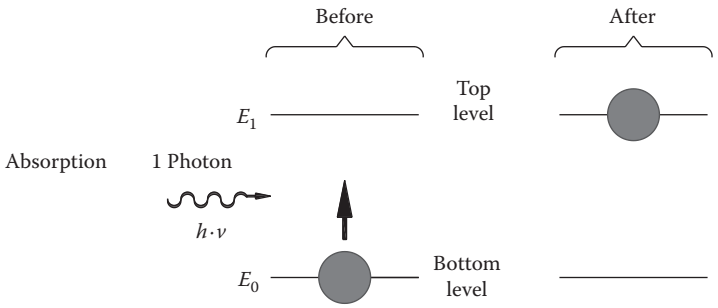


FIGURE 5.2 Quantum transition between two levels presenting the phenomenon of stimulated absorption (From Kusiński J.: *Lasers and its Application in Material Engineering.* Scientific publisher Akapit, Kraków, 2000.) is also involved in the emission and maintaining of thermally unbalanced state. (From Major B.: *Ablation and Sedimentation with Pulse WN.* Akapit, Kraków, 2000.)

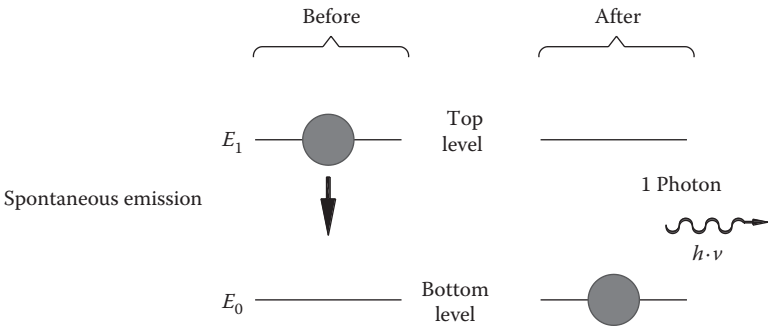


FIGURE 5.3 Quantum transition between two levels illustrating the phenomenon of spontaneous emission. (From Kusiński J.: *Lasers and its Application in Material Engineering.* Scientific publisher Akapit, Kraków, 2000.)

go to its ground energy state of E_0, emitting an identical quantum of radiation that was previously absorbed. This is a phenomenon of spontaneous emission of radiation (Figure 5.3). Due to the random nature of the spontaneous decay of the excited atoms, photons are emitted by different particles of matter where the radiation is incoherent. There is a difference compared to other light sources, where the radiation has a spontaneous character of the emission, whereas in lasers there is used the stimulated emission, although in all quantum phenomena spontaneous radiation plays an important role in strengthening and initiation of vibration excitation; the spontaneous radiation is also involved in the emission and maintaining of thermally unbalanced state [42].

If the quantum system in the excited state (with the energy E_1) is affected by the same photon of radiation, which has been previously absorbed (Figure 5.4), such an emission is called stimulated emission [42,46].

Only in this case is there a forced transition of the system to the ground energy state E_0 and there occurs two photons of radiation: incident and emitted, with the same properties. Both photons move in the same direction. Photons can excite further

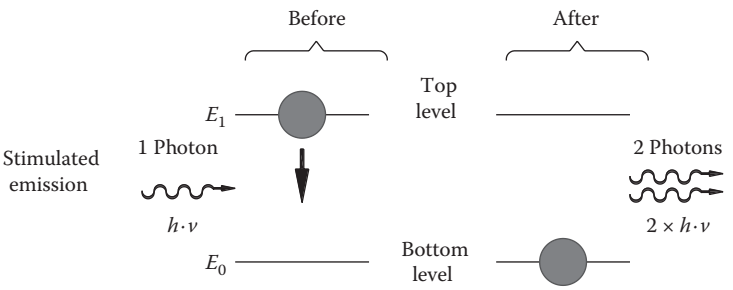


FIGURE 5.4 Quantum transition between two levels illustrating the phenomenon of stimulated emission. (From Kusiński J.: *Lasers and its Application in Material Engineering.* Scientific publisher Akapit, Kraków, 2000.)

photons, and when the conditions are right, the process can grow exponentially. There is, therefore, a process of strengthening of the radiation. Between spontaneous emission and stimulated emission, there are clear differences. The spontaneous emission involves the creation of a single photon, while the effect of stimulated emission is always a second photon. The phenomenon of stimulated emission is the basis for the operation of all amplifiers and quantum generators.

Stimulated emission is based on preliminary excitation of the active material by transferring the atoms and particles to an excited state, and then by the simultaneous emission of the energy accumulated. In the case of stimulated emission of radiation, the incident and emitted have the same frequency, the same phase as well as plane of polarization and direction of propagation. Radiation of such a system, has the properties of a single coherent radiation, that is, propagates exactly in the same direction, has the same frequency, is in phase and is polarized in the same way. This kind of radiation emits lasers and is commonly known as laser radiation [42,58].

Under the conditions of thermodynamic equilibrium, electrons of a set of quantum systems occupy energy levels that are closer to the nuclei in atoms and molecules; occupying higher energy levels are less intensive. To achieve the laser emission, it is necessary that the two conditions are fulfilled [43]:

- A population inversion of the energy levels
- Creation of conditions promoting stimulating resonance

The population inversion affects the redistribution of the energy levels of a set of quantum systems suitable for thermodynamic equilibrium. There should be more atoms in an excited state than in ground state, because only then is it possible to get a surplus of emitted photons over the absorbed ones. It is, therefore, necessary to inverse the occupations of atoms, that is energy rich set of quantum systems, called active laser medium. One method of obtaining the population inversion involves the irradiation of the laser active medium. Excitation occurs due to the absorption of pumping radiation by the active medium. This process is called optical pumping. The population inversion can also be obtained by electrical pumping or in the case of high-power gas lasers by gas-dynamic pumping [43,59].

Laser radiation is distinguished by the following features [60–63]:

- Beam emitted in the one given direction determined by the optical resonator axis.
- Minimum beam divergence, because the laser light is coherent, the divergence angle is small in the range of a few mill radians.
- Radiation intensity distribution in the beam cross section, for the basic type of vibration—basic module marked TEM_{00} (transverse electro-magnetic) described by the Gauss function, for which there is the largest radiation intensity on the axis, for the multimode operation this distribution is modified.
- A beam capable of focus with a simple optical system achieving a spot with a small diameter, typically from 10 to 300 μm and enhanced power density.

- The possibility of continuous and pulsed laser working, for which even higher power density can be achieved.
- High power density associated with the occurrence of a large electric field of the electromagnetic wave, which may be accompanied by an electric discharge and ionization of its optical properties.
- The wavelength of the radiation emitted by various lasers from about 200 nm to 10.6 μm. In the treatment of materials primarily emitting lasers have been used with a wavelength ranging from about 200 nm to 10.6 μm.
- The occurrence of highly monochromatic radiation, where the spectral width measured in the frequency scale Δv or in wavelength scale $\Delta\lambda$ is very small.
- Coherent radiation, temporally and spatially, that is, there is a fixed phase relationship to the beam and time between any points of its cross section.
- High radiation energy, in case of pulse laser energy the density of pulses can even reach 10^4–10^7 W/mm^2, at the pulse time of the order of few milliseconds, and the power density reaches 10^9–10^{11} W/mm^2 by pulse duration of few picoseconds. In the case of continuous laser, the power density is obtained in the range from 10^3–10^7 W/mm^2.

Technologies of laser surface treatment of engineering materials:

- Technologies of laser heat treatment, for example, surface hardening, annealing
- Laser surface melting and alloying
- Laser cladding
- Rapid prototyping technologies
- Laser cleaning and surface layer removing
- Laser soldering
- Marking, punching, engraving, and laser cutting
- Using of laser radiation for synthesis of materials–laser ablation, including laser chemical vapor deposition (LACVD) as well as laser physical vapor deposition (LAPVD)
- Laser appliance in photovoltaic
- Laser technologies in the medicine

5.1.4 Surface Layer Systems Characteristics

As a result of the rapid development of technology there is an increase of the requirements for materials in terms of mechanical properties, corrosion, and erosion resistance or resistance to high temperatures. Analyzing a given element in terms of its internal structure as well as working conditions, it should be noted that the product properties are dependent on two factors: the internal structure of the material from which it is made and the condition of the outer surface having a direct contact with environmental factors during manufacturing process and also service life of working

surface. Also, economic considerations require the use of the surface layers, which reveals adequate properties of the product, using at the same time for production cheap materials for the core element from which such high mechanical properties are generally not required.

The total cycle of the product life depends not only on the capabilities of the mechanical loads throughout the active cross section of the material, in case of metals and its alloys mostly heat treated, or its physical and chemical properties, but also very often depends on the structure and properties of the surface layers. To provide the required functional properties of the produced elements with the desired properties can be achieved by manufacturing of elements on the basis of existing materials, as well as development of new materials with unknown properties, and in many cases through the use of surface engineering techniques that allow the development of microstructure, phase, and chemical composition, internal stresses in the surface layers of the treated material, and thus the formation of their functional properties [75–77].

Despite the fact that the top layer of elements cannot be performed independently of the substrate, however, the core material requirements of the product are generally different from that of the surface layer.

The outer layer is most often determined as the outside layer of an object, where phenomena occur mainly associated with its treatment and service. The top surface layer is formed spontaneously as a result of the applied technology to the given product, or is produced artificially in a given element. The structure and properties of the surface layer has a significant impact on the behavior of the product during operation and service. The basic features of the surface layer, which are roughness, structure, and physicochemical properties depend on the technology and the surface treatment of the element and also depend on the applied technologies ensuring special properties as well as the type of the core material. These features may change spontaneously during operation and service or under the influence of external factors. Functional properties of the surface layer depends also on the type of the core material as well as on its initial state and the type of treatment applied. From the point of view of surface layer wear resistance, the most important parameters are surface morphology, structure of the material, mechanical properties, and thermal and chemical characteristics. Key properties of the surface layer are shown in Figure 5.5. Wear of the surface layer of engineering materials is widespread and a widely recognizable phenomenon. There are many variations of this process, as well as a number of factors that are responsible for its occurrence. The process of wear is a complex phenomenon, considered as an interdisciplinary field connecting many disciplines, including mechanics, physics, chemistry, automation, material engineering, economics, biology, construction, information technology, and others. The variety of forms of wear tends the modern scientists to conduct an extensive research on the various processes that affect the damage of surface layers. Most often investigated wear mechanisms are tribological ones, caused by friction-induced processes, with attention to the fact that they account for about 80% of all cases of currently existing wear mechanisms. Wear, or damage of the surface of a solid state material, refers primarily to the process of machinery and equipment exploitation and as a result the necessary servicing or in extreme cases, to replace the damaged item. In

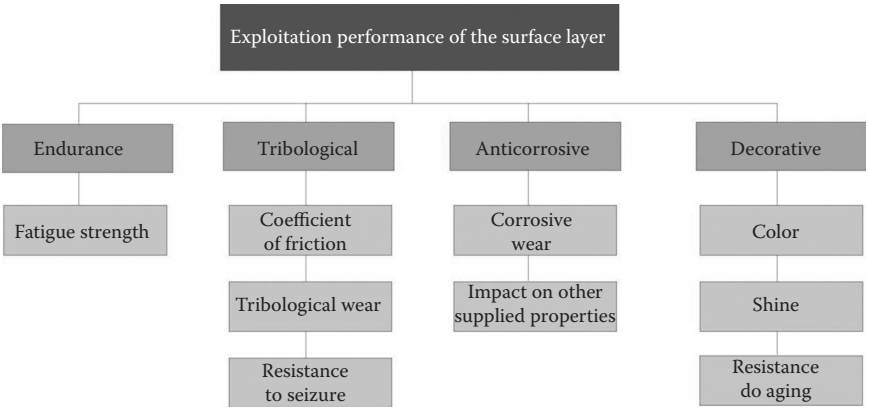


FIGURE 5.5 The most important exploitation properties of the surface layer. (From Dobrzański. L.A.: Basics of material science metal science. *Engineering Materials with Basics of Material Design*. WNT, Gliwice–Warszawa, 2006.)

designing the various machinery elements or even the whole device attention should paid particularly to the working elements and its resistance to damage, both tribological (mechanical, fatigue, adhesion, and others) and nontribological (corrosion, diffusion, cavitation, and others). Therefore, as an important step in the design process is the selection of material, that is often made due to occurred destructive processes in the environment of the working element. Attention should also be paid to the fact that the production of new materials, including the coated ones gives the possibility to discover pioneering, yet unidentified mechanisms of wear or identify a broader spectrum of already existing ones [34,35,76,78].

Due to the variety of core materials and a wide range of processing parameters, it is difficult to develop a general model of the surface layer. There are, however, a number of simplified models, the simplest of which is a three-zone model proposed by Kolm, shown in Figure 5.6.

The outer zone is a layer of particles of natural origin, mixed together with spalled particles of the core material. The outer zone is coated, from the direction of the ambient medium in the form of adsorbed gases such as oxygen, nitrogen, and water steam molecules. The central zone has a strong distortion of the particles in comparison to the core material. This zone is crucial for the functional properties of a surface. The internal zone is composed of no deformed particle, with a structure different from those of the core material, and is caused by changes that occur, for example, under the influence of heat [75,78].

Model of a surface layer proposed by Kolm can be extended so that it correspond to the actual construction of the surface layer. For this reason, there has been developed the model of surface layer proposed by Griffitsha, consisting of nine zones [35,78,79].

1. Outer zone occurring during absorption of organic particle on the surface
2. Zone occurring during absorption of water
3. Zone occurring during absorption of gases

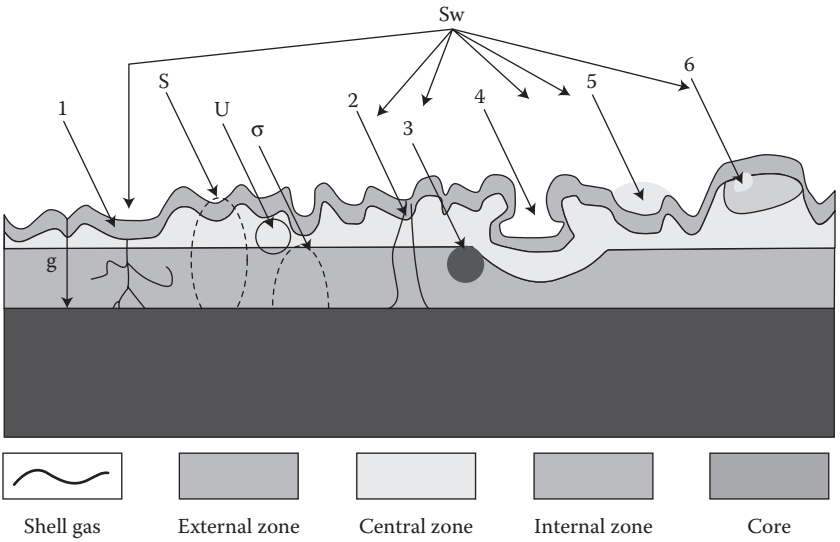


FIGURE 5.6 Scheme of the cross section of a solid-state material according to the three-zone model. Characteristic factors of the surface layer: g—thickness, S—structure, U—strengthening, σ—residual stresses, Sw—defects: 1—microcracks, 2—interstice, 3—shrinkage porosity, 4—roughness, 5—gap, 6—inclusion. (From Kusiński J.: *Lasers and its Application in Material Engineering*. Scientific publisher Akapit, Kraków, 2000.)

4. Zone of metal oxides occurring during chemical reaction of metal and diffusion of oxygen through the oxide layer
5. Zone occurring during grain reinforcement of metal on the surface, caused by interaction between the tool and material during treatment, the so-called Beilby zone
6. Zone enclosing the area of plastic deformed and textured metal layer
7. Zone enclosing the area of the only plastic deformed surface layer
8. Zone, enclosing the area of elastic and tension strain, occurring in the surface layer
9. Core material

Outer layers and coatings are conventionally called the surface layers. Different surface layers can be prepared using the same techniques; the techniques are both traditional as well as newly introduced into industrial practice. Each of the preparation methods of the surface layer allows the achievement of a particular type, and thickness and is divided into a number of subtypes, these same methods can be implemented using a variety of processes. Depending on the type of phenomenon occurring during manufacture of the surface layers the methods can be divided into six groups (Figure 5.7), where each of them allows the production of a proper type of surface layer with different thicknesses and applications [35,75,77].

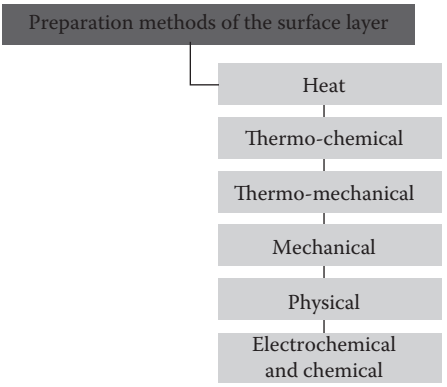


FIGURE 5.7 Manufacturing methods of surface layers. (From Dobrzański. L.A.: Basics of material science metal science. *Engineering Materials with Basics of Material Design*. WNT, Gliwice–Warszawa, 2006.)

5.1.5 Wear of Parts and the Machines

Wear of working surfaces of hot work tool steels.

The use of working surfaces of machine parts and equipment is defined as the reduction of their functional properties caused by many different physical and chemical processes occurring during their lifetime, which occurs mainly due to their working conditions. The variety of wear mechanisms tends the modern scientists to conduct extensive research on the various processes that affect and damage the surface layers. The most common forms are those presented in this work on tribological mechanisms, friction processes, with attention to the fact that they are responsible for about 80% of all cases of existing wear damages. Wear-caused damage of the surface of a solid material refers primarily to the process of proper machinery and equipment application and as a result the necessary servicing or in extreme cases, to replacement of the damaged element. In designing the various assemblies of machinery or even the entire device it should pay particular attention to the wear resistance of the working elements on both tribological damage (mechanical, fatigue, adhesion, and others) as well as nontribological (corrosion, diffusion, cavitation, and others). Therefore, an important step in the design is the selection of material, which is often carried out in relation to some of the destructive processes occurring in the working environment [80–82].

Wear resistance should be understood as the damage of solid material surface, consisting of a gradual loss of material from the surface layer due to its motion relative to the element being in contact. When wear occurs over a long time, a gradual reduction in the weight and dimensional change of the object takes place. This process occurs at the contact surface of the metal materials, nonmetals, flowing liquids, solid particles, or liquid droplets as well as in a flowing gas. Wear includes also oxidation, corrosion as well as cracking, fatigue, and deformation caused by hard particles.

Wear is determined as the process of changes in the surface layer of a solid material, which results in the measurable wear calculated by volume of the loss material, by weight or measured linear (Figure 5.8).

Generally, the wear processes can be divided into three subgroups, that is, consumption due to [81]:

a. Causes: tribological and nontribological
b. Process: stabilized and not stabilized:
   - Stabilized wear: occurs if during the lifetime of the machine the wear process proceeds in a stable way and has a constant intensity.
   - Not stabilized wear: occurs when the wear intensity is variable during the exploitation process.
c. Effects: normal and emergency-related:
   - Normal wear: processes taking place under the same conditions as the normal friction.
   - Emergency wear—not allowed in machine exploitations, leads to damages of machine elements [83–86].

As a result of wear of the working surface of the object there follows a significant deterioration of its functional properties.

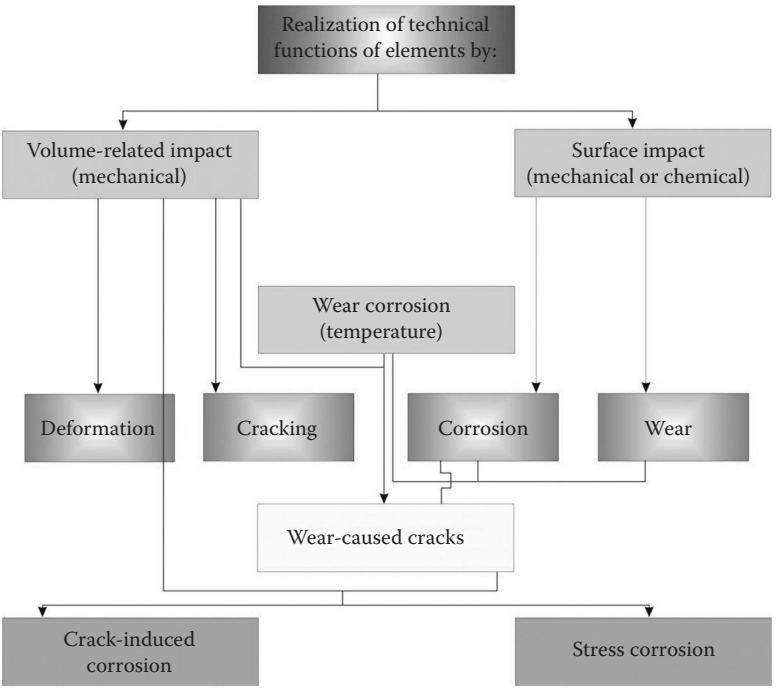


FIGURE 5.8 Interdependence of surface and volume interaction. (From Gierek A.: *Tribological Wear.* Scripts of Silesian University of Technology, Gliwice, 2005.)

The working surfaces of tools frequently get wear by a combined or separate impact of the friction processes (abrasion and adhesion), loads, high temperatures, erosion, and cavitation or corrosion.

On the basis of the obtained results of the causes, analyses of machine parts and equipment wear, it was found that approximately 50% of the parts is wear by abrasion wear, 15% by adhesive wear, 8% by erosion fretting, 5% of wear is the result of corrosion, and about 14% of the cumulative effect of corrosion, erosion, and abrasion [80].

In the case of the described alloying hot work tool steels, the most common cause of wear of the working tools surfaces is those made of steel material (dies, punches, mandrels, molds, etc.). The occurred thermal fatigue is due to the cyclic heating and cooling of the surface layer. Often, the thermal stresses exceed the fatigue strength temperature, the yield strength, causing sometimes the creation of cracks with a characteristic mesh shape on the tool working surface, which grow during further operation.

Thermal fatigue—cyclic changes in temperature cause the formation of variable thermal stresses associated with the temperature gradient and the physic-mechanical properties of the heterogeneity of the phases that occurred in the material. With an increase in the number of thermal cycles followed by structural changes in the mechanical characteristics and the reduction in the surface layer, the thermal stress often exceeds the temperature of the fatigue strength, sometimes also the yield strength. As a result of thermal fatigue after a certain time on the surface of the operating characteristic mesh formed cracks during the deepening of further work cycles, and consequently to a subsequent spalling of material from the surface of the particles and accelerated wear. Fatigue crack nucleation occurs within the grain or interphase boundaries, precipitates and inclusions hinder the movement of dislocations against these obstacles under the influence of thermal stress [87].

In practice, the thermal fatigue never occurs in pure form, but the sum with the other phenomena, that is, [82,86,87]:

- Cyclic mechanical stress (thermo-mechanical fatigue)—structural changes in the material during the thermo-mechanical fatigue are accelerated by the introduction of a large number of network defects, arising from the interaction of the thermal and mechanical stresses. Transitional work hardening is associated with increased dislocation density during plastic deformation of the matrix; in the initial cycle it is removed by heat-activated processes. The result is a decrease of mechanical properties associated with coagulation of the carbides, recrystallization, and the presence of matrix microcracks in the material.
- Corrosion processes (thermal and corrosion fatigue)—corrosive effect on metal forming tool material occurs primarily during operation of casting molds using under pressure. High temperature and pressure intensifying diffusion processes by which the concentration of elements in the treated alloy increases in the tool surface layer. Thermo-corrosion wear can also be caused by using cooling agents or lubricants on the working surface.

- Wear resistance at high temperature–wear and adhesion at elevated temperatures occurring at high surface pressures, not preferred while lubrication and impact of cyclic thermal and mechanical loads.

Adhesion wear caused by adhesion occurs by reciprocal friction of the metal surface and by the absence of lubricants. Because any metal surface regardless of the accuracy of machining is characterized by inequalities, the tops, and depressions, so as a result of mutual shifting of the friction surfaces of plastic deformation in the microregions of the working layer are formed metallic local adhesion areas. As a result of relative sliding of surface friction there occurs destruction of these joints and pulling out the metal particles, which results in the creation of new surface roughness and distribution of the pull-out metal particles on the friction surfaces.

The value of the loading force on the friction surfaces and the temperature has an effect on the wear of the adhesive processes occurring. In the case of high temperature and high pressure there may occur the phenomenon of fusions friction that is a combination of a metallic adjoining area in the same way as in diffusion welding. This type of adhesive wear is also called thermal wear—an adhesive wear of the second type, occurring usually in the situation of a significant overshoot of operating parameters, leading to an enhanced heating of the wear surfaces of the elements.

Intensity of adhesive wear of the joined objects is dependent on the friction conditions, which affect the rate of formation of oxide films. Metallic materials are applied for machine parts and are not only characterized by a high adhesive bonding but are also able to create oxide layers that prevent adhesive wear. This type of wear is referred as a metal-to-metal friction, and the most subjected to adhesive wear are machine parts and equipment, which are not lubricated parts of the supporting surfaces.

In case when the material loss in the surface layer is caused by the separation of particles of the layer as a result of scratch, fissures, or microcutting, and in the friction area there are present loose or constrained abrasive particles and considerably harder surface irregularities, then the wear process takes place. Three basic types of wear have been distinguished (Figures 5.9 through 5.11) [81,82,87–89]:

1. Wear that occurred by scratch or fissuring of the abrasive material, which takes place at low load. This is the least complex process of wear occurring when the working surface is peeled off by brushing of fine particles, which are in contact with the solid material. These particles slide over the surface at a constant speed.
2. Wear by micromachining (grinding) with an abrasive material, which works with a large load force. It occurs when small hard abrasive particles are pressed with great load force to the working surface of an element and move relative to the surface. As a result of very large pressure forces there occurs crushing of the brittle particles to smaller ones with sharp edges.
3. Wear by scratching of the surface with large molecules, which operates at very high load. Molecules with a high molecular weight, such as, for example, fragments of rock or ore, are fed with high force against the element surface, causing thereby the formation of deep grooves and surface irregularities. Increasing scratching speed can be both large or small.

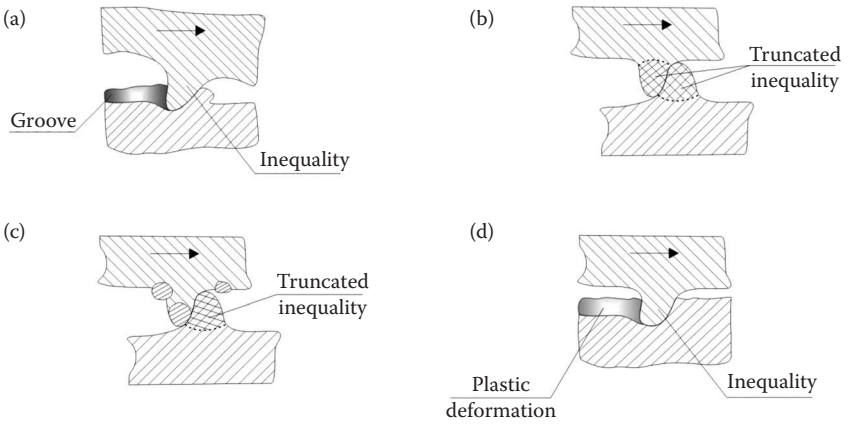


FIGURE 5.9 Models of basic wear processes (a) plowing, (b) cutting of inequalities, (c) cutting of inequalities with the abrasive material by inequality protrusion, (d) plastic deformation of the element material. (From Klimpel A.: *Hard Facing and Thermal Spray Technologies*. WNT, Warsaw, 2000.)

Under specific operating conditions there may occur other types of adhesive wear:

1. Wear by oxidation occurs during the presence of sliding and rolling friction, involving the destruction of the surface layer during the time of friction as a result of the separation of oxide films resulting from the absorption of oxygen from the atmosphere in the areas of friction.
2. Scuffing is the rapid wear of the surface as a result of breaking of the oil film under a high load and the cooperating elements in connection with mechanical and adhesive wear.

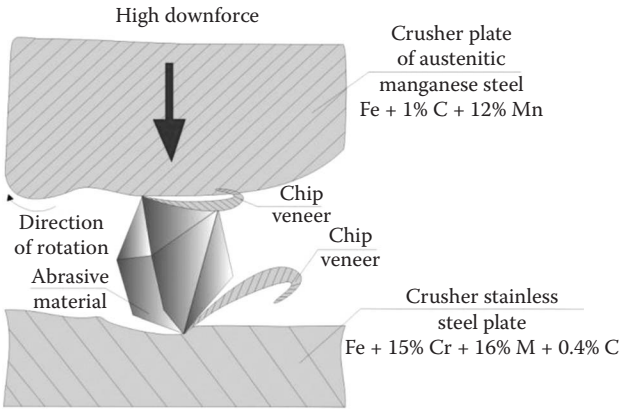


FIGURE 5.10 Micromachining wear process (polishing) with high loads. (From Klimpel A.: *Hard Facing and Thermal Spray Technologies*. WNT, Warsaw, 2000.)

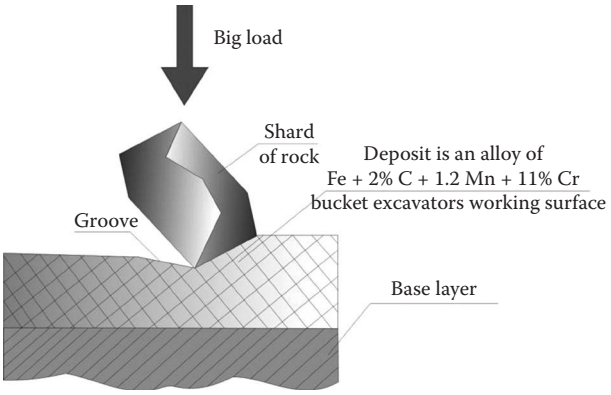


FIGURE 5.11 Grooving wear process with large particles by high load. (From Klimpel A.: *Hard Facing and Thermal Spray Technologies.* WNT, Warsaw, 2000.)

3. Fatigue wear occurs as a result of the summation of deformations in the surface layer, which are caused by the combined effects of residual stress and stress from external loads. In the areas of stress concentration, fatigue microcracks are formed, which grow during continued operation of places of the macrocracks. This results in a loss of cohesion of the material and peeling the metal particles after it reaches fatigue limit by the various metal layer areas and the associated mass loss of the element.
4. Wear known as spalling occurs by rolling friction of the hard metal with a high yield stress, and is a process in which gradual stresses increase in the top surface layer of two wear elements without lubrication. It occurs as a result of the impact of the cyclic stresses, which leads to the formation of microfatigue. Subsequent cyclic stresses rise within the Hertz-stress range to a dispersion of the characteristics microcracks and causes drop out from the wear surface layer of shell-like metal particles. The intensity of the destruction depends on the thickness of the plastically deformed layer and intensity of the plastic deformation.
5. Pitting is a form of fatigue damage caused by the impact of cyclic stresses during the rolling or sliding friction in the surface layer in the presence of oil and at stresses within a range of Hertz stress. Wear takes place in this process in three stages: first, by fatigue and crack initiation; second, by the development and propagation of cracks by supporting of the present oil; third, at the end of plucking, by the oil the metal particles from the surface layer.
6. Fretting is a kind of wear that occurs due to the interaction of mechanical, thermal, chemical, and electrical phenomena during relative small mutual displacement while wearing the surface elements. It has a nature of abrasive fatigue wear as a result of cyclical oscillations with small amplitude. Metal particles that are detached from the surface layer are placed around the contact areas of friction and act as an additional accelerating abrasive factor. In case where the contact area is located in a corrosive environment, the nature of the wear includes also corrosion and is known as fretting.

5.2 INVESTIGATION PROCEDURE

5.2.1 Aim of the Work

The aim of this work was to increase the mechanical and functional properties, including, in particular, wear and thermal fatigue resistance of hot work tool steels 55NiCrMoV7, 32CrMoV12-28, X40CrMoV5-1, X38CrMoV5-3, as well as to investigate the effect of laser alloying of the top layer of the steels, on their structure and properties. The basis for comparison is the hot work tool steels subjected to conventional heat treatment. The processes of laser surface alloying was performed using high power diode laser (HPDL), whereas as the alloying materials carbide powders of the type WC, NbC, VC, TiC, and TaC were used.

5.2.2 Material for Investigation

Investigations were carried out on test pieces from the 55NiCrMoV7, 32CrMoV12-28, X40CrMoV5-1, and X38CrMoV5-3 hot work high-speed tool steels with the compositions according to PN-EN ISO 4957:2004 standard. Chemical composition of the steels are given in Table 5.3. The investigated steels were molten in the electric vacuum furnace at the pressure of about 1 Pa, cast into ingots weighing about 250 kg, and were roughed at the temperature range 1100–900°C into the O.D. 76 mm bars 3 m long, which were soft annealed. The samples were subjected to heat treatment consisting of quenching and tempering, performed twice (Figure 5.12). Surfaces of specimens were ground on magnetic grinder after heat treatment. Particular attention was paid to prevent development of microcracks that might disqualify the specimen from further examination. Next, powder layer of the NbC, TaC, TiC, VC, or WC carbides with the average thickness of 0.05 mm bound with the inorganic binding agent was put down properly onto the degreased specimens. The siliceous liquid glass consisting of the Na_4SiO_4 orthosilicate and $Na_2Si_2O_5$ sodium disilicate was used as a binding agent in the form of the syrup-like solution obtained under the increased pressure. Selected properties of powders are given in Table 5.4.

Rofin DL 020 HPDL (Figure 5.13) was used for surface alloying with carbides 55NiCrMoV7, 32CrMoV12-28, X40CrMoV5-1, and X38CrMoV5-3 steels; its technical specification is given in Table 5.5. The laser used is a high power unit, a versatile one, and used in materials engineering among others for cladding, surface melting, and alloying. The laser system consists, among others, of the following modules:

TABLE 5.3
Chemical Compositions of the Hot Work Tool Steels [PN-EN ISO 4957:2004]

	Mass Concentration of the Elements (%)								
Steel Grade	**C**	**Mn**	**Si**	**Cr**	**W**	**Mo**	**V**	**P**	**S**
55NiCrMoV7	0.55	0.75	0.25	1.1	–	0.50	0.10	0.025	0.019
32CrMoV12-28	0.308	0.37	0.25	2.95	–	2.70	0.535	0.020	0.020
X40CrMoV5-1	0.41	0.44	1.09	5.40	0.01	1.41	0.95	0.015	0.010
X38CrMoV5-3	0.372	0.43	0.42	4.95	–	2.72	0.42	0.022	0.022

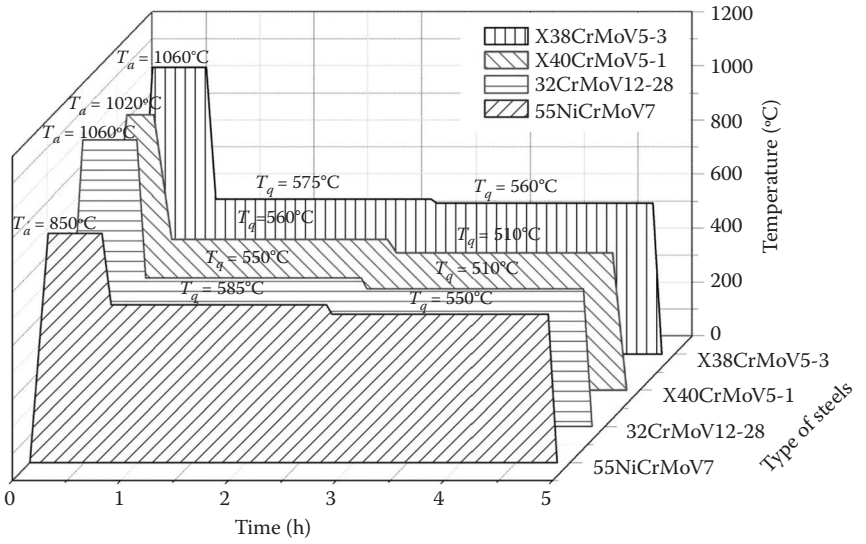


FIGURE 5.12 The heat treatment of investigated steels. (From Klimpel A.: *Hard Facing and Thermal Spray Technologies*. WNT, Warsaw, 2000.)

laser head, rotating work table, movable in the X–Y plane, protective gas nozzle, power supply and cooling systems, and the computer system controlling the laser operation and work table positioning. The rectangular or linear spot size is its significant advantage apart from its versatility, reliability, and small size. The laser alloyed layers were made using the powders shown in Table 5.4 in the power range from 1.2 to 2.3 kW. Dimensions of the laser beam focused on the material surface are 1.8×6.8 mm. The working focal length (measured from the protective glass in the head) is 92 mm. Laser surface alloying was carried out perpendicularly to the longer side of the focused beam with the multimode energy distribution, which makes it possible to obtain the wide face of a single alloyed bead.

It was found out in the preliminary investigations that the maximum laser beam traverse speed at which the process is stable is 0.5 m/min. Further experiments were carried out at the constant laser beam traverse speed, changing the laser beam power

TABLE 5.4
Selected Properties of Carbide Powders

Powder	Average Grain Size (μm)	Melting Point (°C)	Density (g/cm³)	Hardness, HV
Niobium carbide	10	3500	7.6	2100
Tantalum carbide	10	3880	15.03	1725
Titanium carbide	3	3140	4.25	2800
Vanadium carbide	1.5	2830	5.36	2850
Tungsten carbide	5	2770	15.6	2600

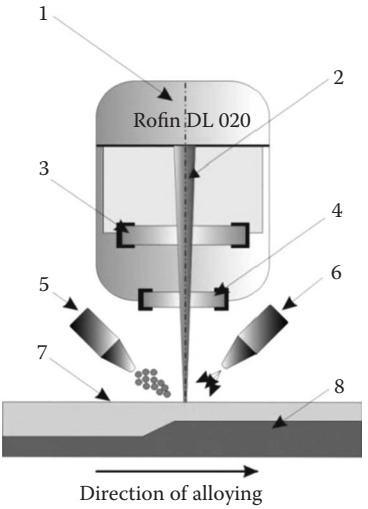


FIGURE 5.13 Working scheme of the HPDL laser used for surface alloying of the hot work tool steel samples. 1—laser head, 2—laser beam, 3—focusing leans, 4—protective glass, 5—alloying material, 6—protective gas nozzle, 7—alloyed layer, 8—core material. (From Klimpel A.: *Hard Facing and Thermal Spray Technologies*. WNT, Warsaw, 2000.)

TABLE 5.5
Specification of the HPDL Rofin DL 020 Diode Laser

Laser radiation wavelength (nm)	808 ± 5
Laser beam output power (continuous wave) (W)	2300
Power range (W)	100–2500
Laser beam focal length (mm)	82/32
Laser beam spot dimensions (mm)	1.8 × 6.8
Power density range in the laser beam plane (kW/cm^2)	0.8–36.5

in the 1.2–2.3 kW range during alloying the surface layer of the test pieces. It was revealed that the argon blow-in with the flow rate of 20 L/min through the Ø 12 mm circular nozzle oppositely directed in respect to the alloying direction provides full alloying zone protection. The test pieces were machined after alloying, to remove the nonremelted layer of the used carbides.

5.2.3 Investigation Methodology

Test pieces from the 55NiCrMoV7, 32CrMoV12-28, X40CrMoV5-1, and X38CrMoV5-3 steels subjected to the standard heat treatment and laser alloyed were cut in the plane perpendicular to the alloying direction on the Struers Discotom-2 device. The cutting disk was water cooled. The prepared test pieces were hot-mounted in the thermosetting resin within 12 min, out of which 7 min were for heating the resin up and the specimens were cooled for 5 min. The microsections

were prepared by grinding on abrasive papers and buffing on diamond abrasive compounds using Struers devices, with subsequent etching. Etching time was selected experimentally for each investigated material's surface layer form. Metallographic examinations were made on the Leica MEF4A light microscope equipped with the Leica-Qwin computer image analysis system at magnifications of 100–1000× and on the Opton DSM-940 scanning electron microscope and scanning electron microscope SUPRA 35 supplied by ZEISS equipped with electron gun of the FEG type and GEMINI column, In-Lens detector, secondary electrons detector, back scattered detector, as well as the TRIDENT XM4 system from EDAX consisting of: energy dispersive x-ray spectrometer (EDS), wavelength dispersive spectrometer (WDS), detector for electron backscattered diffraction (EBSD), dedicated software, database ICDD (The International Centre for Diffraction Data). The Leica-Qwin computer image analysis system was used for thickness examination of the particular zones of the surface layer and for measurement of areas of grains. The saved examination results of the average grain size and dendrite lengths in the particular zones were analyzed statistically.

Diffraction and chemical composition examinations in microareas and of the thin foil structures were made on the JEOL 3010 HRTM transmission electron microscope at the accelerating voltage of 300 kV, equipped with the Oxford EDS LINK ISIS x-ray energy dispersive spectrometer. Thin foils were made from lamellae diced on the electro-discharge machine from the test pieces for the structural examinations, from which disks with 3.2 mm O.D. were cut out, followed by mechanically thinned and ion polished in the electrolyte on the Struers TENUPOL-2 electrolytic polishing device and on the Gatan 691 ion polishing device. The diffraction patterns from the transmission electron microscope were solved using the "Eldyf" computer program. Analysis of the crystallographic relationships occurring between the phases identified in the diffraction patterns from thin foils was made using the stereographic projections.

The x-ray qualitative and quantitative microanalysis and analysis of the surface distribution of the alloying elements in the test pieces of the investigated steel, subjected to the standard heat treatment and laser surface alloying, were made on using the XPert diffractometer from Philips, recording with steep every 0.05° and count time 5–10 s, using filtered x-ray Kα1, with a wavelength of $\lambda = 154{,}056$ nm from the lamp with a copper anode, and Kα1, with a wavelength of $\lambda = 179{,}021$ nm from the lamp with a cobalt anode supplied with a voltage 40 kV by current of 30 mA. The measurements were carried out in the angle range 2θ between 20° and 140°.

Hardness tests were made on specimens subjected to the standard heat treatment and laser surface alloying, using the HPDL at various parameters, making 10 measurements for each condition and calculating their average value. Test results were analyzed statistically. Hardness was measured on the ground and buffed front surfaces of specimens on the hardness tester supplied by Zwick ZHR 4150TK, according to the standard PN-EN ISO 6508-1:2007 (U) in the mode "loading–unloading."

The values of the microhardness measurement of the laser-treated surface layer, were made on the Vickers hardness tester with an automatic measuring path-TECH FUTURE 700ARS FM-50 with a predetermined load of 100 g, and along laser path axis. Loading and unloading rate is 6.62 mN/s, at a measurement time of 15 s.

Abrasion wear resistance tests of the surface layers in the metal–ceramic material arrangement were carried out on a device developed in the Department of Welding of the Silesian University of Technology according to the ASTM standard. Two test pieces of each type of the investigated laser alloyed surface layers were examined according to the requirements of the standard. The ceramic material—quartz sand with the granularity of 212–300 μm—was delivered by the nozzle with the flow rate of about 350 g/min during the test. The nozzle was between the examined test piece and the rubber circle with the diameter of 229 mm. The test piece was loaded with the constant force of 130 N and was pressed down to the rotating rubber wheel. The test pieces before and after the grindability examinations were weighed on the analytical balance with the accuracy of 0.0001 g to check the mass loss, depending on the used particles and laser power. The 55NiCrMoV7, 32CrMoV12-28, X40CrMoV5-1, and X38CrMoV5-3 conventionally heat-treated steels were used as reference materials (Figure 5.14).

Thermal fatigue tests for the 55NiCrMoV7, 32CrMoV12-28, X40CrMoV5-1, and X38CrMoV5-3 steels were carried out on a machine in the Institute of Engineering Materials and Biomaterials. The test pieces were induction heated by a heating coil encompassing half of the test piece perimeter powered by the ELCAL REL–15 induction generators with the current frequency of 400 kHz and maximum power of 15 kW. The test piece rotating at about 25 rpm was immersed in the overflow tank at a depth of ca. 20 mm, cooling with running water. Experiments were carried out for each type of the test pieces alloyed with the hard particles at different laser power values (Figure 5.15).

The maximum temperature of the surface of test pieces did not exceed 580°C ± 1%. It was measured at the output of the test piece from the heating coil using the

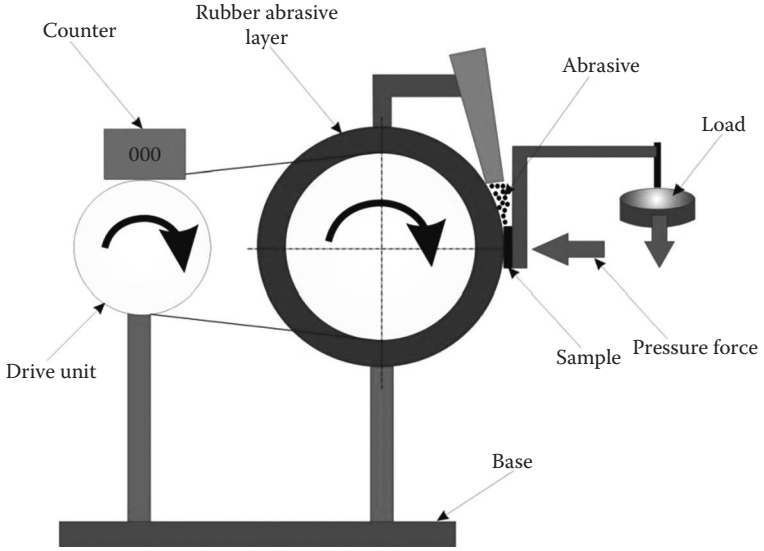


FIGURE 5.14 Scheme of the stand for wear resistance investigations in the metal–ceramic material arrangement, according to the standard ASTM G65.

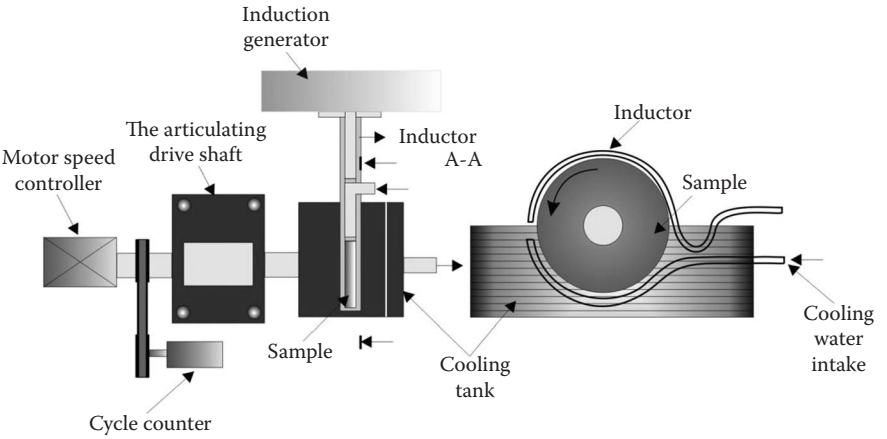


FIGURE 5.15 Scheme of the stand for thermal fatigue investigations.

MINOLTA LAND Cyclops 152 optical pyrometer and it was regulated using the generator. Temperature changes in the test pieces surface layer during the thermal cycle were registered on the *x–y* logger connected with the thermocouple welded with the standard sample at 0.2 mm depth under the heated surface. Fragments were cut out for metallographic examinations from the test pieces subjected to 5000 thermal cycles; the examinations were carried out in the Leica MEF4A light microscope using the Leica Qwin computer image analysis system. Examinations were made on the Opton–DSM 940 scanning electron microscope and scanning electron microscope SUPRA 35 from ZEISS of surfaces of the test pieces after thermal fatigue. The average cracks depth, the maximum cracks depth (calculated as an average from three deepest cracks) and the number of cracks per 1 mm of the test piece perimeter were assumed as criteria specifying the thermal fatigue resistance of the investigated steels.

Temperature measurement during laser surface alloying was carried out using the noncontact digital IMPAC IS 140 pyrometer designed for measurement of temperature of metals and ceramics. The pyrometer is connected through the RS232 port to the PC computer on which the InfraWin PC application is installed making it possible to log the temperature change cycles.

5.3 TECHNICAL APPLICATION

Modern industrial applications require parts with special properties such as high corrosion and wear resistance and hardness. The most effective and economical approach to improve surface ability of machine parts and high surface stresses is by creating surface layers that would possess a high level of corrosion and wear resistance.

The diversity of requirements for materials and the economic impact of material loss due to surface degradation have led to the development of a variety of efficient and cost-effective surface modification processes. Some of these processes create a protective layer by modifying the latter approach, which allows for wider ranges

of coating material and thickness to be used, and permits accurate tailoring of surface properties to local service requirements. Examples of well-established surface treatment techniques are painting, electroplating, aluminum anodizing, induction hardening, carburizing, nitriding, thermal spraying, CVD, PVD, and so on. The thickness of the surface layer that affects resistance to surface deterioration depends on the relevant phenomenon. In general, to resist mechanical interactions the thickness of the treated layer must be greater than the depth of maximum Hertzian stress. Accordingly, a major classification criterion for coatings is the thickness of the protective layer. Some processes produce thin protective layers (in the submicrometer or micrometer ranges), whereas other processes, such as thermal spraying and cladding, produce coatings with thickness ranging from a few hundred micrometers to a few centimeters. This distinction is very important, because thin layers cannot resist intense mechanical stresses, but may be adequate to decrease the friction coefficient and resist corrosion and some forms of wear. Thick protective layers are preferred for high surface stress conditions or intense wear.

Recently, many methods have been used to overcome wear problem. However, a number of applied tasks concerning reliability and durability are not solved up to now. For example, there are now satisfactory methods to improve wear resistance of friction joints working at severe conditions: high loads and contact pressures, washout of lubricant from the contact area, corrosive medium, and so on. In this case, the nature of a friction surface interaction is closed to dry friction. It leads to high linear wear and fast destruction of mechanical parts. The wear behavior of friction joints of an oil-drilling equipment (bearings, seals, gates, etc.) are a typical illustration of the mentioned problem.

Over the past few years, the improvement of surface layers by different methods has attracted many investigators. Changing the microstructure contributes to many advantages such as corrosion, fatigue, and wear resistance. Surface melting and rapid solidification of surface layers by laser treatments can contribute to interesting properties and structures. This technology allows us to convey large amount of energy in a very short time on the exact point of the surface. It provides high power densities of 10^8–10^9 W/m^2. High energy laser beam can produce high rate unstable heat on the surface of bulk alloy and afford fabrication of layers with appropriate properties and structures. The cooling rates afforded by high power lasers are exactly in the bounds of the quench rates necessary for "amorphization," and therefore surface engineering by high power laser provides the chosen tool for this investigation into the fabrication of amorphous or nanoscale surface layers. Depending on the thickness of the melt layer, a cooling rate in the order of 10^4–10^6 K/s can be achieved. Because of precision of the process, short time and local effect of laser surface treatment, it can also be considered in precise industrial applications. Fine crystalline materials obtained under the rapid cooling rate can exhibit high properties over micron-sized materials. Laser surface treatment of steels and production of nanocrystalline structures on the surface of different alloys by laser beam exhibit attractive properties such as low friction, high hardness, and good wear resistance. Steels are suitable for all mechanical applications due to their high strength and ductility, good machining, and low price. However, their composition and surface hardening has the major role in wear conditions.

Laser alloying of surfaces has attracted a great deal of attention for technical applications. By laser alloying of materials it is possible to improve hardness as well as wear and corrosion resistance of the surface without affecting the bulk material.

The spectrum of applications for hot work steels is broad and the tools manufactured with them are used in a variety of fields. Hot work tool steels are used for the noncutting forming of work pieces made of iron and nonferrous metals as well as alloy derivatives at high temperatures. They are applied in processes such as pressure die casting, extrusion, and drop forging as well as in tube and glass product manufacturing.

A hot work tool steel's functionality is defined by its chemical composition, the technology applied for production, and the ensuing heat treatment. Selecting the right steel grade and means of employment leads to considerable cost savings and increased production reliability for the user. The following processing methods—and the steel grades most recommended for them—will be covered [http://www.dew-stahl.com]:

- Pressure die casting
- Extrusion
- Forging
- Glass product manufacturing
- Tube manufacturing

Laser surface treatment is one of the most advanced and technically avant garde technologies used currently in the engineering of material surfaces. Surface treatment of manufactured elements with the application of such means as laser is nowadays a very common and innovative technology due to its seemingly unlimited potential, for example, large material savings, treatment accuracy, considerable improvement of the properties of the treated materials, applicability of full automation processes, and so on. Such a treatment can also contribute to better resistance to corrosion and wear. It can raise hardness and afford better resistance to abrasion between surfaces of relatively small size. The cost of laser treatment is the only limitation when considering the application of this method on large surfaces. Covering a large surface for decorative reasons or to protect it against corrosion with the use of laser techniques is more expensive than traditional methods, for example, painting or electrolytic coating. The application is grounded both from the economical viewpoint and due to the fact that laser surface treatment in many cases ensures the acquisition of higher mechanical properties of the treated surfaces, for example, gear teeth or cutting bits, which would be impossible to achieve using conventional methods of surface treatment.

5.4 MICROSTRUCTURE AND PROPERTIES

5.4.1 Structural Characteristic of the Surface

As a result of laser remelting or alloying with ceramic powders WC, VC, TaC, TiC, and NbC of the surface layers of hot work tool steel X40CrMoV5-1, X38CrMoV5-3, 32CrMoV12-28, and 55NiCrMoV7 using HPDL, an increase in characteristic

nonuniformity of the surface topography and the shape of alloyed bead were achieved, which largely depends on the alloying parameters, in particular the power of the laser beam. The surface of the melt bead obtained during the laser surface melting process has a lower surface roughness, a more regular shape, and reveals a lack of cracks compared to the alloyed bead with carbide powders. In the case of the alloying process, the high absorption coefficient of the laser radiation on the layer of preplaced carbides results in strong convection movement in the melt pool driven by surface tension, thereby causing an increase in the surface shape irregularity and roughness of the obtained surface layers (Figures 5.16 through 5.23).

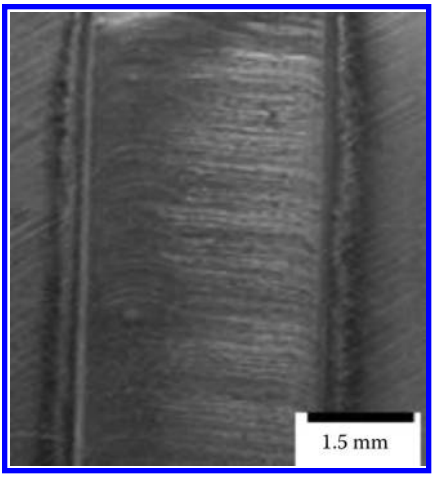


FIGURE 5.16 The surface of the melt bead after laser surface melting of the X40CrMoV5-1 steel; laser power 2.0 kW.

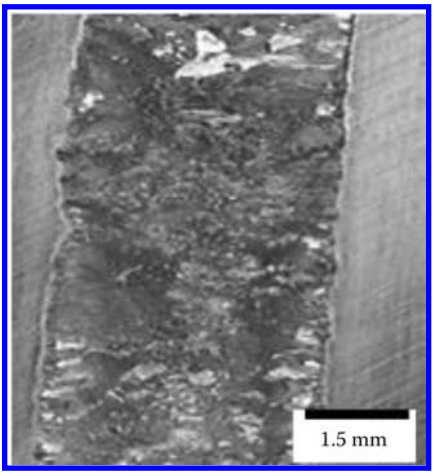


FIGURE 5.17 The surface of the alloyed bead after laser surface alloying of the X40CrMoV5-1 steel with WC powder; laser power 2.0 kW.

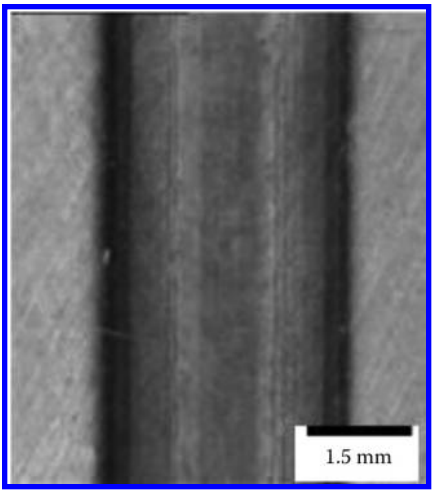


FIGURE 5.18 The surface of the melt bead after laser surface melting of the X38CrMoV5-3 steel; laser power 1.2 kW.

The result of laser remelting or alloying using the ceramic powder put on the surface to form a paste and the substrate to obtain a surface layer, which consists of three zones, starting from the top layer rich in nondissolved particles located on the surface layer of the treated steel, followed by the second zone, the melting zone (RZ) enriched with the alloying material (depending on the type of applied ceramic powder WC, VC, TaC, TiC, NbC), and a heat-affected zone (HAZ), as well as transition zones between the remelting zone and the HAZ, and between the HAZ and the substrate material. The depth of the melted zone and HAZ, at a constant laser beam traverse speed and the thickness of ceramic paste film, depends largely on the

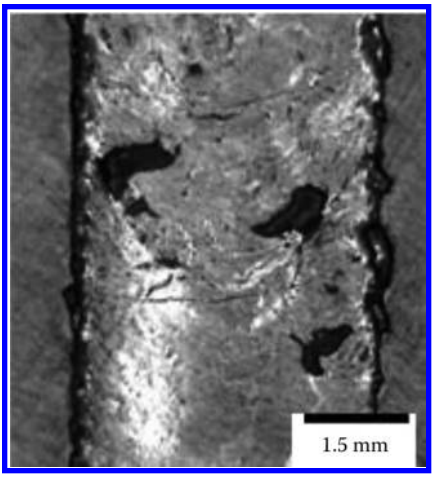


FIGURE 5.19 The surface of the alloyed bead after laser surface alloying of the X38CrMoV5-3 steel with WC powder; laser power 2.3 kW.

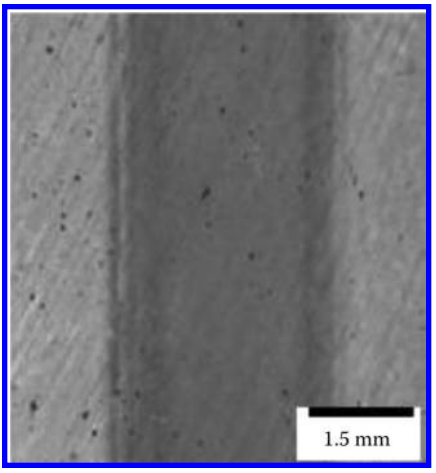


FIGURE 5.20 The surface of the melt bead after laser surface melting of the 32CrMoV12-28 steel; laser power 1.2 kW.

applied laser power. Power of the laser beam also affects the shape of the bottom of the melted zone and convexity of melted bead, what is directly connected with intensity of convection movement in the melt pool. When using higher laser power during the alloying process there appears a strong convexity of the face of laser melted bead, and on the edges of the bead there are created a number of flashes and discontinuities (Figures 5.24 through 5.31).

The cross-sections structure of all the four investigated grades of tool steels characterized below allows to confirm the occurrence of the above-mentioned zones in the laser-treated surface zone (Figures 5.24 through 5.31). Furthermore, in each case

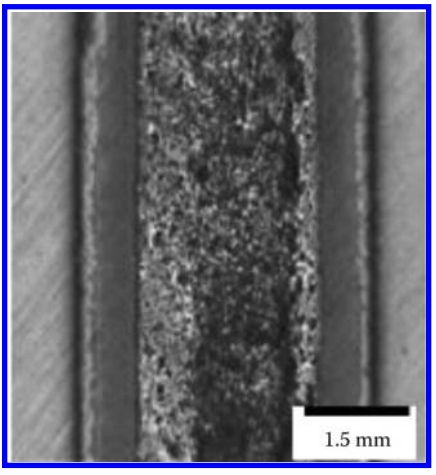


FIGURE 5.21 The surface of the alloyed bead after laser surface alloying of the 32CrMoV12-28 steel with WC powder; laser power 2.3 kW.

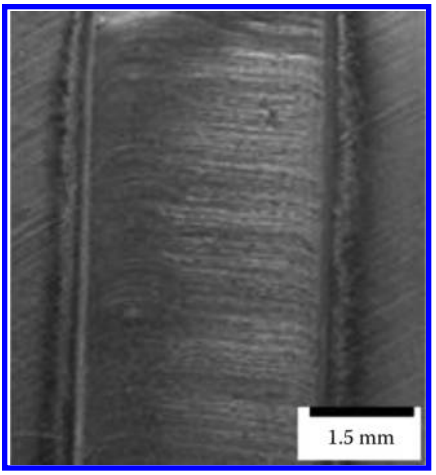


FIGURE 5.22 The surface of the melt bead after laser surface melting of the 55NiCrMoV7steel; laser power 2.3 kW.

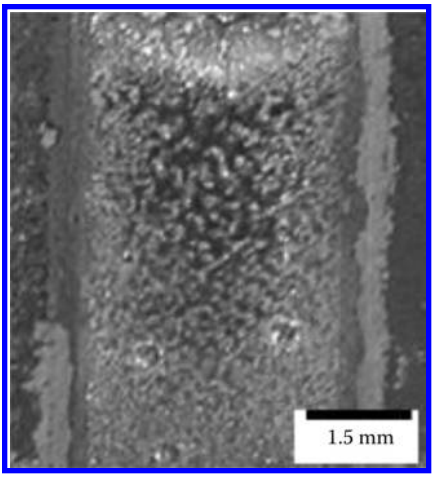


FIGURE 5.23 The surface of the alloyed bead after laser surface alloying of the 55NiCrMoV7 steel with NbC powder; laser power 2.0 kW.

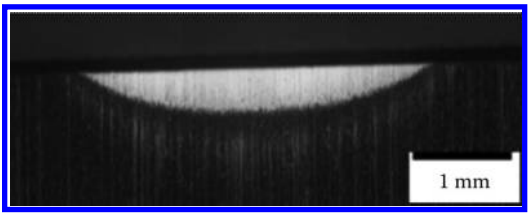


FIGURE 5.24 Surface layer of the X40CrMoV5-1 steel after laser surface melting, laser power 1.2 kW.

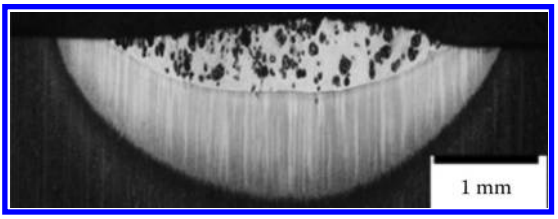


FIGURE 5.25 Surface layer of the X40CrMoV5-1 after alloying with the WC powder, laser power 2.3 kW.

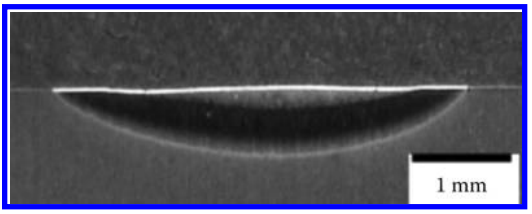


FIGURE 5.26 Surface layer of the X38CrMoV5-3 steel after laser surface melting, laser power 2.0 kW.

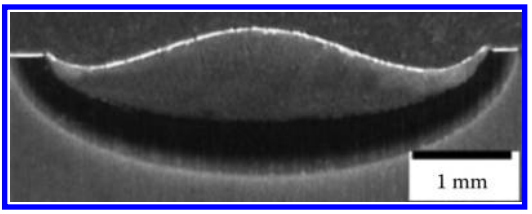


FIGURE 5.27 Surface layer of the X38CrMoV5-3 after alloying with the TaC powder, laser power 2.3 kW.

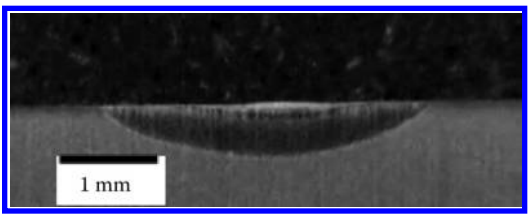


FIGURE 5.28 Surface layer of the 32CrMoV12-28 steel after laser surface melting, laser power 1.6 kW.

there was found the occurrence of the applied WC, TaC, and NbC powder grains (Figures 5.25, 5.27, 5.29, 5.31) in the surface layer. Differences in the specific examined steels grades, concerning mainly the impact of the laser power on the thickness of the individual zones was also found.

Analyzing all the possible cases of laser surface melted steel, it was revealed that in case of the laser power level of 1.2 kW for the steel X38CrMoV5-3 there does not

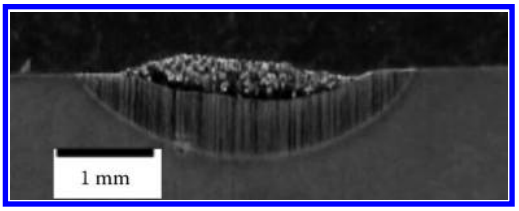


FIGURE 5.29 Surface layer of the 32CrMoV12-28 after alloying with the WC powder, laser power 2.3 kW.

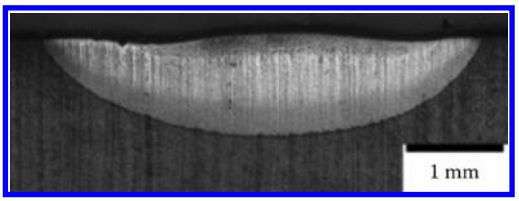


FIGURE 5.30 Surface layer of the 55NiCrMoV7 steel after laser surface melting, laser power 2.0 kW.



FIGURE 5.31 Surface layer of the 55NiCrMoV7 after alloying with the NbC powder, laser power 2.0 kW.

occur at all the remelted zone (RZ), while the remelting zone of minimum thickness of 0.12 mm was found in case of the 32CrMoV12-28 steel surface layer remelted with a laser power of 1.2 kW. The maximum melting depth was also obtained in case of 32CrMoV12-28 steel for laser power of 2.3 kW and is equal to 0.81 mm.

The highest thickness of the remelting zone of an alloyed steel, equal to 2.21 mm, was identified in case of tantalum carbide alloying with 2.3 kW laser beam in case of the steel X38CrMoV5. The highest thickness of the HAZ was found in case of alloying for the X40CrMoV5-1 steel alloyed with tantalum carbide powder for a laser power of 2.3 kW.

Concerning steel after alloying, it can be found that the maximum thickness of the surface layer equal to 3.51 mm at a laser power of 2.3 kW was stated for the 55NiCrMoV7 steel alloyed with the NbC ceramic powder.

The thickness of the particular zones, building the composite layer formed in the surface layer after laser remelting or alloying, depends largely on the power of the laser beam and the type of alloying material. For each of the following carbide powder was used; the thickness of the RZ and HAZ increases and is directly proportional to the applied laser power (Figures 5.32 through 5.39).

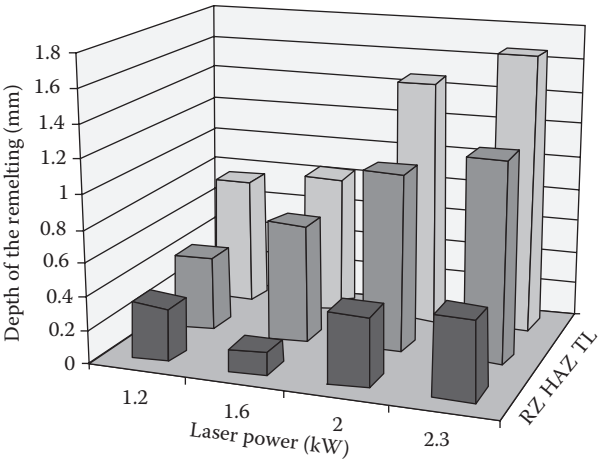


FIGURE 5.32 Influence of the laser power on the thickness of the RZ and HAZ of the X40CrMoV5-1 steel after remelting with the laser power range between 1.2 and 2.3 kW, TL—top layer.

The selection of the powders used for alloying is primarily due to the expected impact on improving the mechanical properties of the surface layer, confirmed on the basis of available literature data sources.

5.4.1.1 Morphology and Microstructure of the Laser-Treated Surface Layer

In the microstructure of laser-remelted or laser-alloyed zone was found the occurrence of dendrites, where their growth occurs from the boundary of the remelted

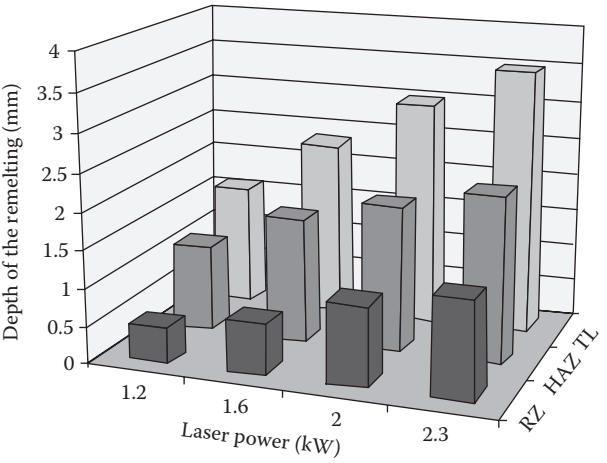


FIGURE 5.33 Influence of the laser power on the thickness of the RZ and HAZ of the X40CrMoV5-1 steel after alloying with TaC powder in the power range between 1.2 and 2.3 kW, TL—top layer.

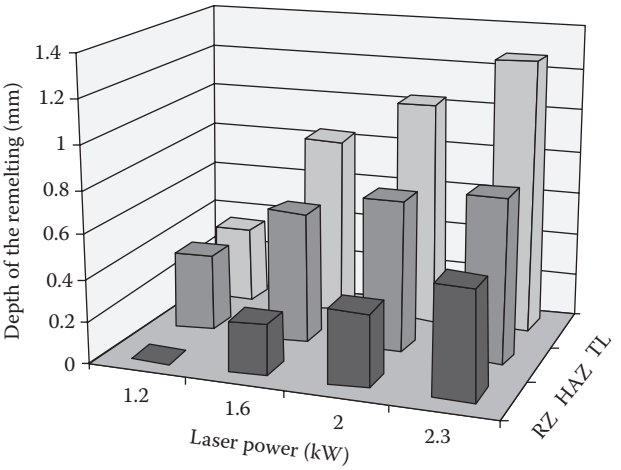


FIGURE 5.34 Influence of the laser power on the thickness of the RZ and HAZ of the X38CrMoV12-28 steel after remelting with the laser power range between 1.2 and 2.3 kW, TL—top layer.

zone and HAZ in the direction of heat transfer. The band occurring between the RZ and the HAZ is the area composed of fine dendrites, which are crystallized at the beginning of the crystallization, just after the stop of the laser beam impact on the treated material (Figures 5.40 through 5.55).

As a result of the solidification process of nondissolved carbides there are formed small grains whose growth direction corresponds to the direction of the largest

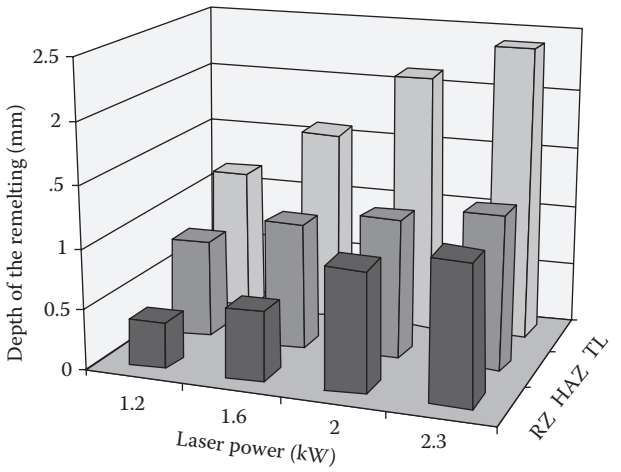


FIGURE 5.35 Influence of the laser power on the thickness of the RZ and HAZ of the X38CrMoV12-28 steel after alloying with NbC powder in the power range between 1.2 and 2.3 kW, TL—top layer.

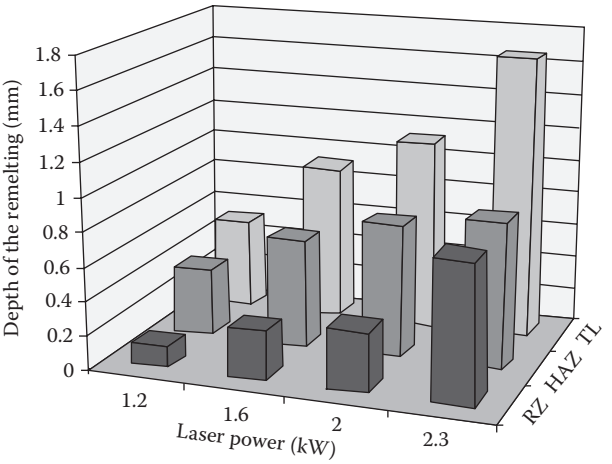


FIGURE 5.36 Influence of the laser power on the thickness of the RZ and HAZ of 32CrMov12-28 steel after remelting with the laser power range between 1.2 and 2.3 kW, TL—top layer.

gradient of temperature associated with the heat transfer from of the entire mass of the sample coming from the laser treatment process. The process of solidification of the substrate material (X40CrMoV5-1, 32CrMoV12-28, 55NiCrMoV7, X38CrMoV5-3) has an effect on the occurrence of areas of varied morphology in the investigated steels. In the central part of the melted zone, the direction of heat transfer changes, and this process is carried out in all directions, the created structure is composed of fine uniaxial crystals corresponding to a carbide mash (Figures 5.56 through 5.67).

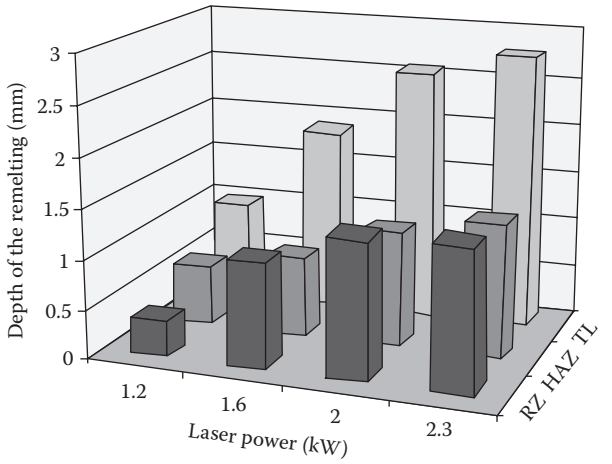


FIGURE 5.37 Influence of the laser power on the thickness of the RZ and HAZ of the 32CrMov12-28 steel after alloying with TaC powder in the power range between 1.2 and 2.3 kW, TL—top layer.

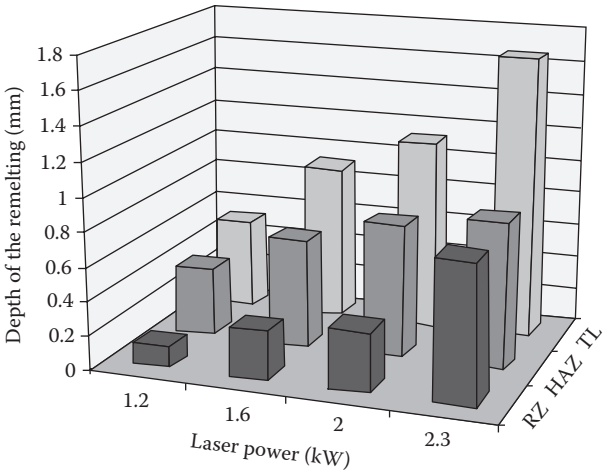


FIGURE 5.38 Influence of the laser power on the thickness of the RZ and HAZ of 55NiCrMoV7 steel after remelting with the laser power range between 1.2 and 2.3 kW, TL—top layer.

The main mechanism contributing to the improvement of the functional properties of the surface layers is solution strengthening, as well as the dispersive effect of the particles with a relatively large diameter. An important fact seems to be that all the powders were partially dissolved in the matrix, or were only remelted as confirmed by the chemical composition investigation of the steel matrix carried out using EDS. The nature of the occurred solution-strengthening is dependent on

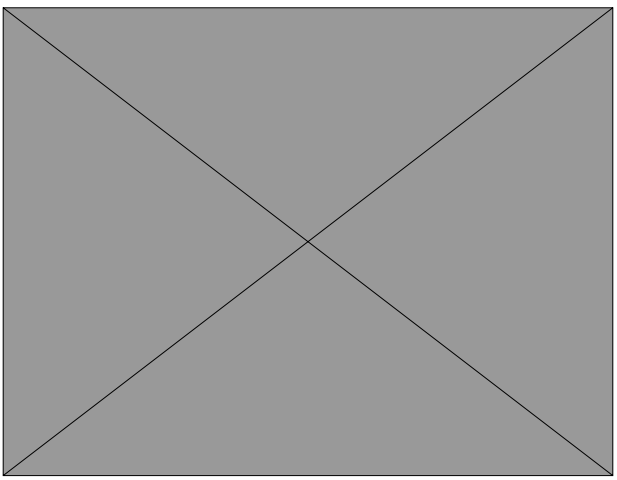


FIGURE 5.39 Influence of the laser power on the thickness of the RZ and HAZ of the 55NiCrMoV7 steel after alloying with TiC powder in the power range between 1.2 and 2.3 kW, TL—top layer.

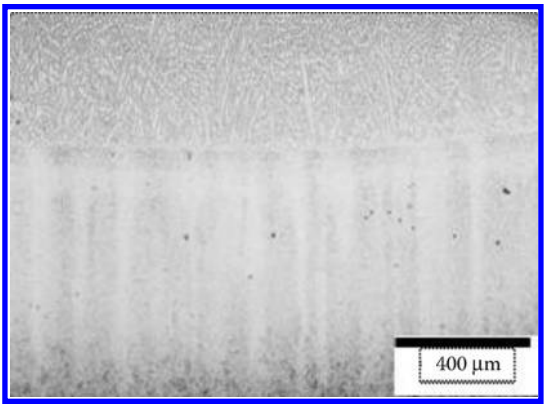


FIGURE 5.40 The cross-sectional morphology of the surface layer of X40CrMoV5-1 steel after surface melting; laser power 2.3 kW.

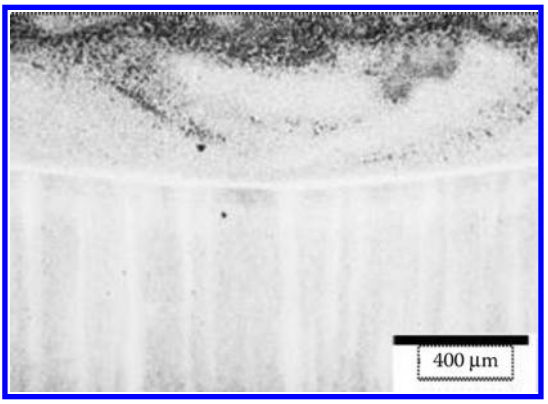


FIGURE 5.41 The cross-sectional morphology of area adjacent to the fusion line, after surface alloying of X40CrMoV5-1 steel with VC; laser power 1.6 kW.

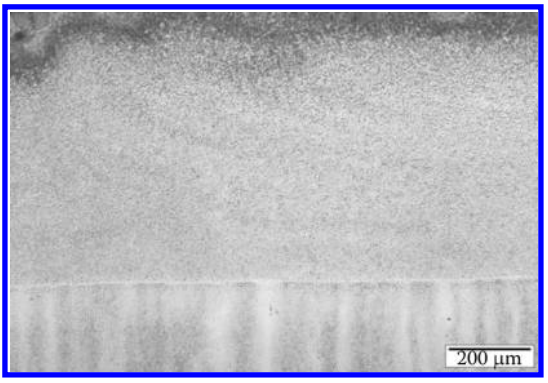


FIGURE 5.42 The cross-sectional morphology of area adjacent to the fusion line, after surface alloying of X40CrMoV5-1 steel with VC; laser power 2.3 kW.

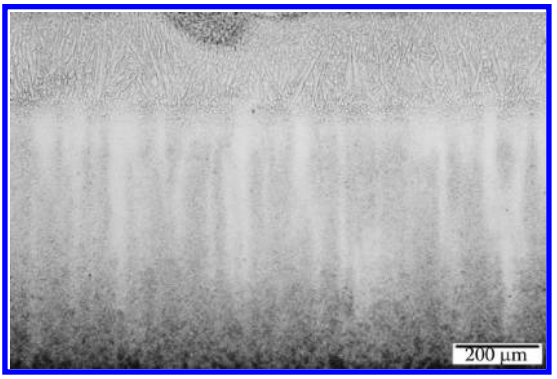


FIGURE 5.43 The cross-sectional morphology of area adjacent to the fusion line, after surface alloying of X40CrMoV5-1 steel with TiC; laser power 1.2 kW.

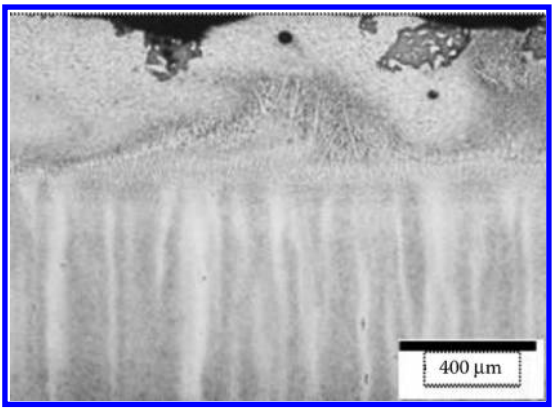


FIGURE 5.44 The cross-sectional morphology of area adjacent to the fusion line, after surface alloying of X40CrMoV5-1 steel with TiC; laser power 1.6 kW.

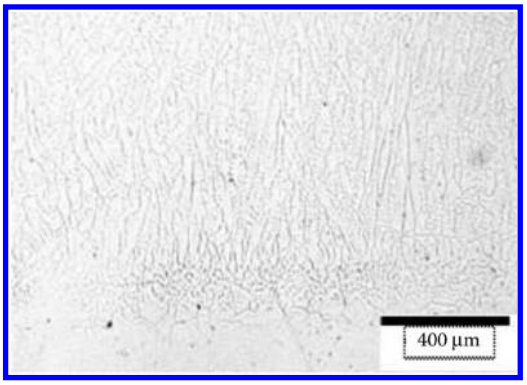


FIGURE 5.45 The cross-sectional morphology of the surface layer of X38CrMoV5-3 steel after surface melting; laser power 2.3 kW.

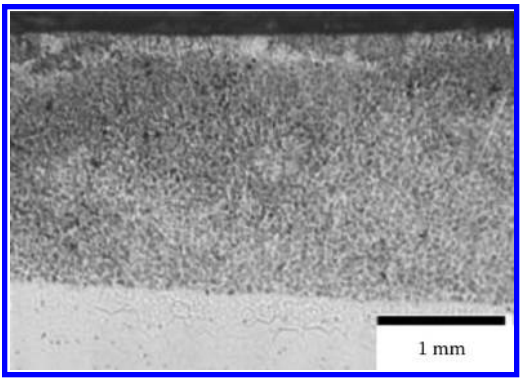


FIGURE 5.46 The cross-sectional morphology of area adjacent to the fusion line, after surface alloying of X38CrMoV5-3 steel with NbC; laser power 1.2 kW.

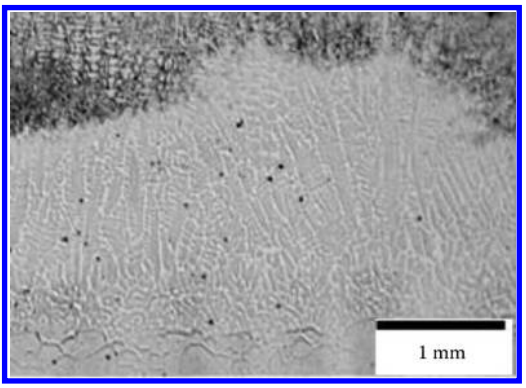


FIGURE 5.47 The cross-sectional morphology of area adjacent to the fusion line, after surface alloying of X40CrMoV5-1 steel with NbC; laser power 1.6 kW.

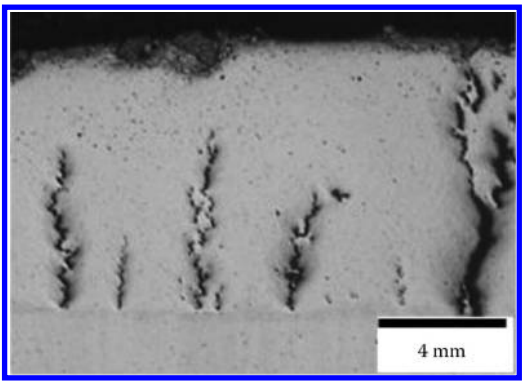


FIGURE 5.48 The cross-sectional morphology of area adjacent to the fusion line, after surface alloying of X38CrMoV5-3 steel with VC; laser power 2.3 kW.

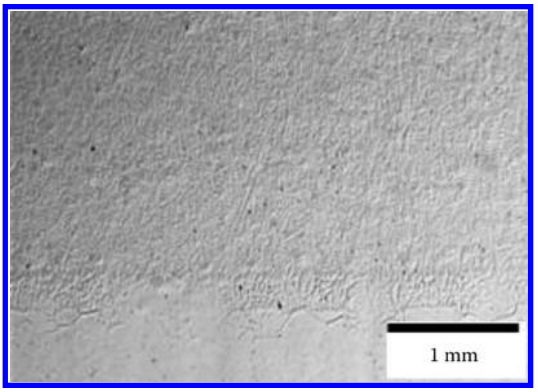


FIGURE 5.49 The cross-sectional morphology of area adjacent to the fusion line, after surface alloying of X38CrMoV5-3 steel with TaC; laser power 1.6 kW.

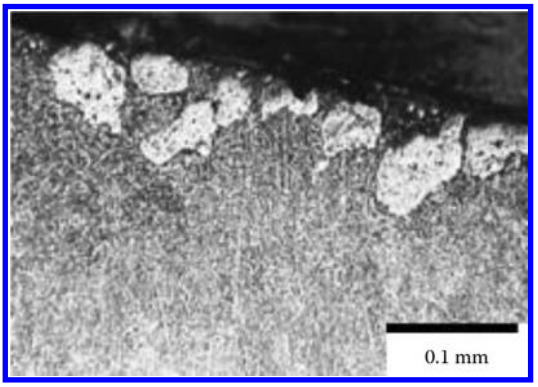


FIGURE 5.50 The cross-sectional morphology of area adjacent to the fusion line, after surface alloying of 32CrMoV12-28 steel with TaC; laser power 1.6 kW.

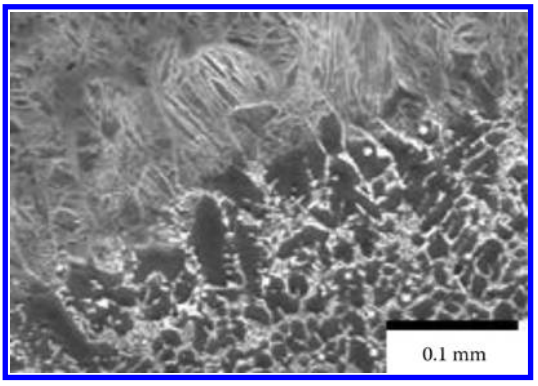


FIGURE 5.51 The cross-sectional morphology of area adjacent to the fusion line, after surface alloying of 32CrMoV12-28 steel with TiC; laser power 1.6 kW.

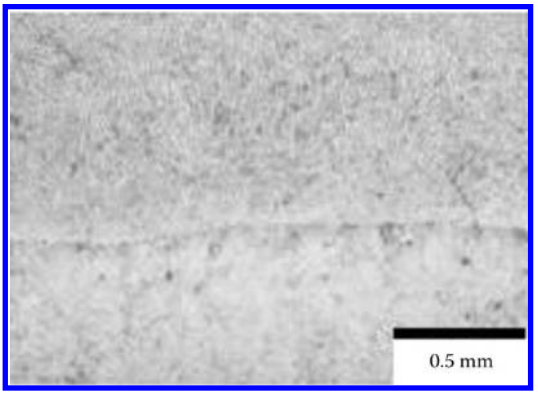


FIGURE 5.52 The cross-sectional morphology of area adjacent to the fusion line, after surface alloying of 32CrMoV12-28 steel with TiC; laser power 1.2 kW.

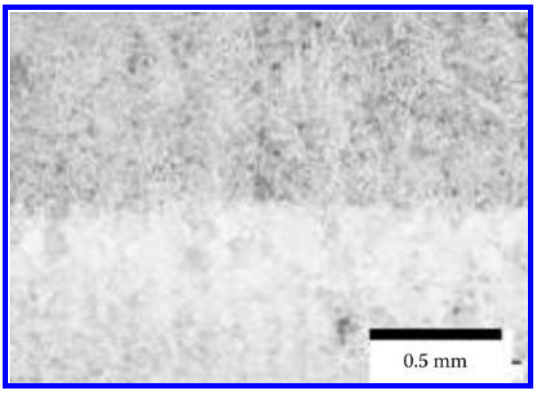


FIGURE 5.53 The cross-sectional morphology of area adjacent to the fusion line, after surface alloying of 55NiCrMoV7-1 steel with VC; laser power 2.3 kW.

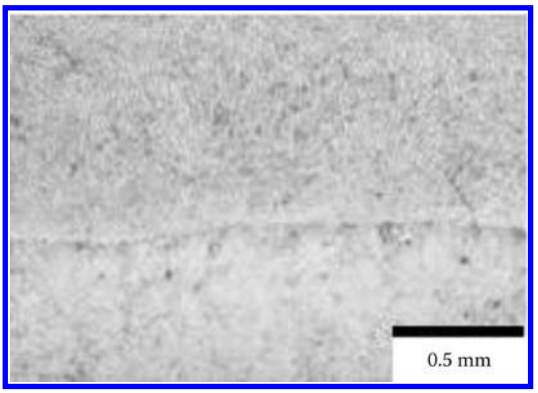


FIGURE 5.54 The cross-sectional morphology of area adjacent to the fusion line, after surface alloying of 32CrMoV12-28 steel with VC; laser power 2.0 kW.

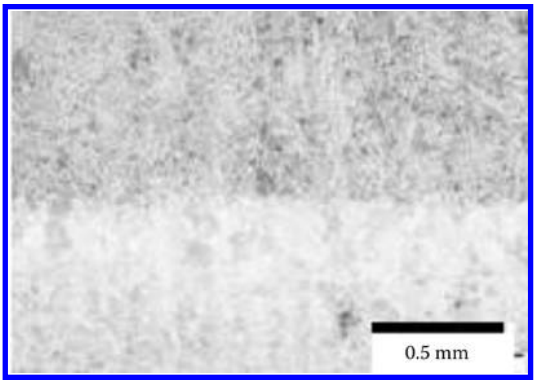


FIGURE 5.55 The cross-sectional morphology of area adjacent to the fusion line, after surface alloying of 32CrMoV12-28 steel with TaC; laser power 2.0 kW.

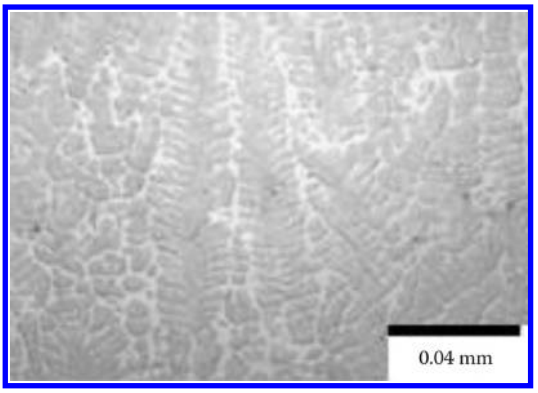


FIGURE 5.56 Central zone of the remelted surface layer after remelting of the X40CrMoV5-1 steel after alloying with TiC, laser power 1.2 kW.

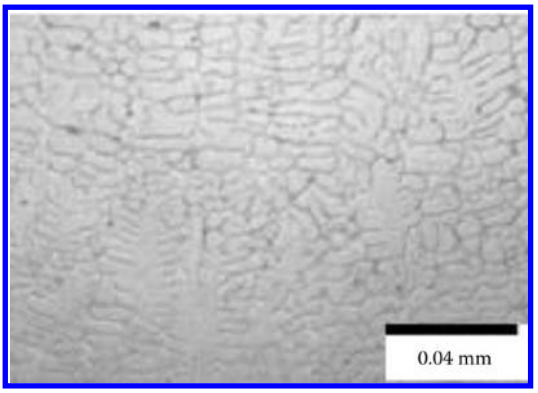


FIGURE 5.57 Central zone of the remelted surface layer after remelting of the X40CrMoV5-1 steel after alloying with TaC, laser power 1.6 kW.

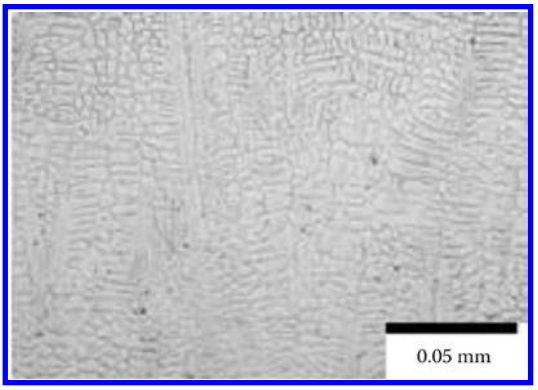


FIGURE 5.58 Central zone of the remelted surface layer after remelting of the X40CrMoV5-1 steel after alloying with TaC, laser power 2.3 kW.

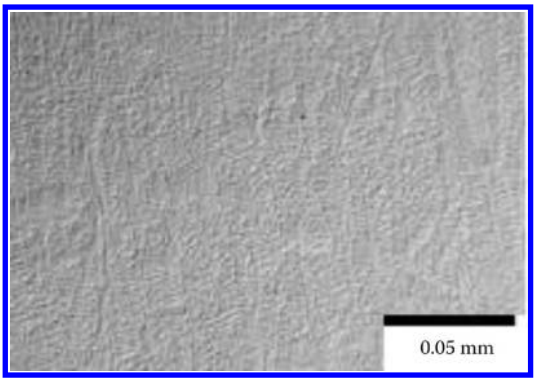


FIGURE 5.59 Central zone of the remelted surface layer after remelting of the X38CrMoV5-3 steel after alloying with NbC, laser power 2.3 kW.

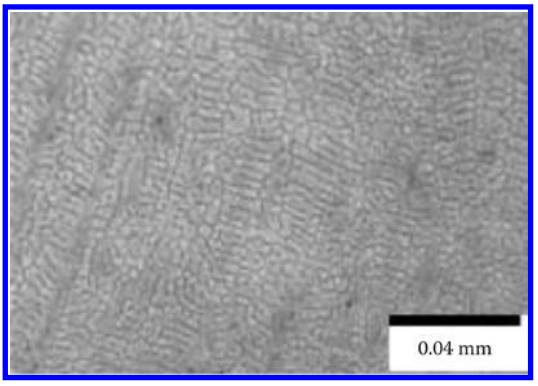


FIGURE 5.60 Central zone of the remelted surface layer after remelting of the X38CrMoV5-3 steel after alloying with TaC, laser power 2.3 kW.

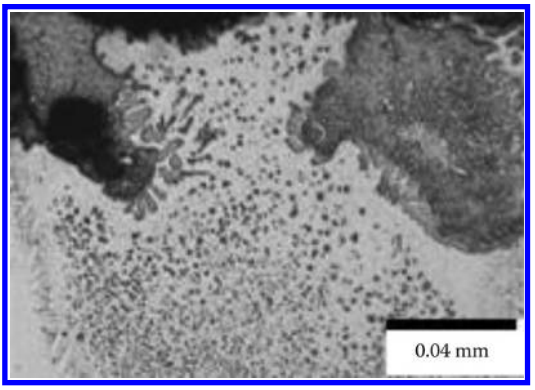


FIGURE 5.61 Central zone of the remelted surface layer after remelting of the X38CrMoV5-3 steel after alloying with TiC, laser power 1.6 kW.

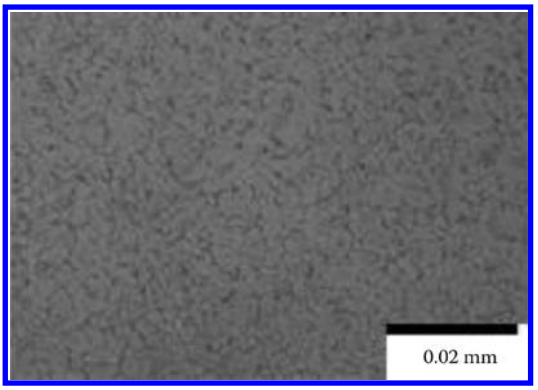


FIGURE 5.62 Central zone of the remelted surface layer after remelting of the 32CrMoV12-28 steel after alloying with TiC, laser power 2.0 kW.

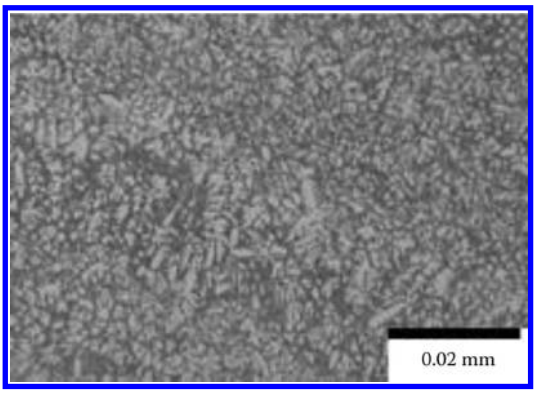


FIGURE 5.63 Central zone of the remelted surface layer after remelting of the 32CrMoV12-28 steel after alloying with TiC, laser power 2.3 kW.

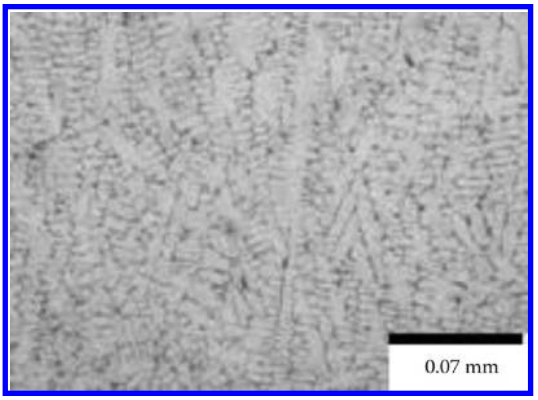


FIGURE 5.64 Central zone of the remelted surface layer after remelting of the 55NiCrMoV7 steel after alloying with TiC, laser power 2.3 kW.

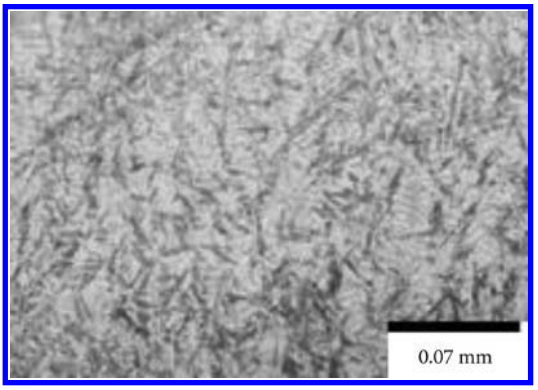


FIGURE 5.65 Central zone of the remelted surface layer after remelting of the 55NiCrMoV7 steel after alloying with VC, laser power 1.2 kW.

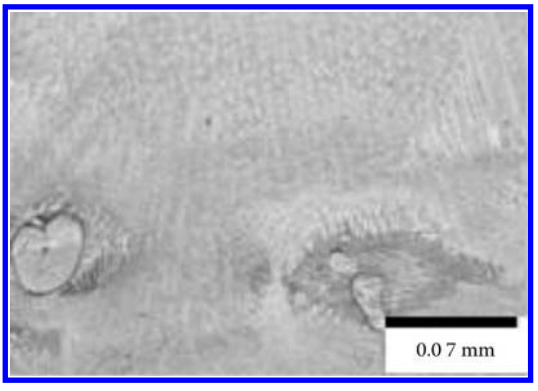


FIGURE 5.66 Central zone of the remelted surface layer after remelting of the 55NiCrMoV7 steel after alloying with VC, laser power 1.6 kW.

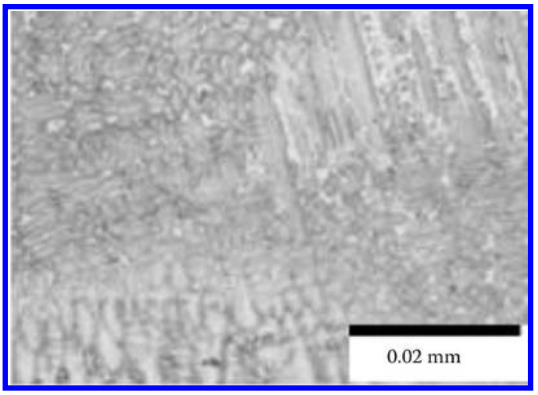


FIGURE 5.67 Central zone of the remelted surface layer after remelting of the 55NiCrMoV7 steel after alloying with WC, laser power 1.6 kW.

the structure of the crystal lattice of the carbide phase and can be, for example, interstitial.

As a result of laser alloying the occurrence of the following strengthening mechanisms in the formed surface layer with a quasicomposite nature was confirmed:

1. Solution strengthening by dissolving the alloying elements in the matrix
2. Grain refinement by rapid crystallization
3. Strengthening with secondary phases arising as a result of the dissolution of the used ceramic powders and next crystallization
4. A strain-strengthening mechanism occurred as a result of excessive stress in the surface layer due to the composite surface layer

In the central area of the RZ there were clusters of nonalloyed carbide material. During laser alloying, an intensive mixing of the liquid metal of the fed ceramic material takes place due to the convective movements caused by temperature difference between the melted metal and the bottom of the remelting surface. The dynamics of this process gives rise to the occurrence of huge turbulences in the liquid phase, which solidifies due to rapid crystallization of the remelted steel and appear as a "frozen" structure (Figures 5.68 through 5.71).

Microstructure of laser alloyed or remelted steel depends on several factors, including the laser scan rate, the crystallization start temperature, as well as the type of alloying material. Based on metallographic investigations carried out by light microscope and scanning electron microscope, it was found that the structure of the solidifying material after laser remelting and alloying reveals a zone-like nature and is of differentiated morphology associated with the crystallization of the tested steels (Figures 5.72 through 5.89). There is also observed a characteristic multiple change in the direction of crystal growth.

After laser alloying of the steels in the remelting zone and on the boundary of the liquid and solid phases a dendritic structure is found, which is formed in accordance with the direction of heat transfer.

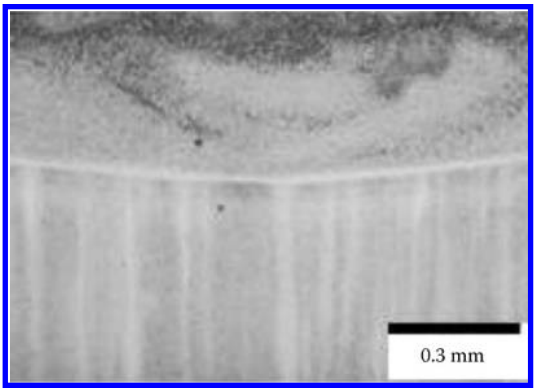


FIGURE 5.68 The cross-sectional morphology of area adjacent to the fusion line, after surface alloying of X40CrMoV5-1 steel with VC; laser power 1.6 kW.

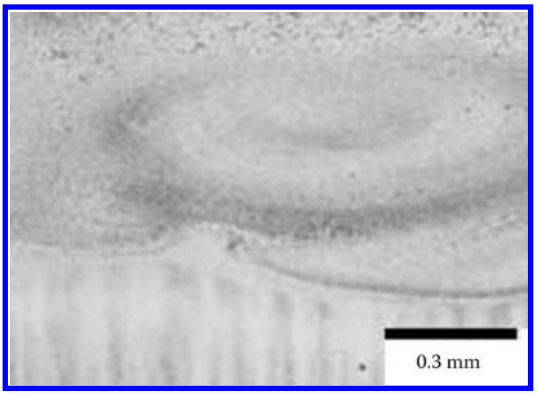


FIGURE 5.69 The cross-sectional morphology of area adjacent to the fusion line, after surface alloying of X40CrMoV5-1 steel with TiC; laser power 2.3 kW.

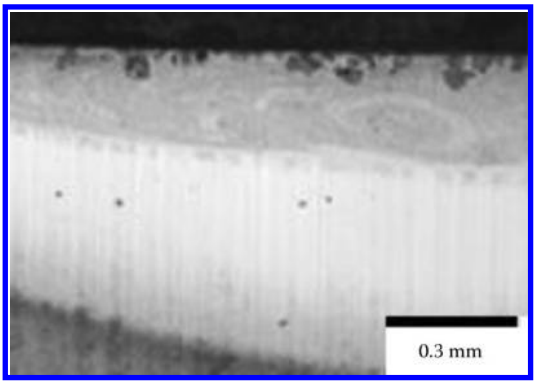


FIGURE 5.70 The cross-sectional morphology of area adjacent to the fusion line, after surface alloying of X38CrMoV5-3 steel with TaC; laser power 1.2 kW.

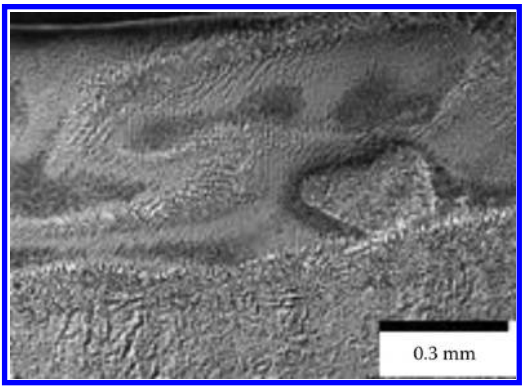


FIGURE 5.71 The cross-sectional morphology of area adjacent to the fusion line, after surface alloying of X40CrMoV5-1 steel with WC; laser power 1.1 kW.

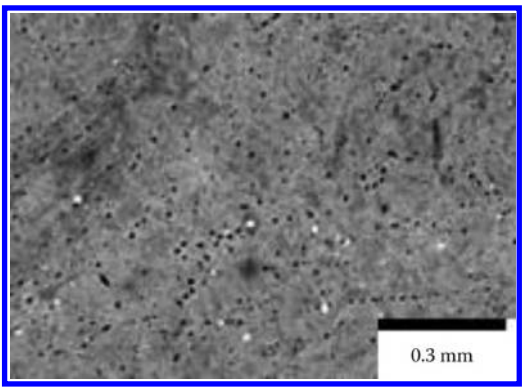


FIGURE 5.72 The cross-sectional morphology of the surface layer of X40CrMoV5-1 steel after surface melting; laser power 1.2 kW.

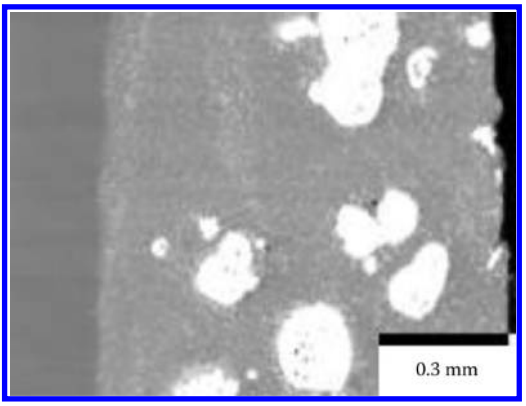


FIGURE 5.73 The cross-sectional morphology of area adjacent to the fusion line, after surface alloying of X40CrMoV5-1 steel with WC; laser power 1.6 kW.

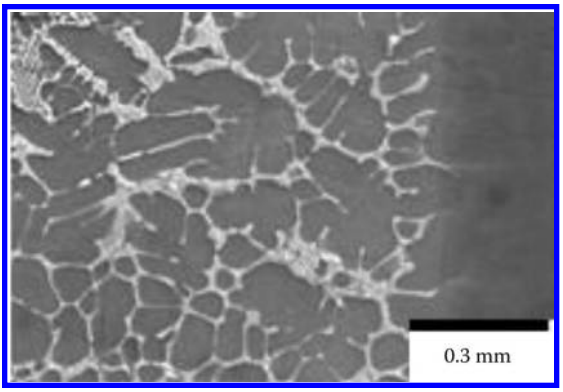


FIGURE 5.74 The cross-sectional morphology of area adjacent to the fusion line, after surface alloying of X40CrMoV5-1 steel with WC; laser power 2.0 kW.

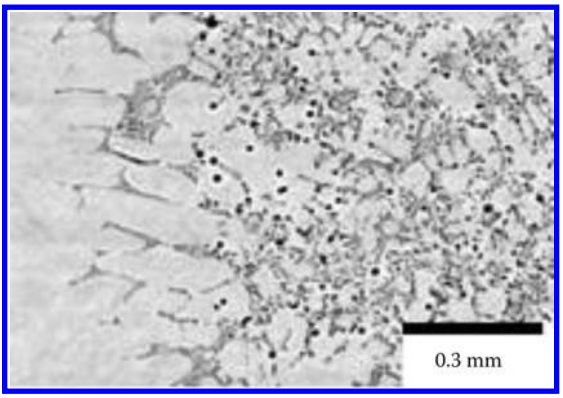


FIGURE 5.75 The cross-sectional morphology of area adjacent to the fusion line, after surface alloying of X40CrMoV5-1 steel with VC; laser power 1.6 kW.

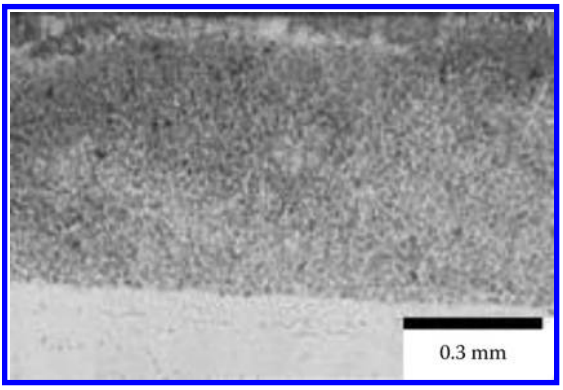


FIGURE 5.76 The cross-sectional morphology of area adjacent to the fusion line, after surface alloying of X38CrMoV5-3 steel with NbC; laser power 1.2 kW.

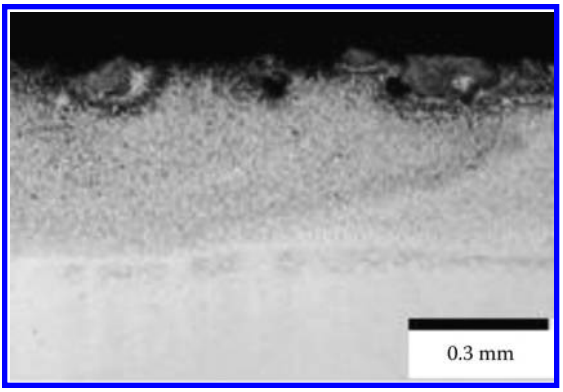


FIGURE 5.77 The cross-sectional morphology of area adjacent to the fusion line, after surface alloying of X38CrMoV5-3 steel with VC; laser power 1.2 kW.

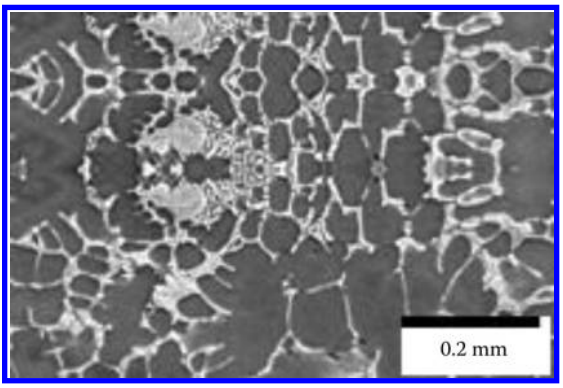


FIGURE 5.78 The cross-sectional morphology of area adjacent to the fusion line, after surface alloying of X40CrMoV5-1 steel with WC; laser power 1.2 kW.

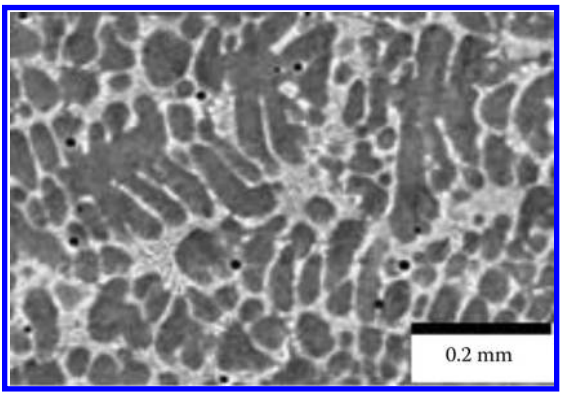


FIGURE 5.79 The cross-sectional morphology of area adjacent to the fusion line, after surface alloying of X40CrMoV5-1 steel with NbC; laser power 1.2 kW.

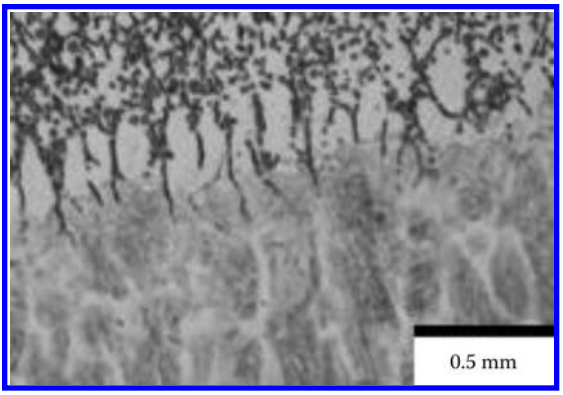


FIGURE 5.80 The cross-sectional morphology of area adjacent to the fusion line, after surface alloying of X38CrMoV5-3 steel with TiC; laser power 2.0 kW.

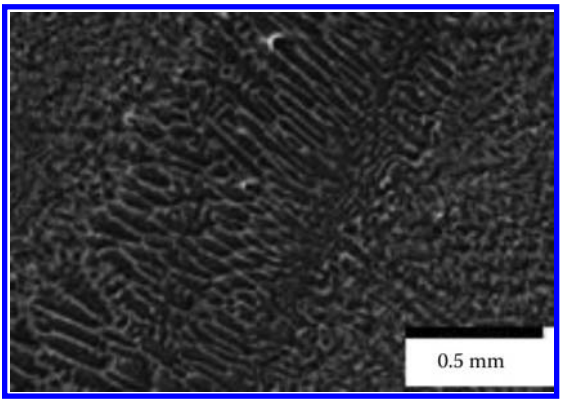


FIGURE 5.81 The cross-sectional morphology of area adjacent to the fusion line, after surface alloying of X38CrMoV5-3 steel with NbC; laser power 2.0 kW.

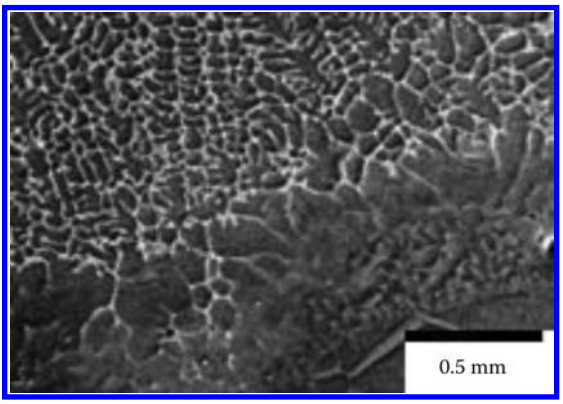


FIGURE 5.82 The cross-sectional morphology of area adjacent to the fusion line, after surface alloying of X38CrMoV5-3 steel with TaC; laser power 1.6 kW.

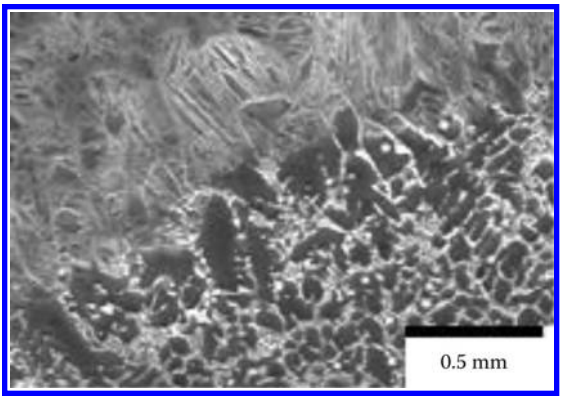


FIGURE 5.83 The cross-sectional morphology of area adjacent to the fusion line, after surface alloying of 32CrMoV12-28 steel with TiC; laser power 1.6 kW.

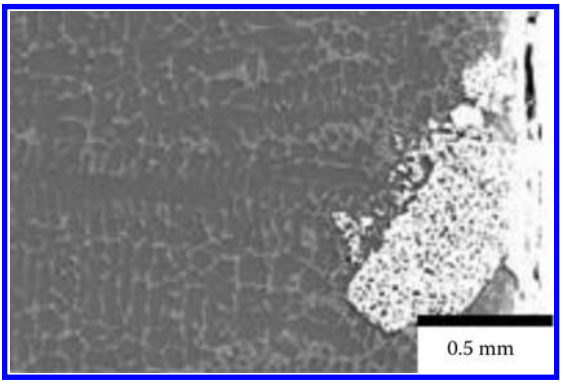


FIGURE 5.84 The cross-sectional morphology of area adjacent to the fusion line, after surface alloying of X40CrMoV5-1 steel with TaC; laser power 1.2 kW.

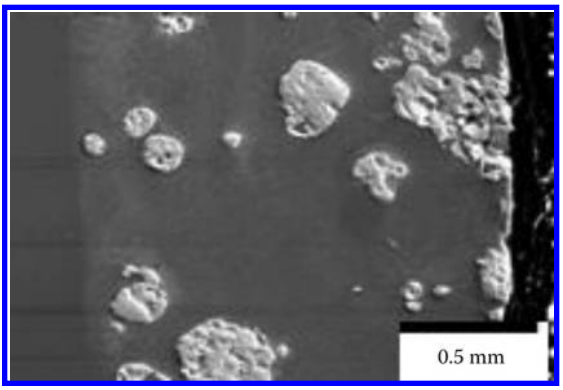


FIGURE 5.85 The cross-sectional morphology of area adjacent to the fusion line, after surface alloying of X40CrMoV5-1 steel with WC; laser power 2.3 kW.

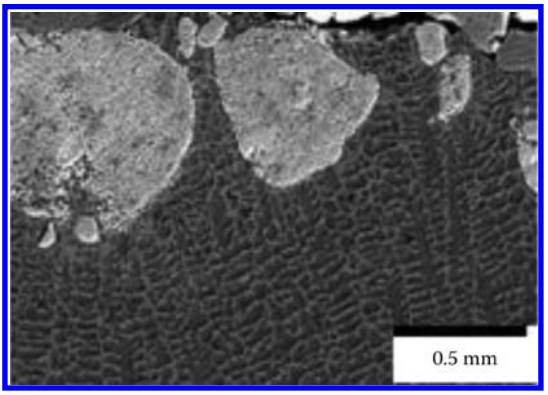


FIGURE 5.86 The cross-sectional morphology of area adjacent to the fusion line, after surface alloying of X32CrMoV12-28 steel with TaC; laser power 2.0 kW.

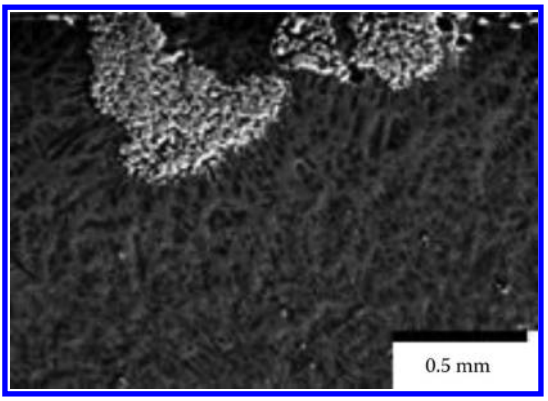


FIGURE 5.87 The cross-sectional morphology of area adjacent to the fusion line, after surface alloying of X32CrMoV12-28 steel with NbC; laser power 1.2 kW.

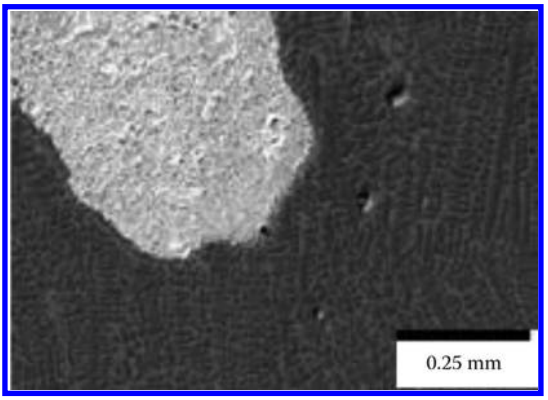


FIGURE 5.88 The cross-sectional morphology of area adjacent to the fusion line, after surface alloying of X38CrMoV5-3 steel with TaC; laser power 2.0 kW.

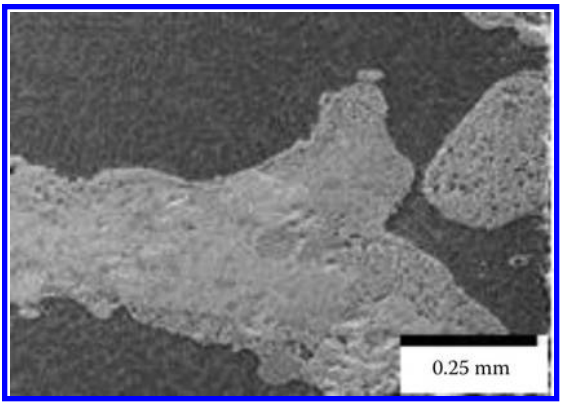


FIGURE 5.89 The cross-sectional morphology of area adjacent to the fusion line, after surface alloying of 55NiCrMoV7steel with TaC; laser power 2.3 kW.

The subsequent stages of crystal growth are closely related to the behavior of preferred growth orientation—the direction of crystal growth in a direction of the largest gradient of temperature, assuming that the whole sample of the material takes the heat from the alloying and remelting process. In the structure there were also observed clusters of undissolved carbides in the steel matrix (Figures 5.85 through 5.89).

5.4.1.2 Phase and Chemical Composition of the Surface Layers

In order to determine or identify the phases present in the produced surface layer by x-ray diffraction qualitative phase analysis was performed, based on which it was found that in the surface layer of the investigated hot work tool steels X40CrMoV5-1, X38CrMoV5-3, 32CrMoV12-28, and 55NiCrMiV7 there occurs the Feα phase after standard heat treatment as well as laser remelted or alloyed. In all analyzed cases there was also identified, as originating from the use for alloying carbide powders, WC, NbC, TaC, TiC, and VC (Figures 5.90 and 5.91).

Moreover, the hot work tool steel 32CrMoV12-28 alloyed with tungsten carbide powder, also reveals the occurrence, beside the Feα and WC phase, identified on the x-ray pattern also reflections derived from the $M_{23}C_6$ and M_7C_3 phases, as well as the retained austenite picks. Some of the identified reflections are shifted toward lower reflection angles, which may be caused by the high fragmentation of structure that affects the crystallographic lattice parameter and can be caused by stresses generated in the composite surface layer in comparison with the values found in the JCPDS database, as occurs usually in case of the surface layers obtained by laser surface treatment.

Point-wise and line-wise chemical composition analysis presented in Figures 5.92 through 5.101 confirms the presence and distribution of elements contained in investigated steels: X40CrMoV5-1, 32CrMov12-28, X38CrMoV5-1, and 55NiCrMoV7 as well as elements derived from the alloying ceramic powder: W, Nb, V, Ti, or Ta. Based on the analysis of the chemical composition of the surface layer of the remelted or alloyed steels the segregation of the used carbides WC,

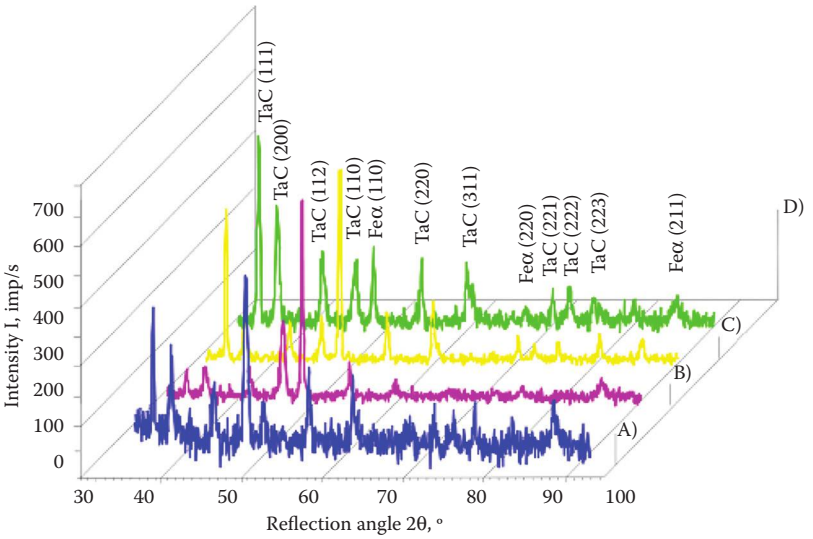


FIGURE 5.90 X-ray diffraction pattern of the 32CrMoV12-28 steel alloyed with TaC powder, laser power 1.2–2.3 kW.

NbC, VC, TaC, and TiC was confirmed, which was caused by convection movement distributing the ceramic powder particles in the molten material according to the heat transfer during the laser surface treatment. After laser remelting of all the investigated steels only the Feα phase was identified. In case of laser alloying of the investigated steels using WC powder, the reflections originating from the

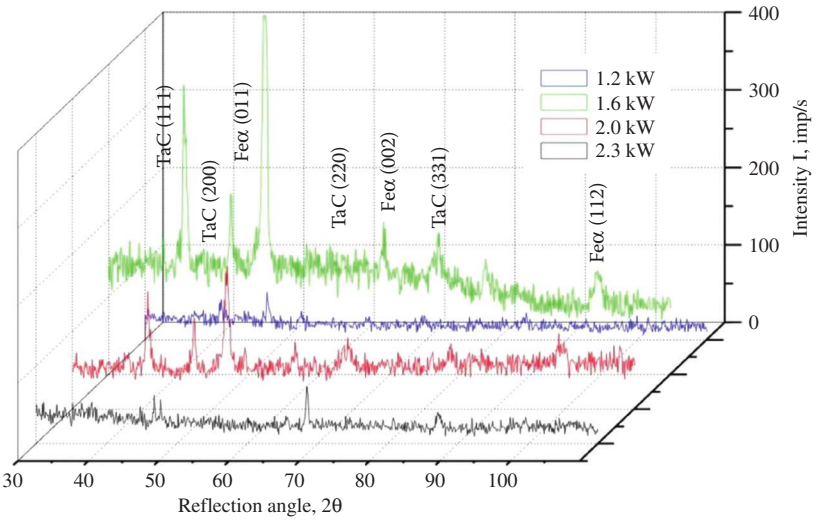


FIGURE 5.91 X-ray diffraction pattern of the X40CrMoV5-1 steel alloyed with TaC powder, laser power 1.2–2.3 kW.

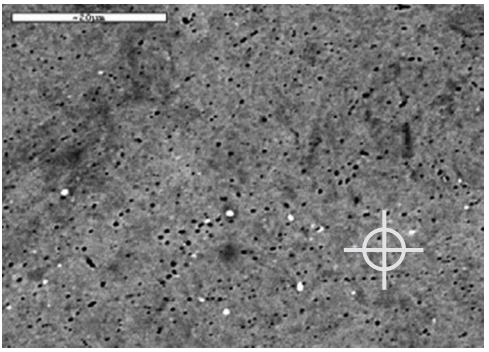


FIGURE 5.92 Central area of the remelting zone of the X40CrMoV5-1 steel after laser alloying, laser power 1.2 kW.

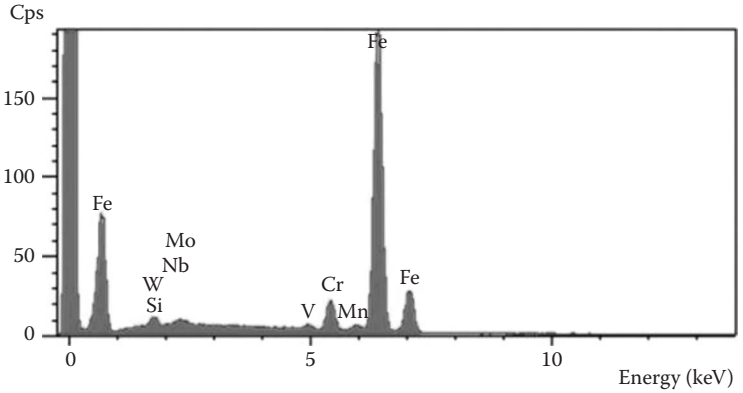


FIGURE 5.93 EDS analysis of the chemical composition of the X40CrMoV5-1 steel after laser remelting, laser power 1.2 kW.

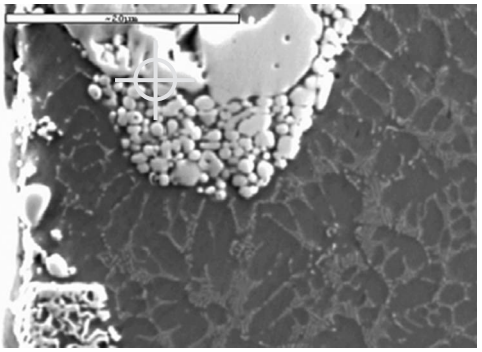


FIGURE 5.94 Alloying material in the surface layer of the X40CrMoV5-1 steel after laser alloying with TaC powder TaC, laser power 1.2 kW.

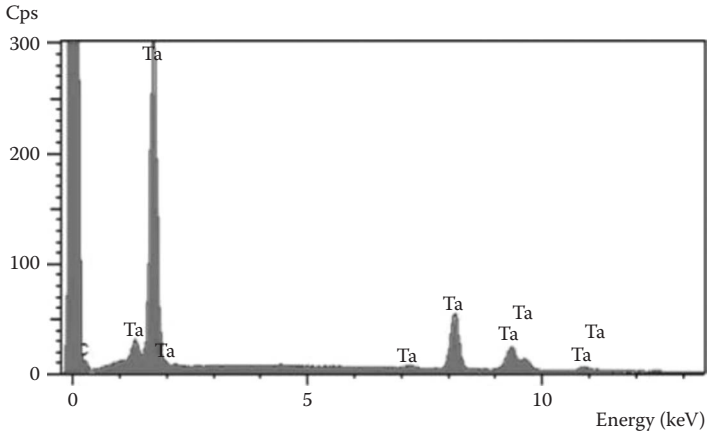


FIGURE 5.95 EDS analysis of the chemical composition of the X40CrMoV5-1 steel after laser alloying with TaC powder, laser power 1.2 kW.

M_7C_3 phase were identified, as well as the retained austenite. EDS microanalysis diagrams provide information on the chemical composition, which can be used as basic information for further phase identification using electron or x-rays diffraction techniques—identify a particular phase.

For a comprehensive metallographic analysis, electronographic investigations were made confirming the occurrence of different phases in the laser-treated steels. Investigations of thin foils on transmission electron microscopy show that the structure of the quenched steel and double tempering consists of tempered martensite with dispersed M_7C_3-type carbide precipitates (Figure 5.102). The martensite laths are maintained at high dislocation density, and some laths are partially twinned. On the basis of thin foil investigations of the surface layer of the hot work tool steel alloyed with vanadium carbide (VC), niobium, tantalum, and titanium there were found the respective alloying carbides placed at grain boundaries, for example, of the type NbC, TaC, and VC (Figure 5.103). The matrix of the surface layer after alloying consists of lath martensite with high density of dislocations that may arise due to residual stress in the previously solidified material. The laths of martensite are very small, irregularly shaped, and are in a very large extent twinned. The martensite in the steel surface layer are embedded also fine carbides of the M_3C or M_7C_3 type (Figure 5.104). The presence of M_4C_3-type carbide precipitation is also confirmed in the VC alloyed steel. These carbides are located on the boundaries of the martensite laths and on the boundaries of the microtwins.

The structure of the hot work tool steel X38CrMoV5-3 in the quenched and tempered state consists of martensite with few MC-type carbides, which did not dissolve during austenitizing. The investigations carried out have confirmed the occurrence of the partially twinned martensite laths, in the area where the dispersive carbides M_7C_3 and $M_{23}C_6$ can be identified, as well as a high density of dislocations arising probably due to residual stress in the previously solidified material. However, the structure of the laser-treated steel consists of martensite with residual austenite, which laths are

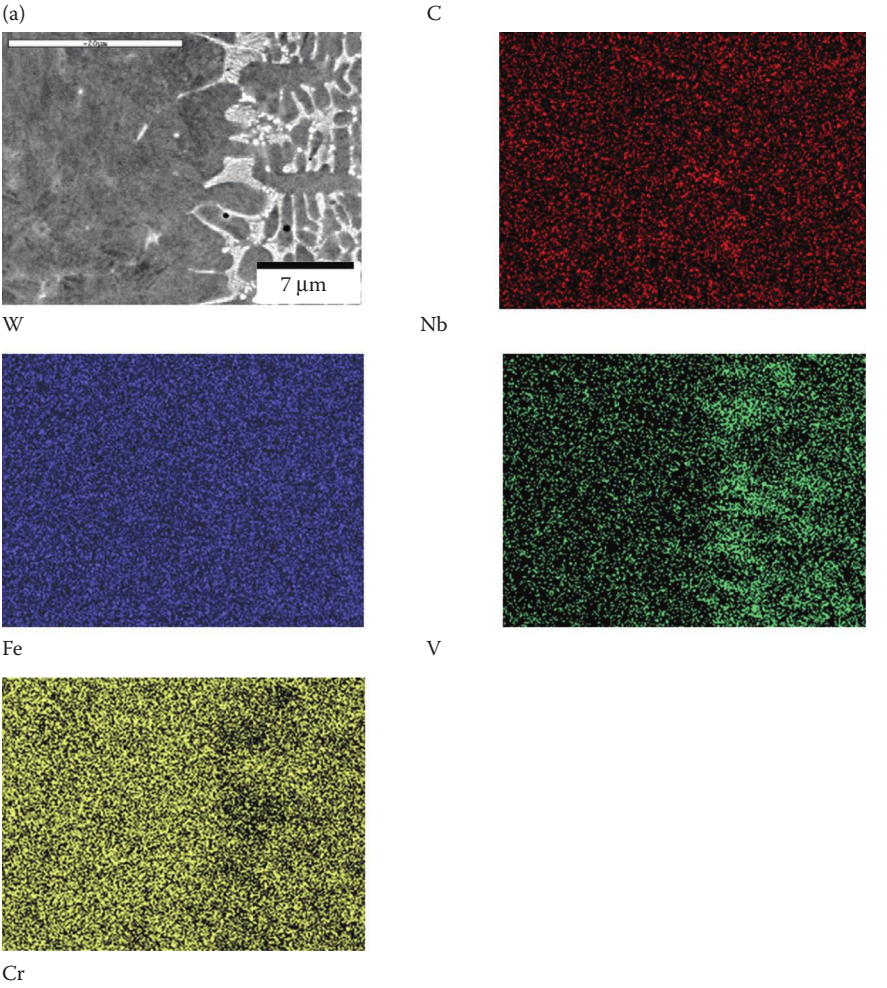


FIGURE 5.96 Small eutectics on the boundary of the remelting zone of the surface layer of X40CrMoV5-1 steel after laser alloying with NbC powder, laser power 1.2 kW, secondary electron image (a) and chemical composition area analysis.

characterized by high dislocation density, irregular shape, and are smaller compared to the martensite identified in the steel treated according to the conventional heat treatment. In the case of laser alloying of the investigated steel with VC powder at the grain boundaries there is a mesh of carbides of the M_7C_3 i $M_{23}C_6$ type, and inside some grains there are small carbides of the V_2C and VC type (Figure 5.105). Thin foil investigations made on transmission electron microscopy on the 32CrMoV12-28 steel after a conventional heat treatment revealed that the structure of this steel is composed of tempered martensite, which is in the twinned form (Figure 5.106). However, as a result of laser alloying of this steel with VC powder, there is confirmed the occurrence of a mesh of dispersive carbides, determined mainly at the grain

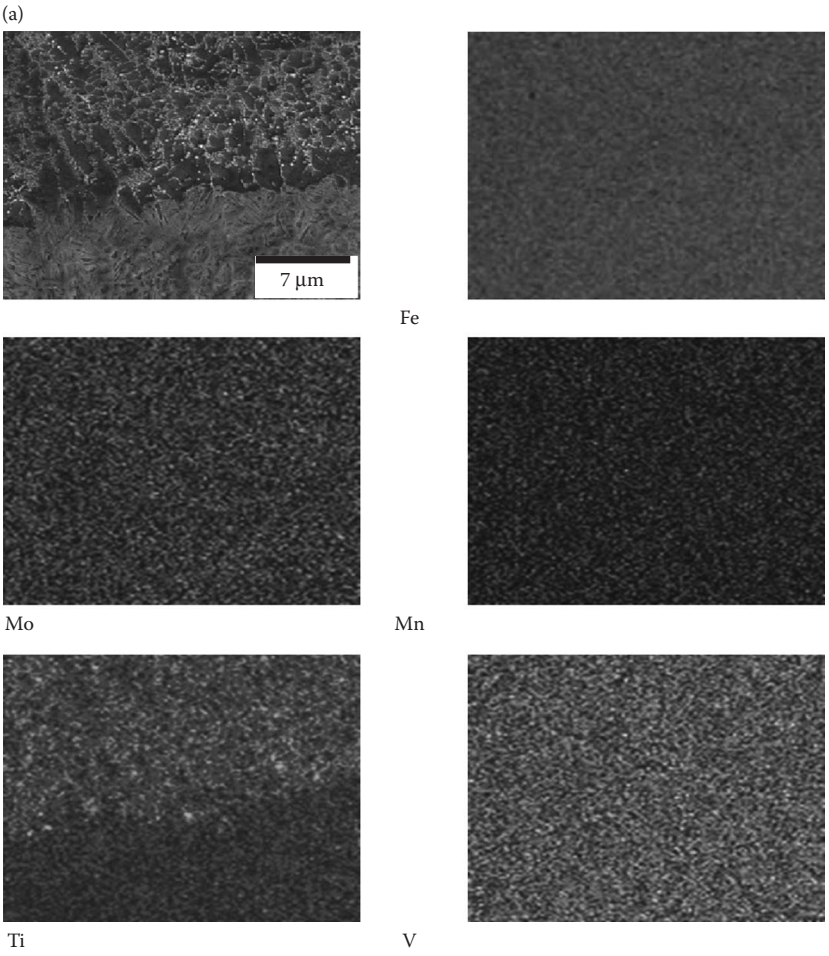


FIGURE 5.97 Boundary of the remelting zone of the surface layer of the 32CrMov12-28 steel after laser alloying with TiC powder; laser power 2.0 kW; secondary electron image (a) and chemical composition area analysis.

boundaries (Figure 5.107). In some cases, there are formed fine dispersed carbides on the side of the grains.

5.4.2 Toughness Measurements of the Obtained Surface Layers

5.4.2.1 Hardness Measurement

The investigations were performed on the samples subjected to laser remelting and alloying, as well as for the samples made of steel subjected to the conventional heat treatment.

In most cases, the laser surface treatment increases the hardness of the investigated steels, which increases with increasing laser power used for melting or alloying.

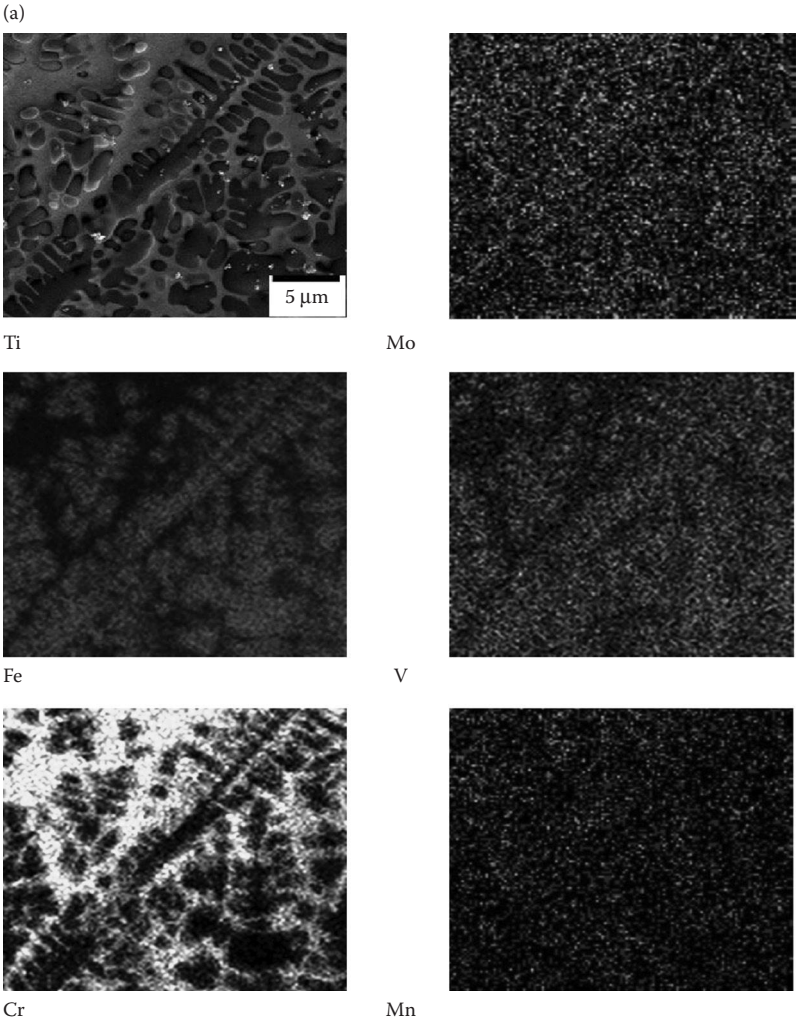


FIGURE 5.98 Alloying material in the middle zone of the surface layer of the X38CrMoV5-3 steel after laser alloying with TiC powder; laser power 2.0 kW; secondary electron image (a) and chemical composition area analysis.

As a result of laser alloying the occurrence of the following strengthening mechanisms in the formed surface layer with a quasicomposite nature was confirmed:

1. Solution strengthening by dissolving the alloying elements in the matrix.
2. Grain refinement by rapid crystallization.
3. Strengthening with secondary phases arising as a result of the dissolution of the used ceramic powders and next crystallization.
4. A strain-strengthening mechanism occurred as a result of excessive stress on the surface layer due to the composite surface layer.

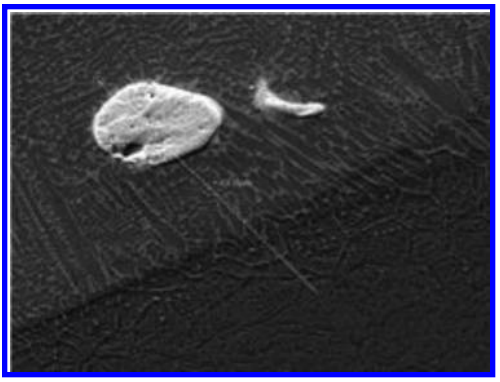


FIGURE 5.99 Remelting zone in the surface zone of the 55NiCrMoV7 steel after laser alloying of the WC, laser power 2.3 kW.

For the X40CrMoV5-1 steel, the maximum hardness (HRC 62.6) was obtained for the alloyed surface layer with VC with the laser beam power of 2.0 kW and a titanium carbide powder TiC (62.1 HRC) at a laser power 2.3 kW. The lowest hardness (HRC 55.3) of the surface layer was obtained by alloying with titanium carbide TiC at laser power of 1.2 kW. Comparing the hardness of the conventionally heat-treated steels, it was found that the lowest increase in hardness (HRC 54.5) shows only the remelted surface layer treated with a power of 1.2 kW. The hardness of the X40CrMoV5-1 steel after standard heat treatment is equal to 53.9 HRC, which demonstrate that the process of laser remelting and alloying with powders of WC, NbC, VC, TiC, or TaC carbides increases the average hardness of the surface layer.

The highest hardness of 61.6 HRC was obtained for laser remelting of the X38CrMoV5-3 steel after remelting with the laser beam power of 2.0 kW, and the lowest value—60.9 HRC after the remelting with the laser power of 1.2 kW. The hardness of the surface layer of the steel alloyed with carbide powders is comparable to the hardness of the material subjected to the standard heat treatment,

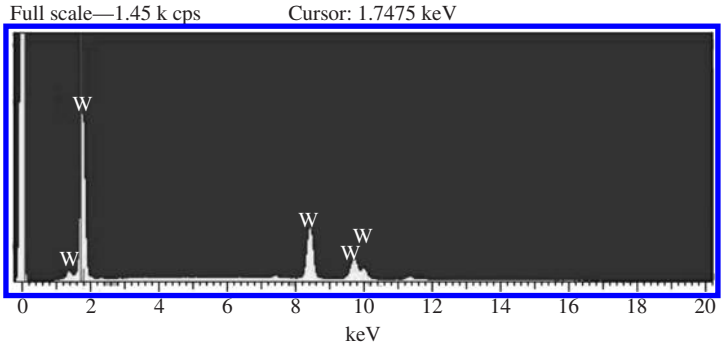


FIGURE 5.100 EDS analysis of the chemical composition of the 55NiCrMoV7 steel after laser alloying with WC, laser power 2.3 kW.

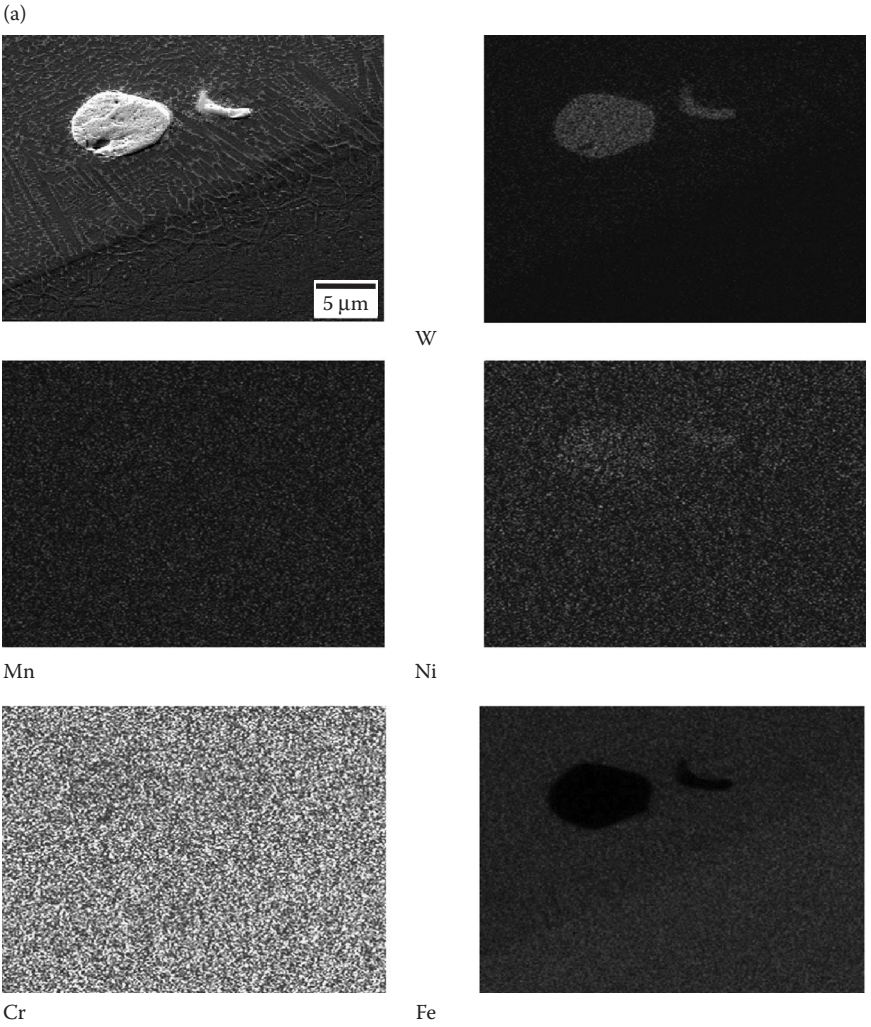


FIGURE 5.101 Boundary of the remelting zone and HAZ of the surface layer of the 55NiCrMoV7 steel after alloying with WC powder, laser power 2.3 kW: secondary electron image (a) and chemical composition area analysis.

with a hardness of 51.8 HRC, which increases over the entire range of the used laser power, that is, 1.2–2.3 kW. The maximum hardness of the surface layer obtained by alloying for niobium carbide NbC treated with a laser power of 2.3 kW is 63.9 HRC, tantalum carbide TaC treated with laser power of 2.3 kW is 67.4 HRC, VC treated with laser power of 2.3 kW is 59.7 HRC. In case of laser alloying of titanium carbide TiC powder there was a significant decrease of hardness for all the used laser ceramic powers, in comparison to the material subjected to the standard heat treatment. In most cases, the hardness of the surface layer of alloy hot work tool

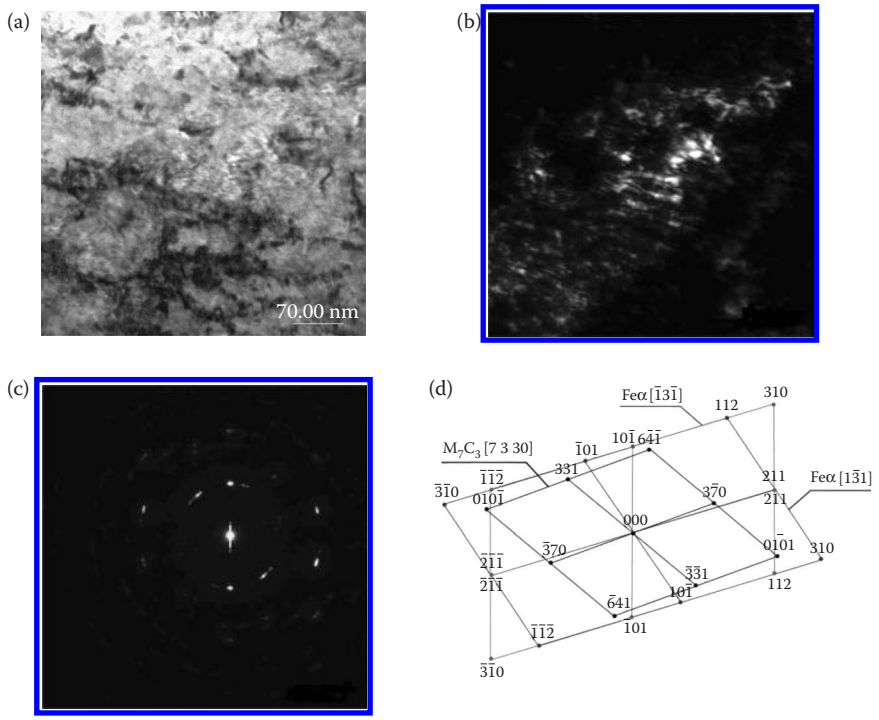


FIGURE 5.102 Thin foil structure of the X40CrMoV5-1 heat-treated steel; (a) bright-field image, (b) dark-field image from the reflexes $[\bar{1}\,\bar{1}\,\bar{2}]$ Feα and $[0\,1\,0\,\bar{1}]$ M_7C_3, (c) diffraction pattern from the area in (a), (d) solution of the diffraction pattern from (b).

steel 32CrMoV12-28 subjected to laser alloying with carbide powders increased in comparison to steel subjected to a conventional heat treatment only. The highest increase in hardness has a laser-alloyed steel with the powders tantalum carbide, niobium carbide TaC, and NbC.

For the 55NiCrMoV7 steel the highest hardness (HRC 68.1) of the surface layer is obtained for the WC carbide alloyed steel with a laser power of 2.3 kW. The highest hardness (HRC 61.87) of the top layer of the investigated steel subjected to laser remelting was obtained after remelting with a laser power of 2.0 kW. The lowest hardness (HRC 43,67) is characteristic for the remelted surface layer with laser beam power of 1.2 kW. The hardness of the surface layer of the steel alloyed with VC, tungsten carbide, tantalum carbide, and niobium carbide increases proportionally with the increase of the laser beam power used for alloying. The highest hardness (HRC 65,36) of the surface layer after laser alloying of tantalum carbide was obtained for the laser beam power of 2.3 kW, and has achieved for titanium carbide (64.96 HRC) at a power of 1.6 kW, VC (66.4 HRC) at a power of 2.3 kW, and niobium carbide (63.7 HRC) at a power of 2.3 kW. In the case of laser alloying of the tool steel with titanium carbide the hardness has decreased by about 2 HRC after alloying with a laser with a power of 2.0 kW and 2.3 kW. In

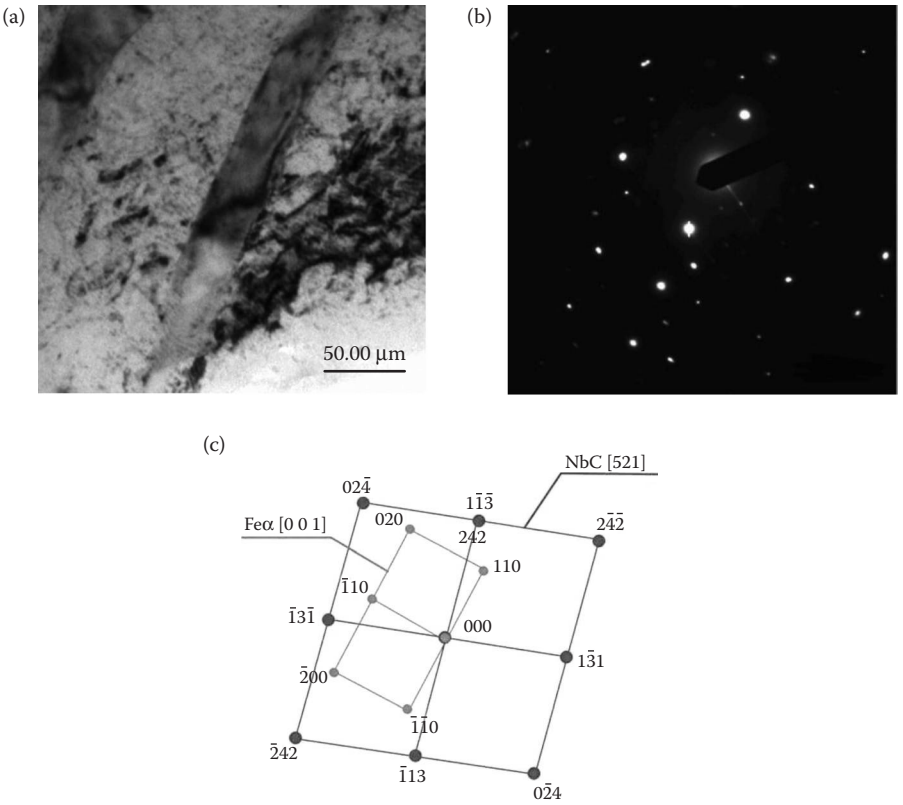


FIGURE 5.103 Thin foil structure of the X40CrMoV5-1 steel after alloying with NbC carbide powder, laser power 1.2 kW, (a) bright-field image, (b) diffraction pattern from the area in (a), (c) solution of the diffraction pattern from (b).

Figure 5.108, the average hardness change of the surface layer of the investigated steels is presented.

5.4.2.2 Microhardness Measurement

Microhardness is the property of a material that enables it to resist plastic deformation, usually by penetration. There are elastic and dynamic processes to measure hardness. The usual method to achieve a hardness value is to measure the depth or area of an indentation left by an indenter of a specific shape, with a specific force applied for a specific time. The Vickers hardness test method, also referred to as a microhardness test method, is mostly used for small parts, thin sections, or case depth work, for the reason to distinguish between ceramic particles and steel matrix. Referring to the foregoing considerations, it was found that in most cases of laser remelting or alloying of the carbide powders there was an increase of the microhardness. In all cases, the microhardness of the surface layer of heat-treated steel, laser alloyed or remelted was found an appearance of area in which a clear decrease of

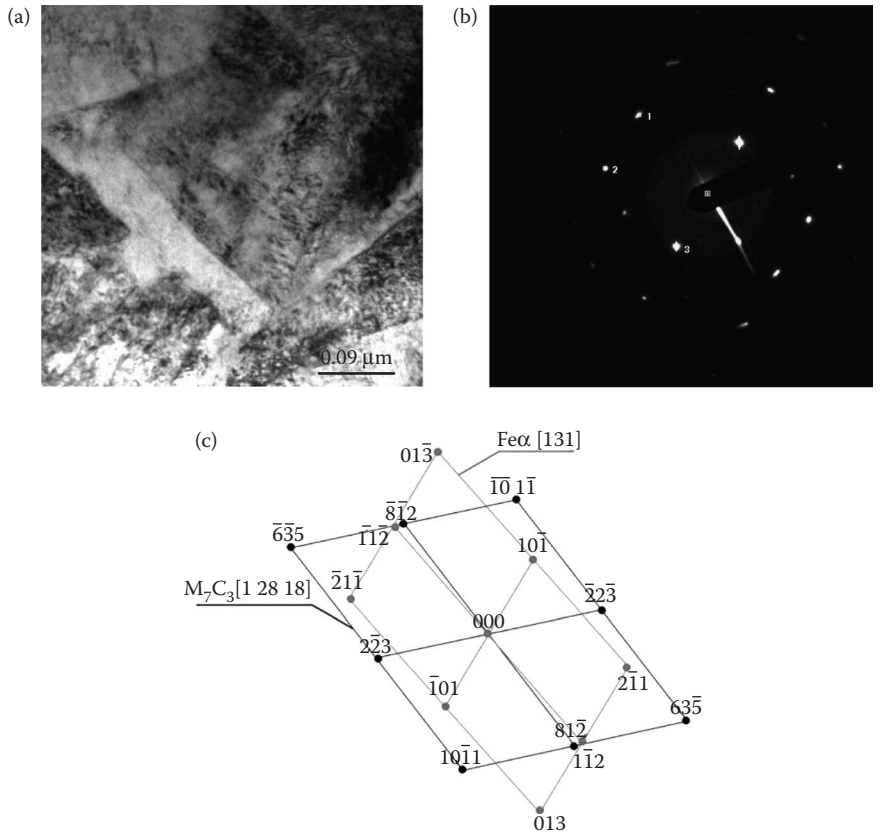


FIGURE 5.104 Thin foil structure of the X40CrMoV5-1 steel after alloying with NbC carbide powder, laser power 2.0 kW, (a) bright-field image, (b) diffraction pattern from the area in (a), (c) solution of the diffraction pattern from (b).

hardness occurs over the entire width of the HAZ and the base metal. This is an effect of lowering the hardness of the steel during annealing through the laser processing, during which the steel is heated to a temperature above the melting temperature.

In case of the X40CrMoV5-1 steel the highest microhardness of the remelting zone was observed for steel alloyed with titanium carbide 1010 $HV_{0,05}$ and niobium carbide 1005 $HV_{0,05}$ for the laser power of 2.3 kW. The lowest microhardness was found in case of the tantalum carbide alloyed steel 400 $HV_{0,05}$ and tungsten carbide 404 $HV_{0,05}$ at a laser power of 1.6 kW. There was found an increase of microhardness with increasing degradation level in all groups of ceramic powders. The highest microhardness has a layer obtained by alloying of the steel with niobium carbide NbC (1005 $HV_{0,05}$) and titanium carbide TiC (1010 $HV_{0,05}$) with the laser power in the range from 1.6 to 2.3 kW. In other cases, the increase of microhardness after laser treatment was obtained for laser remelted steel and was equal to 285 $HV_{0,05}$ for the laser power of 2.3 kW, for steel alloyed with tungsten carbide the value was 250

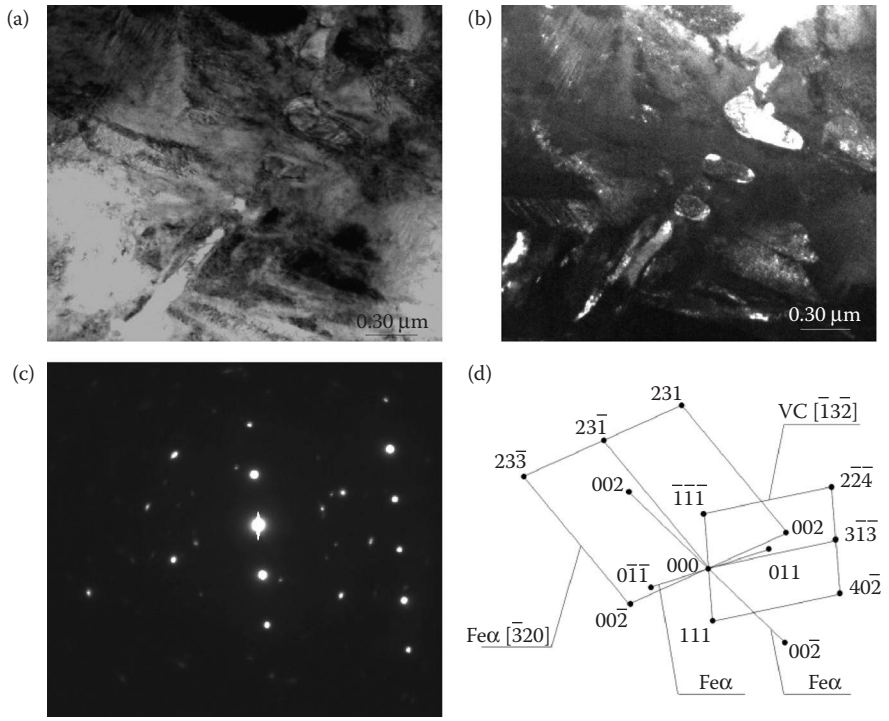


FIGURE 5.105 Thin foil structure of the X38CrMoV5-3 steel after alloying with VC carbide powder, laser power 2.0 kW, (a) bright-field image, (b) dark-field image, (c) diffraction pattern from the area in (a), (d) solution of the diffraction pattern from (b).

$HV_{0,05}$ and for tantalum carbide 380 $HV_{0,05}$ with laser power of 2.3 kW as well as for VC 391 $HV_{0,05}$ at the laser power of 1.6 kW.

The highest increase in microhardness for the X38CrMoV5-3 steel in comparison to the material after a conventional heat treatment ranges from 679 HV0.01 after the alloying with tantalum carbide powder with a laser power of 1.6 kW. For other alloying particles, an average increase in the microhardness of the surface layer in case of VC was 471 HV0.01 for the applied laser power of 2.0 kW, and 332 HV0.01 for niobium carbide at a laser power of 1.2 kW as well as 196 HV0.01 for titanium carbide, with a laser power 2.0 kW. The highest microhardness is characteristic for surface layers of the 32CrMoV12-28 steel, obtained after alloying with tantalum carbide TaC and niobium carbide NbC. The best microhardness value based on the obtained investigation results was found in the case of steel samples alloyed with titanium carbide TiC.

In case of the 55NiCrMoV7 steel, the highest microhardness in the remelting zone was observed for steel alloyed with tantalum carbide TaC powder, which was equal to 1352 HV0.05 and niobium carbide NbC with a value of 1283 HV0.05 for the laser beam power of 1.6 kW. The lowest microhardness was found in steel samples alloyed with tungsten carbide WC—625 HV0.05 with a laser power of 1.6 kW, and titanium

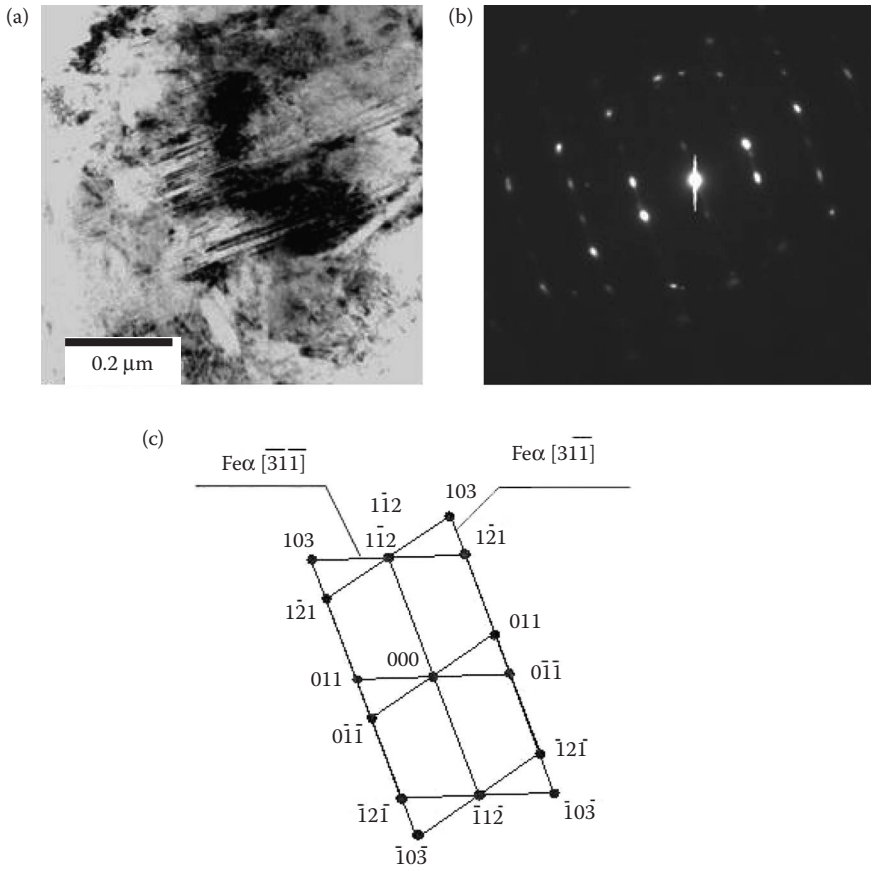


FIGURE 5.106 Thin foil structure of the 32CrMoV12-28 steel quenched at 1040°C and annealed at 550°C, (a) bright-field image, (b) diffraction pattern from the area in (a), (c) solution of the diffraction pattern from (b).

carbide TaC with 959 HV0.05 for a laser power of 1.2 kW. In all the analyzed cases, after laser remelting or alloying the microhardness increased significantly compared to the steel after standard heat treatment. The surface layer of the steel subjected to remelting reveals the largest growth of microhardness with HV0 238,05 and was observed in the case of laser power usage of 2.3 kW. For other carbide powders used, the average increase in the microhardness of the surface layer is equal: for VC 412 HV0.05 with the laser power of 2.0 kW, for tantalum carbide TaC 513 HV0.05 for the laser power of 1.2 kW, for niobium carbide NbC 429 HV0.05 for the laser power of 1.2 kW, for titanium carbide TiC 509 HV0.05 for a laser power of 2.3 kW, and for tungsten carbide WC—345 HV0.05 for a laser power of 2.3 kW (Figure 5.109).

On the basis of the microhardness results of the performed investigations on the cross section, it was found that the pattern of the cross-section microhardness increase is similar for all analyzed cases. The diagram below shows that the X40CrMoV5-1 steel microhardness is evidently different from the values of other steels by about

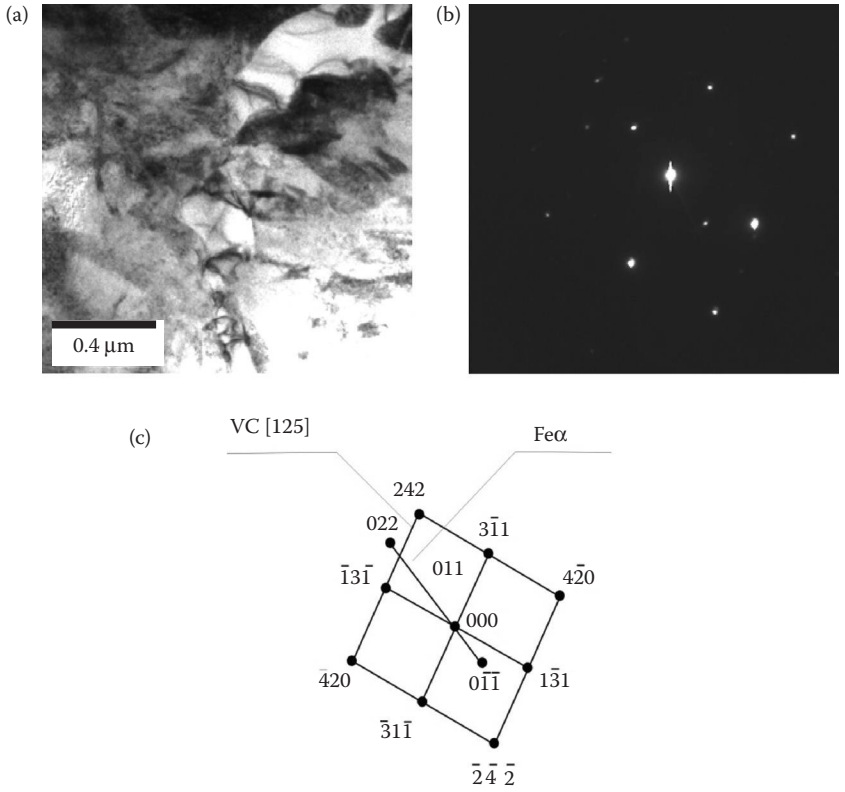


FIGURE 5.107 Thin foil structure of the 32CrMoV12-28 steel after alloying with VC carbide powder, laser power 2.0 kW, (a) bright-field image, (b) diffraction pattern from the area in (a), (c) solution of the diffraction pattern from (b).

500 HV even for the highest individual result, which may be caused by poor feeding of the ceramic powder particles due to differing concentrations of carbon in the matrix material. Other characteristics of the other steels exhibit a similar shape to that of the cross-section microhardness profile.

5.4.2.3 Wear Resistance Measurements in the Metal–Metal Arrangement

In order to compare the wear resistance under conditions simulating the operating conditions of hot work tool steels in as-cast after the conventional heat treatment and laser surface treatment, the wear tests were performed in the arrangement metal–quartz sand with a given load of 130 N.

It is supposed that an important factor for improving the wear resistance will be found in the dispersion of the ceramic particles embedded in the steel matrix being one of the occurred strengthening mechanisms affecting the phase and precipitation network of the steel microstructure after alloying with ceramic powders in case of titanium and VCs. In addition to the impact of the particles dispersion in the matrix, it also seems to be important that the wear resistance of the surface layer can be improved with

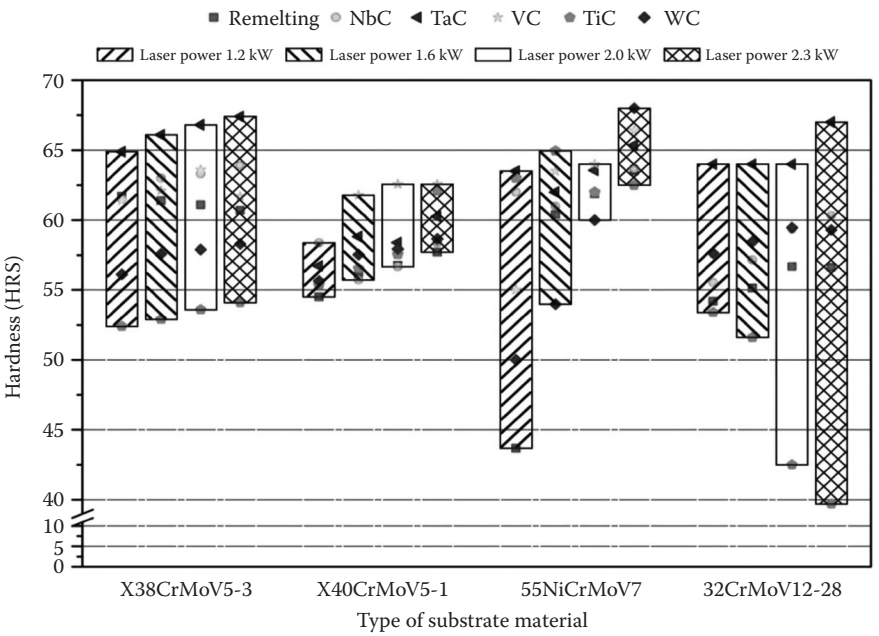


FIGURE 5.108 Average hardness change of the surface layer of hot work tool steels laser remelted or alloyed with the laser power in the range 1.2–2.3 kW.

relatively large particles of the ceramic powders including TaC and NbC fed into the matrix. The wear resistance of the investigated steels, as well as heat-treated condition after various surface treatment operations are shown in the form of the average mass loss. The results of the wear tests confirmed that both the heat treatment and change of the carbon concentration in the investigated steels in the range of approximately 0.3 to 0.55%, causes significant increase in their wear resistance.

The smallest average weight loss of the steel in a state after heat treatment is characteristic for the steel 55NiCrMoV7 after remelting with laser power of 1.2 kW. In contrast, the best wear resistance, both in the state after heat treatment, as well as after laser treatment has the X38CrMoV5-3 steel alloyed with laser power of 2.3 kW. When using a laser power of 1.2 kW the surface layer obtained by using most of the examined particles completely wears during the wear resistance test; what results also in wear of the matrix material during the wear test, while using a laser power of 2.3 kW—the outer layers have discontinuities in form of cracks and microcracks, what also reduce the wear resistance. The smallest average weight loss in a state after the laser treatment, characteristic for the 55NiCrMoV7-1 steel is obtained after alloying with titanium carbide powder with a laser power of 2.3 kW. In contrast, the best wear resistance after the laser surface treatment of the steel has the X40CrMoV5-1 steel alloyed with tungsten carbide powder with a laser power of 1.6 kW. The wear resistance of the composite layers produced by feeding of ceramic powders in some variants is higher than the wear resistance of steel not subjected to surface laser treatment (Figure 5.110). All properties changes of the laser treated

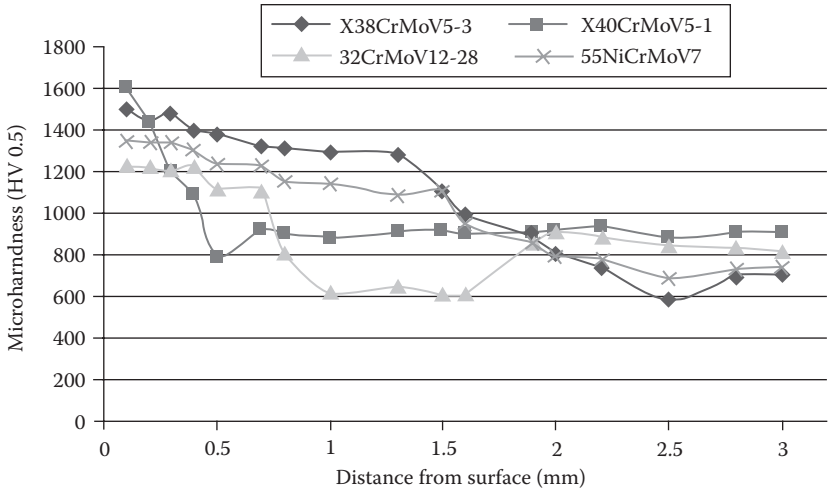


FIGURE 5.109 Microhardness changes of the surface layer of the X38CrMoV5-3 steel after alloying with TaC powder, X40CrMoV5-1 steel after alloying with NbC powder, steel 32CrMoV12-28 after alloying with TaC powder, laser power 1.6 kW, steel 55NiCrMoV7-28 after alloying with TaC powder, laser power 1.6 kW.

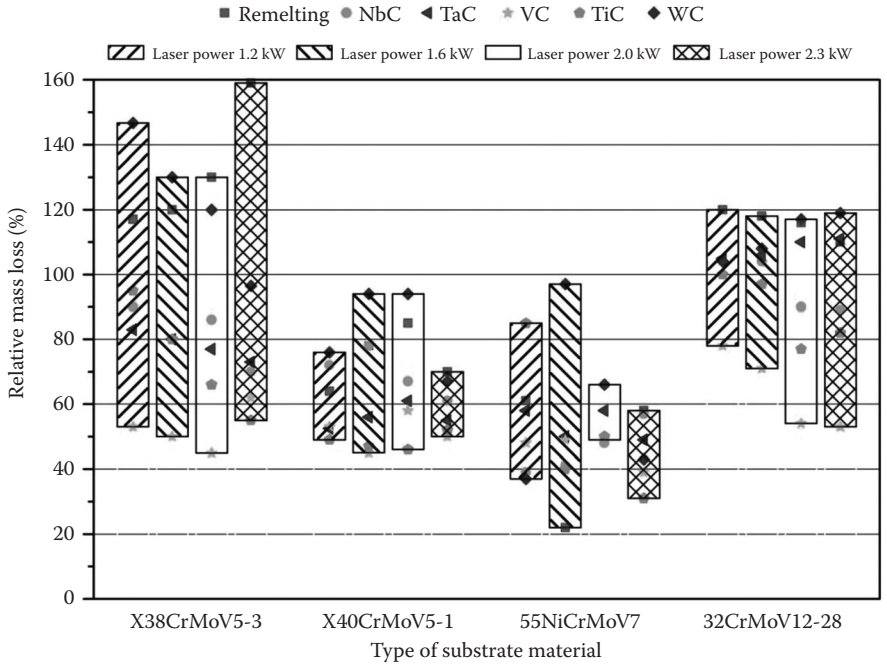


FIGURE 5.110 Relative mass loss measured during the wear resistance test of the hot work tool steels (100%—mass loss of the standard heat-treated sample, not laser treated with ceramic powders).

steels are closely related to changes in the structure, chemical composition, and phase in the surface layer. The highest increase in wear resistance, and thus the lowest weight loss steels are characterized by a carbon concentration above 0.4% with the laser-fed carbide particles: VC, TaC, TiC, and compared to the samples after standard heat treatment.

On the basis of the obtained results, it was found that there is a relationship between the laser power used for alloying and the abrasion resistance of the tested steels, which consists of correlated increase of hardness and wear resistance compared to the applied laser power.

Laser remelting of the surface layer of the investigated steel without alloying additives into the liquid metal, used in the whole range of laser power, causes fragmentation of the dendritic structure, the direction of crystallization of the direction of heat transfer from the laser interaction zone. As a result of laser alloying with tungsten carbide powder WC as well as niobium carbide NbC, VC, titanium carbide TiC, or tantalum carbide TaC there occurs in the steel surface fragmentation of the structure, precipitation hardening caused by the embedded but partially dissolved carbides as well as strengthening of the additives-enriched and alloyed surface layer coming from dissolving carbides.

Alloying using powders containing carbides WC, NbC, VC, TiC, or TaC, within the full accessible laser beam power range causes the alloying material to partially dissolve in the matrix, wherein with the increase of the laser power there is reduced the proportion of carbides, which are partially dissolved in the surface layer of the steel and form conglomerates with a characteristic configuration corresponding according to the thermal turbulences in the liquid metal. As a result of the crystallization of the surface layer saturated with carbon and respectively W, Nb, V, Ti, and Ta in the interdendritic space there crystallize carbides of these elements in characteristic eutectic systems.

The general observations found confirmed by the specific values obtained as a result of the investigations performed during the wear resistance test. The highest resistance and the lowest mass loss, relative to the weight loss of the sample subjected to a conventional steel to heat treatment, are characteristics of the X40CrMoV5-1 steel alloyed with VC powder and titanium carbide TiC with laser power of 1.6 kW and 2.0 kW, respectively. The elevated levels of titanium are confirmed in the remelting zone by the fed TiC particles. The highest weight loss is characteristic for the surface layer alloyed with tungsten carbide powder WC with a laser power of 1.6 and 2.0 kW laser as well as remelted only with a laser power of 2.0 kW, which is associated with a slight dissolution of the WC powder particles embedded in the investigated steel matrix. In the case of X38CrMoV5-3 steel the highest wear resistance, and thus the lowest mass loss relative to the mass loss of the sample steel subjected to a standard heat treatment was found for the sample alloyed with VC with laser at a power of 2.0 kW. The highest mass loss among all the particles' powders used was observed for the surface layer alloyed with tungsten carbide WC with the laser power of 2.3 kW. The lowest mass weight, and thus the highest wear resistance is characteristic for the 32CrMoV12-28 steel surface layer obtained by an alloying laser with VC powder and titanium carbide TiC. The highest wear resistance of the surface layers reveals the material treated with a laser beam power of 2.0 kW, with

the exception of tungsten and tantalum carbide powers. In the case of tantalum carbide powder the highest wear resistance was obtained after alloying with laser beam power of 1.6 kW, and in the case of tungsten carbide powder—with a power of 1.2 kW. The lowest wear resistance of all the samples is measured for steel subjected only to laser remelting. In the case of the hot work tool steel 55NiCrMoV7-1 laser alloyed with carbide powders in the lowest mass loss relative to the mass loss of the sample after standard heat treatment, and thus the highest wear resistance of the top layer was obtained for the steel alloyed with titanium carbide TiC powder with a laser power of 2.3 kW as well as with VC powder with a laser power of 2.3 kW. The lowest mass loss for the investigated 55NiCrMoV7-1 steel after laser remelting was the laser beam power of 2.3 kW. In case of alloying with tungsten carbide powder WC with the highest laser beam power (2.3 kW) fine cracks were developed in the surface material, which causes a decrease in the measured wear resistance. Straightening mechanism inform of the grain refinement in the laser-treated surfaces due to the recrystallization process as a result of the high stress provided in the rapid crystallization of the quasicomposite steel surface.

On Figures 5.111 through 5.118 there are presented the wear test paths on the surface layer of the tool steels X40CrMoV5-1, X38CrMoV5-3, 32CrMoV12-28, and 55NiCrMoV7 after the wear resistance test according to the ASTM-G65 standard.

5.4.3 Thermal Fatigue

Investigations concerning thermal fatigue resistance of the laser-treated hot work tool steel have shown that the laser remelting or alloying and the type of powder used for alloying have a significant impact on increasing the resistance of steel on the process of thermal fatigue. Thermal fatigue resistance of the laser alloyed steel is higher than that of steel after standard heat treatment, which indicates the application potential of this technology for the manufacture or regeneration of selected hot work tool steels. Figures 5.119 through 5.128 show the structure of the samples subjected to the test after standard thermal fatigue and laser treatment.

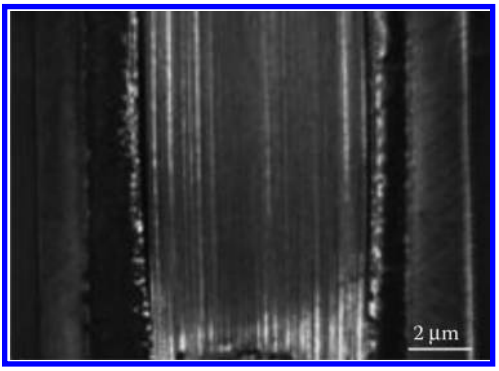


FIGURE 5.111 Surface after wear test according to the ASTM-G65 standard of the X40CrMoV5-1 steel alloyed with TiC powder, laser power 1.2 kW.

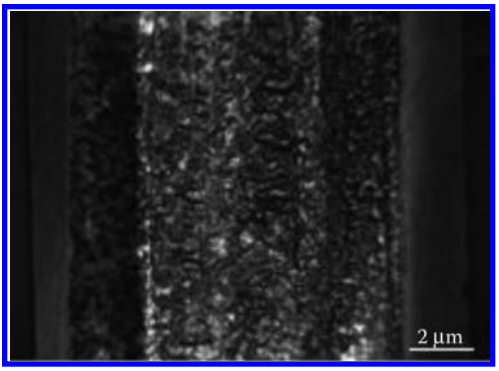


FIGURE 5.112 Surface after wear test according to the ASTM-G65 standard of the X40CrMoV5-1 steel alloyed with WC powder, laser power 1.2 kW.

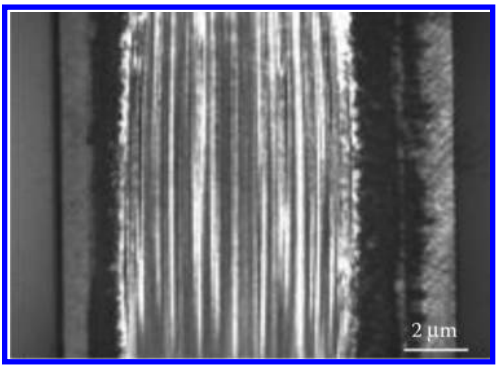


FIGURE 5.113 Surface after wear test according to the ASTM-G65 standard of the 32CrMoV12-28 steel alloyed with TiC powder, laser power 2.0 kW.

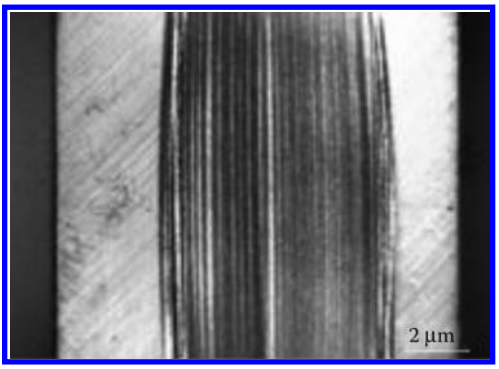


FIGURE 5.114 Surface after wear test according to the ASTM-G65 standard of the 32CrMoV12-28 without laser remelting or alloying.

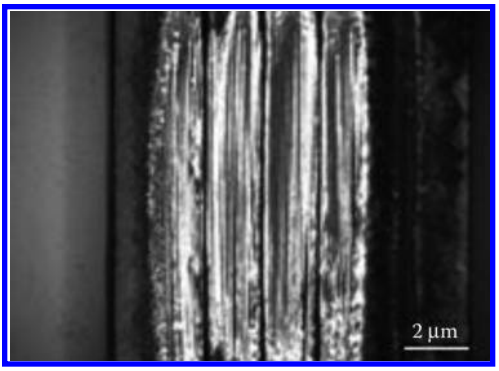


FIGURE 5.115 Surface after wear test according to the ASTM-G65 standard of the X38CrMoV5-3 steel alloyed with VC powder, laser power 2.0 kW.

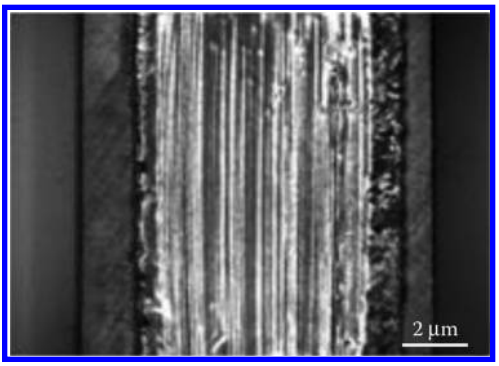


FIGURE 5.116 Surface after wear test according to the ASTM-G65 standard of the X38CrMoV5-3 steel alloyed with WC powder, laser power 1.6 kW.

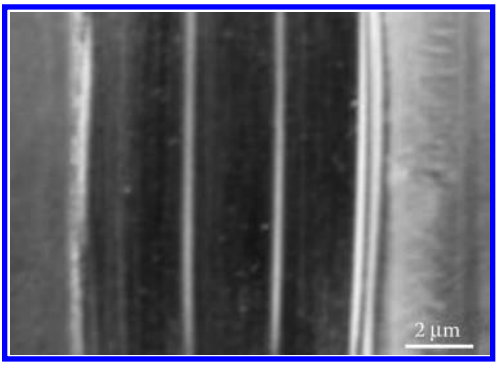


FIGURE 5.117 Surface after wear test according to the ASTM-G65 standard of the 55NiCrMoV7 after laser remelting, laser power 1.6 kW.

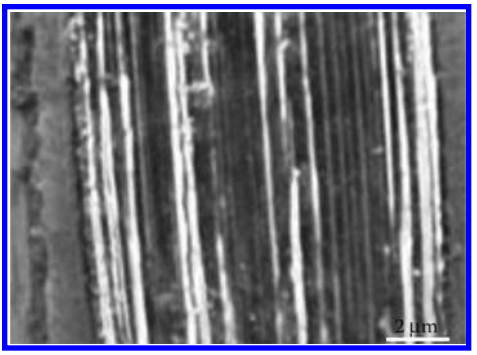


FIGURE 5.118 Surface after wear test according to the ASTM-G65 standard of the 55NiCrMoV7-1 steel alloyed with WC powder, laser power 1.6 kW.

The parameters that were examined during the performed tests were the average depth of the cracks and the maximum depth of the cracks. First, the samples were tested after heat treatment, and then after alloying of the surface layer. Based on the given results it is evident that after remelting there is only a small amount of subsurface defect and grain refinement, it is also of significance that the alloying

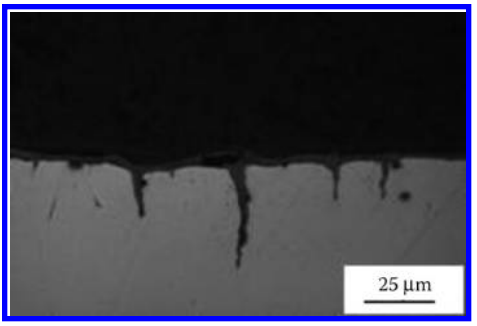


FIGURE 5.119 Cracks on the cross section of the X40CrMoV5-1 steel remelted with laser power of 2.3 kW, created during the thermal fatigue test.

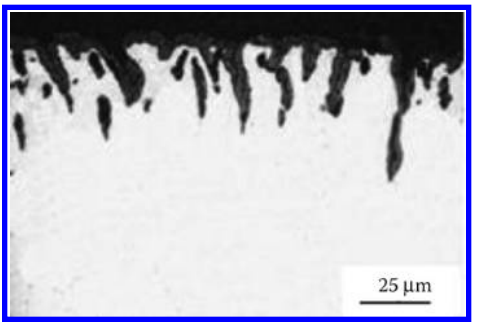


FIGURE 5.120 Cracks on the cross section of the heat treated X38CrMoV5-3 steel, created during the thermal fatigue test.

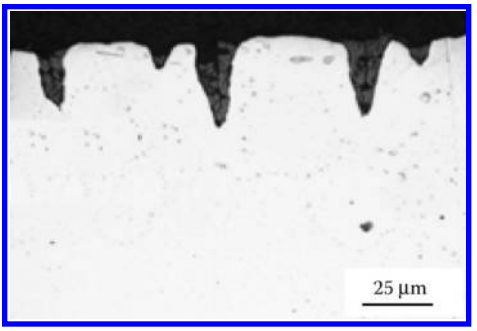


FIGURE 5.121 Cracks on the cross section of the 32CrMoV12-28 steel alloyed with TaC, laser power o 2.0 kW, created during the thermal fatigue test.

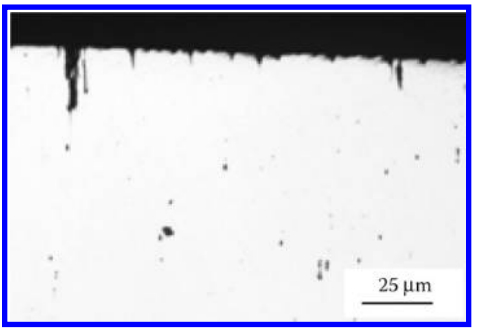


FIGURE 5.122 Cracks on the cross section of the 55NiCrMoV7 steel alloyed with TiC, laser power 1.2 kW, created during the thermal fatigue test.

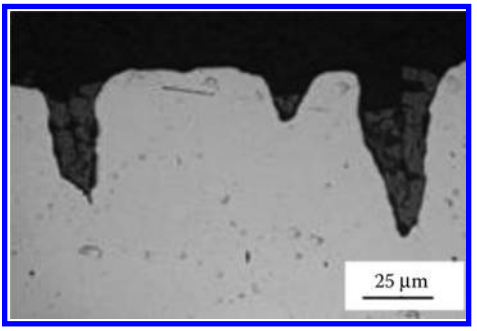


FIGURE 5.123 Cracks on the cross section of the 32CrMoV12-28 remelted, laser power of 1.2 kW, created during the thermal fatigue test.

elements may have passed into the matrix increasing their creep resistance, similar to the embedded particle in the matrix improving their distribution, size, as well as the synergy effect of all these factors together.

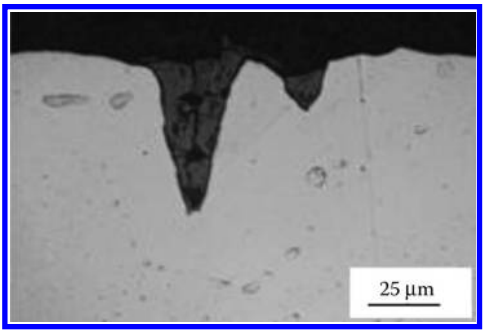


FIGURE 5.124 Cracks on the cross section of the 32CrMoV12-28 steel remelted, with laser power of 1.6 kW, created during the thermal fatigue test.

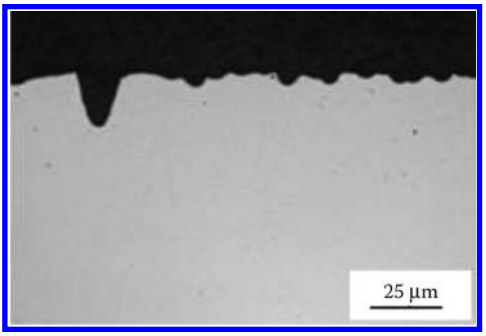


FIGURE 5.125 Cracks on the cross section of the 32CrMoV12-28 remelted, laser power of 2.0 kW, created during the thermal fatigue test.

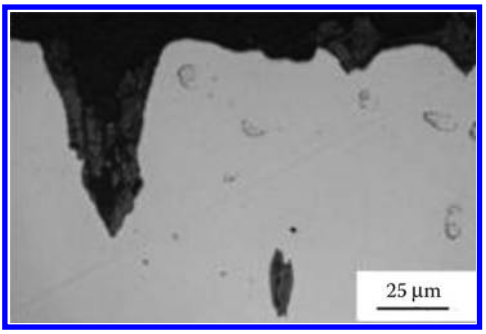


FIGURE 5.126 Cracks on the cross section of the 32CrMoV12-28 alloyed with NbC, laser power of 1.6 kW, created during the thermal fatigue test.

It is recognizable that, despite the treatment parameters by means of titanium and VCs in almost every considered case the surface layers have superior structure and higher resistance.

The average cracks depth of the X40CrMoV5-1 steel in the case of the alloyed layer with VC in the range of 0.022–0.024 mm, for titanium carbide 0.02–0.01 mm,

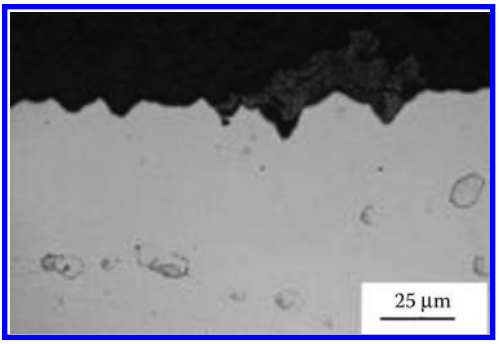


FIGURE 5.127 Cracks on the cross section of the 32CrMoV12-28 alloyed with NbC, laser power of 2.0 kW, created during the thermal fatigue test.

and tantalum carbide 0.02–0.01 mm. Figure 5.129 shows the average depth of the cracks of the X40CrMoV5-1 steel laser alloyed with different carbide powders.

The value of the maximum crack depth is in the range of 0.05–0.04 mm for VC alloyed steel, 0.03–0.02 mm for steel alloyed with titanium carbides 0.04–0.01 mm for steel alloyed with tantalum carbide with applied laser beam of power of 1.2–2.3 kW. As a result of the performed tests, it was found that the highest resistance to thermal fatigue is characterized for steel alloyed with VC powders, titanium and tantalum carbides TiC and TaC. The lowest thermal fatigue resistance of the performed test indicates that the outer layers obtained by laser melting and alloying with tungsten carbide used the entire range of laser power.

The highest thermal fatigue resistance of the steel surface layers exhibit the X38CrMoV5-3 steel, which is obtained by alloying with titanium and VC powders. In the case of alloying with carbide a few small cracks were found on the surface layer formed after the tests with 5000 heat cycles. The laser alloyed steel with TaC and WC powder carbides reveals that cracks and delamination of the surface layer occurred after 1000 thermal cycles. Figure 5.130 shows the average crack depth of the X38CrMoV5-3 steel after laser alloying with different carbide powders.

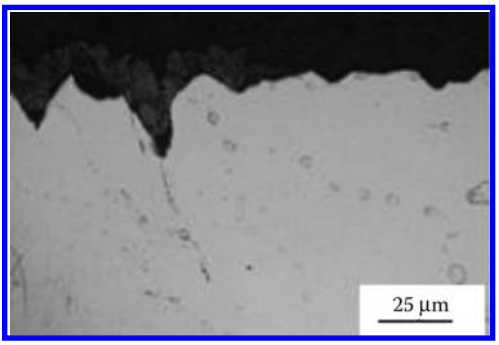


FIGURE 5.128 Cracks on the cross section of the 32CrMoV12-28 alloyed with VC, laser power of 1.6 kW, created during the thermal fatigue test.

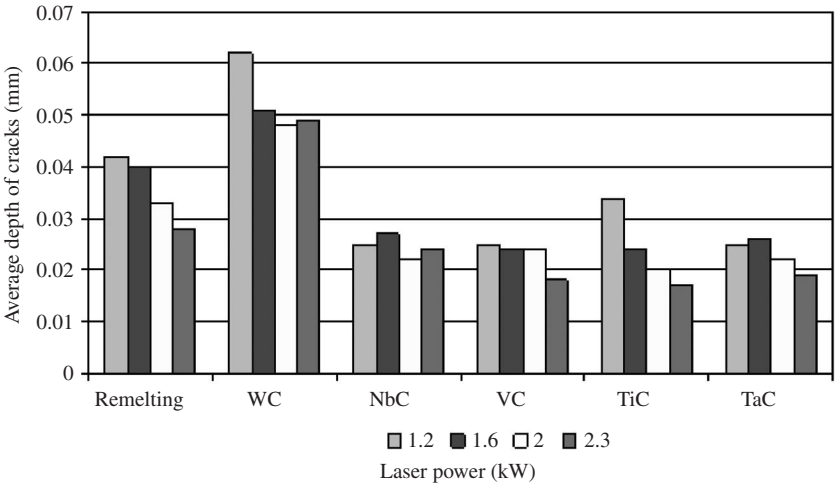


FIGURE 5.129 Comparison of average crack depth of the X40CrMoV5-1 steel surface layer after laser remelting or alloying with different ceramic carbide powders after the thermal fatigue test.

Also in the case of steel 32CrMoV12-28 the highest resistance to thermal fatigue during the test performed under the given conditions is characterized for the steel surface layers obtained after alloying of VC powder and titanium carbide powder. In this case, only small pits were observed on the sample surface, while observing no significant appearance of cracks. The best thermal fatigue resistance of the alloys are characterized for the tantalum carbide and niobium carbide powders. It was

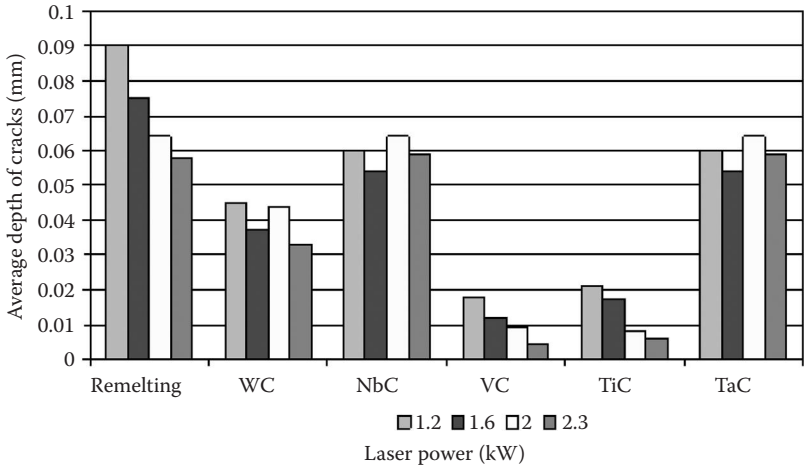


FIGURE 5.130 Comparison of average crack depth of the X38CrMoV5-3 steel surface layer after laser remelting or alloying with different ceramic carbide powders after the thermal fatigue test.

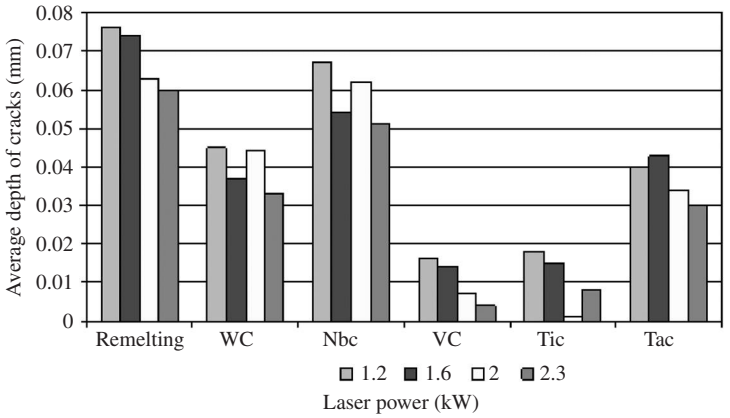


FIGURE 5.131 Comparison of average crack depth of the 32CrMoV12-28 steel surface layer after laser remelting or alloying with different ceramic carbide powders after the thermal fatigue test.

also found that there is a relationship between the power applied to the laser beam machining, and the size and the number of cracks formed in the surface layer of steel tested. As a result of laser melting of the beam power of 1.6 kW more cracks formed in the surface layer than the alloyed laser beam power of 2.0 kW. This relationship is true for all alloying powders used for the carbides. Figure 5.131 shows the average depth of the cracks for the 32CrMoV12-28 laser alloyed steel with carbide powders subjected to the thermal fatigue test.

The parameters of the laser surface treatment, including the type of the alloying material and/or power of the laser beam, have a clear effect on the thermal fatigue resistance of the 55NiCrMoV7 steel. In case of laser alloying with WC tungsten carbide powder after the thermal fatigue test there occurs an increase in the number and depth of cracks. The average depth of cracks obtained in the steel surface layer after conventional heat treatment is equal to 0.95 mm. In the case of steel subjected to laser alloying the smallest average cracks depth of 0.18 mm was observed for steel alloyed with VC at a laser power of 2.3 kW and 0.23 mm in case of alloying with TiC titanium carbide at a laser power of 2.3 kW.

5.5 SUMMARY AND CONCLUSION

The increase in requirements on engineering materials used for machine parts and equipment, as well as the development of new technologies, including the constitution of surface layers needs a constant search for new solutions to the production of surface-machined parts that meet the established performance requirements. The investigations are performed to describe the phenomena occurring on the surface of solids in modern manufacturing techniques and are carried out by many research centers in the country and all over the world in the field of surface engineering. Laser processing techniques of surface layers are certainly a group of manufacturing

techniques aimed at increasing the service life of the surface layers of components made from hot work tool steels, and thus also improving the functional properties of the final product. Different wear mechanisms, in particular tribological and corrosion, significantly limit the maximum lifetime of the finished components. Therefore, there is a need for new solutions to improve the wear and corrosion resistance of the surface layer of the constructional material. A lot of research work was carried out in the national and international research centers concerning implementation of laser in producing of surface layers. The research results presented in this work have shown, in particular, that the surface layers produced by laser surface melting and also laser surface alloying with carbide powders, have a longer durability and service reliability in comparison with those obtained using conventional surface treatment methods. Mechanisms concerning the influence of carbides on structure and properties occurring during the laser processing can be divided depending on the material dissolution of the ceramic powders in the matrix, which is influenced both by the type of carbide used and the laser power. As a result of laser surface melting of steel substrate (without alloying with carbide powders) there occurs a slight increase in the surface layers properties compared to corresponding values obtained for conventional methods resulting from the standard heat treatment. Increase in the laser power used for surface melting also causes increase of the thickness of fusion zone, however, the HAZ produced during surface melting process is much smaller when compared to HAZ obtained during surface alloying process. It results from lower absorption coefficient of the laser radiation on the metal surface in comparison to absorption coefficient of carbide particles. Also, roughness of the surface layers of steel increases compared to the roughness of the untreated surface, which is associated with the occurrence of strong convection movement in the melt pool driven by surface tension and also fast crystallization rate. Under the influence of very high temperature during the laser treatment the surface layer material and the additional material evaporates, forming thereby a specific surface area with very high roughness on the alloyed surface. If the power of the laser beam is relatively low, the structure is quite uniform with a flat bottom of the fusion zone. The increase of the applied laser power affects a larger undulation of the fusion zone. Significant influence on the formation of the melt pool has an uneven heating, which is also a reason for the formation of large surface tension gradient. As a result of the laser surface melting of steel its thermal fatigue resistance is slightly higher than that obtained after standard heat treatment.

As a result of the laser alloying with carbide powders there may occur a partial dissolving of these alloying material in the liquid metal. There is also the possibility that the carbide particles remain undissolved or form conglomerates due to feeding of the undissolved carbide powder particles into the molten metal substrate. Increasing the laser power causes a decrease in the amount of the undissolved carbides, which increase the dispersion hardening of the steel matrix in the surface layer. During laser treatment, followed by a strong circulation of liquid metal, and after the end of the laser treatment, rapid solidification of the surface layer occurs. With the increase of the laser power there occurs a reduction in the value of undissolved carbides in the steel matrix. It was found that in each case, that is, independent of the processing

parameters there is an increase of the surface roughness, which is caused by the presence of strong convection movements in melt pool caused by a high power of the laser beam and the associated rapid crystallization connected with the influence of the protective gas stream. High demands put on today's user make it necessary to find universal solutions, allowing a combination of a low-cost substrate having the best possible mechanical and functional properties with properly chosen machining technology of the surface. If, therefore, the recycling costs will be calculated as the sum of the cost of materials, labor, and energy, so it can be assumed that they are in the range from a few to several tens of percentage of the value of the whole produced part. Therefore, the achieved economic effects after taking into account the profit from the application of the produced layer with improved properties compared to the untreated material may be more cost effective. So the use of laser surface treatment is justified from an economic point of view, and also because in most cases it provides higher mechanical and functional properties of the machined surfaces, so that they can meet the particularly high working conditions established for modern tools.

REFERENCES

1. Adamiec P., Dziubiński J.: *Production and Properties of Surface Layers of Transport Machines Elements*. Publisher of Silesian University of Technology, Gliwice, 2005.
2. Barbacki A., Dynak K., Kawalec M.: Microstructure and roughness of WNL steel after quenching and machining. *Material Engineering*, 2005, 303–305.
3. Adamczyk J.: *Engineering of Steel Products*. Monograph, Publisher of Silesian University of Technology, Gliwice, 2000.
4. Berkowski L.: *Technical Council Entitled: Tools for Cold and Hot Plastic Deformation*. PWN Publisher, Lublin, 1978, p. 35.
5. Blicharski M.: *Material Engineering*. Steel, Warszawa, WNT, 2004.
6. Dobrzański. L.A.: Basics of material science metal science. *Engineering Materials with Basics of Material Design*. WNT, Gliwice—Warszawa, 2006.
7. Dobrzański L.A., Hajduczek E., Marciniak J., Nowosielski R.: *Heat Treatment of Tool Materials*. Skrypt Nr 1390, Politechnika Śląska, Gliwice, 1990.
8. Dobrzański L.A., Mazurkiewicz J., Hajduczek E.: Hot work tool steel 47CrMoWVTiCeZr16–28–8. *Proceedings of the 3rd Scientific Conference on Materials, Mechanical and Manufacturing Engineering*. Gliwice–Wisła, 2005, pp. 193–202.
9. Głowacka M.: *Metal Science*. Publisher of Gdansk Technical University, Gdańsk, 1996.
10. Białecki M.: *Alloying Hot Work Steels*. Institute of Iron Metallurgy, Katowice, 1979, p. 124–128.
11. Przybyłowicz K.: *Metal Science Questions and Answers*. WNT, Warszawa, 2004.
12. Przybyłowicz K., Depczyński W., Konieczny M.: Influence of power density of the laser radiation on structure and properties of as cast high speed steel. *Material Engineering*, 1999, 12–17.
13. Sieniawski J., Filip R., Mrówka G., Pleszekow E.: Effect of laser treatment on microstructure of Ti-6Al-4V titanium alloy. *Proceedings of the 10th Jubilee International Scientific Conference Achievements in the Mechanical and Materials Engineering*, AMME'2001, Gliwice—Kraków—Zakopane, 2001, pp. 523–526.
14. Adamczyk J., Hajduczek E., Dobrzański L.A., Przybył M.: Structure mechanical properties of tool steels WCLVZ i WNL. *Foundry News*, 1983, 246–251.
15. Dobrzański L.A., Hajduczek E., Marciniak J., Nowosielski R.: *Metal Science and Heat Treatment of Tool Materials*. Warszawa, WNT, 1990.

16. Adamczyk J., Hajduczek E., Dobrzański L.A., Dragon K.: *Structure and Mechanical Properties of Tool Steel 5H4M3V2F i 4H3V3MFK*. X, Brno—Bratislava, CSRS, 1984, t. 2, pp. 67–72.
17. Ciszewski A., Radomski T., Szummer A.: *Material Science*. Publisher of Warsaw University of Technology, Warszawa, 1996.
18. Dobrzański. L.A.: *Metal Science and Heat Treatment*. Science and pedagogic publisher, Warszawa, 1997.
19. Adamczyk J.: Directions of development of tool steels and improvement of tool quality. *Foundry News*, 6, 1983, 171–178.
20. Klimpel A., Lisiecki A., Janicki D., Wochnik P.: Heat treatment and laser alloying of tool steels. *Welding Review*, 8–10, 2002, 169–171.
21. Sweda R.: Novalas—Taking laser into the 21st century. *Laser Initiative*, 11, 1998, 18–21.
22. Woldan A., Kusiński J., Tasak E., Kąc S.: Influence of laser alloying of carbon steel with chromium on structure and properties of the surface layer. *Material Engineering*, 2000, 478–481.
23. Adamczyk J., Hajduczek E.: Phase composition od surface layer of WCLV steel boronised by diffusion. *III International Conference* Carbides, nitrides, borides, Poznań–Kołobrzeg, 1984, pp. 272–278.
24. Dobrzański L.A., Mazurkiewicz J., Hajduczek E.: Structure and chemical composition of carbides in quenched tool steels Cr-Mo-W-V i Cr-Mo-V for hot work. *Proceedings of the Scientific Conference Materials, Mechanical and Manufacturing Engineering*, M^{3}E'2000, Gliwice, 2000, pp. 83–88.
25. Hajduczek E., Dobrzański L.A.: Trends of development and wear structure of hot work tool steels. *Foundry News*, 41, 1985, 259–269.
26. Adamczyk J., Hajduczek E., Griner S.: The thermal fatigue resistance of conventionally and vacuum melted of hot-work tool steel. *X Hüttenmännische Materialprüfertagung (Foundry materials investigations Symposium, Balatonaliga),* Hungary, 1979, 126–130.
27. Hetmańczyk M.: *Material Science Basics*. Issue II, Gliwice, 1999.
28. Gierek A.: *Tribological Wear*. Scripts of Silesian University of Technology, Gliwice, 2005.
29. Ciftci I.: Machining of austenitic stainless steels using CVD multi-layer coated cemented carbide tools. *Tribology International*, 39, 2006, 565–569.
30. Dobrzański L. A.: *Material Science and Heat Treatment of Metal Alloys*. Publisher of Silesian University of Technology, Gliwice, 1987.
31. Dobrzański L. A. (red.): Encyclopedia of material science. Metale. Polymers. Ceramics. *Composites*, Publisher of Verlag Dashöfer, Warszawa, 2003.
32. Dobrzański. L. A.: *Metallic Engineering Materials*. WNT, Warszawa, 2004.
33. Dobrzański. L.A.: *Material Science with Basics of Material Engineering*. WNT, Warszawa, 1999.
34. Młynarczyk A., Jakubowski J.: *Surface Treatment and Protective Coatings*. Publishing by the Poznan Technical University, Poznań, 1998.
35. Tkaczyk S.: Surface layer of metals. *Achievements in the Mechanical and Materials Engineering*, Publishing by the Silesian University of Technology, Gliwice, 1994, pp. 351–358.
36. Namysło A.: Structure and mechanical properties of WCLV steel after heat treatment. *Foundry News*, 1, 1985, 3–8.
37. Labisz K. *Structure and Properties of Laser Remelted and Alloyed Shot Work Tool Steel 32CrMoV12–28.* PhD thesis, Main library of the Silesian University of Technology, Gliwice, 2005.
38. Mazurkiewicz J.: *Comparison of Structure and Properties of Tool Steels WLWT and WCLV for Hot Work*. PhD thesis, Main bibliotheca of the Silesian University of Technology, Gliwice, 2000.

39. Piec M: *Structure and Properties of Laser Remelted and Alloyed Shot Work Tool Steel X38CrMoV5-3*. PhD thesis, Main library of the Silesian University of Technology, Gliwice, 2005.
40. Dobrzański. L.A.: *Material Science and Heat Treatment*. WSiP, Warsaw, 1997.
41. Karłow N.W.: *Lectures of Laser Physics*. WNT, Warszawa, 1989.
42. Major B.: *Ablation and Sedimentation with Pulse WN*. Akapit, Kraków, 2000.
43. Wesołowski K.: *Metal Science and Heat Treatment*. WNT, Warszawa, 1978.
44. Anna Schellenberg.: *Encyclopedia of Technics and Chemistry*. Issue IV, WNT, Warszawa, 1993.
45. Dubik A.: *100 Words about Laser and Laser Radiation*, WMON, 1989.
46. Kusiński J.: *Lasers and its Application in Material Engineering*. Scientific publisher Akapit, Kraków, 2000.
47. Przybyłowicz K.: *Material Science*. WNT, Warszawa, 2000.
48. Piec M., Dobrzański L.A., Labisz K., Jonda E., Klimpel A.: Laser alloying with WC Ceramic Powder in hot work tool steel using a high power diode laser (HPDL). *Advanced Materials Research*, 15–17, 2007, 193–198.
49. Dobrzański L.A., Jonda E., Labisz K.: Comparison of the abrasion wear resistance of the laser alloyed hot work tool steels. *Archives of Materials Science and Engineering*, 55/2, 2012, 85–92.
50. Dobrzański L.A., Jonda E., Pakieła W., Bilewicz M.: Improvement of wear resistance of the hot work tool steel by laser surface feeding with ceramic powders. *Archives of Materials Science and Engineering,* 60/2, 2013, 64–71.
51. Bachmann F.: *The Laser of Tomorrow—Diode Laser, Schweisstechnische Lehr- und Versuchsanstalt*. Duisburg, Germany, 1997, pp. 1–17.
52. Nowicki N.: *Lasers in Electron Technology and Material Treatment*. WNT, Warszawa, 1978.
53. Abramowicz H.: *Introduction to Laser Spectroscopy*. PWN, Warszawa, 2000.
54. Dziadoń A., Konieczny M., Gajewski M.: Enrichment of the surface layer of the alloy AlMg3 with nickel-silicon sediment by laser. *Material Engineering*, 2003, 84–87.
55. Domański R.: *Laser Radiation-Influence of Laser on Solid Materials*. Warszawa, WNT, 1990.
56. Kaczmarek F.: *Basics of Laser Treatment*. WNT, Warszawa, 1983.
57. Kaczmarek F.: *Introduction to Laser Physics*. PWN, Warszawa, 1986.
58. Staub F.: *Material Science*. Silesian technical Publisher, Katowice, 1994.
59. Starzyński G.: *Surface Layer and its Modification AIPPT PN*. IPPT PAN Publisher, Warsaw, 1996.
60. Klimpel A., Mazur M.: *Welding Manual*. Publisher of Silesian University of Technology, Gliwice, 2004.
61. Kujawski A., Szczepański P.: *Lasers—Physical Basics*. Publisher of Warsaw technical University, Warszawa, 1999.
62. Kusiński J.: Laser technique in processes of surface treatment and material synthesis, current state and development perspectives. *Material Engineering*, 2002, 26–32.
63. American standard ASTM G65-00, Standard Test Method for Measuring Abrasion Using the Dry Sand/Rubber Wheel Apparatus.
64. Dubik A.: *Laser Application*. Warszawa, WNT, 1991.
65. Tański T.: Determining of laser surface treatment parameters used for light metal alloying with ceramic powders. *Materialwissenschaft und Werkstofftechnik (Materials Science and Engineering Technology) 45/5*, 2014, 333–343.
66. Labisz K., Tański T., Janicki D.: HPDL energy absorption on anodised cast Al-Si-Cu alloys surfaces during remelting. *Archives of Foundry Engineering*, 12/2, 2012, 45–48.

67. Labisz K., Tański T., Dobrzański L.A.: HPDL laser alloying of heat treated Al-Si-Cu alloy. *Archives of Materials Science and Engineering*, 54/1, 2012, 13–21.
68. Dobrzański L.A., Tański T., Domagała J., Malara Sz., Klimpel A.: Laser surface treatment of Mg-Al-Zn alloys, (Strojarstvo). *Journal for Theory and Application in Mechanical Engineering*, 53/1, 2011, 5–10.
69. Labisz K.: Microstructure and mechanical properties of HPDL laser treated cast aluminium alloys. *Materials Science and Engineering Technology 2014, Mat.-wiss. u. Werkstofftech*., 45, 314–324. doi: 10.1002/mawe.201400231.
70. Dobrzański L.A., Labisz K., Jonda E., Klimpel A.: Comparison of the surface alloying of the 32CrMoV12-28 tool steel using TiC and WC powder. *Journal of Materials Processing Technology,* 191/1/3, 2007, 321–325.
71. Jonda E., Labisz K., Pakieła W.: Influence of the HPDL surface treatment of the X40CrMoV5–1 and 32CrMoV12-28 tool steels on wear resistance. *Archives of Materials Science and Engineering,* 64/2, 2013, 152–159.
72. Labisz K., Jonda E., Tański T., Borek W., Czaja M.: High power diode laser application for metals surface treatment based on wear resistance investigation. *Advanced Materials Research*, 1036, 2014, 482–489.
73. Jonda E., Lukaszkowicz K.: Influence of the HPDL surface treatment of the X40CrMoV5-1 tool steel on wear resistance advanced materials research. *Advanced Materials Research*, 1036, 2014, 428–433.
74. Tanski T., Labisz, K., Lukaszkowicz K.: Structure and properties of diamond-like carbon coatings deposited on non-ferrous alloys. *Solid State Phenomena*, 199, 2013, 170–175.
75. Dobrzański. L.A.: Basics of material science. *Engineering Materials with Material Design Basics*. WNT, Gliwice—Warszawa, 2002.
76. Blicharski M.: *Surface Engineering*. Scientific Technical Publisher, Warszawa, 2009 (in Polish).
77. Łaskawiec J.: *Surface Engineering*. Publishing by the Silesian University of Technology, Gliwice, 1997.
78. Burakowski T., Wierzchoń T.: *Surface Engineering of Metals*, Warszawa, WNT, 1995.
79. Ostrowski B., Budzynowski T., Ziewiec W.: Surface layer and its heat treatment as a factor of growth of the machine element stability. *Material Engineering*, 2002, 18–25.
80. Klimpel A.: *Hard Facing and Thermal Spray Technologies*. WNT, Warsaw, 2000.
81. Legutko S.: Basics of machines and devices exploitation. *WSiP*. 2004, ISBN 83-02-08998-2.
82. Zawora J.: *Basics of Machine Technology*. WSiP publisher, Warsaw, 2007.
83. Krajewski S.: Tribology—Wear processes science, www.eduforum.pl.
84. Tubielewicz K., Kęsy M.: Influence of adhesive wear on parameters of the cast iron surface layer. *Tribology: Friction, Wear, Lubrication*, 4, 2008, 259–266.
85. Tubielewicz K., Turczyński K., Tubielewicz M.: Strength indicators of cold-pressed joints. *Technology and Montage Automation*, 2004, 3–4.
86. Weroński A., Zwierzchowski M.: Coatings increasing the wear resistance of selected motor parts. *Welding Review 5*, SIMP Publisher, Warsaw, 2003.
87. Dobrzański L.A.: *Material and Metal Science Basics*. WNT, Gliwice-Warszawa, 2002.
88. Patent PRL Nr 106274, Adamczyk J., Griner S., Hajduczek E., Dobrzański L.: The way to investigate material resistance, particularly of metals and its alloys concerning thermo-mechanical fatigue and the device for material fatigue investigations, 1980.
89. Adamczyk J., E. Hajduczek E.: Boronising of WCLV tool steel for hot work. *Conference Proceedings on Problems of Modern Thermo-Mechanical Treatment*, Warszawa, 1984, z. 1, p. 169–175.
90. Polish standard: Chemical composition of hot work tool steels PN-EN ISO 4957:2002.

6 Interfacial Adhesion of Film/Substrate System Characterized by Nanoindentation

Mingyuan Lu and Han Huang

CONTENTS

6.1 Introduction 316
6.2 Adhesion Measurement of Films 318
6.2.1 Adhesion 318
6.2.2 Interfacial Delamination 319
6.2.3 Adhesion Measurement Techniques 319
6.2.3.1 Peel Test 321
6.2.3.2 Pull-Off Test 321
6.2.3.3 Scratch 322
6.2.3.4 Bending Test 322
6.2.3.5 Stressed Over Layer 322
6.2.3.6 Blister Test 323
6.2.3.7 Nanoindentation 323
6.2.4 Nanoindentation for Assessing Interfacial Toughness of Film/Substrate System 323
6.2.4.1 Conventional Nanoindentation Methods 323
6.2.4.2 Cross-Sectional Nanoindentation Methods 330
6.2.4.3 AE-Assisted Nanoindentation Method 333
6.2.5 Summary 335
6.3 Delamination in SiN/GaAs Film/Substrate Systems during Nanoindentation 335
6.3.1 Methodology 335
6.3.2 Nanoindentation-Induced Delamination in SiN/GaAs Film/Substrate Systems 337
6.3.2.1 Mechanical Properties of GaAs Substrate and SiN Films 337
6.3.2.2 Deformation of GaAs Substrate 337
6.3.2.3 Deformation of SiN/GaAs Film/Substrate Systems 339
6.3.2.4 Verification of Delamination Using Secondary Indentation 340

6.3.2.5 Verification of the Delamination Mechanic Using FEM..... 342
6.3.2.6 Optimization of the Load Profile..... 345
6.4 Evaluation of the Interfacial Toughness of SiN/GaAs Film/Substrate Systems..... 350
6.4.1 Delamination Energy Release..... 351
6.4.1.1 Griffith Energy Balance..... 351
6.4.1.2 Method I: Dual-Indentation..... 352
6.4.1.3 Method II: Preexisting Crack Supposition..... 356
6.4.2 Plate Bending Models..... 358
6.4.2.1 Model I: Centrally Loaded Plate with Uniformly Distributed Load..... 359
6.4.2.2 Model II: Hertz Contact Loaded Plate..... 360
6.4.3 Interfacial Energy Release Rate G_{in} of SiN/GaAs Systems..... 361
6.4.3.1 Dual-Indentation Method..... 361
6.4.3.2 Preexisting Crack Supposition Method..... 364
6.5 Summary..... 365
References..... 368

6.1 INTRODUCTION

Thin films are extensively used in microelectromechanical systems (MEMS). Different types of dissimilar material interfaces are encountered in contemporary MEMS structures, including metal–metal, metal–ceramic, polymer–metal, and polymer–ceramic interfaces. The toughness of the material interface is important if the semiconductor devices are to operate reliably; adhesion failures are major obstacle in bringing new devices to market and achieving full capability [1–3]. Accordingly, interfacial delamination issue in MEMS continues to pose significant challenges to both design and process engineers.

An important film/substrate structure in any MEMS component is a stiff dielectric film on the semiconductor substrate. Such a film may be SiO_2 for silicon or SiN for gallium arsenide (GaAs). Interfacial failures in these film/substrate systems would result in loss of gate control of capacitors, substrate degradation due to moisture incursion, and eventually the collapse of the systems. As such, careful adhesion evaluation of these ceramic/semiconductor interfaces is essential for gauging the structural integrity, performance, and reliability of semiconductor devices.

As thin films have been extensively used in numerous MEMS structures and packaged devices, the assessment of thin film adhesion properties becomes imperative [4,5]. Many methods for quantifying the adhesive strength have been developed in the last few decades, such as indentation, scratching, stressed overlayer testing [1,6], tape peel testing [7–9], four/three-point bending [2,10], laser spallation [11–14], cavitation testing, Rockwell imprint test, and particle blasting [1,15,16]. Those methods are not only different in testing approach, but also have different requirements for samples and testing conditions. Sometimes they could provide contradictory results. It has been challenging to find a general acceptable assessment technique or an analytical approach to determine the adhesion toughness for all sorts of film/substrate

systems, taking into account the complexity of material microstructure, external loading conditions, and testing environments.

Nanoindentation has been used for measuring the mechanical properties of thin films, such as elastic modulus, hardness, and fracture toughness [5,17–27]. Besides inducing elastic and plastic deformation in a film/substrate structure, indentation can also cause nucleation and propagation of an interfacial crack, which permits the use of this technology in testing interfacial adhesion [28]. The phenomenon of interfacial fracture induced by indentation has spurred intense interest, and indentation has thus been accepted as an effective technique to measure the interfacial toughness of thin coating/substrate systems [29,30]. Great efforts have also been directed toward developing analytical models for quantifying adhesion by nanoindentation in the past two decades [6,17,18,31–37]. A number of models were established for quantifying interfacial adhesion in terms of toughness (K_{in}) and energy release rate (G_{in}) via nanoindentation.

A variety of recognized indentation techniques can be used to determine how well a coating is bonded to the substrate. In fact, from a thermodynamic standpoint, the true adhesion (or true work of adhesion) of an interface is the amount of energy required to create free surfaces from the bonded materials [38]. However, in most of the indentation techniques, the thin film and/or the substrate subjected concentrated contact stresses usually experience plastic deformation and even fracture, so it is difficult to extract the true adhesive energy from the total energy measured. What is measured is the practical adhesion (or practical work of adhesion), $W_{A,P}$. Nonetheless, by minimizing the influence of the other concurrent processes in an indentation test, the measured adhesion can be very close or even equivalent to the intrinsic adhesion of an interface.

The scope of this chapter is to present a comprehensive view of the application of nanoindentation adhesion measurement to a typical ceramic/semiconductor film/substrate structure. Our development of adhesion evaluation techniques for the SiN/GaAs film/substrate systems was used as a paradigm, as such a structure is common in semiconductor components. Further, this system represents a general genre of hard and brittle dielectric film on a malleable semiconductor substrate. Thus, the methodologies and models introduced in this work can be applied to other analogous structures with ease.

In this chapter, we first review the most commonly used adhesion measurement methods. In particular, emphasis is given to the current state of the art in adhesion evaluation using nanoindentation techniques and the existing models for quantifying adhesion. In Section 6.3, we then introduce the process and methodologies for studying the delamination mechanics in SiN/GaAs film/substrate systems. This section first deals with the measurement of the mechanical properties and the analysis of the deformation behavior and delamination mechanics. The finite element modeling (FEM) technique is then introduced for verifying the validity of the analysis. At last, some guidance is provided for optimizing the testing scheme to minimize the plastic deformation in the film/substrate system and maximize the stresses responsible for delamination. Section 6.4 introduces two energy-based methods and two plate bending models for the evaluation of adhesion. The methods are reported with a description of the testing method and the basis upon which the analysis is founded. The examples of application to SiN/GaAs film/substrate systems are provided at the end.

6.2 ADHESION MEASUREMENT OF FILMS

6.2.1 Adhesion

The adhesion of thin films is of paramount importance in nearly all applications; therefore, the need for reliable techniques to quantitatively measure an interfacial adhesion is quite patent. In the past few decades, there has been a burst of activity in devising new or improving the existing techniques for film adhesion assessment. More than 350 different techniques for measuring adhesion have been documented in the literature, according to a survey by K.L. Mittal in 1995 [39]. In spite of the abundance of techniques, there has always been a great deal of discord and confusion as to what exactly is being measured and how reliable the measurement is in an adhesion test. Therefore, for any attempt to develop adhesion measurement techniques, understanding the definition of adhesion and the adhesion failure mechanism at a fundamental level is often a matter of central importance.

The term "adhesion" refers to the attraction between two dissimilar surfaces; whereby they are drawn into intimate contact by physical or chemical forces, and it is necessary to do work in order to separate them [3,6,40]. Adhesion can be divided into three categories: (1) fundamental adhesion, (2) thermodynamic or reversible adhesion, and (3) practical adhesion [39]. Fundamental adhesion is the intrinsic property of an interface and is defined as the summation of all interfacial intermolecular interactions between the contacting materials. The types of bonding between two surfaces include ionic, covalent, coordinate, metallic, hydrogen and van der Walls forces, and so on. If the type of interactions between the two surfaces and the number of interacting units per unit area are known, then fundamental adhesion can be calculated. Nevertheless, this basic definition of adhesion is not very helpful as it is not possible either to calculate the magnitude or to measure such adhesion forces in a practical system.

Thermodynamic adhesion, also known as reversible adhesion or the true work of adhesion [3], describes the change in free energy when an interface is formed or separated and can be expressed using the Young–Dupré equation [41]

$$U_s = \gamma_{s1} + \gamma_{s2} - \gamma_{s1}\gamma_{s2} \tag{6.1}$$

in which U_s is the true work of adhesion, γ_{s1} and γ_{s2} represent the surface free energies of the two materials, respectively, and $\gamma_{s1}\gamma_{s2}$ is the interfacial specific free energy. U_s can then be determined by contact-angle measurements [42,43] and atomic simulations [44]. The thermodynamic adhesion is an intrinsic property that depends on the type of bondings at the interface and is therefore equivalent to the fundamental adhesion described above.

The practical adhesion, or practical work of adhesion, is the force or work required to debond the film irrespective of the locus of failure. The practical adhesion includes the true work of adhesion, the energy required to deform both the film and the substrate, as well as the energy consumed in other energy-dissipated processes involved in an interfacial delamination event [37,39,42]. The contribution of other energy-dissipated processes is often considered negligible, such as heat in

acoustic emission (AE) and fracto-emission [45], and so on. The practical work of adhesion can thus be written as

$$W_{A,P} = U_s + W_f + W_s + W_{\text{fric}} \tag{6.2}$$

where W_f and W_s are the work/energy used in plastic deformation of the film and the substrate, respectively, and W_{fric} is the energy loss due to friction. Since the film and/or the substrate plastic deformation during delamination is often inevitable, the extraction of U_s from the total energy measured in interfacial delamination is complicated. Therefore, it is usually very difficult to measure U_s for technologically important structures. In fact, most of the reported techniques measured the practical adhesion, $W_{A,P}$. However, a continued effort has been made to minimize the influence of "other factors" so that the energy/work measured in a delamination event can be as close as possible to the true work of adhesion. Concurrently, a number of less-destructive or nondestructive techniques were developed for the purpose of quantifying adhesion with minimized influence of the "other factors."

6.2.2 Interfacial Delamination

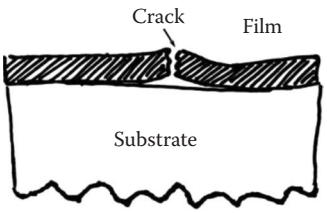
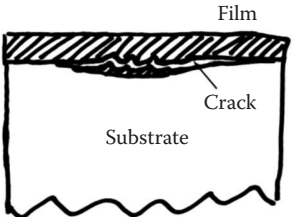
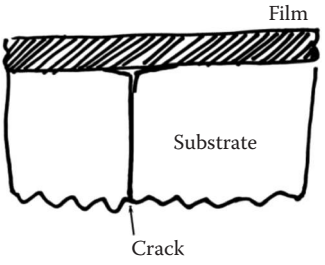
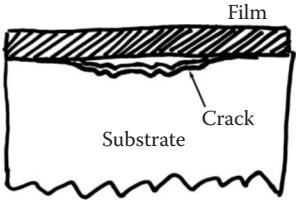
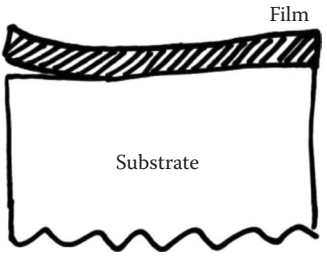
Interfacial delamination is the phenomenon whereby a film separates from a substrate typically driven by mechanical stress. Delamination can also be generated by thermal stress, shock waves, corrosion, and electron-static force. However, this chapter is primarily concerned with mechanical stress-induced delamination. Generally, this mechanical force cannot be directly applied to the interface molecules, and instead is positioned some distance away, wedging, pulling, or peeling the materials apart. As the force is gradually raised, a critical point is reached where a crack runs between the molecules at the interface and the film/substrate structure separates. It is noted that only if the film/substrate bonds are sufficiently weak with respect to bonds within the film or substrate, will the crack be expected to move along the interface. In such instance, competitive processes would be suppressed because the fracture at the interface would dominate. Nevertheless, in most cases, it is difficult to achieve an absolutely clean film/substrate separation, as no fracture occurs exclusively within the coating or within the substrate [42,46]. The challenge then is to devise techniques that can generate interfacial delamination with minimal film and substrate damage. This enables accurate computation of the adhesion properties using models with the least assumption and idealization.

Prior to the evaluation of interfacial adhesion, it is necessary to distinguish the different interfacial failure mechanisms. The general failure modes that may lead to interfacial delamination in a film/substrate system are categorized in Table 6.1.

6.2.3 Adhesion Measurement Techniques

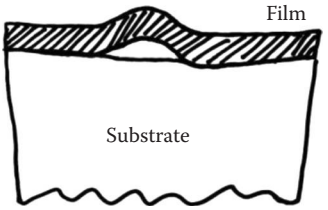
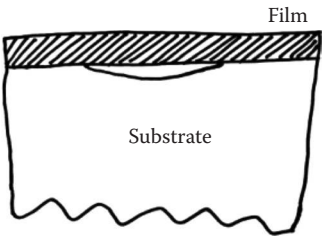
Many methods for quantifying the interfacial adhesion have been developed in the last few decades. Those methods not only differ in their testing approaches, but also have different requirements for sample and testing conditions. This might lead to

TABLE 6.1
Classification of Interfacial Delamination Modes in Film/Substrate System

Delamination Mechanics	Schematics	Description
Film fracture-induced interfacial delamination		Through-thickness crack in the film propagates to the interface and deflects to cause delamination
		Crack in the film parallel to the interface deflects to the interface to cause delamination
Substrate fracture-induced interfacial delamination		A crack in the substrate diverts to the interface to cause delamination
		Crack in the substrate parallel to the interface deflects to the interface to cause delamination
Interfacial crack initiates at the interface		Edge flaw extends resulting in delamination

(*Continued*)

TABLE 6.1 (*Continued*)
Classification of Interfacial Delamination Modes in Film/Substrate System

Delamination Mechanics	Schematics	Description
		Buckling caused by compressive stress in the film
		Plastic deformation in the substrate results in tension at the interface that cause delamination

Source: Chen, J. J. and S. J. Bull. 2011. *Journal of Physics D-Applied Physics* 44(3); Lipkin, D. M., D. R. Clarke, and A. G. Evans. 1998b. *Acta Materialia* 46(13): 4835–4850.

contradictory results. There is not one generally acceptable assessment technique to determine the adhesion for all types of film/substrate systems. Thus, a number of the most "well-known" techniques are introduced here and their advantages and limitations in application are also discussed.

6.2.3.1 Peel Test

The peel test was the earliest and also the simplest quantitative test proposed for determining the adhesion of thin films. The test uses a pressure-sensitive adhesive tape to peel off the coating in order to determine the peel force per unit tape width [47]. Jacquet [48] first used this method in 1934 to measure the adhesion of a copper coating on nickel substrate. In 1965, a peel test was developed to determine the peel strength of plated plastics on substrates by Saubestre [49] and has been used extensively ever since. A modified peel test was developed by Baglin in 1985, in which the use of adhesive tape was avoided by coating the film of interest with a 10 μm copper film; the peel force was applied directly to the unattached end of the copper film [50]. The advantages of the peel test are the simplicity and minimal cost. The main limitation, however, is that the test is only suitable for very thick and weakly bonded coatings.

6.2.3.2 Pull-Off Test

The pull-off test is also a simple method for adhesion measurements, first reported in 1976 [7]. In a typical pull-off test, cylindrical rods/studs are glued to the film of interest

using structural adhesives or cements and the normal applied force required to remove the film are thus measured [7,51,52]. This method is suitable for quantitative measurements of thin film adhesion over a wide range. One of the obvious limitations of this method (as with all methods requiring some sort of bond to the film for transmitting the force) is the strength of the bond itself, that is, the adhesives and cements used.

6.2.3.3 Scratch

The use of a scratch method to quantitatively evaluate the adhesion of thin films was first reported by Heavens in 1950 [53]. In a typical scratch test for adhesion [53–55], a sharp stylus was drawn across the film. The critical load P_c applied by stylus, which is required to cause peeling, is taken as a measure of film adhesion. P_c is often used to compare different materials but this is only valid if the same failure mode occurs. Attributed to the simplicity and high degree of reproducibility, the scratch adhesion test has been extensively used. However, this method is usually considered as semiquantitative because it can be affected by various extrinsic (instrument-specific) factors and intrinsic (coating/substrate system) parameters. Extrinsic factors include scratch speed and loading rate, and so on. Intrinsic parameters include coating thickness, substrate hardness, surface roughness, and so forth. In recent years, various analytical models using linear elastic fracture mechanics (LEFM) principles were developed for analyzing the scratch test data, which enabled the computation of interfacial toughness from P_c. Also, thanks to the highly resolved load and displacement sensing capability of the latest scratch testing machines, its application was extended from microscale to nanoscale [56].

6.2.3.4 Bending Test

The bending test is commonly applied to ceramic coating on a metal substrate where through-thickness fracture in the coatings diverts to the interface to cause interfacial delamination [2,10,57–59]. The four-point bending (4PB) test in particular provides a reliable and repeatable means to quantify the interfacial property. In a 4PB test, the bent region between the central rollers is subject to only bending, which allows a relatively simple analysis. Bending tests are usually used to measure the adhesion of thick films on the scale of tens or hundreds of micrometers in thickness [60]. It has been shown that the success rate of 4PB tests decreases with decreasing film thickness, making testing of ultrathin film interfaces increasingly difficult [61,62]. In addition, as thin film interfaces are engineered to be tougher, delamination becomes more difficult to induce using bending tests.

6.2.3.5 Stressed Over Layer

This method requires a thick superlayer to be deposited on top of the film of interest, capable of storing large amount of residual stress [1,63]. The superlayer provides additional driving force for initiating interfacial delamination without altering the properties of the interface. However, this method requires an additional sample preparation, which involves adjusting the thickness and the residual stress of the superlayer so that the controlled delamination occurs. Additionally, the interfacial adhesion between the stressed superlayer and the test film should be greater than the adhesion between the film and the substrate, which is not always achievable [6].

6.2.3.6 Blister Test

In a blister test, pressure is applied on a free-standing film to cause film delamination [64,65]. This method requires etching the substrate to obtain a free-standing thin film window. In order to cause a film deflection special apparatus is needed to apply pressure in the center of the free-standing film through a narrow groove formed in the substrate. The corresponding analysis is relatively straightforward. However, etching may lead to contamination of the interface, which may greatly affect the interfacial properties. Furthermore, this method is not applicable to thin films with a thickness less than 2 μm due to possible wrinkling effects [66].

6.2.3.7 Nanoindentation

Nanoindentation can also cause initiation and propagation of an interfacial crack, which allows for the quantitative study of interfacial adhesion [28]. The phenomenon of interfacial fracture induced by nanoindentation has been of significant research interest and nanoindentation has thus been accepted as an effective technique to measure the interfacial toughness of thin film/substrate structures [29,30]. In fact, nanoindentation may be considered the most effective technique for investigating thin-film adhesion, as it is able to generate interfacial cracks on a sufficiently small scale and at a specific site. Nanoindentation has now become a very important tool for measuring thin film adhesion; in the last few decades, there has been considerable activity and tremendous interest in developing adhesion measurement methods using nanoindentation techniques. Thus, a review on adhesion assessment by nanoindentation techniques is provided in the following section to give a snapshot of the available methodologies and the latest novel concepts being developed.

6.2.4 Nanoindentation for Assessing Interfacial Toughness of Film/Substrate System

6.2.4.1 Conventional Nanoindentation Methods

Nanoindentation provides a controllable means to generate interfacial cracks on a sufficiently small scale to investigate the adhesion properties of thin films and has thus been considered as an effective tool to characterize the interfacial properties of thin films. The response of indentation-induced delamination with respect to load–displacement relationship has been extensively investigated [6,36,60]. The force and depth at the critical moment have been used to calculate the interfacial toughness. Indenting has caused various types of fracture in the film/substrate structures, which was found to be dependent on the properties of the film materials and the indenter geometry [67,68]. Different deformation mechanics require different analytical approaches or models.

6.2.4.1.1 Delamination without Cracks in Films

For ductile films, fracture within the film is unlikely to occur, however the plastic deformation could significantly contribute to the occurrence of delamination [69–71]. Simple models could be established to analyze the interfacial failure in a

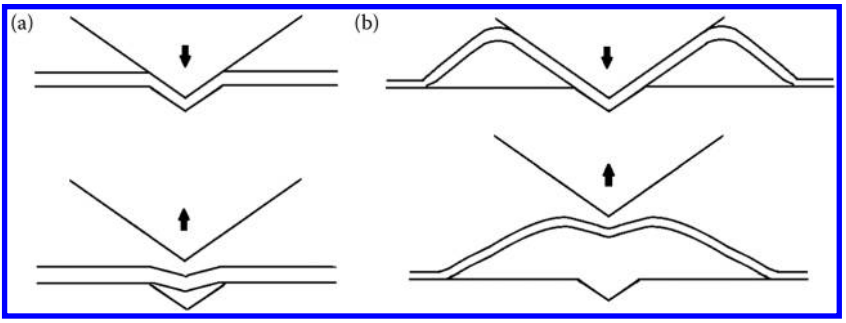


FIGURE 6.1 Schematic illustration of delamination mechanism of ductile films with (a) good adhesion and (b) poor adhesion to the substrate. (From Chen, J., and S. J. Bull. 2007. *Journal of Physics D-Applied Physics* 40 (18):5401–5417.)

film/substrate system if no cracking occurred in the film. As shown in Figure 6.1a, during loading the film remains attached to the substrate. Provided that the interfacial toughness is sufficiently high to withstand the shear stress generated at the interface, the interface maintains intact until the tension that is built up during unloading tears apart the film and the substrate (Figure 6.1a). For the films/coatings with poor adhesion, double buckling may occur during loading and can develop into single buckling during unloading as the interfacial crack propagates toward the middle of the indent (Figure 6.1b). Note that the interfacial properties and mechanical properties of both the film and substrate dictate how the film/substrate structure delaminates. In addition, the ratio of indentation depth over coating thickness affects the interfacial crack modes.

Early in 1984, Marshall and Evans [17,72,73] investigated the fracture mechanics involved in the indentation-induced thin film delamination by use of conical probes. Their model related the crack extension to the residual stress and the fracture toughness of the interface. This provided an analytical basis for using controlled indentation cracking to quantitatively measure the interface toughness and to evaluate indentation-induced delamination in thin films. An elastic circular clamped plate model (treating the detached film as an axisymmetric blister) was used. The energy release rate, G_{in}, for the interfacial cracking of an indented prestressed film could be computed as

$$G_{\text{in}} = t(1-v)\left\{(1-\alpha)\sigma_R^2 + \sigma_0\left[\frac{1+v}{2} - (1-\alpha)\left(1-\frac{\sigma_c}{\sigma_0}\right)^2\right]\right\} / E \qquad (6.3)$$

where E and v are the thin film's Young's modulus and Poisson ratio, respectively; t is the film thickness; σ_R is the residual stress in the film; α is a constant (equals to 1 for the case without buckling and 0.383 for buckling); and σ_0 and σ_c are indentation stress and critical buckling stress, respectively. A similar approach was developed by Rosenfeld et al., where FEM was used to validate the analytical model [18]. Kirese

and Gerberich [74,75], later extended the application of Marshall and Evan's model to ductile films with one or multiple stress-bearing superlayers. They later validated the modified model using the nanoindentation result. Nevertheless, Kriese's models were limited by idealized assumptions. First, the clamped plate assumption neglected the strain relaxation of the film and the elastic recovery of the impression volume. Second, imperfections in the film could affect the accurate calculation of critical buckling stress.

FEM is a versatile tool for determining the mechanical properties of advanced materials [76–78]. It has also been widely used to investigate indentation-induced delamination mechanics [79–83]. By approximating the delamination formation as an annular plate model, Rosenfeld et al. [18] carried out the FEM analysis to the interfacial crack initiation and propagation and determined the dimension of the opening between the delaminated film and substrate. In a study undertaken by Abdul-Baqi et al. [35], the indentation-induced delamination of an elastic thin film on a plastic substrate under a spherical indenter was simulated using the cohesive zone model. The study focused on the delamination during loading. Parametric FEM study was performed to investigate the effects of interfacial strength and substrate yield strength on delamination. It was found that the interfacial crack initiated outside of the contact zone in a tangential mode and propagated both toward and away from the indentation center. However, this model did not take into account the influence of residual stress and ignored the cracking in the film structure. In a later study [84], a model that emphasized the indentation-induced normal delamination during unloading was established. The indentation P–h curve exhibited a discontinuity in the unloading phase; this was attributed to delamination. The critical interfacial strength above which delamination was suppressed for a given film/substrate system at a specific penetration depth was calculated, as well as the energy consumed by the delamination process. The objective of their study was to reveal the delamination mechanics of indentation-induced delamination for film/substrate interfaces with given properties. Their study focused only on the simulation; and hence experimental results are still required for convincing validation. The primary assumption of the above-mentioned models assumes the detached film segment is intact except for delamination, so they are not applicable to the cases where crack occurs in the film or substrate material.

6.2.4.1.2 Delamination With Cracks in Films

Interfacial delamination is often accompanied with cracking and subsequent spalling in the thin film/coating, especially for hard coatings. The onset of through-thickness cracking was indicated by abrupt decrease in stiffness or a discontinuity in the P–h curves [20,81,85–87]. There are primarily two types of cracking or fracture that is associated with the indenting of a brittle coating on a substrate: (i) through-thickness fracture caused by bending stresses when the film is bent into the deformed substrate or bent over the material piled-up around the contact area of indentation; and (ii) interfacial fractures at the weakest interface.

For most hard and brittle coatings, excluding superhard coatings such as diamond or diamond-like carbon films [70], the coatings are insufficiently strong to maintain intact subjected to contact stress. So through-thickness cracks take place

along with interfacial cracking occurred simultaneously. Complex failure mechanisms have been used to describe the delamination of brittle coatings [60,88,89]. A simplified three stages nanoindentation fracture mechanism for a hard amorphous carbon coating on silicon substrate was demonstrated by Li et al. [88]. As shown in Figure 6.2, the indenting process had three stages: (i) the formation of a ring-shaped through-thickness crack due to high stress generated at the contact area, especially the tensile stress around the contact edge; (ii) the occurrence of delamination at the periphery of a second ring-shaped through-thickness crack and partial spalling. Corresponding discontinuities in the *P*–*h* curves were observed during indentation; and (iii) secondary through-thickness crack forms and chipping may occur. Crack formation depends on the material properties of the film and substrate, as well as the stress distribution at the indentation site. In that study, only the energy release from through-thickness cracking was computed, but the assessment of the interfacial toughness was not performed. Nevertheless, the three-stage cracking behavior might be specific for the coating materials studied.

For films exhibiting only annular cracking (no radial crack exist), as shown in Figure 6.3, modeling as the rebounding of a centrally loaded disc on the basis of elastic equilibrium was proposed by Hainsworth et al. [37,91]. The model associated the energy release with only the dimension of the interfacial crack,

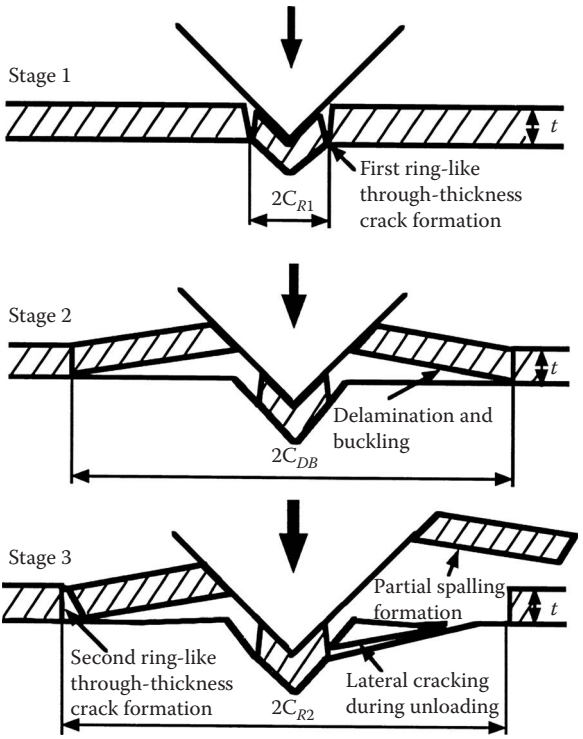


FIGURE 6.2 Fracture mechanism of a brittle coating system. (From Cannon, R. M. et al. 1991. *Acta Metallurgica Et Materialia* 39 (9):2145–2156.)

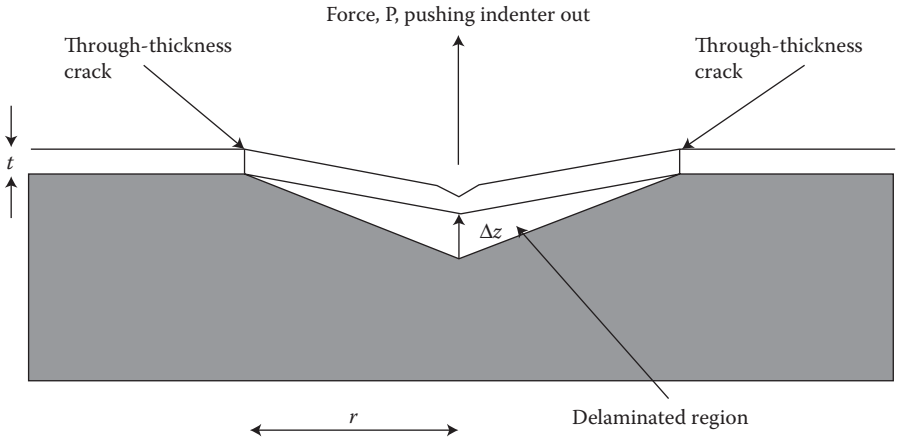


FIGURE 6.3 Schematic illustration of debonding mechanism of a hard coating with annular cracks. (From Hainsworth, S. V., M. R. McGurk, and T. F. Page. 1998. *Surface and Coatings Technology* 102 (1–2):97–107.)

neglecting the contribution of the annular cracking. The fundamental assumption of this model was the equilibrium between the elastic strain energy released from a deflexed coating and the energy absorbed in generating the interfacial crack, with some additional work done to push the indenter up. The debonding energy release rate was given by

$$G_{\text{in}} = \frac{W_d}{\pi r^2} = \frac{2Et^2(\sigma_m - \sigma_r)^2}{3\pi r^2} \tag{6.4}$$

$$W_d = \frac{2\pi Et^3(\delta_m - \delta_r)}{3C_R^2} \tag{6.5}$$

where W_d is the work for delamination, r is the radius of the interfacial crack, δ_m and δ_r are the maximum and residual depth, respectively, and E is the modulus of the coating material. This model has been regarded as analytically ideal among other models.

Nevertheless, Chen et al. [36] suggested that the Hainsworth model overestimated the interfacial toughness as they believed that considerable strain energy could still remain within the bent film after its detachment from the substrate; in addition, a part of the released energy was consumed by through-thickness cracking prior to debonding. They performed the adhesion assessment for a TiO_xN_y coating and for an ITO/Ag/ZnO/TiO_2 multilayer on a glass substrate using the extra linear recovery in the unloading section of the *P–h* curves. As shown in Figure 6.4, the linear section at the end of the unloading curve was the response from the detached coating rebounding and pushing the indenter upwards. By extrapolating the initial part of the unloading curve before detaching of the coating took place, the difference between the

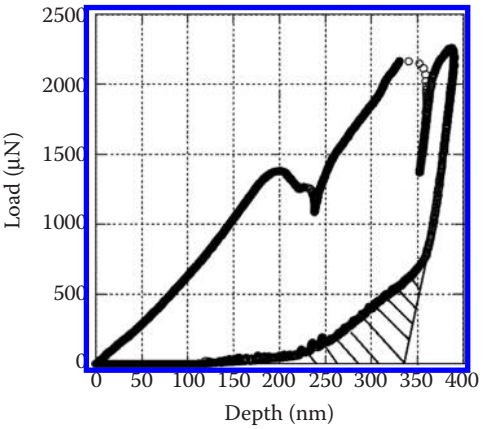


FIGURE 6.4 Extra linear elastic recovery in the *P–h* curve observed during unloading for a 400 nm TiO_xN_y coating on a glass substrate. (From Chen, J. and S. J. Bull. 2007. *Journal of Physics D-Applied Physics* 40 (18):5401–5417.)

extrapolated and experimental unloading curves could be revealed. Determination of the energy release for delamination was obtained by calculating the area of difference (the crosshatched area) in Figure 6.4.

Besides the extra linear recovery model, Chen et al. also applied the lateral cracking induced delamination model that was proposed by Marshall et al. [72] for measuring the interfacial strength of a brittle coating system, G_{in}, given by

$$G_{in} = \frac{P_0 A_0^2}{\delta_0} (\cot \theta)^{2/3} \left(\frac{H^4}{E} \right) \tag{6.6}$$

where P_0 is the threshold load for lateral cracking, A_0 and δ_0 are dimensionless constants ($A_0 = 3/4$ and $\delta_0 = 1200$), and θ is the half-included angle of the indenter. Reasonable agreement in interfacial toughness between experiments and simulation was achieved when applying this model for a variety of brittle coating systems [36,92].

To evaluate the energy dissipation for delamination and chipping in an organic–inorganic coating on glass substrate, Malzbender and Toonder et al. [19,93,94] proposed an energy model based on a sufficient number of indentations made at different loads. The irreversible work of deformation (W_{irr}) was determined by computing the areas between the loading and unloading curves, as illustrated in Figure 6.5. The onset of delamination could change the slope of the W_{irr}–P curve and chipping could be related to the step jump of the curve. The work for delamination (W_{irr}^d) was then defined as the energy difference between the energy at a certain delamination radius r_d and the extrapolated energy for plastic deformation of the coating. Likewise, the energy released from chipping (W_{irr}^c) was obtain by calculating the difference in W_{irr}

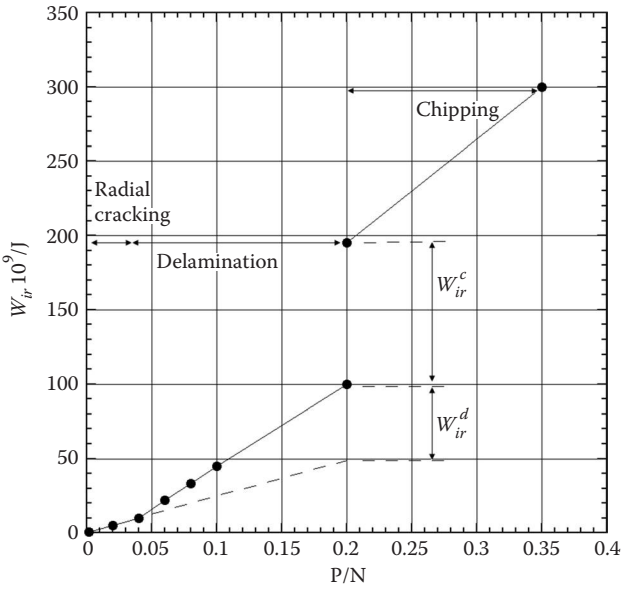


FIGURE 6.5 Irreversible energy release during indentation as a function of the applied load for a sol-gel coating on glass. (From Den Toonder, J. et al. 2002. *Journal of Materials Research* 17 (1):224–233.)

before and after chipping. This method was well accepted as an effective approach to assess the adhesive properties of brittle organic–inorganic film/substrate system and has been applied to inorganic coatings, such as TiAlSiN by Nakonechna et al. [95]. A possible disadvantage of this method is the significant time required to test a number of indents over a wide range of loads. Further, this model was only applicable to cases where a discontinuity in *P*–*h* curves could be observed. Toonder et al. [93] later suggested a more elaborated model for adhesion assessment by adopting the Thouless' model [96], which took care of a particular deformation combination, delamination followed by chipping, where the interfacial fracture energy, U_{in}, was expressed as

$$U_{\text{in}} = 1.42\frac{Et^5}{L^4}\left(\frac{(\beta\pi/2)+(a/L)}{\beta\pi+(a/L)}\right)+\frac{t(1-v)\sigma_r^2}{E} + \frac{3.36(1-v)t^3\sigma_r}{L^2}\left(\frac{(a/L)+(\beta\pi/2)}{(a/L)+\beta\pi}\right) \tag{6.7}$$

in which L, a, and β are dimensional parameters that define the geometry of the chipped piece (Figure 6.6), and E and t are the elastic modulus and thickness of the coating, respectively.

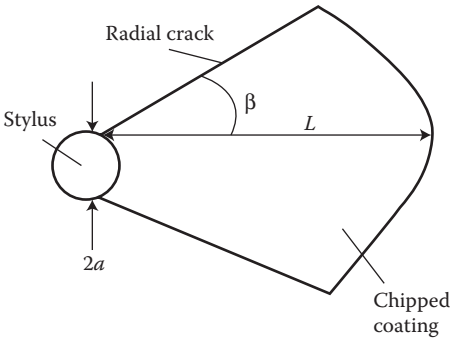


FIGURE 6.6 The geometry of a chipped segment of coating. (From Den Toonder, J. et al. 2002. *Journal of Materials Research* 17 (1):224–233.)

6.2.4.2 Cross-Sectional Nanoindentation Methods

The conventional nanoindentation method has proven to be valuable for measuring the adhesion behavior of a thin film deposited on a substrate. However, its reliability of assessment depends heavily on the theoretical analysis and simulation of the complicated cracking or debonding physics involved. Additionally, direct observation of indentation-induced delamination is challenging as interfacial fracture is hidden under the indented surface. In an effort to eliminate such an issue, a more direct approach was developed, in which indentation was made on the cross section of the film/substrate structure, either at the interface or on the substrate near the interface, as shown in Figure 6.7.

Chicot et al. used cross-sectional indentation to evaluate the adhesion of thermal spray coatings [97–101]. In the studies, a Vickers indenter was used to indent at the interface, where the length of the cracks generated at the interface were measured and used as important parameters for computing the interfacial toughness. In Sanchez's study [102], the interfacial adhesion of Si_xN_y-SiO_2/Si films/substrate systems was investigated. The indentation using a standard Berkovich indenter was made on a silicon substrate that was several micrometers away from the interface of interest. During indenting, radial cracks first initiated at the two corners of the pyramidal indenter closest to the interface and later propagated to the interface. At some stage of indenting, the material could be chipped off from the substrate. This aided the advancement of the interfacial crack, reflected in the *P–h* curve as a jump-in displacement. Analytical approaches based on a circular plate and beam models were established to determine the adhesion toughness in terms of the critical interfacial energy release rate (G_{in}), in which interfacial adhesion was quantitatively interpreted. The energy release rate by use of the circular plate model for the interface was given by

$$G_{in} = \frac{D(1-v^2)u_0^2}{(a-b)^4}(1-\lambda)^4(F+\lambda F') \tag{6.8}$$

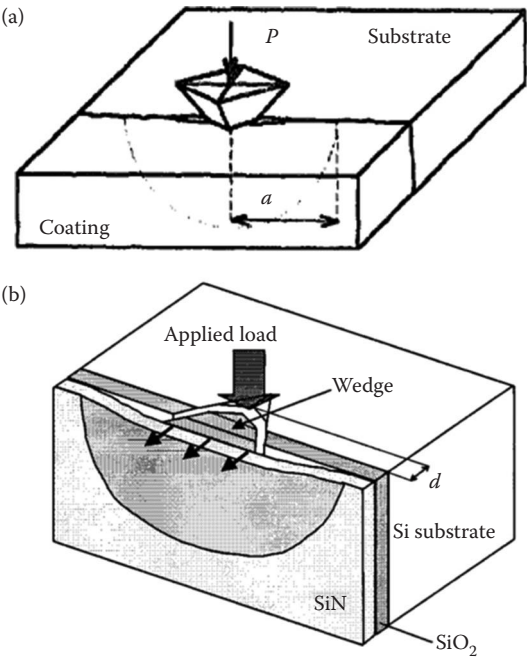


FIGURE 6.7 Schematic illustration of cross-sectional indentation performed (a) at the interface (From Chicot, D., P. Demarecaux, and J. Lesage. 1996. *Thin Solid Films* 283 (1–2):151–157; Hadad, M. et al. 2007. *Surface Engineering* 23 (4):279–283.) and (b) on the substrate near the interface (From Scherban, T. et al., 2003. *International Journal of Fracture* 119 (4–2):421–429.).

$$F(\lambda) = \frac{2\ln\lambda + (1+\lambda/1-\lambda)\ln^2\lambda}{[(1+\lambda)\ln\lambda + 2(1-\lambda)]^2} \tag{6.9}$$

where D is the flexural rigidity of the plate, ν the Poisson's ratio of the coating material, a and b are the delamination radius and contact radius, respectively, u_0 the maximum film deflection, t the film thickness, and $\lambda = a/b$. However, the elastic plate and beam theories are not applicable for metallic films because of the significant plastic energy stored in the film. Models that can more accurately describe the adhesion property are thus needed for ductile films.

When applying cross-sectional nanoindentation (CSN) to metallic film systems, a primary concern is the significant plasticity induced in the vicinity of the delaminated film. Quantitative measure of the interfacial toughness has to take into account the energy consumed in the deformation of a ductile film. For this purpose, Eric et al. performed the CSN on copper films deposited on silicon substrate [103]. In this study, the delamination of the copper films was evaluated in the context of edge chipping and a theoretical model was developed by considering the significant plastic deformation of copper. The critical interfacial energy release rate, G_{in}, was obtained

by subtracting the energy dissipation involved in the film plastic deformation from the total yield, that is,

$$\Delta U_e + \Delta U_p + G_{\text{in}}\,\Delta A = 0 \tag{6.10}$$

then we have

$$G_{\text{in}} = -\frac{\Delta U}{\Delta A} = -\frac{\Delta U_e + \Delta U_p}{\Delta A} \tag{6.11}$$

where A is the deboned area, U_e is the energy released during crack growth, and U_p is the energy used to plastically deform the ductile film. Besides, the geometrical ratio of the delamination created blister was calculated and applied as a simple index for adhesion evaluation. The geometrical ratio of the blister dimension is given as

$$S = \frac{U_f}{a - b} \tag{6.12}$$

where U_f, a, and b are the residual displacement, the semilength of the delaminated blister and semiwidth of the silicon chip, respectively. All these parameters could be measured from the SEM image of the delamination area, as demonstrated in Figure 6.8. The higher S indicated stronger adhesion.

Recently, a great effort was directed toward applying the CSN technique to the interconnect/pattern film structures [32,69,99,105]. Though not quantitatively, the CSN was used to investigate the crack propagation behavior at the complex interface [64], as shown in Figure 6.9. In combination with the FEM modeling, the crack path at a given indentation condition could be predicted and good agreement between simulation and experimental results were obtained. Moreover, some quantitative attempts at the adhesion evaluation of the patterned films were very promising.

The CSN method has been proven to be a useful tool for characterizing the adhesion of films on a brittle substrate, but is not readily applicable for films on a substrate

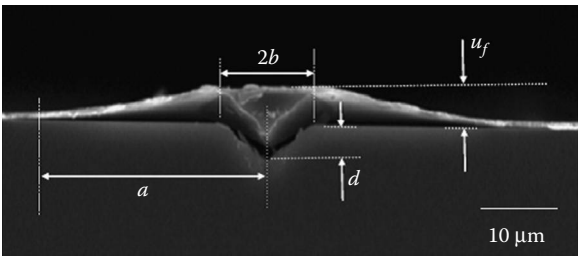


FIGURE 6.8 Cross-sectional indentation applied to ductile–brittle interface (Cu film on Si substrate). (From Roy, S. et al. 2007. *International Journal of Fracture* 144 (1):21–33.)

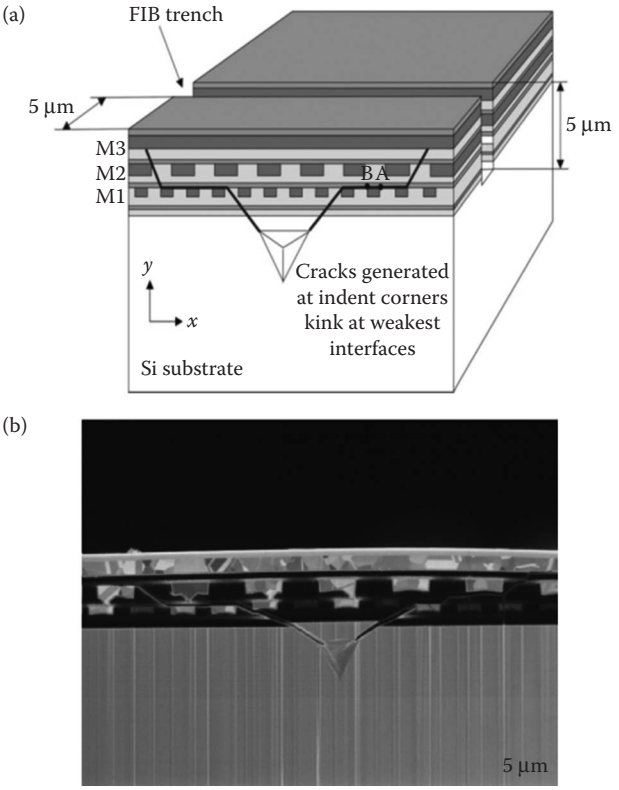


FIGURE 6.9 Schematic illustration of cross-sectional indentation applied to (a) the interconnect structure; (b) the SEM image of indentation-induced delamination to the cross section of the patterned film. (From Deaña, I. et al., 2006. *Acta Materialia* 54 (13):3453–3462.)

that does not have preferentially orientated cleavage planes, because the initiation and propagation of a crack in such a substrate are hard to control. Moreover, tedious experimental trials have to be undertaken to obtain the critical parameters for precisely controlling the delamination, including the orientation of the tip, the indentation position with respect to the interface and the applied load. Additionally, CSN models cannot be used if tearing the film occurs due to strong adhesion or lack of ductility.

6.2.4.3 AE-Assisted Nanoindentation Method

Crack initiation and propagation are extremely short-lived events, which generates instantaneous or explosion-like energy release, propagating as transient elastic waves away from the crack. This "wave-package" could be detected as AE events using sensors placed on the surface of the structure or sample of interest [106].

Numerous studies were carried out to investigate the indentation deformation behavior of a variety of materials using the AE sensors, as AE signals are sensitive to the surface or subsurface changes in a material. The AE nanoindentation

technique has been proven to be capable of identifying the initial stages of yielding, fracture, phase transformation, and different types of dislocation nucleation in bulk materials [80,107,108]. Pioneering applications of the AE-assisted indentation into a film/substrate system indicated that the onset of cracking and delamination of the film/substrate structure induced AE signals of high intensity, which enabled a better understanding of indentation-induced delamination [106,109–111].

Shiwa et al. [110] investigated the application of AE for adhesion testing that used a spherical probe to indent TiN films on silicon substrate. In this study, they demonstrated that AE was capable of detecting the onset of cracking in the TiN film during loading and the interfacial delamination at the interface upon unloading. Based on the AE signals detected, the indenting process was split into six stages. In the initial stage (or stage I), the film/substrate structure deformed elastically during loading, followed by the initiation of circular cracks in the film or the occurrence of shear faulting (stage II). At the end of loading the circular crack propagated and plastic deformation of the substrate occurred (stage III). During unloading, interfacial delamination occurred (stage IV), followed by the phase transformation of silicon (stage V) and then propagation of the interfacial crack (stage VI). SEM examination of the indented cross section allowed for the development of a relationship between the cracking and delamination at the contact site with the specific AE peaks detected. Similarly, Swain and Wittling [109] undertook the AE-assisted nanoindentation for delamination testing of TiN films on different substrates by use of Berkovich and spherical indenters to investigate the effect of indenter geometry on the AE spectra. To understand the adhesive behavior of diamond films, Fan et al. [111,112] used AE-assisted indentation on hard diamond films deposited on various substrates, but using a Rockwell indenter. They demonstrated that analyzing AE signal was very helpful in differentiating between failure stages, such as initiation and propagation of delamination. With the aid of AE monitoring, the critical load related to the onset of delamination could be determined accurately. Belmonte et al. [113] also studied the adhesion behavior of diamond films coated on both polished and ground silicon nitride. By the use of an AE-assisted nanoindentation method, and with the aid of SEM observation of the indents, the AE spectra were related to the extensive delamination behavior or spalling of the diamond film/ceramic structure.

For adhesion testing using nanoindentation method, AE techniques provide a powerful tool for correlating the indentation response with instantaneous plastic behaviors of film/substrate systems. The research works discussed here demonstrated the application of AE for a variety of hard coatings, which helped improve our understanding of the mechanism of interfacial failure. However, reliable analysis by use of this technique requires a more comprehensive study on how to interpret AE signals; the validation of relationship between indentation-induced plastic behavior and AE features and the examination of the surface and subsurface microstructures in terms of different failure modes are also required. Although AE-assisted nanoindentation method is still in its infancy of development, its capability promises a wide range of applications in dealing with practical issues associated with adhesion assessment of thin film/substrate structures.

6.2.5 Summary

Characterizing the interfacial property of thin film/substrate systems is challenging because their delamination mechanisms can be quite different, depending on the mechanical properties of the film and the substrate, and their bonding characteristics at the interface. This section provided a critical review on the measurement of interfacial adhesion of film/substrate system with the focus on the nanoindentation-based methods.

It is apparent that the previous investigations of indentation-induced delamination enabled the improved understanding of the mechanisms of interfacial failures in a more controllable manner. In those studies, FEM simulation was often combined with the experimental indentation to interpret the mechanisms of delamination and interfacial cracking. Various theoretical and empirical models were thus proposed based on those studies. Nevertheless, owing to the complexity of interface delamination and indentation-induced stress distribution, those models might not always provide an accurate measure of interfacial toughness, though qualitative assessment of the adhesion strength could be achieved. Newly developed techniques, such as the cross-sectional nanoindention and the AE-assisted nanoindentation methods, are increasingly used in recent years. CSN enabled the direct posttesting examination with aid from electronic microscopy; while AE-assisted nanoindentation provides a more accurate assessment of failure modes at interfaces.

6.3 DELAMINATION IN SiN/GaAs FILM/SUBSTRATE SYSTEMS DURING NANOINDENTATION

6.3.1 Methodology

Nanoindentation is a flexible, accurate, and rapid tool for initiating delamination in film-substrate systems for adhesion measurement. The data obtained from an indentation process that initiated a delamination can be used to determine the interfacial adhesion; however, developing the testing protocol to initiate delamination is a crucial first step. Shown in Figure 6.10 is a typical process to follow when examining a film/substrate structure using nanoindentation techniques. This flowchart provides a step-by-step guide for devising the optimized testing procedure to generate controlled interfacial delamination with minimal damage to the film/substrate structure. It is important to note that a least-destructive indentation procedure used for inducing delamination is essential for quantifying the true/intrinsic property of the interface in the following step.

An understanding of the mechanical properties and deformation behaviors of both the substrate and the film is of particular importance for interfacial failure study, especially for submicron thin films. That is because the elastic–plastic deformation of both substrate and film determines the stress distribution at the interface and hence the interfacial failure. Therefore, prior to studying the delamination behavior, it is necessary to measure the mechanical properties of the substrate and film materials as well as to investigate their deformation behaviors separately. As the interfacial crack is subsurface structure, it is often challenging to observe the delamination

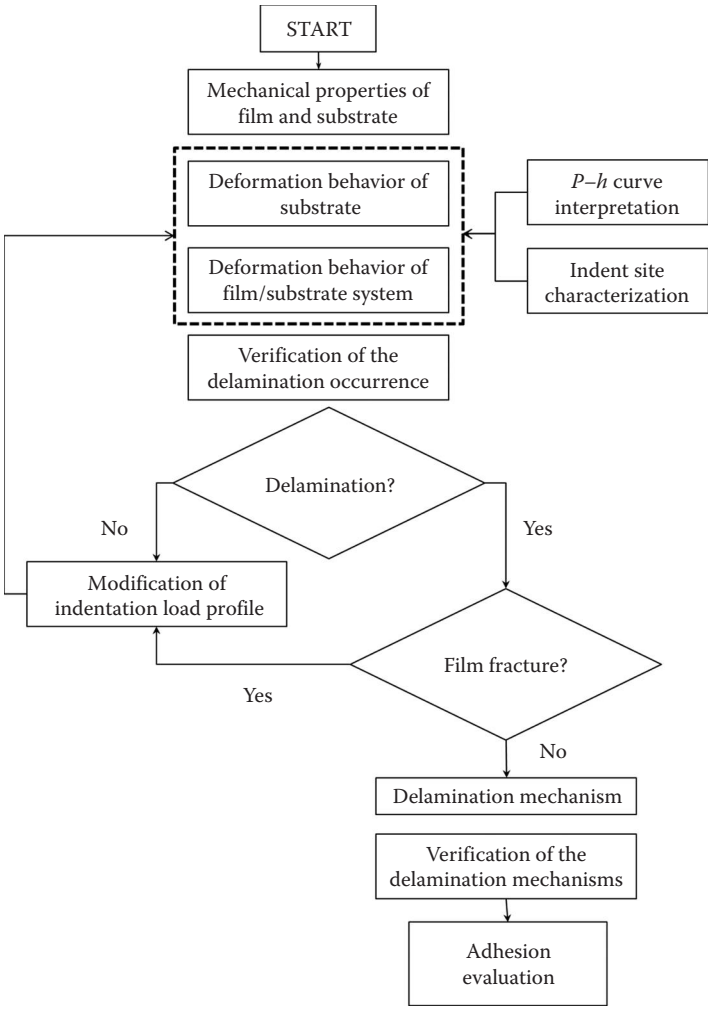


FIGURE 6.10 The flowchart showing the process for determining the interfacial delamination mechanisms in film/substrate systems.

directly using microscopies, especially when the film is not transparent. To confirm that interfacial delamination does occur, additional characterization is needed, such as secondary indentation (see Section 6.3.2.4) and indentation impression cross sectioning, and so on. After the occurrence of delamination is confirmed, the mechanisms that support the interfacial failure can be studied and verified using various modeling techniques [114,115]. If delamination cannot be generated during indentation, the indentation load profile will need to be modified until controlled delamination occurs. In the circumstance that the occurrence of delamination is accompanied with through-thickness fracture in the film structure, the indentation load profile should also be improved, such as reducing the applied load.

6.3.2 Nanoindentation-Induced Delamination in SiN/GaAs Film/Substrate Systems

6.3.2.1 Mechanical Properties of GaAs Substrate and SiN Films

As mentioned earlier, for most of the adhesion tests, the knowledge of mechanical properties of both film and substrate is required. Especially, the elastic modulus is always needed in formulating the interfacial toughness (K_{in}) and energy release rate (G_{in}) [1,6,116]. A suitable procedure uses a Berkovich indenter to measure the elastic modulus and hardness of the substrate and film. The Berkovich tip is used to induce substantial plasticity at the lowest possible indentation load and depth. It is particularly important to use a sharp-pointed indenter to measure the properties of a film so that the plasticity is within the coating and occurs before the substrate yield stress is exceeded; use of blunt indenters may cause the film and substrate to deform simultaneously [117]. The elastic modulus (E) and hardness (H) can be calculated from the indentation P–h curve using the Oliver–Pharr method [118–120]. However, for submicron thin films, the substrate effect is often unavoidable; in this case, a deconvolution method [25–27] may be applied to determine the true E and H of the film from the measured results.

Nanoindentations were carried out on a GaAs bare wafer and SiN films using a Berkovich indenter to measure the elastic modulus E and hardness H. The reduced modulus E_r and H were determined from fitting the upper portion of the unloading part of the P–h curves, as per the methodology developed by Oliver and Pharr [119,121]. The elastic modulus, E, of the material is given by [118]

$$\frac{1}{E_r} = \frac{1 - \nu^2}{E} + \frac{1 - \nu_i^2}{E_i} \tag{6.13}$$

where E and E_i are the elastic modulus of the specimen and the diamond indenter, respectively, ν_i is the Poisson's ratio of the indenter, and ν is the Poisson's ratio of the material being tested. In this study, the values $E_i = 1141$ GPa, $\nu_i = 0.07$, and $\nu_{GaAs} = 0.31$ [24,120] were used to calculate the E of the GaAs. For SiN films, however, the substrate effect cannot be neglected, especially in this case when the SiN films' thicknesses are in submicron scale (Table 6.2). Therefore, an empirical power law was used to deconvolute the films' properties from the measured properties of film/substrate systems [25–27]. Again, the E of SiN film was then calculated using Equation 6.13. The Poisson ratio of SiN, ν_{SiN}, is 0.27 in the calculation. The values of E and H of the GaAs substrate and SiN films obtained are summarized in Table 6.2. As shown in the table, the SiN films are stiffer and harder than the GaAs substrate.

6.3.2.2 Deformation of GaAs Substrate

To accurately characterize a delamination event during testing, the deformation behavior of the film/substrate system must first be understood. The response of a film/substrate system to indentation comprises the deformation of both substrate and thin film. In the case of SiN film on GaAs substrate, particularly, plastic deformation

TABLE 6.2
Elastic Modulus *E* and Hardness *H* of the SiN Films and GaAs Substrate

Sample	Film Thickness (nm)	Elastic Modulus (GPa)	Hardness (GPa)
Compressive SiN	222	152.1	17.2
	489		
	814		
DL-com SiN	207	133.2	15.1
	495		
	787		
Dense SiN	215	148.2	15.7
	523		
	843		
Cap SiN	227	156	16.8
	530		
	842		
Standard SiN	182	115.4	12.7
	520		
	823		
GaAs	6600	120.6	8.03

Source: Lu, M. and H. Huang. 2015. Interfacial energy release rates of SiN/GaAs film/substrate systems determined using a cyclic loading dual-indentation method. *Thin Solid Films* (in press).

of the substrate is required in order to initiate interfacial delamination. Therefore, the substrate deformation should be studied individually, which will provide useful insight into the collective response from indenting the film/substrate systems.

Nanoindentation was carried out on the GaAs bare wafer sample to examine the evolution of the damage. The nanoindentation system used was a Hysitron Triboindenter, equipped with an in situ atomic force microscope (AFM) for indent impression examination. In this case, a conical indenter with a tip radius of 10 μm was used.

Figure 6.11 shows the *P*–*h* curves of the indentation on GaAs at 30 mN and 100 mN. For indentation at a load of 30 mN, GaAs deformed elastically with no plastic deformation occurred. In the case shown, an indentation to a peak load of 100 mN resulted in a marked step in the loading curve. This event is referred to as a "pop-in." The pop-in event is attributed to plane slip in GaAs, occurring at a critical threshold value. When the load is fully released, the extent of the plastic deformation is demonstrated by the residual displacement shown in Figure 6.11. The occurrence of pop-in is equivalent to a "yield point" for GaAs. As shown in Figure 6.12, for small loads very little residual depth is observed indicating full elastic recovery of the material; however, beyond 40 mN pop-in events start to occur and significant residual depth can be observed indicating permanent plastic deformation.

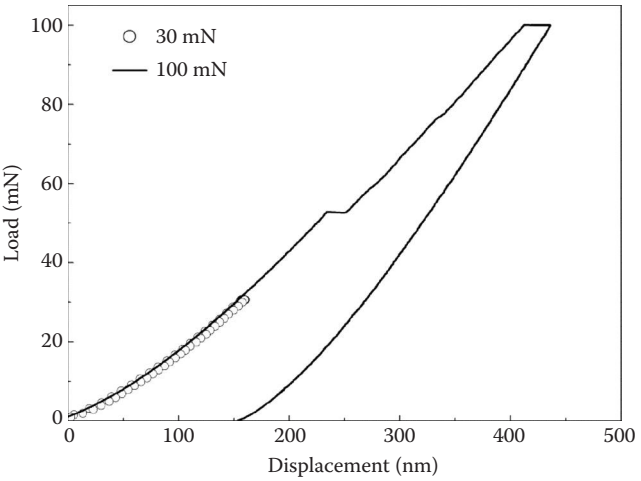


FIGURE 6.11 *P–h* curves of indentation made on the GaAs (001) bare wafer at loads of 30 and 100 mN. (From Lu, M. et al., 2013. *Journal of Materials Research* 28 (08):1047–1055.)

6.3.2.3 Deformation of SiN/GaAs Film/Substrate Systems

For studying the adhesion of film/substrate systems, conical indenters with a spherical apex are preferred, as conical tips cause less stress concentration to the film and thus less likely initiate cracks to the film structure than indenters with sharp edges [114,116,122]. While developing an indentation procedure for a specific film/substrate combination, examination of the indent sites using atomic force microscopy (AFM) or scanning electron microscopy (SEM) are useful to characterize the

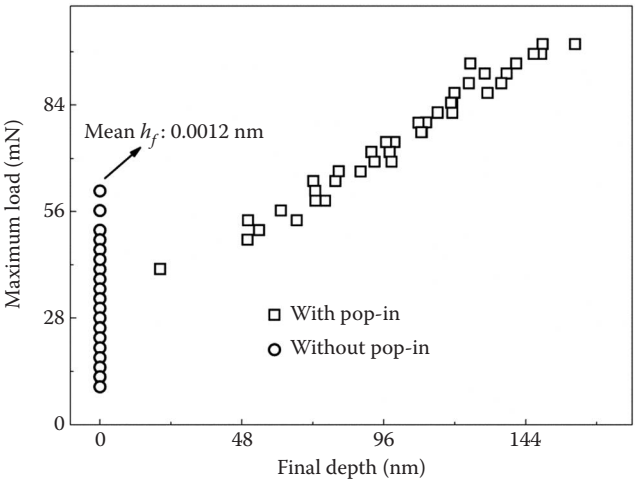


FIGURE 6.12 The relationship between the maximum load and the final indentation depth. (From Lu, M. et al., 2013. *Journal of Materials Research* 28 (08):1047–1055.)

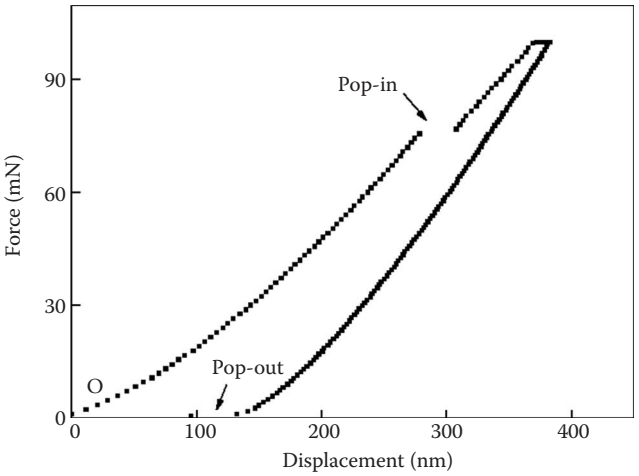


FIGURE 6.13 A typical *P–h* curve of indentations made at 100 mN on the 489 nm compressive SiN film/GaAs film/substrate system.

deformation at the site and ensure that the indent is well formed and free of fracture. In situ imaging technique is most suitable as indentation impressions are often very small and difficult to be observed using various microscopies.

Accordingly, a conical indenter with tip radius of 10 μm was used to study the deformation of SiN/GaAs film/substrate system. The *in situ* AFM was used to examine the indent impression. The typical *P–h* curve of 100 mN indentation on a SiN/GaAs film/substrate system is shown in Figure 6.13. Both pop-in and pop-out can be observed. As discussed earlier, pop-in is caused by the plane-slip occurrence in the GaAs substrate, whereas delamination at the interface is responsible for the pop-out. The deformation mechanism of SiN/GaAs film/substrate system under indentation is illustrated in Figure 6.14. The GaAs substrate has lower hardness, and hence experiences more plastic deformation during loading, while the SiN film deforms more elastically, bending into the dented GaAs substrate. As a consequence, during unloading more elastic recovery occurs in the SiN film than in the substrate, resulting in tensile stress developed at the film/substrate interface. When the tensile stress at the interface exceeds the interfacial strength, an interfacial crack is initiated and propagated quickly along the interface, causing the film to delaminate from the substrate. The recovery of the delaminated film, in the manner of a centrally deflected plate, results in a sudden load on the tip. As indentation is a load-controlled process, such a push causes the indenter to recede quickly, generating a "pop-out."

6.3.2.4 Verification of Delamination Using Secondary Indentation

It is always desirable to undertake additional characterization to confirm the occurrence of interfacial delamination. As most of the films are not transparent, it is very challenging to observe the interfacial crack hidden underneath the film. Often, focused ion beam (FIB) milling is required to cross section the indent site as such subsurface crack can be seen using SEM [122,123]. Although this method provides

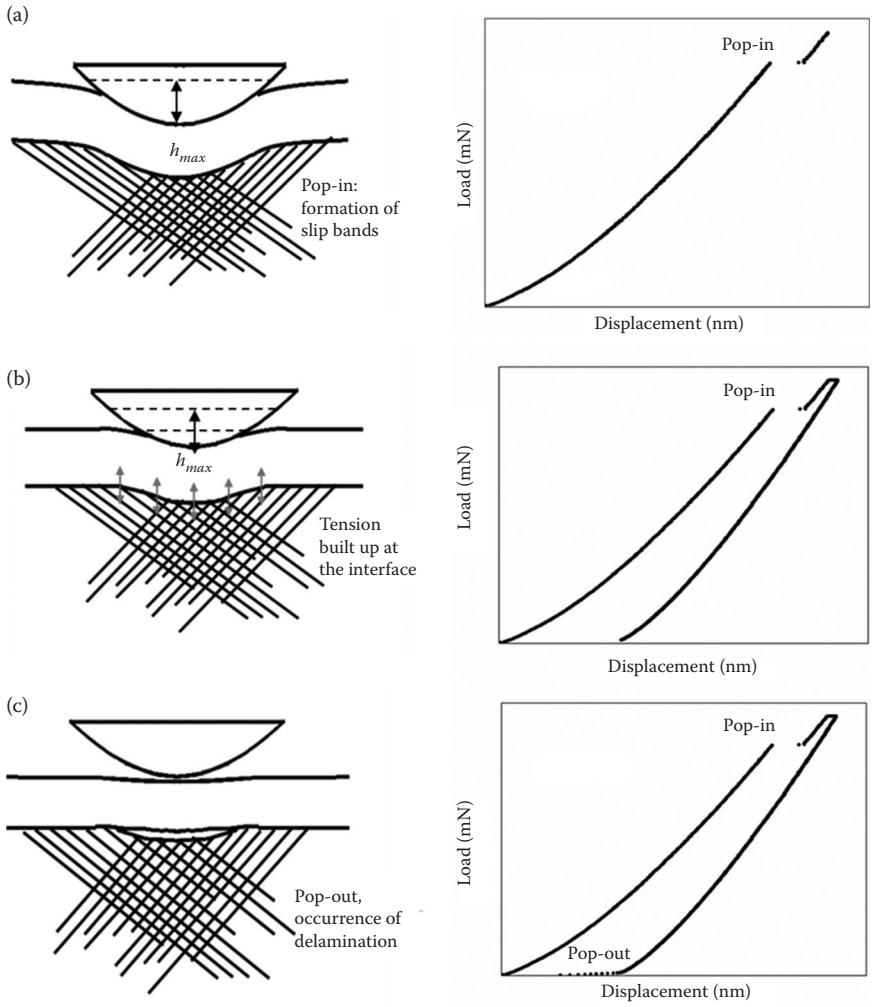


FIGURE 6.14 Schematic illustration of the deformation mechanism of SiN/GaAs film/substrate structure under nanoindentation: (a) elastic–plastic deformation of the SiN/GaAs bilayer during loading; (b) tension building up at the bilayer interface during unloading; (c) occurrence of delamination and the formation of pop-out at the end of unloading. (From Lu, M. et al. 2013. *Journal of Materials Research* 28 (08):1047–1055.)

a direct solution, the sectioning process is often rather difficult and time-consuming, as the indentation impressions are typically shallow and very small. An alternative method, namely secondary indentation [114,115], is thus introduced here. This method provides a simple and fast approach to characterize the delaminated film without causing any damage to the film/substrate structure.

This method involves conducting a second indentation on the spot where delamination occurred in a previous indentation process. Figure 6.15 shows the *P*–*h* curve obtained from the secondary indentation. The previous indentation was

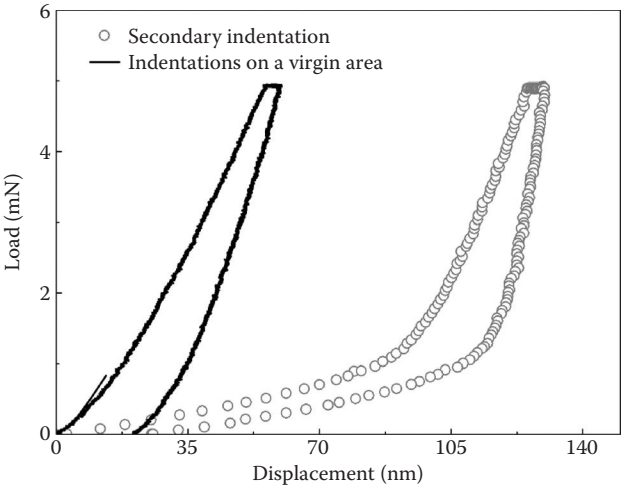


FIGURE 6.15 The *P–h* curve of a secondary indentation at 5 mN made on the spot firstly indented at 100 mN on the 489 nm compressive SiN film. The curve in solid line was obtained from the first indentation on a virgin area using the same loads. (From Lu, M. et al. 2013. *Journal of Materials Research* 28 (08):1047–1055.)

performed at a load of 100 mN. The secondary indentation was performed at the same spot using a load of 5 mN. Here, a much smaller load was used in the second indentation to prevent the film being damaged. For comparison, the *P–h* curve of the indentation performed at 5 mN but at a virgin area is also included. It is seen in Figure 6.15 that in the *P–h* curve of the secondary indentation a dramatic increase in displacement is observed (within the range of approximately 0–70 nm), both at the beginning of loading and the end of unloading with only a slight increase in load. This unique characteristic clearly suggests that the films, after the first indentation, were locally detached from the substrate and thus behaved like suspending membranes or plates.

6.3.2.5 Verification of the Delamination Mechanic Using FEM

A major limitation of most studies in delamination mechanism to date has been the lack of experimental confirmation of subsurface interfacial crack evolution. FEM techniques have the advantage of analyzing stress distribution and elastic–plastic deformation in the film/substrate system [84,122]. FEM offers an improved understanding of indentation-induced delamination phenomena and thus an approach to test the validity of the proposed delamination mechanics.

FEM analysis was carried out using the ANSYS program to study the stress evolution and deformation behavior associated with indentation-induced delamination in the SiN/GaAs system. A 2D axisymmetric FEM model was established to simulate the indenting process. The specimen was modeled 10 times larger than the indented area. The bottom of the substrate was constrained using fixed boundaries. The mesh used had a graduated mesh size, which consisted of

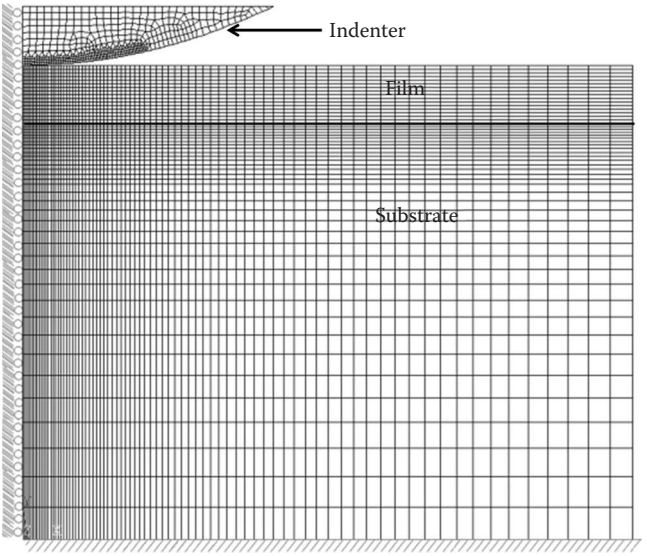


FIGURE 6.16 The 2D axisymmetric finite element model for indentation on SiN/GaAs film/substrate structure using a conical indenter with spherical apex. (From Lu, M. et al. 2013. *Journal of Materials Research* 28 (08):1047–1055.)

11547 quadrilateral elements, as shown in Figure 6.16. Both the substrate and the film were treated as perfectly plastic materials. Their elastic moduli used in the model were obtained from nanoindentation testing. Yield strengths were obtained through matching the peak load numerically with the maximum load used in the indentation for a given indentation depth. The interface was modeled using a cohesive zone law [124] where the cohesive energy (i.e., the energy release rate in linear fracture mechanics, Γ), is governed by a constitutive equation known as the traction-separation law

$$\Gamma = e\sigma_{\max}\bar{\delta}_n\left[1-(1+\Delta_n)e^{-\Delta_n}e^{-\Delta_t^2}\right] \tag{6.14}$$

where $\Delta_n = \delta_n/\delta_n$, $\Delta_t = \delta_t/\delta_t$, $\sigma_{\max}$ is the maximum normal traction at the interface, δ_n and δ_t are the normal and tangential interfacial separation, $\bar{\delta}_n$ is the normal separation across the interface where the maximum normal traction is attained with $\delta_t = 0$, and $\bar{\delta}_t$ is the shear separation where the maximum shear traction is attained when $\delta_t = \frac{1}{\sqrt{2}}\bar{\delta}_t$. The traction T acting on the interface is decomposed into T_n and T_t in both normal and tangential directions, which can be expressed as

$$T_n = \frac{\partial\Gamma(\delta)}{\partial\delta_n} = e\sigma_{\max}\Delta_n e^{-\Delta_n}e^{-\Delta_t^2} \tag{6.15}$$

$$T_t = \frac{\partial \Gamma(\delta)}{\partial \delta_t} = 2e\sigma_{\max} \frac{\bar{\delta}_n}{\bar{\delta}_t} \Delta_t (1 + \Delta_n) e^{-\Delta_n} e^{-\Delta_t^2} \tag{6.16}$$

In the cohesive zone model [124], traction and strain energy release rate that govern the occurrence of delamination were preset. In other words, interfacial failure occurred when the tension at the interface exceeded the preset threshold, assuming that no through-thickness cracking took place. During modeling, an iterative approach was used to optimize the traction and the energy release rate through minimizing the difference between the computed unloading curve and the experimentally obtained target. Once the best fit was obtained, the modeling was terminated and the stress at the depth of delamination was then analyzed.

Since this study focused on the indentation-induced interfacial failure and the corresponding pop-out event was occurred during unloading, the associated mechanism of the pop-in was thus not modeled in order to simplify the FEM simulation. In the FEM model, only the unloading section of the *P–h* curve was used as the optimization target. Figure 6.17 shows the *P–h* curves obtained from the FEM simulation, in

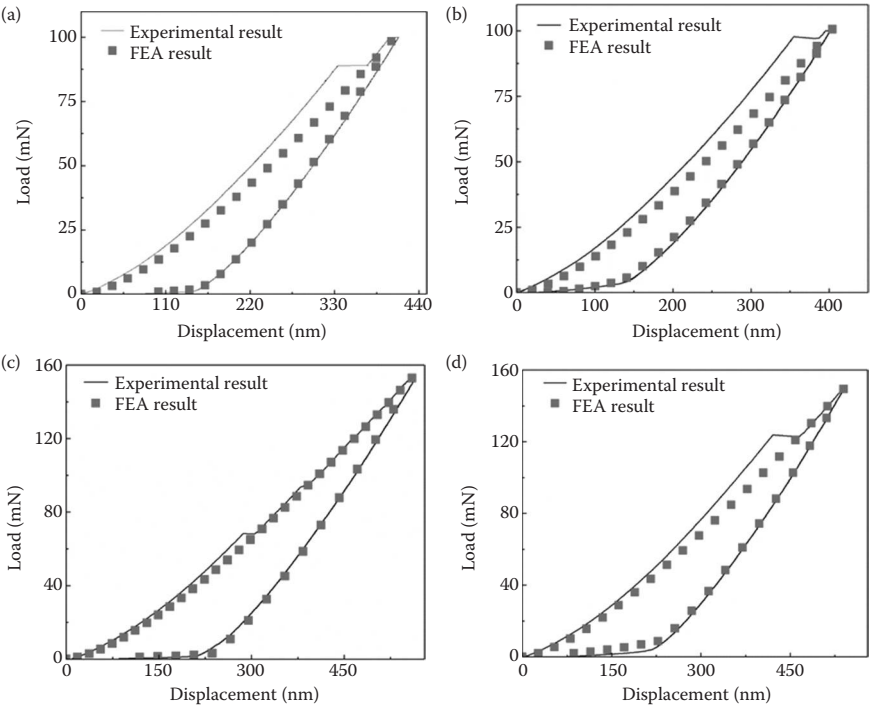


FIGURE 6.17 Comparison of *P–h* curves between experiment and the simulation for different loads and film thickness: (a) 100 mN 489 nm; (b) 100 mN 814 nm; (c) 150 mN, 489 nm; (d) 150 mN, 814 nm. (From Lu, M. et al. 2013. *Journal of Materials Research* 28 (08):1047–1055.)

comparison to those obtained from the indentation tests. The traction and the strain energy release rate input into the model for the 489 nm film, which led to the best fit shown in Figure 6.17a, were 400 MPa and 1.13 J, respectively. The same properties were then used in the model for the 814 nm film. The FEM results appeared to be in excellent agreement with the testing, as shown in Figure 6.17, indicating that the cohesive zone model was appropriate to characterize the debonding of the film to the substrate.

The stress contour underneath the indenter snapped at the moment of delamination for the 489 nm film is shown in Figure 6.18a. It is clearly seen that at debonding a considerable tensile stress of about 400 MPa was built up at the interface toward the indent center. The delamination was initiated at the location near the indenting center and propagated almost instantaneously both toward the center and away from the center. Figure 6.18b shows the stress distribution when the indenter completely detached from the specimen. At this stage, tension was released at the center, but a significant tensile stress still concentrated at the interfacial crack tip.

The FEM analysis clearly demonstrated that tension at the interface was built up with the further withdrawal of the indenter during unloading, as shown in Figure 6.18a. When the tensile stress at the interface exceeded the interfacial adhesion strength, an interfacial crack was initiated and propagated quickly along the interface, causing the film to delaminate from the substrate. The delaminated film recovering elastically upward like a centrally deflected plate would give the tip a push. Since the indentation was a load-control process, such a push thus made the tip to recede quickly, generating a "pop-out."

6.3.2.6 Optimization of the Load Profile

6.3.2.6.1 The Minimum and Maximum Loads

To be able to study the interfacial failure, the interfacial delamination needs to be generated and recorded by the nanoindentation. It may be found that during the development of a delamination process for a specific film/substrate system that a particular load profile works best. It is required that the substrate undergoes sufficient plastic deformation and only limited plastic deformation occurred to the film; hence during tip withdrawal the generous elastic recovery of the film generates tension at the interface that lead to the initiation of delamination.

Figure 6.19 shows the three representative deformation patterns observed from the P–h curves of the nanoindentation test under different load: (i) no plastic deformation occurred in GaAs substrate during loading and the film remained attached to the substrate after unloading (Figure 6.19a and d); (ii) the GaAs substrate deformed plastically during loading and the film detached from the substrate during unloading (Figure 6.19b and e); (iii) annular through-thickness crack occurred in the film during loading (Figure 6.19c and f). It is illustrated that below a certain minimum load, delamination will not occur; however, if a very high load is used the film may fracture. A balance is thus required to initiate delamination without causing excessive film damage. In particular, the minimum applied load should be above the pop-in threshold load and the maximum applied load should be below the film fracture threshold.

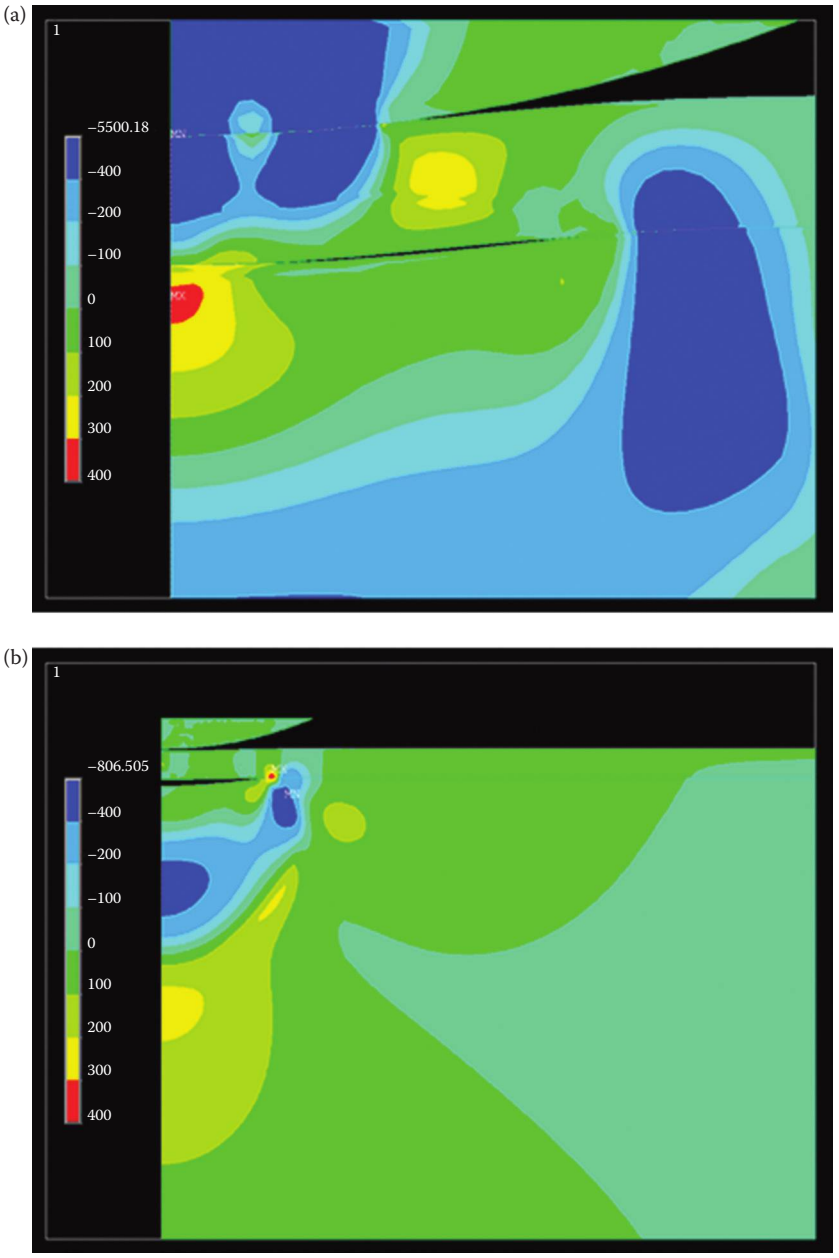


FIGURE 6.18 Cross-sectional view of the normal stress contours (a) at the initiation moment of interfacial crack and (b) after the indenter completely lost contact with the indented surface. (From Lu, M. et al. 2013. *Journal of Materials Research* 28 (08):1047–1055.)

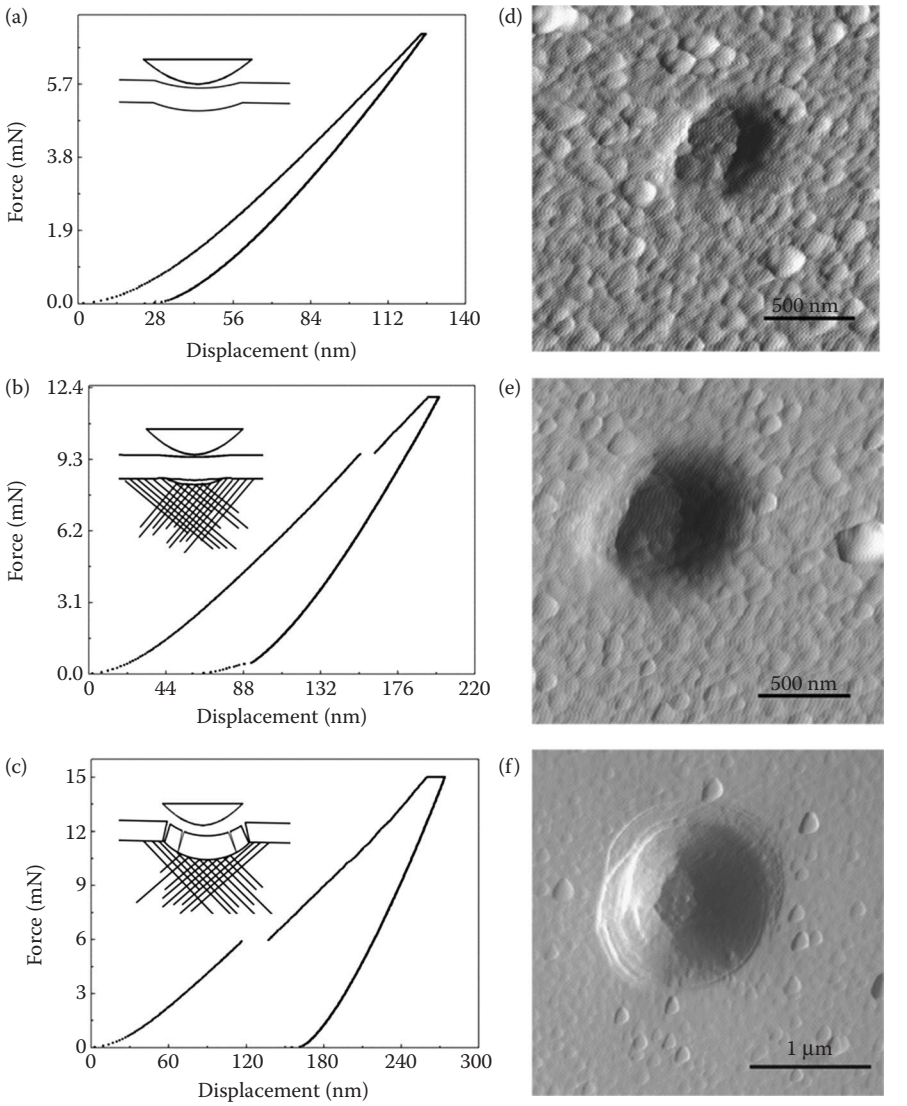


FIGURE 6.19 The *P–h* curves at load of (a) 6, (b) 12, and (c) 15 mN. The AFM images in (d), (e), and (f) are the indents corresponding to the respective *P–h* curves at the left side. Three deformation patterns are shown: (i) substrate recovered completely and the film remained attached to the substrate ((a) and (d)); (ii) the substrate plastically deformed and the film detached from the substrate ((b) and (e)); (iii) through-thickness cracks occurred in the film ((c) and (f)). The indentations were made on the 222 nm compressive SiN on GaAs substrate. (From Lu, M. and H. Huang. 2014. *Journal of Materials Research* 29 (06):801–810.)

6.3.2.6.2 Cyclic Loading Indentation For "Tough" Interface

The indentation contact stress in malleable and strongly adhered films tends to be consumed by plastic deformation rather than being transferred to elastic strain energy, which reduces the driving force for interfacial crack initiation and propagation [1,35]. To detach a well-adhered film from a substrate, two techniques are often used. One is to deposit a thick superlayer on top of the film of interest [1,75]. The superlayer is capable of storing large amount of residual stress and thus provides additional driving force for initiating interfacial delamination without altering the properties of the interface [125]. This method requires additional sample preparation, which involves adjusting the thickness and the residual stress of the superlayer so that controlled delamination occurs [6]. The alternative approach is to use cyclic indentation [34,126–128], during which indentation cycles are done repeatedly at a given load. The interfacial delamination is initiated by the progress of plastic deformation zone in both the film and substrate during each indenting cycle. Compared to the superlayer method, the cyclic indentation method is more controllable and does not require supplementary sample preparation, although the additional plastic deformation resulted from cyclic indentation may potentially weaken the interface through fatigue degradation.

Some SiN/GaAs film/substrate structure could not be delaminated by means of regular indentation, for great plastic deformation was produced in these SiN films during loading. We therefore developed a cyclic loading indentation method used to induce interfacial delamination to these well-adhered SiN/GaAs interfaces [129]. This method used a cyclic loading process that comprised multiple cycles of loading-unloading with incremental increase of applied load and 50% partial unloading fraction from cycle to cycle. Figure 6.20 compares the *P*–*h* curves obtained from a

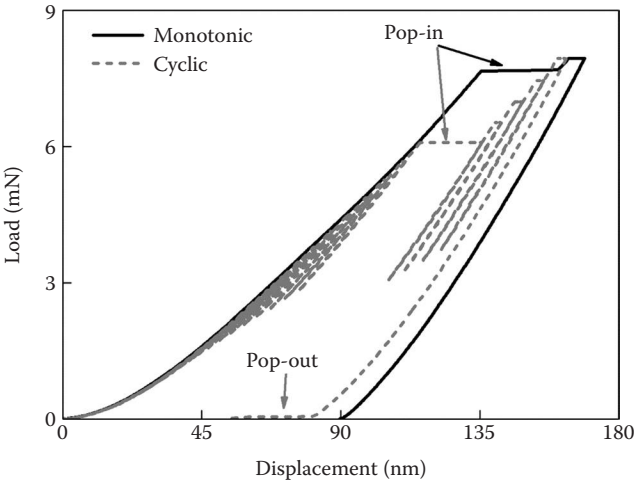


FIGURE 6.20 The *P*–*h* curves of a monotonic loading and a cyclic loading (33 cycles) indentations. The standard SiN film used was 180 nm in thickness; the maximum load was 8 mN. (From Lu, M. and H. Huang. 2015. Interfacial energy release rates of SiN/GaAs film/substrate systems determined using a cyclic loading dual-indentation method. *Thin Solid Films* (in press).)

monotonic loading indentation and a cyclic loading indentation (33 cycles). For the *P–h* curve of the monotonic loading indentation, no pop-out was observed during unloading. In contrast, the *P–h* curve of the cyclic loading indentation showed a significant pop-out event, which signified the occurrence of interfacial delamination. The result shows that the cyclic loading indentation could effectively initiate interfacial delamination in the SiN/GaAs film/substrate systems, in which the regular monotonic loading indentation failed to do so.

It was also found that cyclic loading resulted in increased hardness and hence a shallower indent impression (Figure 6.21), attributed to the localized densification in the amorphous SiN films induced by the imposed cyclic strain. This hardening effect provides some insight into the interfacial delamination mechanic of SiN/GaAs film/substrate systems under cyclic loading indentation. Figure 6.22 schematically illustrates the delamination mechanism of SiN/GaAs film/substrate system under cyclic loading indentation. For comparison, the deformation of the studied film/substrate system in a monotonic loading indentation is provided in Figure 6.22a and b. During monotonic loading, the substantial plastic deformation resulted in a pronounced encroachment of the deformed SiN film conformed into the cavity formed due to the plastic deformation of the substrate. In this process, generous strain energy was used in plastically bending the film toward the substrate and the residual elastic strain energy was thus insufficient to break the interfacial bonds. In the case of cyclic loading indentation, the indented SiN film was hardened, which impeded the plastic flow in the deformed SiN film (Figure 6.22c and d). More contact strain was thus stored in the flexed film in the form of elastic strain energy in cyclic loading than a monotonic loading. As a result, interfacial delamination was more likely initiated driven by the tensile stress being generating during unloading, with more aid of the stored elastic strain energy in the flexed film. As this process did not generate additional plastic flow to the system, the influence of fatigue degradation on the interfacial property is negligible.

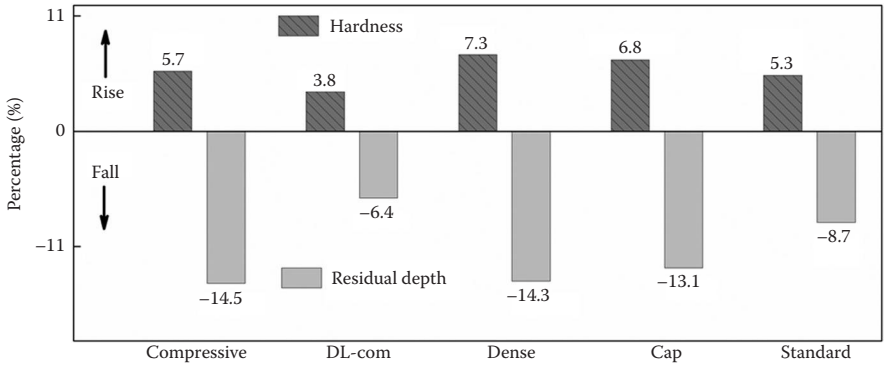


FIGURE 6.21 The relative difference (in percentage) in hardness and residual depth between the values measured using monotonic loading indentation and cyclic loading (50 cycles) indentation. (From Lu, M. and H. Huang. 2015. Interfacial energy release rates of SiN/GaAs film/substrate systems determined using a cyclic loading dual-indentation method. *Thin Solid Films* (in press).)

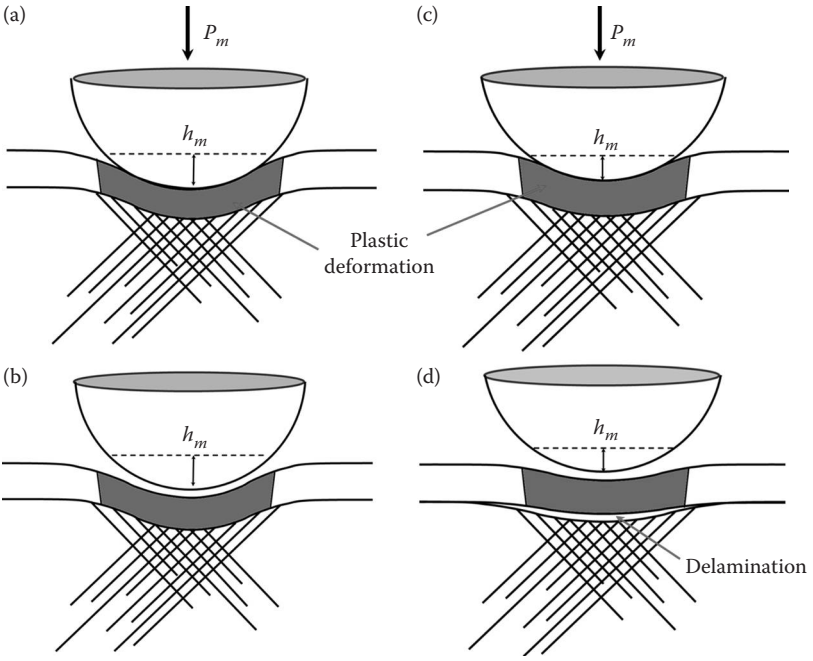


FIGURE 6.22 Schematic illustration showing different deformation behaviour under different loading conditions: (a) monotonically loading till maximum load is reached; (b) film remain attached to the substrate after monotonic loading indentation; (c) cyclically loading till maximum load is reached; and (d) interfacial delamination under cyclic-loading indentation. (From Lu, M. and H. Huang. 2015. Interfacial energy release rates of SiN/GaAs film/substrate systems determined using a cyclic loading dual-indentation method. *Thin Solid Films* (in press).)

6.4 EVALUATION OF THE INTERFACIAL TOUGHNESS OF SiN/GaAs FILM/SUBSTRATE SYSTEMS

A number of models have been established for quantifying the interfacial toughness (K_{in}) or energy release rate (G_{in}) via nanoindentation; among those, stress field and energy analyses are two major approaches. Stress field analysis required an intense modeling process [130–132], whereas the energy method may be applied directly to the indentation data output [19,93,115]. Using continuum linear elasticity theory, the energy method has been applied to evaluate the surface energy associated with the formation of interfacial cracks [37].

In a nanoindentation test, the summation of the energy consumed in plastic deformation and the stored elastic energy within the material being tested may be obtained by computing the integral of the load–displacement (P–h) curve obtained during an indentation process [117]. A study undertaken by Hainsworth et al. attributed the extra linear recovery at the ending of unloading to the occurrence of delamination [37]. Under the assumption that the mechanical work involved had limited contribution, they considered the elastic and the elastic strain energy stored in the

flexed film was equal to the surface energy of the interfacial crack. Wei et al. also approximated the elastic energy stored in the deflexed film as the energy associated with delamination, when studying the interfacial adhesion of SiO_2/Si and DLC/Si film/substrate systems [34,128]. Both approaches modeled the deflection of the delaminated film as a circular membrane. Chen et al. modified the extra linear recovery method by taking into account both the elastic strain energy and the external mechanical work [6,36,133]. By extrapolating the initial part of an unloading curve, the difference between the extrapolated and the actual unloading curves was used to calculate the dissipated energy of the interfacial cracking. Those studies laid the foundation for the characterization of the thin film interfacial adhesion properties. However, as film/substrate structures exhibit quiet different delamination characteristics [6], these approaches cannot currently be considered to be broadly applicable.

The Griffith energy balance concept is often employed to obtain the energy release rate G_{in} of interfacial delamination. In a film/substrate system containing an interfacial crack of area A, the incremental increase of the crack surface energy (or released delamination energy) U_s for a crack extension area A can be expressed as the interfacial energy release rate [6,134]

$$G_{\text{in}} = U_s / A \tag{6.17}$$

Therefore, in order to calculate G_{in}, U_s and A need to be measured. In this section, two approaches to measure U_s and two models established for A estimation will be introduced.

Before we introduce the methodologies, it is worthy to point out that the measured delamination energy release in this work is in fact the practical work of adhesion, $W_{A,P}$. As discussed earlier, $W_{A,P}$ comprises the true work of adhesion (or crack surface energy), U_s, the energy used in plastic deformation of film and substrate, W_f and W_s respectively, as well as the energy loss due to friction W_{fric}, according to Equation 6.2. In the case of interfacial delamination in an SiN/GaAs film/substrate system, as both the film and substrate are hard brittle materials and the interfacial bond is relatively weak, W_f and W_s accompanied with the initiation and propagation of an interfacial crack can be considered negligible. Further, because the film and substrate separate in the manner of mode I (opening mode) fracture at the interface during indentation unloading, energy loss due to friction can also be neglected. Therefore, the practical adhesion $W_{A,P}$ is considered to be equivalent to U_s.

6.4.1 Delamination Energy Release

6.4.1.1 Griffith Energy Balance

It is assumed that the interfacial fracture occurred in a film/substrate structure acted as a reversible thermodynamic system, where the film and substrate were considered as two elastic bodies. The net energy of a static crack is given by [36,37,134]

$$U = U_e + U_s - W \tag{6.18}$$

where U_e is the strain energy stored in the elastic medium, U_s is the free energy required to generate the entire crack surface, the negative work $-W$ is the potential energy of the externally applied loading component. To obtain the thermodynamic equilibrium by balancing all the three energy terms, it is required that [134]

$$U = 0 \tag{6.19}$$

It is important to note that in the Griffith's model the external force at the outer boundary does positive work by pulling apart the two elastic bodies and the elastic strain energy builds up accordingly as the crack proceeds. In contrast, in the indentation-induced delamination model, the indenter does negative work (compressive) and the elastic strain energy in the film is negative (released energy). Defining W_d as the external work done by the indenter, U_e as the elastic strain energy in the deflected film, the equilibrium of the delamination system takes the form

$$-U_e + U_s + W_d = 0 \tag{6.20}$$

Rearranging Equation 6.20, we obtain the energy required to generate the interfacial crack surface, written as

$$U_s = U_e - W_d \tag{6.21}$$

6.4.1.2 Method I: Dual-Indentation

6.4.1.2.1 Load Function

The dual-indentation method is developed to obtain the quantity of the two energy terms U_e and W_d for calculating U_s [116,129]. Two indentation load functions of the dual-indentation methods are shown in Figure 6.23, namely monotonic loading dual-indentation and cyclic loading dual-indentation. The monotonic loading dual-indentation is effective in testing film/substrate systems with low interfacial adhesion. In this dual-indentation scheme (Figure 6.23a), an initial indentation is followed by a second indentation, with each having the same loading and unloading conditions. The unloading portion of the first indentation ceases when the load reaches 0.01 mN, so the contact between the indenter and the film can be maintained. An intermediate holding period of 1 s is applied prior to the second indentation, which aims to attenuate the hysteresis in the elastic recovery of the film. For the cyclic loading dual-indentation (Figure 6.23b), the loading process of the first indentation was composed of 33 cycles of loading–unloading with incremental increase of applied load and 50% partial unloading fraction from cycle to cycle. In each cycle, loading, holding, and unloading times were all 1 s. The cyclic loading dual-indentation, however, can be applied to measure the adhesion of both weakly and strongly bonded interfaces. The application of a cyclic loading phase improves the success rate in generating interfacial delamination to malleable films that strongly adhered to the substrate. As mentioned earlier, cyclic loading leads to the hardening of the indented film and thus impedes the plastic flow during the loading phase. More contact strain is thus stored

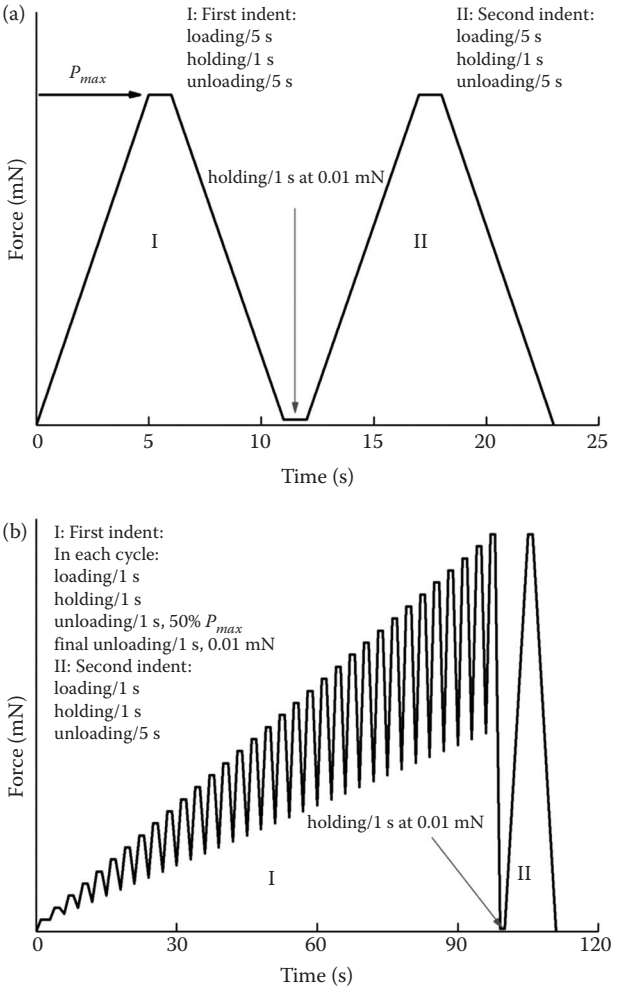


FIGURE 6.23 The load functions of (a) monotonic loading and (b) cyclic loading dual-indentations. (From Lu, M. and H. Huang. 2014. *Journal of Materials Research* 29 (06): 801–810; Lu, M. and H. Huang. 2015. Interfacial energy release rates of SiN/GaAs film/substrate systems determined using a cyclic loading dual-indentation method. *Thin Solid Films* (in press).)

in the flexed film in the form of elastic strain energy, which later drives the initiation and extension of interfacial crack (see Section 6.3.2.6.2).

6.4.1.2.2 Load–Displacement (P–h) Curves

The typical *P–h* curve of a monotonic dual-indention test on the SiN/GaAs film/substrate system is shown in Figure 6.24a. The loading and unloading curves of the second indentation are approximately congruent, indicating the indentation was elastically dominated. The minor hysteresis observed in the *P–h* curve of the secondary

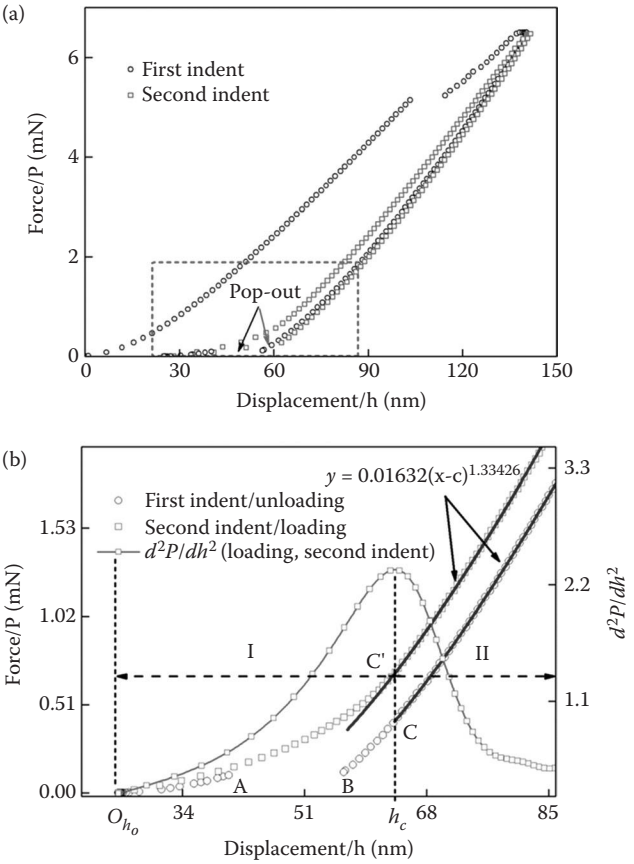


FIGURE 6.24 The *P–h* curves (a) of a monotonic loading dual-indentation on 222 nm compressive SiN film; (b) is the enlarged image of the areas marked in the dashed rectangles in (a), showing the second derivative of the final indent loading portion and the curve fitting result using Hertz elastic contact theory. (From Lu, M. and H. Huang. 2014. *Journal of Materials Research* 29 (06):801–810.)

indentation suggests that a small amount of plasticity occurred. The occurrence of the pop-out event at the near end of the second unloading curve was due to the further extension of the interfacial crack (originally generated in the first indentation). Nevertheless, this method considers only the crack generated in the first indentation, due to the complex nature of the crack propagation in the secondary indentation.

The loading curve of the second indentation was used to compute the delamination energy release (U_s) and the area being detached from the substrate or the delaminated area (A). The initial portion of the loading curve includes the responses of the detached film to elastic bending followed by the elastic deformation of both SiN and GaAs. Thus, it is essential to identify the point of gradient discontinuity, at which the detached film completed the deflection or regained contact with the substrate, in order to accurately obtain U_s and A. Mathematically, the second derivative of the

curve, that is, d^2P/dh^2 in this case, will exhibit a cusp at the gradient discontinuity point. For this purpose, the second derivative, d^2P/dh^2, of the loading curve was calculated and the d^2P/dh^2 is plotted as a function of the penetration depth, h, in Figure 6.24b.

The two loading stages are evident in Figure 6.24b, delineated by the gradient cusp point at $h = h_c$, that is, Point C'. The stage I of the P–h curve (or the curve OC') exhibits a distinctive elbow shape, indicating that the suspended film deflected downward in the reloading stage. The film regained contact with the substrate at the point C'. The total deflection ω of the suspending film in the reloading stage equals $(h_c–h_o)$, as shown in Figure 6.24b. From point C' onward (i.e., stage II), the reattached film/substrate system started to deform elastically as an integrated body. The reloading process is schematically shown in Figure 6.25. As shown in Figure 6.24b, the Hertz contact curves (the solid lines) [94,117,135,136] were expressed as

$$P = K(h - c)^{\beta} \tag{6.22}$$

where K is a constant determined by the reduced modulus E_r and the radius of the indenter, and β is determined by the geometry of the indenter and c is a constant (c is equal to residual displacement h_f in fitting elastic unloading curve). Also, in Figure 6.24b, the loading curve of the second indentation and the unloading curve of the first indentation are fitted using the same function, that is, $P = 0.01632(h–c)^{1.33426}$. This suggests that the elastic deformation in the second indentation commencing from C' is reversible.

In the P–h curve of a cyclic loading dual-indentation on SiN films, all the deformation and delamination characteristics are the same as the ones observed in the

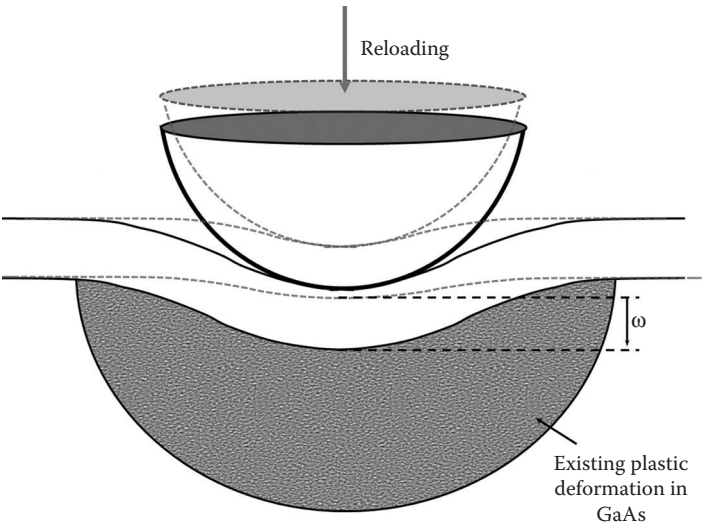


FIGURE 6.25 Reloading the delaminated film. (From Lu, M. and H. Huang. 2014. *Journal of Materials Research* 29 (06):801–810.)

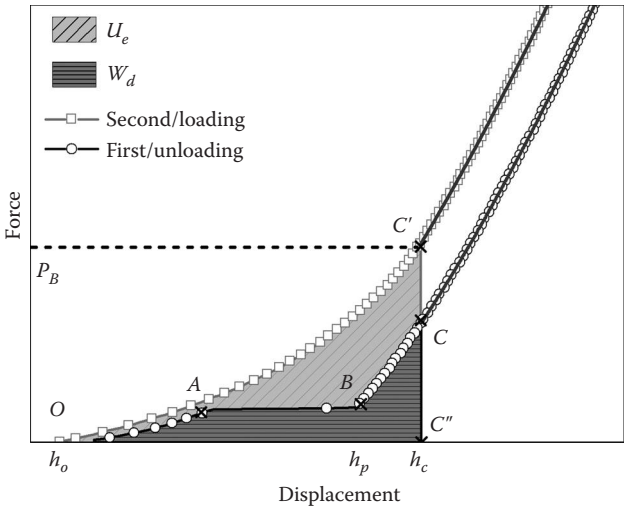


FIGURE 6.26 Schematic illustration of the energy calculation model. (From Lu, M. and H. Huang. 2014. *Journal of Materials Research* 29 (06):801–810.)

P–h curve of a monotonic loading dual-indentation, except for the replacement of the monotonic loading with the cyclic loading. Thus, the energy model developed for the monotonic loading dual-indentation can be applied to the calculation of the energy release caused by cyclic loading dual-indentation.

6.4.1.2.3 Calculation of U_s

Figure 6.26 shows how the energy used for delamination can be obtained from a *P–h* curve of the dual-indentation. As shown in Figure 6.26, curve *OC′* is the loading curve of the second indentation and is the response of the elastic bending of the detached film prior to contact with the substrate. Therefore, the area underneath the *OC′*, that is, the area enclosed by *OC′C″O*, is the stored elastic strain energy of the deflected film at $h = h_c$. The equivalent mechanical work W_d by the indenter can be calculated by integrating the unloading section over the corresponding displacement range of h_o–h_c, that is, the area enclosed by *OABCC″O*. Therefore, according to Equation 6.17, the surface energy U_s can be approximated by the area enclosed by *OC′CBAO*.

6.4.1.3 Method II: Preexisting Crack Supposition

6.4.1.3.1 Assumptions

Assuming two film/substrate systems, the interface of system 1 has a finite interfacial strength, as shown in Figure 6.27a [115]. System 2 has the same film and substrate as system 1 but has a preexisting crack that is identical to the indentation-induced crack in system 1 (Figure 6.27b), as shown in Figure 6.27c. The imaginary crack is assumed to be closed, that is, the film and the substrate are still in contact prior

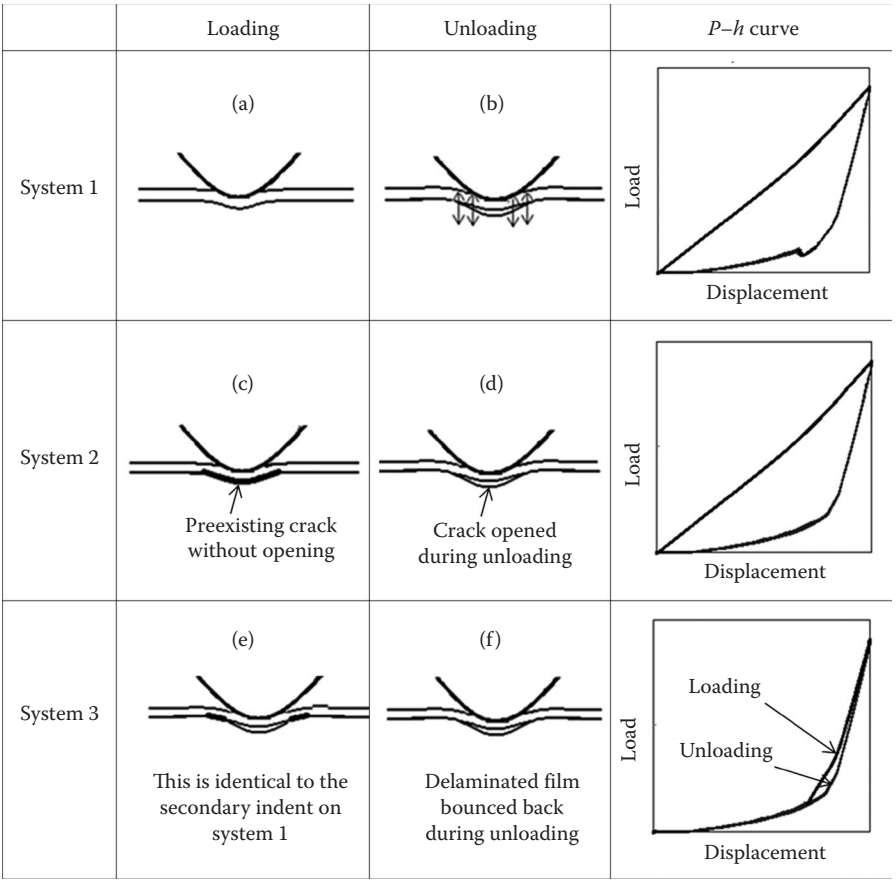


FIGURE 6.27 Schematic illustration of indentation-induced deformation during loading and unloading and the corresponding *P–h* curves of system 1(a,b), 2(c,d), and 3(e,f). (From Xie, H. and H. Huang. 2013. *Journal of Materials Research* 28 (22):3137–3145.)

to loading. During indenting, the beginning state and the state in the end for both cases are exactly the same. Therefore, the elastic and plastic work/energy consumed in both processes should be equal. However, for system 1, additional work is used to create interfacial crack. Subtracting the total energy involved in the indentation on system 2, W_{t2}, from the one from indentation on system 1, W_{t1}, the delamination energy U_s can be obtained:

$$U_s = W_{t1} - W_{t2} \tag{6.23}$$

Equation 6.23 indicates that delamination energy equals the difference of the mechanical work done by the indenter on the two systems without and with a preexisting crack, that is, system 1 and 2, shown in Figure 6.27a.

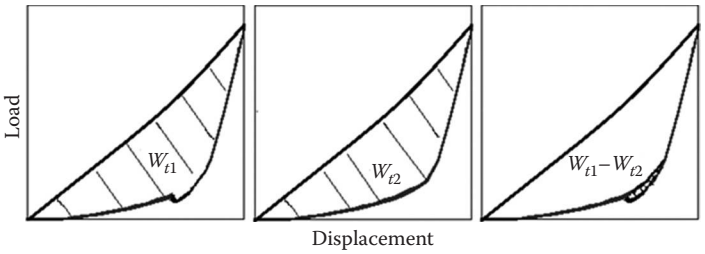


FIGURE 6.28 Determination of the energy released for delamination U_s. (From Xie, H. and H. Huang. 2013. *Journal of Materials Research* 28 (22):3137–3145.)

6.4.1.3.2 Determination of U_s

If the *P–h* curves of the two systems can be obtained from indentation testing, U_s can be obtained, as shown in Figure 6.28. In Figure 6.28, $W_{t1} - W_{t2}$ is the difference of work done during indenting on systems 1 and 2. System 1 is a normal film/substrate system, whose *P–h* curve can be obtained from the nanoindentation test. However, system 2 is imaginary, whose *P–h* curve cannot be obtained directly. From stress analysis, it is understood that the preexisting crack does not affect the indentation loading but does affect unloading. Therefore, the loading curve of system 2 should be identical to that of system 1. To obtain the unloading curve of system 2, we can image a system that has an open preexisting crack, that is, system 3, shown in Figure 6.27e and f, and the crack will not propagate during further indenting. The crack will be closed during loading, creating a state identical to that in Figure 6.27c. During unloading, the film will bounce back, returning to the state prior to the indentation. System 3 is in fact the secondary indentation of the system shown in Figure 6.27b. Thus, we can perform the secondary indentation on the same position of the first indentation system 1 to achieve the unloading curve of system 2. By combining the loading curve of the first indentation and the unloading curve of the secondary indentation of system 1, the *P–h* curve of system 2 is obtained. $W_{t1} - W_{t2}$ can thus be determined experimentally, as shown in Figure 6.28.

6.4.2 Plate Bending Models

To calculate G_{in} using Equation 6.17, the delaminated area, A, must be measured. As the interfacial delamination occurred beneath the film, it was extremely challenging to measure the delaminated area. FIB milling has the capability to cross section the delaminated area for such measurement. However, it is difficult to locate the delaminated area accurately since the indents are normally very shallow. Furthermore, the ion beam milling may introduce microstructural modifications/damage during cross sectioning [137,138]. Therefore, the estimation of the delaminated area using a plate-bending model is important. The behavior of flexed plates of equivalent geometry to the suspending film structure can be examined by solving the corresponding governing equations with the boundary conditions being appropriately assumed.

Rosenfeld et al. [18] used an annular plate model with plane stress condition along the axial direction to approximate the strain energy in the debonded coating

with known geometry. Similarly, in Hainsworth's study [37], a centrally loaded disc model was used to derive the stored elastic energy in the flexed annular coating, and a model of a circular membrane under uniform pressure was applied by Pal et al. [128] for stress analysis of the detached film. However, in these above-mentioned studies, the plate-bending models were used to obtain the energy by use of stress/strain analysis of known plate geometries. Here, we introduce the application of plate bending models for delamination area estimation, when the dimension of the "plate" studied is unknown. Two models were used, based on which the area of the interfacial crack, A, in a SiN/GaAs system could be estimated using the film deflection and loading conditions obtained directly from the indentation P–h curve.

Under the assumption that the spherical apex of a conical indenter generated a circular delaminated area, a circular plate model was employed for computation of the delaminated area. A rigidly clamped edge was also assumed in the model because no through-thickness fracture was generated. Therefore, considering delaminated film as a uniformly loaded circular plate at the concentric circular area with its edge being firmly clamped is appropriate to simulate the deflection of the delaminated film.

6.4.2.1 Model I: Centrally Loaded Plate with Uniformly Distributed Load

In this model [116,129], the detached film structure is approximated as a clamped circular plate, as shown in Figure 6.29. The delamination area can then be calculated based on the deflection of the clamped circular plate using corresponding circular plate deflexion rule. This model is proposed for estimating the delamination area generated by indentation in film/substrate system using a conical indenter. In this model, the indentation is treated as uniformly distributed load at a concentric circular area of a radius of b,

$$b = [R_i^2 + (R - h_c)^2]^{1/2} \tag{6.24}$$

where R_i is the radius of the indenter ($R_i = 3$ μm) and h_c is the contact depth for an typical spherical contact [119] determined by

$$h_c = h - \frac{0.72P}{dP/dh} \tag{6.25}$$

The radius of the delamination area a is associated with the deflection ω of the suspending film, which is written as [139]

$$\omega = \frac{P_0 b^2 (a^2 - 0.75b^2 + b^2 \ln(b/a))}{16D} \tag{6.26}$$

where P_0 is the load intensity and D is the flexural rigidity of the plate, expressed as

$$P_0 = \frac{P}{2\pi b^2} \tag{6.27}$$

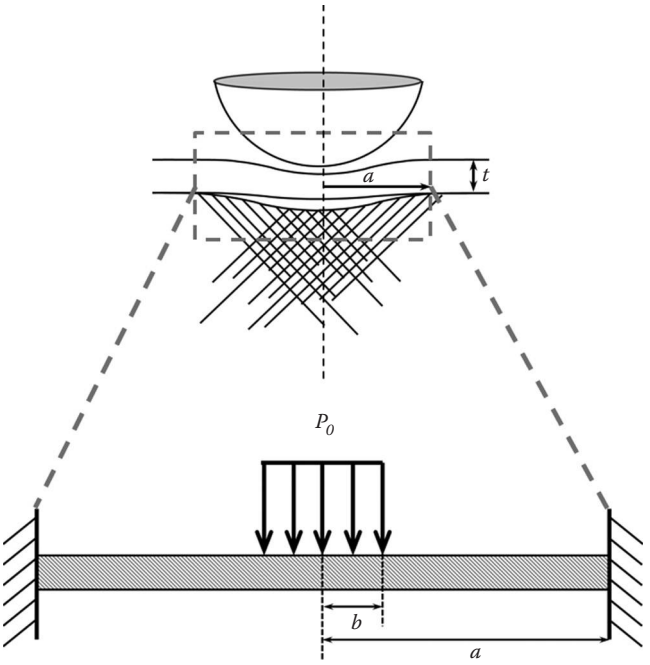


FIGURE 6.29 The centrally loaded clamped circular plate model for delamination area estimation. (From Lu, M. and H. Huang. 2014. *Journal of Materials Research* 29 (06):801–810.)

$$D = \frac{Et^3}{12(1-\upsilon^2)} \tag{6.28}$$

where E, t, and υ are the elastic modulus, the thickness, and the Poisson's ratio of the film, respectively. Once a is known, G_{in} can be calculated by

$$G_{\text{in}} = \frac{U_s}{A} = \frac{U_e - W_d}{2\pi a^2} \tag{6.29}$$

6.4.2.2 Model II: Hertz Contact Loaded Plate

Likewise, the detached film is treated as a circular plate with clamped boundaries in this model [115,140]. The total deflection of the plate can be estimated by treating the system as two springs in series, in which the penetration of the indenter and deflection of the plate superpose

$$\omega = \delta_{\text{Hertz}} + \delta_{Plate} = \left(\frac{9P^2}{16R_iE^2}\right)^{\frac{1}{3}} + \frac{3Pa^2(1-v^2)}{4\pi Et^3} \tag{6.30}$$

in which E and ν are the elastic modulus and passion's ratio of the plate/film, respectively. The plate radius, a, can be obtained by fitting the "extra linear recovery" of the P–h curve, which is the portion after delamination occurrence, using Equation 6.29.

6.4.3 Interfacial Energy Release Rate G_{in} of SiN/GaAs Systems

6.4.3.1 Dual-Indentation Method

The methodology for adhesion measurement is shown in Figure 6.30 [116,129]. Successful quantification of G_{in} using the proposed model is only possible if the delamination occurs during an indentation process without the occurrence of any film fracture. Therefore, it is necessary to explore the optimal loading condition for inducing interfacial delamination. Normal monotonic loading indentations with varied maximum load were first performed. If delamination was generated by indentation without any film fracture, monotonic loading dual-indentation would be employed [116]. For some film/substrate systems, in which a normal indentation could not introduce interfacial delamination, cyclic loading dual-indentation would be applied instead [129]. After the dual-indentations were performed, the computation of G_{in} was carried out using the data retrieved directly from the dual-indentation P–h curves [116]. The calculation of the energy associated with the generation of an interfacial crack U_s was based on the methods described previously in Section 6.4.1.2.

Figure 6.31 shows the calculated U_s for 12 different SiN/GaAs systems. It is seen that the increased indentation load resulted in greater delamination energy release. Apparently, a deeper penetration generated a larger delamination area; the resultant net surface energy was thereby higher. The centrally loaded circular plate model (model I) introduced previously was used to estimate the delamination area. The initial loading curve (OC') of the second indentation shown in Figure 6.26 was approximated as the loading process on a circular plate under concentric loading. Therefore, the maximum deflection ω and the load at the maximum deflection P were obtained directly from the indentation measurements. After the area A was obtained, Equation 6.29 was used to calculate G_{in}. The values of G_{in} computed are plotted against the penetration depth in Figure 6.32. For the films with the same thickness, the values of G_{in} appear to be independent of the indentation condition used. However, the G_{in} value increased with the increase in film thickness. For all the 12 film specimens being tested, the standard deviations of the G_{in} values are in the range of 3.2%–13.8% of the average G_{in}.

For the film/substrate systems with relatively strong interfacial adhesion, that is, standard SiN films on GaAs, normal indentation cannot induce interfacial delamination, so cyclic loading indentation has to be used, as shown in Figure 6.30. The values of U_s and G_{in} of the standard SiN films obtained from cyclic loading indentation are shown in Figure 6.33a and b, respectively. Likewise, U_s appears to increase when the indentation depth is greater, because higher penetration generates larger delamination area, therefore higher surface energy released. In Figure 6.33b, the G_{in} values are plotted as a function of the indentation depth too. It is seen that for a specific

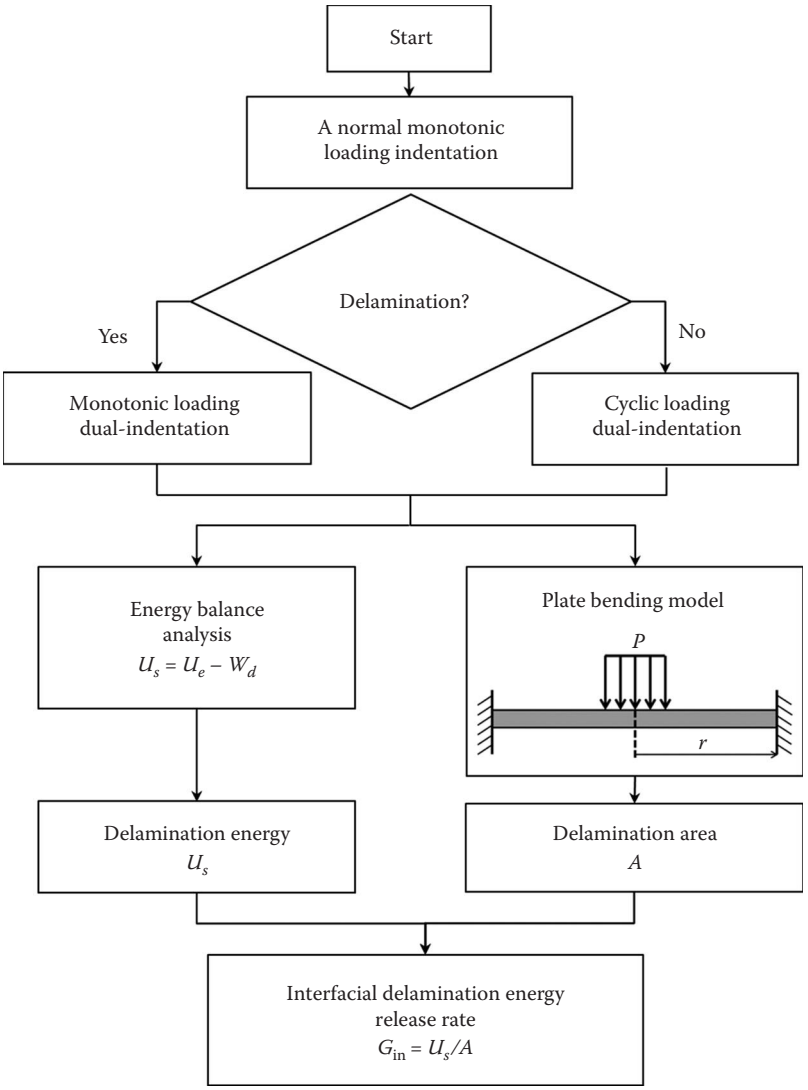


FIGURE 6.30 The flowchart of the energy-based method for the evaluation of interface energy release rate. (From Lu, M. and H. Huang. 2015. Interfacial energy release rates of SiN/GaAs film/substrate systems determined using a cyclic loading dual-indentation method. *Thin Solid Films* (in press).)

film/substrate system, the values of G_{in} do not vary regardless of the change in the indentation condition used. The system with a smaller film thickness has a higher G_{in} value. The result is in good agreement with those measured by the monotonic loading dual-indentation.

As discussed earlier, cyclic loading generates little plastic deformation to the indented film, thus the property of the interface is not affected. It is proven that G_{in}

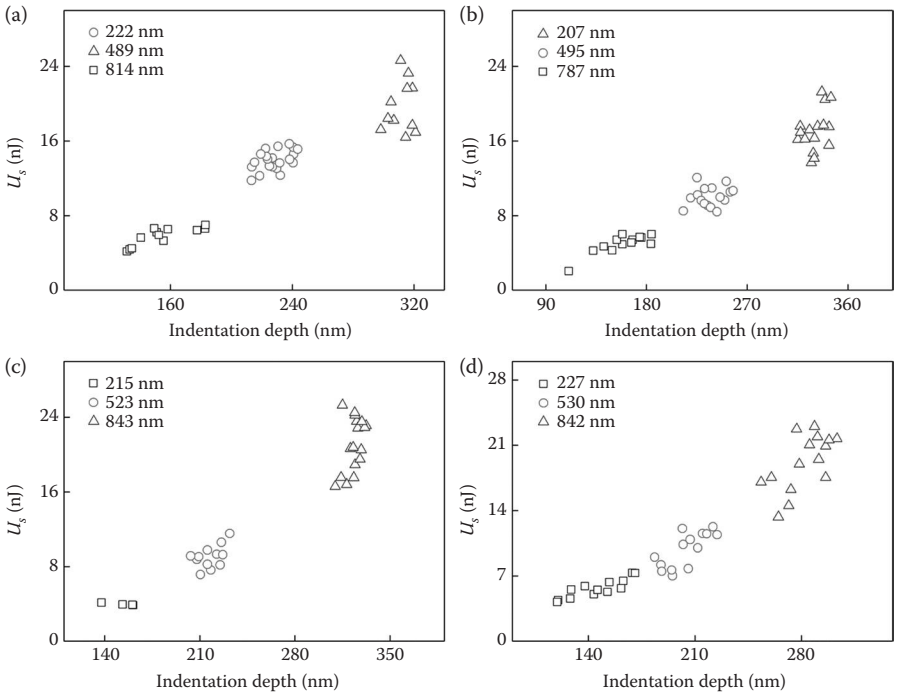


FIGURE 6.31 Delamination energy release U_s of SiN films determined by monotonic loading dual-indentation: (a) compressive; (b) DL-com; (c) dense; (d) cap. (From Lu, M. and H. Huang. 2014. *Journal of Materials Research* 29 (06):801–810.)

values for all the specimens tested obtained from the two approaches are in good agreement as shown in Figure 6.34, with relatively small deviations, indicating the G_{in} values measured by the cyclic loading indentation are reliable. Noted the result for standard SiN specimens is only from the cyclic loading indentation as the monotonic loading indentation failed to generate delamination in this case. Accordingly, these specimens have the highest values of G_{in}.

Using the proposed energy method, reasonable estimation of interfacial energy release rate G_{in} were obtained for different SiN/GaAs film/substrate samples, with very small variation in the G_{in} values. As the G_{in} measured is the intrinsic property of a specific bilayer system, G_{in} should not vary with testing conditions. The calculated G_{in} values in this study were shown to be independent on the indentation load/penetration, which agrees with the theoretical concept of the energy release rate of an interface.

The energy release rate is shown to decrease with an increase in film thickness, as shown in Figure 6.32, although all the other fabrication conditions remained the same. The effect of film thickness on the interfacial toughness has been reported in a number of studies [1,141–143], and is thought to be associated primarily with variation in residual stress levels in thin films. It is well accepted that residual stresses, developed during film deposition, significantly undermine the interfacial adhesion at

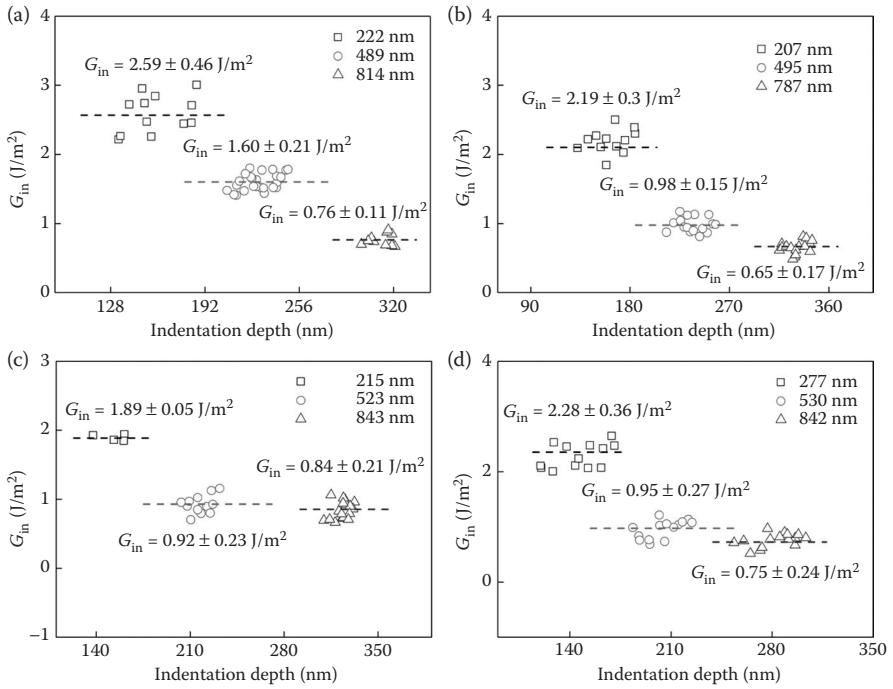


FIGURE 6.32 Delamination energy release rate G_{in} of SiN films determined by monotonic loading dual-indentation: (a) compressive; (b) DL-com; (c) dense; (d) cap; (f) standard (with different HCL pretreatments) obtained from monotonic loading dual-indentation. (From Lu, M. and H. Huang. 2014. *Journal of Materials Research* 29 (06):801–810.)

the film/substrate interface by providing a crack driving force [3,17,144]. Therefore, it is reasonable to postulate that the decrease in G_{in} of the SiN/GaAs bilayer with an increase in film thickness may be attributed to the change in residual stress. In this case, higher residual compressive stress could be induced in thicker films, and thus results in lower values of G_{in}.

6.4.3.2 Preexisting Crack Supposition Method

The *P–h* curves of the first and the second indentations of two specimens, namely 523 nm dense and 489 nm compressive SiN, were obtained [115]. The first indentation curve was subtracted by the secondary indentation curve and all those curves obtained after subtraction are plotted in Figure 6.35. The area enclosed by the curves gives the values of U_s ($W_{t1} - W_{t2}$) for a given load. It should be noted that in Figure 6.35, the displacement coordinate was shifted to separate the curves generated using different loads, but such shifting would not affect the calculation. It is seen that "humps" occasionally occurred during the unloading of the first indentation, but the unloading curves of the secondary indentation are smooth. The area enclosed was calculated using trapezoidal integration with MATLAB®. The delamination area *A* was estimated using the Hertz contact-loaded plate model (model II). The delamination energy release rate, G_{in}, values were then calculated using Equation 6.13. The

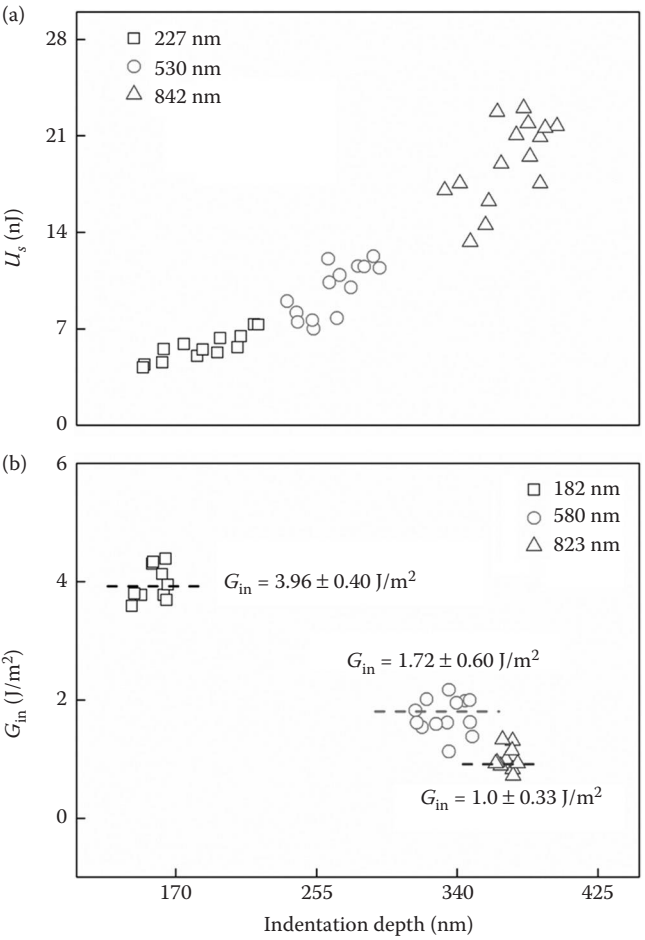


FIGURE 6.33 (a) Delamination energy U_s and (b) interfacial energy release rate G_{in} of the standard SiN films of various thicknesses obtained using the (33 cycles) cyclic loading dual-indentation. (From Lu, M. and H. Huang. 2015. Interfacial energy release rates of SiN/GaAs film/substrate systems determined using a cyclic loading dual-indentation method. *Thin Solid Films* (in press).)

results are summarized in Table 6.3. For comparison, the G_{in} values derived using dual-indentation method are also provided in Table 6.3. It is shown that the G_{in} values obtained from the two methods are in reasonable agreement.

6.5 SUMMARY

The state of art in adhesion evaluation techniques for thin film/substrate systems has been reviewed in this chapter. In particular, a comprehensive overview was presented examining the techniques using nanoindentation. Two methods for measuring the interfacial adhesion of a variety of SiN/GaAs film/substrate systems using

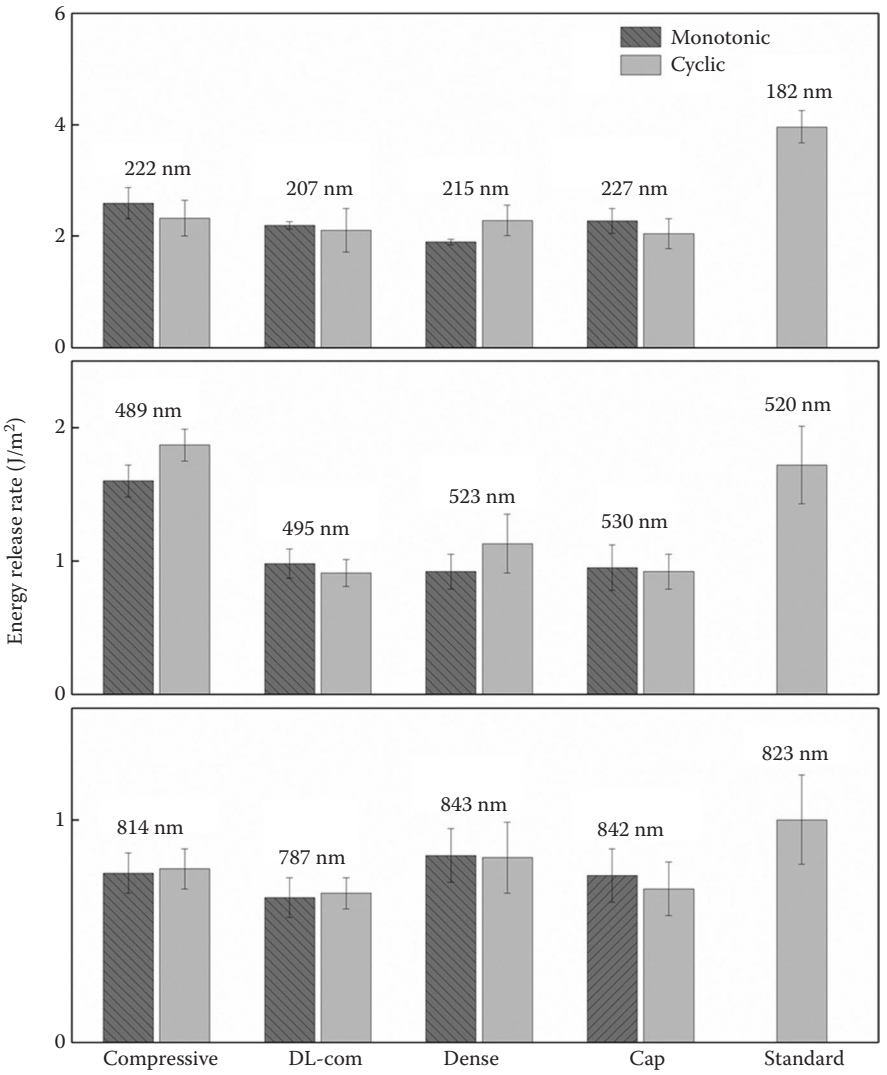


FIGURE 6.34 Comparison of the energy release rates G_{in} obtained using monotonic loading and cyclic loading dual-indentations. The values inside the plots represent the film's thickness. (From Lu, M. and H. Huang. 2015. Interfacial energy release rates of SiN/GaAs film/substrate systems determined using a cyclic loading dual-indentation method. *Thin Solid Films* (in press).)

nanoindentation were then introduced. Two energy-based methods for deriving the released energy related to an interfacial delamination event and two plate bending models for estimating the area of the interfacial crack surface were described. Although these approaches were developed for the specific SiN/GaAs film/substrate systems, they can be implemented to measure the interfacial adhesion properties of other dielectric/semiconductor film/substrate structures with ease.

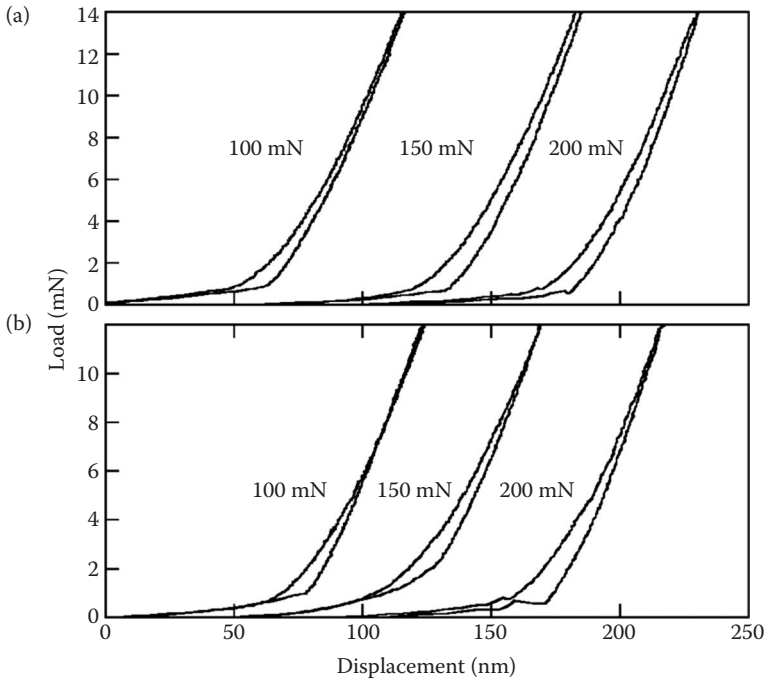


FIGURE 6.35 The subtracted P–h curves for calculating W_{t1}-W_{t2} under three different indentation loads of 100, 150, and 200 mN for the two SiN films: (a) 523 nm dense, and (b) 489 nm compressive. (From Xie, H. and H. Huang. 2013. *Journal of Materials Research* 28 (22):3137–3145.)

TABLE 6.3
Comparison of the G_{in} Values Obtained Using the Preexisting Crack Supposition Method and the Dual-Indentation Method

Specimens	Thickness (nm)	P_{max} (MPa)	G_{in} (J/m^2)	Average G_{in} (J/m^2)	G_{in} (J/m^2, Dual-Indentation)
Dense	523	100	0.91	1.00	0.92
		150	1.04		
		200	1.06		
Compressive	489	100	1.38	1.06	1.60
		150	0.72		
		200	1.09		

Source: Xie, H. and H. Huang. 2013. *Journal of Materials Research* 28 (22):3137–3145.

REFERENCES

1. Volinsky, A. A., J. B. Vella, and W. W. Gerberich. 2003. Fracture toughness, adhesion and mechanical properties of low-K dielectric thin films measured by nanoindentation. *Thin Solid Films* 429 (1–2):201–210.
2. Dauskardt, R. H., M. Lane, Q. Ma, and N. Krishna. 1998. Adhesion and debonding of multi-layer thin film structures. *Engineering Fracture Mechanics* 61 (1):141–162.
3. Khanna, V. K. 2011. Adhesion-delamination phenomena at the surfaces and interfaces in microelectronics and MEMS structures and packaged devices. *Journal of Physics D-Applied Physics* 44 (3):034004.
4. Yu, H. Y., S. C. Sanday, and B. B. Rath. 1990. The effect of substrate on the elastic properties of films determined by the indentation test—Axisymmetric boussinesq problem. *Journal of the Mechanics and Physics of Solids* 38 (6):745–764.
5. Huajian, G., C. Cheng-Hsin, and L. Jin. 1992. Elastic contact versus indentation modeling of multi-layered materials. *International Journal of Solids and Structures* 29 (20): 2471–2492.
6. Chen, J. J. and S. J. Bull. 2011. Approaches to investigate delamination and interfacial toughness in coated systems: An overview. *Journal of Physics D-Applied Physics* 44 (3):034001.
7. Jacobsson, R. 1976. Measurement of the adhesion of thin films. *Thin Solid Films* 34 (2):191–199.
8. Hegemann, D., H. Brunner, and C. Oehr. 2003. Plasma treatment of polymers for surface and adhesion improvement. *Nuclear Instruments and Methods in Physics Research Section B: Beam Interactions with Materials and Atoms* 208 (0):281–286.
9. Kim, J., K. S. Kim, and Y. H. Kim. 1989. Mechanical effects in peel adhesion test. *Journal of Adhesion Science and Technology* 3 (1):175–187.
10. Litteken, C., R. Dauskardt, T. Scherban, G. Xu, J. Leu, D. Gracias, and B. Sun. 2003. Interfacial adhesion of thin-film patterned interconnect structures. Interconnect Technology Conference, 2003. *Proceedings of the IEEE 2003 International*, 2–4 June 2003.
11. Gupta, V., A. S. Argon, J. A. Cornie, and D. M. Parks. 1990. Measurement of interface strength by laser-pulse-induced spallation. *Materials Science and Engineering a-Structural Materials Properties Microstructure and Processing* 126:105–117.
12. Gupta, V., A. S. Argon, D. M. Parks, and J. A. Cornie. 1992. Measurement of interface strength by a laser spallation technique. *Journal of the Mechanics and Physics of Solids* 40 (1):141–180.
13. Van Dijk, K., V. Gupta, A. K. Yu, and J. A. Jansen. 1998. Measurement and control of interface strength of RF magnetron-sputtered Ca-PO coatings on Ti-6A1-4V substrates using a laser spallation technique. *Journal of Biomedical Materials Research* 41 (4):624–632.
14. Youtsos, A. G., M. Kiriakopoulos, and T. Timke. 1999. Experimental and theoretical/numerical investigations of thin films bonding strength. *Theoretical and Applied Fracture Mechanics* 31 (1):47–59.
15. Gäbler, J., L. Schäfer, B. Menze, and H.-W. Hoffmeister. Micro abrasive pencils with CVD diamond coating. *Diamond and Related Materials* 12 (3–7):707–710.
16. Steinmann, P. A. and H. E. Hintermann. 1989. A review of the mechanical tests for assessment of thin-film adhesion. *Journal of Vacuum Science & Technology A: Vacuum, Surfaces, and Films* 7 (3):2267–2272.
17. Evans, A. G. and J. W. Hutchinson. 1984. On the mechanics of delamination and spalling in compressed films. *International Journal of Solids and Structures* 20 (5):455–466.

18. Rosenfeld, L. G., J. E. Ritter, T. J. Lardner, and M. R. Lin. 1990. Use of the microindentation technique for determining interfacial fracture energy. *Journal of Applied Physics* 67 (7):3291–3296.
19. Malzbender, J. and G. de With. 2000. Energy dissipation, fracture toughness and the indentation load-displacement curve of coated materials. *Surface & Coatings Technology* 135 (1):60–68.
20. Ding, J., Y. Meng, and S. Wen. 2000. Mechanical properties and fracture toughness of multilayer hard coatings using nanoindentation. *Thin Solid Films* 371 (1–2):178–182.
21. Malzbender, J., G. de With, and J. M. J. den Toonder. 2000. Elastic modulus, indentation pressure and fracture toughness of hybrid coatings on glass. *Thin Solid Films* 366 (1–2):139–149.
22. Zhu, L. N., B. S. Xu, H. D. Wang, and C. B. Wang. 2010. Determination of hardness of plasma-sprayed FeCrBSi coating on steel substrate by nanoindentation. *Materials Science and Engineering a-Structural Materials Properties Microstructure and Processing* 528 (1):425–428. doi: 10.1016/j.msea.2010.09.028.
23. Saha, R. and W. D. Nix. 2002. Effects of the substrate on the determination of thin film mechanical properties by nanoindentation. *Acta Materialia* 50 (1):23–38.
24. Huang, H., X. Z. Hu, Y. Liu, M. Bush, K. Winchester, C. Musca, J. Dell, and L. Faraone. 2005. Characterization of mechanical properties of silicon nitride thin films for MEMS devices by nanoindentation. *Journal of Materials Science & Technology* 21:13–16.
25. Jung, Y. G., B. R. Lawn, M. Martyniuk, H. Huang, and X. Z. Hu. 2004. Evaluation of elastic modulus and hardness of thin films by nanoindentation. *Journal of Materials Research* 19 (10):3076–3080.
26. Huang, H., K. Winchester, Y. Liu, X. Z. Hu, C. A. Musca, J. M. Dell, and L. Faraone. 2005. Determination of mechanical properties of PECVD silicon nitride thin films for tunable MEMS Fabry-Perot optical filters. *Journal of Micromechanics and Microengineering* 15 (3):608–614.
27. Huang, H., K. J. Winchester, A. Suvorova, B. R. Lawn, Y. Liu, X. Z. Hu, J. M. Dell, and L. Faraone. 2006. Effect of deposition conditions on mechanical properties of low-temperature PECVD silicon nitride films. *Materials Science and Engineering a-Structural Materials Properties Microstructure and Processing* 435:453–459.
28. Ma, K. J., A. Bloyce, and T. Bell. 1995. Examination of mechanical properties and failure mechanisms of TiN and Ti-TiN multilayer coatings. *Surface & Coatings Technology* 76 (1–3):297–302.
29. DeBoer, M. P. and W. W. Gerberich. 1996. Microwedge indentation of the thin film fine line. 1. Mechanics. *Acta Materialia* 44 (8):3169–3175.
30. DeBoer, M. P. and W. W. Gerberich. 1996. Microwedge indentation of the thin film fine line. 2. Experiment. *Acta Materialia* 44 (8):3177–3187.
31. Zhang, S. and X. M. Zhang. 2012. Toughness evaluation of hard coatings and thin films. *Thin Solid Films* 520 (7):2375–2389.
32. Gallois-Garreignot, S., F. Chave, J. P. Gonchond, B. Gautheron, V. Fiori, D. Nelias, and Ieee. 2009. *Thin films interfacial adhesion characterization by Cross-Sectional Nanoindentation: Application to pad structures*, *2009 11th Electronics Packaging Technology Conference*. New York: IEEE.
33. Bull, S. J. and E. G. Berasetegui. 2006. An overview of the potential of quantitative coating adhesion measurement by scratch testing. *Tribology International* 39 (2):99–114.
34. Wei, P. J., W. L. Liang, C. F. Ai, and J. F. Lin. 2009. A new method for determining the strain energy release rate of an interface via force-depth data of nanoindentation tests. *Nanotechnology* 20 (2):025701.
35. Abdul-Baqi, A. and E. Van der Giessen. 2001. Indentation-induced interface delamination of a strong film on a ductile substrate. *Thin Solid Films* 381 (1):143–154.

36. Chen, J. and S. J. Bull. 2007. Indentation fracture and toughness assessment for thin optical coatings on glass. *Journal of Physics D-Applied Physics* 40 (18):5401–5417.
37. Hainsworth, S. V., M. R. McGurk, and T. F. Page. 1998. The effect of coating cracking on the indentation response of thin hard-coated systems. *Surface and Coatings Technology* 102 (1–2):97–107.
38. Venkataraman, S., D. L. Kohlstedt, and W. W. Gerberich. 1996. Continuous microscratch measurements of the practical and true works of adhesion for metal/ceramic systems. *Journal of Materials Research* 11 (12):3133–3145.
39. Mittal, K. L. 1995. *Adhesion Measurement of Films and Coatings*. Zeist, Netherlands: VSP.
40. Wake, W. C. 1982. *Adhesion and the Formulation of Adhesives*. London, UK: Applied Science Publishers.
41. Padday, J. F. and N. D. Uffindell. 1968. The calculation of cohesive and adhesive energies from intermolecular forces at a surface. *The Journal of Physical Chemistry* 72 (5):1407–1414.
42. Lipkin, D. M., D. R. Clarke, and A. G. Evans. 1998. Effect of interfacial carbon on adhesion and toughness of gold-sapphire interfaces. *Acta Materialia* 46 (13):4835–4850.
43. Furuya, A., N. Hosoi, and Y. Ohshita. 1995. Evaluation of cu adhesive energy on barrier metals by means of contact angle measurement. *Journal of Applied Physics* 78 (10): 5989–5992.
44. Lin, Z. S. and P. D. Bristowe. 2007. Microscopic characteristics of the Ag(111)/ZnO(0001) interface present in optical coatings. *Physical Review B* 75 (20):13.
45. Dickinson, J.T. 1989. *Fracto-Emission from Interfacial Failure.* MRS Online Proceedings Library, 153:331.
46. Brown, S. D. 1994. Adherence failure and measurement: Some troubling questions. *Journal of Adhesion Science and Technology* 8 (6):687–711.
47. Hull, T. R., J. S. Colligon, and A. E. Hill. 1987. Measurement of thin film adhesion. *Vacuum* 37 (3–4):327–330.
48. Jacquet, P. A. 1934. Adhesion of electrolytic copper deposits. *Transactions of the Electrochemical Society* 66 (1):393–426.
49. Saubestre, E. B., L. J. Durney, J. Hajdu, and E. Bastenbeck. 1965. The adhesion of electrodeposits to plastics. *Plating* 52:982.
50. Baglin, J. E. E. and G. J. Clark. 1985. Ion beam bonding of thin films. *Nuclear Instruments and Methods in Physics Research Section B: Beam Interactions with Materials and Atoms* 7–8, Part 2 (0):881–885.
51. Kikuchi, A., S. Baba, and A. Kinbara. 1983. Measurements of the adhesion of evaporated metal films (II). *Journal of the Vacuum Society of Japan* 26(5):475–479.
52. Zhang, S., Y. S. Wang, X. T. Zeng, K. A. Khor, W. J. Weng, and D. E. Sun. 2008. Evaluation of adhesion strength and toughness of fluoridated hydroxyapatite coatings. *Thin Solid Films* 516 (16):5162–5167.
53. Heavens, O. S. 1950. Some factors influencing the adhesion of films produced by vacuum evaporation. *Journal de Physique et Le Radium* 11 (7):355–360.
54. Weaver, Charles. 1975. Adhesion of thin films. *Journal of Vacuum Science & Technology* 12 (1):18–25.
55. Laugier, M. T. 1984. An energy approach to the adhesion of coatings using the scratch test. *Thin Solid Films* 117 (4):243–249.
56. He, A. and H. Huang. 2013. Nanoscratch characteristics and interfacial adhesion energy of SiN/GaAs film/substrate bilayer systems. *International Journal of Surface Science and Engineering* 7 (4):382–396.
57. Charalambides, P. G., J. Lund, A. G. Evans, and R. M. McMeeking. 1989. A test specimen for determining the fracture resistarim of bimaterial interfaces. *Journal of Applied Mechanics-Transactions of the Asme* 56 (1):77–82.

58. Harry, E., A. Rouzaud, M. Ignat, and P. Juliet. 1998. Mechanical properties of W and W(C) thin films: Young's modulus, fracture toughness and adhesion. *Thin Solid Films* 332 (1–2):195–201.
59. Nie, P. L., H. P. Lv, T. Zhou, X. Cai, and P. K. Chu. 2010. Interfacial adhesion measurement of a ceramic coating on metal substrate. *Journal of Coatings Technology and Research* 7 (3):391–398.
60. Zhang, S., D. Sun, Y. Q. Fu, and H. J. Du. 2005. Toughness measurement of thin films: A critical review. *Surface & Coatings Technology* 198 (1–3):74–84.
61. Roham, S., K. Hardikar, and P. Woytowitz. 2004. Crack penetration and deflection at a bimaterial interface in a four-point bend test. *Journal of Materials Research* 19 (10): 3019–3027.
62. Birringer, R. P., P. J. Chidester, and R. H. Dauskardt. 2011. High yield four-point bend thin film adhesion testing techniques. *Engineering Fracture Mechanics* 78 (12):2390–2398.
63. Bagchi, A. and A. G. Evans. 1996. A new procedure for measuring the decohesion energy for thin ductile films on substrates—Reply. *Journal of Materials Research* 11 (8): 2112–2113.
64. Lai, Y.-H. and D. A. Dillard. 1994. A study of the fracture efficiency parameter of blister tests for films and coatings. *Journal of Adhesion Science and Technology* 8 (6):663–678.
65. Liang, J.-L., J. P. Bell, and A. Mehta. 1993. Adhesion (fracture energy) of electropolymerized poly(n-octyl maleimide-co-styrene) coatings on copper substrates using a constrained blister test. *Journal of Adhesion Science and Technology* 7 (8):869–884.
66. Small, M. K. and W. D. Nix. 1992. Analysis of the accuracy of the bulge test in determining the mechanical-properties of thin-films. *Journal of Materials Research* 7 (6):1553–1563.
67. Ritter, J. E., T. J. Lardner, L. Rosenfeld, and M. R. Lin. 1989. Measurement of adhesion of thin polymer-coatings by indentation. *Journal of Applied Physics* 66 (8):3626–3634.
68. Swain, M. V. and J. Menčík. 1994. Mechanical property characterization of thin films using spherical tipped indenters. *Thin Solid Films* 253 (1–2):204–211.
69. Molina-Aldareguia, J. M., I. Ocaña, D. González, M. R. Elizalde, J. M. Sánchez, J. M. Martínez-Esnaola, J. Gil-Sevillano et al. 2007. Adhesion studies in integrated circuit interconnect structures. *Engineering Failure Analysis* 14 (2):349–354.
70. Li, X. and B. Bhushan. 1998. Measurement of fracture toughness of ultra-thin amorphous carbon films. *Thin Solid Films* 315 (1–2):214–221.
71. Tsui, T. Y., J. Vlassak, and W. D. Nix. 1999a. Indentation plastic displacement field: Part I. The case of soft films on hard substrates. *Journal of Materials Research* 14 (6):2196–2203.
72. Marshall, D. B. and A. G. Evans. 1984. Measurement of adherence of residually stressed thin-films by indentation. 1. Mechanics of interface delamination. *Journal of Applied Physics* 56 (10):2632–2638.
73. Rossington, C., A. G. Evans, D. B. Marshall, and B. T. Khuriyakub. 1984. Measurements of adherence of residually stressed thin-films by indentation. 2. Experiments with Zno/Si. *Journal of Applied Physics* 56 (10):2639–2644.
74. Kriese, M. D., W. W. Gerberich, and N. R. Moody. 1999. Quantitative adhesion measures of multilayer films: Part II. Indentation of W/Cu, W/W, Cr/W. *Journal of Materials Research* 14 (7):3019–3026.
75. Kriese, M. D., W. W. Gerberich, and N. R. Moody. 1999. Quantitative adhesion measures of multilayer films: Part I. Indentation mechanics. *Journal of Materials Research* 14 (7):3007–3018.
76. Huang, H. and M. B. Bush. 1997. Finite element analysis of mechanical properties in discontinuously reinforced metal matrix composites with ultrafine micro structure. *Materials Science and Engineering: A* 232 (1–2):63–72.

77. Liu, S., Y. T. Gu, and H. Huang. 2009. Determination of Elastic Modulus of Thin Coating Materials Using Nanoindentation and Finite Element Analysis. In *Advances in Abrasive Technology Xii*, edited by H. Huang, L. Zhang, J. Wang, Z. Jiang, L. Zhou and X. P. Xu, 392–397. Stafa-Zurich: Trans Tech Publications Ltd.
78. Liu, S., Y. T. Gu, and H. Huang. 2011. A new tip area function for instrumented nanoindentation at extremely small contact depths. *Materials Science and Engineering a-Structural Materials Properties Microstructure and Processing* 528 (27):7948–7951.
79. Laursen, T. A. and J. C. Simo. 1992. A study of the mechanics of microindentation using finite-elements. *Journal of Materials Research* 7 (3):618–626.
80. Yonezu, A. and X. Chen. 2010. Evaluation of elastoplastic properties and fracture strength of thick diamond like carbon film by indentation. *Diamond and Related Materials* 19 (1):40–49.
81. Tsui, T. Y., J. Vlassak, and W. D. Nix. 1999. Indentation plastic displacement field: Part II. The case of hard films on soft substrates. *Journal of Materials Research* 14 (6):2204–2209.
82. Bhattacharya, A. K. and W. D. Nix. 1988. Analysis of elastic and plastic deformation associated with indentation testing of thin films on substrates. *International Journal of Solids and Structures* 24 (12):1287–1298.
83. Chen, X. and J. J. Vlassak. 2001. Numerical study on the measurement of thin film mechanical properties by means of nanoindentation. *Journal of Materials Research* 16 (10):2974–2982.
84. Abdul-Baqi, A. and E. Van der Giessen. 2001. Delamination of a strong film from a ductile substrate during indentation unloading. *Journal of Materials Research* 16 (5):1396–1407.
85. Moody, N. R., R. Q. Hwang, S. Venka-Taraman, J. E. Angelo, D. P. Norwood, and W. W. Gerberich. 1998. Adhesion and fracture of tantalum nitride films. *Acta Materialia* 46 (2):585–597.
86. Palacio, J. F., S. J. Bull, J. Neidhardt, and L. Hultman. 2006. Nanoindentation response of high performance fullerene-like CNx. *Thin Solid Films* 494 (1–2):63–68.
87. Chen, J. and S. J. Bull. 2006. Assessment of the toughness of thin coatings using nanoindentation under displacement control. *Thin Solid Films* 494 (1–2):1–7.
88. Li, X.D., D.F. Diao, and B. Bhushan. 1997. Fracture mechanisms of thin amorphous carbon films in nanoindentation. *Acta Materialia* 45 (11):4453–4461.
89. Li, X. D. and B. Bhushan. 1999. Micro/nanomechanical and tribological characterization of ultrathin amorphous carbon coatings. *Journal of Materials Research* 14 (6):2328–2337.
90. Cannon, R. M., B. J. Dalgleish, R. H. Dauskardt, T. S. Oh, and R. O. Ritchie. 1991. Cyclic fatigue-crack propagation along ceramic/metal interfaces. *Acta Metallurgica Et Materialia* 39 (9):2145–2156.
91. Page, T. F. and S. V. Hainsworth. 1993. Using nanoindentation techniques for the characterization of coated systems—A critique. *Surface & Coatings Technology* 61 (1–3):201–208.
92. Chen, J. J. and S. J. Bull. 2009. Finite element analysis of contact induced adhesion failure in multilayer coatings with weak interfaces. *Thin Solid Films* 517 (13):3704–3711.
93. Den Toonder, J., J. Malzbender, G. de With, and R. Balkenende. 2002. Fracture toughness and adhesion energy of sol-gel coatings on glass. *Journal of Materials Research* 17 (1):224–233.
94. Chen, J. J. 2012. Indentation-based methods to assess fracture toughness for thin coatings. *Journal of Physics D-Applied Physics* 45 (20):203001.
95. Nakonechna, O., T. Cselle, M. Morstein, and A. Karimi. 2004. On the behaviour of indentation fracture in TiAlSiN hard thin films. *Thin Solid Films* 447–448 (0):406–412.

96. Thouless, M. D. 1998. An analysis of spalling in the microscratch test. *Engineering Fracture Mechanics* 61 (1):75–81.
97. Chicot, D., P. Demarecaux, and J. Lesage. 1996. Apparent interface toughness of substrate and coating couples from indentation tests. *Thin Solid Films* 283 (1–2):151–157.
98. Hadad, M., G. Marot, P. Demarecaux, D. Chicot, J. Lesage, L. Rohr, and S. Siegmann. 2007. Adhesion tests for thermal spray coatings: Correlation of bond strength and interfacial toughness. *Surface Engineering* 23 (4):279–283.
99. Scherban, T., D. Pantuso, B. Sun, S. El-Mansy, J. Xu, M. R. Elizalde, J. M. Sanchez, and J. M. Martinez-Esnaola. 2003. Characterization of interconnect interfacial adhesion by cross-sectional nanoindentation. *International Journal of Fracture* 119 (4–2):421–429.
100. Chicot, D., P. Araujo, N. Horny, A. Tricoteaux, and J. Lesage. 2005. Application of the interfacial indentation test for adhesion toughness determination. *Surface and Coatings Technology* 200 (1–4):174–177.
101. Chicot, D., L. Gil, K. Silva, F. Roudet, E. S. Puchi-Cabrera, M. H. Staia, and D. G. Teer. 2010. Thin film hardness determination using indentation loading curve modelling. *Thin Solid Films* 518 (19):5565–5571.
102. Sanchez, J. M., S. El-Mansy, B. Sun, T. Scherban, N. Fang, D. Pantuso, W. Ford, M. R. Elizalde, J. M. Martinez-Esnaola, A. Martin-Meizoso, J. Gil-Sevillano, M. Fuentes, and J. Maiz. 1999. Cross-sectional nanoindentation: A new technique for thin film interfacial adhesion characterization. *Acta Materialia* 47 (17):4405–4413.
103. Felder, Eric, Sébastien Roy, and Evelyne Darque-Ceretti. 2011. Characterization of the adhesion of thin film by cross-sectional nanoindentation: Analysis of the substrate edge chipping and the film delamination. *Comptes Rendus Mecanique* 339 (7–8):443–457.
104. Roy, S., E. Darque-Ceretti, E. Felder, and H. Monchoix. 2007. Cross-sectional nanoindentation for copper adhesion characterization in blanket and patterned interconnect structures: Experiments and three-dimensional FEM modeling. *International Journal of Fracture* 144 (1):21–33.
105. Ocaña, I., J. M. Molina-Aldareguia, D. Gonzalez, M. R. Elizalde, J. M. Sánchez, J. M. Martínez-Esnaola, J. Gil Sevillano et al. 2006. Fracture characterization in patterned thin films by cross-sectional nanoindentation. *Acta Materialia* 54 (13):3453–3462.
106. Von Stebut, J., F. Lapostolle, M. Bucsa, and H. Vallen. 1999. Acoustic emission monitoring of single cracking events and associated damage mechanism analysis in indentation and scratch testing. *Surface & Coatings Technology* 116:160–171.
107. Dong, Z. G., H. Huang, and R. Kang. 2010. An investigation of the onset of elastoplastic deformation during nanoindentation in MgO single crystal (001) and (110) planes. *Materials Science and Engineering: A* 527 (16–17):4177–4184.
108. Irwan, R. and H. Huang. 2008. Mechanical properties and fracture characteristics of cemented tungsten carbide with fine microstructure studied by nanoindentation. *International Journal of Surface Science and Engineering* 2 (1–2):29–40.
109. Swain, M. V. and M. Wittling. 1995. Comparison of acoustic emission from pointed and spherical indentation of TiN films on silicon and sapphire. *Surface & Coatings Technology* 76–77 (1–3):528–533.
110. Shiwa, M., E. R. Weppelmann, A. Bendeli, M. V. Swain, D. Munz, and T. Kishi. 1994. Acoustic emission and precision force-displacement observations of spherical indentations into TiN films on silicon. *Surface and Coatings Technology* 68–69:598–602.
111. Fan, Q. H., J. Gracio, and E. Pereira. 1999. Comparison of the adhesion of diamond coatings using indentation tests and micro-Raman spectroscopy. *Journal of Applied Physics* 86 (10):5509–5514.
112. Fan, Qi Hua, J. Grácio, Nasar Ali, and E. Pereira. 2001. Comparison of the adhesion of diamond films deposited on different materials. *Diamond and Related Materials* 10 (3–7):797–802.

113. Belmonte, M., A. J. S. Fernandes, F. M. Costa, F. J. Oliveira, and R. F. Silva. 2003. Adhesion behaviour assessment on diamond coated silicon nitride by acoustic emission. *Diamond and Related Materials* 12 (3–7):733–737.
114. Lu, M., H. Xie, H. Huang, J. Zou, and Y. He. 2013. Indentation-induced delamination of plasma-enhanced chemical vapor deposition silicon nitride film on gallium arsenide substrate. *Journal of Materials Research* 28 (08):1047–1055.
115. Xie, H. and H. Huang. 2013. Characterization of the interfacial strength of SiNx/GaAs film/substrate systems using energy balance in nanoindentation. *Journal of Materials Research* 28 (22):3137–3145.
116. Lu, M. and H. Huang. 2014. Determination of the energy release rate in the interfacial delamination of silicon nitride film on gallium arsenide substrate via nanoindentation. *Journal of Materials Research* 29 (06):801–810.
117. Anthony, C. and A. C. Fischer-Cripps. 2004. Nanoindentation. In *Mechanical Engineering Series*, edited by F. Ling Frederick, New York: Springer-Verlag, pp. 132–136.
118. Oliver, W. C. and G. M. Pharr. 1992. An improved technique for determining hardness and elastic-modulus using load and displacement sensing indentation experiments. *Journal of Materials Research* 7 (6):1564–1583.
119. Oliver, W. C. and G. M. Pharr. 2004. Measurement of hardness and elastic modulus by instrumented indentation: Advances in understanding and refinements to methodology. *Journal of Materials Research* 19 (1):3–20.
120. Pharr, G. M. and W. C. Oliver. 1992. Measurement of thin-film mechanical-properties using nanoindentation. *MRS Bulletin* 17 (7):28–33.
121. Pharr, G. M., W. C. Oliver, and F. R. Brotzen. 1992. On the generality of the relationship among contact stiffness, contact area, and elastic-modulus during indentation. *Journal of Materials Research* 7 (3):613–617.
122. Singh, R. K., M. T. Tilbrook, Z. H. Xie, A. Bendavid, P. J. Martin, P. Munroe, and M. Hoffman. 2008. Contact damage evolution in diamond like carbon coatings on ductile substrates. *Journal of Materials Research* 23 (1):27–36.
123. Chang, S. Y. and Y. S. Lee. 2007. Analyses of interface adhesion between Cu and SiCN etch stop layers by nanoindentation and nanoscratch tests. *Japanese Journal of Applied Physics Part 1-Regular Papers Brief Communications & Review Papers* 46 (4B):1955–1960.
124. Needleman, A. 1987. A continuum model for void nucleation by inclusion debonding. *Journal of Applied Mechanics-Transactions of the Asme* 54 (3):525–531.
125. Bagchi, A., G. E. Lucas, Z. Suo, and A. G. Evans. 1994. A new procedure for measuring the decohesion energy for thin ductile films on substrates. *Journal of Materials Research* 9 (7):1734–1741.
126. Dharma R., T. M. Kato, and K. Nakasa. 2003. Backward deviation and depth recovery of load–displacement curves of amorphous SiC film under repeating nanoindentation. *Acta Materialia* 51 (12):3585–3595.
127. Raju, T. D., K. Nakasa, and M. Kato. 2003. Relation between delamination of thin films and backward deviation of load-displacement curves under repeating nanoindentation. *Acta Materialia* 51 (2):457–467.
128. Wei, P. J., S. B. Chio, W. L. Liang, and J. F. Lin. 2011. Determining buckling strain energy release rate through indentation-induced delamination. *Thin Solid Films* 519 (15):4889–4893.
129. Lu, M. and H. Huang. 2015. Interfacial energy release rates of SiN/GaAs film/substrate systems determined using a cyclic loading dual-indentation method. *Thin Solid Films* (in press).
130. Lawn, B. R., A. G. Evans, and D. B. Marshall. 1980. Elastic-plastic indentation damage in ceramics—The median-radial crack system. *Journal of the American Ceramic Society* 63 (9–10):574–581.

131. Marshall, D. B., S. S. Chiang, A. G. Evans, and B. R. Lawn. 1981. Elastic-plastic indentation damage in ceramics—The lateral crack system. *American Ceramic Society Bulletin* 60 (3):384–384.
132. Alvarado-Rivera, J., J. Muñoz-Saldaña, and R. Ramírez-Bon. 2011. Determination of fracture toughness and energy dissipation of SiO2-poly(methyl metacrylate) hybrid films by nanoindentation. *Thin Solid Films* 519 (16):5528–5534.
133. Chen, J. J. and S. J. Bull. 2006. Assessment of the adhesion of ceramic coatings. *Advances in Science and Technology* 45:1299.
134. Lawn, B. R. 1993. *Fracture of Brittle Solids*. New York, USA: Cambridge University Press.
135. Johnson, K. L. 1895. *Contact Mechanics*. Cambridge, UK: Cambridge University Press.
136. Ma, L., D. J. Morris, S. L. Jennerjohn, D. F. Bahr, and L. E. Levine. 2012. The role of probe shape on the initiation of metal plasticity in nanoindentation. *Acta Materialia* 60 (12):4729–4739.
137. Mayer, J., L. A. Giannuzzi, T. Kamino, and J. Michael. 2007. TEM sample preparation and FIB-induced damage. *Mrs Bulletin* 32 (5):400–407.
138. Bei, H., S. Shim, M. K. Miller, G. M. Pharr, and E. P. George. 2007. Effects of focused ion beam milling on the nanomechanical behavior of a molybdenum-alloy single crystal. *Applied Physics Letters* 91 (11):111915–111913.
139. Timoshenko, S. and S. Woinowsky-Krieger. 1959. *Theory of Plates and Shells*. New York, US: McGraw-Hill.
140. Scott, O. N., M. R. Begley, U. Komaragiri, and T. J. Mackin. 2004. Indentation of freestanding circular elastomer films using spherical indenters. *Acta Materialia* 52 (16):4877–4885.
141. Pobedinskas, P., J.-C. Bolsée, W. Dexters, B. Ruttens, V. Mortet, J. D'Haen, J. V. Manca, and K. Haenen. 2012. Thickness dependent residual stress in sputtered AlN thin films. *Thin Solid Films* 522 (0):180–185.
142. Zhang, X. C., C. J. Liu, F. Z. Xuan, Z. D. Wang, and S. T. Tu. 2010. Effect of residual stresses on the strength and fracture energy of the brittle film: Multiple cracking analysis. *Computational Materials Science* 50 (1):246–252.
143. Nazarpour, S. and A. Cirera. 2011. Variation of adhesive force at the interface of Pd and SrTiO3 as a consequence of residual stresses. *Journal of Physics D-Applied Physics* 44 (3).
144. Evans, A. G. and J. W. Hutchinson. 1995. The thermomechanical integrity of thin films and multilayers. *Acta Metallurgica et Materialia* 43 (7):2507–2530.

7 Advanced Hard Coatings with Enhanced Toughness and Resistance to Cracking

Jindrich Musil

CONTENTS

7.1 Physics behind Unique Properties of Nanocomposite Coatings 378
7.2 Nanocomposite Coatings with Enhanced Hardness H 379
7.2.1 Classification of Hard Nanocomposite Coatings According to Phases 382
7.3 Hard Nanocomposite Coatings with Enhanced Toughness 383
7.3.1 Toughness and Toughening Mechanisms 383
7.3.2 Principle of Formation of Hard Coatings with Enhanced Toughness 384
7.3.3 Classification of Coatings According to Mechanical Properties and Important Ratios 386
7.4 Hard Coatings with Low Effective Young's Modulus E^* and High Ratio $H/E^* \geq 0.1$ 387
7.4.1 Control of H/E^* Ratio by Deposition Parameters Used in the Formation of Coating 389
7.4.2 Control of H/E^* Ratio by Addition of Selected Me Element in Coating 391
7.4.3 Control of H/E^* Ratio by Energy $\mathcal{E}$ Delivered to the Growing Coating 391
7.4.3.1 Effect of Substrate Heating 392
7.4.3.2 Effect of Ion Bombardment of Growing Coating 393
7.4.4 Control of H/E^* Ratio by Combined Action of Deposition Parameters, Added Elements, and Energy $\mathcal{E}$ 395
7.4.5 Highly Elastic Multielement Compound Coatings with $H/E^* \geq 0.1$ 399
7.5 Hard Coatings Resistant to Cracking 401
7.5.1 Methods Used for Assessment of Resistance of Coating to Cracking 401
7.5.1.1 Indentation Test and Fracture Toughness 402
7.5.1.2 Bending Test 414
7.5.2 Design of Hard Flexible Coatings Resistant to Cracking 419
7.6 Flexible Multifunctional Coatings 423

7.6.1 Two-Functional Tribological Hard nc-TiC/a-C Nanocomposite Coatings 424
7.6.2 Two-Functional Highly Transparent Si-Zr-O Nanocomposite Coatings 428
7.6.3 Three-Functional Highly Elastic, Antibacterial Al-Cu-N Nanocomposite Coatings Resistant to Cracking 430
7.6.3.1 Two-Functional Cr-Cu-O Coatings 430
7.6.3.2 Three-Functional Al-Cu-N Coatings 431
7.7 Overlayer Protecting Brittle Coatings against Cracking 433
7.7.1 Generation of Cracks at Surface of Bended Brittle Material 434
7.7.2 Overlayer Preventing Cracking 435
7.7.3 Protection of Brittle Layer against Cracking by Zr-Si-O Overlayer in Compression 437
7.7.4 Multilayer Coating Resistant to Cracking 439
7.7.4.1 Effect of Thickness Overlayer on Protection of Brittle Film against Cracking 442
7.8 Summary of Main Issues 443
7.9 Trends of Next Development of New Advanced Hard Nanocomposite Coatings 444
Appendix 1: Effect of Addition of Selected Elements and Delivery of Energy $\mathcal{E}$ in Coating on Its Growth 446
A1.1 Effect of Added Elements 447
A1.2 Effect of Energy $\mathcal{E}$ Delivered to Growing Coating 448
A1.3 Effect of Speed of Delivered Energy in Growing Coating and Speed of Energy Extraction from Created Coating Material 451
Acknowledgments 454
References 454

7.1 PHYSICS BEHIND UNIQUE PROPERTIES OF NANOCOMPOSITE COATINGS

Nanocomposite coatings represent a new generation of materials [1–41] and references therein. They are composed of at least two separated phases with nanocrystalline (nc-) and/or amorphous (a-) structure or their combinations. The nanocomposite materials, due to very small (≤10 nm) grains and a significant role of boundary regions surrounding individual grains, exhibit enhanced or even completely new unique properties compared with the conventional materials composed of larger (≥100 nm) grains. New properties of the nanocomposite materials are caused by the increase of the ratio of the grain surface S and its volume V, and occur when the ratio S/V > 0.1. The high ratio S/V (>0.1) results in the dominance of the grain boundary regions increasing with decreasing grain size d, reduced action of the grain volume, stopping of the generation of dislocations, and the promotion of new processes such as the grain boundary sliding or the grain boundary enhancement due to an interatomic interaction between the atoms of neighboring grains. It means that dramatic changes in properties and behavior of the nanocomposite materials compared with that of the conventional materials are the result of (1) *the strong*

change of the geometrical structure of material, particularly the size d and the shape of grain and the separation distance w between grains, and (2) *the enhanced chemical and electronic bonding between atoms* of neighboring phases or grains. These are main reasons why the nanocomposite coatings can exhibit enhanced and new unique properties.

7.2 NANOCOMPOSITE COATINGS WITH ENHANCED HARDNESS H

The enhanced hardness of the coating can be due to (i) the macrostress generated in coating during its growth, (ii) the film micro- and nanostructure, and/or (iii) short covalent bonds between atoms. The enhanced hardness of nanocomposite based on its micro- and nanostructure strongly depends on the size and shape of nanograins and the structure of individual phases, see Figure 7.1. From Figure 7.1 it can be seen that there is a critical value of the grain size $d_c \approx 10$ nm at which a maximum value of hardmess H_{max} of the coating is achieved. The critical grain size d_c is connected with stopping of the generation of dislocations. The region around the maximum hardness H_{max}, that is, around $d = d_c$, corresponds to a continuous transition from the activity of *the intragranular deformation*

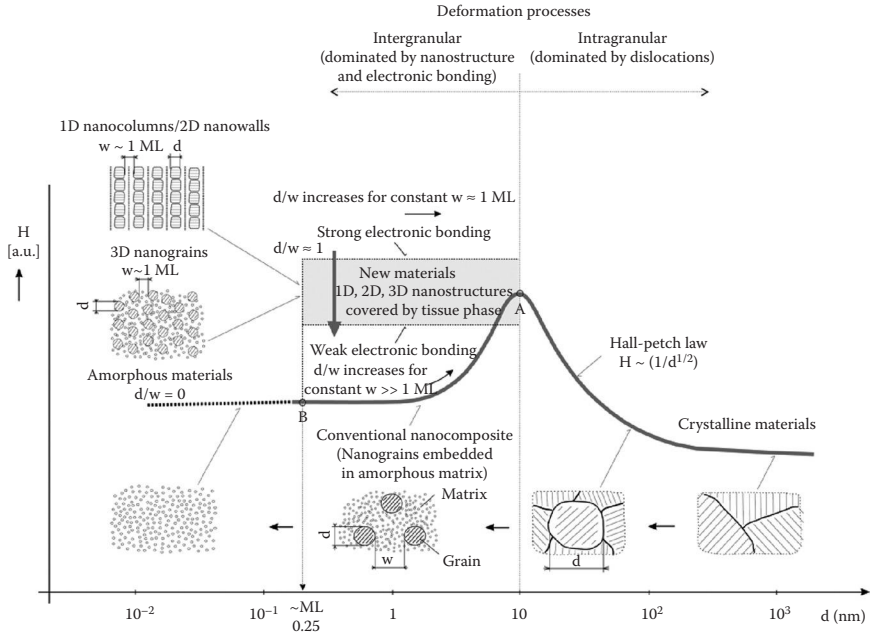


FIGURE 7.1 Hardness H of material as a function of size d and shape of grains. ML is the monolayer, d is the grain size, and w is the separation distance between nanograins. (Musil J., P. Baroch, P. Zeman: *Plasma Surface Engineering Research and its Practical Applications*, Wei R. (Ed.), Kerala, pp. 1–34. Copyright 2008, Research Signpost.)

processes at $d > d_c$, dominated by the dislocations and described by the Hall–Petch law [42,43], to the activity of *the intergranular deformation processes* at $d < d_c$ dominated by interactions between atoms of neighboring phases or grains and/or by the small-scale sliding in grain boundaries. In materials composed of small grains with $d \le d_c$ the ratio $S/V \ge 0.1$ and the dislocations are not generated. Therefore, the nanostructure of the material starts to play a dominant role. The properties of materials containing grains with $d \le d_c$ strongly depend on the size of grains, the separation distance w between grains, the elemental composition of grains, the chemical and electronic bonding between atoms of neighboring grains or surrounded phases, the crystallographic orientation of grains, and the phase composition of the nanocomposite.

It was found that there are at least four types of nanostructures that result in the enhanced hardness of nanocomposite coatings: (1) the bilayers with nanosize period λ, (2) the columnar nanostructure, (3) the nanograins surrounded by a very thin (~1–2 ML) tissue phase, and (4) the mixture of nanograins with different crystallographic orientations and/or different phases, see Figure 7.2; here $\lambda = h_1 + h_2$, h_1 and h_2 are the thickness of first and second layer of the bilayer, respectively, and ML denotes the monolayer.

Also, it is worthwhile to note that the hardness H of the nanocomposite coatings cannot be caused by its nanostructure only. Very often the hardness H of the nanocomposite coating can be caused by the compressive macrostress ($\sigma < 0$) generated in the coating during its growth. Therefore, at first, it is necessary to measure the value of macrostress σ in the coating. Only in the case when the compressive macrostress σ is low it can be declared that the enhanced hardness of nanocomposite coating is due to its nanostructure.

This fact is illustrated in Figure 7.3 where the hardness H of TiN and CrN nitride films sputtered under (a) a strong ion bombardment as a function of macrostress σ (Figure 7.3a) and (b) a weak ion bombardment as a function of grain size d

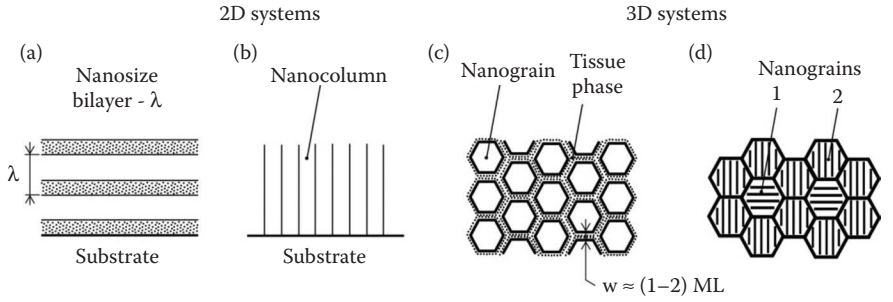


FIGURE 7.2 Schematic illustration of four nanostructures of the nanocomposite coating with enhanced hardness: (a) nanosize bilayers, (b) columnar nanostructure, (c) nanograins surrounded by a tissue phase, and (d) mixture of nanograins with different crystallographic orientation. (Reprinted from *Surface and Coatings Technology*, 207, Musil J., Hard nanocomposite coatings: Thermal stability, oxidation resistance and toughness, 50–65, Copyright 2012, with permission from Elsevier.)

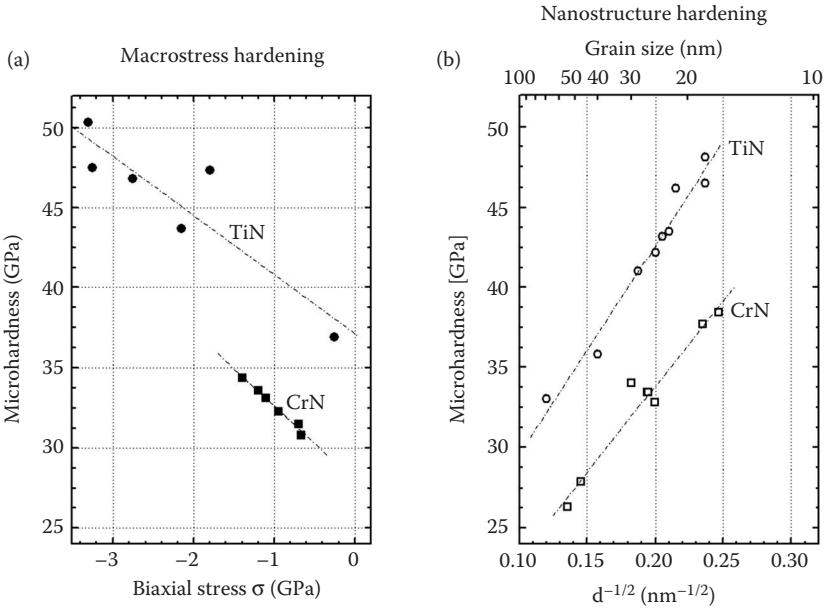


FIGURE 7.3 Hardness of TiN and CrN nitride films sputtered under (a) strong ion bombardment dominated by (a) the biaxial compressive stress σ and (b) the weak ion bombardment dominated by the grain size d (films with stresses close to zero $\sigma \leq -0.5$ GPa; TiN [45], CrN [46]), respectively. (Reprinted from *Thin Solid Films*, 415, Mayrhofer P.H. et al., A comparative study on reactive and nonreactive unbalanced magnetron sputter deposition of TiN coatings, 151–159, Copyright 2001, with permission from Elsevier; Reprinted from *Surface and Coatings Technology*, 142–144, Mayrhofer P.H., G. Tischler, C., Mitterer, Microstructure and mechanical properties of Cr-N coatings by reactive unbalanced magnetron sputtering, 78–84, Copyright 2001, with permission from Elsevier.)

(Figure 7.3b) are displayed [44]. In the film formed under the strong ion bombardment (high U_s, high i_s, and low a_D) and fast atoms bombardment (low sputtering gas pressure p_T) high compressive stresses are generated; here U_s is the substrate bias, i_s is the substrate ion current density, a_D is the deposition rate of film, and p_T is the total pressure of sputtering gas mixture ($Ar + N_2$). The hardness H in such films is mainly determined by high values of σ and H increases with increasing compressive macrostress σ, see Figure 7.3a. Similar results are also reported, for instance, in References 45 through 50.

However, the films sputtered under a weak ion bombardment exhibit a low compressive macrostress ($|\sigma| \leq 0.5$ GPa) and its hardness H increases with decreasing grain size d according to the Hall–Petch law $\sigma = \sigma_0 + k(d)^{-1/2}$; here σ is the yield stress, σ_0 is the lattice frictional stress required to move individual dislocations, and k is the positive constant called the Hall–Petch slope [42,43]. Recently, the following low (≤1 GPa) stress, superhard (≥40 GPa), several μm thick (typically 4 μm) sputtered films: Al-Cu-N films with H = 47 GPa and $\sigma = -0.2$ GPa [51], Al-Si-Cu-N films with H = 39.5 GPa and $\sigma = -0.8$ GPa [52], $TiB_{x\,=\,2.4}$ films with H = 73 GPa and

$\sigma = -0.1$ GPa [53] and (Ti,Al,V)N_x films with H = 50,7 GPa and $\sigma = -0.5$ GPa [54] were prepared. In all cases, the energy $\mathcal{E}$ delivered to the growing film was optimized by decreasing of the energy $\mathcal{E}_{bi}$ delivered by bombarding ions, that is, by decreasing of the substrate bias U_s and the substrate ion current density i_s and by increasing of the deposition rate a_D and the substrate heating, that is, by increasing of the ratio T_s/T_m; here T_s is the substrate temperature and T_m is the melting temperature of film material. For more details see Appendix 1.

In many cases, both the macrostress σ and the nanostructure (grain size d) can decide simultaneously on the coating hardness H. Therefore, very often it is very difficult to determine the factor responsible for the enhanced hardness H—the macrostress σ or the nanostructure only or a combined action of both factors. Therefore, it is very important to assess the value of the energy $\mathcal{E}$ delivered to the growing film. More details on the energy $\mathcal{E}$ delivered to the growing film are given in Appendix 1.

7.2.1 Classification of Hard Nanocomposite Coatings According to Phases

According to the hardness H, the nanocomposite coatings can be divided into three groups: (1) the hard coatings with hardness H < 40 GPa, (2) the superhard coatings with hardness H ranging from ~40 to ~80 GPa, and (3) the ultrahard coatings with hardness H > 80 GPa. More important is, however, the physical classification of hard nanocomposite coatings based on their phase composition. According to the phase composition two-phase hard and superhard nanocomposite coatings can be divided in two groups:

1. *Hard phase/hard phase nanocomposites* composed of two hard phases, for example, nc-Me_1N/a-Me_2N, etc.
2. *Hard phase/soft phase nanocomposites* composed of one hard and one soft phase, for example, nc-Me_1N/Me_3, etc.

Here, Me_1 = Ti, Zr, W, Ta, Cr, Mo, Al, and so on, are the elements forming hard nitrides, Me_2 = Si, B, and the like are the glass forming metalloid elements, and Me_3 = Cu, Ni, Ag, Au, Y, and so on are the soft metals.

Also, it is worthwhile to note that the nanocomposite coatings with enhanced hardness and further unique properties can be formed by (1) the addition of selected elements in the base material and (2) the nanocrystallization of amorphous and x-ray amorphous multielement materials. The energy $\mathcal{E}$ delivered to the growing coating must be, however, carefully controlled (i) to minimize the macrostress σ generated in the coating during growth to avoid its delamination from the substrate, (ii) to produce a high density coating with a smooth surface and void-free microstructure, (iii) to prevent changes of the structure, elemental, and phase composition of the nanocomposite coating and thereby to avoid changes of its properties, and (iv) to prevent the substrate overheating with the aim to avoid the destruction of heat sensitive substrates. More details are given in reference [39,40].

7.3 HARD NANOCOMPOSITE COATINGS WITH ENHANCED TOUGHNESS

Until recently, attention was concentrated on the hardness H of nanocomposite materials (coatings), the ways of the hardness H enhancement, and the achievement of the coating hardness H approaching or even exceeding that of the diamond. Many new advanced single-phase and nanocomposite coatings based on (i) nitrides, particularly the composites of the type nc-MeN/a-Si_3N_4 with low (≤10 at.%) Si content where Me = Ti, Zr, Ta, V, Nb, Hf, Cr, Mo, W, Al, and so on, (ii) oxides, (iii) oxynitrides, (iv) carbides, (v) carbonitrides, and (vi) borides and other compounds were successfully developed. Some of these coatings exhibit the enhanced hardness H achieving up to 50–70 GPa but none of them exhibit the hardness H approaching that of the diamond. It means that the diamond still remains the hardest material. However, these new advanced coatings exhibit many new unique properties.

Simultaneously, it was recognized that the hard materials are often very brittle. The brittleness of material increases with increasing hardness H. The brittleness of hard coatings strongly limits their practical utilization. It concerns mainly hard ceramic materials based on oxides that are widely used in many applications either as protective or functional coatings. This is a main reason why many laboratories across the world try to develop new advanced ceramic coatings with low brittleness and sufficiently high (≥20 GPa) hardness [17,19,23,28,55–61]. Despite the fact that the hardness H is one of the most important mechanical properties of the material, a correct selection of the coating material for a given application cannot be based on its hardness H only. The material must exhibit not only the high hardness H but also a sufficient toughness because the coating toughness can be more important than its hardness H for many applications. Therefore, it is vitally important to master the formation of the hard coatings with a high toughness. The hard coatings with enhanced toughness represent a new class of advanced nanocomposite coatings, see Figure 7.4.

7.3.1 Toughness and Toughening Mechanisms

The toughness of the material is defined as its resistance to cracking under loading by an external force F. It means that the toughness of material is defined as its ability to absorb the deformation energy without a fracture (rupture) of material. However, when the deformation of material (the strain ε) is increased, always a critical value $\varepsilon = \varepsilon_r$ at which the rupture of material occurs is achieved. Therefore, the resistance of material to fracture is called the fracture toughness. The fracture toughness is defined by the strain ε_r at its rupture (failure). It means that the toughness of material can be enhanced only in case when the value of ε_r is increased. It can be achieved only in the case when the crack initiation in the material is hindered or at least the propagation of cracks is reduced.

There are several toughening mechanisms that can be used to enhance the toughness of materials [19,56]. The main toughening mechanisms are the following: (1) ductile phase toughening, that is, the addition of a ductile phase (metal) in the ceramic matrix, (2) nanograin toughening based on the strengthening of grain boundaries resulting in the crack bending or branching, (3) multilayer coating

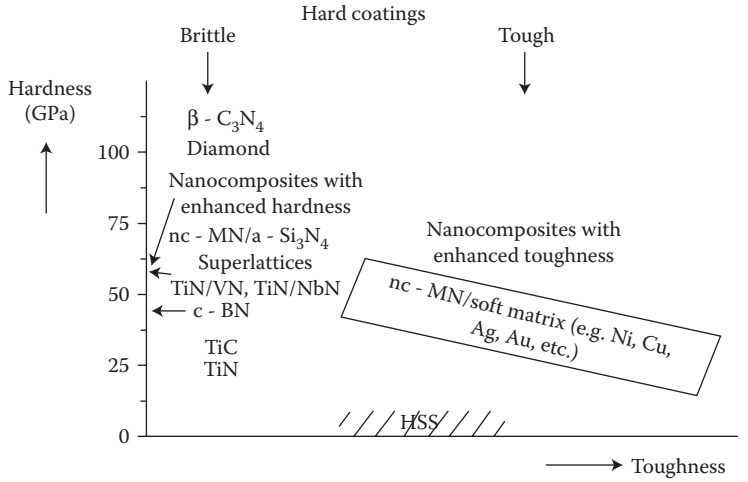


FIGURE 7.4 Schematic representation of hard nanocomposite coatings in the plane hardness H versus toughness. (With kind permission from Springer Science+Business Media: *Czechoslovak Journal of Physics*, Magnetron sputtering of alloy-based films and its specificity, B48, 1998, 1209–1224, Musil J., J. Vlček. Copyright 1998, Institute of Physics, Academy of Sciences of the Czech Republic.)

structure toughening based on the alternation of brittle and ductile layers, (4) fiber or nanotube toughening based on bridging or deflection of cracks, (5) phase transformation toughening based on the extraction of the fracture energy and consuming it for the phase transformation, and (6) compressive stress toughening that prevents cracks formation by their closing [19].

All toughening mechanisms are important and very useful in the design of the hard coating with enhanced toughness. The main aim of all toughening methods is to prevent crack propagation by the extraction or at least by the reduction of the fracture energy. However, these *toughening methods give no instructions on what should be mechanical properties of the material of coating, which is resistant to cracking.* This task is the subject of Sections 7.3.2 and 7.3.3 and the Section 7.4.

7.3.2 Principle of Formation of Hard Coatings with Enhanced Toughness

Hard nanocomposite coatings with enhanced toughness are coatings that are simultaneously hard and tough. The way to produce hard and tough coatings indicates the Hooke's law

$$\sigma = E \cdot \varepsilon \tag{7.1}$$

Here, σ is the stress (load) and ε is the strain (deformation). If we need to form the material that allows a high elastic deformation prior to a failure, that is, to form

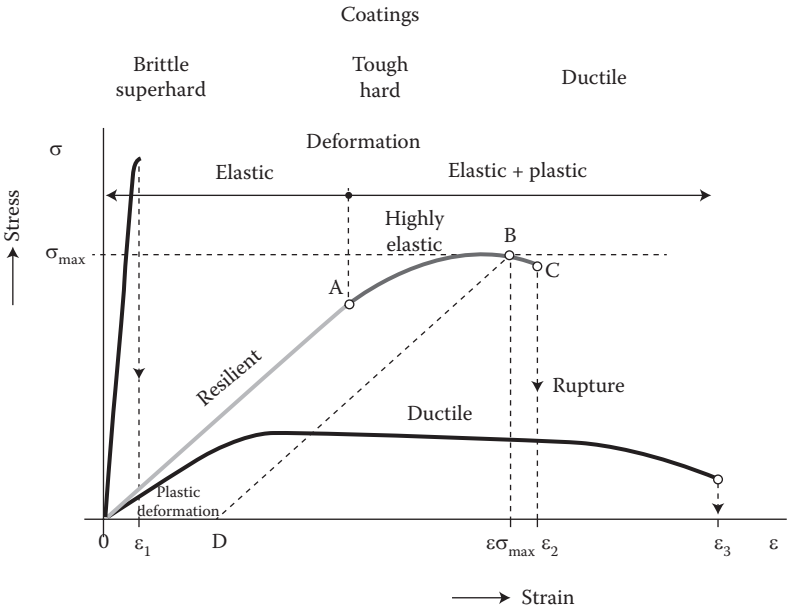


FIGURE 7.5 Schematic illustration of stress σ versus strain ε curves of superhard (brittle), hard (tough), hard (resilient), and ductile coatings. Resilient coatings exhibit no plastic deformation (line 0A). (Reprinted from *Surface and Coatings Technology*, 207, Musil, J., Hard nanocomposite coatings: Thermal stability, oxidation resistance and toughness, 50–65, Copyright 2012, with permission from Elsevier.)

the material with a high value ε at a given value σ, its Young's modulus E must be reduced. It means that the materials with the lowest value of Young's modulus E at a given hardness H (σ = const) need to be developed. It is a simple solution but a very difficult task. A possible behavior of the material can be best illustrated in the stress σ versus strain plane. The stress σ versus strain ε dependences for brittle, tough, resilient, and ductile hard coatings are schematically displayed in Figure 7.5.

Superhard materials are very brittle, exhibit almost no plastic deformation, and a very low strain to failure $\varepsilon = \varepsilon_1$. Hard and tough materials exhibit both elastic and plastic deformation. The material withstanding a higher strain $\varepsilon_1 < \varepsilon \leq \varepsilon_{\sigma max}$ without its cracking exhibits a higher toughness. The toughness of material is higher in the case when a greater value of $\varepsilon_{\sigma max}$ is achieved at higher values of σ_{max}. Such materials exhibit a high strength and a high elastic recovery $W_e \geq 60\%$ (the line AB). Hard and tough materials with no plastic deformation (the line 0A) are the resilient hard coatings with 100% elastic recovery W_e. On the contrary, materials with $\sigma < \sigma_{max}$ and $\varepsilon_{\sigma max} < \varepsilon \leq \varepsilon_3$ are ductile and exhibit a lower strength and a high plastic deformation. The hardness H of hard, tough, and highly elastic coatings, ranging from about 15 to 25 GPa, is, however, sufficient for many applications. The main advantage of the highly elastic coatings with a low plastic deformation is their enhanced resistance to cracking. These are reasons, why the hard, tough, and highly elastic hard coatings are now intensively developed in many laboratories across the world. The hard and

simultaneously tough coatings represent *a new generation of advanced hard nanocomposite coatings*.

This analysis shows that a new task in the development of new advanced hard nanocomposite coatings with enhanced toughness is to master the formation of coatings with (i) the low value of the effective Young's modulus E^* and (ii) a high value of the elastic recovery W_e. The hard coatings with low values of E^* and high values of W_e were already successfully prepared, for instance, see References 39 and 62 through 68. Also, it was found that the hard nanocomposite coatings with enhanced toughness and enhanced resistance to cracking should exhibit the high ratio $H/E^* \geq 0.1$ and the high elastic recovery $W_e \geq 60\%$. More details are given below and in Reference 39.

7.3.3 Classification of Coatings According to Mechanical Properties and Important Ratios

Properties of coatings given in stress versus strain diagram and displayed in Figure 7.5 can be briefly characterized as follows. *The brittle coatings* are hard but easily broken coatings. *The tough coatings* are strong, not easily weakened, cut, worn, or broken coatings. *The ductile coatings* exhibit (i) a high plastic deformation, that is, they can be pressed or pulled into shape without a need to be heated, and (ii) almost zero elasticity, that is, they keep the shape created by pressing also after being pressed or pulled. *The elastic coatings* partially spring back into the original shape after being stretched (extended). *The resilient coatings* exhibit zero plastic deformation and fully spring back to the original shape when the load is removed.

The mechanical properties of the coating are its hardness H, the effective Young's modulus $E^* = E/(1 - \nu^2)$, and the elastic recovery W_e; here, E is Young's modulus and ν is Poisson's ratio. However, important is also the mechanical behavior of coating. It is well characterized by two ratios H/E^* and H^3/E^{*2}. *The ratio* H/E^* is proportional to the resistance to wear and the elastic strain ε up to a rupture (failure) of the coating at $\varepsilon = \varepsilon_2$ [17], see Figure 7.5. It means that the higher the ratio H/E^* the higher is the resistance of coating to wear and failure [17,23,28,57]. Therefore, the ratio H/E^* can be used as a parameter enabling to predict whether the coating will crack or be resistant to cracking. Recently, it was found experimentally that the coatings with the high ratio $H/E \geq 0.1$ are resistant to cracking [39,62–68]. *The ratio* H^3/E^{*2} is proportional to the resistance of the coating to plastic deformation [69]; it means that the H^3/E^{*2} ratio is proportional to the elastic deformation of the coating. Also, it is worthwhile to note that a low value of the effective Young's modulus E^* is very desirable as it allows the given load L to be distributed over a wider area of material and thereby makes it possible to increase both the elastic strain to failure ε_r and the resistance of the coating to cracking. Here, it is worthwhile to note that there is a great difference in the physical basis of both ratios H/E^* and H^3/E^{*2}.

The ratio H^3/E^{*2} cannot be used as a measure of the resistance of the coating to cracking. It is illustrated on the properties of sputtered Al-Cu-O films [62]. A detailed investigation of mechanical properties of different Al-Cu-O films showed that the Al-Cu-O film with different values of H, E^*, W_e, and σ can exhibit different values of the ratio H/E^* and simultaneously the same values of the ratio H^3/E^{*2}, see

TABLE 7.1
Comparison of the Resistance to Cracking of Two nc-(Al_{8-2x}, Cu_{3x}) O_{12}/a-(Al-Cu-O) Composite Films with Different Values of the Ratio H/E^*, the Same Values of the Ratio H^3/E^{*2} and Different Values of Macrostress σ

Film	h (nm)	H (GPa)	E^* (GPa)	W_e (%)	H/E^*	H^3/E^{*2}	σ (GPa)	Cracks
1	2020	16.7	135	71	0.124	0.26	–2.2	No
2	1850	19.4	170	70	0.114	0.25	–1.5	Yes

Source: Blažek J. et al.: *Applied Surface Science*, 258, 2011, 1762–1767.
Note: Cracking of films was assessed by the indentation test using the diamond indenter impressed in the film at load L = 1 N.

Table 7.1. Both films, denoted as film 1 and film 2, were assessed as to their resistance to cracking during loading by the diamond indenter at a high load L = 1 N; more details on this test is given below in Section 7.5. Due to different values of H, E^*, and σ, both films exhibit completely different behavior under loading. The film 1 does not crack under loading. On the contrary, film 2 easily cracks. This experiment indicates that (1) the ratio H^3/E^{*2} cannot be used for the assessment of the resistance of film to cracking but it assesses well the elasticity of film (for both films the same value of the elastic recovery W_e was measured) and (2) the achievement *of the lowest value of E^* is probably further key parameter which decides on the magnitude of the resistance of the film to cracking*. The confirmation of this hypothesis, however, requires a special investigation, which still needs to be carried out.

7.4 HARD COATINGS WITH LOW EFFECTIVE YOUNG'S MODULUS E^* AND HIGH RATIO $H/E^* \geq 0.1$

The formation of highly elastic hard coatings with a low effective Young's modulus E^* resulting in a high ratio $H/E^* \geq 0.1$ is possible. The possibility of the formation of such coatings indicate the experimental relationship between the coating hardness H and its effective Young's modulus E^* reported more than 10 years ago [23,70–72], see Figures 7.6 and 7.7. Figure 7.6 shows that the film hardness H has not to be always exactly 1/10 of the effective Young's modulus E^* as is often roughly assumed. Experimental points are dispersed on both sides around the straight line $H = 0.1\ E^*$. There is, however, a question as to how and under what conditions such coatings can be formed.

Figure 7.7 displays $H = f(E^*)$ dependences of five Ti-N, Ti-Al-N, Zr-N, Zr-Cu-N, and Al-Cu-N nitride coatings prepared by magnetron sputtering [40,70–72]. In this figure, a straight line $H/E^* = 0.1$, which divides the H-E^* plane in two regions of coatings with high $H/E^* > 0.1$ and low $H/E^* < 0.1$, is also displayed. From Figure 7.7 it is seen that experimental points corresponding to individual nitrides are quite well distributed along mutually separated straight lines. This figure clearly shows that (1) the coating material with the same hardness H, for instance, H = 30 GPa

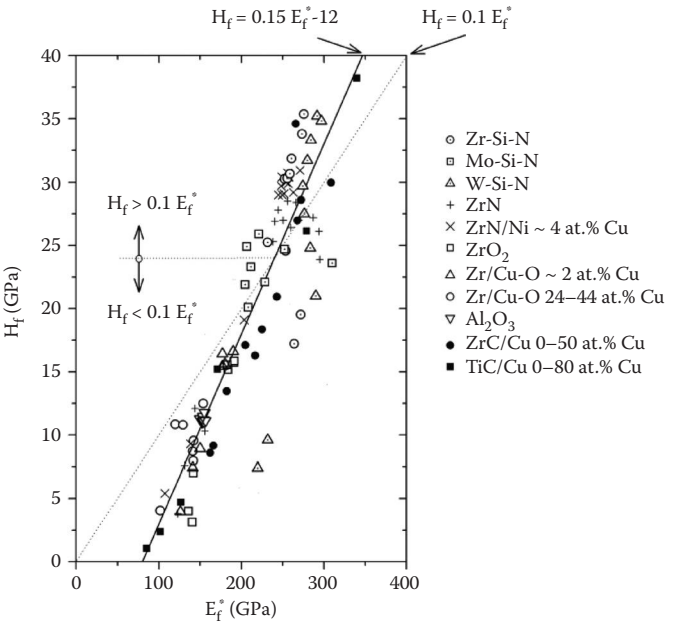


FIGURE 7.6 The relationships between the hardness H_f and effective Young's modulus E_f^* of several selected oxide, nitride, and carbide films prepared by magnetron sputtering under different deposition conditions. The index f denotes the film. (Reprinted from *Surface and Coatings Technology*, 201, Musil, J., M. Jirout, Toughness of hard nanostructured ceramic thin films, 5148–5152, Copyright 2007, with permission from Elsevier.)

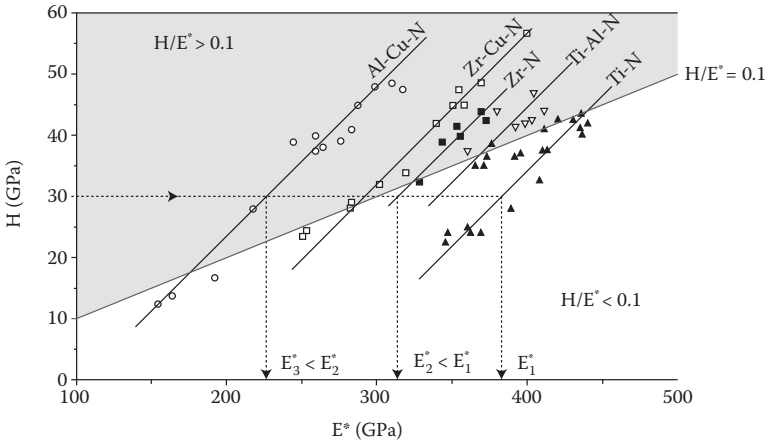


FIGURE 7.7 Control of the effective Young's modulus E^* of the Me-N binary nitride coatings with the same hardness H by the addition of Cu and Al elements; Me = Ti, Zr, and Al. (Reprinted from *Comprehensive Materials Processing, 4*, Musil J., P. Zeman, P. Baroch, Hard nanocomposite coatings, 325–353, Copyright 2014, with permission from Elsevier.)

as shown in this figure, and different elemental composition can exhibit different values of the effective Young's modulus E^*, (2) the value of E^* of the Me_1-Me_2-N nitride coating depends not only on the element Me_2 added to the Me_1N binary nitride but also on the element Me_1, which forms the binary nitride, (3) not all nitrides exhibit a high ratio $H/E^* > 0.1$, and (4) the coating material with the ratio $H/E^* > 0.1$ can be achieved only in the case when both elements Me_1 and Me_2 are correctly selected.

The finding that hard coatings with high ratio $H/E^* \geq 0.1$ can be formed is very important because these coatings exhibit new unique properties. This finding is a main reason why the formation of highly elastic hard coatings with a high $H/E^* \geq 0.1$ is now a new task in the development of new advanced hard nanocomposite coatings with enhanced toughness. The coatings with a high ratio $H/E^* \geq 0.1$ should exhibit the lowest possible value of the effective Young's modulus E^* at a given hardness H. However, it is very difficult because the hardness H and the effective Young's modulus E^* are two mutually coupled quantities. Magnitudes of the hardness H and the effective Young's modulus E^* of coating strongly depend on the deposition parameters used in its formation. The values of H and E^* are controlled not only by the elemental composition of coating as shown above but also by its structure, elemental, and phase composition, microstructure and macrostress σ, that is, the values of H and E^* are controlled by the energy $\mathcal{E}$ delivered to the growing coating by the substrate heating (T_s) and particularly by the bombarding ions and condensing atoms. At present, there are no general rules that allow to predict how to prepare the coatings with high ratio $H/E^* > 0.1$.

The coatings with high ratio $H/E^* > 0.1$ can be formed by four methods, that is, by

1. The control of deposition parameters used in the formation of coatings.
2. The addition of one or more selected Me_n elements in the base coating material; n is the number of added element.
3. The control of the energy $\mathcal{E}$ delivered to the growing coating by (i) the substrate heating (T_s) and (ii) the condensing particles (p), and (iii) the bombarding ions (U_s, i_s, a_D); here p is the pressure of sputtering gas, U_s is the substrate bias, i_s is the substrate ion current density, and a_D is the deposition rate of coating.
4. The simultaneous selection of (i) the kind and amount of elements added in the coating and (ii) the amount of energy $\mathcal{E}$ delivered to the coating during its growth.

7.4.1 Control of H/E^* Ratio by Deposition Parameters Used in the Formation of Coating

The formation of hard coatings with high ratio $H/E^* > 1$ and high elastic recovery $W_e \geq 60\%$ is a difficult but possible task. The possibility of creation of these coatings is illustrated on formation of the Zr-Al-O coatings with a low ratio $Zr/Al < 1$ and a high ratio $Zr/Al > 1$ by reactive sputtering using a pulsed dual magnetron under different deposition conditions [65], see Figure 7.8. From Figure 7.8 it is seen that

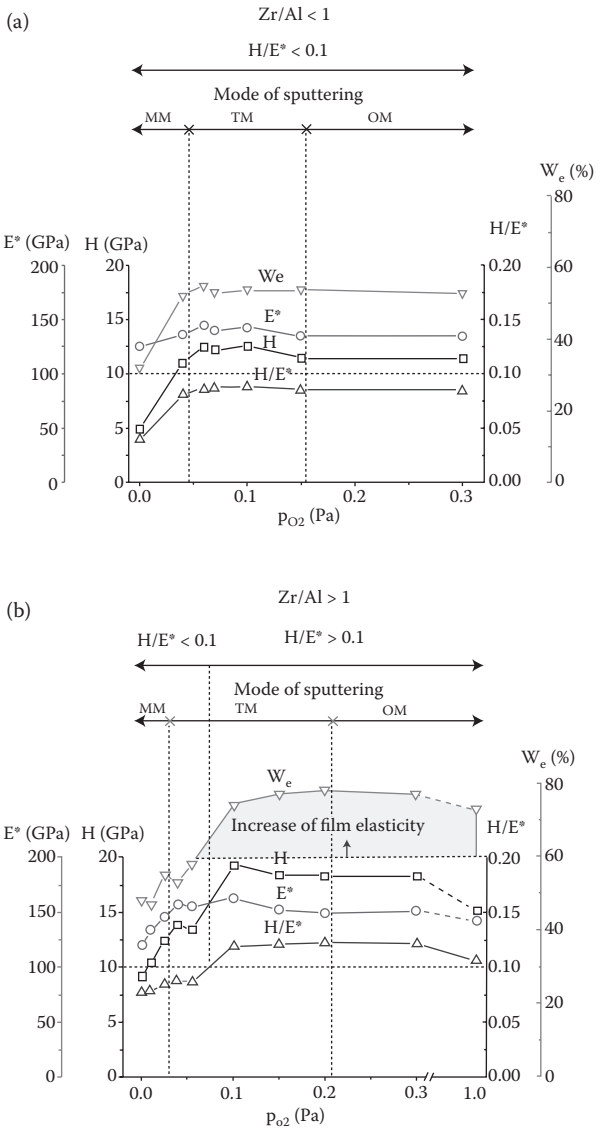


FIGURE 7.8 Hardness H, effective Young's modulus E^*, elastic recovery W_e, and ratio H/E^* of Zr-Al-O films with (a) low ratio Zr/Al < 1 and (b) high ratio Zr/Al > 1 sputtered, using a dual magnetron operated at an AC pulse mode, on Si(100) substrate at $U_s = U_{fl}$, $T_s = 500°C$, $p_T = p_{Ar} + p_{O2} = 1$ Pa, and $I_{da} = 1$ and 2 A, respectively, as a function of partial pressure of oxygen p_{O2}; here I_{da} is the magnetron current averaged over the pulse period T, MM, TM, and OM are the metallic, transition, and oxide modes of sputtering, respectively. (Reprinted from *Surface and Coatings Technology*, 207, Musil J. et al., The effect of addition of Al in ZrO_2 thin film on its resistance to cracking, 355–360, Copyright 2012, with permission from Elsevier.)

a. The partial pressure of oxygen p_{O2} very effectively influences the hardness H, effective Young's modulus E^*, and elastic recovery W_e of the Zr-Al-O film.
b. The mechanical properties of Zr-Al-O films strongly depend on the ratio Zr/Al.
c. The Zr-Al-O films with a low ratio Zr/Al < 1 exhibit a low ratio $H/E^* \leq 0.1$, are softer and less elastic compared with the Zr-Al-O films with a high ratio Zr/Al > 1, which can exhibit a high ratio $H/E^* > 0.1$.
d. All Zr-Al-O films with high ratio $H/E^* > 0.1$ exhibit a high hardness $H \approx 18$ GPa and a high elastic recovery $W_e \geq 60\%$.

This experiment clearly shows that (1) the mechanical properties of Zr-Al-O film depend not only on the deposition conditions used in sputtering but also on its elemental composition, (2) the formation of the Zr-Al-O film with a high ratio $H/E^* \geq 1$ requires to select a correct combination of the deposition parameters and the elemental composition of film, and (3) the Zr-Al-O films with $H/E^* \geq 1$ are highly elastic and exhibit a high elastic recovery $W_e \geq 60\%$.

7.4.2 Control of H/E^* Ratio by Addition of Selected Me Element in Coating

The possibility of the formation of highly elastic hard coatings with a high ratio $H/E^* \geq 0.1$ by the addition of one or several selected Me elements in the base material was already experimentally demonstrated for Al-Cu-N, Zr-Cu-N, ZrN, Ti-Al-N, and Ti-N nitride coatings, see Figure 7.7. Recently, the highly elastic hard Al-Cu-O [62], Zr-Al-O [63,65] (Figure 7.8) oxide coatings and Al-O-N [64] oxynitride coatings with high ratio $H/E^* \geq 0.1$ and enhanced resistance to cracking were also successfully reactively sputtered on substrates held at $U_s = U_{fl}$. The last three experiments demonstrate that highly elastic hard coatings with a high ratio $H/E^* \geq 0.1$ can be prepared not only in the nitride systems but also in the oxide systems such as oxide/oxide nanocomposites and in the oxynitride systems such as nitride/oxide nanocomposites.

Besides, it is worthwhile to note that not only a correct selection of (i) the deposition parameters and (ii) the elements Me_2 added in the base coating material is important for the formation of the highly elastic hard coatings with a high ratio $H/E^* \geq 0.1$ but also a correct amount of the energy $\mathcal{E}$ delivered to the growing coating is necessary.

7.4.3 Control of H/E^* Ratio by Energy $\mathcal{E}$ Delivered to the Growing Coating

The addition of Me element in the base coating material is a very effective way to influence its structure and the phase composition. Similar effect can be achieved also in the case when the energy $\mathcal{E}$ delivered to the growing coating by the heating and/or

incident and bombarding particles (fast atoms and ions) is correctly controlled. This fact is illustrated in Figures 7.9 and 7.10.

7.4.3.1 Effect of Substrate Heating

The effect of substrate heating on formation of the coating with a high ratio $H/E^* \geq 0.1$ is illustrated on mechanical properties of the Sn-Cu-O coating sputtered on (i) the unheated substrate (T_s = RT) and (ii) the heated substrate (T_s = 250°C) substrate, see Figure 7.9. In this figure, the evolution of hardness H, effective Young's modulus E^*, and elastic recovery W_e of the Sn-Cu-O oxide film with constant ~10 at.% Cu, sputtered at two values of the substrate temperature T_s = RT and 250°C, with increasing negative substrate bias U_s is displayed. In both figures the Sn-Cu-O films with $H/E^* > 0.1$ are enclosed by dotted closed curves. The comparison of both figures (Figure 7.9a and b) clearly shows that the Sn-Cu-O film sputtered on the unheated substrate exhibits the high ratio $H/E^* > 0.1$ only in the case when the film is deposited at $U_s = -200$ V. On the other hand, there is a relatively wide range of negative biases U_s ranging from approximately −100 to approximately −200 V in which the Sn-Cu-O films sputtered at T_s = 250°C exhibit the high ratio $H/E^* > 0.1$. This difference is due to a higher energy $\mathcal{E}$ delivered to the film sputtered on heated substrate (T_s = 250°C). This experiment demonstrates that not only the addition of a selected Me element in the base coating material, in our case Cu in the SnO_2 film, but also a sufficient energy $\mathcal{E}$ delivered to the growing film is necessary to form the Sn-Cu-O films with high ratio $H/E^* > 0.1$. It means that a correct combination of the added Me element, its content in the film, and the sufficient amount of the energy $\mathcal{E}$ delivered to the growing film is needed to form the films with a high ratio $H/E^* > 0.1$. This requirement is not currently fulfilled in the deposition of films. It is a main reason why so far most of the deposited films exhibit a low ratio $H/E^* < 0.1$ only.

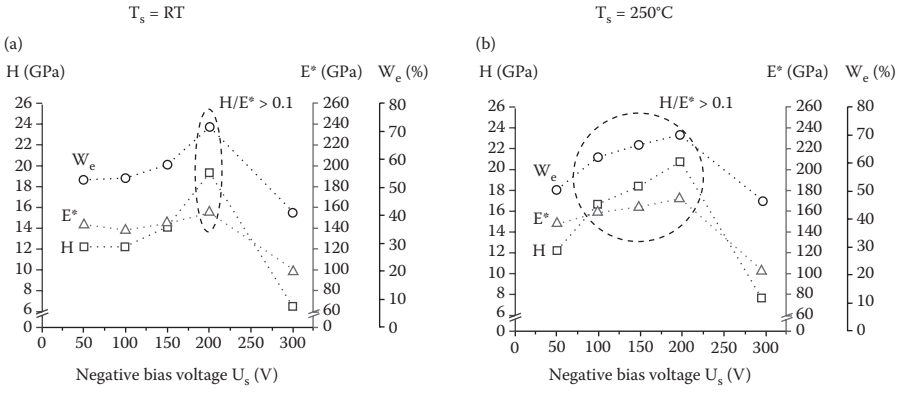


FIGURE 7.9 Hardness H, effective Young's modulus E^*, and elastic recovery W_e of the Sn-Cu-O film with ~10 at.% Cu sputtered at (a) T_s = RT (unheated substrate) and (b) T_s = 250°C as a function of negative substrate bias U_s. (Reprinted from Musil J. et al., *Journal of Vacuum Science and Technology* A, 32(2), 2014, 021504–1 to 6. Copyright 2014, with permission from American Vacuum Society.)

7.4.3.2 Effect of Ion Bombardment of Growing Coating

The effect of the ion bombardment on formation of the coating with a high ratio $H/E^* \geq 0.1$ is illustrated on mechanical properties of the Sn-Cu-O coating reactively sputtered in a mixture of $Ar + O_2$ on (i) the unheated (T_s = RT) and (ii) the heated (T_s = 250 and 500°C) Si(100) substrates held at $U_s = U_{fl}$ and three values of the negative substrate bias U_s = –100, –150, and –200 V, see Figure 7.10. Figure 7.10a shows the hardness H of Sn-Cu-O coating as a function of the effective Young's modulus E^* and Figure 7.10b shows the elastic recovery W_e of Sn-Cu-O coating as a function of the ratio H/E^*.

Results displayed in Figure 7.10a and b show that

1. The dependence $H = f(E^*)$ does not exactly follow the line $H/E^* = 0.1$. The line along which experimental points (not shown in Figure 7.10a) are distributed is steeper than the line $H/E^* = 0.1$. It means that both the coatings with a low ratio $H/E^* < 0.1$ and the coatings with a high ratio $H/E^* \geq 0.1$ can be produced.
2. The Sn-Cu-O coatings sputtered on unheated substrates (T_s = RT) exhibit a low ratio $H/E^* \leq 0.1$ only.
3. All Sn-Cu-O coatings with a high ratio $H/E^* \geq 0.1$ are highly elastic with the elastic recovery $W_e \geq 60\%$.
4. The hardness H of the Sn-Cu-O coating increases with increasing negative bias U_s, that is, with increasing (i) energy $\mathcal{E}_{bi}$ of bombarding ions and (ii) substrate heating (T_s), see points denoted by letters g, d, a in Figure 7.10a. The elastic recovery W_e also increases with increasing negative bias U_s, see Figure 7.10b.

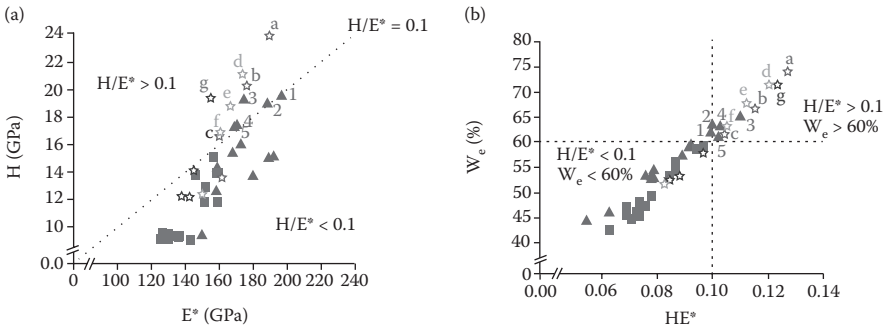


FIGURE 7.10 (a) Hardness $H = f(E^*)$ and (b) elastic recovery $W_e = f(H/E^*)$ of the Sn-Cu-O film with high ~10 at.% Cu content sputtered at (i) T_s = RT and $U_s = U_{fl}$, (squares), (ii) T_s = 500° C and $U_s = U_{fl}$ (triangles), (iii) T_s = RT, U_s = –200, –150, –100, –50 V (star g, the film deposited at U_s = –200 V), (iv) T_s = 250°C and U_s = –200, –150, –100, –50 V (stars d,e,f, the films deposited at U_s = –200, –150, and –150 V, respectively), and (v) T_s = 500°C and U_s = –200, –150, –100, –50 V (stars a,b,c). Points denoted by numbers correspond to films prepared at T_s = 500° C and $U_s = U_{fl}$. Stars corresponding to films with $H/E^* < 0.1$ prepared at negative substrate bias $U_s < 0$ are not denoted. (Reprinted from Musil J. et al., *Journal of Vacuum Science and Technology* A, 32(2), 2014, 021504–1 to 6. Copyright 2014, with permission from American Vacuum Society.)

Changes in mechanical properties of the Sn-Cu-O coating strongly influence its other properties. It is illustrated on a tribological behavior of the Sn-Cu-O coating, see Figure 7.11. The tribological properties of the Sn-Cu-O coating also correlate well with its mechanical properties, see Figure 7.11a and b. Here, the coefficient of friction μ and wear rate k of the Sn-Cu-O coating are displayed as a function of its hardness H, effective Young's modulus E^*, elastic recovery W_e, and H/E^* ratio. The friction coefficient μ and wear rate k were measured using a ball-on-disk tribometer (CSM) in ambient air with WC ball (∅ = 6 mm) rotating at radius r = 3 mm under the load L = 2 N at the velocity v = 0.05 m/s and sliding distance l = 1000 m (53052 revolutions). The wear loss is defined as the coating volume lost (removed) per the sliding distance l.

From results displayed in Figure 7.11 the following issues can be drawn:

1. The coefficient of friction μ of the Sn-Cu-O film sputtered at $T_s = 500°C$ and $U_s = U_{fl}$ decreases with increasing hardness H, effective Young's modulus E^*, elastic recovery W_e, and ratio H/E^*. The lowest values of μ are achieved at high values of ratio $H/E^* \geq 0.1$. It shows that not only is a high

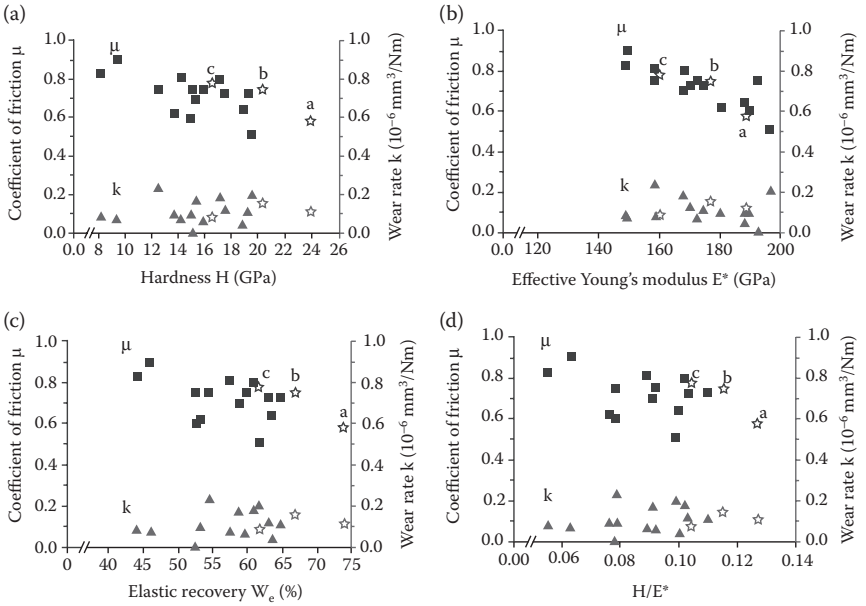


FIGURE 7.11 Coefficient of friction μ (squares) and wear rate k (triangles) of Sn-Cu-O film with high ~10 at.% Cu content sputtered on Si (100) (i) substrates heated at $T_s = 500°C$ and held at floating potential $U_s = U_{fl}$ (full symbols) and (ii) unheated substrates (T_s = RT) held at negative bias U_s = –200, –150, and –100 V (open symbols: stars a, b, c, respectively) measured at RT as a function of (a) hardness H, (b) effective Young's modulus E^*, (c) elastic recovery W_e, and (d) H/E^* ratio. (Reprinted from Musil J. et al., *Journal of Vacuum Science and Technology A*, 32(2), 2014, 021504–1 to 6. Copyright 2014, with permission from American Vacuum Society.)

TABLE 7.2
Deposition Parameters, Thickness h, Deposition Rate a_D, Mechanical and Tribological Properties of Sn-Cu-O Films with High (~10 at.%) Cu Content Sputtered at $T_s = 500°C$, $p_{Ar} = 0.4$ Pa, $p_{O2} = 0.6$ Pa, and Three Values of Negative Substrate Bias U_s

Film	U_s (V)	h (nm)	a_D (nm/min)	H (GPa)	E^* (GPa)	W_e (%)	H/E^*	μ	k (10^{-6} mm^3/N m)
a	–200	2570	14	23.9	189	73.8	0.127	0.58	0.11
b	–150	3080	17	20.3	177	66.8	0.115	0.75	0.15
c	–100	2870	19	16.6	160	61.5	0.104	0.78	0.08

hardness H necessary but also the low effective Young's modulus E^* resulting in a high H/E^* ratio is important. The fact that the films with high ratio $H/E^* \geq 0.1$ also exhibit high values of $W_e \geq 60\%$, see above in Figure 7.8, indicates that only a correct combination of high H, low E^*, and high W_e can ensure minimum values of the coefficient of friction of Sn-Cu-O films.

2. The coefficient of friction μ of the Sn-Cu-O film can be further decreased by the ion bombardment of film during its growth due to increase of its H, H/E^* ratio, and W_e, see Table 7.2.
3. The coefficient of wear k of the Sn-Cu-O film is very low of about ~1×10^{-6} mm^3/Nm and almost does not depend on H, E^*, W_e, and H/E^* ratio.

In summary, it can be concluded *that mechanical properties of the coating can be used to optimize its operational properties*, for example, the minimal coefficient of friction μ and the minimal wear rate k for a given material can be achieved by an optimization of the mechanical properties of coating. This finding can be utilized in the design of coatings with optimal properties.

7.4.4 Control of H/E^* Ratio by Combined Action of Deposition Parameters, Added Elements, and Energy $\mathcal{E}$

Usually, in deposition of the coating three factors—(1) deposition parameters, (2) the addition of elements in the base material of coating, and (3) the energy $\mathcal{E}$ delivered in the growing coating—operate simultaneously and decide on the value of the H/E^* ratio. The combined effect of these three factors on the H/E^* ratio is illustrated on mechanical properties of the coatings prepared by a reactive magnetron sputtering.

In the reactive sputtering, the coatings can be produced in three basic sputtering modes: (1) the metallic mode (MM), (2) the transition mode (TM), and (3) reactive mode (RM), see Figure 7.12; for more details see, for instance, the references [74,75]. Properties of coatings deposited in individual modes of sputtering strongly differ due to (i) the incorporation of different amount of atoms of reactive gas in the coating and (ii) the different amount of energy $\mathcal{E}_{bi}$ delivered to the growing coating by bombarding ions. The amount of RG in the sputtering gas mixture strongly

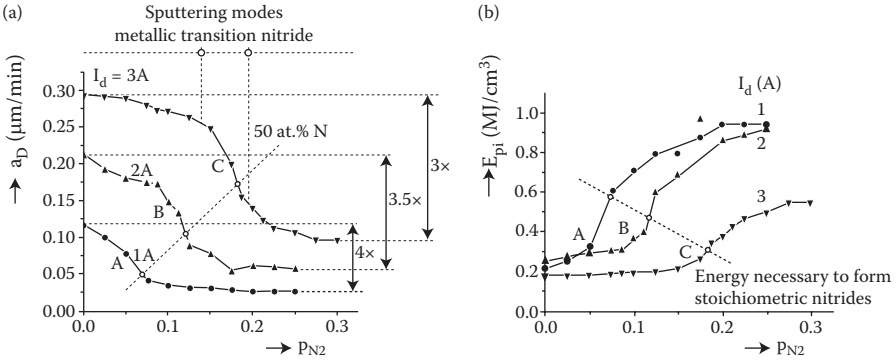


FIGURE 7.12 (a) Deposition rate a_D of Ti(Fe)N_x films and (b) energy $\mathcal{E}_{bi}$ delivered to them during their growth by bombarding ions as a function of partial pressure of nitrogen p_{N2}. The films were sputtered at $U_s = -100$ V, $T_s = 300°C$, $d_{s\text{-}t} = 60$ mm, $p_T = p_{Ar} + p_{N2} = 0.5$ Pa and (i) $I_d = 1$ A, $i_s = 0.5$ mA/cm^2, (ii) $I_d = 2$ A, $i_s = 1$ mA/cm^2, and (iii) $I_d = 3$ A, $i_s = 1$ mA/cm^2. (Reprinted from *Materials Surface Processing by Directed Energy Techniques*, Musil J., J. Vlček, P. Baroch, Magnetron discharges for thin films plasma processing, Chapter 3, 67–106, Copyright 2006, with permission from Elsevier.)

influences the deposition rate a_D of sputtered coating due to the target poisoning and changing of the sputtering yield of the target material. The energy $\mathcal{E}_{bi}$ also strongly depends on a_D, see Figure 7.12. It means that the deposition rate a_D is of key importance in the reactive sputtering of coatings. The energy $\mathcal{E}_{bi}$ delivered to the growing coating by bombarding ions in collisionless plasma is defined by the following formula [76–79]:

$$\mathbf{E}_{bi}[\mathrm{J/cm^3}] \approx U_s i_s / a_D \tag{7.2}$$

where U_s is the substrate bias and i_s is the substrate ion current density; more details are given in the Appendix 1. From Equation 7.2 it is seen that the value of $\mathcal{E}_{bi}$ depends not only on U_s but also on the substrate ion current density i_s and the deposition rate a_D of coating. The magnitude of i_s strongly depends also on the design of magnetron and the power delivered to magnetron [79]. In general, the deposition rate a_D increases with increasing magnetron discharge voltage U_d due to an increase of the sputtering yield of the target material. Besides, it is worthwhile to note that the deposition rate a_D depends also on the magnetron design, particularly on the magnitude of parallel component of magnetic field $B_{||}$ on the target surface, dimensions of the sputtered target, sputtering gas pressure p, and the perfection of the plasma confinement above the sputtered target; for more details see Reference 79.

Figure 7.12 clearly shows that the deposition rate a_D of reactively sputtered coatings decreases with increasing partial pressure of reactive gas p_{N2}. On the contrary, the energy $\mathcal{E}_{bi}$ increases with increasing p_{N2}. It means that the lowest energy $\mathcal{E}_{bi}$ is delivered to the growing film in the metallic mode (MM) and the highest energy $\mathcal{E}_{bi}$ in the reactive mode (RM) of sputtering. This is a main reason why, different

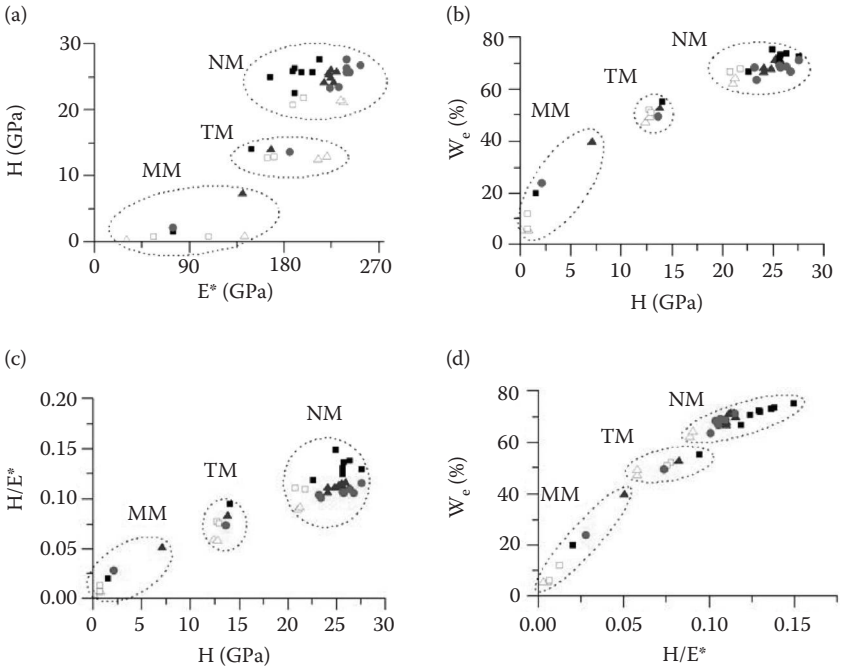


FIGURE 7.13 (a) $H = f(E^*)$, (b) $W_e = f(H)$, (c) $H/E^* = f(H)$, and (d) $W_e = f(H/E^*)$ of Al-Si-N coatings reactively sputtered at $U_s = U_{fl}$, $T_s = 500°C$, $p_T = p_{Ar} + p_{N2} = 0.7$ Pa on Si(111), steel, and sintered Al_2O_3 substrates; here U_{fl} is the floating potential. Open symbols correspond to the coatings with a low (<10 at.%) Si content, full symbols correspond to the coatings with a high (~40 at.%) content of Si; squares, circles, and triangles correspond to coatings deposited on Si (111), sintered Al_2O_3, and steel substrates, respectively. (Reprinted from *Surface and Coatings Technology*, 202, Musil J. et al., Properties of magnetron sputtered Al-Si-N thin films with a low and high Si Content, 3485–3493, Copyright 2008, with permission from Elsevier.)

combinations of three key deposition parameters, that is, a_D, E_{bi}, and p_{RG} (decides on the content of RG atoms in film), result in different properties of sputtered films.

These facts are illustrated on mechanical properties of the Al-Si-N coating reactively sputtered in an $Ar + N_2$ sputtering gas mixture, see Figure 7.13. The Al-Si-N coatings were reactively sputtered from Al/Si targets composed of a Si plate (∅ 28 mm) fixed to the cathode by an Al ring with an inner diameter $∅_i = 15$ or 26 mm using a dual magnetron. More details are given in References 80 and 81. Figure 7.13 displays mechanical properties (H, E^*, W_e, H/E^*) of the Al-Si-N coating with low (<10 at.%) and high (~40 at.%) Si content formed in individual modes of reactive sputtering. NM denotes the nitride mode of sputtering.

From Figure 7.13 it is seen that

1. The hardness H increases with increasing effective Young's modulus E^* and the elastic recovery W_e increases with increasing H.

2. The H/E^* ratio increases with increasing H and the elastic recovery W_e increases with increasing H/E^* ratio.
3. The Al-Si-N coatings with high ratio $H/E^* \geq 0.1$ exhibit a high hardness H ranging from ~20 to ~30 GPa and a high elastic recovery $W_e \geq 60\%$.
4. The Al-Si-N coatings with high ratio $H/E^* \geq 0.1$ are sputtered in the nitride mode (NM) of sputtering only.

Last finding (point 4) indicates that the formation of films with high ratio $H/E^* \geq 0.1$ requires a sufficiently high amount of energy $\mathcal{E}_{bi}$ to be delivered to the growing film. Such films can be prepared only in the NM of sputtering at lowest deposition rate a_D, compared with films deposited at much higher a_D in the TM and MM modes of sputtering, when the highest energy $\mathcal{E}_{bi}$ is delivered to the growing film, see Figure 7.12. Here, it is worthwhile to note that the energy $\mathcal{E}_{bi}$ can be controlled not only by the variation of the partial pressure of reactive gas p_{RG}, that is, by the variation of amount of RG atoms incorporated in the film, but also by the variation of (i) the negative substrate bias U_s and (ii) the substrate ion current density i_s at a given value of p_{RG}, see Equation 7.2. It makes possible to produce films with almost the same elemental composition but with a controlled H/E^* ratio including the films with a high ratio $H/E^* \geq 0.1$. The effect of $\mathcal{E}_{bi}$ on H, E^*, W_e, H/E^*, and σ of reactively sputtered film is illustrated on physical and mechanical properties of the Ti(Ni)N films prepared by a dc reactive sputtering using a dual magnetron, see Table 7.3.

Data given in Table 7.3 show the evolution of (i) the energy $\mathcal{E}_{bi}$, (ii) the film deposition rate a_D, and (iii) the mechanical properties of the Ti(Ni)N films with increasing negative substrate bias U_s. The Ti(Ni)N films were deposited on Si(100) substrates at target/substrate distance $d_{s\text{-}t} = 60$ mm by dc reactive sputtering using dual magnetron with TiNi (90/5 at.%) targets tilted to vertical axis at 20° for 120 min. From this table it can be seen that the increase of negative bias U_s results in increase of (a) the substrate ion current i_s, (b) the energy $\mathcal{E}_{bi}$, (c) the hardness H and elastic recovery W_e, (d) the H/E^* ratio, and (e) the compressive macrostress in film ($\sigma < 0$). The negative

TABLE 7.3
Evolution of Hardness H, Effective Young's Modulus E^*, Elastic Recovery W_e, H/E^* Ratio, and Macrostress σ in Ti(Ni)N Films Prepared by DC Reactive Sputtering using Dual Magnetron Operated at Discharge Current $I_d = 0.5$ A Supplied by an Advanced Energy Pinnacle Plus +5/5 kW Power Supply

U_s (V)	i_s (mA/cm²)	$\mathcal{E}_{bi}$ (MJ/cm³)	h (nm)	a_D (nm/min)	H (GPa)	E^* (GPa)	W_e (%)	H/E^*	σ (GPa)
–25	0.6	0.538	2000	16.7	14.2	208	49	0.068	–0.31
–50	1.4	2.511	1800	15.0	20.6	230	61	0.090	–0.55
–75	1.6	64.560	1700	14.2	24.9	208	70	0.112	–0.88

Source: Musil J., R. Jílek, R. Čerstvý: *Journal of Materials Science and Engineering*, A4(1), 2014, 27–33.

substrate bias U_s is responsible for a slight decrease of the film deposition rate a_D and an increase of the compressive macrostress σ with increasing absolute value of $|U_s|$. The combined action of U_s and i_s is responsible for the increase of H, W_e, and H/E^* ratio of the Ti(Ni)N film with increasing $\mathcal{E}_{bi}$. The most important issue of this experiment is the finding that the hard Ti(Ni)N films with high ratio $H/E^* \geq 0.1$ and high elastic recovery $W_e > 60\%$ can be formed only in case when a sufficient energy $\mathcal{E}_{bi}$ is delivered to the growing film. For more details on the effect of the energy $\mathcal{E}_{bi}$ delivered to the growing film on its mechanical properties, see above also Section 7.4.3.2.

In summary, it can be concluded *that both the addition of selected Me elements in a base coating material and the energy E_{bi} delivered to the coating during its growth are the two key parameters* determining final properties of sputtered coatings. In reactive sputtering of films it is impossible to separate effects of these two key parameters. It is a main reason why the reactive sputtering of films with prescribed properties is an extremely complicated deposition process.

7.4.5 Highly Elastic Multielement Compound Coatings with $H/E^* \geq 0.1$

Several examples given above clearly show that the coatings with high ratio $H/E^* \geq 0.1$ are highly elastic and exhibit a high elastic recovery $W_e \geq 60\%$. This relation between the H/E^* ratio and the elastic recovery W_e seems to be of a general validity. This fact demonstrates the values of the H/E^* ratio and W_e of different coatings reported in many papers, see Table 7.4. In this table some mechanical properties, that is, values of hardness H, effective Young's modulus E^*, elastic recovery W_e, and H/E^* ratio, of ternary nitrides, oxides, oxinitrides, carbonitrides, and multielement equal-mole compounds are given. The values of T_s and U_s are also given in Table 7.4 because the energy $\mathcal{E}$ delivered in the coating during its growth by (i) heating (T_s) and (ii) bombarding and condensing particles (U_s, i_s, a_D, $p_T = p_{Ar} + p_{RG}$) is of key importance for the formation of coatings with a high ratio $H/E^* \geq 0.1$. As can be seen, not all deposition parameters and mechanical properties (H, E^*, W_e, H/E^*) are, however, reported in published papers and many of them are missing in Table 7.4. It is due to the fact that, up to now, a main attention in the formation of hard coatings was concentrated only on their enhanced hardness and almost no attention was devoted to the development of coatings with enhanced toughness and enhanced resistance to cracking. Therefore, no special attention was devoted to the finding of an optimal combination of the deposition parameters and the energy $\mathcal{E}$ necessary to form highly elastic, hard coatings with a high ratio $H/E^* \geq 0.1$. Despite this fact, Table 7.4 clearly shows that (i) the formation of highly elastic coatings with a high ratio $H/E^* \geq 0.1$ is possible and (ii) the coatings with high ratio $H/E^* \geq 0.1$ always exhibit high values of elastic recovery $W_e \geq 60\%$.

Table 7.4 shows that multielement coatings can also exhibit a high ratio $H/E^* \geq 0.1$. These coatings can be as the nonequal-mole as equal-mole compounds. The multielement equal-mole coatings, also called "high entropy alloy compounds," exhibit thermodynamically stable simple solid-solution structures, good mechanical properties, high thermal stability, high corrosion, and wear resistance due to their strong amorphization [82–92]. Differences in properties of the multielement equal-mole coatings containing metal elements only and those containing a mixture of metal

TABLE 7.4
Brief Survey of the Mechanical Properties of Nitride, Carbide, Boride, C-N Based, B-N Based, B-C-N Based, and Multimetal Element Nitride, Carbonitride Coatings with High Ratio $H/E^* \geq 0.1$ and High Elastic Recovery $W_e \geq 60\%$ Recently Reported and the Substrate Temperature T_s and the Substrate Bias U_s Used in Their Formation

Coating	Kind of Coating	U_s (V)	T_s (°C)	H (GPa)	E^* (GPa)	W_e (%)	H/E^*	Reference
Al-Si-N	Nitride	U_{fl}	500	25	180	73	0.139	[81]
Zr-Si-N	Nitride	−100	500	30	260	66	0.115	[93]
Ti-Si-N	Nitride	n.r.	300	34	275	–	0.124	[94]
V-Si-N	Nitride	−50	500	52	–	>80	–	[95]
Al-Cu-N	Nitride	−100	300	47	313	84	0.150	[51]
Cr-Zr-Si-N	Nitride	–	120	32.7	253	–	0.129	[96]
Ti-Al-V-N	Nitride	−100	300	42	387	74	0.108	[54]
Al-Si-Cu-N	Nitride	−100	500	47	298	86	0.157	[97]
Ti-Al-Si-Cu-N	Nitride	−200	200	24	218	–	0.110	[98,99]
TiC_x	Carbide	n.r.	200	24.2	237	–	0.102	[100]
Ti-Si-C	Carbide	−400	400	30	230	–	0.130	[101]
Ti-Si-C-N	C-N based	–	–	55	300	80	0.183	[102]
Ti-Si-C-N	C-N based	−40	400	42.4	300	–	0.140	[103]
Zr-Si-C-N	C-N based	−40	400	29.6	241	–	0.120	[104]
Si-B-C-N	B-C-N based	−100	350	47	290	88	0.162	[105]
Si-B-C-N	B-C-N based	−100	350	–	–	–	–	[106]
Si-B-C-N	B-C-N based	U_{fl}	350	22	170	75	0.124	[107]
Ti-B	Boride	−50	550	73	487	82	0.149	[53]
TiB_2	Boride	−100	<100	23	200	–	0.115	[108]
TiB_2-Ni	Boride	−30	300	44	438	66	0.100	[61]
$HfB_{2.7}$	Boride	−50	500	44	396	87	0.110	[109]
TaB_2	Boride	+75	500	44	348	–	0.126	[110]
Hf-B-N	B-N based	–	–	9.4	176	–	0.053	[111]
Ta-B-N	B-N based	–	–	18	174	54	0.103	[112]
Cr-Ti-B-N	B-N based	−150	250	28.4	259	–	0.110	[113]
Zr-B-C-N	B-C-N based	U_{fl}	450	37	275	85	0.135	[114]
Ti-B-C-N-Si	B-C-Si-N based	−50	RT	≥35	–	>50	≥0.095	[115]
$(AlCrTaTiZr)NC_y$	Carbonitride	−150	RT	31	270	76	0.115	[116]
(AlCrTaTiZr)N	Nitride	n.r.	RT	–	–	–	≤0.100	[85]
$(TiAlCrSiV)_xN_y$	Nitride	n.r.	RT	31.2	300	–	0.104	[86]
(AlCrTaTiZr)N	Nitride	−100	100	~35	~350	–	~0.100	[87]
(AlCrMoSiTi)N	Nitride	−100	300	33	275	–	0.120	[88]
(AlCrNbSiTiV)N	Nitride	−100	300	41	360	–	0.114	[89]
(AlBCrSiTi) N	Nitride	−50	300	23	257	–	0.089	[90]
(TiVCrZrHf)N	Nitride	−200	450	33	276	–	0.119	[91]
(TiVCrZrHf)N	Nitride	−100	500	33.5	–	–	–	[92]

Note: None of these coatings were tested for their resistance to cracking so far. The symbol "–" denotes that no values are reported, n.r. denotes the substrate bias, U_s is not reported (it is not clear if the substrate is floating or grounded).

and metalloid elements (Si, B, C, P, etc.) were not sufficiently explained so far. Despite these facts, it is however reasonable to expect that multielement coatings with $H/E^* \geq 0.1$ will be highly elastic, flexible, and will exhibit an enhanced resistance to cracking. No experiment demonstrating these expectations was, however, performed so far. Therefore, the first main task should be to demonstrate that the multielement coatings with $H/E^* \geq 0.1$ are highly elastic and exhibit high values of elastic recovery $W_e \geq 60\%$. Besides, a fully open question remains: What should be (i) an optimal microstructure of the multielement coating that ensures its high ratio $H/E^* \geq 0.1$, high elastic recovery $W_e \geq 60\%$, compressive macrostress σ, and enhanced resistance to cracking and (ii) the energy $\mathcal{E}$ necessary to form these multielement coatings? Again, it is necessary to underline that a detailed investigation of the interrelationships between the energy $\mathcal{E}$ delivered to the growing coating and its microstructure, mechanical, and physical properties, because these parameters are of key importance for the development of new advanced flexible and multielement coatings. Therefore, besides the investigation of the effect of the elemental composition of multielement coating on its properties, higher attention should be devoted also to the energy $\mathcal{E}$ necessary for its formation.

In summary, it can be concluded that the demonstration of possibility to form highly elastic multielement coatings with high ratio $H/E^* \geq 0.1$ *opens a new direction in the development of advanced flexible multielement coatings.*

7.5 HARD COATINGS RESISTANT TO CRACKING

A low value of the effective Young's modulus E^* resulting in a high ratio $H/E^* \geq 0.1$ is the necessary condition, which the hard coatings with enhanced toughness must fulfill. The high ratio $H/E^* \geq 0.1$ of the hard coating is not, however, a sufficient condition to form hard coatings resistant to cracking. The resistance of hard coatings to cracking strongly depends also on its

i. Elastic recovery W_e.
ii. Microstructure.
iii. Macrostress σ was generated in the coating during its growth.

Relationships among the resistance of hard coating to cracking, the ratio H/E^*, the elastic recovery W_e, the microstructure of coating, and the macrostress σ generated in growing coating are analyzed below in detail. At first, basic methods used for an assessment of the resistance of coating to cracking are briefly described.

7.5.1 Methods Used for Assessment of Resistance of Coating to Cracking

For the assessment of the resistance of coating to cracking different methods were developed [23,63,117–140]. There are, however, three basic methods that are usually used for the determination of the fracture toughness: (1) the stretching of coating (the stretch test), (2) the loading of coating by the diamond indenter at a high load L (the indentation test), and (3) the bending of coating (the bending test). Principles of these

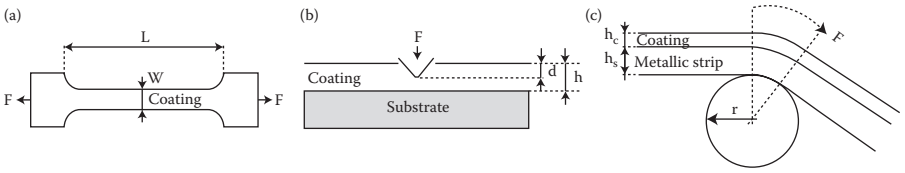


FIGURE 7.14 Schematic illustration of (a) the stretch test, (b) the indentation test, and (c) the bending test used in assessment of the resistance of thin films and coatings to cracking.

tests are schematically illustrated in Figure 7.14. All the three methods are destructive and are based on an evaluation of the force F necessary for the breaking of the coating (Figure 7.14a) or for the generation of cracks in the coating (Figure 7.14b and c). The tested coating is deposited on a substrate. The substrate used in stretch test has a special shape as shown in Figure 7.14a. The shape of substrate for the indentation test is not important because the diamond indenter impression in the coating is very small. The substrate used in the bending test is a thin metallic strip with small width and typical dimensions $60 \times 10 \times 0.1$ mm^3. Below, only the indentation test and the bending test are described because these tests are very convenient for the assessment of the fracture toughness of thin films and coatings.

7.5.1.1 Indentation Test and Fracture Toughness

In the indentation test, the diamond indenter is impressed in the coating under a high load L of about ~1 N. During this test cracks are formed in the coating. The length of cracks is commonly used for the determination of the fracture of bulk materials. The length of the crack is defined in Figure 7.15. Under assumption of the plane strain conditions, the fracture toughness is related to the rate of strain energy released by the following formula [19,128]:

$$K_c = \sigma_f [\pi a/(1 - \nu^2)]^{1/2} \tag{7.3}$$

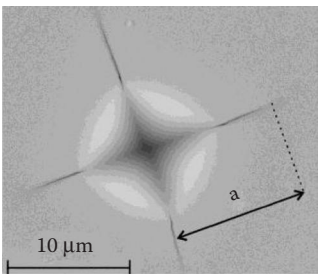


FIGURE 7.15 SEM photo of the diamond indenter impression in 2190 nm thick a-Al_2O_3 coating deposited on Si (100) substrate at load 0.8 N and definition of the length a of the crack. (Adapted from Blažek J.: Pulsed reactive magnetron sputtering of thin films containing copper and characterization of the physical and mechanical properties. PhD thesis, Department of Physics, Faculty of Applied Sciences, University of West Bohemia, Plzen, Czech Republic, 2013.)

Here, σ_f is the fracture strength, a is the length of crack, and ν is the Poisson's ratio. K_c is called the critical stress intensity factor and the fracture toughness increases with increasing K_c. However, this formula can be used only for thick films with a minimum thickness $h_{min} = 2.5(K_c/\sigma_y)^2$ [121]; here, σ_y is the yield stress. For brittle materials with $(K_c/\sigma_y)^2 \approx 0.1$ mm [117] the minimum film thickness is $h_{min} \approx 0.25$ mm. It means that the toughness of the films with the thickness ≤10,000 nm should not be calculated from Equation 7.3, which was derived for the bulk materials.

Despite this limitation, the indentation test can give important information on the resistance of thin films and coatings to cracking. This test must be, however, carried out under correct conditions. These conditions, formulated on the basis of results of many experiments, are described below in detail. It was found that the resistance of the film to cracking depends on many factors. The main factors are the following: (1) the film thickness h, (2) the hardness H_s, and effective Young's modulus E_s^* of the substrate, (3) the hardness H_f and effective Young's modulus E_f^* of the film, (4) the macrostress σ generated in the film, and (5) the microstructure of film. Also, it is important to note that the values of the hardness H_f and the effective Young's modulus E_f^* of the film are strongly influenced by (i) the elements added in the base material of the film and their amounts in the film, and (ii) the energy delivered to the film during its growth. Last two factors also play a key role in the formation of the films resistant to cracking. Effects of all factors on the resistance of the film to cracking given above are further briefly described.

7.5.1.1.1 Effect of the Film Thickness

At first, it is necessary to eliminate the effect of the substrate on the generation of cracks in the film. The effect of the substrate on the cracks formation in the film is very strong, see Figure 7.16. In this figure, photos of the diamond indenter impressions into the Zr-Cu-O film, sputtered simultaneously, that is, under the same deposition conditions, on three different substrates—steel, glass, and Si(100)—at a high load L = 1 N are shown. The cracks generated during the film loading are

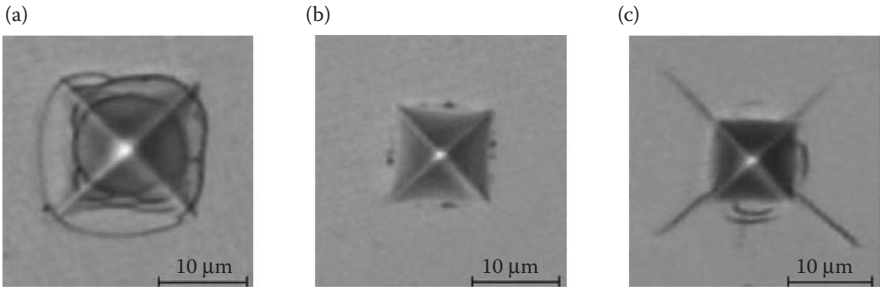


FIGURE 7.16 Photos of diamond indenter impressions into 2000 nm thick amorphous Zr-Cu-O film with 38 at.% Cu and tensile macrostress $\sigma_{Si(100)} = 0.3$ GPa (measured at Si(100) substrate only) deposited on (a) 15330 steel, (b) glass, and (c) Si (100) substrates at load L = 1 N. (Reprinted from *Surface and Coatings Technology*, 200, Jirout M., J. Musil, Effect of addition of Cu into ZrOx film on its properties, 6792–6800, Copyright 2006, with permission from Elsevier.)

very different. Circular cracks are formed in the film deposited on the soft substrate (steel), that is, when $H_f > H_s$; here, H_f and H_s are the hardness of the film and the substrate, respectively. On the contrary, radial cracks are formed in the film deposited on the Si (100) substrate, which is harder (H_s) than the film (H_f); that is, when $H_f < H_s$. It indicates that a transition between the circular and radial cracks with no cracks in the film should exist for the substrate with the hardness H_s not too low and too high compared with the film hardness H_f. Such transition was really found and no cracks were formed in the film deposited on the glass substrate. This experiment clearly shows that the formation of cracks depends on the hardness H_s of the substrate and also indicates that the ratio of the depth d of diamond indenter impression in film and the thickness h of film, that is, the d/h ratio, also plays important role in the assessment of the resistance of film to cracking, see Table 7.5.

The effect of the substrate on the film cracking can be eliminated if the ratio $d/h \leq 0.5$, see Table 7.6 and Figure 7.17. In this figure, the photos of the diamond indenter impression in the W-Si-N film with thickness (a) h = 5700 nm and (b) h = 4100 nm deposited on the 15330 steel substrates are compared. Physical and mechanical properties of these films are given in Table 7.6. This table shows that the values of H_f and E_f^* of the W-Si-N film almost do not depend on the film thickness h. A slightly lower values H_f and E_f^* of the thicker film are connected with a higher energy $\mathcal{E}$ delivered to it during its growth due to a longer deposition time needed for its formation. This experiment shows that there is a direct proportionality among the film thickness h, the value of diamond indenter load L, and the formation of cracks. As expected, no cracks are formed when the ratio $d/h \leq 0.5$. However, the film cracks if the depth d of the diamond indenter impression under the same load L approaches to the film thickness h or is even greater, that is, in the case when the ratio $d/h \geq 1$ as shown in Table 7.6 and displayed in Figure 7.17.

In summary, it can be concluded *that in the case when we want to avoid the cracking of film during the indentation test, the ratio d/h has to be of about* ~0.5 *or lower.*

TABLE 7.5
Mechanical Properties of Zr-Cu-O film with 38 at.% Cu Deposited on Steel, Glass, and Si (100) Substrate Used in the Indentation Test Demonstrating the Effect of the Substrate on the Formation of Cracks in the Film

Material Zr-Cu-O	$H_{f,s}$ (G^*Pa) 10	$E^*_{f,s}$ (GPa) 120	$H_{f,s}/E^*_{f,s}$ 0.083	W_e (%) Film 50 Substrates	Structure Amorphous	d/h (%)	Cracks in Film on Different Substrates
Steel	2.9	212	0.014	10	Polycrystalline	201	Circular
Glass	7.1	69	0.103	57	Amorphous	177	None
Si (100)	12.6	132	0.095	57	Single crystal	158	Radial

Note: Indentation test was performed at load L = 1 N. Mechanical properties of the Zr-Cu-O film (H_f, E_f^*) deposited on Si(100) substrate were measured by the microindentation at a low load L = 20 mN resulting in a low ratio $d/h < 0.1$.

TABLE 7.6
Physical and Mechanical Properties of Two W-Si-N Film Sputtered on 15330 Steel Substrate Used in Indentation Test Demonstrating the Effect of the Film Thickness h on Cracks Formation in the Film

Film	h (nm)	H_f (GPa)	E_f^* (GPa)	H_f/E_f^*	$E_f^*/E_{f,s}^*$	d/h	Cracks in Film on Steel Substrate
a	5700	31.7	280	0.113	1.32	0.49	None
b	4100	34.8	297	0.117	1.42	0.82	Yes

Source: For more details see Musil J. and M. Jirout, *Surface and Coatings Technology*, 201, 2007, 5148–5152.

Note: Indentation test was performed at load L = 1 N. Mechanical properties of film (H_f, E_f^*) were measured by the microindentation at low load L = 20 mN resulting in d/h < 0.1.

7.5.1.1.2 Effect of the Effective Young's Modulus of Substrate

The resistance of film to cracking strongly depends not only on the hardness H_s of the substrate as shown in Table 7.5 but also on its effective Young's modulus E_s^* and the ratio E_f^*/E_s^* of the effective Young's moduli of the film and the substrate, respectively, see Figure 7.18. In this figure, the photos of the diamond indenter impressions in the Mo-Si-N, Zr-Si-N, and W-Si-N films deposited on Si (100) and 15330 steel substrates are compared. Physical and mechanical properties of these films are given in Table 7.7. All three films are x-ray amorphous; for more details see References 93 and 141 through 145.

From Figure 7.18 it can be seen that even relatively hard films with a high hardness H_f ranging from ~25 to ~32 GPa do not crack if (1) the film is x-ray amorphous

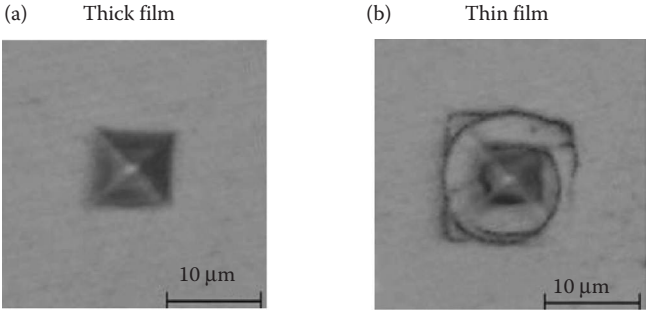


FIGURE 7.17 Illustration of the effect of the thickness h of the W-Si-N film on its cracking during indentation test. Photos of diamond indenter impressions in (a) 5700 nm and (b) 4100 nm thick W-Si-N deposited on 15330 steel substrate at load L = 1 N. (Reprinted from *Surface and Coatings Technology*, 201, Musil J., M. Jirout, Toughness of hard nanostructured ceramic thin films, 5148–5152, Copyright 2007, with permission from Elsevier.)

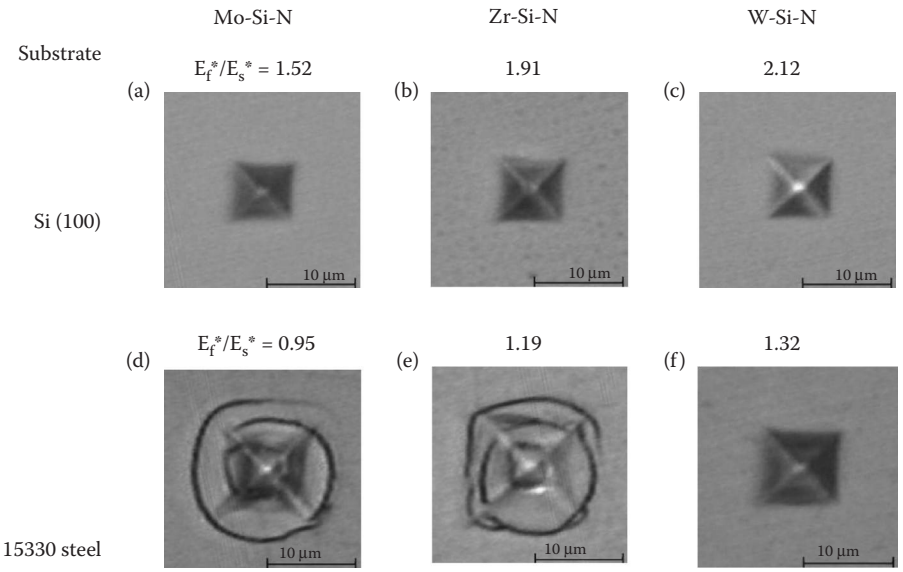


FIGURE 7.18 Illustration of the E_f^*/E_s^* ratio effect on the cracking of Mo-Si-N, Zr-Si-N, and W-Si-N films in the indentation test. Photos of diamond indenter impression in the x-ray amorphous a-(Mo-Si-N) (a,d), a-(Zr-Si-N) (b,e), and a-(W-Si-N) (c,f) films with high content (>50 vol.%) of Si_3N_4 phase deposited on Si (100) and 15330 steel substrates at load L = 1 N. (Reprinted from *Surface and Coatings Technology*, 201, Musil J., M. Jirout, Toughness of hard nanostructured ceramic thin films, 5148–5152, Copyright 2007, with permission from Elsevier.)

and in compression ($\sigma < 0$, see Table 7.7), (2) the substrate is hard ($H_s \leq 0.5\ H_f$), and (3) the effective Young's modulus of substrate is lower than that of the film, that is, $E_s^* < E_f^*$. On the contrary, cracks are formed in films deposited on the soft steel substrate when $E_f^*/E_s^* < 1.3$. It means that a high ratio $E_f^*/E_s^* > 1.3$ is the necessary condition that has to be fulfilled to avoid the film cracking.

In summary it can be concluded that the resistance of film to cracking is determined not only by the mechanical properties of the film but also by the mechanical properties of the substrate. It means that the resistance of film to cracking is the result of a combined action of the film and the substrate. If we want to know a real resistance of the film to cracking, only thick films, which fully eliminate or at least strongly suppress the influence of substrate on the measurement of the film resistance to cracking, must be used in the indentation test. Besides the mechanical properties of the film and the substrate there are also other parameters that influence the resistance of film to cracking. These parameters are the macrostress σ in film, the film microstructure, the kind and amount of the element added in the base material of film, the energy $\mathcal{E}_{bi}$ delivered to the growing film by bombarding ions, and the phase transformation in the film material. The effect of all these parameters of the film cracking is briefly analyzed in the next paragraphs.

TABLE 7.7
Physical and Mechanical Properties of the Mo-Si-N, Zr-Si-N, and W-Si-N Films with High Content (>50 vol.%) of Si_3N_4 Phase Deposited on Si (100) and 15330 Steel Substrates

Film	h (nm)	$H_{f,s}$ (GPa)	$E^*_{f,s}$ (GPa)	H_f/E^*_f	E^3_f/E^{*2}_f	σ (GPa)	d/h	E^*_f/E^*_{Si}	Cracks	E^*_f/E^*_{steel}	Cracks
Mo-Si-N	3100	25.4	201	0.126	0.41	–2.2	0.81	1.52	No	0.94	Yes
Zr-Si-N	5200	30.3	252	0.120	0.44	–1.1	0.63	1.91	No	1.19	Yes
W-Si-N	5300	31.7	280	0.113	0.41	–1.6	0.45	2.12	No	1.32	No
Si (100)		12.6	132								
15330 steel		2.9	212								

Source: Musil J. et al.: *Thin Solid Films*, 478, 2005, 238–247; Musil J., P. Dohnal, P. Zeman: *Journal of Vacuum Science and Technology*, B23, 2005, 1568–1575; Musil J. et al.: *Surface and Coatings Technology*, 200, 2006, 3886–3895; Zeman P., J. Musil: *Applied Surface Science*, 252, 2006, 8319–8325; Daniel R. et al.: *Surface and Coatings Technology*, 201, 2006, 3368–3376; Musil J., P. Zeman: *Solid State Phenomena*, 127, 2007, 31–36.

Note: Indentation test was performed at a high load L = 1 N. Mechanical properties of film (H_f, E^*_f) were measured by the microindentation at a low load L = 20 mN resulting in d/h < 0.1.

7.5.1.1.3 Effect of the Macrostress in Film

The macrostress σ generated in the film during its growth also plays an important role in the film resistance to cracking. This fact is illustrated in Figure 7.19. In this figure, the resistance of cracking of two Al-Cu-O films with almost the same thickness h and different compressive macrostress (σ < 0) are compared: (1) the Al-Cu-O film with a low compressive macrostress σ = –1.5 GPa (the film A) and (2) the Al-Cu-O film with a higher compressive macrostress σ = –2.2 GPa (the film B). The macrostress σ was controlled by the total pressure $p_T = p_{Ar} + p_{O2}$ of a sputtering $Ar + O_2$ gas mixture used in the film deposition. As expected, the film sputtered at a lower value of p_T exhibits a higher compressive macrostress σ. The resistance of these films to cracking was assessed by the indentation test at a high load L = 1 N of the diamond indenter. Mechanical properties of these films, measured at a low load L = 20 mN, are given in Table 7.8. More details are given in Reference 62.

Results of the indentation test of both Al-Cu-O films are displayed in Figure 7.19. The film A with a lower compressive macrostress σ exhibits clear radial cracks. However, the film B with the same content of Cu and a higher compressive macrostress σ exhibits no cracks. This experiment clearly indicates that a higher compressive macrostress helps to close cracks in the film after deloading of the diamond indenter. Besides, Table 7.8 shows that both films exhibit almost the same values of the elastic recovery W_e and the H^3/E^{*2} ratio, which is proportional to the resistance of film to the plastic deformation, but very different values of E^* and H/E^* ratio. It indicates that a decisive role in the assessment of the resistance of film to cracking

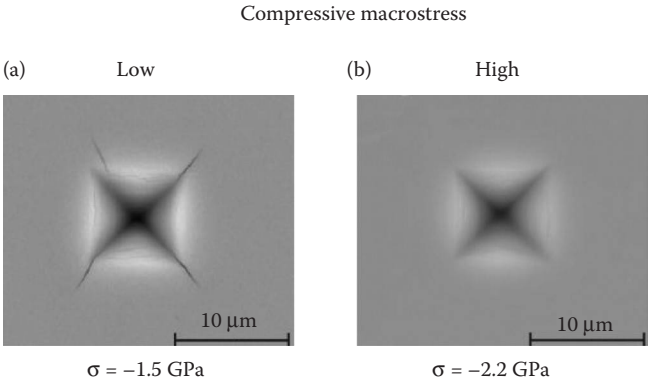


FIGURE 7.19 SEM images of diamond indenter impression in Al-Cu-O films with the same (≈6.4 at.%) Cu content but with (a) low σ = –1.5 GPa (the film A) and (b) high σ = –2.2 GPa (the film B) compressive macrostress generated at a high diamond indenter load L = 1 N. Mechanical properties of these films, measured at a low load L = 20 mN, are given in Table 7.8. (Reprinted from *Applied Surface Science*, 258, Blažek J. et al., Properties of nanocrystalline Al-Cu-O films reactively sputtered by dc pulse dual magnetron, 1762–1767, Copyright 2011, with permission from Elsevier.)

plays the H/E^* ratio and not the H^3/E^{*2} ratio. The ratio H^3/E^{*2} is proportional to the elastic deformation of the film. Therefore, the same values of the ratio H^3/E^{*2} correspond to the same values of the elastic recovery W_e, see Table 7.8. The Al-Cu-O film with a higher value of (i) the compressive macrostress σ and (ii) the H/E^* ratio and a lower value of the effective Young's modulus E^* exhibits no cracks. Similar results were reported also in References 23 and 60. It is very probable that the lowest absolute value of the effective Young's modulus E^* achieved at a given hardness H of the film is a key parameter that decides about the resistance of film to cracking. The confirmation of the last statement needs special investigation, which unfortunately was not carried out so far.

TABLE 7.8
Hardness H, Effective Young's Modulus E^*, Elastic Recovery W_e, H/E^*, and H^3/E^{*2} Ratios of Two Sputtered Al-Cu-O Films with Different Values of the Compressive Macrostress σ

Film	p_T (Pa)	Cu (at.%)	h (nm)	H (GPa)	E^* (GPa)	W_e (%)	H/E^*	H^3/E^{*2} (GPa)	σ (GPa)	Cracks
A	1.5	6.5	1850	19.4	170	70.0	0.114	0.252	–1.5	Yes
B	0.5	6.2	2020	16.7	135	71.0	0.124	0.256	–2.2	No

Source: Blažek J. et al.: *Applied Surface Science*, 258, 2011, 1762–1767.
Note: All mechanical properties were measured at the diamond indenter load L = 20 mN.

In summary, it can be concluded that the compressive macrostress ($\sigma < 0$), which can close cracks, can be used as a self-healing tool for the coatings exposed to a heavy loading. However, it is worthwhile to note that the tensile macrostress ($\sigma > 0$) in the coating is undesirable because it enhances its cracking under loading, see Section 7.5.1.1.4.

7.5.1.1.4 Effect of the Microstructure of Film

The microstructure of the film also strongly influences its resistance to cracking. It is well known that the microstructure of the film can be, according to deposition parameters used in its formation, either a porous microstructure with voids or a dense microstructure free of voids. The porous microstructure is composed of columns separated by voids and corresponds to that of the zone I of the Thornton's structural zone model (SZM) [146]. However, the dense, free-of-voids microstructure corresponds to the zone T neighboring with the zone I.

Experiments performed so far clearly show that the coatings with columnar microstructure composed columns separated by voids easily crack. Cracks propagate along boundaries of columns. This fact is illustrated in Figure 7.20 where (a) the fracture cross section of ~1300 nm thick TiC/a-C:H composite coating and (b) the surface morphology of this coating after loading by the diamond indenter at the load L = 190 mN are displayed [147]. Photos of SEM micrographs given in Figure 7.20 clearly show that (i) the TiC/a-C:H film has a columnar microstructure (corresponding to the zone I of the Thornton's SZM) composed of columns perpendicular to the film/substrate interface, (ii) the TiC/a-C:H film easily cracks under loading of its surface by the diamond indenter at high loads L, and (iii) the crack readily propagates

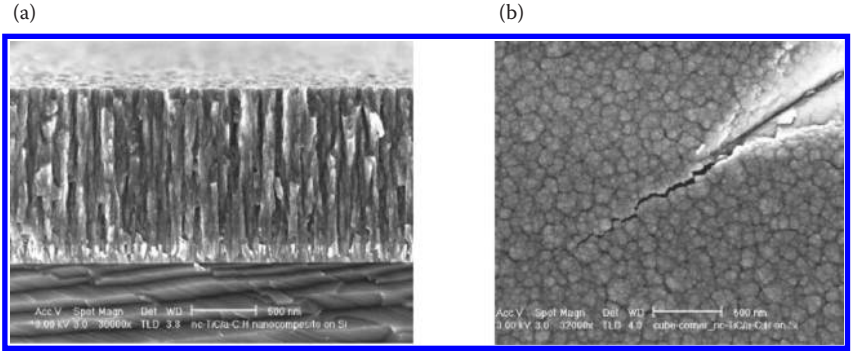


FIGURE 7.20 Photos of SEM micrographs show (a) the fracture cross section of ~1300 nm thick TiC/a-C:H composite coating (29 at.% Ti, 49 at.% C, and 22 at.% H) sputtered on Si-wafer in argon/acetylene atmosphere at $U_s = -100$ V, $T_s = RT$ (there is no intentional heating of the substrate but its temperature T_s was increased during deposition by ion bombardment to 185°C), $p_T = p_{Ar} + p_{C2H2} = 0.327$ Pa, $\phi_{C2H2} = 80$ sccm and (b) the surface morphology of coating with a crack generated by diamond indenter impressed in it at normal load L = 190 mN. (Reprinted from *Surface and Coatings Technology*, 207, Musil J., Hard nanocomposite coatings: Thermal stability, oxidation resistance and toughness, 50–65, Copyright 2012, with permission from Elsevier.)

through boundary regions separating individual columns. A similar result is reported also in Reference 148.

These findings indicate that the film microstructure can dominate over the mechanical properties of both the film and the substrate as to the resistance of film to cracking. Therefore, the films with enhanced resistance to cracking should have a dense, free-of-voids microstructure with fibrous grains corresponding to the zone T of the Thornton's SZM. Moreover, it is worthwhile to mention that the films produced in the zone T exhibit a compressive macrostress ($\sigma < 0$). It means that *the dense, free-of-voids microstructure and the compressive macrostress* ($\sigma < 0$) *in the film are further conditions necessary to produce hard films and coatings with enhanced resistance to cracking.*

7.5.1.1.5 Effect of the Addition of Selected Element in Base Material

The addition of a selected element in the base material of film can strongly influence its physical and mechanical properties. Therefore, the film can exhibit different resistances to cracking according to the kind and content of element added in its base material. Mainly, the mechanical properties of film are responsible for changes of its resistance to cracking. This fact is demonstrated on a mechanical behavior of the Al-Cu-O coatings in the indentation test, see Figure 7.21. This figure shows the photos of SEM images of the impression of the diamond indenter in the Al-Cu-O film with different Cu content. Physical and mechanical properties of these films are given in Table 7.9.

Figure 7.21 shows the effect of the amount of Cu added in the Al_2O_3 film on its cracking during loading by the diamond indenter at the high load L = 1 N. This figure shows that only the pure Al_2O_3 film (0 at.% Cu) and the Al-Cu-O film with a low (2 at.%) content of Cu exhibit clear radial cracks. No cracks are formed in the Al-Cu-O films with a higher (>2 at.%) content of Cu. This finding correlates well with changes of the mechanical properties of Al-Cu-O film caused by increase of the Cu content in the film, see Table 7.9. Simultaneously, this experiment indicates that the resistance of the Al-Cu-O film to cracking increases with

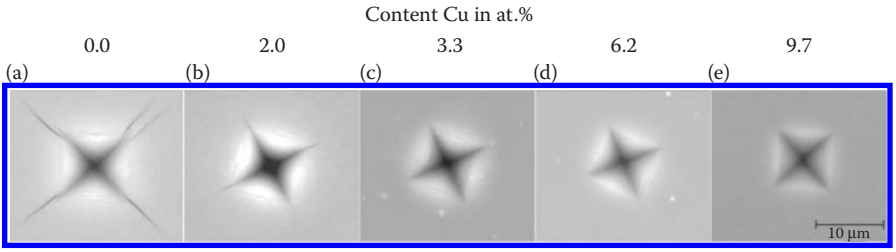


FIGURE 7.21 SEM images of diamond indenter impression in (a) nc–(γ-Al_2O_3)/a-Al_2O_3 and (b)–(e) nc–(Al_{8-2x}, Cu_{3x})O_{12}/a–(Al-Cu-O) composite films formed at a high load L = 1 N. Mechanical properties of these films are given in Table 7.9. (Reprinted from *Applied Surface Science*, 258, Blažek J. et al., Properties of nanocrystalline Al-Cu-O films reactively sputtered by dc pulse dual magnetron, 1762–1767, Copyright 2011, with permission from Elsevier.)

TABLE 7.9
Hardness H, Effective Young's Modulus E^*, Elastic Recovery W_e, H/E^* Ratio, and H^3/E^{*2} Ratio of the Al-Cu-O Films with Different Cu Content and Macrostress σ Generated in Them during Sputtering

Film	Cu (at.%)	h (nm)	H (GPa)	E^* (GPa)	W_e (%)	H/E^*	H^3/E^{*2} (GPa)	σ (GPa)	Cracks
a	0	2520	7.3	100	49.4	0.073	0.04	–0.40	Yes
b	2.0	1930	10.0	111	57.5	0.090	0.08	–2.23	Yes
c	3.3	1900	14.5	130	66.6	0.112	0.18	–2.32	No
d	6.2	2020	16.7	135	71.0	0.124	0.26	–2.24	No
e	9.7	2070	18.5	143	74.8	0.129	0.31	–2.20	No

Note: Mechanical properties were measured at a low value of the diamond indenter load L = 20 mN. Indentation test was performed at high load L = 1 N.

increasing amount of Cu in the film. However, the amount of Cu incorporated in the Al-Cu-O film has to overpass a critical value of Cu content, which ensures that the Al-Cu-O film is highly elastic and exhibits a high ratio $H/E^* \geq 0.1$ and a high value of the elastic recovery $W_e \geq 60\%$. The Al-Cu-O films with $H/E^* > 0.1$ and $W_e > 60\%$ are well resistant to plastic deformation ($H^3/E^{*2} > 0.1$). More details are given in Reference 39.

The experiment described in this paragraph demonstrates that (1) the resistance of film to cracking can be controlled by the addition of selected element in the base material of film via variation of its mechanical properties. Besides, this experiment shows that *high values of (i) the H/E^* ratio* ($H/E^* \geq 0.1$) *and (ii) the elastic recovery* W_e ($W_e \geq 60\%$) *are further necessary conditions, which ensure that the film will exhibit an enhanced resistance to cracking.*

7.5.1.1.6 Effect of Energy Delivered to Growing Film by Bombarding Ions

Main parameter that can be used to form a highly elastic film with a high ratio $H/E^* \geq 0.1$ and high value of elastic recovery $W_e \geq 60\%$ is not only the addition of a selected element in the base material of film but also the energy $\mathcal{E}_{bi}$ delivered to the film by bombarding ions during its growth. This fact is illustrated on properties of (Ti,Ni)N films [67]. The increase of the negative substrate bias U_s used in sputtering increases the power density W_s at the substrate and it makes possible to produce harder, highly elastic (Ti,Ni)N films with high ratio $H/E^* \geq 0.1$, high value of the elastic recovery $W_e > 60\%$, and compressive macrostress ($\sigma < 0$), which are resistant to cracking, see Table 7.10. This fact is illustrated in Figure 7.22. In this figure the cracking resistance of the (Ti,Ni)N film sputtered at low ($W_s = 0.02$ W/cm^2) and high ($W_s = 0.13$ W/cm^2) ion bombardment is compared. The resistance of (Ti,Ni)N films to cracking was assessed by the indentation test at a high load L = 200 mN of diamond indenter.

This experiment shows that the energy $\mathcal{E}_{bi}$ delivered to the growing film by bombarding ions, similarly as the addition of a selected element in the base material

TABLE 7.10
Hardness H, Effective Young's Modulus E^*, Elastic Recovery W_e, H/E^* and H^3/E^{*2} Ratio of the (Ti, Ni) N Films Sputtered from TiNi (90/10 at.%) Targets at Different Values of Negative Substrate Bias U_s and Macrostress σ Generated in Them during Sputtering

	i_s	W_s	a_D	h	H	E^*	W_e		σ		
U_s (V)	(mA/cm²)	(W/cm²)	(nm/min)	(nm)	(GPa)	(GPa)	(%)	H/E^*	(GPa)	d/h	Cracks
–25	0.6	0.02	15.9	2100	15.4	228	49	0.068	0.17	0.46	Yes
–75	1.8	0.13	13.6	1800	24.7	228	71	0.104	–0.46	0.43	No

Note: All mechanical properties were measured at the diamond indenter load L = 20 mN. Indentation test was performed at high diamond indenter load L = 200 mN. Here, d is the depth of diamond indenter impression in coating at load L = 200 mN.

of film, also strongly influences mechanical properties of the sputtered film. The energy $\mathcal{E}_{bi}$ increases the hardness H, the H/E^* ratio, and the elastic recovery W_e of film and converts its tensile macrostress ($\sigma > 0$) to a compressive macrostress ($\sigma < 0$).

In summary, it can be concluded that the ion bombardment of growing film makes it possible to form the films with high ratio $H/E^* \geq 0.1$ and high elastic recovery $W_e \geq 60\%$. Such films exhibit an enhanced resistance to cracking. Also, it is worthwhile to note that the addition of (i) the selected element and (ii) the energy $\mathcal{E}_{bi}$ in the film are two complementary processes, which operate simultaneously in the formation of the films with enhanced resistance to cracking.

7.5.1.1.7 Effect of the Phase Transformation Toughening

Besides the substrate, mechanical properties of the film, its macrostress and microstructure also its phase transformation toughening enhances the resistance of film

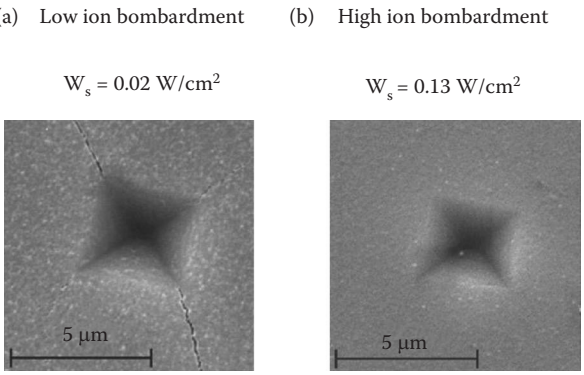


FIGURE 7.22 Photos of the SEM images of diamond indenter impression in (Ti,Ni)N film sputtered at (a) low (W_s = 0.02 W/cm²) and (b) high (W_s = 0.13 W/cm²) ion bombardment formed at high load L = 200 mN.

to cracking. The enhancement of the resistance of film to cracking by the phase transformation toughening is based on an extraction of the fracture energy and its consumption for the phase transformation of the film material. This process can be started by the pressure of the diamond indenter penetrating in the film during the indentation test. This fact is illustrated in Figure 7.23. In this figure, optical microscope (OM) images of an impression of the diamond indenter in two Zr-Al-O films with low (53%) and high (75%) value of the elastic recovery W_e are compared. The Zr-Al-O film with low value of $W_e = 53\%$ is denoted as the film A, the Zr-Al-O film with high value of $W_e = 75\%$ is denoted as the film B. Physical and mechanical properties of these films are given in Table 7.11.

This experiment shows that a less elastic film A with $W_e = 53\%$ exhibits well bounded impressions due to its strong plastic deformation. When the diamond indenter load L is increased to 1 N small round cracks are formed because the ratio $d/h \approx 0.5$ and the substrate starts to influence the indentation test. On the contrary, a highly elastic film B with $W_e = 75\%$ exhibits a round diffused deformation zone. This zone is believed to be a region in which the tetragonal t–ZrO_2 phase of Zr-Al-O film was converted into the monoclinic m–ZrO_2 phase as was already demonstrated in the experiment described in Refs. [149–152]. No tendency to cracks formation is observed probably due to cracks closing (self-healing) by the high compressive macrostress ($\sigma = -1$ GPa) and the high elastic recovery ($W_e = 75\%$) of Zr-Al-O film.

In summary, it can be concluded that all experiments given in this section show that less elastic films with a low value of the elastic recovery $W_e < 60\%$ and a low ratio $H/E^* < 0.1$ easily crack. However, *highly elastic films with a high value of the elastic recovery* $W_e \geq 60\%$ *and high ratio* $H/E^* \geq 0.1$ *exhibit an enhanced resistance to cracking.* To avoid an effect of the substrate on the resistance of coating, *the load L*

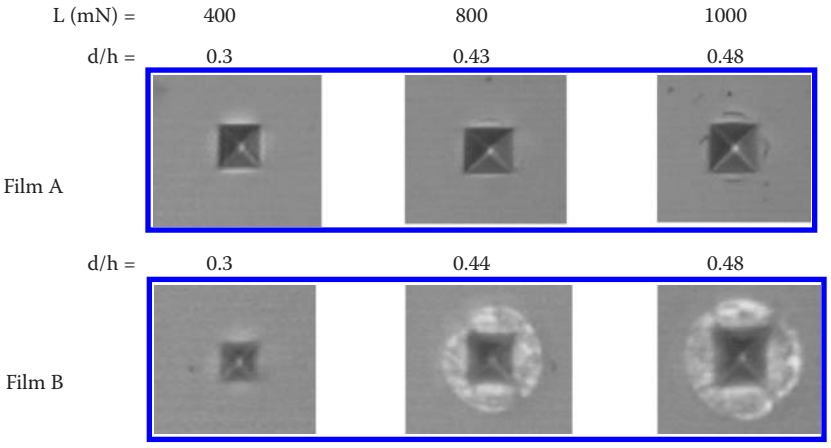


FIGURE 7.23 Photos of the optical microscope (OM) images of diamond indenter impression in the surface of Zr-Al-O film with low (53%) and high (75%) value of the elastic recovery W_e created at high values of diamond indenter load L = 400, 800, and 1000 mN.

TABLE 7.11
Thickness h, Hardness H, Effective Young's Modulus E^*, Elastic Recovery W_e, Ratio H/E^* of Zr-Al-O Film with Low (53%) and High (75%) Values of W_e Sputtered at the Average Discharge Current $I_{da} = 2$ A, Substrate Temperature $T_s = 500°C$, Substrate Bias $U_s = U_{fl}$, Total Sputtering Gas Pressure $p_T = p_{Ar} + p_{O2} = 1$ Pa using AC Pulse Dual Magnetron on Si(100) Substrates

Film	p_{O2} (Pa)	h (nm)	a_D (nm/min)	σ (GPa)	H (GPa)	E^* (GPa)	W_e (%)	H/E^*	Cracks
A	0.05	5000	110	0.4	13.6	142	53	0.050	Yes
B	0.13	5100	63	−1.0	17.9	152	75	0.118	No

Note: Values of H, E^*, and W_e were measured at low value of diamond indenter load L = 10mN.

in the indentation test has to be selected in such a way that the ratio $d/h \leq 0.5$; here, d is the depth of the diamond impression in the film at a load L.

7.5.1.2 Bending Test

The resistance of coating to cracking can be easily assessed by its bending when the coating is deposited on a flexible substrate. This test, called the bending test, imitates the coating deformation in a more realistic way. The principle of the bending test is shown in Figure 7.24 [39,63]. The coating is deposited on a metallic strip and the coated strip is bended around a fixed cylinder of radius r_1 using a moving cylinder of radius r_2 up to an angle $\alpha = \alpha_c$ at which cracks in the coating occur. The maximum angle α up to which the coated strip can be bended is 180°. If no cracks in the coating are formed, the coating is considered as resistant to cracking in bending around the fixed cylinder of radius r_1. The resistance of coating to cracking is the higher the smaller is radius r_1 of the fixed cylinder.

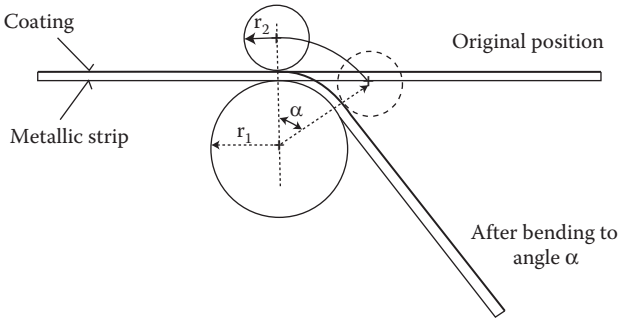


FIGURE 7.24 Schematic illustration of bending test used to create cracks in the coating deposited on a metallic strip. r_1 and r_2 is the radius of fixed and moving cylinder, respectively. (Reprinted from *Surface and Coatings Technology*, 207, Musil J., Hard nanocomposite coatings: Thermal stability, oxidation resistance and toughness, 50–65, Copyright 2012, with permission from Elsevier.)

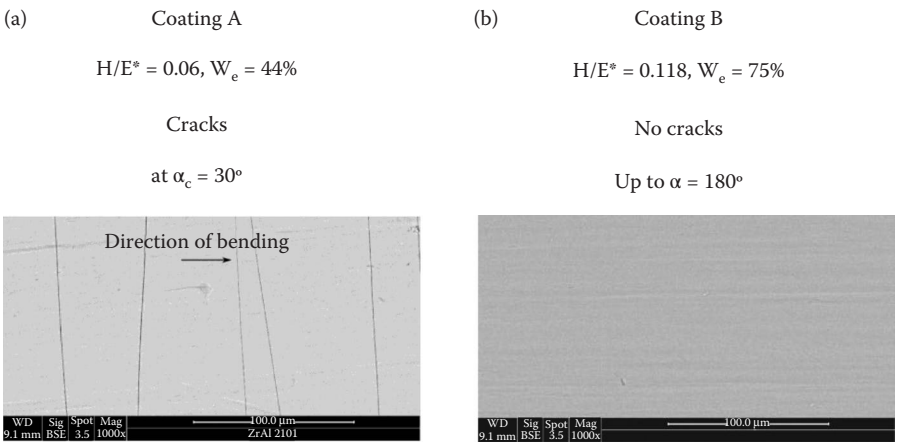


FIGURE 7.25 Surface morphology of ~3000 nm thick Zr-Al-O coating deposited on Mo strip after bending around steel cylinder of radius $r_1 = 12.5$ mm. (Reprinted from *Surface and Coatings Technology*, 206, Musil J., Sklenka J., Cerstvy R., Transparent Zr-Al-O oxide coatings with enhanced resistance to cracking, 2105–2109, Copyright 2012, with permission from Elsevier.)

The cracking of the coating during bending of the coated metallic strip, as in the indentation test, also strongly depends on mechanical properties of the coating, mainly on the H/E^* ratio and the elastic recovery W_e. This fact is illustrated in Figure 7.25. In this figure, as example, the surface morphology of the brittle and tough Zr-Al-O coatings deposited on Mo strip after bending around the fixed cylinder of radius $r_1 = 12.5$ mm is shown. The following two Zr-Al-O coatings were selected for this experiment: (1) the Zr-Al-O coating with a low ratio $H/E^* < 0.1$ and a low elastic recovery $W_e = 44\%$ (coating A), and (2) the Zr-Al-O coating with a high ratio $H/E^* > 0.1$ and a high elastic recovery $W_e = 75\%$ (coating B). Both coatings were deposited on the Mo strip ($80 \times 15 \times 0.1$ mm^3) and then bended around the cylinder of radius $r_1 = 12.5$ mm.

Figure 7.25 shows that the coating A with the low ratio $H/E^* = 0.06$ cracks already after bending at the angle $\alpha_c = 30°$; cracks are perpendicular to the direction of bending of the coated Mo strip. On the contrary, *the coating B with the high ratio* $H/E^* = 0.118$ *exhibits strongly enhanced resistance to cracking and no cracks are created even after bending up to angle* $\alpha = 180°$. The enhanced resistance to cracking of the coating B is due to the fact that the material with $H/E^* > 0.1$ is tough and more elastic compared to the coating A with $H/E^* \leq 0.1$ whose material is brittle and less elastic. The load L applied to the coating B is distributed over a wider area and thereby its resistance to cracking is enhanced.

7.5.1.2.1 Comparison of Cracks Generated in Coating by Bending and Indentation

In assessment of the resistance of coating to cracking it is important to know whether cracks are caused by the coating material only or whether cracks are

TABLE 7.12
Deposition Parameters, Physical, and Mechanical Properties of Sputtered Al-Cu-N Coatings Whose Surface Morphology is Displayed in Figure 7.26 and Results of the Assessment of their Resistance to Cracking by the Indentation and Bending Test

Coating	h (nm)	a_D (nm/min)	T_s (°C)	U_s (V)	i_s (mA/cm²)	σ (GPa)	Cu content (at.%)	H (GPa)	E^* (GPa)	W_e (%)	H/E^*	d/h	Cracks Indentation	Cracks Bending
Coating A	1810	60	400	−100		−2.4	7.5	19.3	170	69	0.114	1.30	Yes	No
Coating B	2780	49	400	−100	1.5	−0.7	10.7	19.3	169	71	0.114	yes	No	Yes

Note: d is the depth of diamond indenter at load L = 1 N.

generated also as a consequence of other factors, for example, by the substrate. This fact is illustrated on the Al-Cu-N coatings with different thickness h and different values of the compressive macrostress ($\sigma < 0$). Deposition parameters, thickness h, deposition rate a_D, macrostress σ, and mechanical properties of these coatings are given in Table 7.12. The Al-Cu-N coatings were deposited on the Si (100) substrate for the indentation test and on the Mo strip for the bending test. The thinner Al-Cu-N coating with a higher compressive macrostress is denoted as the coating A, the thicker Al-Cu-N coating with a lower compressive macrostress is denoted as the coating B. Both coatings were tested by the indentation using the diamond indenter at a high load L = 1000 mN and also by the bending method in which the Mo strip coated by the Al-Cu-N coating was bended around a fixed cylinder of radius r_1 = 12.5 mm. Results of these tests are displayed in Figure 7.26. More details are given in Reference 140.

From Figure 7.26 it is clearly seen that the coating A with a high compressive macrostress $\sigma = -2.4$ GPa cracks in nanoindentation test but does not cracks in bending test. In the case of the coating B with a lower compressive macrostress $\sigma = -0.7$ GPa the situation is completely opposite; the coating B exhibits no cracks in the nanoindentation but it cracks in the bending test. This apparent paradox can be, however, explained by the dominant influence of the substrate over that of the compressive macrostress σ in the coating A on its resistance to cracking and the

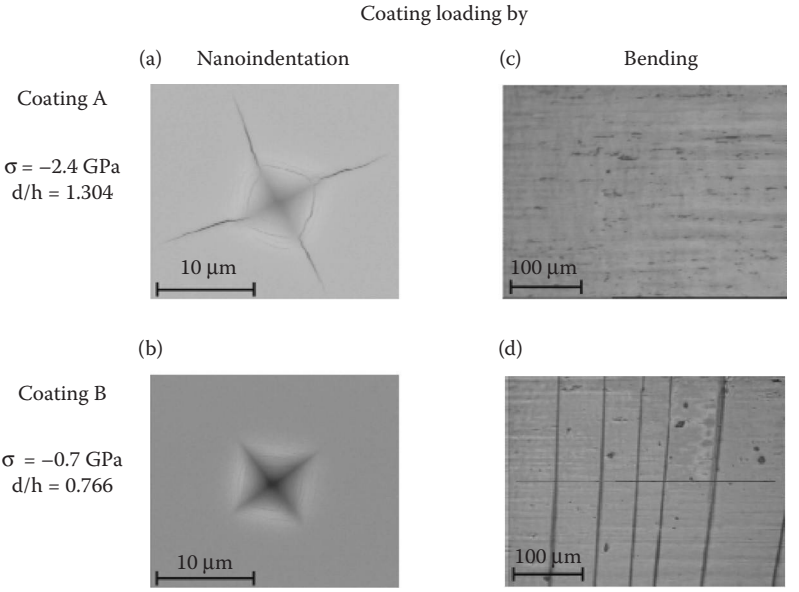


FIGURE 7.26 Photos of the SEM images of (a,b) indentation impression in surface and (c,d) surface morphology after bending of highly elastic Al-Cu-N coatings with the same hardness H = 19.3 GPa and high ratio $H/E^* = 0.114$ and thickness (i) h = 2780 nm (the photos b,d), and (ii) h = 1660 nm (the photos a,c). Nanoindentation test was performed at diamond indenter load L = 1 N. The Mo strip covered by Al-Cu-N coating was bended around cylinder of radius r = 12.5 mm.

dominant influence of the compressive macrostress σ over that of the substrate in the coating B. The dominant effect of the substrate in the coating A is due to a high ratio d/h > 1. On the contrary, no cracks formation in the coating B during indentation indicates a negligible influence of the substrate on cracking of the coating B due to its higher thickness resulting in a low ratio d/h < 1. Low compressive macrostress σ = −0.7 GPa in the coating B is, however, insufficient to close cracks created in this coating during bending. The high compressive macrostress σ = −2.4 GPa fully compensates a tensile macrostress (σ > 0) generated in the coating A during its bending.

The findings given above are of fundamental importance in the assessment of the resistance of coating to cracking. This experiment clearly shows that the assessment of the resistance of the same coating to cracking by indentation and bending can give completely opposite results. It means, always when the resistance of the coating to cracking is measured by the indentation method the ratio d/h should be ≤ 0.5 to avoid the effect of substrate on indentation test, and in papers reporting on the resistance of coating to cracking assessed by the indentation the ratio d/h should be given to avoid a wrong information.

In summary it can be concluded that

1. The measurement of the resistance of the coating to cracking by the nanoindentation can be strongly influenced by the substrate mainly in cases when the thickness h of coating is small and the ratio d/h ≥ 1.
2. The resistance of the coating against cracking can be correctly measured by the indentation only in the case when the ratio d/h ≤ 0.5. Therefore, the value of ratio d/h should be always given in reports on the fracture toughness of the coating measured by the indentation.
3. The measurement of the resistance of the coating to cracking by bending a metallic strip coated by tested coating avoids an effect of mechanical properties of the substrate on the measurement and thus it seems to be more reliable compared with the nanoindentation test. *The compressive macrostress* (σ < 0) *in the coating compensates a tensile macrostress* (σ > 0) *generated in bending and clearly shows its beneficial role in the enhancement of the resistance of coating to cracking due to self-healing of generated cracks.*

7.5.1.2.2 Effect of Coating Microstructure

Also, it is worthwhile to note that the Zr-Al-O coatings with Zr/Al > 1 and $H/E^* > 0.1$ resistant to cracking are the nc-ZrO_2/a-Al_2O_3 composites composed of ZrO_2 nanograins embedded in the amorphous a-Al_2O_3 matrix [65]. The cross-section microstructure of this coating is very dense, see Figure 7.27. This figure shows that the Zr-Al-O coatings with Zr/Al > 1 and $H/E^* > 0.1$ exhibits a dense, free-of-voids microstructure penetrated by interrupted nanocolumns perpendicular to the coating/substrate interface. This microstructure strongly differs from the columnar microstructure composed of densely packed columns separated by voids, corresponding to that of the zone I of the Thornton's SZM displayed below in Figure 7.29, which very easily cracks along boundaries of columns, see Figure 7.20. It means that the high

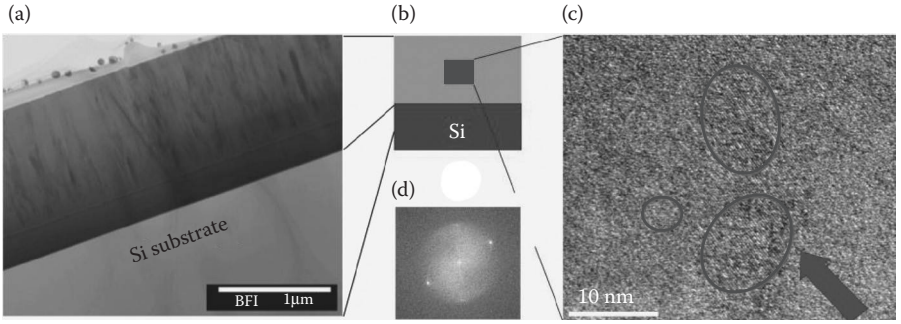


FIGURE 7.27 Photo of (a) SEM image (c) HRTEM image of the cross section of Zr-Al-O film with Zr/Al > 1 deposited on Si (100) substrate and (d) the Fast Fourier Transformation (FFT) image from the place denoted by the square in schematic figure of film/Si substrate couple denoted by (b). (Reprinted from *Surface and Coatings Technology*, 207, Musil J. et al., The effect of addition of Al in ZrO_2 thin film on its resistance to cracking, 355–360, Copyright 2012, with permission from Elsevier.)

ratio $H/E^* > 0.1$ and the high elastic recovery $W_e \geq 60\%$ are necessary conditions but not sufficient ones to ensure the enhanced resistance of the coating to cracking. The dense, free-of-voids microstructure of the coating is also of key importance for the enhancement of its resistance to cracking.

In summary, it can be concluded that *the coatings well resistant to cracking under loading have to* (i) *be highly elastic* ($W_e > 60\%$), (ii) *exhibit the high ratio* $H/E^* > 0.1$ *and the compressive macrostress* ($\sigma < 0$), and (iii) *have the dense, voids-free microstructure*. This finding is of great importance for many applications in which the coating is deposited on flexible substrates, for instance, in flexible electronics, nano- and micromechanics, formation of multifunctional coatings, and so on.

7.5.2 Design of Hard Flexible Coatings Resistant to Cracking

Detailed investigation described above clearly showed that there are general rules based on which it is possible to start a design of hard coatings resistant to cracking. These general rules were discovered during a detailed investigation of the interrelationships between the deposition parameters of coatings and their properties. It was found that the coatings resistant to cracking should exhibit simultaneously the following properties

1. The low effective Young's modulus E^* resulting in a high ratio $H/E^* \geq 0.1$ and the high elastic recovery $W_e \geq 60\%$
2. The compressive macrostress ($\sigma < 0$)
3. The dense, voids-free microstructure

All these properties (H, E^*, W_e, H/E^* ratio, macrostress σ, microstructure, elemental, and phase composition) of hard coatings resistant to cracking are controlled by

(1) the energy $\mathcal{E}_p = \mathcal{E}_{ca} + \mathcal{E}_{bi}$ delivered to the growing coating by condensing atoms ($\mathcal{E}_{ca}$) and bombarding ions ($\mathcal{E}_{bi}$) and the substrate heating (T_s), and (2) the elements added in the base material of coating, which moreover decide also on the value of the melting temperature T_m of the coating material. The relationships among the energy $\mathcal{E}_{bi}$, the macrostress σ generated in the growing coating, the melting temperature T_m of coating material, and the microstructure of the coating are clearly illustrated in Figures 7.28 through 7.30.

Figure 7.28 shows the macrostress σ as a function of the energy $\mathcal{E}_{bi}$. The effect of the melting temperature T_m on the magnitude and kind of macrostress σ and on the microstructure of coating are also clearly seen from this figure. From Figure 7.28, four general very important issues can be drawn:

1. The macrostress σ changes from tensile (σ > 0) to compressive (σ < 0) with increasing energy $\mathcal{E}_{bi}$.
2. There is a critical value of $\mathcal{E}_{bi} = \mathcal{E}_c$ at which films exhibit zero macrostress σ = 0.
3. The magnitude of the macrostress σ and the critical energy $\mathcal{E}_c$ depend on the melting temperature T_m of the coating material.

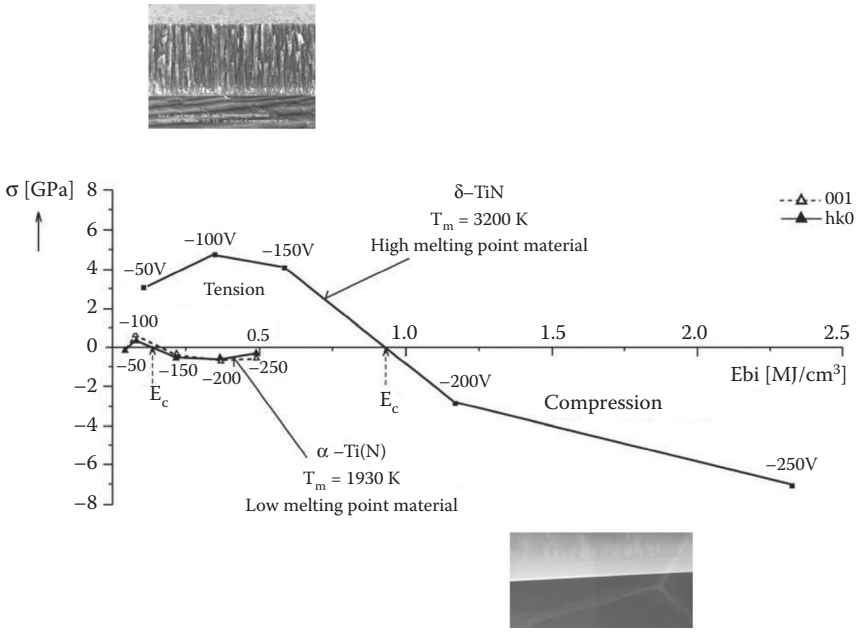


FIGURE 7.28 Macrostress σ in sputtered α–Ti (N) and δ–$TiN_{x\approx1}$ films as a function of energy $E_{bi} = U_s i_s / a_D$ delivered to them by bombarding ions at $p_T = p_{Ar} + p_{N2} = 5$ Pa and $T_s = 350°C$, that is, at $T_s/T_m = 0.32$ and 0.19 for the α–Ti(N) and the δ–$TiN_{x\approx1}$films, respectively. (Reprinted from *Surface and Coatings Technology*, 60, Musil J. et al., Relation of deposition conditions of Ti-N films prepared by dc magnetron sputtering to their microstructure and macrostress, 484–488, Copyright 1993, with permission from Elsevier.)

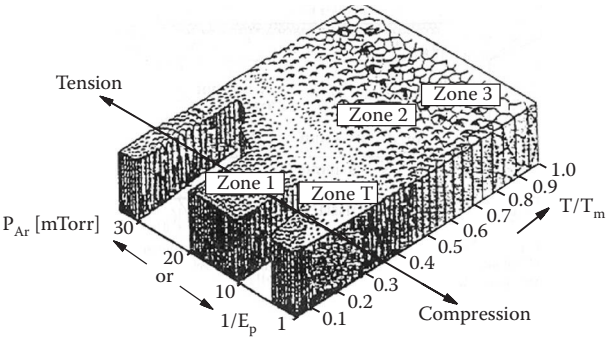


FIGURE 7.29 Structural zone model (SZM) of sputtered metallic films developed by J.A. Thornton. (Adapted with permission from Thornton, J. A.: *Metal Finishing* 1979, 77(5), 83–87. Copyright 1979, Metal & Plastics Publications, Inc.)

4. The macrostress σ and the critical energy $\mathcal{E}_c$ increase with increasing T_m of coating material.

The macrostress σ generated in the growing film also very well correlates with its microstructure; see Figure 7.29 and photos inserted in Figure 7.28. Figure 7.29 shows the evolution of the film microstructure in 3D representation as a function of the T_s/T_m ratio (the equilibrium heating of substrate) and the sputtering pressure

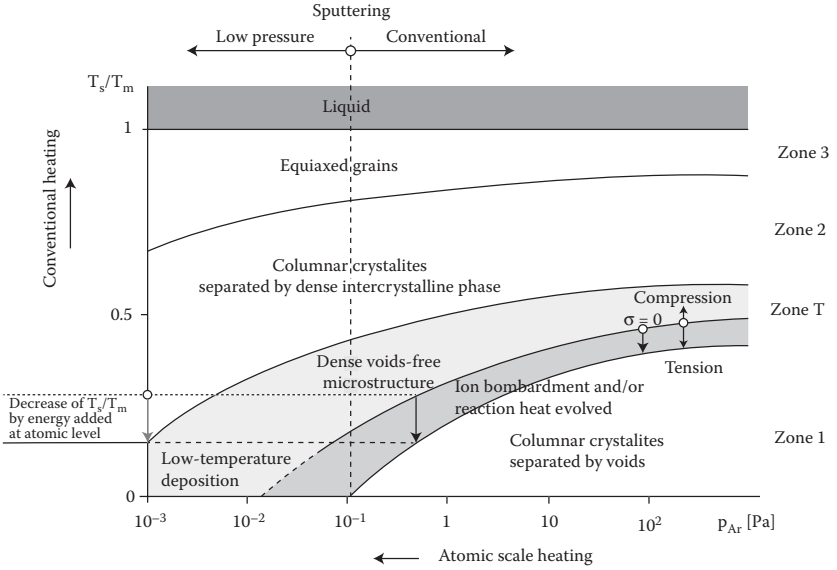


FIGURE 7.30 Thornton's structural zone model (SZM) of sputtered films extended to the region of low sputtering gas pressures. (Reprinted from *Vacuum*, 50, Musil, J., Low-pressure magnetron sputtering 363–372, Copyright 1998, with permission from Elsevier.)

of argon p_{Ar}, that is, as a function of *the energy* $\mathcal{E}_p$ *delivered to growing film by incident neutral particles* (the nonequilibrium heating). The evolution of the film microstructure displayed in Figure 7.29 is called the structural zone model (SZM). The SZM of sputtered metallic films was developed by J.A.Thornton in 1977 [146]. The SZM is divided in four zones: (1) zone 1 composed of the tapered crystallites separated by voids, (2) zone T composed of the fibrous grains embedded in voids-free amorphous matrix, (3) zone 2 composed of the columnar grains separated by dense intercrystalline boundaries [154], and (4) zone 3 composed of the recrystallized grain structure. The boundary between zone 1 and zone T corresponds to zero macrostress $\sigma = 0$ and separates the films with a low-density microstructure composed of columns separated by voids (the zone 1) from the films with a dense, voids-free microstructure composed of fibrous grains embedded in an amorphous intergrain phase (the zone T). This is a main reason why properties of the films formed in zone 1 and zone T so strongly differ and why the films formed in zone T exhibit unique properties.

Many experiments performed so far show that the films formed in zone T exhibit not only dense, voids-free microstructure composed of tiny fibrous grains embedded in an amorphous matrix and compressive macrostress $\sigma < 0$ but also a high ratio $H/E^* \geq 0.1$ and high values of the elastic recovery $W_e \geq 60\%$. It means that films formed in the zone T can automatically exhibit an enhanced resistance to cracking. However, a sufficient energy $\mathcal{E}$ has to be delivered in films during their growth.

The boundary between zone 1 and zone T can be influenced by (1) the energy $\mathcal{E}_{bi}$ delivered to the growing film by bombarding ions when films are formed at negative substrate biases $U_s < 0$ [155,156] and (2) by the energy $\mathcal{E}_{fn}$ delivered by fast neutral particles, which is controlled by the pressure p of sputtering gas and is increased by decreasing p. The shift of the boundary between zone 1 and zone T makes it possible to form films with the microstructure of zone T at low values of T_s/T_m ratio, even at unheated substrates (T_s = RT). Here, it is important to underline that the deposition of the films with microstructure corresponding to zone T of the Thornton's SZM at low values of T_s/T_m ratio is possible also without an ion bombardment ($U_s = U_{fl}$) of the growing film, simply by sputtering of the film at very low values of the sputtering gas pressure p, see Figure 7.30. However, new low-pressure magnetrons need to be developed for the formation of films at very low pressures p [157]. The possibility to form the films with the microstructure corresponding to the zone T of the Thornton's SZM at low substrate temperatures $T_s \leq 100°$ C is of great potential for many advanced applications, namely for flexible electronics, flat panel displays, MEMS systems, formation of functional films on polymer foils and fabrics, and so on. The formation of nanocrystalline or even crystalline films with the microstructure corresponding to zone T at low substrate temperatures $T_s \leq 100$°C can be realized also by the addition of selected elements in the film because the melting temperature T_m of such films decreases compared to pure films and the T_s/T_m ratio increases.

In summary, it can be concluded that the analysis reported in this section clearly shows that *the formation of films with microstructure corresponding to zone T of the Thornton's SZM requires deliver to films during their growth a sufficiently high*

energy $\mathcal{E}$ to exceed the critical energy $\mathcal{E}_c$ at which the films with zero macrostress ($\sigma = 0$) *are created*. The magnitude of the critical energy $\mathcal{E}_c$ depends on (i) the sputtering gas pressure p, (ii) the melting temperature T_m of the film material, (iii) the substrate bias U_s and the substrate ion current density i_s, (iv) the kind and amount of the element added in the film, and (v) the contamination of film by oxygen O and nitrogen N from a residual atmosphere in the deposition chamber at low deposition rates a_D of the film.

7.6 FLEXIBLE MULTIFUNCTIONAL COATINGS

Coatings that exhibit two or several functions are called *the two- or multifunctional coatings*. The material of such coatings has to exhibit a unique combination of mechanical properties, elemental and phase composition, and microstructure. It is a quite difficult task because every property of the coating requires different combination of deposition parameters (CDPs) used in its creation, see Figure 7.31. From Figure 7.31a it can be seen that the one-functional coating with a property 1 can be prepared in a certain range of deposition parameters, for instance, the sputtering gas pressure p ranging from p_1 to p_2. Standard properties of the coating can be achieved in a wider range of sputtering gas pressure p. On the contrary, unique properties of the coating are already achieved in a narrower range of p. In the case when the property of coating, for example, the hardness H, is required to be unique and maximal, the CDPs must be optimized, for instance, the pressure p_{max} must be used as shown in Figure 7.31a. The optimalization of the CDPs is relatively easy in the formation of the one-functional materials. However, more complicated is the creation of the two- and multifunctional materials. Regions of the CDPs enabling to form materials with two- or several functions simultaneously are usually overlapping or even mutually separated. It means that the formation of two-functional materials is a quite difficult task and almost always is not possible to form the coating with two unique properties having maximal possible values simultaneously, for instance, transparent conductive oxides (TCO's) with the highest possible optical transparency and the highest possible electric conductivity. The formation of three-functional materials is still more complicated.

Experiments, however, indicate that the formation of two- and multifunctional materials is possible and their unique properties can be optimized, see Figure 7.31. The maxima of different properties of the material are at different points on the horizontal axis as shown in Figure 7.31b and these maxima can be shifted along horizontal axis by the variation of further process parameters, for instance, by the variation of the substrate temperature T_s, substrate bias U_s, and so on. This way, a separation distance between the maxima of individual properties can be reduced and two- or even three-functional materials can be formed, see Figure 7.31b and c. The main role in the reduction of the separation distance is played by the energy $\mathcal{E}$ delivered to the coating during its growth and/or during its postdeposition treatment, for example, thermal annealing, ion implantation, and so on. As examples, the two-functional nc-TiC/a-C nanocomposite coatings with the low coefficient of friction

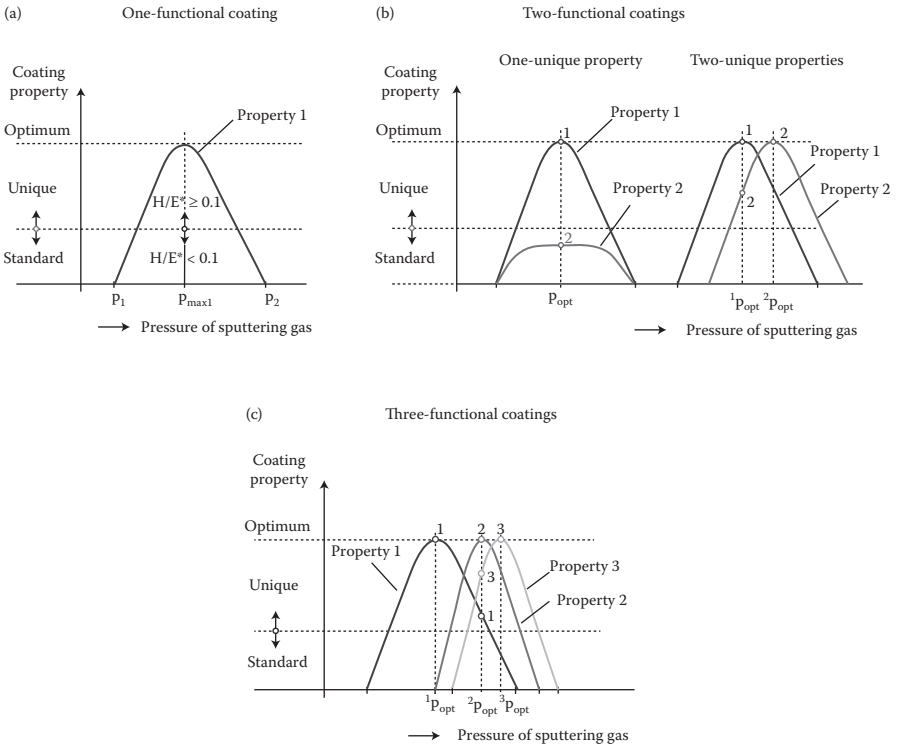


FIGURE 7.31 Schematic illustration of combination of deposition parameters (CDPs) used in formation of one-, two-, and three-functional coatings. (a) CDP optimized for the formation of coating with one unique function (e.g., hard coatings with high ratio $H/E^* \geq 0.1$), (b) CDP optimized for the formation of coating with two unique functions, and (c) CDP optimized for the formation of coating with three unique functions.

μ and the low wear rate k and the three-functional Al-Cu-N nanocomposite coating with (i) the high killing activity of *Escherichia coli* bacteria, (ii) the high flexibility, and (iii) the high resistance to cracking are given.

7.6.1 Two-Functional Tribological Hard nc-TiC/a-C Nanocomposite Coatings

Every tribological coating must contain a "friction phase," which controls its coefficient of friction μ and wear rate k. The presence of friction phase in the coating is, however, insufficient to achieve minimum values of μ and k. The mechanical properties of the coating also play an important role in decreasing of μ and k. This fact is illustrated on the interrelationships between the tribological (μ, k) and the mechanical (H, E^*, W_e) properties of the nc-TiC/a-C nanocomposite coating, see Figures 7.32 through 7.34. In Figure 7.32, the coefficient of friction

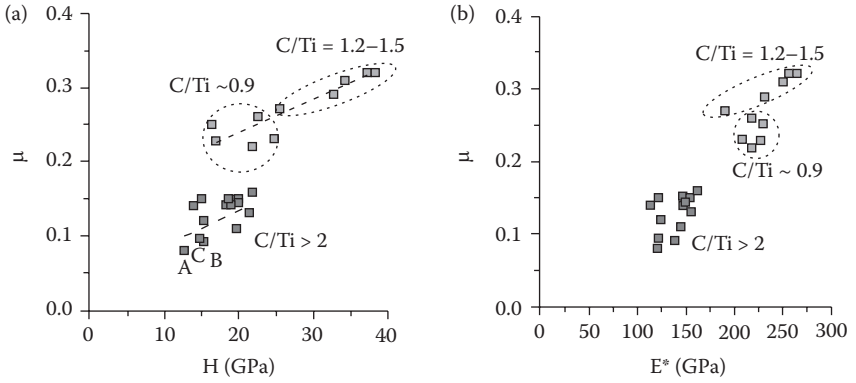


FIGURE 7.32 Friction coefficient μ of 3000 nm thick Ti-C coating with low (≤2) and high (>2) value of the C/Ti ratio as a function of (a) hardness H and (b) effective Young's modulus E^*. (Figures are based on data in Musil J. et al.: *Journal of Vacuum Science and Technology A*, 28(2), 2010, 244–249.)

μ is displayed as a function of the hardness H and the effective Young's modulus E^* of the Ti-C coating, that is, as the functions μ = f (H), Figure 7.32a, and μ = f (E^*), Figure 7.32b.

From Figure 7.32 it can be seen that μ = f (H) is an ambiguous function of H. Two values of μ can be obtained for the same value of H. However, the dependence μ = f (E^*) is an unambiguous function. The friction μ of the nc-TiC/a-C coating decreases with decreasing value of the effective Young's modulus E^*. From this figure it can be seen that *the lowest value of the friction* μ *exhibits the Ti-C coating with the lowest value of* E^*. It is an important finding. However, it is worthwhile to note that the lowest value of E^* is not a sufficient condition to reach the lowest value of friction μ. This fact shows the interrelationships between the hardness H, the elastic recovery W_e, and the ratio H/E^* of the Ti-C coating, see Figure 7.33.

Figure 7.33 shows that the Ti-C coatings with (i) the high ratio C/Ti > 2, (ii) the hardness H ranging from ~12 to ~22 GPa, (iii) the high ratio $H/E^* \geq 0.1$ ranging from ~0.1 to ~0.15, and (iv) the high elastic recovery W_e ranging from ~60 to ~80% exhibit the lowest values of E^*. It means that for the reduction of the friction coefficient μ important is also the C/Ti ratio (the film elemental composition), the high ratio H/E^* ranging from ~0.1 to ~0.15, and the high coating elasticity ($W_e \geq 60\%$). The fact that the ratio H/E^* is not too high (up to ~0.15 only) is also important. The increase of the ratio H/E^* above 0.15 is connected not only with the increase of H but mainly with the increase of E^* what results in increase of the coefficient of friction μ as shown in Figure 7.32. It means that an increase of the H/E^* ratio only is not a sufficient indicator for the production of coatings with the lowest coefficient of friction μ, see Figures 7.33 and 7.34.

Figure 7.34 shows an evolution of the coefficient of friction μ and the wear rate k of the Ti-C coating with different ratio C/Ti with increasing H/E^* ratio. From this figure it is seen that the lowest values of both the coefficient of friction μ and

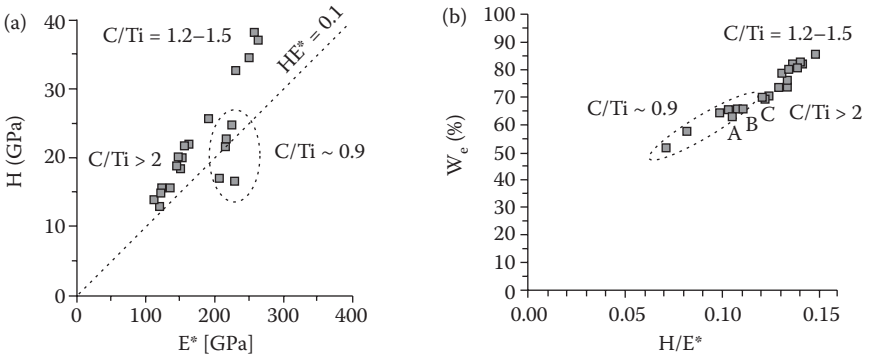


FIGURE 7.33 Hardness H and elastic recovery W_e of 3000 nm thick Ti-C coating with low (≤2) and high (>2) value of the C/Ti ratio as a function of (a) effective Young's modulus E^* and (b) ratio H/E^*.

wear rate k exhibit the Ti-C coatings with a high ratio C/Ti > 2 only. These coatings are carbon rich, two-phase nc-TiC/a-C nanocomposite coatings composed of the nc-TiC grains embedded in an amorphous a-C matrix as the evolution of the structure of Ti-C coating with increasing C/Ti content, displayed in Figure 7.35, clearly shows. This figure shows the evolution of the structure of the Ti-C coating, magnetron sputtered from a composed (Ti + C) target (C (99.99) round plate fixed to the cathode body with Ti (99.5) ring of different inner diameter) on unheated Si (100) substrates at $I_d = 0.5$ A, $U_s = U_{fl}$, $d_{s\text{-}t} = 60$ mm, and $p_{Ar} = 1$ Pa, with increasing C/Ti ratio; for more details see Reference 158. The Ti-C coatings with C/Ti ≤ 1.5 are

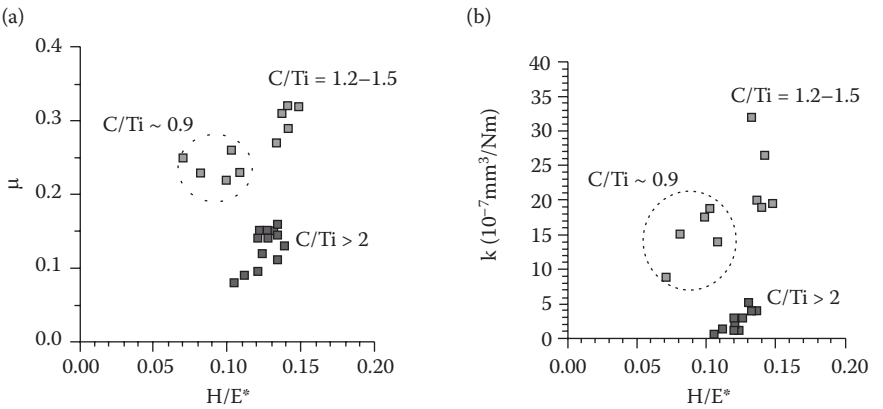


FIGURE 7.34 Coefficient of friction μ (a) and wear rate k (b) of 3000 nm thick Ti-C coating with low (≤1), medium (1.2–1.5) and high (>2) value of the C/Ti ratio as a function of ratio H/E^*. (Figures are based on data in Musil J. et al.: *Journal of Vacuum Science and Technology A*, 28(2), 2010, 244–249.)

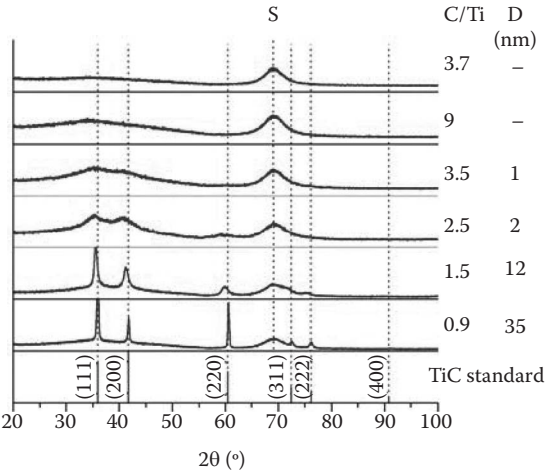


FIGURE 7.35 Evolution of structure of TiC/a-C coating decreases with increasing C/Ti ratio. S denotes the reflection from Si substrate. The dotted lines show positions of x-ray reflections from powder TiC standard. (Reprinted with permission from Musil J. et al.: *Journal of Vacuum Science and Technology A*, 28(2), 2010, 244–249. Copyright 2010, Američan Vacuum Society.)

polycrystalline coatings characterized with TiC (111), TiC (200), and TiC (220) x-ray reflections. The polycrystalline Ti-C coatings gradually change with increasing C/Ti ratio through nanocrystalline coatings with C/Ti ratio ranging from ~2.5 to ~3.5 to x-ray amorphous a-(Ti,C) coatings at a high ratio C/Ti ≥ 3.5. The nanocrystalline nc-TiC/a-C coatings are composed of the TiC nanocrystals embedded in the a-C matrix. The intensity of x-ray reflections from the nanocrystalline coatings decreases and their width increases with increasing C/Ti ratio up to a full disappearance of TiC reflections in a broad x-ray amorphous peak of the a-C phase. The size D of TiC grains increases with increasing C/Ti ratio, see Figure 7.35 and Reference 158. At present, it is not however, fully clear whether the decrease of the intensity of x-ray reflection is due to the decrease of the size of TiC grains or to the decrease of the number of TiC grains.

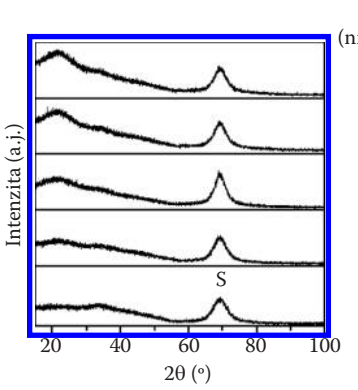
In summary it can be concluded *that the coefficient of friction* μ *and the wear rate k of the Ti-C coating can be optimized by tuning of its mechanical properties.* Recent experiments indicate that (i) the lowest value of the effective Young's modulus E^* achieved at a given hardness H and resulting in the high $H/E^* \geq 0.1$ and (ii) the high elastic recovery $W_e \geq 60\%$ are of key importance in the formation of the nc-TiC/a-C coatings with the lowest values of the coefficient of friction μ and the wear rate k. This finding indicates that *the coatings with a low ratio* $H/E^* < 0.1$ *should not exhibit the best tribological properties*, that is, the lowest coefficient of friction μ and the lowest wear rate k.

7.6.2 Two-Functional Highly Transparent Si-Zr-O Nanocomposite Coatings

Highly transparent SiO_2 coatings with a low amount (≤3 at.%) of Zr were reactively deposited from a molten magnetron target composed of Si round plate fixed to the magnetron cathode body by a Zr ring [159]. The Si-Zr-O coatings were deposited on Si(100) and glass substrates held on a floating potential U_{fl} ($U_s = U_{fl}$) at the substrate temperature $T_s = 500°C$, the target power density $W_{ta} \geq 27$ W/cm^2 , and the total sputtering gas pressure $p_T = p_{Ar} + p_{O2} = 1$ Pa using a pulsed dual magnetron supplied by an AC pulse MSS-10 power supply and operated with repetition frequency $f_r = 0.83$ kHz in bipolar mode; W_{ta} is the target power density averaged over the pulse period $T = 1/f_r$.

The Si-Zr-O coatings sputtered at higher partial pressures of oxygen $p_{O2} \geq 0.2$ Pa and higher target power densities $W_{ta} \geq 27$ W/cm^2 are x-ray amorphous [160], see Figure 7.36. These coatings were deposited at a high deposition rate a_D increasing from ~55 to ~533 nm/min with the target power density W_{ta} increasing from 27 to 85 W/cm^2. Under these conditions the sputtering of Si-Zr-O coatings is enhanced by an evaporation of atoms from the molten Si target. The evaporation of target atoms dominates over sputtering of atoms at the target power densities $W_{ta} \geq 60$ W/cm^2. This process is *called the ionized magnetron evaporation*. More details are given in Refs. [159,160].

All x-ray amorphous Si-Zr-O coatings are perfectly optically transparent, see Figure 7.37. There is almost no difference in the optical transparency of the uncoated glass substrate and the glass substrate coated by several micrometers thick Si-Zr-O films. Also, there are no interference maxima and minima superposed on the dependence $T = f(\lambda)$. It indicates that the index of refraction of the Si-Zr-O coating with a low amount of Zr and the glass is almost the same and no



a_D (nm/min)	W_{ta} (W/cm^2)	h (nm)
533	85.3	8000
315	72.6	6300
150	54.7	4500
88	40.7	2650
55	27.5	1640

FIGURE 7.36 Evolution of XRD patterns of Si-Zr-O coatings deposited from molten Si target at $U_s = U_{fl}$, $T_s = 500°C$, $p_T = p_{Ar} + p_{O2} = 1$ Pa with increasing target power density W_{ta} (From Šatava V.: Reactive magnetron deposition of selected oxide films and their properties, PhD thesis, 2011, Department of Physics, Faculty of Applied Sciences, University of West Bohemia, Plzen, Czech Republic.)

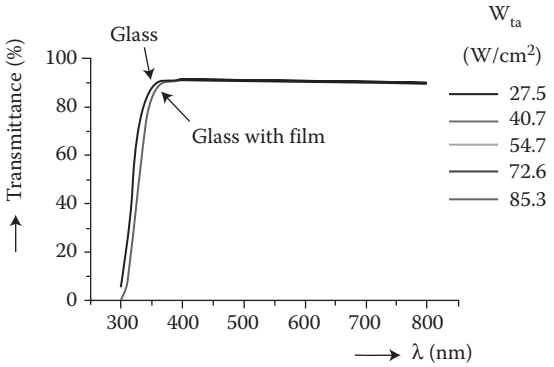


FIGURE 7.37 Transmittance T of more than 5000 nm thick Si-Zr-O films sputtered on the microscopic glass substrate at different values of W_{ta} as a function of wavelength λ of incident electromagnetic wave. (Reprinted from *Thin Solid Films*, 519, Musil J., V. Šatava, P. Baroch, High-rate reactive deposition of transparent SiO_2 films containing low amount of Zr from molten magnetron target, 775–777. Copyright 2010, with permission from Elsevier.)

reflections of incident electromagnetic waves at the glass/coating interface takes place. The coated glass exhibits a very small shift of transmittance T of the coated glass to longer wavelengths only. Both parameters—the high deposition rate a_D (increasing with increasing W_{ta}) and the evaporation from the molten target (dominating at high target loadings, that is, at the target power densities $W_{ta} > 60$ W/cm^2)—slow down the crystallization of the deposited film due to a decrease of the energy $\mathcal{E}$ delivered to it at high deposition rates a_D, see Equation 7.2; more details are given in the Appendix 1.

The Si-Zr-O coatings with a low amount (≤3 at.%) of Zr exhibit also very interesting mechanical properties, see Table 7.13. The most important is the finding that all as-deposited Si-Zr-O coatings with a low content of Zr (≤3 at.%) exhibit high ratios $H/E^* \geq 0.1$ and $H^3/E^{*2} \geq 0.14$ and high values of the elastic recovery $W_e \geq 70\%$. It indicates that the highly elastic Si-Zr-O coatings with ≤3 at.% Zr (1) should be

TABLE 7.13
Variable Parameters (p_{O2}, W_{ta}), Deposition Rate a_D, Thickness h, and Mechanical Properties of Si-Zr-O Coating Sputtered on Microscopic Glass Substrates at $U_s = U_{fl}$, $T_s = 500°C$, $d_{s-t} = 80$ mm, $p_T = p_{Ar} + p_{O2} = 1.1$ Pa

Film No.	p_{O2} (Pa)	W_{ta} (W/cm²)	a_D (nm/min)	h (nm)	H (GPa)	E^* (GPa)	W_e (%)	H/E^*	H^3/E^{*2} (GPa)
1	0.20	27.5	55	1640	9.1	73	70	0.125	0.141
2	0.28	40.7	88	2650	9.0	68	71	0.132	0.158
3	0.34	54.7	150	4500	9.3	66	73	0.141	0.185
4	0.41	72.6	315	6300	9.3	64	76	0.145	0.196
5	0.65	85.3	533	8000	9.5	63	76	0.151	0.216

well resistant to plastic deformation (high ratio H^3/E^{*2}) and (2) exhibit an enhanced resistance to cracking due to a high ratio $H/E^* \geq 0.1$ and a high elastic recovery $W_e > 60\%$; for more details see Section 7.5 where conditions under which the coating is resistant to cracking are described in detail.

In summary, it can be concluded that the highly elastic Si-Zr-O coatings with a low (≤3 at.%) Zr content are *the two-functional Si-Zr-O coatings*. These coatings are (1) highly transparent for electromagnetic waves at $\lambda \geq 350$ nm (the measurement was carried out up to 800 nm only) and (2) flexible due to high values of (i) the ratio $H/E^* > 0.1$ and (ii) the elastic recovery $W_e \geq 70\%$.

7.6.3 Three-Functional Highly Elastic, Antibacterial Al-Cu-N Nanocomposite Coatings Resistant to Cracking

Antibacterial coatings are usually designed as one-functional antibacterial coatings or two-functional antibacterial/protective coatings. However, in most cases the mechanical properties of two-functional antibacterial/protective coatings are insufficient to exhibit an enhanced resistance to cracking. Therefore, three-functional antibacterial/protective/flexible coatings are now under development. As examples, the two-functional Cr-Cu-O coatings and the three-functional antibacterial/protective/flexible Al-Cu-N coatings are described in this section in detail.

7.6.3.1 Two-Functional Cr-Cu-O Coatings

Recently, new two-functional antibacterial/protective x-ray amorphous a-(Cr-Cu-O) coatings were developed [66]. It was shown that the antibacterial activity of a-(Cr-Cu-O) coatings strongly depends on the Cu content and 100% killing of the *E. coli* bacteria at their surfaces is achieved only in the case when a Cu content in the Cr-Cu-O coating is >15 at.%. The antibacterial activity needs no external activation. The a- (Cr-Cu-O) coatings with >15 at.% Cu effectively kill bacteria in daylight as in the dark. This fact is clearly illustrated in Figures 7.38 and 7.39.

Figure 7.38 shows photos of Petri dishes covered with bacterial suspensions, which was in a contact with the amorphous a-(Cr-Cu-O) films containing various amount of Cu in the dark for 5 h [66]. Black points on these photos are colony units (CUs) of *the E. coli* bacteria. No bacteria are killed in the suspension, which was in contact with the uncoated Si substrate. However, a very efficient killing of bacteria is seen on the photos of Petri dishes covered with the bacterial suspensions, which were in a contact with the a-(Cr-Cu-O) films containing ≥22 at.% Cu. Figure 7.39 shows the efficiency of killing of *the E. coli* bacteria in daylight and in the dark. More details are given in Reference 66.

The hardness H of the Cr-Cu-O coating decreases with increasing Cu content from $H \approx 6$ GPa to $H \approx 3.7$ GPa at 15 and 28 at.% Cu content in the coating, respectively. The Cr-Cu-O films with ≥15 at.% Cu content are sufficiently hard to ensure the mechanical protection of surfaces. However, these coatings exhibit low values of (i) the ratio $H/E^* < 0.1$ and (ii) the low elastic recovery $W_e < 50\%$ and thus they are not resistant to cracking in bending. It means that *the Cr-Cu-O oxide coatings with a high* (≥15 *at.%*) *Cu content are the two-functional antibacterial/protective coatings*

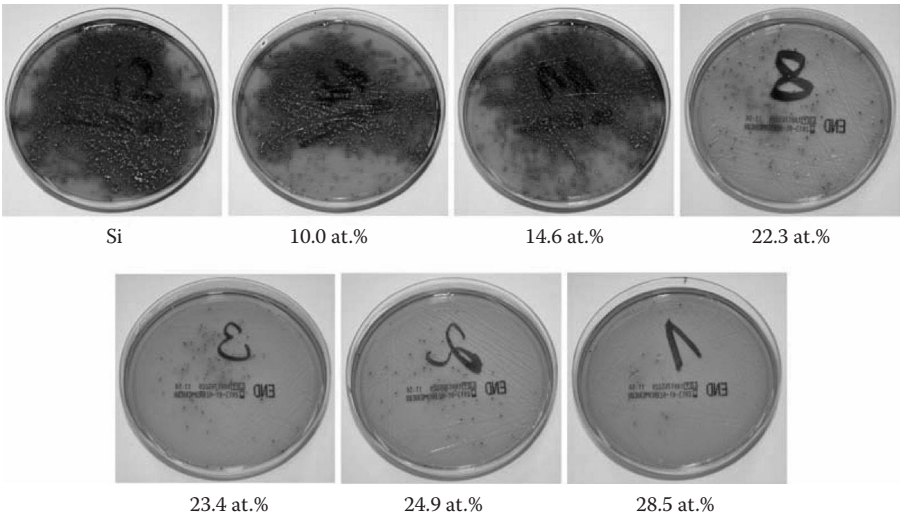


FIGURE 7.38 Photos of Petri dishes with Endo agar and bacterial colonies cultivated from bacterial suspensions which were in contact with a-(Cr-Cu-O) coatings with various at.% of Cu in the dark for 5 h. The films were sputtered on Si(100) substrate at floating potential ($U_s = U_{fl}$) and $T_s = 500°C$. (Reprinted from *Applied Surface Science*, 276, Musil J. et al., Antibacterial Cr-Cu-O films prepared by reactive magnetron sputtering, 660–666, Copyright 2013, with permission from Elsevier.)

only. These coatings exhibit a strong antibacterial activity and ensure quite a good mechanical protection of surfaces, for instance, against its surface scratching.

7.6.3.2 Three-Functional Al-Cu-N Coatings

Recently, new flexible antibacterial Al-Cu-N coatings were developed [161]. The Al-Cu-N nitride coatings exhibit substantially higher (i) hardness ($H \approx 20$ GPa), (ii) H/E^* ratio ($H/E^* > 0.1$), (iii) elastic recovery ($W_e \geq 70\%$), and strongly enhanced resistance to cracking compared with the antibacterial Al-Cu-O oxide coatings, see Table 7.14 and Figure 7.40.

Here, i_{sp} is the averaged substrate ion current density over negative pulse of substrate bias U_{sp}.

In Table 7.14 main deposition parameters of the Cr-Cu-O and Al-Cu-N coatings, their physical and mechanical properties are summarized. While the antibacterial Al-Cu-O coating with ≥15 at.% Cu deposited on a Mo strip ($55 \times 15 \times 0.15$ mm^3) easily cracks during bending around the cylinder of radius r = 12.5 mm, no cracks are formed in the antibacterial Al-Cu-N coating, see Figure 7.40. Also, a high antibacterial activity of the Al-Cu-N coating is achieved at a lower Cu content compared with antibacterial Cr-Cu-O coatings with a high (≥15 at.%) Cu content. Almost 100% killing of *E. coli bacteria* is achieved already at the surface of the Al-Cu-N coating with ~10 at.% Cu. Next advantage of the Al-Cu-N nitride coatings compared with the Cr-Cu-O oxide coatings is their higher hardness H, higher elastic recovery $W_{e,}$ and higher deposition rate a_D of their production; more details

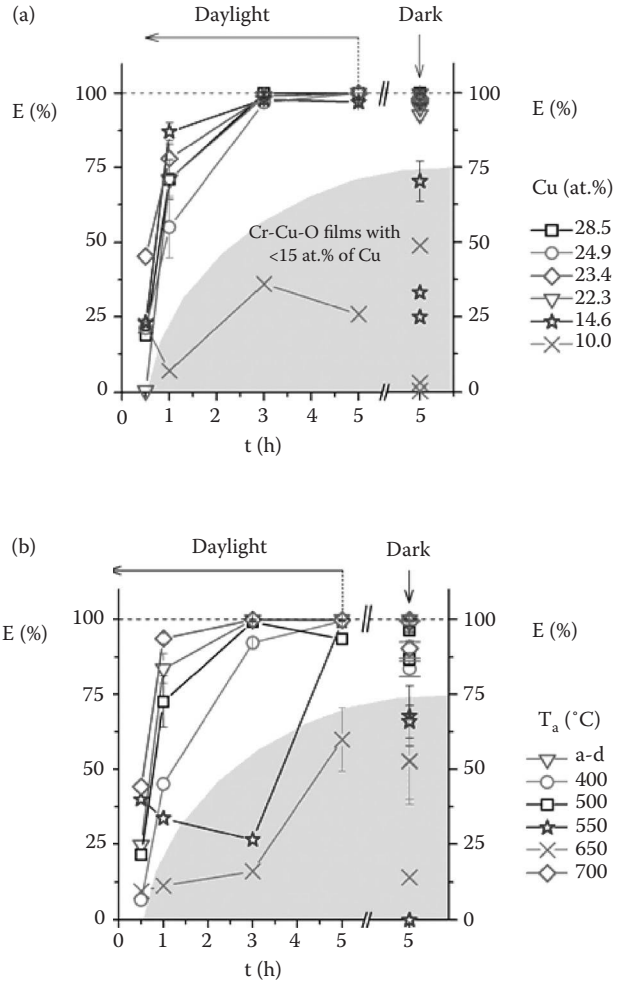


FIGURE 7.39 Antibacterial efficiency *E* of (a) as-deposited Cr-Cu-O films with various Cu content (b) Cr-Cu-O films with various structure induced by a postdeposition rapid thermal annealing (RTA) to different maximum temperature $T_{a\,max}$ against the bacteria *E. coli* as a function of the contact time t in the daylight and in the dark. (Reprinted from *Applied Surface Science*, 276, Musil J. et al., Antibacterial Cr-Cu-O films prepared by reactive magnetron sputtering, 660–666, Copyright 2013, with permission from Elsevier.)

are given in Reference 161. All these facts clearly show that the Al-Cu-N nitride is *the three-functional coating*. The Al-Cu-N coating is (1) antibacterial, (2) protective against the mechanical damage, and (iii) flexible (bendable without cracking). This experiment demonstrates that in the case of the Al-Cu-N coating it is possible to find a combination of the deposition parameters (CDPs) at which, compared to the Cr-Cu-O coating, the coating simultaneously fulfils three functions as it is schematically shown above in Figure 7.31c.

TABLE 7.14
Thickness h, Deposition Rate a_D, Deposition Parameters, Physical, and Mechanical Properties of Sputtered Cr-Cu-O and Al-Cu-N Coatings Whose Surface Morphology is Displayed in Figure 7.40 and Results of the Assessment of Their Resistance to Cracking by Bending

Coating	h (nm)	a_D (nm/min)	T_s (°C)	U_{sp} (V)	i_{sp} (mA/cm^2)	σ (GPa)	Cu (at.%)	H (GPa)	E^* (GPa)	W_e (%)	H/E^*	Cracks Bending
Cr-Cu-O	2190	18.3	500	U_{fl}	–	0.1	19.5	3.2	70	36	0.046	Yes
Al-Cu-N	2730	63.5	400	−100	1.38	−1.7	9.6	21.9	180	74	0.122	No

Note: i_{sp} is the averaged substrate ion current density over negative pulse of substrate bias U_{sp}.

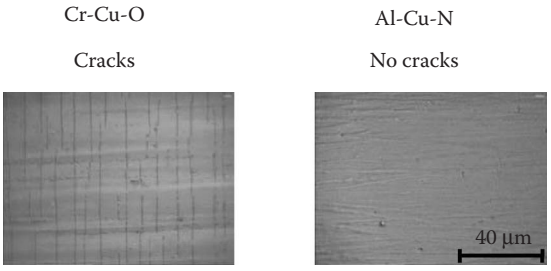


FIGURE 7.40 Surface morphology of Cr-Cu-O oxide coating with $H/E^* < 0.1$ and Al-Cu-N coating with $H/E^* > 0.1$ on Mo strip ($55 \times 15 \times 0.15$ mm^3) after bending around cylinder of radius r = 12.5 mm, respectively. Mechanical properties were measured on Si(100) substrates at a low diamond load L = 20 mN.

7.7 OVERLAYER PROTECTING BRITTLE COATINGS AGAINST CRACKING

The cracking of brittle materials and coatings during bending and/or loading is a well-known fact. This undesirable phenomenon, however, results in catastrophic consequences such as, for instance, the interruption of (i) the coating protection of the substrate and (ii) the function of the functional coatings deposited on flexible substrates, the breaking of brittle materials such as the glass, and so on. Therefore, in the development of new advanced materials and coatings it is vitally important to find and to master a way to prevent cracking of coatings or at least to enhance their resistance to cracking. Recently, great attention has been devoted to the solution of this problem [39,63,65,162–166].

In this section, one way that allows prevent cracking of coatings and cracking at surfaces of brittle materials is described. This method is based on the deposition of a special overlayer on the brittle coatings and materials. Properties of this special overlayer are further described in detail.

7.7.1 Generation of Cracks at Surface of Bended Brittle Material

It is well known that brittle materials easily crack. During bending of the brittle material, for example, the metallic strip (foil), cracks are formed in its surface, see Figure 7.41. These surface cracks are caused by a tension stress $\sigma > O$ generated in the upper part of the brittle strip during bending. Simultaneously, the bottom part of brittle strip is in compression ($\sigma < O$). The surface cracks are initiators of breaking of the materials and coatings. In the case, when the coating cracks its function is interrupted, for example, the interruption of a passage of the electric current results in a failure of electrical circuits and electronics components, the protection of the substrate surface against oxidation, corrosion, erosion can be lost, and so on. These are serious reasons why the formation of cracks at surfaces of bend brittle materials and coatings should be avoided.

Magnitudes of stresses generated in the bend metallic strip can be calculated as follows. During bending a strain ε is generated in the metallic strip due to stretching of its surface layer (top layer) at $r = r_1 + h$. The strain ε in the inner layer (bottom layer) of metallic strip, that is, at the surface of fixed cylinder at $r = r_1$, is opposite, see Figure 7.41. Under the assumption that the metallic strip is a homogenous material the strain ε in the metallic strip is distributed linearly, according to Equation 7.4 [140,167]

$$\varepsilon(r, r_0) = (r - r_0)/r_0 \tag{7.4}$$

Here, $r_0 = r_1 + h/2$. From Equation 7.4 it is seen that the strain ε is negative ($\varepsilon < 0$) for $r < r_0$ and the strain ε is positive ($\varepsilon > 0$) for $r > r_0$. It means that outer layers of the

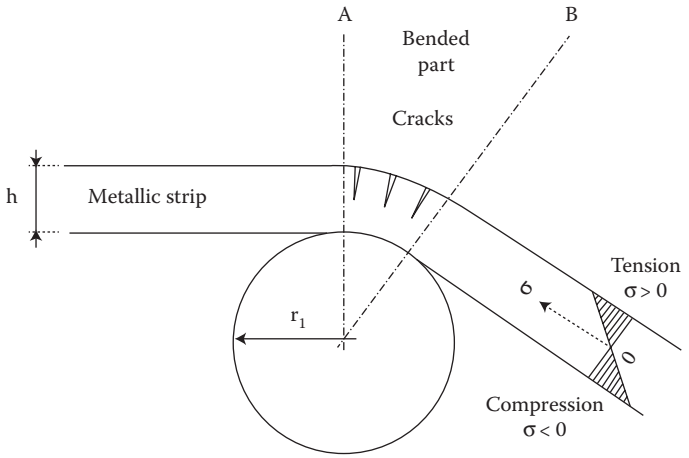


FIGURE 7.41 Schematic illustration of cracks generated at the surface of metallic strip during its bending around the fixed cylinder of radius r_1 and the distribution of stress generated inside the strip. The stress is generated inside the bended part of metallic strip only. (Reprinted from *Surface and Coatings Technology*, 240, Musil J., J. Sklenka, J. Procházka, Flexible over-layer coating preventing cracking of thin films deposited on flexible substrates, 275–280, Copyright 2014, with permission from Elsevier.)

metallic strip with $r > r_0$ are in tension ($\sigma > 0$) and inner layers with $r < r_0$ are in compression ($\sigma < 0$) as shown in Figure 7.41. Under the assumption that $r_1 > h$ the strain ε in the top and bottom layer of the bended metallic strip can be calculated from the following formulas:

$$\varepsilon(r_1 + h) \approx h/2r_1 \tag{7.5}$$

$$\varepsilon(r_1) \approx -h/2r_1 \tag{7.6}$$

Here, h is the thickness of the metallic strip. This formula shows that the strain ε generated in the metallic strip during bending increases with (i) increasing thickness h of the coating and (ii) decreasing radius r_1 of the fixed cylinder. It means that bending of the metallic strip around the fixed cylinder with smaller radius r_1 represents a harder test of the metallic strip against cracking.

The macrostress σ_{bst} generated in the top and bottom layer of the metallic strip (st) during bending can be calculated from the Hooke's law $\sigma = E.\varepsilon$ defined by Equation 7.1. After substitution of Equations 7.5 and 7.6 in the Equation 7.1 we obtain

$$\sigma_{bst} = \sigma_0 \pm E_{st}(1 - \nu_{st}^2)\, h/2r_1 \tag{7.7}$$

Here, σ_0 is the macrostress of the metallic strip before bending, the sign+ is valid for the top layer and the sign – is valid for the bottom layer of the coating, E_{st} and ν_{st} are Young's modulus and Poisson's ratio of the metallic strip, respectively. In the case that there is no stress in the metallic strip prior to its bending then the macrostress σ_{bst} generated in the bended metallic strip can be calculated from the following formula:

$$\sigma_{bst} = \pm E_{st}(1 - \nu_{st}^2)\, h/2r_1 \tag{7.8}$$

From this formula it is possible to calculate the magnitude of tensile stress at surface of bended strip. For Mo strip with $E_{st} = E_{Mo} = 315$ GPa, $\nu_{st} = \nu_{Mo} = 0.31$ [168], $h = 0.1$ mm and radius of fixed cylinder $r_1 = 10$ mm the tensile stress at surface of bended Mo strip $\sigma_{bst} = -1.4$ GPa.

Also, it is worthwhile to note that the absolute prolongation of the length L_2 of the bended top layer of metallic strip at radius $r = r_1 + h$ compared to the length L_1 of the bended bottom layer of metallic strip at radius $r = r_1$ depends on the metallic strip thickness h and the angle α of bending of the metallic strip and can be calculated from the following formula:

$$\Delta L = L_2 - L_1 = 2\pi(r_1 + h)\alpha/2\pi - 2\pi r_1\alpha/2\pi = h\alpha \tag{7.9}$$

7.7.2 Overlayer Preventing Cracking

One possible way to avoid the formation of surface cracks on the bended surface of the brittle material is to coat its surface by a special overlayer coating as shown in

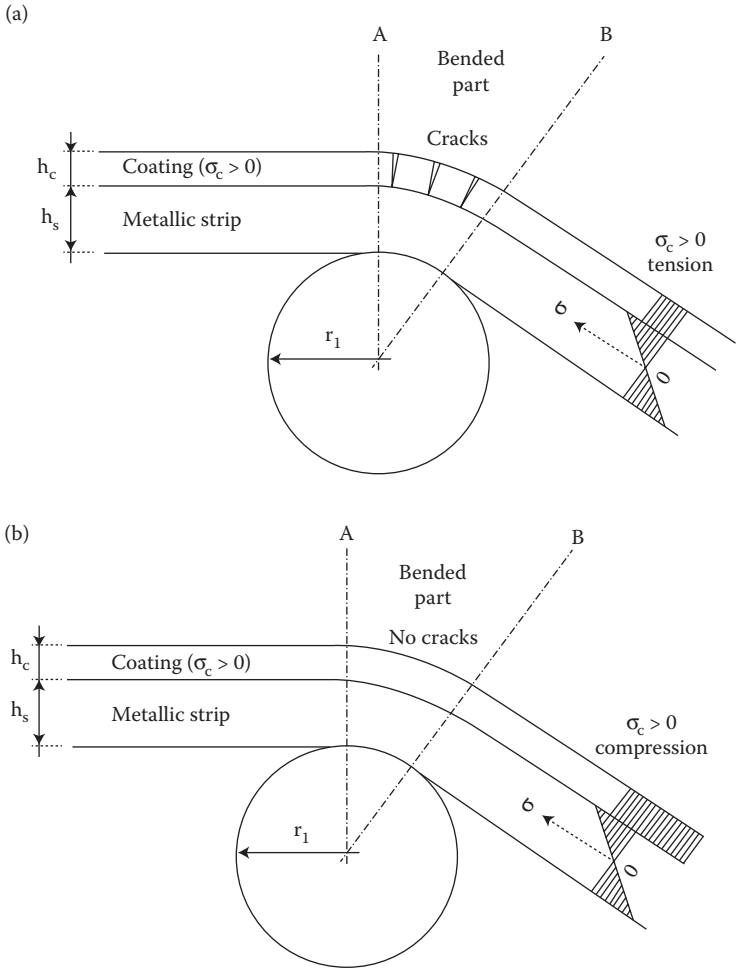


FIGURE 7.42 Schematic illustration of bended metallic strip covered by (a) the coating in tension ($\sigma > 0$) and (b) the coating in compression ($\sigma < 0$). The stress is generated inside the bended part of coated metallic strip only. (Reprinted from *Surface and Coatings Technology*, 240, Musil J., J. Sklenka, J. Procházka, Flexible over-layer coating preventing cracking of thin films deposited on flexible substrates, 275–280, Copyright 2014, with permission from Elsevier.)

Figure 7.42. The principle of this method is based on the conversion of the tensile stress at the interface between the bended material and the coating to the compressive stress ($\sigma < 0$). It means that the interface stress $\sigma_{interface}$ must be negative.

$$\sigma_{interface} = \sigma_{bst} + \sigma_{bc} < 0 \tag{7.10}$$

Here, σ_{bst} is the macrostress at the surface of bended strip and σ_{bc} is the macrostress of the overlayer coating. The macrostress σ_{bc} is composed of two components

$$\sigma_{bc} = \sigma_{ib} + \sigma_c \tag{7.11}$$

The component σ_{ib} is the macrostress generated in the coating during its bending and the component σ_c is the macrostress generated in the coating during its growth. The macrostress σ_{ib} can be calculated from the following formula:

$$\sigma_{ib} = \pm E_c(1 - \nu_c^2)h_c/2r_l \tag{7.12}$$

Here, E_c and ν_c is Young's modulus and Poisson's ratio of coating material and h_c is the thickness of coating. The value of σ_{ib} is considerably lower than the macrostress σ_{bst} of the metallic strip due to a low ratio of h_c/h, for instance in our case $h_c/h = 10^3$ nm$/10^5$ nm $= 10^{-2}$. Besides, due to a very low thickness h_c of the coating the compressive macrostress ($\sigma < 0$) at the bottom and tensile macrostress ($\sigma > 0$) on top of bended coating can compensate each other. However, the macrostess σ_c is generated in the coating during its growth achieves high values of about 1 GPa and higher. Therefore, the macrostress σ_{ib} can be neglected in Equation 7.11 and $\sigma_{bc} \approx \sigma_c$. It means that the distribution of macrostress σ_c across the coating thickness h_c can be in the first approximation considered as approximately constant, see Figure 7.42.

In the case when the macrostress σ_{bc} of the overlayer coating is tensile ($\sigma_{bc} > 0$) the formation of cracks cannot be avoided because the tensile macrostress $\sigma_{interface}$ at the surface of bended strip is enhanced $\sigma_{interface} = \sigma_{bst} + \sigma_{bc} > \sigma_{bst} > 0$ (Figure 7.42a). The macrostress $\sigma_{inerface}$ can be negative only in the case (i) when the macrostress σ_c of the overlayer coating is compressive ($\sigma_c < 0$), and (ii) its absolute value $|\sigma_{bc}| > |\sigma_{bst}|$ because the macrostress of bended strip σ_{bst} at its surface is tensile ($\sigma_{bst} > 0$), that is, $\sigma_{interface} = \sigma_{bst} + \sigma_{bc} < 0$, see Figure 7.42b. This principle was tested on the metallic strip coated by the brittle coating.

7.7.3 Protection of Brittle Layer Against Cracking by Zr-Si-O Overlayer in Compression

The verification of the hypothesis that the overlayer with compressive macrostress ($\sigma < 0$) can prevent cracking of the brittle coating were performed with Zr-Si-O coatings. For this experiment two coatings, denoted as A and B, with precisely defined properties given in Table 7.15 were sputter deposited on a Mo strip ($60 \times 10 \times 0.1$ mm^3):

1. The coating A is the single-layer Zr-Si-O coating with low ratio $H/E^* = 0.08$, low elastic recovery $W_e = 50\%$, and tensile macrostress $\sigma = 0.25$ GPa. The coating A is a brittle coating.
2. The coating B is composed of two layers: (a) the Zr-Si-O film with low ratio $H/E^* = 0.08$, low elastic recovery $W_e = 50\%$, and tensile macrostress $\sigma = 0.25$ GPa bottom layer (the layer 1), and (b) the Zr-Si-O film with high ratio $H/E^* = 0.1$, high elastic recovery $W_e = 68\%$, and compressive macrostress $\sigma = -1.5$ GPa upper layer (the layer 2). The layer 1 is the same as the coating A.

TABLE 7.15
Elemental Composition, Thickness h, Deposition Rate a_D, Macrostress σ, Hardness H, Effective Young's Modulus E^*, and H/E^* Ratio of the Layer 1 and the Layer 2 used in the Coating A and B Deposited on Si(100) Substrate; here $E^* = E/(1-\nu^2)$, E is Young's Modulus and ν is Poisson's Ratio

Layer No.	Zr (at.%)	Si (at.%)	O (at.%)	H (nm)	a_D (nm/min)	σ (GPa)	H (GPa)	E^* (GPa)	W_e (%)	H/E^*	Cracks in Bending
Layer 1	29	15	56	3000	133	0.25	12.6	161	50	0.078	Yes
Layer 2	30	1	69	3000	6	−1.50	17.1	167	68	0.102	No

Source: Reprinted from *Surface and Coatings Technology*, 240, Musil J., J. Sklenka, J. Procházka, Flexible over-layer coating preventing cracking of thin films deposited on flexible substrates, 275–280, Copyright 2014, with permission from Elsevier.

Note: Mechanical properties of the film were measured by microindentation at diamond indentation load L = 20 mN.

Both Zr-Si-O coatings were tested by bending around the fixed cylinder of the same radius r with the aim to show that (1) the coating A is brittle and easily cracks and (2) the coating B is tough and does not crack. The overlayer coating (layer 2) prevents cracking of the coating B. Results of this experiment are displayed in Figure 7.43.

As expected, the single-layer coating A with the low ratio $H/E^* < 0.1$, low elastic recovery $W_e < 60\%$, and tensile macrostress $\sigma > 0$ easily cracks in bending around the cylinder of radius r = 12.5 mm already at a small bending angle $\alpha \approx 30°$, see Figure 7.43a. However, the two-layer coating B in which the same layer 1 as in the coating A is covered by the layer 2 with high ratio $H/E^* \approx 0.1$, high elastic recovery $W_e > 60\%$, and compressive macrostress $\sigma < 0$ exhibits no cracks even after bending up to angle $\alpha = 180°$ around the cylinder with the same radius r = 12.5 mm, see Figure 7.43b. This experiment clearly demonstrates that the brittle coating can be protected against cracking by the highly elastic overlayer with high ratio $H/E^* \geq 0.1$, high elastic recovery $W_e \geq 60\%$, and compressive macrostress $\sigma < 0$.

Also, it is worthwhile to note that there is a strong difference in the cross-section morphology of the brittle coating (the layer 1) and the tough overlayer (the layer 2), see Figure 7.44a. From Figure 7.44a it is seen that while the layer 1 exhibits a dense featureless microstructure, the layer 2 exhibits a dense, voids-free columnar microstructure. The structure of the layer 1 is x-ray amorphous. However, the structure of the layer 2 is polycrystalline with strong (101) and (112) reflections from t-ZrO_2 phase, see Figure 7.44b. More details are given in Reference 68.

In summary, it can be concluded that the brittle coating can be protected against cracking by the highly elastic overlayer with high ratio $H/E^* \geq 0.1$, high elastic recovery $W_e > 60\%$, and compressive macrostress $\sigma < 0$.

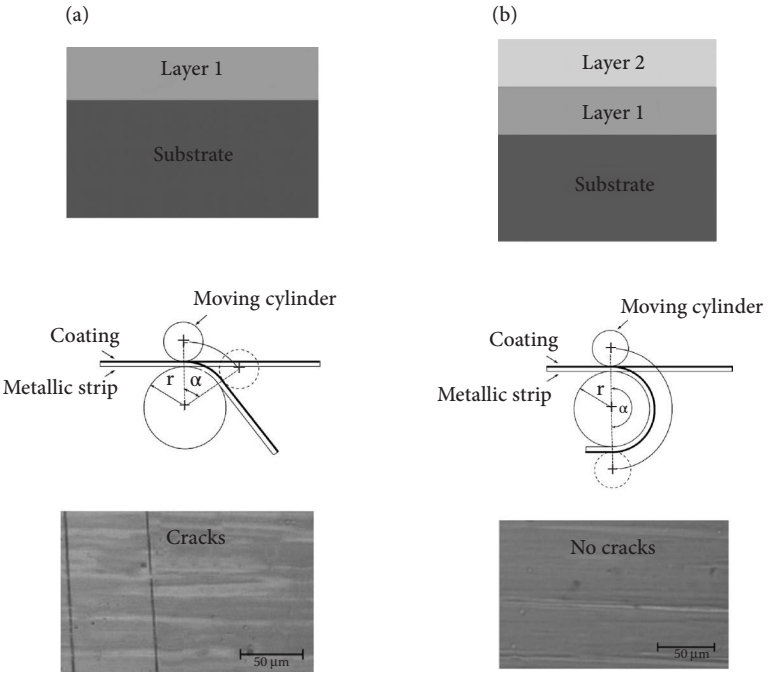


FIGURE 7.43 Schematic illustration of coating/substrate geometry, method of bending of the coated Mo strip, and photos of surface morphology of (a) single-layer Zr-Si-O coating A with low ratio $H/E^* < 0.1$, low elastic recovery $W_e < 60\%$, and tensile macrostress $\sigma > 0$ (the layer 1) and (b) two-layer Zr-Si-O coating B composed of bottom layer with low ratio $H/E^* < 0.1$, low elastic recovery $W_e < 60\%$ and tensile macrostress $\sigma > 0$ (the layer 1) and the upper layer with high ratio $H/E^* \geq 0.1$, high elastic recovery $W_e > 60\%$ and compressive macrostress $\sigma < 0$ (the layer 2) after bending around the cylinder with diameter of $r = 12.5$ mm. Properties of the layer 1 and the layer 2 are given in Table 7.15. (Reprinted from *Surface and Coatings Technology*, 240, Musil J., J. Sklenka, J. Procházka, Flexible over-layer coating preventing cracking of thin films deposited on flexible substrates, 275–280, Copyright 2014, with permission from Elsevier.)

7.7.4 Multilayer Coating Resistant to Cracking

The role of the layer in compression ($\sigma < 0$) was tested also in a multilayered coating. Three-layer and four-layer Zr-Si-O coatings composed of alternating layers in tension ($\sigma > 0$) and compression ($\sigma < 0$) were sputtered on a Mo strip ($60 \times 10 \times 0.1$ mm^3), see Figure 7.45. The layer in tension is denoted as the layer 1 (L_1) and the layer in compression is denoted as the layer 2 (L_2). The elemental composition of both layers is given in Table 7.15. The first layer deposited at the substrate was always the layer 1 with $\sigma > 0$ (in tension). The thicknesses h_n of individual layers in the coating and its mechanical properties are given in Table 7.16; the index n denotes the number of layer in the coating.

From Figure 7.45 it can be seen that the alternation of the layers in tension and compression strongly influences the resistance of the coating to cracking. Always,

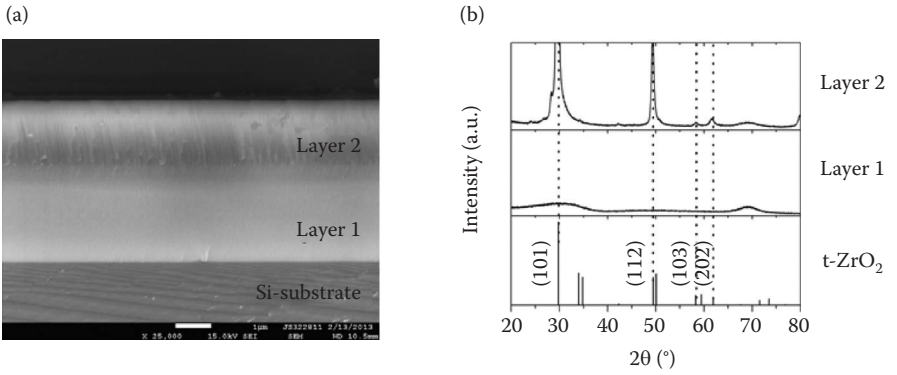


FIGURE 7.44 (a) SEM image of cross-section morphology of the coating B composed of two different layers: (1) the brittle layer 1 which is the Zr-Si-O film with low ratio $H/E^* = 0.08$ in tension and (2) the tough layer 2 which is the Zr-Si-O film with high ratio $H/E^* = 0.102$ in compression and (b) XRD patterns of the layer 1 and 2 deposited separately on two Si substrates. (Reprinted from *Surface and Coatings Technology*, 240, Musil J., J. Sklenka, J. Procházka, Flexible over-layer coating preventing cracking of thin films deposited on flexible substrates, 275–280, Copyright 2014, with permission from Elsevier.)

when the top layer is in tension ($\sigma > 0$) the coating cracks and when the top layer is in compression ($\sigma < 0$) the coating does not crack, that is, the coating exhibits enhanced resistance to cracking. This is a very important phenomenon, which could be used in the formation of new advanced very thick (10–100 μm) coatings. The experiment described above indicates that the multilayer coating composed of the layers with alternating macrostress σ could be used also in the formation of new

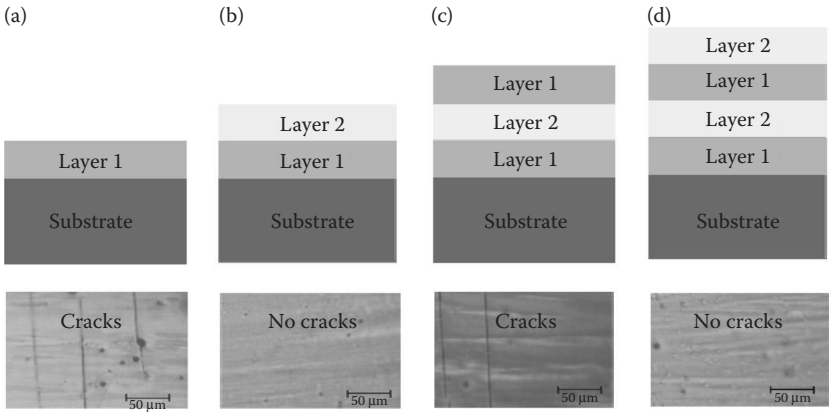


FIGURE 7.45 Surface morphology of (a) single layer, (b) two-layer, (c) three-layer, and (d) four-layer coating deposited on Mo strip after bending around fixed cylinder of radius r = 12.5 mm. (Reprinted from *Surface and Coatings Technology*, 240, Musil J., J. Sklenka, J. Procházka, Flexible over-layer coating preventing cracking of thin films deposited on flexible substrates, 275–280, Copyright 2014, with permission from Elsevier.)

TABLE 7.16
Thickness h_n of Individual Layers in the Multilayer Zr-Si-O Coatings, their Mechanical Properties, Macrostress σ in the Top Layer, and Cracks Formation in Multilayer Coating during Bending of Coated Mo Strip Around Fixed Cylinder of Radius r = 12.5 mm

Coating	Content of Layers	h_1 (nm)	h_2 (nm)	h_3 (nm)	h_4 (nm)	h_T (nm)	H (GPa)	E^* (GPa)	W_e (%)	H/E^*	Macrostress in Top Layer	Cracks in Bending
Coating A	L_1	3000	–	–	–	3000	12.6	161	50	0.078	Tension	Yes
Coating B	$L_1 + L_2$	3000	3000	–	–	6000	17.6	165	70	0.107	Compression	No
Coating C	$L_1 + L_2 + L_3$	2500	2500	2500	–	7500	12.2	149	56	0.082	Tension	Yes
Coating D	$L_1 + L_2 + L_3 + L_4$	2400	2400	2400	2400	9600	16.6	157	70	0.106	Compression	No

Source: Reprinted from *Surface and Coatings Technology*, 240, Musil J., J. Sklenka, J. Procházka, Flexible over-layer coating preventing cracking of thin films deposited on flexible substrates, 275–280, Copyright 2014, with permission from Elsevier.

Note: Mechanical properties of the film were measured by microindentation at load L = 20 mN.

advanced coatings with new unique properties. However, many questions remain still open. For instance, what is a minimum thickness of the layer in compression which is sufficient to prevent the cracking of the multilayer coating, what is the effect of alternating layers on physical properties of the multilayer coating, what is the thermal stability of the multilayer coating, what is the thermal conductivity of the multilayer coating composed of layers with macrostress σ alternating from tension ($\sigma > 0$) to compression ($\sigma < 0$), and so on.

7.7.4.1 Effect of Thickness Overlayer on Protection of Brittle Film Against Cracking

The knowledge of the effect of the overlayer thickness on a protection of brittle films against cracking is also very important. Therefore, the protective overlayer with different thickness h was deposited on the brittle layer and the resistance of the coating, composed of the brittle layer and the protective overlayer, to cracking was tested by the bending test. The layer 1 and layer 2 were used as a brittle film and a protecting overlayer, respectively. The thickness of the layer 1 was 3000 nm and the thickness of overlayer ranged from 50 to 8000 nm; the mechanical properties of the layer 1 and layer 2 are given in Table 7.15. The overlayer with different thickness was sputtered under the same deposition conditions as the layer 2. The main aim of this experiment was to find the thinnest overlayer, which can still prevent cracking of brittle coatings, see Figure 7.46.

The two-layer coatings were sputtered on a Mo strip ($60 \times 10 \times 0.1$ mm^3) and bended around a fixed cylinder of radius r = 10 mm. The surface morphology of the two-layer coatings with the overlayer thickness 50, 500, and 3300 nm after their bending around a fixed cylinder of radius r = 10 mm is shown in Figure 7.46. This figure clearly shows that even a very thin overlayer with thickness 50 nm is sufficient to prevent cracking of the brittle coating, see Figure 7.46b. This fact is very interesting from a scientific point of view and also very important from a practical point of view. Important is also the fact that the brittle coating can be protected

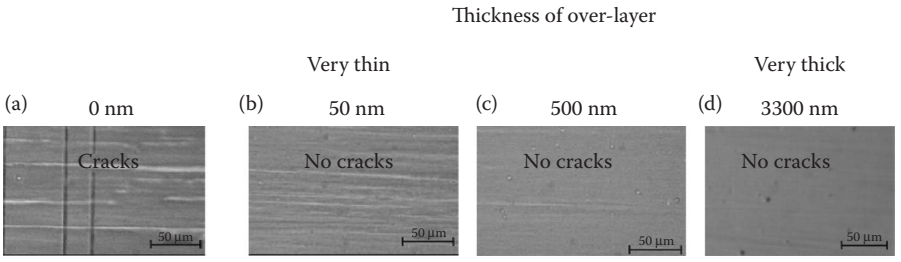


FIGURE 7.46 Surface morphology of two-layer coatings composed of the 3000 nm thick brittle layer (the layer 2) and the 50, 500, and 3300 nm thick overlayer (the layer 2) deposited on Mo strip after bending around fixed cylinder of radius r = 10 mm. For a comparison cracks in the brittle coating (the layer 1 only) not protected by an overlayer is shown in Figure 7.46a. (Reprinted from *Surface and Coatings Technology*, 240, Musil J., J. Sklenka, J. Procházka, Flexible over-layer coating preventing cracking of thin films deposited on flexible substrates, 275–280, Copyright 2014, with permission from Elsevier.)

against cracking by very thick overlayer, see Figure 7.46d. These findings open new possibilities in the design of new advanced protective and functional coatings. This phenomenon is now under detailed investigation in our laboratories and obtained results will be published in a separate paper.

7.8 SUMMARY OF MAIN ISSUES

Main results reported in this chapter can be shortly summarized as follows:

1. The nanocomposite coatings which are simultaneously hard, tough, highly elastic (HTHE) are called the HTHE nanocomposite coatings. The HTHE coatings represent a new generation of advanced hard coatings, which are resistant to cracking. Main characteristics of the HTHE coatings are:
   a. High hardness H = ~15– ~ 25 GPa
   b. Low effective Young's modulus E^* resulting in a high ratio $H/E^* \geq 0.1$
   c. High elastic recovery We ≥ 60%
   d. Dense, voids-free microstructure.
2. The addition of selected elements (ASE) in the base material of the coating and the energy $\mathcal{E}$ delivered to the coating during its growth or a postdeposition treatment of coating are two key factors, which enable to form the HTHE coatings.
3. The HTHE nanocomposite coatings represent a huge potential for many applications, for instance, for flexible electronics, flat panel displays, microelectromechanic systems (MEMS), functional coatings on flexible substrates, and so on.
4. The combined action of both factors, the ASE and the energy $\mathcal{E}$, makes it possible to combine excellent mechanical properties with other functions and this way form new advanced two- or multifunction nanocomposite coatings, for instance, low friction/low wear coatings, antibacterial/flexible coatings, antifouling/flexible coatings, low friction/flexible coatings, low wear/flexible coatings,, transparent/flexible coatings, antibacterial/protective/flexible coatings, corrosion resistant/oxidation resistant/flexible coatings, and so on.
5. Already a small amount of the added element in the base material of the coating is sufficient to result in new unique properties of the nanocomposite coating.

Based on the results presented in this chapter, the following main tasks in the development of *the new advanced HTHE nanocomposite coatings* are expected to be solved:

1. The demonstration of a simultaneous existence of the enhanced hardness, toughness, elasticity, and resistance to cracking in other material systems different from oxides and nitrides, for instance, in alloys, metallic glasses, nanocomposites based on borides, boronitrides, carbides, carbonitrides, and so on.

2. The investigation of the relationships between the resistance to cracking of new advanced HTHE nanocomposite coatings and their microstructure.
3. The determination of the thermal stability of the HTHE nanocomposite coatings.
4. The investigation of the efficiency of the substrate protection against oxidation and corrosion by the HTHE nanocomposite coatings.
5. The development of new advanced multifunctional coatings based on the HTHE nanocomposite coatings with new unique properties, for instance, biocompatible/antibacterial/flexible coatings, corrosion resistant/erosion resistant/flexible coatings, low wear/high friction/flexible coatings, highly transparent/highly electric conductive/flexible coatings, and so on.
6. The development of new multilayer coatings composed of layers with alternating tensile ($\sigma > 0$) and compressive ($\sigma < 0$) macrostress.
7. The development of new advanced coatings based on the HTHE nanocomposite coatings for medicine and biology applications, fuel cells, hydrogen generation by water splitting, storage of energy, and so on.

7.9 TRENDS OF NEXT DEVELOPMENT OF NEW ADVANCED HARD NANOCOMPOSITE COATINGS

The next development of new advanced hard nanocomposite coatings will be based on new strong ideas utilizing physical and physicochemical processes not used so far. Particularly, the following three processes should be underlined.

1. The extremely fast heating and cooling of the growing film at atomic level.
2. The electronic bonding between the atoms of different phases in the nanocomposite materials.
3. The nonepitaxial growth of the crystalline phase on the amorphous phase of nanocomposite materials.

The extremely fast heating and cooling at atomic level can be used, for instance, for the low-temperature ($T_s \leq 100°C$) formation of high-temperature crystalline phases in coatings and flexible glasses made of the alloys and compounds, such as nitrides, oxides, carbides, borides, their combinations, and so on, without an equilibrium substrate heating. The principle of the formation of the high-temperature phases in the alloy coating and the flexible glasses without the equilibrium substrate heating is illustrated in Figure 7.47a and b, respectively. From these figures it is seen that pure high-T phases or fully flexible glasses can be formed only in the case when the cooling rate of the created material is extremely fast, that is, in the case when the time t_c of cooling is such short that the high-T phase cannot be converted in low-T phases. Such extremely fast cooling ($\geq 10^{13}$ K/s) can be achieved only at atomic level and thus can be realized using the physical vapor deposition processes, for example, using the magnetron sputtering of coating. It means that not only *the amount of the energy* $\mathcal{E}$ delivered to the growing coating is important but also *the speed of the delivery of the energy* $\mathcal{E}$ in the growing coating and *the*

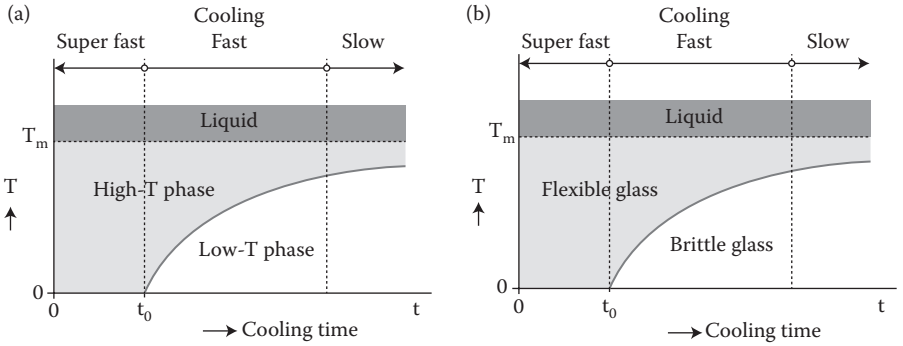


FIGURE 7.47 Schematic illustration of formation of (a) high-temperature phase coating material and (b) flexible glasses without the equilibrium substrate heating by the extremely fast heating and cooling of the growing film at atomic level. (Reprinted from *Comprehensive Materials Processing*, 4, Musil J., P. Zeman, P. Baroch, Hard Nanocomposite Coatings, 325–353, Copyright 2014, with permission from Elsevier.)

speed of the energy $\mathcal{E}$ extraction from the created coating material, that is, the speed of cooling, are of key importance in the formation of the coatings with new unique properties.

In nanostructured and nanocomposite materials composed of small ($d \leq 10$ nm) grains, the electronic charge transfer between the atoms at surfaces of neighboring grains with the different (i) elemental and phase composition, (ii) structure, and (iii) Fermi energy plays a very important role in the film growth [13]. The electronic charge transfer between atoms strongly influences final physical and functional properties of the film. This phenomenon called "*electronic effect*," which occurs at every interface of two phases, is enhanced in the nanostructured and nanocomposite coatings when the surface area of contacting grains or regions with ordered or disordered structure increases due to the decrease of the size d of grains or contacting immiscible disordered regions. The electronic charge transfer between the atoms at surfaces of neighboring A and B grains with a different elemental composition is illustrated in Figure 7.48.

A nonepitaxial growth of the crystalline phase on the amorphous phase in nanocomposite materials is a great challenge for the development of new multilayer coatings, for instance, the formation of multilayers with alternating amorphous ($\sigma > 0$) and crystalline ($\sigma < 0$) layers, see Figure 7.49. A typical example of such new multilayer coating is the system composed of alternating amorphous and crystalline Zr-Si-O layers; more details are given in Ref. [68]. It can be expected that this new concept of multilayer coating could enable to produce extremely thick (tens to hundreds nanometers) coatings for extreme environments. At present, there are only few papers devoted to this type of multilayer coating [169–177]. Therefore, the interaction between the crystalline and the amorphous phase still needs to be investigated in detail to obtain necessary knowledge for the perfect understanding of physics on processes in this multilayer coating and for the realization of new applications.

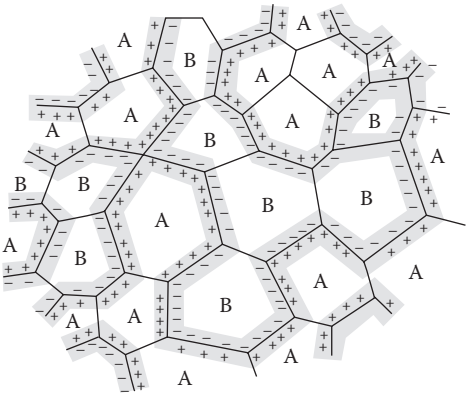


FIGURE 7.48 Schematic illustration of space charge regions in two-phase nanocomposites composed of two regions (grains) denoted by letters A and B. Gray areas denote electronically coupled atoms of A and B grains [13]. (Reprinted with kind permission from Springer Science+Business Media: *Nanostructured Coatings*, Physical and mechanical properties of hard nanocomposite films prepared by reactive magnetron sputtering, 2006, 407–463, Musil J.)

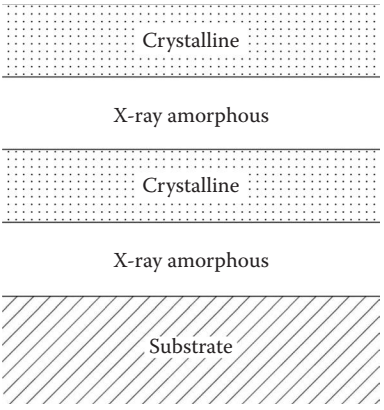


FIGURE 7.49 Multilayer coating composed of alternating x-ray amorphous and crystalline layers.

APPENDIX 1: EFFECT OF ADDITION OF SELECTED ELEMENTS AND DELIVERY OF ENERGY $\mathcal{E}$ IN COATING ON ITS GROWTH

The addition of selected elements and the delivery of energy $\mathcal{E}$ in the coating are two basic methods used to control of the growth of coating. Both methods are briefly described below.

A1.1 Effect of Added Elements

The addition of a selected element into a base material as shown above is one of possible methods used to control the structure, phase, and elemental composition of the nanocomposite coating. This method is based on the stopping of grains growth of one phase by a segregation of the second phase to grain boundaries of first one in the formation of nanocrystalline composite materials or in the suppression of the nanocrystalline phase creation at the expense of a dominant creation of the amorphous phase in the formation of x-ray amorphous composite materials composed of the nanocrystalline regions (fibrous grains, crystallites) embedded in the amorphous matrix. The effect of the amount of the added element in the base material of coating on its structure was investigated in detail by Barna and Adamik. They developed the structural zone model (SZM) describing the evolution of coating microstructure as a function of the T_s/T_m ratio for different amounts of impurities or element added in the coating [178,179]; here T_s is the substrate temperature and T_m is the melting temperature of coating material. This SZM is given in Figure A1.1a.

From Figure A1.1 it can be clearly seen that the addition of selected elements in the film results in conversion of the columnar microstructure into a fine grained microstructure. The T_s/T_m ratio up to which this conversion takes place increases

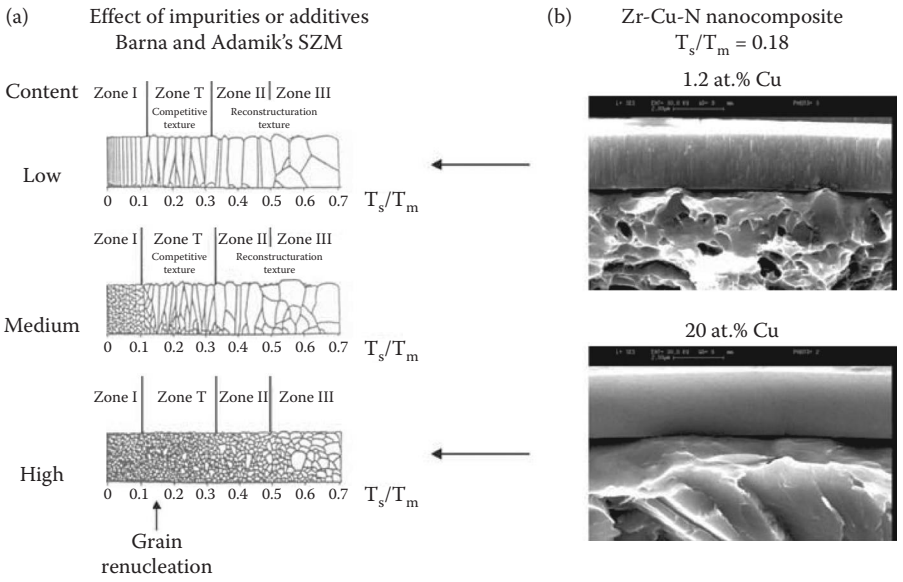


FIGURE A1.1 (a) Barna and Adamik structural zone model (SZM) of coatings with low, medium, and high amount of added element as a function of T_s/T_m [178,179] and (b) the cross-section microstructure of sputtered Zr-Cu-N nitride film with a low (1.2 at.%) and a high (20 at.%) amount of Cu [180,181]. (Reprinted from *Comprehensive Materials Processing*, 4, Musil J., P. Zeman, P. Baroch, Hard Nanocomposite Coatings, 325–353, Copyright 2014, with permission from Elsevier.)

with increasing amount of the added element. For comparison of the SZM with the experiment, the microstructure of Zr-Cu-N films with a low (1.2 at.%) and a high (20 at.%) Cu content sputtered at the same value of ratio $T_s/T_m = 0.18$ are also given in this figure, see Figure A1.1b. As expected, from this figure it is seen that while the film with a low Cu content has a clear columnar microstructure at the low value of ratio $T_s/T_m = 0.18$, the film with a high Cu content exhibits at the same value of T_s/T_m a dense, fibrous voids-free ("poorly defined") microstructure corresponding to the zone T of the Thornton's SZM, see Figure 7.29. The microstructures of both Zr-Cu-N films are in good agreement with the SZM proposed by Barna and Adamik. However, it is worthwhile to note that this agreement is not only caused by the amount of added elements but can also be caused by a change of the melting temperature T_m of material of the created film. Namely, it is well known that the addition of added elements in the base material decreases its melting temperature T_m and thus the T_s/T_m ratio can increase even at a constant value of the substrate temperature T_s. This way the transition zone T of the Thornton's SZM can be achieved at lower values of T_s. It means that the films with a dense, fibrous voids-free ("poorly defined") microstructure can be formed at lower values of the substrate temperature T_s compared with that of noncontaminated Zr-N films.

In summary, it can be concluded that these experiments indicate that the decrease of T_m in materials with added elements also plays a key role in the formation of films with a dense, fibrous voids-free ("poorly defined") microstructure. Therefore, a next investigation of the origin of film microstructure should be concentrated also on the determination of melting temperature T_m of the film material as a function of added elements in the base material, that is, $T_m = f$ (kind and amount of added elements).

Pure amorphous materials can be formed only in the case when a low energy $\mathcal{E}$, not sufficient to induce the nanocrystallization of the amorphous phase, is delivered to the growing film. Therefore, the amount of the energy $\mathcal{E}$ delivered to the growing coating should be always correctly determined or at least roughly estimated.

A1.2 Effect of Energy $\mathcal{E}$ Delivered to Growing Coating

The energy delivered to the growing coating has also a crucial effect on its structure, microstructure, elemental and phase composition, and physical properties [54,76–78,182]. The energy can be delivered by (i) the substrate heating $\mathcal{E}_{sh}$, (ii) the conversion of the kinetic energy $\mathcal{E}'_p$ of bombarding ions ($\mathcal{E}_{bi}$) and fast neutrals ($\mathcal{E}_{fn}$) incident on the surface of growing film, (iii) the heat evolved during formation of the compound $\mathcal{E}_{ch}$ (the energy released in exothermic chemical reactions), (iv) the heating from the sputtered magnetron target $\mathcal{E}_{mt}$, which almost always is not perfectly cooled, and (v) the radiation from the plasma $\mathcal{E}_{rad}$. The total energy $\mathcal{E}_T$ delivered to the growing coating can be expressed by the following formula [182]

$$\mathcal{E}_T = \mathcal{E}_{sh}(T_s, t_d) + \mathcal{E}_p(U_s, i_s, a_D, p_T, t_d) + \mathcal{E}_{ch}(t_d, T_a) + \mathcal{E}_{mt}(W_d, t_d, d_{s-t}) + \mathcal{E}_{rad}(t_d) \tag{A.1}$$

where t_d is the time of the film deposition, T_a is the annealing temperature, $p_T = p_{Ar} + p_{RG}$ is the total pressure of sputtering gas mixture, p_{Ar} and p_{RG} are the partial pressures of argon and reactive gas (RG), respectively, $W_d = (U_d I_d)/S$ is the magnetron target power density, I_d and U_d are the magnetron current and voltage, respectively, S is the whole area of magnetron target and $d_{s\text{-}t}$ is the substrate-to-target distance. The energy delivered to the growing coating by incident particles $\mathcal{E}_p$ is composed of two terms

$$\mathcal{E}_p = \mathcal{E}_{bi} + \mathcal{E}_{fn} \tag{A.2}$$

In the simplest case of a collisionless, fully ionized plasma when $\mathcal{E}_{fn} = 0$, the energy $\mathcal{E}_p$ can be expressed in the following form [76]:

$$\mathcal{E}_p[J/cm^3] = \mathcal{E}_{bi} = \mathcal{E}_i(\nu_i/\nu_{ca}) = (U_s - U_p)i_s/a_D \approx (U_s i_s)/a_D \tag{A.3}$$

where $\mathcal{E}_i$ is the energy of one ion, ν_i and ν_{ca} is the flux of ions and condensing atoms, respectively, U_s is the substrate bias, U_p is the plasma potential, i_s is the substrate ion current density, and a_D is the film deposition rate.

Equation A.3 shows two important facts:

1. The energy $\mathcal{E}_{bi}$ delivered to the growing film by bombarding ions can be easily calculated from measured deposition parameters (U_s, i_s) and the film deposition rate $a_D = h/t_d$ calculated from measured film thickness h and deposition time t_d.
2. The energy $\mathcal{E}_{bi}$ strongly depends not only on U_s and i_s but also on the film deposition rate a_D. This fact is of extraordinary importance, particularly in (i) reactive sputtering of compounds such as nitrides, oxides, and other compounds, and (ii) high-rate sputtering of coatings. The decrease of a_D in the reactive sputtering of the compounds results in the increase of the energy $\mathcal{E}_{bi}$ delivered to the growing film due to a slower growth of the film what contributes to the nanocrystallization of amorphous films and to the improvement of a crystallinity of the crystalline coatings. On the contrary, the high-rate sputtering of films results in the decrease of the energy $\mathcal{E}_{bi}$ delivered to the growing coating and slows down its crystallization.

In the case of higher sputtering pressures p_T, the energy $\mathcal{E}_{bi}$ is lower than that defined by Equation A.3 in consequence of collisions between particles and $\mathcal{E}_{bi}$ has to be determined from Equation A.4

$$\mathcal{E}_{bi}[J/cm^3] \approx (U_s i_s) \exp(-L/\lambda_i)/a_D \tag{A.4}$$

where L is the thickness of the voltage sheath at the surface of biased substrate and λ_i is the ion mean free path of ions reflecting losses of the ion energy in the sheath caused by collisions. The ions mean free path can be calculated from the Dalton law

as λ_i [cm] ≈ 0.4/p_T [Pa] [183]. The thickness of high-voltage ($U_s \gg U_{fl}$) sheath can be calculated from the Child–Langmuir equation for the dc sheath; here U_{fl} is the floating potential. The sheath thickness L can be calculated from the formulas given in Ref. [184]. More details are given in the references [20,54,77–79,182].

Generally, the sputtering discharges are not fully ionized (in low-power discharges the ionization of sputtered atoms is usually low) and contain many fast neutrals with energies ranging from several eV to several tens of eV. Therefore, in discharges generated at low (≤0.1 Pa) sputtering pressures p the deposited film grows under a combined action of the energy delivered to the growing film by both the bombarding ions $\mathcal{E}_{bi}$ and the fast neutral atoms $\mathcal{E}_{fn}$. According to the Dalton law the mean free path $\lambda_{mfp} \approx 40$ mm at p = 0.1 Pa. Hence, when the sputtering is carried out at low pressures p ≤ 0.1 Pa and at small substrate-to-target distances $d_{s\text{-}t} \approx 50$ mm, the energy of sputtered atoms does not decrease (due to no collisions with the background gas atoms) and highly energetic atoms arrive at the surface of growing coating. This energy is identical or even higher than the surface energy $\mathcal{E}_{surf}$ of atoms. Thus, the film growth in discharges generated at low pressures is strongly influenced also by the energy of incident and condensing energetic atoms [185]. The surface energy $\mathcal{E}_{surf}$ of atoms is relatively low and varies in the range from 1 to 8 eV for majority of materials [186]. At present, only first two terms in Equation A.1, that is, $\mathcal{E}_{sh}$ (T_s, t_d) and $\mathcal{E}_p$ (U_s, i_s, a_D, p_T, t_d), are considered as main sources of the total energy $\mathcal{E}_T$ influencing the film growth. The energy $\mathcal{E}_{ch}$, third term in Equation A.1, is also very important for the film growth. In future, it can be expected that also the energy $\mathcal{E}_{ch}$ released in exothermic reactions or consumed in endothermic reactions will be utilized in the development of new technological processes of the formation of next generation of advanced materials. At present, the energy $\mathcal{E}_{ch}$ is exploited for the generation of self-sustained waves in nanostructured multilayer coatings and foils [187,188]. Last two terms in Equation A.1 play an important role in the formation of films on heat-sensitive substrates such as polymer foils, polycarbonate, substrates for flexible electronics, and so on. Therefore, the target power density of magnetron cathode must be limited to a value at which the heat transferred from the sputtered magnetron target to the substrate does not cause a destruction of the heat sensitive substrate.

The effect of the ion energy $\mathcal{E}_i'$ and the flux of ions ν_i on the coating microstructure is illustrated in Figure A1.2. This figure displays the cross-section microstructure and the surface morphology of the TiN films reactively sputtered in a mixture argon and nitrogen at three values of (i) the substrate bias U_s and (ii) the substrate ion current density i_s [189]. Both the microstructure and the surface morphology of the TiN film dramatically change with increasing U_s and i_s. Already a small increase of U_s and i_s is sufficient for the conversion of a columnar microstructure to a dense featureless microstructure. The increase of U_s results in a gradual smoothening of the coating surface. When the substrate bias U_s is high (in our case $U_s = -100$ V), the ion bombardment of the growing coating is strong and the growing films is partially resputtered. It results in the slowdown of the growth of sputtered film and its smaller thickness h, compared with that of the film deposited at lower values of negative substrate bias U_s, when the films are deposited at the same deposition time t_d. All changes of the film microstructure also result in changes of its mechanical

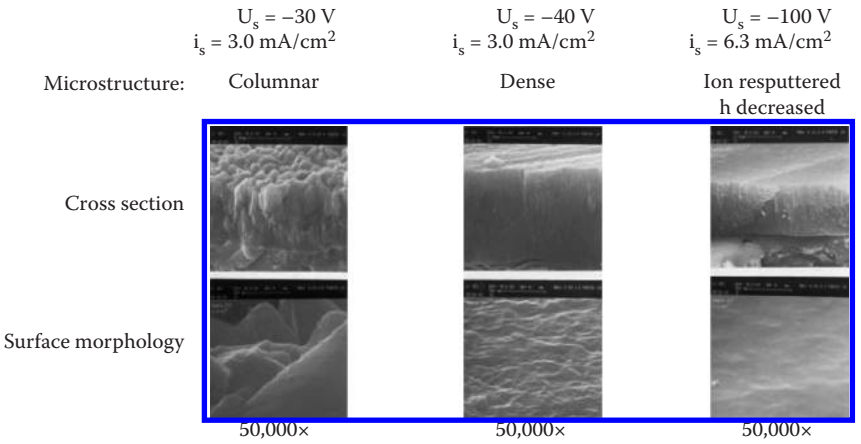


FIGURE A1.2 Effect of substrate bias U_s and substrate ion current density i_s on microstructure of ≥3000 nm thick TiN films reactively sputtered at total pressure $p_T = p_{Ar} + p_{N2} = 5$ Pa and target-to-substrate distance $d_{s\text{-}t} = 200$ mm. (Reprinted from *Surface and Coatings Technology*, 39/40, Kadlec S. et al., Reactive deposition of TiN films using unbalanced magnetron, 487–497, Copyright 1989, with permission from Elsevier.)

properties. Therefore, process parameters used in the film deposition must be carefully selected if the formation of the film with prescribed properties is required.

In conclusion of this section, it is worthwhile to note that hard low-stress sputtered films can be formed if a low energy ions (negative biases ($|U_s| \leq 50$ V) and high ion fluxes ($i_s \geq 1$ mA/cm^2) are used [20,44]. The substrate ion current density i_s must be increased in the case when the sputtering gas pressure p_T increases, the energy $\mathcal{E}_i$ decreases due to ion collisions with atoms and the total energy $\mathcal{E}_T$ delivered to the growing coating is required to be kept constant. The magnitude of ion flux ν_i is, however, limited by the substrate temperature T_s permitted in a given application.

A1.3 Effect of Speed of Delivered Energy in Growing Coating and Speed of Energy Extraction from Created Coating Material

For the development of new advanced coatings with unique properties, not only is the amount of energy $\mathcal{E}_T$ delivered to them during their growth important but also the speed of the energy delivery ($d\mathcal{E}_T/dt$) in the growing coating and the speed of the energy extraction ($-d\mathcal{E}_T/dt$) from the created coating, that is, the speed of the cooling of created coating material. This fact is illustrated in the formation of a single-phase Ti (Fe) coating with high-temperature (high-T) phase on an unheated substrate by magnetron sputtering, that is, in the formation of coating without an equilibrium substrate heating at high temperatures $T_s \gg$ RT [190], see Figures 7.47a and A1.3. Figure A1.3 shows the phase diagram of the Ti–Fe alloy in which the region where the high-T (βFe) phase can be formed is given in red color. From this figure it is seen

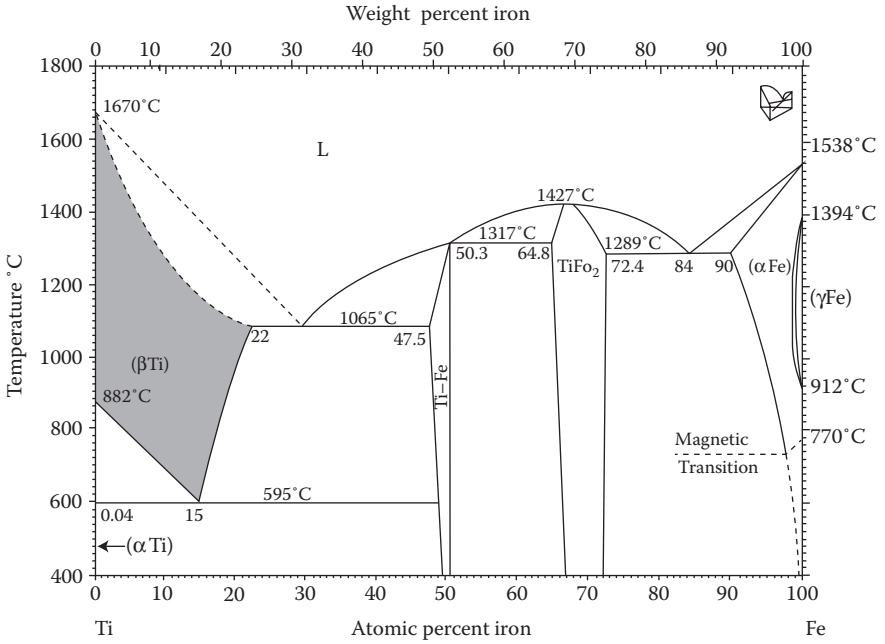


FIGURE A1.3 Modified phase diagram of Ti–Fe alloy [191]. (Reprinted from *Comprehensive Materials Processing*, 4, Musil J., P. Zeman, P. Baroch, Hard nanocomposite coatings, 325–353, Copyright 2014, with permission from Elsevier.)

that the high-T (βFe) phase can be formed at temperatures T > 600°C and Fe contents less than 22 at.% Fe.

However, it is worthwhile to note that during a slow cooling the high-T (βTi) phase will be converted in the low-T (αTi) phase. It means that the formation of the βTi(Fe) coating with a high-T (βFe) phase using a slow equilibrium substrate heating and cooling is impossible. To form the Ti(Fe) coating with a high-T (βFe) phase and to avoid its conversion in a low-T (αFe) phase an extremely fast nonequilibrium heating and cooling of created coating material is necessary. It can be realized at an atomic level only when the energy necessary to form the Ti(Fe) coating with a high-T (βFe) phase is delivered to the created material by energetic incident and condensing particles in very small atomic scale regions and simultaneously the created coating material is extremely rapidly cooled by the energy dissipation in a cold vicinity of the place where the energy was delivered. This principle of formation of the Ti(Fe) coating with a high-T (βFe) phase is schematically shown above in Figure 7.47.

Figure 7.47 clearly shows that the formation of the one-phase coating with high-T phase is possible only in the case when the time of cooling t_c is less than t_0. The cooling time t_0 is very short and corresponds to extremely fast cooling $\geq 10^{13}$ K/s, which can be reached in processes performed at atomic level only. In the case when cooling time $t_c > t_0$, the two-phase coating composed of a mixture the high-T phase and the

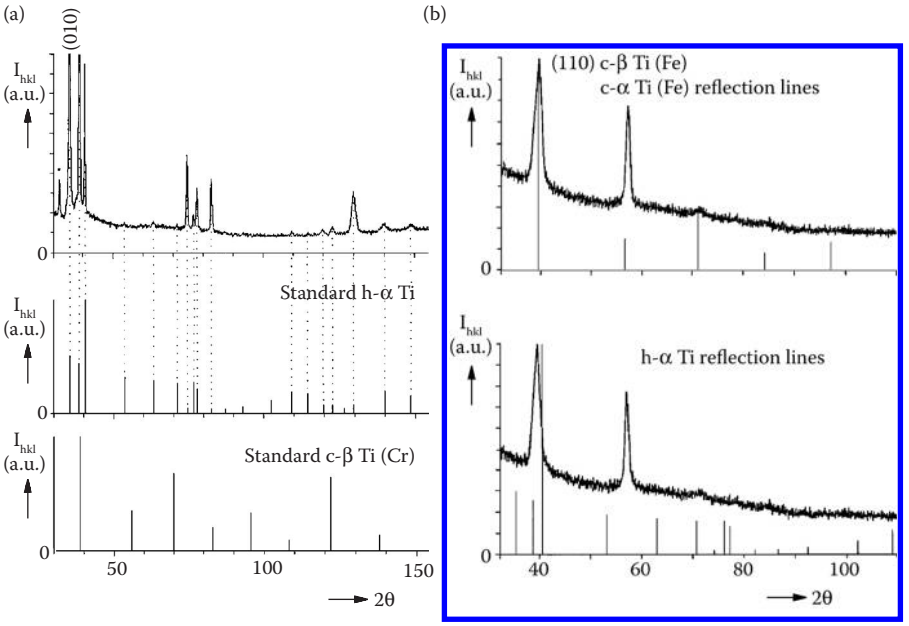


FIGURE A1.4 Comparison of structure of (a) the pure Ti (99.5 at.%) film and (b) the TiFe (90/10 at.%) alloy film magnetron sputtered at substrate temperature $T_s < 100°C$. Figure is based on data in Reference 190. (Reprinted with permission from Musil J. et al.: *Journal of Vacuum Science and Technology A*, A14(4), 1996, 2247–2250, Copyright 1996, American Vacuum Society.)

low-T phase is formed. It means that the cooling time t_c can be used to control (i) the mutual content of the high-T and the low-T phase in the created coating material and thereby (ii) the properties of coating. Recent experiments indicate that this principle could be used in the formation of highly elastic coatings with enhanced resistance to cracking.

The possibility of the creation of coatings with a pure high-T phase without the substrate heating according to the principle described above and illustrated in Figure 7.47 was experimentally demonstrated in magnetron sputtering of the pure Ti (99.5 at.%) and TiFe (90/10 at.%) alloy coatings [190], see Figure A1.4. This experiment clearly shows that by the addition of a small amount of Fe in Ti the one-phase TiFe (90/10 at.%) coating with a high-T (βTi) phase can be formed without equilibrium substrate heating.

In summary, it can be concluded that the coatings with a pure high-T phase can be formed on unheated substrates if (i) a correctly selected element is added in the correct amount in the base material and (ii) the energy necessary for the coating growth is delivered in the created coating material at atomic level. It means that for the development of new advanced coatings with unique properties not only is a correct *amount of the energy* $\mathcal{E}_T$ delivered to them during their growth *important* but also *the speed of the energy delivery* $(d\,\mathcal{E}_T/dt)$ and *the speed of cooling* $(-d\,\mathcal{E}_T/dt)$ of the created coating material.

ACKNOWLEDGMENTS

This work was supported in part by the Grant Agency of the Czech Republic (GACR) under project P 108/12/0393. The author greatly appreciates Professor RNDr. Jaroslav Vlcek, CSc, head of the Department of Physics at the University of West Bohemia in Plzen, Czech Republic, for stimulating discussions and more than 30 PhD students, who participated in the solution of partial tasks of the project "Hard Nanocomposite Coatings" solved at the Department of Physics, Faculty of Applied Sciences, University of West Bohemia in Plzen, Czech Republic from 1995 to 2014, for their enthusiasm and hard work.

REFERENCES

1. Gleiter H.: Nanocrystalline materials. *Progress in Materials Science*, 33, 1989, 223–315.
2. Birringer R.: Nanocrystalline materials. *Materials Science and Engineering A*, 117, 1989, 33–43.
3. Siegel R.W.: Cluster-assembled nanophase materials. *Annual Review of Materials Science*, 21, 1991, 559–579.
4. Siegel R.W.: What do we really know about the atomic-scale structures of nanophase materials? *Journal of Physics and Chemistry of Solids*, 55(10), 1994, 1097–1106.
5. Siegel R.W., G.E. Fougere: Grain size dependent mechanical properties in nanophase materials. In *Materials Research Society Symposium Proceedings*, Grant H.J., Armstrong R.W., Otooni M.A., K. Ishizaki (Eds.), Warrendale, PA, Materials Research Society, Vol. 362, 1995, pp. 219–229.
6. Vepřek S. and S. Reiprich: A concept for the design of novel superhard coatings. *Thin Solid Films*, 265, 1995, 64–71.
7. Gleiter H.: Nanostructured materials: State of the art and perspectives. *Nanostructured Materials*, 6, 1996, 3–14.
8. Yip S.: The strongest size. *Nature*, 391, 1998, 532.
9. Voevodin A.A., J.S. Zabinski: Superhard, functionally gradient, nanolayered and nanocomposite diamond-like carbon coatings for wear protection. *Diamond and Related Materials*, 7, 1998, 463–467.
10. Musil J.: Hard and superhard nanocomposite coatings. *Surface and Coatings Technology*, 125, 2000, 322–330.
11. Gleiter H.: Nanostructured materials: Basic concepts and microstructure. *Acta Materialia*, 48, 2000, 1–29.
12. Vepřek S.: Nanostructured superhard materials: Chapter 4. In *Handbook of Ceramic Hard Materials*, Riedel R. (Ed.), WILEY-VCH, Weinheim, 2000, pp. 104–139.
13. Gleiter H.: Tuning the electronic structure of solids by means of nanometer-sized microstructures. *Scripta Materialia*, 44, 2001, 1161–1168.
14. Demyashev G.M., A.L. Taube, E.E. Siores: Superhard nanocomposite coatings. In *Handbook of Organic-Inorganic Hybrid Materials and Nanocomposite*, Nalwa H.S. (Ed.), Valencia, CA, USA, American Scientific Publishers, Vol. 1, 2003, pp. 1–61.
15. Patscheider J.: Nanocomposite hard coatings for wear protection. *MRS Bulletin*, 28(3), 2003, 180–183.
16. Zhang S., D. Sun, Y. Fu, H. Du: Recent advances of superhard nanocomposite coatings: A review. *Surface and Coatings Technology*, 167, 2003, 113–119.
17. Leyland A., A. Matthews: On the significance of the H/E ratio in wear control: A nanocomposite coating approach to optimised tribological behaviour. *Wear*, 246, 2000, 1–11.

18. Andrievski R.A.: Nanomaterials based on high-melting carbides, nitrides and borides. *Russian Chemical Reviews*, 74(12), 2005, 1061–1072.
19. Zhang S., D. Sun, Y. Fu, H. Du: Toughening of hard nanostructured thin films: A critical review. *Surface and Coatings Technology*, 198, 2005, 2–8.
20. Musil J.: Physical and mechanical properties of hard nanocomposite films prepared by reactive magnetron sputtering, Chapter 10. In *Nanostructured Coatings*, DeHosson J.T.M., A. Cavaleiro (Eds.), New York, Springer Science + Business Media, LCC, 2006, pp. 407–463.
21. Mayrhofer P.H., C. Mitterer, L. Hultman: Microstructural design of hard coatings. *Progress in Materials Science*, 51, 2006, 1032–1114.
22. Lu C., Y.W. Mai, Y.G. Shen: Recent advances on understanding the origin of superhardness in nanocomposite coatings: A critical review. *Journal of Materials Science*, 41, 2006, 937–950.
23. Musil J., M. Jirout: Toughness of hard nanostructured ceramic thin films. *Surface and Coatings Technology*, 201, 2007, 5148–5152.
24. Musil J.: Properties of hard nanocomposite thin films, Chapter 5. In *Nanocomposite Films and Coatings*, London, Zhang S. and N. Ali (Eds.), London, Imperial College Press, 2007, pp. 281–328.
25. Musil J., P. Baroch, P. Zeman: Hard nanocomposite coatings. Present status and trends, Chapter 1. In *Plasma Surface Engineering Research and its Practical Applications*, Wei R. (Ed.), Kerala, Research Signpost, 2008, pp. 1–34.
26. Wei R.: Plasma enhanced magnetron sputtering deposition of superhard, nanocomposite coatings, Chapter 3. In *Plasma Surface Engineering Research and its Practical Applications*, Wei R. (Ed.), Kerala, Research Signpost Publisher, 2008, pp. 87–115.
27. Pogrebjank A.D., A.P. Shpak, N.A. Azarenkov, V.M. Beresnev: Structure and properties of hard and superhard nanocomposite coatings. *Physics-Uspekhi*, 52, 2009, 29–54.
28. Matthews A., A. Leyland: *Materials Related Aspects of Nanostructured Tribological Coatings*. SVC Bulletin, Spring, 2009, pp. 40–44.
29. Korotaev A.D., B.D. Borisov, Yu.V. Moshkov, S.V. Ovchinnikov, Yu.P. Pinzhin, A.N. Tyumentsev: Elastic stress state in superhard multielement coatings. *Physical Mesomechanics*, 12(5–6), 2009, 269–279 (in Russian).
30. Musil J.: Recent progress in hard nanocomposite coatings, Part 1, *Galvanotechnik*, 8, 2010, 1856–1867, Part 2, *Galvanotechnik*, 9, 2010, 2116–2121.
31. Hauert R., J. Patscheider: From alloying to nanocomposites—Improved performance of hard coatings. *Advanced Materials*, 2(5), 2000, 247–259.
32. Sandu C.S., F. Medjani, R. Sanjines, A. Karimi, F. Levy: Structure, morphology and electrical properties of sputtered Zr-Si-N thin films: From solid solution to nanocomposite. *Surface and Coatings Technology*, 201, 2006, 4219–4229.
33. Lu Y.H., Y.G. Shen: Nanostructure transition: From solid solution Ti(N,C) to nanocomposite nc-Ti(N,C)/a-(C,CN_x). *Applied Physics Letters*, 90, 2007, 221913.
34. Sandu C.S., F. Medjani, R. Sanjines: Optical and electrical properties of Zr-Si-N thin films: From solid solution to nanocomposite. *Reviews on Advanced Materials Science,* 15, 2007, 173–178.
35. Hultman L.: Thermal stability of nitride thin films. *Vacuum*, 57(1), 2000, 1–30.
36. Andrievskii R.A.: Thermal stability of nanomaterials. *Russian Chemical Reviews*, 71(10), 2002, 853–866.
37. Hultman L., C. Mitterer: Thermal stability of advanced nanostructured wear-resistnt coatings, Chapter 11. In *Nanostructured Coatings*, DeHosson J.T.M. and A. Cavaleiro (Eds.), New York, Springer Science + Business Media, 2006, pp. 464–510.
38. Raveh A., I. Zukerman, R. Shneck, R. Avni, I. Fried: Thermal stability of nanostructured superhard coatings: A review. *Surface and Coatings Technology*, 201, 2007, 6136–6142.

39. Musil J.: Hard nanocomposite coatings: Thermal stability, oxidation resistance and toughness. *Surface and Coatings Technology*, 207, 2012, 50–65.
40. Musil J., P. Zeman, P. Baroch: Hard Nanocomposite Coatings. In *Comprehensive Materials Processing, Volume 4, Coatings and Films, Chapter 4.13*, Cameron D. (Ed.), Elsevier Ltd., 2014, pp. 325–353.
41. Veprek S.: Recent search for new superhard materials: Go nano!. *Journal of Vacuum Science and Technology*, A31(5), 2013, 050822-1-33.
42. Hall E.O.: The deformation and ageing of mild steel: III Discussion and results. *Proceedings of the Physical Society*, B64, 1951, 747–753.
43. Petch N.J.: The cleavage strength of polycrystals. *Journal of the Iron and Steel Institute*, 174, 1953, 25–28.
44. Mitterer C., P.H. Mayrhofer, J. Musil: Thermal stability of PVD hard coatings. *Vacuum*, 71, 2003, 279–284.
45. Mayrhofer P.H., F. Kunc, J. Musil, C. Mitterer: A comparative study on reactive and nonreactive unbalanced magnetron sputter deposition of TiN coatings. *Thin Solid Films*, 415, 2001, 151–159.
46. Mayrhofer P.H., G. Tischler, C. Mitterer: Microstructure and mechanical properties of Cr-N coatings by reactive unbalanced magnetron sputtering. *Surface and Coatings Technology*, 142–144, 2001, 78–84.
47. Musil J., S. Kadlec, V. Valvoda, R. Kužel, Jr., R. Černý: Ion-assisted sputtering of TiN films. *Surface and Coatings Technology*, 43–44, 1990, 259–269.
48. Musil J., S. Kadlec, J. Vyskočil, V. Valvoda: New results in dc reactive magnetron deposition of TiN_x films. *Thin Solid Films*, 167, 1988, 107–119.
49. Valvoda V., R. Kužel, Jr., R. Černý, J. Musil: Structure of TiN coatings deposited at relatively high rates and low temperatures by magnetron sputtering. *Thin Solid Films*, 156, 1988, 53–63.
50. Kulikovsky V., P. Bohač, F. Franc, A. Deineka, V. Vorlíček, L. Jastrabík: Hardness, intrinsic stress, and structure of the a-C and a-C:H films prepared by magnetron sputtering. *Diamond and Related Materials*, 10, 2001, 1076–1081.
51. Musil J., H. Hrubý, P. Zeman, H. Zeman, R. Čerstvý, P.H. Mayrhofer, C. Mitterer: Hard and superhard nanocomposite Al-Cu-N films prepared by magnetron sputtering. *Surface and Coatings Technology*, 142–144, 2001, 603–609.
52. Musil J., H. Zeman, J. Kasl: Relationship between structure and mechanical properties in hard Al-Si-Cu-N films prepared by magnetron sputtering. *Thin Solid Films*, 41, 2002, 121–130.
53. Kunc F., J. Musil, P.H. Mayrhofer, C. Mitterer: Low-stress superhard Ti-B films prepared by magnetron sputtering. *Surface and Coatings Technology*, 174–175, 2003, 744–753.
54. Poláková H., J. Musil, J. Vlček, J. Alaart, C. Mitterer: Structure- hardness relations in sputtered Ti-Al-V-N films. *Thin Solid Films*, 444, 2003, 189–198.
55. Musil J., J. Vlček: Magnetron sputtering of alloy-based films and its specificity. *Czechoslovak Journal of Physics*, B48, 1998, 1209–1224.
56. Mishra R.S., A.K. Mukherjee: Processing of high hardness-high toughness alumina matrix nanocomposites. *Materials Science and Engineering*, A 301, 2001, 97–101.
57. Leyland A., A. Matthews: Design criteria for wear-resistant nanostructured and glassy-metal coatings. *Surface and Coatings Technology*, 177–178, 2004, 317–324.
58. Kuntz J.D., G.D. Zhan, A.K. Mukherjee: Nanocrystalline-matrix ceramic composites for improved fracture toughness. *MRS Bulletin*, January 2004, 22–27.
59. Zhang S., H.L. Wang, S.E. Ong, D. Sun, X.L. Bui: Hard yet tough nanocomposite coatings—Present status and future trends. *Plasma Processes and Polymers*, 4, 2007, 219–228.
60. Jirout M., J. Musil: Effect of addition of Cu into ZrO_x film on its properties. *Surface and Coatings Technology*, 200, 2006, 6792–6800.

61. Wang H., B. Wang, S. Li, Q. Xue, F. Huang: Toughening magnetron sputtered TiB_2 coatings by Ni addition. *Surface and Coatings Technology*, 232, 2013, 767–774.
62. Blažek J., J. Musil, P. Stupka, R. Čerstvý, J. Houška: Properties of nanocrystalline Al-Cu-O films reactively sputtered by dc pulse dual magnetron. *Applied Surface Science*, 258, 2011, 1762–1767.
63. Musil J., J. Sklenka, R. Čerstvý: Transparent Zr-Al-O oxide coatings with enhanced resistance to cracking. *Surface and Coatings Technology*, 206, 2011, 2105–2109.
64. Musil J., M. Meissner, R. Jílek, T. Tolg, R. Čerstvý: Two-phase single layer Al-O-N nanocomposite films with enhanced resistance to cracking. *Surface and Coatings Technology*, 206, 2012, 4230–4234.
65. Musil J., J. Sklenka, R. Čerstvý, T. Suzuki, M. Takahashi, T. Mori: The effect of addition of Al in ZrO_2 thin film on its resistance to cracking. *Surface and Coatings Technology*, 207, 2012, 355–360.
66. Musil J., J. Blažek, K. Fajfrlík, R. Čerstvý, Š. Prokšová: Antibacterial Cr-Cu-O films prepared by reactive magnetron sputtering. *Applied Surface Science*, 276, 2013, 660–666.
67. Musil J., R. Jílek, R. Čerstvý: Flexible Ti-Ni-N thin films prepared by magnetron sputtering. *Journal of Materials Science and Engineering*, A4(1), 2014, 27–33.
68. Musil J., J. Sklenka, J. Procházka: Flexible over-layer coating preventing cracking of thin films deposited on flexible substrates. *Surface and Coatings Technology*, 240, 2014, 275–280.
69. Tsui T.Y., G.M. Pharr, W.C. Oliver, C.S. Bhatia, R.L. White, S. Anders, A. Anders, I.G. Brown: Nanoindentation and nanoscratching of hard carbon coatings for magnetic disks. *Materials Research Society Symposium Proceedings*, 383, 1995, 447–451.
70. Musil J., F. Kunc, H. Zeman, H. Poláková: Relationships between hardness, Young's modulus and elastic recovery in hard nanocomposite coatings. *Surface and Coatings Technology*, 154, 2002, 304–313.
71. Musil J., J. Vlček: Magnetron sputtering of hard nanocomposite coatings and their properties. *Surface and Coatings Technology*, 142–144, 2001, 557–566.
72. Musil J., J. Vlček, F. Regent, F. Kunc, H. Zeman: Hard nanocomposite coatings prepared by magnetron sputtering. *Key Engineering Materials*, 230–232, 2002, 613–622.
73. Musil J., M. Hromádka, R. Čerstvý, Z. Soukup, J. Savková: Mechanical and tribological properties of Sn-Cu-O films prepared by reactive magnetron sputtering. *Journal of Vacuum Science and Technology*, A 32(2), 2014, 021504–1 to 6.
74. Musil J., P. Baroch, J. Vlček, K.H. Nam, J.G. Han: Reactive magnetron sputtering of thin films. *Present status and trends, Thin Solid Films*, 475, 2005, 208–218.
75. Musil J., P. Baroch: High-rate pulsed reactive magnetron sputtering of oxide nanocomposite coatings. *Vacuum*, 87, 2013, 96–102.
76. Musil J.: Sputtering systems with enhanced ionization for ion plating of hard wear resistant coatings. *Proceedings of the 1st Meeting on the Ion Engineering Society of Japan* (IESJ-92), Tokyo, Japan, 1992, pp. 295–304.
77. Musil J., H. Polaková, J. Šůna, J. Vlček: Effect of ion bombardment on properties of hard reactively sputtered single-phase films. *Surface and Coatings Technology*, 177–178, 2004, 289–298.
78. Musil J., J. Šůna: The role of energy in formation of sputtered nanocomposite films. *Materials Science Forum*, 502, 2005, 291–296.
79. Musil J., J. Vlček, P. Baroch: Magnetron discharges for thin films plasma processing, Chapter 3. In *Materials Surface Processing by Directed Energy Techniques*, Pauleau Y. (Ed.), 2006, Oxford, UK, Elsevier Science Publisher B.V., pp. 67–106.
80. Musil J., M. Šašek, P. Zeman, R. Čerstvý, D. Heřman, J.G. Han, V. Šatava: Properties of magnetron sputtered Al-Si-N thin films with a low and high Si Content. *Surface and Coatings Technology*, 202, 2008, 3485–3493.

81. Šašek M.: Magnetron sputtering of oxide and nitride films with high thermal stability, Ph.D. thesis, 2012, Department of Physics, University of West Bohemia, Czech Republic, (in Czech).
82. Yeh J.W., S.K. Chen, S.J. Lin, J.Y. Gan, T.S. Chin, T.T. Shun, C.H. Tsau, S.Y. Chang: Nanostructured high-entropy alloys with multiple principal elements: Novel alloy design concepts and outcomes. *Advanced Engineering Materials*, 6(5), 2004, 299–303.
83. Chen T.K., T.T. Shun, J.W. Yeh, M.S. Wong: Nanostructured nitride films of multi-element high-entropy alloys by reactive DC sputtering. *Surface and Coatings Technology*, 188–189, 2004, 193–200.
84. Chen T.K., M.S. Wong, T.T. Shun, J.W. Yeh: Nanostructured nitride films of multi-element high-entropy alloys by reactive DC sputtering. *Surface and Coatings Technology*, 200, 2005, 1361–1365.
85. Lai C.H., S.J. Lin, J.W. Yeh, S.Y. Chang: Preparation and characterization of AlCrTaTiZr multi-element nitride coatings. *Surface and Coatings Technology*, 201, 2006, 3275–3280.
86. Lin C.H., J.G. Duh, J.W. Yeh: Multi-component nitride coatings derived from Ti-Al-Cr-Si-V target in RF magnetron sputter. *Surface and Coatings Technology*, 201, 2007, 6304–6308.
87. Lai C.H., M.H. Tsai, S.J. Linm J.W. Yeh: Influence of substrate temperature on structure and mechanical properties of multi-element (AlCrTaTiZr)N coatings. *Surface and Coatings Technology*, 201, 2007, 6993–6998.
88. Chang H.W., P.K. Huang, J.W. Yeh, A. Davison, C.H. Tsau, C.C. Yang: Influence of substrate bias, deposition temperature and post-deposition annealing on the structure and properties of multi-principal-component (AlCrMoSiTi)N coatings. *Surface and Coatings Technology*, 202, 2008, 3360–3366.
89. Huang P.K., J.W. Yeh: Effect of nitrogen content on structure and mechanical properties of multi-element (AlCrNbSiTiV)N coating. *Surface and Coatings Technology*, 203, 2009, 1891–1896.
90. Tsai C.W., S.W. Lai, K.H. Cheng, M.H. Tsai, A. Davison, C.H. Tsau, J.W. Yeh: Strong amorphization of high-entropy AlBCrSiTi nitride film. *Thin Solid Films*, 520, 2012, 2613–2618.
91. Tsai D.C., S.C. Liang, Z.C. Chang, T.N. Lin, M.H. Shiao, F.S. Shieu; Effects of substrate bias on structure and mechanical properties of (TiVCrZrHf)N coatings. *Surface and Coatings Technology*, 207, 2012, 293–299.
92. Tsai D.C., Z.C. Chang, L.Y. Kuo, T.J. Lin, T.N. Lin, F.S. Shieu: Solid solution coating of (TiVCrZrHf)N with unusual structure evolution. *Surface and Coatings Technology*, 217, 2013, 84–87.
93. Musil J., R. Daniel, P. Zeman, O. Takai: Structure and properties of magnetron sputtered Zr-Si-N films with a high (≥25 at.%) Si content. *Thin Solid Films*, 478, 2005, 238–247.
94. Chawla V., R. Jayaganthan, R. Chandra: A study of structural and mechanical properties of sputter deposited nanocomposite Ti-Si-N thin films. *Surface and Coatings Technology*, 204, 2010, 1582–1589.
95. Huang F., F. Ge, P. Zhu, H. Wang, F. Meng, S. Li: Superhard V-Si-N coatings (>50 GPa) with the cell-like nanostructure prepared by magnetron sputtering. *Surface and Coatings Technology*, 232, 2013, 600–605.
96. Kim D.J., J.H. La, B.S. Kim, A.Y. Lee: Synthesis and characterization of CrZr-Si-N coatings using Cr-Zr-Si- segment targets by unbalanced magnetron sputtering. *Surface and Coatings Technology*, 259, 2014, 71–76.
97. Zeman H., J. Musil, J. Vlček, P.H. Mayrhofer, C. Mitterer: Thermal annealing of sputtered Al-Si-Cu-N films. *Vacuum*, 72, 2004, 21–28.

98. Shi J., A. Kumar, L. Zhang, X. Jiang, Z.L. Pei, J. Gong, C. Sun: Effect of Cu addition on properties of Ti-Al-Si-N nanocomposite films deposited by cathodic vacuum arc ion plating. *Surface and Coatings Technology*, 206, 2012, 2947–2953.
99. Shi J., C.M. Muders, A. Kumar, X. Jiang, Z.L. Pei, J. Gong, C. Sun: Study on nanocomposite Ti-Al-Si-Cu-N films with various Si contents deposited by cathodic vacuum arc ion plating. *Applied Surface Science*, 258, 2012, 9642–9649.
100. Polychronopoulou K., C. Rebholz, M.A. Baker, L. Theodorou, N.G. Demas, S.J. Hinder, A.A. Polycarpou, C.C. Doumanidis, K. Bobel: Nanostructure, mechanical and tribological properties of reactive magnetron sputtered TiC_x coatings. *Diamond & Related Materiále*, 17, 2008, 2054–2061.
101. Hassani S., J.-E. Klemberg-Sapieha, L. Martinu: Mechanical, tribological and erosion behavior of super-elastic hard Ti-Si-C coatings prepared by PECVD. *Surface and Coatings Technology*, 205, 2010, 1426–1430.
102. Jedrzejowski P., J.E. Klemberg-Sapieha, L. Matinu: Quaternary hard nanocomposite TiC_xNy/SiCN coatings prepared by plasma enhanced chemical vapor deposition. *Thin Solid Films*, 466, 2004, 189–196.
103. Wei R., E. Langa, C. Rincon, J.H. Arp: Deposition of thick nitrides and carbonitrides for sand erosion protection. *Surface and Coatings Technology*, 201, 2006, 4453–4459.
104. Ho L.W., J.W. Lee, H.W. Chen, Y.C. Chan, J.G. Duh: Structure and mechanical properties evaluation of Cr-Ti-B-N coatings. *Thin Solid Films*, 544, 2014, 380–385.
105. Vlček J., S. Potocký, J. Čižek, J. Houška, V. Peřina, J. Zemek, Y. Setsuhara, S. Konuna: Reactive magnetron sputtering of hard Si-B-C-N films with high-temperature oxidation resistance. *Journal of Vacuum Science and Technology* A, 23(6), 2005, 1513–1521.
106. Čapek J., S. Hřeben, P. Zeman, J. Vlček, R. Čerstvý, J. Houška: Effect of the gas mixture composition on high-temperature behavior of magnetron sputtered Si-B-C-N coatings. *Surface and Coatings Technology*, 203, 2008, 466–469.
107. Vlček J., P. Calta, P. Steidl, P. Zeman, R. Čerstvý, J. Houška, J.Kohout: Pulsed reactive magnetron sputtering of high-temperature Si-B-C-N films with high optical transparency. *Surface and Coatings Technology*, 226, 2013, 34–39.
108. Sanchez C.M.T., B.R. Plata, M.E.H. Maia da Costa, F.L. Freire Jr.: Titanium diboride thin films produced by dc magnetron sputtering: Structural and mechanical properties. *Surface and Coatings Technology*, 205, 2011, 3698–3702.
109. Dub S.N., A.A. Goncarov, S.S. Ponomarev, V.B. Filippov, G.N. Tolmaceva, A.V. Agulov: Mechaniceskije svojstva nanokrystalliceskich tonkich plenok $HfB_{2.7}$. *Sverchtverdyje Materialy*, 3, 2011, 9–19 (in Russian).
110. Goncarov A.A., V.A. Konovalov, S.N. Dub, V.A. Stupak, V.V. Petukhov: Structure, composition, and physicomechanical characteristics of tantalum diboride films. *The Physics of Metals and Metallography*, 107, 2009, 285–290.
111. Goncarov A.A., S.N. Dub, A.V. Agulov: Structure, composition, and physicomechanical characteristics of HfB_2 and Hf-B-N films. *The Physics of Metals and Metallography*, 114(1), 2013, 95–101.
112. Dub S.N., A.A. Goncarov, V.V. Petuchov: Vlijanije azota na mechaniceskije svojstva tonkich plenok Ta-B-N. *Sverchtverdyje Materialy*, 2, 2009, 3–11 (in Russian).
113. Ho L.W., J.W. Lee, H.W. Chen, Y.C. Chan, J.G. Duh: Structure and mechanical properte evaluation of Cr-Ti-B-N coatings. *Thin Solid Films*, 544, 2013, 380–385.
114. Vlček J., P. Steidl, J. Kohout, R. Čerstvý, P. Zeman, S. Prokšová, V. Peřina: Hard nanocrystalline Zr-B-C-N films with high electrical conductivity prepared by pulsed magnetron sputtering. *Surface and Coatings Technology*, 215, 2013, 186–191.
115. Jang J., E. An, I.W. Park, D.G. Nam, I. Jo, J. Lin, J.J. Moore, K.H. Kim, I. Park: Microstructure and mechanical properties of Ti-B-C-N-Si nanocomposite films deposited by unbalanced magnetron sputtering. *Journal of Vacuum Science and Technology*, A 31(6), 2013, 061401–1 to 7.

116. Lin S.Y., S.Y. Chang, Y.C. Huang, F.S. Shieu, J.W. Yeh: Mechanical performance and nanoindenting deformation of (AlCrTaTiZr)NC_y multi-component coatings co-sputtered with bias. *Surface and Coatings Technology*, 206, 2012, 5096–5102.
117. Jayatilaka A.D.S.: *Fracture of Engineering Brittle Materials*. Applied Science Publishers, London, 1979.
118. Lawn B.R., A.G. Evan, D.B. Marshall: Elastic/plastic indentation damage in ceramics: The median/radial crack system. *Journal of the American Ceramic Society*, 63, 1980, 574–581.
119. Cook R.F., G.M. Pharr: Direct observation and analysis of indentation damage in ceramics. *Journal of the American Ceramic Society*, 73, 1990, 787–817.
120. Leung D.K., M.Y. He, A.G. Evans: Cracking resistance of nanoscale layers and films. *Journal of Materials Research*, 10, 1995, 1693–1699.
121. Brown W.F. Jr., J.E. *Srawley: ASTM STP*, 410, 1996, 12.
122. Broek D.: *Elementary Engineering Fracture Mechanics*. Kluwer Academic Publishers, Dordrecht, 1997.
123. Li X., D. Diao, B. Bhunshan: Fracture mechanisms of thin amorphous carbon films in nanoindentation. *Acta Materialia*, 45, 1997, 4453–4461.
124. Li X., B. Bhunshan: Measurement of fracture toughness of ultra-thin amorphous carbon films. *Thin Solid Films*, 315, 1998, 214–221.
125. Jaeger G., I. Endler, M. Heilmaier, K. Bartsch, A. Leonhardt: A new method of determining strength and fracture toughness of thin hard coatings. *Thin Solid Films*, 377–378, 2000, 382–388.
126. Tsui T.Y., Y.-Ch. Joo: A new technique to measure through film thickness fracture toughness. *Thin Solid Films*, 401, 2001, 203–210.
127. Kamiya S., H. Kimura, M. saka, H. Abe: A new method for measurement of the toughness of brittle thin films. *Thin Solid Films*, 389, 2001, 180–186.
128. Callister W.D. Jr.: *Materials Science and Engineering*. Introduction, 6th edition, Wiley, New York, 2003.
129. Zhang S., D. Sun, Y. Fu, H. Du: Toughness measurement of ceramic thin films by two-step uniaxial tensile method. *Thin Solid Films*, 469–470, 2004, 233–238.
130. Xia Z., W.A. Curtin, B.W. Sheldon: A new method to evaluate the fracture toughness of thin films. *Acta Materialia*, 52, 2004, 3507–3517.
131. Jungk J.M., B.L. Boyce, T.E. Buchheit, T.A. Friedmann, D. Yang, W.W. Gerberich: Indentation fracture toughness and acoustic energy release in tetrahedral amorphous carbon diamond-like thin films. *Acta Materialia*, 54, 2006, 4043–4052.
132. Galvan D., Y.T. Pei, J.Th. M. De Hosson: Deformation and failure mechanism of nanocomposite coatings under nano-indentation. *Surface and Coatings Technology*, 200, 2006, 6718–6726.
133. Lopez O.B., M. Hoffman, A. Bendavid, P. Martin: The use of the scratch test to measure the fracture strength of brittle thin films. *Thin Solid Films*, 518, 2010, 4911–4917.
134. Hirakata H., O. Nishijima, N. Fukuhara, T. Kondo, A. Yonezu, K. Minoshima: Size effect on fracture toughness of freestanding copper nano-films. *Materiále Science and Engineering*, A 528, 2011, 8120–8127.
135. Panin A.V., A.R. Shugurov, M.S. Kazachenok, V.P. Sergeev: Effect of the nanostructuring of a Cu substráte on the fracture of heat-resistant Si-Al-N coatings dutiny uniaxial pension. *Technical Physics*, 57(6), 2012, 779–786.
136. Zhang S., X. Zhang: Toughness evaluation of hard coatings and thin films. *Thin Solid Films*, 520, 2012, 2375–2389.
137. Zhang X., S. Zhang: Rethinking the role that the "step" in the load-displacement curves can play in measurement of fracture toughness for hard coatings. *Thin Solid Films*, 520, 2012, 3423–3428.
138. Borrero-Lopez O., M. Hoffman, A. Bendavid, P.J. Martin; The use of the scratch test to measure the fracture strength of brittle thin films. *Thin Solid Films*, 518, 2013, 4911–4917.

139. Kachold F.S., M.A. Lodes, S.M. Rosiwal, R.F. Singer: Direct measurement of Young's modulus, fracture strength and fracture toughness of nanocrystalline diamond foil by means of tensile testing. *Acta Materialia*, 61, 2013, 7000–7008.
140. Blažek J.: Pulsed reactive magnetron sputtering of thin films containing copper and characterization of the physical and mechanical properties. Ph.D. thesis, Department of Physics, Faculty of Applied Sciences, University of West Bohemia, Plzen, Czech Republic, 2013.
141. Musil J., P. Dohnal, P. Zeman: Physical properties and high-temperature oxidation resistance of sputtered Si_3N_4/MoN_x nanocomposite coatings. *Journal of Vacuum Science and Technology*, B23, 2005, 1568–1575.
142. Musil J., R. Daniel, J. Soldán, P. Zeman: Properties of reactively sputtered W-Si-N films. *Surface and Coatings Technology*, 200, 2006, 3886–3895.
143. Zeman P., J. Musil: Difference in high-temperature oxidation resistance of amorphous Zr-Si-N and W-Si-N films with a high Si content. *Applied Surface Science*, 252, 2006, 8319–8325.
144. Daniel R., J. Musil, P. Zeman, C. Mitterer: Thermal stability of magnetron sputtered Zr-Si-N films. *Surface and Coatings Technology*, 201, 2006, 3368–3376.
145. Musil J., P. Zeman: Hard amorphous a-Si_3N_4/MeN_x nanocomposite coatings with high thermal stability and high oxidation resistance. *Solid State Phenomena*, 127, 2007, 31–36.
146. Thornton J.A.: (i) Recent developments in sputtering—Magnetron sputtering. *Metal Finishing*, 77(5), 1979, 83–87 and (ii) High rate thick films growth. *Ann. Rev. Mater. Sci*., 7, 1977, 239–260.
147. Pei Y.T., D. Galvan, J.Th.M. De Hosson: Nanostructure and properties of TiC/a-C:H composite coatings. *Acta Materialia*, 53, 2005, 4505–4521.
148. Li W.Z., M. Evaristo, A. Cavaleiro: Influence of Al on the microstructure and mechanical properties of Cr-Zr-(Al)-N coatings with low and high Zr content. *Surface and Coatings Technology*, 206, 2012, 3764–3771.
149. Casellas D., F.L. Cumbrera, F. Sanchez-Bajo, W. Forsling, L. Llanes, M. Anglada: On the transformation toughening of Y-ZrO_2 ceramics with mixed Y-TZP/PSZ microstructures. *Journal of the European Ceramic Society*, 21, 2001, 765–777.
150. Carvie R.C., R.H. Hannink, R.T. Pascoe: Ceramic steel? *Nature* (London), 258, 1975, 703–704.
151. McMeeking R., A.G. Evans: Mechanics of transformation toughening in brittle materials. *J.A. Ceramic Society*, 65, 1986, 242–250.
152. Evans A.G., R.N. Cannon: Toughening of brittle solids by martensitic transformations. *Acta Materialia*, 34, 1986, 761–800.
153. Musil J., V. Poulek, V. Valvoda, R. Kužel Jr., H.A. Jehn, M.E. Baumgartner: Relation of deposition conditions of Ti-N films prepared by dc magnetron sputtering to their microstructure and macrostress. *Surface and Coatings Technology*, 60, 1993, 484–488.
154. Movchan B.A., A.V. Demchishin: Study of the structure and properties of thick vacuum condensates of nickel, titanium, tungsten, aluminum oxide and zirconium oxide. *Phys. The Physics of Metals and Metallography*, 28, 1969, 83–90.
155. Messier R., A.P. Giri, R.A. Roy: Revised structure zone model for thin film physical structure. *Journal of Vacuum Science and Technology*, A2(2), 1984, 500–503.
156. Anders A.: A structure zone diagram including plasma-based deposition and ion etching. *Thin Solid Films*, 518, 2009, 4087–4090.
157. Musil J.: Low-pressure magnetron sputtering. *Vacuum*, 50(3–4), 1998, 363–372.
158. Musil J., P. Novák, R. Čerstvý, Z. Soukup: Tribological and mechanical properties of nc-TiC/a-C nanocomposite thin films. *Journal of Vaccum Science and Technology A*, 28(2), 2010, 244–249.
159. Musil J., V. Šatava, P. Baroch: High-rate reactive deposition of transparent SiO_2 films containing low amount of Zr from molten magnetron target. *Thin Solid Films*, 519, 2010, 775–777.

160. Šatava V.: Reactive magnetron deposition of selected oxide films and their properties, PhD thesis, 2011, Department of Physics, Faculty of Applied Sciences, University of West Bohemia, Plzen, Czech Republic.
161. Musil J., J. Blažek, K. Fajfrlik, R. Čerstvý: Flexible antibacterial Al-Cu-N coatings. *Surface and Coatings Technology*, 264, 2015, 114–120.
162. Chu J.P., J.S.C. Jang, J.C. Huang et al.: Thin film metallic glasses: Unique properties and potential applications. *Thin Solid Films*, 520, 2012, 5097–5122.
163. Chu J.P., J.E. Greene, J.S.C. Jang et al.: Bendable bulk metallic glass: Effects of a thin, adhesive, strong, and ductile coating. *Acta Materialia*, 60, 2012, 3226–3238.
164. Jia H., F. Liu, Z. An, W. Li, G. Wang, J.P. Chu, J.S.C. Jang, Y. Gao, P.K. Liaw: Thin-film metallic glasses for substrate fatigue-property improvements. *Thin Solid Films*, 561, 2014, 2–27.
165. Wisitsorasak A., P.G. Wolynes: On the strength of glasses. *Proceedings of the National Academy of Sciences (PNAS)*, 2013, doi: 10.1073/pnas.1214130109/-/DCSupplemental.
166. Kilczewski S.M., S.R. Thies, J.J. Swab, J.C. Wright, A.J. Gott, M.H. Gaviola, P.J. Patel: The effect of a glass coating on the strength of damaged soda-lime-silicate glass, Poster presentation ICACC-S4-P069–2013, at the 37th International Conference and Exposition on Advanced Ceramics and Composites, January 27-February 1, 2013, Daytona Beach, Florida, USA.
167. Boljanovic V.: *Sheet Metal Forming Processes and Die Design*, New York, Industrial Press, 2004, p. 219.
168. *Handbook of Physical Quantities*, Grigorov I.S. and E.Z. Meilikhov (Eds.), 1997, Boca Raton, FL, USA, p. 49.
169. Chen C.R. J. Pascual, F.D. Fisher, O. Kolednik, R. Danzer: Prediction of the fracture toughness of a ceramic multilayer composite—Modeling and experiments. *Acta Materialia*, 55, 2007, 409–421.
170. Cepeda-Jimenez C.M., M. Pozuelo, J.M. Garcia-Infanta, O.A. Ruano, F. Carreno: Influence of the aluminium thickness at the interfaces on the fracture mechanisms of aluminium multilayers. *Materials Science and Engineering A*, 496, 2008, 133–142.
171. Pascual J., T. Lube, R. Danzer: *Journal of the European Ceramic Society*, 28, 2008, 1551–1556.
172. Panin V.E., V.E. Egorushkin: Deformable solid as a nonlinear hierarchically organized system. *Physical Mesomechanics*, 14(5), 2013, 207–223.
173. Panin V.E., V.P. Sergeev, D.D. Moiseenko, Ju. I. Pochivalov: Scientific basis for the design of heat- and wear-resistant multilayer Si-Al-N/Zr-Y-O coatings. *Fiziceskaja Mesomechanika*, 14(6), 2011, 5–14 (in Russian).
174. Panin V.E., V.E. Egorushkin, L.S. Derevyagina, E.E. Deryugin: Nonlinear wave processes of crack propagation in brittle and brittle-ductile fracture. *Physical Mesomechanics*, 16(3), 2013, 183–190.
175. Zhang Y., Y. Zhai, F. Li, S. Zhang, P. Zhang, S. Zhang: Effect of microstructure and mechanical properties difference between sub-layers on the performance of alternate hard and soft diamond-like carbon multilayer films. *Surface and Coatings Technology*, 232, 2013, 575–581.
176. Soares T.P., C. Aguzzoli, G.V. Soares, C.A. Figueroa, I.J.R. Baumvol: Physicochemical and mechanical properties of crystalline/amorphous CrN/Si_3N_4 multilayers. *Surface and Coatings Technology*, 237, 2013, 170–175.
177. Nakatani M., J. Nishimura, S. Hanaki, H. Uchida: Crack-healing behavior induced by oxidation in SiN/SiC nanolaminated films. *Thin Solid Films*, 556, 2014, 68–73.
178. Barna P.B., M. Adamik: Growth mechanisms of polycrystalline thin films. In *Science and Technology of Thin Films*, Matacotta, F.C. and G. Ottaviani (Eds.), World Scientific Publishing Co, Singapore, 1995, 1–28.

179. Barna P.B., M. Adamik: Formation and characterization of the structure of surface coatings. In *Protective Coatings and Thin Films*, Pauleau, Y. and P.B. Barna (Eds.), 1997, Kluwer Academic Publishers, the Netherlands, 279–297.
180. Musil J., J. Vlček: Magnetron sputtering of hard nanocomposite coatings and their properties. *Surface and Coatings Technology*, 142–144, 2001, 557–566.
181. Musil J., J. Vlček, P. Zeman, Y. Setsuhara, S. Miyake, S. Konuma, K. Yabuta, H. Saito, M. Kumagai: Morphology and microstructure of hard and superhard Zr-Cu-N nanocomposite coatings. *Japanese Journal of Applied Physics*, 41, Part 1, 11A, 2002, 6529–6533.
182. Musil J., J. Šícha, D. Heřman, R. Čerstvý: Role of energy in low-temperature high-rate formation of hydrophilic TiO_2 thin films using pulsed magnetron sputtering. *Journal of Vacuum Science and Technology A*, 25(4), 2007, 666–674.
183. Vlček J., K. Rusňák, V. Hájek, L. Martinu: Reactive magnetron sputtering of CN_x films: Ion bombardment effects and process characterization using optical emission spectroscopy. *Journal of Applied Physices*, 86, 1999, 3646–3655.
184. Lieberman M.A., A.J. Lichtenberg: *Principles of Plasma Discharges and Materials Processing*. Wiley Interscience, New York, 1994.
185. Šůna J., J. Musil, P. Dohnal: Control of macrostress σ in reactively sputtered Mo-Al-N films by total gas pressure. *Vacuum*, 80, 2006, 588–592.
186. Iriarte G.F., F. Engelmark, I.V. Katardiev: Reactive sputter deposition of highly oriented AlN films at room temperature. *Journal of Materials Research*, 17(6), 2002, 1469–1475.
187. Merzhanov A.G., I.P. Borovinskaya: Self-propagated high-temperature synthesis of refractory inorganic compounds. *Doklady Akademii Nauk SSSR*, 204, 1972, 366–369.
188. Rogachev A.S.: Exothermic reaction waves in multilayer nanofilms. *Russian Chemical Reviews*, 77(1), 2008, 21–37.
189. Kadlec S., J. Musil, W.-D. Munz, G. Hakanson, J.-E. Sundgren: Reactive deposition of TiN films using unbalanced magnetron. *Surface and Coatings Technology*, 39/40, 1989, 487–497.
190. Musil J., A.J. Bell, J. Vlček, T. Hurkmans: Formation of high temperature phases in sputter deposited Ti-based films below 100°C. *Journal of Vacuum Science and Technology A*, A14(4), 1996, 2247–2250.
191. *Smithells Metal Reference Book*, 6th Edition, Brandes E.A. (Ed.), Butterworths, London, Metallurgically important compounds, pp. 8–24.

8 Characterization of Coating Adhesion Strength

Kun Zhou, Zhaoxiang Chen, and Hsin Jen Hoh

CONTENTS

8.1 Introduction 466
8.2 Mechanics of Interface Fracture 467
8.2.1 Concepts of Fracture Mechanics 467
8.2.2 Interfacial Fracture Mechanics 468
8.3 Coating Adhesion Evaluation Methods 470
8.3.1 Sandwich Specimen-Based Methods 471
8.3.1.1 DCB Specimen 471
8.3.1.2 Four-Point Bend Specimen 474
8.3.1.3 Brazil Nut Specimen 478
8.3.1.4 Double-Cleavage Drilled Compression Specimen 481
8.3.1.5 Lap Shear Specimen 483
8.3.1.6 Direct Pull-Off Specimen 486
8.3.2 Bimaterial Specimen-Based Methods 490
8.3.2.1 Indentation Test 490
8.3.2.2 Scratch Test 494
8.3.2.3 Peel Test 497
8.3.2.4 Blister Test 500
8.3.2.5 Tensile Test 503
8.3.2.6 Laser Spallation Test 504
8.3.3 Supplementary Techniques 506
8.3.3.1 Photoelasticity Technique 508
8.3.3.2 Coherent Gradient Sensing Technique 509
8.3.3.3 Moiré Interferometry Technique 511
8.3.3.4 Speckle Interferometry Technique 512
8.3.3.5 DIC Technique 514
8.4 Conclusions 515
Acknowledgments 516
References 516

8.1 INTRODUCTION

A coating is a layer of material that is applied over the surface of a substrate, for purposes that may be protective, decorative, or functional.[1] Unique functions may be introduced through such surface modification, such as electrical insulation and moisture protection in electronic applications,[2] corrosion resistance in biomedical applications,[3] thermal barrier for aerospace applications,[4] and a variety of other functions.[5–7] The performance and reliability of such coatings depend on the mechanical integrity of the coating/substrate systems, that is, adhesion of the coating to substrate. Poor adhesion results in delamination or spallation of coatings that will expose the underlying substrate to severe environmental conditions, such as corrosive gases and liquids, abrasive particles and elevated temperatures, resulting in premature failure.[8–10] Proper evaluation of the coating adhesion is important in assessing its fitness for service and detecting need for corrective measures.[11]

In general, there are four mechanisms of coating adhesion (Figure 8.1): (a) interfacial adhesion in which the adhesive forces act upon a well-defined thin interface; (b) interdiffusion adhesion in which the coating and substrate diffuse into each other, resulting in a thicker interfacial region; (c) intermediate layer adhesion in which the coating and substrate are separated by one or more layers of materials of different chemical compositions; (d) mechanical interlocking adhesion in which the coating–substrate interface is relatively rough.[12] Among these mechanisms, the interdiffusion and mechanical interlocking adhesion typically exhibit higher strength. The adhesion strength of a coating to a substrate is also dependent on variables such as the thermal and elastic mismatch between the coating and the substrate, the thickness of the coating and the presence of defects at or near the interface.[13–15] A good understanding of the adhesion and damage mechanisms in coating/substrate systems is necessary to quantify the effects of these variables on coating adhesion.

In current practice, the adhesion of coatings to the substrate is usually measured by mechanical methods and may be supplemented by optical techniques. Mechanical methods can be broadly classified based on their specimen type into either sandwich specimen-based or bimaterial specimen-based methods. Supplementary techniques, such as the photoelasticity or digital image correlation (DIC), are usually used in conjunction with one of the mechanical methods of testing to provide additional evaluation.

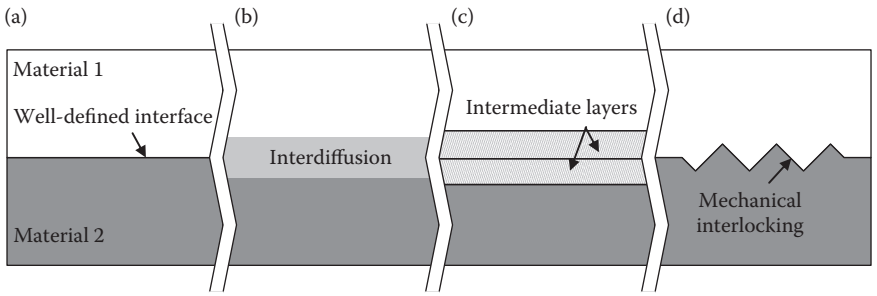


FIGURE 8.1 Four mechanisms of coating adhesion.

This chapter describes the most widely employed evaluation methods and supplementary techniques used in measuring the coating adhesion strength. The theory relevant to understanding the quantification of interface fracture is presented in Section 8.2, followed by a discussion of the measurement methods and supplementary techniques in Section 8.3. In the discussion of the measurement methods, details of the setup are sufficiently described to enable evaluation of the coating adhesion to be carried out, with external references recommended for further details.

8.2 MECHANICS OF INTERFACE FRACTURE

This section lays down the theoretical foundations necessary to quantify interfacial fracture of coating adhesion. In general, two methods may be adopted to establish the coating adhesion strength of various coating–substrate systems evaluated by different testing methods: first, using maximum stress to quantify the adhesion strength needed to separate the coating and substrate; second, being the fracture mechanics approach. The first approach was the primary method before the advent of fracture mechanics. Evaluation of coating adhesion strength was quantified by "strength" based on stress analysis, commonly known as "bond strength" or "adhesion strength." This bond or adhesion strength is defined as the maximum stress that the coating–substrate interface can sustain before separation of the coating and substrate occurs. On the contrary, fracture mechanics considers the presence of defects in addition to the applied stress, resulting in a more complicated approach. In this section, a brief discourse on fracture mechanics is given, followed by a discussion of interfacial fracture mechanics.

8.2.1 Concepts of Fracture Mechanics

Before the introduction of fracture mechanics, general mechanical stress design was based on the maximum allowable stress, with failure expected once a critical stress level was reached. The critical stress could refer to the ultimate tensile stress for uniaxial tension, or the criterions such as the Tresca or von Mises for multiaxial conditions. However, it was found that failure frequently occurred before the critical stress was reached, caused by factors such as the presence of defects, harsh environmental conditions, and poor maintenance.

The pioneer of fracture mechanics, Griffith was motivated by the discrepancies between the theoretical atomic bond strength of glass (~20 GPa) and the stress needed to fracture glass fibers (~170 MPa).[16] He found that the stress required to fracture glass increased as the fiber diameter decreased, prompting investigation into the presence of defects. To explain how these flaws adversely affects material strength, Griffith considered equilibrium between the elastic energy provided by the external load and energy needed to propagate the crack in a linear elastic material, with the strain energy release rate G:

$$G = \frac{\partial(W - U)}{\partial A}, \tag{8.1}$$

where W is the work done by external forces, U is the elastic energy stored in the system, and A is the crack area. When G exceeds a critical value G_c, crack propagation occurs. For interfacial fracture, crack propagation will result in detachment of the coating from the substrate.

Irwin[17] introduced the stress intensity factor (SIF) K to simplify characterization of the state of stresses and displacements near the crack tip. Similar to G, crack propagation is predicted when K exceeds a critical value K_c known as the plane strain fracture toughness. The definition of the SIF is

$$\begin{aligned} K_{\mathrm{I}} &= \lim_{r\to 0}\sqrt{2\pi r}\,\sigma_{yy}(r,0) \\ K_{\mathrm{II}} &= \lim_{r\to 0}\sqrt{2\pi r}\,\sigma_{xy}(r,0) \\ K_{\mathrm{III}} &= \lim_{r\to 0}\sqrt{2\pi r}\,\sigma_{yz}(r,0) \end{aligned} \tag{8.2}$$

For a center crack in a plate, the SIF is given by

$$K_{\mathrm{I}} = \sigma_{yy}\sqrt{\pi a}, \tag{8.3}$$

where a refers to half of the crack size. For a crack in a homogeneous material, G is related to K by

$$G = \frac{K^2}{\bar{E}} \tag{8.4}$$

where $\bar{E} = E$ for plane stress and $\bar{E} = E/(1-\nu^2)$ for plane strain, in which E is Young's modulus and ν is Poisson's ratio. For homogeneous linear elastic solids, either G or K is sufficient to characterize the failure.

However, the parameters do not apply to materials that exhibit ductile behavior, which could be caused by inelastic deformation or a blunt crack tip. The size of such a plastic region can be estimated by models introduced by Irwin[18] and Dugdale.[19] An appropriate fracture criterion is the crack tip opening displacement (CTOD),[20] suitable where significant plastic deformation precedes fracture.

8.2.2 Interfacial Fracture Mechanics

The interface crack is more complicated than the crack in a homogeneous material because mixed-mode fracture is often exhibited at the interface of two dissimilar materials. The foundations of linear elastic fracture mechanics is the asymptotic analysis of the stress and strain fields near the crack tip. Asymptotic analysis of the stress and strain fields near the crack tip of open interface cracks by Williams[21] gives the stresses σ and displacements u as

$$\begin{aligned} \sigma &\sim r^{-1/2}(\sin,\cos)(\varepsilon \log r), \\ u &\sim r^{1/2}(\sin,\cos)(\varepsilon \log r), \end{aligned} \tag{8.5}$$

where

$$\varepsilon = \frac{1}{2\pi}\ln\left(\frac{1-\beta}{1+\beta}\right), \tag{8.6}$$

while β is the second Dundurs parameter,[22] given by

$$\beta = \frac{\mu_2(\kappa_1 - 1) - \mu_1(\kappa_2 - 1)}{\mu_2(\kappa_1 + 1) + \mu_1(\kappa_2 + 1)}, \tag{8.7}$$

where μ_j ($j = 1, 2$) denotes the shear modulus of each material; $\kappa_j = 3 - 4\nu_j$ for plane strain and $\kappa_j = (3 - \nu_j)/(1 + \nu_j)$ for plane stress, in which ν_j is Poisson's ratio of the material.

The stress and displacement elastic solutions in Equation 8.5 exhibit oscillatory behavior. In pure mode I loading, the interpenetration zone caused by this behavior is negligible. However, when remote shear loading is present, the interpenetration zone length is no longer negligible. Various attempts have been made to resolve this oscillatory behavior,[23] most prominent being the contact zone model by Comninou.[24] It is predicted that the contact zone could be up to almost a third of the crack length under mixed-mode loading.

Due to the nature of the stresses in Equation 8.5, using the SIF definition in Equation 8.2 for interfacial cracks results in logarithmically infinite values. Another problem with the elastic solution is that the fracture modes I and II are coupled. Consequently, a complex interfacial SIF K^* is used to characterize the stress fields ahead of an interfacial crack tip[25,26] in Figure 8.2:

$$\begin{aligned} \sigma_{yy} + i\sigma_{xy} &= \frac{K^*}{\sqrt{2\pi r}} r^{i\varepsilon}, \\ K^* &= K_I + iK_{II}. \end{aligned} \tag{8.8}$$

The strain energy release rate for the interfacial crack with the oscillatory solution G_o is related to the complex interfacial SIF K^*[25,27] by

$$G_o = \frac{\bar{E}_1 + \bar{E}_2}{2\cosh^2(\pi\varepsilon)\bar{E}_1\bar{E}_2}|K^*|^2, \tag{8.9}$$

where $\bar{E}_j = E_j/(1 - \nu_j^2)$ for plane strain, while $\bar{E}_j = E_j$ for plane stress. In the contact zone model of Comninou,[23] the critical interfacial strain energy release rate G_c is

$$G_c = \frac{\bar{E}_1 + \bar{E}_2}{2\bar{E}_1\bar{E}_2}(1 - \beta^2)(K_{II}^c)^2, \tag{8.10}$$

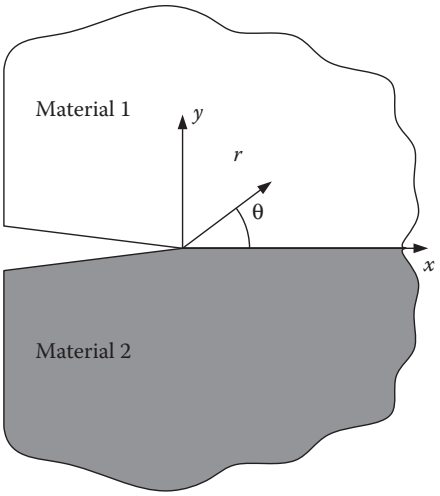


FIGURE 8.2 An interfacial crack between two dissimilar materials.

where the K_{II}^{c} is known for the problem of an interface crack under uniform tension T as

$$K_{II}^{c} = T[\pi a(1 + 4\varepsilon^2)]^{1/2}. \tag{8.11}$$

In addition to the stated energy release rate, another important parameter for a crack in a bimaterial interface is the loading phase angle Ψ, which is related to the ratio of the normal to shear stresses ahead of the interfacial crack tip. The phase angle Ψ is defined as[27,28]

$$\Psi = \tan^{-1}\left(\frac{\mathrm{Im}(K^* L^{i\varepsilon})}{\mathrm{Re}(K^* L^{i\varepsilon})}\right) = \tan^{-1}\left(\frac{K_{II}}{K_I}\right) \tag{8.12}$$

where the functions Im(·) and Re(·) take the imaginary and the real part of the complex variable, respectively. Ψ is independent of the reference length L used to characterize the remote field and is an arbitrary length parameter. An example of the arbitrary reference length L is the smaller thickness of the two materials that form the interface.[27]

For interface fracture, two parameters are required: the loading phase angle Ψ and either the strain energy release rate or complex SIF K^*.

8.3 COATING ADHESION EVALUATION METHODS

Approaches based on strength and stress can be measured by a number of simple techniques such as the lap shear test[29] and pull-off test.[8] The introduction of fracture mechanics allowed the coating adhesion to be quantified by interfacial fracture toughness, which is related to the amount of energy required to initiate or propagate

the crack. The interfacial fracture toughness is a measure of the resistance of the interface to interfacial crack initiation and propagation. However, the interfacial fracture toughness usually depends on the mode mixity and requires more than one quantity to be characterized, unlike the adhesion strength where a single parameter is sufficient. The interfacial fracture toughness of coating/substrate systems can be measured by employing tests such as the double cantilever beam (DCB),[30] four-point bending,[31] Brazil-nut,[32] and indentation.[33]

In this section, the various test methods are classified based on their specimen material configuration. The two configurations are the sandwich specimen and the bimaterial specimen. A third group of techniques described are supplementary techniques, because they are generally applied in conjunction with one of the specimen test methods.

8.3.1 Sandwich Specimen-Based Methods

The main theory behind sandwich specimen-based testing in evaluating coating adhesion was developed by Suo and Hutchinson.[34] This specimen is prepared by bonding a coating between two halves of a substrate material. By ensuring that the coating thickness is small compared to the crack length and other dimensions of the specimen, the specimen can be considered homogeneous. Hence, classical fracture mechanics applies and solutions are available for evaluation of the fracture toughness or strain energy release rate. In addition, the complication due to inhomogeneity introduced by this thin coating can be ignored. It is a common practice to use the fracture toughness or strain energy release rate of a homogeneous specimen to characterize the interfacial crack between substrate and coating layer.[34]

In this section, sandwich specimens to be discussed include the DCB specimen,[30] four-point bend specimen,[31] Brazil-nut specimen,[32] double-cleavage drilled compression (DCDC) specimen,[35] lap shear specimen,[29] and pull-off specimen.[36]

8.3.1.1 DCB Specimen

One of the earliest sandwich specimen tests was the DCB specimen, first proposed and developed by Berndt and McPherson[37] for evaluation of coating adhesion. In the DCB test setup (Figure 8.3), the coating is sandwiched between two beams of substrate material with a preexisting crack along the coating/substrate interface. Under tensile loading, the crack begins to propagate along the interface; the propagation is monitored by an optical microscope while the CTOD is measured by an extensometer placed on the specimen. The experiment is performed by increasing the displacement of the loading point at a constant rate. The applied load is measured by a load cell, in which the peak load is associated with the onset of interfacial crack growth while the load drop is associated with the interfacial crack jump. When stable interfacial crack growth occurs, the displacement ramp is interrupted, allowing the DCB specimen to be unloaded and returned to rest. Subsequently, the specimen is reloaded with constant displacement rate until crack growth occurs. Several loading/unloading cycles are performed until complete specimen failure.

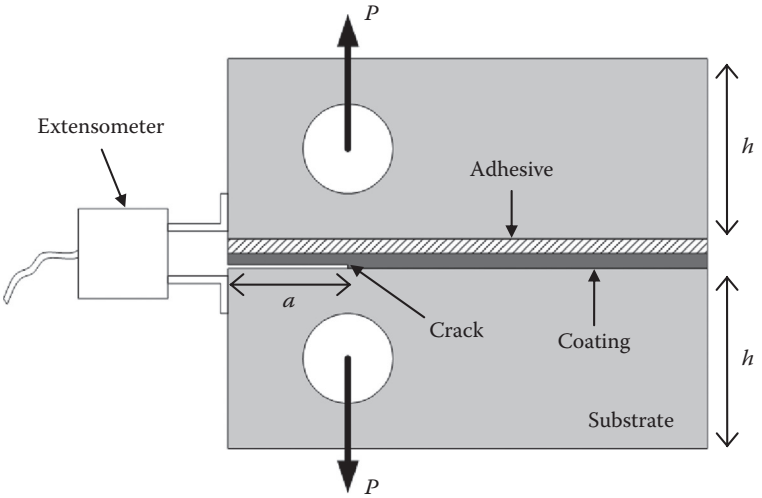


FIGURE 8.3 Specimen configuration for DCB testing of coating adhesion. (Modified with permission from Ostojic, P. and McPherson, R. *Journal of the American Ceramic Society* 71(10), 1988: 891–99.)

The DCB test can be employed to quantitatively determine the critical interfacial strain energy release rate G_c of the coating/substrate system. As explained earlier, when the coating thickness is small compared with the length scale of the overall geometry of the DCB specimen and the ratio of the crack length to the beam half-height is large, the existence of this thin coating layer can be ignored. As such, G_c can be determined[38] by

$$G_c = \frac{P_c^2}{2b}\frac{\mathrm{d}C}{\mathrm{d}a} = \frac{4P_c^2}{Eb^2}\left(\frac{3a^2}{h^3} + \frac{1}{h}\right), \tag{8.13}$$

where P_c is the critical tensile load, b the beam width, C the loading point compliance, a the crack length, and E Young's modulus, Poisson's ratio is assumed $\nu = 1/3$ and h the substrate height. The expression of G_c is thus dependent on P_c and a. Once G_c is known, the interfacial SIF can be calculated by Equation 8.9. The phase angle shift caused by the thin coating layer is typically small unless the elastic mismatch between the coating and the substrate is significantly large, indicating predominantly mode I loading.

The advantages of the DCB test include stable and controllable crack growth that allows multiple fracture toughness readings to be taken from a single specimen, compared with other simple techniques such as the pull-off test and single edge notched specimen where the interfacial failure is often catastrophic. Furthermore, because the DCB test measures the interface fracture energy at a phase angle Ψ of about 0° (nearly mode I), this allows the measured energy to be closely related to the intrinsic interfacial adhesion energy under mode I loading. This attribute makes the DCB test a popular method for evaluating the adhesion of coating/substrate systems.[30,37]

In the field of microelectronics, measurement of G_c is carried out under the condition $a \gg h$, by which Equation 8.13 becomes

$$G_c = \frac{12P_c^2a^2}{Eb^2h^3}. \tag{8.14}$$

Using this result, Lee[39] found the DCB more suitable than shear tests for characterizing interfacial adhesion between packaging materials, because the shear tests failed cohesively for all temperature conditions tested. Similarly, Loo et al.[40] demonstrated that the DCB specimen could be employed to evaluate interfacial fracture toughness of the solder joint with good repeatability. Dai et al.[41] used a modified form of Equation 8.14 to quantify the interfacial adhesion of a flip-chip on an organic substrate.

The disadvantage of the DCB test is that the crack length has to be measured to determine the interfacial strain energy release rate. It may be difficult or even impossible to accurately measure the crack length optically by a traveling microscope in certain situations, such as in an environmental chamber or during cyclic loading.

To alleviate this, a contoured DCB specimen (Figure 8.4) was designed such that its compliance is linearly proportional to crack length.[42] Hence, dC/da in Equation 8.13 is constant and the applied tensile load P_c is the only measured parameter required to establish the critical energy release rate G_c, dispensing with measurement of crack length a. In addition, this test method does not require the introduction of a sharp crack in the specimen. Specimen loading could start with a blunt crack and once propagation commences, the average load is used to calculate G_c. Later, Li et al.[38] suggested that for the convenience of specimen preparation, a tapered DCB specimen with machined flat surfaces is preferable to the contoured DCB specimen (Figure 8.4). When the beam is machined into a straight surface instead of a curved one, the compliance of the tapered DCB specimen still yields an experimentally

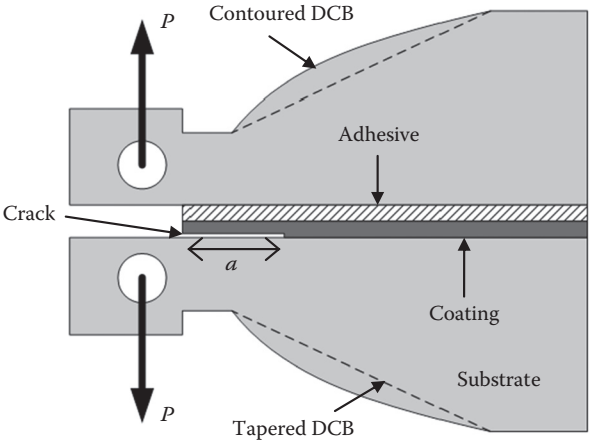


FIGURE 8.4 Contoured and tapered DCB specimens. (Modified with permission from Li, C.-J., Wang, W.-Z., and He, Y. *Journal of the American Ceramic Society* 86(8), 2003: 1437–39.)

reasonable linear relation with the crack length, despite the beam height difference. The measured mean values of interfacial fracture toughness G_c of plasma-sprayed Al_2O_3 coatings using the tapered DCB specimen ranged from 13 to 27 J/m^2 for the Al_2O_3 coatings at different spray distances. These values agree well with those obtained by the conventional DCB specimen test and confirm the feasibility of the tapered DCB method for the measurement of fracture toughness of thermal sprayed coatings.[38,43]

The tapered DCB test has been applied to study the adhesion of epoxy-amine to metals.[44] The addition of reactive liquid rubber further improved the critical strain energy release rate G_c from 120 to 320 J/m^2. The tapered DCB has also been employed in studying fatigue crack propagation in microcapsule-toughened epoxy.[45] It was shown that the addition of microcapsules decreased the fatigue growth rate and increased fatigue life.

The DCB test is well-suited for measuring mode I interfacial fracture toughness. Multiple fracture toughness readings can be taken from a single DCB specimen, making the test preferable when material is expensive or scarce. This test has no stringent restrictions on the mechanical properties of materials used for the coatings and substrates and thus can be applied to a wide range of coating/substrate systems.

8.3.1.2 Four-Point Bend Specimen

Charalambides et al.[46,47] developed the four-point bend specimen (Figure 8.5) to determine critical energy release rate G_c at bimaterial interfaces under approximately equal shear and normal displacement loading. In the specimen, a central notch serves as the interfacial crack initiation site when loaded under four-point bending, where the crack is assumed to propagate symmetrically with respect to the notch. However, this setup is limited to coating/substrate systems with relatively high fracture toughness at the coating layer to prevent vertical cracking in the layer.[48,49] Despite its limitations, it is still commonly used because of its simplicity.[50,51]

To overcome the limitations of the original setup, Hofinger et al.[49] proposed a simple modification to the four-point bend specimen to allow for evaluation of the critical interfacial energy release rate G_c of thin, brittle, and strongly adhering coatings, leading to the sandwich form in Figure 8.6. A stiffener was introduced, bonded

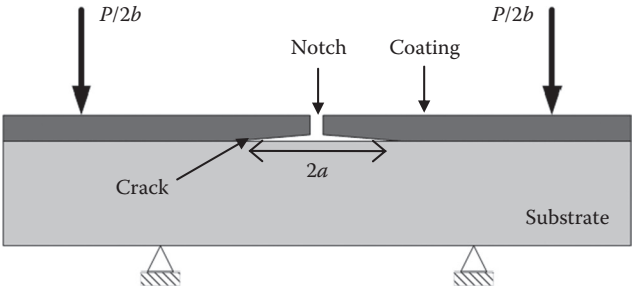


FIGURE 8.5 Geometry of original four-point bend specimen. (Modified with permission from Charalambides, P. G. et al., *Mechanics of Materials* 8(4), 1990: 269–83.)

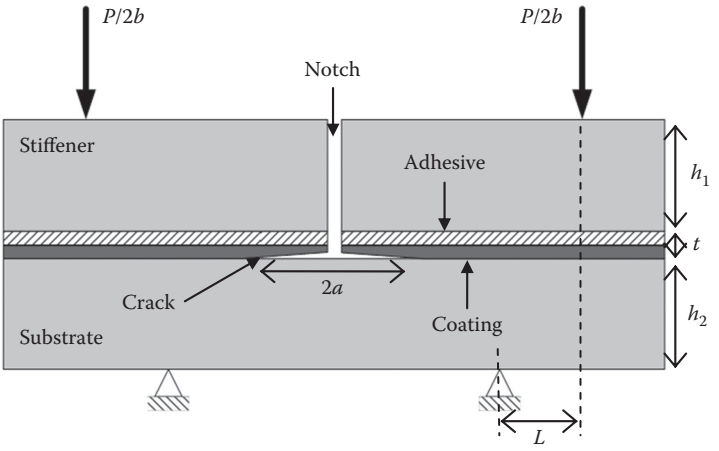


FIGURE 8.6 Geometry of sandwich four-point bend specimen. (Modified with permission from Hofinger, I. et al., *International Journal of Fracture* 92(3), 1998: 213–20.)

on top of the thin brittle surface. This stiffening plate suppresses the vertical cracking and segmentation of the brittle coating, while the increased thickness caused by the stiffener increases stored strain energy, which promotes crack propagation at the interface. The resulting critical energy release rate[49] is given by

$$G_c = \frac{P_c^2 L^2}{8\bar{E}b^2}\left(\frac{1}{I_2} - \frac{1}{I_c}\right) \tag{8.15}$$

where P_c is the critical load; L is the spacing between the inner and outer loading lines; b is the width of the specimen. Second moments of inertia I_2 and I_c are given by

$$I_2 = \frac{h_2^3}{12}$$
$$I_c = \frac{h_2^3}{3} + \kappa\frac{t^3}{3} + \mu\left(\frac{h_1^3}{3} + h_1^2 t + t^2 h_1\right) - \frac{[h_2^2 - \kappa t^2 - \mu(h_1^2 + 2th_1)]^2}{4(h_2 + \kappa t + \mu h_1)} \tag{8.16}$$

in which $\kappa = (\bar{E}_t/\bar{E}_2)$, $\mu = (\bar{E}_1/\bar{E}_2)$. Elastic modulus is $\bar{E} = E/(1 - \nu^2)$ for plane strain as in Equation 8.4, where subscript 1 refers to the stiffener, 2 to the substrate, and t to the coating/adhesive.

When the stiffener and substrate are of identical material $\bar{E}_1 = \bar{E}_2 = \bar{E}$ and height $h_1 = h_2 = h$, while the coating dimensions are small relative to other dimensions, the sandwich four-point bend specimen is mostly homogeneous. Under such conditions, the homogeneous critical strain energy release rate G_c can be used to characterize the interfacial crack as proposed by Suo and Hutchinson.[34]

Simplifying Equation 8.15 to that of a homogeneous four-point bend specimen (without a sandwiched layer)[31]

$$G_c = \frac{21P_c^2L^2}{16\bar{E}b^2h^3} \tag{8.17}$$

This four-point bend specimen test method possesses advantages of: (a) availability of a closed-form solution for the critical interfacial strain energy release rate G_c; (b) the resulting G_c exhibits steady-state characteristics, which makes accurate crack length monitoring noncritical; (c) relatively simple specimen preparation because a specimen with a rectangular cross section is usually used for testing; and (d) straightforward specimen mounting and dismounting, with no special grip required.

The main disadvantage of the four-point bending specimen lies in the complexity of the preparation of precracks. A second disadvantage is that the condition of symmetric interfacial crack propagation with respect to the central notch is rarely achieved in actual experiments; asymmetric crack propagation is more common. For such cases, the calculated G_c may be incorrect. There are two main causes for the asymmetric crack propagation.[52,53] First, for a very stiff four-point bend beam specimen under a small load, even very small shape distortions of the specimen (~100 μm) or misalignments of the test rig can cause significant loading asymmetry.[52] Second, the presence of imperfect precracks or variations in material properties along the interface can also result in asymmetrical crack propagation.[53]

To overcome the problem of asymmetric crack propagation, Howard et al.[52] modified the bend loading arrangement to include a floating platen (Figure 8.7). This modified four-point bend rig is self-aligned and flexible to use. It ensures that a uniform moment is applied to the specimen between the inner loading rollers, leading to symmetrical propagation of crack tips at both sides of the specimen. The linear variable displacement transducers (LVDTs) function to monitor the

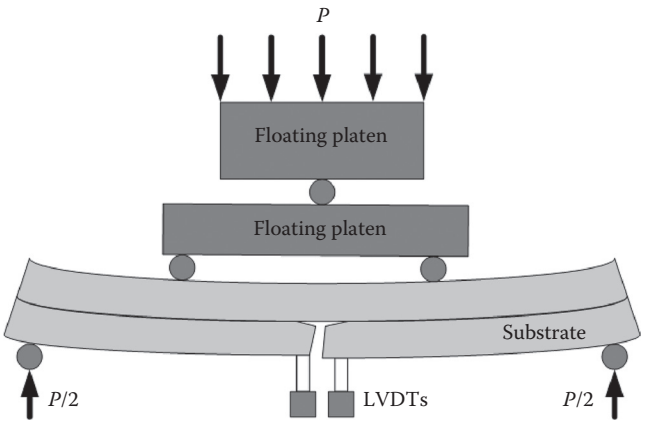


FIGURE 8.7 Modified four-point bending specimen loading arrangement using a floating platen. (Modified with permission from Howard, S. J., Phillipps, A. J., and Clyn, T. W. *Composites* 24(2), 1993: 103–12.)

vertical displacements of the debonded ligaments. This floating platen four-point bend fixture was applied by Clifford et al.[54] to characterize the interface fracture toughness of glass-reinforced plastic (GRP) to steel. The fracture toughness is shown to significantly increase with increasing surface roughness, reaching a plateau at $R_a \approx 3$ μm. Fracture toughness increased due to the increase in surface area caused by the surface roughness, and at the plateau, the crack path ceased to follow the actual interface. Wang and Siegmund[53] obtained improved fracture toughness results using this setup. They also developed equations for calculating the fracture toughness when the two half cracks are asymmetrical. The two fracture toughness values obtained correspond to the two load plateaus caused by asymmetrical crack propagation. However, the floating platen loading arrangement in Figure 8.7 is still less adopted as it is more complicated compared to the setups in Figures 8.5 and 8.6.

Hence, the sandwich four-point bend test in Figure 8.6 is still the preferred method in the evaluation of coating adhesion, especially for evaluating the performance of thermal barrier coatings (TBCs). Yamazaki et al.[55] evaluated the delamination resistance of a TBC system with this method. They found that the average critical energy release rate G_c was independent of the loading rate and the interface roughness, but increased with aging time. Théry et al.[56] employed the method to compare the performance of two different TBCs. They found that the two bond coats have similar adhesion evolution, but different microstructural degradation and failure mechanisms. The Pt-modified β-NiAl bond coat failure was caused by interfacial voids and extensive rumpling, while the Zr-doped β-NiAl bond coat interface remained smooth with no interfacial voids. Failure was attributed to high compressive stresses within the thermally grown oxide layer. Chen et al.[31] also employed the sandwich four-point bend specimen to evaluate the interfacial crack growth resistance in plasma-sprayed TBCs. G_c was found to increase with crack extension until a steady value of ~170 J/m^2. Through *in situ* observation of crack propagation and subsequent finite element analysis, it was concluded that the rising R-curve behavior was caused by crack bridging in the wake zone, which shielded the crack tip from the far-field loading. Zhao et al.[57] studied atmospheric plasma sprayed TBCs and found that delamination occurred mainly within the TBC. The energy release rate G_c increased from ~50 J/m^2 for as-sprayed TBCs to ~120 J/m^2 for TBCs exposed at 1150°C for 200 h, with a loading phase angle of about 42°. X-ray microtomography was used to track the 3D evolution of the microstructure in a nondestructive manner.

The sandwich four-point bend specimen can also be employed for adhesion measurement of multilayered thin-film structures and composite structures. Zou et al.[58] characterized the interfacial toughness of Si_3N_4/BN composites. Their test was improved by adopting a small sandwich specimen and introducing a weak crack path directly connecting to the interphase, compared to the conventional four-point bend test in which large specimens were usually adopted and precracks were created by three-point bending. Their measured results showed that the interfacial toughness of Si_3N_4/BN composites increased as the volume fraction of the Si_3N_4 interphase modifier increased. The improved specimen was found to be very effective in measuring the interfacial toughness of Si_3N_4/BN composites. Gan et al.[59] quantified

the interfacial adhesion energy of multilayered thin-film structures. The adhesion energy of the SiC/polyarylene ether (PAE) interface was measured to be 26.2 J/m^2 higher than that of other reported SiN/PAE interfaces. Yan et al.[60] proposed the use of the cohesive zone model instead of the fracture toughness to study multilayered nanoscale components. The cohesive zone model parameters calibrated by a 200 nm nanocantilever test were shown to be capable of predicting crack propagation in millimeter-sized four-point bending specimens.

The sandwich four-point bend test is suitable for determining the mixed-mode interfacial fracture toughness, unlike the DCB test, which measures only mode I interfacial fracture toughness. Furthermore, it is widely applicable to many types of coatings, from soft flexible coatings to hard brittle coatings. It is not only limited to a bilayer system but may also be applied to a multilayer system. However, preparation of specimen precracks is tricky, and the cracks may not propagate symmetrically about the notch.

8.3.1.3 Brazil Nut Specimen

The Brazil nut specimen, also known as the Brazilian disk, was proposed by Carneiro and Barcellos[61] in Brazil to measure the tensile strength of concrete. The specimen was later adopted to study the mixed-mode fracture of homogeneous materials.[62,63] In their test setup, shown in Figure 8.8a, a uniform disk-shaped specimen containing a precrack passing through the center is loaded in compression along a diameter of an angle θ to the crack plane. Using different orientations of the precrack with respect to the loading direction enables a wide range of phase angles to be studied. For example, for θ = 0°, crack deformation is in mode I; for mode II crack deformation, θ is between 19° and 32°, depending on the ratio of crack length to specimen

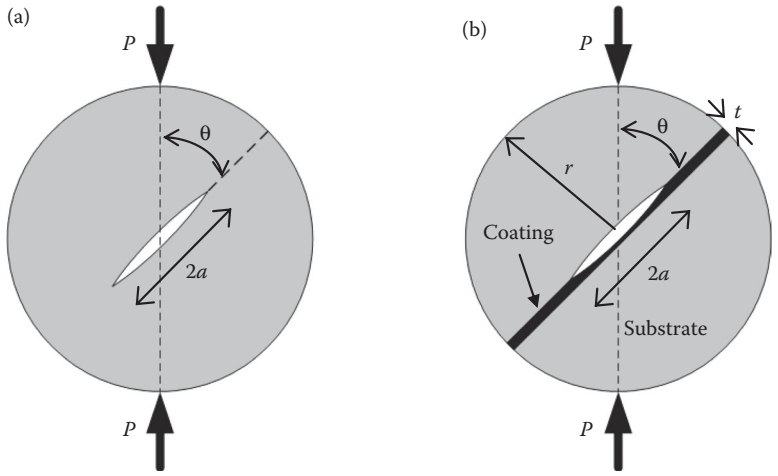


FIGURE 8.8 (a) Brazil nut specimen geometry. (Modified with permission from Atkinson, C., Smelser, R. E., and Sanchez, J. *International Journal of Fracture* 18(4), 1982: 279–91.) (b) Brazil-nut-sandwich specimen geometry. (Modified with permission from Wang, J. S. and Suo, Z. *Acta Metallurgica Et Materialia* 38(7), 1990: 1279–90.)

radius a/r.[64] Above this value, the mode I SIF becomes negative. For this specimen, the real and imaginary parts of the SIF are given by

$$K_{\mathrm{I}} = \frac{Pf_{\mathrm{I}}}{br}\sqrt{\frac{a}{\pi}}, \tag{8.18}$$

$$K_{\mathrm{II}} = \frac{Pf_{\mathrm{II}}}{br}\sqrt{\frac{a}{\pi}}, \tag{8.19}$$

where P is the load applied in compression, a is the semicrack length, b and r are the disk thickness and radius, respectively. The nondimensional factors f_{I} and f_{II} are functions of the compression angle θ, crack length a, and radius r, and were evaluated by Atkinson et al.[62] as

$$\begin{aligned} f_{\mathrm{I}} &= \sum_{i=1}^{n} T_i \left(\frac{a}{r}\right)^{2i-2} A_i(\theta), \\ f_{\mathrm{II}} &= 2\sin 2\theta \sum_{i=1}^{n} S_i \left(\frac{a}{r}\right)^{2i-2} B_i(\theta), \end{aligned} \tag{8.20}$$

where the first five values of coefficients T_i and S_i, as well as angular constants $A_i(\theta)$ and $B_i(\theta)$ are given in Tables 8.1 and 8.2. A simplified relation was obtained by Shetty et al.[65] for mode I by providing a cubic fit to the results of Atkinson et al.[62] as

TABLE 8.1
First Five Coefficients of Equation 8.20

a/r	0.1	0.2	0.3	0.4	0.5	0.6
T_1	1.014998	1.060049	1.135551	1.243134	1.387239	1.578258
T_2	0.503597	0.514907	0.533477	0.559734	0.594892	0.642124
T_3	0.376991	0.382430	0.391640	0.404603	0.421949	0.445387
T_4	0.376991	0.383392	0.393835	0.408597	0.428353	0.454861
T_5	0.314159	0.318086	0.325033	0.334831	0.347941	0.365559
S_1	1.009987	1.039864	1.089702	1.160796	1.257488	1.390654
S_2	0.502341	0.509959	0.522272	0.539824	0.563966	0.597985
S_3	0.376363	0.379956	0.386086	0.394822	0.406869	0.424037
S_4	0.376363	0.380584	0.387518	0.397403	0.410966	0.430072
S_5	0.314159	0.316245	0.320834	0.327411	0.336447	0.349219

Source: Modified with permission from Atkinson, C., Smelser, R. E., and Sanchez, J. *International Journal of Fracture* 18(4), 1982: 279–91.

TABLE 8.2
First Five Angular Constants of Equation 8.20

A_1	$1 - 4\sin^2\theta$
A_2	$8\sin^2\theta\,(1 - 4\cos^2\theta)$
A_3	$-12\sin^2\theta\,(1 - 12\cos^2\theta + 16\cos^4\theta)$
A_4	$16\sin^2\theta\,(1 - 24\cos^2\theta + 80\cos^4\theta - 64\cos^6\theta)$
A_5	$-20\sin^2\theta\,(1 - 40\cos^2\theta + 240\cos^4\theta - 448\cos^6\theta + 256\cos^8\theta)$
B_1	1
B_2	$-5 + 8\cos^2\theta$
B_3	$-3 - 8\cos 2\theta\,(2 - 3\cos^2\theta)$
B_4	$3 - 16\cos 2\theta - 12\,(\cos 2\theta)^2 + 32(\cos 2\theta)^3$
B_5	$5 + 16\cos 2\theta - 60(\cos 2\theta)^2 - 32(\cos 2\theta)^3 + 80(\cos 2\theta)^4$

Source: Modified with permission from Atkinson, C., Smelser, R. E., and Sanchez, J. *International Journal of Fracture* 18(4), 1982: 279–91.

$$f_{\mathrm{I}} = 0.991 + 0.141\left(\frac{a}{r}\right) + 0.863\left(\frac{a}{r}\right)^2 + 0.886\left(\frac{a}{r}\right)^3. \tag{8.21}$$

For small crack approximations, where $a/r < 0.6$, Atkinson et al.[62] gives the values of f_{I} and f_{II} as

$$\begin{aligned} f_{\mathrm{I}} &= 1 - 4\sin^2\theta + 4\sin^2\theta(1 - 4\cos^2\theta)\left(\frac{a}{r}\right)^2, \\ f_{\mathrm{II}} &= \left[2 + (8\cos^2\theta - 5)\left(\frac{a}{r}\right)^2\right]\sin 2\theta. \end{aligned} \tag{8.22}$$

The energy release rate G can be calculated from

$$G = \frac{1}{\bar{E}}(K_{\mathrm{I}}^2 + K_{\mathrm{II}}^2) = (f_{\mathrm{I}}^2 + f_{\mathrm{II}}^2)\frac{P^2 a}{\bar{E}b^2 r^2 \pi} \tag{8.23}$$

where $\bar{E} = E/(1 - \nu^2)$ is the elastic modulus of the beam as in Equation 8.4. The corresponding mode mixity Ψ of Equation 8.12 is given by

$$\Psi = \tan^{-1}\left(\frac{K_{\mathrm{II}}}{K_{\mathrm{I}}}\right) = \tan^{-1}\left(\frac{f_{\mathrm{II}}}{f_{\mathrm{I}}}\right). \tag{8.24}$$

Later modification by Wang and Suo[66] brought about the Brazil nut sandwich or sandwich Brazil nut specimen (Figure 8.8b). In this specimen, the coating is bonded

between two identical substrate halves and a precrack is introduced at the interface. If the coating layer thickness is much smaller than other characteristic dimensions of the specimen, the SIF solution for a homogeneous disk shown in Figure 8.8a can be used for the sandwich Brazil nut specimen shown in Figure 8.8b.

The advantage of the sandwich Brazil nut specimen is that it can be loaded in pure mode I, pure mode II, or any mixed mode in between. Thus, a wealth of interface fracture information at different modes can be provided by simple compression loading. In addition, this specimen is compact and the test does not require sophisticated loading fixtures. The main disadvantage is that interfacial crack propagation tends to occur in an unstable manner.

The sandwich Brazil nut specimen has been a valuable tool in practice for the study of interfacial fracture behavior. Pang et al.[67] characterized mixed-mode fracture toughness of adhesive bonded joints using this specimen and found mode II fracture toughness to be generally higher than mode I fracture toughness. Banks-Sills and Schwartz[68] studied sandwich Brazil nut specimen composed of aluminum adherents joined by a thin epoxy, with the precrack placed within the coating. They found that the crack propagated within the epoxy but ran into the lower interface for two loading angles in which $K_{II}/K_I < 0.9$. Tong et al.[32] studied the interfacial fracture toughness of synthetic bone-cement interface using the sandwich Brazil nut specimen with polyurethane (which is a material analogous to cancellous bone) as substrates and bone cement as the interlayer. The solution for the critical strain energy release rate G_c at the chosen phase angle Ψ was obtained using finite element analysis. At phase angles $\Psi \approx 45°$ and $|\Psi| < 18°$, the measured values of G_c were 47 and 20 J/m^2 on average, respectively. Rahbar et al.[69] studied the adhesion of hard and soft layers by measuring the interfacial fracture energies between parylene and 316L stainless steel bonded by epoxy over a range of mode mixities. They showed that the experimental values agree well with the adhesion model of Derjaguin-Muller-Toporov (DMT). Tan et al.[70] employed the sandwich Brazil nut specimen to study interfacial creep crack growth along interfaces of different adhesives and marble in order to identify suitable materials for the restoration of statues and other marble structures. They identified that the combination of mixed thermosetting/thermoplastic polymer resins (Paraloid B-72/Epotek) provides best resistance to subcritical crack growth.

The key advantage of the Brazil nut specimen is that it can conveniently evaluate the interfacial fracture toughness as a function of the loading mode. This is because this specimen can be easily loaded in pure mode I, pure mode II, or any mode mix between modes I and II. Moreover, there is no stringent restriction on mechanical properties of the materials used for the coatings and substrates. The main disadvantage is that the interfacial crack tends to propagate in an unstable manner.

8.3.1.4 Double-Cleavage Drilled Compression Specimen

Janssen developed the DCDC specimen,[35] with the experimental setup shown in Figure 8.9a. The DCDC specimen is a rectangular bar with a circular hole at the center. When uniform axial compression is applied to the DCDC specimen, Poisson's effect will cause tensile stresses to be concentrated at the crowns of the central hole. Under increased compression, a mode I crack is generated at each crown once the tensile stresses at the crowns reach the fracture strength of the material. The

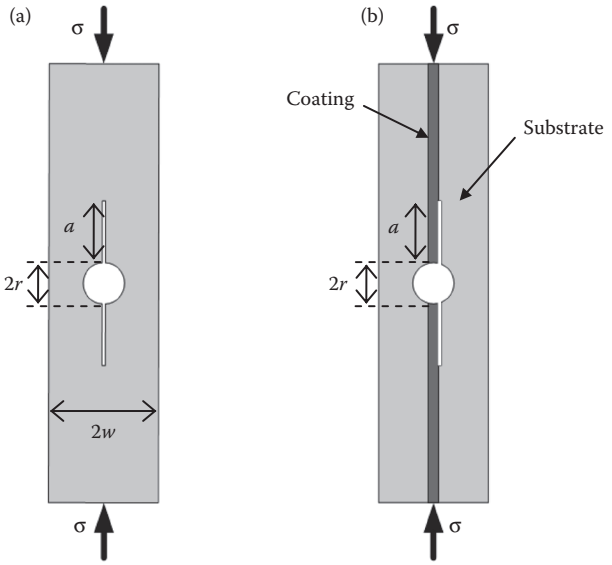


FIGURE 8.9 (a) DCDC specimen geometry. (Modified with permission from Plaisted, T. A., Amirkhizi, A. V., and Nemat-Nasser, S. *International Journal of Fracture* 141(3–4), 2006: 447–57.) (b) Sandwich DCDC specimen geometry. (Modified with permission from Turner, M. R. et al., *Acta Metallurgica Et Materialia* 43(9), 1995: 3459–65.)

generated crack will propagate along the midplane of the specimen and finally be arrested by frictionally constrained end conditions.[71–74]

The advantage of the DCDC specimen lies in its long stretch of stable crack growth,[75] which allows the crack to be monitored by optical microscopy. This enables *in situ* observation and video recordings of crack extension. Other advantages of the DCDC specimen include the experimental simplicity of axial compression, autoprecracking, and controllable crack growth.[76]

Although this specimen is usually used for the determination of mode I fracture toughness, a wide range of mode mixities (from $\Psi = 0°$ to 64°) can be achieved by varying the locations of the hole and longitudinal crack (Figure 8.9a).[77,78] The strain energy release rate G_c under mode I loading condition can be evaluated by the analytical solution developed by He et al:[77]

$$G_c = \frac{\sigma^2 \pi r}{\bar{E}} \left[\frac{w}{r} + \left(0.235 \frac{w}{r} - 0.259 \right) \frac{a}{r} \right]^{-2}, \tag{8.25}$$

where σ is the applied compressive stress; $\bar{E} = E/(1 - \nu^2)$ is the elastic modulus of the beam as in Equation 8.4; r is the hole radius; w is the half width of the specimen; and a is the crack length. Equation 8.25 is applicable when the specimen geometries are varied within the ranges $2 \le w/r \le 4$ and $w/r \le a/r \le 15$.

For coating evaluation, the DCDC specimen can be extended to study interface fracture by sandwiching a thin layer of coating or film between the two beams

of the substrate material (Figure 8.9b). The interfacial crack has almost the same energy release rate as that for the monolithic material, under the condition that the sandwiched layer is thin compared with the in-plane dimensions of the specimen. Therefore, the interfacial energy release rate of a sandwich DCDC specimen can be evaluated using Equation 8.25. A notable advantage of this specimen for the study of interfacial fracture is that the cracks tend to propagate along the interface even when the interfacial fracture toughness greatly exceeds the toughness of the adjoining materials.[74] During the test, when cracks attempt to propagate into the adjoining materials rather than be confined at the interface, the cracks are subjected to a substantial mode II loading; this loading will deflect the cracks back toward the interface. Hence, the DCDC specimen displays a strong preference for interface fracture.

The sandwich DCDC specimen was originally used by Turner et al.[74] Their specimen was validated by a model system consisting of a thin polymer layer between two glass beams. Their experimental results demonstrated the unique capability of the DCDC specimen for measuring mode I interfacial fracture toughness. Subsequently, Turner and Evans[79] investigated the mechanism of mode I crack propagation along the gold–sapphire interface in both humid and dry environments. Through *in situ* experimental observations, the intrinsic mechanisms that allow debonding to occur along the oxide–metal interfaces were identified. Lipkin et al.[80] investigated the effect of interfacial carbon on adhesion and toughness of gold–sapphire interfaces. The full details of the crack extension along the interface were recorded by a real-time video recording system and a linear variable differential transformer for position tracking. The variation in each quantity with interfacial carbon was independently measured and the possible origins of the observed sensitivity of adhesion to carbon heat treatment were discussed. Results showed that the adhesion was reduced by the carbon heat treatment. Ritter et al.[81] employed the sandwich DCDC specimen to study the resistance of silane bonded epoxy–glass interfaces to subcritical crack growth under static and cyclic loading in both high and low humidity environments. Their tests separated the effects of stress corrosion and cyclic fatigue on crack growth. The sandwich specimen has also been used by Hasegawa and Kagawa[82] to study the Cu-Al_2O_3 metal–ceramic interface under mode I cyclic loading. In their experiment, Cu acted as the coating layer. They showed that fatigue decohesion occurred along the interface in a straight manner, and was independent of the thickness of the Cu layer. This decohesion behavior was observed to differ from that under quasistatic loading.

The sandwich DCDC specimen possesses a unique and notable advantage of the crack tending to propagate along the interface, making this specimen a most suitable choice when the interfacial fracture toughness exceeds the fracture toughness of the adjoining materials. In addition, allowing the specimen to be automatically precracked greatly simplifies experimental requirements. There is no particular requirement for the mechanical properties of the materials used for the coatings and substrates. This specimen is usually used for the determination of mode I interfacial fracture toughness.

8.3.1.5 Lap Shear Specimen

The lap shear specimen has been widely used for evaluating the performance of adhesives or adhesively bonded joints.[83,84] For such tests, several standard test methods

have been designed. Two of the most commonly used are the ASTM D1002[85] and ASTM D3164.[86] In recent years, this specimen has also been adopted and modified to determine the shear adhesion strength of coatings or films to the substrate.[87,88] In this test, a partly coated sample is bonded to a substrate sheet using strong epoxy glue, with the coating facing the substrate sheet,[89] as shown in Figure 8.10a. During the test, the tensile load is applied parallel to the coating–substrate interface to induce the coating detachment. The shear adhesion strength of the coating–substrate interface is calculated as the ratio between the measured maximum force and the bonding area.

This test is popular for two main reasons. First, it can simulate the actual application conditions of some coatings very well due to its unique loading mode. For instance, the biocompatible ceramic coatings applied on the dental implant screw are usually subject to significant shear stress during their installation and service,[90] so the adhesion evaluation of such coatings using the lap shear test is more meaningful. Second, this test method is very easy to use. Specifically, the lap shear specimen is easy to prepare and testing can be performed in a commercial tensile test machine. Furthermore, data analysis of this method is also very simple.

However, it should be noted that this test method suffers from two main disadvantages.[91,92] First, the offset of the partly coated sample and the substrate sheet (Figure 8.10a) causes the lap shear specimen to experience a bending motion in addition to the shear loading during the test. Thus, the stress distribution in the lap is not uniform but concentrated near the ends. In fact, the determined shear strength is an average value, depending not only on the interfacial adhesion of the coating/substrate, but also on the geometry of the specimen. Although these measured average values can be used for comparing effects of different process parameters on the coating adhesion, care must be taken in using these values for the purpose of practical engineering design. In order to overcome the asymmetric nature of this test, tabs are bonded to the ends of the coated sample and the substrate sheet (Figure 8.10b) to alleviate or eliminate the undesirable bending moment.[93]

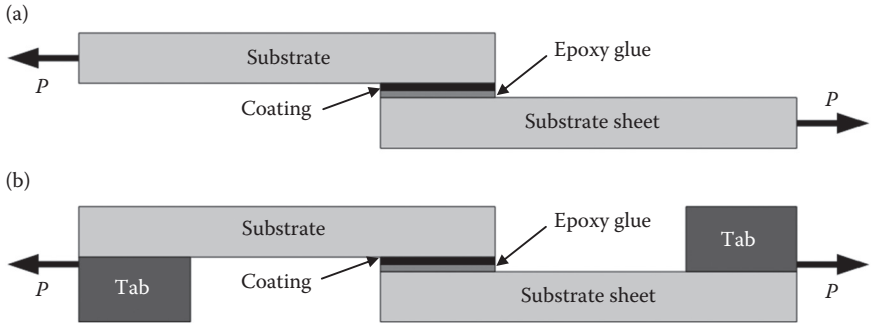


FIGURE 8.10 (a) Conventional lap shear specimen geometry. (Modified with permission from Mascia, L., Dhillon, J., and Harper, J. F. *Journal of Applied Polymer Science* 47(3), 1993: 487–98.) (b) Modified lap shear specimen geometry with tabs. (Modified with permission from Ochoa-Putman, C. and Vaidya, U. K. *Composites Part A: Applied Science and Manufacturing* 42(8), 2011: 906–15.)

Second, this test is very dependent on the properties of epoxy glue used to bond the coated sample and the substrate sheet, especially its shear strength. The shear strength of the epoxy glue must be larger than the shear adhesion strength of the coating–substrate interface. If the latter is larger, the interfacial failure of the coating/substrate system will not occur. Instead, shear fracture will take place in the interior of the epoxy glue or along other weaker interfaces. Therefore, the problem of selecting or fabricating very strong glue is paramount in this test. In addition, the selected epoxy glue should have good adhesion property with the coating and the substrate sheet so that the shear strength of the glue–coating interface or the glue–substrate sheet interface is larger than that of the coating–substrate interface. Due to the possibility of undesirable fractures, such as in the interior of epoxy glue or along the glue–coating or glue/substrate sheet interfaces, it is necessary to observe and characterize fracture surfaces after the lap shear test to determine the failure modes and locations. The measured adhesion data are valid only when failures occur along the substrate–coating interface.

As mentioned above, one important application of the lap shear test is to evaluate the shear adhesion strength of biocompatible ceramic coatings to their substrates.[29,94] For instance, Boulton et al.[94] characterized the shear adhesion strength of adhesively bonded or plasma-sprayed hydroxyapatite coatings to Ti6Al4V substrates using this test. They further tested the effects of environmental degradation using Ringers solution at 37°C on the adhesion properties of the above coatings. Their measurement results revealed that the adhesively bonded hydroxyapatite coating exhibited an excellent initial adhesion to the substrate and it also possessed better durability than the plasma sprayed coating in Ringers solution. After the lap shear test, observation of fracture surfaces revealed that in all cases failures occurred at the substrate–coating interface, indicating that the measured data were valid. Similarly, Wei et al.[29] used the lap shear test to measure the interfacial bond strength of electrophoretically deposited hydroxyapatite coatings on three kinds of substrate: pure titanium, titanium alloy Ti6Al4V, and 316L stainless steel. They found that the measured interfacial shear strength depended on the substrate type. The coatings on the 316L stainless steel substrate exhibited the highest shear adhesion strength (~22 MPa), comparing quite favorably with the shear strength of bovine cortical bone (~34 MPa). In contrast, the coatings on the titanium and Ti6Al4V substrates had much lower shear adhesion strength, which were ~11 and 14 MPa, respectively.

In addition to the hydroxyapatite coatings, the shear adhesion strength of TiO_2 coatings for biomedical application has also been measured using the lap shear test.[95,96] Lin et al.[95] investigated the effect of anodizing voltage on anodic TiO_2 coating adhesion. Results showed that the coating adhesion deteriorated at higher anodizing voltages. They ascribed such deterioration to the defects formed in coatings at relatively high anodizing voltages. Furthermore, a structure/adhesion relation had been established in their study, serving as a basis and reference for improving the adhesion strength of anodic TiO_2 coating on titanium substrate. Chen et al.[96] employed the lap shear test to investigate the shear fracture characteristics of porous anodic TiO_2 layer before and after hot water treatment. They found that the shear fracture characteristics depended on the microstructural features of untreated and treated oxide layers. For the untreated TiO_2 layer, the shear fracture took place primarily along

the cavity-containing layer. For the treated TiO_2 layer, the bottom surface of newly formed nanostructured layer was weaker and the shear fracture took place along this surface. The measured average shear adhesion strength of TiO_2 layer before and after water treatment were ~11.6 and 8.9 MPa, respectively, indicating a decrease by about 23% after water treatment.

Another important application of the lap shear test is to investigate the adhesion of metallic coatings with composite substrates or composite coatings with metallic substrates.[97,98] For instance, Liu et al.[97] studied the influence of metallic bond coat on the adhesion between thermal resistant coatings and carbon fiber reinforced thermosetting polyimide substrate using the shear test. Results showed that both bond coat materials and the substrate pretreatment influenced the adhesion strength of coatings to the substrate significantly. Specifically, Al and Zn are possible candidates for the bond coat material and preheating of the substrate as they improve the shear adhesion strength by up to 14.2 MPa. Chrobak et al.[98] examined the adhesion between composite coatings and an Al-based alloy substrate by the lap shear test. It was found that the examined composite coatings exhibited an average adhesion value of ~2.1 MPa.

In short, the key advantages of the lap shear test include its unique shear loading mode and the simplicity of operation. This test relies on a strong epoxy glue to remove the coating from the substrate with an applied shear loading. Therefore, selecting or fabricating suitable epoxy glue is of importance in this test. This test applies to many types of coatings, from flexible metallic coatings to brittle ceramic coatings. Generally, the coating itself should have larger shear strength than that of the coating–substrate interface so as to insure the occurrence of interfacial failure.

8.3.1.6 Direct Pull-Off Specimen

The direct pull-off test is a widely used standard method in industrial and scientific laboratories, following ASTM standard C633.[99] The basic principle of this test is to form a bond with the coating and then pull the coating off in the perpendicular direction. Compared with the sandwich specimens mentioned previously, this test determines the interfacial adhesion strength rather than interfacial fracture toughness.[8,9,100] The direct pull-off specimen is illustrated in Figure 8.11. Preparation of this specimen consists of coating one face of a cylindrical substrate fixture and

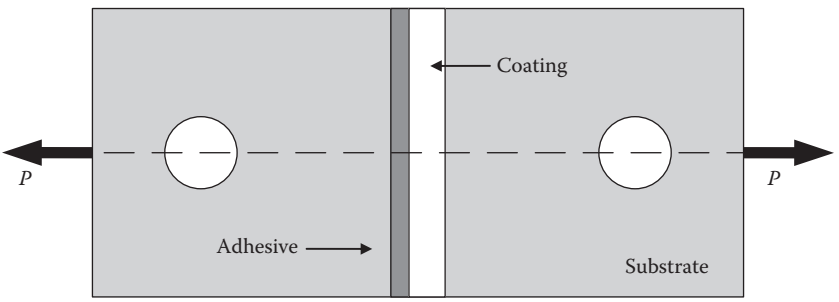


FIGURE 8.11 Schematic drawing of the direct pull-off specimen. (Modified with permission from Filiaggi, M. J. and Pilliar, R. M. *Journal of Materials Science* 26(19), 1991: 5383–95.)

bonding this coating to the face of a cylindrical loading fixture with an epoxy resin. The prepared specimen is subjected to a tensile load until its fracture. The interfacial adhesion strength is determined by dividing the maximal tensile force by the cross-sectional area of the specimen.

The direct pull-off test has two notable advantages. First, specimen preparation is relatively simple and the test is easily implemented. This is because the specimen has a simple cylindrical shape and the test can be performed using a general tensile test machine. Furthermore, data acquisition of this method is also very simple since only the maximal tensile force and the cross-sectional area of the specimen need to be measured. Second, this test method has a wide-ranging applicability to a variety of coating/substrate systems.

However, it should be noted that although this test has been used for a long time and standardized by ASTM, it still suffers from some disadvantages.[100–102] First, despite the relatively simple data acquisition, data interpretation of this test is very difficult due to the wide scatter in measurement results. Such scatter is caused by the variety of fracture modes. During this test, several types of fracture can occur separately or together. It could be (a) a clean interfacial fracture when the failure appears at the interface between the coating and the substrate; (b) a cohesive fracture when the failure occurs within the coating or within the epoxy glue; and (c) a combination of the first two fracture modes. Therefore, care must be taken in using these measured values for the purpose of practical engineering design. Furthermore, due to the high possibility of undesirable fracture locations, for example, fracture within the epoxy glue or the coating, it is necessary to observe and characterize fracture surfaces after the test to determine validity of measurement results.

In addition, this test is highly dependent on the tensile strength of epoxy glue used to bond the coated sample and the loading fixture.[103,104] That is to say, the strength of the epoxy glue should be larger than the adhesion strength of the coating to the substrate. Subsequently, the maximum adhesion that can be measured by this test is limited and this test can only be applied to relatively weakly adhering coatings. Other limitations of this test include the following: (a) careful alignment is necessary to ensure the uniform loading across the interface; (b) the epoxy glue may penetrate into the porous coating and modify its adhesion property; and (c) additional stress may be produced during setting of the epoxy glue. All these factors have potential influences on the adhesion strength measured.

Yilmaz et al.[36] investigated the effect of bond coat on the bonding strength of plasma-sprayed Al_2O_3 coatings using the direct pull-off test. It was found that the tested samples exhibited a variety of fracture modes. For the Al_2O_3 coating without bond coat (Figure 8.12a), the failure mode is a combination of adhesive fracture along the Al_2O_3 coating–substrate interface and cohesive fracture within the Al_2O_3 coating. For the Al_2O_3 coating with bond coat (Figure 8.12b), the fracture mode is more complex since two kinds of cohesive fractures (within the bond coat and the Al_2O_3 coating, respectively) and one adhesive fracture along the substrate–bond coat interface have been identified. Such a fracture mode indicated that the measured bonding strength of coating is a mix of cohesive and adhesive strength. The Al_2O_3 coating with bond coat exhibited a higher strength value, indicating that the bond coat improved the adhesion of Al_2O_3 coating to the substrate. Similarly, Liu et al.[105]

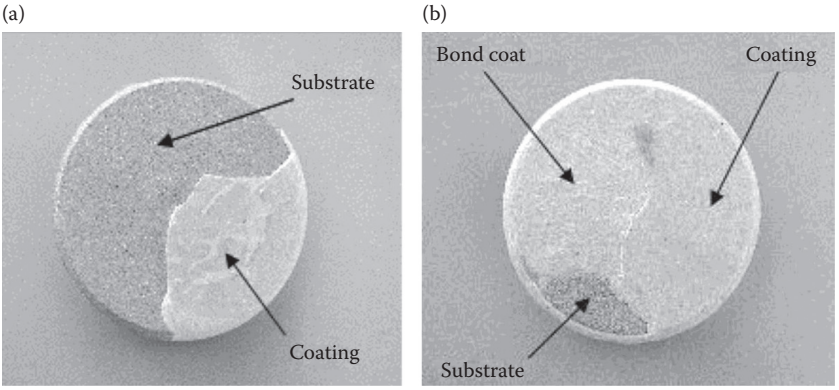


FIGURE 8.12 The fracture macrograph of coatings after the pull-off test: (a) pure Al_2O_3 without bond coat, (b) pure Al_2O_3 with bond coat. (Reprinted with permission from Yilmaz, S. et al., *Vacuum* 77(3), 2005: 315–21.)

used the pull-off test to investigate the effects of cathodic voltages on the bonding strength of ceramic coatings formed on NiTi alloy by microarc oxidation. Results clearly showed that the bonding strength of the coating decreased with the increasing cathodic voltages. Specifically, when the cathodic voltage increased from 10 to 30 V, the measured average strength value decreased from 37.8 to 18.2 MPa. A noteworthy thing is that the coating was not stripped from the substrate when the applied cathodic voltage is 0 V. In this case, all fractures occurred within the epoxy resin, indicating that the bonding strength of the coating exceeded the tensile strength of the epoxy resin. This example clearly exhibited the limitation of the pull-off test.

In short, the key advantages of the pull-off test include its wide-ranging application, minimal cost, and the simplicity of operation. This test has no stringent restrictions on the coating or substrate materials, and it can be applied to both flexible metallic coatings and brittle ceramic coatings. However, it should be noted that since this test relies on a strong epoxy glue to pull the coating off the substrate, it is more suitable for the adhesion measurement of relatively weakly adhering coatings.

A summary of the various reviewed sandwich specimen-based methods are given in Table 8.3. Overall, the reviewed sandwich specimens can be employed to perform quantitative strength analysis or fracture mechanics analysis of coating adhesion. The analysis is important for understanding factors contributing to coating adhesion, and is also important for further numerical simulations and lifetime predictions. However, some of the sandwich specimens still possess some shortcomings, such as relatively sophisticated experimental techniques or complicated specimen preparation, which could have undesirable effects on the resulting experimental coating evaluation. Preparation of the sandwich specimen is typically done through diffusion bonding, which may alter both the coating microstructure and interfacial adhesion. This is because the bonding process usually takes a long time and sometimes at a relatively high temperature. Thus, sandwich specimens are not suitable for coatings with interconnected pores or coatings that are temperature-sensitive. Furthermore, sandwich specimens may not satisfactorily simulate the stress/strain

TABLE 8.3
Comparison of the Various Sandwich Specimen-Based Methods

	Strength/Fracture Toughness Measurement	Experimental Setup	Results and Data Processing	Other Notes
DCB	+ Suitable for measurement of mode I interfacial G_c – Unsuitable for mode II	– Crack length measurement may be difficult under certain situations – Tapered or contoured shapes require machining	+ Multiple readings of G_c can be taken from one specimen due to stable and controllable crack growth	+ Suitable for a wide range of coating/substrate systems
Four-point bend	+ Suitable for measurement of mode I, mode II, and mixed mode interfacial G_c	+ No mounting required – Complex precrack preparation – Complicated floating platen arrangement if used	+ Accurate crack length monitoring is noncritical due to steady-state G_c – Asymmetric crack growth more common	+ Suitable for a wide range of coating/substrate systems
Brazil nut	+ Suitable for measurement of mode I, mode II, and mixed mode interfacial fracture toughness	+ Compact setup + No sophisticated loading fixtures required	– Unstable interfacial crack propagation	+ Suitable for a wide range of coating/substrate systems
DCDC	+ Suitable for measurement of mode I and mixed mode interfacial fracture toughness	+ Simple axial compression + Automatically precracked.	+ Controllable crack growth + Crack tends to propagate along the interface	+ Suitable for a wide range of coating/substrate systems
Lap shear	+ Suitable for measurement of shear adhesion strength	+ Easy to prepare and test	+ Simple data interpretation + Simulates actual application conditions – Bending motion present	– Dependent on the epoxy glue – Coating to have larger shear strength than interface
Direct pull-off	+ Suitable for measurement of adhesion strength	+ Simple specimen preparation – Requires careful alignment	+ Simple data acquisition – Wide scatter of results	– Dependent on the epoxy glue – Better for weakly adhering coatings

The symbols "+" and "–" denote advantage and disadvantage characteristic, respectively.

loading environment that real manufactured parts must endure because the sandwich structure could present a different stress state at the interface compared to the expected stress state under service conditions.

8.3.2 Bimaterial Specimen-Based Methods

The second category of adhesion measurement techniques are based on bimaterial specimens that are relatively simple to perform and provide good qualitative or quantitative results. The adhesion evaluation of coatings using bimaterial specimens does not usually involve the attachment of new devices to the coating. This avoids possible epoxy penetration into the coating, minimizing distortion on interfacial adhesion compared to what will be expected in service. In this section, the bimaterial specimen-based test methods discussed include indentation,[101] scratch,[106] peel,[107] blister,[108] tensile,[109] and laser spallation[110] tests.

8.3.2.1 Indentation Test

Indentation is a simple, convenient, and commonly used technique for evaluating mechanical properties of bulk materials. Many important mechanical properties such as hardness, Young's modulus, and fracture toughness can be easily acquired by this test.[111–113] However, when it comes to the coating/substrate system, the situation becomes more complicated because the deformation and fracture of a coated system depends not only on the coating microstructure and toughness, but also on the properties of the substrate and the coating–substrate interface.[101,114–116] This significantly increases the difficulty in performing the mechanical analysis and determining the corresponding mechanical properties of coatings.

Despite the relatively complicated deformation and fracture behaviors occurring during the indentation test, this technique has been successfully used for adhesion evaluation of brittle coatings to ductile substrates.[101,115–117] Figure 8.13 shows the schematic of indentation test at the surface of a coating/substrate system and the two stages of brittle coating deformation and fracture.[117] First, the applied indentation load drives the indenter into the coating/substrate system and induces a through-thickness coating fracture around the indenter tip (Figure 8.13a). The through-thickness coating fracture is mainly caused by the brittle nature of the coating and the plastic deformation of the substrate, which promotes the coating fracture by applying the bending stresses on the coating.[117,118] After the first stage, the interfacial fracture in the form of coating delamination or buckling will occur with the further increase in the indentation load, and stress concentrated at the end of the interfacial crack (Figure 8.13b). Theoretically, the stress concentration at the end of the interfacial crack can be relaxed gradually by continuous interfacial crack propagation. However, a secondary though-thickness coating fracture may occur around the impression, causing coating spallation.[117,118]

Based on the surface morphology observation of the coated system after the indentation test, Drory and Hutchinson[114] concluded that there were three types of coating delamination (Figure 8.14): (a) delamination leaving behind a very narrow annular plate of coating; (b) delamination with an unbuckled annular plate of coating left behind the crack tip; and (c) delamination with a buckled annular plate of coating

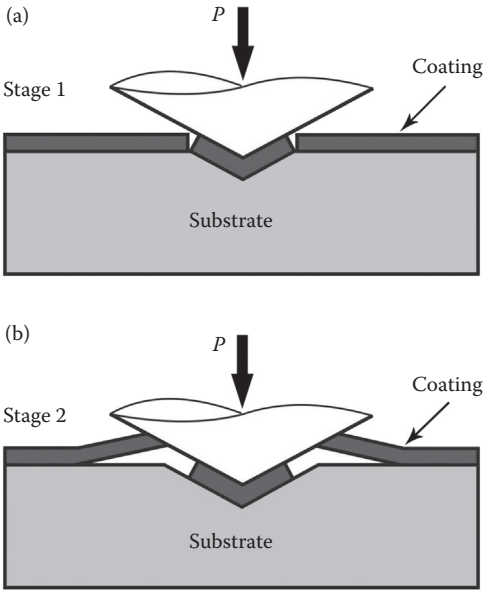


FIGURE 8.13 Schematic of indentation test at the surface of a coating/substrate system and the two stages of brittle coating deformation and fracture. (Modified with permission from Li, X., Diao, D., and Bhushan, B. *Acta Materialia* 45(11), 1997: 4453–61.)

left behind the crack tip. They developed solutions to evaluate the coating adhesion from the measurement of the applied indentation load, delamination radius, coating thickness, and coating/substrate material properties. Considering the most common model shown in Figure 8.14b as an example, the interfacial energy release rate value is given by

$$G_c = \frac{(1 - \nu_c^2)h}{2E_c}[\sigma_r(R) - \sigma_r(R^-)]^2, \tag{8.26}$$

where v_c, h, and E_c are Poisson's ratio, thickness, and Young's modulus of the coating, respectively, and $\sigma_r(R)$ and $\sigma_r(R^-)$ are the radial stress components at the inner and outer edges of the annular plate, respectively.

The indentation test at the surface of a coating/substrate system has some remarkable advantages such as the simplicity of operation and ready availability of commercial equipment. Therefore, it is used widely for coating adhesion evaluation as a convenient and economic measurement method. For example, Xie and Hawthorne[119] measured the adhesion of sol–gel derived composite coatings to a 316 stainless steel substrate by the indentation-based method. The sol–gel derived coatings had low cohesive strength and high brittleness, making the coating adhesion evaluation difficult. In this test, the indenter was driven through the coating and into the underlying substrate. The brittle nature of the coating and the extensive plastic deformation of the substrate resulted in the formation and propagation of annular crack along

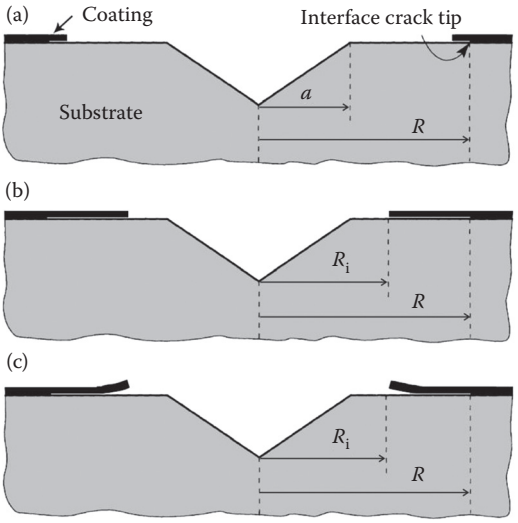


FIGURE 8.14 Coating delamination caused by indentation. (Modified with permission from Xie, Y. and Hawthorne, H. M. *Surface and Coatings Technology* 172(1), 2003: 42–50.)

the coating–substrate interface. The radius of the annular crack was measured and used to calculate the interface fracture toughness, along with the coating thickness, residual stress, and mechanical properties of the coating and substrate. Calculation results showed that the indentation method is sensitive enough to differentiate the adhesions of the coatings processed by different conditions. The interfacial fracture toughness of the coatings studied ranged between 25 and 73 J/m^2 for various coating processing temperatures and substrate treatment methods. This study demonstrated the effectiveness of the indentation test for coating adhesion evaluation.

However, it should be pointed out that the indentation test at the surface of a coating/substrate system is only suitable for the systems of brittle coatings weakly bonded to ductile substrates. This is because a ductile and strongly adhered coating usually experiences large deformation before it delaminates from the substrate. Such large deformation occurring around the coating–substrate interface makes the calculation of coating adhesion rather complicated. Furthermore, the calculation of the radial stress in Equation 8.26 is rather complicated due to the complexity of the tri-axial stress state of the indentation, the different elastic and plastic properties of the coating and substrate, and the existence of the interface. Fortunately, the indentation test offers an additional possibility to investigate the coating adhesion: the indentation can also be performed perpendicular to the cross section of the coating/substrate system to induce the interfacial fracture, as shown in Figure 8.15. This technique was developed by Chicot et al.[116] and was named the interfacial indentation test. In this test, one diagonal line of the Vickers indenter is first aligned along the coating–substrate interface, and then an increasing indentation load is applied to induce a semicircular interfacial crack.[101,115,116] The critical load P_c required to initiate the interface fracture is recorded automatically by the indentation machine, and

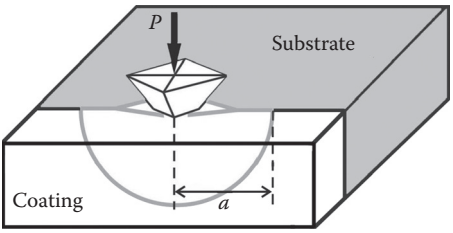


FIGURE 8.15 The interfacial indentation test. (Modified with permission from Chicot, D., Démarécaux, P., and Lesage, J. *Thin Solid Films* 283(1–2), 1996: 151–57.)

the interfacial crack length a_c is measured through optical observation after the test. The above-measured values are used to calculate the apparent interfacial fracture toughness of the coating/substrate system:[120]

$$K = 0.015 \frac{P_c}{a_c^{3/2}} \left(\frac{E}{H} \right)_{\mathrm{I}}^{1/2} \tag{8.27}$$

In Equation 8.27, the ratio $(E/H)_{\mathrm{I}}$ characterizes the global behavior of the coating/substrate system and is defined by the following equation:

$$\left(\frac{E}{H} \right)_{\mathrm{I}}^{1/2} = \frac{(E/H)_{\mathrm{S}}^{1/2}}{1 + (H_{\mathrm{S}}/H_{\mathrm{C}})^{1/2}} + \frac{(E/H)_{\mathrm{C}}^{1/2}}{1 + (H_{\mathrm{C}}/H_{\mathrm{S}})^{1/2}}, \tag{8.28}$$

where E is Young's modulus, H is the hardness, and the subscripts I, S, and C stand for interface, substrate, and coating, respectively.

The most important advantage of the interfacial indentation test is that the measured interface fracture resistance is uniquely related to the interfacial bonding.[118–120] This is because the indentation load is applied directly on the coating–substrate interface and a crack confined at the interface has been induced. Other advantages include short data acquisition time, simplicity of operation and mechanical analysis, and ready availability of commercial equipment.[118–120] Furthermore, the interfacial indentation test has wider applications than the conventional one and it can be applied to many kinds of coatings such as alloy, composite, and ceramics[121–123]. For example, Bourse et al.[121] characterized the interfacial adhesion of bronze–aluminum alloy coatings to a steel substrate. The obtained results show that the critical load measured by interfacial indentation depends on the substrate roughness before spraying. Specifically, the higher substrate roughness leads to higher critical load and better coating adhesion. Marcano et al.[122] studied the adhesion of vacuum plasma-sprayed Cr_3C_2-NiCr coatings to plain carbon steel. They found that the interfacial toughness value is well related to the coating thickness. When the coating thickness increases from 150 to 450 μm, the interfacial toughness changes from 7.6 to 10.1 MPa $m^{1/2}$. For the ceramic coatings, Sadeghi-Fadaki et al.[123] investigated the interfacial adhesion between plasma-sprayed yttria-stabilized zirconia (YSZ) coatings and mild

carbon steel substrate. Results showed that the spray parameters such as powder feed rate and spray distance play an important role in regulating coating adhesion.

Despite the wide application of interfacial indentation test, there are some difficulties in using this technique.[118–121] First, it is not easy to measure the interfacial crack length during the test. This is mainly caused by two reasons: (a) the crack may deviate across the coating instead of being confined at the interface, particularly when the coating has a low cohesive strength; (b) the complex coating microstructures around the interface, for example, the existence of pores and intersplat microcracks, hinders accurate determination of crack length. Second, the interfacial indentation test requires careful preparation of the specimen cross section to facilitate the subsequent fracture morphology observation and crack length measurement. This requirement results in a more tedious sample preparation than the surface indentation test.

The above discussion focuses on the coating adhesion evaluation using conventional microindentation. It is worth noting that nanoindentation has gained increased attention in recent years because it can induce a highly localized deformation or fracture.[124] In nanoindentation, very small loads and indenter sizes are used and thus the indentation area may be only several micrometers or nanometers. Due to the relatively small indentation depth and area, the nanoindentation test ensures that the mechanical property measurement of thin coatings is not affected significantly by the substrate.[125,126] This feature makes the nanoindentation particularly suitable for adhesion evaluation of thin coatings. For example, Chen et al.[127] investigated the adhesion of very thin (sub-100 nm) coatings on glass using the nanoindentation technique. The results agreed very well with the intrinsic interface adhesion obtained from atomistic simulations. Their study has demonstrated the effectiveness of nanoindentation for adhesion evaluation of thin coatings or films.

In summary, the indentation tests possess the advantages of simple operation, small quantity of specimen materials, minimal cost, and ready availability of commercial equipment. These advantages enable the tests to be easily implemented both in the laboratory and on the manufacturing line. As to the application, the indentation test at the coating surface is usually used for brittle coatings on ductile substrates, while the interfacial indentation test is used for a variety of coating/substrate systems. The main limitation of the conventional indentation test lies in the complex mechanical analysis, while the interfacial indentation test has the difficulty in crack length measurement.

8.3.2.2 Scratch Test

The scratch test for coating adhesion evaluation was first developed by Heavens in 1950.[128] This test is performed by drawing a spherically tipped diamond indenter across the coating surface. Meanwhile, the applied normal load on the indenter is increased until the detachment of the coating. The schematic drawing of this test is shown in Figure 8.16. The critical normal load required to induce coating detachment is taken as a semiquantitative measure of the coating adhesion, but it is greatly influenced by mechanical properties of coating/substrate systems.[129] Because dissimilar coating/substrate systems usually have varying mechanical responses and thus exhibit different fracture modes, this test can only be used to compare the

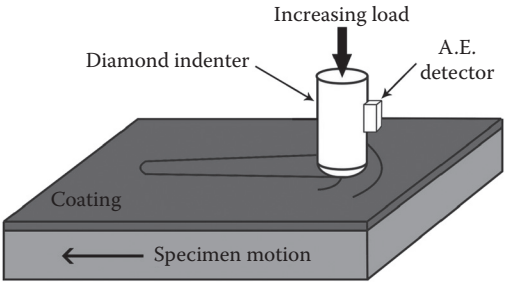


FIGURE 8.16 Schematic of scratch adhesion test. (Modified with permission from Xie, Y. and Hawthorne, H. M. *Surface and Coatings Technology* 172(1), 2003: 42–50.)

adherence of coating/substrate systems with similar nature. In this test, it is crucial to detect the occurrence of coating detachment, and thus many detection techniques have been developed, including acoustic emission, *in situ* force measurement and deformation morphology observation.[130–132] Among these techniques, the acoustic emission technique is more suitable for detecting the fracture or detachment of brittle coatings; while the *in situ* measurement of tangential friction and normal forces have more advantages in determining the fracture of ductile coatings. The *in situ* microscopic observation method can be applied to both brittle and ductile coatings, but this method involves more complicated experimental operation.

The scratch test usually causes three types of coating failures.[106,133,134] They are adhesive, cohesive, and mixed failure. Among these failures, the coating detachment ahead of the indenter belongs to the adhesive failure. It is the most important failure mode because it is directly related to the coating adhesion evaluation. Other failure modes mainly include coating deformation, delamination, and through-thickness fragmentation. These failures belong to cohesive or mixed failure. They may occur before or along with the adhesive failure. During the scratch test, when the induced compressive stress in the coating exceeds a critical value, the coating adhesive failure usually can be easily induced.[106] However, it should be noted that it is not easy to establish the correct relationship between the measured critical load and the actual coating adhesion strength due to the coexistence of other coating failure modes. In addition to the contributions from different failure modes, the measured critical load is also strongly affected by testing conditions, including scratching speed, loading rate, indenter tip radius, and indenter wear.[132]

Obviously, the determination of coating adhesion strength from the scratch test results involves complex mechanical analysis. In this area, Benjamin and Weaver[135] first deduced an expression for the critical shearing force for coating removal using the plasticity theory. However, assumptions they used during their analysis were too simple compared with the actual process of coating removal. Later, Laugier[136] modeled the coating adhesion behavior in terms of the strain energy released during the coating removal. He proposed that when the critical scratch load is reached, the compressive stressed coating in the region ahead of the indenter reduces its stored energy by detaching from the substrate. Such energy description is applicable to both ductile and brittle coatings. Provided that the work for coating ductile deformation

or brittle fragmentation is small, it can be ignored during the determination of coating adhesion energy. Recently, a mathematical model was developed by Xie and Hawthorne[106,133] to calculate the distribution of compressive stresses in a thin coating induced by the scratch indenter. Furthermore, a simple but useful equation was derived from the model to rank the adhesion of different coating systems.

Despite its relatively complex data analysis, the scratch test is a popular method for assessing the adhesion of thin, hard, and well-adhering coatings. Compared with other methods, the scratch test is fairly reliable, easy to use, and no special specimen shape or preparation is required. Therefore, scratch adhesion testing has increasingly been used in engineering and research. Jaworski et al.[137] characterized the mechanical properties of suspension plasma-sprayed TiO_2 coatings using this test. They measured two important mechanical parameters, including the critical load to remove the coating and the scratch hardness. The critical load was used to characterize the adhesion strength of coatings, while the scratch hardness was employed to estimate the cohesion strength of coatings. They found that the spray distance has a significant effect on the adhesion of coatings, while the suspension feed rate has less significant influences. Sander et al.[138] developed a modified scratch test to measure the scratch resistance and adhesion of thin hard coatings on relatively soft substrates. In their test, the diamond Rockwell-C stylus was replaced by ball bearings as the indenter. Such cost-effective and easily replaceable indenter allows the coating adhesion evaluation without damaging large amounts of expensive diamond indenters. Barnes et al.[139] measured the adhesion strength of calcium phosphate (CaP) coatings to carbonate urethane substrates using the scratch test. Results indicate that the adhesion strengths of CaP coatings were influenced by the aging time. Specifically, the coating that was aged for 3 years exhibited considerably lower adhesion strength due to the suspected "drying out" effect. Also, their test results demonstrated that the scratch test is an effective technique for obtaining comparative values of adhesion strength for hard coatings on a compliant substrate.

The major difficulty of the scratch test is that it is affected by a number of intrinsic and extrinsic factors that are not adhesion-related. Thus, the measured critical normal load is only a semiquantitative measure of the coating/substrate adhesion.[140] Therefore, when employing this method for adhesion assessment, a careful analysis of the failure modes of the coatings subsequent to the scratch test is necessary and important for a proper analysis of the implication of the test results.

The scratch test usually is performed on the coating surface and thus it is more suitable for the adhesion evaluation of thin coatings due to the limited scratch depth. In order to apply this method to thick coatings, Lopez et al.[141] developed a modified scratch method, shown in Figure 8.17. This test consists of scratching the cross section of a coating/substrate system at several levels of constant load and the indenter is moved from the substrate through the coating to the coating surface. During this test, there are generally two types of failure: the cone-shaped fracture near the coating surface and the interfacial fracture along the coating–substrate interface. The former fracture is related to the coating cohesion strength and the latter indicates the coating adhesion strength. Assuming that the pattern of interfacial crack is in a half-penny shape, it is possible to evaluate the coating adhesion toughness by calculating the critical SIF. Vencl et al.[142] measured the adhesion of thick plasma sprayed coating with this

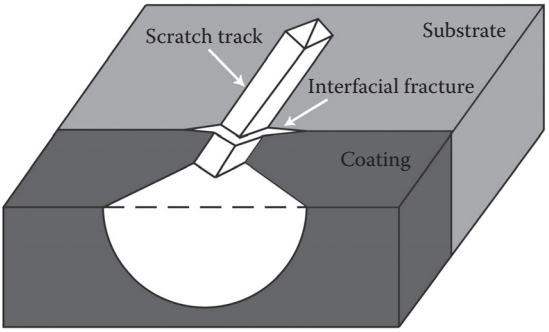


FIGURE 8.17 Schematic of the scratch adhesion test on the cross section of coating/substrate system. (Reprinted with permission from Vencl, A. et al., *Tribology International* 44(11), 2011: 1281–88.)

method. The results obtained were compared to the results from the most commonly applied tensile test. It was found that coatings with higher scratch bond strength also had higher tensile bond strength. These results showed that the scratch test on the cross section of coating/substrate system could be used as a supplement of some standard test method as a coating characterization and quality control technique.

8.3.2.3 Peel Test

The peel test was developed by the aerospace industry where it was used to measure the adhesion of laminated structural components.[143] This test originated from the tape test.[144] In the tape test, a piece of adhesive tape is pressed against a weakly adherent coating, and then the tape is removed to observe whether the coating is peeled off. Unlike the tape test in which only the tape is used, the peel test employs either a tape or a special clamp to grasp and detach the flexible coatings. The tape test is only suitable for the adhesion evaluation of relatively thin and weakly adherent coatings since it relies on the adhesive tape to detach the coating. Hence, the peel test has wider applicability than the tape test; it is also suitable for the adhesion evaluation of relatively thick and strongly adherent coatings.

Several standard peel test methods have been developed, such as multiangle fixed arm peel, T-peel, and mandrel-assisted peel.[145–148] Figure 8.18 illustrates the T-peel test and the 90° peel test around a mandrel. The T-peel test is preferred when the substrate and coating are both relatively thin and flexible strips, as shown in Figure 8.18a. For example, the standardized T-peel test was adopted by Zumelzu and Gipoulou[107] to investigate the adhesion between organic coatings and electrolytic tinplate. They found that gold-plated epoxy–phenolic coatings exhibited better adhesion to tinplates than aluminum plating coatings. Furthermore, this study validated that the T-peel test is a good method to determine the mechanical adhesion between the organic coatings and the metal substrates used in the canning industry. The 90° peel test is the most commonly used peel test method and it is suitable for flexible coatings on rigid substrate plates.[146] In fact, the peel test can be performed not only at 90° but also at any angles between 0° and 180°, and the varying peel angles provide

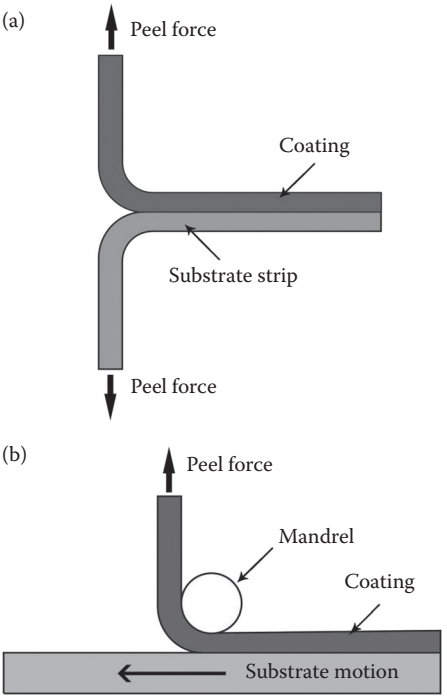


FIGURE 8.18 Schematic drawings of the (a) T-peel test and (b) 90° peel test around a mandrel. (Modified with permission from Nase, M. et al., *Polymer* 49(25), 2008: 5458–66; Sexsmith, M. and Troczynski, T. *Journal of Thermal Spray Technology* 5(2), 1996: 196–206.)

information about the effect of mode mixity on the coating adhesion strength. In addition to the peel angle, other peel parameters also have significant influences on the measured peel force. For example, Nase et al.[149] have shown that the peel force increased exponentially with an increase in the peel rate.

In the peel test, the crack continuously propagates along the coating–substrate interface in a stable manner, and the peel force versus displacement curve can be recorded to represent the adhesion of the coating at different positions. Thus, the effect of the inhomogeneity of the substrate surface on the coating adhesion is revealed by this test. Horgnies et al.[150] characterized the adhesion of polyurea coatings to a concrete surface by the peel test. Results showed that the coating adhesion depended mainly on the mechanical anchorage between the concrete surface and polyurea coatings.

The conventional peel test can only be applied to tough and flexible coatings because of the significant coating deformation that occurs during the peeling process. In order to expand the application of the peel test to brittle coatings, a novel peel test was developed by Sexsmith and Troczynski.[151] They used the developed test to perform the adhesion evaluation of thermal sprayed ceramic coatings. Figure 8.19 illustrates the brief experimental procedure for this test. First, the metallic substrate foil is attached to a massive copper block, and then its surface is partially

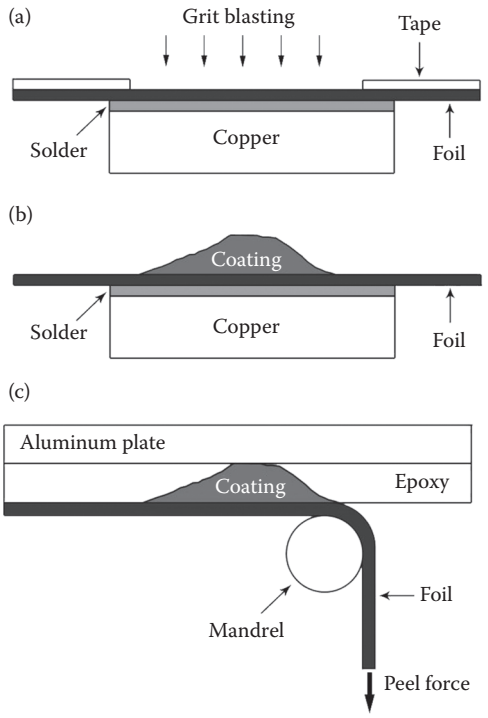


FIGURE 8.19 Schematic of the novel peel test. (Modified with permission from Sexsmith, M. and Troczynski, T. *Journal of Thermal Spray Technology* 3(4), 1994: 404–11.)

sand-blasted (Figure 8.19a). Subsequently, the ceramic coating is deposited onto the sand-blasted foil surface. As such, the copper block underneath provides the necessary mechanical support and also serves as a heat sink (Figure 8.19b). After that, the assembly of the block, foil, and coating is glued to a stiff aluminum plate using a strong epoxy, and the copper block is subsequently removed. The metallic foil, which serves as the substrate in the coating/substrate system, is then peeled from the coating, causing a crack to propagate precisely along the interface (Figure 8.19c). With this arrangement, the ductile substrate rather than the brittle coating is peeled, effectively avoiding the deformation and fracture of ceramic coatings. Sexsmith and Troczynski[151] successfully applied this modified peel test for adhesion measurement of thermal sprayed coatings. By directly measuring the force required to peel the foil, they characterized the adhesion variation across the sample easily. Similarly, Kurzweg et al.[152] employed this modified peel test to evaluate the adhesion of thermally sprayed hydroxyapatite (HAP) coatings. They found that an appropriate bond interlayer between the metallic substrate and the HAP coatings improved the adhesion of HAP coatings.

In the peel test, a stable and continuously propagating crack is produced along the coating–substrate interface, allowing the study of adhesion as a function of the interfacial crack position. Therefore, the inhomogeneity effect of the substrate surface on

coating adhesion can be investigated using the peel test, which is its most important advantage. There are two major disadvantages for the conventional peel test. First, it only applies to tough and flexible coatings. Second, this test spent the majority of the mechanical energy on deforming the coating but only a small quantity on the interfacial fracture. Consequently, it is not easy to extract adhesion energy from peel test data. As for the novel peel test discussed above, it can be used for brittle ceramic coatings, but requires a very complex specimen preparation.

8.3.2.4 Blister Test

The blister test is one of the few techniques capable of obtaining stable interfacial crack growth in a controlled manner. Dannenberg[153] first applied this technique to measure the adhesion of polymer coatings to metallic substrates. Figure 8.20a is a schematic representation of the standard blister test.[108] The test specimen consists of a perforated substrate with a flexible overlying coating, and either liquid or gas is pressurized through the hole in the substrate against the underside of the coating.[108,154] During the test, the coating experiences a two-stage deformation under the applied pressure.[154] The first deformation stage is usually called the bulge test. In this stage, the applied pressure causes the coating to deflect outward with an equilibrium shape. Currently, the elastic modulus and the residual stress of the coating can be determined by mechanical analysis of the coating deformation. With further increase in the applied pressure, the coating gradually detaches from the underlying substrate, forming a blister with the shape of a spherical cap (Figure 8.20a). At this stage, the coating/substrate interfacial adhesion energy can be quantitatively determined from the geometry of the blister and the applied pressure.

Through the two-stage deformation of the coating, both the coating elastic properties and adhesion energy can be measured from a single blister test. Therefore, the standard blister test has been used widely for coating adhesion evaluation. For example, Wang[155] measured the interfacial properties between an elastic tape and poly(methyl methylcrylate) substrates using this test. The adhesive fracture energy, residual stress, and the elastic modulus of the tapes were determined from the test.

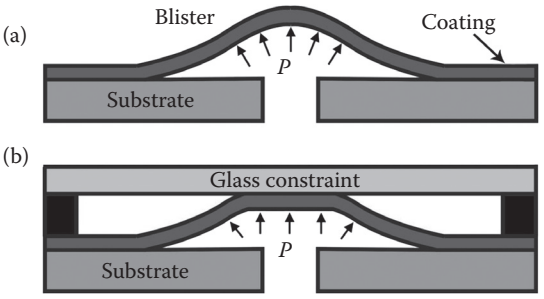


FIGURE 8.20 (a) Schematic of the standard blister test. (Modified with permission from Taheri, N., Mohammadi, N., and Shahidi, N. *Polymer Testing* 19(8), 2000: 959–66.) (b) Schematic of the constrained blister test. (Modified with permission from Parsons, M. et al., *Journal of Adhesion* 68(1–2), 1998: 45–63.)

Also, the effect of the volume flow rate of the injected fluid on the adhesion was investigated. Results showed that the adhesive fracture energy was about 3.0 ± 0.5 J/m^2 and the flow rate of the injected fluid did not have a pronounced effect on the measured interfacial strength.

During the blister test, the coating undergoes very large deformation so that it may rupture prior to debonding from the substrate. In order to avoid the occurrence of premature coating fracture, some improvements and refinements have been made to the blister test. For example, Chang et al.[156] and Napolitano et al.[157] developed a constrained blister test (Figure 8.20b) to limit the vertical displacement and rupture of the coating by placing a flat glass constraint above the blister. This glass constraint also promotes the radial coating detachment. In addition, it allows the coating deformation to be observed from the top. Parsons et al.[158] evaluated the adhesion between electrical tape and polystyrene using the constrained blister test. They successfully minimized the energy spent for the tape deformation by lowering the distance of the constraint above the tape, and obtained the intrinsic adhesion energy from the test results.

In addition to the constrained blister test, other modifications also have been made. For example, Allen and Senturia[159] developed an island blister test to reduce stresses on the coating. Dillard and Bao[160] later proposed a peninsular blister test, which has a steadier delamination front than the island blister test. These two modifications both effectively alleviate the coating fracture problem. However, the conventional blister test still faces another problem: catastrophic debonding that often occurs once a critical pressure is reached. A significant improvement was made by Wan and his coworkers[161–163] to overcome this problem. They developed a unique blister test driven by a fixed amount of gas trapped at the coating–substrate interface. Unlike the conventional blister test loaded by constant pressure which usually leads to catastrophic crack propagation, this improved blister test is driven by an internal thermal expansion of trapped gas for achieving stable crack growth. Furthermore, this novel test allows coating adhesion investigation at an elevated temperature. Koenig et al.[164] used this type of blister test to measure the adhesion energy of graphene sheets with a silicon oxide substrate. They obtained the adhesion energy of 0.45 ± 0.02 J/m^2 for monolayer graphene and 0.31 ± 0.03 J/m^2 for specimens containing two to five graphene sheets. Such a strong adhesion was attributed to the extreme flexibility of graphene. This flexibility allows graphene to conform to the topography of the very smooth substrates.

The above-mentioned blister tests were all driven by pressure. This feature limited their applications due to two reasons. The first is that these tests require a complicated pressure control system; the second reason is that a sophisticated experimental setup is necessary to continuously monitor changes in pressure and blister dimension. Therefore, a more convenient method named the shaft-loaded blister test was proposed by Malyshev and Salganik,[165] attracting attention in recent years. In this version of blister test shown in Figure 8.21, the deformation and detachment of the overhanging coating is driven by a spherically capped shaft instead of the pressure. The shaft-loaded test is an attractive alternative to pressurized tests due to its simpler experimental setup. Furthermore, the load–shaft displacement and the blister central deflection are easily controlled and measured.

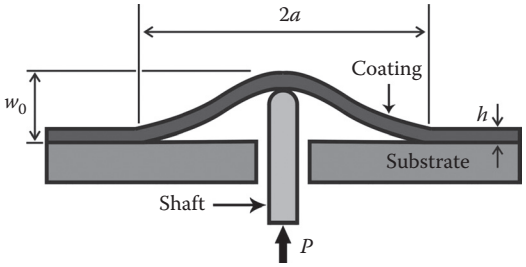


FIGURE 8.21 Schematic of the shaft-loaded blister test. (Modified with permission from Malyshev, B. M. and Salganik, R. L. *International Journal of Fracture Mechanics* 1(2), 1965: 114–28.)

An analytic solution has been developed by Wan and Mai[166,167] to derive the interfacial strain energy release rate for the shaft-loaded blister test. During stable crack growth, the applied load P, central deflection w_0, and radius of debonding a are predicted to increase linearly. From the slope of P versus w_0, the strain energy release rate G can be calculated by

$$G = \frac{1}{\pi^2 Eh}\left(\frac{P}{w_0}\right)^2, \tag{8.29}$$

where E and h are elastic modulus and thickness of the coating, respectively. Alternatively, G also can be calculated from the slope of P versus a:

$$G = \left(\frac{1}{16\pi^4 Eh}\right)^{1/3}\left(\frac{P}{a}\right)^{4/3}, \tag{8.30}$$

or from the slope of w_0 versus a:

$$G = \frac{Eh}{16}\left(\frac{w_0}{a}\right)^4, \tag{8.31}$$

Due to the significant convenience in experimental operation and data analysis, the shaft-loaded blister test has found increasing use in engineering and research. For instance, O'Brien et al.[168] evaluated the interfacial adhesion of a pressure-sensitive adhesive tape to a rigid substrate using the shaft-loaded blister test. In their study, the analytical solutions given by Equations 8.29 through 8.31 were adopted to calculate the interfacial adhesion energy G. Results showed that for a thin adhesive coating, accurate values of G were obtained using Equation 8.30 independent of the coating stiffness. Xu et al.[169] studied the elastic response and delamination behavior of a thin film of photoresist deposited on a silicon wafer. They found that under shaft loading, the thin film underwent a pure bending mode at small deformation

and then gradually transformed to a pure stretching mode at larger deformation. The film-substrate delamination behavior has been successfully measured under displacement control mode. Recently, Na et al.[170] measured the adhesion work of electrospun polymer membrane on a commercial cardboard substrate. In this study, the elastic response of the polymer membrane was analyzed and its adhesion energy to the substrate was measured. The average value of the adhesion work was found to be 206 ± 26 mJ/m^2.

The blister test has a number of advantages, the main one being that both the elastic properties and adhesion energy of the coating can be obtained from the blister test, simply by increasing the value of the applied pressure gradually. Other significant advantages include the following: (a) a fully quantitative analysis of interfacial adhesion energy is available; (b) the axisymmetric fracture surface minimizes the effect of specimen nonuniformity; and (c) testing the environmental degradation of the coating/substrate system is possible by choosing the degrading fluid or gas as the pressurizing medium. The main disadvantages of the blister test lie in the relatively complicated specimen preparation and high experimental requirements. In addition, this test is usually limited to soft flexible polymeric or metallic coatings because hard brittle coatings will tend to crack before forming a blister.

8.3.2.5 Tensile Test

Recently, Elambasseril and Ibrahim[109] developed a tensile test with circumferentially notched specimen to determine the interfacial fracture toughness of coatings. Figure 8.22 is a schematic representation of the circumferentially notched tensile (CNT) specimen.[109] The test specimen consists of cylindrical substrate with a coating-covered notch in the middle. Prior to the coating deposition, a thin layer of gold is electroplated on the masked substrate to form a precrack at different locations on the notch. During the test, a uniform axial tensile load is applied on the coated CNT specimen until coating failure. Occurrence of the coating failure is monitored by acoustic emission technique. The applied force corresponding to the coating failure is recorded as the critical tensile load, which can be applied to the finite element model to calculate the critical J-integral J_C. With the obtained J_C, the complex critical SIF K_C^* can be evaluated by

$$\left|K_C^*\right| = \sqrt{\frac{E^* J_C}{(1-\beta^2)}}. \tag{8.32}$$

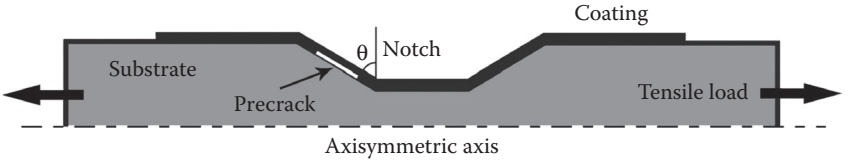


FIGURE 8.22 Schematic of the tensile test with circumferentially notched specimen. (Modified with permission from Elambasseril, J. and Ibrahim, R. N. *Materials Science and Engineering A* 529(1), 2011: 406–16.)

In Equation 8.32, β is from Equation 8.2 and E^* are given as

$$E^* = \frac{2E_1E_2}{E_1 + E_2}, \tag{8.33}$$

where μ_j ($j = 1, 2$ designating materials 1 and 2) is the material shear modulus and E_j is Young's modulus according to Equation 8.4.

The CNT technique has a number of advantages. Compared with the sandwich specimens, the CNT specimen simulates the service conditions of coatings more closely and hence realistically quantifies their mechanical integrity. In addition, this technique can be used to investigate the mixed-mode coating failure by varying the notch angle θ. In addition, this technique has wide applicability to many kinds of coatings. Elambasseril and Ibrahim[171,172] used this technique to quantitatively evaluate the adhesion of nickel coatings to a mild steel substrate. Their measured interfacial fracture toughness exhibited good agreement with the results of other researchers.

Nevertheless, it should be pointed out that this technique still suffers from some limitations. First, the determination of the critical load is not easy. This test depends on an acoustic emission system to monitor the coating failure and then determine the corresponding critical load. But it is difficult to collect and analyze the acoustic signals due to the occurrence of both cohesive and adhesive failures of the coating. Second, the data analysis is relatively complex for this test due to the requirement of finite element modeling, which could be an impediment for the adoption of this technique. Third, in situ observation of interfacial crack initiation and propagation is almost impossible during testing.

8.3.2.6 Laser Spallation Test

The laser spallation is an experimental technique first developed to evaluate the adhesion of thin films to substrates.[173] In this technique, an energy absorbing coating layer is deposited onto the substrate such that it is on the opposite side of the substrate–coating interface of interest. A pulse laser, usually Nd:YAG, is made to focus on this energy absorbing layer (Figure 8.23). This results in a sudden expansion of the layer, generating a compressive shockwave toward the substrate–coating interface. This compressive pulse strikes the interface and is partially transmitted into the coating. The reflection of this compressive pulse results in a tension pulse at the free surface of the coating, which leads to delamination when a critical pulse amplitude is applied.

However, these earlier experiments did not quantify the interface toughness, which can be determined by measuring the free surface velocity of the coating during crack initiation. Quantification of the critical stress amplitude of delamination was first achieved through a computer simulation of the process, verified by a piezoelectric crystal probe capable of mapping out the profile of the stress pulse generated by the laser.[174]

Over the years, Gupta and coworkers[175] have further improved the laser spallation technique. Their refined experimental setup, shown in Figure 8.24, is now widely

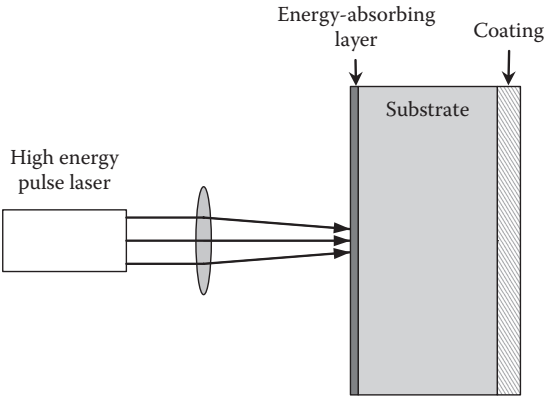


FIGURE 8.23 Early setup of the laser spallation experiment. (Modified with permission from Gupta, V., Yuan, J., and Pronin, A. *Journal of Adhesion Science and Technology* 8(6), 1994: 713–47.)

adopted. In this setup, the free surface velocity is determined by relating measurements of a laser Doppler velocity interferometer and displacement interferometer to mechanics simulation. A constraining material is added to eliminate the thermal stress tail problem that affected earlier approaches.

The advantage of this nonmechanical method is that no gripping scheme is needed, which disturbs the surface and may cause damage to the film–substrate interface. In addition, the very high strain rates in laser spallation prevent inelastic deformations, which affect measurements of other techniques.

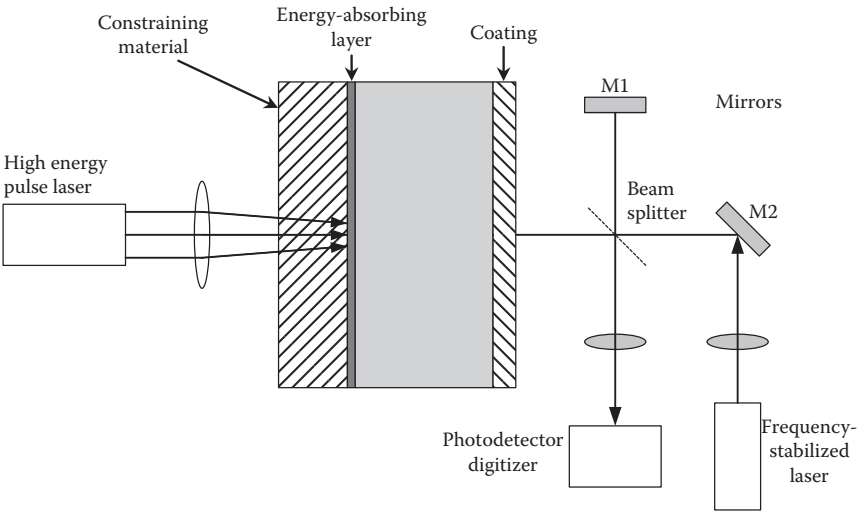


FIGURE 8.24 Improved laser spallation setup with Doppler interferometry. (Modified with permission from Gupta, V., Yuan, J., and Pronin, A. *Journal of Adhesion Science and Technology* 8(6), 1994: 713–47.)

The main disadvantage of the laser spallation technique is the necessity of high-precision equipment to measure parameters caused by the high strain rates.[176] Another disadvantage is the need for special backing and absorbing layers, which limit the possible sample configurations.

This technique has found applications in many areas. For example, the interfacial strength of polycrystalline CVD diamond film deposited on a sintered SiC substrate was estimated to be larger than 222 MPa.[110] Acoustic emission and laser ultrasonics were employed to accurately determine spallation initiation.

Kobayashi et al.[177] have used the technique to study zirconia–steel interface strength. The zirconia coating was deposited by a gas tunnel-type plasma spraying method. The measure interface strength ranged from 206 to 501 MPa. It was found that the interface strength increased with a decrease in the spray distance and speed. An increase in the coating and substrate thickness also improved interface strength.

The laser spallation technique has been used to quantify the interface strength of critical layers of integrated circuit packages. For example, the adhesion strength of polymer dielectric interfaces in a multilayer thin film stack was evaluated.[178] The adhesive strength of poly-p-phenylenebenzobisoxazole (PBO) on Si_xN_y-passivated single crystal Si substrates was determined for different formulations of PBO and thicknesses of Si_xN_y. The thicker 400 nm Si_xN_y showed higher interface strengths than the 30 nm layer, due to the higher surface roughness of the thicker Si_xN_y. In another study, the effects of moisture on the interfacial strength were evaluated.[179] For samples at 38°C, the interfacial strength was found to decrease linearly with increasing interfacial moisture concentration.

In short, the key advantages of the laser spallation technique include its nonreliance on gripping and very high strain rates that prevent inelastic deformations, giving accurate readings of interfacial strength. However, the detection of these very high strain rates indicates that very precise equipment and careful setup is required. This test applies to hard coatings, integrated circuit packaging interfaces, and cell–biomaterial interfaces.

A brief summary of the various bimaterial specimen-based methods is given in Table 8.4. It shows the advantages and disadvantages of the different setups.

8.3.3 Supplementary Techniques

In recent years, with the development of computers, charged coupled device (CCD) cameras, and laser light technology, optical techniques have improved tremendously and are applied in many engineering fields.[180–182] For the interfacial fracture study or adhesion evaluation of a bimaterial system, the crack tip along the bimaterial interface represents a highly singular stress field and evaluation of the associated strain gradient is difficult using conventional experimental methods.[183,184] An efficient alternative relies on optical techniques, which are noncontact and yield rich information about the stress and displacement fields, as well as their derivatives for strain evaluation.[183–185]

For the adhesion evaluation of the coating–substrate interface, the interfacial displacement and strain fields determined by optical techniques are directly related to the interfacial strain energy release rate, which is an important parameter representing coating adhesion. Thus, it is beneficial to evaluate coating adhesion by

TABLE 8.4
Comparison of the Various Bimaterial Specimen-Based Methods

	Strength/Fracture Toughness Measurement	Experimental Setup	Results/Data Processing	Other Notes
Indentation	+ Suitable for measurement of interfacial G_c	+ Simple setup + Availability of commercial equipment	– Complex when large deformation occurs at the interface	– Better for brittle coatings weakly bonded to ductile substrates
Scratch	+ Provides semiqualitative evaluation of coating adhesion	+ No special specimen shape or preparation required. + Easy to use – Needs detection of coating detachment	– Complex mechanical analysis due to presence of many factors	+ Fairly reliable + Suitable for brittle coatings
Peel	+ Provides semiqualitative evaluation of coating adhesion	+ Simple setup	– Difficult to extract adhesion energy from data as most mechanical energy is spent on deforming coating	+ Has wider applicability than the tape test. – Suitable for tough and flexible coatings
Blister	+ Suitable for measurement of interfacial G_c + Measures elastic modulus and residual stress of the coating	– Requires a complicated pressure control system – Needs continuous monitoring of pressure and blister dimensions	+ Stable and controlled interfacial crack growth	– Limited to soft flexible polymeric or metallic coatings because hard brittle coatings will tend to crack before forming a blister
Tensile	+ Suitable for investigating mixed-mode coating failure by varying the notch angle	– In situ observation of interfacial crack initiation and propagation almost impossible	– Complicated data analysis due to finite element modeling – Difficult to determine critical load	+ Simulates service conditions more closely than sandwich specimens
Laser spallation	+ Suitable for measurement of interfacial G_c	+ No gripping scheme needed. – Requires high-precision equipment – Needs special backing and absorbing layers	+ Inelastic deformations prevented by very high strain rates – Complex analysis to relate measurement to simulation	– Sample configurations may be limited by special backing and absorbing layers

The symbols "+" and "–" denote advantage and disadvantage characteristics, respectively.

the combined technique of optical techniques and mechanical methods mentioned above.[186,187] The mechanical methods are used to generate an interfacial delamination in the coating/substrate system, and optical techniques are employed to evaluate the extension of the generated delamination to characterize the coating adhesion.

There are a number of optical techniques that can be used to characterize the displacement field and stress state near the crack tip, such as photoelasticity, coherent gradient sensing, moiré interferometry, speckle interferometry, and DIC.[183,185,188,189] In this section, the basic principles and application of these optical techniques for interfacial adhesion evaluation will be reviewed briefly.

8.3.3.1 Photoelasticity Technique

The photoelasticity technique utilizes the birefringence property of certain transparent materials for stress measurement.[190–195] As shown in Figure 8.25, when a ray of polarized light passes through a birefringent material under the action of mechanical stress, it experiences two refractive indices. The magnitude of the refractive indices at each point in the material is directly related to the stress state at that point. After passing the light beams through an analyzer sheet, the interference fringes of light beams are obtained. These fringes are stress-dependent and can be used for calculating the stress throughout the material.

Notable early works on photoelastic investigations of bimaterial interfaces were made by Miskioglu et al.[190] and Lu and Chiang.[191] Miskioglu et al.[190] extracted interfacial SIF from photoelastic data for a bimaterial system consisting of casting PL-2 liquid plastic and Homalite-100 precast sheet. They determined the direction of the applied load for continued interfacial crack propagation by the use of the extracted SIF and finite element method, and found good agreement between the two methods. Lu and Chiang[191] determined a complex SIF from the isochromatic fringe patterns for a center-cracked bimaterial specimen consisting of two dissimilar photoelastic resins. The above-mentioned works demonstrated that the photoelastic technique is applicable to the problem of bimaterial interfaces. Later, Singh and Shukla[192] used photoelasticity to investigate dynamic fracture along the interface of polymer/metal bimaterials. The influence of various fracture parameters on the isochromatic fringe pattern was considered. These parameters include the crack-tip velocity, the mode

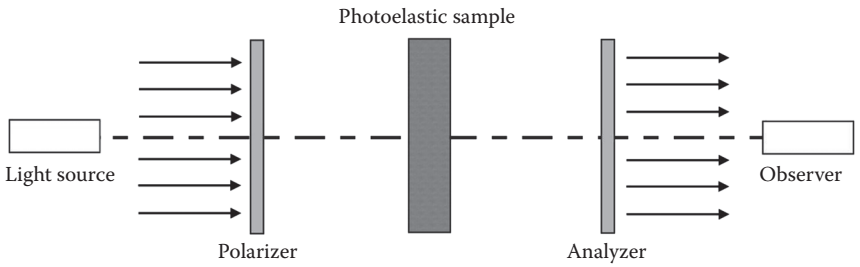


FIGURE 8.25 Schematic of the photoelastic investigation system. (Modified with permission from Sadek, S. and Iskander, M. *Modeling with Transparent Soils*, 27–44. Heidelberg, Berlin: Springer, 2010.)

mixity, and the nonsingular stress field component. Afterwards, studies on how to properly interpret dynamic isochromatic fringe patterns were also conducted.[193,194] For the application of photoelasticity technique in the mechanical evaluation of the coating/substrate system, Fabbri and Messori[196] evaluated the state of residual plane stress present in the polycarbonate slabs by the photoelasticity analysis before and after the poly-silica coating application and curing. Results showed that the thermal curing resulted in less residual stresses than the microwave-assisted curing, leading to better coating scratch resistance.

The photoelastic approach is commonly used for interfacial fracture and adhesion study. The disadvantage is that analysis of the obtained isochromatic fringes is a time-consuming and relatively complex process, often requiring a skilled technician with rich experience. Therefore, further effort should be made to simplify the analysis and reduce the time required.

8.3.3.2 Coherent Gradient Sensing Technique

Coherent gradient sensing (CGS) is a double grating lateral-shearing interferometric technique that provides real-time fringes representing crack-tip deformation or stress state.[197–201] This technique can be used with both opaque (reflection mode) and transparent (transmission mode) solids. When it is used in the reflection mode with opaque solids, it measures in-plane gradients of out-of-plane displacements. Instead, when it is used in the transmission mode with isotropic transparent solids, it measures in-plane gradients of stresses. Figure 8.26 shows the schematics of the CGS setup in transmission and reflection modes. The setups consist of a collimated coherent laser beam, a pair of high-density gratings, a filtering aperture, a positive lens, and an observer. When the transmitted or reflected wavefront emerges from the specimen, it is first processed by two gratings. Then, the light field emerging from the gratings is collected by the filtering lens and its diffraction spots are displayed on its back focal plane. Finally, information regarding the gradients is obtained on the image plane by placing a filtering aperture.

The CGS technique was first developed and applied to the field of fracture mechanics by Tippur and his coworkers.[197–200] Tippur et al.[197] first used the reflection CGS to quantitatively measure the gradients of out-of-plane displacements around a crack tip in a three-point bend fracture specimen under static loading. A good agreement between mode I SIF evaluated from surface slope fringes and the analytical results demonstrated the feasibility of CGS to experimental fracture mechanics investigations. Later, Tippur et al.[198] extended this method to the case of transparent solids using the transmission CGS.

Afterwards, the possibility of using this technique for interfacial fracture mechanics study was explored.[199,200,202] Tippur and Rosakis[199] studied a bimaterial three-point bend specimen made of polymethyl methacrylate (PMMA) and aluminum sheets of equal thickness bonded along a straight interface. Crack-tip deformations were observed in the PMMA half of the specimen using the transmission CGS. The experimentally measured SIF agreed well with numerically calculated values. Subsequently, Tippur and Ramaswamy[200] employed a modified edge notched flexural specimen to investigate the mixed-mode interface fracture of the PMMA/aluminum bimaterial system. They achieved a wide range of crack tip mode mixity

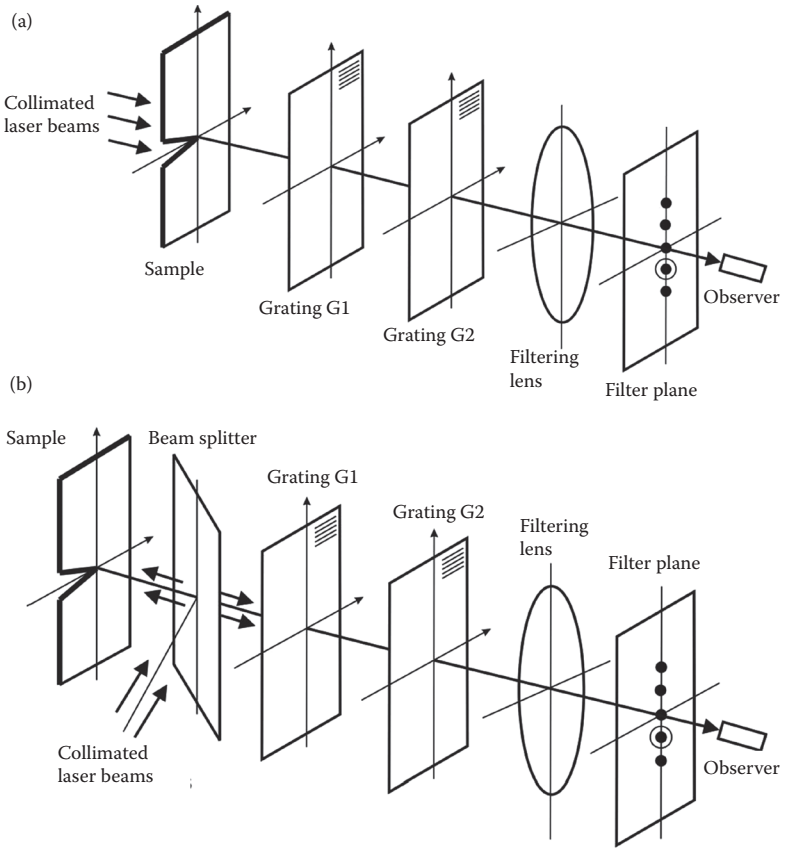


FIGURE 8.26 Schematics of the CGS setup in transmission (a) and reflection (b) modes. (Modified with permission from Tippur, H. V. A review. *Fatigue and Fracture of Engineering Materials and Structures* 33(12), 2010: 832–58.)

using this specimen geometry and CGS technique was used to map crack tip deformations in real time. The experimental measurements and the predictions based on flexural analysis of bimaterial beams were found to be in good agreement. Also, they established a critical energy release rate versus mode mixity map for the present PMMA/aluminum bimaterial system using their optical measurements. The experiments by Tippur's group have inspired several follow-up works on interfacial fracture of bimaterials. For example, Kimberley and Lambros[202] studied the interfacial crack kinking phenomenon in PMMA/Homalite-100 bimaterial panels using transmission CGS and high-speed photography. For the film/substrate systems, the CGS technique was usually used to measure the film curvature which is typically related to the stress state in films.[203,204] Rosakis et al.[203] demonstrated the capability of CGS in measuring curvature in a variety of thin films. Liu et al.[204] reported the systematic absolute/relative error limits of the CGS system in film curvature measurements at arbitrary temperature.

The CGS technique gives full field information in real time and the measurement sensitivity is easily controllable. Furthermore, it involves a simple optical setup and is relatively insensitive to random vibrations and rigid body motions. Nowadays, this optical technique is used widely in the study of quasistatic as well as dynamic crack-tip fields in homogeneous and composite materials.[202,205–207]

8.3.3.3 Moiré Interferometry Technique

Moiré interferometry is an optical method for the measurement of in-plane deformation of solids, caused by mechanical force, temperature change, or other environmental factors.[180,208] Figure 8.27 shows the optical setup for moiré interferometry test.[209] This method relies on an interferometer formed by coherent light and a diffraction grating bounded onto the sample surface. The bounded diffraction grating is used to replicate the surface deformation of the sample. During the test, the interferometer directs two pairs of collimated wavefronts to the diffraction grating at specific angles. When the sample deforms under loading, the diffraction grating deforms accordingly. The deformation of the diffraction grating causes the diffracted wavefronts to interfere with each other, producing fringe patterns that represent the in-plane deformation displacements on the sample surface.

Moiré interferometry has been extensively used for the study of interfacial fracture problems.[210–214] Wang and Chiang[210,211] investigated the deformation fields of interfacial cracks in adhesive joints. The obtained moiré fringe patterns provided a means for the determination of the remote SIF. Nishioka et al.[212] used the

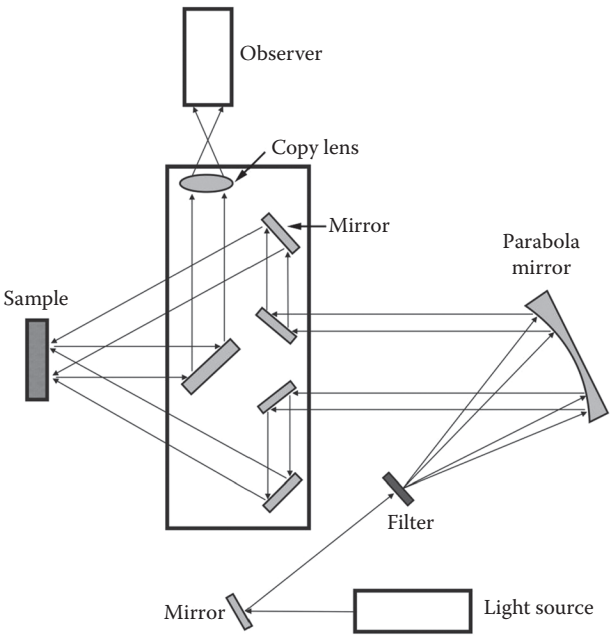


FIGURE 8.27 Optical setup for moiré interferometry test. (Modified with permission from Kang, B. S. J. et al., *Materials Science and Engineering A* 239–240(1–2), 1997: 344–52.)

phase-shifting moiré interferometry to investigate the interfacial crack-tip behavior of an epoxy/aluminum bimaterial specimen. With the measured displacement fields by moiré interferometry, the SIF and separated mode I and II energy release rates were evaluated. Mohammed and Liechti[213] investigated crack nucleation from bimaterial corners using an epoxy/aluminum specimen loaded under four-point bending. Displacements near the corner were measured using moiré interferometry in addition to the usual measurement of load and an associated displacement. The local displacement measurements revealed that the interface was not rigid as commonly assumed. This finding led to the modification of the initial assumption of a rigid interface and a cohesive zone model was chosen to represent the interface in the subsequent finite element analyses. Savalia and Tippur[214] used the moiré interferometry to map the evolution of debonding between the inclusion-matrix pair in a composite by recording crack opening displacements. In the mechanical evaluation of the coating/substrate system, Tang et al.[215] studied the interfacial failure mechanism of TBCs by the moiré interferometry technique combined with a three-point bending test. They determined the crack opening displacement and *J*-integral of the coating specimen with the aid of the experimental results from moiré interferometry.

In short, the moiré interferometry technique combines the simplicity of geometrical moiré with the high sensitivity of optical interferometry for measuring in-plane displacements and has had a proven record of applications in fracture mechanics.

8.3.3.4 Speckle Interferometry Technique

Like the moiré interferometry technique, the speckle interferometry technique also utilizes interference fringes for deformation measurement.[182,216,217] The difference between them is that the moiré interferometry technique relies on the superposition of two gratings to form a moiré fringe pattern, while the speckle interferometry technique uses a speckle effect to produce interference fringes. When an optically rough surface is illuminated by a coherent light such as laser, it will exhibit a granular appearance, creating a speckle effect. The formed speckle pattern can be regarded as a point property of the sample surface. These speckles will experience the same displacement changes as the sample surface. The speckle interferometry technique has been categorized into speckle photography, speckle correlation, and electronic speckle pattern interferometry (ESPI). Here, we focus on the ESPI technique.

The ESPI technique links the speckle interferometer with a computer-based image detection and processing system, producing the fringe interference pattern electronically.[216,218,219] The experimental setup for out-of-plane measurement is shown in Figure 8.28. In this technique, the laser beam is split. One beam is directed onto the sample to take a laser-illuminated sample picture, and the obtained picture is stored in the computer system. The other beam is directed onto the photo receiver in the sensor as the reference beam. This reference beam is superimposed on the light scattered by the sample, and the produced image is also stored in the computer system. The difference between the two images yields quantitative information about the displacements and strains of the test sample. The ESPI technique is an important advancement in the development of speckle photography techniques. The electronic detection and processing system employed shortens the analysis time for speckle photography greatly, resulting in the display of the measurement information in real time. Furthermore, this

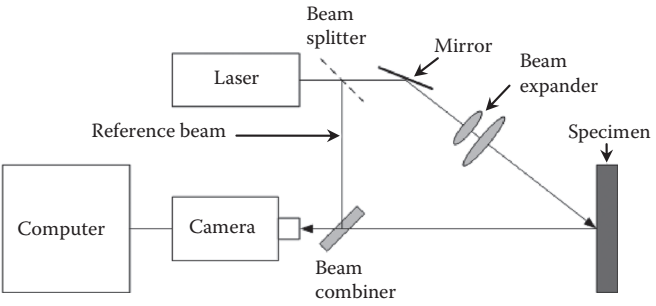


FIGURE 8.28 Experimental setup for out-of-plane ESPI.

technique also applies to nonhomogeneous materials due to its advantage of full-field measurement. Thus, the full-field deformation measurement of anisotropic materials such as composites and joints can be performed by this technique.

The laser speckle technique has been proven to be an effective tool in investigating the fracture mechanics problems.[218,220,221] This is because the wavelength of laser light is on the order of tenths of microns and this feature achieves displacement measurements at detailed resolution. The high measurement resolution is very useful in determining surface deformation of samples and identifying initiation of failure. Tay et al.[218] used the laser speckle technique to measure the extent of the elastic–plastic boundary ahead of a static mode I crack under small-scale yielding. The results show that the shape and size of the plastic zone near a notch agree reasonably well with the theoretical prediction, demonstrating the effectiveness of this technique for fracture mechanics analysis. Moore and Tyrer[221] measured the opening-mode SIF by using the ESPI technique. By comparing the measurement results with theoretical values, it was found that all cumulative ESPI measurement results fall within ±10% of the theoretical values. This comparison highlighted the high sensitivity of ESPI technique and demonstrated that the SIF can be calculated accurately with this technique.

The speckle interferometry technique also applies to fracture analysis of bimaterial interface.[222–224] Chiang and Lu[222] investigated the displacement field around a bimaterial interfacial crack by using the laser speckle technique. The results showed that while tangential displacement jump agreed very well with the theoretical predictions, the opening displacement jump was much larger than theoretical values. The authors speculated that some nonlinear effect may play a role, leading to the difference between measurement results and predictions. Frybort et al.[223] employed the ESPI technique to investigate the mechanical interactions at the interface of wood–cement composites. The ESPI technique was used to visualize the interfacial bonding between the wood and the cement. Combining the ESPI results with the surface roughness of wood strands, it was found that the surface with a comparatively higher roughness bonded well to the cement matrix, while the less rough surface failed earlier during the shrinkage of wood strands. For coating adhesion evaluation, Dolinko and Kaufmann[186] studied the feasibility of evaluating coating adhesion by the ESPI and bending test combined technique. In this study, the ESPI technique was used to measure the deflections produced by the small delamination in the

coated specimen subjected to the four-point bending test. The delamination length depended on the coating adhesion strength. Thus, by measuring the deflections of the debonded region, they obtained a quantitative estimation of coating adhesion. Similarly, Tendela and Kaufmann[187] evaluated coating adhesion by a technique that combined radial in-plane speckle interferometer and a microindentation test. This technique was based on the measurement of the radial in-plane displacement field on the surface of the coated specimen to characterize the coating adhesion. They demonstrated that the ESPI technique can be successfully used to measure the small local deformations generated by the microindentation.

The speckle interferometry technique offers the advantages including being noncontacting, full-field measurement, and high sensitivity for the study of fracture mechanics and interfacial adhesion. The major drawback of this technique is that the measured deformation information is easily affected by several random and systematic parameters, such as optical noises, environmental perturbations, misalignments, and collimation faults of the laser beams.

8.3.3.5 DIC Technique

The DIC technique is an optical nondestructive and noncontacting method used to measure deformation, displacement, and strain. The target object needs to possess a pattern, for example, lines, grids, or random arrays. An example of the DIC setup is shown in Figure 8.29. The changes in the pattern before and after any phenomena are acquired utilizing the cameras, and analyzed in the computer digital image processing software to obtain full-field information of the object. The DIC has the advantage of allowing measurements independent of the target object size. However, it is limited by the resolution of the imaging system and the quality of the object pattern.

Early work in the area of image correlation was performed by Hobrough in the 1950s.[225] When digitized images were available, algorithms were developed for nonengineering applications such as character recognition, microscopy, and radiology. Peters and Ranson[226] then pioneered the use of the DIC to study deformations in material systems.

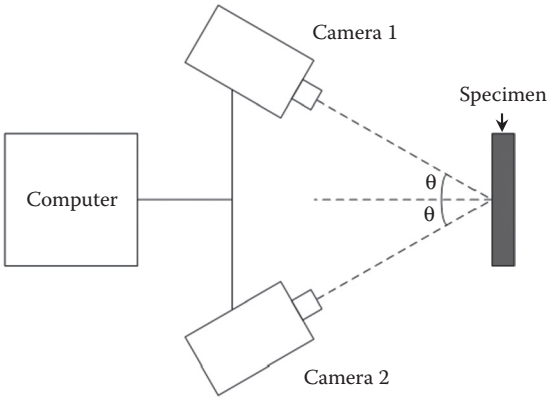


FIGURE 8.29 Schematic of the 3D DIC setup.

Wu et al.[227] utilized the DIC to monitor the strain full/local field strain in a brittle coating/ductile substrate system under tension loading. The strains were subsequently used to evaluate the fracture strength in coating and interfacial adhesion strength, determined to be 35.0 ± 4.6 and 14.1 ± 3.2 MPa, respectively.

The DIC technique is also applicable to small-scale testing. Eberl et al.[228] proposed a microbeam bending test methodology incorporating DIC to determine the elastic properties and strength of electron beam physical vapor deposition (EB-PVD) coatings. The DIC also captured details of the crack initiation and propagation of interfacial cracks.

In addition, the DIC technique has been frequently used together with other methods. For example, it was combined with the acoustic emission method to monitor cracking formation and coating delamination and to determine fracture toughness of a TBC system subjected to bending.[229] The fracture toughness of top coating/bond coat interface was estimated to be 103–129 J/m^2 by a shear-lag model. It has been used with high-speed photography to monitor the dynamic torsion testing of tungsten carbide-cobalt (WC-Co) cermets.[230] The deformation events of the coating–substrate system during the tests were observed using high-speed photography and correlated to specific points along the stress–strain curve. The events observed include formation of a mode III crack and heavy plastic deformations that lead to ductile failure. The approach has also been coupled with micro-Raman spectroscopy and the finite element method to study stress relaxation of diamond coatings deposited on Ti-substrates.[231]

The DIC has also been used to determine the performance of TBCs. Song et al.[232] studied the thermal deformation of EB-PVD TBCs using the DIC. In thermal sprays, the DIC is used to measure the strip curvature, from which the stress profile in each deposition step is determined by the finite element method.[233] DIC has also been used with focused ion beam (FIB) milling to assess residual stress relaxation.[234] Zhou et al.[235] employed the DIC and with acoustic emission to monitor real-time tensile failure of air plasma-sprayed TBC. The characteristics of the acoustic emission signals are used to study the failure modes of the TBC, while strain-maps of the DIC system help delineate the fracture stages.

The DIC technique is a unique auxiliary approach to determining the deformation and material properties of coatings that can be adapted for use with many types of experimental setups.

8.4 CONCLUSIONS

In summary, this chapter discusses the approaches widely used to evaluate coating adhesion. For each technique, the experimental setup, underlying principles, and typical applications are reviewed. The discussion in this chapter shows that there is no single method that is applicable for all coating/substrate systems. Each approach has its own merits and limitations, depending on the targeted applications and the characteristics of the coating/substrate system. Proper selection of the testing method or a combination of methods is therefore vital to obtain useful and reliable data. The deficiencies of each method highlighted indicate that there is room for improvement toward the development of more efficient, reliable, and universally applicable methods for evaluating coating adhesion.

ACKNOWLEDGMENTS

The authors acknowledge the support from the Agency for Science, Technology, and Research (A*STAR), Singapore (Grant No: SERC 1123004027 and SERC 1122904015).

REFERENCES

1. Goldschmidt, A. and Streitberger, H. J. *BASF Handbook on Basics of Coating Technology*. Hannover, Germany: Vincentz Network, 2003.
2. Licari, J. J. *Coating Materials for Electronic Applications: Polymers, Processing, Reliability, Testing*. New York: Noyes Publications, 2003.
3. Sankara Narayanan, T. S. N., Park, I. S., and Lee, M. H. Strategies to improve the corrosion resistance of microarc oxidation (MAO) coated magnesium alloys for degradable implants: Prospects and challenges. *Progress in Materials Science* 60(0), 2014: 1–71.
4. Padture, N. P., Gell, M., and Jordan, E. H. Thermal barrier coatings for gas-turbine engine applications. *Science* 296(5566), 2002: 280–84.
5. Lima, R. S. and Marple, B. R. Thermal spray coatings engineered from nanostructured ceramic agglomerated powders for structural, thermal barrier and biomedical applications: A review. *Journal of Thermal Spray Technology* 16(1), 2007: 40–63.
6. Wood, R. J. K. Tribo-corrosion of coatings: A review. *Journal of Physics D: Applied Physics* 40(18), 2007: 5502–21.
7. PalDey, S. and Deevi, S. C. Single layer and multilayer wear resistant coatings of (Ti,Al) N: A review. *Materials Science and Engineering A* 342(1–2), 2003: 58–79.
8. Valli, J. A review of adhesion test methods for thin hard coatings. *Journal of Vacuum Science & Technology A: Vacuum, Surfaces, and Films* 4(6), 1986: 3007–14.
9. Mittal, K. L. Adhesion measurement of thin films. *Electro Component Science and Technology* 3(1), 1976: 21–42.
10. Lin, C. K. and Berndt, C. C. Measurement and analysis of adhesion strength for thermally sprayed coatings. *Journal of Thermal Spray Technology* 3(1), 1994: 75–104.
11. Chen, Z. X., Zhou, K., Lu, X., and Lam, Y. C. A review on the mechanical methods for evaluating coating adhesion. *Acta Mechanica* 225, 2014: 431–52.
12. Hull, T., Colligon, J., and Hill, A. Measurement of thin film adhesion. *Vacuum* 37(3–4), 1987: 327–30.
13. Mellali, M., Fauchais, P., and Grimaud, A. Influence of substrate roughness and temperature on the adhesion/cohesion of alumina coatings. *Surface and Coatings Technology* 81(2–3), 1996: 275–86.
14. Singh, R. K., Gilbert, D. R., Fitz-Gerald, J., Harkness, S., and Lee, D. G. Engineered interfaces for adherent diamond coatings on large thermal-expansion coefficient mismatched substrates. *Science* 272(5260), 1996: 396–98.
15. Takadoum, J. and Houmid Bennani, H. Influence of substrate roughness and coating thickness on adhesion, friction and wear of TiN films. *Surface and Coatings Technology* 96(2–3), 1997: 272–82.
16. Griffith, A. A. The phenomena of rupture and flow in solids. *Philosophical Transactions of the Royal Society of London. Series A, Containing Papers of a Mathematical or Physical Character* 221, 1921: 163–98.
17. Irwin, G. R. Analysis of stresses and strains near the end of a crack traversing a plate. *Journal of Applied Mechanics* 24, 1957: 361–64.
18. Irwin, G. R. Linear fracture mechanics, fracture transition, and fracture control. *Engineering Fracture Mechanics* 1(2), 1968: 241–57.

19. Dugdale, D. S. Yielding of steel sheets containing slits. *Journal of the Mechanics and Physics of Solids* 8(2), 1960: 100–04.
20. Wells, A. A. Unstable crack propagation in metals: Cleavage and fracture. Paper presented at the Proceedings of the Crack Propagation Symposium, Cranfield, 1961.
21. Williams, M. L. The stresses around a fault or crack in dissimilar media. *Bulletin of the Seismological Society of America* 49(2), 1959: 199–204.
22. Dundurs, J. Discussion: Edge-bonded dissimilar orthogonal elastic wedges under normal and shear loading (Bogy, D. B., 1968, *ASME Journal of Applied Mechanics*, 35, pp. 460–466). *Journal of Applied Mechanics* 36(3), 1969: 650–52.
23. Comninou, M. An overview of interface cracks. *Engineering Fracture Mechanics* 37(1), 1990: 197–208.
24. Comninou, M. The interface crack. *Transactions of the ASME. Series E, Journal of Applied Mechanics* 44(4), 1977: 631–6.
25. Rice, J. R. Elastic fracture mechanics concepts for interfacial cracks. *Journal of Applied Mechanics* 55(1), 1988: 98–103.
26. Rice, J. R. and Sih, G. C. Plane problems of cracks in dissimilar media. *Journal of Applied Mechanics* 32(2), 1965: 418–23.
27. Klingbeil, N. W. and Beuth, J. L. Interfacial fracture testing of deposited metal layers under four-point bending. *Engineering Fracture Mechanics* 56(1), 1997: 113–25.
28. Hutchinson, J. W. and Suo, Z. Mixed mode cracking in layered materials. In *Advances in AppliedMechanics*, edited by J.W. Hutchinson and T. Y. Wu, 63–191. New York: Academic Press Inc., 1992.
29. Wei, M., Ruys, A. J., Swain, M. V., Kim, S. H., Milthorpe, B. K., and Sorrell, C. C. Interfacial bond strength of electrophoretically deposited hydroxyapatite coatings on metals. *Journal of Materials Science: Materials in Medicine* 10(7), 1999: 401–09.
30. Ostojic, P. and McPherson, R. Determining the critical strain energy release rate of plasma-sprayed coatings using a double-cantilever-beam technique. *Journal of the American Ceramic Society* 71(10), 1988: 891–99.
31. Chen, Z. X., Qian, L. H., and Zhu, S. J. Determination and analysis of crack growth resistance in plasma-sprayed thermal barrier coatings. *Engineering Fracture Mechanics* 77(11), 2010: 2136–44.
32. Tong, J., Wong, K. Y., and Lupton, C. Determination of interfacial fracture toughness of bone-cement interface using sandwich Brazilian disks. *Engineering Fracture Mechanics* 74(12), 2007: 1904–16.
33. Chen, J. Indentation-based methods to assess fracture toughness for thin coatings. *Journal of Physics D: Applied Physics* 45(20), 2012: 203001.
34. Suo, Z. and Hutchinson, J. W. Sandwich test specimens for measuring interface crack toughness. *Materials Science and Engineering A* 107(C), 1989: 135–43.
35. Janssen, C. Sample for fracture mechanics studies on glass. Paper presented at the 10th International Congress on Glass, Kyoto, Japan, 1974.
36. Yilmaz, S., Ipek, M., Celebi, G. F., and Bindal, C. The effect of bond coat on mechanical properties of plasma-sprayed Al_2O_3 and Al_2O_3-13 wt% TiO_2 coatings on AISI 316L stainless steel. *Vacuum* 77(3), 2005: 315–21.
37. Berndt, C. C. and McPherson, R. A fracture mechanics approach to the adhesion of flame and plasma sprayed coatings. Paper presented at the International Conference on Manufacturing Engineering, Melbourne, Australia, 1980.
38. Li, C.-J., Wang, W.-Z., and He, Y. Measurement of fracture toughness of plasma-sprayed Al_2O_3 coatings using a tapered double cantilever beam method. *Journal of the American Ceramic Society* 86(8), 2003: 1437–39.
39. Lee, T. K. Interfacial adhesion studies using double cantilever beam method and shear testing. Paper presented at the Electronics Packaging Technology Conference (EPTC 2007), Singapore, 2007.

40. Loo, S. Z. Y., Lee, P. C., Lim, Z. X., Yantara, N., Tee, T. Y., Tan, C. M., and Chen, Z. Interface fracture toughness assessment of solder joints using double cantilever beam test. *International Journal of Modern Physics B* 24(1–2), 2010: 164–74.
41. Dai, X., Brillhart, M. V., and Ho, P. S. Adhesion measurement for electronic packaging applications using double cantilever beam method. *Components and Packaging Technologies, IEEE Transactions on* 23(1), 2000: 101–16.
42. Mostovoy, S., Crosley, P., and Ripling, E. J. Use of crack-line-loaded specimens for measuring plane-strain fracture toughness. *Journal of Materials* 2(3), 1967: 661–81.
43. Wang, W. Z., Li, C. J., and Ye, F. X. Effect of specimen geometry on fracture toughness measurement of plasma-sprayed ceramic coatings by the tapered double cantilever beam approach. *Vacuum* 73(3–4), 2004: 649–54.
44. Meiller, M., Roche, A. A., and Sautereau, H. Tapered double cantilever beam test used as a practical adhesion test for metal/adhesive/metal systems. *Journal of Adhesion Science and Technology* 13(7), 1999: 773–88.
45. Brown, E. N., White, S. R., and Sottos, N. R. Fatigue crack propagation in microcapsule-toughened epoxy. *Journal of Materials Science* 41(19), 2006: 6266–73.
46. Charalambides, P. G., Lund, J., Evans, A. G., and McMeeking, R. M. A test specimen for determining the fracture resistance of bimaterial interfaces. *Journal of Applied Mechanics* 56(1), 1989: 77–82.
47. Charalambides, P. G., Cao, H. C., Lund, J., and Evans, A. G. Development of a test method for measuring the mixed mode fracture resistance of bimaterial interfaces. *Mechanics of Materials* 8(4), 1990: 269–83.
48. Chandra, L. and Clyne, T. W. Characterization of the strength and adhesion of diamond films on metallic substrates using a substrate plastic straining technique. *Diamond and Related Materials* 3(4–6), 1994: 791–98.
49. Hofinger, I., Oechsner, M., Bahr, H. A., and Swain, M. V. Modified four-point bending specimen for determining the interface fracture energy for thin, brittle layers. *International Journal of Fracture* 92(3), 1998: 213–20.
50. Agrawal, A. and Karlsson, A. M. On the reference length and mode mixity for a bimaterial interface. *Journal of Engineering Materials and Technology, Transactions of the ASME* 129(4), 2007: 580–87.
51. Li, H., Khor, K. A., and Cheang, P. Adhesive and bending failure of thermal sprayed hydroxyapatite coatings: Effect of nanostructures at interface and crack propagation phenomenon during bending. *Engineering Fracture Mechanics* 74(12), 2007: 1894–903.
52. Howard, S. J., Phillipps, A. J., and Clyn, T. W. The interpretation of data from the four-point bend delamination test to measure interfacial fracture toughness. *Composites* 24(2), 1993: 103–12.
53. Wang, B. and Siegmund, T. A modified 4-point bend delamination test. *Microelectronic Engineering* 85(2), 2008: 477–85.
54. Clifford, S. M., Manger, C. I. C., and Clyne, T. W. Characterisation of a glass-fibre reinforced vinylester to steel joint for use between a naval GRP superstructure and a steel hull. *Composite Structures* 57(1–4), 2002: 59–66.
55. Yamazaki, Y., Schmidt, A., and Scholz, A. The determination of the delamination resistance in thermal barrier coating system by four-point bending tests. *Surface and Coatings Technology* 201(3–4), 2006: 744–54.
56. Théry, P. Y., Poulain, M., Dupeux, M., and Braccini, M. Adhesion energy of a YPSZ EB-PVD layer in two thermal barrier coating systems. *Surface and Coatings Technology* 202(4–7), 2007: 648–52.
57. Zhao, Y., Shinmi, A., Zhao, X., Withers, P. J., Van Boxel, S., Markocsan, N., Nylen, P., and Xiao, P. Investigation of interfacial properties of atmospheric plasma sprayed thermal barrier coatings with four-point bending and computed tomography technique. *Surface and Coatings Technology* 206(23), 2012: 4922–29.

58. Zou, L., Huang, Y., and Wang, C. A. The characterization and measurement of interfacial toughness for Si_3N_4/BN composites by the four-point bend test. *Journal of the European Ceramic Society* 24(9), 2004: 2861–68.
59. Gan, Z., Mhaisalkar, S. G., Chen, Z., Zhang, S., Chen, Z., and Prasad, K. Study of interfacial adhesion energy of multilayered ULSI thin film structures using four-point bending test. *Surface and Coatings Technology* 198(1–3), SPEC. ISS. 2005: 85–89.
60. Yan, Y., Sumigawa, T., Shang, F., and Kitamura, T. Cohesive zone criterion for cracking along the Cu/Si interface in nanoscale components. *Engineering Fracture Mechanics* 78(17), 2011: 2935–46.
61. Carneiro, F. L. L. B., and Barcellos, A. Concrete tensile strength. *RILEM Bulletin* 13, 1953: 103–07.
62. Atkinson, C., Smelser, R. E., and Sanchez, J. Combined mode fracture via the cracked Brazilian disk test. *International Journal of Fracture* 18(4), 1982: 279–91.
63. Awaji, H. and Sato, S. Combined mode fracture toughness measurement by the disk test. *Journal of Engineering Materials and Technology, Transactions of the ASME* 100(2), 1978: 175–82.
64. Ayatollahi, M. R. and Aliha, M. R. M. Cracked Brazilian disc specimen subjected to mode II deformation. *Engineering Fracture Mechanics* 72(4), 2005: 493–503.
65. Shetty, D. K., Rosenfield, A. R., and Duckworth, W. H. Fracture toughness of ceramics measured by a chevron-notch diametral-compression test. *Journal of the American Ceramic Society* 68(12), 1985: 325–27.
66. Wang, J. S. and Suo, Z. Experimental determination of interfacial toughness curves using Brazil-nut-sandwiches. *Acta Metallurgica Et Materialia* 38(7), 1990: 1279–90.
67. Pang, H. L. J., Bong, S. N., Shi, X. Q., and Wang, Z. P. Mixed mode fracture toughness characterization for interface and interlayer cracks in adhesive bonded joints. Paper presented at the Electronic Materials and Packaging (EMAP 2000), Hong Kong, 2000.
68. Banks-Sills, L. and Schwartz, J. Fracture testing of Brazilian disk sandwich specimens. *International Journal of Fracture* 118(3), 2002: 191–209.
69. Rahbar, N., Wolf, K., Orana, A., Fennimore, R., Zong, Z., Meng, J., Papandreou, G., Maryanoff, C., and Soboyejo, W. Adhesion and interfacial fracture toughness between hard and soft materials. *Journal of Applied Physics* 104(10), 2008: 103533.
70. Tan, T., Rahbar, N., Buono, A., Wheeler, G., and Soboyejo, W. Sub-critical crack growth in adhesive/marble interfaces. *Materials Science and Engineering A* 528(10–11), 2011: 3697–704.
71. Pallares, G., Ponson, L., Grimaldi, A., George, M., Prevot, G., and Ciccotti, M. Crack opening profile in DCDC specimen. *International Journal of Fracture* 156(1), 2009: 11–20.
72. Fett, T., Rizzi, G., Guin, J. P., López-Cepero, J. M., and Wiederhorn, S. M. A fracture mechanics analysis of the double cleavage drilled compression test specimen. *Engineering Fracture Mechanics* 76(7), 2009: 921–34.
73. Plaisted, T. A., Amirkhizi, A. V., and Nemat-Nasser, S. Compression-induced axial crack propagation in DCDC polymer samples: Experiments and modeling. *International Journal of Fracture* 141(3–4), 2006: 447–57.
74. Turner, M. R., Dalgleish, B. J., He, M. Y., and Evans, A. G. A fracture resistance measurement method for bimaterial interfaces having large debond energy. *Acta Metallurgica Et Materialia* 43(9), 1995: 3459–65.
75. Jenne, T. A., Keat, W. D., and Larson, M. C. Limits of crack growth stability in the double cleavage drilled compression specimen. *Engineering Fracture Mechanics* 70(13), 2003: 1697–719.
76. Ayatollahi, M. R. and Bagherifard, S. Numerical analysis of an improved DCDC specimen for investigating mixed mode fracture in ceramic materials. *Computational Materials Science* 46(1), 2009: 180–85.

77. He, M. Y., Turner, M. R., and Evans, A. G. Analysis of the double cleavage drilled compression specimen for interface fracture energy measurements over a range of mode mixities. *Acta Metallurgica Et Materialia* 43(9), 1995: 3453–58.
78. Olvera, D., Zimmermann, E. A., and Ritchie, R. O. Mixed-mode toughness of human cortical bone containing a longitudinal crack in far-field compression. *Bone* 50(1), 2012: 331–36.
79. Turner, M. R. and Evans, A. G. An experimental study of the mechanisms of crack extension along an oxide/metal interface. *Acta Materialia* 44(3), 1996: 863–71.
80. Lipkin, D. M., Clarke, D. R., and Evans, A. G. Effect of interfacial carbon on adhesion and toughness of gold-sapphire interfaces. *Acta Materialia* 46(13), 1998: 4835–50.
81. Ritter, J. E., Jacome, G. S., Pelch, J. R., Russell, T. P., and Lardner, T. J. Controlling subcritical crack growth at epoxy/glass interfaces. *Journal of Electronic Packaging, Transactions of the ASME* 124(4), 2002: 328–33.
82. Hasegawa, M. and Kagawa, Y. Decohesion behavior in copper-sapphire interface under mode I cyclic loading. *Materials Science and Engineering A* 417(1–2), 2006: 158–65.
83. Balkova, R., Holcnerova, S., and Cech, V. Testing of adhesives for bonding of polymer composites. *International Journal of Adhesion and Adhesives* 22(4), 2002: 291–95.
84. Di Bella, G., Galtieri, G., Pollicino, E., and Borsellino, C. Mechanical characterization of adhesive joints with dissimilar substrates for marine applications. *International Journal of Adhesion and Adhesives* 41, 2013: 33–40.
85. ASTM. Standard Test Method for Apparent Shear Strength of Single-Lap-Joint Adhesively Bonded Metal Specimens by Tension Loading (Metal-to-Metal). 6. West Conshohocken, PA: ASTM International, 2010.
86. ASTM. Standard Test Method for Strength Properties of Adhesively Bonded Plastic Lap-Shear Sandwich Joints in Shear by Tension Loading. 4. West Conshohocken, PA: ASTM International, 2003.
87. Lewis, F. and Mantovani, D. Methods to investigate the adhesion of soft nano-coatings on metal substrates—application to polymer-coated stents. *Macromolecular Materials and Engineering* 294(1), 2009: 11–19.
88. Pandiyaraj, K. N., Selvarajan, V., Deshmukh, R. R., and Gao, C. Modification of surface properties of polypropylene (PP) film using DC glow discharge air plasma. *Applied Surface Science* 255(7), 2009: 3965–71.
89. Mascia, L., Dhillon, J., and Harper, J. F. Adhesion enhancement of rubbery and ductile polyolefin coatings on glass fibers for epoxy composites and effects on failure mechanism. *Journal of Applied Polymer Science* 47(3), 1993: 487–98.
90. Zhang, C., Leng, Y., and Chen, J. In vitro mechanical integrity of hydroxyapatite coatings on ti-6Al-4V implants under shear loading. *Journal of Biomedical Materials Research* 56(3), 2001: 342–50.
91. Baldan, A. Adhesively-bonded joints in metallic alloys, polymers and composite materials: Mechanical and environmental durability performance. *Journal of Materials Science* 39(15), 2004: 4729–97.
92. Berg, S., Kim, S. W., Grajewski, V., and Fromm, E. Effect of contamination on mechanical properties and adhesion of magnetron-sputtered TiN coatings on high speed steel substrates. *Materials Science and Engineering A* 139(C), 1991: 345–51.
93. Ochoa-Putman, C. and Vaidya, U. K. Mechanisms of interfacial adhesion in metal-polymer composites—Effect of chemical treatment. *Composites Part A: Applied Science and Manufacturing* 42(8), 2011: 906–15.
94. Boulton, L. M., Gregson, P. J., Tuke, M., and Baldwin, T. Adhesively bonded hydroxyapatite coating. *Materials Letters* 12(1–2), 1991: 1–6.
95. Lin, C. S., Chen, M. T., and Liu, J. H. Structural evolution and adhesion of titanium oxide film containing phosphorus and calcium on titanium by anodic oxidation. *Journal of Biomedical Materials Research—Part A* 85(2), 2008: 378–87.

96. Chen, Z. X., Wang, W. X., Takao, Y., Matsubara, T., and Ren, L. M. Microstructure and shear fracture characteristics of porous anodic TiO_2 layer before and after hot water treatment. *Applied Surface Science* 257(16), 2011: 7254–62.
97. Liu, A., Guo, M., Gao, J., and Zhao, M. Influence of bond coat on shear adhesion strength of erosion and thermal resistant coating for carbon fiber reinforced thermosetting polyimide. *Surface and Coatings Technology* 201(6), 2006: 2696–700.
98. Chrobak, A., Kubisztal, M., Kubisztal, J., and Haneczok, G. Adhesion coefficient and elastic properties of composite coatings on metallic substrate. *Surface and Coatings Technology* 204(12–13), 2010: 2077–80.
99. ASTM. Standard Test Method for Adhesion or Cohesion Strength of Thermal Spray Coatings. 8. West Conshohocken, PA: ASTM International, 2013.
100. Filiaggi, M. J. and Pilliar, R. M. Mechanical testing of plasma-sprayed ceramic coatings on metal substrates: Interfacial fracture toughness and tensile bond strength. *Journal of Materials Science* 26(19), 1991: 5383–95.
101. Marot, G., Lesage, J., Démarécaux, P., Hadad, M., Siegmann, S., and Staia, M. H. Interfacial indentation and shear tests to determine the adhesion of thermal spray coatings. *Surface and Coatings Technology* 201(5), 2006: 2080–85.
102. Kim, H. M., Miyaji, F., Kokubo, T., and Nakamura, T. Bonding strength of bonelike apatite layer to Ti metal substrate. *Journal of Biomedical Materials Research* 38(2), 1997: 121–27.
103. Hong, M. H., Lee, D. H., Kim, K. M., and Lee, Y. K. Improved bonding strength between TiO2 film and Ti substrate by microarc oxidation. *Surface and Interface Analysis* 42(6–7) 2010: 492–96.
104. Ou, S. F., Lin, C. S., and Pan, Y. N. Microstructure and surface characteristics of hydroxyapatite coating on titanium and Ti-30Nb-1Fe-1Hf alloy by anodic oxidation and hydrothermal treatment. *Surface and Coatings Technology* 205(8–9), 2011: 2899–906.
105. Liu, F., Xu, J. L., Yu, D. Z., Wang, F. P., and Zhao, L. C. Effects of cathodic voltages on the structure and properties of ceramic coatings formed on NiTi alloy by micro-arc oxidation. *Materials Chemistry and Physics* 121(1–2), 2010: 172–77.
106. Xie, Y. and Hawthorne, H. M. A model for compressive coating stresses in the scratch adhesion test. *Surface and Coatings Technology* 141(1), 2001: 15–25.
107. Zumelzu, E. and Gipoulou, G. A T-peel test to assess the adhesive properties of organic coatings applied to electrolytic tinplate. *Surface Coatings International Part B: Coatings International* 85(1), 2002: 35–38.
108. Taheri, N., Mohammadi, N., and Shahidi, N. An automatic instrument for measurement of interfacial adhesion of polymeric coatings. *Polymer Testing* 19(8), 2000: 959–66.
109. Elambasseril, J. and Ibrahim, R. N. Determination of interfacial fracture toughness of coatings using circumferentially notched cylindrical substrate. *Materials Science and Engineering A* 529(1), 2011: 406–16.
110. Ikeda, R., Cho, H., Sawabe, A., and Takemoto, M. Laser spallation method to measure strength against Mode-I decohesion of CVD diamond films. *Diamond and Related Materials* 14(3–7), 2005: 631–36.
111. Oliver, W. C. and Pharr, G. M. Measurement of hardness and elastic modulus by instrumented indentation: Advances in understanding and refinements to methodology. *Journal of Materials Research* 19(1), 2004: 3–20.
112. Kruzic, J. J., Kim, D. K., Koester, K. J., and Ritchie, R. O. Indentation techniques for evaluating the fracture toughness of biomaterials and hard tissues. *Journal of the Mechanical Behavior of Biomedical Materials* 2(4), 2009: 384–95.
113. Ranade, A. N., Rama Krishna, L., Li, Z., Wang, J., Korach, C. S., and Chung, Y. W. Relationship between hardness and fracture toughness in Ti-TiB_2 nanocomposite coatings. *Surface and Coatings Technology* 213, 2012: 26–32.

114. Drory, M. D. and Hutchinson, J. W. Measurement of the adhesion of a brittle film on a ductile substrate by indentation. *Proceedings of the Royal Society A: Mathematical, Physical and Engineering Sciences* 452(1953), 1996: 2319–41.
115. Qi, H., Yang, X., and Wang, Y. Interfacial fracture toughness of APS bond coat/substrate under high temperature. *International Journal of Fracture* 157(1–2), 2009: 71–80.
116. Chicot, D., Démarécaux, P., and Lesage, J. Apparent interface toughness of substrate and coating couples from indentation tests. *Thin Solid Films* 283(1–2), 1996: 151–57.
117. Li, X., Diao, D., and Bhushan, B. Fracture mechanisms of thin amorphous carbon films in nanoindentation. *Acta Materialia* 45(11), 1997: 4453–61.
118. Xie, Y., Zhang, X., Robertson, M., Maric, R., and Ghosh, D. Measurement of the interface adhesion of solid oxide fuel cells by indentation. *Journal of Power Sources* 162(1), 2006: 436–43.
119. Xie, Y. and Hawthorne, H. M. Measuring the adhesion of sol-gel derived coatings to a ductile substrate by an indentation-based method. *Surface and Coatings Technology* 172(1), 2003: 42–50.
120. Lesage, J. and Chicot, D. Models for hardness and adhesion of coatings. *Surface Engineering* 15(6), 1999: 447–53.
121. Bourse, G., Xü, W. J., Mouftiez, A., Vandevoorde, L., and Ourak, M. Interfacial adhesion characterization of plasma coatings by V(z) inversion technique and comparison to interfacial indentation. *NDT and E International* 45(1), 2012: 22–31.
122. Marcano, Z., Lesage, J., Chicot, D., Mesmacque, G., Puchi-Cabrera, E. S., and Staia, M. H. Microstructure and adhesion of Cr_3C_2-NiCr vacuum plasma sprayed coatings. *Surface and Coatings Technology* 202(18), 2008: 4406–10.
123. Sadeghi-Fadaki, S. A., Zangeneh-Madar, K., and Valefi, Z. The adhesion strength and indentation toughness of plasma-sprayed yttria stabilized zirconia coatings. *Surface and Coatings Technology* 204(14), 2010: 2136–41.
124. Lee, C. Y., Dupeux, M., and Tuan, W. H. Cross-sectional indentation technique for thick film interfacial adhesion characterisation. *Surface Engineering* 25(2), 2009: 97–100.
125. Chen, J. and Bull, S. J. Approaches to investigate delamination and interfacial toughness in coated systems: An overview. *Journal of Physics D: Applied Physics* 44(3), 2011: 034001.
126. Xie, H. and Huang, H. Characterization of the interfacial strength of SiNx/GaAs film/substrate systems using energy balance in nanoindentation. *Journal of Materials Research* 28(22), 2013: 3137–45.
127. Chen, J., Lin, Z., Bull, S. J., Phillips, C. L., and Bristowe, P. D. Experimental and modelling techniques for assessing the adhesion of very thin coatings on glass. *Journal of Physics D: Applied Physics* 42(21), 2009: 214003.
128. Heavens, O. Some factors influencing the adhesion of films produced by vacuum evaporation. *Journal de Physique et Le Radium* 11(7), 1950: 355–60.
129. Laugier, M. The development of the scratch test technique for the determination of the adhesion of coatings. *Thin Solid Films* 76(3), 1981: 289–94.
130. Richard, P., Thomas, J., Landolt, D., and Gremaud, G. Combination of scratch-test and acoustic microscopy imaging for the study of coating adhesion. *Surface and Coatings Technology* 91(1–2), 1997: 83–90.
131. Valli, J. and Mäkelä, U. Applications of the scratch test method for coating adhesion assessment. *Wear* 115(1–2), 1987: 215–21.
132. Steinmann, P. A., Tardy, Y., and Hintermann, H. E. Adhesion testing by the scratch test method: The influence of intrinsic and extrinsic parameters on the critical load. *Thin Solid Films* 154(1–2), 1987: 333–49.
133. Xie, Y. and Hawthorne, H. M. Effect of contact geometry on the failure modes of thin coatings in the scratch adhesion test. *Surface and Coatings Technology* 155(2–3), 2002: 121–29.

134. Bull, S. J. Failure mode maps in the thin film scratch adhesion test. *Tribology International* 30(7), 1997: 491–98.
135. Benjamin, P. and Weaver, C. Measurement of adhesion of thin films. *Proceedings of the Royal Society of London. Series A. Mathematical and Physical Sciences* 254(1277), 1960: 163–76.
136. Laugier, M. T. An energy approach to the adhesion of coatings using the scratch test. *Thin Solid Films* 117(4), 1984: 243–49.
137. Jaworski, R., Pawlowski, L., Roudet, F., Kozerski, S., and Petit, F. Characterization of mechanical properties of suspension plasma sprayed TiO2 coatings using scratch test. *Surface and Coatings Technology* 202(12), 2008: 2644–53.
138. Sander, T., Tremmel, S., and Wartzack, S. A modified scratch test for the mechanical characterization of scratch resistance and adhesion of thin hard coatings on soft substrates. *Surface and Coatings Technology* 206(7), 2011: 1873–78.
139. Barnes, D., Johnson, S., Snell, R., and Best, S. Using scratch testing to measure the adhesion strength of calcium phosphate coatings applied to poly(carbonate urethane) substrates. *Journal of the Mechanical Behavior of Biomedical Materials* 6, 2012: 128–38.
140. Bull, S. J. and Berasetegui, E. G. An overview of the potential of quantitative coating adhesion measurement by scratch testing. *Tribology International* 39(2), 2006: 99–114.
141. Lopez, E., Beltzung, F., and Zambelli, G. Measurement of cohesion and adhesion strengths in alumina coatings produced by plasma spraying. *Journal of Materials Science Letters* 8(3), 1989: 346–48.
142. Vencl, A., Arostegui, S., Favaro, G., Zivic, F., Mrdak, M., Mitrović, S., and Popovic, V. Evaluation of adhesion/cohesion bond strength of the thick plasma spray coatings by scratch testing on coatings cross-sections. *Tribology International* 44(11), 2011: 1281–88.
143. Spies, G. J. The peeling test on redux-bonded joints: A theoretical analysis of the test devised by aero research limited. *Aircraft Engineering and Aerospace Technology* 25(3), 1953: 64–70.
144. Jacobsson, R. Measurement of the adhesion of thin films. *Thin Solid Films* 34(2), 1976: 191–99.
145. Nase, M., Zankel, A., Langer, B., Baumann, H. J., Grellmann, W., and Poelt, P. Investigation of the peel behavior of polyethylene/polybutene-1 peel films using *in situ* peel tests with environmental scanning electron microscopy. *Polymer* 49(25), 2008: 5458–66.
146. Sexsmith, M. and Troczynski, T. Peel strength of thermal sprayed coatings. *Journal of Thermal Spray Technology* 5(2), 1996: 196–206.
147. Guermazi, N., Haddar, N., Elleuch, K., and Ayedi, H. F. On the peel behavior of polymer coating-steel system: Effect of hygrothermal aging. *Advances in Polymer Technology* 29(3), 2010: 185–96.
148. Roy, D., Simon, G. P., Forsyth, M., and Mardel, J. Modification of thermoplastic coatings for improved cathodic disbondment performance on a steel substrate: A study on failure mechanisms. *International Journal of Adhesion and Adhesives* 22(5), 2002: 395–403.
149. Nase, M., Langer, B., Baumann, H. J., Grellmann, W., Geißler, G., and Kaliske, M. Evaluation and simulation of the peel behavior of polyethylene/polybutene-1 peel systems. *Journal of Applied Polymer Science* 111(1), 2009: 363–70.
150. Horgnies, M., Willieme, P., and Gabet, O. Influence of the surface properties of concrete on the adhesion of coating: Characterization of the interface by peel test and FT-IR spectroscopy. *Progress in Organic Coatings* 72(3), 2011: 360–79.
151. Sexsmith, M. and Troczynski, T. Peel adhesion test for thermal spray coatings. *Journal of Thermal Spray Technology* 3(4), 1994: 404–11.

152. Kurzweg, H., Heimann, R. B., and Troczynski, T. Adhesion of thermally sprayed hydroxyapatite-bond-coat systems measured by a novel peel test. *Journal of Materials Science: Materials in Medicine* 9(1), 1998: 9–16.
153. Dannenberg, H. Measurement of adhesion by a blister method. *Journal of Applied Polymer Science* 5(14), 1961: 125–34.
154. Dupeux, M. and Bosseboeuf, A. Application of the blister test to adhesion energy measurements in metal/ceramic film-on-substrate systems, Chapter 27. In *Interfacial Science in Ceramic Joining*, edited by A. Bellosi, T. Kosmač and A. P. Tomsia. NATO ASI Series, 319–27. Dordrecht, The Netherlands: Springer, 1998.
155. Wang, C. Measurements of interfacial strength from the blister test. *Journal of Applied Polymer Science* 73(10), 1999: 1899–912.
156. Chang, Y.-S., Lai, Y.-H., and Dillard, D. A. The constrained blister—A nearly constant strain energy release rate test for adhesives. *The Journal of Adhesion* 27(4), 1989: 197–211.
157. Napolitano, M. J., Chudnovsky, A., and Moet, A. The constrained blister test for the energy of interfacial adhesion. *Journal of Adhesion Science and Technology* 2(1), 1988: 311–23.
158. Parsons, M., Polyakova, A., Stepanov, E. V., Hiltner, A., and Baer, E. Evaluation of the constrained blister test for measuring adhesion. *Journal of Adhesion* 68(1–2), 1998: 45–63.
159. Allen, M. G. and Senturia, S. D. Application of the island blister test for thin film adhesion measurement. *The Journal of Adhesion* 29(1–4), 1989: 219–31.
160. Dillard, D. A. and Bao, Y. The peninsula blister test: A high and constant strain energy release rate fracture specimen for adhesives. *The Journal of Adhesion* 33(4), 1991: 253–71.
161. Wan, K.-T. A novel blister test to investigate thin film delamination at elevated temperature. *International Journal of Adhesion and Adhesives* 20(2), 2000: 141–43.
162. Wan, K.-T. and Breach, C. D. Thermodynamics of a stable blister delamination at elevated temperature. *Journal of Adhesion* 66(1–4), 1998: 183–202.
163. Wan, K.-T. and Mai, Y.-W. Fracture mechanics of a new blister test with stable crack growth. *Acta Metallurgica Et Materialia* 43(11), 1995: 4109–15.
164. Koenig, S. P., Boddeti, N. G., Dunn, M. L., and Bunch, J. S. Ultrastrong adhesion of graphene membranes. *Nature Nanotechnology* 6(9), 2011: 543–46.
165. Malyshev, B. M. and Salganik, R. L. The strength of adhesive joints using the theory of cracks. *International Journal of Fracture Mechanics* 1(2), 1965: 114–28.
166. Wan, K.-T., Di Prima, A., Ye, L., and Mai, Y.-W. Adhesion of nylon-6 on surface treated aluminium substrates. *Journal of Materials Science* 31(8), 1996: 2109–16.
167. Wan, K.-T. and Mai, Y.-W. Fracture mechanics of a shaft-loaded blister of thin flexible membrane on rigid substrate. *International Journal of Fracture* 74(2), 1996: 181–97.
168. O'Brien, E. P., Ward, T. C., Guo, S., and Dillard, D. A. Strain energy release rates of a pressure sensitive adhesive measured by the shaft-loaded blister test. *Journal of Adhesion* 79(1), 2003: 69–97.
169. Xu, X., Shearwood, C., and Liao, K. A shaft-loaded blister test for elastic response and delamination behavior of thin film-substrate system. *Thin Solid Films* 424(1), 2003: 115–19.
170. Na, H., Chen, P., Wan, K. T., Wong, S. C., Li, Q., and Ma, Z. Measurement of adhesion work of electrospun polymer membrane by shaft-loaded blister test. *Langmuir* 28(16), 2012: 6677–83.
171. Elambasseril, J. and Ibrahim, R. N. Validity requirements of circumferentially notched tensile specimens for the determination of the interfacial fracture toughness of coatings. *Composites Part B: Engineering* 43(5), 2012: 2415–22.

172. Elambasseril, J. and Ibrahim, R. N. Quantitative evaluation of the adhesion of metallic coatings using cylindrical substrate. *Materials and Design* 33(1), 2012: 641–51.
173. Vossen, J. L. Measurements of film-substrate bond strength by laser spallation. In *Adhesion Measurement of Thin Films, Thick Films and Bulk Coatings ASTM STP 640*, edited by K. L. Mittal, 122–33. Philadelphia, PA: American Society for Testing and Materials, 1978.
174. Gupta, V., Argon, A. S., Cornie, J. A., and Parks, D. M. Measurement of interface strength by laser-pulse-induced spallation. *Materials Science and Engineering: A* 126(1–2), 1990: 105–17.
175. Gupta, V., Yuan, J., and Pronin, A. Recent developments in the laser spallation technique to measure the interface strength and its relationship to interface toughness with applications to metal/ceramic, ceramic/ceramic and ceramic/polymer interfaces. *Journal of Adhesion Science and Technology* 8(6), 1994: 713–47.
176. Lacombe, R. Overview of most common adhesion measurement methods. In *Adhesion Measurement Methods*, edited by R. Lacombe, 7–73. Florida, USA: CRC Press, 2005.
177. Kobayashi, A., Jain, A., Gupta, V., and Kireev, V. Study on the interface strength of zirconia coatings by a laser spallation technique. *Vacuum* 73(3–4), 2004: 533–39.
178. Kandula, S. S. V., Hartfield, C. D., Geubelle, P. H., and Sottos, N. R. Adhesion strength measurement of polymer dielectric interfaces using laser spallation technique. *Thin Solid Films* 516(21), 2008: 7627–35.
179. Jain, A., Gupta, V., and Basu, S. N. A quantitative study of moisture adsorption in polyimide and its effect on the strength of the polyimide/silicon nitride interface. *Acta Materialia* 53(11), 2005: 3147–53.
180. Ifju, P. G. and Han, B. Recent applications of moiré interferometry. *Experimental Mechanics* 50(8), 2010: 1129–47.
181. Sciammarella, C. A. and Sciammarella, F. M. Industrial applications of optical techniques that measure displacements. *Journal of Failure Analysis and Prevention* 5(2), 2005: 61–72.
182. Sciammarella, C. A. Overview of optical techniques that measure displacements: Murray lecture. *Experimental Mechanics* 43(1), 2003: 1–19.
183. Krishnan, A. and Xu, L. R. Systematic evaluation of bonding strengths and fracture toughnesses of adhesive joints. *Journal of Adhesion* 87(1), 2011: 53–71.
184. Liechti, K. M. and Hanson, E. C. Nonlinear effects in mixed-mode interfacial delaminations. *International Journal of Fracture* 36(3), 1988: 199–217.
185. Liechti, K. M. Moiré of crack-opening interferometry in adhesive fracture mechanics. *Experimental Mechanics* 25(3), 1985: 255–61.
186. Dolinko, A. E. and Kaufmann, G. H. Feasibility study of a digital speckle pattern interferometry and bending test combined technique to investigate coating adhesion. *Optics and Lasers in Engineering* 46(3), 2008: 230–35.
187. Tendela, L. P. and Kaufmann, G. H. Evaluation of coating adhesion using a radial speckle interferometer combined with a micro-indentation test. *Optics and Lasers in Engineering* 50(6), 2012: 817–22.
188. Tippur, H. V. and Xu, L. M. Measurement of interfacial fracture parameters using coherent gradient sensing (CGS). *Strain* 31(4), 1995: 143–49.
189. Tippur, H. V. Coherent gradient sensing: A Fourier optics analysis and applications to fracture. *Applied Optics* 31(22), 1992: 4428–39.
190. Miskioglu, I., Villmann, C. R., Pawloski, J. S., and Pariseau, D. M. A photoelastic and FEM analysis of interfacial crack propagation. *Experimental Mechanics* 31(2), 1991: 135–39.
191. Lu, H. and Chiang, F. P. Photoelastic determination of stress intensity factor of an interfacial crack in a bi-material. *Journal of Applied Mechanics, Transactions ASME* 60(1), 1993: 93–100.

192. Singh, R. P. and Shukla, A. Characterization of isochromatic fringe patterns for a dynamically propagating interface crack. *International Journal of Fracture* 76(4), 1996: 293–310.
193. Ricci, V., Shukla, A., and Kavaturu, M. Using strain gages to investigate subsonic dynamic interfacial fracture in an isotropic-isotropic bimaterial. *Engineering Fracture Mechanics* 70(10), 2003: 1303–21.
194. Shukla, A. High-speed fracture studies on bimaterial interfaces using photoelasticity: A review. *Journal of Strain Analysis for Engineering Design* 36(2), 2001: 119–42.
195. Sadek, S. and Iskander, M. Optical measurement of strain and stress. In *Modeling with Transparent Soils*, edited by M. Iskander, 27–44. Heidelberg, Berlin: Springer, 2010.
196. Fabbri, P., Messori, M., Toselli, M., Veronesi, P., Rocha, J., and Pilati, F. Enhancing the scratch resistance of polycarbonate with poly(ethylene oxide)-silica hybrid coatings. *Advances in Polymer Technology* 27(2), 2008: 117–26.
197. Tippur, H. V., Krishnaswamy, S., and Rosakis, A. J. A coherent gradient sensor for crack tip deformation measurements: Analysis and experimental results. *International Journal of Fracture* 48(3), 1991: 193–204.
198. Tippur, H. V., Krishnaswamy, S., and Rosakis, A. J. Optical mapping of crack tip deformations using the methods of transmission and reflection coherent gradient sensing: A study of crack tip K-dominance. *International Journal of Fracture* 52(2), 1991: 91–117.
199. Tippur, H. V. and Rosakis, A. J. Quasi-static and dynamic crack growth along bimaterial interfaces: A note on crack-tip field measurements using coherent gradient sensing. *Experimental Mechanics* 31(3), 1991: 243–51.
200. Tippur, H. V. and Ramaswamy, S. Measurement of mixed-mode fracture parameters near cracks in homogeneous and bimaterial beams. *International Journal of Fracture* 61(3), 1993: 247–65.
201. Tippur, H. V. Coherent gradient sensing (CGS) method for fracture mechanics: A review. *Fatigue and Fracture of Engineering Materials and Structures* 33(12), 2010: 832–58.
202. Kimberley, J. and Lambros, J. Dynamic crack kinking from a PMMA/Homalite interface. *Experimental Mechanics* 44(2), 2004: 158–66.
203. Rosakis, A. J., Singh, R. P., Tsuji, Y., Kolawa, E., and Moore Jr, N. R. Full field measurements of curvature using coherent gradient sensing: Application to thin film characterization. *Thin Solid Films* 325(1–2), 1998: 42–54.
204. Liu, C., Zhang, X., Zhou, J., and Zhou, Y. A general coherent gradient sensor for film curvature measurements: Error analysis without temperature constraint. *Optics and Lasers in Engineering* 51(7), 2013: 808–12.
205. Kitey, R. and Tippur, H. V. Dynamic crack growth past a stiff inclusion: Optical investigation of inclusion eccentricity and inclusion-matrix adhesion strength. *Experimental Mechanics* 48(1), 2008: 37–53.
206. Yao, X. F., Yeh, H. Y., and Chen, X. B. Visualization of crack tip behaviour in functionally gradient materials using coherent gradient sensing (CGS). *Modelling and Simulation in Materials Science and Engineering* 13(4), 2005: 621–32.
207. Yao, X. F., Yeh, H. Y., and Xu, W. Fracture investigation at V-notch tip using coherent gradient sensing (CGS). *International Journal of Solids and Structures* 43(5), 2006: 1189–200.
208. Post, D., Han, B., and Ifju, P. Moiré methods for engineering and science—Moiré interferometry and shadow moiré. In *Photomechanics*, edited by P.K. Rastogi. Topics in Applied Physics, 151–96 New York: Springer Berlin Heidelberg, 2000.
209. Kang, B. S. J., Yao, Q., Li, Z., and Liu, C. T. Investigation on environmental assisted fracture behavior of iron aluminides using moire interferometry. *Materials Science and Engineering A* 239–240(1–2), 1997: 344–52.

210. Wang, Y. Y., Chiang, F. P., Barsoum, R. S., and Chou, S. T. Study of deformation field of interface crack in adhesive joint. *Engineering Fracture Mechanics* 44(2), 1993: 175–84.
211. Wang, Y. Y. and Chiang, F. P. Deformation fields of interfacial cracks in adhesively bonded DCBs. *Engineering Fracture Mechanics* 55(2), 1996: 181–89.
212. Nishioka, T., Yao, J., Sakakura, K., and Epstein, J. S. Measurements of near-tip displacement fields, separated J integrals and separated energy release rates for interfacial cracks using phase-shifting moiré interferometry. *JSME International Journal, Series A* 43(4), 2000: 334–42.
213. Mohammed, I. and Liechti, K. M. Cohesive zone modeling of crack nucleation at bimaterial corners. *Journal of the Mechanics and Physics of Solids* 48(4), 2000: 735–64.
214. Savalia, P. C. and Tippur, H. V. A study of crack-inclusion interactions and matrix-inclusion debonding using moiré interferometry and finite element method. *Experimental Mechanics* 47(4), 2007: 533–47.
215. Tang, M., Xie, H., Zhu, J., and Wu, D. The failure mechanisms of TBC structure by moiré interferometry. *Materials Science and Engineering A* 565, 2013: 142–47.
216. Bhaduri, B., Krishna Mohan, N., and Kothiyal, M. P. A dual-function ESPI system for the measurement of out-of-plane displacement and slope. *Optics and Lasers in Engineering* 44(6), 2006: 637–44.
217. Krishna Mohan, N., and Rastogi, P. Recent developments in digital speckle pattern interferometry. *Optics and Lasers in Engineering* 40(5–6), 2003: 439–45.
218. Tay, T. E., Yap, C. M., and Tay, C. J. Crack tip and notch tip plastic zone size measurement by the laser speckle technique. *Engineering Fracture Mechanics* 52(5), 1995: 879–85,87–93.
219. Haggerty, M., Lin, Q., and Labuz, J. F. Observing deformation and fracture of rock with speckle patterns. *Rock Mechanics and Rock Engineering* 43(4), 2010: 417–26.
220. Tajik, N., Soltani, N., and Sedighiani, K. Fracture parameter analysis on a double edge crack problem by the method of Electronic Speckle Pattern Interferometry (ESPI). *Procedia Engineering* 10, 2011: 3267–3272.
221. Moore, A. J. and Tyrer, J. R. Evaluation of fracture mechanic's parameters using electronic speckle pattern interferometry. *Journal of Strain Analysis for Engineering Design* 29(4), 1994: 257–62.
222. Chiang, F. P. and Lu, H. Measurement of displacement field around an interfacial crack in a bimaterial sheet. *Engineering Fracture Mechanics* 41(6), 1992: 939–49.
223. Frybort, S., Mauritz, R., Teischinger, A., and Müller, U. Investigation of the mechanical interactions at the interface of wood-cement composites by means of electronic speckle pattern interferometry. *BioResources* 7(2), 2012: 2483–95.
224. Vermeltfoort, A. T., Martens, D. R. W., and Van Zijl, G. P. A. G. Electronic speckle pattern interferometry observation of brick-mortar interface behaviour under compression. *Canadian Journal of Civil Engineering* 34(11), 2007: 1467–74.
225. Sutton, M. A., Orteu, J. J., and Schreier, H. W. *Image Correlation for Shape, Motion and Deformation Measurements: Basic Concepts, Theory and Applications*. New York, USA: Springer, 2009.
226. Peters, W. H. and Ranson, W. F. Digital imaging techniques in experimental stress analysis. *Optical Engineering* 21(3), 1982: 427–31.
227. Wu, D. J., Mao, W. G., Zhou, Y. C., and Lu, C. Digital image correlation approach to cracking and decohesion in a brittle coating/ductile substrate system. *Applied Surface Science* 257(14), 2011: 6040–43.
228. Eberl, C., Gianola, D. S., and Hemker, K. J. Mechanical characterization of coatings using microbeam bending and digital image correlation techniques. *Experimental Mechanics* 50(1), 2010: 85–97.

229. Mao, W. G., Wu, D. J., Yao, W. B., Zhou, M., and Lu, C. Multiscale monitoring of interface failure of brittle coating/ductile substrate systems: A non-destructive evaluation method combined digital image correlation with acoustic emission. *Journal of Applied Physics* 110(8), 2011: 084903.
230. Barthelat, F., Wu, Z., Prorok, B. C., and Espinosa, H. D. Dynamic torsion testing of nanocrystalline coatings using high-speed photography and digital image correlation. *Experimental Mechanics* 43(3), 2003: 331–40.
231. Ahmed, F., Krottenthaler, M., Schmid, C., and Durst, K. Assessment of stress relaxation experiments on diamond coatings analyzed by digital image correlation and micro-Raman spectroscopy. *Surface and Coatings Technology* 237, 2013: 255–60.
232. Song, M., Guo, H., Abbas, M., and Gong, S. Thermal deformation of Y_2O_3 partially stabilized ZrO_2 coatings by digital image correlation method. *Surface and Coatings Technology* 216, 2013: 1–7.
233. Zhu, J., Xie, H., Hu, Z., Chen, P., and Zhang, Q. Residual stress in thermal spray coatings measured by curvature based on 3D digital image correlation technique. *Surface and Coatings Technology* 206(6), 2011: 1396–402.
234. Korsunsky, A. M., Sebastiani, M., and Bemporad, E. Residual stress evaluation at the micrometer scale: Analysis of thin coatings by FIB milling and digital image correlation. *Surface and Coatings Technology* 205(7), 2010: 2393–403.
235. Zhou, M., Yao, W. B., Yang, X. S., Peng, Z. B., Li, K. K., Dai, C. Y., Mao, W. G., Zhou, Y. C., and Lu, C. In-situ and real-time tests on the damage evolution and fracture of thermal barrier coatings under tension: A coupled acoustic emission and digital image correlation method. *Surface and Coatings Technology* 240, 2014: 40–47.

9 Sliding-Contact Fracture of Brittle Layers

Oscar Borrero-Lopez and Mark Hoffman

CONTENTS

9.1 Introduction 529
9.2 Scratch Test 530
9.2.1 Experimental Method 533
9.2.2 Focused Ion Beam Microscopy for Observation of Subsurface Fracture in Coated Systems 536
9.3 Fracture Modes on Scratching of Brittle Layers 539
9.3.1 Stress Field Originated by a Sliding Contact 540
9.3.1.1 Bulk Material 540
9.3.1.2 Coated System 544
9.3.2 Isotropic Films 548
9.3.3 Columnar Films 553
9.3.4 Thin Wafers with a Diamond Structure 558
9.3.5 Substrate Effects and Size Effects 560
9.4 Fracture Analysis of Thin Films Using the Scratch Test 564
9.4.1 Stress Approach 565
9.4.1.1 Fracture Strength 566
9.4.1.2 Fracture Toughness 571
9.4.1.3 Stress Intensity Factor Solutions 573
9.4.2 Energy Approach 577
9.4.3 Semiquantitative Approach 581
9.5 Concluding Remarks 584
References 585

9.1 INTRODUCTION

Sliding is one of the most common contact configurations for materials used in engineering applications. It occurs wherever contacting parts are in relative motion, for example, in rotors, stators, pistons, and other wear parts of both large- and small-scale engines (i.e., microelectromechanical systems, MEMS). Moreover, sliding contacts may appear when third bodies impact a material at low angle, for example, slurry pump impellers. In sliding contacts, the friction between the contacting bodies creates relatively complex stress fields due to the presence of tangential forces in addition to normal forces. This, in turn, results in a wider range of possible failure

modes in materials subjected to sliding compared to uniaxial contact loaded normal to the surface.

Modern engineering materials are often coated with hard material layers so as to impart both mechanical protection and increase load-bearing capacity, and also to improve functionality, biocompatibility, or aesthetics. These layers are usually brittle and thus prone to failure by fracture, originated by high tensile stress on preexisting defects, both intrinsic and extrinsic. Examples of coated systems where brittle behavior may pose a risk to structural integrity include optical coatings (both dielectric, e.g., TiO_2; and antireflective, e.g., MgF_2) on glass [1], antifriction coatings (e.g., carbon-based layers [2]) on MEMS silicon, dielectric films (e.g., SiO_2) in semiconductors, and antireflective coatings (e.g., Si_3N_4) on solar-grade silicon [3]. Moreover, free-standing thin brittle layers can be found in a number of state-of-the-art engineering applications; for example, in ever-miniaturizing optoelectronic devices [4] or in piezoelectric transducers in MEMS [5].

This chapter is concerned with the fracture of brittle layers, both coatings/films and small-scale free-standing elements, originated by sliding contacts. The aim is to provide the fundamentals for assessing the key mechanical properties that affect performance–fracture strength and fracture toughness. For this particular contact configuration, the experimental technique that is best suited is the scratch test. This technique stands out for its simplicity and almost universal applicability—its use in coated systems is in fact standardized [6]. The scratch test not only allows for the investigation of damage (deformation and fracture) of materials subject to sliding contact, but also for property assessment in combination with the appropriate analytical or numerical modeling tools. The occurrence of purely brittle failure combined with the ease of modeling make elastic systems best suited for the assessment of fracture properties of films by means of scratch test.

Based on the above, the chapter begins with a detailed description of the relevant experimental methodologies—scratch tests and advanced microscopy techniques that can be simultaneously employed to assess surface and subsurface damage. Next, a review is presented of the most common failure modes of brittle layers subjected to sliding contacts as a function of material structure, that is, isotropic and anisotropic. The failure modes are explained in combination with analysis of stresses in sliding contacts. Subsequently, procedures are outlined for property assessment, namely fracture strength and fracture toughness, through the combination of experiments and theoretical analyses. Three different approaches—stress-based, energy-based, and semiquantitative—are presented, and their practical applicability to coated systems is discussed within the framework of fracture mechanics. The chapter concludes with a summary of the main points and concluding remarks.

9.2 SCRATCH TEST

The single point scratch test is a relatively simple experimental technique, standardized for the assessment of the adhesion strength of coating materials and thin films [6]. Briefly, in a typical scratch test of coating adhesion, an indenter of prescribed geometry is dragged across the surface of the system, while the normal load, F_N, is progressively increased, until different damage modes appear, as depicted in

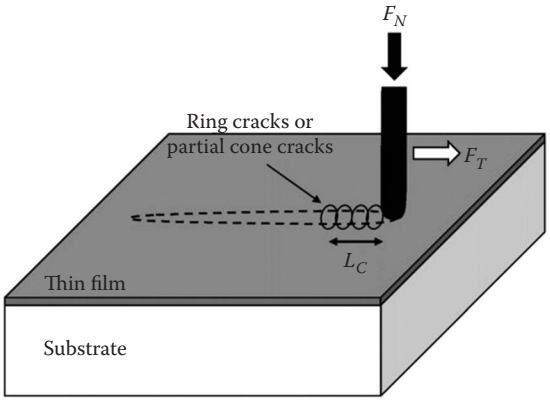


FIGURE 9.1 Schematic of the scratch test in a coated system. F_N and F_L are the normal and tangential loads, respectively. The distance between the position where crack initiation takes place and the end of the scratch is denoted by L_C, and can be used to assess the critical failure load. (From Borrero-Lopez O., *Thin Solid Films*, 2010;518:4911.)

Figure 9.1. The lateral or tangential force, F_L, is related to the normal load through the coefficient of friction (f): $F_L = fF_N$. Critical loads for initiation of the failure modes involving detachment of the coating from the substrate (adhesive failure) are assessed indirectly by acoustic emission or from discontinuities in the load–displacement curves, or calculated *a posteriori* upon direct microscopic examination. From the critical load values fundamental and practical adhesion can, in principle, be ascertained.

The main difficulty with this methodology is the fact that the resulting failure modes depend on the coating/substrate system, and are thus a function of mechanical properties, residual stresses, coating thickness, roughness, and so on. Major failure modes, as compiled by Bull [8,9] and in the ASTM standard, include through-thickness cracking, buckling, and chipping, which will be reviewed in more detail in Section 9.3.2. Moreover, not all the failure modes that arise upon scratching of coated systems are related to coating detachment. An example is cracking of the coating without debonding, which is termed cohesive failure, and cannot be used to assess adhesion. Finally, the stress states at the coating/substrate interface are typically multiaxial, which hinders calculations of adhesion strength [10]. Equations for quantitative estimation of strength do exist, but are specific to given failure modes; for example, the Benjamin and Weaver model [11] for the critical shear stress for removal of fully plastic coatings, or the expression by Evans [12] for the critical buckling stress of hard films on softer substrates, among others. The above limitations hinder the use of the scratch test for adhesion assessment at a fully quantitative level and, in practice, it is mostly used comparatively at a semiquantitative level, as shown in Figure 9.2.

In addition to adhesion, it is relatively common to use the scratch test in order to assess coating hardness. In fact, the scratch hardness is the oldest form of hardness assessment [13]. Two magnitudes are typically used for this purpose: the scratch

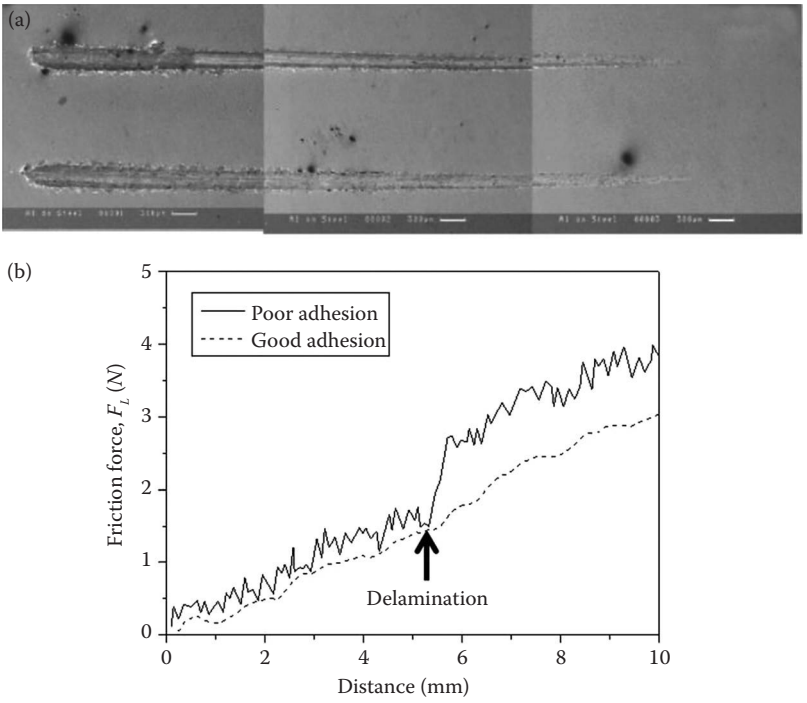


FIGURE 9.2 (a) Scanning electron micrographs of scratch tracks in a 100 nm aluminum coating on steel; a relatively thick coating with poor adhesion exposes the substrate suddenly at a given applied load (top); a relatively thin coating with improved adhesion shows a gradual transition (bottom). (b) Friction forces corresponding to the top (solid line) and bottom (broken line) scratch tests. The former shows a sharp increase in friction associated with delamination of the film. (Replotted from Bull SJ, and Berasetegui EG. *Tribology International*, 2006;39:99.)

hardness, H_s, and the ploughing hardness, H_p, which, by assuming perfectly plastic behavior, can be calculated using the following expressions [14]:

$$H_S = \frac{F_N}{A_S} \tag{9.1}$$

$$H_P = \frac{f_p F_N}{A_P} \tag{9.2}$$

where f_p is the ploughing friction coefficient [15], A_S is the projected load-bearing area, and A_P is the projected contact area in the direction normal to sliding. Thus, the scratch hardness provides information about the resistance to normal deformation, and the ploughing hardness about the resistance to lateral deformation in the sliding contact. A_S and A_P can be estimated from the physical dimensions of the scratch track through simple expressions [14].

Hardness values obtained from scratch tests are supplementary to those obtained by uniaxial indentation techniques, which are most appropriate when the materials are to be subject to loading configurations involving lateral forces and friction. However, because of the approximation of a purely plastic behavior, hardness values obtained by indentation techniques are generally preferred. Moreover, as in indentation of coatings and films, the hardness values obtained by Equations 9.1 and 9.2 are affected by the deformation of the supporting substrate. But while in indentation a reference penetration depth is assumed in order to minimize the substrate influence (the so-called 10% rule [16]), in a scratch test the limit is less clear. For this reason, and similar to what occurs with adhesion strength, scratch and plowing hardness values are used only semiquantitatively in practice.

This chapter reviews the use of the scratch test beyond its commonest uses of assessment of coating adhesion and hardness. In particular, it demonstrates the measurement of important fracture properties of coatings, such as strength and toughness, from controlled cohesive failure modes in elastic systems. We begin by describing the experimental procedure in scratch tests.

9.2.1 Experimental Method

As indicated in ASTM C1624–05, the primary components of a standardized apparatus for scratch testing include a test frame with a force application system, a stylus mount, a mechanical stage with displacement control (two axis, X and Y), and force sensors. In addition, the system typically includes detectors of acoustic emission (attached to the stylus mount) and displacement detectors. During testing, force displacement as well as data acquisition are generally computer controlled. A schematic is shown in Figure 9.3.

In the standardized scratch test, the stylus is a Rockwell-C (cone apex angle $2\theta = 120°$) diamond indenter of radius $R = 200\ \mu m$, as shown in Figure 9.4. The effective tip geometry thus depends on the penetration depth; it can be regarded as a sphere for low penetration depths, and as a cone for higher depths. The transition takes place at a depth of $(1 - \sin\theta)R = 26.8\ \mu m$ [17]. Because brittle systems are

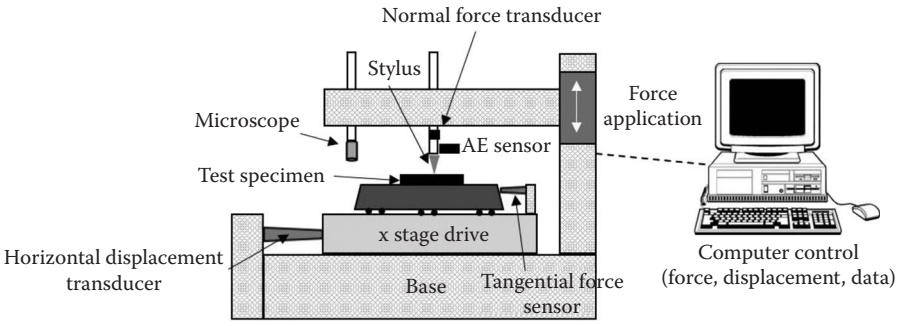


FIGURE 9.3 Schematic of the standardized equipment for scratch testing. (Redrawn from A.s.f.t.a. materials, Standard ASTM C1624-05, Vol. 15.01 *Refractories, Activated Carbon; Advanced Ceramics*. ASTM International, 2005.)

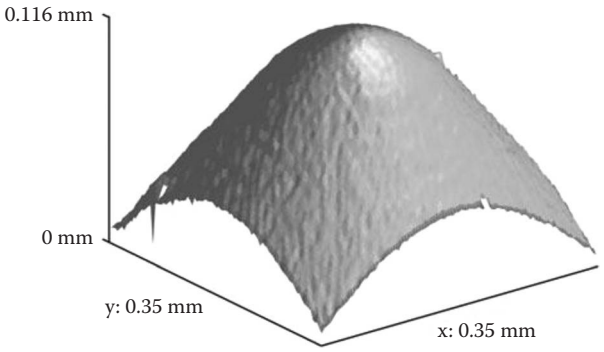


FIGURE 9.4 Three-dimensional reconstruction of a Rockwell indenter tip (radius of 200 μm and a half-apex angle $\theta = 60°$) obtained with a profilometer. (Taken from Akono AT, Randall NX, and Ulm FJ. *Journal of Materials Research*, 2012;27:485.)

typically very hard, the penetration depths that are necessary to induce fracture during scratch tests are rather low, typically within the spherical region of the tip. Thus, in the following discussions, a spherical contact will be assumed. For a spherical tip, the relationship between the scratch width (w) and the depths (h) is [14]

$$w = 2\sqrt{2Rh - h^2} \tag{9.3}$$

As with all indentation experiments, care must be taken to ensure that the tip is clean and free of damage (e.g., rounding, cracking, chipping, wear, etc.) prior to testing. Routine inspection by optical microscopy normally suffices, but more thorough examination may be pursued by using scanning electron microscopy (SEM), interferometry, profilometry, or interference microscopy.

Regarding specimen size and geometry, there are no major restrictions so long as the sample can be securely fixed to the mounting fixture, and well aligned (i.e., with its surface plane parallel to the fixture). Specimen dimensions are typically of a few centimeters, and it must be ensured that the coating is uniform along the whole surface. This issue is, however, less critical in scratching than in uniaxial indentation, as the sliding indenter samples a larger area of the specimen in each test rather than an isolated point. Finally, while a mirror-finished surface is not strictly necessary, roughness should be low enough to prevent the tip from bouncing during testing and to facilitate subsequent imaging. It is recommendable that the surface roughness be measured prior to testing as it may influence the stylus drag and contact stresses, and thus the critical load values obtained. Moreover, the defect population at the surface is expected to be closely related to the roughness, which has important implications for the measurement of fracture properties, as discussed in more detail in Section 9.4.

The scratch adhesion test is generally performed at ambient conditions and without lubrication, although in principle it is possible to adapt the apparatus to modify the environmental conditions during testing. There are two main test modes,

depending on whether the normal load is maintained constant (constant load test, CL) or increased progressively (progressive load test, PL). Typically, PL scratch tests are performed in order to identify the different damage modes as a function of the applied load and more efficiently assess relative performance between different coatings. Finer details of a specific damage mode can be obtained by conducting CL tests at prescribed loads of interest. In the more common PL test, the standard horizontal displacement rate is set to $v = 10$ mm/min, and the loading rate, $\dot{F}_N$, is 10 N/min when the maximum load, $F_{N,\max}$, is below 20 N; or 100 N/min, when $F_{N,\max}$, is above 20 N. The total scratch length, L, is lower than 10 mm (test duration below 1 min), and the spacing between consecutive scratches is at least 1 mm.

During a scratch test, the applied normal load, the lateral force (and from it, the coefficient of friction), and the acoustic emission signal are monitored as a function of the sliding distance. The occurrence of damage modes may be inferred indirectly, from the peaks in the acoustic emission signal (i.e., high frequency waves upon release of stored elastic energy by the fracture), or from discontinuities in the load–distance curves or in the coefficient of friction (e.g., stick-slip). However, not all failure events produce detectable changes in acoustic emission or in the friction. Moreover, signal peaks do not offer information *a priori* about the type of failure mode. Thus, the most reliable and comprehensive method to elucidate failure is microscopic examination of the scratch track after testing. The simplest technique for *postmortem* examination is optical microscopy. Indeed, from calibrated optical micrographs, the sliding distances at which the different failure modes take place can be readily measured. Alternatively, if the initial load ($F_{N,0}$) is low and does not produce a visible mark on the surface, the distance to the end of the scratch (L_C, see Figure 9.1) can be used. From L_C, calculation of critical loads (normal) is straightforward using the loading and horizontal displacement rates:

$$F_{N,C} = F_{N,0} + \frac{(L - L_C)\dot{F}_N}{v} \tag{9.4}$$

The critical load corresponding to a given failure mode may be converted into a critical stress value, but this requires a detailed knowledge of the stress state at the contact, which is not easy in coated systems subjected to both normal and lateral forces (see Section 9.3.1). Moreover, the stochastic nature of brittle failure results in a distribution of critical load values, instead of a well-defined single value. This requires a number of tests to be conducted, in order to define the distribution, typically via a two-parameter Weibull function. This process is demonstrated in detail in Section 9.4.1.

In many cases, particularly in contemporary functional applications, the films of interest are indeed very thin, that is, hundreds, or even tens of nanometer [18]. For that reason, there is a growing need to perform scratch tests at small scales. First, film properties (friction, elastic modulus, hardness) need to be estimated with minimal influence from the substrate, which requires probing smaller volumes by using smaller tips and forces. In addition, smaller probes are more likely to initiate damage

modes of comparable size to the characteristic length scale of films (i.e., thickness), which is required for their scale-like fracture characterization. Thus, micro- and nanoscratch testing is becoming increasingly common.

Scratch testing at small scales is typically conducted using depth-sensing indentation instruments equipped with a lateral force sensor. Normal loads range between one and hundreds of mN, although the newest equipment is able to test even lower loads, in the order of μN. The typical normal loading rate is about 10% of the maximum load per second. Typical scratching velocities are in the order of units of μm per second, with a maximum of 100 μm/s [19]. Micro- and nanoscratch tests can also be performed in atomic force microscopes (AFM). Indeed, modern instruments combine both indentation and AFM stages. This allows imaging of the scars after indentation, which is otherwise difficult given their small size.

9.2.2 Focused Ion Beam Microscopy for Observation of Subsurface Fracture in Coated Systems

The main limitation of the experimental procedures described for *postmortem* assessment of failure modes occurring in a scratch test is that conventional microscopy techniques only allow for surface observations. Optical microscopy is convenient in the sense that it is relatively inexpensive and requires little sample preparation, but it can only assess the surface projection of occurring cracks. Subsurface damage modes cannot be observed in this way, which is critical in sliding contact of coated systems, particularly when coatings are not transparent. This is because in some cases, cross-sectional fracture, for example, radial and lateral cracks [20,21], may be initiated before damage can be detected at the surface level.

Other techniques such as SEM or AFM are able to improve the resolution and limited depth of field of optical microscopy, but suffer from the same inability to reveal subsurface damage. It is of course possible to prepare cross sections for subsequent SEM imaging, for example, by mechanical cutting and polishing at selected sites, or by using alternative techniques such as ball cratering [22] (i.e., grinding a crater in the scratch track with a relatively large sphere). However, these methods are typically time-consuming, and involve a high risk of distorting the crack geometry in the process.

Fortunately, in recent years, the development of modern microscopy techniques has made it possible to overcome some of the limitations of conventional methods for *postmortem* observation. Among these new techniques, focused ion beam (FIB) milling stands out for its ease of use and versatility. Its basic practice for subsurface assessment of damage modes in coated systems is summarized below [23]. An FIB system is physically similar to an SEM, and has the same vacuum requirements and sample preparation, mainly to ensure the electrical conductivity of the specimens. The main difference is that, instead of "light" electrons, an FIB uses a beam of "heavy" ions (typically Ga^+, generated from a liquid source) accelerated at high voltage, which is able to sputter material away from the specimen surface. Thus, unlike SEM, FIB is a destructive technique. Depending on the current, the ion beam can be used to mill relatively large areas (higher currents, in excess of 2000 pA) or to finely

polish selected cross sections (lower currents, about 150 pA). The latter treatment is required in order to minimize the damage, that is, roughening resulting from ion implantation introduced by the high currents during milling, prior to cross-sectional imaging. The milling time can be optimized by selecting wedge-shaped patterns, which are deeper at the surface to be imaged. This enables observation of the cross section by tilting the stage, as shown schematically in Figure 9.5. In simpler single beam microscopes, imaging is typically carried out with secondary electrons, generated by scanning the polished cross section with the ion beam at low currents (values ~70 pA). Alternatively, the newer dual-beam systems incorporate an electron beam that allows simultaneous SEM imaging without stage tilting. Imaging with low-energy secondary ions is also possible. Interestingly, FIB microscopy allows a contrast mechanism not possible in a conventional SEM: ion channeling, which makes it possible to distinguish between areas with different crystal orientation.

In addition to conventional two-dimensional imaging, modern FIB systems offer the opportunity of three-dimensional reconstruction of features such as cracks through software-controlled, progressive slicing and imaging, or serial sectioning, as shown in Figure 9.6. While the procedure of image acquisition is typically automated, it is time-consuming due to the large number of slices needed to attain submicron resolution—typically numbering in the hundreds. In addition, the prolonged milling makes charging issues more likely to appear in susceptible systems. Three-dimensional reconstructions are certainly very useful at elucidating the evolution of novel damage modes, but are perhaps excessive for routine assessment of well-documented damage modes, which can be readily inferred from surface images.

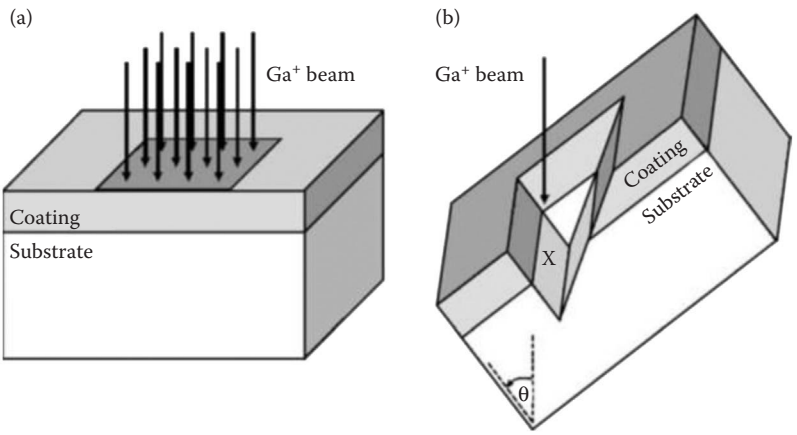


FIGURE 9.5 Schematic of cross-sectional milling at high ion current (a) and imaging at low ion current (b) using a single-beam FIB microscope. Note that cross-sectional imaging requires that the stage be tilted to an angle that affects the observed dimensions in the micrograph. (Taken from Cairney JM, Munroe PR, and Hoffman M. *Surface & Coatings Technology* 2005;198:165.)

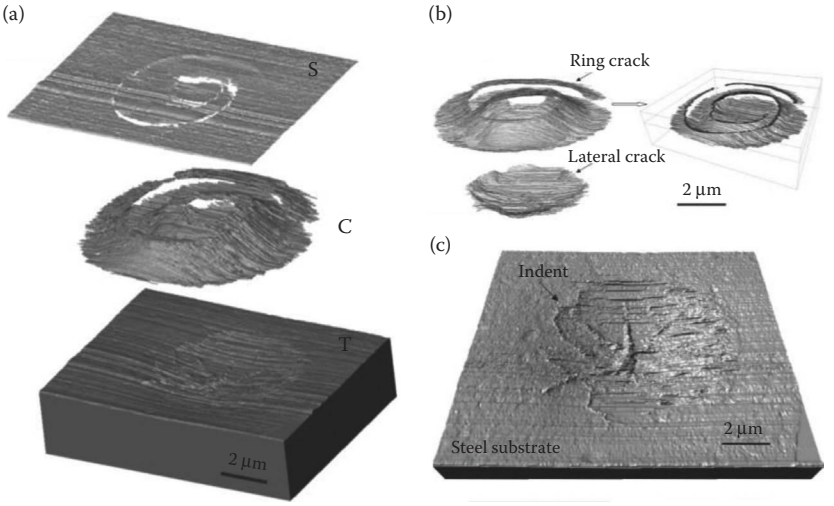


FIGURE 9.6 (a) Three-dimensional reconstruction of cracking upon nanoindentation with a spherical 5 µm tip of a diamond-like coating on a steel substrate. The coating surface (denoted by S), the cracks in the coating (C), and the substrate surface (T) are shown separately. (b) Three-dimensional images showing relevant cracking modes individually. (c) Three-dimensional image showing locally deformed regions in the substrate surface. The images were obtained software-assisted (Amira 3.1; TGS Inc., Chantilly, VA) superposition of some 300 micrographs obtained by progressive slicing and imaging. (Taken from Xie ZH. et al., *Journal of Materials Research*, 2006;21:2600.)

Finally, an added benefit of FIB is the ease of preparation of thin lamellae for high-resolution transmission electron microscopy (TEM), otherwise very challenging to obtain in coated systems by conventional methods. The process, albeit time-consuming, is software-controlled and fully automated, and has the capability of revealing small-scale details of damage modes, as shown in Figure 9.7.

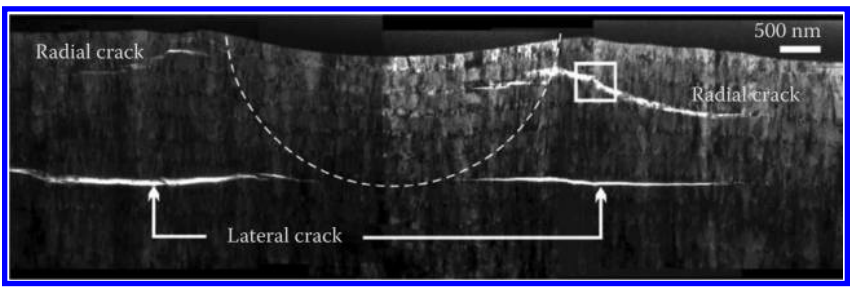


FIGURE 9.7 Montage of cross-sectional TEM images perpendicular to the sliding direction in a microscratch (tip radius 5 µm, normal load 210 mN) on TiSiN/TiN multilayer on a steel substrate showing different subsurface fracture modes. (Taken from Wow C. et al., *Journal of the American Ceramic Society*, 2011;94:1598.)

9.3 FRACTURE MODES ON SCRATCHING OF BRITTLE LAYERS

Brittle solids are largely resistant under compression. Thus, fracture of a brittle material is the result of large tensile stresses and favorably oriented defects. When the stress acting on a given defect and located in a given region exhausts the fracture strength, cracking takes place. The geometry of an opening crack depends on the particular orientation of the tensile stress (e.g., radial, hoop, mixed) during propagation and, in some systems, on the interaction of the crack with critical features in the microstructure (e.g., crack deflection by inclusions).

Experimentally, it is observed that when a brittle material is loaded normally with a blunt indenter, the main fracture mode taking place is the formation of ring-like cracks, nucleating near the edges of the indenter in the surface region. These evolve to cone cracks extending below the surface and forming an angle with the horizontal (e.g., approximately 22° for a steel ball on isotropic soda-lime glass) on further loading, hence the characteristic cone shape. Extensive analyses of the stress field and flaws that cause fracture in Hertzian contacts have been undertaken in the past, in the field of indentation mechanics [20,26]. From these studies, it is well established that ring cracks are the result of highest first principal stresses (i.e., maximum tensile), $\sigma_{1max} \equiv \sigma_{max}$, at the edges of the Hertzian contact, which have a radial direction on the surface. Subsequent opening of cone cracks is also driven by high tensile stresses at the cross section. The resulting trajectory approximately follows the surface formed by the second and third principal stresses (σ_2–σ_3); for glass, this forms a 22° angle with the horizontal. Moreover, indentation mechanics has allowed expressions for the crack propagation criteria. Typically, such expressions are simple relations between the critical load ($F_{N,C}$) and the indenter radius (r), namely $F_{N,C} \propto r$ (Auerbach's law) for small r, and $F_{N,C} \propto r^2$, for large r.

In this context, the presence of a coating, with different structure and properties (both mechanical properties and residual stresses originated during processing) than the substrate, modifies the contact stress field, which results in additional damage modes as a function of coating thickness. These include ring, cone, and radial cracks, as summarized in Figure 9.8 for the case of a relatively compliant substrate, that is, $E_C > E_S$ [27], which is the typical situation in the case of hard, protective coatings—E_C and E_S are the elastic modulus of the coating and the substrate, respectively. Indentation mechanics is able to assess the occurrence of one fracture mode or the other, depending on the location and orientation of the maximum tensile stress in each case. The formation of radial cracks, starting at the lower layer of the coating due to its bending over the relatively compliant substrate, is of particular importance, as this damage mode cannot be detected from the surface when the coating is not transparent. Radial cracks generated at the interface may eventually reach the coating surface leading to chipping, and thus pose a serious risk for the structural integrity.

Sliding contacts represent a yet more complex case than normal Hertzian contacts, due to the combination of normal and lateral forces. This results in a wide variety of damage modes, particularly in coated systems with mismatches in structure and properties. The present section reviews the failure modes occurring on scratching of brittle coatings in three representative cases: (i) isotropic films and anisotropic

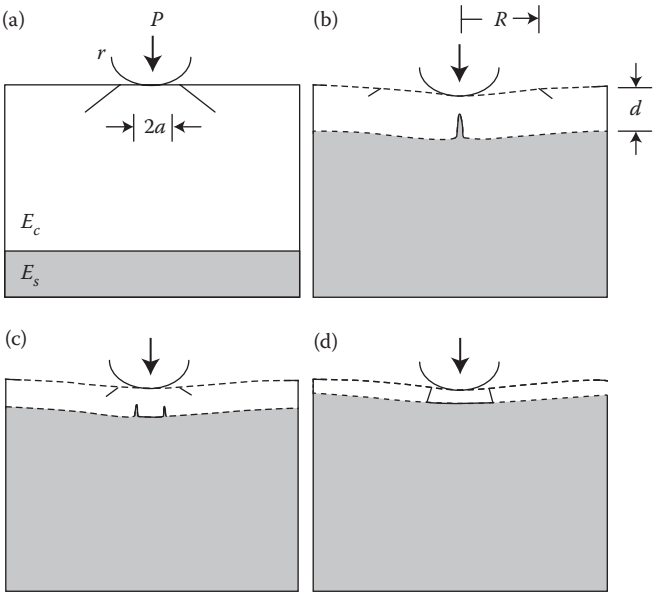


FIGURE 9.8 Schematic of the main damage modes occurring upon uniaxial indentation at load P with a sphere of radius r (contact radius a) of a coated system ($E_C > E_S$) as a function of coating thickness (d): (a) cone cracks in the coating; (b) and (c) ring cracks at the top surface (at distance R from loading axis), and radial cracks at the bottom surface of the coating; (d) through-thickness ring cracks. (Taken from Chai H, and Lawn BR. *Journal of Materials Research* 2004;19:1752.)

layers, both (ii) columnar, and (iii) with a diamond structure. Within the framework of indentation mechanics, the different mechanisms are explained from the stress field in sliding contact of a coated system.

9.3.1 Stress Field Originated by a Sliding Contact

9.3.1.1 Bulk Material

The stress field in a semiinfinite (i.e., uncoated) elastic medium under sliding contact was determined analytically by Hamilton and Goodman in 1966 [28], by adding the lateral frictional force to the Hertzian contact solution. As mentioned in Section 9.2, the magnitude of the friction force is fF_N, where f is the coefficient of friction. Figure 9.9a and b show that the first principal stress (σ_1; the maximum tensile stress, responsible for fracture) contours on the surface and below the surface for two different f values [29]. Also represented as broken lines are trajectories of the principal stresses σ_2 (surface) and σ_3 (cross section). As in the Hertzian case, the σ_2–σ_3 stress trajectory surface indicates cone crack path.

Figure 9.9c and d show, respectively, the profile of σ_1 at the surface along the sliding direction (x) at the vicinity of the point of loading ($x = 0$), and a schematic of the region under maximum tensile stress (σ_{max}) as a function of f and F_N [30]. The figures

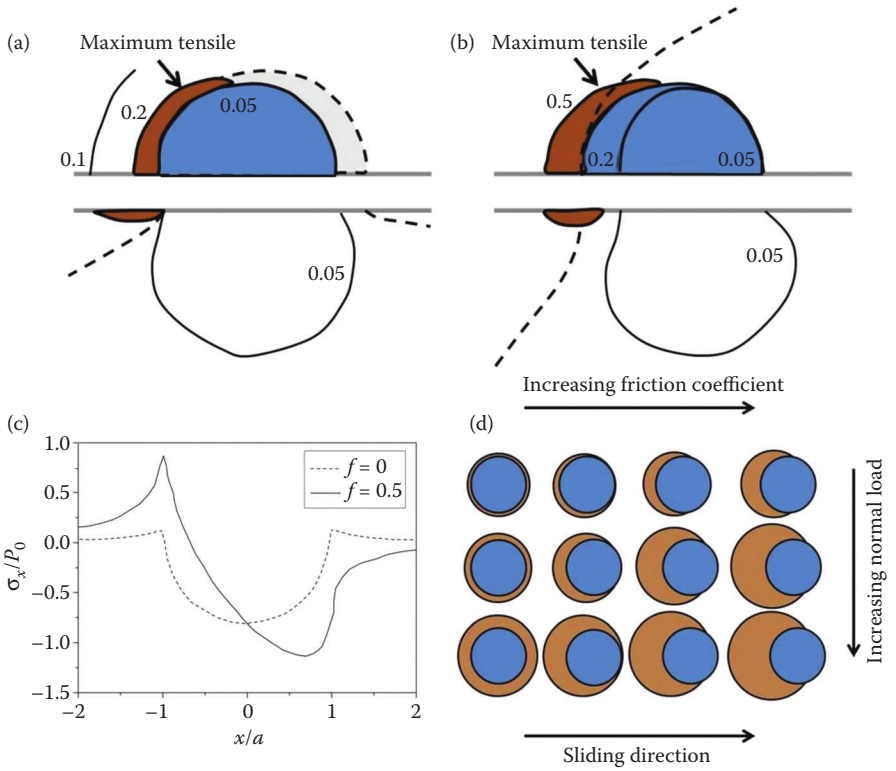


FIGURE 9.9 (a) and (b) show half top surface (up) and longitudinal cross section (down) of first principal stress (relative to Hertzian pressure) contours upon sliding contact of an elastic, isotropic solid with a spherical indenter, for $f = 0.1$ (a), and $f = 0.5$ (b). Broken lines correspond to the σ_2 (surface) and σ_3 (cross section) stress trajectories from the place of highest tensile stress. (Redrawn from Lawn BR. *Proceedings of the Royal Society of London Series a-Mathematical and Physical Sciences*, 1967;299:307.) (c) Maximum stress as a function of distance x along the sliding axis, where $x = 0$ is the normal loading axis. (Replotted from Hamilton GM, and Goodman LE. *Journal of Applied Mechanics*, 1966;33:371.); P_0 denotes the Hertzian pressure and a the contact radius; (d) Schematic showing the region under higher tensile stress (brown) behind the contact region (blue) as a function of normal load (F_N) and friction (top view). (Redrawn from Leu HJ, and Scattergood RO. *Journal of Materials Science*, 1988;23:3006.)

provide relevant information about crack initiation in a sliding contact: (i) the magnitude of the stress responsible for cracking, σ_{max}, increases with increasing f and F_N; (ii) σ_{max} shifts toward the trailing edge of the contact upon increasing f; and (iii) the region under (σ_{max}) expands with increasing f and F_N. From the analysis by Hamilton and Goodman, the σ_{max} value is given by the expression shown in Equation 9.5:

$$\sigma_{max} = (1 + 1.15f)\left(\frac{1}{2} - \upsilon\right)\left(\frac{F_N}{\pi a^2}\right) \tag{9.5}$$

From the Hertzian theory, the contact radius, a, is given by

$$a = \frac{4}{3}\frac{kF_N r}{E} \tag{9.6}$$

$$k = \frac{9}{16}\left[(1-\upsilon^2) + \frac{E}{E'}(1-\upsilon'^2)\right] \tag{9.7}$$

In the equations above, r is the indenter radius, and the magnitudes E and E', υ and υ' are the elastic properties (Young's modulus and Poisson's ratio) of the material and the indenter, respectively. Moreover, the stress field allows the geometry of the fracture modes upon sliding contact to be estimated. In particular, the Hamilton and Goodman elastic stress field suggests rather similar fracture mechanisms to those in normal, Hertzian contacts (i.e., cone-shaped cracks), but with two important differences. First, crack initiation takes place from critical defects located at the trailing edge of the sliding contact, and is more likely to occur as the values of f and F_N are increased. This is because increasing f and F_N results in higher stresses and a larger area at the trailing edge under σ_{max}, which makes it more likely to find a critical defect. Second, crack propagation is disturbed by the fact that the tip moves along as sliding proceeds. As a result, instead of a single crack, sliding contact of a brittle solid typically produces a succession of cracks, as is observed experimentally (Figure 9.10a)—once a first crack pops in, it provides a critical defect for nucleation of a subsequent crack as the tip slides to the next site, and so forth.

The shape of the cracks depends ultimately on the coefficient of friction. Indeed, the curvature of the broken lines in Figure 9.9a and b (σ_2–σ_3 lines), which mark the

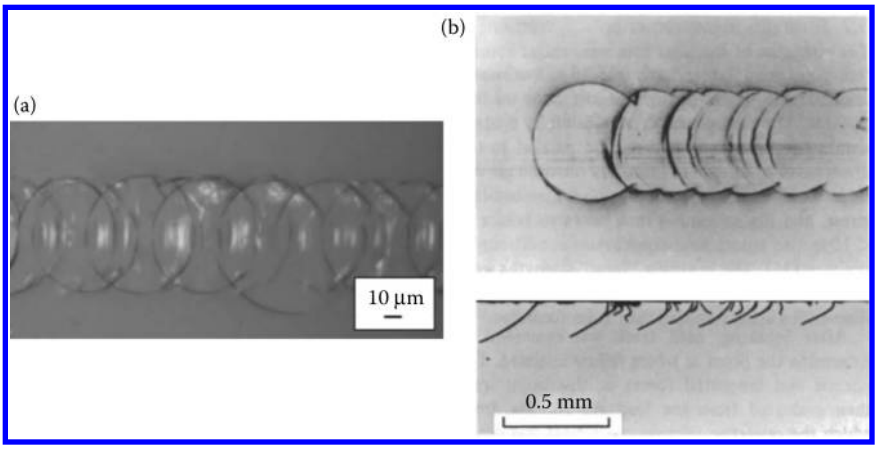


FIGURE 9.10 (a) Optical micrograph showing partial cone cracks on the surface of a soda-lime glass specimen under sliding contact with a spherical indenter. (From Borrero-Lopez O, Vodenitcharova T, and Hoffman M. *Scripta Materialia*, 2010;63:997.); (b) Comparison of surface and cross-sectional damage. (From Lawn BR, Wiederhorn SM, and Roberts DE. *Journal of Materials Science*, 1984;19:2561.)

most likely crack trajectories, is observed to decrease with increasing *f*. If the *f* value is sufficiently high, the curvature becomes so low that cracks are not actually able to fully complete the Hertzian cone. This is consistent with the experimental observations, see, for example, the projected geometry in Figure 9.10b. Due to their sometimes incomplete shape, the cracks originated on sliding contacts are commonly termed partial cone cracks.

It is difficult to directly observe partial cone cracks in three dimensions, unless the material is transparent. An example is shown in Figure 9.11, where partial cone cracks were simulated in glass by off-axis normal loading [33]. The asymmetric nature of the partial cone cracks can be clearly appreciated in contrast with conventional cone cracks (Figure 9.11b). An alternative to reconstructing partial cone cracks in three dimensions is the use of novel imaging techniques, for example, FIB serial sectioning. However, it is worth noting that little additional information can be gained from three-dimensional imaging, compared to two-dimensional projections (Figure 9.10) from which relevant features for toughness analysis (e.g., cone angle, crack length) can be determined.

Indentation mechanics has shown that in partial cone cracks an Auerbach-type law is only valid for very small coefficients of friction, and so generally the critical load for cracking is proportional to r^2. Beyond the critical load, the width of the partial cone cracks (W) increases proportionally to $F_N^{1/3}$, as observed experimentally by Leu and Scattergood [30].

In addition to tensile stresses, high shear stresses are of interest in sliding contacts. They can have an effect on cracking, albeit indirectly, by providing critical sites for nucleation. Indeed, in the uniaxial loading case ($f = 0$), the maximum shear stress appears at a distance $0.5a$ below the contact, along the loading axis, and can generate plastic or quasiplastic damage [26]. In sliding, however, the frictional force moves

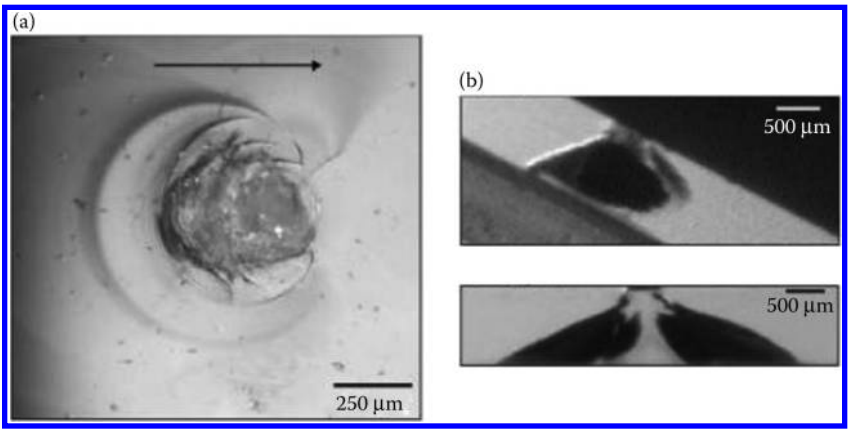


FIGURE 9.11 (a) Optical micrograph showing partial cone cracks on the surface of a soda-lime glass plate on a polycarbonate foundation under off-axis loading with a blunt indenter (simulates sliding contact); (b) Cross-sectional view of the partial cone crack (top) in comparison with a conventional cone crack obtained upon axial loading (bottom). (From Kim JH. et al., *Journal of Dental Research*, 2008;87:671.)

the Von-Mises stress ahead of the normal loading axis, and closer to the surface, toward the leading edge of the indenter [34]. This shift is precisely what makes shear stresses more relevant to cracking in the sliding case. In particular, while the occurrence of plasticity has the effect of dissipating elastic stresses at the trailing edge, shear faulting ahead of the tip may provide critical defects for initiation of cracks at the trailing edge, as the indenter moves forward. This could result in fracture at stresses lower than the fracture strength of the material without shear faults.

9.3.1.2 Coated System

Extrapolation of the stress analysis to the case of a coated system is not straightforward. Indeed, the Hamilton and Goodman solution can only be taken as an approximation for the thickest coatings, when the substrate is less likely to influence the response of the coating. Diao et al. have suggested that, in a wide range of elastic systems, for $t/a > 0.6f + 0.2$, being t the coating thickness, the effect of the substrate could be neglected [35]. The latter would be the scratch analogous to the well-known 10% rule in the case of uniaxial depth-sensing indentation [16]. As an example, for a coating thickness of 1 μm, and for a coefficient of friction of 0.1, treating the coating as a bulk material would require a contact radius lower than 3.8 μm. In practice, this would be satisfied by microindentations with blunt indenters of a maximum of 5 μm. As the coefficient of friction increases, the condition becomes more restrictive, and the substrate can only be neglected for very small contact radii (lower than 2.6 μm). The problem with such small contact radii is that plasticity effects need to be considered (see Section 9.3.5), and the elastic solution is less representative of the actual stress field. The latter is also the case for systems in which the substrate is a ductile material.

In general, for thin films, and/or larger contact radii and coefficients of friction, the presence of a substrate with different structure and properties needs to be taken into account for the calculation of the elastic contact stresses. The stress analysis of a coated system under sliding contact is of increased complexity than the bulk case, due to the discontinuity of the stress field at the interface. Thus, it has typically been attempted by using numerical methods. For example, O'Sullivan and King [36] employed a least-squares iterative approach to calculate surface and subsurface elastic stress components for different coefficients of friction, coating thickness and elastic modulus ratios (coating/substrate). Oliveira and Bower [37] performed both stress and fracture analyses, but approximating the contact pressure distribution by the Hertzian distribution. The finite-element (FE) method has also been employed, for example, by Ihara et al. [38], Komvopoulos [39], and Diao et al. [35], who studied similar sets of variables. More recently, newer, commercially available software packages, such as Elastica® (ASMEC GmbH, Radeberg, Germany) [40,41], have been used, which are able to provide relatively simple and quick calculations of the elastic stress fields (analytical) for a relevant interval of contact conditions [42,43].

Regardless of the method, the calculations and simulations of the elastic stress field reveal some general trends relevant to the study of damage modes in sliding contacts. In particular, the first principal stress (maximum tensile; the main component directly responsible for crack opening) always shows a maximum on the

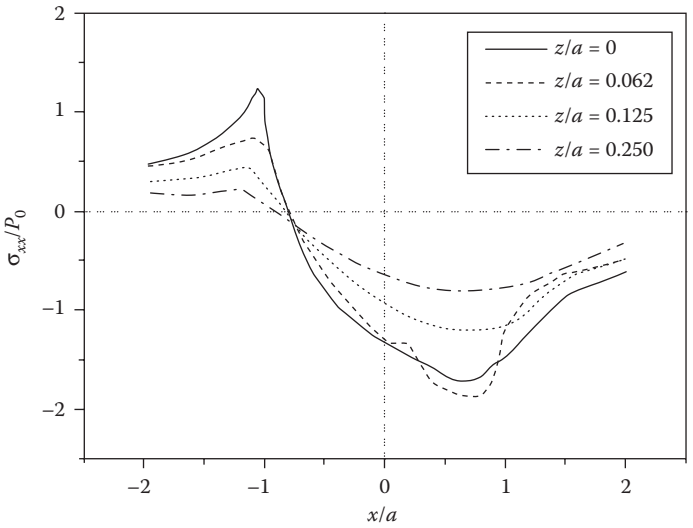


FIGURE 9.12 Contact stress (σ_{xx}) upon scratching of an elastic, isotropic-coated system, as a function of distance along sliding axis (x) to the normal loading axis ($x = 0$). The four curves correspond to different vertical distances (z) from the surface ($z = 0$), and were obtained from FE simulations considering a coating of thickness $0.125a$ and elastic modulus $E_C = 2E_S$ (C and S denote coating and substrate, respectively). P_0 represents the Hertzian pressure and a the contact radius. (Redrawn from Diao DF, Kato K, and Hayashi K. *Tribology International*, 1994;27:267.)

surface of the coating, at the trailing edge of the contact. The extent of the stress decreases by increasing the depth into the coating and into the substrate, as shown in Figure 9.12. Despite the decrease, it should be noted that the stress remains tensile in the region just behind the loading axis, and thus may also cause fracture if a critical defect is encountered. A region of particular interest is the interface, where defects are likely to be found [44], and which typically has a lower cohesive strength than the coating and the substrate, although this depends on the specific processing conditions of each system.

For a given coating/substrate combination, both the magnitude of the maximum tensile stress and the size of the region subjected to it are found to increase with increasing the coefficient of friction and the applied load, as in the bulk case. In addition, the maximum tensile stress increases with increasing the coating stiffness respective to the substrate (i.e., E_C/E_S). Representative results from numerical solution by O'Sullivan and King are shown in Figure 9.13. Thickness also has an effect, and generally the maximum tensile stress decreases with increasing the coating thickness relative to the contact radius (Figure 9.13c).

Based on their simulations, Diao et al. [35] attempted a relatively simple equation for the determination of σ_{max} as a function of the applied load (i.e., the equivalent for a coated system of the Hamilton and Goodman expression given by Equation 9.5).

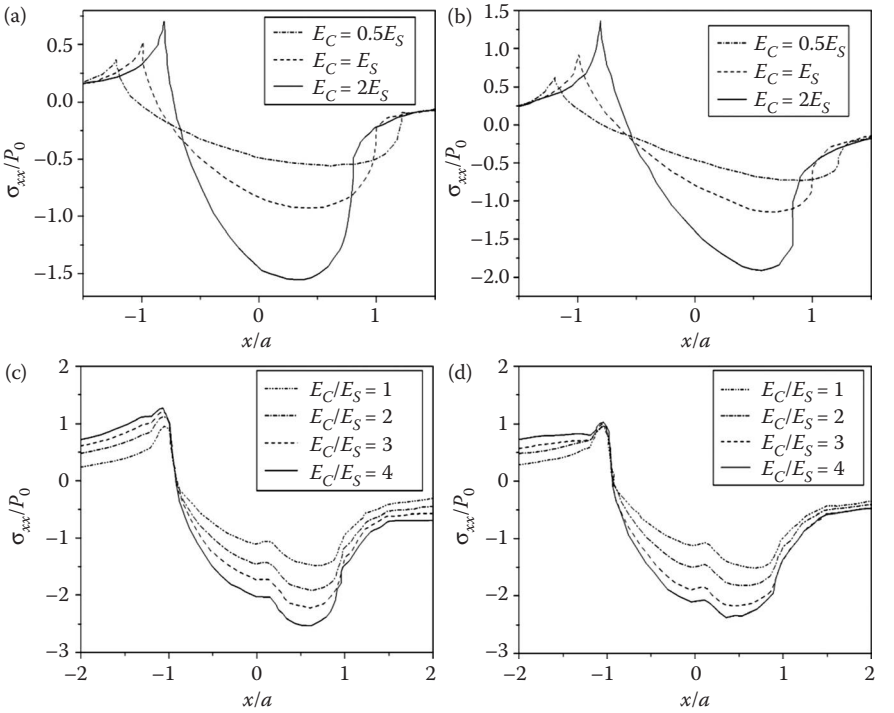


FIGURE 9.13 Effects of coating stiffness, coefficient of friction, and coating thickness on the contact stress at the surface ($z = 0$) upon scratching of an elastic, isotropic coated system along x. (a)–(b) compare two different coefficients of friction: 0.25 and 0.5, respectively. (Redrawn from Osullivan TC, and King RB. *Journal of Tribology-Transactions of the Asme*, 1988;110:235); (c)–(d) compare two coatings of different thickness: 0.25a and 0.50a, respectively. (From Diao DF, Kato K, and Hayashi K. *Tribology International*, 1994;27:267.) P_0 represents the Hertzian pressure and a the contact radius. Subscripts C and S denote coating and substrate, respectively.

Because their simulations found that σ_{max} increased with increasing E_C/E_S at different rates depending on the E_C/E_S value, an exponential function was proposed:

$$\sigma_{max} = 2f\left(\frac{F_N}{\pi a^2}\right)e^{\beta}, \tag{9.8}$$

where the parameter β can be obtained from:

$$\beta = 0.21 - 0.08\left(\frac{t}{a}\right) + \left[0.175 - 0.6\left(\frac{t}{a}\right)\right]\left(\frac{E_c}{E_S} - 1\right), \tag{9.9}$$

for $0.125 \leq t/a \leq 0.25$; and

$$\beta = 0.3 - 0.60\left(\frac{t}{a}\right) + \left[0.04 - 0.07\left(\frac{t}{a}\right)\right]\left(\frac{E_C}{E_S} - 1\right), \tag{9.10}$$

for $0.25 < t/a < 0.5$.

The above expression was found to agree well with the results of the FE simulations in the intervals $0.1 \le f \le 0.7$, $0.125 \le t/a \le 0.6$, and $1 \le E_C/E_S \le 4$. This covers a wide range of representative properties in hard coatings, but does not take into account residual stresses. Residual stresses are present in many systems of interest, particularly in films obtained from nonequilibrium processes (e.g., deposition from a vapor phase, or from a high energy source). Their magnitude can be up to the hundreds of MPa or units of GPA—comparable to that of the contact stresses—and are typically regarded as equibiaxial (tensile or compressive). Compressive residual stresses on the surface lower the tensile contact stresses, and make the coating more resistant to fracture; tensile residual stresses have the opposite effect, and assist at crack opening. In order to obtain the net tensile stress on the film surface, the residual stresses* need to be superimposed in the simulations of contact stress. Alternatively, the net tensile stress can be estimated by adding (if tensile) or subtracting (if compressive) the measured residual stress from the maximum contact stress value, obtained by Equation 9.8 or by simulations that consider the system free from internal stress.

In addition to the maximum tensile stress, high shear stresses are also important. This is because shear stresses can cause plastic deformation damage (e.g., shear faults), which may be a precursor of fracture, as explained in the previous section. Moreover, in coatings shear stresses are also directly related to delamination of the coating at the interface. As in the bulk case, under uniaxial, normal loading ($f = 0$), the Von-Mises stress has a maximum at $0.5a$ below the surface, along the loading axis. As the friction is increased, the maximum moves ahead of the normal loading axis, and closer to the coating surface, that is, toward the leading edge of the contact [36], as shown in Figure 9.14 for the case of $E_C = 2E_S$. This shift is more pronounced for the case of thinner coatings, relative to the contact radius. Similar to what happens with the maximum tensile stress, the magnitude of the Von-Mises stress in the coating increases with increasing the elastic modulus of the coating relative to the substrate (i.e., E_C/E_S), the applied load and the coefficient of friction, as shown in Figure 9.14. Thickness also has a marked effect, and the Von-Mises stress decreases with increasing the coating thickness relative to the contact radius [36].

The Von-Mises stress becomes the most important component in the case of ductile systems (coating or substrate), where plastic deformation is more likely to take place than fracture. The influence of plastic deformation of a soft substrate on the stress field in the coating can also be included in numerical models in order to refine the predictions of the stress values, but at the cost of complexity. For this reason, such analyses have attracted less attention than the purely elastic case [10,46]. Nevertheless, the simpler elastic stress analyses are able to predict the regions under the relevant stresses, and thus suffice for assessing the fracture modes on most elastic

* Residual stresses are routinely assessed experimentally by measuring the curvature that the stressed film induces on a thin substrate after deposition, and using Stoney's equation [45].

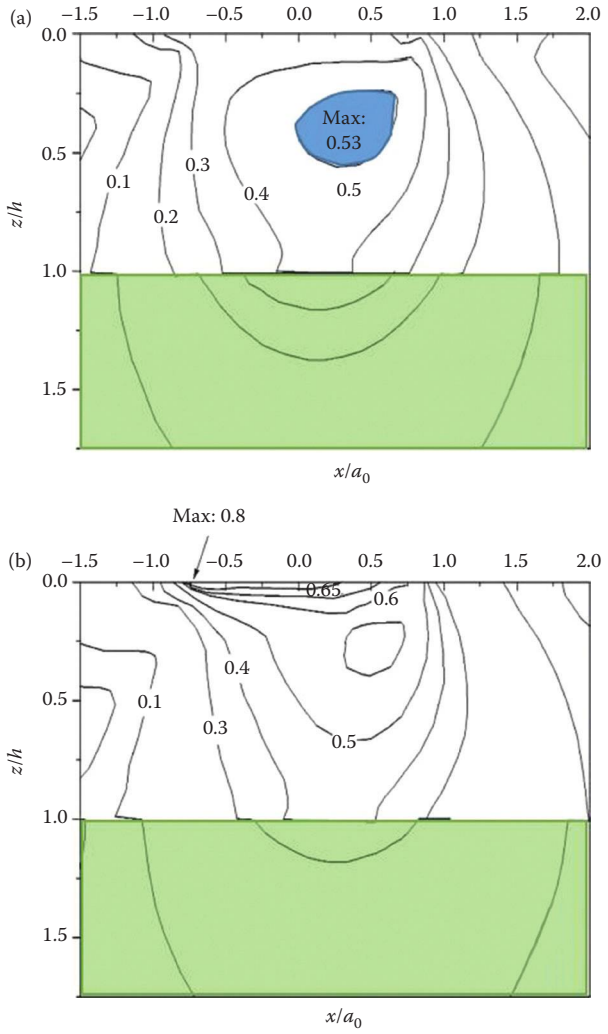


FIGURE 9.14 Contour of the Von-Mises stress (relative to the contact pressure) upon scratching of a coated system ($E_C = 2E_S$) for $f = 0.25$ (a) and $f = 0.5$ (b). The sliding direction is x, and h and a represent the coating thickness and the Hertzian contact radius, respectively. (Replotted from Osullivan TC, and King RB. *Journal of Tribology-Transactions of the Asme*, 1988;110:235.)

coatings on elastic substrates, which are typically the best-suited model systems for measurement of fracture properties of films, the main focus of the present chapter.

9.3.2 Isotropic Films

From the structural point of view, isotropic films represent the simplest case scenario, whereby the microstructure is not expected to interfere significantly with

crack initiation and propagation. Most crystalline films, particularly those obtained from a vapor phase, have a columnar, anisotropic structure. An exception is that of modern nanocomposite films in which, typically, impurities present during deposition hinder the columnar growth, resulting in equiaxed grains with no preferential orientation [47]. Thus, the main categories of isotropic films comprise amorphous films and crystalline nanocomposites.

The first necessary ingredient for fracture is the presence of defects. Visual characterization of defects prior to testing in amorphous solids (e.g., conventional glasses) is traditionally considered to be a difficult task [20], further hindered in submicron size films, which require high-resolution imaging techniques. Moreover, both surface and subsurface regions are of interest. One of the problems is that techniques with the appropriate resolution, such as TEM, are extremely site-specific, that is, they only allow images of small lamellae; whereas the stochastic of defect distribution require large surface areas and cross sections to be imaged in order to be able to find defects. Considering the duration of TEM sample preparation procedures, *a priori* defect characterization by high-resolution electron microscopy is an enormous challenge.

Alternatively, assessment of critical defects in thin films is typically carried out *a posteriori*, by means of fractographic observations after mechanical testing. For example, cross-sectional FIB examination after nanoindentation of diamond-like carbon (DLC) films deposited in a mirror-finished silicon substrate revealed crack-like defects of size below 100 nm at the interface [44]. It is, however, acknowledged that the nature of defects in the smallest systems is far from clear, that is, whether they are crack-like or embryonic defects with intensely concentrated residual stress fields [48]. Moreover, defect populations at the surface, perhaps most relevant to sliding contact, are not necessarily the same as at the interface. In Section 9.4.1.1, we show how surface defects can be assessed indirectly from the scratch test.

When both the film and the substrate are elastic, the stress analyses presented in the previous section predict largest tensile stresses on defects at the trailing edge of the contact upon sliding. This is illustrated in Figure 9.15a, for scratching of a DLC film deposited on a glass substrate. The linear elastic stress field is simulated on the surface at the point of contact as a function of position along the sliding direction (x) using the commercial software Elastica, for the loading conditions at the moment of failure (as calculated via Equation 9.4). The simulations show that the maximum tensile stress (σ_1) at the trailing edge is $\approx$ 1.4 GPa, which represents the fracture strength of the film. At the forward edge of the contact, the stress is compressive. Moreover, the radial orientation of the first principal stress on the film surface results in formation of partial cone cracks, much like the ones obtained in bulk amorphous brittle materials such as soda-lime glass. This has been observed experimentally by means of optical microscopy in DLC (opaque), amorphous SiC (opaque), and amorphous TiO_2 (transparent) films on glass substrates, as shown in Figure 9.15b [7].

Subsurface observations by means of FIB microscopy (Figure 9.16) are able to confirm that damage starts on the surface of the film. Indeed, examinations before the first surface crack reveal a damage-free subsurface, and do not show evidence of possible cross-sectional fracture modes such as median or lateral cracks. However, the observations normal to surface at the first cracking site reveal propagation of

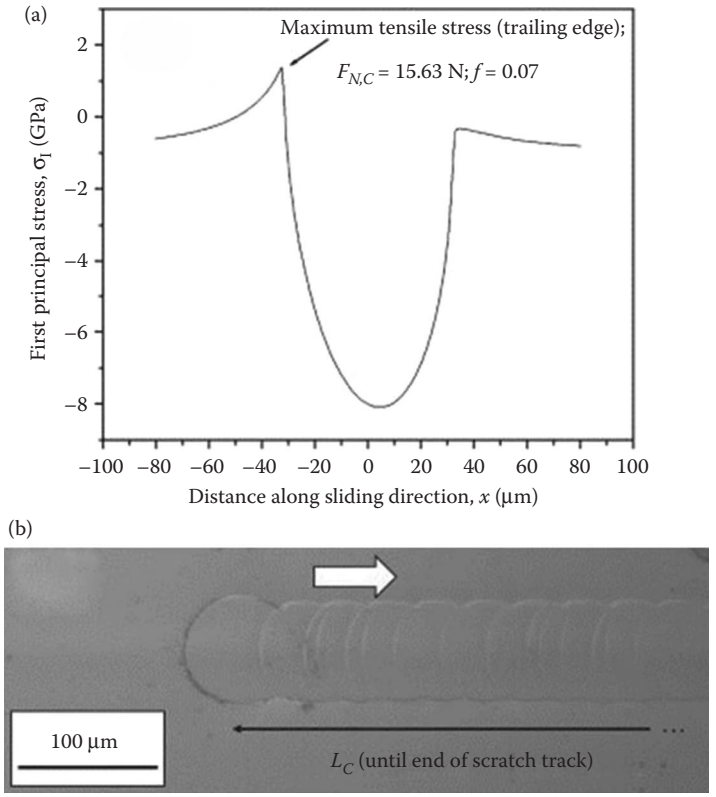


FIGURE 9.15 (a) Elastica simulation of the first principal stress on the surface as a function of distance along the sliding direction, upon scratching (tip radius 200 μm) a DLC film (thickness-1 μm). The point $x = 0$ represents the stylus position at the moment of first cracking occurrence, at an applied normal load of 15.63 N, as measured from the optical micrograph at the end of the test (b). The white arrow indicates the sliding direction. (From Borrero-Lopez O. et al., *Thin Solid Films*, 2010;518:4911.)

the crack into the cross section of the coating, and subsequently into the substrate, following a cone-like configuration. Thus, this cracking mode in the film is through-thickness. It is worth noting that film fracture does not necessarily involve its detachment from the substrate, which is characteristic of cohesive failure, in contrast with adhesive failure (i.e., delamination). Axial views of the cross section (Figure 9.16) reveal steps due the sliding of the fracture surfaces with respect to each other at higher normal loads, but nonetheless the film remains physically adhered to the substrate at the interface.

As indicated in the previous section, the actual shape of the partial cone cracks can be affected by the coefficient of friction. This may result in cracks with different radii of curvature, that is, more or less circular. In the most extreme cases, the crack shape can be rather straight, as shown schematically in Figure 9.17. The fracture modes represented are the so-called chevron tensile cracks and arc tensile cracks.

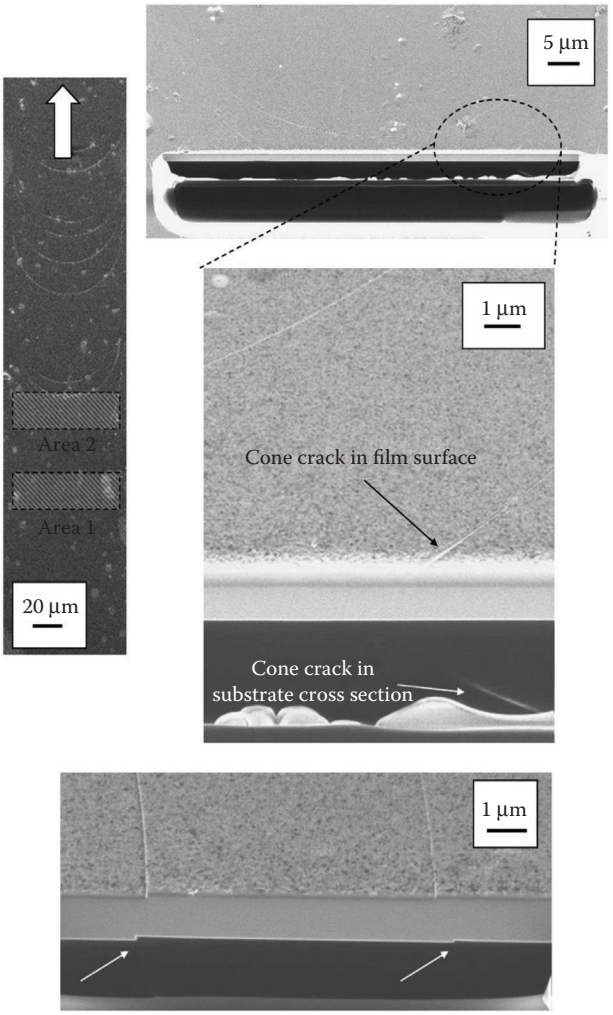


FIGURE 9.16 FIB micrographs of a scratch track in a SiC film (1.2 µm) on a glass substrate. The image on the left-hand side is a top view of the scratch. The white arrow indicates the scratch direction. The images on the right-hand side (top) are cross-sectional details of area 2 (after cracking). At the bottom: steps at the interface due to trough-thickness propagation. Cross sections viewed at a 45° angle. (From Borrero-Lopez O. et al., *Thin Solid Films*, 2010;518:4911.)

However, it is important to note that crack shapes deviating from the more conventional partial cone cracks can also result from anisotropy of the film, as discussed in Section 9.3.3. Regardless of their actual shape, all the fracture modes in elastic systems show a characteristic concave geometry, with some degree of forward crack propagation (i.e., along the scratch direction, from the trailing edge), and toward the edge of the scratch track, before arresting.

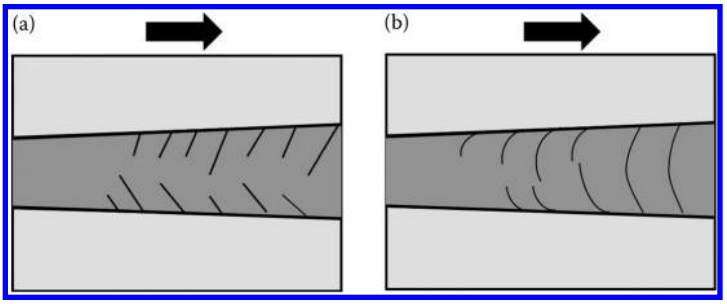


FIGURE 9.17 Schematic (top view) of relevant fracture modes upon scratching of coated systems: (a) Forward chevron tensile cracks; and (b) Arc tensile cracks. The black arrow indicates the sliding direction. (Redrawn from A.s.f.t.a. materials, Standard ASTM C1624-05, Vol. 15.01 *Refractories, Activated Carbon; Advanced Ceramics.* ASTM International, 2005.)

Upon increasing the applied load, the frequency of cracking increases. When the load is sufficiently high, the tensile stress acting on the surface is not solely responsible for fracture. Indeed, interfacial stresses eventually reach a critical value, which can also cause failure. Cracks initiated at the interface typically propagate along that region, detaching the coating from the substrate. Delamination cracks extend out of the scratch track, forming an angle (close to 45° in as shown in Figure 9.18), as the compressive stresses ahead of the tip (e.g., see Figure 9.12) block propagation along the sliding direction. Similar to what occurs with lateral cracks upon indentation of bulk materials, when the tip moves forward and the applied load is released, the interfacial cracks typically propagate upward into the coating, driven by the elastic recovery of the surrounding region. Delamination cracks reaching the surface cause relatively large chipping, which extends ahead of the tip when sliding finishes (Figure 9.18).

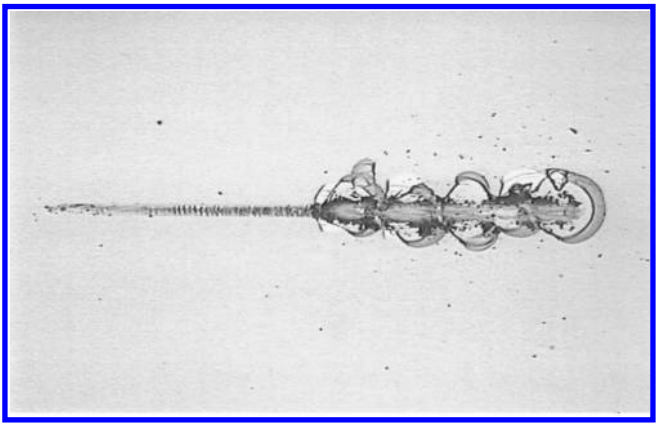


FIGURE 9.18 Scratch track of a particle-filled sol–gel coating on a glass substrate. Tip radius and scratch length were 150 μm and 1 mm, respectively. (From Malzbender J. et al. *Materials Science & Engineering R-Reports*, 2002;36:47.)

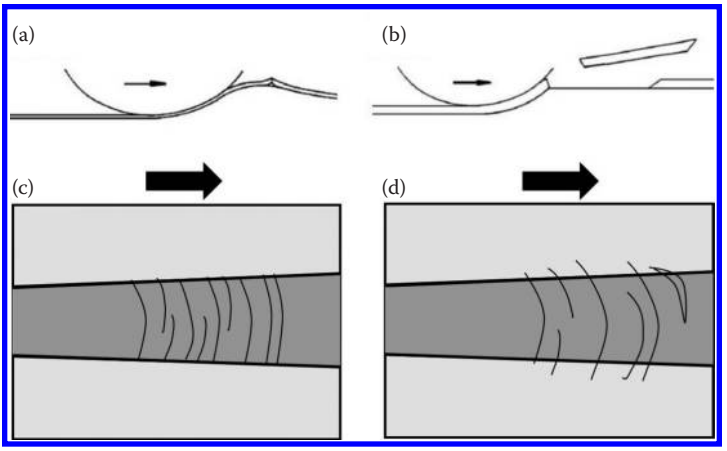


FIGURE 9.19 (a) Schematic (cross section) of the formation of buckling cracks upon sliding contact of a coated system, due to deformation of the substrate ahead of the indenter; (b) Wear particle formation due to propagation and coalescence of buckling cracks. (From Bull SJ. *Wear*, 1999;233:412.) (c) Schematic (top view) of surface markings characteristic of buckling cracks; (d) Wider marks indicate wear. The black arrow indicates the sliding direction. (Redrawn from A.s.f.t.a. materials, Standard ASTM C1624-05, Vol. 15.01 *Refractories, Activated Carbon; Advanced Ceramics*. ASTM International, 2005.)

Additional damage modes appear when elastic–plastic substrates are employed. Indeed, plastic deformation of a relatively compliant or soft substrate ahead of the scratch stylus due to the high shear stress (see Figure 9.14) can indirectly cause relatively high tensile stress on the surface of the brittle film by buckling, and subsequent fracture when the tensile stress exhausts the film strength, as shown schematically in Figure 9.19a. Buckling cracks are typically irregularly spaced, and have an opposite curvature to the tensile cracks originated in purely elastic systems (i.e., convex). This failure mode is more common for thinner films–thicker films effectively impart protection to the substrate from contact damage and limit the plastic deformation necessary for film buckling—and can be catastrophic when cracks propagate along the interface, leading to adhesive failure by spall particle formation (Figure 9.19b), which is a form of severe wear.

9.3.3 Columnar Films

In the previous section, it was shown how the elastic stress field predicts that the shape of partial cone cracks can be modified by increasing the coefficient of friction, which results in cracks becoming less circular. Crack geometry can also be distorted by the anisotropic structure in crystalline films. Most crystalline films possess a columnar structure, especially those obtained from a vapor phase. Columnar grains typically have a larger height than width, depending on the deposition conditions, and relatively weak grain boundaries that may affect crack propagation [47].

The effect of a columnar structure on scratch failure of an elastic system has been demonstrated for TiO_2 films of submicron thickness on a glass substrate [49].

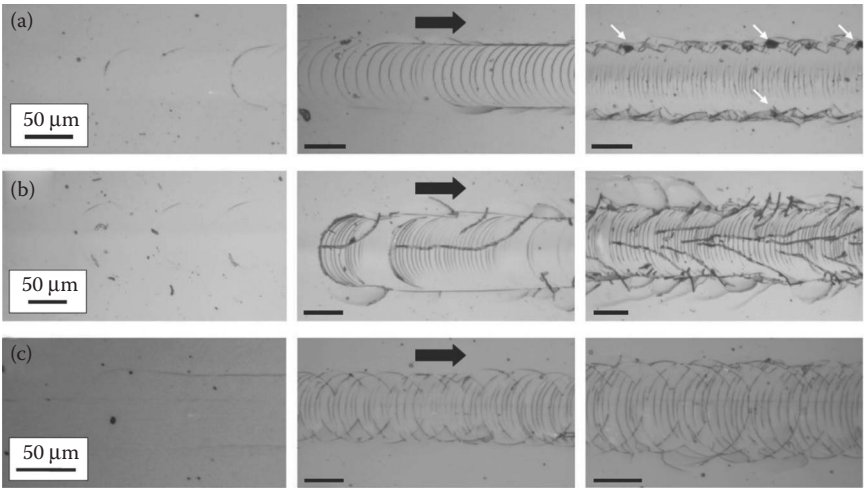


FIGURE 9.20 Optical micrographs representative of the surface damage arising from scratch tests (tip radius 200 µm) in TiO_2 submicron films of different structure on glass substrates: (a) Rutile; (b) Anatase; and (c) Amorphous. The black arrow indicates the sliding direction. Scale bars represent 50 µm. (From Borrero-Lopez O. et al., *Thin Solid Films*, 2011;519:7925.)

Figure 9.20 compares three TiO_2 films, two of them with a crystalline structure (anatase and rutile, respectively), and one amorphous. The coefficient of friction and residual stress were measured to be approximately the same for the three systems (~0.09). Thus, it was be determined that the observed differences in the geometry of scratch cracks were related to structure. Indeed, the amorphous film shows rather circular cracks. The low value of the coefficient of friction in this case does not result in significant distortion of the σ_2–σ_3 surfaces with respect to the Hertzian case, and as a result cracks are able to fully complete a ring contour. Since the crystalline films show the same coefficient of friction, the same elastic stress field can be expected, but in this case the rings do not close, and instead cracks show an arc geometry. This is because cracks originated at the trailing edges of the contact do not follow the paths of maximum stress (σ_2–σ_3 surfaces), but rather propagate along relatively weak grain boundaries, which pose lower resistance, as shown schematically in Figure 9.21.

Intercolumnar crack propagation or intercolumnar shear is well-known in films with a columnar microstructure, and can be observed in detail by cross-sectional TEM samples prepared by FIB (Figure 9.22a). Intergranular crack propagation can also be assessed by examination of the scratch cracks with the FIB/SEM (Figure 9.22b), where approximately vertical trajectories of the cracks through the film cross section are observed (in some cases the columns can be tilted slightly under the action of the applied stress [50]). This contrasts with ~22° crack propagation angles of cone cracks in the amorphous glass substrate [20,26].

The columnar microstructure results in new fracture modes in the rutile and anatase films, in addition to the arc tensile cracks. In particular, high stresses at the edge of the contact result in relative sliding between the grains in that region, which

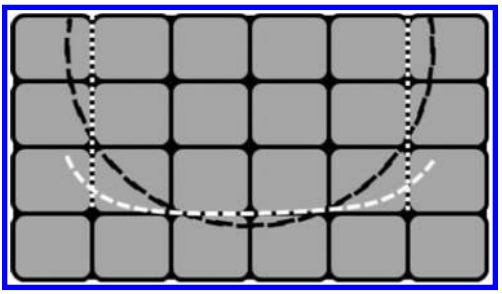


FIGURE 9.21 Schematic surface projection of the scratch crack trajectories in a columnar film with low coefficient of friction: arc-like (white dashed line), and longitudinal (white dotted line). The arc cracks deviate from the circular prediction based on the stress field (black line; crack path in an amorphous film) due to the presence of weak grain boundaries. Grains and contact size not to scale.

originate longitudinal cracks running parallel to the sliding direction. It is observed that the longitudinal cracks propagate through the film and into the substrate, where they eventually arrest, unless interaction with structural defects deflect them back to the surface as shown in Figure 9.23, which can lead to localized wear. At higher normal loads, longitudinal cracks become a more serious risk for the structural integrity of the film as they start to branch out. Indeed, when combined with lateral cracks at the cross section, they result in formation of wear particles, leading to rapid material removal from both the substrate and the film (Figure 9.24). The material removal can be observed as black patches around the edges of the scratch in the optical micrographs, highlighted by white arrows in Figure 9.20.

Finally, when the frequency of tensile cracks is very high and the arc cracks are very close to each other, as in the rutile film in Figure 9.20b, cross-linking or channeling between cracks may take place. This results in an additional type of

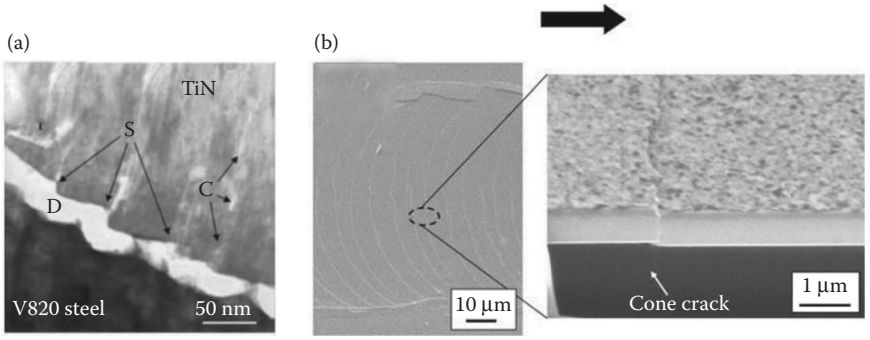


FIGURE 9.22 (a) Bright-field cross-sectional TEM image of a columnar TiN coating on a steel substrate after nanoindentation, showing intercolumnar cracking. (From Ma LW. et al., *Surface & Coatings Technology*, 2005;192:11); (b) FIB micrographs of the scratch track on a TiO_2 film (rutile structure) on glass, surface image (left), and cross-sectional detail of the circled area at higher magnification, viewed at 45° angle (right). The black arrow indicates the sliding direction. (From Borrero-Lopez O. et al., *Thin Solid Films*, 2011;519:7925.)

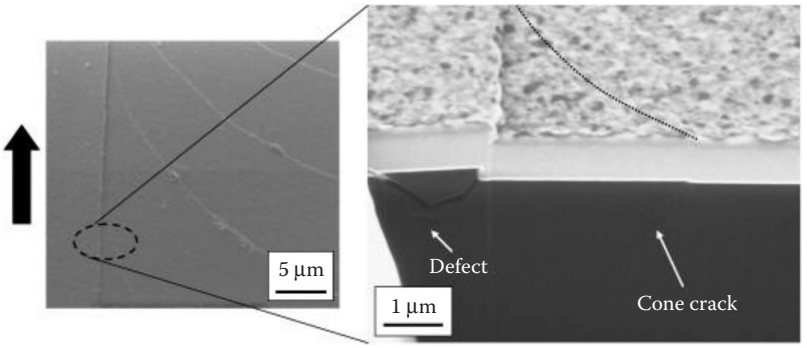


FIGURE 9.23 FIB micrographs of a longitudinal crack at intermediate load upon scratching of TiO_2 film (rutile) on glass. The image on the left-hand side is a top view of the scratch. The image on the right-hand side is a cross-sectional detail of the circled area. The arc-like crack is highlighted at the surface by the pointed line. The black arrow indicates the sliding direction. The cross section is viewed at a 45° angle. (From Borrero-Lopez O. et al., *Thin Solid Films*, 2011;519:7925.)

failure (channel cracks), with an axial geometry, that is, extending along the sliding direction, although deflection toward the edges of the contact, where large tensile stresses are also present, is observed in some instances. This fracture mode is largely restrained to the film surface, as shown in Figure 9.25, and involves delamination or adhesive failure.

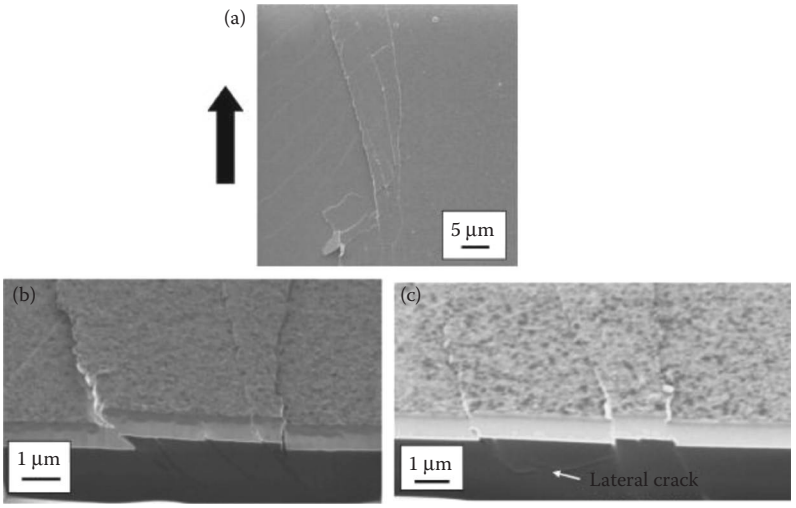


FIGURE 9.24 FIB micrographs of scratch cracking of a TiO_2 film (rutile) on a glass substrate: (a) Surface view; (b) and (c): Cross-sectional images showing formation of wear particles due to the coalescence of vertical and lateral cracks, viewed at 45° angle. The black arrow indicates the sliding direction. (From Borrero-Lopez O. et al., *Thin Solid Films*, 2011;519:7925.)

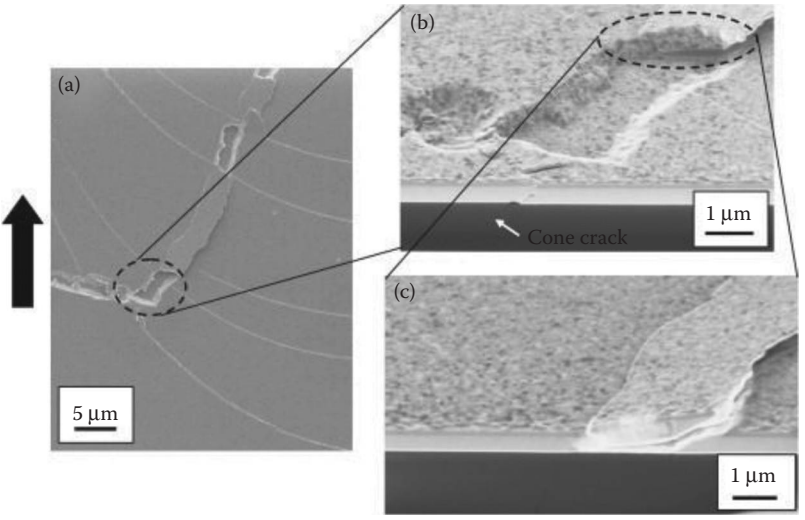


FIGURE 9.25 FIB micrographs showing channel-like cracks that originated on scratching of a TiO_2 film (anatase) on a glass substrate: (a) Top view; (b) Cross-sectional detail of the circled area in (a); (c) Cross-sectional detail of the circled area in (b). The black arrow indicates the sliding direction. The cross sections are viewed at a 45° angle. (From Borrero-Lopez O. et al., *Thin Solid Films*, 2011;519:7925.)

A special case of interest pertaining to anisotropic structures is that of mutilayer and graded films. These are novel structures that can be tailored to have superior contact properties (hardness, stiffness) at the surface while being resistant to the propagation of cracks through the cross section, that is, damage tolerant [52–54]. Moreover, the design can minimize elastic mismatch and residual stress at the film/substrate interface, thereby decreasing the probability of large spallation and delamination [55]. Thus, mutilayer/graded systems typically show improved properties compared to single-layer films. With regard to sliding contact, the main difference between multilayer and single-layer coatings is that, because of the different mechanical properties of the individual layers (mainly elastic modulus) in the former, the σ_2–σ_3 surfaces that dictate the trajectory of the cracks at the cross section vary from layer to layer. In particular, one of the commonest multilayer structure, consisting of alternating layers, results in zig-zag cross-sectional crack propagation [22], but maintaining the cone shape. If the layer composition (and thus the elastic modulus) is varied gradually, it is possible to achieve a significant distortion of the macroscopic crack trajectory from its cone geometry. For example, Wo et al. [25] observed that, on scratching of a TiSiN/TiN multilayer coating (total thickness of 2 µm) on steel with a 5 µm sphere, the partial cone cracks become approximately parallel to the surface by including a graded TiN transition layer, which prevents crack penetration into the substrate (Figure 9.26c). Using FIB progressive sectioning, the three-dimensional shape of the cracks was reconstructed, as shown in Figure 9.26, clearly revealing the deviation from the conventional partial cone crack geometry. Another possibility in this type of multilayer structures is crack deflection at interfaces, which

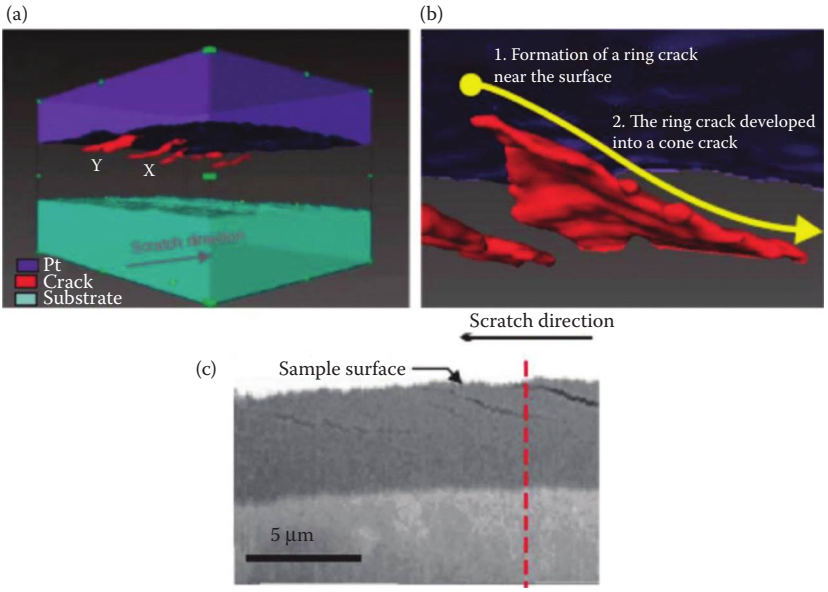


FIGURE 9.26 (a) Three-dimensional reconstruction of surface and subsurface cracking that originated on scratching (tip radius 5 μm) of a TiSiN/TiN multilayer coating on a steel substrate. The image was obtained by software-assisted (Avizo Fire 6.0, FEI, Hillsboro, OR) superposition of some 125 micrographs obtained by progressive slicing and imaging with a FIB. (b) Enlarged detail of crack Y showing initiation point and propagation path. (c) Two-dimensional image reconstruction obtained from the three-dimensional reconstruction showing a cross section parallel to the scratch direction. (From Wow C. et al., *Journal of the American Ceramic Society*, 2011;94:1598.)

also tends to open cracks parallel to the surface and can cause the delamination of a section of the coating. Finally, the inclusion of relatively ductile Ti interlayers have been shown to supress intercolumnar shearing in TiN multilayered films. However, for high applied loads, the supression of intercolumnar shearing results in rupture of the columnar grains located near the interface with a steel substrate [50].

9.3.4 Thin Wafers with a Diamond Structure

A significantly more important distortion of the geometry of cracks originated on sliding contact of brittle layers takes place when the layers show a single-crystal structure. Perhaps, nowhere is this distortion clearer than in crystals with the diamond structure. This is a very relevant case, since many materials of great importance in technological applications possess this structure. The most renowned case is that of group IV semiconductors, such as silicon and germanium, which are the gold standard in microelectronic and optoelectronic devices.

In the case of scratching of a brittle layer with a diamond structure, fracture along relatively "easy" cleavage planes (i.e., planes with lower surface energy, γ) distorts the shape of the partial cone cracks. Indeed, cleavage planes make it energetically

more favorable for cracks to open along weaker planes located near the maximum contact tensile stress, thus deviating from the predicted shape [56]. This is illustrated in Figure 9.27 for scratching of single-crystal silicon wafers. The actual crack shapes depend on the orientation of the cleavage planes with respect to the stress field, as shown by Leu and Scattergood [30]. More recently, Vodenitcharova et al. [57] have predicted the most favorable planes for fracture by means of numerical simulations using the FE method. In particular, the cleavage planes can be determined by resolving the stress field into the different planes intersecting the wafer surface. The cleavage plane is the one for which the resolved tensile stress requires the smallest Griffith-type defect to satisfy the condition for crack initiation: that is, when the stress intensity factor reaches the fracture toughness.

The method described above reveals that the cleavage planes in silicon wafers are typically {111} and {110} planes. The intersection of the cleavage planes with

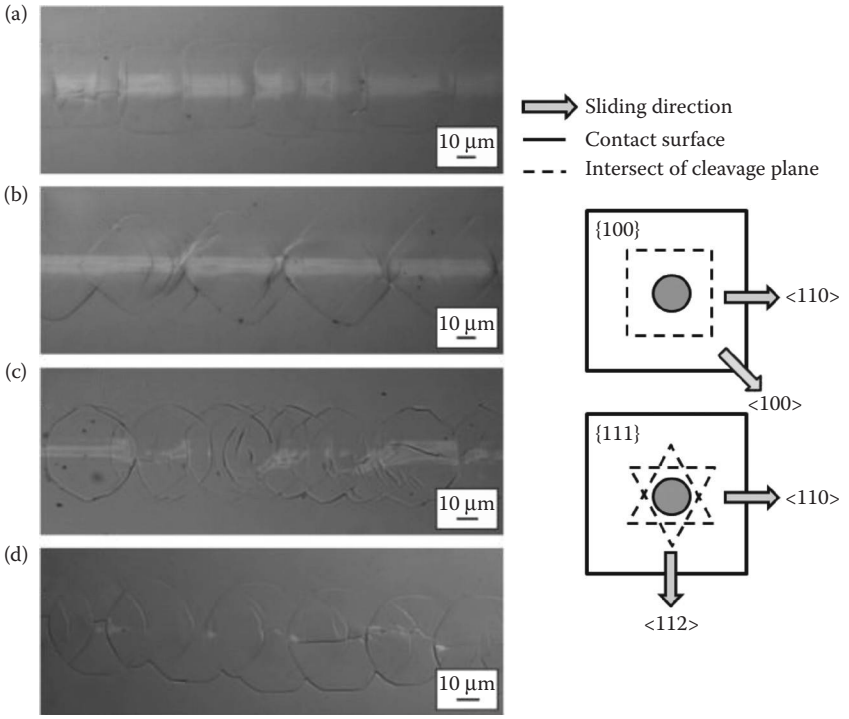


FIGURE 9.27 On the left-hand side: characteristic surface fracture patterns upon scratching (tip radius 200 µm) single-crystal silicon. (a) {1 0 0} wafer along the [1 1 0] direction; (b) {1 0 0} wafer along the [1 0 0] direction; (c) {1 1 1} wafer along the [1 1 2] direction; and (d) {1 1 1} wafer along the [1 1 0] direction. (From Vodenitcharova T, Borrero-Lopez O, and Hoffman M. *Acta Materialia*, 2012;60:4448.) On the right-hand side: schematic drawing of crack pattern formation on sliding of single-crystal silicon. Dashed lines show {1 1 1} cleavage plane intersections with {1 0 0} and {1 1 1} surfaces. The gray circle represents the contact point, and arrows indicate sliding directions. (From Leu HJ, and Scattergood RO. *Journal of Materials Science*, 1988;23:3006.)

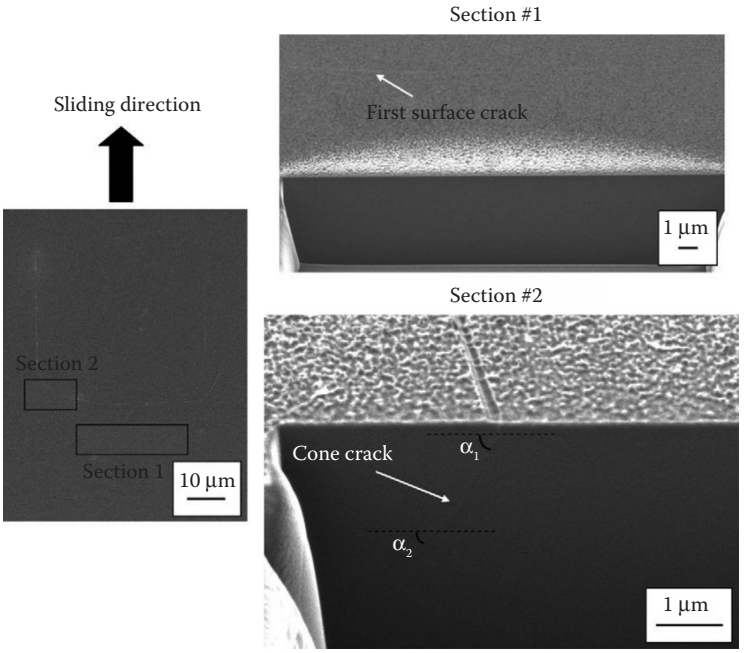


FIGURE 9.28 FIB micrographs showing the first scratch fracture of a {1 0 0} wafer upon sliding along the [1 1 0] direction. The micrograph on the left-hand side shows the surface pattern. The micrographs on the right-hand side show cross-sectional details of Sections 1 and 2, respectively. The cross-sectional images are viewed at a 45° angle. (From Vodenitcharova T, Borrero-Lopez O, and Hoffman M. *Acta Materialia*, 2012;60:4448.)

{100} and {111} surfaces (most typical in commercially available wafers) is shown schematically in Figure 9.27. This results in square-shaped cracks when scratching the surface of a {100} wafer, and dodecagonal cracks when scratching the surface of a {111} wafer, as observed experimentally. The specific orientation of the cracks depends on the orientation of the cleavage planes relative to the sliding direction—for example, see ⟨100⟩{100} cracks rotated 45° with respect to ⟨100⟩{110} cracks in Figure 9.27. While initial crack propagation is dominated by the cleavage planes with the lowest fracture energy, the Hertzian contact stress eventually takes over at the cross section. This is illustrated in Figure 9.28, for the case of a {100} wafer scratched along the [110] direction. The cross-sectional FIB micrograph reveals a change in the crack angle, from ≈54° to ≈22°. The former coincides with the angle that {111} cleavage planes form with the wafer surface, while the latter is the angle that the surface of highest Hertzian stress forms in isotropic materials, thus demonstrating its prevalence.

9.3.5 Substrate Effects and Size Effects

Unless they are very thick, coatings cannot be considered independent of the substrate. Because deformation of the film nearly always results in deformation of the

supporting foundation to some extent, substrate effects are well-known to be very important in modulus and hardness determination by means of nanoindentation. In particular, a relatively stiff and hard substrate leads to mechanical property overestimation, and vice versa. For this reason, indentations are typically either performed at depths below 10% of film thickness, or at progressively decreasing depths followed by extrapolation to zero indentation depth for deconvolution of the film property [16].

For the same reasons, substrate effects are important in fracture during scratching. Indeed, as discussed in Section 9.3.1.2, the substrate properties influence the contact stresses during sliding. This cannot only affect the critical values for cracking, but also modify the fracture modes in a given coating. For example, the same brittle film may fail by buckling if the substrate is plastic, and by partial cone cracking if the substrate is elastic. Importantly, differences are also to be expected when using substrates of the same nature (e.g., elastic), depending on their properties relative to the coating. Borrero-Lopez et al. [58] investigated substrate effects on the microscratch fracture of a DLC film (thickness 1 μm) on elastic foundations. Silicon and glass substrates which were relatively stiff and compliant compared to the film, respectively, were considered. In scratching of both systems, high tensile stress appears on the DLC film surface, at the trailing edge of the contact (Figure 9.29). The stiff silicon substrate results in somewhat higher stress compared to the compliant glass substrate. But at the same time, the stiff substrate bears a higher load, and thus shows a higher stress, than the compliant substrate.

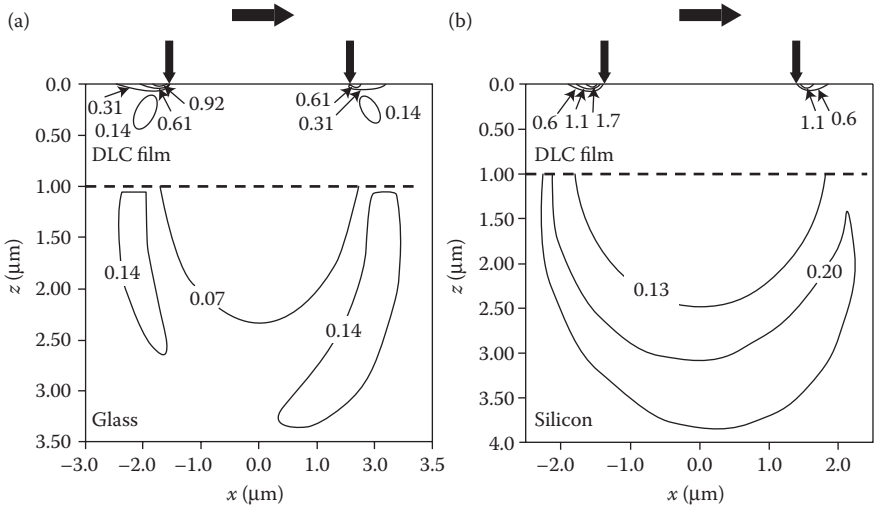


FIGURE 9.29 Cross-sectional tensile stresses (first principal) upon scratching (tip radius 5 μm) of a DLC film (thickness 1 μm, elastic modulus 106 GPa) on soda-lime glass (a) and silicon (b) substrates, simulated with Elastica. The simulated normal load is 100 mN. Cartesian coordinates are employed, being x the sliding axis, with $x = 0$ as the normal loading axis. The horizontal arrows indicate the sliding direction. Dashed lines represent the interface between the film and the substrate, and the vertical arrows indicate the limits of the contact region. Stress units are in GPa. (From Borrero-Lopez O. et al. *Diamond and Related Materials*, 2010;19:1273.)

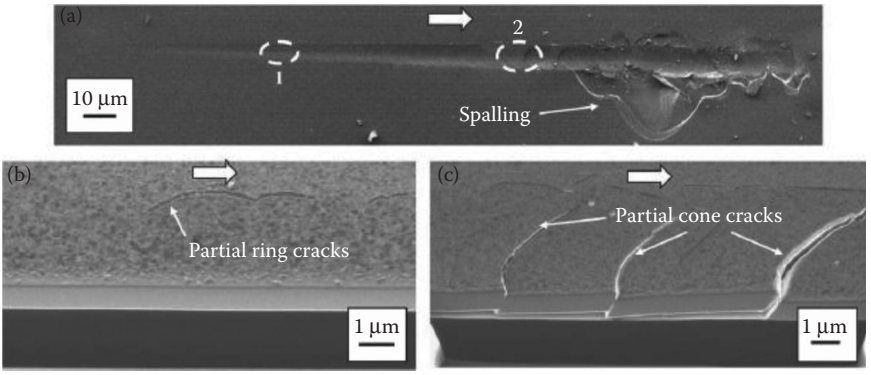


FIGURE 9.30 FIB micrographs of a scratch track in a DLC film on a glass substrate: (a) Surface view; (b) Cross-sectional view of the system at circled region 1 (first surface crack); (c) Cross-sectional view of the system at circled region 2. The thick arrows indicate the sliding direction. Cross sections are viewed at a 45° angle. (From Borrero-Lopez O. et al., *Diamond and Related Materials*, 2010;19:1273.)

The differences in stress as a function of substrate properties translate into differences in observed fracture modes (Figures 9.30 and 9.31). While surface observations point at partial cone cracking in both systems, the cross-sectional examinations reveal a very different fracture mechanism. In particular, the system with the compliant glass substrate shows conventional cracking, initiated in the film surface at the trailing edge of the contact, and subsequently propagated through the film thickness forming an angle with the surface. The partial cone cracks deflect at the interface and delaminate the film from the substrate. However, the surface cracks observed in

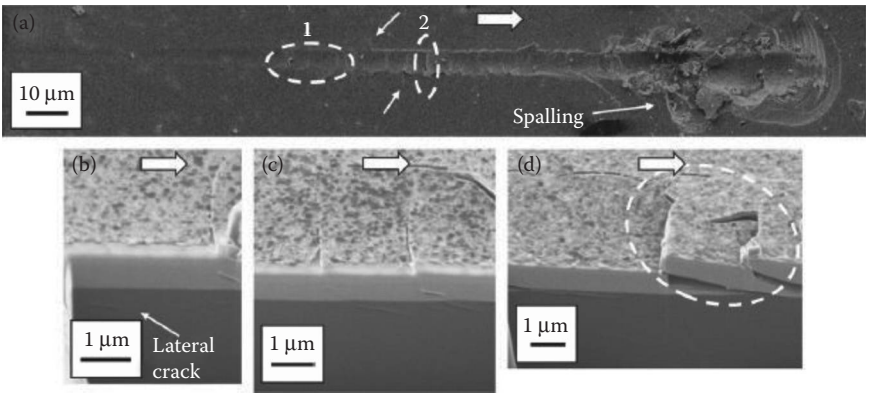


FIGURE 9.31 FIB micrographs of a scratch track in DLC film on a silicon substrate: (a) Surface view; (b) Cross-sectional view of the system at circled region 1 (first surface crack); (c) Cross-sectional view of the system at circled region 1 (after first surface crack); and (d) Cross-sectional view of the system at circled region 2. The thick arrows indicate the sliding direction. Cross sections are viewed at a 45° angle. (From Borrero-Lopez O. et al., *Diamond and Related Materials*, 2010;19:1273.)

the system with the stiff silicon substrate do not show appreciable curvature, typical of conventional ring/cone cracks. Instead, cracks are somewhat straight and perpendicular to the sliding direction. This suggests fracture initiation in the substrate, in a plane parallel to the surface and ahead of the normal loading axis, where high stresses are also present (Figure 9.29b). Subsequent crack propagation upward is driven by the tensile stress at the trailing edge. The process is shown schematically in Figure 9.32.

In addition to substrate effects, size effects are also important in scratch fracture. First, the size of the region under the maximum tensile stress increases with increasing the contact radius, which, for a given stress, makes it more likely to include critical defects for crack initiation. This is expected to result in differences in the fracture strength that can be calculated by means of scratch testing (see Section 9.4.1.1). In addition, as the tip becomes smaller, stress concentrations become larger, which can cause plastic deformation from very low loads. Thus, there is usually an elastic/brittle–plastic/ductile transition on scratching as a function of tip size.

The elastic–plastic transition is demonstrated in Figure 9.33 for the case of a single layer of silicon, by comparing the fracture pattern arising upon scratching with a relatively large tip (200 μm) and a significantly smaller (5 μm) tip. It can be seen that with the larger tip, the scratch groove is mostly elastic, with no visible traces of plasticity. Indeed, a brittle fracture mode (partial cone cracks) is evident along the sliding direction. On the contrary, a relatively deep plastic groove appears when scratching is performed with the smaller tip. In actuality, the response is quasiplastic. In particular, cracks emanating from the edges of the plastic groove, forming an angle with the sliding direction, can also be observed (white arrows in Figure 9.33). Such cracks are the result of median cracks forming under the surface during loading, below the plastically deformed region, and opening normally to the surface upon unloading,

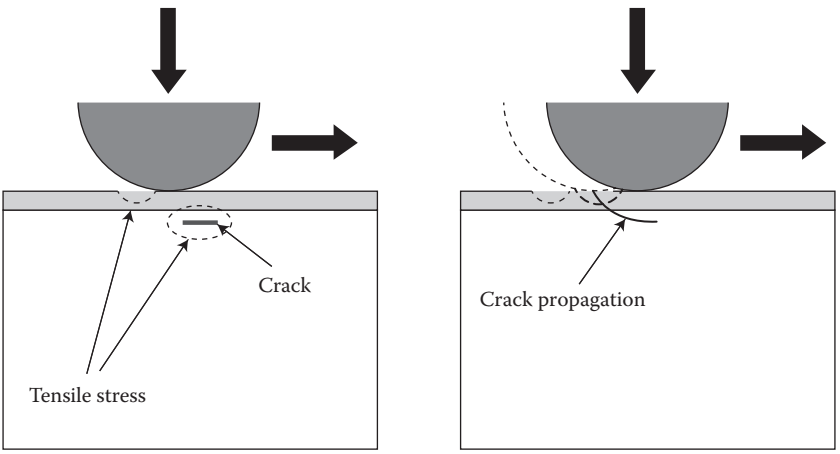


FIGURE 9.32 Schematic showing initiation and propagation at the cross section of subsurface cracks originated upon sliding contact of a brittle film on a stiff substrate. Vertical and horizontal arrows indicate the normal loading axis, and the sliding direction, respectively. Not at scale. (From Borrero-Lopez O. et al., *Diamond and Related Materials*, 2010;19:1273.)

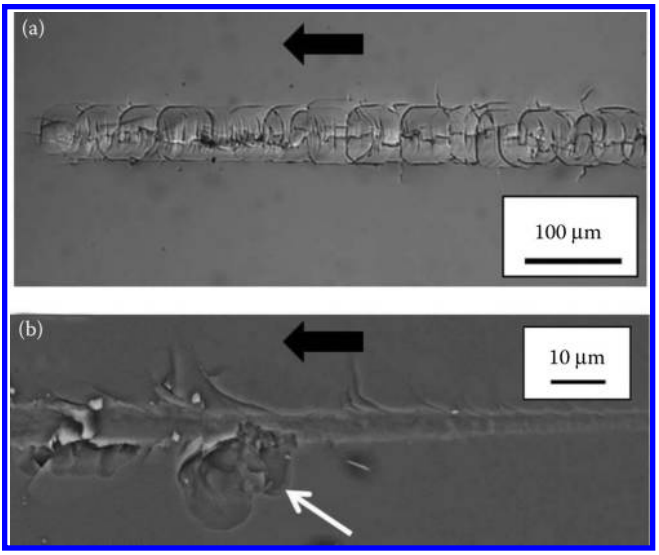


FIGURE 9.33 Surface damage arising on scratching of single-crystal silicon: (a) with a 200 µm tip; and (b) with a 5 µm tip. White arrow point at spall particle formation upon coalescence of lateral and radial cracks. Black arrows indicate the sliding direction.

driven by the residual stress field due to the elastic recovery of the region surrounding the plastic zone. Such cracks are very similar to radial cracks emanating from indentations (uniaxial) with sharp tips [21]. However, in the case of a sliding contact, the residual stress field moves along a sliding direction (Section 9.3.1), which results in cracks that are not normal to the scratch track, but form an angle smaller than 90°.

The transitions between damage modes as a function of tool size have relevant implications in machining of materials. Indeed, since scratch tests can be taken as simulations of cutting processes, it follows that on cutting brittle materials, smaller tools would be preferred in order to achieve more efficient cutting by ductile mechanisms, which also produces less attendant strength-degrading damage in the as-cut parts. However, in cutting with small tips the load needs to be carefully controlled, as secondary fracture modes may appear when the stresses are too high. While some of these fracture modes, for example, isolated radial cracks, result in limited damage, their combination with other subsurface cracks such as lateral cracks may be very deleterious. This is shown in Figure 9.33, where at higher loads, radial cracks coalesce with lateral cracks to form large spall particles (white arrow) producing severe abrasive wear.

9.4 FRACTURE ANALYSIS OF THIN FILMS USING THE SCRATCH TEST

In the analysis of fracture, the magnitudes of fracture strength, σ_F, and fracture toughness, K_C, are typically used to assess the resistance to crack initiation and propagation, respectively. For brittle solids with strong ionic/covalent bonds, fracture strength

values should be very high in theory. However, in practice, actual strengths are significantly lower than theoretical values due to the presence of defects. Toughness of ceramics is typically very low, although it can be improved to some extent by microstructural control, activating various mechanisms for crack energy dissipation ahead of and/or behind the tip [20]. While determination of fracture strength and toughness is standardized, application of conventional methods to coated systems poses a challenge due to specimen size (i.e., thickness) and influence of the substrate. Thus, alternative methodologies have been developed for small-scale specimens, but these can also require relatively complex experimental techniques (e.g., free-standing film micromachining, micromechanical testing) [59–61]. The scratch test can be used for the purpose of strength and toughness assessment, which provides a somewhat simpler alternative, mainly because it does not require specimen machining. Three main approaches will be described here for the characterization of fracture properties by scratching, most useful specifically for the many practical applications involving sliding contacts. In particular, a stress approach, an energy approach, and finally a simpler and quicker, semiquantitative approach are explained as follows.

9.4.1 Stress Approach

Fracture of brittle materials takes place when preexisting, stress intensifying, crack-like defects become unstable and propagate under the action of applied stress. Within the framework of linear elastic fracture mechanics (LEFM), the stress field near a crack-like defect can be derived as a function of a scaling parameter called the stress intensity factor, K. For the simplest case of a uniaxial loading configuration, the K factor is related to the tensile stress, σ, through the following expression [20,21]:

$$K = \sigma Y \sqrt{c}, \tag{9.11}$$

where Y is a dimensionless geometrical factor and c is the size of the precursor defect. In scratching, assuming a uniaxial tensile stress is of course a simplification, but not a crucial one for the purposes of fracture assessment. Indeed, based on the stress analysis in sliding contacts outlined in Section 9.3, fracture is most likely initiated at the trailing edge of the contact, where tensile stresses are highest. This is the case in some of the commonest fracture modes observed in brittle systems: partial cone cracks and arc-like cracks (Section 9.3.2). Moreover, the maximum contact stresses are oriented radially on the surface, which renders a uniaxial tension state in each volume element at the edge of the contact circle, as shown schematically in Figure 9.34.

Linear elastic fracture mechanics establishes that failure takes place when the stress intensity factor reaches the critical value of the fracture toughness, K_C. This corresponds to the tensile stress at the trailing edge, reaching the maximum stress that the precursor defect can withstand prior to becoming unstable, the fracture strength, that is, when $\sigma_{max} = \sigma_F$. In that case, Equation 9.11 becomes

$$K_C = \sigma_F Y \sqrt{c} \tag{9.12}$$

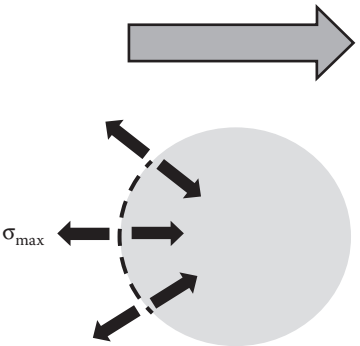


FIGURE 9.34 Schematic of a model contact surface upon sliding with a spherical indenter. The dashed line represents the trailing edge of the contact, where tensile stresses are highest (σ_{max}). Tensile stresses at the trailing edge are oriented radially, as indicated by black arrows. The gray arrow indicates the sliding direction.

Thus, using this approach, fracture properties of coatings and films can be obtained from scratch tests. The main requisite is that the failure mode be cohesive fracture initiated by the maximum tensile stress at the trailing edge of the contact. There are two possibilities: (i) estimation of strength from tests at progressive load increase and subsequent calculation of toughness using Equation 9.12 (Sections 9.4.1.1 and 9.4.1.2); and (ii) direct calculation of toughness from tests at constant load (Section 9.4.1.3). The former requires knowledge of the population of critical defects (geometry, size), while the latter requires that the applied load be sufficiently high to cause fracture. The methodology for the quantitative assessment of strength and toughness by means of scratch tests is presented in the following subsections.

9.4.1.1 Fracture Strength

Fracture strength measurement in bulk, brittle systems is standardized [62]. In a strength test, a specimen of simple geometry (dog-bone, bar, or disk) is progressively—and preferably swiftly, in order to measure inert strength—loaded in tension until failure takes place. Unlike in toughness measurements, specimens do not need to be prenotched, that is, they fail as a result of their "natural" flaws. The critical fracture load is ascertained from the experimental load–displacement curve, and in combination with a model (analytical or FE) of the stress in the specimen as a function of the applied load, allows determination of the fracture strength. Typically, flexure experiments (uniaxial three- and four-point bending [63], or biaxial ball-on-ring [64]) are preferred over uniaxial tensile tests due to difficulties associated with dog-bone shaped specimen machining and gripping in the latter.

Regardless of the loading configuration, strength testing is experimentally very challenging. Indeed, stochastic distributions of defects in a ceramic inevitably result in variations of strength, as can be inferred from Equation 9.12. Statistical treatment of the strength scatter requires a large number of specimens to be tested, which involves large machining and polishing efforts—one specimen only provides one strength value. Machining of test specimens out of brittle materials is difficult as it

is, but is particularly challenging in the case of small-scale systems such as coatings. Nanomechanical testing of micromachined, free-standing films has been carried out in recent times, especially in MEMS materials, but is technologically complex [61].

The scratch test meets the requirements for strength measurement when failure takes place by partial cone and arc-like cracks. Indeed, sliding induces a controlled and quantifiable tensile stress state (Section 9.3.1) at the region where fracture initiate—the trailing edge of the contact (see Figure 9.34)—and loading is swift, as the tip moves to a fresh spot of the sample with increasing the applied force. In addition, the scratch test has significant advantages compared to the more conventional methodologies for strength testing of coatings. In particular, in a scratch test the films can be tested as deposited in the substrate. The effect of the substrate (i.e., property mismatch) can be readily included in the stress model. Testing films as deposited avoids the introduction of spurious damage and release of residual stresses during specimen micromachining of free-standing films—it tests the actual system, and not a model. Moreover, several scratch tests can be performed in a single specimen, as long as the spacing between the scratches is large enough so that they do not interfere with each other. From the experimental point of view, scratching is much easier than conventional methodologies for strength testing.

A further advantage of the scratch test is that it allows the influence of surface defects to strength to be assessed independently. Indeed, in a scratch test, fracture typically initiates at the film surface, from localized tensile stress in that region. Thus, defects occurring there are ultimately responsible for failure. This is relevant since defect populations are not necessarily homogenous along the film cross section. Indentation-based methodologies are available in order to assess defect populations at the film/substrate interface [65]. The combination of both types of tests provides an alternative for characterization of defect populations in thin films, albeit indirectly, as shown schematically in Figure 9.35.

As mentioned earlier, the practical applicability of the scratch test to measure fracture strength of brittle layers relies on finding a suitable film/substrate combination, one in which the first failure mode corresponds to brittle fracture of the coating at the trailing edge. The preferred fracture mode is partial cone cracking, which can be achieved relatively easily by using elastic, stiff substrates. This is the case, for example, with micrometric thickness DLC, amorphous SiC, and TiO_2 films on glass substrates (see Figures 9.15 and 9.20 in Sections 9.3.2 and 9.3.3). The procedure for strength measurement in these systems by means of scratch testing is outlined as follows.

First of all, a statistically significant number of scratch experiments at progressively increasing load are conducted, no less than 25–30. A maximum normal load of 20 N is typically sufficient to induce film fracture in purely brittle materials with the standardized scratch equipment—in plastic systems, higher loads are required. After testing, optical microscopy examination of the scratches and analysis of the calibrated images are carried out. This allows for the determination of the critical (i.e., lowest) load for fracture in each scratch, using Equation 9.4. For fracture strength assessment, the critical load values need to be converted into strength values. This requires simulation of the stress state in the system as a function of the applied normal load, the coefficient of friction, and materials properties (elastic). Specifically,

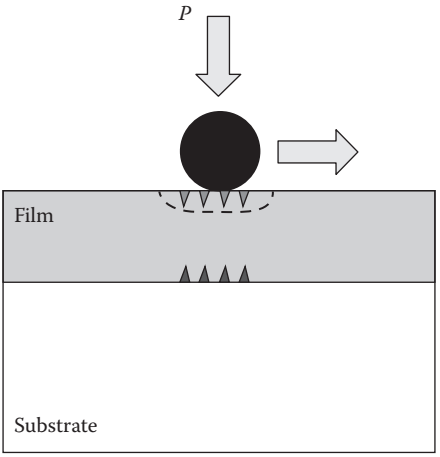


FIGURE 9.35 Schematic of a model-coated system (cross section) under a combination of normal (vertical arrow) and lateral (horizontal arrow) contact forces. If the substrate is relatively compliant, uniaxial normal contact induces film bending and thus probes defects at the interface. Upon sliding, the maximum tensile stress moves toward the film surface, behind the trailing edge, which probes defects in that region (circled).

since partial cone cracks originate at the trailing edge of the contact, for a given load value the fracture strength is taken as the maximum tensile stress in that region. As mentioned in Section 9.3.3, if residual stresses are present, the net σ_{max} value on the surface can be obtained by superimposing their value to the contact stress. For sufficiently thick films, the effect of the substrate could be neglected, and the analytical solution by Hamilton and Goodman (Equation 9.5) may be used, as has been done by a number of authors [25,66]. However, in general, the effect of the substrate needs to be considered in the stress model, as discussed in Section 9.3.1.2.

In the example of a DLC film on glass (Figure 9.15), a normal load of 15.6 N and a coefficient of friction of 0.07 (measured experimentally) result in a fracture strength value of 1.38 GPa, calculated using the commercially available software package Elastica—the residual stress in the film were input into the simulation, thus obtaining the intrinsic strength value of the film. If the analytical solution by Diao et al. is used (Equation 9.8), taking $\beta \approx 0.3$ as a rough approximation, and estimating the Hertzian radius from the optical micrograph in Figure 9.15, a value of 1.3 GPa is obtained. The agreement between the two calculations is quite reasonable, but shows that comparison between different systems should only be made when the stress data have been obtained using the same procedure. In this context, the most accurate estimations of contact stress in coated systems are achieved by FE simulations, which can be calibrated against the experimental data (i.e., by fitting to the load–displacement curves).

By conducting the procedure described above for all the scratches in the specimen, the values for the fracture strength distribution, resulting from the stochastics in defect population, are readily obtained. The actual form of the strength distribution is unknown, but an empirical Weibull function [62] is often employed. The

Weibull model of brittle fracture considers the specimen as the product of individual volume elements, and makes a "weakest link" assumption, meaning that failure of the weakest element results in failure of the whole specimen. This evolves into an exponential function for the probability of survival of the elements, which can be integrated over the total volume (V) of the specimen, giving the following three-parameter distribution function:

$$P_f = 1 - \exp\left[-\int_V \left(\frac{\sigma - \sigma_{\min}}{\sigma_0}\right)^m dV\right] \tag{9.13}$$

P_f is the probability of failure of the specimen at the applied stress σ; and the parameters m, σ_0, and $\sigma_{\min}$ are material properties termed, respectively, Weibull modulus (shape parameter), characteristic strength (scale parameter), and minimum strength (below which no failures will occur). The minimum strength is usually assumed to be equal to zero, which results in a two-parameter distribution. For a given loading geometry, Equation 9.13 can be integrated, giving a simpler expression:

$$P_f = 1 - \exp\left(-\frac{\sigma}{\sigma^*}\right)^m \tag{9.14}$$

The parameter σ^* is the characteristic strength in the geometry under consideration. It is related to σ_0 and to the volume of the specimen under tensile stress, which gives rise to size effects, as will be discussed at the end of the section.

For representation of the strength distribution, a probability of failure is assigned to each strength value, typically by ranking the experimental values from lowest to highest, and using $P_f(\sigma_F^i) = (i - 0.5)/N$, $i = 1, \ldots, N$, being N the total number of measured strength values. According to Equation 9.14, plotting $\ln(\ln(1/1 - P_f))$ *versus* $\ln(\sigma_F)$ allows estimation of the Weibull parameters by fitting a straight line to the experimental data—the slope gives the modulus, and the characteristic strength can be obtained from the intercept. The Weibull plots of amorphous SiC, TiO_2, and DLC films on glass obtained in this way are shown in Figure 9.36. Characteristic strength values of 2, 1.28, and 1.25 GPa (including residual stress in the simulations); and Weibull moduli of 14.9, 4.3, and 6.2 were obtained for SiC, TiO_2, and DLC, respectively [7]. These values are within the expected range for ceramic materials, according to conventional strength tests—of course, values obtained from different test methods cannot be directly compared [21]. In the context of fracture mechanics, the higher strength and reliability of the SiC film can be attributed to the presence of a narrower distribution of smaller surface defects in that film. Moreover, considering the scarce experimental data available in the literature, crystalline thin films have been reported to result in higher scratch strength values than amorphous films of the same composition. This was demonstrated in micrometer thick TiO_2 films, where high compressive stresses in the crystalline structures (rutile and anatase) were deemed responsible for their superior fracture strength, a factor 1.6–1.8 larger than the strength of their amorphous counterpart [49].

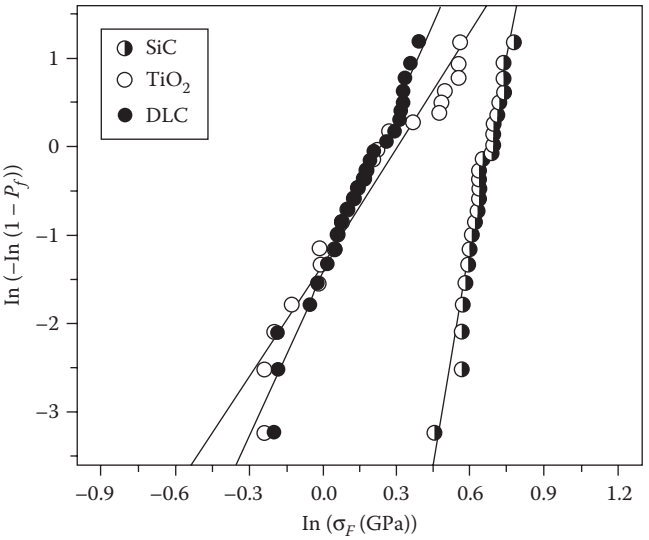


FIGURE 9.36 Weibull plot (probability of failure, P_f, *vs.* strength, σ_F) for DLC (thickness 1 μm), SiC (thickness 1.2 μm) and TiO_2 (thickness 0.7 μm) films. The points correspond to experimental data obtained from scratch tests of the coatings as deposited on soda-lime glass substrates. On each sample, 25 different experimental points were considered. The solid lines are the best linear fits to the experimental data. (From Borrero-Lopez O. et al., *Thin Solid Films*, 2010;518:4911.)

The significance of Weibull plots of fracture strength is that they provide essential information for the reliable design of brittle components by indicating the stress interval within which materials can be safely used. The safety limits, however, should be extrapolated with care from simple laboratory conditions to complicated stress configurations and different component sizes in practice. The conversion is done by calculating loading factors, which inform about the volume of the material under the maximum tensile stress (for uniaxial tension, the loading factor is 1). Moreover, real multiaxial stress fields are expected to result in a larger fraction of defects that are favorably oriented for propagation compared to uniaxial stress states, which can result in failure at lower loads than predicted from laboratory tests [21].

Particular attention must be paid to the size of the indenter used in the scratch test, due to the occurrence of size effects. Size effects are one of the most important consequences of the statistical nature of brittle fracture, and are well established in the case of conventional strength testing by tensile and flexure testing [21]. As anticipated in Section 9.3.5, in a scratch test, since the size of the stress field scales with the contact area, the radius of the indenter determines the volume of the sample that is subjected to the maximum tensile stress (at the trailing edge). Given that the probability of finding a critical defect increases with increasing the size of the probed region, it is to be expected that larger indenters result in lower values of fracture strength.

It is important to note that, because small contact radii are also more likely to induce a plastic response instead of cracking (see Figure 9.33), it is not always

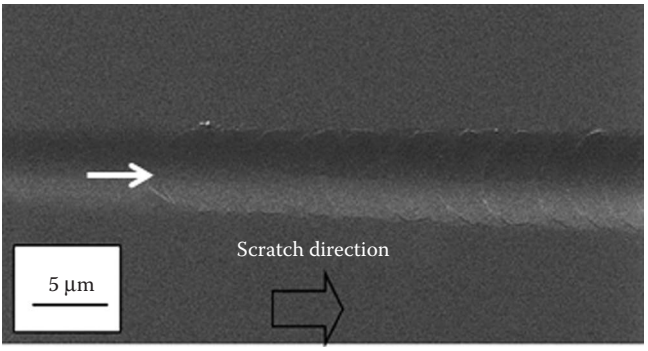


FIGURE 9.37 Partial ring cracks upon sliding contact (tip radius 5 μm) of a DLC film (thickness 1 μm) on a soda-lime glass substrate. The white arrow indicates the first crack observed on the surface, which was used to estimate the fracture strength of the film (from the calculated critical load value).

possible to measure fracture strength using small tips. One system in which it was possible to investigate size effects is the DLC film on a glass substrate analyzed earlier ($\sigma^* = 1.25$ GPa, $m = 6.2$ with a 200 μm indenter). When microscratch tests are performed with a 5 μm tip, partial cone cracks are observed to be the dominant fracture mechanism (Figure 9.37), which allows comparison with the results obtained from macroscratch tests. In particular, from the microscratch tests, a characteristic strength of 2.3 GPa is obtained (almost double as in the macroscratch case).

The scratch test has some advantages for investigations of size effects. First, sample preparation and test procedures are significantly simpler than in conventionally employed uniaxial tension of dog-bone specimens. In addition, because the volume under the maximum tensile stress increases with increasing the contact area, scratch tests with different radii allow defect populations at different regions of the film to be sampled, that is, closer to surface or more toward the bulk of the films. This is important in many films of technological importance, which are metastable phases obtained from non-equilibrium processes, for example, deposition from a vapor phase, or high energy plasma spraying. In such systems, defect populations and residual stresses are likely not to be homogeneous in the film [44]. The microscratch test is thus ideally suited to indirectly ascertain structural variations, which are otherwise very difficult to pick up via conventional strength testing.

9.4.1.2 Fracture Toughness

The stress approach to fracture allows estimation of the fracture toughness of brittle layers from their fracture strength, by using Equation 9.12 with a suitable Y factor. In particular, in a sliding contact with a blunt indenter, for a favorably oriented defect—that is, perpendicular to the tensile stress, which is more likely to be opened under its action—at the trailing edge of the contact, the Y factor of a through-thickness surface crack in a semiinfinite body, that is, $Y = 1.12\sqrt{\pi}$, can be assumed, as shown schematically in Figure 9.38.

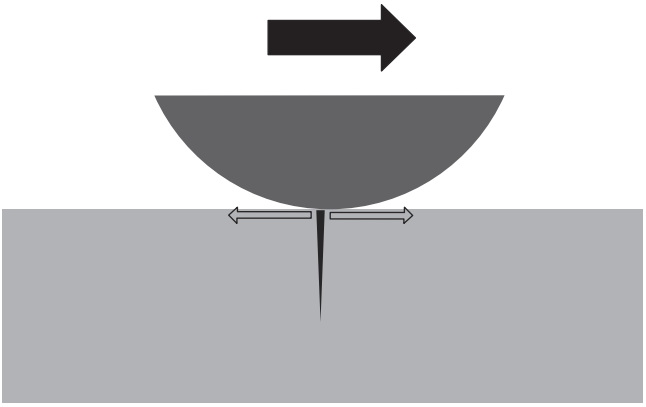


FIGURE 9.38 Schematic (cross section) of a crack-like surface defect favorably oriented upon sliding contact of an elastic, isotropic solid using a spherical indenter. The thin arrows indicate the tensile stresses (directed radially along the contact edge) acting on the defect, at the trailing edge of the contact. The thick arrow indicates the sliding direction.

Estimation of the fracture toughness using Equation 9.12 also requires knowledge of the critical defect size, c, *a priori*. In fracture toughness testing of conventional bulk specimens this step is avoided by prenotching specimens with sharp cracks of known size [21]. This is not directly feasible in scratch tests, where the exact cracking point of the specimen is not known. In the absence of controlled defects, one would need to measure the size of the flaws that are active in actuality. In this context, the most accurate way to determine the critical defect size is by means of *postmortem* fractographic analysis after the strength tests. But again, while fractographic observations are relatively simple in the bulk case after standardized strength testing (uniaxial tensile tests, bending, or biaxial flexure), they are not possible in scratch tests. Indeed, in a tensile/flexure test the specimen typically breaks into few fragments, which allow microscopic inspection of the fracture surfaces in order to locate and characterize the critical defect. This may be time-consuming, especially considering the large number of specimens in strength testing, but nonetheless feasible in most cases. However, in a scratch test the flanks of the cracks remain closed, and unfortunately it is not possible to separate them to inspect the fracture surfaces since the film is adhered to the substrate (i.e., by definition the nature of the failure is cohesive).

Based on the above, one has to assume a defect size in order to estimate the fracture toughness by means of Equation 9.12. Given the nature of the scratch test, where the highest tensile stresses are located at the film surface, a sensible first approximation is to consider that the flaws are proportional to the surface roughness of the film, that is, $c \approx 1\text{–}10R_a$. Surface roughness values can be readily measured by means of profilometry or AFM microscopy. In films deposited from a vapor phase, film roughness tends to mimic that of the substrate, and is typically very low, that is, within the nanometer range. For example, in the amorphous SiC, DLC, and TiO_2 films on glass substrates considered earlier in the section, R_a values of 1.1 nm, 1.4 nm, and 8.8 nm were measured by AFM. Substituting in Equation 9.12, the fracture toughness values

(K_C) of the films are estimated to be 0.13–0.42 MPa·m$^{1/2}$ (SiC), 0.10–0.30 MPa·m$^{1/2}$ (DLC), and 0.24–0.75 MPa·m$^{1/2}$ (SiC), which are within the values typically reported for brittle thin films.

The stress approach may also be applied to systems that are not purely elastic, as long as the contributions of plasticity to stress are taken into account in the stress model. For example, Holmberg et al. [67] estimated the fracture toughness of TiN films on ductile substrates (steel), by simulating the elastic–plastic stress field using FE. A fracture toughness value of 7 MPa·m$^{1/2}$ was obtained for a 2 μm thickness coating by scratching, which compared well with a 7.5 MPa·m$^{1/2}$ value obtained by other authors using four-point bending [68].

An alternative to assuming a critical defect size is to carefully polish specimens, that is, after film deposition, to a known grit size prior to scratching. This is expected to create a homogeneously distributed population of surface defects centered at that size, which can be confirmed by profilometry analysis, and would be the scratch equivalent of a prenotched specimen. The grit size used in the polishing treatment must be small enough to ensure a clear observation of the specimen surface in the optical microscope. Typically, a 1 μm polishing ensures good image quality in a reflected light microscope while introducing defects that are significantly larger than the "natural" flaws in most coatings. Thinner films will require a smaller polishing grit. One of the challenges associated with the introduction of "artificial" defects on the film surface by mechanical polishing is that the process might also modify the film properties (e.g., by releasing residual stresses or introducing impurities) or even detach the film from the substrate in very sensitive cases, or if the applied force during polishing is not carefully controlled.

In the calculation of fracture toughness with specimens polished after deposition, in Equation 9.12, c must be replaced by the final polishing grit, and σ_F by the stress at which the fracture polished specimen is first observed. This failure stress will be lower than the fracture strength, and can be calculated by any of the stress models outlined in Section 9.3.1.2 by substituting the critical load value at which fracture takes place, as measured in the scratch track.

9.4.1.3 Stress Intensity Factor Solutions

The method presented in Section 9.4.1.2 is based on the approximation of a uniform, uniaxial tensile stress (at the trailing edge of the sliding contact) causing fracture (Equation 9.11). While in the case of partial cone cracks and arc-like cracks the approximation is adequate, in actuality the stress intensity factor can be calculated in a more precise way using a variety of methods, which in principle allow calculations of K_C from other fracture modes. Some of these methods (e.g., Green function, weight function) are based on the integration of the stress field along an existing crack of length c, assisted by a function ($h(x,c)$), where x represents the location along the crack, to weight the stress toward its values closest to the tip [21]:

$$K = \int_0^c h(x,c)\sigma(x)dx \tag{9.15}$$

In general, the weight function employed must be derived for a specific crack-component configuration. A typical function used in brittle solids is the Green function, which is proportional to $(c^2–x^2)^{-1/2}$ for the case of a through-thickness crack. If the crack is homogeneously loaded, then $\sigma(x) = \sigma$ = constant, and Equation 9.15 reduces to Equation 9.11.

For the case of scratching, the exact function $\sigma(x)$ for a crack located at the trailing edge of the contact needs to be derived. The complexity of coated systems makes numerical simulations (FE) more appropriate (see Section 9.3.1.2). Subsequent integration of Equation 9.15 then allows analytical expressions of the fracture toughness as a function of the applied load, the dimensions of a well-developed crack and material properties—similar to the well-established toughness assessment by means of uniaxial indentation [20]. Such expressions are best suited to scratch tests at constant load (unlike strength assessment, which is typically undertaken in combination with tests at increasing load). To simplify the analysis, approximations are typically made. Some examples are presented below.

Lawn et al. [32] estimated the stress intensity factor upon sliding contact of a bulk material when the observed fracture mode is that of partial cone cracking, the commonest damage mode in brittle systems. In order to describe partial cone cracks, a tangential friction force can be superposed to the Roesler solution (critical cone depth vs. K) for conventional cone cracks in uniaxial Hertzian contact [69]. The frictional component is accommodated by increasing the applied load and rotating the coordinate system by a certain angle, both proportionally to f. The following expression can be obtained [14]:

$$K_C = \chi \frac{F_N \sqrt{1+f^2}}{(1+(a/c'\cos\alpha))^{3/2}} \frac{1}{(c')^{3/2}} + Z\sigma_r (c')^{1/2} \left(1 + \frac{a}{c'\cos\alpha}\right)^{1/2} \tag{9.16}$$

Here, σ_r is the residual stress in the coating, a is the Hertzian contact radius, c' is the depth of the cone crack generated at the load F_N (constant load scratch test), and α its angle relative to the surface; Z is a crack shape factor [70], and χ is a parameter related to the indenter geometry and materials properties. An analogous expression to Equation 9.16 is conventionally used for estimation of fracture toughness from uniaxial indentation with radial cracks [20]. In particular, for radial cracks in uniaxial Berkovich indentation, it is well-known that the Z and χ parameters take values of 1.26, and $0.016(E/H)^{1/2}$, respectively. However, for partial cone cracks these parameters need to be calibrated specifically, which is quite challenging. Moreover, routine c' and α measurements on the scratch track are complicated, and is certainly not feasible to do a three-dimensional reconstruction of the cracks in all cases. Thus, approximations need to be made. Malzbender et al. [14] have applied Equation 9.16 to thick, particle-filled sol–gel coatings on glass. For this specific system, they approximated a Z factor to 0.52, using the equivalent expression for radial cracks, in combination with experimental observations of the partial cone cracks at the onset of delamination by optical microscopy. In order to fit the toughness values to reference values measured by Berkovich indentation (0.1–0.4 $MPa \cdot m^{1/2}$), a χ factor of 0.011 was determined.

Other stress intensity factor solutions have been proposed for damage modes differing from partial cone cracks, which may appear in systems with some degree of ductility. In particular, for scratching of a bulk material with a conical indenter (radius R, semiangle θ), in which the observed fracture mode is arc-like cracking, Hoehn et al. calculated the stress intensity factor, assuming (i) cracks originated from the bottom (instead of the surface as is the case of purely brittle systems) of the scratch groove opening in mode I, perpendicular to the tensile stress along the sliding direction, and (ii) cracks extending fully across the scratch width [71]. The following expression was derived as a function of the applied load:

$$K_C = \frac{2F_N f}{R^2 \cot\theta}\left(\frac{l}{\pi}\right)^{1/2} \sin^{-1}\frac{R}{l}, \tag{9.17}$$

where $2l$ is the total crack length perpendicular to the sliding axis ($l \geq R$) at the considered load. These simplifications result in an expression that does not directly take into account the material properties, but that allows the fracture toughness to be estimated in a simple way from scratch tests at constant load (F_N), by direct measurements of the cracks within the track.

The expression above was applied to a ductile NiAl free-standing intermetallic (i.e., bulk system), for which crack opening from the bottom of the scratch track was confirmed. In this case, it was noted that the indentation component of the contact would have an opposite effect to the trailing stress. Thus, a "zeroth-order" correction was applied by subtracting a uniaxial indentation K factor [20] from Equation 9.17. In this way, a fracture toughness value of 5.95 MPa·m$^{1/2}$ was obtained, which agreed relatively well with reference values obtained by other methods.

Veldkamp et al. [72] have derived an expression for the scratch toughness of a bulk material in which the fracture mode consists of cracks extending from the edge of the scratch track, at an angle from the sliding direction (see Figures 9.33 and 9.39). As mentioned in Section 9.3.5, such cracks are not one of the main fracture modes on sliding of brittle systems, but may appear in elastic/plastic systems when sharper tips are employed or in the more ductile systems. For sliding of a conical tip of semiangle θ, the following expression was derived for the stress intensity factor as a function of the applied load:

$$K_C = \frac{AF_N \cot g\theta}{\sqrt{d^2(d - Bd_p)}} \tag{9.18}$$

where d is the half-width of the crack, d_p is the half-width of the groove, and A and B are constants. As in the previous expression, Equation 9.18 does not directly include materials properties, which could be introduced by adjusting the constants.

Akono et al. [17] considered the case in which the failure mode is subsurface lateral cracking, originated at the bottom of the indenter tip and extending parallel to the surface (see Figure 9.40). As with the previous case, this fracture mode is more likely to appear in systems with a higher degree of ductility and with smaller/sharper

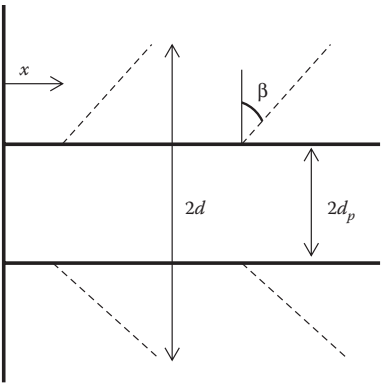


FIGURE 9.39 Schematic of a scratch track, from above. The sliding direction (horizontal) is indicated as x. The angle of the cracks (dashed lines) from the vertical line is β, and the magnitudes d and d_p are the half-widths of the crack and the groove, respectively. (Adapted from Veldkamp JDB, Hattu N, and Snijders VACS, *Flaws and Testing*, vol. 3. 1978. p.273.)

indenters. The following expressions were derived as a function of the lateral force (F_L), for scratching with conical (semiangle θ) and spherical probes, respectively:

$$K_C \propto \frac{\cos\theta}{h^{3/2}\left[\sin\theta\right]^{1/2}} F_L \tag{9.19}$$

$$K_C \propto \frac{1}{h^{3/2}} F_L \tag{9.20}$$

where h is the penetration depth (Figure 9.40). As mentioned in Section 9.2.1, in the study of fracture of hard materials such as ceramics, penetration depths are

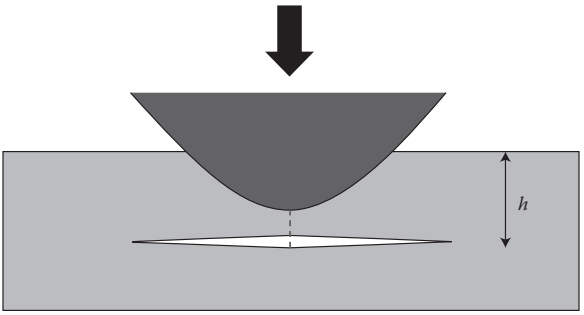


FIGURE 9.40 Schematic of the formation of lateral cracks, extending parallel to the surface upon scratching of a material with elastic–plastic behavior using a conical tip (with spherical end). The vertical arrow represents the normal loading direction. The sliding direction is perpendicular to the represented surface. Not at scale. (Replotted from Akono AT, Randall NX, and Ulm FJ. *Journal of Materials Research*, 2012;27:485.)

low and the tests take place in the spherical part of the standardized Rockwell tip. While Equations 9.19 and 9.20 are not directly dependent on materials properties, they are to be calibrated in comparison with experimental F_L versus h curves, which takes into account the materials response. This method was applied to polymeric and metallic materials likely to undergo subsurface cracking emanating from the bottom of tip, as well as to some glass ceramics. The calculated K_C values agree reasonably well with reference values from the literature, for both brittle and ductile materials.

It is important to note that in the derivation of Equations 9.16 through 9.20, a single-layer was assumed, that is, a bulk material. Thus, strictly, such expressions cannot be applied to coated systems. This is because the substrate significantly disrupts the stress field on the film cracks $\sigma(x)$ in Equation 9.15. For example, Malzbender and de With [73] have reported relatively large size effects by using Equation 9.18 in hybrid, organic–inorganic coatings (thickness is between 0.5 and 4 μm) on glass. In particular, they found that the measured K_C increased significantly with increasing the tip radius, which was attributed to increasing energy dissipation by plastic deformation of the underlying substrate as the probe size increases and the contact stress reaches deeper into it. However, it could be justified to use stress intensity factor solutions in coated systems, as an approximation in certain cases. For example, in those systems in which detection of critical loads at first failure is challenging, as is the case with subsurface fracture modes. The approximation will work better for thicker coatings where substrate effects are less pronounced.

9.4.2 Energy Approach

Fracture toughness can be related to the amount of energy dissipated during crack propagation (G). For propagation in equilibrium conditions, the relationship is through the following expression [20]:

$$G_C = \frac{K_C^2(1-\upsilon^2)}{E} \tag{9.21}$$

In a scratch experiment, the work done by the tip can be approximated by integrating the normal load *vs.* displacement, that is, the F_N–h curve. This is because the contribution by the lateral force is usually much smaller than that of the normal force (the coefficient of friction is typically lower than 1), and thus can be neglected [74]. Part of the work is converted into elastic energy (reversible), and the rest is irreversibly dissipated into plastic and fracture energies, and also heat. The irreversibly dissipated energy can be estimated from the area between the loading and unloading curves. Moreover, in those specific cases where a cracking event leaves a distinguishable mark in the F_N–h curve, the fracture energy ($U_{fracture}$) can be calculated indirectly.

Of all the possible fracture modes, chipping cracks (Section 3.2; Figure 9.18) are most likely to result in detectable pop-in marks in the F_N–h curve, due to the

additional penetration of the tip upon cracking at a given load, and are best suited for toughness estimations. Moreover, chipping cracks originate at the interface and extend toward the surface, thus probing the response of the coating to crack extension through its entire thickness. For a chipping crack of size L (see Figure 9.41), the fracture toughness can then be calculated as a function of coating thickness (t) and elastic properties (E_C, υ_C) through the following equation [14]:

$$K_{IC} = \left[\frac{E_C U_{fracture}^{chipping}}{(1 - \upsilon_C^2)\pi t L} \right]^{1/2} \tag{9.22}$$

When the crack does not propagate normally to the coating, but instead forms an angle δ, the thickness may be replaced by an effective thickness (t'), which is simply t divided by sin δ.

On estimating $U_{fracture}^{chipping}$ from F_N–h curves, a function form needs to be assumed. In the simplest case, it can be taken $F_N \sim h^2$. In experiments undertaken in load-control mode, anticipating a fully elastic, or a fully plastic behavior, $U_{fracture}^{chipping}$ can be calculated, respectively, from

$$U_{fracture}^{chipping} = \frac{2}{3} F_{N,C}(h_{Cf} - h_{Ci}) \tag{9.23}$$

$$U_{fracture}^{chipping} = F_{N,C}(h_{Cf} - h_{Ci}) \tag{9.24}$$

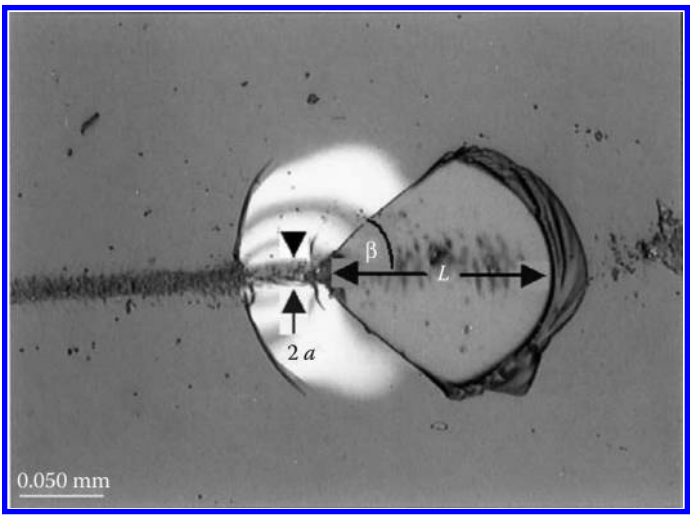


FIGURE 9.41 Optical micrograph showing chipping upon scratching (tip radius 150 μm) of a sol–gel coating (thickness 2 μm) on a glass substrate. (From Malzbender J. et al., *Materials Science & Engineering R-Reports*, 2002;36:47.)

where $F_{N,C}$ is the critical load at which cracking takes place, and h_{Ci} and h_{Cf} are the critical tip displacements at the beginning and the end of the F_N–h step related to chipping (see Figure 9.42). In practice, the actual $U_{fracture}^{chipping}$ values lie in between the values provided by Equation 9.23 and Equation 9.24, in the more general case of elastic–plastic behavior.

The above method has been applied to measure the fracture toughness of particle-filled sol–gel coatings (thicknesses about 10 μm, i.e., quite thick) on glass, as a function of particle fraction [14]. Values in the range $0.2 \le K_C$ (MPa·m$^{1/2}$) ≤ 0.4 were obtained, which increased with increasing the fraction of filling particles in between 0 and 0.7. Moreover, the values were quite similar to those obtained by uniaxial indentation (by using both energy and stress methods). However, it was observed that K_C estimated by Equation 9.23 was somewhat higher than what was obtained by the other methods, despite being intended as a lower limit. This brings into question the simplistic assumptions of a $F_N \sim h^2$ loading curve on scratching, and of purely elastic behavior, as well as the neglect of the lateral force. Indeed, in practice other mechanisms for energy dissipation take place in addition to chipping fracture. In particular, buckling ahead of the indenter was indicated as the most likely mechanism for

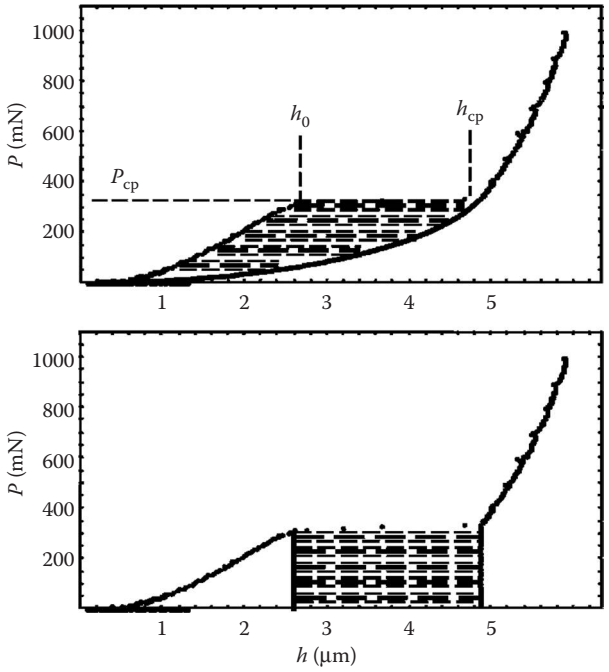


FIGURE 9.42 Load (P)–displacement (h) curves obtained from scratching (tip radius 150 μm) of a sol–gel coating (thickness 11 μm) on a glass substrate. The large step is originated by chipping of the coating (as in Figure 9.41). The shaded areas in the left-hand side and right-hand side curves correspond to the energy assuming elastic and plastic deformation of the system, respectively. (From Malzbender J. et al., *Materials Science & Engineering R-Reports*, 2002;36:47.)

additional tip penetration on scratching of the sol–gel films on glass. Other possibilities may include plastic deformation of the coating and/or substrate, interfacial detachment, or friction. Despite these considerations, the similarities between the values obtained by scratching and the more common uniaxial indentation methods confirm the feasibility of using the former at the quantitative level.

A similar method was proposed by Li and Bhushan initially for uniaxial indentation [19,75], which can also be applied to scratch tests if one neglects the contribution (for low values) of the coefficient of friction. In this method, Equation 9.22 is also used to calculate the fracture toughness, but $U_{fracture}^{chipping}$ is estimated differently. In particular, the F_N–h curve is extrapolated at the discontinuity site associated with fracture, as shown in Figure 9.43. The fracture energy in chipping is then approximated by the difference between the extrapolated and the recorded curves, that is, the area ABC in Figure 9.43. Malzbender et al. [14] argued that the dissipated energy is in actuality given by the area OAB in Figure 9.43, and thus, this method provides only a lower limit for the fracture toughness (analogous to Equation 9.23).

As mentioned previously, fracture toughness assessment by energy methods typically require systems with discontinuities or pop-in marks in the F_N–h curves. Nevertheless, estimations could also be possible in cases where no features are visible in the scratch curves; for example, by applying the method proposed by Chen and Bull for uniaxial indentation [76]. This method is based on the simulation of an imaginary F_N–h curve, obtained by averaging the effect of a crack on the deformation during loading. The fracture toughness can be related to the difference between the imaginary and the actual F_N–h curves, but in the case of scratch fracture simulation of the imaginary curve it is expected to be somewhat more complex, due to the presence of lateral forces.

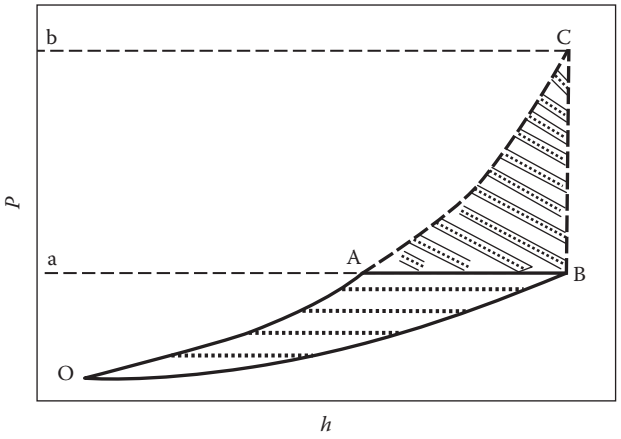


FIGURE 9.43 Schematic load (P)–displacement (h) plot for the estimation of the energy $U_{fracture}^{chipping}$ using the methods by Li and Bhushan (area ABC) and the purely elastic loading case (area OAB). (From Malzbender J. et al., *Materials Science & Engineering R-Reports*, 2002;36:47.)

From the practical point of view, the stress approach has some advantages. One is that, once it is confirmed that the discontinuity in the F_N–h curve corresponds to a given cracking mode (e.g., chipping), the subsequent observation and microscopy measurements in the scratch track are very simple. Another advantage is that substrate effects are not significant as the F_N–h curve is the combined response of the coating and the substrate. As long as pop-ins take place, using different substrates should lead to different L, $F_{N,C}$, h_{Cf}, and h_{Ci} values, but to an essentially similar amount of energy dissipated by the coating, and thus fracture toughness value.

Finally, it is also worth noting that, although accurate F_N–h curves can easily be obtained in standardized scratch testers, the high sensitivity required in order to detect small-scale fracture events (often in micrometric and submicrometric coatings) through discontinuities or pop-ins makes micro- and nanoscratch experiments more suitable for toughness assessment via the energy approach.

9.4.3 Semiquantitative Approach

A critical step in the method presented in Sections 9.4.1.1 and 9.4.1.2 for strength and toughness analysis is the simulation of the stress state (best by FE) at the contact, in order to relate critical loads to stress values. The complexity of the contact stress state in scratching and the property mismatch at the coating/substrate interface can make this step time-consuming. Moreover, the occurrence of plastic deformation in some systems further complicates the stress field. One way to make the scratch test more practical in order to quickly assess fracture properties of films is simply to measure the critical loads at which cracking is observed on the film surface [7,49,57,77–82]. This is, to use the scratch test at a qualitative, or semiquantitatve level, mainly to compare materials tested under the same conditions, in order to gain information relatively quickly about the strength and toughness of coatings and thin films, as is done with the assessment of adhesion strength (Section 9.2).

For the purpose of semiquantitative assessment of strength, researchers have employed the critical load at which first cracking takes place, $F_{N,C}$. In principle, higher critical loads would be indicative of a higher resistance to crack initiation. Although the critical load is clearly not equal to the fracture strength, it allows the comparison at the qualitative, or semiquantitative, level of films tested under similar (preferably identical) conditions. As noted earlier, using the standard Rockwell tip (200 μm), conventional brittle coatings fracture at moderate normal loads, below 20 N, for example, SiC, TiO_2, DLC, or CrN [7,49,77,83]. In this context, it has been shown that the critical load of ceramic-based coatings can be increased by engineering the structure with additions of more ductile phases. For example, Voevodin et al. [77] have reported critical loads of up to 40 N in composite DLC coatings with Ti additions (columnar structure; thickness ~3 μm) on steel.

Nanocomposite microstructure, with ceramic nanocrystals embedded in a ductile amorphous matrix, has also been anticipated to have a high resistance to cracking. One type of such microstructure with outstanding performance is the so-called "chameleon" structure (i.e., able to change reversibly upon contact), based on hard carbide nanocrystals embedded in an amorphous, low-friction DLC phase. Voevodin

and Zabinski [79] have reported critical loads as high as 60 N and 70 N for WC/DLC and TiC/DLC nanocomposite films (0.5 μm) on steel.

It is important to note that the effect of residual stress, which can be readily computed in the FE simulations of the stress state (or subsequently added/subtracted from critical stress values obtained in the simulations), needs to be dealt with differently in the assessment of scratch fracture at the semiquantitative level. Indeed, residual stresses in a coating do affect its critical load. In particular, compressive and tensile residual stresses require higher and lower loads for crack opening, respectively. There is no simple solution to obtain the intrinsic critical load of the film, independent of residual stress. Ligot et al. [84] have used a multipass scratch test, in which scratches are performed in the same position/track until the critical load value does not vary between the *i*-th pass and the following. For submicron W films on polymeric substrates, 5–6 passes were sufficient to achieve a stable critical load value (~3–5 N, depending on film thickness). However, as the residual stress is released with each additional pass, new defects (i.e., extrinsic) are also being created. For this reason, the critical load values obtained by this method cannot be considered as intrinsic either.

In addition to assessing resistance to crack initiation, scratch tests at the semiqualitative level can inform about fracture reliability, which requires statistical analysis. In particular, higher values of the Weibull modulus indicate a narrower, better defined, interval of the scratch loads that induce cracking. This information is very important for the machining of brittle materials. Indeed, the commonest cutting mechanism is abrasion, which often has the undesirable byproduct of strength-degrading cracks. In order to remove machining cracks, subsequent surface treatments are employed; for example, mechanical polishing. In this context, knowledge of the reliability, that is, interval of loads that are less likely to generate cracks, is of great help in order to select cutting parameters that could avoid (or at least minimize) subsequent polishing.

One relevant example is that of single-crystal silicon. As mentioned in Section 9.3.4, the structural anisotropy of this material affects the crack shape, depending on the orientation of the cleavage planes relative to the wafer surface and the sliding direction. In addition, there is a marked effect in the critical load at which fracture takes place. This is because a given set of normal and lateral forces on scratching are resolved differently in the different cleavage planes, depending on their intersection (i.e., angle) with the surface. Moreover, energy dissipation by phase transformation (brittle to ductile) is more likely to occur when scratching is performed along certain directions, which adds to the variability.

Vodenitcharova et al. [57] have analyzed the reliability of single-crystal silicon by performing scratch tests along the most relevant directions in {100} and {111} wafer surfaces (Figure 9.44). It was found that the variability of critical loads for first fracture was higher along the {100}<110> and {111}<112> directions (i.e., lower *m*) than along {100}<100> and {111}<110> directions (i.e., higher *m*). This means that in the {100}<110> and {111}<112> directions, high scratch loads result in a lower probability of failure. But at the same time, a low *m* means that even at low loads, there is a finite probability of cracking. On the contrary, {100}<100> and {111}<110> directions require higher loads for crack initiation, and are thus considered stronger

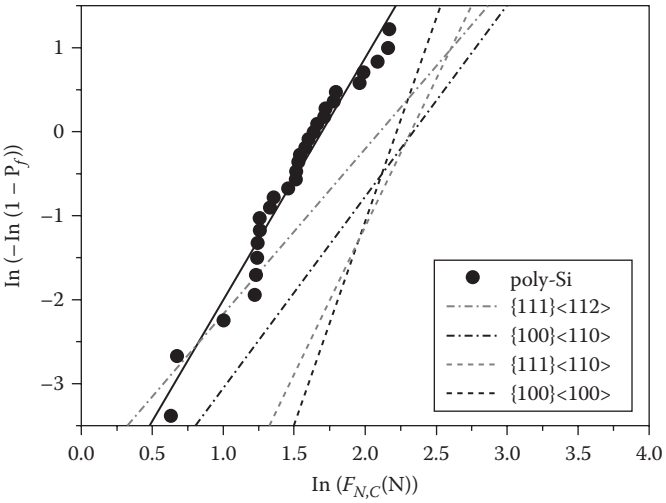


FIGURE 9.44 Weibull plot (probability of failure, P_f, vs. failure load, F_C) for scratching of silicon: broken lines represent the best fits to the experimental data obtained from scratching along relevant directions of single-crystal silicon. Symbols correspond to experimental data in polycrystalline silicon, and the solid line is the best linear fit to the poly-Si data. (From Borrero-Lopez O. et al., Submitted, 2014.)

directions, preferred for safer machining. Underlying the higher variability of the {100}<110> and {111}<112> directions is the increased probability of phase transformation when sliding is conducted along those directions—for a given applied load, the resulting hydrostatic stress is higher, as a result of the structural anisotropy.

More recently, Borrero-Lopez et al. [82] have investigated the scratching reliability in the special case of large-grained polycrystalline silicon wafers (thickness 200 μm), the functional unit in many commercially available solar cells. It was obtained that the Weibull modulus in the polycrystalline case was the average of the relevant directions in the single-crystal case (Figure 9.44). While grain boundaries were not identified as the main cause of crack initiation, they were observed to increase the extent of already initiated damage, and thus the recommendation for safer machining was to cut along those ingot directions where the largest grains may be present, or alternatively to use smaller tools in order to achieve a higher degree of plastic deformation, but taking into account the considerations discussed at the end of Section 9.3.5 in order to avoid secondary cracking.

In order to gain semiquantitative information about toughness, that is, resistance to crack propagation, the difference between the loads for initial and final cracking (i.e., damage resulting in the complete peel off of the coating) should be considered instead. Based on this idea, Zhang et al. [81] have defined a "scratch crack propagation resistance" (CPR) as follows:

$$CPR = F_{N,C1}(F_{N,C2} - F_{N,C1}) \tag{9.25}$$

where $F_{N,C1}$ is the load (normal) for first cracking, or "lower critical load," and $F_{N,C2}$ is the load at which delamination/chipping takes place, or "higher critical load." In Equation 9.25, the difference between the critical loads is multiplied by $F_{N,C1}$ to account for the contribution to toughness arising from the resistance to crack initiation. Equation 9.25 has been applied in order to assess grain size and intergranular phase effects on the mechanical properties of submicron nanocomposite TiN-SiN_x films, by means of microscratch tests ($r = 15$ μm) [81]. The method clearly suffices for such comparative purposes, and is able to provide quick and useful information in order to identify processing conditions that result in the best performance.

It is worth noting that, unless the thickness is sufficiently large, comparative analysis of CPR should only be made between coatings/films on the same substrate and surface roughness/surface condition. This is because the substrate and roughness have marked effects on the stress field and the surface defects, respectively, and thus on the attendant fracture modes and critical loads [58]. Moreover, semiquantitative assessment of fracture toughness is ideally to be used in combination with cross-sectional examination e.g., by FIB) of selected scratches to ensure that chipping or through-thickness cracking is related to propagation of cracks initiated in the film. While this is indeed the commonest case in brittle films, in some cases, particularly when using highly brittle substrates, delamination can have its origin in fracture events in the latter.

9.5 CONCLUDING REMARKS

1. Sliding with a blunt tool results in a complex contact stress field, which can be simplified by considering a maximum tensile stress (most relevant to fracture) located on the surface, at the trailing edge of the contact, due to the frictional force, and a maximum shear stress (most relevant to plastic deformation) below the surface and ahead of the normal loading axis.
2. Scratching of brittle coated systems at progressively increasing loads results in a variety of initial fracture modes (i.e., cohesive failure), depending mainly on film and substrate properties and contact parameters. For brittle coatings on brittle substrates, tensile cracks initiated at the trailing edge of the contact (including partial cone and arc-like cracks), are the most common. When ductile substrates are employed, buckling cracks ahead of the contact are in the dominant mode. Crack geometry is ultimately controlled by the coefficient of friction, residual stress, and material structure.
3. Substrate and contact size affect the occurring damage modes and the critical loads upon sliding contact. In particular, larger tips result in larger regions under maximum tensile stress, which make it more likely to encounter critical defects for fracture. Decreasing the contact size makes it more likely to increase the extent of plasticity, which may result in additional quasiplastic damage modes.
4. Cohesive, brittle failure modes allow scratch tests to be used beyond their commonest use of adhesion strength assessment. In particular, fracture properties (strength, toughness) of brittle coatings and films can be assessed both at the quantitative and at semiquantitative levels.

5. Quantitative assessment of fracture strength can be undertaken from tests at progressive load using a stress-based approach, which requires: (i) a controlled, brittle failure mode, that is, tensile cracks at the trailing edge of the contact; and (ii) detailed knowledge of the contact stress state as a function of the applied load, via analytical or FE models. Fracture toughness can be subsequently estimated by using fracture mechanics and assuming a *Y* factor for the critical defects.
6. Quantitative assessment of fracture toughness can be undertaken from tests at constant load (sufficiently high to induce cracking) using a stress-based approach, based on calculation of the stress intensity factor assuming a given failure mode as a function of the applied load and crack geometry.
7. Quantitative assessment of fracture toughness can be undertaken from tests at progressive load using an energy-based approach, by calculating energy dissipated in crack propagation from discontinuities in load–displacement curves in selected substrate–film combinations that induce delamination cracks.
8. Semiquantitative assessment of fracture strength can be undertaken from tests at progressive load, by comparing critical loads for initial cracking from test conducted in identical conditions. For fracture toughness, semiquantitative assessment can be achieved from the relative difference between the critical loads for initial and final cracking.
9. Quantitative assessment by the energy-based approach (when possible) and by the stress-based approach are best suited to thin films and coatings, as they take into account the contribution of substrate properties to the stress field.

REFERENCES

1. Zhang XT, Fujishima A, Jin M, Emeline AV, and Murakami T. Double-layered TiO_2–SiO_2 nanostructured films with self-cleaning and antireflective properties. *Journal of Physical Chemistry B*, 2006;110:25142.
2. Wang DF, and Kato K. Tribological evaluation of carbon coatings with and without nitrogen incorporation applicable to MicroElectroMechanical systems. *Sensors and Actuators a-Physical*, 2001;93:251.
3. Aberle AG. Surface passivation of crystalline silicon solar cells: A review. *Progress in Photovoltaics*, 2000;8:473.
4. Chung K, Lee CH, and Yi GC. Transferable GaN layers grown on ZnO-coated graphene layers for optoelectronic devices. *Science*, 2010;330:655.
5. Dubois MA, and Muralt P. Properties of aluminum nitride thin films for piezoelectric transducers and microwave filter applications. *Applied Physics Letters*, 1999;74:3032.
6. A.s.f.t.a. materials, Standard test method for adhesion strength and mechanical failure modes of ceramic coatings by quantitative single point scratch testing. Standard ASTM C1624-05, Vol. 15.01 *Refractories, Activated Carbon; Advanced Ceramics*. ASTM International, 2005. DOI no.: 10.1520/C1624-05R10.
7. Borrero-Lopez O, Hoffman M, and Bendavid A, Martin PJ. The use of the scratch test to measure the fracture strength of brittle thin films. *Thin Solid Films*, 2010;518:4911.
8. Bull SJ. Failure modes in scratch adhesion testing. *Surface & Coatings Technology* 1991;50:25.
9. Bull SJ. Failure mode maps in the thin film scratch adhesion test. *Tribology International* 1997;30:491.

10. Bull SJ, and Berasetegui EG. An overview of the potential of quantitative coating adhesion measurement by scratch. *Tribology International*, 2006;39:99.
11. Benjamin P, and Weaver C. Measurement of adhesion of thin films. *Proceedings of the Royal Society of London Series a-Mathematical and Physical Sciences*, 1960;254:163.
12. Evans HE. Modeling oxide spallation. *Materials at High Temperatures*, 1994;12:219.
13. Tabor D. *The Hardness of Metals*. Oxford, UK: Oxford University Press, 1951.
14. Malzbender J, den Toonder JMJ, Balkenende AR, and de With G. Measuring mechanical properties of coatings: A methodology applied to nano-particle-filled sol-gel coatings on glass. *Materials Science & Engineering R-Reports*, 2002;36:47.
15. Bull SJ. Can scratch testing be used as a model for the abrasive wear of hard coatings? *Wear*, 1999;233:412.
16. Fischer-Cripps AC. *Nanoindentation*. New York: Springer, 2004.
17. Akono AT, Randall NX, and Ulm FJ. Experimental determination of the fracture toughness via microscratch tests: Application to polymers, ceramics, and metals. *Journal of Materials Research*, 2012;27:485.
18. Scott WW, and Bhushan B. Corrosion and wear studies of uncoated and ultra-thin DLC coated magnetic tape-write heads and magnetic tapes. *Wear*, 2000;243:31.
19. Bhushan B, and Li XD. Nanomechanical characterisation of solid surfaces and thin films. *International Materials Reviews*, 2003;48:125.
20. Lawn BR. *Fracture of Brittle Solids*. Cambridge,UK: Cambridge University Press, 1993.
21. Green DJ. *An Introduction to the Mechanical Properties of Ceramics*. Cambridge, UK: Cambridge University Press, 1998.
22. Panjan P, Cekada M, and Navinsek B. A new experimental method for studying the cracking behaviour of PVD multilayer coatings. *Surface & Coatings Technology* 2003;174:55.
23. Cairney JM, Munroe PR, and Hoffman M. The application of focused ion beam technology to the characterization of coatings. *Surface & Coatings Technology* 2005;198:165.
24. Xie ZH, Munroe PR, McGrouther D, Singh RK, Hoffman M, Bendavid A, Martin PJ, and Yew S. Three-dimensional study of indentation-induced cracks in an amorphous carbon coating on a steel substrate. *Journal of Materials Research*, 2006;21:2600.
25. Wow C, Munroe PR, Xie ZH, Zhou ZF, and Li KY. Three-dimensional visualization of scratch-induced subsurface damage in TiSiN/TiN multilayer coating using focused ion beam-scanning electron microscopic tomography technique. *Journal of the American Ceramic Society*, 2011;94:1598.
26. Lawn BR. Indentation of ceramics with spheres: A century after Hertz. *Journal of the American Ceramic Society*, 1998;81:1977.
27. Chai H, and Lawn BR. Fracture mode transitions in brittle coatings on compliant substrates as a function of thickness. *Journal of Materials Research* 2004;19:1752.
28. Hamilton GM, and Goodman LE. Stress field created by a circular sliding contact. *Journal of Applied Mechanics*, 1966;33:371.
29. Lawn BR. Partial cone crack formation in a brittle material loaded with a sliding spherical indenter. *Proceedings of the Royal Society of London Series a-Mathematical and Physical Sciences*, 1967;299:307.
30. Leu HJ, and Scattergood RO. Sliding contact fracture on glass and silicon. *Journal of Materials Science*, 1988;23:3006.
31. Borrero-Lopez O, Vodenitcharova T, and Hoffman M. Anisotropy effects on the reliability of single-crystal silicon. *Scripta Materialia*, 2010;63:997.
32. Lawn BR, Wiederhorn SM, and Roberts DE. Effect of sliding friction forces on the strength of brittle materials. *Journal of Materials Science*, 1984;19:2561.
33. Kim JH, Kim JW, Myoung SW, Pines M, and Zhang Y. Damage maps for layered ceramics under simulated mastication. *Journal of Dental Research*, 2008;87:671.

34. Johnson KL. *Contact Mechanics*. Cambridge, UK: Cambridge University Press, 1987.
35. Diao DF, Kato K, and Hayashi K. The maximum tensile-stress on a hard coating under sliding friction. *Tribology International*, 1994;27:267.
36. Osullivan TC, and King RB. Sliding contact stress-field due to a spherical indenter on a layered elastic half-space. *Journal of Tribology-Transactions of the Asme*, 1988;110:235.
37. Oliveira SAG, and Bower AF. An analysis of fracture and delamination in thin coatings subjected to contact loading. *Wear*, 1996;198:15.
38. Ihara T, and Shaw MC, and Bhushan B. A finite-element analysis of contact stress and strain in an elastic film on a rigid substrate. *Journal of Tribology-Transactions of the Asme*, 1986;108:534.
39. Komvopoulos K. Finite-element analysis of a layered elastic solid in normal contact with a rigid surface. *Journal of Tribology-Transactions of the Asme*, 1988;110:477.
40. Schwarzer N, Whittling M, Swain M, and Richter F. The analytical solution of the contact problem of spherical indenters on layered materials: Application for the investigation of TiN films on silicon. *Thin Solid Films*, 1995;270:371.
41. Schwarzer N. Arbitrary load distribution on a layered half space. *Journal of Tribology-Transactions of the Asme*, 2000;122:672.
42. Chudoba T, Schwarzer N, and Richter F. Steps towards a mechanical modeling of layered systems. *Surface & Coatings Technology*, 2002;154:140.
43. Linss V, Chudoba T, Karniychuk M, and Richter F. Combination of normal and lateral force-displacement measurements as a new technique for the mechanical characterization of surfaces and coatings. *Thin Solid Films*, 2006;494:179.
44. Borrero-Lopez O, Hoffman M, Bendavid A, and Martin PJ. Reverse size effect in the fracture strength of brittle thin films. *Scripta Materialia*, 2009;60:937.
45. Freund LB, and Suresh S. *Thin Film Materials. Stress, Defect Formation and Surface Evolution*. Cambridge, UK: Cambridge University Press, 2008.
46. Mao K, Sun Y, and Bell T. Contact mechanics of engineering surfaces: State of the art. *Surface Engineering*, 1994;10:297.
47. Petrov I, Barna PB, Hultman L, and Greene JE. Microstructural evolution during film growth. *Journal of Vacuum Science & Technology A*, 2003;21:S117.
48. Lawn BR. Fracture and deformation in brittle solids: A perspective on the issue of scale. *Journal of Materials Research*, 2004;19:22.
49. Borrero-Lopez O, Hoffman M, Bendavid A, and Martin PJ. Mechanical properties and scratch resistance of filtered-arc-deposited titanium oxide thin films on glass. *Thin Solid Films*, 2011;519:7925.
50. Xie ZH, Hoffman M, Munroe P, Singh R, Bendavid A, and Martin PJ. Microstructural response of TiN monolithic and multilayer coatings during microscratch testing. *Journal of Materials Research*, 2007;22:2312.
51. Ma LW, Cairney JM, Hoffman M, and Munroe PR. Deformation mechanisms operating during nanoindentation of TiN coatings on steel substrates. *Surface & Coatings Technology*, 2005;192:11.
52. Fratzl P, Gupta HS, Fischer FD, and Kolednik O. Hindered crack propagation in materials with periodically varying Young's Modulus—Lessons from biological materials. *Advanced Materials*, 2007;19:2657.
53. Xu J, Zhao XL, Munroe P, Xie ZH. Synergistic toughening of hard, nacre-mimetic $MoSi_2$ coatings by self-assembled hierarchical structure. *Scientific Reports*, 2014;4.
54. Xu J, Li ZY, Xie ZH, and Munroe P. Uniting superhardness and damage-tolerance in a nanosandwich-structured Ti-B-N coating. *Scripta Materialia*, 2014;74:88.
55. Singh RK, Zhou ZF, Li LKY, Munroe P, Hoffman M, and Xie ZH. Design of functionally graded carbon coatings against contact damage. *Thin Solid Films*, 2010;518:5769.
56. Lawn BR. Hertzian fracture in single crystals with diamond structure. *Journal of Applied Physics*, 1968;39:4828.

57. Vodenitcharova T, Borrero-Lopez O, and Hoffman M. Mechanics prediction of the fracture pattern on scratching wafers of single crystal silicon. *Acta Materialia*, 2012;60:4448.
58. Borrero-Lopez O, Hoffman M, Bendavid A, and Martin PJ. Substrate effects on the mechanical properties and contact damage of diamond-like carbon thin films. *Diamond and Related Materials*, 2010;19:1273.
59. Zhang S, Sun D, Fu YQ, and Du HJ. Toughness measurement of thin films: A critical review. *Surface & Coatings Technology*, 2005;198:74.
60. Zhang S, and Zhang XM. Toughness evaluation of hard coatings and thin films. *Thin Solid Films*, 2012;520:2375.
61. Hemker KJ, and Sharpe WN. Microscale characterization of mechanical properties. *Annual Review of Materials Research*, 2007;37:93.
62. A.s.f.t.a. materials, Standard practice for reporting uniaxial strength data and estimating Weibull distribution parameters for advanced ceramics. vol. C 1624–05. Philadelphia, PA, USA, 2007.
63. A.s.f.t.a. materials, Standard test method for flexural strength of advanced ceramics at ambient temperature. Standard ASTM C1161. Vol. 15.01 *Refractories, Activated Carbon; Advanced Ceramics*. ASTM International, 2003. DOI: 10.1520/C1161.
64. A.s.f.t.a. materials, Standard test method for monotonic equibiaxial flexural strength of advanced ceramics at ambient temperature. Standard ASTM C1499. Vol. 15.01 *Refractories, Activated Carbon; Advanced Ceramics*. ASTM International, 2005. DOI: 10.1520/C1499.
65. Borrero-Lopez O, Hoffman M, Bendavid A, and Martin PJ. A simple nanoindentation-based methodology to assess the strength of brittle thin films. *Acta Materialia*, 2008;56:1633.
66. Malzbender J, and de With G. Scratch testing of hybrid coatings on float glass. *Surface & Coatings Technology*, 2001;135:202.
67. Holmberg K, Laukkanen A, Ronkainen H, Wallin K, and Varjus S. A model for stresses, crack generation and fracture toughness calculation in scratched TiN-coated steel surfaces. *Wear*, 2003;254:278.
68. Wiklund U, Bromark M, Larsson M, Hedenqvist P, and Hogmark S. Cracking resistance of thin hard coatings estimated by four-point bending. *Surface & Coatings Technology*, 1997;91:57.
69. Roesler FC. Indentation hardness of glass as an energy scaling law. *Proceedings of the Physical Society of London Section B*, 1956;69:55.
70. Broek D. *Elementary Engineering Fracture Mechanics*, Dordrecht, Netherlands: Springer, 1982.
71. Hoehn JW, Venkataraman SK, Huang H, and Gerberich WW. *Materials Science and Engineering a-Structural Materials Properties Microstructure and Processing*, 1995;192:301.
72. Veldkamp JDB, Hattu N, and Snijders VAC. Crack formation during scratching of brittle materials. In: Bradt RC, Hasselman DPH, Lange FF, editors. *Flaws and Testing*, vol. 3. New York: Springer, 1978. p. 273.
73. Malzbender J, and de With G. Analysis of scratch testing of organic-inorganic coatings on glass. *Thin Solid Films*, 2001;386:68.
74. den Toonder J, Malzbender J, de With G, and Balkenende R. Fracture toughness and adhesion energy of sol-gel coatings on glass. *Journal of Materials Research*, 2002;17:224.
75. Li XD, Diao DF, and Bhushan B. Fracture mechanisms of thin amorphous carbon films in nanoindentation. *Acta Materialia*, 1997;45:4453.
76. Chen J, and Bull SJ. Indentation fracture and toughness assessment for thin optical coatings on glass. *Journal of Physics D-Applied Physics*, 2007;40:5401.

77. Voevodin AA, Rebholz C, Schneider JM, Stevenson P, and Matthews A. Wear-resistant composite coatings deposited by electron enhanced closed field unbalanced magnetron sputtering. *Surface & Coatings Technology* 1995;73:185.
78. Harry E, Rouzaud A, Juliet P, Pauleau Y, and Ignat M. Failure and adhesion characterization of tungsten-carbon single layers, multilayered and graded coatings. *Surface & Coatings Technology*, 1999;116:172.
79. Voevodin AA, and Zabinski JS. Supertough wear-resistant coatings with 'chameleon' surface adaptation. *Thin Solid Films*, 2000;370:223.
80. Pei YT, Galvan D, and De Hosson JTM. Nanostructure and properties of TiC/a-C : H composite coatings. *Acta Materialia*, 2005;53:4505.
81. Zhang S, Sun D, Fu YQ, and Du HJ. Effect of sputtering target power on microstructure and mechanical properties of nanocomposite nc-TiN/a-SiNx thin films. *Thin Solid Films*, 2004;447:462.
82. Borrero-Lopez O, Vodenitcharova T, Quadir MZ, and Hoffman M. Scratch fracture of polycrystalline silicon wafers. Submitted, 2014.
83. Shum PW, Li KY, Zhou ZF, and Shen YG. Structural and mechanical properties of titanium–aluminium–nitride films deposited by reactive close-field unbalanced magnetron sputtering. *Surface & Coatings Technology*, 2004;185:245.
84. Ligot J, Benayoun S, and Hantzpergue JJ. Analysis of cracking induced by scratching of tungsten coatings on polyimide substrate. *Wear*, 2000;243:85.

Index

A

a-C film, *see* amorphous carbon film (a-C film)
Acoustic emission (AE), 319, 495
  AE-assisted nanoindentation method, 333–334
  application for adhesion testing, 334
  with DIC technique, 515
  signal, 137, 334, 535
Addition of selected elements (ASE), 443, 446–448
Adhesion, 28, 318–319
  wear, 244, 245
Adhesion measurement of films; *see also* Coating adhesion strength; Nanoindentation
  bending test, 322
  blister test, 323
  interfacial delamination, 319
  interfacial property of thin film/substrate systems, 335
  measurement techniques, 319
  peel test, 321
  pull-off test, 321–322
  scratch method, 322
  stressed over layer method, 322
AE, *see* Acoustic emission (AE)
AFM, *see* Atomic force microscopy (AFM)
Al-Cu-N coatings
  antibacterial coatings, 430
  comparison of cracks generated in coating, 415, 417
  deposition parameters, physical, and mechanical properties, 416
  three-functional Al-Cu-N coatings, 431–433
Al-Si-N coatings, 397
American Society for Testing and Materials standards (ASTM standards), 2
  ASTM C1624–05 standards, 533
  ASTM D1002 and ASTM D3164 standards, 484
  C633 standard, 466
Amorphization, 253, 399
amorphous carbon film (a-C film), 19
  investigating fracture mechanisms, 213–214
  nanoindentation fracture mechanism, 326
Antibacterial coatings, 430
  three-functional Al-Cu-N coatings, 431–433
  two-functional Cr-Cu-O coatings, 430–431
Arc tensile cracks, 550, 552
ASE, *see* Addition of selected elements (ASE)
ASTM standards, *see* American Society for Testing and Materials standards (ASTM standards)
Atomic force microscopy (AFM), 338, 339, 536
  bending modulus of thin films, 183
  indentation-induced through-thickness cracks, 151
  indentation on ECRCVD DLC coating on silicon, 79
  in situ AFM for indent impression, 340
  spontaneous blister on glass, 140
  tip blunting, 129
Auerbach's law, 539, 543
Austenitizing temperature, 230

B

Bending test, 322, 401, 402, 414
  Al-Cu-N coatings deposition parameters and properties, 416
  effect of coating microstructure, 418–419
  comparison of cracks, 415–418
  cracking of coating, 415
  DIC technique and, 515
Berkovich indenter, 68, 210, 211, 213
  crack parameters for, 211
  indentation, 330
  lateral crack in coated glass, 144
  load–displacement curve of nanoindentation, 80, 81
  load–displacement relation, 187
  nanoindentations on GaAs, 337
  pressure–volume relation, 188
  radial cracking at Vickers indentation, 67
  radial cracks, 210
Berkovich tip, 127, 128, 137, 154, 197, 198, 199, 337
Bimaterial specimen-based methods, 490; *see also* Sandwich specimen-based methods
  blister test, 500–503
  comparison of methods, 507
  indentation test, 490–494
  laser spallation test, 504–506
  peel test, 497–500
  scratch test, 494–497
  tensile test, 503–504
Blister test, 323, 500
  advantages and disadvantages, 503
  analytic solution, 502

Blister test (*Continued*)
constrained blister test, 501
film-substrate delamination behavior, 503
shaft-loaded test, 501, 502
two-stage deformation of coating, 500–501
Bombarding ions, 11, 389
effect of energy delivered to growing film, 406, 411–412, 422
energy delivery to growing coating, 396
Bond strength, 467
Boundary atoms, 4, 5
Brazilian disk, *see* Brazil nut specimen
Brazil nut specimen, 478
advantage of sandwich, 481
angular constants of equation, 480
coefficients of equation, 479
SIF, 479
Bridging contribution to debond energy ($G_{bridging}$), 208
Brittle coatings
cracks generation, 434–435
fracture mechanism, 326
multilayer coating resistance to cracking, 439–443
overlayer preventing cracking, 435–437
overlayer protection against cracking, 433
Zr-Si-O overlayer in compression, 437–439
Brittle fracture, 2, 15, 563
size effects, 570
Weibull model of, 568
Brittle layers fracture, 530; *see also* Scratch test
bulk material, 540–544
coated system, 544–548
columnar films, 553–558
fracture modes on scratching, 539
isotropic films, 548–553
sliding contacts, 539–540
stress field originating by sliding contact, 540
substrate effects and size effects, 560–564
thin wafers with diamond structure, 558–560
Bulge test, 92, 94
Bulging of films, 92
bulge test for section of long rectangular membrane, 94
microfabrication of precrack, 94
Bulk material, 540
crack initiation in sliding contact, 541
Hertzian theory, 542
indentation mechanics, 543
plasticity, 544

C

Calcium phosphate coatings (CaP coatings), 496
CaP coatings, *see* Calcium phosphate coatings (CaP coatings)
Carbides, 230
carbide-forming elements, 231
plasticity in, 52
powder properties, 248
solidification process, 262, 263
Carbon nanofiber (CNF), 23
Carbon nanotube (CNT), 17, 21, 23, 27, 504
Carbon nanotube toughening (CNT toughening), 21; *see also* Ductile phase toughening
as-fabricated highly orientated CNT/Al_2O_3 composites, 25
CNT bridging longitudinal Al_2O_3 matrix and tube pull-out, 25
crack deflection at CNT/Al_2O_3 interface, 25
fracture surface of composite and fracture toughness, 22
fracture toughness behavior of Si-C-N nanocomposites, 23
HR-TEM image and CNT anchored, 24, 27
nanotube tangling, 23
nc-TiC/(CNFs:a-C)0. 05 coating, 26
in situ growth, 22
CCD cameras, *see* Charged coupled device cameras (CCD cameras)
CDPs, *see* Combination of deposition parameters (CDPs)
Centrally loaded plate with uniformly distributed load, 359–360
Ceramic coatings, 84, 123, 124, 499; *see also* Hard-yet-tough ceramic coatings
bending test, 322
biocompatible, 484, 485
Brittle behavior, 57
cathodic voltage effects, 488
displacement-controlled nanoindentation, 74
hardness and toughness in, 1–3
interfacial adhesion, 493
Ceramics, 123
CNTs and, 21
contact area, 128
phase transformation toughening, 28
toughness, 145
CGS technique, *see* Coherent gradient sensing technique (CGS technique)
CH, *see* Channeling crack (CH)
“Chameleon” structure, 581
Channel cracking
indent-induced channel cracking, 87
indent-induced partial-penetration radial fracture, 87
multistrain flexure test, 84
multistrain specimen and test configuration, 85
pattern, 111
residual stresses, 88
SEM images of ta-C coating fracture, 88
sphere indentation test, 86
stress intensity factor of coating, 83

3D channeling of crack, 84
toughness evaluation, 83
Channeling crack (CH), 195
Charged coupled device cameras (CCD cameras), 506
Charpy test, 49
Chemical vapor deposition (CVD), 9, 11, 253
Chevron tensile cracks, 550, 552
Chromium, 227, 230
Chromium–molybdenum steels, 229
Circumference crack, *see* Indentation-induced picture-frame crack
Circumferential cracking and spallation, 71
boundaries of irreversible work, 73
debates about extraction of irreversible work, 71–77
displacement-controlled nanoindentation, 74, 76
energy irreversibly dissipated during indentation, 75
extrapolating total work *vs.* displacement curve, 76
fracture energy of coating, 74
for fracture toughness of thin hard coatings, 77–83
instability analyses of 1D blister, 77
load-and depth-controlled force–displacement curves, 83
load–displacement curves, 79, 80, 81
mechanical properties of coatings, 78
stages in nanoindentation fracture and load–displacement curve, 72
Circumferential cracking pattern, 49
Circumferentially notched tensile specimen (CNT specimen), 503, 504
Closed loop indentation, 130, 131
CNF, *see* Carbon nanofiber (CNF)
CNT, *see* Carbon nanotube (CNT)
CNT specimen, *see* Circumferentially notched tensile specimen (CNT specimen)
CNx film, 101
etching of sacrificial layer, 103
five freestanding film strips, 106
properties of sputter-deposited, 102
sample preparation for testing, 102, 103
testing results of fracture toughness of, 104–105
upper and lower boundaries of fracture toughness, 107
Coated system, 544
coating stiffness effects, 546
coating/substrate combination, 545
contact stress, 545
exponential function, 546
FIB microscopy for subsurface fracture observation, 536–538
maximum tensile stress, 547
for thin films, 544
Von-Mises stress, 547–548
Coating, 466
Coating adhesion strength, 466; *see also* Adhesion measurement of films
bimaterial specimen-based methods, 490, 507
blister test, 500–503
Brazil nut specimen, 478–481
CGS technique, 509–511
DCB specimen, 471–474
DCDC specimen, 481–483
DIC technique, 514–515
direct pull-off specimen, 486–488, 490
evaluation methods, 470
four-point bend specimen, 474–478
indentation test, 490–494
interface fracture mechanics, 467–470
lap shear specimen, 483–486
laser spallation test, 504–506
mechanisms, 466
Moiré interferometry technique, 511–512
peel test, 497–500
photoelasticity technique, 508–509
sandwich specimen-based methods, 471, 489
scratch test, 494–497
speckle interferometry technique, 512–514
supplementary techniques, 506
tensile test, 503–504
COD, *see* Crack opening displacement (COD)
Coherent gradient sensing technique (CGS technique), 509
film/substrate systems, 510
for interfacial fracture mechanics, 509–510
in study of quasistatic fields, 511
in transmission, 510
Cohesive zone model (CZM), 165, 167, 169
Colloidal crystal templating, 186
Columnar films, 553; *see also* Isotropic films
anisotropic structures, 557
columnar microstructure results, 554–555
crack geometry, 553
frequency of tensile cracks, 555–556
intercolumnar crack propagation, 554
mutilayer/graded systems, 557
scratch cracking of TiO_2 film, 556
surface projection of scratch crack trajectories, 555
Ti interlayers, 558
Combination of deposition parameters (CDPs), 423, 424, 432
Compressive stress
biaxial, 11, 381
distribution, 496
failure, 477
from ion bombardment, 19
microblasting effect, 60, 61
residual, 364
toughening, 28, 29

Cone crack, 141–142, 539, 540; *see also* Partial cone crack
Contact area, 128, 209, 210, 212, 216, 326
Contact stiffness, 126, 210, 217
Conventional nanoindentation, 130, 323
  delamination with cracks in films, 325–330
  delamination without cracks in films, 323–325
Corrosion, 253, 309
  processes, 243
  stress-corrosion cracking, 202, 203
  stress, 93, 205
CPR, *see* Crack propagation resistance (CPR)
Crack-growth rate, *see* Crack velocity
Crack opening displacement (COD), 146
Crack propagation, 468, 542
  asymmetric, 476–477
  catastrophic, 501
  CSN and, 332
  fatigue, 474
  intercolumnar, 554
  interfacial, 481, 508
  intergranular, 554
  materials toughness, 17
  resistance to, 3, 15, 144, 583
  stability, 195
  theory, 15, 17
Crack propagation resistance (CPR), 53
Crack shape factor, 69, 574
Crack tip opening displacement (CTOD), 468, 471
Crack velocity, 200, 202, 203
CrAlN coatings, 8
  cross-sectional morphology, 12
  high-resolution TEM lattice images, 12
  XRD spectra and lattice parameter, 10
Cross-sectional nanoindentation methods (CSN methods), 330, 331
  blister dimension geometrical ratio, 332
  energy release rate, 330
  experimental trials, 333
  to ductile–brittle interface, 332
Crystal atoms, 4, 5
CSN methods, *see* Cross-sectional nanoindentation methods (CSN methods)
CTOD, *see* Crack tip opening displacement (CTOD)
Cube-corner
  diamond indenter, 55, 56, 69
  geometry, 87, 194
  indentation, 194
Cutting-tool coatings, 59–60
CVD, *see* Chemical vapor deposition (CVD)
Cyclic loading indentation
  for “tough” interface, 348–350
  for film/substrate systems, 361
Cyclic mechanical stress, 243
CZM, *see* Cohesive zone model (CZM)

D

Dalton law, 449–450
DCB specimen, *see* Double cantilever beam specimen (DCB specimen)
DCDC specimen, *see* Double-cleavage drilled compression specimen (DCDC specimen)
de Boer’s and Gerberich’s methods, 197
Delamination
  without cracks in films, 323–325
  with cracks in films, 325–330
  GaAs substrate deformation, 337–339
  GaAs substrate mechanical properties, 337
  load profile optimization, 345–350
  nanoindentation-induced delamination, 337
  SiN films mechanical properties, 337
  SiN/GaAs film/substrate systems, 335, 339–340
  verification, 340–345
  work for, 328–329
Delamination energy release, 351
  dual-indentation, 352–356
  Griffith energy balance, 351–352
  preexisting crack supposition, 356–358
Depth-sensing indentation method, 186–187, 536
Derjaguin-Muller-Toporov model (DMT model), 481
Diamond-like carbon coatings (DLC coatings), 15, 19, 77, 79
  depth-at-failure, 58
  hardness, 31
  residual stress, 16
Diamond-like carbon films (DLC films), 549
  effects on microscratch fracture, 561
  FIB micrographs of scratch track, 562
  on glass, 568
  partial ring cracks, 571
  scratching, 549, 550
  tensile stresses, 561
  Weibull plot, 570
Digital image correlation technique (DIC technique), 466, 514–515
Dimensionless scratch durability ratio, 53
Direct pull-off specimen, 486
  advantages, 487, 488
  fracture macrograph of coatings after, 488
  sandwich specimens, 488, 490
Disordered porous thin films, 188, 209; *see also* Highly ordered porous thin films
  analytical models, 203
  CH, 195
  cohesive failure of low-κ thin film, 191
  crack bridging phenomenon, 207
  crack propagating rate, 207
  crack velocity, 202
  cube-corner geometry, 194

cube-corner indentation, partially cracked film, 194
effects of parameters, 200
elastic modulus, 188, 190
failure and toughening mechanisms, 202–209
failure process in low-κ thin film, 193
FIB cross section of blister, 191
fracture toughness and interfacial toughness, 190–201
interfacial toughness, 196, 197, 208
linear relationship between energy release rate, 205
load–displacement curves, 193, 201
nanoindentation load–displacement depth curves, 198
optical image of TiW/400 nm low-κ thin film blister, 191
plane strain modulus and hardness, 189
porosity, 189
residual stress in and fracture toughness, 193
SIF, 192
simplified molecular reaction mechanisms, 206
stability of crack propagation, 195
subcritical crack-growth curves, 204
superlayer indentation, 191
surfactant-enhanced nanobubble cavitations formation, 208
wedge indentation on MSSQ thin film, 199
Displacement control (Dp-ctrl), 157
indentation, 74
lower and upper limits of fracture dissipated energy for, 160
nanoindentation, 74, 76
DLC coatings, *see* Diamond-like carbon coatings (DLC coatings)
DMT model, *see* Derjaguin-Muller-Toporov model (DMT model)
"Dog-bone" shape film, 89
Doping ductile phase, 20
Double-cleavage drilled compression specimen (DCDC specimen), 471, 482
advantage, 482
for coating evaluation, 482–483
Poisson's effect, 481–482
sandwich DCDC specimen, 483
Double cantilever beam specimen (DCB specimen), 95, 96, 471, 472
advantages, 472
coating adhesion, 472
contoured and tapered, 473
disadvantage, 473
eight-node anisotropic elements, 99
tapered DCB test, 474
Dp-ctrl, *see* Displacement control (Dp-ctrl)
Dual-indentation method, 352, 361
energy release rate (G^{in}) values comparison, 367
load-displacement curves, 353–356
load function, 352–353
plastic deformation to indented film, 362–363
SiN films delamination energy release, 363, 364
SiN/GaAs systems, 361
surface energy calculation, 356
Ductile fracture, 2, 15
Ductile phase toughening, 17; *see also* Carbon nanotube toughening (CNT toughening)
DLC, 19
doping ductile phase, 20
HRTEM image, 18
nc-Me_nN/a-SiN_x, 18
plasticity, 20, 21
scratch tracks, 20
Dunders parameter, 83

E

EB-PVD, *see* Electron beam physical vapor deposition (EB-PVD)
EBSD, *see* Electron backscattered diffraction (EBSD)
EDS, *see* Energy dispersive x-ray spectrometer (EDS)
Effective Young's modulus (E^*), 356, 387; *see also* Young's modulus (E)
control of E*, 388
E_f^*/E_s^* ratio effect, 406
H/E* ratio control by deposition parameters, 389–391, 395–399
H/E* ratio control by energy, 391–395
H/E* ratio control by selected Me element addition, 391
with low E* and high ratio H/E*, 387
mechanical properties of substrate, 406
Mo-Si-N, Zr-Si-N, and W-Si-N physical and mechanical properties, 407
multielement compound coatings, 399–401
of substrate effect, 405
Eight-node anisotropic elements, 99
Elastic–plastic deformation, 74, 153, 155, 335, 341
Elastic–plastic transition, 563
Elastic recovery parameter, 51
"Eldyf" computer program, 250
Electron backscattered diffraction (EBSD), 250
Electron beam physical vapor deposition (EB-PVD), 515
TBCs, 64, 65, 515
Electronic speckle pattern interferometry (ESPI), 512–514
Elevated temperature nanoimpact tests, 60
Emergency wear, 242
Empirical power law, 337
relationship, 133
End milling tests, 60, 61
Energy-balance approach, 2

Energy-based models, 149; *see also* Stress-based models
analyzing irreversible work and plastic work, 154–155
associated load–displacement curve, 151
extrapolate load–displacement curve, 150–153
extrapolate total work–displacement curve, 153–154
extrapolating irreversible work *vs*. load, 155–156
fracture-dissipated energy, 156–161
fracture evolution in brittle coating, 150
indentation-induced fracture, 152
indentation-induced through-thickness cracks, 151
interfacial fracture-dissipated energy assessment, 161–164
ld–dp method, 152, 153
nanoindentation-induced fracture, 149, 150
picture frame cracks and load–displacement curve, 154
toughness results of carbon coating on silicon, 154
work of indentation, 155
Energy approach, 577
chipping upon scratching, 578
fracture toughness assessment, 580
load-control mode, 578
particle-filled sol–gel coatings fracture toughness, 579
in scratch experiment, 577
stress approach, 581
Energy delivery
atom transition, 234
in coating, 446
effect of delivered energy speed, 451–453
effect to growing film by bombarding ions, 411, 412
to growing coating, 448–451
Energy dispersive x-ray spectrometer (EDS), 250, 284, 285, 286
Energy release rate (G_c), 213
Enhanced hardness
Hall–Petch law, 381–382
hard nanocomposite coatings classification, 382
hardness of TiN and CrN nitride films, 381
nanocomposite coatings with, 379
nanostructures, 380
Enhanced toughness
coatings classification, 386–387
hard coatings formation principle, 384–386
hard nanocomposite coatings with, 383
toughness and toughening mechanisms, 383–384
ESPI, *see* Electronic speckle pattern interferometry (ESPI)
"Expanding cavity" model, 69
Experimental test procedure, 56
Extended finite element method (XFEM), *see* Partition-of-unity

F

FEA, *see* Finite element analysis (FEA)
FEM, *see* Finite element modeling (FEM)
FESEM images, *see* Field emission scanning electron microscopy images (FESEM images)
FIB, *see* Focused ion beam (FIB)
Field emission scanning electron microscopy images (FESEM images), 23, 197, 199, 200
Film(s), 49; *see also* Fully densed thin films; Isotropic films; Porous thin films
strain, 99
Film microbridges
microtensile testing, 95
precracked CNx, 103
preparation, 98
Film/substrate system interfacial toughness assessment, nanoindentation for, 323
Finite element analysis (FEA), 128
CZM implementation, 165, 167
ideal pyramidal Berkovich geometry, 51
Finite element modeling (FEM), 70, 165, 317, 325, 335, 544
delamination mechanic verification using, 342–345
displacement of silicon substrate, 99–100
nanoimpact FEM simulation, 56
55NiCrMoV7 steels, 251
ASTM-G65 standard, 301, 302, 303
boundary of remelting zone, 287, 290
central zone of remelted surface layer, 272, 273, 274
comparison of average crack depth of, 308
cracks on cross section of, 304, 305, 306
cross-sectional morphology, 268–270, 280, 281, 282
EDS analysis of chemical composition, 289
influence of laser power on thickness of RZ and HAZ, 264
investigations, 247, 249–250
laser power influence on RZ and HAZ thickness, 263
after laser surface melting, 259, 260
remelting zone in surface zone of, 289
surface layer after alloying with WC powder, 260
surface of alloyed bead after laser surface alloying, 257, 258
surface of melt bead after laser surface melting, 257, 258
thermal fatigue tests, 251

thin foil structure, 295, 296
X-ray diffraction pattern, 283
Flexible multifunctional coatings, 423
antibacterial Al-Cu-N nanocomposite coatings, 430–433
CDPs, 423, 424
nc-TiC/a-C nanocomposite coatings, 424–427
Si-Zr-O nanocomposite coatings, 428–430
Focused ion beam (FIB), 92, 191
cross-sectional milling, 537
microscopy for subsurface fracture observation, 536–537
milling, 340, 515
montage of cross-sectional TEM images, 538
three-dimensional reconstruction, 537, 538
Four-point bending test (4PB test), 322
specimen, 474–478
Fracture
mechanics, 467–468
probability, 57
Fracture-dissipated energy
existing toughness limits models, 157
fracture toughness, 161
initial toughness bound model, 157
lower and upper limits, 160
lower bound method, 159
modeling limits, 156, 160
toughness limits model, 158
Fracture strength, 566
DLC film on glass, 568
model-coated system, 568
scratch test, 567, 571
size effects, 570
three-parameter distribution function, 569
Weibull plot for DLC, 570
Fracture toughness, 48, 144, 383, 402, 571
addition of selected element in base material, 410–411
bulging of films, 92, 94
displacement of silicon substrate, 100
*E** of substrate effect, 405–407
effect of energy delivered to growing film, 411–412
extraction, 98
film strain, 99
film thickness effect, 403–405
fully densed thin films, 213–215
inchworm actuation method, 89
macrostress effect in film, 407–409
macrotension of substrate, 95–111
measurement, 210–211
membrane deflection method, 89–90
microscale fracture specimen preparation and testing, 90
microscratch fracture toughness measurement, 66
microstructure of film effect, 409–410
microtensile testing for standalone thin films, 88
phase transformation toughening effect, 412–414
quantitative characterization for hard coatings, 65
residual stress, 101
stress approach, 573
stylus drawn along coated sample, 67
surface roughness values, 572–573
tension by residual stress, 91, 92
3D finite element model, 66
toughness evaluation from radial cracks, 67–70
Frank–Read source, 6
Fretting, 246
Friction phase, 424
Fully densed thin films, 211; *see also* Porous thin films
fracture toughness measurement, 213–215
load–displacement curve, 215
pile-up or sink-in of materials, 212
stages in nanoindentation fracture for film/substrate system, 214
Young's Modulus and hardness measurement, 211–213

G

GaAs, *see* Gallium arsenide (GaAs)
GACR, *see* Grant Agency of Czech Republic (GACR)
Gallium arsenide (GaAs), 316
P–h curves of indentation, 339
pop-in event, 338
substrate deformation, 337
substrate mechanical properties, 337
Glass-reinforced plastic (GRP), 477
Gradient structure toughening, 28; *see also* Multilayering structure toughening
a-C gradient coating, 29
CrASiN nanocomposites, 30
gradient layer coatings, 30
hardness of graded DLC coatings, 31
scratch adhesion strength of nonhydrogenated DLCs, 31
Grain-boundary reinforcement, hardening via, 5–7
Grain-size refinement, ceramic coating hardening via, 3–5
Grant Agency of Czech Republic (GACR), 454
Griffith energy balance, 351–352
Growing coating
coating mechanical properties, 395
effect of delivered energy speed, 451–453
H/E* ratio control by energy delivery, 391
ion bombardment effect, 393
Sn-Cu-O coating, 394
substrate heating effect, 392

Growth stress, 139, 140
GRP, *see* Glass-reinforced plastic (GRP)

H

H_2O_2, *see* Hydrogen peroxide (H_2O_2)
*H3/E*2 ratio*, 386
Half-Penny-like radial cracks, 145, 148
  COD, 146
  Meyer's hardness, 147
  pop-in in load–displacement curve, 147
  toughness of ceramics and glass, 145
  triangular pyramid indenter, 147
  Young's modulus and hardness of coating, 145
Half Penny radial crack, 142
Hall–Petch
  effect, 5, 6, 14
  law, 381–382
  relation, 4
HAP coatings, *see* Hydroxyapatite coatings (HAP coatings)
Hard-yet-tough ceramic coatings, 3, 15
  coating hardness as function of size of grains, 5
  compressive stress toughening, 28
  crystal and boundary atoms, 4, 5
  grain-boundary reinforcement, hardening via, 5–7
  grain-size refinement, hardening via, 3–5
  ion bombardment, hardening via, 11–13
  multilayering, hardening via, 13–15
  nc-TiN/a-Si_3N_4 hardness, 6, 7, 8
  nc-$TiSi_2$ hardness, 6, 7
  optimization of coatings architecture, toughening through, 28–36
  phase transformation toughening, 28
  schematic of current status of hard ceramic coatings, 4
  solid-state solution and precipitation, hardening via, 7–11
  toughening agent, toughening through, 17–27
Hard coatings
  bending test, 414–419
  combined action, H/E* ratio control by, 395–399
  control of effective Young's modulus, 388
  deposition parameters, H/E* ratio control by, 389–391
  design of hard flexible coatings, 419–423
  energy, H/E* ratio control by, 391–395
  formation principle, 384–386
  fracture toughness, 402–414
  indentation test, 402–414
  with low effective Young's modulus E* and high ratio H/E*, 387
  methods for assessment, 401
  multielement compound coatings, 399–401
  resistance to cracking, 401
  selected Me element addition, H/E* ratio control by, 391
Hard nanocomposite coatings, 382
  with enhanced toughness, 383–387
  nc-Me_nN/a-SiN_x, 18
  trends of next development, 444–446
Hardness (*H*), 1–3, 82, 183; *see also* Enhanced hardness; Young's modulus (*E*)
  of as-deposited CrAlN coatings, 9
  in ceramic coatings, 1–3
  of coatings, 132–136
  of graded DLC coatings, 31
  of hot work tool steels, 230
  measurement, 209–210, 211–213, 287–292
  in monolayer and multilayer DLC, 16
  of nc-TiN/a-Si3N4, 8
  scratch toughness *vs*., 36
  of SiN films and GaAs substrate, 338
  tests, 250
Hardness measurement, 209–210, 287; *see also* Microhardness measurement
  average hardness change, 292, 297
  55NiCrMoV7 steel, 291
  fully densed thin films, 211–213
  highest hardness of 61. 6 HRC, 289
  strengthening mechanisms, 288
Hard, tough, highly elastic (HTHE), 443–444
HAZ, *see* Heat-affected zone (HAZ)
H/E* *ratio*, 386
  control by deposition parameters, 389–391, 395–399
  control by energy, 391–395
  control by selected Me element addition, 391
  highly elastic multielement compound coatings, 399–401
Heat-affected zone (HAZ), 256, 260, 262, 264, 290, 293, 309
Hertz contact loaded plate, 360–361
Hertzian theory, 542
High-Al coatings, 60
High-resolution transmission electron microscope image (HRTEM image), 18
  carbon nanofiber, 27
  of multilayer coating, 35
  nc-CrAlN/a-SiN_x, 18
  of Zr-Al-O film, 419
High entropy alloy compounds, *see* Multi-element equal-mole coatings
Highly ordered porous thin films, 181; *see also* Disordered porous thin films
  porous anodic alumina thin film, 182–183
  SEM images, 181
  silica foam thin film, 186–188
  TiO_2 nanotube array thin film, 183–186

High power diode laser (HPDL), 247
hardness tests, 250
Rofin DL 020 Diode Laser specification, 249
working scheme, 249
Hot work tool steels, 226
adhesion wear, 244
approximate chemical composition, 227
chemical compositions, 247
chromium, 227
chromium–molybdenum and tungsten steels, 229
functionality, 254
grooving wear process with large particles, 246
heat treatment, 230–231
heat treatment of investigated steels, 248
influence of tempering temperature on hardness, 232
interdependence of surface and volume interaction, 242
investigation methodology, 249–252
material for investigation, 247–249
micromachining wear process with high loads, 245
models of wear processes, 245
nickel, 228
production technology, 231–232
properties, 228
selected properties of carbide powders, 248
stand for thermal fatigue investigations, 252
stand for wear resistance investigations, 251
thermal fatigue, 243
wear of parts and machines, 241–246
wear process subgroups, 242
HPDL, *see* High power diode laser (HPDL)
HRTEM image, *see* High-resolution transmission electron microscope image (HRTEM image)
HSSQ, *see* Hydrogen-silsesquioxane (HSSQ)
HTHE, *see* Hard, tough, highly elastic (HTHE)
Hydrogen-silsesquioxane (HSSQ), 188, 189
Hydrogen peroxide (H_2O_2), 205
Hydroxyapatite coatings (HAP coatings), 485–486, 499
Hysitron triboscope, 125

I

ICDD, *see* International Centre for Diffraction Data (ICDD)
Impact-time data analysis, 56
Impact toughness, 49, 53; *see also* Scratch toughness; Toughness for hard coatings
correlation between fractional potential energy and probe depth, 57
correlation between plasticity index, 62
cutting-tool coatings, 59–60
experimental test procedure, 56
impact and erosion of TBC in aero-engines, 63–65
impact test on TiAlCrN and AlTiN coatings, 58
interfacial toughness, 58–59
load dependence, substrate, and microstructural influences on, 62–63
nanoimpact testing, 54–55
nanoimpact tests on TiAlN and AlCrN, 61
postdeposition coating modification, 60, 62
progression of damage with continued impact, 56–58
TiFeN and TiFeMoN films impact performance, 64
Inchworm actuation method, 89, 90
Indentation-induced cracking
cohesive zone, 165
indentation-induced picture-frame crack, 168
indentation modeling, 166
load drop in load–displacement curve, 166
numerical analysis, 165, 168
traction–separation relations, 165
VCCT, 167, 168
Indentation-induced fracture detection, 136
AE signal, 137
Kexp curve, 137, 138
plot of instantaneous loading rate, 138, 139
Indentation-induced picture-frame crack, 168
Indentation; *see also* Dual-indentation method
fracture toughness, 144
geometry, 70
hardness, 2
irreversible energy release during, 329
mechanics, 543
Indentation plasticity, 49
elastic recovery parameter, 51
load–displacement curve, 50
plasticity index, 49, 50
variation in relative wear rate, 52
Indentation tests, 124, 144, 402, 490
addition of selected element in base material, 410–411
coating adhesion evaluation, 494
coating delamination, 492
E^* of substrate effect, 405–407
effect of energy delivered to growing film, 411–412
film thickness effect, 403–405
indentation-induced fracture detection, 136–138
interfacial, 493
macrostress effect in film, 407–409
microstructure of film effect, 409–410
nanoindentation, 124–131
phase transformation toughening effect, 412–414

Indentation tests (*Continued*)
at surface of coating/substrate system, 491
Young's modulus and hardness of coatings, 132–136
Initial impact, 63
In situ conversion, 231
In situ inspection in testing, 98
Interface elastic modulus (E_{int}), 164
Interface fracture mechanics, 467
fracture mechanics, 467–468
interfacial fracture mechanics, 468–470
Interfacial delamination, 77, 196, 319, 325, 345, 348, 349
characterization, 340–341
under cyclic-loading indentation, 350
driving force, 75, 77, 322
energy release rate, 351
fracture-dissipated energy, 163
in low-κ/substrate systems, 197
mechanic of SiN/GaAs film/substrate systems, 349
mechanisms in film/substrate systems, 336
modes in film/substrate system, 320–321
in SiN/GaAs film/substrate system, 351
wedge indentation, 197
Interfacial energy release rate, 361
dual-indentation method, 361–364
energy-based method for evaluation, 362
preexisting crack supposition method, 364–365
SiN/GaAs systems, 361
Interfacial fracture-dissipated energy assessment, 161
energy dissipated and release rate for delamination, 161, 162
extra linear elastic recovery in load–displacement curve, 162
sequential indentation-induced deformation, 163
unloading curves of sequential indentations, 164
unloading induced delamination, 162
Interfacial fracture mechanics, 468
interface crack, 468, 470
stress and displacement elastic solutions, 469
Interfacial indentation test, 493, 494
Interfacial toughness, 58–59, 196, 197
delamination energy release, 351–358
Griffith energy balance, 351–352
interfacial energy release rate, 361–365
plate bending models, 358–361
SiN/GaAs film/substrate systems, 350
International Centre for Diffraction Data (ICDD), 250
International Union of Pure and Applied Chemistry (IUPAC), 179
Ion bombardment, ceramic coating hardening via, 11–13
Irreversible work difference method, 154
Isotropic films, 548
buckling cracks, 553
delamination cracks, 552
DLC films, 549
FIB micrographs of scratch track in SiC film, 551
subsurface observations, 549–550
IUPAC, *see* International Union of Pure and Applied Chemistry (IUPAC)

K

Knoop indentation, 97
Kzanowski's model for image force effect, 15

L

LACVD, *see* Laser chemical vapor deposition (LACVD)
Lap shear specimen, 483
advantages, 486
application, 485
conventional geometry, 484
hydroxyapatite coatings, 485–486
stress distribution, 484
LAPVD, *see* Laser physical vapor deposition (LAPVD)
Laser-treated surface layer toughness
hardness measurement, 287–292
hot work tool steels, 226–232
laser, 233–237
microhardness measurement, 292–296
morphology and microstructure, 261–282
phase and chemical composition, 282–287
structural characteristic of surface, 254
surface layer of 32CrMoV12–28 steel, 259, 260
surface layer of 55NiCrMoV7 steel, 260
surface layer of X38CrMoV5–3 steel, 259
surface layer of X40CrMoV5–1 steel, 258, 259
surface layer systems characteristics, 237–241
surface of alloyed bead after laser surface alloying of 32CrMoV12–28 steel, 257
surface of alloyed bead after laser surface alloying of 55NiCrMoV7 steel, 258
surface of alloyed bead after laser surface alloying of X38CrMoV5–3 steel, 256
surface of alloyed bead after laser surface alloying of X40CrMoV5–1 steel, 255
surface of melt bead after laser surface melting of 32CrMoV12–28 steel, 257
surface of melt bead after laser surface melting of 55NiCrMoV7 steel, 258
surface of melt bead after laser surface melting of X38CrMoV5–3 steel, 256
surface of melt bead after laser surface melting of X40CrMoV5–1, 255

technical application, 252–254
thermal fatigue, 300–308
wear of parts and machines, 241–246
wear resistance measurements in metal–metal arrangement, 296–300
LASER, *see* Light Amplification by Stimulated Emission of Radiation (LASER)
Laser chemical vapor deposition (LACVD), 237
Laser physical vapor deposition (LAPVD), 237
Laser spallation test, 504
advantage, 505
applications, 506
early setup, 505
Laser speckle technique, 513
Laser surface treatment, 254
effect on material hardness, 287–288
parameters, 308
short time and local effect, 253
technologies of engineering materials, 237
Lateral cracks, 142–144, 148–149
Ld-ctrl, *see* Load control (Ld-ctrl)
LEFM, *see* Linear elastic fracture mechanics (LEFM)
Leica-Qwin computer image analysis system, 250, 252
Lift-off process, 106
Light Amplification by Stimulated Emission of Radiation (LASER), 233
application in material engineering, 233
features, 236–237
interaction of photons with atoms, 233
optical pumping, 236
physical basics, 233
spontaneous emission constant, 234, 235
stimulated emission, 235, 236
technologies, 237
Line-wise chemical composition analysis, 282
Linear elastic deformation, 167
Linear elastic fracture mechanics (LEFM), 17, 322, 565
Linear variable displacement transducers (LVDTs), 476
Load-displacement curves, 353
energy calculation model, 356
loading curve of second indentation, 354–355
reloading delaminated film, 355
on SiN/GaAs film/substrate system, 353–354
Load control (Ld-ctrl), 157
close-loop, 132
force–displacement curves, 83
indentation work, 159
lower and upper limits of fracture dissipated energy, 160
lower bound method, 159
toughness limits models, 157
Load function, 352–353
Load profile optimization, 345
cyclic loading indentation for "tough" interface, 348–350
deformation behavior, 350
maximum loads, 345
minimum loads, 345
normal stress contours, 346
P–h curves at load, 347
Load support, 63
Loose-columnar aluminum layer, 106
Al patterns, 110
boundaries of fracture toughness of CuZr film, 110
etching away, 107
lift-off process, 106
loose Al/ZnO sacrificial layer, 109
sputter-deposited Al films structure, 109
surface topographies of *dense* Al layer, 108
Loose Al/ZnO sacrificial layer, 109
Low-κ dielectric materials, 190
Low-κ thin films, 188
Lower critical load, 52, 584
LVDTs, *see* Linear variable displacement transducers (LVDTs)

M

Macroporous silica, 186, 187
Macrostress effect in film, 407–409
Al-Cu-O films, 407
H^3/E^{*2} ratio, 408
self-healing tool for coatings, 409
Macrotension of substrate, 95
advantage, 111
CNx film case study, 101–106
crack on silicon wafer substrate, 97
film microbridges preparation, 98
fracture toughness extraction, 98–101
loading stage, 96
loose-columnar aluminum layer, 106–110
in situ inspection in testing, 98
substrate configuration, 95–96
substrate crack, 97
substrate precrack preparation, 97–98
testing stage, 96
Maxwell–Boltzmann statistics, 203
MD modeling, *see* Molecular dynamics modeling (MD modeling)
Median crack, 68, 142
Membrane deflection method, 89–90
MDE setup and monochromatic images, 92
microfabrication steps, 91
optical image of Au membranes, 91
MEMS, *see* Microelectromechanical systems (MEMS)
Metallic mode (MM), 395, 396

Methyl-silsesquioxane thin film (MSSQ thin film), 197, 199
FESEM images, 199, 200
interfacial toughness, 208
nanoindentation load–displacement depth curves, 198
Meyer's hardness, 147
Microblasting, postdeposition coating modification by, 60, 62
Microelectromechanical systems (MEMS), 86, 316, 443, 529
Microhardness measurement, 292, 296; *see also* Hardness measurement
X38CrMoV5–3 steel, 294, 298
X40CrMoV5–1 steel, 293
Microhardness test method, *see* Vickers hardness test method
Microindentation, 124, 494, 514
Microtensile testing, 49
MINOLTA LAND Cyclops 152 optical pyrometer, 252
MM, *see* Metallic mode (MM)
Modified four-point bend rig, 476
Moduli-perturbation method, 132
Moiré interferometry technique, 511–512
Molecular dynamics modeling (MD modeling), 6
MSSQ thin film, *see* Methyl-silsesquioxane thin film (MSSQ thin film)
Multi-element equal-mole coatings, 399
Multilayer and/or superlattice coatings, 13
Multilayer coating resistance to cracking, 439
multilayer Zr-Si-O coatings, 441
effect of thickness overlayer, 442–443
Multilayering, ceramic coating hardening via, 13–15
Multilayering structure toughening, 30; *see also* Gradient structure toughening
cross-sectional images of indentation, 33
cross-section TEM micrograph, 35
hardness *vs.* scratch toughness, 36
HRTEM image, 35
mechanisms, 32
scratch channels and indent marks of monolayer coatings, 33
surface view of indentation with load, 31, 32
TiN/AlTiN, 31
variation of hardness, critical load for cracking, and fracture toughness, 34
Multiple impacts, 56
Multistrain flexure test, 84
Multiwalled nanotube (MWNT), 21, 22, 23

N

Nanocomposite coatings, 6, 378; *see also* Hard coatings; Hard nanocomposite coatings
with enhanced hardness, 379–382
HTHE, 443–444
physics behind unique properties, 378–379
Nanoimpact testing, 54, 55
nanoimpact behavior of fused silica and Si(100)
repetitive nanoimpacts applications, 54
single nanoimpacts applications, 54
Nanoindentation-induced delamination, 337
GaAs substrate deformation, 337–339
GaAs substrate mechanical properties, 337
load profile optimization, 345–350
SiN films mechanical properties, 337
SiN/GaAs film/substrate systems deformation, 339–340
verification using FEM, 342–345
verification using secondary indentation, 340–342
Nanoindentation, 124, 317; *see also* SiN/GaAs film/substrate systems
AE-assisted nanoindentation method, 333–334
AFM image, 129
alternative expressions, 130
Berkovich tip, 127
conventional nanoindentation methods, 323–330
CSN methods, 330–333
for film/substrate system interfacial toughness assessment, 323
hardness, 128
head and positioning table, 125
load–displacement curve, 126, 132
Nano Indenter® with coil and magnetic gauge, 125
O&P method, 131
pile-up and sink-in during, 129
surface profile for indentation, 127
test approaches, 130–131
Nanoindentation testing, 209
contact stiffness, 210
fracture toughness measurement, 210–211
fully densed thin films, 211–215
indentation load–displacement data, 209
porous thin films, 215–217
Young's Modulus and hardness measurement, 209–210
Nanoindentation tests, 32
failure mechanisms during, 141
fracture mode, 141
lateral cracks, 143
radial cracks, 142, 143
substrate bending induced picture-frame crack, 143
types of cracks, 142
Nano Indenter® with coil and magnetic gauge, 125
Nanotube tangling, 23

nc-Me_nN/a-SiN_x nanocomposite coating, 18
hardness *vs.* scratch toughness and fracture behavior, 19
HRTEM image, 18
Nickel, 228
Normal wear, 242
Not stabilized wear, 242

O

Oliver and Pharr method (O&P method), 128, 129, 131
Oliver–Pharr method, 2
OM, *see* Optical microscopy (OM)
One-dimensional blister model (1D blister model), 74
instability analyses, 77
Optical microscopy (OM), 413, 536
Optical pumping, 236
Organosilicate glasses (OSG), 188, 189
interfacial toughness, 201
low-κ OSG thin film, 199
material hardness, 190–191
spin-on glass, 190
water diffusion, 203
OSG, *see* Organosilicate glasses (OSG)
Overlayer protecting brittle coatings against cracking, 433

P

PAE, *see* Polyarylene ether (PAE)
Palmqvist radial cracks, 142, 148
Partial cone crack, 542, 543, 549–551, 553, 557, 562, 563, 565, 567, 568, 571, 574, 575
Partition-of-unity, 167
pc-CrAlN, *see* polycrystalline CrAlN (pc-CrAlN)
Peel test, 321, 497
to brittle coatings, 498–499
disadvantages for, 500
inhomogeneity effect, 499–500
novel peel test, 499
T-peel test, 497, 498
Phase transformation toughening, 28
effect, 412–414
Physical vapor deposition (PVD), 8
PI, *see* Plasticity index (PI)
Picture-frame cracks, 143, 154
indentation-induced, 168
Pile-up or sink-in of materials, 212
Pitting, 246
Plane strain
condition, 48
fracture toughness, 468
Plastic deformation, 20, 323, 338, 349, 553
AE events, 137
asperities, 49–50
of element material, 245
hardness and, 2, 3
indentation–induced crack, 168
interfacial delamination, 348
mechanism of crystalline material, 3, 4
microhardness, 292
Palmqvist radial crack and, 142
substrate, 167, 319, 490
Plasticity, 20, 21, 59, 337
indentation, 49–52, 111
nanocrystalline, 6
room temperature, 60
toughness estimation, 3
Plasticity index (PI), 49, 50, 52, 62
Plate bending models, 358
centrally loaded plate with uniformly distributed load, 359–360
Hertz contact loaded plate, 360–361
PMMA, *see* Polymethyl methacrylate (PMMA)
Point-wise chemical composition analysis, 282
Poisson ratio, 51, 127, 128
Poly-p-PBO, *see* Poly-p-phenylenebenzobisoxazole (Poly-p-PBO)
Poly-p-phenylenebenzobisoxazole (Poly-p-PBO), 506
Polyarylene ether (PAE), 478
polycrystalline CrAlN (pc-CrAlN), 34
Polymethyl methacrylate (PMMA), 509, 510
Pop-in event, 338
Pop-out event, 340, 349
Porosity, 182, 183, 189, 215
elastic modulus as function, 190
interfacial toughness of MSSQ thin films, 208
interfacial toughness of OSG films, 201
Porous anodic alumina thin film, 182; *see also* Silica foam thin film; TiO_2 nanotube array thin film
hardness and elastic modulus with respect to porosity, 183
load–displacement curves of nanoindentation tests, 184
SEM images of indents on type II, 185
Porous materials, 179
Porous thin films, 180, 215; *see also* Fully densed thin films
contact area, 216
disordered porous thin films, 188–189
fundamental mechanical properties, 181
highly ordered porous thin films, 181–188
load–displacement curves, 216
substrate, 217
Postdeposition coating modification, 60
Postmortem, 536
Practical adhesion, 318–319
Practical work of adhesion, *see* Practical adhesion

Precursor polymer routes, 21
Preexisting crack supposition, 356
  assumptions, 356–358
  method, 364–365
  surface energy determination, 358
Pressure–volume relations (*p–V* relations), 187, 188
Pull-off test, 321–322
PVD, *see* Physical vapor deposition (PVD)
p–V relations, *see* Pressure–volume relations (*p–V* relations)

Q

Quasi-static fracture toughness, 54

R

Radial cracking
  indentation method, 68
  pattern, 49
Radial cracks, 142, 143, 145
  expanding cavity model, 69
  half-Penny-like radial cracks, 145–148
  indentation geometry and crack growth, 70
  Palmqvist radial cracks, 148
  patterns of brittle material, 68
  toughness evaluation, 67
Rapid thermal annealing (RTA), 23
Reaction-controlled regime, 202
Reactive gas (RG), 449
Reactive mode (RM), 395, 396
Remelted zone (RZ), 260
Repetitive nanoimpacts applications, 54
Residual stress, 101, 547
  film bridges images, 93
  tension by, 91, 92
Residual stress in coating, 138
  AFM image, 140
  growth, thermal, and total residual stresses change with temperature, 140
  sin 2ψ method, 141
  thermal stress, 139
  XRD, 140
Reversible adhesion, *see* Thermodynamic adhesion
RG, *see* Reactive gas (RG)
Rigid substrate hypothesis, 86
RM, *see* Reactive mode (RM)
Rockwell C-Brale indentation test, 33
RTA, *see* Rapid thermal annealing (RTA)
RZ, *see* Remelted zone (RZ)

S

SAD pattern, *see* Selected area diffraction pattern (SAD pattern)
Sandwich Brazil nut specimen, 481
Sandwich four-point bend
  specimen, 475, 477
  test, 477, 478
Sandwich four-point bend specimen, 475–476, 477–478
Sandwich specimen-based methods, 471; *see also* Bimaterial specimen-based methods
  Brazil nut specimen, 478–481
  comparison of methods, 489
  DCB specimen, 471–474
  DCDC specimen, 481–483
  direct pull-off specimen, 486–488, 490
  four-point bend specimen, 474–478
  lap shear specimen, 483–486
Scanning electron microscopic image (SEM image), 137, 339, 409, 534, 536
  anodic alumina thin film, 181
  cohesive failure of low-κ thin film, 191
  of cube-corner indentation, 194
  of diamond indenter impression, 402, 408, 410, 412
  of FIB-sectioned impact craters, 63
  of FIB cross section of blister, 191
  for indentation-induced crack, 137
  of indentation-induced delamination, 333
  of indentation-induced fracture, 152
  of indentation-induced through-thickness cracks, 151
  ordered silica foam thin film, 181
  of picture frame cracks, 154
  porous silicon low dielectric constant thin film, 180
  of ta-C coating fracture, 88
  TiO_2 nanotube array thin film, 181
  typical precrack, 94
  worn surface of cemented carbide grade, 52
  of Zr-Al-O film, 419
Schmid's law, 14
Scratch adhesion
  profile, 53
  test, 534–535
Scratch CPR, *see* Scratch crack propagation resistance (Scratch CPR)
Scratch crack propagation resistance (Scratch CPR), 17, 53, 583–584
Scratch test, 52, 322, 494, 530; *see also* Thin films fracture analysis
  applying tensile test, 498
  causes coating failures, 495
  in coated system, 531
  on coating/substrate system, 497
  experimental method, 533–536
  failure modes, 531
  focused ion beam microscopy, 536–538
  hardness values, 533
  intrinsic and extrinsic factors, 496
  scratch adhesion test, 495

scratch hardness, 532
single point, 530–531
standardized equipment for, 533
Scratch toughness, 49, 52–53, 65
Scuffing, 245
Selected area diffraction pattern (SAD pattern), 18
SEM image, *see* Scanning electron microscopic image (SEM image)
Semiquantitative approach, 581
CPR, 583
fracture toughness, 584
nanocomposite microstructure, 581–582
single-crystal silicon, 582
Shaft-loaded test, 501, 502
SIF, *see* Stress intensity factor (SIF)
Silica foam thin film, 186; *see also* Porous anodic alumina thin film; TiO_2 nanotube array thin film
depth-sensing indentation method, 186–187
indentation deformation mechanisms, 187
normalized load–displacement relation in macroporous silica, 187
p–V relations, 188
residual Berkovich indentation impression, 187
Silsesquioxane (SSQ), 188
spin-on glass, 190
thin film, 193
SiN/GaAs film/substrate systems
deformation, 339–340
delamination during nanoindentation, 335
delamination energy release, 351–358
GaAs substrate deformation, 337–339
GaAs substrate mechanical properties, 337
Griffith energy balance, 351–352
interfacial energy release rate, 361–365
interfacial toughness evaluation, 350
load profile optimization, 345–350
nanoindentation-induced delamination, 337
plate bending models, 358–361
SiN films mechanical properties, 337
verification using FEM, 342–345
verification using secondary indentation, 340–342
Single-walled nanotube (SWNT), 21
Single nanoimpacts applications, 54
Sliding-contact fracture; *see also* Brittle layers fracture
failure modes, 530
sliding contacts, 529
stress field originating by sliding contact, 540–544
Sliding, 529
Sneddon equation, 127
Solid-state solution and precipitation, hardening via, 7
CrAlN coatings, 8, 10, 12
optimized Al/Cr atomic ratio, 8, 9
Solidification process, 262, 263
Spalling, 214, 228, 246
Spark plasma sintering process (SPS process), 21
Speckle interferometry technique, 512
advantages, 514
ESPI, 512, 513
laser speckle technique, 513
Sphere indentation, 84, 86
Spontaneous emission
constant, 234, 235
of radiation, 235
SPS process, *see* Spark plasma sintering process (SPS process)
Sputter-deposited Al films structure, 109
SSQ, *see* Silsesquioxane (SSQ)
Stabilized wear, 242
Standard MEMS patterning method, 102
Stimulated absorption, 234
Stimulated emission, 235, 236
Stoney equation, 101, 141
Strain rates, 54
Stress-based models, 144; *see also* Energy-based models
indentation fracture toughness, 144
lateral cracks, 148–149
radial cracks, 145–148
tensile test, 144
Stress-corrosion cracking, 202
Stress approach, 469, 565
fracture strength, 566–571
fracture toughness, 571–573
stress intensity factor solutions, 573–577
Stressed over layer method, 322
Stress field
analysis, 350
bulk material, 540–544
coated system, 544–548
contact, 195, 539, 584
elastic, 549, 554
multiaxial, 570
repulsive, 4
residual, 146, 549, 564
wedging, 195
Stress intensity factor (SIF), 192, 468
for damage modes, 575
lateral cracks formation, 576
organic–inorganic coatings, 577
for scratching, 574
scratch track, 576
solutions, 573
Structural zone model (SZM), 409, 422, 447
Thornton's, 421
Struers Discotom-2 device, 249
Substrate displacement, 99, 100
Substrate effects, 560
compliant glass substrate, 562
elastic–plastic transition, 563

Substrate effects (*Continued*)
heating effect, 392
in scratch fracture, 561, 563
and size effects, 560
surface damage, 564
Substrate indentation method, 69
Superlayer indentation, 191
Super toughening effect, 59
Supplementary techniques, 506
CGS technique, 509–511
DIC technique, 514–515
Moiré interferometry technique, 511–512
photoelasticity technique, 508–509
speckle interferometry technique, 512–514
Surface layer systems, 237, 240
exploitation properties, 239
manufacturing methods, 241
nine zones, 239–240
properties, 238
solid-state material, 240
Surfactant-enhanced nanobubble cavitations, 208
SWNT, *see* Single-walled nanotube (SWNT)
SZM, *see* Structural zone model (SZM)

T

T-peel test, 497, 498
TBCs, *see* Thermal barrier coatings (TBCs)
TCO, *see* Transparent conductive oxides (TCO)
TEM, *see* Transmission electron microscopy (TEM)
TEM_{00}, *see* Transverse electro-magnetic (TEM_{00})
Tempering, 231
temperature, 227, 231, 232
10% rule, 533, 544
Tensile test, 144, 503–504
Tension by residual stress, 91, 92
Ternary nanocomposite, 6
Thermal barrier coatings (TBCs), 63, 477
impact and erosion of, 63
influence of thermal aging, 65
mechanisms of erosive damage on EB-PVD TBCs, 63
Thermal fatigue, 243, 300
average cracks depth of X40CrMoV5–1 steel, 305
comparison of average crack depth of 32CrMoV12–28 steel, 308
comparison of average crack depth of X38CrMoV5–3 steel, 307
comparison of average crack depth of X40CrMoV5–1 steel, 307
cracks on cross section of 32CrMoV12–28 steel, 304, 305, 306
cracks on cross section of 55NiCrMoV7 steel, 304
cracks on cross section of heat treated X38CrMoV5–3 steel, 303
cracks on cross section of X40CrMoV5–1 steel, 303
highest thermal fatigue resistance of steel surface layers, 306
performed tests, 303
Thermal stress, 139, 196, 243
Thermodynamic adhesion, 318
Thin film fracture analysis
energy approach, 577–581
fracture strength, 566–571
fracture toughness, 571–573
using scratch test, 564
semiquantitative approach, 581–584
stress approach, 565
stress intensity factor solutions, 573–577
Thin films, 316
Thin hard coatings and films, toughness evaluation of, 48–49
Thin wafers with diamond structure, 558–560
32CrMoV12–28 steels, 251
Thorton–Messier structure–zone diagram, 11
Thornton's SZM, 421
3D finite element model, 66
Three-functional Al-Cu-N coatings, 431–433
Three-functional highly elastic, antibacterial Al-Cu-N nanocomposite coatings, 430
three-functional Al-Cu-N coatings, 431–433
two-functional Cr-Cu-O coatings, 430–431
TiO_2, *see* Titanium dioxide (TiO_2)
TiO_2 nanotube array thin film, 183; *see also* Porous anodic alumina thin film; Silica foam thin film
advantage, 184
densification behavior, 186
fracture stress, 186
fracture stress and strain relationship, 186
Young's modulus, 185
Titanium dioxide (TiO_2), 181, 182
TM, *see* Transition mode (TM)
"Tough" interface, cyclic loading indentation for, 348–350
Toughening mechanisms, 383–384
Toughening whiskers, 23
Toughness, 15, 48, 383–384
in ceramic coatings, 1–3
indentation plasticity, 49–52
limits model, 158
qualitative assessment, 49
scratch toughness, 52–53
Traction-separation law, 343
Traction–separation relations, 165
Transitional work hardening, 243
Transition mode (TM), 395
Transmission electron microscopy (TEM), 538

Transparent conductive oxides (TCO), 423
Transport-limited regime, 202
Transverse electro-magnetic (TEM_{00}), 236
Triangular pyramid indenter wedging open radial crack, 147
TRIDENT XM4 system, 250
True work of adhesion, *see* Thermodynamic adhesion
Tungsten carbide-cobalt cermets (WC-Co cermets), 515
Tungsten steels, 229
Two-functional Cr-Cu-O coatings, 430–431
Two-functional highly transparent Si-Zr-O nanocomposite coatings, 428
  evolution of XRD patterns, 428
  Si-Zr-O coatings, 428
  Si-Zr-O coatings with low amount, 429–430
Two-functional tribological hard nc-TiC/a-C nanocomposite coatings, 424
  evolution of coefficient of friction, 425–426
  nanocrystalline nc-TiC/a-C coatings, 427
  Ti-C coatings, 425

U

Uniaxial tensile testing, 88
Uniformly distributed load, centrally loaded plate with, 359–360
Unloading curve, 126
Unloading stiffness, *see* Unloading curve

V

Vanadium carbide (VC), 285
VC, *see* Vanadium carbide (VC)
VCCT, *see* Virtual crack closure technique (VCCT)
Vickers hardness test method, 292
Vickers indentation, 89, 95, 98, 102
  crack patterns of a brittle material, 68
  radial cracking, 67
Vickers indenter, 67, 68, 210
  crack parameters for, 211
Virtual crack closure technique (VCCT), 167
  for four-noded element, 168
Von-Mises stress, 547

W

Wave-package, 333
Wavelength dispersive spectrometer (WDS), 250
Wear resistance measurements, 296, 300
  alloying using powders, 299
  ASTM-G65 standard of 32CrMoV12–28 steel, 301
  ASTM-G65 standard of 55NiCrMoV7, 302, 303
  ASTM-G65 standard of X38CrMoV5–3 steel, 302
  ASTM-G65 standard of X40CrMoV5–1 steel, 300, 301
  55NiCrMoV7–1 steel, 297
  relative mass loss, 298

X

X-ray diffraction (XRD), 140
  of CrAlN coatings, 10
  patterns of Si-Zr-O coatings, 428
X38CrMoV5–3 steels, 251
  alloying material in middle zone of surface layer of, 288
  after alloying with TaC powder, 259
  after alloying with WC powder, 260
  after laser surface melting, 259
  ASTM-G65 standard of, 302
  central zone of remelted surface layer, 271, 272
  comparison of average crack depth of, 307
  cracks on cross section of heat treated X38CrMoV5–3 steel, 303
  cross-sectional morphology, 266, 267, 268, 275, 277, 278, 279, 281
  influence of laser power on thickness of RZ and HAZ, 262
  investigations, 247, 249–250
  surface of alloyed bead after laser surface alloying, 256
  surface of melt bead after laser surface melting of, 256
  thermal fatigue tests, 251
  thin foil structure, 294
X40CrMoV5–1 steels, 251
  alloying material in surface layer of, 284
  after alloying with WC powder, 259
  ASTM-G65 standard of, 300, 301
  central area of remelting zone, 284
  central zone of remelted surface layer, 270, 271
  comparison of average crack depth, 307
  cracks on cross section, 303
  cross-sectional morphology, 265, 266, 267, 275, 276, 277, 278, 280
  EDS analysis of chemical composition of, 284, 285
  influence of laser power on thickness of RZ and HAZ, 261
  investigations, 247, 249–250
  after laser surface melting, 258
  small eutectics on boundary of remelting zone of surface layer, 286
  surface of alloyed bead after laser surface alloying, 255
  surface of melt bead after laser surface melting, 255

X40CrMoV5–1 steels (*Continued*)
thermal fatigue tests, 251
thin foil structure, 291, 292, 293
X-ray diffraction pattern, 283
XRD, *see* X-ray diffraction (XRD)

Y

Young–Dupré equation, 318
Young's equation, 84, 85
Young's modulus (*E*), 71, 73; *see also* Effective Young's modulus (*E**)
of as-deposited CrAlN coatings, 9
of coatings, 132, 145
composite hardness, 134
empirical power law relationship, 133
as function of displacement, 185
hard film on soft substrate, 134
measurement, 209–210, 211–213
of MWNT, 21
simulated hardness for softer but stiffer coating, 136
simulated relative hardness, 135
stiffness of elastic elements, 133
Yttria-stabilized zirconia coatings (YSZ coatings), 493

Z

"Zeroth-order" correction, 575